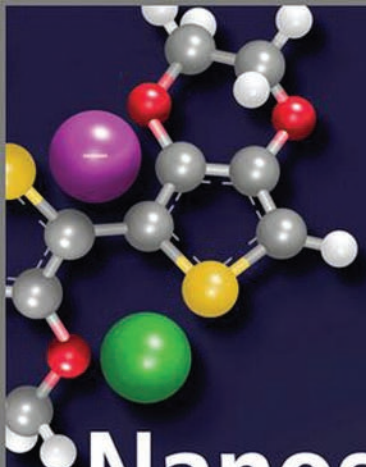

Editor

Ali Eftekhari

Nanostructured Conductive Polymers

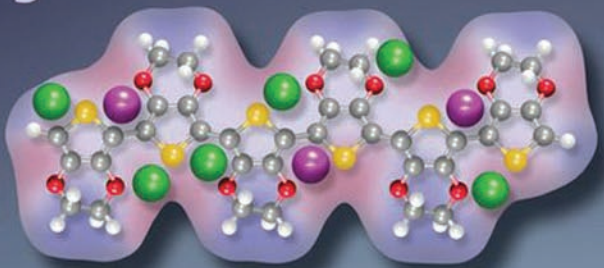

WILEY

Nanostructured Conductive Polymers

Nanostructured Conductive Polymers

Edited by

ALI EFTEKHARI

Department of Chemistry, Ohio Institute of Technology, Cleveland, Ohio, USA

WILEY

A John Wiley and Sons, Ltd., Publication

This edition first published 2010

Registered office
John Wiley & Sons Ltd, The Atrium, Southern Gate, Chichester, West Sussex, PO19 8SQ, United Kingdom

Library of Congress Cataloging-in-Publication Data

Nanostructured conductive polymers / edited by Ali Eftekhari.
p. cm.
Includes bibliographical references and index.
ISBN 978-0-470-74585-4 (cloth)
1. Nanostructured materials. 2. Conducting polymers. I. Eftekhari, Ali, 1979–
TA418.9.N35N3522 2010
620.1′92—dc22

2010005168

A catalogue record for this book is available from the British Library.

ISBN Cloth: 978-0-470-74585-4

Set in 10/12pt Times by Integra Software Services Pvt. Ltd., Pondicherry, India
Printed and bound in Great Britain by CPI Antony Rowe, Chippenham, Wiltshire

Contents

Preface

In October 2000 when the winners of Nobel Prize in Chemistry were announced, I sent a greeting card to Alan J. Heeger for congratulating him on this honor and his pioneering works on conductive polymers. Professor Heeger replied me by the following note ''This Prize was awarded to the field of semconducting and metallic polymers. You, as one with direct research experience in this field, have a right to be proud.'' A few months later I was in a position to defend a research proposal, and in reply to the question of one of the panelists ''Is it a well-established subject with practical potentials or just fancy subject for academic projects'', I had a convincing answer, and felt the glory of that award.

Nanotechnology and conductive polymers approximately have the same age, but contrary to the field of conductive polymers, which was abruptly introduced in a Short Communication, nanotechnology was emerged gradually through journey from micro-technology to smaller scales. There are two distinguishable aspects about nanotechnology, but this distinction is usually ignored: advancing our technology by taking control at smaller scales (an advanced form of microtechnology), or entering a new world at nanoscale because its scale is comparable with the molecular size. The fame of nanotechnology belongs to the latter one, but most of research studies are restricted to the first aspect.

Due to the interdisciplinary nature of nanotechnology, researchers from various disciplines have been involved in the rapid growth of nanotechnology as a promising field of study. One of the most active areas is polymer nanotechnology owing to the size of polymer chains. Advancement of nanotechnology tools has provided a rare opportunity to investigate individual chains of polymers. On the other hand, polymers as a member of soft matter family have incredible flexibility for the preparation of various nanostructures, particularly for nano-devices.

The emerging field of conductive polymers itself is indeed an interdisciplinary field, as the essential conductivity has well connected this field to other disciplines (which were not usually associated with polymer materials) from electrochemistry to electrical engineering. Now the emerging field at the interface of nanotechnology and conductive polymers covers a vast variety of quite different disciplines; which calls for more collaboration between researchers with different professions and knowledge. The present book and similar volumes aim to introduce new opportunities by linking different topics involved in this emerging field.

The present book does not claim to provide an ultimately comprehensive resource on the field, and it is almost impossible; but as far as possible, I tried to collect most active areas of research. More than 80 referees assisted me to assure the scientific quality of this book. Although all chapters were solicited in advance, some of contributions were rejected as they did not meet the required standard, and there was insufficient time to call for a replacement by another author. In addition, some authors agreed to deliver their manuscripts by the given deadline but simply declined to submit their contributions in due time. Thus, the audience may feel that some topics have been missed.

As a matter of fact, we are still far from ultimate control at nanoscale as claimed by the mission of nanotechnology; thus, the subjects discussed here are mainly at the interface of transition from micro- to nano-world. This is indeed a transition from the first to second decade of third millennium. This book builds a bridge to the forthcoming decade in which we expect to witness incredible advancement in the realms of nanotechnology. The present book aims to lead researchers from different disciplines in this direction and somehow unite them to think about emerging problems from quite different perspectives.

The book starts with an introductory chapter about conductive polymers. For those who are familiar with nanotechnology, this chapter is a guiding star; and for polymer scientists, it is a reminder that from where we have started. The two next chapters are typical ones to introduce the realms of nanostructured conductive polymers. Polyaniline is considered as a prototype and among most popular conductive polymers. Chapter 3 discusses some interesting features in surface studies of conductive polymer, while surface analysis is always a key concept in the realm of nanotechnology.

The second part of the book commences with a series of papers devoted to a variety of nanomaterials made of conductive polymers, and later introduces some important properties of conductive polymers and methodology of the field. Electrospining is an effective method for the preparation of a variety of nanomaterials, and it has been widely utilized for the fabrication of conductive polymers. Carbon nanotubes are indeed the most dominant prototype of nanomaterials, as they are among the first prototypes of nanomaterial which were introduced to the market in abundance; thus, nanocomposites based on carbon nanotubes have attracted a considerable attention, particularly due to the special conductivity of carbon nanotubes and conductive polymers. Due to the intrinsic difference between inorganic and polymer materials (soft matter vs. rigid structure), this type of composites has long attracted a noticeable attention. Now structural entanglement at nanoscale has provided rare opportunities for the formation of interesting nanocomposites. This is of particular interest when dealing with inorganic materials and conductive polymers which both have ionic properties and conductivity, and the resulting nanocomposites have a wide variety of applications. Metallic nanoparticles are usually too small, leading to severe difficulties in handling the nanomaterials, and soft structure of polymers is an appropriate medium to host such tiny nanoparticles. Again electrical conductivities of both ingredients of this class of nanocomposites lead to potential applications.

Like all types of polymers, conductive polymers are first characterised by spectroscopic techniques, and this is of particular importance for nanostructured materials too. Atomic force microscopy (AFM) is a powerful (and relatively inexpensive) microscopic technique for surface studies at nanoscale, and sometimes this is essential for the investigation of conductive polymers. Despite available limitations, progress in nanodevices has provided

new opportunities for the study of single molecules. Study of single wires of polymers is quite easy due to the size of the polymer chains. An interesting feature recently reported is the possibility of preparation of micro- and nano-containers of conductive polymers which can have potential applications. Magnetic properties and electron transfer in nanocomposites made of conductive polymers are complicated which need profound investigations. An important application of conductive polymers is in solar cells, but to reach effective performances, it is necessary to inspect charge transfer theoretically.

The last part of the book reviews some important applications of conductive polymers which have been evolved by the birth of nanotechnology. Chemical and electrochemical sensors based on conductive polymers have been effectively fabricated during the past decades, and now nanomaterials have significantly improved the sensor performances. In recent years a noticeable attention has been paid to polymer-based actuators, and according to potential applications at smaller scales, nanostructured-based polymers play key roles in this case. From the first electrochemical synthesis of conductive polymers, they have been propounded for the protection of metal surfaces against corrosion as a thin layer could be simply electrodeposited. Possibility for the coating of uniform with small thickness has made this idea more practical. Electrochemically prepared conductive polymers show excellent electrocatalytic properties (and particularly in electroactive composites) and due to the enhanced electrochemical properties of nanostructured materials, this is an open issue in the realms of nanotechnology. Polymers are generally a dominant category in biomaterials, and due to the fictional prospective of nanotechnology to make a revolution in medicine, it is always interesting to inspect biomedical applications of polymer nanomaterials. Taking control at nanoscale provides golden opportunities; for instance, conductive polymers are not limited to polymers which are originally conductive, but it is possible to make conductive polymer-based nanocomposites by nanofillers.

The subjects quoted above are among hot topics in the interfacial field between conductive polymers and nanotechnology, which have been elaborately discussed by leading scientists. Each chapter reviews the past by citing key references through a comprehensive review of the literature, discusses the present by reporting recent and forthcoming achievements, and draws the future by introducing a prospective of the topic under consideration. As emphasised before, the present book should play a role in transition from the present to future as we are just in the beginning of a new stage in the realms of nanotechnology. Until now we were engaged with the birth of nanotechnology, but now it is the time for maturing this rapidly growing field. We witnessed many incredible but random achievements in different disciplines associated with nanotechnology; however, now we need to conduct the scientific research in desirable ways to reach planned goals.

At last but not least, I need to thank those people whose names are not printed in this book, but the publication of this volume would not have been possible without their hard efforts. The list of people from scientific referees to technical staff is too long to be incorporated here; but I must send my special thanks to Alexandra Carrick, Emma Strickland, and Richard Davies. I could not forget how they have worked with me with patience on a daily basis. One may think it is just formalities and as a part of publication industry everyone does her/his duty; but the fact is that in such a complicated process, sincere collaborations and mutual understanding between all parties involved can lead to the publication of a brilliant volume. Definitely, it was the case for the present book, and

I hope we are successful in contributing to the scientific community. Although it was a team work, any failure returns to me as the coordinator of this book project; thus, I strongly appreciate any comment, which will be invaluable for me in editing prospective volumes.

Ali Eftekhari
January 2010

Foreword

In the recent decades, the field of conductive polymers has been one of the most exciting fields of science and technology. It has brought together scientists from many disciplines and countries. This great progress has involved synthesis of materials closely linked to physical characterisation. With the development of this field, a wide range of applications have been envisaged, presenting their own research challenges and stimulating further innovation. It discovery, provided new materials and frequently also reflected back on our understanding at a more fundamental level. Throughout, the interplay of structure and properties has been at the heart of the subject, and now this book reviews the field with particular emphasis on nanostructure. It elegantly captures the key features of the field outlined above: the quest to make materials, relate their properties to their structure, the favourable interplay of basic and applied research, and the realisation of materials that could only have been dreamt of in the past.

The opening chapter by Campbell Scott gives an eloquent, insightful and personal history of the subject by a leading researcher whose career has spanned, what he describes as, the modern age of materials. The subsequent chapters show an enormous range of ways of synthesising and preparing nanostructured conductive polymers in many different forms – nanofibres, nanorods, nanotubes, nanospheres and even ''brain-like'' morphologies. Besides covering chemical and electrochemical synthesis methods, the chapters are devoted to advanced processing techniques for nanostructure fabrication, such as electrospinning and soft lithography. Conductive polymers can be blended with a range of other materials such as nanoparticles and carbon nanotubes, leading to nanocomposite materials with additional properties. Many interesting examples discussed in this volume range from magnetic composite materials to conductive nanogreases.

The development of nanostructured conductive polymers also requires the development of advanced characterisation techniques, and this aspect of current research is captured in several chapters. A detailed review of Atomic Force Microscopy (AFM) covers the wide range of related scanning probe microscopes that are particularly relevant to soft materials. It also shows how techniques such as conductive AFM go beyond structural measurements to image the functional properties of materials relevant to applications such as solar cells. A wide range of spectroscopic techniques has also been reviewed, showing how they can be applied to learn about the interactions between conductive polymers and nanostructured

hosts. In addition, rheological measurements as well as the impact of nanostructure on electrical and optical properties have been described.

This book covers the remarkable range of applications emerging for nanostructured conductive polymers. These applications generally exploit the increased surface area of nanostructured materials, often to do something very new. One very important example is of polymer solar cells, where nanoscale phase separation lies at the heart of charge generation and extraction. Another exciting application domain is the use of nanostructured conductive polymers as biomaterials, including the development of neural interfaces. Other applications described include sensors, actuators, corrosion protection and electrocatalysis.

Each chapter provides a comprehensive review by a leading researcher. But a bigger picture emerges from reading all the chapters together – it reveals how we are now working with new classes of materials, new techniques and how the quest to link properties to structure is advancing at the nanoscale. The ensemble of all the chapters captures the excitement and potential of this field, whilst beautifully demonstrating the interdisciplinary and international nature of modern science.

Ifor Samuel, St Andrews,
May 2010

List of Contributors

Agnese Abrusci, Optoelectronics Group, Cavendish Laboratory, Cambridge, U.K.

Alain Pailleret, CNRS UPR, Laboratoire d'Electrochimie et de Chimie Analytique, Ecole Nationale Supérieure de Chimie de Paris, Paris, France.

Anthony J. Killard, Sensors and Separations Group, School of Chemical Sciences, Dublin City University, Dublin, Ireland.

David Cocke, Integrated Composites Laboratory (ICL), Dan F. Smith Department of Chemical Engineering, Lamar University, Beaumont, Texas, USA.

Di Zhang, Integrated Composites Laboratory (ICL), Dan F. Smith Department of Chemical Engineering, Lamar University, Beaumont, Texas, USA.

Dustin Thomas, Department of Material and Metallurgical Engineering, South Dakota School of Mines and Technology, Rapid City, SD, USA .

Edgar Ap. Sanches, Institute of Physics of São Carlos (IFSC), University of São Paulo, São Carlos, SP, Brazil.

Fabio de Lima Leite, Federal University of São Carlos (UFSCar), Sorocaba, SP, Brasil.

Gordana Ćirić-Marjanović, Faculty of Physical Chemistry, University of Belgrade, Belgrade, Serbia.

Gustavo M. do Nascimento, Departamento de Química Fundamental, Universidade de São Paulo, São Paulo, Brazil.

Haiping Hong, Department of Material and Metallurgical Engineering, South Dakota School of Mines and Technology, Rapid City, SD, USA.

Hyacinthe Randriamahazaka, Laboratoire Interfaces Traitements et Dynamique des Systèmes (ITODYS), UMR 7086, CNRS –Université Denis Diderot Paris, Paris, France.

I. Baltog, National Institute of Materials Physics, Bucharest, Romania.

Ian A. Howard, Max Planck Institute for Polymer Research, Mainz, Germany.

Ioannis S. Chronakis, Swerea IVF, Swedish Institute for Industrial Research and Development, Mölndal, Sweden.

J. Campbell Scott, IBM Almaden Research Center, San Jose CA.

Jadranka Travas-Sejdic, Polymer Electronics Research Centre, The University of Auckland, Auckland, New Zealand.

Jalal Ghilane, Laboratoire Interfaces Traitements et Dynamique des Systèmes (ITODYS), UMR 7086, CNRS –Université Denis Diderot Paris, Paris, France.

Jean-Christophe Lacroix, Laboratoire Interfaces Traitements et Dynamique des Systèmes (ITODYS), UMR 7086, CNRS –Université Denis Diderot Paris, Paris, France.

Jing Li, Nanotechnology Branch, NASA Ames Research Center, CA, USA.

Jiyong Huang, National Center for Nanoscience and Technology, Beijing, P. R. China.

Laura A. Poole-Warren, Graduate School of Biomedical Engineering, University of New South Wales, Sydney NSW, AUSTRALIA.

M. Baibarac, National Institute of Materials Physics, Bucharest, Romania.

Marcelo A. de Souza, Departamento de Química Fundamental, Universidade de São Paulo, São Paulo, Brazil.

Mark Horton, Department of Material and Metallurgical Engineering, South Dakota School of Mines and Technology, Rapid City, SD, USA.

Neil C. Greenham, Optoelectronics Group, Cavendish Laboratory, Cambridge, U.K.

Nigel H. Lovell, Graduate School of Biomedical Engineering, University of New South Wales, Sydney NSW, AUSTRALIA.

Oleg Semenikhin, Department of Chemistry, University of Western Ontario, London, Ontario, Canada.

Osvaldo N. Oliveira Jr., Institute of Physics of São Carlos (IFSC), University of São Paulo, São Carlos, SP, Brazil.

Paul A. Kilmartin, Polymer Electronics Research Centre, The University of Auckland, Auckland, New Zealand.

Pauline Smith, Army Research Lab, Aberdeen Proving Ground, MD, USA.

Pierre Camille Lacaze, Laboratoire Interfaces Traitements et Dynamique des Systèmes (ITODYS), UMR 7086, CNRS –Université Denis Diderot Paris, Paris, France.

Rabin Bissessur, Department of Chemistry, University of Prince Edward Island, Charlottetown, Canada.

Richard H. Friend, Optoelectronics Group, Cavendish Laboratory, Cambridge, U.K.

Rylie A. Green, Graduate School of Biomedical Engineering, University of New South Wales, Sydney NSW, AUSTRALIA.

S. Lefrant, Institut des Matériaux Jean Rouxel, Nantes, France.

Sebastian Westenhoff, Department of Chemistry, Biochemistry & Biophysics, University of Gothenburg, Gothenburg, Sweden.

Shaolin Mu, Department of Chemistry, Yangzhou University, Yangzhou, China.

Sungchul Baek, Graduate School of Biomedical Engineering, University of New South Wales, Sydney NSW, AUSTRALIA.

Suying Wei, Department of Chemistry and Physics, Lamar University, Beaumont, TX, USA.

Vessela Tsakova, Institute of Physical Chemistry, Bulgarian Academy of Sciences, Sofia, Bulgaria.

Walter Roy, Army Research Lab, Aberdeen Proving Ground, MD, USA.

Ya Zhang, School of the Environment, Nanjing University, Nanjing, China.

Yi Luo, Department of Electrical and Computer Engineering, Carnegie Mellon University, Pittsburgh, PA, USA.

Yijiang Lu, Nanotechnology Branch, NASA Ames Research Center, CA, USA.

Yixuan Chen, Department of Electrical and Computer Engineering, Carnegie Mellon University, Pittsburgh, PA, USA.

Zhanhu Guo, Integrated Composites Laboratory (ICL), Dan F. Smith Department of Chemical Engineering, Lamar University, Beaumont, Texas, USA.

Zhixiang Wei, National Center for Nanoscience and Technology, Beijing, P. R. China.

Part One

1

History of Conductive Polymers

J. Campbell Scott

IBM Almaden Research Center, San Jose CA

1.1 Introduction

It is generally recognized that the modern study of electric conduction in conjugated polymers began in 1977 with the publication by the group at the University of Pennsylvania [1] describing the doping of polyacetylene. Although there was some prior work dating back to World War II (see the review by Hush [2]) and even reports of electrochemical synthesis the nineteenth century [3], the Nobel Committee recognized the seminal contribution of Heeger [4], MacDiarmid [5] and Shirakawa [6] by awarding them the Nobel Prize for Chemistry in 2000. Shirakawa, who was based at the Tokyo Institute of Technology, had been visiting the lab of his collaborators at Pennsylvania at the time of the breakthrough research.

The story of polyacetylene is an example of a fortunate confluence of circumstances that is often under-appreciated in the history of scientific progress. In the 1970s, there was worldwide interest in the unique properties of materials with such a high degree of anisotropy that they can be considered one-dimensional (1D) systems. The Pennsylvania group, of which I was privileged to be a member until 1975, was jointly led by a chemist, Tony Garito, and a physicist, Alan Heeger, and was recognized worldwide as a primary center for that field. Early focus was on the study of charge-transfer salts, in which planar, conjugated, small molecules were stacked like poker chips. Experiments revealed a Peierls transition [7,8] and suggested the observation of Frölich superconductivity [9,10]. The emphasis then shifted to linear polymers as chemist, Alan MacDiarmid, entered into a

Nanostructured Conductive Polymers Edited by Ali Eftekhari

collaboration with Heeger, to examine poly(sulfur-nitride), a crystalline solid, consisting of chains of alternating sulfur and nitrogen atoms, that exhibits metallic conduction [11] down to liquid helium temperatures, and has a superconducting transition at 0.26 K [12].

In the midst of this research, MacDiarmid was traveling in Japan and visited the laboratory of Hideki Shirakawa who was studying the Ziegler–Natta-catalyzed polymerization of acetylene. Standard practice was to use a concentration of the organometallic catalyst at the millimolar level. It is a catalyst after all. These low concentrations led to the infamous 'insoluble, intractable, black precipitate,' but Shirakawa had discovered that with concentrations closer to molar, he obtained a shiny 'metallic' film coating the wall of the reaction vessel. MacDiarmid returned to Pennsylvania, where he and Heeger quickly arranged to invite Shirakawa for a sabbatical visit.

The pieces were all in place. Scientifically, it was understood that pristine polyacetylene is a Peierls semiconductor, as evidenced by its bond-alternating structure; it was known that charge transfer to molecular donors or acceptors would result in partially filled bands and that the resulting incommensurability of the Fermi wave-vector would destabilize the Peierls phase. The interdisciplinary team had the ideal expertise: the chemists, led by Shirakawa and MacDiarmid, brought their synthetic expertise to the preparation of the polymer films; the physicists, led by Heeger and post-doc C. K. Chiang, brought physical measurement and interpretation of material properties, not just electrical conductivity, but also structural and spectroscopic. Together, they applied vapor-phase doping of molecular acceptors (halogens) and a donor (ammonia).

The publication by Chiang *et al*. [1] led to a huge surge in interest in 'synthetic metals.' In less than a decade, most of the monomer building blocks that we know today had been identified and many procedures for polymeric synthesis had been established. The chemical structures are illustrated in Figure 1.1. (In the nomenclature used in Figure 1.1, polyacetylene would be called polyvinylene. This is because some – 'common' – names derive from the compound that is polymerized, while others, more correctly according to IUPAC conventions, use the monomeric unit in the product polymer.)

An interesting sociological aspect of the research on conjugated polymers has been the evolving target for technological application, and hence emphasis on particular physical properties, that has motivated the research in the ensuing 30 years. Initially, and through the early 1980s, high electrical conductivity was the primary driving force. There were suggestions to replace (copper) electrical wiring in everything from printed circuit boards to home, and even grid, power distribution with inexpensive, light-weight polymeric conductors. As issues of processability, limits on conductivity, and environmental stability became more apparent these grand schemes fell by the wayside. Nevertheless, in certain niche applications, electrical conductivity is the primary attribute. For example, antistatic coatings are important in many textiles and in the roll-to-roll processing of polymer webs. Photographic film is a good example of the latter application and is the reason that Bayer initiated, in conjunction with Agfa, their development of the Baytron series of products based on poly(ethylenedioxythiophene) (PEDOT) doped with poly(styrene sulphonate) PSS. (PEDOT-PSS is currently marketed by H. C. Starck Corp. as their Clarion line of conductive coatings.)

When the Holy Grail of copper replacement receded over the horizon, the emphasis in the late 1980s and early 1990s shifted to the optical properties. Since there is typically a large oscillator strength in the HOMO–LUMO transition of undoped conjugated polymers,

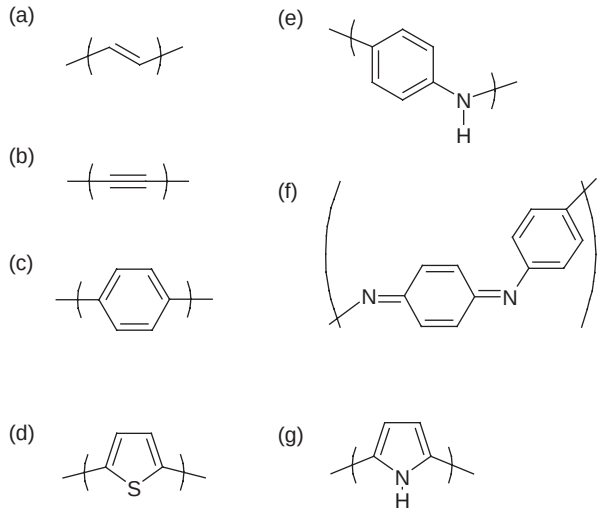

Figure 1.1 *Chemical structures for monomers of the conjugated polymers discussed in this chapter: (a) vinylene (the repeat unit of polyacetylene); (b) ethynylene (polydiacetylene is alternating vinylene-ethynylene); (c) phenylene; (d) thiophene; (e) leucoemeraldine form of polyaniline; (f) pernigraniline form of polyaniline (the number of protons can vary between the two limits); (g) pyrrole*

they are often highly colored and fluorescent. At that time there was great interest in nonlinear optics, as researchers were developing new materials, both organic and inorganic, for application in optical switches, modulators and the like. It was experimentally demonstrated [13] and theoretically understood [14,15] that many conjugated polymers also possess extremely high third-order optical nonlinearity. Although much interesting science emerged from this line of research, to my knowledge no technology is based on it.

Second-order nonlinearity and electro-optic response are much more amenable to device application. There are few conjugated polymers with intrinsic second-order nonlinearity, since homopolymers and alternating copolymers tend to have a center of symmetry. (This is not necessarily always so, since head-to-tail polymerization of an asymmetric monomer does not have mirror symmetry.) In 1990, the Cambridge group under the leadership of Richard Friend was investigating the electro-optic response of poly(phenylene vinylene). The story goes (I have heard several versions, probably with some embellishment) that graduate student Jeremy Burroughes had turned off the lab lights in order to minimize stray light, and applied a dc voltage to a sandwich-structured device – just the conditions required to observe the resulting electroluminescence. Of course, the publication of this observation [16] spawned an enormous worldwide research effort to optimize the materials and device structures (polymer light-emitting diodes or PLEDs) for use in flat-panel displays, signage and lighting.

The semiconductive properties of conjugated polymers are also exploited for application in thin-film organic field-effect transistors (OFETs). The earliest materials examined were polyacetylene [17], polythiophene [18], and an oligomer of thiophene [19]. In these

devices the polymer forms the channel between the source and drain electrodes of the device. The number of charge carriers in the channel is modulated by the voltage applied to the gate electrode. The conductance of the channel is proportional to the number of charge carriers and to their mobility. Hence, charge-carrier mobility is the primary metric in screening materials for use in OFETs. As several other chapters in this volume discuss in detail, polymer morphology at the nanoscale plays a crucial role in dictating the mobility. In any conductor a high degree of order is essential to achieve high mobility, since disorder leads to scattering, trapping at defects, and localization. However, as discussed by Kline *et al*. [20] among others, highly crystalline polymers are not necessarily ideal, because the crystallites are typically much smaller than the channel length, in which case the mobility is limited by transfer across grain boundaries. It seems preferable to have a high degree of polymer chain alignment, but with few grain boundaries and with many chains bridging between adjacent domains. Nano-morphology is key.

Another application which relies on the optical and semiconducting properties of conjugated polymers is solar-energy conversion. In this case, each photon of solar radiation is absorbed to generate an exciton – a bound electron–hole pair. The onset of absorption is below the HOMO–LUMO gap by an energy corresponding to the exciton binding energy. In contrast to many inorganic semiconductors used in solar cells, the exciton binding energy in conjugated polymers is several tenths of an electronvolt and therefore many times thermal energy (kT) at ambient temperature. Therefore excitons in conjugated polymers do not readily dissociate to create free electrons and holes. Excitonic solar cells rely on a hetero-junction to dissociate the excitons. In this device structure, an electron-transport material (n-type) is adjacent to a hole-transport material (p-type). If the energy level offsets (HOMO and LUMO of the n- and p-type materials) are sufficient compared to the binding energy, the exciton may dissociate at the interface. The exciton may be created in either the n- or p-type material or both, the difference being the absorption spectra and magnitudes of the binding energy.

Here again, nano-morphology plays a key role. The exciton has a characteristic lifetime, dictated by the sum of its radiative (re-emission) and non-radiative (heat-producing) decay rates. It is also mobile, diffusing through one of the polymeric semiconductors with a characteristic diffusivity. If the exciton lives long enough to diffuse to the n–p interface, high carrier-generation efficiency can be achieved. Since the exciton diffusion length in conjugated polymers is typically of the order of 5–10 nm, the n- and p-type materials must be blended at this length scale. Such 'bulk heterojunctions' were first demonstrated by the Santa Barbara [21] and Cambridge [22] groups.

There is an additional constraint on the nature of the mixing, namely that the hole-transporting p-type phase be continuous to the cathode, while the electron-transporting n-type phase connect to the anode. Controlling the morphology of such bi-continuous networks is the goal of recent research on self-assembled block copolymers.

Most of this volume is devoted to the characterization and application of doped conjugated polymers, i.e. to their highly conducting 'metallic' state. I have touched upon some of the issues relating to the nano-morphology of undoped conjugated polymers, and to their application as semiconductors, because it is usually helpful to understand properties of the 'pristine' material prior to analyzing the effect of dopants. The remainder of this chapter is divided into sections devoted to, respectively, the work that preceded the Pennsylvania publication ('archeology and prehistory'), its immediate impact ('the dawn

of the modern era'), and the 'materials revolution,' which brought careful refinement of synthesis and processing, and thereby enables today's applications.

1.2 Archeology and Prehistory

Today's conductive polymer workhorses are primarily derivatives of polypyrrole, polyaniline and polythiophene. Each of these was known to the chemical community long before the work on doping of polyacetylene. The earliest publication that I am aware of concerns the oxidative polymerization of 'indigo' (i.e. aniline) by nitric acid [23]. This was soon, at the pace of ninteenth century science, followed by a paper 'On the production of a blue substance by the electrolysis of sulphate of aniline' [3]. The background was the industrial revolution, when chemists were exploring the usefulness of coal by-products and just post-Faraday, electrochemistry was in its infancy. Aniline was particularly interesting because it was a reagent in the synthesis of many of the dyes that we associate with the deep crimsons and purples of the Victorian era. Fritsche [23] and Letheby [3] had undoubtedly synthesized some form of polyaniline, long before the concept of linear polymerization [24,25], and long before the concept of frontier orbitals, which is so important in understanding organic chromophores, was developed by Fukui [26]. More on the early history of polyaniline can be found in the paper by Mohilner *et al.* [27] and in the review by MacDiarmid and Epstein [28]. By the 60s, it was recognized that the oxidation product of aniline was a linear oligomer or polymer [27], and the effect of acid on its conductivity had been discovered [29].

Likewise, chemical coupling to form oligomers and polymers of pyrrole, thiophene and many other heterocycles was begun in the nineteenth and early twentieth centuries (see citations in [30]). The resulting materials were poorly characterized, partly because of the rudimentary analytical techniques of the day, and partly because of their insolubility. In particular, it was rarely clear whether the products were branched or linear. Nevertheless, by the 60s [30], it became routine to measure the electrical conductivity of the product. The science learned was marginally useful, but a catalog of monomers was generated for future use.

An important development occurred in the late 60s in the studies by Wegner [31,32] of the polymerization of diacetylenes. He showed that single crystals of the monomer derivatives can be polymerized topotactically, essentially retaining the original crystal structure. For the first time, a class of conjugated polymers was amenable to crystallographic analysis: bond lengths and angles could be determined, and would serve as a reference for future structural studies of less well-ordered materials, and as input to *ab initio* molecular-orbital calculations. Initially, most interest on the physical properties of polydiacetylenes focused on their photoconductivity. We shall return to their dark conductivity below.

At the same time, in his lab in Tokyo, Hideki Shirakawa was applying Ziegler–Natta polymerization to the simplest conceivable monomer – acetylene, C_2H_2. By a 'fortuitous error' he discovered the effect of using $1000 \times$ the usual concentration of a particularly soluble organometallic catalyst. When he bubbled acetylene gas through the solution, a shiny, silvery film was deposited on the walls of the tube. The morphology of these films

consists of well-separated fibrils, leading to a high degree of porosity and large internal surface area, ideal for gas-phase doping. The visitor from Penn, MacDiarmid, was fascinated by what he saw in his lab.

While this work was being pursued in the chemical community, several groups of physicists, together with their chemist collaborators, were studying 'highly conducting one-dimensional solids' [33]. Many of the materials of interest were organic charge-transfer salts, of which TTF-TCNQ is probably the best-known example. The scientific interest lay in the intriguing phenomena associated with one-dimensional electronic structures. Peierls [7] had postulated that a 1D electronic system would spontaneously distort, and therefore could not be metallic at low temperature. This Peierls transition was observed in TTF-TCNQ at a temperature of about 40 K [8]. The low, and experimentally accessible, transition temperature is due to non-negligible interchain interactions and to the partial charge transfer from the TTF donor to the TCNQ acceptor. In contrast, in sp^2-conjugated polymers there is one π-electron per carbon atom. Thus a chain with equal bond lengths would result in a half-filled band. The Peierls distortion is then a simple dimerization of the chain, resulting in alternating long and short C—C bonds. The gain in electronic energy dominates the cost in lattice energy and results in a high transition temperature, well above the decomposition temperature of the organic polymers of interest.

Thus by the mid-70s, much of the preparative polymer chemistry and the physical understanding of conduction processes in 1D were well established.

1.3 The Dawn of the Modern Era [6]

Highly doped inorganic semiconductors are 'degenerate' because the donor (acceptor) impurity band overlaps the bottom of the conduction band (top of the valence band), leading to a nonzero density of states at the Fermi level. The result is a material with conductivity similar to that of a metal, and unlike the thermally activated response of the original semiconductor. This concept does not apply directly to doped conjugated polymers since energy of the dopant ion is typically not close in energy to the transport bands. The motivation to investigate the effects of doping on the conductivity of polyacetylene arose instead from experience with charge-transfer salts. The ground state of the system does not consist of neutral impurities that release mobile charge carriers as the temperature is raised, but rather of charged ions (anion or cation) with the counter-charge in the valence or conduction band of the polymer. The carriers are attracted to the opposite charge on the ions, but because of the relatively large molecular sizes and the screening effects of other carriers, the binding energy is low and at room temperature the carriers are quite mobile.

This concept – mobile charge carriers in the valence (HOMO) or conduction (LUMO) band of the polymer, with the counter-charges on ionic species – provides the fundamental framework for the subsequent development of polymeric conductors.

Following the 1977 publication by the Pennsylvania team, the field exploded. Dozens of research groups began programs to understand better the properties of polyacetylene and to search for new and better materials. There was considerable emphasis on determining the

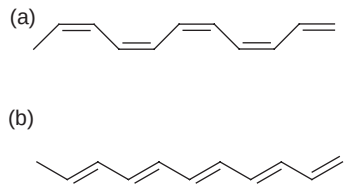

Figure 1.2 *(a)* cis *and (b)* trans *isomers of polyacetylene*

details of (what we would now call) its nanomorphology. There are two isomeric forms of polyacetylene $(CH)_x$: *cis* and *trans*, which can be readily distinguished by their vibrational (infrared and Raman) spectroscopy. The mechanism of Ziegler–Natta polymerization leads initially to the generation of the *cis* form, but this is metastable at room temperature and mild heating or exposure to vapor-phase dopants converts it to *trans*.

The fibrous morphology created during synthesis is highly crystalline. Since the fibrils are only about 200 nm in diameter, about 1 μm long and randomly oriented, the X-ray diffraction patterns yield only lattice spacings, not the full crystal structure. Ray Baughman and others members of the polymer chemistry group at Allied Chemical (as it then was) combined the X-ray diffraction results with molecular modeling to elucidate the crystal structure of the pristine isomers, and to determine the approximate location of the dopant ions [34]. Initially, iodine was of particular interest because it formed linear polyatomic ionic species (I_3^-, I_5^-, etc) residing in 'channels' between the polymer chains.

There was a great deal of debate about the homogeneity of doping, and its effect on the conductivity. There were those who argued that the doping was homogeneous and random, and that the concentration of charge carriers increases up to the point where their mutual screening induces a Mott insulator–metal transition. Others proposed highly inhomogeneous doping, essentially the growth of metallic 'islands' in an otherwise insulating polymer matrix. In this scenario, the macroscopically observed insulator–metal transition is due to the growth of the islands to the point where they coalescence into percolating conductive pathways. Although the controversy was never fully resolved to the satisfaction of all parties, it was nevertheless a great motivator, driving innovative research that ultimately contributed to a detailed understanding of the excitations of conjugated chains, their spectral and magnetic signatures, and their interactions.

A polymer chain of *trans*-$(CH)_x$ has the unusual property of geometric degeneracy – there are mirror-image distinct states, but possessing the same energy (see Figure 1.3).

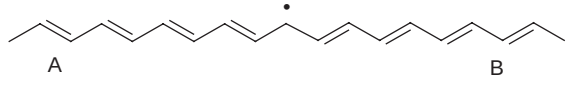

Figure 1.3 *Bonding structure of a soliton in polyacetylene. The configurations A, to the left, and B, to the right, are equivalent, but there is a defect where they meet. The central carbon atom shares electrons in three σ-bonds, but the fourth (π) electron is unpaired. The system is charge-neutral, but has spin ½*

Su, Schrieffer and Heeger (SSH) [35] addressed the nature of the topological defect that must be created at the junction between two mirror-image chains. The mathematical description of the defect belongs to a class of solution of nonlinear differential equations, and is known as a soliton. The solitons in *trans*-$(CH)_x$ exhibit reversed spin-charge relations: the neutral species has spin ½, while the addition or removal of an electron results in a nonmagnetic state. The soliton is not localized on a single carbon atom, as depicted in Figure 1.3, but is spread over roughly a dozen atoms, according to the parameters of the SSH Hamiltonian. Many of the theoretically predicted features of solitons were subsequently confirmed by experiment over the next few years: electron spin resonance was observed in undoped polyacetylene, and diminished at low dopant concentrations; measurements of the hyperfine coupling strength to the protons confirmed its delocalization; the presence of a mid-gap state was confirmed by photo-induced (pump-probe) absorption; and the symmetry changes induced by optical excitation or by doping were deduced from the infrared modes that appeared.

The science of polyacetylene is fascinating, but as a polymeric conductor its material properties are not at all suited to technological application. It is insoluble in any common solvent; it has little mechanical strength, especially in its doped state, and cannot be molded nor effectively stretch-aligned; it is not stable in air. Immediately the effort began to find new polymers and better ways of processing. Exploration proceeded on many fronts, from the substitution of one or both hydrogen atoms in acetylene, to polymerization processes other than Ziegler–Natta catalysis, to the use of completely different monomers and to electrochemical oxidation.

An example of side-group substitution is poly(phenylacetylene). The phenyl group imparts considerably better stability. Due to steric packing constraints, it also changes the conformation of the backbone from planar zig-zag to helical. However, the crystallinity is considerably reduced, doping is not so effective and the conductivities obtained were lower than the unsubstituted polymer. The improvement in material properties was rather modest and not sufficiently encouraging to offset the loss in conductance, so PPA is one of many technological dead-ends encountered at that time.

Among the more successful synthetic procedures were those developed by Feast at Durham, [36] who developed a ring-opening synthesis procedure for polyacetylene derivatives. Meanwhile Naarmann at BASF showed the benefits of dissolving the Ziegler–Natta organometallic catalyst in a viscous solvent [37]. These routes permitted better morphological control and led to higher conductivity in the doped state, but still suffered from the inherent limitations of polyene chemistry.

Completely different monomers were called for. Before long, three of today's workhorses had been identified: pyrrole, aniline and thiophene. In Japan, Yamamoto [38] and in Germany, Kossmehl [39] synthesized polythiophene doped with pentafluoroarsenate. At the same time, the possibilities of electrochemical polymerization were recognized. At the IBM Lab in San Jose, Diaz used oxidative electrochemical polymerization to prepare polypyrrole [40] and polyaniline. [41] Electrochemical synthesis forms the polymer in its doped state, with the counter-ion (usually an anion) incorporated from the electrolyte. This mechanism permits the selection of a wider range of anions, including those which are not amenable to vapor-phase processes, such as perchlorate and tetrafluoroborate. Electrochemical doping also overcomes an issue associated with dopants

such as pentafluoroarsenate, neutral in the gas phase, but leading to hexafluoroarsenate anions in the doped compound, with the production of other species as by-products which are not easy to identify or trace. An additional advantage of synthesis in an electrochemical cell is that the dopants can also be removed by applying an appropriate reverse voltage. The polymer is neutralized ('dedoped'), while the new covalent bonds between monomers remain.

The polymers formed by electrochemical oxidation are also insoluble, and therefore still not generally useful as general-purpose electrical conductors. In addition, it was not always possible to control coupling sites between monomers. For example in polypyrrole, 2-5 coupling predominated, but reaction at the 3 or 4 sites could not be ruled out [42]. Oxidative coupling, for example with ferric chloride, was found to lead to similar poor control over the molecular structure and to insoluble polymeric adducts. The goal of high conductivity in a solution-processable polymer remained elusive. It would require a further decade of painstaking chemical research to develop procedures for the large-scale production of soluble metallic polymers.

Polyaniline is unique among the conducting polymers in its doping characteristics. Rather than changing its oxidation state (i.e. carrier density) by addition or removal of electrons, doping is accomplished by removal or addition of protons [28], using strong bases (e.g. ammonium hydroxide) or protonic acids (e.g. hydrochloric or sulfuric). The net effect is similar: electrons in partially filled frontier orbitals are responsible for carrying the current; overall charge neutrality is maintained by the protons bound to the backbone nitrogen atom and by the anion of the protonic acid.

In spite of the synthetic difficulties, the wide selection of new materials being provided by the chemists encouraged exploration of new physical phenomena among the physical chemists and physicists. Virtually none of these new polymers exhibits the topological degeneracy that is found in *trans*-$(CH)_x$. Therefore their charge species are not solitons, but rather polarons and, perhaps, bipolarons (see Figure 1.4). The question arose as to whether the cost in lattice energy to form two polarons would exceed Coulomb repulsion and lead to a net binding energy stabilizing the bipolaron. Magnetic and spectroscopic data [43,44] reveals that bipolarons were the dominant species in moderately doped polypyrrole. Many subsequent studies have shown that bipolarons are the species most frequently encountered when conjugated polymers are doped.

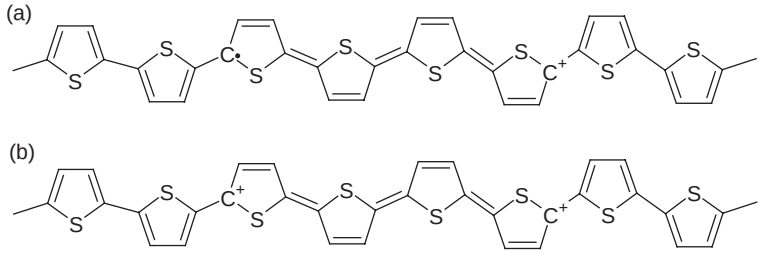

Figure 1.4 *Bonding structure of (a) a polaron and (b) a bipolaron in polythiophene*

1.4 The Materials Revolution

By the mid-80s it was clear to most researchers that success on the conductivity side had taken its toll on polymer processability. Attention turned back to restoring the solubility and mechanical properties of the polymer. Polyaniline received the most attention initially. The nonconductive emeraldine base form is soluble in *N*-methylpyrrolidone [28] and films can be cast. Subsequent doping with a protonic acid from aqueous solution, or *in situ* with a photo-acid generator [45], is necessary to achieve conductivity. Polyaniline is also soluble in sulfuric acid, not the most convenient of solvents. Nevertheless it proved possible to spin fibers [46], cast films and extrude sheets of conductive polyaniline sulfate, but the laboratory experiments did not make the transition into large-scale manufacturing.

A major advance in the solubilization of polyaniline was 'self-doping' by the attachment of a sulfonic acid side group to the backbone ring [47,48]. The resulting material is essentially a 'polyzwitterion' with the acid proton transferring to the basic amine backbone. The polymer is then soluble in mildly basic aqueous solutions and can be coated over large areas.

Almost simultaneously, another breakthrough occurred when it was realized that the protonic acid dopant could be selected or modified to act as a surfactant. Homologs of toluene sulfonic acid were the first examples examined [49], and camphor sulphonic acid proved to be one of the most interesting and promising acid surfactants [50], solubilizing polyaniline in *m*-creosol.

During the same period, the German chemical company, Bayer AG, was developing a soluble polythiophene derivative (PEDOT-PSS), motivated primarily by the need for electrostatic dissipation during the coating of photographic film. At the time, Bayer owned the photography company Agfa. Web-coating of the polymer substrate ('celluloid') leads to significant static charge build-up, and uncontrolled discharge amid the vapors of organic solvents was a major concern. The early phases of this research began in the late 80s, but the company considered it highly proprietary, applying for patents in Germany in 1988. The US patent was issued in 1991 [51]. There are no publications in the scientific literature until the company began to consider offering evaluation quantities for other applications [52]. Then, some of the details of the chemistry [53] and physical properties [54] began to appear.

Thus, by the mid-90s, the scientific foundations were well established, and methods had been developed to overcome the difficulties of achieving both conduction and processability in the same material. Many potential applications had already been identified and patents filed. New companies were started and more established companies initiated new business units, both on the supply side as vendors of the materials and on the demand side as developers of technological applications. Naturally, most of this work was hidden behind closed doors and presentations were aimed more at venture capitalists than at the scientific community. Publicity was generated, not by talks at scientific conferences, but rather by carefully managed press releases. The subsequent history is probably better documented by a business analyst than by a scientist.

The scientific story, however, does not end there. The identification of new potential applications demanded modifications and improvements in the materials, which in turn revealed more interesting and possibly useful properties. In 1993, Joel Miller, who had

recently moved to the University of Utah after working at Xerox and then DuPont, published a pair of articles listing, first, the attributes and potential applications [55] and then the existing commercially available products [56] based on conducting polymers. The latter list is dominated by applications dependent on electrochemical properties: batteries, electrolytic capacitors and electrodes for plating baths. Antistatic coatings, usually as blends in other polymers, for textiles and in electronic packaging are also prevalent. The list of potential applications spans the gamut from biochemical sensors to protection against lightning strikes in aircraft. One barely anticipated application now represents a major part of polymer production is in anticorrosive coatings [57]. In retrospect, it is not surprising that these electrochemically active materials might provide some benefit, but the detailed mechanism(s) of the protection are still an active area of research. A second unanticipated use is for electrodes in flat-panel displays, particularly polymer light-emitting diodes. The original motivation was to find a flexible replacement for indium tin oxide (ITO)-coated glass, but the conductivity of polymers was insufficient to carry the necessary current. However, it was found that a layer of various polyanilines or PEDOT [58,59] on top of ITO led to improved device performance and greatly enhanced lifetime. This 'hole-injection layer' is now one of the primary uses of PEDOT-PSS.

Intrinsic, i.e. undoped, conjugated polymers are now of great interest for their semiconducting properties. Research, development and commercialization have continued as applications for light-emitting diodes, field-effect transistors, photo-detectors, solar cells and chemical sensors were identified. For these technologies exquisite control over the chemistry is required in order to minimize defects which may limit performance and lifetime. Attention must also be paid to termination of the polymer chains, and to the elimination and/or removal of the trace amounts of polymerization catalysts. The methods of polymer chemistry, developed originally for careful control of the molecular structure of commodity polymers, were applied and adapted. Precise coupling and condensation reactions, using functionalized monomers as precursors, ensure that the resulting polymer has the desired linear structure. The range of chemical methods (Knoevenagel, Heck, Suzuki, Yamamoto and others) is described in the excellent review by Kraft *et al.* [60], who were primarily interested in luminescent polymers at the time.

Two of the earliest conjugated polymers are no longer the subject of active research as conducting materials. Polydiacetylene is the most highly crystalline polymer, and therefore the one with the highest potential carrier mobility. However, it has proved impossible to dope to any significant degree. It is being developed for sensor applications because of its optical properties and biocompatibility. Polyacetylene is chemically the simplest conjugated polymer, and although it provided a great deal of interesting science and proved to be a model for many other materials, it is not itself technologically useful.

1.5 Concluding Remarks

The history of research on conjugated polymers reveals its highly interdisciplinary nature and the importance of collaboration. Prior to the 70s, there was much in the chemical literature about the synthesis of many of the materials that form the basis for today's inventory, but the synthetic chemists were generally not experienced in the preparation of

samples suitable for detailed physical characterization. Similarly, although physicists had begun to study the organic solid state, the research was mainly on small molecules which chemical supply companies could provide. The major breakthroughs began when chemists and physicists began to work together to design and synthesize specific molecular structures to achieve the desired physical properties.

Such 'structure–function' relationships form the paradigm of modern materials science, and in the 80s and 90s many academic materials/chemical/polymer engineering departments were rebuilding to include a greater emphasis on soft-matter and electronic properties. They recruited young faculty members with degrees in chemistry or physics, with the result that the boundaries between these various departments has become blurred.

From the very beginning of the modern era, there was strong involvement of theorists. Theoretical physicists were particularly interested in the topological defects inherent in 1D systems, and the reversed spin-charge relationships of solitons and polarons. Quantum chemists focused on the molecular-orbital theory of extended structures. Both disciplines struggled with the relative importance of electron correlations and electron–phonon interactions.

As potential applications were identified, researchers from other engineering fields became involved. Electrical engineers brought their expertise in electronics, optoelectronics and display technology. Materials engineers joined with electrochemists to study anticorrosion coatings. Bioengineers recognized the potential for sensors and bioanalytical assays. The list of author affiliations of this volume testifies to the success of this interdisciplinary approach.

A historical review such as this is not only about the science and the published literature. It is also about the people involved and their interactions. The scientific progress which is summarized in this chapter is the result of collective endeavor, with a large number of scientists making contributions with various levels of impact. They came together at several exciting international topical conferences, particularly during the 80s. The 'Conference on Organic Conductors and Semiconductors' was first held in Siofok, Hungary in 1976, and took place annually until 1982. It acquired the name 'International Conference on Synthetic Metals' (ICSM) in Helsingor, Denmark in 1980. Since 1982, ICSM has been held every two years, most recently in Porto de Galinhas, Brazil, in 2008. There had been several other *ad hoc* conferences and workshops during the prior decade, notably in Saarbrucken, Germany in 1974, and at Lake Arrowhead, California in the same year, where many of the researchers cited among the references came to know each other, exchanged ideas and frequently engaged in heated discussions. The journal, *Synthetic Metals*, was initiated in 1979 expressly to serve this subfield of the scientific community, and continues to this day with editors, contributors and referees from around the world. *Organic Electronics* began publication in 2000, and organic electronics as a topic comprises a major fraction of the articles in *Advanced Materials*, and *Advanced Functional Materials*.

Advances in science do not occur in a vacuum. They are based on prior research, which in many cases may not have seemed relevant at the time. Progress is punctuated, with periods of great activity interspersed with times of relative quiet. Breakthroughs occur due to the development of new instrumentation, the discovery of a new material, and/or because of the efforts of particularly passionate and skilled scientists. In many cases, the subjects of the initial scientific excitement turn out not to be the leading candidates for

technological application. Their usefulness lies in the science lessons that they teach us, and conjugated polymers from aniline and pyrrole blacks in Victorian times, to polydiacetylene and polyacetylene in the 70s, to today's poly(phenylene vinylene)s and poly(spiro-bifluorene)s, have taught us many interesting lessons.

Acknowledgments

I have benefited over the years from many discussions with the authors of the papers cited, and those of many other papers which time and space preclude. I thank them for their explanations and inspiration. I also thank Dr Gillian Eade for a critical reading of the manuscript. Any omissions (and I know that there are many) and errors are mine and I apologize to those whose work I may have seemed to overlook. This chapter is not really a history of science. If it were to be so, I would have interviewed many of the protagonists involved in the research, and requested copies of their correspondence, lab notebooks and notes. Nor is it a comprehensive review of the literature which is, at this point, too vast and diversified to encapsulate into a single short article. Rather it is my recollection of the important events which subsequently shaped the field, and my own opinion about what constitutes 'important.' I have attempted to cite the earliest, most seminal papers and to include appropriate and accessible reviews. Finally, I wish to thank Alan Heeger, my thesis advisor until 1975, and a mentor ever since.

References

[1] C. K. Chiang, C. R. Fincher, Y. W. Park, A. J. Heeger, H. Shirakawa, E. J. Louis, S. C. Gau, and A. G. McDiarmid, Electrical conductivity in doped polyacetylene, *Phys. Rev. Lett.*, **39**, 1098–1101 (1977).

[2] N. S. Hush, An overview of the first half-century of molecular electronics, *Ann. N. Y. Acad. Sci.*, **1006**, 1–20 (2003).

[3] H. Letheby, On the production of a blue substance by the electrolysis of sulphate of aniline, *J. Chem. Soc*., 161–163 (1862).

[4] A. J. Heeger, Semiconducting and metallic polymers: the fourth generation of polymeric materials, *Curr. Appl. Phys.*, **1**, 247–267 (2001).

[5] A. G. Macdiarmid, 'Synthetic metals': a novel role for organic polymers, *Curr. Appl. Phys.*, **1**, 269–279 (2001).

[6] H. Shirakawa, The discovery of polyacetylene film – the dawning of an era of conducting polymers, *Curr. Appl. Phys.*, **1**, 281–286 (2001).

[7] R. E. Peierls, *Quantum Theory of Solids*, Oxford University Press, London, 1955.

[8] F. Denoyer, R. Comès, A. F. Garito, and A. J. Heeger, X-ray-diffuse-scattering evidence for a phase transition in tetrathiafulvalene tetracyanoquinodimethane (TTF-TCNQ), *Phys. Rev. Lett.*, **35**, 445–449 (1975).

[9] H. Frohlich, On the theory of superconductivity: the one-dimensional case, *Proc. Roy. Soc. A*, **223**, 296–305 (1954).

[10] L. B. Coleman, M. J. Cohen, D. J. Sandman, F. G. Yamagishi, A. F. Garito, and A. J. Heeger, Superconducting fluctuations and the Peierls instability in an organic solid, *Solid State Commun.*, **12**, 1125–1132 (1973).

[11] V. V. Walatka, M. M. Labes, and J. H. Perlstein, Polysulfur Nitride—char22a One-Dimensional Chain with a Metallic Ground State, *Phys. Rev. Lett.*, **31**, 1139–1142 (1973).
[12] R. L. Greene, G. B. Street, and L. J. Suter, Superconductivity in polysulfur nitride (SN)x, *Phys. Rev. Lett.*, **34**, 577–579 (1975).
[13] F. Kajzar, S. Etemad, G. L. Baker, and J. Messier, $X^{(3)}$ of trans-$(CH)_x$: Experimental observation of ^2A_g excited state, *Synth. Metals*, **17**, 563–567 (1987).
[14] Z. G. Soos and S. Ramasesha, Valence bond approach to exact nonlinear optical properties of conjugated systems, *J. Chem. Phys.*, **90**, 1067–1076 (1989).
[15] S. N. Dixit, D. Guo, and S. Mazumdar, Essential-states mechanism of optical nonlinearity in π-conjugated polymers, *Phys. Rev. B*, **43**, 6781–6784 (1991).
[16] J. H. Burroughes, D. D. C. Bradley, A. R. Brown, R. N. Marks, K. Mackey, R. H. Friend, P. L. Burns, and A. B. Holmes, Light-emitting diodes based on conjugated polymers, *Nature*, **347**, 539–541 (1990).
[17] F. Ebisawa, T. Kurokawa, and S. Nara, Electrical properties of polyacetylene/polysiloxane interface, *J. Appl. Phys.*, **54**, 3255–3259 (1983).
[18] H. Koezuka, A. Tsumura, and T. Ando, Field-effect transistor with polythiophene thin film, *Synth. Metals*, **18**, 699–704 (1987).
[19] G. Horowitz, D. Fichou, X. Peng, Z. Xu, and F. Garnier, A field-effect transistor based on conjugated alpha-sexithienyl, *Solid State Commun.*, **72**, 381–384 (1989).
[20] R. J. Kline, M. D. McGehee, E. N. Kadnikova, J. S. Liu, J. M. J. Frechet, and M. F. Toney, Dependence of regioregular poly(3-hexylthiophene) film morphology and field-effect mobility on molecular weight, *Macromol.*, **38**, 2219–3312 (2005).
[21] C. H. Lee, G. Yu, D. Moses, K. Pakbaz, C. Zhang, N. S. Sariciftci, A. J. Heeger, and F. Wudl, Sensitization of the photoconductivity of conducting polymers by C_{60}: Photoinduced electron transfer, *Phys. Rev. B*, **48**, 15425–15433 (1993).
[22] J. J. M. Halls, K. Pichler, R. H. Friend, S. C. Moratti, and A. B. Holmes, Exciton diffusion and dissociation in a poly(p-phenylenevinylene)/C_{60} heterojunction photovoltaic cell, *Appl. Phys. Lett.*, **68**, 3120–3122 (1996).
[23] J. Fritsche, Vorläufige notiz über ein neues zersetzungsproduct des indigo durch salpetersäure, *J. Prakt. Chem.*, **16**, 507–508 (1839).
[24] H. Staudinger, Über polymerisation, *Ber. Chem.*, **53**, 1073–1085 (1920).
[25] W. H. Carothers, Polymers and polyfunctionality, *Trans. Faraday Soc.*, **32**, 39–49 (1936).
[26] K. Fukui, T. Yonezawa, and H. Shingu, A molecular orbital theory of reactivity in aromatic hydrocarbons, *J. Chem. Phys.*, **20**, 722–725 (1952).
[27] D. M. Mohilner, R. N. Adams, and W. J. Argersinger, Investigation of the kinetics and mechanism of the anodic oxidation of aniline in aqueous sulfuric acid solution at a platinum electrode, *J. Am. Chem. Soc.*, **84**, 3618–3622 (1962).
[28] A. G. MacDiarmid and A. J. Epstein, Polyanilines: a novel class of conducting polymers, *Faraday Discuss.*, **88**, 317–332 (1989).
[29] L. T. Yu, M. S. Borredon, M. Jozefowicz, G. Belorgey, and R. Buvet, Experimental Study of direct current conductivity of macromolecular compounds, *J. Polym. Sci. Part C-Polym. Symp.*, **16**, 2931 (1967).
[30] M. Armour, A. G. Davies, J. Upadhyay, and A. Wasserman, Colored electrically conducting polymers from furan, pyrrole and thiophene, *J. Polym. Sci. A*, **1**, 1527–1538 (1967).
[31] G. Wegner, Topochemical reactions of monomers with conjugated triple bonds I. polymerization of 2.4-hexadiyn-1.6-diols derivatives in crystalline state, *Z. Naturf.*, **24b**, 824 (1969).
[32] G. Wegner, Topochemical polymerization of monomers with conjugated triple bonds, *Makromol. Chem.*, **154**, 35–48 (1972).
[33] J. T. Devreese, R. P. Evrard, and V. E. van Doren, (Eds), *Highly Conducting One-Dimensional Solids*, Plenum, New York and London, 1979.
[34] R. H. Baughman, S. L. Hsu, G. P. Pez, and A. J. Signorelli, The structures of *cis*-polyacetylene and highly conducting derivatives, *J. Chem. Phys.*, **68**, 5405–5409 (1978).
[35] W. P. Su, J. R. Schrieffer, and A. J. Heeger, Solitons in polyacetylene, *Phys. Rev. Lett.*, **42**, 1698–1701 (1979).

[36] W. Feast and J. Winter, An improved synthesis of polyacetylene, *J. Chem. Soc. Chem. Commun.,* 202–203 (1985).
[37] H. Naarmann and N. Theophilou, New process for the production of metal-like, stable polyacetylene, *Synth. Metals*, **22**, 1–8 (1987).
[38] T. Yamamoto, K. Sanechika, and A. Yamamoto, Preparation of thermostable and electric-conducting poly(2,5-thienylene), *J. Polym. Sci., Polym. Lett. Ed.*, **18**, 9–12 (1980).
[39] G. Kossmehl and G. Chatzitheodorou, Electrical conductivity of poly(2,5-thiophenediyl)-arsenic pentafluoride-complexes, *Makromol. Chem., Rapid Commun.*, **2**, 551–555 (1981).
[40] A. Diaz, K. Kanazawa, and G. Gardini, Electrochemical polymerization of pyrrole, *J. Chem. Soc: Chem. Commun*., 635–636 (1979).
[41] A. F. Diaz and J. A. Logan, Electroactive polyaniline films, *J. Electroanal. Chem.*, **111**, 111–114 (1980).
[42] J. Bargon, S. Mohmand, and R. J. Waltman, Electrochemical synthesis of electrically conducting polymers from aromatic compounds, *IBM J. Res. Dev.*, **27**, 330–341 (1983).
[43] J. C. Scott, P. Pfluger, M. T. Krounbi, and G. B. Street, Electron-spin-resonance studies of pyrrole polymers – evidence for bipolarons, *Phys. Rev. B*, **28**, 2140–2145 (1983).
[44] J. C. Scott, J. L. Bredas, K. Yakushi, P. Pfluger, and G. B. Street, The evidence for bipolarons in pyrrole polymers, *Synth. Metals*, **9**, 165–172 (1984).
[45] M. Angelopoulos, G. E. Asturias, S. P. Ermer, A. Ray, E. M. Scherr, A. G. MacDiarmid, M. Akhtar, Z. Kiss, and A. J. Epstein, Polyaniline: solutions, films and oxidation state, *Molec. Cryst. Liq. Cryst.*, **160**, 151–163 (1988).
[46] A. Andreatta, Y. Cao, J. C. Chiang, A. J. Heeger, and P. Smith, Electrically-conductive fibers of polyaniline spun from solutions in concentrated sulfuric acid, *Synth. Metals*, **26**, 383–389 (1988).
[47] J. Yue, Z. H. Wang, K. R. Cromack, A. J. Epstein, and A. G. MacDiarmid, Effect of sulfonic acid group on polyaniline backbone, *J. Am. Chem. Soc.*, **113**, 2665–2671 (1991).
[48] X.-L. Wei, Y. Z. Wang, S. M. Long, C. Bobeczko, and A. J. Epstein, Synthesis and Physical Properties of Highly Sulfonated Polyaniline, *J. Am. Chem. Soc.*, **118**, 2545–2555 (1996).
[49] Y. Cao, P. Smith, and A. J. Heeger, Counter-ion induced processibility of conducting polyaniline and of conducting polyblends of polyaniline in bulk polymers, *Synth. Metals*, **48**, 91–97 (1992).
[50] Y. Cao and P. Smith, Liquid-crystalline solutions of electrically conducting polyaniline, *Polymer*, **34**, 3139–3143 (1993).
[51] F. Jonas, G. Heywang, W. Schmidtberg, J. Heinze, and M. Dietrich, Method of imparting antistatic properties to a substrate by coating the substrate with a novel polythiophene, US Patent 5035926, 30 July 1991.
[52] G. Heywang and F. Jonas, Poly(alkylenedioxythiophene)s – new, very stable conducting polymers, *Adv. Mater.*, **4**, 116–118 (1992).
[53] M. Dietrich, J. Heinze, G. Heywang, and F. Jonas, Electrochemical and spectroscopic characterization of polyalkylenedioxythiophenes, *J. Electroanal. Chem*, **369**, 87–92 (1994).
[54] I. Winter, C. Reese, J. Hormes, G. Heywang, and F. Jonas, The thermal ageing of poly(3,4-ethylenedioxythiophene). An investigation by X-ray absorption and X-ray photoelectron spectroscopy, *Chem. Phys.*, **194**, 207–213 (1995).
[55] J. S. Miller, Conducting polymers – materials of commerce, *Adv. Mater.*, **5**, 587–589 (1993).
[56] J. S. Miller, Conducting polymers – materials of commerce, *Adv. Mater.*, **5**, 671–676 (1993).
[57] D. W. DeBerry, Modification of the electrochemical and corrosion behavior of stainless steels with an electroactive coating, *J. Electrochem. Soc.*, **132**, 1022–1026 (1985).
[58] S. Karg, J. C. Scott, J. R. Salem, and M. Angelopoulos, Increased brightness and lifetime of polymer light-emitting diodes with polyaniline anodes, *Synth. Metals*, **80**, 111–117 (1996).
[59] S. A. Carter, M. Angelopoulos, S. Karg, P. J. Brock, and J. C. Scott, Polymeric anodes for improved polymer light-emitting diode performance, *Appl. Phys. Lett.*, **70**, 2067–2069 (1997).
[60] A. Kraft, A. C. Grimsdale, and A. B. Holmes, Electroluminescent conjugated polymers – Seeing polymers in a new light, *Angew. Chem. Internat. Ed.*, **37**, 402–428 (1998).

2

Polyaniline Nanostructures

Gordana Ćirić-Marjanović

Faculty of Physical Chemistry, University of Belgrade,
Studentski Trg 12-16, 11158 Belgrade, Serbia

2.1 Introduction

Polyaniline (PANI) is one of the most extensively studied conducting polymers because of its simple synthesis [1] and doping/dedoping chemistry [2], low cost, high conductivity, and excellent environmental stability. PANI has a wide applicability in rechargeable batteries [3], erasable optical information storage [4], shielding of electromagnetic interference [5], microwave- and radar-absorbing materials [6], sensors [7], indicators [8], catalysts [9], electronic and bioelectronic components [10], membranes [11], electrochemical capacitors [12], electrochromic devices [13], nonlinear optical [14] and light-emitting devices [15], electromechanical actuators [16], antistatic [17] and anticorrosion coatings [18]. Its electromagnetic and optical properties depend mostly on its oxidation state and degree of protonation [19]. The green emeraldine salt form of PANI is conducting ($\sim$1–10 S cm^{-1} for granular powders) [1]. It contains, depending on the synthetic route, various proportions of diamagnetic [(—B—NH^{+}=Q=NH^{+}—)$_n$(—B—NH—)$_{2n}$](A^{-})$_{2n}$ and paramagnetic [(—B—NH$^{+\bullet}$—B—NH—)$_n$](A^{-})$_n$ units (in the preceeding formulae B, Q and A^{-} denote a benzenoid ring, quinonoid ring and dopant anion, respectively). The blue emeraldine base [(—B—N=Q=N—)$_n$(—B—NH—)$_{2n}$], the colorless leucoemeraldine base [(—B—NH—)$_n$], and violet pernigraniline base forms [(—B—N=Q=N—)$_n$] are insulating. The preparation of bulk quantities of conducting granular PANI is usually performed

Nanostructured Conductive Polymers Edited by Ali Eftekhari

by the oxidative polymerization of aniline with ammonium peroxydisulfate (APS) in an acidic aqueous solution (initial pH < 2.0) [1]. Colloidal PANI nanoparticles are prepared by dispersion polymerization of aniline in the presence of various colloidal stabilizers [20,21]. The average size of colloidal PANI nanoparticles decreases with increasing stabilizer/aniline ratio. PANI colloids often have nonspherical (rice grain, needle-like, etc.) core-shell morphology. The colloidal nanoparticle core most likely has a composite nature, i.e. it is composed of both the PANI and the incorporated stabilizer, while the shell is formed by the stabilizer.

Nowadays, conducting PANI nanostructures are the focus of intense research owing to their significantly enhanced dispersibility and processability, and substantially improved performance in many applications, in comparison with granular and colloidal PANI [22–27]. The continuously growing interest in the study of zero-dimensional (0-D) (solid nanospheres), one-dimensional (1-D) (nanofibers (nanowires), nanorods (nanosticks), nanoneedles, rice-like nanostructures, nanotubes), two-dimensional (2-D) (nanoribbons (nanobelts), nanosheets (nanoplates, nanoflakes, nanodisks, leaf-like nanostructures), nanorings (cyclic nanostructures), net-like nanostructures), and three-dimensional (3-D) PANI nanostructures (hollow nanospheres, dendritic and polyhedral nanoparticles, flower-like, rhizoid-like, brain-like, urchin-like, and star-like nanostructures, etc.) has dramatically increased in recent years (Figure 2.1). The major focus of research has been the preparation, characterization, processing, and application of PANI nanofibers (PANI-NFs) and nanotubes (PANI-NTs). PANI-NFs are 1-D PANI nanoobjects of cylindrical profile with diameters ≤100 nm, without a discernible internal cavity, while PANI-NTs are 1-D PANI nanoobjects with an internal cavity. PANI nanowires (conducting or semiconducting doped PANI-NFs) and PANI nanorods (short and straight PANI-NFs) are also referred

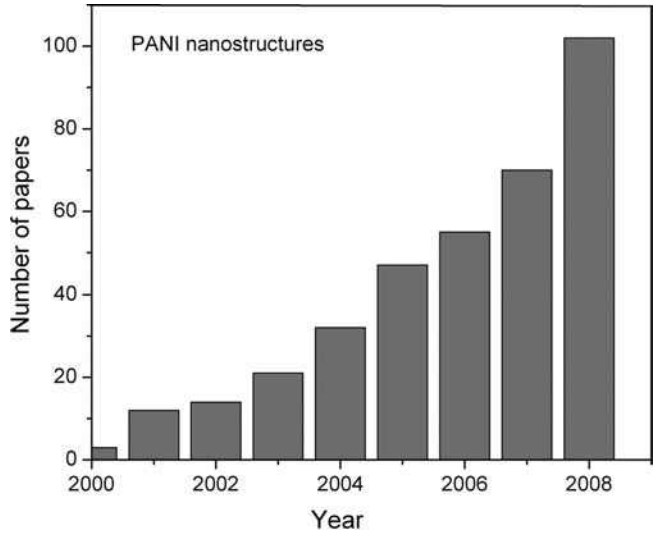

Figure 2.1 *The number of articles devoted to the synthesis, characterization and application of PANI nanostructures, published by the American Chemical Society, Elsevier, John Wiley & Sons, Wiley-VCH, the Royal Society of Chemistry, Springer, and the Institute of Physics during the last decade*

throughout the manuscript as PANI-NFs. It should be noted that numerous articles in leading international journals, having in title or abstract terms 'nanofibers' ('nanowires', 'nanorods') and/or 'nanotubes' of PANI, are in fact devoted to the study of submicrofibrous/submicrotubular PANI materials (100 nm ≤ diameters ≤ 1 μm) and their mixtures with PANI-NFs and/or PANI-NTs.

Extensive research in a broad field of preparation and characterization of nanostructured composite PANI materials, containing PANI nanostructures and micro-/submicro-/nanoparticles of various metals, oxides, organic/bio-organic compounds, and biological materials, has developed intensively with the aim to design nanomaterials with unique physicochemical properties and applicability. Therefore the objective of this review is not only to provide insight into the recent developments regarding preparation, characterization, processing, and application of pure PANI nanostructures, but also to give comprehensive information about composite materials which contain PANI nanostructures. It should be noted that the PANI nanocomposites prepared by the formation of PANI thin solid films on the surface of other nanostructured materials (nanofibers and nanotubes of various inorganic, organic and biological materials e.g. carbon nanotubes (CNTs), nanorods of tobacco mosaic virus, etc.) are not the subject of this review.

2.2 Preparation

2.2.1 Preparation of Polyaniline Nanofibers

2.2.1.1 Physical Methods of Preparation

Electrospinning

Unlike conventional fiber-spinning techniques (wet spinning, dry spinning, melt spinning, gel spinning), which are capable of producing fibers of blends of nonspinnable conducting PANI emeraldine salt (e.g. camphorsulfonate) and spinnable polymers (e.g. poly(ethylene oxide) (PEO), poly(methylmetacrylic acid) (PMMA)) with diameters down to the micrometer range, electrospinning is a process capable of producing corresponding submicrofibers and nanofibers, as well as pure PANI-NFs [28–39]. This electrostatic processing method uses a high-voltage electric field to form solid fibers from a polymeric blend fluid stream (solution or melt) delivered through a millimeter-scale nozzle. Due to the inherent properties of the electrospinning process, which can control the deposition of nanofibers onto a target substrate, complex 3-D nanofiber areas can be formed. Nanofibers of blends of PANI camphorsulfonate and PEO have a minimum fiber diameter of 5 nm [31]. Nanofibers of pure PANI doped with sulfuric acid (H_2SO_4) show conductivity of a single fiber of $\sim 0.1\ S\ cm^{-1}$, and average and a minimum fiber diameters of 139 nm and 96 nm, respectively [29].

Ultrasonication

Branched conducting PANI-NFs buried in the crystals of camphorsulfonic acid (CSA) have been prepared from *m*-cresol solution of granular PANI and excessive CSA [40]. After the

CSA was dissolved through ultrasonication in deionized water, networks of PANI-NFs with spherical nodes, nanoparticles, leaf-vein-shaped nanofibers, etc. were obtained, depending on the strength of the ultrasonic treatment. PANI–CSA nanofibers having diameters 1–2 nm were produced by bath sonication of aqueous dispersions of larger nanofibers (30–50 nm diameter) [41].

Spin Coating

Thin films of parallel undoped PANI-NFs have been deposited by spin coating an *N*-methyl pyrrolidone solution of undoped PANI [42], synthesized by MacDiarmid's method [43], on freshly cleaved highly oriented pyrolytic graphite. These PANI-NFs films preserved nanostructured morphology upon doping with CSA, while the ordering was almost entirely lost upon doping with hydrochloric acid (HCl). Thin films of parallel PANI-NFs doped with CSA have also been prepared by spin coating of *m*-cresol solution of PANI-CSA [42].

2.2.1.2 Chemical Oxidative Polymerization of Aniline

Hard (Physical) Template Methods

***Nanoporous Hard-Template Method*:** The standard hard-template method is an effective and straightforward route for fabricating PANI-NFs with diameters determined by the diameter of the pores in the template [44]. Conducting PANI-NFs have been synthesized in a 3-nm-wide hexagonal channel system of the aluminosilicate MCM-41 [45]. Adsorption of aniline vapor into the dehydrated host, followed by reaction with peroxydisulfate, led to encapsulated PANI-NFs in the protonated emeraldine salt form, with chain lengths of several hundred aniline rings. Uniform and ordered PANI-NFs were prepared within the anodic aluminum oxide (AAO) template [46–48], and polycarbonate (PC) track-etched membrane [48]. PANI-NFs with lengths from sub-micrometre to several micrometres and with diameters 20–250 nm were formed via the selection of pore diameter, monomer, counterions, and synthetic conditions [49]. PANI-NFs were prepared by the oxidative polymerization of aniline with sodium chlorite in an acidic aqueous suspension of diatomite [50]. The holes in porous diatomite acted as a template at the early stage of polymerization. The porous structure of diatomite was destroyed during the polymerization due to the transformation of silica in diatomite to silicic acid, which served as a dopant in the final nanofibrillar composite material.

The disadvantages of the nanoporous hard-template method are the generally tedious post-synthetic processes, which are required in order to remove the templates, and the destruction of nanostructures during the post-synthetic process, i.e. the formation of undesirable aggregated structures after removal of the templates.

***Nanostructured Seed Template Method*:** Seeding an ordinary chemical oxidative polymerization of aniline with very small amounts (usually $<1\%$) of nanofibers (inorganic or organic), and single-walled carbon nanotube (SWCNT) bundles, changes the morphology of the nonfibrillar PANI emeraldine salt quantitatively to nanofibers having an average diameter in the range 20–60 nm, as has been revealed by scanning (SEM) and transmission (TEM) electron microscopies (Figure 2.2) [51]. The general shape of the seed (nanofibers vs. nanospheres) controls the overall morphology of the resulting precipitate, while differences in the length, diameter, etc., of the nanostructured seed templates do not

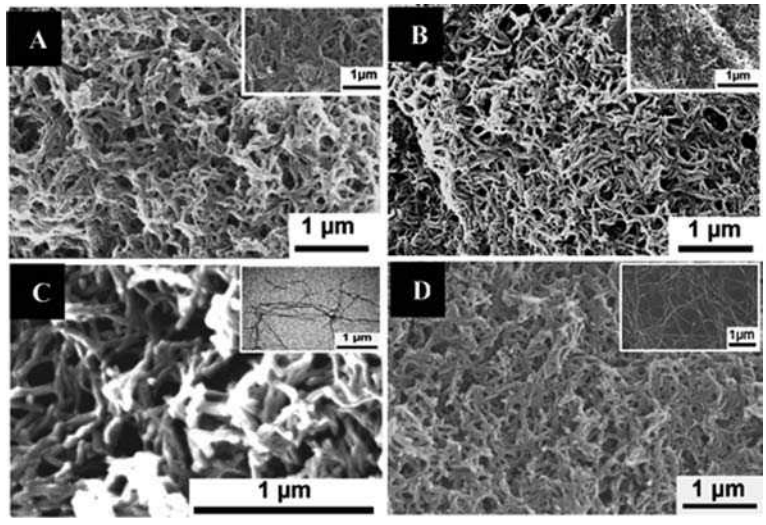

Figure 2.2 *SEM images of emeraldine-HCl nanofibers synthesized by seeding the reaction using the following: (A) 1.5 mg of emeraldine-HCl nanofibers (SEM image inset), (B) 1.6 mg of HiPco SWNTs (SEM image inset), (C) 1.0 mg of the hexapeptide AcPHF6 (TEM image inset), and (D) 4 mg of V_2O_5 nanofibers (SEM image inset) [51]. (Reprinted with permission from Journal of the American Chemical Society, Synthesis of Polyaniline Nanofibers by "Nanofiber Seeding" by Zhang, Goux and Manohar, 126, 14, 4502–4503. Copyright (2004) American Chemical Society)*

have a significant impact. It has been revealed that stirring of the reaction solution has a dramatic effect on the morphology of PANI synthesized by the nanostructured seed template method [52]. It was found that when no stirring is applied, a large amount of new nanofibers appear in the product, while the morphological change of the pre-added fibers is unremarkable. In contrast, if the reaction is stirred, granular nanoparticles will gradually grow on the pre-added fibers and the surface roughness and thickness of the pre-added fibers increase with the addition of the oxidant, leading to the formation of coral-like fibers. PANI-NFs were also synthesized using SWCNTs [53], chlorophyllin nanorods [54], and composite nanofibers of methyl orange/ferric chloride ($FeCl_3$) [55], as nanostructured seed templates.

PANI nanostructures formed (or present) during the very early stages of the polymerization govern bulk formation of similar nanostructures. It has been proposed that polymerization first occurs on the surface of the nanofiber template whose morphology is mirrored by the growing polymer chain [51]. A film of pernigraniline salt has been formed on the walls of the reaction flask, magnetic stir bar, etc., well before any precipitate was observed in bulk. This *in situ* deposited film of fibrillar pernigraniline salt can then seed fresh polymer growth, triggering a continuous seeding process that results in a bulk precipitate in which the nanoscale morphology of the original seed template is transcribed over many length scales.

***Nanostructured Template Method*:** HCl-doped PANI-NFs having a long nanosize fibril structure have been prepared by an inverse microemulsion polymerization process using

nanosize Ni particles as inorganic template [56]. By using barium ferrite nanoparticles of different morphologies as nucleation sites, PANI-NFs/barium ferrite nanocomposites with novel coralloid structures were synthesized [57]. Cage-like ferromagnetic PANI-NFs/cobalt ferrite composite nanostructures, in which PANI-NFs (minimum diameter ~15 nm) entwined around an octahedral cobalt ferrite magnet acting as the nucleation site or template, were obtained by using $FeCl_3$ as oxidant and dopant [58]. Nanocomposites of PANI nanorods and multi-walled carbon nanotubes (MWCNTs) coated with PANI were prepared by *in situ* aniline polymerization in the presence of MWCNTs and perchloric acid ($HClO_4$) as nanostructured template and dopant, respectively [59]. PANI nanorods have recently been synthesized by the oxidation of aniline with APS in the presence of silicotungstic acid using Cu nanowires as the template [60].

Soft (Chemical) Template Methods

The soft-template methods are based on the use of structure-directing molecules, such as various soluble oligomers and polymers, as well as surfactants and amphiphilic acids which are able to form, alone or with aniline, aggregates such as cylindrical micelles, and other supramolecular 1-D aggregates.

***Oligomer- and Polymer-Assisted Synthesis*:** Chiral PANI-NFs (minimum diameter 20 nm) have been synthesized by the oxidative polymerization of aniline, with incremental addition of APS as an oxidant, in concentrated CSA solutions in the presence of aniline oligomers [61,62]. When aniline dimer 4-aminodiphenylamine (4-ADPA) was added to the polymerization of aniline, the produced nanofibers were longer and less entangled than those typically observed [63]. The addition of 4-ADPA can even induce nanofiber formation under synthetic conditions that generally do not favor a nanofibrillar morphology, e.g. in concentrated aqueous solutions (5M) of salts such as sodium chloride, or in nonaqueous solvents (acetonitrile). Self-dispersible conducting PANI-NFs were synthesized by the oxidative polymerization of aniline in the presence of oligosaccharide β-cyclodextrin [64,65].

Granular PANI powder dissolved in dimethyl sulfoxide was used as a template to induce the polymerization of aniline and hence to prepare PANI-NFs having a conductivity of $\sim 35\ S\ cm^{-1}$ [66]. PANI-NFs were synthesized in the presence of poly(acrylic acid) (PAA) [67,68]. 'Flower-like' dendritic superstructure comprising of densely packed PANI-NFs was obtained when polymerization was templated by a water-soluble polyelectrolyte copolymer poly(acrylamide-co-acrylic acid) as the dopant and support matrix [69]. Poly(3-thiopheneacetic acid) was used both as a dopant and template to prepare PANI-NFs by the oxidation of aniline with APS and $FeCl_3 \cdot 6H_2O$ [70]. The diameter, crystallinity and conductivity of the prepared PANI-NFs were strongly affected by the oxidant. In particular, the diameter of the nanofibers obtained by using $FeCl_3 \cdot 6H_2O$ was measured to be 20–30 nm, which was significantly thinner than that of the PANI-NFs obtained by using APS (130 nm). Yu *et al.* demonstrated a facile route to the synthesis of large quantities of uniform PANI alginate nanofibers guided by sodium alginate as a biopolymeric template [71]. Deoxyribonucleic acid (DNA)-templated PANI-NFs and their networks were synthesized using the oxidative polymerization of aniline with APS [72], hydrogen peroxide/horseradish peroxidase (H_2O_2/HRP) [72–74], $FeCl_3 \cdot 6H_2O$ [75], or by photo-oxidation using a Ru complex as photo-oxidant [72]. A novel method for facile synthesis of uniform straight PANI-NFs (nanosticks) by the oxidative polymerization of aniline with APS in

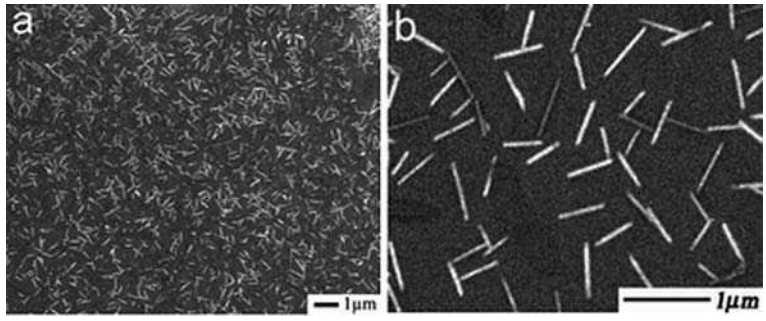

Figure 2.3 *Typical SEM images of PANI synthesized in cholic acid/PEG 400 hydrogel: (a) low magnification; (b) high magnification. (Reprinted with permission from Macromolecules, Facile Synthesis of Straight Polyaniline Nanostick in Hydrogel by L. Meng, Y. Lu, X. Wang et al., 40, 2981–2983. Copyright (2007) American Chemical Society)*

an acidic hydrogel system, in the presence of cholic acid/poly(ethylene glycol) (PEG) 400 complex as hydrogelator, has recently been reported (Figure 2.3) [76]. Ordered PANI-NFs arrays were obtained in the presence of high concentrations (11 M of one repeat unit) of poly(vinyl alcohol) (PVA) [77]. Promoting mass transfer for the polymerization carried out under very low aniline concentration in a high-viscosity aqueous system, created by dissolving a high-molecular-weight PEO, was beneficial for the preparation of uniform PANI-NFs [78].

***Surfactant- and Amphiphilic Acid-Assisted Synthesis*:** PANI-NFs have been prepared by oxidative polymerization of aniline in the presence of nonionic surfactants (Triton X-100) [79,80], anionic surfactants (sodium dodecylsulfate (SDS)) [81,82], cationic surfactants (cetyltrimethylammonium bromide (CTAB)) [83], a mixture of ionic surfactants (CTAB and sodium dodecylbenzenesulfonate (SDBS)) [84], amphiphilic ionic liquid (1-hexadecyl-3-methylimidazolium chloride) [85], and amphiphilic acids e.g., 4-{n-[4-(4-nitrophenylazo)-phenyloxy]propyl}-aminobenzenesulfonic acid, where n = 2, 3, 4, 6, 8, or 10 [86,87], azobenzenesulfonic acid [88], β-naphthalenesulfonic acid (β-NSA) [89–94], dodecylbenzenesulfonic acid (DBSA) [91], *p*-aminobenzenesulfonic acid (*p*-ABSA) [95], *p*-toluenesulfonic acid (*p*-TSA, Figure 2.4) [92,96,97], CSA [92], 4-[4-hydroxy-2((*Z*)-pentadec-8-enyl)phenylazo]benzenesulfonic acid [98–101], 4-(3-dodecyl-8-enylphenyloxy)butanesulfonic acid [102], Allura Red AC [103], monosulfonated dendrons [G_3-SO_3H, $12G_2$-SO_3H] [104], saturated fatty acids [105,106], dicarboxylic acids [107,108], amino acids [109], salicylic acid [110,111], acrylic acid [112], perfluorosebacic acid [113,114], and perfluorooctanesulfonic acid [115]. The use of a mixture of surfactants and acids is known to be effective, especially in the production of 3-D PANI-NF networks [116] and PANI-NF-covered rectangular PANI submicrotubes [117]. The PANI-NFs have also been obtained by the oxidative polymerization of aniline with APS in a CTAB–lauric acid complex coacervate gel template [118]. Parallel arrays of PANI-NFs have been synthesized on atomically flat surfaces using adsorbed aggregates of surfactant molecules and aniline as templates [119]. The formation of PANI-NFs in the presence of amphiphilic acids was found to depend mostly on the initial acid/aniline ratio.

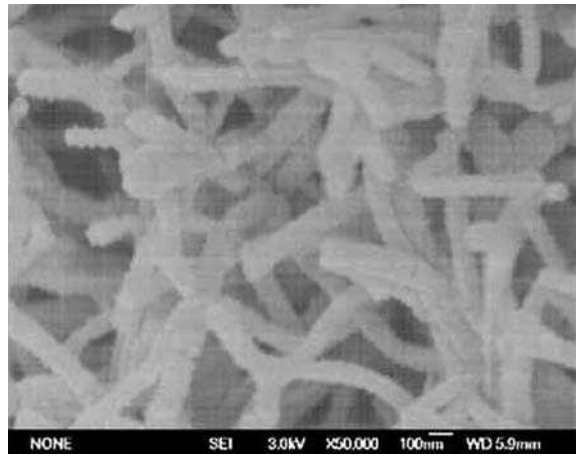

Figure 2.4 *SEM image of the PANI-NFs doped with* p-*TSA; [APS]/[aniline] = 1:1, reaction time = 12h; [aniline] = 0.2 M, [acid]/[aniline] = 0.5:1. (Reprinted with permission from Macromol. Rapid Commun., Nanoscaled Polyaniline Fibers prepared by ferric chloride as an oxidant by L. Zhang, M. Wan and Y. Wei, 27, 366–371. Copyright (2006) Wiley-VCH)*

Micelles of amphiphilic acids and/or corresponding aniline salts were tentatively proposed to interpret the formation of PANI-NFs and other nanostructures. The formation of supramolecular aggregates was indicated by dynamic light-scattering (DLS) measurements in the case of NSA [89] and 4-[4-hydroxy-2((*Z*)-pentadec-8-enyl)phenylazo]-benzenesulfonic acid [100,101], and by the dependance of the concentration on emission intensity of a luminescent dopant in the case of 4-[4-hydroxy-2((*Z*)-pentadec-8-enyl)phenylazo]-benzenesulfonic acid [99]. However, the existence of cylindrical micelles under an applied concentration range of acids has never been unambiguously proved for the investigated amphiphilic acid/aniline systems. The most recent indirect proof of the existence of cylindrical micelles in an aqueous solution of aniline and 4-[4-hydroxy-2((*Z*)-pentadec-8-enyl)phenylazo]- benzenesulfonic acid [101] was based on TEM images of rod-like nanocrystallites found in dried sample.

Nanofibers of self-doped PANI have been synthesized by the oxidation of aniline with APS in an aqueous solution in the presence of *o*-ABSA [120,121] and *m*-ABSA [122]. Helical PANI-NFs were prepared by using chiral CSA as a dopant [123]. Chiral PANI-NFs (nanorods) and Au microspheres, which can be easily separated, were obtained by the oxidative polymerization of aniline with potassium tetrachloroaurate(III) in the presence of (+)-CSA [124]. PANI hollow microspheres containing PANI-NFs (20–30 nm in diameter) were prepared by inversed microemulsion polymerization in the presence of NSA as dopant [125]. Electromagnetic functionalized PANI composites of microspherical hydroxyl iron magnet (core) and PANI–NSA nanofibers (shell) were prepared [126]. Synthesis of dendritic PANI-NFs in a surfactant gel was performed by Li *et al.* [127]. Nanocomposites containing PANI nanorods and magnetite (Fe_3O_4) nanoparticles were synthesized by DBSA-assisted synthesis [128]. Combined amphiphilic acid-assisted and hard-template synthesis of highly oriented PANI-NFs, growing out of the nanoporous

template, was performed through 4-{3-[4-(4-nitrophenylazo)phenyloxy]propyl}-aminobenzenesulfonic-acid-assisted oxidative polymerization of aniline with APS in the presence of a hydrophilic track-etched nanoporous alumina template [129]. The length of these nanofibers can be roughly controlled by the polymerization time.

Template-Free Methods

It is now clear that PANI-NFs are naturally formed during chemical oxidative polymerization of aniline in aqueous solutions [52,130–132]. It was found that PANI-NFs are formed as soon as the polymerization begins (Figure 2.5b), upon slow addition of the oxidant/dopant solution to the aniline/dopant solution (Figure 2.5a) [130]. Since the nanofibers are exposed to aniline and oxidant, they are subject to secondary growth. Agglomerates of PANI particles accompanied by a few nanofibers are found as a consequence of severe secondary growth (Figure 2.5c). It was concluded that if secondary growth can be suppressed, the yield of PANI-NFs in the final product could be greatly increased. By suppressing the secondary growth of irregular particles, through a not-shaken–not-stirred method, aqueous/organic interfacial polymerization, rapid-mixing reactions, dilute polymerization, etc., essentially pure PANI-NFs can be obtained.

***Not-Shaken–Not-Stirred Method*:** Highly dispersible PANI-NFs can be reproducibly prepared from a conventional reaction simply by not mechanically agitating the reaction and carrying it out at an elevated temperature (Figure 2.6) [52]. It was shown that

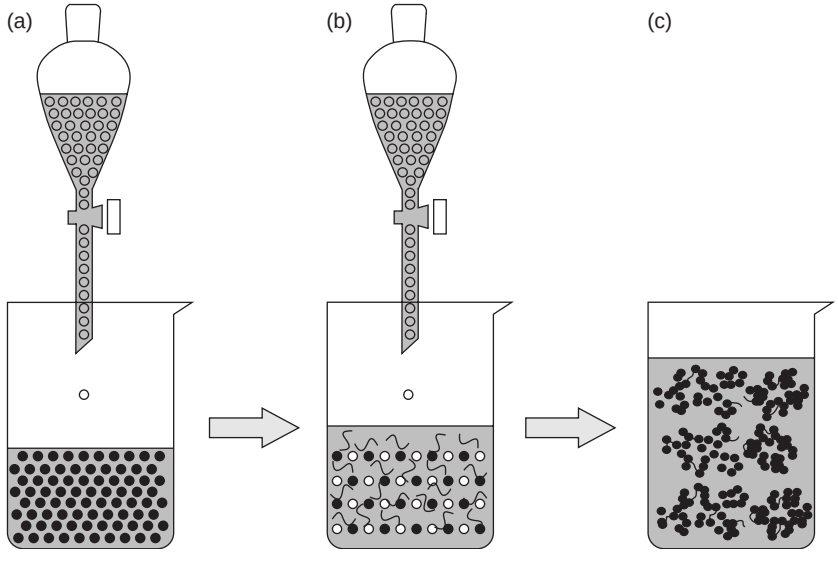

Figure 2.5 *Schematic diagram illustrating the formation of PANI agglomerates during conventional chemical synthesis [the oxidant (open circles), aniline (solid circles)]. (Reprinted with permission from Angewandte Chemie Int. Ed., Nanofiber formation in the chemical polymerization of aniline: A mechanistic study by J. Huang and R. B. Kaner, 43, 5817–5821. Copyright (2004) Wiley-VCH)*

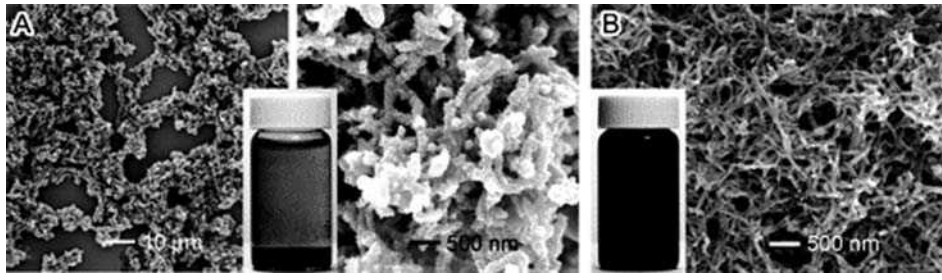

Figure 2.6 *SEM images of PANI synthesized by reacting aniline in 1.0 M HCl with APS in 1.0 M HCl at 25 °C. (A) The APS solution was added dropwise into the stirred aniline solution. (B) The APS solution was added dropwise into the aniline solution without stirring. (Reprinted with permission from the Journal of the American Chemical Society, Shape and Aggregation Control of nanoparticles: Not shaken, not stirred by D. Li and R. B. Kaner, 128, 968–975. Copyright (2006) American Chemical Society)*

mechanical agitation, usually a common method for disrupting aggregates, unexpectedly triggered aggregation of PANI during the course of the synthesis. The study of the effect of the reaction temperature on the size of the resulting PANI-NFs has shown that nanofibers obtained in the absence of stirring at low temperatures (0 °C) have rough surfaces and are accompanied by granular particulates. In contrast, there are almost no granular particulates in product prepared at elevated temperatures (60 °C) [52].

The behavior of nucleation of PANI nanoparticles plays a crucial role in the aggregation of the resulting particulates. It was revealed that nanofibers, characterized by smooth surfaces and fairly uniform sizes, were exclusively formed at the initial stage of conventional polymerization as a result of homogeneous nucleation [52]. As the polymerization proceeds under shear, granular nanoparticulates gradually grow on these nanofibers (heterogeneous nucleation), leading to the formation of coral-like aggregates. The observation that a considerable amount of granular nanoparticulates appear in product prepared with stirring suggested that stirring favors heterogeneous nucleation. It has been suggested that the molecules to be nucleated will form transient nanoscale ordered regions or embryos prior to nucleation. Stirring could destroy these transient ordered regions or dilute local concentrations of PANI molecules, thereby decreasing the probability of homogeneous nucleation. It has been noticed that the PANI chains in nanofibers have more extended conformation in comparison with granular PANI. Mechanical shear is likely able to make the PANI chains in the solution more coiled, hindering homogeneous nucleation. On the other hand, mechanical shear could enhance collisions between embryonic nuclei and the preformed particles or the reactor surfaces, which may decrease the activation energy of heterogeneous nucleation and thereby facilitate this mode of nucleation. In addition, mechanical agitation also enhances mass transfer in the reaction solution and makes newly formed PANI molecules diffuse toward preformed particles faster, leading to greater probability of heterogeneous nucleation. The observation of the nucleation behavior of PANI under shear enabled Li and Kaner [52] to propose a new aggregation mechanism for PANI particles. At the initial stage, as PANI-NFs form in solution via homogeneous nucleation (Figure 2.7) they will be forced to collide with each

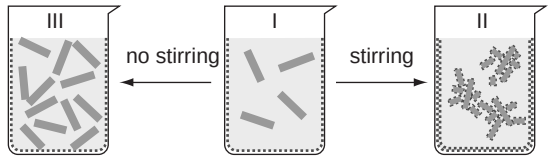

Figure 2.7 *Schematic illustration of the formation and aggregation of PANI particles. The green fibers and purple dots represent PANI particles that result from homogeneous and heterogeneous nucleation, respectively. (Reprinted with permission from the Journal of the American Chemical Society, Shape and Aggregation Control of nanoparticles: Not shaken, not stirred by D. Li and R. B. Kaner, 128, 968–975. Copyright (2006) American Chemical Society)*

other due to mechanical shear and Brownian motion. Under shear, heterogeneous nucleation occurs on the surfaces of these particles, including the contact points of the preformed particles. The nuclei at the collision points will function like a nanoscale glue to link the particles together, causing aggregation of the preformed particles. Subsequent growth of the nuclei and the formation of new heteronuclei on their surfaces will further solidify the aggregation. In contrast, in the absence of stirring, heterogeneous nucleation is suppressed and the nanofibers are produced continuously and therefore well dispersed.

***Aqueous/Organic Interfacial Polymerization*:** The polymerization is performed in an immiscible organic (carbon tetrachloride, benzene, toluene, or carbon disulfide)/aqueous biphasic system to separate the byproducts (inorganic salts, oligomers, etc.) according to their solubility in the organic and aqueous phases [133]. The PANI-NFs have lengths extending from 500 nm to several micrometers. The average diameter of the nanofibers can be tuned by the type of acid, e.g. from 30 nm using HCl to 120 nm using $HClO_4$ (Figure 2.8) [131]. Gram-scale products can be synthesized that contain almost exclusively nanofibers (>95%), which tend to agglomerate into interconnected nanofiber networks rather than bundles. The synthesis is easily scalable and reproducible. It has been demonstrated

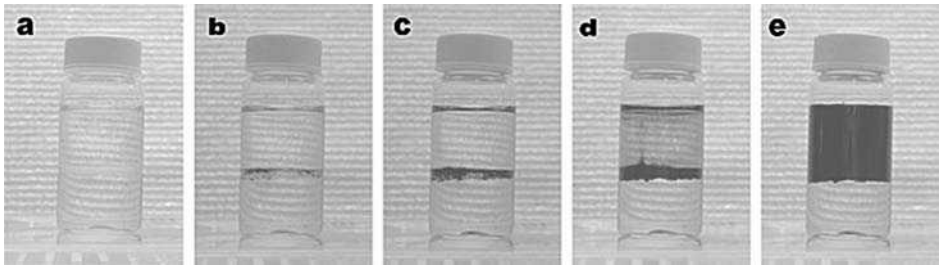

Figure 2.8 *Snapshots showing interfacial polymerization of aniline in a water/chloroform system. From (a) to (e), the reaction times are 0, 1.5, 2.5, 4, and 10 min, respectively. The top layer is an aqueous solution of 1.0 M $HClO_4$ and APS; the bottom layer is aniline dissolved in chloroform. (Reprinted with permission from Journal of the American Chemical Society, A General Chemical Route to Polyaniline Nanofibers by J. Huang and R. B. Kaner, 126, 3, 851–855. Copyright (2004) American Chemical Society)*

[131,134] that the interfacial polymerization method is a very general route to create PANI-NFs. The shape and size of the nanofibers does not appear to be affected by the solvent. Therefore, an organic solvent that is heavier than water (methylene chloride, etc.) is preferred due to safety considerations, since the water layer seals the organic vapor within the reaction vessel. The syntheses can be accomplished in one pot with a wide choice of reagent concentrations over a broad range of temperatures. The major disadvantages of interfacial polymerization are low synthetic yields (6–10 wt %) and the waste stream of organic solvents that must be treated.

It was observed that the reaction time significantly affects the morphology of PANI-NFs [135,136]. A three-phase system (organic solvent/paraffin oil/water) was also used in an interfacial polymerization [137]. The morphology and the average diameter of PANI-NFs obtained by interfacial polymerization can be controlled by using surface-active dopants and/or surfactants in the aqueous phase [138–140]. In the modified interfacial polymerization method, aniline dissolved in xylene was directly added into the aqueous solution of the oxidant with stirring [141]. The polymerization was carried out at the interface formed between the organic liquid drops and the water. A simple, two-step process for the synthesis of conducting PANI-NFs bound directly to the surface of an Au substrate, using an interfacial polymerization technique, has been reported [142]. PANI-NFs were prepared by an interfacial method in the presence of HCl [135,143–150], HCl and SDS [151], $HClO_4$ [152–154], CSA [53], poly(styrenesulfonic acid) (PSSA) [155,156], DL-tartaric acid [157], DBSA [158], *p*-TSA [159], cerium(IV) oxide nanoparticles [160], and magnesium carbonate particles [161]. Long PANI-NFs with lengths of up to tens of microns, bundled together by single PANI-NFs with diameters of ca. 3–5 nm, were prepared by the interfacial chemical oxidative copolymerization of aniline dimers 4-ADPA and 2-ADPA [162]. Ag nanoparticle/PANI-NF and Pt nanoparticle/PANI-NF nanocomposites were generated by the interfacial oxidative polymerization of aniline with silver methanesulfonate and hexachloroplatinic acid, respectively [149].

The measurement of *in situ* UV-visible spectra showed the existence of 'expanded and partly doped' macromolecular intermediates in the interfacial polymerization of aniline [163,164]. It was hypothesized that the expanded macromolecular conformation performed a macromolecular template function in the formation of PANI-NFs. Interfacial polymerization represents an effective method for suppressing secondary growth of irregular PANI particles i.e. heterogeneous nucleation [130]. Assuming that the aniline and the oxidant (APS) are efficiently separated by the boundary between the aqueous and the organic phase, it was first proposed that the interfacial oxidative polymerization occurs only at this interface, where all the components needed for polymerization come together. PANI then forms as nanofibers. Since these newly formed nanofibers are in the doped emeraldine salt form, they are hydrophilic and can rapidly move away from the interface and diffuse into the water layer. In this way, as the nanofibers form they are continuously withdrawn from the reaction front, thus avoiding secondary growth and allowing new nanofibers to grow at this interface. However, investigation of the effect of stirring on the interfacial polymerization of aniline has indicated that the interfacial polymerization of aniline is much more complex process [52]. It was realized that aniline dissolved in an organic phase can easily migrate into the aqueous acidic phase. Thus, the reaction is similar to conventional polymerization of aniline, in which an aniline solution is added dropwise into the oxidant solution. The essential reason for the formation of high-quality

PANI-NFs with this method is the fact that the reaction is not stirred. It can be concluded that interfacial polymerization without stirring represents a special case of the not-shaken–not-stirred method. A recent morphological study of the formation of PANI-NFs has revealed a crucial influence of the aniline concentration on the morphology of the product of interfacial polymerization of aniline [165]. It was found that at relatively low concentration of aniline (≤0.05 M), pure nanofibers can be isolated at all stages of interfacial polymerization, indicating that the interface effectively prevents secondary growth of PANI, while the higher aniline concentration (≥0.1 M) enhances the diffusion rate of aniline from the organic phase into water phase. This leads to a rapid increase in the aniline concentration in water, and the secondary growth of PANI is inevitable, resulting in a larger-sized PANI product. It has recently been assumed that in interfacial polymerization the situation at the interface corresponds roughly to polymerization in an acidity range pH 2.5–4.0, i.e. the polymerization includes the stage of slow accumulation of phenazine nucleates [166]. The formation of initiation centres for chain growth is reduced and the phenazine nucleates are able to self-assemble into columns or stacks, representing supramolecular aggregates formed *in situ*, which govern further PANI-NF growth.

***Rapid-Mixing Method*:** This method is based on the idea of the consumption of all the reactants during the primary growth of PANI-NFs. The secondary growth will be greatly suppressed since no reactants will be available for further reaction. To achieve this goal, the acidified oxidant (APS) solution is added into the acidic aqueous solution of aniline all at once [130,134], rather than slowly feeding it in by titration or syringe-pumping. Sufficient mixing should be achieved (magnetic stirrer or shaker) to evenly distribute the oxidant and aniline molecules before polymerization. Fast-mixing reactions carried out at different temperatures (8 °C, 20 °C, 100 °C) all yielded high-quality nanofibers (Figure 2.9). Rapid-mixing reactions in less polar solvents have produced less perfect

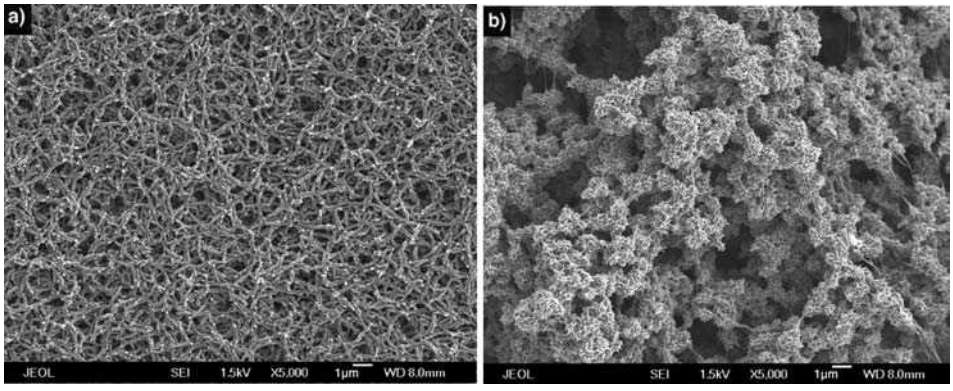

Figure 2.9 *SEM images showing the morphology of PANI synthesized from (a) a rapidly mixed reaction and (b) a slowly mixed reaction. High-quality nanofibers are obtained in the rapidly mixed reaction, while irregular agglomerates form in the slowly mixed reactions. (Reprinted with permission from Angewandte Chemie Int. Ed., Nanofiber formation in the chemical polymerization of aniline: A mechanistic study by J. Huang and R. B. Kaner, 43, 5817–5821. Copyright (2004) Wiley-VCH)*

nanofibers, due to the decrease of the affinity of the hydrophylic PANI emeraldine salt for the solvent, indicating that water is the best solvent for the synthesis of nanofibers. PANI-NFs were successfully prepared by simply introducing an initiator into a rapidly mixed reaction between aniline and oxidant [167]. Recent morphological studies on the formation of PANI-NFs films [168] and powders [165] have revealed a crucial influence of the aniline concentration on the morphology of the product of the rapid-mixing polymerization of aniline. At lower concentration of aniline (0.005 M) pure nanofibers were isolated at all stages of rapid-mixing polymerization, while at higher aniline concentration (0.05 M) the diameters of the nanofibers increased with increasing reaction time, and the fiber surfaces became coarser, indicating the growth of PANI-NFs [165]. At the end, mixtures of large-sized irregular PANI particles and agglomerates of PANI-NFs with larger diameters were obtained. A morphological study of a rapid-mixing polymerization with an aniline concentration of 0.5 M showed that, though the initially formed products were all PANI-NFs, only the final PANI products prepared by using a low molar ratio of APS/aniline (0.25–0.50) and low temperature (0 °C) were nanofibers [169]. Two-dimensional network structures of PANI-NFs on solid substrates coated with Au nanoparticles and modified with 4-aminothiophenol were recently obtained by rapid mixing of aniline and APS solutions [170].

***Dilute Polymerization*:** PANI-NFs have been successfully synthesized by chemical oxidative polymerization of aniline at a substantially lower concentration of aniline (≤0.01 M) [171–173], compared with that used to synthesize granular PANI powders (0.1–0.4 M) [1]. It was demonstrated that different dopant acids produced PANI-NFs with similar length ranges up to several micrometers, and similar morphologies – nanofiber structures of interconnected networks. The diameters of the PANI-NFs were tunable by the appropriate selection of dopant acids. During dilute polymerization, aligned PANI-NFs were simultaneously formed on the available substrates present in the reaction mixture [174]. It was revealed that a decrease in the concentration of aniline/APS leads to the formation of less branched PANI-NFs with larger diameters [132]. A 'stirring effect' for dilute polymerization was observed. For the same synthetic conditions, stirred solutions yielded shorter nanofibers with smaller diameters. Nonfibrous particulates were found in all nanofibrillar PANI samples. The quantities of particulates increased with the concentration of aniline/APS. It was proved that the morphology of PANI-NFs was strongly dependent on the concentrations of both monomer and oxidant. The combination of the dilute polymerization method with soft-template methods is also known. Thus, PANI-NFs were synthesized by surfactant-assisted chemical oxidative polymerization of aniline in dilute aqueous organic acids [41,175]. High-yield synthesis (85%) of conducting PANI-NFs by the slow addition of an acidic (HCl) aqueous solution of aniline to a vigorously stirred acidic (HCl, CSA, $HClO_4$, H_2SO_4 and PA120) aqueous solution of APS (pseudo highly dilute conditions) has recently been developed [176].

Large, colorless aggregates were observed by static and dynamic light-scattering measurements during the induction period of an oxidative polymerization of aniline with APS in dilute acidic aqueous solutions [177]. These aggregates are believed to be dianilinium peroxydisulfate ion clusters whose shape (rod-like) plays an important role in the initial formation of PANI-NFs. The formation of the interconnected, branched nanofiber networks by dilute polymerization was explained as follows [171]. Competition between a

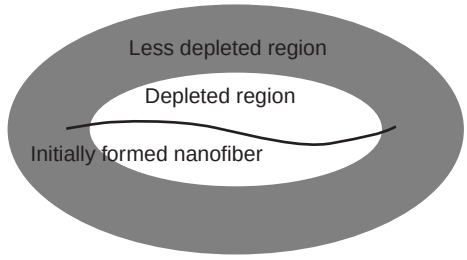

Figure 2.10 *Schematic representation of the growth and elongation of an initially formed nanofiber in a dilute solution. (Reprinted with permission from Synthetic Metals, A Simple Approach to Control the Growth of Polyaniline Nanofibers by N.-R. Chiou and A. J. Epstein, 153, 69–72. Copyright (2005) Elsevier Ltd)*

directional nanofiber growth process and formation of additional nucleation centers takes place in the case of high aniline concentrations in solution. Once a high density of nucleation centers is generated, the interfacial energy between the reaction solution and nanofibers may be minimized, and hence rapid precipitation occurs in a disordered manner, yielding irregular shapes. In a dilute solution, the number of nucleation sites formed on the surface of the nanofibers may be reduced, thus allowing PANI to grow only as a 1-D nanostructure. In general, molecules of aniline and oxidants are depleted in the vicinity of initially formed nanofibers in the initial stage of polymerization (Figure 2.10).

It has been proposed that PANI-NFs are able to continuously grow and elongate in one direction because their ends extend to the less depleted regions (Figure 2.10) [132]. The formation of PANI-NFs by dilute polymerization has also been explained on the basis of the proposed organization of the phenazine nucleates into stacks or cylindrical structures [166]. It was proposed that short and structurally uniform oligomers, i.e. phenazine-containing aniline trimers, are produced under acidic conditions. The growth rate of short oligomers to higher oligomers is low due to the low concentration of aniline. Because of that, during the extended induction period, nucleates self-assemble into columns or stacks, which represent templates formed *in situ* for further PANI-NF growth during the single exothermic phase.

***Photo-Assisted Synthesis*:** Thin films of PANI-NFs have been synthesized using UV irradiation of aqueous solutions of aniline, nitric acid (HNO_3), and APS [178]. UV-irradiation was used in the one-step fabrication of a PANI-NF vapor sensor [179]. The synthesis of PANI-NFs under UV light illumination at lower temperatures has also been reported [180]. The acceleration effect of photo-assistance on the polymerization can promote homogeneous nucleation and elongation of the nanofibers, leading to easy preparation of PANI-NFs with tuneable diameters. Chiral PANI-NFs were easily prepared with low aniline concentrations, at higher CSA concentrations, at room temperature, without stirring, and with UV-light illumination [181]. Well-confined uniform PANI-NFs were synthesized by using photo-assisted chemical oxidative polymerization of aniline in the presence of different dopant acids [182].

***Radiolythic Synthesis*:** PANI-NFs can be produced by irradiating aqueous solutions of aniline, APS, and HCl with γ-rays [183]. This template-free radiolytic synthesis of PANI-NFs can be carried out completely in an aqueous phase. The synthesized PANI is virtually

entirely nanostructured, with the presence of less than 5% of globular PANI structures. Composite materials consisting of PANI-NFs decorated with noble-metal (Ag or Au) nanoparticles have also been synthesized with γ-radiolysis [184,185]. The mechanism of formation of the PANI-NFs appears to be related to the formation, during irradiation, of hollow spheres, which coalesce in a way reminiscent of diffusion-limited colloidal aggregation [183].

***Sonochemical Synthesis*:** Ultrasonic irradiation has been applied to the synthesis of PANI-NFs in a conventional oxidant dropwise addition [186–188]. An ultrasonic irradiation-assisted polymerization method was used to prepare PANI-NFs by using high concentrations of mineral or organic acid [189]. The diameter of nanofibers ranged from about 50 nm using HNO_3, to more than 110 nm with $HClO_4$ as the dopant. The sonochemical method was combined with the not-shaken–not-stirred method and surfactant-assisted synthesis [99]. PANI-NFs were successfully prepared sonochemically with H_2O_2 as the oxidant [190]. A single-step sonochemical procedure to synthesize hybrid vanadium(V) oxide (V_2O_5)/PANI-NFs, starting from crystalline V_2O_5 and aniline in aqueous medium, was presented [191]. The graphite nanosheets/PANI nanorods composites were fabricated via ultrasonic polymerization of aniline in the presence of graphite nanosheets [192]. PANI-NFs were chemically prepared through ultrasonic irradiated polymerization with varying ultrasonic power, frequency, and reaction temperature. It was found that PANI-NFs with smoother surfaces and uniform diameters could be achieved by increasing the ultrasonic power or the reaction temperature in the studied ranges; a higher reaction temperature was also beneficial for producing PANI-NFs with larger aspect ratios [193].

***Solid-State Mechanochemical Synthesis*:** Facile template-free solid-state mechanochemical synthesis of highly branched PANI-NFs with coralloid tree-like superstructure, via the oxidative polymerization of aniline hydrochloride with $FeCl_3 \cdot 6H_2O$, has been demonstrated [194]. The synthetic yield (~8%) was comparable to that of the solution interfacial polymerization method. Solid-phase mechanochemical synthesis of branched PANI-NFs was also achieved by using anhydrous $FeCl_3$ as the oxidant [195].

***Dopant-Free Template-Free Method*:** The oxidative polymerization of aniline with APS, starting in an alkaline aqueous solution and finishing at $pH < 2$ due to the formation of H_2SO_4 as the by-product, was the first example of dopant-free template-free synthesis of PANI-NFs (nanorods) [196]. The influence of the initial alkali concentration and reaction temperature on the morphology of PANI-NFs, prepared by alkali-guided synthesis, has been studied [197]. A simple way to quantitatively prepare well-controlled PANI-NFs by changing the redox potential of the oxidants in the oxidative polymerization of aniline, in water without added acid, has recently been revealed [198]. It has been observed that the diameter of the nanofibers (d) significantly decreases with decreasing redox potential of the oxidants (E_{ox}). An experimental formula has been established:

$$\log d = 0.69 + 0.71\, E_{ox} \tag{2.1}$$

According to this formula, for a given oxidant the resultant nanofiber diameter can be predicted. The dopant-free template-free method not only provides a quantitative way of controlling the diameter of the PANI-NFs, but also simplifies the reagents. PANI-NFs were successfully prepared by using the dopant-free template-free method through the

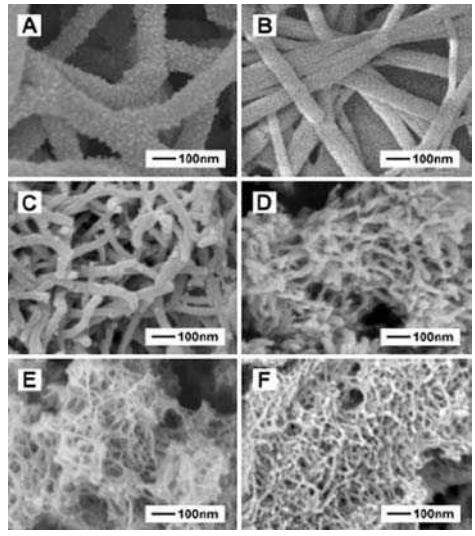

Figure 2.11 *SEM images of the PANI-NFs prepared by using the dopant-free template-free method in the presence of different oxidants: (A) APS/aniline = 1, the average outer diameter* d *is ca. 130 nm; (B)* H_2O_2*/aniline = 10,* d ≈ *85 nm; (C) cerium(IV) sulfate/aniline = 2,* d ≈ *45 nm; (D)* $FeCl_3$*/aniline = 3,* d ≈ *18 nm; (E) ferric sulfate/aniline = 4,* d ≈ *13 nm; (F) cupric chloride/aniline = 6,* d ≈ *12 nm. Synthesis conditions: aniline = 0.1 M, reaction temperature: 0–5 °C; reaction time: 15 h. (Reprinted with permission from Advanced Materials, Controlling the diameter of polyaniline nanofibers by adjusting the oxidant redox potential by H. Ding, M. Wan and Y. Wei, 153, 69–72. Copyright (2007) Wiley-VCH)*

oxidation of aniline with APS, cerium(IV) sulfate, $FeCl_3$, ferric sulfate, cupric chloride, and H_2O_2 (Figure 2.11). Chiou *et al.* have reported a successful synthesis of a highly uniform, relatively long PANI-NFs via a self-assembly process assisted by the presence of excess oxidant (APS), without the use of any acid in the initial step [199]. When the oxidative polymerization of aniline was carried out with APS in dilute aniline aqueous solution ($\sim 10^{-2}$ M) in the absence of any doping acid, a micromat of PANI-NFs with hierarchical structure was obtained [200]. 3-D rose-like microstructures of PANI, which are self-assembled from 2-D nanosheets consisting of 1-D nanofibers, were synthesized by the dopant-free template-free method in the presence of APS as both oxidant and dopant under a high relative humidity of 80% [201]. A chemical one-step method, which represents a modified dopant-free template-free method, has been proposed to prepare electromagnetic functional composite PANI/Fe_3O_4 nanofibers, with a diameter of 20 nm, which show high conductivity and super-paramagnetic properties [202]. In this approach $FeCl_3$ acts as the oxidant and dopant in synthesis of PANI, as well as the precursor for the synthesis of Fe_3O_4.

***Hydrophobic Surface Method*:** Manohar's group proved that the nature of available surfaces, such as the walls of the reaction vessel, magnetic stir bar, etc., play an important role in PANI-NF formation [203]. Since rod-like aggregates, formed in systems that

yielded PANI-NFs [177] would be highly hydrophobic, it was suspected that the presence of hydrophobic surfaces can promote the formation of PANI-NFs. Therefore a conventional PANI synthesis was carried out in a glass vessel containing a rolled-up hydrophobic sheet of poly(ethylene terephthalate) (PET) [203]. It was observed that the reaction rate increased significantly, and the morphology changed dramatically, from granules, which were formed without the presence of PET sheet, to entirely PANI-NFs. The reaction was initiated on the PET surface, as evidenced by the dark blue color of *in situ*-deposited pernigraniline film that was much thicker than corresponding films on a glass surface.

***Miscellaneous Template-Free Methods*:** Self-assembled PANI-NFs have been prepared by the oxidative polymerization of aniline with APS in an acidic aqueous solution in the presence of HCl [172,204–206], HCl and ethanol [207], HCl and colloidal Au particles [208], H_2SO_4 [204], *o*-phosphoric acid (H_3PO_4) [204], H_3PO_4 and Fe_3O_4 nanospheres [209], HNO_3 [210], tetrafluoroboric acid [204], $HClO_4$ [59], selenious acid [211], hydrophilic organic acids, e.g., oxalic acid [112], citric acid [112], tartaric acid [112], and 5-sulfosalicylic acid [212], PEG [213], molybdic acid [214], and gadolinium chloride [215]. Rod-like nanostructures, as well as nano/microspheres with rod-like nanostructures pointing out to the sphere surface, have recently been prepared by the oxidation of aniline with APS in citrate/phosphate buffer (pH = 3) [216,217]. Since the oxidation was performed under slightly acidic conditions (pH >2), known to be favorable for aniline oligomerization rather than polymerization, this interesting nanostructured material could be referred as oligoaniline rather than PANI. Besides the most frequently used APS as the oxidant in the preparation of PANI-NFs, facile template-free syntheses of PANI-NFs in an acidic aqueous solution using chloroauric acid [218], $FeCl_3$ [92,205,206,219,220], vanadic acid [221], V_2O_5 [222], H_2O_2 [223,224] and silver nitrate [225] (Figure 2.12) as the oxidants, have also been reported. Self-assembled

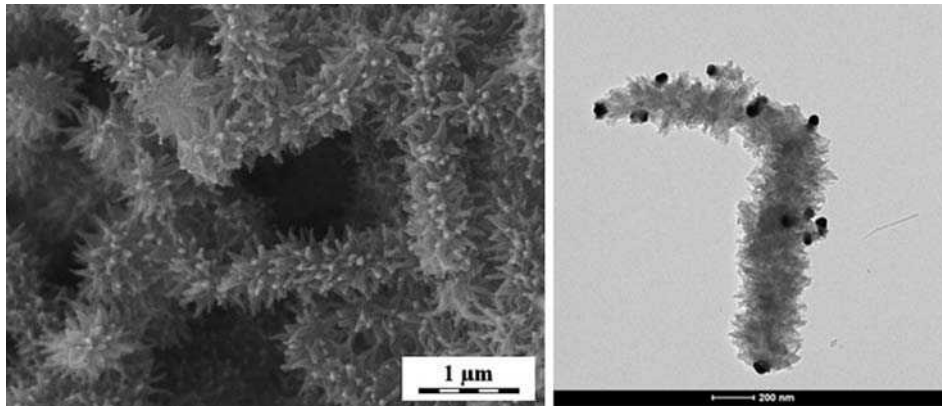

Figure 2.12 *SEM (left) and TEM (right) of PANI-NFs–Ag composite; 0.2 M aniline was oxidized with 0.5 silver nitrate in 0.4 M HNO_3. (Reprinted with permission from Polymer, The oxidation of aniline with silver nitrate to polyaniline-silver composites by N. V. Blinova, J. Stejskal, M. Trchova et al., 50, 1, 50–56. Copyright (2009) Elsevier)*

PANI-NFs with long lengths were prepared by co-use of APS and sodium hypochlorite [226]. PANI-NFs synthesized by using both potassium biiodate and sodium hypochlorite as oxidants showed high electrical conductivity greater than $100\,S\,cm^{-1}$ [227]. When *p*-phenylenediamine was used as an additive for the chemical polymerization of aniline, an increased polymerization rate resulted in improvements to the nanofibers formed [63]. It has been shown that the addition of phenol assisted the deaggregation of PANI chains during the template-free growth of PANI-NFs [228]. High-molecular-weight PANI, synthesized by combining a neutral salt technique with MacDiarmid's method, showed a mass of honeycombed clews, which are tenuous, interconnected PANI fibrillar networks with characteristic cross-sectional fibril dimensions of a few tens of nanometers [229]. HCl-doped PANI-NFs were chemically prepared by adding inorganic salts (e.g. lithium chloride, sodium chloride, magnesium chloride, and aluminium chloride) as the additives via a self-assembly process, and aggregated to form chrysanthemum flower-like microstructures [230]. A simple method based on chemical polymerization under centrifugal forces was used to achieve synthesis of large particles of PANI-NFs [231]. Thin PANI-NFs of 20 nm diameter connecting the submicrometre PANI particles were observed when the template-free polymerization took place in ice, in the presence of both strong (H_2SO_4) and weak acids (acetic acid) [232]. Self-doped PANI-NFs have been prepared by chemical polymerization of *m*-anilineboronic acid in 1-propanol [233]. A template-free approach to synthesize aligned PANI-NF arrays with individual fiber diameters of ~100 nm, lengths of ~600 nm and a packing density of ~40 pieces μm^{-2} on a passivated Au substrate via a facile wet chemical process has been reported [234]. The Au surface was first modified using 4-aminothiophenol, followed by the oxidation of aniline with APS in an aqueous medium in the presence of tartaric acid.

2.2.1.3 Electrochemical Oxidative Polymerization of Aniline

Electrosynthesis provides an effective and convenient approach to the production of PANI-NFs and other nanostructures [235]. The resulting nanostructures are usually oriented on the electrode surfaces and their properties are easily controlled.

Electrochemical Template Methods

An AAO template-based electrochemical process [236] has been adopted to fabricate PANI-NFs by using an AAO membrane [237], a composite AAO/Au electrode attached to a stainless steel [238] or a Pt sheet [48,239], or an AAO template on a Ti/Si substrate [240], as the working electrode. It was shown that the morphologies of PANI-NFs synthesized electrochemically in AAO membranes were better than those synthesized in PC track-etched membranes [48]. The morphology of PANI-NFs grown electrochemically in AAO templates was found to be strongly influenced by the supporting electrolyte concentration, the potential of the electropolymerization, the growth time, and the monomer concentration [241]. Increasing the H_2SO_4 concentration during growth induces a transition from solid nanofibers with tubular ends to open nanofibers. Current transient data for nanofiber growth were interpreted quantitatively in terms of instantaneous and progressive nucleation and growth models, and this analysis was consistent with the observed concentration and potential dependence of nanofiber vs. nanotube growth. It was emphasized that anodization and electropolymerization can occur at the same time in a single

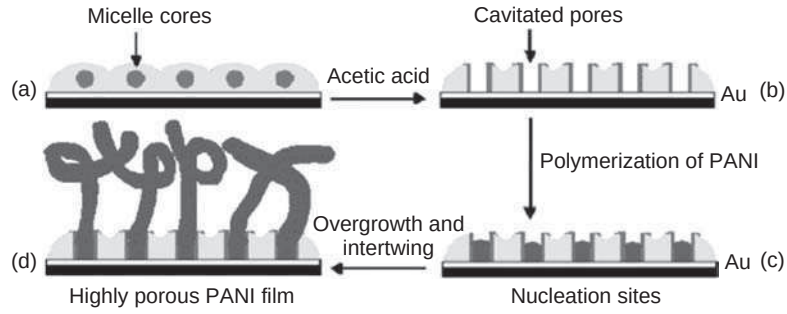

Figure 2.13 *Schematic illustration of the process of fabricating a porous PANI-NF film by a galvanostatic method using porous poly(styrene-block-2-vinylpyridine) diblock copolymer films as templates. (Reprinted with permission from Langmuir, One-Step Route to the Fabrication of Highly Porous Polyaniline Nanofiber Films by Using PS-b-PVP Diblock Copolymers as Templates by X. Li, S. Tian, Y. Ping et al., 21, 21, 9393–9397. Copyright (2005) American Chemical Society)*

electrochemical process [242]. PANI-NF–Au core-shell nanostructures have been fabricated electrochemically within AAO membranes [243]. A galvanostatic method to control both the nucleation and growth of highly porous PANI nanofiber films, using porous poly(styrene-block-2-vinylpyridine) (PS-b-PVP) diblock copolymer films as templates, was also reported (Figure 2.13) [244]. Highly dense arrays of ordered and aligned PANI-NFs on indium tin oxide (ITO) substrate, found to exhibit excellent electrochemical capacitance of 3407 $F\,g^{-1}$, have been fabricated using supramolecular assemblies of block copolymer as scaffold material [245].

It was found that 5,10,15,20-tetrakis(4-sulfonatophenyl)porphyrin [246] and Co-porphyrin [247], which are known to aggregate in a one-dimensional direction in water, acted as soft templates for electrochemical polymerization of aniline to PANI-NFs on ITO and glassy carbon electrodes, respectively. A technique for the patterning of conducting PANI-NFs on metallic (Au, Pt) substrates was also reported [248,249]. Electrochemical template-free synthesis of PANI-NFs was initially preceded by the formation of a thin compact 2-D layer, which had been spread horizontally from the edge of an Au electrode across a silica float-glass surface. This encumbered nanofiber patterning during the fabrication of nanofiber devices, since it led to electrical short-circuiting of the metal contacts before the nanofibers had fully developed. The use of amine-terminated self-assembled monolayers, 3-aminopropyltriethoxysilane, to inhibit the spread of PANI-NFs growth onto adjacent silica float-glass surfaces was also demonstrated.

The electropolymerization of aniline on both DNA monolayer and single poly(dG)–poly(dC) DNA molecules, leading to the PANI-NFs, was reported [250]. The synthesis includes the formation of an electrostatic complex between the negatively charged DNA and positively charged anilinium ions, followed by electrochemical oxidation and polymerization of the anilinium ions on the DNA template. The polymerization was carried out on a flame-annealed Au substrate modified with a positively charged self-assembled 4-aminothiophenol monolayer.

Electrochemical Template-Free Methods

***Voltammetric Methods*:** PANI-NFs of interconnected network-like structures have been prepared by electrochemical oxidation of aniline in an aqueous ethanol solution of HCl [251] and an aqueous solution of potassium nitrate/ HNO_3 at pH = 0 [252], using the cyclic voltammetry method. PANI-NFs with different sizes were synthesized by using cyclic-voltammetry at different potential scan rates, in the presence of ferrocenesulfonic acid [253,254] and CSA [255]. The potential scan rate controls the formation and growth of PANI nuclei, which plays a key role in controlling nanofiber sizes. PANI-NFs were also fabricated by a combined potentiodynamic electrodeposition and mechanical break junction method [256], and potentiodynamic electropolymerization from surfactant sodium bis(2-ethylhexyl) sulfosuccinate reverse hexagonal liquid crystalline phase [257]. PANI deposited by potentiodynamic technique on porous carbon substrate was found to possess a network morphology of nanofibers, and superior capacitance properties [258]. Potentiodynamic electrochemical synthesis was used to controllably synthesize PANI-NFs with a mean diameter of 48 nm on Au electrodes [259]. Hybrid films of PANI and manganese oxide with an open nanofibrous structure, for electrochemical supercapacitors, were obtained through potentiodynamic deposition from solutions of aniline and manganese(II) sulfate at pH 5.6 [12]. γ-Manganese(IV) oxide (γ-MnO_2) nanoparticle-coated PANI-NFs on carbon electrodes were prepared by potentiodynamic deposition of PANI and MnO_2 from a single pot [260]. A standard pulse voltammetric method was used to synthesize PANI-NFs in HCl solution on a Pt electrode [261]. Self-doped PANI-NFs were deposited on Pt electrodes by a reverse pulse voltammetric method [262].

***Potentiostatic Methods*:** A potentiostatic method has been used to synthesize PANI-NFs deposited on stainless steel electrodes [263–265] and in an acidic aqueous solution containing methanol [266]. High-quality nanofibrous PANI film was synthesized on Ti electrodes from an aqueous solution of aniline and HNO_3 by a pulse potentiostatic method [267]. PANI-NFs were also prepared by a template-free constant potential method on a stainless steel electrode [268]. Both the hydrophilicity and the lipophilicity of the modified stainless steel surface were enhanced by the nanostructured PANI, and a super-amphiphilic surface was obtained in this way.

***Galvanostatic Methods*:** Conducting PANI-NFs have been grown galvanostatically on Au electrodes modified with self-assembled monolayers of well-separated thiolated cyclodextrins in an alkanethiol 'forest' [269]. Thiolated aniline monomer was anchored to the surface within the cyclodextrin cavity and formed an initiation point for PANI-NF growth. Large-scale oriented PANI-NFs have been synthesized by one-step galvanostatic deposition on an Al electrode in the presence of oxalic acid [270]. The use of template-free electrochemical polymerization at low and constant current levels to fabricate individual PANI-NFs of controlled dimension and high aspect ratio between Au electrodes [271], or PANI-NF–electrode junctions, in which a number of PANI-NFs of uniform diameter intertwine to form nanoframeworks between Pt electrodes [272,273], has been described. PANI-NFs with interconnected network-like structures have also been electrochemically prepared on stainless steel substrates by galvanostatic electrolysis [274]. PANI and gels (mixtures of oligomer, dopant, and aniline) have been formed simultaneously during

electrochemical deposition. The gels play an important role in the formation of PANI-NFs. The PANI formed in the early stage of polymerization was subject to secondary growth along one dimension, since the nucleation sites were suppressed by the wrapped gels. The film of PANI-NFs was deposited onto the surface of a stainless steel electrode through galvanostatic polymerization of aniline, undoped [275,276] or doped with PSSA by a sequential doping–dedoping–redoping process [277], resulting in a PANI-NF or PANI-NF/PSSA spatial matrix, respectively, and utilized for the fabrication of Pt particle-loaded catalyst electrode for the oxidation of methanol. PANI-NF/carbon black nanocomposites have been prepared by the galvanostatic oxidative polymerization of aniline in the presence of $HClO_4$ and carbon black [278]. Thin films of the interconnected network of PANI-NFs have been fabricated galvanostatically from an aqueous solution of the monomer encompassing the ionic liquid, 1-ethyl-3-methylimidazolium bromide [279]. It was demonstrated that PANI–Ag nanocomposite prepared by chronopotentiometry in water-in-ionic liquid microemulsion was nanofibrous with homogeneously dispersed Ag nanoparticles (∼5 nm diameter) [280].

Miscellaneous Electrochemical Methods

Fully sulfonated PANI-NFs have been synthesized by electrochemical polymerization of orthanilic acid using a three-step electrochemical deposition procedure in a mixed solvent of acetonitrile and water [281]. The uniform oriented PANI-NFs were prepared through controlled nucleation and growth during a stepwise electrochemical deposition process in which a large number of nuclei were first deposited on the substrate using a large current density. After the initial nucleation, the current density was reduced stepwise in order to grow the oriented nanowires from the nucleation sites created in the first step [282,283]. A stepwise deposition method was employed to create ordered conducting PANI-NFs with remarkably enhanced capacitance compared with those prepared by a one-step deposition method [284]. The unsymmetrical square-wave current method, which is characterized by the combination of an anodic aniline polymerization and a cathodic metal electrodeposition, was used to produce a nanocomposite film of PANI-NFs and Ag nanoparticles [285]. A novel template-free process was developed to synthesize the PANI-NFs using a controlled multipotential method [239]. Self-doped PANI microrings of PANI-NFs have been successfully generated electrochemically (Figure 2.14) [286]. The PANI-NFs forming rings had a diameter of 100 nm, and the ring diameter was tunable from several to dozens of micrometers, depending on used current densities. The bubble template formation mechanism of the microrings was proposed. PANI-NFs doped with [60]fullerene have been prepared by an electrochemical method in an aqueous medium at pH ∼1 through a copolymerization process of aniline and *o*-, *m*-, and *p*-aminobenzylamine-C_{60} derivatives [287–289].

The formation of PANI-NFs during electrochemical polymerization has been attributed to the combined effect of an electrophilic substitution reaction mainly taking place at the *para* position of aniline or its oligomers, and aniline oligomers with 1-D structures [290]. It was discovered that the PANI film formed on the electrode exhibited a lamellar structure. Firstly, a thin compact 2-D PANI layer was formed during the initial stage of electrodeposition. Subsequently, microgranular, nanorod-shaped, and nanofibrillar PANI layers were formed from bottom to top, respectively.

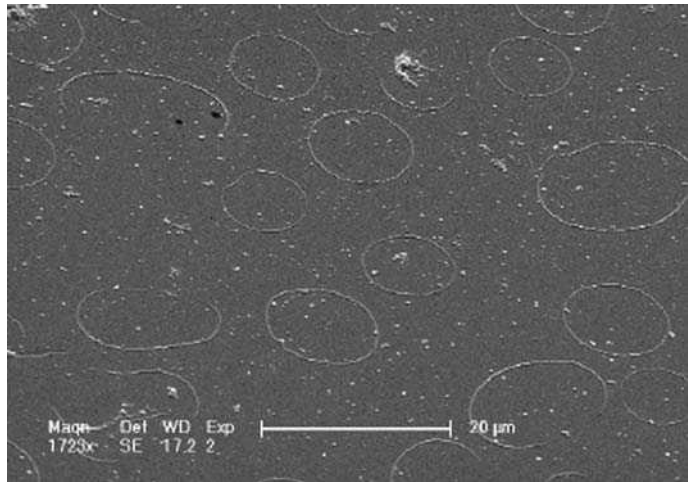

Figure 2.14 *SEM image of microrings electrodeposited at current density of 10 mA cm^{-2} for 45 min in aqueous solutions of 0.05 M aniline hydrochloride and 0.05 M o-ABSA. (Reprinted with permission from Nanotechnology, Direct electrochemical generation of conducting polymer micro-rings by J. Song, D. Han, L. Guo and L. Niu, 17, 824–829. Copyright (2006) Institute of Physics)*

2.2.1.4 Miscellaneous Methods

Thin films of PANI oligomers can be gradually converted into thick conductive PANI-NFs films doped with HCl and HNO_3, using a two-pot alternate oxidation of oligoanilines with APS and reduction of formed pernigraniline-like oligoanilines with aniline [291]. PANI-NFs have been prepared by the oxidation of aniline with V_2O_5 in water without added acid, followed by the reaction of the obtained nanocomposite powder with hexadecylamine in ethanol solution, and hydrothermal treatment [292,293]. Dissolved granular PANI emeraldine base forms a nanofibrous inclusion complex with α-cyclodextrin [294,295], and a mixture of α-cyclodextrin and α,ω-diamino-PEG [296]. Since the conducting PANI-NFs were fully covered by α-cyclodextrin molecular nanotubes as an insulator, these inclusion complexes were regarded as insulated molecular wires. Nanofibrous PANI films were prepared by chemical oxidative polymerization of aniline on Si substrates, which were surface modified by amino-silane ($(CH_3O)_3$—Si—$(CH_2)_3NH(CH_2)_2$—NH_2) self-assembled monolayers [297]. A novel strategy was developed in order to prepare PANI-NFs on polymer substrates [298,299]. The strategy involved two main steps, i.e. a grafting polymerization of acrylic acid onto the surface of a polypropylene film and a subsequent oxidative polymerization of aniline on the grafted surface. In these structures, the PAA brushes not only acted as templates, but also as dopants of PANI, and thereby the PANI-NFs could be strongly bonded with the substrate. An ice-templating method has recently been developed to prepare PANI microflakes stacked by uniform PANI-NFs with diameters in the range 22–32 nm [300]. A post-synthetic method for producing PANI-NFs of various doping (oxidation) states, by simultaneous doping and electrodeposition from electrolyte solutions of granular PANI *p*-toluenesulfonate, using constant applied voltage

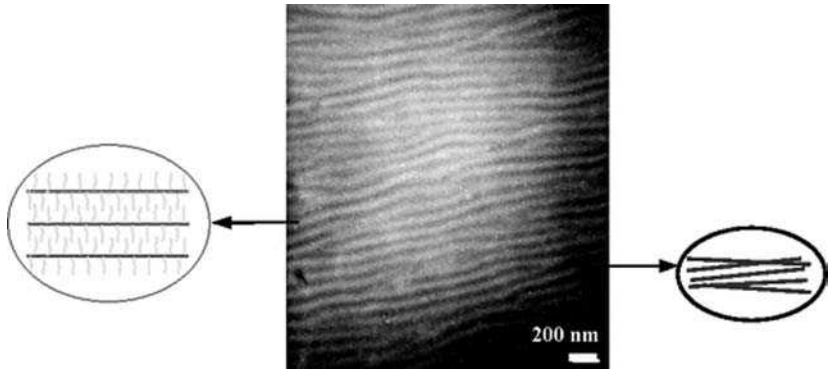

Figure 2.15 *The highly oriented conducting PANI-NFs formed in the complexes of the PANI emeraldine base with a phosphoric acid-terminated PEO (from Table of Contents of Reference 302). (Reprinted with permission from Macromolecules, Highly Oriented Nanowires from the Hierarchical Self-Assembly in Supramolecular Complex of Polyaniline with ω-Methoxypoly(ethylene oxide) Phosphates by B. Nandan, J.-Y. Hsu, A. Chiba et al., 40, 3, 395–398. Copyright (2007) American Chemical Society)*

and varying deposition time, was recently presented [301]. The highly oriented conducting PANI-NFs were formed by an unique hierarchical self-assembly of the complexes of the emeraldine base form of PANI with a phosphoric acid-terminated PEO (Figure 2.15) [302]. The Langmuir–Blodgett technique was explored to produce dopant (CSA and *p*-TSA)-induced nanostructures, especially nanorods and nanoparticles of the conducting PANI emeraldine salt on a Si substrate [303]. An easily scalable method for the production of self-doped PANI-NFs through functionalization of PANI-NFs by post-polymerization reflux in the presence of a nucleophile has been reported [304]. The extent of carboxylate side-chain attachment was controlled simply by altering the amount of nucleophile added during reflux. An efficient method for fabricating PANI-NFs (50–80 nm in diameter and up to few tens of micrometers in length) at room temperature on a microsecond timescale was demonstrated by the irradiation of the freestanding PANI film with the pulsed electron beam (10–200 keV) of a plasma focus device [305]. A nanofibrous PANI thin film was also fabricated using a plasma-induced polymerization method [306]. Uniform thin films containing PANI-NFs have recently been fabricated by a flash dry deposition method [307]. A mixture of PANI nanorods and nanoparticles was prepared by passing aniline vapor through an aqueous acidic solution of APS [308].

2.2.2 Preparation of Polyaniline Nanotubes

2.2.2.1 Chemical Oxidative Polymerization of Aniline

Hard (Physical) Template Methods

***Nanoporous Hard-Template Methods*:** PANI-NTs have been prepared by the chemical oxidative polymerization of aniline within the pores of PC nanoporous membranes

[48,309–314]. The PC membrane was used as a dividing wall in a two-compartment cell containing separated aqueous solutions of aniline and oxidant [309–311]. The aniline and the oxidant diffuse toward each other through the pores of the PC membrane and react, to yield the PANI-NTs. At short polymerization times, a thin skin of PANI lines the pore walls. With increasing polymerization time, the PANI grows in thickness. In the case of the single-compartment cell [48,312–314] it was found that the PANI is first formed in the polymerization solution (the solution containing the monomer and oxidant, where the PC membrane is placed), and then it precipitates within the nanopores of the PC membrane [312,313]. A highly ordered PANI-NT array was prepared by the oxidative polymerization of aniline with APS using a nanoporous AAO template [48,315]. An array of PANI-NTs was synthesized by chemical oxidative polymerization of aniline in the pores of an alumina membrane, and then an alumina/PANI-NTs membrane was used as a second-order template for electrodeposition of Fe [316], Co [317], or Ni nanowires [318] within the PANI-NTs. A route for producing PANI-NTs using inner eggshell membrane and fiber mats imitating eggshell membrane (electrospun PVA fiber mats), as a template, was demonstrated [319]. It was found that the pore size of the template played a key role in the formation of the PANI-NTs. When the pore size of the PVA fiber mats is similar to that of the inner eggshell membrane, PANI-NTs can be obtained. A facile approach to the synthesis of conducting PANI-NTs decorated with uniform dispersed Ag nanoparticles, using an UV-irradiation method and nitrocellulose fiber mats as a suitable template in the presence of silicotungstic acid, has recently been reported [320]. Silver nitrate was used as a single oxidant in this work. Compared with other methods, the nitrocellulose fiber mats template can be easily removed, while the PANI/Ag tubular morphology remains.

***Nanostructured Hard-Template Method*:** The use of sulfonated MWCNTs [MWCNT—$(OSO_3H)_n$] as the template for the formation of PANI-NTs has been reported [321]. PANI-NTs doped with MWCNT—$(OSO_3H)_n$ were synthesized by the oxidation of aniline with APS in an aqueous dispersion of MWCNT—$(OSO_3H)_n$, using an initial ratio of aniline/MWCNT—$(OSO_3H)_n \geq 2$. A MnO_2 template-based fabrication technique for PANI-NTs has also been reported [322]. The templates used were cryptomelane-phase (β and ε) MnO_2 nanowires, and β-MnO_2 nanotubes. These nanostructured templates shaped the PANI-NTs and also acted as an oxidant in the aniline polymerization. This effect causes the template to be spontaneously removed after the reaction, because the MnO_2 is reduced to soluble Mn^{2+} ions, whereas the aniline is oxidatively polymerized. PANI-NTs were successfully prepared by using thin glass tubes as a single template in the presence of silicotungstic acid and APS, which were used as dopant and oxidant, respectively [323]. The method employed here was a simple and effective way to prepare multifunctional PANI-NTs. The uniform PANI-NTs were prepared successfully by using natural tubular aluminosilicates as templates [324]. The halloysite nanotubes were coated with PANI via *in situ* chemical oxidative polymerization and the templates were then etched with HCl/hydrofluoric acid solution. PANI-NTs were also prepared by dissolution of the PMMA core of PANI/PMMA nanocables (PANI hydrogen-sulfate-coated PMMA nanofibers) in chloroform [37]. The PMMA can also be melted by heating the fibers up to 150 °C. PANI-NTs with Pd nanoparticles attached onto their inner walls were synthesized via a three-step nanostructured hard-template method [325]. First, sulfonated electrospun polystyrene (PS) nanofibers were coated with Pd nanoparticles through *in situ* reduction of Pd^{2+}

ions on the surface of sulfonated PS nanofibers. Afterwards a self-assembly method was used to coat the composite with a PANI layer. The final product was obtained by dissolution of the sulfonated PS nanofibers in tetrahydrofuran. Self-assembled peptide (diphenylalanine) nanofibers [326] and electrospun nitrocellulose nanofibers [327] were also used as a template for the synthesis of PANI-NTs.

Soft (Chemical) Template Methods

***Surfactant- and Amphiphilic Acid-Assisted Synthesis*:** PANI-NTs have been prepared by the oxidative polymerization of aniline with APS in an aqueous solution in the presence of SDS [82,328], SDBS [329], a mixture of ionic surfactants (CTAB and SDBS) [204], polymeric acids [330] e.g. poly(methyl vinyl ether-alt-maleic acid) [331–334] (Figure 2.16), poly(3-thiopheneacetic acid) [70], PSSA and PAA (Figure 2.16) [333],

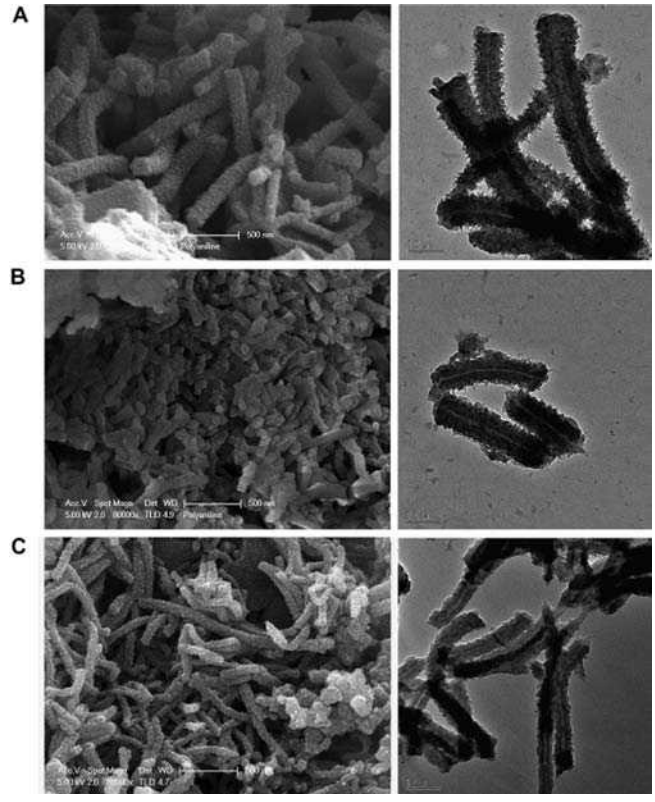

Figure 2.16 *SEM and TEM images of PANI-NTs obtained from solutions that contained different polymeric acids: (A) PSSA, (B) PAA and (C) poly (methyl vinyl ether-alt-maleic acid). The synthesis conditions were 0.1 M aniline, 2 wt% of the polyacid, which were reacted for 16 h at 3°C. (Reprinted with permission from Current Applied Physics, Polyaniline nanotubes doped with polymeric acids by L. Zhang, H. Peng, J. Sui et al., 8, 3–4, 312–315. Copyright (2008) Elsevier Ltd)*

and amphiphilic acids e.g. 4-{n-[4-(4-nitrophenylazo)phenyloxy]propyl}-ABSA (n = 2, 3, 4, 6, 8, or 10) [86,87], fullerenol with six —OSO_3H groups [$C_{60}(OSO_3H)_6$] [335], a sulfonated dendrimer containing 24 terminal groups of 3,6-disulfonaphthylthiourea (PAMAM4.0-[naphthyl$(SO_3H)_2]_{24}$) [335], a monosulfonated dendron [G_3-SO_3H] [104], β-NSA [89,93,336,337], α-NSA [337], 1,5-naphthalenedisulfonic acid [337], azobenzenesulfonic acid [88], CSA [338–343], 2-acrylamido-2-methyl-1-propanesulfonic acid [344], 4-[4-hydroxy-2((Z)-pentadec-8-enyl)phenylazo]-benzenesulfonic acid [99,101], DBSA [345,346], naphthol blue black [347], salicylic acid [328,348], stearic acid [106], propionic acid [349], acetic acid [232,350–354], dicarboxylic acids [107], and amino acids [109,330,355,356]. PANI-NTs were synthesized from different aqueous buffer solutions of aniline [citric acid/phosphate (pH 3 and pH 4) and HCl/phthalate (pH 3)] in the presence of the amino acid alanine [357]. The probability of nanotube formation during the amphiphilic acid-assisted synthesis depended on various factors, such as the aniline concentration, amphiphilic acid/aniline ratio, oxidant/monomer ratio, reaction temperature, and reaction time. The PANI-NTs have also been obtained by the oxidative polymerization of aniline with APS in a CTAB–lauric acid complex coacervate gel template [118]. Optically active PANI-NTs have been prepared in the presence of (S)-(–)-2-pyrrolidone-5-carboxylic acid and (R)-(+)-2-pyrrolidone-5-carboxylic acid [358], as well as L-CSA and D-CSA as chiral dopants [359]. Nanotubes of self-doped PANI were synthesized by the oxidation of aniline with APS in an aqueous solution, in the presence of 5-aminonaphthalene-2-sulfonic acid [360], *o*-ABSA [121,361,362], *m*-ABSA [363], and 1-amino-2-naphthol-4-sulfonic acid, which were incorporated into PANI chains [364]. Nanocomposites containing PANI-NTs accompanied with PANI-NFs, and Fe_3O_4 nanoparticles [365,366], titanium dioxide (TiO_2) nanoparticles [367,368], a mixture of TiO_2 nanoparticles and Fe_3O_4 microparticles [369,370], a mixture of TiO_2 nanoparticles with SWCNTs or MWCNTs [371], and Au nanoparticles [208] were synthesized by amphiphilic acid (β-NSA, CSA, hexanoic acid)-assisted synthesis. Stearic acid-assisted preparation of PANI-NTs/clay nanocomposite has recently been reported [372].

The mechanism of formation of PANI-NTs in the presence of amphiphilic acids is still open to discussion. The formation of PANI-NTs in the presence of amphiphilic acids has been found to be highly susceptible to the initial acid/aniline ratio (the initial pH). PANI-NTs are formed only for selected compositions with an aniline surplus, i.e. where there was a mixture of nonprotonated aniline and its salt in aqueous solution (slightly alkaline, neutral, or slightly acidic conditions) at the beginning of polymerization. When acid is in substantial surplus (highly acidic reaction solutions) PANI-NTs are not formed. Cylindrical micelles of aniline salts with amphiphilic acids have been tentatively proposed by Wan's group to govern the formation of PANI-NTs and other nanostructures [89], which is why the surfactant- and amphiphilic acid-assisted synthesis is frequently referred to as the micelle soft-template method. It is supposed that the core of micelle is made up of hydrophobic bulky groups of amphiphilic acids, while the shell of micelle is made up of the anions (sulfonate, carboxylate) of amphiphilic acids and anilinium cations. The nonprotonated aniline diffuses into micelles forming aniline-filled micelles. The initial concentration of nonprotonated aniline and the initial pH value, i.e. the initial [amphiphilic acid]/[aniline] ratio, will influence the initial size of micelles. DLS results have shown that the average diameters of the initially formed micelles, as well as the average diameters of the finally formed PANI-NTs decreases with decreasing initial [amphiphilic acid]/[aniline]

ratio. When oxidant (APS) diffuses into the aniline-filled micelles, polymerization of nonprotonated aniline molecules will occur in the micelles. It has been proposed that the anilinium cations on the surface of the micelles can also be oxidized. As the polymerization proceeds, the micelles can form large spheres through accretion or tubes/fibers through elongation, depending on the local reaction conditions. It was assumed that if the polymerization reaction on the surface of the micelles dominates, nanotubes will be obtained; otherwise, nanofibers are formed. It was concluded that the polymerization process on the surface of the micelles combined with the elongation process dominates in the case of PANI-NT synthesis. As additional indirect evidence that micelles govern the formation of PANI-NTs by the oxidative polymerization of aniline in the presence of amphiphilic acids, it was noticed that the diameter of PANI-NTs depends on the ionic strength of reaction solution and the polarity of the solvent, parameters known to have significant influence on micelle size. Xia *et al.* [347] have also tentatively proposed cylindrical micelles of aniline salts with amphiphilic acids as the structure-directing supramolecular aggregates which govern the growth of PANI-NTs. It should be noted that, contrary to this micellar mechanistic approach, it was found that a surfactant function of the dopant is not a prerequisite for the formation of PANI-NTs [204]. It was proved that the addition of the surfactant and its concentration only affected the size of PANI-NTs.

Stejskal's group criticized the concept of micellar templates and pointed out that the existence of cylindrical template micelles had been assumed, but their presence had never been proven [350]. In addition, the observed inner diameter of the PANI-NTs is much larger than the diameter of the potential micelles produced by aniline salts, unless they were considerably swollen with aniline base. It was recognized that the morphology of PANI, granular or tubular, depends on the acidity profile of the reaction rather than on the chemical nature of the acid (Figure 2.17). It was proposed that, during the course of aniline oxidation, pH-dependent self-assembly of aniline oligomers rather than that of aniline monomers, predetermined the final PANI morphology. A study of the synthesis of PANI-NTs in the presence of acetic acid [350,351] clearly showed that the oxidative polymerization process has two distinct exothermic phases (separated by an athermal period): (1) the oxidation of the neutral aniline molecules and the initially produced low-molecular-weight aniline oligomers at low acidity, $pH > 4$; followed by (2) the oxidation of the anilinium cations after the acidity becomes higher, $pH < 2$. The two phases of oxidation give different products, oligoanilines (some of them as rod-like crystals) with a molecular weight of several thousands and the mixed *ortho* and *para* coupling of aniline molecules, and PANI-NTs, respectively. The 2–3 wt% content of sulfur in deprotonated samples suggests that the oxidation products are partly sulfonated/sulfated. The oxidation of *ortho* coupled anilines combined with intramolecular cyclization produces phenazine units, as indicated by FTIR spectra. It was proposed that the nanosized oligoaniline crystallites serve as starting templates for the nucleation of PANI-NTs. Further growth of nanotubes proceeds by the self-organization of the phenazine units or their blocks located at the ends of the PANI chains. It has recently been assumed that during the athermal phase (pH 2.5–4.0) chain-growth reactions are reduced and only a slow accumulation of phenazine nucleates takes place [166]. This is favorable for the regular organization of phenazine nucleates. Low-molecular-weight oligoanilines with a high content of phenazine rings crystallize easily to produce 1-D structures and crystalline offshoots on the body of the amorphous precipitate. It has been shown that such offshoots serve as templates initiating

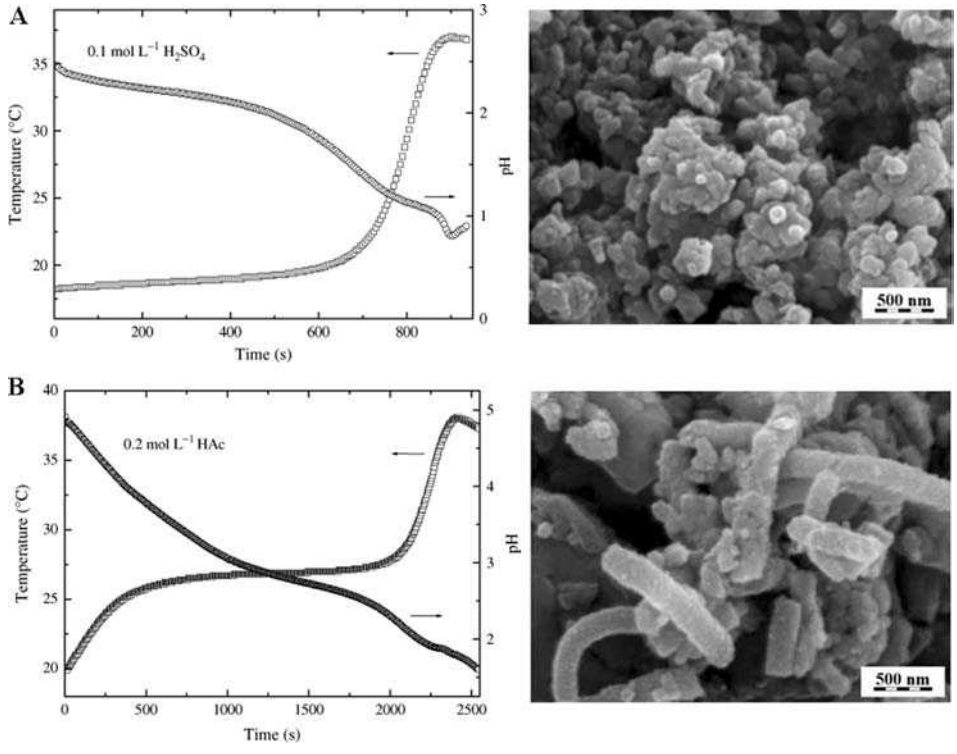

Figure 2.17 *Changes in temperature (squares) and acidity (circles) during oxidation of 0.2 M aniline with 0.25 M APS in (A) 0.1 M H_2SO_4, (B) 0.2 M acetic acid. Corresponding morphologies (granular, H_2SO_4; tubular, acetic acid) are also shown. (Reprinted with permission from Polymer International, Polyaniline nanotubes: conditions of formation by E. N. Konyushenko, J. Stejskal, I. Šeděnková et al., 55, 31–39. Copyright (2005) John Wiley & Sons Ltd)*

the growth of PANI-NTs [351]. The diameter of the offshoot determines the inner diameter of the growing nanotube. Because they have various diameters, the inner diameters of PANI-NTs have a broad distribution.

***Miscellaneous Soft-Template Methods*:** Novel Y-junction PANI-NTs, accompanied with nanorods, have been selectively prepared using *in situ* self-assembly of water-soluble Fe_3O_4 nanoparticles coated with PEG(5)-nonylphenylether and cyclodextrin as templates and pH control in an aqueous medium [373]. A chemical oxidative route to synthesize oriented arrays of conducting PANI-NTs in HCl solution by hydrogen-bonding directionality in the presence of a crown ether derivative (CE-SO_3K) has also been reported [374].

Template-Free Methods

***Falling pH Method*:** PANI-NTs have been synthesized by the falling pH method, i.e. the oxidative polymerization of aniline with APS in an aqueous solution, starting at pH > 4.0

and finishing at pH < 2.0, in the presence of inorganic acids e.g. HCl [204], H_2SO_4 [204], H_3PO_4 [204,336], tetrafluoroboric acid [204], and molybdic acid [214]. Lower reaction temperatures (e.g. 0–4 °C) were found to be favorable for the formation of PANI-NTs [204]. The oxidative polymerization of aniline with APS in 1 M methanol aqueous solution acidified with HCl also led to PANI-NTs [375]. Nanocomposites containing PANI-NTs and Fe_3O_4 nanoparticles were synthesized by the falling pH method in the presence of H_3PO_4 [209]. PANI-NTs aggregated to form nanotube dendrites when a template-free synthesis was performed in the presence of hydroxycarboxylic acids (lactic acid, succinic acid, malic acid, tartaric acid, and citric acid) [112,349,376]. PANI-NTs were successfully synthesized by the falling pH method in the presence of hydrophilic organic acids e.g. 5-sulfosalicylic acid [377].

In the absence of a surfactants or amphiphilic acids, micelles formed by anilinium cations and inorganic or hydrophilic organic anions (hydroxycarboxylates) have been considered by Wan's group as soft templates [204]. As the polymerization proceeds, the micelles become big spheres through accretion or tubes/rods through elongation, depending on the local conditions, similarly to surfactant- and amphiphilic acid-assisted syntheses. Contrary to the micellar model, the self-assembly of phenazine-containing oligoanilines was proposed to govern the evolution of the supramolecular structure of the final PANI products, synthesized by the falling pH method [350,377]. The dissolution of fully oxidized oligoanilines from the core(nonconducting oligoanilines)/shell(conducting PANI) structured nanorods, caused by their protonation at pH ≤ 2, has recently been proposed to contribute in the formation of PANI nanotubes [377]. This hypothesis was supported by TEM observation of nanorods having partly dissolved cores. The morphology evolution of PANI-NTs during a falling pH process, in the presence of DL-tartaric acid, showed that the PANI-NTs followed a nucleation, agglomeration, or self-growing process, sequentially [376]. It was proposed that PANI-NTs derived, most probably, from self-growth of as-formed bubble-like ribbons. PANI-NTs formation by self-curling has also been proposed [375]. Electron microscopy images revealed the flake-like intermediates, formed in the initial stage of the falling pH process of aniline polymerization, which then curled into PANI-NTs as the polymerization proceeded [375]. It was suggested that the phenazine-like oligoaniline units served as the axis for PANI nanotube curling. It has recently been revealed that the morphology of the oligoanilines directly correlates with the morphology of PANI-NTs [378]. When the oligoanilines are rod-shaped with rectangular cross-section the resulting PANI-NTs have rectangular holes and outer contours. PANI-NTs have circular cross-sections when the oligoanilines are platelet-shaped.

***pH-Stat Method*:** PANI-NTs have also been obtained by the oxidation of aniline with APS in an aqueous solution, in the presence of *p*-TSA, at constant acidity (pH = 2, and 3) [379]. The products of pH-3-stat synthesis are a mixture of nanotubes and nanofibers, the yield of these nanostructures is 80–90%, while the products of pH-2-stat synthesis are a mixture of nanotubes (10–20%) and granular particles.

***Dopant-Free Template-Free Method*:** PANI-NTs have been prepared by the oxidative polymerization of aniline with APS in water without added acid (Figure 2.18) [199,350,380,381]. This is a facile and efficient approach to synthesize PANI-NTs because it not only omits hard templates and post-treatment template removal, but also simplifies reagents. A modification of the dopant-free template-free method of PANI-NTs synthesis

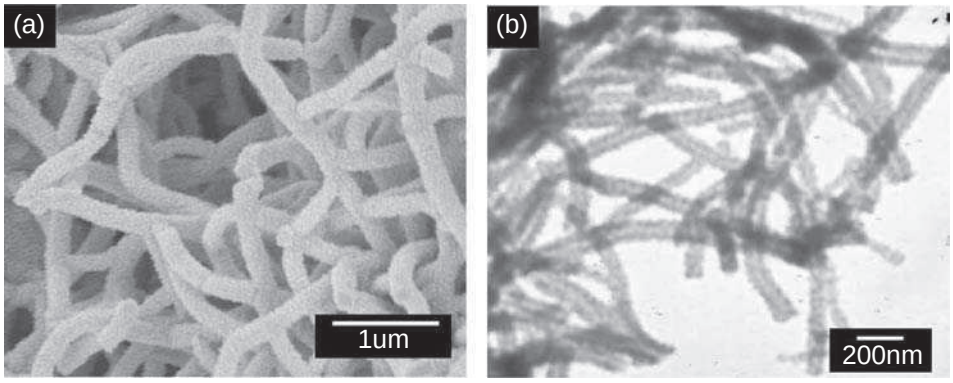

Figure 2.18 *Typical (a) SEM and (b) TEM of PANI-NTs prepared by dopant-free template-free method. (Reprinted with permission from Macromolecular Chemistry and Physics, Formation mechanism of polyaniline nanotubes by a simplified template-free method by H. Ding, J. Shen, M. Wan and Z. Chen, 209, 8, 864–871. Copyright (2008) Wiley-VCH)*

was reported by Chiou *et al.* [199]. They have performed a synthesis of the highly uniform, relatively long PANI-NTs, in addition to PANI-NFs, by using an excess of oxidant (APS). It should be noted that the first dopant-free template-free synthesis of PANI-NTs was a simple alkali (NaOH)-guided template-free method performed by Wang *et al.* [196]. The synthesis of PANI-NTs with the introduction of methanol in aqueous solutions was recently reported [382]. A dopant-free template-free method has recently been successfully used in the preparation of PANI-NTs/zeolite [383] and PANI-NTs/silica nanocomposites [384].

Aniline oligomers are produced in the first exothermic part of the oxidation of aniline in water without added acid, the PANI during the second exothermic phase [381]. It has been proposed that the aniline oligomers are insoluble in water, and that they aggregate to constitute a template-like structure, which further predetermines the directional growth of PANI, that is, the production of nanotubes. The occurrence of nanotubes is clearly associated with the presence of oligoaniline crystal-like structures that act as templates for nanotubes growth. It was recently found that the important stage of PANI-NTs self-assembly during dopant-free template-free synthesis, as well as during pH-stat and falling pH syntheses, seems to be based on the aggregation of small 15–30nm conducting PANI nanoparticles onto smooth oligoaniline nanorods that act as templates [385]. The presence of phenazine-like units in PANI, is also invariably connected with the existence of nanotubes [381,386]. The formation of phenazine units during the dopant-free template-free synthesis of PANI-NTs, experimentally proved by FTIR [381] and Raman spectroscopies [386] correlates well with the quantum-chemical predictions of the molecular structure of fully oxidized low-molecular-weight oligoanilines (linear pernigraniline-like, as well as branched phenazine-like (pseudomauveine)) formed during the early stages of the oxidation of aniline with APS in water, without added acid (**A**, Figure 2.19) [387–389]. Recently, an alternative pathway to phenazine-containing oligoaniline intermediates in the aniline–peroxydisulfate system was proposed [390]. Surwade *et al.* suggested that chemical oxidative polymerization of aniline with peroxydisulfate in aqueous solutions at pH

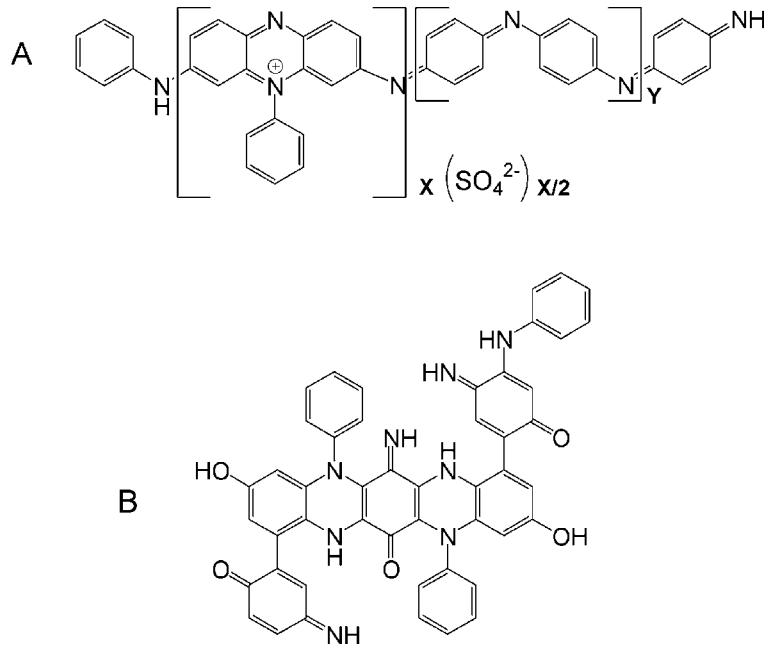

Figure 2.19 *Proposed structures of phenazine-containing oligoanilines: A [387–389] and B [390]*

2.5–10 led to oligoanilines which are believed to be mixtures of Michael-type adducts of benzoquinone monoimine and aniline at various stages of hydrolysis (**B**, Figure 2.19) [390]. It was suggested that phenazinium units act as discotics that guide the stacking of oligomers as they are produced during the oxidation of aniline, thus providing the necessary organization and order that predetermine the growth of nanotubes [381]. The sulfonation and/or sulfation of PANI, occurring at the same time, may help to stabilize the produced structures by internal protonation, that is, by ionic bonding between sulfonate/sulfate groups and protonated imine sites in neighboring polymer chains. Chiou *et al.* have proposed a micellar model based on the 'surfactant' role of aniline dimer cation-radicals, which could aggregate to form different sizes and types of micelle [199]. However, the mechanistic details of this model are not supported by quantum-chemical studies of the early stages of the oxidative polymerization of aniline with APS [387,388]. Moreover, the surfactant role of cation-radicals of a major aniline dimer, 4-ADPA, is not consistent with their pronounced charge/spin delocalization [387]. A recent study of the evolution of PANI-NTs morphology during the oxidative polymerization of aniline with APS in aqueous solution without added acid has revealed that the morphology changes from hollow spheres to short and long tubes [380]. It was proposed that a micelle composed of the aniline monomer itself in aqueous solution served as a soft template in forming PANI nanospheres at the initial stage. These nanospheres then linearly aggregate to form PANI-NTs by the coordination of the polymerization and elongation processes, as well as hydrogen-bond formation as the driving force.

***Ultrasonic Irradiation Assisted Template-Free Method*:** PANI-NTs containing Fe_3O_4 nanoparticles have been synthesized under ultrasonic irradiation of the aqueous dispersions of aniline, APS, H_3PO_4, and a quantitative amount of aniline-dimer-COOH-capped Fe_3O_4 nanoparticles [391]. It has been found that PANI-NTs can be produced by an ultrasonic irradiation-assisted template-free method when the concentration of the dopant acid (HCl, HNO_3, H_2SO_4, H_3PO_4, $HClO_4$, CSA) is low [189].

***Interfacial Polymerization*:** Thin PANI-NTs with an average outer diameter of 28 nm have been synthesized by interfacial polymerization in a calcium carbonate-stabilized oil/water emulsion [161]. PANI-NTs were synthesized by simply tuning the concentration of APS in a two-phase (toluene solution of aniline/acetic acid aqueous solution of APS) medium [392], or by tuning the concentration of DL-tartaric acid in a two-phase (toluene solution of aniline/DL-tartaric acid aqueous solution of APS) medium [393]. The difference in the PANI morphologies was attributed to the difference in the relative rates of interfacial nucleation to aqueous nucleation.

***Miscellaneous Template-Free Methods*:** PANI-NTs, having cavities of various diameters, have been found as by-products of PANI-NF synthesis through the oxidation of aniline with silver nitrate in aqueous solutions of HNO_3 [225]. Ag was obtained as nanoparticles accompanying macroscopic Ag flakes in the resulting PANI/Ag composite.

Electrochemical Oxidative Polymerization of Aniline

The electrochemical synthesis of PANI-NTs has been performed by using a composite Au/Cr/PC anode [311] or Pt/PC anode [313], i.e. metallic layers deposited through evaporation onto one side of the PC membrane, or by attaching the PC membrane to a Pt electrode with a little bit of Ag paste [48]. Doped and dedoped PANI-NTs have been synthesized by the electrochemical polymerization method, using alumina nanoporous templates [48,238]. It was observed that the PANI-NTs were transformed from a conducting state to a semiconducting (or insulating) state during the template removal, using template-dissolving solvents [238]. Nanoporous thin PC films supported on conductive substrates (Au-coated Si wafers or ITO glass) were used to electrosynthesize PANI-NT brushes [394]. PANI-NTs were synthesized electrochemically on modified ITO glass in a room-temperature ionic liquid, 1-butyl-3-methyl-imidazolium hexafluorophosphate containing 1 M trifluoroacetic acid [395]. PANI-NTs were deposited on Al thin films using the polarographic technique [396]. The current density–voltage profile shows a behavior typical of Schottky diode.

Miscellaneous Methods

Au/PANI-CSA coaxial nanocables have been successfully synthesized by the oxidation of aniline with chloroauric acid in the presence of CSA [397]. PANI-CSA nanotubes were obtained by dissolving the Au nanowire core of the Au/PANI-CSA nanocables. Purified flagella fibers displaying an anionic aspartate–glutamate loop peptide with 18 carboxylate groups were used to initiate formation of PANI-NTs [398].

2.2.3 Preparation of Miscellaneous Polyaniline Nanostructures

2.2.3.1 Nanoneedles and Rice-like Nanostructures

Single crystalline PANI nanoneedles have been synthesized using an interfacial polymerization (Figure 2.20) [399,400]. Interfacial crystallization at the liquid/liquid interface allowed PANI to form single crystalline nanocrystals in a rice-like shape with dimensions of 63 nm × 12 nm. An important growth condition necessary to yield highly crystalline conducting PANI was extended crystallization time at the liquid/liquid interfaces to increase the degree of crystallization. As compared to other interfacial polymerization methods, lower concentrations of monomer and oxidant solutions were employed to further extend the crystallization time. While other interfacial PANI growth yielded noncrystalline polymer fibers, this interfacial method produced single crystalline PANI nanocrystals. The resulting PANI nanoneedles have a fast conductance switching time between the insulating and conducting states on the order of milliseconds.

Highly crystalline PANI with uniform rice-like nanostructures, ca. 50–130 nm in diameter and 130–260 nm in length were prepared in the presence of DBSA without stirring (Figure 2.21) [401]. The formation of aniline/DBSA salts insoluble in the reaction system without stirring is believed to be favorable for the formation of these uniform rice-like nanostructures.

2.2.3.2 Nanoribbons

PANI nanoribbons, also known as nanobelts, have been synthesized by a self-assembly process using the chemical oxidative polymerization of aniline in a surfactant gel, formed by mixing an acetic acid solution of aniline and CTAB with an aqueous solution of APS

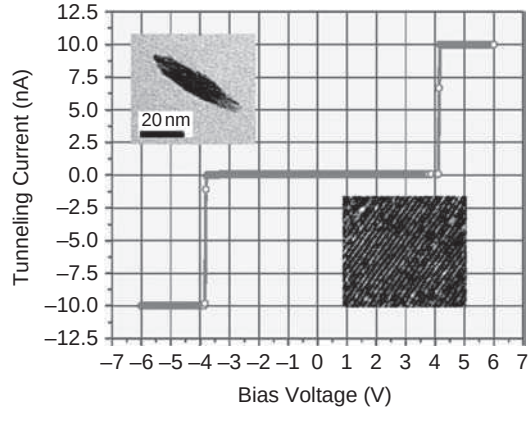

Figure 2.20 *Tunneling current vs. bias voltage for PANI nanoneedles (from Table of Contents of Reference 399). (Reprinted with permission from ACS Nano, Liquid/liquid Interfacial Polymerization to grow Single Crystalline Nanoneedles of Various Conducting Polymers by N. Nuraje, K. Su, N.-I. Yang and H. Matsui, 2, 3, 502–506. Copyright (2008) American Chemical Society)*

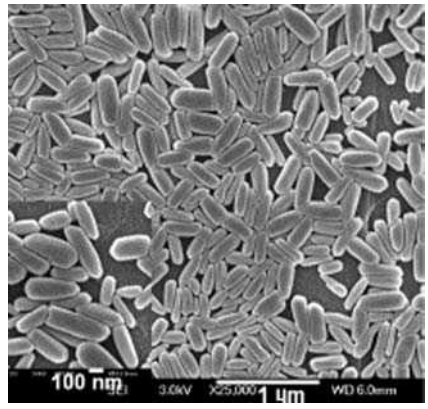

Figure 2.21 *Highly crystalline PANI with uniform rice-like nanostructures. (Reprinted with permission from Materials Chemistry and Physics, Uniform rice-like nanostructured polyanilines with high crystallinity prepared in dodecylbenzene sulfonic acid micelles by J. Yang, Y. Ding and J. Zhang, 112, 2, 322–324. Copyright (2008) Elsevier Ltd)*

and cooling the mixture to −7 °C (Figure 2.22) [402]. The typical thickness and length of these PANI nanoribbons were in the range of 40–50 nm and several micrometers, respectively. FTIR and UV-vis results indicated that their molecular structure corresponds to emeraldine. The dispersion of aniline and 4-(3-dodecyl-8-enylphenyloxy)butanesulfonic acid in water/toluene mixture produced vesicles templates for PANI nanoribbons [102]. Grafting polymerization of acrylic acid onto the surface of a polypropylene film followed by the oxidative polymerization of aniline on the grafted surface led to PANI nanoribbons [299]. Fully enclosed horizontal nanochannels, in a prearranged array on a substrate and with built-in electrical contacts and chemical access regions, were used as growth templates for electrochemical synthesis of conducting PANI nanoribbons [403]. In this 'grow-in-place'

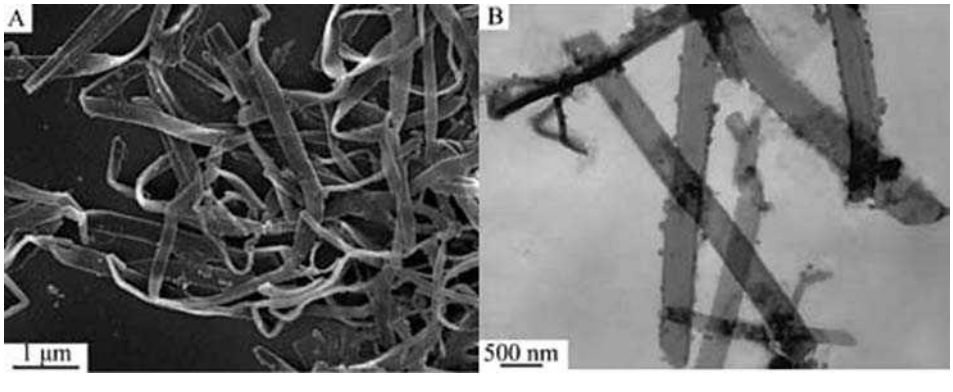

Figure 2.22 *(A) SEM and (B) TEM images of PANI nanoribbons. (Reprinted with permission from Macromolecular Rapid Communications, Synthesis of Polyaniline Nanobelts by G. Li, H. Peng, Y. Wang et al., 25, 1611–1614. Copyright (2004) Wiley-VCH)*

approach, the nanochannel templates were part of the final array structure and remained after fabrication of the nanoribbons. The built-in electrical contacts, which provided the electrical potential for electrochemical polymerization, also remained and became contacts/interconnects to the array components. The grow-in-place architecture and methodology removed the need for template dissolution, any post-synthesis nanoribbon 'grow-and-then-place' manipulation, and any post-synthesis electrical contacting. The grow-in-place approach may also be used for chemical polymerization. However, electrochemical polymerization is superior since it does not suffer from diffusion-limited growth and allows precise placement of the nanoribbons in the growth channel. Nanoribbons of PANI doped with H_2SO_4 or HCl were prepared via electrospinning by using a coagulation bath as the collector after optimizing the fabrication parameters [404].

2.2.3.3 Cyclic and Spiral Nanostructures

Cyclic nanostructured polyanilines (Figure 2.23) have been synthesized by means of a simple modified aqueous/organic interfacial polymerization with the aid of PAA [405]. The cyclic PANI nanostructures were formed by severe secondary overgrowth through the electrostatic interaction between aniline/oligoaniline and PAA chains. The average diameter of the obtained cyclic structure was ca. 400 nm and its conductivity was $\sim 1\ S\ cm^{-1}$.

The synthesis of spiral PANI nanostructures (2-D ordered spirals comprised of single-strand PANI-NFs) by chemical oxidative polymerization using a hydrated surfactant sodium dodecylsulfonate crystallite template was recently described [406]. It was found that a spiral dislocation structure on the surface of a hydrated sodium dodecylsulfonate crystallite was responsible for the growth of the spiral PANI nanoarchitecture. It was revealed that APS has a strong tendency to induce the formation of a spiral dislocation structure in hydrated sodium dodecylsulfonate crystallites. A mechanism of adsorption of oligoanilines on the steps of dislocation has been proposed for the growth of PANI spirals.

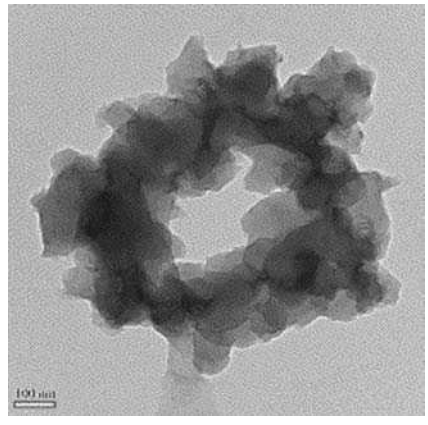

Figure 2.23 *TEM image of the cyclic PANI nanostructure. (Reprinted with permission from Polymer, Cyclic polyaniline nanostructures from aqueous/organic interfacial polymerization induced by polyacrylic acid by S. Liu, K. Zhu, Y. Zhang and J. Xu, 47, 22, 7680–7683. Copyright (2006) Elsevier Ltd)*

2.2.3.4 Nanosheets

PANI nanosheets (nanoplates, nanoflakes, nanodisks) can be assembled at the organic/aqueous interface or in solution by controlling the diffusion rate and the induction time of the interfacial polymerization of aniline [137]. Well-defined nanosheets with a leaf-like morphology (3.3 μm in length, 1.4 μm in width, and 150 nm in thickness, Figure 2.24a) were formed in the presence of PEO-poly(propylene oxide)-PEO, the amphiphilic triblock copolymer F127 [407]. The edges of such leaf-like PANI seem to be coarse and some fibrous structures can be observed (Figure 2.24c). The leaf-like structures of PANI are composed of nanofibers with diameters of ca. 25 nm. Such nanofibers are aligned in parallel along the long axis and short axis (Figure 2.24b) and then result in the mat-like arrays (Figure 24d). Surfactant-assisted synthesis of PANI nanosheets has recently been achieved by a one-pot process in the presence of SDS [82]. PANI nanosheets have been synthesized successfully by the chemical oxidative polymerization of aniline by a self-assembly process without the use of any acid [408], or in the presence of selenious acid

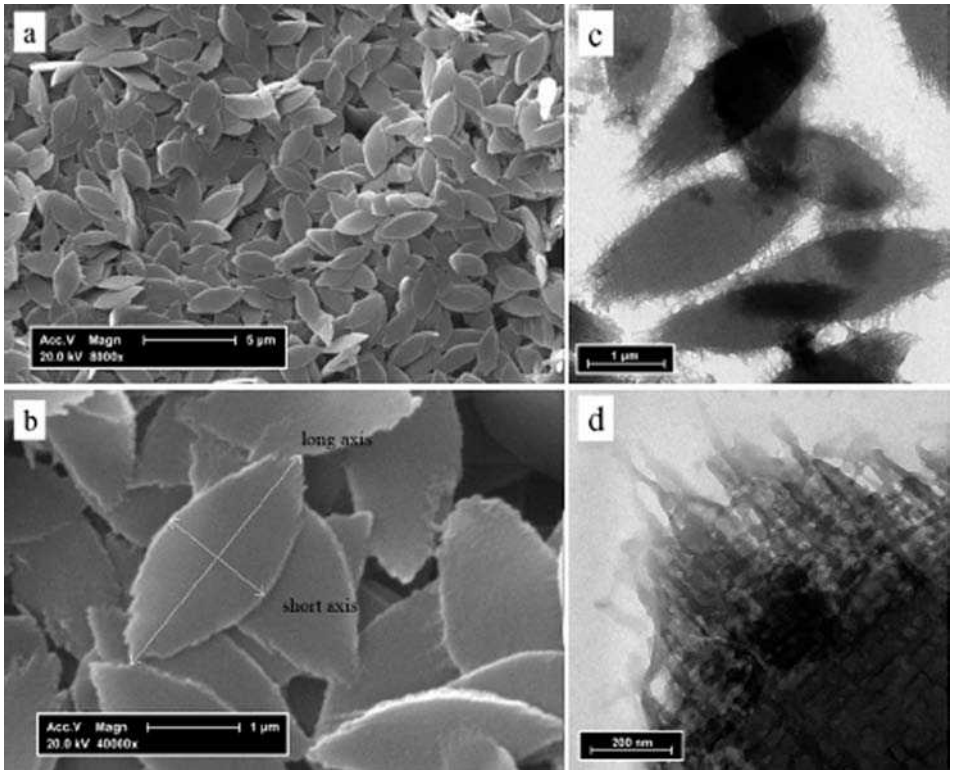

Figure 2.24 *(a,b) SEM and (c,d) TEM images of leaf-like PANI synthesized in the presence of F127. Synthetic conditions: [F127] = 1.6 × 10^{-4} M; [aniline] = 1.0 × 10^{-2} M; [APS]/[aniline] = 1.0:1; 20°C. (Reprinted with permission from Advanced Materials, Nanostructure-based leaf-like polyaniline in the presence of an amphiphilic triblock copolymer by J. Han, G. Song and R. Guo, 19, 2993–2999. Copyright (2007) Wiley-VCH)*

[211] and *p*-TSA [97]. 3-D rose-like PANI microstructures, which are self-assembled from 2-D nanosheets consisted of 1-D nanofibers, were synthesized by a template-free method in the presence of APS as both oxidant and dopant under a high relative humidity of 80% [201]. When the relative humidity increased from 25 to 80%, not only does the morphology of the micro/nanostructured PANI undergo a change from 1-D nanofibers to 2-D nanosheets to 3-D rose-like microstructures, but also an increase in crystallinity was observed. It has been proposed that a cooperation effect of the oriented water molecules at the vapor-water interface and a difference in hydrogen bonding energies between the interface and the bulk induced by the relative high humidity results in the formation of the 3-D rose-like microstructures self-assembled from 2-D nanosheets.

2.2.3.5 Nanolines and Nanodots

Nanolithography of PANI nanopatterns by the enzymatic oxidative polymerization of aniline in the presence of H_2O_2, using HRP-modified atomic force microscopy (AFM) tips, has recently been developed [409]. Tailored PANI nanostructures were created through controlled movement and positioning of the enzyme-modified AFM tip. A PANI line nanostructure on the blank mica substrate with a length of 3 μm, a width of about 350 nm and an average height of 5 nm was formed. Controlled biocatalytic patterning of PANI nanodots has also been reported [409].

2.2.3.6 Solid and Hollow Nanospheres

Synthesis of colloidal PANI nanospheres (PANI-NSs) by dispersion polymerization has been comprehensively reviewed [20,21]. Besides the dispersion polymerization, solid PANI-NSs have also been prepared by a self-assembly method in the presence of amino acids [109], selenious acid [211,410], and *p*-TSA [97]. The synthesis of PANI-NSs by aqueous/ionic liquid interfacial polymerization [411] and a simple alkali-guided template-free method [196,412] has been described. It has recently been shown that the oxidative polymerization of aniline with H_2O_2, catalyzed with metallic Au supported on carbon and Ti, leads to the PANI-NSs in high yields [413]. A strategy which involves two main steps, i.e. a grafting polymerization of acrylic acid onto the surface of a polypropylene film and subsequently an oxidative polymerization of aniline on the grafted surface, was developed in order to prepare PANI-NSs [299]. A simple and noncovalent method for coating MWCNTs with PANI-NSs, using a microemulsion aniline polymerization, has recently been presented [414]. PANI-NSs/Ag nanocomposite was obtained through an UV-irradiation method [415]. Uniform and ordered PANI-NSs were synthesized by electropolymerization of aniline in aqueous HCl solution using the constant-potential in the presence of a magnetic field [416]. Fully sulfonated PANI-NSs have been obtained by electrochemical homopolymerization of orthanilic acid [281]. PANI-NSs have recently been prepared within a lamellar liquid crystal template formed by the nonionic surfactant Triton X-100 [417]. Structural evolution and electrocatalytic application of nitrogen-doped carbon shells synthesized by pyrolysis of near-monodisperse PANI-NSs have also recently been reported [418].

Hollow PANI-NSs have been synthesized by the oxidative polymerization of aniline with APS in aqueous medium comprising poly(caprolactone)-PEO(1000)-poly(caprolactone) amphiphilic triblock copolymer micelles [419]. Hollow PANI-NSs were also

prepared by surface charge control of PS nanoparticle templates when PANI was electrochemically synthesized around the templates [420].

2.2.3.7 Polyhedral Nanoparticles

Using a γ-irradiation technique, hexagonal PANI nanoparticles have been prepared in the hexagonal lyotropic liquid crystalline phases of a non-ionic and biodegradable surfactant alkyl polyglucoside (GP215 CS UP) in water and/or medium and long chain alkanes, used as a template [421].

2.2.3.8 Comb- and Honeycomb-Shaped Nanostructures

Comb-shaped PANI nanostructures have been constructed upon complexation with zinc dodecylbenzenesulfonate [422]. Highly conducting PANI (600–1000 $S\,cm^{-1}$) with a nanoporous honeycomb-like morphology was prepared using self-stabilized dispersion polymerization [423–425]. It was suggested that the propagation reaction proceeded stepwise at the interface of heterogeneous biphasic chloroform/water system thus leading to the minimization of undesirable side reactions, such as *ortho* and *meta* substitutions and cross-linking. The nanoporous honeycomb-like PANI nanostructure became finer and the solubility of PANI was improved when PANI was prepared with oxygen bubbling [425].

2.2.3.9 Urchin-Like Nanostructures

Urchin-like PANI nanostructures (Figure 2.25A), composed of radially aligned uniform nanotubes (Figure 2.25B) and a core (Figure 2.25C), have been synthesized using tartaric acid as the dopant [112]. The core is comprised of vestigial PANI nanorods and nanoparticles. The PANI-NTs are often found to be linked together to form Y-junctions (Figure 2.25D) and then assembled into PANI dendrites. The geometrical shape of the individual PANI-NT is a cone with length of several micrometers and a wall thickness of 30–50 nm (Figure 2.25E). The outer diameters decrease from 400 to 80 nm along the length of the cone. Urchin-like PANI micro/nanostructures were found to originate from the self-assembly of PANI nanoplates, which then grew into microstructures with highly oriented PANI-NFs of 30 nm diameter and 1 μm length on the surface [426]. Hollow, urchin-like carbon spheres with electromagnetic function have recently been prepared by the carbonization of template-free-synthesized urchin-like PANI micro/nanostructures containing $FeCl_3$ [427].

2.2.3.10 Brain-Like Nanostructures

A solid-state synthesis has been explored to prepare PANI nanostructures with many convolutions, which resemble the cerebral cortex of the brain (Figure 2.26), via the oxidative polymerization of solid anilinium citrate with chlorine gas [428]. A reversible doping/dedoping process (i.e., conducting state/insulating state) for the brain-like nanostructures was realized by using HCl gas/ammonia gas.

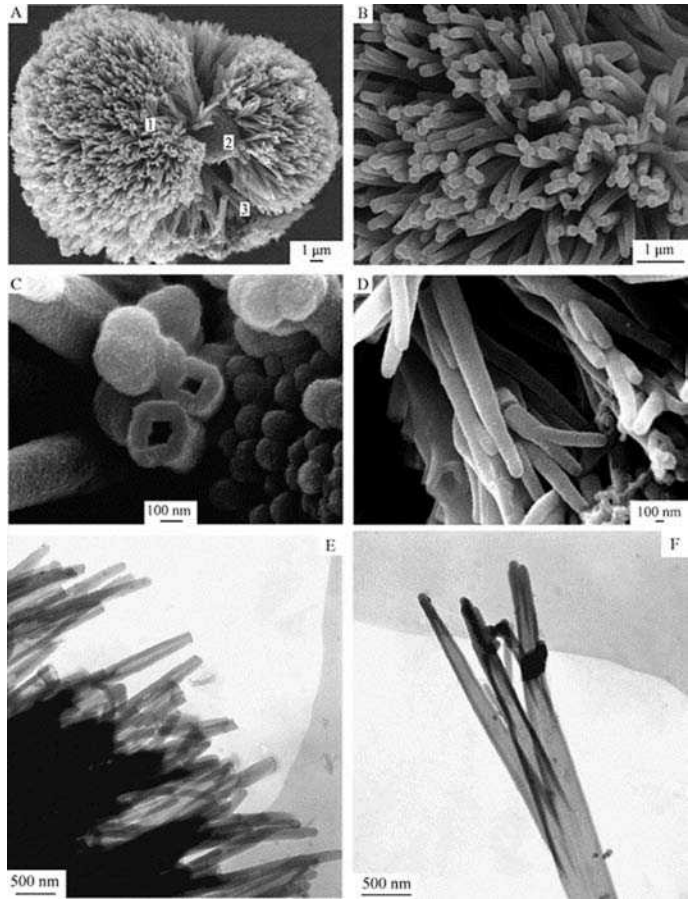

Figure 2.25 *SEM and TEM images of the urchin-like PANI nanostructures: (A) low magnification SEM image; (B), (C), and (D) show magnified SEM images of boxes 1, 2, and 3 in (A), respectively; (E) TEM image of the edge of PANI nanostructures; (F) TEM image of a representative PANI dendrite. (Reprinted with permission from Polymer, Synthesis of radially aligned polyaniline dendrites by G. Li, S. Pang, G. Xie et al., 47, 4, 1456–1459. Copyright (2006) Elsevier Ltd)*

2.2.3.11 Flower-Like and Rhizoid-Like Nanostructures

Flower-like and rhizoid-like nanostructures of pure PANI doped with H_2SO_4 or HCl have been prepared via electrospinning by using a coagulation bath as the collector [404]. PANI 'sunflowers' with arrays of oriented nanorods were synthesized by chemical oxidative polymerization of aniline in the presence of CTAB and HNO_3 [429]. A method for the fabrication of screen-printed electrodes modified with cauliflower-like PANI nanostructures was developed [430]. PS nanoparticles were self-assembled onto a PANI-modified screen-printed electrode with the help of the negatively charged polyelectrolyte poly(sodium 4-styrenesulfonate) and positively charged poly(diallyldimethylammonium chloride). The

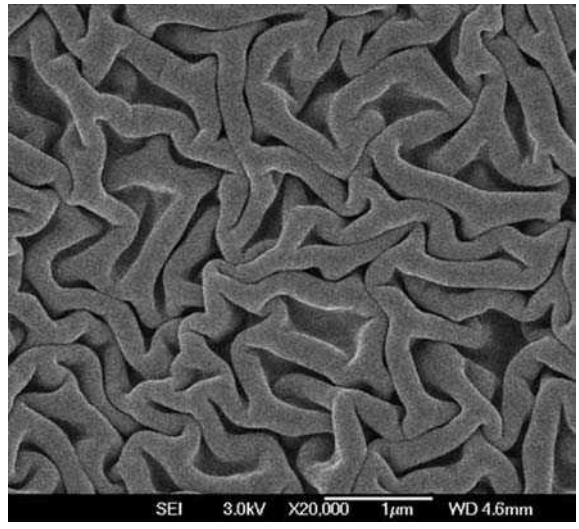

Figure 2.26 *SEM image of the brain-like PANI nanostructure. (Reprinted with permission from Macromolecular Rapid Communications, A new route for the preparation of brain-like nanostructured polyaniline by Y. Zhu, J. Li, M. Wan et al., 28, 1339–1344. Copyright (2007) Wiley-VCH)*

self-assembled PS nanoparticles could then act as a template for the electrosynthesis of an additional layer of PANI. It was found that the additional layer of PANI preferred to grow around the PS nanoparticles, and a highly nodular, cauliflower-like nanostructure of PANI was thus formed on the electrode surface.

2.2.3.12 Net-Like, Star-Like, and Feather-Like Nanostructures

Net-like and star-like PANI nanostructures (Figure 2.27) were prepared by controlling the monomer/stabilizer ratio (Triton X-100 and PEG-600), pH, and the reagent adding method and rate, in diffusion polymerization [80].

Feather-like PANI nanostructures (Figure 2.28) have been fabricated by using a simultaneous redoping–reprecipitation approach [431]. The protonation reaction happening at the same time as the reprecipitation was confirmed to be the key point for the formation of the special polycrystalline nanostructures.

2.2.3.13 Miscellaneous Hierarchical Nanostructures

PANI tower-shaped hierarchical nanostructures were prepared by a limited hydrothermal reaction [432]. The growth process is quite different from that of traditional inorganic layer-like superstructures. The conductivity of the superstructures was about 10^{-2} to 10^{-1} S cm^{-1}. Fabrication of spherical and cubic PANI shells with hierarchical nanostructures, by using MnO_2 hollow hierarchical nanostructures with different morphologies as reactive templates in a controlled manner, has also been reported [433].

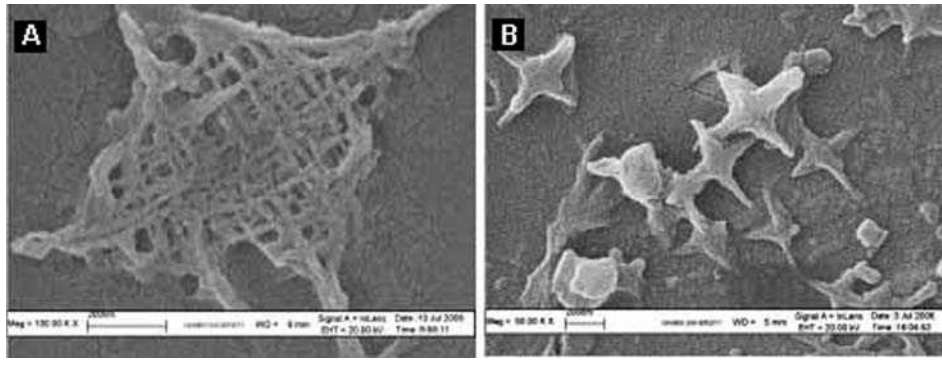

Figure 2.27 *SEM images of net-like (A) and star-like (B) PANI nanostructures. (Reprinted with permission from Comptes Rendus Chimie, The design, synthesis and characterisation of polyaniline nanophase materials by J. Chen, Y. Xu, Y. Zheng et al., 11, 1–2, 84–89. Copyright (2008) Elsevier Ltd)*

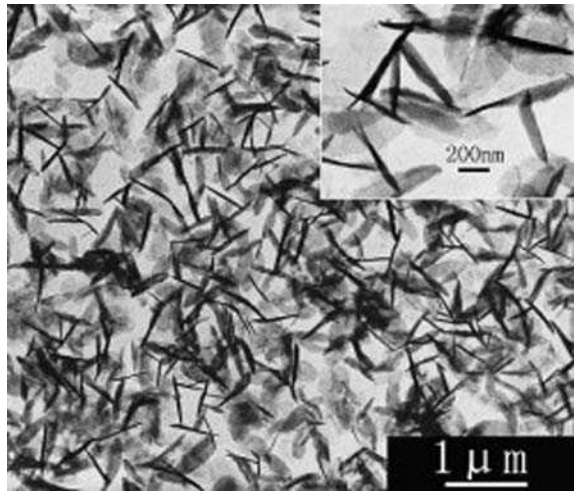

Figure 2.28 *SEM images of feather-like PANI nanostructures. (Reprinted with permission from European Polymer Journal, Polycrystalline polyaniline with strong infrared absorption by T. Dai and Y. Lu, 44, 11, 3417–3422. Copyright (2008) Elsevier Ltd)*

2.3 Structure and Properties

2.3.1 Structure and Properties of Polyaniline Nanofibers

The spectroscopic features (FTIR, UV-vis) of both powders and films of PANI-NFs are essentially identical to conventional nonfibrillar PANI in the emeraldine oxidation state [51,131]. UV-vis absorption and X-ray diffraction studies have shown that the PANI-NFs,

synthesized by dilute polymerization, have optical spectra and diffraction patterns similar to those previously reported for nonfibrous PANI [171]. Recent solid-state ^{13}C and ^{15}N NMR experiments showed that the PANI-NFs synthesized by rapid mixing in the presence of strong acid resemble standard PANI in structure [434]. These spectroscopic findings also support the conclusion that nanofibrous PANI has a very similar chemical structure to granular PANI. It has been noticed that the conformation of PANI chains in nanofibers is slightly different from that of granular particles [52]. A film cast from a nanofiber dispersion exhibited higher absorbance in the near-infrared region than a film composed of granular particulates prepared on a glass slide via *in situ* deposition from the same reaction solution, indicating a more extended conformation of the PANI chains in the nanofibers. Resonance Raman spectral profiles of PANI-NSA nanofibers suggested a lower protonation state than that of the emeraldine salt form, as well as cross-linking between PANI chains [90]. The cross-linking was also indicated by nonquaternary suppression ^{15}N NMR experiment [434]. Increased cross-linking upon heating has been observed [435]. The changes in the resonance Raman, FTIR and EPR spectra of the PANI-NFs, prepared through interfacial polymerization, have revealed an increase in the torsion angles of $C_{ring}—N—C_{ring}$ segments, owing to the increased formation of bipolarons in the PANI-NFs backbone compared with PANI prepared by conventional routes [147]. Small-angle neutron scattering (SANS), NMR, and wide-angle and small-angle X-ray scattering measurements confirmed the existence of more ordered molecular conformation and supramolecular packing in PANI-NFs, in comparison with granular PANI [436]. SANS indicated very sharp, well-organized interfaces in the PANI-NFs.

Four-probe pressed-pellet conductivities for PANI emeraldine hydrochloride nanofibers are in the range 2–10 S cm^{-1} [51], similar to conventional PANI emeraldine hydrochloride powder [1]. Maximum conductivities of PANI-NFs prepared by various template and template-free methods are given in Tables 2.1 and 2.2, respectively.

Table 2.1 *Maximum conductivity of PANI-NFs prepared by template methods*

Method of PANI-NFs preparation	Maximum conductivity (S cm^{-1})	Refs.
Nanoporous hard template	0.29	50
Nanostructured seed template	21.1	54
Nanostructured template	5.2	58
Oligomer- and polymer-assisted	34.5	66
Surfactant- and amphiphilic acid-assisted	0.98	92

Table 2.2 *Maximum conductivity of PANI-NFs prepared by template-free methods*

Method of PANI-NFs preparation	Maximum conductivity (S cm^{-1})	Refs.
Aqeous/organic interfacial	13.5	141
Rapid mixing	20.3	169
Dilute polymerization	4.0	171
Radiolythic	0.02	184
Sonochemical	10.2	188
Dopant-free	2.6	198
Miscellaneous	112.0	227

There is also no significant difference between PANI-NFs and conventional PANI in their aqueous electrochemistry: the cyclic voltammogram of PANI emeraldine hydrochloride nanofibers displays the two redox peaks characteristic of conventional PANI [51]. There is, however, a significant difference in the capacitance for PANI-NFs. A capacitance of 122 F g^{-1} was obtained for PANI emeraldine hydrochloride nanofibers synthesized using PANI-NFs as the seed template, as compared to 33 F g^{-1} in nonfibrillar PANI emeraldine hydrochloride [51]. Elevated capacitance values were obtained for all seeded systems. The charge/discharge cycles were also found to be more symmetrical for nanofibers, which is consistent with their increased available surface area, and is expected to improve the kinetics of the various processes involved. Electrochemical performance of PANI-NFs, synthesized by interfacial polymerization, and PANI/MWCNT composite as electrode material for aqueous redox supercapacitors was evaluated [153]. The initial specific capacitance of the two-electrode cell was 554 F g^{-1} at a constant current of 1.0 A g^{-1}, using PANI-NFs as electrode material, but this value rapidly decreased on continuous cycling. In order to improve the cycleability of the supercapacitor, a composite of PANI with MWCNTs was synthesized by *in situ* chemical polymerization. A high initial specific capacitance of 606 F g^{-1} was obtained with good retention on cycling. The electrochemical supercapacitive behavior of PANI-NFs (nanorods) fabricated on aniline-primed conducting ITO substrate via electroless surface polymerization, using APS as oxidant and selenious acid as efficient dopant, was also demonstrated [410].

Higher coloration efficiency, larger charge capacity, enhanced cycling stability and faster color-bleach rates were observed for nanofibrillar PANI films, obtained by electropolymerization from an aqueous medium in the presence of an ionic liquid (1-ethyl, 3-methylimidazolium bromide), as compared to that shown by nonfibrillar PANI films fabricated from PEG solution [279].

PANI-CSA nanofibers, synthesized by an interfacial polymerization method, are readily dispersed in water, which could facilitate environmentally friendly processing and biological applications [133]. The nanofibers are stable in water, in contrast to conventional PANI/CSA thin films, which can be dedoped by water. PANI-NFs synthesized by dilute polymerization were also easily dispersed in various solvents, polar as well as nonpolar, and the resulting suspensions were stable for several minutes [171].

PANI-NFs prepared by interfacial polymerization have shown a bimodal distribution of molecular weights, determined using gel permeation chromatography, similar to that of conventional PANI [131]. However, the area under the high-molecular-weight peak (M_W=550000–800000) was found to be considerably larger than that under the low-molecular-weight peak (M_W=24000). This contrasts with conventional chemically synthesized PANI, for which the low-molecular-weight fraction dominates.

It was found that the antioxidant activity of PANI-NFs was higher than that of conventional PANI, and that it increased with decreasing averaged diameter of the nanofibers [182]. The enhanced antioxidant activity was due to the increased surface area of PANI-NFs. Conductive 3-D microstructures assembled from PANI-NFs doped with perfluorosebacic [113,114] and perfluorooctanesulfonic acid [115], such as hollow rambutan-like spheres [115], hollow dandelion-like [113], and hollow box-like microstructures [114], exhibited superhydrophobic properties. Reversible hydrogen storage behavior of PANI-NFs at room temperature has recently been reported [437].

2.3.2 Structure and Properties of Polyaniline Nanotubes

Hard-template-synthesized PANI-NTs have enhanced conductivity in comparison with conventional PANI [309,310]. Polarized IR spectroscopy data showed that PANI deposited directly on the pore wall is highly ordered relative to subsequently deposited PANI [310]. This ordering of the PANI chains is responsible for the enhancement in conductivity. It was shown that the PANI chains were preferentially aligned perpendicular to the tubule axis. The directly measured conductivity of a single PANI nanotube doped with CSA is very high ($\sim 30\,\mathrm{S\,cm^{-1}}$) [339,340], and its temperature dependence follows the three-dimensional variable range hopping model. However, the bulk conductivity of the PANI-NTs pellets is much smaller than that of the nanotube itself ($3.5 \times 10^{-2}\ \mathrm{S\,cm^{-1}}$), which is due to the large intertubular contact resistance. The results for temperature-dependent conductivity of a nanotubular PANI measured over a wide range of temperatures [336,339,438] have been explained on the basis of phonon-assisted tunneling theory as a free-charge-carrier generation mechanism [439].

The magnetoresistance of single PANI-NT is found to be very small even at 2 K (magnetoresistance $< 5\%$ at 10 T) compared with that of the pellets (40–100% at 10 T), and no evident and stable negative magnetoresistance has been observed above 50 K, indicating that the magnetoresistance in bulk pellet samples made of PANI-NTs is dominated by a random network [440].

The susceptibility data cannot be simply described as Curie-like susceptibility at lower temperatures and temperature-independent Pauli-like susceptibility at higher temperatures [441]. Some unusual transitions were observed in the temperature dependence of susceptibility, for example paramagnetic susceptibility decreased gradually with lowering temperature, which suggests the coexistence of polarons and spinless bipolarons and the possible formation of bipolarons with changing temperature or doping level.

PANI–β-NSA nanotubes show unusually high crystallinity [93]. It has been revealed that PANI-NTs are composed of crystalline and amorphous regions [341]. The crystallinity fraction D_g obtained from the specific heat was about 15% for the measured PANI-NTs, which indicated that most of the PANI chains in the nanotubes were disordered.

A comparison of PANI-NTs synthesized by electrochemical and chemical methods inside the nanopores of AAO membrane and PC track-etched membrane was made [48]. The morphologies of PANI-NTs synthesized electrochemically in AAO membrane were found to be better than those synthesized in PC track-etched membrane. EPR spectra revealed that the degree of delocalization of those nanotubes synthesized electrochemically in the AAO membranes was better. Nanotubes synthesized electrochemically inside the pores of AAO membranes showed an enhancement of the electronic conductivity compared to PANI bulk materials. PANI-NTs synthesized by an electrochemical method showed better properties (morphology, degree of delocalization and conductivity) than the tubes synthesized by a chemical method in the same templates.

The thermal stability and structural variation of the PANI-NT films produced on Si windows during a treatment at 80 °C for three months were studied by FTIR and Raman spectroscopies [442]. The morphology of the films was preserved during the degradation, but the molecular structure had been changed. The results indicate that the spectral changes correspond to deprotonation, oxidation, and chemical cross-linking reactions. The films of

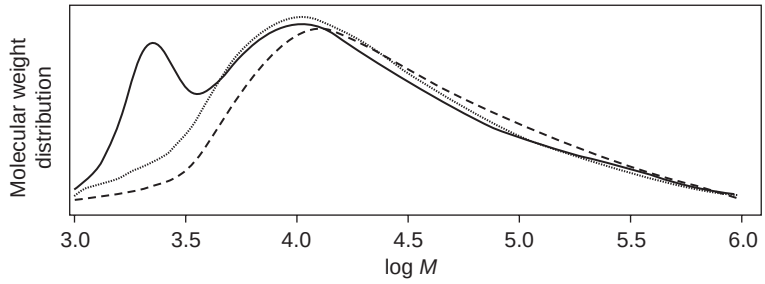

Figure 2.29 *Molecular weight distribution as obtained by gel permeation chromatography for the samples prepared by the oxidation of aniline with APS using different [5-sulfosalicylic acid]/[aniline] mole ratios: 1 (– – –, PANI granules), 0.5 (· · · · · ·, PANI granules) or 0.25 (——, PANI-NTs). (Reprinted with permission from Nanotechnology, Synthesis and characterisation of conducting polyaniline 5-sulfosalicylate nanotubes by A. Janošević, G. Ćirić-Marjanović, B. Marjanović et al., 19, 135606. Copyright (2008) Institute of Physics)*

PANI salts lose their protonating acid and PANI bases are more stable than the salt forms during thermal ageing. PANI-NTs films obtained in water or in the presence of acetic acid are more stable than granular films prepared in solutions of H_2SO_4. The protonated structure is more prone to cross-linking reactions than deprotonated one. The molecular structure corresponding to the nanotubular morphology, which contains the cross-linked phenazine- and oxazine-like groups, is more thermally stable than the molecular structure of the granular morphology. The morphology of PANI-NTs is preserved upon carbonization [443–445].

PANI-NTs are redox active, e.g. reduce silver nitrate to Ag nanoparticles [353], thus forming PANI-NTs/Ag nanocomposites [446]. Granular PANI samples have unimodal molecular weight distributions, while a bimodal distribution with a characteristic oligoaniline peak is observed for PANI-NTs (Figure 2.29) [377].

2.4 Processing and Applications

2.4.1 Processing

Suspensions of PANI-NFs can be cast to form highly porous nanofibrous films without deformation of the nanofiber morphology [171]. PMMA/PANI-NF [151,188] and PAA/PANI-NF [145] composite films have been prepared by solution casting. Processable composites of PANI–β-NSA nanotubes with water-soluble PVA were prepared by simple mixing PANI–β-NSA dispersion in water with aqueous PVA solution, followed by film casting to obtain composite films [93]. Conducting films were prepared by blending self-doped PANI-NTs with low-density polyethylene [364]. Soya oil alkyd-containing nanostructured PANI composite coatings have also been fabricated [447]. It has been demonstrated that a methanol/formic acid mixture could be used as a suitable solvent system for PANI-NFs to achieve sufficient processability [448]. Mixtures of methanol with

increasing fractions of formic acid were used to progressively transform the morphology of PANI, from nanofibers to compact conventional films.

Processable stabilizer-free PANI-NF aqueous colloids are readily prepared by purifying PANI-NFs and controlling the pH, and are self-stabilized via electrostatic repulsions, thus providing a simple and environmentally friendly way to process the conducting polymer in its conductive state both in bulk and at the nanometer level [449,450]. Stabilizer-free PANI-NF aqueous colloids were obtained by the direct dispersing of PANI-NFs prepared in the presence of β-cyclodextrin [64,65]. PANI-NFs, the diameters of which are between 80 and 100 nm, can be steadily dispersed in neutral aqueous solution for about 60 days without any steric or electrostatic stabilizer [65]. Water-dispersible PANI-NFs provide a simple, fast, and inexpensive route towards highly concentrated CNT water dispersions [451,452]. In order to make the isolated PANI-NTs water dispersible, their surface can be modified by complex formation (non-covalent grafting) with hydrophilic PEO-block-PAA copolymer [328].

Melt-processable PANI-NFs doped with superfluous DBSA were synthesized using interfacial polymerization and thermal doping technique [453]. Conducting composites composed of these PANI-DBSA nanofibers, low-density polyethylene, and ethylene-acrylic acid copolymer as compatibilizer were prepared by melt processing. An enhanced photothermal phenomenon with conducting PANI-NFs in which a camera flash causes instantaneous welding has been reported [454]. Under flash irradiation, PANI-NFs 'melt' to form a smooth and continuous film from an originally random network of nanofibers [450]. The fabrication of monolithic microstructures from PANI-NFs has been described [455]. Electrophoretic deposition techniques were used to pattern the PANI-NFs and through a subsequent flash-welding process the PANI-NF mat was bound together into a coherent monolithic porous structure, retaining much of the morphology of non-coherent fiber networks.

Processable PAA/PANI-NF and poly(2-acrylamido-2-methyl propyl-sulfonic acid-acrylic acid)/PANI-NF conducting hydrogels with an interpenetrating polymer network structure have recently been synthesized [456].

Performance improvement of polysulfone ultrafiltration membrane has been achieved by blending with PANI-NFs [457]. Conducting blends of nanostructured PANI and PANI-clay nanocomposites with ethylene vinyl acetate as host matrix have been prepared [458]. A new conducting hybrid biocompatible composite material of PANI-NFs well dispersed in a collagen matrix was fabricated with various PANI-NFs/collagen ratios [459]. PANI-NFs doped by protonic acids can be efficiently dispersed in vinylidene fluoride-trifluoroethylene copolymers [460]. Fabrication of MWCNTs/PANI-NF nanocomposites via electrostatic adsorption in aqueous colloids has been reported [143]. A PANI-NFs/carbon paste electrode was prepared via dopping PANI-NFs into the carbon paste [461].

2.4.2 Applications

2.4.2.1 Sensors

Progress in the development of nanostructured PANI for sensor applications has recently been reviewed [23,24,462,463]. Films of PANI-NFs possess much faster gas-phase

doping/dedoping times compared with conventionally cast films [133]. The nanofiber films show essentially no thickness dependence in their performance. This is consistent with the porous nature of the nanofiber films, which enables gas molecules to diffuse in and out of the fibers rapidly. This also leads to a much greater doping or dedoping over short times for the nanofiber films. The better performance in both sensitivity and time response of PANI-NF film relative to its conventional bulk counterpart is caused by higher effective surface area and shorter penetration depth for target molecules. Using an interfacial polymerization method for the synthesis of PANI-NFs, Kaner's group has developed nanofiber sensors (Figure 2.30) and compared them to conventional PANI sensors [22,464,450]. The changes in electrical resistance were monitored as a function of time as the thin films of PANI-NFs were exposed to the various gases. Five different response mechanisms were explored: acid doping (HCl), base dedoping (ammonia), reduction (hydrazine), swelling (chloroform), and polymer chain conformational changes (methanol). In all cases, the PANI-NFs performed better than conventional thin films. PANI-NF composites with metal salts can be used as a chemical sensors for hydrogen sulfide [465] and arsine [466]. Hydrogen sensors, based on conductivity changes in PANI-NFs [467,468] have been reported. A controlled multipotential process was used to deposit PANI-NF arrays on a lithium niobate substrate with gold finger paired electrodes to form a surface acoustic wave device (hydrogen sensor) [239]. The 64° YX lithium niobate surface acoustic wave transducer coated first with aluminum nitride, and then with PANI-NFs by rapid mixing chemical oxidative method, in the presence of CSA, has demonstrated a large and reproducible response to different concentrations of the hydrogen gas, making it an ideal candidate for hydrogen sensing at room temperature [469]. PANI-NFs deposited on lithium tantalate surface acoustic wave transducers [470], Au and Pt electrodes [471] have also been used as hydrogen gas sensors. The great sensitivity of the Pt/PANI-NF sensor can be used to detect hydrogen at a concentration of 10 ppm [471]. Chemical gas sensors for nitrogen dioxide detection, using PANI-NFs synthesized by an interfacial polymerization method [144] and a plasma-induced polymerization technique [306] have been reported.

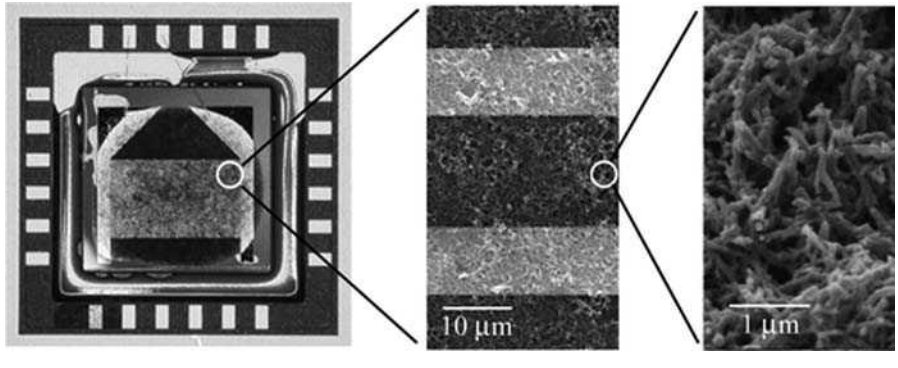

Figure 2.30 *PANI-NF sensors (from Table of Contents of Reference 22). (Reprinted with permission from Nano Letters, Polyaniline Nanofiber Gas Sensors: Examination of Response Mechanisms by S. Virji, J. Huang, R. B. Kaner and B. H. Weller, 4, 3, 491–496. Copyright (2004) American Chemical Society)*

Composites of PANI-NFs, synthesized using a rapid mixing method, with amines have recently been presented as novel materials for phosgene detection [472]. Chemiresistor sensors with nanofibrous PANI films as a sensitive layer, prepared by chemical oxidative polymerization of aniline on Si substrates, which were surface-modified by amino-silane self-assembled monolayers, showed sensitivity to very low concentration (0.5 ppm) of ammonia gas [297]. Ultrafast sensor responses to ammonia gas of the dispersed PANI-CSA nanorods [303] and patterned PANI nanobowl monolayers containing Au nanoparticles [473] have recently been demonstrated. The gas response of the PANI-NTs to a series of chemical vapors such as ammonia, hydrazine, and triethylamine was studied [319,323]. The results indicated that the PANI-NTs show superior performance as chemical sensors. Electrospun isolated PANI-CSA nanofiber sensors of various aliphatic alcohol vapors have been proven to be comparable to or faster than those prepared from PANI-NF mats [474]. An electrochemical method for the detection of ultratrace amount of 2,4,6-trinitrotoluene with synthetic copolypeptide-doped PANI-NFs has recently been reported [475]. PANI-NFs, prepared through the in situ oxidative polymerization method, were used for the detection of aromatic organic compounds [476].

Good biocompatibility of PANI-NFs enables them to become a simple and effective platform for the integration of proteins/enzymes and electrodes, which can provide analytical access to a large group of enzymes for a variety of bioelectrochemical applications. The glucose oxidase (GOx)-PANI-NFs/glassy carbon [477] and GOx-PANI-NFs/carbon cloth [478] electrodes have displayed good features in electrocatalytic oxidation of glucose. An amperometric glucose biosensor prepared by self-assembly of GOx and dendrimer-encapsulated Pt nanoparticles on PANI-NFs has been described [148]. The unique sandwich-like layer structure showed excellent response performance to glucose and provided a favorable microenvironment to keep the bioactivity of GOx and to prevent enzyme leakage. A sensitive glucose biosensor based on a composite of conducting PANI-NFs and Au nanoparticles, which shows excellent reproducibility and good operational stability, was also reported [224]. An amperometric glucose biosensor which had good electrocatalytic activity toward oxidation of glucose and exhibited rapid response, low detection limit, useful linear range, high sensitivity and biological affinity, as well as good stability and repeatability, was developed by electrochemically entrapping GOx on the inner wall of highly ordered PANI-NTs, which were synthesized using an AAO membrane as a template [479]. CSA-doped PANI/PS nanofibers, prepared using the electrospinning technique, have been used for sensing H_2O_2 and glucose [34]. Sensitive H_2O_2 biosensors using HRP immobilized in PS nanoparticles/cauliflower-like nanostructured PANI [430], Au-Pt alloy nanoparticle/PANI-NT/chitosan nanocomposite membranes [480], and processable PANI-NF/chitosan film [159] have been fabricated. Cholesterol biosensors based on cholesterol oxidase covalently immobilized onto electrophoretically deposited PANI film, derived from a PANI-NF colloidal suspension, has been reported [481]. A lipase/glutaraldehyde/PANI-NT/ITO bioelectrode has recently been utilized to estimate triglyceride in serum samples using an impedimetric technique [482].

Sensitive electrochemical DNA biosensors based on electrochemically fabricated PANI-NFs and methylene blue [483], as well as based on the synergistic effect between PANI-NFs and MWCNTs in chitosan film have been successfully prepared [484]. Highly sensitive electrochemical impedance spectroscopic detection of DNA hybridization based

on Au_{nano}–CNT/PANI-NFs films has recently been reported [461]. PANI-NTs doped by poly(methyl vinyl ether-alt-maleic acid) were used to construct a simple electrochemical oligonucleotide sensor, where oligonucleotide probes were covalently grafted onto residual carboxylic acid functionalities on the nanotubes [330,332,485]. The potential pulse amperometry technique was used to obtain a direct and fast electrochemical readout. An ultrasensitive electrochemical DNA biosensor using a conducting PANI-NT array as the signal enhancement element has also been presented [486]. A PANI-NT array with a highly organized structure was fabricated with a well-controlled nanoscale dimension on a graphite electrode using a thin nanoporous layer as a template, and 21-mer oligonucleotide probes were immobilized on these PANI-NTs. In comparison with Au nanoparticle- or CNT-based DNA biosensors, this PANI-NT-array-based DNA biosensor could achieve similar sensitivity without catalytic enhancement, purification, or end-opening processing. The electrochemical results showed that the conducting PANI-NTs array had a signal-enhancement capability, allowing the DNA biosensor to readily detect the target oligonucleotide at concentrations as low as 1.0×10^{-15} M. In addition, this biosensor demonstrated good capability of differentiating the perfect matched target oligonucleotide from one-nucleotide mismatched oligonucleotides, even at a concentration of 4×10^{-14} M. This detection specificity has indicated that this biosensor could be applied to single-nucleotide polymorphism analysis and single-mutation detection. Au nanoparticle/PANI-NT membranes on a glassy carbon electrode were constructed for the electrochemical sensing of the immobilization and hybridization of DNA (Figure 2.31) [487]. The synergistic effect of the two kinds of nanomaterials, Au nanoparticles and PANI-NTs, enhanced dramatically sensitivity for DNA hybridization recognition. The detection limit was 3.1×10^{-13} M. The biosensor also had good selectivity, stability and reproducibility.

A nanogapped microelectrode-based PANI-NF biosensor array was fabricated for ultrasensitive electrical detection of microribonucleic acids (miRNAs) [488]. Deposition of conducting PANI-NFs was carried out by an enzyme-catalyzed method, where the electrostatic interaction between anionic phosphate groups in miRNA and cationic aniline molecules was exploited to guide the formation of the PANI-NFs on the hybridized target miRNA. The conductance of the deposited PANI-NFs was correlated directly to the amount of the hybridized miRNA, with a detection limit of 5.0×10^{-15} M.

A fast and sensitive continuous-flow nanobiodetector for detecting micro-organism cells in a flowing liquid, based on PANI-NFs fabricated as a freestanding nanonetwork in a micro gap between two Au electrodes, was recently developed [489]. A direct-charge transfer biosensor, using antibodies as the sensing element and conducting PANI-NFs as the molecular electrical transducer, was developed for the detection of the foodborne pathogen, *Bacillus cereus* [490]. A new type of nanobiodetector based on a limited number of PANI-NFs has recently been designed and tested against bacteria *Klebsiella pneumoniae*, *Pseudomonas aeruginosa*, *Escherichia coli*, and *Enterococcus faecalis* [491]. The cells 'defects' accumulated in PANI-NFs lead to an abrupt change in their electrical conductivity above a threshold density (the percolation limit). The device works like an 'on–off' switch with nearly linear response above a threshold number of cells in the suspension examined. Nanostructured ultrathin films of self-assembled PANI-NFs cast onto interdigital microelectrodes have been used as efficient sensoactive layers in taste sensors for quality assessment of orange juices [492]. Unique highly

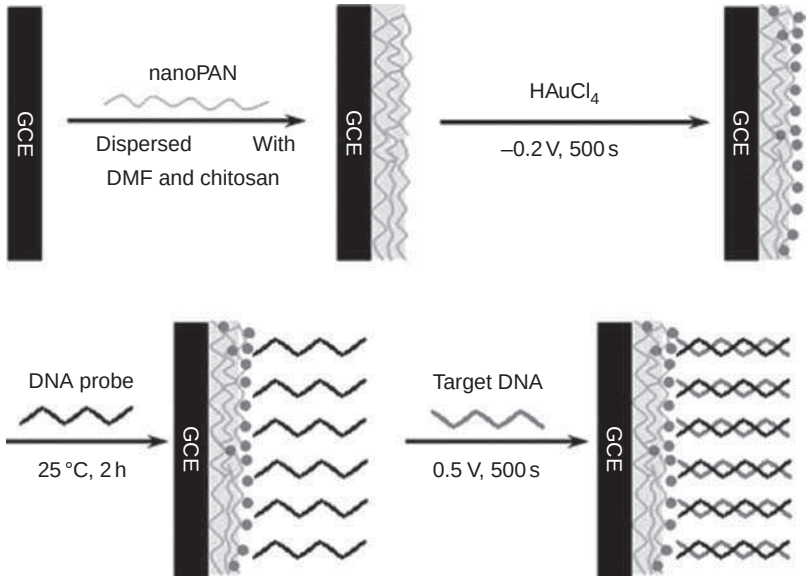

Figure 2.31 *Schematic diagram of the immobilization and hybridization of DNA on Au/nanoPAN/GCE. (Reprinted with permission from Analytica Chimica Acta, Enhanced Sensitivity for deoxyribonucleic acid electrochemical impedance sensor: Gold nanoparticle/polyaniline nanotube membranes by Y. Feng, T. Yang, W. Zhang, C. Jiang and K. Jiao, 616, 2, 144–151. Copyright (2008) Elsevier Ltd) (See colour Plate 1)*

carbonized PANI-NTs as a new, thermally stable nanomaterial for nanosensors and nanodevices with a wide range of possible applications, comparable to CNTs, have been prepared [443].

2.4.2.2 Catalysts

Pd nanoparticles supported on PANI-NFs are efficient semi-heterogeneous catalysts for Suzuki coupling between aryl chlorides and phenylboronic acid, the homocoupling of deactivated aryl chlorides, and for phenol formation from aryl halides and potassium hydroxide in water and air [493]. PANI-NF-supported $FeCl_3$ as an efficient and reusable heterogeneous catalyst for the acylation of alcohols and amines with acetic acid has been presented [494]. Vanadate-doped PANI-NFs and PANI-NTs have proven to be excellent catalysts for selective oxidation of arylalkylsulfides to sulfoxides under mild conditions [412]. Heterogeneous Mo catalysts for the efficient epoxidation of olefins with *tert*-butylhydroperoxide were successfully synthesized using sea urchin-like PANI hollow microspheres, constructed with oriented PANI-NF arrays, as support [495]. Pt- and Ru-based electrocatalyst PANI-NFs—PSSA—Ru—Pt, synthesized by the electrodeposition of Pt and Ru particles into the nanofibrous network of PANI-PSSA, exhibited an excellent electrocatalytic performance for methanol oxidation [496]. A Pt electrode modified by PANI-NFs made the electrocatalytic oxidation reaction of methanol more complete [497]. Synthesis of a nanoelectrocatalyst based on PANI-NF-supported

suprahigh density Pt nanoparticles or Pt/Pd hybrid nanoparticles, without prior PANI-NFs functionalization, has recently been reported [498]. Highly stable and recoverable PANI-NFs [499] and magnetic PANI-NF /iron oxide nanocomposites [500] for enzyme immobilization and recovery have been developed. The covalently attached, highly active and stable immobilized lipase could be used repeatedly. A PANI-NF/Co-porphyrin/glassy carbon composite electrode was able to catalyze oxygen reduction with the number of electrons involved being close to four. In 1 M HCl, this nanocomposite electrode performed comparably to a Pt disk electrode, demonstrating its potential as a non-noble metal electrocatalyst for oxygen reduction [247]. PANI-NTs with Pd nanoparticles attached to their inner walls have been found to be a better catalyst than Pd/C in the catalytic reduction of *p*-nitroaniline [325].

PANI-NTs synthesized by a template method on commercial carbon cloth have been used as the catalyst support for Pt particles for the electro-oxidation of methanol [501]. The Pt-incorporated PANI-NT electrode exhibited excellent catalytic activity and stability compared to 20 wt% Pt supported on VulcanXC 72R carbon and Pt supported on a conventional PANI electrode. The electrode fabrication used in this investigation is particularly attractive to adopt in solid polymer electrolyte-based fuel cells, which are usually operated under methanol or hydrogen. The higher thermal stability of y-MnO2 nanoparticles-coated PANI-NFs on carbon electrodes and their activity in formic acid oxidation permits the realization of Pt-free anodes for formic acid fuel cells [260]. The excellent electrocatalytic activity of Pd/PANI-NFs film has recently been confirmed in the electro-oxidation reactions of formic acid in acidic media, and ethanol/methanol in alkaline medium, making it a potential candidate for direct fuel cells in both acidic and alkaline media [502].

2.4.2.3 Electron Field Emitters and Field-Effect Transistors

Template-synthesized nanofibrilar PANI array membrane [46], which shows a low threshold electric field of 5–6 V μm^{-1} and a maximum emission current density of 5 mA cm^{-2}, was found to be a promising electron field emitter. However, despite the fact that this finding indicated a possible significant role for PANI-NFs in the development of field-emission display technology, no further scientific progress regarding PANI-NF electron field emiters has been made during the last decade. The electrochemical field-effect transistor (FET) behavior of a mesh of PANI-NFs bridging two 10-nm-wide Pt electrodes separated by 2 μm has been investigated [273]. FETs based on single PANI-NFs were fabricated (Figure 2.32) and characterized [503]. The 100-nm-wide and 2.5-μm-long PANI-NF FETs were turned 'on' and 'off' by electrical or chemical signals. A large modulation in the electrical conductivity of up to three orders of magnitude was obtained as a result of varying the electrochemical gate potential of PANI-NFs. Single conducting PANI-NFs FET showed higher electrical performance than FET, based on PANI nanofiber electrode junctions and thin films in terms of their transconductance and on/off current (I_{on}/I_{off}) ratio. Furthermore, the performance of single PANI-NF FETs was found to be comparable to Si nanowire FETs.

Possible applications of PANI-NTs in the construction of nanotip emitters in field-emission displays and polymer-based transistors have been demonstrated [238]. Gate voltage controllable p–n junction diode behavior for polymeric-acid-doped PANI-NTs with Au contacts, configured as a FET, was reported [334].

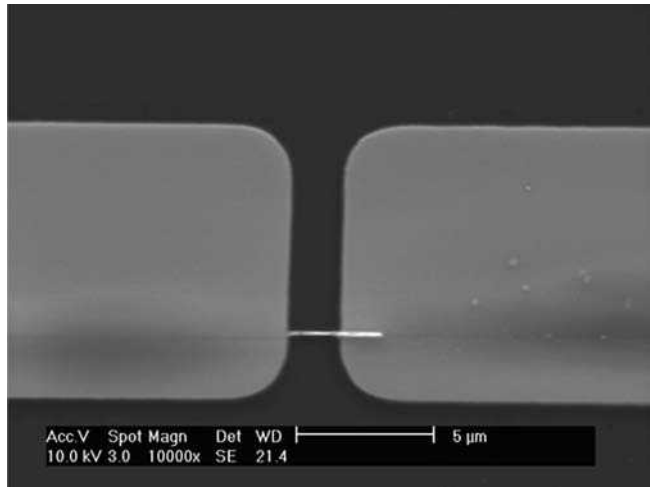

Figure 2.32 *Field-effect transistor based on single conducting PANI-NF. (Reprinted with permission from Journal of Physical Chemistry C, Field-Effect Transistors based on Single Nanowires of Conducting Polymers by A. K. Wanekaya, Mangesh A. Bangat et al., 111, 13, 5218–5221. Copyright (2007) American Chemical Society)*

2.4.2.4 Corrosion Protection

It is well known that nanoparticulate colloidal dispersions of PANI in various paints at low concentrations cause tremendous improvements in corrosion protection [504]. PANI-NFs showed similar anticorrosive effects e.g., carbon steel coated with PANI-NFs has better corrosion protection than that with aggregated PANI. Raman spectroscopy analysis indicated that the surface of carbon steel coated with PANI-NFs formed a better passive layer, which is composed of α-ferric oxide and Fe_3O_4 [146]. The corrosion resistance performance of soya oil alkyd containing nanostructured PANI composite coatings has recently been studied [447]. An array of Fe nanowires within PANI-NTs was obtained using a two-step template synthesis [316]. This PANI-NT envelope may protect the Fe nanowires against a corrosive atmosphere.

2.4.2.5 Data Storage

A nonvolatile digital memory device based on PANI-NFs decorated with Au nanoparticles has been reported (Figure 2.33) [450,505,506]. The device has a simple structure consisting of a plastic composite film sandwiched between two electrodes. An external bias was used to program the 'on' and 'off' states of the device that are separated by a three-orders-of-magnitude difference in conductivity. On–off switching times of less than 25 ns were observed by electrical pulse measurements. The devices possess prolonged retention times of several days after they had been programmed. Write–read–erase cycles have also been demonstrated. The switching mechanism was attributed to an electric-field-induced charge transfer from the PANI-NFs to the Au nanoparticles. The active polymer layer was created

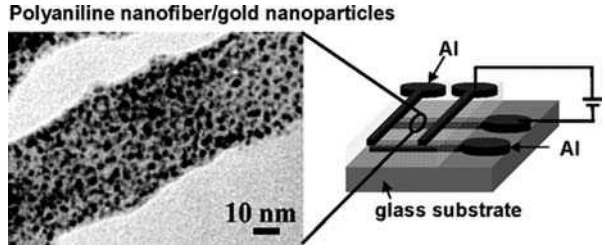

Figure 2.33 *PANI-NFs/Au nanoparticle bistable digital memory device (from Table of Contents of Reference 504). (Reprinted with permission from Nano Letters, Polyaniline nanofiber/Gold Nanoparticle Nonvolatile Memory by R. J. Tseng, J. Huang, J. Ouyang et al., 5, 6, 1077–1080. Copyright (2005) American Chemical Society)*

by growing nanometer size Au particles within 30-nm-diameter PANI-NFs using a redox reaction with chloroauric acid.

2.4.2.6 Actuators

Asymmetric PANI films formed by flash-welding PANI-NF mats, having a completely dense flash-welded top layer ~1 μm thick, while the underlayer of nanofibers remains porous, have demonstrated rapid reversible actuation in the presence of select aqueous acids and bases [507]. The collective movement of the individual nanofibers in the asymmetric film creates a large degree of actuation resembling natural muscle. These continuous single-component bending/curling actuators have several advantages over conventional dual-component bimorph actuators, including ease of synthesis, large degree of bending, patternability, and no delamination, and could be developed for use in microtweezers, microvalves, artificial muscles, chemical sensors, and/or patterned actuator structures [450]. A flexible conducting polymer actuator was fabricated using an electrospun PVA nanofibrous mat followed by *in situ* chemical polymerization with aniline [508]. The PVA/PANI hybrid mat consisted of PANI-NFs grown on the surface of individual PVA nanofibers.

2.4.2.7 Membranes

A gas-diffusion electrode with a catalyst layer containing a mixture of Nafion and PANI-NFs, showing good mechanical properties and acceptable electrochemical activity, has been prepared [509]. This type of modified electrode could potentially be applied in the development of a membrane–electrode assembly. A nanocomposite ultrafiltration membrane with improved permeability has been prepared through the filtration of a PANI-NF aqueous dispersion with a polysulfone ultrafiltration membrane [510], or by blending PANI-NFs with polysulfone ultrafiltration membrane using a phase-inversion process [457]. An unusual nanoscale photothermal effect of PANI-NFs, called ‘flash welding’, has led to the development of new techniques for making asymmetric polymer membranes [450].

2.4.2.8 Solar-Cell Devices

Polymer solar-cell devices based on a blend of poly(3-hexylthiophene) and [6,6]-phenyl-C61-butyric acid methyl ester, and incorporating doped PANI-NTs as an interfacial layer, have been fabricated [511,512]. The power-conversion efficiency of an annealed device incorporating the PANI-NTs layer showed an increase of $\sim$ 26% relative to that of the annealed device lacking the PANI-NTs interfacial layer. The high conductivity, controlled tubular nanoscale morphologies, and mobility of the annealed PANI-NTs layer led to efficient extraction of photogenerated holes to the buffer layer and suppression of exciton recombination, thereby improving the photovoltaic performance.

2.4.2.9 Rechargeable Batteries

PANI-NF/V_2O_5 is a promising nanocomposite material for utilization as a cathode for ion-Li batteries [292,293]. PANI-NFs have been used as a cathode material for rechargeable Li-polymer cells assembled with a gel polymer electrolyte [152], and in an aqueous PANI-Zn rechargeable battery [261]. Dispersions of dedoped PANI-NFs in poly(vinylidene fluoride-hexafluoropropylene)-based gel polymers can be used as electrolyte membranes for rechargeable Li batteries [513]. PANI-NF and PANI-NT arrays, which show superior electrochemical properties to the bulk counterpart, can be applied to Li-polymer thin-film batteries, which are shape-flexible and specifically suitable for powering integrated circuit cards and microelectromechanical systems [514,515].

2.4.2.10 Miscellaneous Applications

PANI-NF emeraldine salts have a high dispersion stability in vinylidene fluoride-trifluoroethylene copolymers and lead to percolative ferroelectric nanocomposites with enhanced electric responses [460]. Nanofibrous PANI has been applied as an electrorheological (ER) fluid [516,517] and exhibited distinctly improved suspended stability and a larger ER effect under electric fields compared to conventional granular PANI ER fluid. Electrospinning was used to fabricate Schottky diodes using PANI-NFs and n-doped Si [518]. PANI-NFs (nanorods) obtained by electroless surface polymerization on a modified ITO surface for electrochemical supercapacitors have been described [410]. Nanofibrous PANI/manganese oxide films [12], PANI-NFs/acetylene black/polytetrafluoroethylene/graphite composite electrode [55], activated carbon electrode modified with PANI-NFs doped with lithium salt [150], PANI-NFs/carboxymethyl cellulose/styrene-butadiene rubber/Ti foil [153], PANI-NFs doped with citric acid [175], PANI-NFs/Ti/Si [240], and PANI-NF-modified stainless-steel electrode [519] were also used to assemble supercapacitors. New PANI-NFs materials for electrochemical redox capacitors, with advantages including low cost, long life cycle and stability in acidic solutions at pH 3, have recently been prepared [262]. Electromagnetic-interference-shielding composite materials were developed from the conductive blends of nanostructured PANI and PANI-clay nanocomposites with ethylene vinyl acetate as the host matrix [458]. A mixture of PANI-NFs, PANI-NTs, TiO_2 nanoparticles, and Fe_3O_4 microparticles showed excellent microwave absorption (>99.4%) at high frequency [370]. Blends of low-density polyethylene, *p*-TSA and nanotubes of self-doped PANI were formulated into films with effective antistatic

properties [364]. Nitrogen-containing CNTs were synthesized by the carbonization of PANI-NTs [443–445].

2.5 Conclusions and Outlook

Breakthrough template (hard- (nanoporous, nanostructured seed) and soft-template (oligomer-, polymer-, surfactant-, and amphiphilic acid-assisted syntheses)), and template-free methods (not-shaken–not-stirred, aqueous/organic interfacial, rapid-mixing, and dilute polymerizations; photo-assisted, radiolythic, sonochemical, solid-state mechanochemical, and electrochemical syntheses; dopant-free, falling pH, pH-stat, and hydrophobic surface methods) in the syntheses of PANI nanostructures have been developed over the last two decades. However, simple and efficient synthesis of well-oriented arrays of PANI nanostructures with controllable morphologies and sizes, especially on a large scale, is still challenging. Despite the fact that a number of studies, experimental as well as theoretical, have been devoted to the understanding of the genesis of PANI nanostructures, the mechanisms of the formation of PANI nanostructures are still unclear. PANI nanostructures possess some unique physical and chemical properties, quite different from the ordinary granular and colloidal PANI, which opens a completely new domain of applications. PANI-NFs, PANI-NTs, and other PANI nanostructures have a wide applicability in sensors, catalysts, electron field emitters, field-effect transistors, corrosion protection, data storage, actuators, membranes, solar cell devices, rechargeable batteries, fuel cells, electrorheological fluids, supercapacitors, electromagnetic interference shielding, microwave absorption, and antistatic coatings. Wherever a high interfacial area between PANI and its environment is important, nanostructured PANI offers the possibility of enhanced performance. Taking into account that conductivity of PANI nanostructures is dominated by the interchain and intertube/fiber contact resistance, elimination of these contact resistances is key to observing pure metal-like behavior of PANI nanostructures and represents a challenge in future investigations. Improved processability of conducting PANI nanostructures is still a challenge in practical applications. It can be expected that the combination of desirable properties of PANI nanostructures and micro-/submicro-/nanoparticles of various metals, oxides, organic/bioorganic compounds, and biological materials, can lead to significant improvements in the technological performances of new composites containing PANI nanostructures.

References

[1] J. Stejskal and R. G. Gilbert, Polyaniline. Preparation of a conducting polymer, *Pure Appl. Chem.*, **74**, 857–867 (2002).
[2] J.-C. Chiang and A. G. MacDiarmid, 'Polyaniline': Protonic acid doping of the emeraldine form to the metallic regime, *Synth. Met.*, **13**, 193–205 (1986).
[3] A. G. MacDiarmid, L. S. Yang, W.-S. Huang, and B. D. Humphrey, Polyaniline: Electrochemistry and application to rechargeable batteries, *Synth. Met.*, **18**, 393–398 (1987).

[4] R. P. McCall, J. M. Ginder, J. M. Leng, K. A. Coplin, H. J. Ye, A. J. Epstein, G. E. Asturias, S. K. Manohar, J. G. Masters, E. M. Scherr, Y. Sun, and A. G. MacDiarmid, Photoinduced absorption and erasable optical information storage in polyanilines, *Synth. Met.*, **41**, 1329–1332 (1991).
[5] D. C. Trivedi and S. K. Dhawan, Shielding of electromagnetic interference using polyaniline, *Synth. Met.*, **59**, 267–272 (1993).
[6] D. A. Makeiff and T. Huber, Microwave absorption by polyaniline–carbon nanotube composites, *Synth. Met.*, **156**, 497–505 (2006).
[7] D. Dutta, T. K. Sarma, D. Chowdhury, and A. Chattopadhyay, A polyaniline-containing filter paper that acts as a sensor, acid, base, and endpoint indicator and also filters acids and bases, *J. Colloid Interface Sci.*, **283**, 153–159 (2005).
[8] A. Drelinkiewicz, A. Waksmundzka-Góra, J. W. Sobczak, and J. Stejskal, Hydrogenation of 2-ethyl-9,10-anthraquinone on Pd-polyaniline(SiO_2) composite catalyst: The effect of humidity, *Appl. Catal. A: Gen.*, **333**, 219–228 (2007).
[9] C. Zhao, S. Xing, Y. Yu, W. Zhang, and C. Wang, A novel all-plastic diode based upon pure polyaniline material, *Microelectron. J.*, **38**, 316–320 (2007).
[10] I. Willner, B. Willner, and E. Katz, Biomolecule–nanoparticle hybrid systems for bioelectronic applications, *Bioelectrochemistry*, **70**, 2–11 (2007).
[11] N. V. Blinova, J. Stejskal, M. Trchová, G. Ćirić-Marjanović, and I. Sapurina, Polymerization of aniline on polyaniline membranes, *J. Phys. Chem. B*, **111**, 2440–2448 (2007).
[12] L.-J. Sun, X.-X. Liu, K. K.-T. Lau, L. Chen, and W.-M. Gu, Electrodeposited hybrid films of polyaniline and manganese oxide in nanofibrous structures for electrochemical supercapacitor, *Electrochim. Acta*, **53**, 3036–3042 (2008).
[13] A. Bessière, C. Duhamel, J.-C. Badot, V. Lucas, and M.-C. Certiat, Study and optimization of a flexible electrochromic device based on polyaniline, *Electrochim. Acta*, **49**, 2051–2055 (2004).
[14] C. Halvorson, Y. Cao, D. Moses, and A. J. Heeger, Third order nonlinear optical susceptibility of polyaniline, *Synth. Met.*, **57**, 3941–3944 (1993).
[15] H. L. Wang, A. G. MacDiarmid, Y. Z. Wang, D. D. Gebier, and A. J. Epstein, Application of polyaniline (emeraldine base, EB) in polymer light-emitting devices, *Synth. Met.*, **78**, 33–37 (1996).
[16] K. Kaneto, M. Kaneko, Y. Min, and A. G. MacDiarmid, 'Artificial muscle': Electromechanical actuators using polyaniline films, *Synth. Met.*, **71**, 2211–2212 (1995).
[17] M. A. Soto-Oviedo, O. A. Araújo, R. Faez, M. C. Rezende, and M.-A. DePaoli, Antistatic coating and electromagnetic shielding properties of a hybrid material based on polyaniline/organoclay nanocomposite and EPDM rubber, *Synth. Met.*, **156**, 1249–1255 (2006).
[18] A. Kalendová, D. Veselý, and J. Stejskal, Organic coatings containing polyaniline and inorganic pigments as corrosion inhibitors, *Progr. Org. Coat.*, **62**, 105–116 (2008).
[19] J. Stejskal, P. Kratochvíl, and A. D. Jenkins, The formation of polyaniline and the nature of its structures, *Polymer*, **37**, 367–369 (1996).
[20] S. P. Armes, Colloidal dispersions of conducting polymers. In *Handbook of Conducting Polymers*, *2nd Edn*., T. A. Skotheim, R. L. Elsenbaumer, and J. R. Reynolds (Eds), Marcel Dekker, New York, 1998.
[21] J. Stejskal, Colloidal dispersions of conducting polymers, *J. Polym. Mater.*, **18**, 225–258 (2001).
[22] S. Virji, J. Huang, R. B. Kaner, and B. H. Weiller, Polyaniline nanofiber gas sensors: Examination of response mechanisms, *Nano Lett.*, **4**, 491–496 (2004).
[23] J. Huang, Syntheses and applications of conducting polymer polyaniline nanofibers, *Pure Appl. Chem.*, **78**, 15–28 (2006).
[24] D. Zhang and Y. Wang, Synthesis and applications of one-dimensional nano-structured polyaniline: An overview, *Mater. Sci. Eng. B*, **134**, 9–19 (2006).
[25] S. Bhadra, D. Khastgir, N. K. Singha, and J. H. Lee, Progress in preparation, processing and applications of polyaniline, *Prog. Polym. Sci.*, **34**, 783–810 (2009).
[26] M. Wan, Some issues related to polyaniline micro-/nanostructures, *Macromol. Rapid Commun.*, **30**, 963–975 (2009).
[27] P. Liu and L. Zhang, Hollow nanostructured polyaniline: Preparation, properties and applications, *Crit. Rev. Solid State Mater. Sci.*, **34**, 75–87 (2009).

[28] I. D. Norris, M. M. Shaker, F. K. Ko, and A. G. MacDiarmid, Electrostatic fabrication of ultrafine conducting fibers: polyaniline/polyethylene oxide blends, *Synth. Met.*, **114**, 109–114 (2000).
[29] A. G. MacDiarmid, W. E. Jones, Jr., I. D. Norris, J. Gao, A. T. Johnson, Jr., N. J. Pinto, J. Hone, B. Han, F. K. Ko, H. Okuzaki, and M. Llaguno, Electrostatically-generated nanofibers of electronic polymers, *Synth. Met.*, **119**, 27–30 (2001).
[30] P. K. Kahol and N. J. Pinto, Electron paramagnetic resonance investigations of electrospun polyaniline fibers, *Solid State Commun.*, **124**, 195–197 (2002).
[31] Y. X. Zhou, M. Freitag, J. Hone, C. Staii, N. J. Pinto, A. T. Johnson, Jr., and A. G. MacDiarmid, Fabrication and electrical characterization of polyaniline-based nanofibers with diameter below 30 nm, *Appl. Phys. Lett.*, **83**, 3800–3802 (2003).
[32] N. J. Pinto, A. T. Johnson, Jr., A. G. MacDiarmid, C. H. Mueller, N. Theofylaktos, D. C. Robinson, and F. A. Miranda, Electrospun polyaniline/polyethylene oxide nanofiber field-effect transistor, *Appl. Phys. Lett.*, **83**, 4244–4246 (2003).
[33] P. K. Kahol and N. J. Pinto, An EPR investigation of electrospun polyaniline-polyethylene oxide blends, *Synth. Met.*, **140**, 269–272 (2004).
[34] D. Aussawasathien, J.-H. Dong, and L. Dai, Electrospun polymer nanofiber sensors, *Synth. Met.*, **154**, 37–40 (2005).
[35] A. G. MacDiarmid, Synthetic metals: a novel role for organic polymers, *Synth. Met.*, **125**, 11–22 (2002).
[36] H. Liu, J. Kameoka, D. A. Czaplewski, and H. G. Craighead, Polymeric nanowire chemical sensor, *Nano. Lett.*, **4**, 671–675 (2004).
[37] A. Attout, S. Yunus, and P. Bertrand, Electrospinning and alignment of polyaniline-based nanowires and nanotubes, *Polym. Eng. Sci.*, **48**, 1661–1666 (2008).
[38] J. H. Jun, K. Cho, J. Yun, K. S. Suh, T. Y. Kim, and S. Kim, Enhancement of electrical characteristics of electrospun polyaniline nanofibers by embedding the nanofibers with Ga-doped ZnO nanoparticles, *Org. Electron.*, **9**, 445–451 (2008).
[39] P. H. S. Picciani, E. S. Medeiros, Z. Pan, W. J. Orts, L. H. C. Mattoso, and B. G. Soares, Development of conducting polyaniline/poly(lactic acid) nanofibers by electrospinning, *J. Appl. Polym. Sci.*, **112**, 744–753 (2009).
[40] C. He, Y. Tan, and Y. Li, Conducting polyaniline nanofiber networks prepared by the doping induction of camphor sulfonic acid, *J. Appl. Polym. Sci.*, **87**, 1537–1540 (2003).
[41] X. Zhang and S. K. Manohar, Polyaniline nanofibers: chemical synthesis using surfactants, *Chem. Commun.*, 2360–2361 (2004).
[42] D. Chaudhuri, S. Datar, R. Viswanatha, D. D. Sarma, and H. Amenitsch, Self-organization of polyaniline nanorods: Towards achieving a higher conductivity, *Appl. Phys. Lett.*, **87**, 093117 (2005).
[43] A. G. MacDiarmid, J. C. Chiang, A. F. Richter, and A. J. Epstein, Polyaniline: a new concept in conducting polymers, *Synth. Met.* **18**, 285–290 (1987).
[44] K. Jackowska, A. T. Bieguński, and M. Tagowska, Hard template synthesis of conducting polymers: a route to achieve nanostructures, *J. Solid State Electrochem.*, **12**, 437–443 (2008).
[45] C.-G. Wu and T. Bein, Conducting polyaniline filaments in a mesoporous channel host, *Science*, **264**, 1757–1759 (1994).
[46] C. W. Wang, Z. Wang, M. K. Li, and H. L. Li, Well-aligned polyaniline nano-fibril array membrane and its field emission property, *Chem. Phys. Lett.*, **341**, 431–434 (2001).
[47] Z. Wang, M. Chen, and H.-L. Li, Preparation and characterization of uniform polyaniline nano-fibrils using the anodic aluminum oxide template, *Mater. Sci. Eng. A.*, **328**, 33–38 (2002).
[48] S. M. Yang, K. H. Chen, and Y. F. Yang, Synthesis of polyaniline nanotubes in the channels of anodic alumina membrane, *Synth. Met.*, **152**, 65–68 (2005).
[49] N.-R. Chiou, L. J. Lee, and A. J. Epstein, Porous membrane controlled polymerization of nanofibers of polyaniline and its derivatives, *J. Mater. Chem.*, **18**, 2085–2089 (2008).
[50] X. Li, X. Li, and G. Wang, Fibrillar polyaniline/diatomite composite synthesized by one-step in situ polymerization method, *Appl. Surf. Sci.*, **249**, 266–270 (2005).

[51] X. Zhang, W. J. Goux, and S. K. Manohar, Synthesis of polyaniline nanofibers by 'nanofiber seeding', *J. Am. Chem. Soc.*, **126**, 4502–4503 (2004).
[52] D. Li and R. B. Kaner, Shape and aggregation control of nanoparticles: Not shaken, not stirred, *J. Am. Chem. Soc.*, **128**, 968–975 (2006).
[53] R. C. Y. King and F. Roussel, Morphological and electrical characteristics of polyaniline nanofibers, *Synth. Met.*, **153**, 337–340 (2005).
[54] T. Thanpitcha, A. Sirivat, A. M. Jamieson, and R. Rujiravanit, Synthesis of polyaniline nanofibrils using an in situ seeding technique, *Synth. Met.*, **158**, 695–703 (2008).
[55] H. Mi, X. Zhang, S. Yang, X. Ye, and J. Luo, Polyaniline nanofibers as the electrode material for supercapacitors, *Mater. Chem. Phys.*, **112**, 127–131 (2008).
[56] J. Li, K. Fang, H. Qiu, S. Li, W. Mao, and Q. Wu, Micromorphology and conductive property of the pellets prepared by HCl-doped polyaniline nanofibers, *Synth. Met.*, **145**, 191–194 (2004).
[57] P. Xu, X. Han, J. Jiang, X. Wang, X. Li, and A. Wen, Synthesis and characterization of novel coralloid polyaniline/$BaFe_{12}O_{19}$ nanocomposites, *J. Phys. Chem. C.*, **111**, 12603–12608 (2007).
[58] H. Ding, X.-M. Liu, M. Wan, and S.-Y. Fu, Electromagnetic functionalized cage-like polyaniline composite nanostructures, *J. Phys. Chem. B.*, **112**, 9289–9294 (2008).
[59] C. Su, G. Wang, and F. Huang, Preparation and characterization of composites of polyaniline nanorods and multiwalled carbon nanotubes coated with polyaniline, *J. Appl. Polym. Sci.*, **106**, 4241–4247 (2007).
[60] Y. Gao, F. Wang, J. Gong, Z. Su, and L. Qu, Polyaniline nanorods and hollow-microspheres prepared by using copper wires or rings as template, *J. Nanosci. Nanotechn.*, **8**, 5972–5976 (2008).
[61] W. Li and H.-L. Wang, Oligomer-assisted synthesis of chiral polyaniline nanofibers, *J. Am. Chem. Soc.*, **126**, 2278–2279 (2004).
[62] W. Li, J. A. Bailey, and H.-L. Wang, Toward optimizing synthesis of nanostructured chiral polyaniline, *Polymer*, **47**, 3112–3118 (2006).
[63] H. D. Tran, Y. Wang, J. M. D'Arcy, and R. B. Kaner, Toward an understanding of the formation of conducting polymer nanofibers, *ACS Nano*, **2**, 1841–1848 (2008).
[64] X. Li, Y. Zhao, T. Zhuang, G. Wang, and Q. Gu, Self-dispersible conducting polyaniline nanofibres synthesized in the presence of β-cyclodextrin, *Colloids and Surfaces A: Physicochem. Eng. Aspects*, **295**, 146–151 (2007).
[65] X. Li, T. Zhuang, G. Wang, and Y. Zhao, Stabilizer-free conducting polyaniline nanofiber aqueous colloids and their stability, *Mater. Lett.*, **62**, 1431–1434 (2008).
[66] S. Xing, C. Zhao, S. Jing, and Z. Wang, Morphology and conductivity of polyaniline nanofibers prepared by 'seeding' polymerization, *Polymer*, **47**, 2305–2313 (2006).
[67] J. H. Hwang and S. C. Yang, Morphological modification of polyaniline using polyelectrolyte template molecules, *Synth. Met.*, **29**, 271–276 (1989).
[68] J. M. Liu and S. C. Yang, Novel colloidal polyaniline fibrils made by template guided chemical polymerization, *J. Chem. Soc., Chem. Commun.*, 1529–1531 (1991).
[69] Q. Sun, M.-C. Park, and Y. Deng, Dendritic superstructure formation of polyaniline prepared using a water-soluble polyelectrolyte copolymer as the support matrix, *Mater. Lett.*, **61**, 3052–3055 (2007).
[70] Z. Zhang, L. Wang, J. Deng, and M. Wan, Self-assembled nanostructures of polyaniline doped with poly(3-thiopheneacetic acid), *React. Funct. Polym.*, **68**, 1081–1087 (2008).
[71] Y. Yu, S. Zhihuai, S. Chen, C. Bian, W. Chen, and G. Xue, Facile synthesis of polyaniline-sodium alginate nanofibers, *Langmuir*, **22**, 3899–3905 (2006).
[72] P. Nickels, W. U. Dittmer, S. Beyer, J. P. Kotthaus, and F. C. Simmel, Polyaniline nanowire synthesis templated by DNA, *Nanotechnology*, **15**, 1524–1529 (2004).
[73] Y. Ma, J. Zhang, G. Zhang, and H. He, Polyaniline nanowires on Si surfaces fabricated with DNA templates, *J. Am. Chem. Soc.*, **126**, 7097–7101 (2004).
[74] P. R. Singh, S. Mahajan, S. Rajwade, and A. Q. Contractor, EC-AFM investigation of reversible volume changes with electrode potential in polyaniline, *J. Electroanal. Chem.*, **625**, 16–26 (2009).
[75] X. Li, M. Wan, X. Li, and G. Zhao, The role of DNA in PANI–DNA hybrid: Template and dopant, *Polymer*, **50**, 4529–4534 (2009).

[76] L. Meng, Y. Lu, X. Wang, J. Zhang, Y. Duan, and C. Li, Facile synthesis of straight polyaniline nanostick in hydrogel, *Macromolecules* **40**, 2981–2983 (2007).
[77] J. Bhadra and D. Sarkar, Self-assembled polyaniline nanorods synthesized by facile route of dispersion polymerization, *Mater. Lett*., **63**, 69–71 (2009).
[78] Y. Li and X. Jing, Morphology control of chemically prepared polyaniline nanostructures: effects of mass transfer, *React. Funct. Polym.*, **69**, 797–807 (2009).
[79] D. M. Sarno, S. K. Manohar, and A. G. MacDiarmid, Controlled interconversion of semiconducting and metallic forms of polyaniline nanofibers, *Synth. Met.*, **148**, 237–243 (2005).
[80] J. Chen, Y. Xu, Y. Zheng, L. Dai, and H. Wu, The design, synthesis and characterization of polyaniline nanophase materials, *Compt. Rend. Chim*., **11**, 84–89 (2008).
[81] T. Jeevananda, J. H. Lee, and Siddaramaiah, Preparation of polyaniline nanostructures using sodium dodecylsulphate, *Mater. Lett.*, **62**, 3995–3998 (2008).
[82] Y.-G. Han, T. Kusunose, and T. Sekino, Facile one-pot synthesis and characterization of novel nanostructured organic dispersible polyaniline, *J. Polym. Sci. Part B: Polym. Phys.*, **47**, 1024–1029 (2009).
[83] X. Wang, M. Shao, G. Shao, Z. Wu, and S. Wang, A facile route to ultra-long polyaniline nanowires and the fabrication of photoswitch, *J. Colloid Interface Sci.*, **332**, 74–77 (2009).
[84] G. Li, Z. Wang, G. Xie, H. Peng, and Z. Zhang, Synthesis of interconnected polyaniline nanofibers in catanionic micelles, *J. Dispersion Sci. Technol.*, **27**, 991–995 (2006).
[85] Z. Miao, Y. Wang, Z. Liu, J. Huang, B. Han, Z. Sun, and J. Du, Synthesis of polyaniline nanofibrous networks with the aid of an amphiphilic ionic liquid, *J. Nanosci. Nanotechn.*, **6**, 227–230 (2006).
[86] H. J. Qiu and M. X. Wan, Nanostructures of polyaniline doped with a novel dopant, *Mater. Phys. Mech*., **4**, 125 (2001).
[87] H. Qiu and M. Wan, Synthesis, characterization, and electrical properties of nanostructural polyaniline doped with novel sulfonic acids (4-{n-[4-(4-nitrophenylazo)phenyloxy]alkyl} aminobenzene sulfonic acid), *J. Polym. Sci. Part A: Polym. Chem*., **39**, 3485–3497 (2001).
[88] K. Huang and M. Wan, Self-assembled polyaniline nanostructures with photoisomerization function, *Chem. Mater*., **14**, 3486–3492 (2002).
[89] Z. Wei, Z. Zhang, and M. Wan, Formation mechanism of self-asembled polyaniline micro/nanotubes, *Langmuir*, **18**, 917–921 (2002).
[90] G. M. do Nascimento, C. H. B. Silva, and M. L. A. Temperini, Electronic structure and doping behavior of PANI-NSA nanofibers investigated by resonance Raman spectroscopy, *Macromol. Rapid Commun*., **27**, 255–259 (2006).
[91] G. M. do Nascimento, C. H. B. Silva, C. M. S. Izumi, and M. L. A. Temperini, The role of cross-linking structures to the formation of one-dimensional nano-organized polyaniline and their Raman fingerprint, *Spectrochim. Acta Part A*, **71**, 869–875 (2008).
[92] L. Zhang, M. Wan, and Y. Wei, Nanoscaled polyaniline fibers prepared by ferric chloride as an oxidant, *Macromol. Rapid Commun.*, **27**, 366–371 (2006).
[93] Z. Zhang and M. Wan, Composite films of nanostructured polyaniline with poly(vinyl alcohol), *Synth. Met.*, **128**, 83–89 (2002).
[94] X. Bai, X. Li, N. Li, Y. Zuo, L. Wang, J. Li, and S. Qiu, Synthesis of cluster polyaniline nanorod via a binary oxidant system, *Mater. Sci. Eng. C* **27**, 695–699 (2007).
[95] G. Li, S. Pang, H. Peng, Z. Wang, Z. Cui, and Z. Zhang, Templateless and surfactantless route to the synthesis of polyaniline nanofibers, *J. Polym. Sci. A: Polym. Chem.*, **43**, 4012–4015 (2005).
[96] L. Zhang, H. Peng, P. A. Kilmartin, C. Soeller, and J. Travas-Sejdic, Poly(3,4-ethylenedioxythiophene) and polyaniline bilayer nanostructures with high conductivity and electrocatalytic activity, *Macromolecules*, **41**, 7671–7678 (2008).
[97] J. Wang, J. Wang, Z. Yang, Z. Wang, F. Zhang, and S. Wang, A novel strategy for the synthesis of polyaniline nanostructures with controlled morphology, *React. Funct. Polym.*, **68**, 1435–1440 (2008).
[98] P. Anilkumar and M. Jayakannan, New renewable resource amphiphilic molecular design for size-controlled and highly ordered polyaniline nanofibers, *Langmuir*, **22**, 5952–5957 (2006).

[99] P. Anilkumar and M. Jayakannan, Fluorescent tagged probing agent and structure-directing amphiphilic molecular design for polyaniline nanomaterials via self-assembly process, *J. Phys. Chem. C*, **111**, 3591–3600 (2007).
[100] P. Anilkumar and M. Jayakannan, Single-molecular-system-based selective micellar templates for polyaniline nanomaterials: control of shape, size, solid state ordering, and expanded chain to coillike conformation, *Macromolecules*, **40**, 7311–7319 (2007).
[101] P. Anilkumar and M. Jayakannan, Divergent nanostructures from identical ingredients: Unique amphiphilic micelle template for polyaniline nanofibers, tubes, rods, and spheres, *Macromolecules*, **41**, 7706–7715 (2008).
[102] P. Anilkumar and M. Jayakannan, Self-assembled cylindrical and vesicular molecular templates for polyaniline nanofibers and nanotapes, *J. Phys. Chem. B*, **113**, 11614–11624 (2009).
[103] H. Xia, J. Narayanan, D. Cheng, C. Xiao, X. Liu, and H. S. O. Chan, Formation of ordered arrays of oriented polyaniline nanoparticle nanorods, *J. Phys. Chem. B*, **109**, 12677–12684 (2005).
[104] C. Cheng, J. Jiang, R. Tang, and F. Xi, Polyaniline nanostructures doped with mono-sulfonated dendrons via a self-assembly process, *Synth. Met.*, **145**, 61–65 (2004).
[105] L. Zhang, L. Zhang, M. Wan, and Y. Wei, Polyaniline micro/nanofibers doped with saturation fatty acids, *Synth. Met.*, **156**, 454–458 (2006).
[106] X. Wang, J. Liu, X. Huang, L. Men, M. Guo, and D. Sun, Controlled synthesis of linear polyaniline tubes and dendritic polyaniline fibers with stearic acid, *Polym. Bull.*, **60**, 1–6 (2008).
[107] Z. Zhang, M. Wan, and Y. Wei, Highly crystalline polyaniline nanostructures doped with dicarboxylic acids, *Adv. Funct. Mater.*, **16**, 1100–1104 (2006).
[108] X. Ma, G. Li, M. Wang, Y. Cheng, R. Bai, and H. Chen, Preparation of a nanowire-structured polyaniline composite and gas sensitivity studies, *Chem. Eur. J.*, **12**, 3254–3260 (2006).
[109] E. Jin, N. Liu, X. Lu, and W. Zhang, Novel micro/nanostructures of polyaniline in the presence of different amino acids via a self-assembly process, *Chem. Lett.*, **36**, 1288 (2007).
[110] J. Chen, D. Chao, X. Lu, and W. Zhang, Novel interfacial polymerization for radially oriented polyaniline nanofibers, *Mater. Lett.*, **61**, 1419–1423 (2007).
[111] X. Wang, X. Feng, Y. Zhao, R. Zhang, and D. Sun, Preparation of dendritic and network PANI/silica composite fibers, *Eur. Polym. J.*, **43**, 3679–3682 (2007).
[112] G. Li, S. Pang, G. Xie, Z. Wang, H. Peng, and Z. Zhang, Synthesis of radially aligned polyaniline dendrites, *Polymer* **47**, 1456–1459 (2006).
[113] Y. Zhu, J. Li, M. Wan, and L. Jiang, Superhydrophobic 3D microstructures assembled from 1D nanofibers of polyaniline, *Macromol. Rapid. Commun.*, **29**, 239–243 (2008).
[114] Y. Zhu, J. Li, M. Wan, and L. Jiang, 3D-boxlike polyaniline microstructures with superhydrophobic and high-crystalline properties, *Polymer*, **49**, 3419–3423 (2008).
[115] Y. Zhu, D. Hu, M. X. Wan, L. Jiang, and Y. Wei, Conducting and superhydrophobic rambutan-like hollow spheres of polyaniline, *Adv. Mater.*, **19**, 2092–2096 (2007).
[116] W. Zhong, J. Deng, Y. Yang, and W. Yang, Synthesis of large-area three-dimensional polyaniline nanowire networks using a 'soft template', *Macromol. Rapid Commun.*, **26**, 395–400 (2005).
[117] C. Zhou, J. Han, and R. Guo, Synthesis of polyaniline hierarchical structures in a dilute SDS/HCl solution: Nanostructure-covered rectangular tubes, *Macromolecules*, **42** 1252–1257 (2009).
[118] A. Garai and A. K. Nandi, Tuning of different polyaniline nanostructures from a coacervate gel/sol template, *Synth. Met.*, **159**, 757–760 (2009).
[119] A. D. W. Carswell, E. A. O'Rear, and B. P. Grady, Adsorbed surfactants as templates for the synthesis of morphologically controlled polyaniline and polypyrrole nanostructures on flat surfaces: from spheres to wires to flat films, *J. Am. Chem. Soc.*, **125**, 14793–14800 (2003).
[120] C.-H. Yang, Y.-K. Chih, H.-E. Cheng, and C.-H. Chen, Nanofibers of self-doped polyaniline, *Polymer* **46**, 10688–10698 (2005).
[121] C.-H. Yang, Y.-K. Chih, M.-S. Tsai, and C.-H. Chen, Self-doped polyaniline nanostructures for casting metal nanorods, *Electrochem. Solid-State Lett.*, **9**, G49–G52 (2006).

[122] C. Zhang, G. Li, and H. Peng, Large-scale synthesis of self-doped polyaniline nanofibers, *Mater. Lett.*, **63**, 592–594 (2009).
[123] Y. Yan, Z. Yu, Y. W. Huang, W. X. Yuan, and Z. X. Wei, Helical polyaniline nanofibers induced by chiral dopants by a polymerization process, *Adv. Mater.*, **19**, 3353–3357 (2007).
[124] X. Zhang, V. Chechik, D. K. Smith, P. H. Walton, and A.-K. Duhme-Klair, Controlled synthesis of optically active polyaniline nanorods and nanostructured gold microspheres using tetrachloroaurate as an efficient oxidant of aniline, *Macromolecules*, **41**, 3417–3421 (2008).
[125] K. Huang, X.-H. Meng, and M. Wan, Polyaniline hollow microspheres constructed with their own self-assembled nanofibers, *J. Appl. Polym. Sci.*, **100**, 3050–3054 (2006).
[126] X. Li, J. Shen, M. Wan, Z. Chen, and Y. Wei, Core–shell structured and electro-magnetic functionalized polyaniline composites, *Synth. Met.*, **157**, 575–579 (2007).
[127] G. Li and Z. Zhang, Synthesis of dendritic polyaniline nanofibers in a surfactant gel, *Macromolecules* **37**, 2683–2685 (2004).
[128] X. Ding, D. Han, Z. Wang, X. Xu, L. Niu, and Q. Zhang, Micelle-assisted synthesis of polyaniline/magnetite nanorods by in situ self-assembly process, *J. Colloid Interface Sci.*, **320**, 341–345 (2008).
[129] H. Qiu, J. Zhai, S. Li, L. Jiang, and M. Wan, Oriented growth of self-assembled polyaniline nanowire arrays using a novel method, *Adv. Funct. Mater.*, **13**, 925–928 (2003).
[130] J. Huang and R. B. Kaner, Nanofiber formation in the chemical polymerization of aniline: A mechanistic study, *Angew. Chem. Int. Ed.*, **43**, 5817–5821 (2004).
[131] J. Huang and R. B. Kaner, A general chemical route to polyaniline nanofibers, *J. Am. Chem. Soc.*, **126**, 851–855 (2004).
[132] N.-R. Chiou and A. J. Epstein, A simple approach to control the growth of polyaniline nanofibers, *Synth. Met.*, **153**, 69–72 (2005).
[133] J. Huang, S. Virji, B. H. Weiller, and R. B. Kaner, Polyaniline nanofibers: Facile synthesis and chemical sensors, *J. Am. Chem. Soc.*, **125**, 314–315 (2003).
[134] J. Huang and R. B. Kaner, The intrinsic nanofibrillar morphology of polyaniline, *Chem. Commun.*, 367–376 (2006).
[135] S. Goel, A. Gupta, K. P. Singh, R. Mehrotra, and H. C. Kandpal, Optical studies of polyaniline nanostructures, *Mater. Sci. Eng. A*, **443**, 71–76 (2007).
[136] F. Yakuphanoglu, R. Mehrotra, A. Gupta, and M. Muñoz, Nanofiber organic semiconductors: The effects of nanosize on the electrical charge transport and optical properties of bulk polyanilines, *J. Appl. Polym. Sci.*, **114**, 794–799 (2009).
[137] J. Wang, J. Wang, X. Zhang, and Z. Wang, Assembly of polyaniline nanostructures, *Macromol. Rapid Commun.*, **28**, 84–87 (2007).
[138] X. Zhang, C. Chan-Yu-King, A. Jose, and S. K. Manohar, Nanofibers of polyaniline synthesized by interfacial polymerization, *Synth. Met.*, **145**, 23–29 (2004).
[139] P. Dallas, D. Stamopoulos, N. Boukos, V. Tzitzios, D. Niarchos, and D. Petridis, Characterization, magnetic and transport properties of polyaniline synthesized through interfacial polymerization, *Polymer*, **48**, 3162–3169 (2007).
[140] J. Li, Q. Jia, J. Zhu, and M. Zheng, Interfacial polymerization of morphologically modified polyaniline: from hollow microspheres to nanowires, *Polym. Int.*, **57**, 337–341 (2008).
[141] S. Xing, H. Zheng, and G. Zhao, Preparation of polyaniline nanofibers via a novel interfacial polymerization method, *Synth. Met.*, **158**, 59–63 (2008).
[142] D. D. Sawall, R. M. Villahermosa, R. A. Lipeles, and A. R. Hopkins, Interfacial polymerization of polyaniline nanofibers grafted to Au surfaces, *Chem. Mater.*, **16**, 1606–1608 (2004).
[143] X.-B. Yan, Z.-J. Han, Y. Yang, and B.-K. Tay, Fabrication of carbon nanotube–polyaniline composites via electrostatic adsorption in aqueous colloids, *J. Phys. Chem. C*, **111**, 4125–4131 (2007).
[144] X. B. Yan, Z. J. Han, Y. Yang, and B. K. Tay, NO_2 gas sensing with polyaniline nanofibers synthesized by a facile aqueous/organic interfacial polymerization, *Sens. Actuators B*, **123**, 107–113 (2007).
[145] Y. Niu, Electromagnetic interference shielding with polyaniline nanofibers composite coatings, *Polym. Eng. Sci.*, **48**, 355–359 (2008).

[146] B. Yao, G. Wang, J. Ye, and X. Li, Corrosion inhibition of carbon steel by polyaniline nanofibers, *Mater. Lett.*, **62**, 1775–1778 (2008).
[147] G. M. do Nascimento, P. Y. G. Kobata, and M. L. A. Temperini, Structural and vibrational characterization of polyaniline nanofibers prepared from interfacial polymerization, *J. Phys. Chem. B*, **112**, 11551–11557 (2008).
[148] L. Xu, Y. Zhu, L. Tang, X. Yang, and C. Li, Dendrimer-encapsulated Pt nanoparticles/polyaniline nanofibers for glucose detection, *J. Appl. Polym. Sci.*, **109**, 1802–1807 (2008).
[149] L.-M. Huang, W.-H. Liao, H.-C. Ling, and T.-C. Wen, Simultaneous synthesis of polyaniline nanofibers and metal (Ag and Pt) nanoparticles, *Mater. Chem. Phys.*, **116**, 474–478 (2009).
[150] J. Fang, M. Cui, H. Lu, Z. Zhang, Y. Lai, and J. Li, Hybrid supercapacitor based on polyaniline doped with lithium salt and activated carbon electrodes, *J. Cent. South Univ. Technol.*, **16**, 434–439 (2009).
[151] P. L. B. Araújo, E. S. Araújo, R. F. S. Santos, and A. P. L. Pacheco, Synthesis and morphological characterization of PMMA/polyaniline nanofiber composites, *Microelectron. J.*, **36**, 1055–1057 (2005).
[152] S. R. Sivakkumar, J.-S. Oh, and D.-W. Kim, Polyaniline nanofibres as a cathode material for rechargeable lithium-polymer cells assembled with gel polymer electrolyte, *J. Power Sources*, **163**, 573–577 (2006).
[153] S. R. Sivakkumar, W. J. Kim, J.-A. Choi, D. R. MacFarlane, M. Forsyth, and D.-W. Kim, Electrochemical performance of polyaniline nanofibres and polyaniline/multi-walled carbon nanotube composite as an electrode material for aqueous redox supercapacitors, *J. Power Sources*, **171**, 1062–1068 (2007).
[154] C. Su, G. Wang, F. Huang, and X. Li, Effects of synthetic conditions on the structure and electrical properties of polyaniline nanofibers, *J. Mater. Sci.*, **43**, 197–202 (2008).
[155] A. R. Hopkins, D. D. Sawall, R. M. Villahermosa, and R. A. Lipeles, Interfacial synthesis of electrically conducting polyaniline nanofiber composites, *Thin Solid Films*, **469–470**, 304–308 (2004).
[156] F.-J. Liu, L.-M. Huang, T.-C. Wen, A. Gopalan, and J.-S. Hung, Interfacial synthesis of platinum loaded polyaniline nanowires in poly(styrene sulfonic acid), *Mater. Lett.*, **61**, 4400–4405 (2007).
[157] M.-C. Park, Q. Sun, and Y. Deng, Polyaniline microspheres consisting of highly crystallized nanorods, *Macromol. Rapid Commun.*, **28**, 1237–1242 (2007).
[158] S. Ding, H. Mao, and W. Zhang, Fabrication of DBSA-doped polyaniline nanorods by interfacial polymerization, *J. Appl. Polym. Sci.*, **109**, 2842–2847 (2008).
[159] Z. Du, C. Li, L. Li, M. Zhang, S. Xu, and T. Wang, Simple fabrication of a sensitive hydrogen peroxide biosensor using enzymes immobilized in processable polyaniline nanofibers/chitosan film, *Mater. Sci. Eng. C*, **29**, 1794–1797 (2009).
[160] Y. He, Interfacial synthesis and characterization of polyaniline nanofibers, *Mater. Sci. Eng. B*, **122**, 76–79 (2005).
[161] Y. He, One-dimensional polyaniline nanostructures synthesized by interfacial polymerization in a solids-stabilized emulsion, *Appl. Surf. Sci.*, **252**, 2115–2118 (2006).
[162] Q. Sun and Y. Deng, Morphology studies of polyaniline lengthy nanofibers formed via dimers copolymerization approach, *Eur. Polym. J.*, **44**, 3402–3408 (2008).
[163] W. Li, M. Zhu, Q. Zhang, and D. Chen, Expanded conformation of macromolecular chain in polyaniline with one-dimensional nanostructure prepared by interfacial polymerization, *Appl. Phys. Lett.*, **89**, 103110 (2006).
[164] W. Li, Q. Zhang, D. Chen, and L. Li, Study on nanofibers of polyaniline via interfacial polymerization, *J. Macromol. Sci., Pure Appl. Chem.*, **43**, 1815–1824 (2006).
[165] Y. Wang and X. Jing, Formation of polyaniline nanofibers: A morphological study, *J. Phys. Chem. B*, **112**, 1157–1162 (2008).
[166] I. Sapurina and J. Stejskal, The mechanism of the oxidative polymerization of aniline and the formation of supramolecular polyaniline structures, *Polym. Int.*, **57**, 1295–1325 (2008).
[167] H. D. Tran and R. B. Kaner, A general synthetic route to nanofibers of polyaniline derivatives, *Chem. Commun.*, 3915–3917 (2006).

[168] S. Xing, C. Zhao, S. Jing, Y. Wu, and Z. Wang, Morphology and gas-sensing behavior of in situ polymerized nanostructured polyaniline films, *Eur. Polym. J.*, **42**, 2730–2735 (2006).
[169] J. Qiang, Z. Yu, H. Wu, and D. Yun, Polyaniline nanofibers synthesized by rapid mixing polymerization, *Synth. Met.*, **158**, 544–547 (2008).
[170] C. Liu, K. Hayashi, and K. Toko, A novel formation process of polyaniline micro-/nanofiber network on solid substrates, *Synth. Met.*, **159**, 1077–1081 (2009).
[171] N.-R. Chiou and A. J. Epstein, Polyaniline nanofibers prepared by dilute polymerization, *Adv. Mater.*, **17**, 1679–1683 (2005).
[172] P.-C. Wang, E. C. Venancio, D. M. Sarno, and A. G. MacDiarmid, Simplifying the reaction system for the preparation of polyaniline nanofibers: Re-examination of template-free oxidative chemical polymerization of aniline in conventional low-pH acidic aqueous media, *React. Funct. Polym.*, **69**, 217–223 (2009).
[173] Z. Hu, J. Xu, Y. Tian, R. Peng, Y. Xian, Q. Ran, and L. Jin, Layer-by-layer assembly of polyaniline nanofibers/poly(acrylic acid) multilayer film and electrochemical sensing, *Electrochim. Acta*, **54**, 4056–4061 (2009).
[174] N.-R. Chiou, C. Lu, J. Guan, L. J. Lee, and A. J. Epstein, Growth and alignment of polyaniline nanofibres with superhydrophobic, superhydrophilic and other properties, *Nature Nanotechnology*, **2**, 354–357 (2007).
[175] A. Subramania and S. L. Devi, Polyaniline nanofibers by surfactant-assisted dilute polymerization for supercapacitor applications, *Polym. Adv. Technol.*, **19**, 725–727 (2008).
[176] H. Zhang, X. Wang, J. Li, and F. Wang, Facile synthesis of polyaniline nanofibers using pseudo-high dilution technique, *Synth. Met.*, **159**, 1508–1511 (2009).
[177] X. Zhang, H. S. Kolla, X. Wang, K. Raja, and S. K. Manohar, Fibrillar growth in polyaniline, *Adv. Funct. Mater.*, **16**, 1145–1152 (2006).
[178] L. K. Werake, J. G. Story, M. F. Bertino, S. K. Pillalamarri, and F. D. Blum, Photolithographic synthesis of polyaniline nanofibres, *Nanotechnology*, **16**, 2833–2837 (2005).
[179] Z.-F. Li, F. D. Blum, M. F. Bertino, C.-S. Kim, and S. K. Pillalamarri, One-step fabrication of a polyaniline nanofiber vapor sensor, *Sens. Actuators B*, **134**, 31–35 (2008).
[180] J. Li, H. Tang, A. Zhang, X. Shen, and L. Zhu, A new strategy for the synthesis of polyaniline nanostructures: From nanofibers to nanowires, *Macromol. Rapid Commun.*, **28**, 740–745 (2007).
[181] J. Li, L. Zhu, W. Luo, Y. Liu, and H. Tang, Correlation between one-directional helical growth of polyaniline and its optical activity, *J. Phys. Chem. C*, **111**, 8383–8388 (2007).
[182] J. Wang, L. H. Zhu, J. Li, and H. Q. Tang, Antioxidant activity of polyaniline nanofibers, *Chinese Chem. Lett.*, **18**, 1005–1008 (2007).
[183] S. K. Pillalamarri, F. D. Blum, A. T. Tokuhiro, J. G. Story, and M. F. Bertino, Radiolytic synthesis of polyaniline nanofibers: A new templateless pathway, *Chem. Mater.*, **17**, 227–229 (2005).
[184] S. K. Pillalamarri, F. D. Blum, A. T. Tokuhiro, and M. F. Bertino, One-pot synthesis of polyaniline–metal nanocomposites, *Chem. Mater.*, **17**, 5941–5944 (2005).
[185] R. A. de Barros and W. M. de Azevedo, Polyaniline/silver nanocomposite preparation under extreme or non-classical conditions, *Synth. Met.*, **158**, 922–926 (2008).
[186] X. Jing, Y. Wang, D. Wu, L. She, and Y. Guo, Polyaniline nanofibers prepared with ultrasonic irradiation, *J. Polym. Sci. A: Polym. Chem.*, **44**, 1014–1019 (2006).
[187] X. Jing, Y. Wang, D. Wu, and J. Qiang, Sonochemical synthesis of polyaniline nanofibers, *Ultrason. Sonochem.*, **14**, 75–80 (2007).
[188] Y. Wang and X. Jing, Transparent conductive thin films based on polyaniline nanofibers, *Mater. Sci. Eng. B*, **138**, 95–100 (2007).
[189] X. Lu, H. Mao, D. Chao, W. Zhang, and Y. Wei, Fabrication of polyaniline nanostructures under ultrasonic irradiation: From nanotubes to nanofibers, *Macromol. Chem. Phys.*, **207**, 2142–2152 (2006).
[190] Y. Wang, X. Jing, and J. Kong, Polyaniline nanofibers prepared with hydrogen peroxide as oxidant, *Synth. Met.*, **157**, 269–275 (2007).
[191] M. Malta, L. H. Silva, A. Galembeck, and M. Korn, Ultrasound-assisted synthesis of hybrid vanadium oxide/polyaniline nanowires, *Macromol. Rapid Commun.*, **29**, 1221–1225 (2008).

[192] Z. Mo, H. Shi, H. Chen, G. Niu, Z. Zhao, and Y. Wu, Synthesis of graphite nanosheets/polyaniline nanorods composites with ultrasonic and conductivity, *J. Appl. Polym. Sci.*, **112**, 573–578 (2009).
[193] Y. Li, Y. Wang, D. Wu, and X. Jing, Effects of ultrasonic irradiation on the morphology of chemically prepared polyaniline nanofibers, *J. Appl. Polym. Sci.*, **113**, 868–875 (2009).
[194] X.-S. Du, C.-F. Zhou, G.-T. Wang, and Y.-W. Mai, Novel solid-state and template-free synthesis of branched polyaniline nanofibers, *Chem. Mater.*, **20**, 3806–3808 (2008).
[195] C.-F. Zhou, X.-S. Du, Z. Liu, S. P. Ringer, and Y.-W. Mai, Solid phase mechanochemical synthesis of polyaniline branched nanofibers, *Synth. Met.*, **159**, 1302–1307 (2009).
[196] X. Wang, N. Liu, W. Zhang, and Y. Wei, Alkali-guided synthesis of polyaniline hollow microspheres, *Chem. Lett.*, **34**, 42–43 (2005).
[197] C. Zhou, J. Han, G. Song, and R. Guo, Fabrication of polyaniline with hierarchical structures in alkaline solution, *Eur. Polym. J.*, **44**, 2850–2858 (2008).
[198] H. Ding, M. Wan, and Y. Wei, Controlling the diameter of polyaniline nanofibers by adjusting the oxidant redox potential, *Adv. Mater.*, **19**, 465–469 (2007).
[199] N.-R. Chiou, L. J. Lee, and A. J. Epstein, Self-assembled polyaniline nanofibers/nanotubes, *Chem. Mater.*, **19**, 3589–3591 (2007).
[200] C. Zhou, J. Han, G. Song, and R. Guo, Polyaniline hierarchical structures synthesized in aqueous solution: Micromats of nanofibers, *Macromolecules*, **40**, 7075–7078 (2007).
[201] Y. Zhu, H. He, M. Wan, and L. Jiang, Rose-like microstructures of polyaniline by using a simplified template-free method under a high relative humidity, *Macromol. Rapid Commun.*, **29**, 1705–1710 (2008).
[202] Z. Zhang, J. Deng, J. Shen, M. Wan, and Z. Chen, Chemical one step method to prepare polyaniline nanofibers with electromagnetic function, *Macromol. Rapid Commun.*, **28**, 585–590 (2007).
[203] S. P. Surwade, N. Manohar, and S. K. Manohar, Origin of bulk nanoscale morphology in conducting polymers, *Macromolecules*, **42**, 1792–1795 (2009).
[204] Z. Zhang, Z. Wei, and M. Wan, Nanostructures of polyaniline doped with inorganic acids, *Macromolecules*, **35**, 5937–5942 (2002).
[205] J. Jang, J. Bae, and K. Lee, Synthesis and characterization of polyaniline nanorods as curing agent and nanofiller for epoxy matrix composite, *Polymer*, **46**, 3677–3684 (2005).
[206] J. Jang and J. Bae, Formation of polyaniline nanorod/liquid crystalline epoxy composite nanowires using a temperature-gradient method, *Adv. Funct. Mater.*, **15**, 1877–1882 (2005).
[207] J. Q. Kan, S. L. Zhang, and G. L. Jing, Effect of ethanol on chemically synthesized polyaniline nanothread, *J. Appl. Polym. Sci.*, **99**, 1848–1853 (2006).
[208] X. Feng, G. Yang, Q. Xu, W. Hou, and J.-J. Zhu, Self-assembly of polyaniline/Au composites: From nanotubes to nanofibers, *Macromol. Rapid Commun.*, **27**, 31–36 (2006).
[209] Z. Zhang, M. Wan, and Y. Wei, Electromagnetic functionalized polyaniline nanostructures, *Nanotechnology*, **16**, 2827–2832 (2005).
[210] X.-G. Li, A. Li, and M.-R. Huang, Facile high-yield synthesis of polyaniline nanosticks with intrinsic stability and electrical conductivity, *Chem. Eur. J.*, **14**, 10309–10317 (2008).
[211] C. A. Amarnath, J. Kim, K. Kim, J. Choi, and S. Daewon, Nanoflakes to nanorods and nanospheres transition of selenious acid doped polyaniline, *Polymer*, **49**, 432–437 (2008).
[212] G. Ćirić-Marjanović, A. Janošević, B. Marjanović, M. Trchová, J. Stejskal, and P. Holler, Chemical oxidative polymerization of dianilinium 5-sulfosalicylate, *Russ. J. Phys. Chem. A*, **81**, 1418–1424 (2007).
[213] W. Zhao, L. Ma, and K. Lu, Facile synthesis of polyaniline nanofibers in the presence of polyethylene glycol, *J. Polym. Res.*, **14**, 1–4 (2007).
[214] L. Zhang, L. Zhang, and M. Wan, Molybdic acid doped polyaniline micro/nanostructures via a self-assembly process, *Eur. Polym. J.*, **44**, 2040–2045 (2008).
[215] S. Zhang, S. Kan, and J. Kan, Chemical synthesis and characterization of polyaniline nanofiber doped with gadolinium chloride, *J. Appl. Polym. Sci.*, **100**, 946–953 (2006).
[216] E. C. Venancio, P.-C. Wang, O. Y. Toledo, and A. G. MacDiarmid, First preparation of optical quality films of nano/micro hollow spheres of polymers of aniline, *Synth. Met.*, **157**, 758–763 (2007).

[217] E. C. Venancio, P.-C. Wang, and A. G. MacDiarmid, The azanes: A class of material incorporating nano/micro self-assembled hollow spheres obtained by aqueous oxidative polymerization of aniline, *Synth. Met.*, **156**, 357–369 (2006).
[218] Y. Wang, Z. Liu, B. Han, Z. Sun, Y. Huang, and G. Yang, Facile synthesis of polyaniline nanofibers using chloroaurate acid as the oxidant, *Langmuir*, **21**, 833–836 (2005).
[219] X.-S. Du, C.-F. Zhou, and Y.-W. Mai, Facile synthesis of hierarchical polyaniline nanostructures with dendritic nanofibers as scaffolds, *J. Phys. Chem. C*, **112**, 19836–19840 (2008).
[220] Z. Zhang, J. Deng, and M. Wan, Highly crystalline and thin polyaniline nanofibers oxidized by ferric chloride, *Mater. Chem. Phys.*, **115**, 275–279 (2009).
[221] G. Li, L. Jiang, and H. Peng, One-dimensional polyaniline nanostructures with controllable surfaces and diameters using vanadic acid as the oxidant, *Macromolecules*, **40**, 7890–7894 (2007).
[222] N. Ferrer-Anglada, J. A. Gorri, J. Muster, K. Liu, M. Burghard, and S. Roth, Electrical transport and AFM microscopy on V_2O_{5-X}–polyaniline nanorods, *Mater. Sci. Eng. C*, **15**, 237–239 (2001).
[223] S. P. Surwade, S. R. Agnihotra, V. Dua, N. Manohar, S. Jain, S. Ammu, and S. K. Manohar, Catalyst-free synthesis of oligoanilines and polyaniline nanofibers using H_2O_2, *J. Am. Chem. Soc*., **131**, 12528–12529 (2009).
[224] Y. Xian, Y. Hu, F. Liu, Y. Xian, H. Wang, and L. Jin, Glucose biosensor based on Au nanoparticles–conductive polyaniline nanocomposite, *Biosens. Bioelectron.*, **21**, 1996–2000 (2006).
[225] N. V. Blinova, J. Stejskal, M. Trchová, I. Sapurina, and G. Ćirić-Marjanović, The oxidation of aniline with silver nitrate to polyaniline–silver composites, *Polymer*, **50**, 50–56 (2009).
[226] A. Rahy, M. Sakrout, S. Manohar, S. J. Cho, J. Ferraris, and D. J. Yang, Polyaniline nanofiber synthesis by co-use of ammonium peroxydisulfate and sodium hypochlorite, *Chem. Mater.*, **20**, 4808–4814 (2008).
[227] A. Rahy and D. J. Yang, Synthesis of highly conductive polyaniline nanofibers, *Mater. Lett.*, **62**, 4311–4314 (2008).
[228] C.-G. Wu, C.-H. Chiang, and U.-S. Jeng, Phenol assisted deaggregation of polyaniline chains: simple route to high quality polyaniline film, *J. Phys. Chem. B*, **112**, 6772–6778 (2008).
[229] D. Chao, J. Chen, X. Lu, L. Chen, W. Zhang, and Y. Wei, SEM study of the morphology of high molecular weight polyaniline, *Synth. Met.*, **150**, 47–51 (2005).
[230] Z. Zhang, J. Deng, L. Yu, and M. Wan, Chrysanthemum flower-like constructed polyaniline nanofibers synthesized by adding inorganic salts as additives, *Synth. Met.*, **158**, 712–716 (2008).
[231] A. Eftekhari, Synthesis of nanostructured large particles of polyaniline, *J. Appl. Polym. Sci.*, **102**, 6060–6063 (2006).
[232] E. N. Konyushenko, J. Stejskal, M. Trchová, N. V. Blinova, and P. Holler, Polymerization of aniline in ice, *Synth. Met.*, **158**, 927–933 (2008).
[233] B. A. Deore, I. Yu, J. Woodmass, and M. S. Freund, Conducting poly(anilineboronic acid) nanostructures: controlled synthesis and characterization, *Macromol. Chem. Phys.*, **209**, 1094–1105 (2008).
[234] Q. Sun, W. Bi, T. F. Fuller, Y. Ding, and Y. Deng, Fabrication of aligned polyaniline nanofiber array via a facile wet chemical process, *Macromol. Rapid Commun.*, **30**, 1027–1032 (2009).
[235] C. Li, H. Bai, and G. Shi, Conducting polymer nanomaterials: electrosynthesis and applications, *Chem. Soc. Rev.*, **38**, 2397–2409 (2009).
[236] Y. Zhao, M. Chen, T. Xu, and W. Liu, Electrochemical synthesis and electrochemical behavior of highly ordered polyaniline nanofibrils through AAO templates, *Colloids Surf. A*, **257–258**, 363–368 (2005).
[237] A. Drury, S. Chaure, M. Kröll, V. Nicolosi, N. Chaure, and W. J. Blau, Fabrication and characterization of silver/polyaniline composite nanowires in porous anodic alumina, *Chem. Mater.* **19**, 4252–4258 (2007).

[238] B. H. Kim, D. H. Park, J. Joo, S. G. Yu, and S. H. Lee, Synthesis, characteristics, and field emission of doped and de-doped polypyrrole, polyaniline, poly(3,4-ethylenedioxythiophene) nanotubes and nanowires, *Synth. Met.*, **150**, 279–284 (2005).
[239] X. Yu, Y. Li, and K. Kalantar-zadeh, Synthesis and electrochemical properties of template-based polyaniline nanowires and template-free nanofibril arrays: Two potential nanostructures for gas sensors, *Sens. Actuators B*, **136**, 1–7 (2009).
[240] G.-Y. Zhao and H.-L. Li, Preparation of polyaniline nanowire arrayed electrodes for electrochemical supercapacitors, *Microporous Mesoporous Mater.*, **110**, 590–594 (2008).
[241] Y. Cao and T. E. Mallouk, Morphology of template-grown polyaniline nanowires and its effect on the electrochemical capacitance of nanowire arrays, *Chem. Mater.*, **20**, 5260–5265 (2008).
[242] J. Choi, S. J. Kim, J. Lee, J. H. Lim, S. C. Lee, and K. J. Kim, Controlled self-assembly of nanoporous alumina for the self-templating synthesis of polyaniline nanowires, *Electrochem. Commun.*, **9**, 971–975 (2007).
[243] M. Lahav, E. A. Weiss, Q. Xu, and G. M. Whitesides, Core–shell and segmented polymer–metal composite nanostructures, *Nano Lett.*, **6**, 2166–2171 (2006).
[244] X. Li, S. Tian, Y. Ping, D. H. Kim, and W. Knoll, One-step route to the fabrication of highly porous polyaniline nanofiber films by using PS-b-PVP diblock copolymers as templates, *Langmuir*, **21**, 9393–9397 (2005).
[245] B. K. Kuila, B. Nandan, M. Böhme, A. Janke, and M. Stamm, Vertically oriented arrays of polyaniline nanorods and their super electrochemical properties, *Chem. Commun*., **38**, 5749–5751 (2009).
[246] T. Hatano, M. Takeuchi, A. Ikeda, and S. Shinkai, New morphology-controlled poly(aniline) synthesis using anionic porphyrin aggregate as a template, *Chem. Lett.*, **32**, 314–315 (2003).
[247] Q. Zhou, C. M. Li, J. Li, and J. Lu, Electrocatalysis of template-electrosynthesized cobalt–porphyrin/polyaniline nanocomposite for oxygen reduction, *J. Phys. Chem. C*, **112**, 18578–18583 (2008).
[248] N. T. Kemp, J. W. Cochrane, and R. Newbury, Patterning of conducting polymer nanowires on gold/platinum electrodes, *Nanotechnology*, **18**, 145610 (2007).
[249] N. T. Kemp, J. W. Cochrane, and R. Newbury, Characteristics of the nucleation and growth of template-free polyaniline nanowires and fibrils, *Synth. Met.*, **159**, 435–444 (2009).
[250] Y. Bardavid, J. Ghabboun, D. Porath, A. B. Kotylar, and S. Yitzchaik, Formation of polyaniline layer on DNA by electrochemical polymerization, *Polymer*, **49**, 2217–2222 (2008).
[251] J. Kan, R. Lv, and S. Zhang, Effect of ethanol on properties of electrochemically synthesized polyaniline, *Synth. Met.*, **145**, 37–42 (2004).
[252] X.-Y. Peng, F. Luan, X.-X. Liu, D. Diamond, and K.-T. Lau, pH-controlled morphological structure of polyaniline during electrochemical deposition, *Electrochim. Acta*, **54**, 6172–6177 (2009).
[253] S. Mu, Novel properties of polyaniline nanofibers coated with polycatechol, *Synth. Met.*, **156**, 202–208 (2006).
[254] S. Mu and Y. Yang, Spectral characteristics of polyaniline nanostructures synthesized by using cyclic voltammetry at different scan rates, *J. Phys. Chem. B*, **112**, 11558–11563 (2008).
[255] R. E. Anderson, A. D. Ostrowski, D. E. Gran, J. D. Fowler, A. R. Hopkins, and R. M. Villahermosa, Diameter-controlled synthesis of polyaniline nanofibers, *Polym. Bull.*, **61**, 563–568 (2008).
[256] H. X. He, C. Z. Li, and N. J. Tao, Conductance of polymer nanowires fabricated by a combined electrodeposition and mechanical break junction method, *Appl. Phys. Lett.*, **78**, 811–813 (2001).
[257] L. Huang, Z. Wang, H. Wang, X. Cheng, A. Mitra, and Y. Yan, Polyaniline nanowires by electropolymerization from liquid crystalline phases, *J. Mater. Chem.*, **12**, 388–391 (2002).
[258] S. K. Mondal, K. Barai, and N. Munichandraiah, High capacitance properties of polyaniline by electrochemical deposition on a porous carbon substrate, *Electrochim. Acta*, **52**, 3258–3264 (2007).
[259] M. G. Xavier, E. C. Venancio, E. C. Pereira, F. L. Leite, E. R. Leite, A. G. MacDiarmid, and L. H. C. Mattoso, Synthesis of nanoparticles and nanofibers of polyaniline by potentiodynamic electrochemical polymerization, *J. Nanosci. Nanotechn.*, **9**, 2169–2172 (2009).

[260] G. K. Surya Prakash, P. Suresh, F. Viva, and G. A. Olah, Novel single step electrochemical route to γ-MnO_2 nanoparticle-coated polyaniline nanofibers: Thermal stability and formic acid oxidation on the resulting nanocomposites, *J. Power Sources*, **181**, 79–84 (2008).
[261] Kh. Ghanbari, M. F. Mousavi, and M. Shamsipur, Preparation of polyaniline nanofibers and their use as a cathode of aqueous rechargeable batteries, *Electrochim. Acta*, **52**, 1514–1522 (2006).
[262] H. R. Ghenaatian, M. F. Mousavi, S. H. Kazemi, and M. Shamsipur, Electrochemical investigations of self-doped polyaniline nanofibers as a new electroactive material for high performance redox supercapacitor, *Synth. Met.*, **159**, 1717–1722 (2009).
[263] V. Gupta and N. Miura, Electrochemically deposited polyaniline nanowire's network: A high-performance electrode material for redox supercapacitor, *Electrochem. Solid-State Lett.*, **8**, A630–A632 (2005).
[264] V. Gupta and N. Miura, Large-area network of polyaniline nanowires prepared by potentiostatic deposition process, *Electrochem. Commun.*, **7**, 995–999 (2005).
[265] V. Gupta and N. Miura, High performance electrochemical supercapacitor from electrochemically synthesized nanostructured polyaniline, *Mater. Lett.*, **60**, 1466–1469 (2006).
[266] S. Zhou, T. Wu, and J. Kan, Effect of methanol on morphology of polyaniline, *Eur. Polym. J.*, **43**, 395–402 (2007).
[267] H. Zhou, J. Wen, X. Ning, C. Fu, J. Chen, and Y. Kuang, Electrosynthesis of polyaniline films on titanium by pulse potentiostatic method, *Synth. Met.*, **157**, 98–103 (2007).
[268] H. Zhang, J. Wang, Z. Zhou, Z. Wang, F. Zhang, and S. Wang, Preparation of nanostructured polyaniline and its super-amphiphilic behavior, *Macromol. Rapid Commun.*, **29**, 68–73 (2008).
[269] S.-J. Choi and S.-M. Park, Electrochemical growth of nanosized conducting polymer wires on gold using molecular templates, *Adv. Mater.*, **12**, 1547–1549 (2000).
[270] L. Jiang and Z. Cui, One-step synthesis of oriented polyaniline nanorods through electrochemical deposition, *Polym. Bull.*, **56**, 529–537 (2006).
[271] K. Ramanathan, M. A. Bangar, M. Yun, W. Chen, A. Mulchandani, and N. V. Myung, Individually addressable conducting polymer nanowires array, *Nano Lett.*, **4**, 1237–1239 (2004).
[272] J. Wang, S. Chan, R. R. Carlson, Y. Luo, G. Ge, R. S. Ries, J. R. Heath, and H.-R. Tseng, Electrochemically fabricated polyaniline nanoframework electrode junctions that function as resistive sensors, *Nano Lett.*, **4**, 1693–1697 (2004).
[273] M. M. Alam, J. Wang, Y. Guo, S. P. Lee, and H.-R. Tseng, Electrolyte-gated transistors based on conducting polymer nanowire junction arrays, *J. Phys. Chem. B*, **109**, 12777–12784 (2005).
[274] Y. Guo and Y. Zhou, Polyaniline nanofibers fabricated by electrochemical polymerization: A mechanistic study, *Eur. Polym. J.*, **43**, 2292–2297 (2007).
[275] F.-J. Liu, L.-M. Huang, T-C. Wen, and A. Gopalan, Large-area network of polyaniline nanowires supported platinum nanocatalysts for methanol oxidation, *Synth. Met.*, **157**, 651–658 (2007).
[276] F.-J. Liu, L.-M. Huang, T.-C. Wen, K.-C. Yin, J.-S. Hung, and A. Gopalan, Composite electrodes consisting of platinum particles and polyaniline nanowires as electrocatalysts for methanol oxidation, *Polym. Compos.*, **28**, 650–656 (2007).
[277] F.-J. Liu, L.-M. Huang, T.-C. Wen, C.-F. Li, S.-L. Huang, and A. Gopalan, Platinum particles dispersed polyaniline-modified electrodes containing sulfonated polyelectrolyte for methanol oxidation, *Synth. Met.*, **158**, 767–774 (2008).
[278] K. Luo, X. Guo, N. Shi, and C. Sun, Synthesis and characterization of core–shell nanocomposites of polyaniline and carbon black, *Synth. Met.*, **151**, 293–296 (2005).
[279] M. Deepa, S. Ahmad, K. N. Sood, J. Alam, S. Ahmad, and A. K. Srivastava, Electrochromic properties of polyaniline thin film nanostructures derived from solutions of ionic liquid/polyethylene glycol, *Electrochim. Acta*, **52**, 7453–7463 (2007).
[280] Z. Zhou, D. He, Y. Guo, Z. Cui, M. Wang, G. Li, and R. Yang, Fabrication of polyaniline–silver nanocomposites by chronopotentiometry in different ionic liquid microemulsion systems, *Thin Solid Films*, **517**, 6767–6771 (2009).

[281] L. Zhang, X. Jiang, L. Niu, and S. Dong, Syntheses of fully sulfonated polyaniline nanonetworks and its application to the direct electrochemistry of cytochrome C, *Biosens. Bioelectron.*, **21**, 1107–1115 (2006).
[282] L. Liang, J. Liu, C. F. Windisch, Jr., G. J. Exarhos, and Y. Lin, Direct assembly of large arrays of oriented conducting polymer nanowires, *Angew. Chem. Int. Ed.*, **41**, 3665–3668 (2002).
[283] J. Liu, Y. Lin, L. Liang, J. A. Voigt, D. L. Huber, Z. R. Tian, E. Coker, B. McKenzie, and M. J. McDermott, Templateless assembly of molecularly aligned conductive polymer nanowires: A new approach for oriented nanostructures, *Chem. Eur. J.*, **9**, 604–611 (2003).
[284] X. Zou, S. Zhang, M. Shi, and J. Kong, Remarkably enhanced capacitance of ordered polyaniline nanowires tailored by stepwise electrochemical deposition, *J. Solid State Electrochem.*, **11**, 317–322 (2007).
[285] H. H. Zhou, X. H. Ning, S. L. Li, J. H. Chen, and Y. F. Kuang, Synthesis of polyaniline-silver nanocomposite film by unsymmetrical square wave current method, *Thin Solid Films*, **510**, 164–168 (2006).
[286] J. Song, D. Han, L. Guo, and L. Niu, Direct electrochemical generation of conducting polymer micro-rings, *Nanotechnology*, **17**, 824–829 (2006).
[287] J. J. Langer, G. Framski, S. Golczak, and T. Gibiński, Fullerene-doped polyaniline, *Synth. Met.*, **119**, 359–360 (2001).
[288] J. J. Langer, G. Framski, and R. Joachimiak, Polyaniline nano-wires, and nano-networks, *Synth. Met.*, **121**, 1281–1282 (2001).
[289] J. J. Langer, G. Framski, and S. Golczak, Polyaniline micro- and nanofibrils, *Synth. Met.*, **121**, 1319–1320 (2001).
[290] H. Zhang, J. Wang, Z. Wang, F. Zhang, and S. Wang, Electrodeposition of polyaniline nanostructures: A lamellar structure, *Synth. Met.*, **159**, 277–281 (2009).
[291] R. Madathil, Multilayer growth of conductive polyaniline: A two-pot, alternate, oxidation and reduction strategy, *Synth. Met.*, **150**, 123–126 (2005).
[292] M. Malta, G. Louarn, N. Errien, and R. M. Torresi, Nanofibers composite vanadium oxide/polyaniline: synthesis and characterization of an electroactive anisotropic structure, *Electrochem. Commun.*, **5**, 1011–1015 (2003).
[293] M. Malta and R. M. Torresi, Electrochemical and kinetic studies of lithium intercalation in composite nanofibers of vanadium oxide/polyaniline, *Electrochim. Acta*, **50**, 5009–5014 (2005).
[294] T. Shimomura, T. Akai, T. Abe, and K. Ito, Atomic force microscopy observation of insulated molecular wire formed by conducting polymer and molecular nanotube, *J. Chem. Phys.*, **116**, 1753–1756 (2002).
[295] T. Akai, T. Shimomura, and K. Ito, HCl-doping of insulated molecular wire formed by emeraldine base polyaniline and molecular nanotube, *Synth. Met.*, **135**, 777–778 (2003).
[296] T. Shimomura, T. Akai, M. Fujimori, S. Heike, T. Hashizume, and K. Ito, Conductivity measurement of insulated molecular wire formed by molecular nanotube and polyaniline, *Synth. Met.*, **153**, 497–500 (2005).
[297] D. S. Sutar, N. Padma, D. K. Aswal, S. K. Deshpande, S. K. Gupta, and J. V. Yakhmi, Preparation of nanofibrous polyaniline films and their application as ammonia gas sensor, *Sens. Actuators B*, **128**, 286–292 (2007).
[298] W. Zhong, X. Chen, S. Liu, Y. Wang, and W. Yang, Synthesis of highly hydrophilic polyaniline nanowires and sub-micro/nanostructured dendrites on poly(propylene) film surfaces, *Macromol. Rapid Commun.*, **27**, 563–569 (2006).
[299] W. Zhong, Y. Wang, Y. Yan, Y. Sun, J. Deng, and W. Yang, Fabrication of shape-controllable polyaniline micro/nanostructures on organic polymer surfaces: Obtaining spherical particles, wires, and ribbons, *J. Phys. Chem. B*, **111**, 3918–3926 (2007).
[300] H. Ma, Yu Gao, Y. Li, J. Gong, X. Li, B. Fan, and Y. Deng, Ice-templating synthesis of polyaniline microflakes stacked by one-dimensional nanofibers, *J. Phys. Chem. C*, **113**, 9047–9052 (2009).
[301] S. Roy, K. Kargupta, S. Chakraborty, and S. Ganguly, Preparation of polyaniline nanofibers and nanoparticles via simultaneous doping and electro-deposition, *Mater. Lett.*, **62**, 2535–2538 (2008).

[302] B. Nandan, J.-Y. Hsu, A. Chiba, H.-L. Chen, C.-S. Liao, S.-A. Chen, and H. Hasegawa, Highly oriented nanowires from the hierarchical self-assembly in supramolecular complex of polyaniline with ω-methoxypoly(ethylene oxide) phosphates, *Macromolecules*, **40**, 395–398 (2007).
[303] S. Manigandan, A. Jain, S. Majumder, S. Ganguly, and K. Kargupta, Formation of nanorods and nanoparticles of polyaniline using Langmuir Blodgett technique: Performance study for ammonia sensor, *Sens. Actuators B*, **133**, 187–194 (2008).
[304] E. Lahiff, T. Woods, W. Blau, G. G. Wallace, and D. Diamond, Synthesis and characterisation of controllably functionalised polyaniline nanofibres, *Synth. Met.*, **159**, 741–748 (2009).
[305] S. R. Mohanty, N. K. Neog, R. S. Rawat, P. Lee, B. B. Nayak, and B. S. Acharya, Self-organized transformation to polyaniline nanowires by pulsed energetic electron irradiation in a plasma focus device, *Phys. Lett. A*, **373**, 1962–1966 (2009).
[306] A. Tiwari, R. Kumar, M. Prabaharan, R. R. Pandey, P. Kumari, A. Chaturvedi, and A. K. Mishra, Nanofibrous polyaniline thin film prepared by plasma-induced polymerization technique for detection of NO_2 gas, *Polym. Adv. Technol.*,In Press, doi:10.1002/pat.1470.
[307] L. Hu, G. Gruner, J. Jenkins, and C.-J. Kim, Flash dry deposition of nanoscale material thin films, *J. Mater. Chem.*, **19**, 5845–5849 (2009).
[308] S. Bhadra and J. H. Lee, Synthesis of higher soluble nanostructured polyaniline by vapor-phase polymerization and determination of its crystal structure, *J. Appl. Polym. Sci.*, **114**, 331–340 (2009).
[309] C. R. Martin, R. Parthasarathy, and V. Menon, Template synthesis of electronically conductive polymers – A new route for achieving higher electronic conductivities, *Synth. Met.*, **55**, 1165–1170 (1993).
[310] R. V. Parthasarathy and C. R. Martin, Template-synthesized polyaniline microtubules, *Chem. Mater.,* **6**, 1627–1632 (1994).
[311] M. Delvaux, J. Duchet, P.-Y. Stavaux, R. Legras, and S. Demoustier-Champagne, Chemical and electrochemical synthesis of polyaniline micro- and nano-tubules, *Synth. Met.*, **113**, 275–280 (2000).
[312] M. Mazur, M. Tagowska, B. Pałys, and K. Jackowska, Template synthesis of polyaniline and poly(2-methoxyaniline) nanotubes: comparison of the formation mechanisms, *Electrochem. Commun.*, **5**, 403–407 (2003).
[313] M. Tagowska, B. Pałys, and K. Jackowska, Polyaniline nanotubules – anion effect on conformation and oxidation state of polyaniline studied by Raman spectroscopy, *Synth. Met.*, **142**, 223–229 (2004).
[314] B. Pałys and P. Celuch, Redox transformations of polyaniline nanotubes. Cyclic voltammetry, infrared and optical absorption studies, *Electrochim. Acta*, **51**, 4115–4124 (2006).
[315] S. Xiong, Q. Wang, and H. Xia, Preparation of polyaniline nanotubes array based on anodic aluminum oxide template, *Mater. Res. Bull.*, **39**, 1569–1580 (2004).
[316] H. Cao, Z. Xu, D. Sheng, J. Hong, H. Sang, and Y. Du, An array of iron nanowires encapsulated in polyaniline nanotubules and its magnetic behavior, *J. Mater. Chem.*, **11**, 958–960 (2001).
[317] H. Q. Cao, Z. Xu, H. Sang, D. Sheng, and C. Y. Tie, Template synthesis and magnetic behavior of an array of cobalt nanowires encapsulated in polyaniline nanotubules, *Adv. Mater.*, **13**, 121–123 (2001).
[318] H. Cao, C. Tie, Z. Xu, J. Hong, and H. Sang, Array of nickel nanowires enveloped in polyaniline nanotubules and its magnetic behavior, *Appl. Phys. Lett.*, **78**,1592 (2001).
[319] Y. Gao, X. Li, J. Gong, B. Fan, Z. Su, and L. Qu, Polyaniline nanotubes prepared using fiber mats membrane as the template and their gas-response behavior, *J. Phys. Chem. C*, **112**, 8215–8222 (2008).
[320] X. Li, Y. Gao, J. Gong, L. Zhang, and L. Qu, Polyaniline/Ag composite nanotubes prepared through UV rays irradiation via fiber template approach and their NH_3 gas sensitivity, *J. Phys. Chem. C*, **113**, 69–73 (2009).
[321] Z. Wei, M. Wan, T. Lin, and L. Dai, Polyaniline nanotubes doped with sulfonated carbon nanotubes made via a self-assembly process, *Adv. Mater.*, **15**, 136–139 (2003).

[322] L. J. Pan, L. Pu, Y. Shi, S. Y. Song, Z. Xu, R. Zhang, and Y. D. Zheng, Synthesis of polyaniline nanotubes with a reactive template of manganese oxide, *Adv. Mater.*, **19**, 461–464 (2007).
[323] Y. Gao, S. Yao, J. Gong, and L. Qu, Preparation of polyaniline nanotubes via 'thin glass tubes template' approach and its gas response, *Macromol. Rapid Commun.*, **28**, 286–291 (2007).
[324] L. Zhang and P. Liu, Facile fabrication of uniform polyaniline nanotubes with tubular aluminosilicates as templates, *Nanoscale Res. Lett.*, **3**, 299–302 (2008).
[325] L. Kong, X. Lu, E. Jin, S. Jiang, C. Wang, and W. Zhang, Templated synthesis of polyaniline nanotubes with Pd nanoparticles attached onto their inner walls and its catalytic activity on the reduction of p-nitroanilinum, *Compos. Sci. Technol.*, **69**, 561–566 (2009).
[326] J. Ryu and C. B. Park, Synthesis of diphenylalanine/polyaniline core/shell conducting nanowires by peptide self-assembly, *Angew. Chem. Int. Ed.*, **48**, 4820–4823 (2009).
[327] B. Xue, S. Qi, J. Gong, Y. Gao, S. Yao, R. Yin, and L. Qu, Synthesis of ultra-fine conducting polyaniline micro/nanotubes using fiber template and their NH_3 gas sensitivity, *J. Nanosci. Nanotechn.*, **7**, 4515–4521 (2007).
[328] P. Petrov, P. Mokreva, C. B. Tsvetanov, and L. Terlemezyan, Colloidal aqueous dispersion of polyaniline nanotubes grafted non-covalently with poly(ethylene oxide)-blockpoly(acrylic acid) copolymer, *Colloid Polym. Sci.*, **286**, 691–697 (2008).
[329] G. Song, J. Han, and R. Guo, Synthesis of polyaniline/NiO nanobelts by a self-assembly process, *Synth. Met.*, **157**, 170–175 (2007).
[330] H. Peng, L. Zhang, P. A. Kilmartin, Z. Zujovic, C. Soeller, and J. Travas-Sejdic, Quantum dots and nanostructured conducting polymers for biosensing applications, *Int. J. Nanotechn.*, **6**, 418–430 (2009).
[331] L. Zhang, H. Peng, C. F. Hsu, P. A. Kilmartin, and J. Travas-Sejdic, Self-assembled polyaniline nanotubes grown from a polymeric acid solution, *Nanotechnology* **18**, 115607 (6 pp) (2007).
[332] L. Zhang, H. Peng, P. A. Kilmartin, C. Soeller, and J. Travas-Sejdic, Polymeric acid doped polyaniline nanotubes for oligonucleotide sensors, *Electroanalysis* **19**, 870–875 (2007).
[333] L. Zhang, H. Peng, J. Sui, P. A. Kilmartin, and J. Travas-Sejdic, Polyaniline nanotubes doped with polymeric acids, *Curr. Appl. Phys.*, **8**, 312–315 (2008).
[334] K. C. Aw, N. T. Salim, H. Peng, L. Zhang, J. Travas-Sejdic, and W. Gao, PN-junction diode behavior based on polyaniline nanotubes field effect transistor, *J. Mater. Sci.- Mater. Electron.*, **19**, 996–999 (2008).
[335] H. Qiu, M. Wan, B. Matthews, and L. Dai, Conducting polyaniline nanotubes by template-free polymerization, *Macromolecules* **34**, 675–677 (2001).
[336] Y. Long, Z. Chen, P. Zheng, N. Wang, Z. Zhang, and M. Wan, Low-temperature resistivities of nanotubular polyaniline doped with H_3PO_4 and β-naphthalene sulfonic acid, *J. Appl. Phys.*, **93**, 2962–2965 (2003).
[337] Z. Zhang, Z. Wei, L. Zhang, and M. Wan, Polyaniline nanotubes and their dendrites doped with different naphthalene sulfonic acids, *Acta Mater.*, **53**, 1373–1379 (2005).
[338] L. Zhang and M. Wan, Synthesis and characterization of self-assembled polyaniline nanotubes doped with D-10-camphorsulfonic acid, *Nanotechnology* **13**, 750–755 (2002).
[339] Y. Long, Z. Chen, N. Wang, Y. Ma, Z. Zhang, L. Zhang, and M. Wan, Electrical conductivity of a single conducting polyaniline nanotube, *Appl. Phys. Lett.*, **83**, 1863–1865 (2003).
[340] Y. Long, L. Zhang, Y. Ma, Z. Chen, N. Wang, Z. Zhang, and M. Wan, Electrical conductivity of an individual polyaniline nanotube synthesized by a self-assembly method, *Macromol. Rapid Commun.*, **24**, 938–942 (2003).
[341] Y. Long, J. Luo, J. Xu, Z. Chen, L. Zhang, J. Li, and M. Wan, Specific heat and magnetic susceptibility of polyaniline nanotubes: inhomogeneous disorder, *J. Phys: Condens. Matter*, **16**, 1123–1130 (2004).
[342] Y. Z. Long, L. J. Zhang, Z. J. Chen, K. Huang, Y. S. Yang, H. M. Xiao, M. X. Wan, A. Z. Jin, and C. Z. Gu, Electronic transport in single polyaniline and polypyrrole microtubes, *Phys. Rev. B*, **71**, 165412 [7 pages] (2005).
[343] Z.-H. Yin, Y.-Z. Long, C.-Z. Gu, M.-X. Wan, and J.-L. Duvail, Current–voltage characteristics in individual polypyrrole nanotube, poly(3,4-ethylenedioxythiophene) nanowire, polyaniline nanotube, and CdS nanorope, *Nanoscale Res. Lett.*, **4**, 63–69 (2009).

[344] N. J. Pinto, P. L. Carrión, A. M. Ayala, and M. Ortiz-Marciales, Temperature dependence of the resistance of self-assembled polyaniline nanotubes doped with 2-acrylamido-2-methyl-1-propanesulfonic acid, *Synth. Met.*, **148**, 271–274 (2005).
[345] B.-Z. Hsieh, H.-Y. Chuang, L. Chao, Y.-J. Li, Y.-J. Huang, P.-H. Tseng, T.-H. Hsieh, and K.-S. Ho, Formation mechanism of a nanotubular polyanilines prepared by an emulsion polymerization without organic solvent, *Polymer*, **49**, 4218–4225 (2008).
[346] K.-S. Ho, Y.-K. Han, Y.-T. Tuan, Y.-J. Huang, Y.-Z. Wang, T.-H. Ho, T.-H. Hsieh, J.-J. Lin, and S.-C. Lin, Formation and degradation mechanism of a novel nanofibrous polyaniline, *Synth. Met.*, **159**, 1202–1209 (2009).
[347] H. Xia, H. S. O. Chan, C. Xiao, and D. Cheng, Self-assembled oriented conducting polyaniline nanotubes, *Nanotechnology*, **15**, 1807–1811 (2004).
[348] L. Zhang and M. Wan, Self-assembly of polyaniline-from nanotubes to hollow microspheres, *Adv. Funct. Mater.*, **13**, 815–820 (2003).
[349] L. Zhang, Y. Long, Z. Chen, and M. Wan, Effect of hydrogen bonding on self-assembled polyaniline nanostructures, *Adv. Funct. Mater.*, **14**, 693–698 (2004).
[350] E. N. Konyushenko, J. Stejskal, I. Šeděnková, M. Trchová, I. Sapurina, M. Cieslar, and J. Prokeš, Polyaniline nanotubes: conditions of formation, *Polym. Int.*, **55**, 31–39 (2006).
[351] J. Stejskal, I. Sapurina, M. Trchová, E. N. Konyushenko, and P. Holler, The genesis of polyaniline nanotubes, *Polymer*, **47**, 8253–8262 (2006).
[352] J. Stejskal, I. Sapurina, M. Trchová, and E. N. Konyushenko, Oxidation of aniline: Polyaniline granules, nanotubes, and oligoaniline microspheres, *Macromolecules*, **41**, 3530–3536 (2008).
[353] J. Stejskal, M. Trchová, L. Brožová, and J. Prokeš, Reduction of silver nitrate by polyaniline nanotubes to produce silver–polyaniline composites, *Chem. Pap.*, **63**, 77–83 (2009).
[354] I. Šeděnková, M. Trchová, J. Stejskal, and J. Bok, Polymerization of aniline in the solutions of strong and weak acids: The evolution of infrared spectra and their interpretation using factor analysis, *Appl. Spectrosc.*, **61**, 1153–1162 (2007).
[355] L. Zhang, H. Peng, Z. D. Zujovic, P. A. Kilmartin, and J. Travas-Sejdic, Characterization of polyaniline nanotubes formed in the presence of amino acids, *Macromol. Chem. Phys.*, **208**, 1210–1217 (2007).
[356] Z. D. Zujovic, L. Zhang, G. A. Bowmaker, P. A. Kilmartin, and J. Travas-Sejdic, Self-assembled, nanostructured aniline oxidation products: A structural investigation, *Macromolecules*, **41**, 3125–3135 (2008).
[357] L. Zhang, Z. D. Zujovic, H. Peng, G. A. Bowmaker, P. A. Kilmartin, and J. Travas-Sejdic, Structural characteristics of polyaniline nanotubes synthesized from different buffer solutions, *Macromolecules*, **41**, 8877–8884 (2008).
[358] Y. Yang and M. Wan, Chiral nanotubes of polyaniline synthesized by a template-free method, *J. Mater. Chem.*, **12**, 897–901 (2002).
[359] L. Zhang and M. Wan, Chiral polyaniline nanotubes synthesized via a self-assembly process, *Thin Solid Films*, **477**, 24–31 (2005).
[360] Z. Wei and M. Wan, Synthesis and characterization of self-doped poly(aniline-*co*-amino-naphthalene sulfonic acid) nanotubes, *J. Appl. Polym. Sci.*, **87**, 1297–1301 (2003).
[361] J. Yuan, Z. Wang, Q. Zhang, D. Han, Y. Zhang, Y. Shen, and L. Niu, Controlled synthesis of 2D Au nanostructure assembly with the assistance of sulfonated polyaniline nanotubes, *Nanotechnology*, **17**, 2641–2648 (2006).
[362] R.-H. Lee, H.-H. Lai, J.-J. Wang, R.-J. Jeng, and J.-J. Lin, Self-doping effects on the morphology, electrochemical and conductivity properties of self-assembled polyanilines, *Thin Solid Films*, **517**, 500–505 (2008).
[363] G. Li, C. Zhang, H. Peng, K. Chen, and Z. Zhang, Hollow self-doped polyaniline micro/nanostructures: Microspheres, aligned pearls, and nanotubes, *Macromol. Rapid Commun.*, **29**, 1954–1958 (2008).
[364] H. Bhandari, V. Bansal, V. Choudhary, and S. K. Dhawan, Influence of reaction conditions on the formation of nanotubes/nanoparticles of polyaniline in the presence of 1-amino-2-naphthol-4-sulfonic acid and applications as electrostatic charge dissipation material, *Polym. Int.*, **58**, 489–502 (2009).

[365] Z. Zhang and M. Wan, Nanostructures of polyaniline composites containing nano-magnet, *Synth. Met.*, **132**, 205–212 (2003).
[366] Y. Long, Z. Chen, J. L. Duvail, Z. Zhang, and M. Wan, Electrical and magnetic properties of polyaniline/Fe_3O_4 nanostructures, *Physica B*, **370**, 121–130 (2005).
[367] S. W. Phang, M. Tadokoro, J. Watanabe, and N. Kuramoto, Microwave absorption behaviors of polyaniline nanocomposites containing TiO_2 nanoparticles, *Curr. Appl. Phys.*, **8**, 391–394 (2008).
[368] L. Zhang and M. Wan, Polyaniline/TiO_2 composite nanotubes, *J. Phys. Chem. B*, **107**, 6748–6753 (2003).
[369] S.-W. Phang and N. Kuramoto, Morphology studies of doped polyaniline micro/nanocomposites containing TiO_2 nanoparticles and Fe_3O_4 microparticles, *Polym. Compos.*, **30**, 970–975 (2009).
[370] S. W. Phang, M. Tadokoro, J. Watanabe, and N. Kuramoto, Effect of Fe_3O_4 and TiO_2 addition on the microwave absorption property of polyaniline micro/nanocomposites, *Polym. Adv. Technol.*, **20**, 550–557 (2009).
[371] S. W. Phang, M. Tadokoro, J. Watanabe, and N. Kuramoto, Synthesis, characterization and microwave absorption property of doped polyaniline nanocomposites containing TiO_2 nanoparticles and carbon nanotubes, *Synth. Met.*, **158**, 251–258 (2008).
[372] V. L. Reena, J. D. Sudha, and C. Pavithran, Role of amphiphilic dopants on the shape and properties of electrically conducting polyaniline-clay nanocomposite, *J. Appl. Polym. Sci.*, **113**, 4066–4076 (2009).
[373] H. Xia, D. Cheng, C. Xiao, and H. S. O. Chan, Controlled synthesis of polyaniline nanostructures with junctions using in situ self-assembly of magnetic nanoparticles, *J. Mater. Chem.*, **15**, 4161–4166 (2005).
[374] H. Xia, D. Cheng, P. Lam, and H. S. O. Chan, Crown ether derivative assisted growth of oriented polyaniline nanotubes, *Nanotechnology*, **17**, 3957–3961 (2006).
[375] Y. F. Huang and C. W. Lin, Exploration of the formation mechanisms of polyaniline nanotubes and nanofibers through a template-free method, *Synth. Met.*, **159**, 1824–1830 (2009).
[376] Q. Sun, M.-C. Park, and Y. Deng, Studies on one-dimensional polyaniline (PANI) nanostructures and the morphological evolution, *Mater. Chem. Phys.*, **110**, 276–279 (2008).
[377] A. Janošević, G. Ćirić-Marjanović, B. Marjanović, P. Holler, M. Trchová, and J. Stejskal, Synthesis and characterization of conducting polyaniline 5-sulfosalicylate nanotubes, *Nanotechnology* **19**, 135606 (2008).
[378] Z. Ding, R. P. Currier, Y. Zhao, and D. Yang, Self-assembled polyaniline nanotubes with rectangular cross-sections, *Macromol. Chem. Phys*., **210**, 1600–1606 (2009).
[379] C. Laslau, Z. D. Zujovic, L. Zhang, G. A. Bowmaker, and J. Travas-Sejdic, Morphological evolution of self-assembled polyaniline nanostuctures obtained by pH-stat chemical oxidation, *Chem. Mater.*, **21**, 954–962 (2009).
[380] H. Ding, J. Shen, M. Wan, and Z. Chen, Formation mechanism of polyaniline nanotubes by a simplified template-free method, *Macromol. Chem. Phys.*, **209**, 864–871 (2008).
[381] M. Trchová, I. Šeděnková, E. N. Konyushenko, J. Stejskal, P. Holler, and G. Ćirić-Marjanović, Evolution of polyaniline nanotubes: The oxidation of aniline in water, *J. Phys. Chem. B*, **110**, 9461–9468 (2006).
[382] Y. F. Huang and C. W. Lin, Introduction of methanol in the formation of polyaniline nanotubes in an acid-free aqueous solution through a self-curling process, *Polymer*, **50**, 775–782 (2009).
[383] G. Ćirić-Marjanović, V. Dondur, M. Milojević, M. Mojović, S. Mentus, A. Radulović, Z. Vuković, and J. Stejskal, Synthesis and characterization of conducting self-assembled polyaniline nanotubes/zeolite nanocomposite, *Langmuir*, **25**, 3122–3131 (2009).
[384] G. Ćirić-Marjanović, Lj. Dragičević, M. Milojević, M. Mojović, S. Mentus, B. Dojčinović, B. Marjanović, and J. Stejskal, Synthesis and characterization of self-assembled polyaniline nanotubes/silica nanocomposites, *J. Phys. Chem. B*, **113**, 7116–7127 (2009).
[385] C. Laslau, Z. D. Zujovic, and J. Travas-Sejdic, Polyaniline nanotube self-assembly: The stage of granular agglomeration on nanorod templates, *Macromol. Rapid Commun*., **30**, 1663–1668 (2009).

[386] G. Ćirić-Marjanović, M. Trchová, and J. Stejskal, The chemical oxidative polymerization of aniline in water: Raman spectroscopy, *J. Raman Spectrosc.*, **39**, 1375–1387 (2008).
[387] G. Ćirić-Marjanović, M. Trchová, and J. Stejskal, MNDO-PM3 Study of the early stages of the chemical oxidative polymerization of aniline, *Collect. Czech. Chem. Commun.*, **71**, 1407–1426 (2006).
[388] G. Ćirić-Marjanović, M. Trchová, and J. Stejskal, Theoretical study of the oxidative polymerization of aniline with peroxydisulfate: Tetramer formation, *Int. J. Quantum Chem.*, **108**, 318–333 (2008).
[389] G. Ćirić-Marjanović, E. N. Konyushenko, M. Trchová, and J. Stejskal, Chemical oxidative polymerization of anilinium sulfate versus aniline: Theory and experiment, *Synth. Met.*, **158**, 200–211 (2008).
[390] S. P. Surwade, V. Dua, N. Manohar, S. K. Manohar, E. Beck, and J. P. Ferraris, Oligoaniline intermediates in the aniline-peroxydisulfate system, *Synth. Met.*, **159**, 445–455 (2009).
[391] X. Lu, H. Mao, D. Chao, W. Zhang, and Y. Wei, Ultrasonic synthesis of polyaniline nanotubes containing Fe_3O_4 nanoparticles, *J. Solid State Chem.*, **179**, 2609–2615 (2006).
[392] Y. He and J. Lu, Synthesis of polyaniline nanostructures with controlled morphology by a two-phase strategy, *React. Funct. Polym.*, **67**, 476–480 (2007).
[393] Q. Sun and Y. Deng, The unique role of DL-tartaric acid in determining the morphology of polyaniline nanostructures during an interfacial oxidation polymerization, *Mater. Lett.*, **62**, 1831–1834 (2008).
[394] L. Dauginet-De Pra and S. Demoustier-Champagne, A comparative study of the electronic structure and spectroelectrochemical properties of electrosynthesized polyaniline films and nanotubes, *Thin Solid Films*, **479**, 321–328 (2005).
[395] D. Wei, C. Kvarnström,T. Lindfors, and A. Ivaska, Polyaniline nanotubules obtained in room-temperature ionic liquids, *Electrochem. Commun.*, **8**, 1563–1566 (2006).
[396] E. G. R. Fernandes, D. A. W. Soares, and A. A. A. DeQueiroz, Electrical properties of electrodeposited polyaniline nanotubes, *J. Mater. Sci. - Mater. Electron.*, **19**, 457–462 (2008).
[397] K. Huang, Y. Zhang, Y. Long, J. Yuan, D. Han, Z. Wang, L. Niu, and Z. Chen, Preparation of highly conductive, self-assembled gold/polyaniline nanocables and polyaniline nanotubes, *Chem. Eur. J.*, **12**, 5314–5319 (2006).
[398] M. T. Kumara, S. Muralidharan, and B. C. Tripp, Generation and characterization of inorganic and organic nanotubes on bioengineered flagella of mesophilic bacteria, *J. Nanosci. Nanotechn.*, **7**, 2260–2272 (2007).
[399] N. Nuraje, K. Su, N. L. Yang, and H. Matsui, Liquid/liquid interfacial polymerization to grow single crystalline nanoneedles of various conducting polymers, *ACS Nano*, **2**, 502–506 (2008).
[400] K. Su, N. Nuraje, L. Zhang, I-W. Chu, H. Matsui, and N.-L. Yang, First preparations and characterization of conductive polymer crystalline nanoneedles, *Macromol. Symp.*, **279**, 1–6 (2009).
[401] J. Yang, Y. Ding, and J. Zhang, Uniform rice-like nanostructured polyanilines with highly crystallinity prepared in dodecylbenzene sulfonic acid micelles, *Mater. Chem. Phys.*, **112**, 322–324 (2008).
[402] G. Li, H. Peng, Y. Wang, Y. Qin, Z. Cui, and Z. Zhang, Synthesis of polyaniline nanobelts, *Macromol. Rapid Commun.*, **25**, 1611–1614 (2004).
[403] C.-Y. Peng, A. K. Kalkan, S. J. Fonash, B. Gu, and A. A. Sen, 'Grow-in-place' architecture and methodology for electrochemical synthesis of conducting polymer nanoribbon device arrays, *Nano Lett.*, **5**, 439–444 (2005).
[404] Q. Z. Yu, Y. Li, M. Wang, and H. Z. Chen, Polyaniline nanobelts, flower-like, and rhizoid-like nanostructures by electrospinning, *Chin. Chem. Lett.*, **19**, 223–226 (2008).
[405] S. Liu, K. Zhu, Y. Zhang, and J. Xu, Cyclic polyaniline nanostructures from aqueous/organic interfacial polymerization induced by polyacrylic acid, *Polymer*, **47**, 7680–7683 (2006).
[406] Y. Wang, W. Chen, D. Zhou, and G. Xue, Synthesis of conducting polymer spiral nanostructures using a surfactant crystallite template, *Macromol. Chem. Phys.*, **210**, 936–941 (2009).
[407] J. Han, G. Song, and R. Guo, Nanostructure-based leaf-like polyaniline in the presence of an amphiphilic triblock copolymer, *Adv. Mater.*, **19**, 2993–2999 (2007).

[408] G. Li, C. Zhang, and H. Peng, Facile synthesis of self-assembled polyaniline nanodisks, *Macromol. Rapid Commun.*, **29**, 63–67 (2008).
[409] X. Luo, V. A. Pedrosa, and J. Wang, Enzymatic nanolithography of polyaniline nanopatterns by using peroxidase-modified atomic force microscopy tips, *Chem. Eur. J.*, **15**, 5191–5194 (2009).
[410] C. A. Amarnath, J. H. Chang, D. Kim, R. S. Mane, S.-H. Han, and D. Sohn, Electrochemical supercapacitor application of electroless surface polymerization of polyaniline nanostructures, *Mater. Chem. Phys.*, **113**, 14–17 (2009).
[411] H. Gao, T. Jiang, B. Han, Y. Wang, J. Du, Z. Liu, and J. Zhang, Aqueous/ionic liquid interfacial polymerization for preparing polyaniline nanoparticles, *Polymer*, **45**, 3017–3019 (2004).
[412] B. Sreedhar, P. Radhika, B. Neelima, N. Hebalkar, and M. V. B. Rao, Synthesis and characterization of polyaniline: nanospheres, nanorods, and nanotubes-catalytic application for sulfoxidation reactions, *Polym. Adv. Technol.*, **20**, 950–958 (2008).
[413] Z. Chen, C. Della Pina, E. Falletta, M. Lo Faro, M. Pasta, M. Rossi, and N. Santo, Facile synthesis of polyaniline using gold catalyst, *J. Catal.*, **259**, 1–4 (2008).
[414] K. R. Reddy, B. C. Sin, C. H. Yoo, D. Sohn, and Y. Lee, Coating of multiwalled carbon nanotubes with polymer nanospheres through microemulsion polymerization, *J. Colloid Interface Sci*., **340**, 160–165 (2009).
[415] X. Li, Y. Gao, F. Liu, J. Gong, and L. Qu, Synthesis of polyaniline/Ag composite nanospheres through UV rays irradiation method, *Mater. Lett.*, **63**, 467–469 (2009).
[416] J. Kan, Y. Jiang, and Y. Zhang, Studies on synthesis and properties of uniform and ordered polyaniline nanoparticles in the magnetic field, *Mater. Chem. Phys.*, **102**, 260–265 (2007).
[417] G. Song, J. Han, J. Bo, and R. Guo, Synthesis of polyaniline nanostructures in different lamellar liquid crystals and application to lubrication, *J. Mater. Sci.*, **44**, 715–720 (2009).
[418] Z. Lei, M. Zhao, L. Dang, L. An, M. Lu, A.-Y. Lo, N. Yu, and S.-B. Liu, Structural evolution and electrocatalytic application of nitrogen-doped carbon shells synthesized by pyrolysis of near-monodisperse polyaniline nanospheres, *J. Mater. Chem.*, **19**, 5985–5995 (2009).
[419] D. Cheng, S.-C. Ng, and H. S. O. Chan, Morphology of polyaniline nanoparticles synthesized in triblock copolymers micelles, *Thin Solid Films*, **477**, 19–23 (2005).
[420] X. Luo, A. J. Killard, A. Morrin, and M. R. Smyth, Electrochemical preparation of distinct polyaniline nanostructures by surface charge control of polystyrene nanoparticle templates, *Chem. Commun.*, 3207–3209 (2007).
[421] L. S. Jan, S. Radiman, M. A. Siddig, S. V. Muniandy, M. A. Hamid, and H. D. Jamali, Preparation of nanoparticles of polystyrene and polyaniline by γ-irradiation in lyotropic liquid crystal, *Colloids Surf. A*, **251**, 43–52 (2004).
[422] S. Valkama, J. Hartikainen, M. Torkkeli, R. Serimaa, J. Ruokolainen, K. Rissanen, G. ten Brinke, and O. Ikkala, Self-organized nanostructures of poly(4-vinylpyridine), polyaniline and polyamides due to metal complexation, *Macromol. Symp.*, **186**, 87–92 (2002).
[423] S. H. Lee, D. H. Lee, K. H. Lee, and C. W. Lee, High-performance polyaniline prepared via polymerization in a self-stabilized dispersion, *Adv. Funct. Mater.*, **15**, 1495–1500 (2005).
[424] K. H. Lee, S. U. Cho, S. H. Park, A. J. Heeger, and C. W. Lee, Metallic transport in polyaniline, *Nature*, **441**, 65–68 (2006).
[425] C. W. Lee, K.-W. Chi, H. Y. Hwang, and H. M. Jeong, Synthesis and properties of high performance nanostructured polyaniline: Effect of initiator dosage and molecular oxygen, *Synth. Met.*, **159**, 1757–1760 (2009).
[426] J. Wang, J. Wang, Z. Wang, and F. Zhang, A template-free method toward urchin-like polyaniline microspheres, *Macromol. Rapid Commun.*, **30**, 604–608 (2009).
[427] Y. Zhu, J. Li, M. Wan, and L. Jiang, Electromagnetic functional urchin-like hollow carbon spheres carbonized by polyaniline micro/nanostructures containing $FeCl_3$ as a precursor, *Eur. J. Inorg. Chem.*, **2009**, 2860–2864 (2009).
[428] Y. Zhu, J. Li, M. Wan, L. Jiang, and Y. Wei, A new route for the preparation of brain-like nanostructured polyaniline, *Macromol. Rapid Commun.*, **28**, 1339–1344 (2007).
[429] T. Wang, W. Zhong, X. Ning, Y. Wang, and W. Yang, Facile synthesis of polyaniline 'sunflowers' with arrays of oriented nanorods, *J. Colloid Interface Sci.*, **334**, 108–112 (2009).

[430] X. Luo, G. D. Vidal, A. J. Killard, A. Morrin, and M. R. Smyth, Nanocauliflowers: A nanostructured polyaniline-modified screen-printed electrode with a self-assembled polystyrene template and its application in an amperometric enzyme biosensor, *Electroanalysis*, **19**, 876–883 (2007).
[431] T. Dai and Y. Lu, Polycrystalline polyaniline with strong infrared absorption, *Eur. Polym. J.*, **44**, 3417–3422 (2008).
[432] J. Fei, Y. Cui, X. Yan, Y. Yang, Y. Su, and J. Li, Formation of PANI tower-shaped hierarchical nanostructures by a limited hydrothermal reaction, *J. Mater. Chem.*, **19**, 3263–3267 (2009).
[433] J. Fei, Y. Cui, X. Yan, Y. Yang, K. Wang, and J. Li, Controlled fabrication of polyaniline spherical and cubic shells with hierarchical nanostructures, *ACS Nano*, **3**, 3714–3718 (2009).
[434] Z. D. Zujovic, G. A. Bowmaker, H. D. Tran, and R. B. Kaner, Solid-state NMR of polyaniline nanofibers, *Synth. Met.*, **159**, 710–714 (2009).
[435] G. M. do Nascimento, C. H. B. Silva, and M. L. A. Temperini, Spectroscopic characterization of the structural changes of polyaniline nanofibers after heating, *Polym. Degrad. Stab.*, **93**, 291–297 (2008).
[436] A. R. Hopkins, R. A. Lipeles, and S.-J. Hwang, Morphology characterization of polyaniline nano- and microstructures, *Synth. Met.*, **158**, 594–601 (2008).
[437] M. U. Niemann, S. S. Srinivasan, A. R. Phani, A. Kumar, D. Y. Goswami, and E. K. Stefanakos, Room temperature reversible hydrogen storage in polyaniline (PANI) nanofibers, *J. Nanosci. Nanotechn.*, **9**, 4561–4565 (2009).
[438] Y. Long, Z. Chen, N. Wang, Z. Zhang, and M. Wan, Resistivity study of polyaniline doped with protonic acids, *Physica B*, **325**, 208–213 (2003).
[439] P. Pipinys and A. Kiveris, Analysis of temperature-dependent conductivity of nanotubular polyaniline on the basis of phonon-assisted tunneling theory, *Physica B*, **355**, 352–356 (2005).
[440] Y. Long, Z. Chen, J. Shen, Z. Zhang, L. Zhang, K. Huang, M. Wan, A. Jin, C. Gu, and J. L. Duvail, Magnetoresistance studies of polymer nanotube/wire pellets and single polymer nanotubes/wires, *Nanotechnology*, **17**, 5903–5911 (2006).
[441] Y. Long, Z. Chen, J. Shen, Z. Zhang, L. Zhang, H. Xiao, M. Wan, and J. L. Duvail, Magnetic properties of conducting polymer nanostructures, *J. Phys. Chem. B*, **110**, 23228–23233 (2006).
[442] I. Šeděnková, M. Trchová, and J. Stejskal, Thermal degradation of polyaniline films prepared in solutions of strong and weak acids and in water – FTIR and Raman spectroscopic studies, *Polym. Degrad. Stab.*, **93**, 2147–2157 (2008).
[443] J. J. Langer and S. Golczak, Highly carbonized polyaniline micro- and nanotubes, *Polym. Degrad. Stab.*, **92**, 330–334 (2007).
[444] M. Trchová, E. N. Konyushenko, J. Stejskal, J. Kovářová, and G. Ćirić-Marjanović, The conversion of polyaniline nanotubes to nitrogen-containing carbon nanotubes and their comparison with multi-walled carbon nanotubes, *Polym. Degrad. Stab.*, **94**, 929–938 (2009).
[445] S. Mentus, G. Ćirić-Marjanović, M. Trchová, and J. Stejskal, Conducting carbonized polyaniline nanotubes, *Nanotechnology*, **20**, 245601 (10pp) (2009).
[446] J. Stejskal, J. Prokeš, and I. Sapurina, The reduction of silver ions with polyaniline: The effect of the type of polyaniline and the mole ratio of the reagents, *Mater. Lett.*, **63**, 709–711 (2009).
[447] U. Riaz, S. Ahmad, and S. M. Ashraf, Comparison of corrosion protective performance of nanostructured polyaniline and poly(1-naphthylamine)-based alkyd coatings on mild steel, *Mater. Corr.*, **60**, 280–286 (2009).
[448] G. F. Li, C. Martinez, J. Janata, J. A. Smith, M. Josowicz, and S. Semancik, Effect of morphology on the response of polyaniline-based conductometric gas sensors: Nanofibers *vs.* thin films, *Electrochem. Solid-State Lett.*, **7**, H44–H48 (2004).
[449] D. Li and R. B. Kaner, Processable stabilizer-free polyaniline nanofiber aqueous colloids, *Chem. Commun.*, 3286–3288 (2005).
[450] D. Li, J. Huang, and R. B. Kaner, Polyaniline nanofibers: A unique polymer nanostructure for versatile applications, *Acc. Chem. Res.*, **42**, 135–145 (2009).
[451] P. Jiménez, W. K. Maser, P. Castell, M. T. Martínez, and A. M. Benito, Nanofibrilar polyaniline: Direct route to carbon nanotube water dispersions of high concentration, *Macromol. Rapid Commun.*, **30**, 418–422 (2009).

[452] W. K. Maser, P. Jiménez, N. O. Payne, R. L. Shepherd, P. Castell, M. in het Panhuis, and A. M. Benito, Nanofibrilar-polyaniline/carbon nanotube composites: Aqueous dispersions and films, *J. Nanosci. Nanotechnol.*, **9**, 6157–6163 (2009).
[453] C. Su, G. Wang, F. Huang, and X. Li, Melt-processed polyaniline nanofibers/LDPE/EAA conducting composites, *Polym. Compos.*, **29**, 1177–1182 (2008).
[454] J. Huang and R. B. Kaner, Flash welding of conducting polymer nanofibres, *Nat. Mater.*, **3**, 783–786 (2004).
[455] B. Shedd, C. O. Baker, M. J. Heller, R. B. Kaner, and H. T. Hahn, Fabrication of monolithic microstructures from polyaniline nanofibers, *Mater. Sci. Eng. B*, **162**, 111–115 (2009).
[456] J. Lin, Q. Tang, D. Hu, X. Sun, Q. Li, and J. Wu, Electric field sensitivity of conducting hydrogels with interpenetrating polymer network structure, *Colloids Surf. A*, **346**, 177–183 (2009).
[457] Z. Fan, Z. Wang, N. Sun, J. Wang, and S. Wang, Performance improvement of polysulfone ultrafiltration membrane by blending with polyaniline nanofibers, *J. Membrane Sci.*, **320**, 363–371 (2008).
[458] J. D. Sudha, S. Sivakala, R. Prasanth, V. L. Reena, and P. Radhakrishnan Nair, Development of electromagnetic shielding materials from the conductive blends of polyaniline and polyaniline-clay nanocomposite-EVA: Preparation and properties, *Compos. Sci. Technol.*, **69**, 358–364 (2009).
[459] H.-S. Kim, H. L. Hobbs, L. Wang, M. J. Rutten, and C. C. Wamser, Biocompatible composites of polyaniline nanofibers and collagen, *Synth. Met.*, **159**, 1313–1318 (2009).
[460] C.-C. Wang, J.-F. Song, H.-M. Bao, Q.-D. Shen, and C.-Z. Yang, Enhancement of electrical properties of ferroelectric polymers by polyaniline nanofibers with controllable conductivities, *Adv. Funct. Mater.*, **18**, 1299–1306 (2008).
[461] N. Zhou, T. Yang, C. Jiang, M. Du, and K. Jiao, Highly sensitive electrochemical impedance spectroscopic detection of DNA hybridization based on Au_{nano}–CNT/PAN_{nano} films, *Talanta*, **77**, 1021–1026 (2009).
[462] Rajesh, T. Ahuja, and D. Kumar, Recent progress in the development of nano-structured conducting polymers/nanocomposites for sensor applications, *Sens. Actuators B*, **136**, 275–286 (2009).
[463] J. Jang, Conducting polymer nanomaterials and their applications, *Adv. Polym. Sci.*, **199**, 189–260 (2006).
[464] J. Huang, S. Virji, B. H. Weiller, and R. B. Kaner, Nanostructured polyaniline sensors, *Chem. Eur. J.*, **10**, 1314–1319 (2004).
[465] S. Virji, J. D. Fowler, C. O. Baker, J. Huang, R. B. Kaner, and B. H. Weiller, Polyaniline nanofiber composites with metal salts: Chemical sensors for hydrogen sulfide, *Small*, **1**, 624–627 (2005).
[466] S. Virji, R. Kojima, J. D. Fowler, R. B. Kaner, and B. H. Weiller, Polyaniline nanofiber−metal salt composite materials for arsine detection, *Chem. Mater.*, **21**, 3056–3061 (2009).
[467] S. Virji, R. B. Kaner, and B. H. Weiller, Hydrogen sensors based on conductivity changes in polyaniline nanofibers, *J. Phys. Chem. B*, **110**, 22266–22270 (2006).
[468] A. Z. Sadek, W. Wlodarski, K. Kalantar-Zadeh, C. Baker, and R. B. Kaner, Doped and dedoped polyaniline nanofiber based conductometric hydrogen gas sensors, *Sens. Actuators A*, **139**, 53–57 (2007).
[469] M. Z. Atashbar, A. Z. Sadek, W. Wlodarski, S. Sriram, M. Bhaskaran, C. J. Cheng, R. B. Kaner, and K. Kalantar-zadeh, Layered SAW gas sensor based on CSA synthesized polyaniline nanofiber on AlN on 64° YX $LiNbO_3$ for H_2 sensing, *Sens. Actuators B*, **138**, 85–89 (2009).
[470] R. Arsat, X. F. Yu, Y. X. Li, W. Wlodarski, and K. Kalantar-zadeh, Hydrogen gas sensor based on highly ordered polyaniline nanofibers, *Sens. Actuators B*, **137**, 529–532 (2009).
[471] J. D. Fowler, S. Virji, R. B. Kaner, and B. H. Weiller, Hydrogen detection by polyaniline nanofibers on gold and platinum electrodes, *J. Phys. Chem. C*, **113**, 6444–6449 (2009).
[472] S. Virji, R. Kojima, J. D. Fowler, J. G. Villanueva, R. B. Kaner, and B. H. Weiller, Polyaniline nanofiber composites with amines: Novel materials for phosgene detection, *Nano Res.*, **2**, 135–142 (2009).

[473] S. Jiang, J. Chen, J. Tang, E. Jin, L. Kong, W. Zhang, and C. Wang, Au nanoparticles-functionalized two-dimensional patterned conducting PANI nanobowl monolayer for gas sensor, *Sens. Actuators B*, **140**, 520–524 (2009).
[474] N. J. Pinto, I. Ramos, R. Rojas, P.-C. Wang, and A. T. Johnson Jr., Electric response of isolated electrospun polyaniline nanofibers to vapors of aliphatic alcohols, *Sens. Actuators B*, **129**, 621–627 (2008).
[475] F. Wang, W. Wang, B. Liu, Z. Wang, and Z. Zhang, Copolypeptide-doped polyaniline nanofibers for electrochemical detection of ultratrace trinitrotoluene, *Talanta*, **79**, 376–382 (2009).
[476] W. Li, N. D. Hoa, Y. Cho, D. Kim, and J.-S. Kim, Nanofibers of conducting polyaniline for aromatic organic compound sensor, *Sens. Actuators B*, **143**, 132–138 (2009).
[477] M. Zhao, X. Wu, and C. Cai, Polyaniline nanofibers: Synthesis, characterization, and application to direct electron transfer of glucose oxidase, *J. Phys. Chem. C*, **113**, 4987–4996 (2009).
[478] Y.-Y. Horng, Y.-K. Hsu, A. Ganguly, C.-C. Chen, L.-C. Chen, and K.-H. Chen, Direct-growth of polyaniline nanowires for enzyme-immobilization and glucose detection, *Electrochem. Commun.*, **11**, 850–853 (2009).
[479] Z. Wang, S. Liu, P. Wu, and C. Cai, Detection of glucose based on direct electron transfer reaction of glucose oxidase immobilized on highly ordered polyaniline nanotubes, *Anal. Chem.*, **81**, 1638–1645 (2009).
[480] X. Wang, T. Yang, Y. Feng, K. Jiao, and G. Li, A novel hydrogen peroxide biosensor based on the synergistic effect of gold-platinum alloy nanoparticles/polyaniline nanotube/chitosan nanocomposite membrane, *Electroanalysis*, **21**, 819–825 (2009).
[481] C. Dhand, S. P. Singh, S. K. Arya, M. Datta, and B. D. Malhotra, Cholesterol biosensor based on electrophoretically deposited conducting polymer film derived from nano-structured polyaniline colloidal suspension, *Anal. Chim. Acta* **602**, 244–251 (2007).
[482] C. Dhand, P. R. Solanki, K. N. Sood, M. Datta, and B. D. Malhotra, Polyaniline nanotubes for impedimetric triglyceride detection, *Electrochem. Commun.*, **11**, 1482–1486 (2009).
[483] N. Zhu, Z. Chang, P. He, and Y. Fang, Electrochemically fabricated polyaniline nanowire-modified electrode for voltammetric detection of DNA hybridization, *Electrochim. Acta* **51**, 3758–3762 (2006).
[484] T. Yang, N. Zhou, Y. Zhang, W. Zhang, K. Jiao, and G. Li, Synergistically improved sensitivity for the detection of specific DNA sequences using polyaniline nanofibers and multi-walled carbon nanotubes composites, *Biosens. Bioelectron.*, **24**, 2165–2170 (2009).
[485] H. Peng, L. Zhang, C. Soeller, and J. Travas-Sejdic, Conducting polymers for electrochemical DNA sensing, *Biomaterials*, **30**, 2132–2148 (2009).
[486] H. Chang, Y. Yuan, N. Shi, and Y. Guan, Electrochemical DNA biosensor based on conducting polyaniline nanotube array, *Anal. Chem.*, **79**, 5111–5115 (2007).
[487] Y. Feng, T. Yang, W. Zhang, C. Jiang, and K. Jiao, Enhanced sensitivity for deoxyribonucleic acid electrochemical impedance sensor: Gold nanoparticle/polyaniline nanotube membranes, *Anal. Chim. Acta*, **616**, 144–151 (2008).
[488] Y. Fan, X. Chen, A. D. Trigg, C.-H. Tung, J. Kong, and Z. Gao, Detection of microRNAs using target-guided formation of conducting polymer nanowires in nanogaps, *J. Am. Chem. Soc.*, **129**, 5437–5443 (2007).
[489] K. Langer, P. Barczyński, K. Baksalary, M. Filipiak, S. Golczak, and J. J. Langer, A fast and sensitive continuous flow nanobiodetector based on polyaniline nanofibrils, *Microchim. Acta*, **159**, 201–206 (2007).
[490] S. Pal, E. C. Alocilja, and F. P. Downes, Nanowire labeled direct-charge transfer biosensor for detecting *Bacillus* species, *Biosens. Bioelectron.*, **22**, 2329–2336 (2007).
[491] J. J. Langer, K. Langer, P. Barczyński, J. Warchoł, and K. H. Bartkowiak, New 'ON-OFF'-type nanobiodetector, *Biosens. Bioelectron.*, **24**, 2947–2949 (2009).
[492] E. S. Medeiros, R. Gregório, R. A. Martinez, and L. H. C. Mattoso, A taste sensor array based on polyaniline nanofibers for orange juice quality assessment, *Sens. Lett.*, **7**, 24–30 (2009).
[493] B. J. Gallon, R. W. Kojima, R. B. Kaner, and P. L. Diaconescu, Palladium nanoparticles supported on polyaniline nanofibers as a semi-heterogeneous catalyst in water, *Angew. Chem. Int. Ed.*, **46**, 7251–7254 (2007).

[494] P. R. Likhar, R. Arundhathi, S. Ghosh, and M. L. Kantam, Polyaniline nanofiber supported $FeCl_3$: An efficient and reusable heterogeneous catalyst for the acylation of alcohols and amines with acetic acid, *J. Mol. Catal. A: Chem.*, **302**, 142–149 (2009).
[495] H. Ding, G. Wang, M. Yang, Y. Luan, Y. Wang, and X. Yao, Novel sea urchin-like polyaniline microspheres-supported molybdenum catalyst: Preparation, characteristic and functionality, *J. Mol. Catal. A: Chem.*, **308**, 25–31 (2009).
[496] F.-J. Liu, L.-M. Huang, T.-C. Wen, C.-F. Li, S.-L. Huang, and A. Gopalan, Effect of deposition sequence of platinum and ruthenium particles into nanofibrous network of polyaniline–poly(styrene sulfonic acid) on electrocatalytic oxidation of methanol, *Synth. Met.*, **158**, 603–609 (2008).
[497] J. Wang, X. Qi, F. Meng, Y. Ning, S. Chen, D. Pang, and Y. Wen, Polyaniline nanofibers: Inducing action of neodymium oxide and inhibiting effect on electrochemical degradation and modified platinum electrode application to the electrocatalytic oxidation of methanol, *J. Phys. Chem. C*, **113**, 1459–1465 (2009).
[498] S. Guo, S. Dong, and E. Wang, Polyaniline/Pt hybrid nanofibers: High-efficiency nanoelectrocatalysts for electrochemical devices, *Small*, **5**, 1869–1876 (2009).
[499] G. Lee, H. Joo, and J.-H. Lee, The use of polyaniline nanofibre as a support for lipase mediated reaction, *J. Mol. Catal. B: Enzym.*, **54**, 116–121 (2008).
[500] G. Lee, J. Kim, and J.-H. Lee, Development of magnetically separable polyaniline nanofibers for enzyme immobilization and recovery, *Enzyme Microb. Tech.*, **42**, 466–472 (2008).
[501] B. Rajesh, K. R. Thampi, J. M. Bonard, H. J. Mathieu, N. Xanthopoulos, and B. Viswanathand, Nanostructured conducting polyaniline tubules as catalyst support for Pt particles for possible fuel cell applications, *Electrochem. Solid-State Lett.*, **7**, A404–A407 (2004).
[502] R. K. Pandey and V. Lakshminarayanan, Electro-oxidation of formic acid, methanol, and ethanol on electrodeposited Pd-polyaniline nanofiber films in acidic and alkaline medium, *J. Phys. Chem. C*, **113**, 21596–21603 (2009).
[503] A. K. Wanekaya, M. A. Bangar, M. Yun, W. Chen, N. V. Myung, and A. Mulchandani, Field-effect transistors based on single nanowires of conducting polymers, *J. Phys. Chem. C*, **111**, 5218–5221 (2007).
[504] B. Wessling and J. Posdorfer, Nanostructures of the dispersed organic metal polyaniline responsible for macroscopic effects in corrosion protection, *Synth. Met.*, **102**, 1400–1401 (1999).
[505] R. J. Tseng, J. Huang, J. Ouyang, R. B. Kaner, and Y. Yang, Polyaniline nanofiber/gold nanoparticle nonvolatile memory, *Nano Lett.*, **5**, 1077–1080 (2005).
[506] R. J. Tseng, C. O. Baker, and B. Shedd, Charge transfer effect in the polyaniline-gold nanoparticle memory system, *Appl. Phys. Lett.*, **90**, 053101 (3 pages) (2007).
[507] C. O. Baker, B. Shedd, P. C. Innis, P. G. Whitten, G. M. Spinks, G. G. Wallace, and R. B. Kaner, Monolithic actuators from flash-welded polyaniline nanofibers, *Adv. Mater.*, **20**, 155–158 (2008).
[508] Y. A. Ismail, M. K. Shin, and S. J. Kim, A nanofibrous hydrogel templated electrochemical actuator: From single mat to a rolled-up structure, *Sens. Actuators B*, **136**, 438–443 (2009).
[509] H. Gharibi, M. Zhiani, R. A. Mirzaie, M. Kheirmand, A. A. Entezami, K. Kakaei, and M. Javaheri, Investigation of polyaniline impregnation on the performance of gas diffusion electrode (GDE) in PEMFC using binary of Nafion and polyaniline nanofiber, *J. Power Sources*, **157**, 703–708 (2006).
[510] Z. Fan, Z. Wang, M. Duan, J. Wang, and S. Wang, Preparation and characterization of polyaniline/polysulfone nanocomposite ultrafiltration membrane, *J. Membrane Sci.*, **310**, 402–408 (2008).
[511] M.-Y. Chang, C.-S. Wu, Y.-F. Chen, B.-Z. Hsieh, W.-Y. Huang, K.-S. Ho, T.-H. Hsieh, and Y.-K. Han, Polymer solar cells incorporating one-dimensional polyaniline nanotubes, *Org. Electron.*, **9**, 1136–1139 (2008).
[512] Y.-K. Han, Y.-J. Lee, and P.-C. Huang, Regioregularity effects in poly(3-hexylthiophene): PCBM-based solar cells incorporating acid-doped polyaniline nanotubes as an interfacial layer, *J. Electrochem. Soc.*, **156**, K37–K43 (2009).

[513] M. Deka, A. K. Nath, and A. Kumar, Effect of dedoped (insulating) polyaniline nanofibers on the ionic transport and interfacial stability of poly(vinylidene fluoride-hexafluoropropylene) based composite polymer electrolyte membranes, *J. Membrane Sci.*, **327**, 188–194 (2009).
[514] F. Cheng, W. Tang, C. Li, J. Chen, H. Liu, P. Shen, and S. Dou, Conducting poly(aniline) nanotubes and nanofibers: Controlled synthesis and application in lithium/poly(aniline) rechargeable batteries, *Chem. Eur. J.*, **12**, 3082–3088 (2006).
[515] J. Chen and F. Cheng, Combination of lightweight elements and nanostructured materials for batteries, *Acc. Chem. Res.*, **42**, 713–723 (2009).
[516] J. Yin, X. Zhao, X. Xia, L. Xiang, and Y. Qiao, Electrorheological fluids based on nanofibrous polyaniline, *Polymer*, **49**, 4413–4419 (2008).
[517] J. Yin, X. Xia, L. Xiang, Y. Qiao, and X. Zhao, The electrorheological effect of polyaniline nanofiber, nanoparticle and microparticle suspensions, *Smart Mater. Struct.*, **18**, 095007 (11pp) (2009).
[518] R. Rivera and N. J. Pinto, Schottky diodes based on electrospun polyaniline nanofibers: Effects of varying fiber diameter and doping level on device performance, *Physica E* **41**, 423–426 (2009).
[519] H. Li, J. Wang, Q. Chu, Z. Wang, F. Zhang, and S. Wang, Theoretical and experimental specific capacitance of polyaniline in sulfuric acid, *J. Power Sourc.*, **190**, 578–586 (2009).

3

Nanoscale Inhomogeneity of Conducting-Polymer-Based Materials

Alain Pailleret[1,2] *and Oleg Semenikhin*[3]

[1]*CNRS, UPR 15, Laboratoire Interfaces et Systèmes Electrochimiques, (LISE, case courrier 133), 4 Place Jussieu, F-75005, Paris, France*
[2]*UPMC Univ Paris VI, UPR 15, Laboratoire Interfaces et Systèmes Electrochimiques, (LISE, case courrier 133), 4 Place Jussieu, F-75005, Paris, France*
[3]*Department of Chemistry, The University of Western Ontario, London, Ontario, Canada*

3.1 Introduction: Inhomogeneity and Nanostructured Materials

Efficient micro- and nanostructuring of conducting polymer-based materials, or introduction of certain patterns of local modifications, is impossible without careful consideration of the inhomogeneity of these materials. If the desired scale of modifications is less than or equal to the typical scale of inhomogeneous features of the material, the modification will not be uniform and thus most probably fail to achieve its goals. Furthermore, the extent of directional modification of the material properties as a result of nanostructuring should also be measured against the inherent distribution of the material properties that existed in the as-prepared material before the modification. For instance, structuring a more inhomogeneous material would obviously require a deeper modification as compared to a less inhomogeneous material.

Nanostructured Conductive Polymers Edited by Ali Eftekhari

Another area where inhomogeneity is extremely important is various organic semiconductor devices such as solar cells and thin-film transistors. Typical thickness of polymer layers in such devices is of the order of 100 nm, which means that any inhomogeneity/disorder on this or similar scale will affect the performance of devices based on such materials. Specifically, one of the effects of inhomogeneity widely discussed in the recent literature is the effect of disorder on the efficiency of charge transport in organic materials, which is crucial for many applications based on conducting and semiconducting organic polymers.

Overall, as a result of all these factors, the prevailing tendency has been to find the ways to reduce the inhomogeneity and produce uniform, high-quality polymer films. Such films will be also the best substrates for micro- and nanostructuring since they would require only limited modification to drastically modify their properties. At the same time, there are cases when inhomogeneity may be beneficial and even crucial for the functioning of polymer-based devices. Regrettably, the scope of this chapter does not allow us to address here in any detail the very rapidly developing fields of such inherently heterogeneous systems as polymer blends, including those used in bulk heterojunction organic solar cells, and polymer-based materials modified with metal nanoparticles.

The field of conducting polymers is quite special because these materials hold great promise for a variety of uses. As a result, the inhomogeneity of such materials has been treated in the context of many diverse applications. Furthermore, the focus of the scientific community has shifted considerably over time, and this has also impacted studies of polymer inhomogeneity. In the early days (roughly two decades from 1980 to 2000, but most prominently in 1990s), most studies were focused on the metallic state of conducting polymers and the metal-to-insulator/insulator-to-metal transitions. The polymer systems most studied at that time were first polyacetylene and later mainly polyaniline and polypyrrole. Electrochemical and related studies of the inhomogeneous distribution of the doping level in such materials were also initiated at that time. In the late 1990s and especially in the 2000s, the attention of the scientific community shifted from metallic to semiconductor polymers and their applications, such as organic light-emitting diodes (OLEDs), organic electronics, and plastic solar cells. As a result, polyaniline and polypyrrole were no longer subjects of major interest and most studies of polymer inhomogeneity were performed in the context of organic electronics applications, first with various poly(phenylene vinylene)s (PPVs) and later with various polythiophenes, especially regio-regular polythiophenes such as poly(3-hexylthiophene) (P3HT). However, despite very different approaches, preparation techniques, and applications discussed in the literature in 1990s and 2000s, the fact remains that all these materials are closely related to each other and the inhomogeneity of polypyrrole and polyaniline should be governed by the same factors as that of poly(phenylene vinylene)s and polythiophenes.

This chapter attempts to review the knowledge accumulated over time on the problem of inhomogeneity of conducting polymers and related materials in various systems and applications and to present a common view of the origins of the inhomogeneity of these materials. Early studies with conducting and semiconducting π-conjugated polymers have accumulated ample experimental evidence that these materials feature significant inhomogeneous disorder. More precisely, these materials were envisaged as consisting of small, ordered, mostly crystalline domains or islands separated by amorphous disordered matrix. These conclusions were made on the basis of indirect data such as X-ray

measurements [1–5] or mobility/conductivity measurements/analysis of the metallic [6–12] and semiconducting [13–20] states of the polymer materials; however, all these studies were based on indirect measurements which could not provide any local and especially nanoscale information and could not relate the measured properties to specific locations or topographic features of the materials under study.

One of the main differences between early and more recent work is that over the last decade various scanning-probe and related techniques such as AFM, SEM, TEM, EDX, as well as various local spectroscopic techniques, have become everyday tools available to wide circles of materials scientists. The widespread use of these techniques has enabled scientists to routinely perform direct local studies of material properties and inhomogeneity on the nanometer scale and obtain unique information not available before. Therefore, one of the main goals of this chapter is to review recent progress achieved in the local studies of conducting polymers and related materials on the nanoscale. Special attention will be also paid to understanding the origins of inhomogeneity, which is of great importance from both the fundamental and practical viewpoints. The most obvious source and manifestation of the material inhomogeneity is its morphology; however, it has not been clear until very recently if polymer inhomogeneity and morphology are in fact even related to each other, and even now further work is required to establish the details of this relationship.

X-ray diffraction and related techniques, especially those using grazing incidence X-ray scattering, have been very instrumental in establishing the degree of crystallinity and disorder in conducting polymer films. However, in most cases, the X-ray data will be reviewed in this chapter only insofar as they provide support for the other structural/local data. A more detailed overview of recent literature on X-ray scattering from conducting and semiconducting polymers is available [21].

3.2 Direct Local Measurements of Nanoscale Inhomogeneity of Conducting and Semiconducting Polymers

3.2.1 Introduction

Before reviewing the results of direct local measurements of nanoscale properties of conducting and semiconducting polymers available in the literature, we believe it would be advantageous to provide in each section a short summary of the technique used for this purpose. We do not feel there is a need to review here general well-known techniques like basic atomic force microscopy (AFM) and scanning/transmission electron microscopy (SEM/TEM); however, there are some techniques, particularly AFM extensions, which may be less familiar to the reader and thus warrant some additional notes. The main advantages of AFM extensions is that they are able to measure simultaneously not only the sample topography, but also a host of other parameters, from which one is able to extract information about various local properties of the samples with the same nanometer resolution, and reference these data to exact locations on the sample surface for which other properties, like topography, have been determined. Among the extensions that have

been especially instrumental in studies of the inhomogeneity of conducting and semiconducting conjugated polymers reviewed in this chapter are Kelvin probe force microscopy (KFM) and electric force microscopy (EFM), which measure the nanoscale distribution of surface electrical potential or electric field; current-sensing atomic force microscopy (CS-AFM) (also known as conducting AFM (CAFM)), which measures the local sample conductivity; scanning near-field optical microscopy (SNOM), which enables one to characterize various local optical properties below the far-field diffraction limit; and phase-imaging atomic force microscopy (PI-AFM), which provides information concerning the nanoscale viscoelasticity and crystallinity of materials. All these techniques feature the same important advantage: the ability to measure important local parameters simultaneously with topography imaging, and with the same high resolution; therefore, they allow one to correlate topography information, such as the surface morphology, with the other parameters characterizing the material inhomogeneity. Specifically, for conducting and semiconducting polymers, this feature is instrumental in deciding if there is a relationship between inhomogeneity and surface morphology, which is of prime importance for elucidating the origins of nanoscale inhomogeneity in these systems.

We also feel that in this introduction we need to provide a brief summary of some of the molecular structures of the conducting and semiconducting polymers under study. While early studies dealt with polymers that featured relatively simple and straightforward structures, such as polyaniline, polypyrrole, and polythiophene, including regio-random and regio-regular poly(3-alkyl thiophene)s, in recent years, new polymeric materials have been developed which, in many cases, feature extremely complex chemical structures. The main driving force here was the search for various donor–acceptor materials incorporating distinct donor and acceptor moieties in the same molecule, for instance for solar-energy conversion and low-bandgap materials, as well as the search for regio-regular materials with better ordering and intermolecular packing than regio-regular poly(3-hexylthiophene) (P3HT).

As far is the latter field is concerned, one of the design ideas was that to ensure better and facile interdigitation of the side chains, which is the main driving force behind the excellent ordering of regio-regular polymer materials, the side-chain density should be decreased. One way of achieving this is to prepare a polymer in which not every thiophene ring bears a side chain. Two examples of such polymers are poly(4,4″-dioctyl-2,2′:5′,2″-terthiophene) (PDOTT) [22] and poly(3,3‴-dialkylquaterthiophene)s (PQT) [23-27], which have two alkyl-substituted thiophene rings flanking one (PDOTT) or two (PQT) nonsubstituted rings. These polymers show excellent charge-carrier mobilities that are generally higher than those found with regio-regular P3HT. Yet another design idea is to introduce various spacer (not thiophene) subunits between regio-regular alkylthiophene units. Among those materials are poly[(5,5′-(3,3′-di-*n*-octyl-2,2′-bithiophene))-*alt*-(2,7-fluoren-9-one)] (PDOBTF) [28], which combines head-to-head coupled di-*n*-octylthiophene and fluorenone subunits, poly(2,5-bis(3-alkylthiophen-2-yl)thieno[3,2-b]thiophene) (PBTTT) [29] and poly(2,6-bis(3-alkylthiophen-2-yl)dithieno[3,2-b;2′,3′-d]thiophene) (PBTDT) [30] with thienothiophene and dithienothiophene spacer subunits, and others. Outside the polythiophene family, important materials are polyfluorenes such as poly(9,9′-dialkylfluorene)s and poly(phenylene vinylene)s, such as poly(2-methoxy-5-(2′-ethylhexyloxy)-1,4-phenylene vinylene) (MEH-PPV). The molecular structures of some of the materials described in the following sections is given in Figure 3.1.

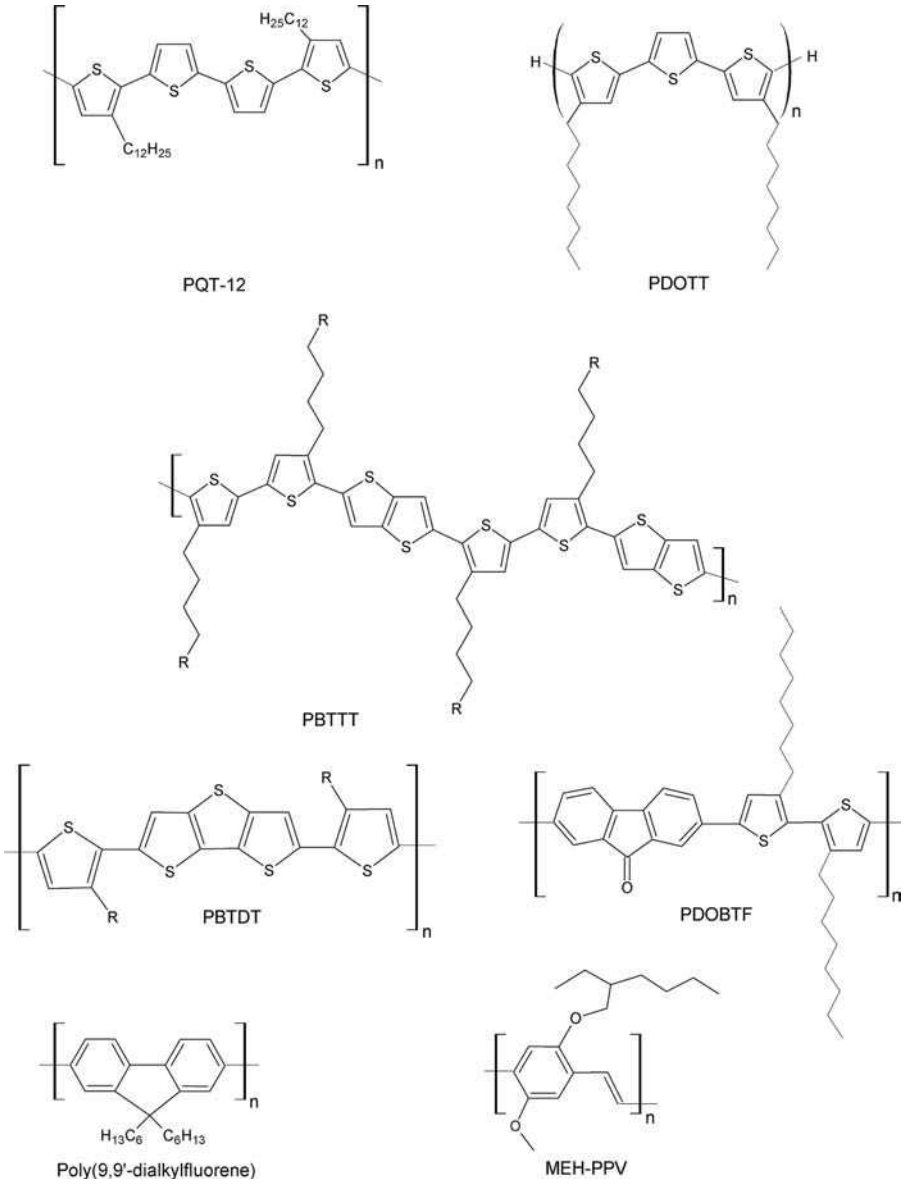

Figure 3.1 *Molecular structures of some of the materials described in this chapter*

3.2.2 Atomic Force Microscopy (AFM), Kelvin Probe Force Microscopy (KFM), and Electric Force Microscopy (EFM)

As far as can be seen from the available literature, the first locally resolved studies of nanoscale inhomogeneity of conducting and semiconducting polymers only appeared in

1996 [31,32]. Semenikhin *et al.* [31] used atomic force microscopy (AFM) and its extension, Kelvin probe force microscopy (KFM), to study the structural inhomogeneity and doping level distribution in undoped polybithiophene (PBT). The Kelvin probe force technique utilizes a conducting tip through which a selectable bias can be applied between the tip and the sample. If the applied bias is equal to the contact potential difference between the tip and the sample, the electric field between the tip and the sample is cancelled, which can be detected with a high accuracy. Therefore, by constantly adjusting the tip–sample bias in the process of scanning so that there is no electric field between them, one can measure with nanometer resolution the lateral distribution of the contact potential difference and therefore of the sample work function, from which other parameters such as chemical composition and/or oxidation degree can be obtained. Using AFM and KFM, Semenikhin *et al.* [31] showed that electrochemically deposited PBT films featured pronounced inhomogeneity, indicated by considerable spatial variations in the local doping level as measured by KFM. Furthermore, the doping-level distribution showed a strong correlation with topography: more doped portions of the polymer formed domains with a typical size of 20–50 nm, which were located in the cores of the polymer grains. These domains were surrounded by relatively undoped regions, predominantly located at the grain periphery. Furthermore, they also found pronounced structural differences between the grain cores and grain periphery; molecular-resolution AFM images obtained at the grain cores showed highly ordered crystalline structures, while the images obtained at the grain periphery showed more disordered structures consisting of separate and more disordered helical polymer chains (Figure 3.2). The presence of the crystalline structure with parameters close to those derived from the molecular-resolution AFM images was confirmed by X-ray diffraction measurements [33].

The changes in the nanoscale inhomogeneity upon electrochemical doping were also investigated [31,34,35]. Kelvin probe force microscopy indicated that the most changes occurred in the more disordered peripheral regions of the polymer grains both in p- and n-type doping, thus confirming the existence of the domain structure and demonstrating that crystalline, more-ordered domains are less open to dopant ion penetration (Figure 3.3). A similar conclusion was later inferred from macroscopic electrochemical measurements (however, without any local structural information) performed with semicrystalline films of poly(3-methylthiophene) [36] and poly(3-hexylthiophene) [37].

Kelvin probe force microscopy and a closely related technique, electric force microscopy (EFM), have proven to be valuable tools to study the structural inhomogeneity of conducting and semiconducting polymers. In particular, they were used to examine the inhomogeneity of such materials as electrochemically polymerized polypyrrole, polyaniline, and polythiophene containing various counter-ions [38-40], as well as spin-coated poly(2-methoxy-5-(2′-ethylhexyloxy)-1,4-phenylene vinylene) (MEH-PPV) [41]. It was confirmed that all these materials have a well-defined inhomogeneous structure, with pronounced variations in the sample work functions, in agreement with the results of Semenikhin *et al.* [31,34,35]. Spin-coated films show considerably less inhomogeneity and much smaller domains as compared to electrochemically prepared polymers [41]. KFM and EFM were also successfully used to study the inhomogeneity of Langmuir–Blodgett (LB) films of an amphiphilic polythiophene modified with hydrophobic and hydrophilic groups [42] and polypyrrole chemically polymerized onto sulfonated polystyrene [43]. Later, the KFM and EFM techniques started to be used to characterize the

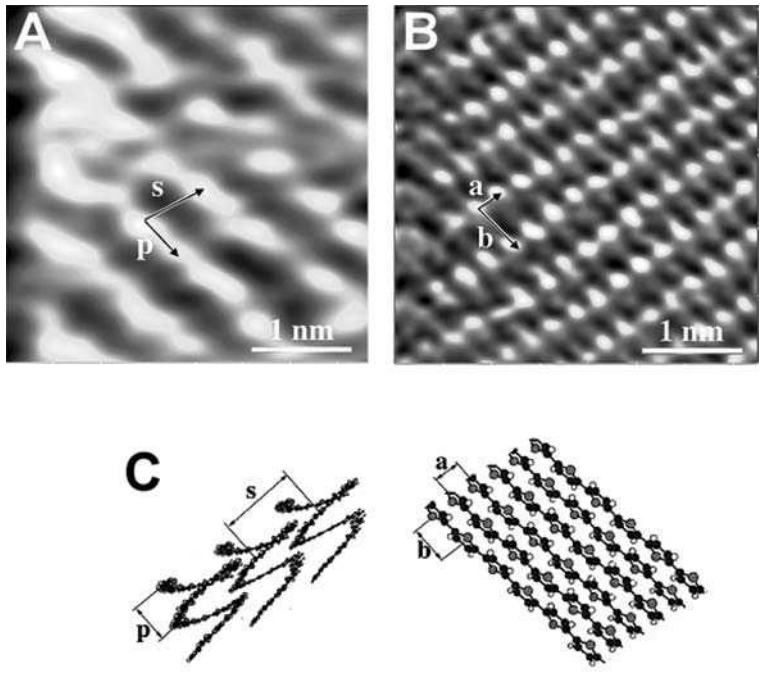

Figure 3.2 *Molecular-resolution AFM images of electrochemically deposited PBT showing typical structures encountered (A) at the grain periphery and (B) at the grain cores. Figure (C) shows schematic drawings of the helical and linear polymer chains proposed for these structures. (Reprinted with permission from the Journal of Physical Chemistry, Atomic Force Microscopy and Kelvin Probe Force Microscopy Evidence of Local Structure Inhomogeneity and Nonuniform Dopant Distribution in Conducting Polybithiophene by Oleg A. Semenikhin et al., 100, 48, 18603–18606. Copyright (1996) American Chemical Society)*

nanoscale properties of polymer blends, especially, in the context of research into bulk heterojunction organic solar cells [44–51]; however, the inhomogeneity in these studies was related primarily to the formation of a blend containing two or more polymers, or a polymer and a fullerene-based electron acceptor, and thus these results cannot be readily compared to the studies of nascent polymers. Some of these papers are described in more detail in a recent review [52].

3.2.3 Current-Sensing Atomic Force Microscopy (CS-AFM)

Electrical conductivity is one of the defining parameters that characterize conducting and semiconducting polymer materials. One of the most important features of these materials is their ability to be doped and undoped, switching from a semiconducting undoped state to electronically conducting doped state. Therefore, mapping the local values of electrical conductivity on the micro- and nanoscale allows one to characterize the inhomogeneous distribution of the doping level in these materials. This is especially important for materials

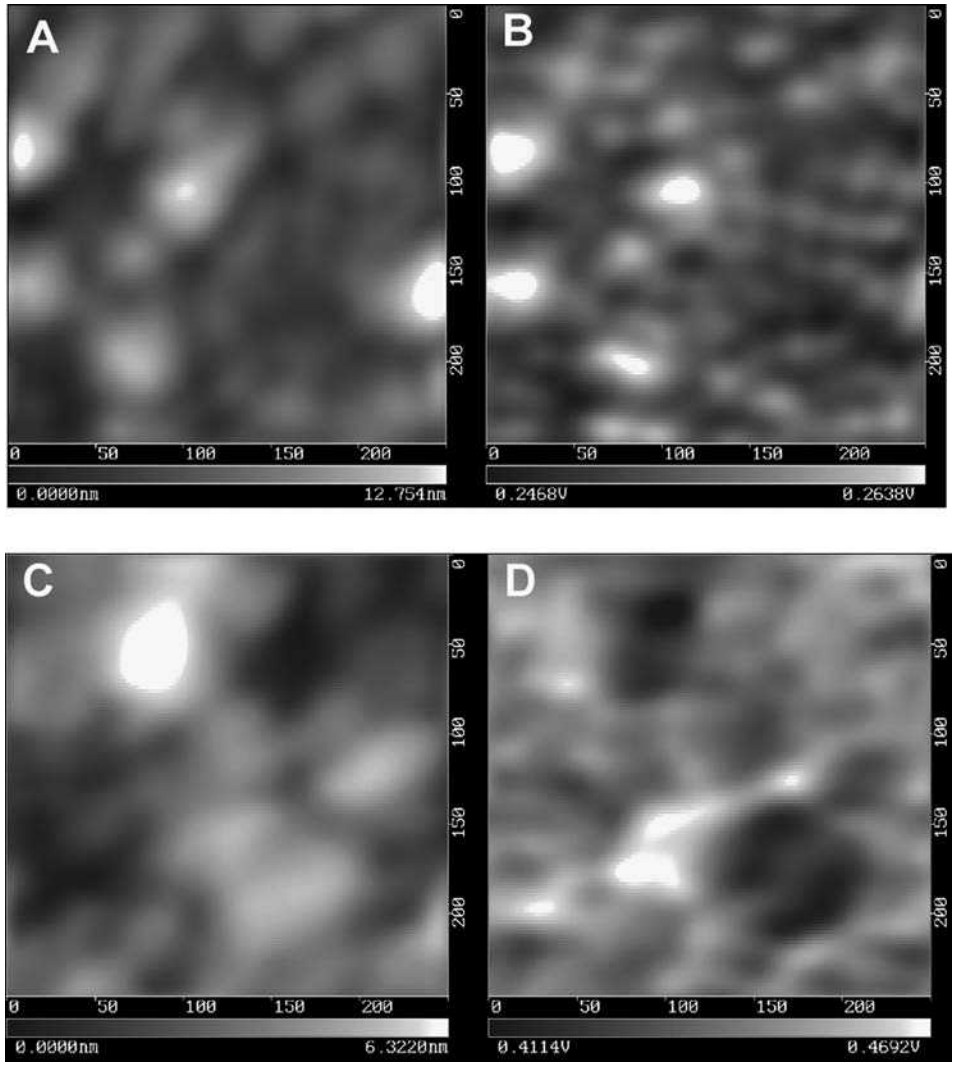

Figure 3.3 *Simultaneous 250 nm × 250 nm KFM images of (A,C) topography and (B,D) surface potential of electrochemically deposited PBT acquired in the KFM feedback mode. Bright spots in the surface potential images (more positive surface potential) correspond to more oxidized polymer. Images A and B represent as-grown PBT, while images C and D show anodically doped polymer. (Reprinted with permission from the Journal of Physical Chemistry, Atomic Force Microscopy and Kelvin Probe Force Microscopy Evidence of Local Structure Inhomogeneity and Nonuniform Dopant Distribution in Conducting Polybithiophene by Oleg A. Semenikhin et al., 100, 48, 18603–18606. Copyright (1996) American Chemical Society; Reprinted with permission from Electrochimica Acta, A Kelvin probe force microscopic study of the local dopant distribution in conducting polybithiophene by O. A. Semenikhin, L. Jiang, T. Iyoda et al., 42, 20–22, 3321–3326. Copyright (1997) Elseveir Ltd)*

prepared by electrochemical or chemical oxidation, since, even if they are later converted to the semiconducting undoped state, they often contain domains of residual dopant localization, sometimes referred to as trapped charge. Local conductivity measurements are also instrumental in localization of conducting metallic islands that are an important feature of inhomogeneous conducting polymers near the metal-to-insulator transition [6–12].

Current-sensing atomic force microscopy (CS-AFM) is a technique that measures, in addition to the surface morphology, the local current flowing between a conducting tip and the area of the sample it is in contact with. To ensure the flow of the electric current, CS-AFM requires a direct electric contact between the sample and the tip, and is a contact-mode technique, although recently some equipment manufacturers have started to develop noncontact electrical characterization techniques such as torsional resonance tunneling AFM. CS-AFM, along with scanning tunneling spectroscopy (STS) reviewed later, is arguably the best technique to measure the local electrical properties of materials on the nanoscale (yet another technique called tunneling AFM, or TUNA, is essentially a version of current-sensing AFM with higher electrical sensitivity). However, unlike STS, CS-AFM does not rely on conductivity as the source of the topography information and can therefore be used for poorly conducting samples such as thick films of semiconducting conjugated polymers.

An important question that arises with relatively thick samples is the relation between the surface and the bulk components of the overall conductivity registered by the CS-AFM technique. This problem does not occur when a film represents a molecular monolayer or consists of a single layer of polymer grains or globules, which is normally the case for very thin films of 10 nm and less [40]. Thicker films typically comprise several layers of polymer grains or globules stacked on top of each other and a charge carrier must pass through several polymer globules in order to travel from the support to the conducting tip and give rise to a CS-AFM current. Therefore, more general analysis of the conductivities of thick polymer samples should be performed using a kind of 3-D percolation approach. However, in most practical cases it seems to be possible to assume that the most important contribution to the overall conductivity is produced by the globules of the topmost polymer layer. The reason for this is that the carriers traveling from the support to the topmost polymer layer will do so using a few of the most conducting pathways. Such conducting pathways may be polymer crystalline domains or grain boundaries. It is probable that every grain of the topmost polymer layer will have access to at least one such conducting pathway, provided that their number is sufficiently large, which is a reasonable assumption for the doped conducting and partially undoped semiconducting polymers most often studied. This mechanism essentially eliminates the variability of the bulk conductivity component of the overall conductivity registered using the CS-AFM technique. However, the variability of the surface conductivity component will remain, since the CS-AFM tip, unlike the grains of the neighboring polymer layers, is in electrical contact with only one area at the grain surface, and a carrier must pass through this area in order to be collected and registered as a CS-AFM current. Therefore, it can be concluded that in most practical cases the CS-AFM current information can be related to the variability in conductivity of the morphological features of the topmost polymer layer rather than the bulk conductivity of the sample.

There have been several CS-AFM studies of conducting polymers and related materials, most notably performed in the group of S.M. Park with various electrochemically polymerized conducting polymers such as polypyrrole [53–55], polyaniline [56,57], polythiophene and derivatives [58], and poly(3,4-ethylenedioxy-thiophene) [59], as well as chemically polymerized poly(*o*-anthranilic acid) (PARA) [60]. There have also been CS-AFM studies of chemically polymerized polyaniline [61,62] and MEH-PPV [63], as well as spin-coated poly(3,4-ethylenedioxythiophene) polystyrenesulfonate (PEDOT:PSS) [64,65]. All these studies universally suggested that the conducting polymer materials, both doped and undoped, showed a considerable nanoscale inhomogeneity and possessed domains with higher and lower conductivity. The domain size was generally of the order of 50–200 nm, although some studies claimed to have observed domains of a smaller size, down to 20 nm. However, the quality of the images was generally not very high because of inherent problems with the conducting tip coating in the CS-AFM technique. AFM tips are generally made of doped silicon. While this material is sufficiently conducting for surface potentiometry techniques such as KFM and EFM, it is not conductive enough for CS-AFM. To make an AFM tip conducting enough for use in the CS-AFM technique, the tips are coated with a conducting coating, typically a very thin metal film. However, this conducting coating is easily damaged in the process of contact-mode scanning, thus requiring the researchers to limit the contact forces and thus the resolution. In particular, the cited studies did not provide a definite answer concerning the correlation between the inhomogeneity, as revealed by CS-AFM, and the surface morphology, as discussed above. In some cases, a correlation was inferred; in the others, no such correlation was found. In the studies on spin-coated PEDOT-PSS, the domain structure of local conductivity was attributed to the variation in the content of less conducting PSS rather than to the properties of the conducting polymer itself [64,65].

The problem of the tip coating was partially overcome with the introduction of conducting AFM tips coated with conductive boron-doped diamond film. Such tips were used by Kantzas *et al.* [66] and O'Neil *et al.* [41] to study the nanoscale inhomogeneity of electrochemically deposited semiconducting polybithiophene (PBT). Boron-doped diamond possesses excellent electrical conductivity and superior antiwear properties, even though the process of coating makes the tips less sharp, thus limiting the resolution as compared to uncoated tips. The use of doped diamond-coated tips allowed Kantzas *et al.* and O'Neil *et al.* to unambiguously demonstrate that the electrical inhomogeneity is related to the morphology of the polymer materials. Specifically (see Figure 3.4), it was shown that there are numerous conducting domains in nominally undoped polybithiophene, which are located in the centers of the polymer grains, while the grain periphery is generally less conducting or insulating. These findings highlight again the conclusion made earlier, on the basis of KFM and EFM data, that there is a correlation between inhomogeneity and surface morphology, which has to be traced back to the formation of the polymer films, specifically to the processes of polymer nucleation and growth [41].

As was the case with KFM and EFM, there have been a few CS-AFM studies of the polymer blends [67–71] generally showing inhomogeneity due to pronounced phase segregation in these systems. Further details can be found in a recent review [52].

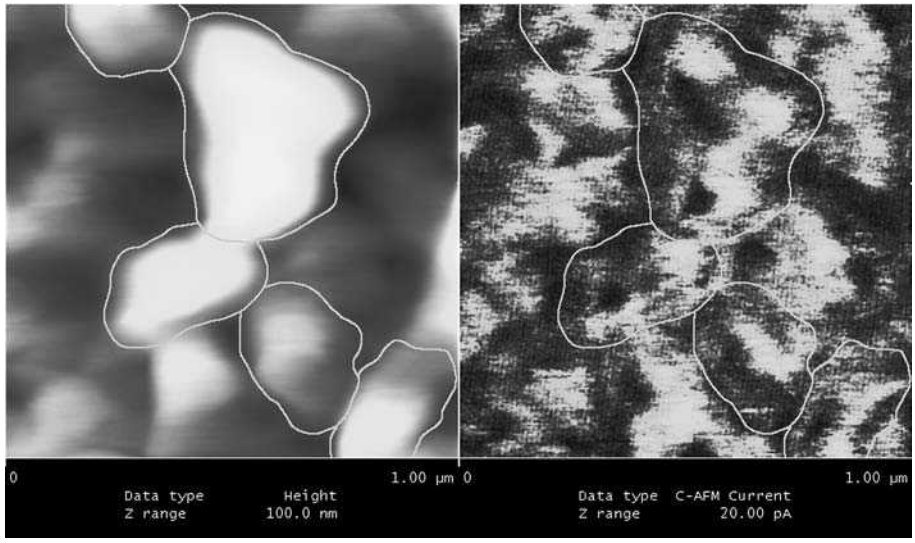

Figure 3.4 *Simultaneous 1 µm × 1 µm CS-AFM images of topography (left) and local current (right) obtained for electrochemically deposited PBT. Bright spots in the current image (more positive current) correspond to more conducting polymer (the tip bias was +500 mV). Several large grains are contoured for easier visualization of the correlation between the topography and the local current images. (Reprinted with permission from Electrochimica Acta, The effect of preparation conditions on the photoelectrochemical properties of polybithiophene based photoelectrodes by T. Kantzas, K. O'Neil and O. A. Semenikhin, 53, 3, 1225–1234. Copyright (2007) Elsevier Ltd)*

3.2.4 Scanning Tunneling Microscopy (STM) and Scanning Tunneling Spectroscopy (STS)

Yet another powerful local characterization technique is scanning tunneling microscopy (STM), which produces topography information by controlling the tunneling current between a sharp conducting tip and the sample surface. While the probability of tunneling, and the tunneling currents, generally depend on the sample local conductivity and density of states, which is a disadvantage of the STM technique, especially for imaging semiconducting samples, STM does produce a very high resolution, generally better than AFM, allowing one to more easily achieve molecular resolution, and the conductivity limitations may not be too severe with thin film samples. Furthermore, one can use a so-called scanning tunneling spectroscopy (STS), also known as current-imaging tunneling spectroscopy (CITS), to measure the tunneling current as a function of the applied bias at certain points of interest in the STM image, and thus determine the local band structure and conductivity of the material, again, in relation to the sample morphology. In a sense, this approach is similar to current-sensing atomic force microscopy (CS-AFM) discussed above; however, while the accuracy of the topography information obtained by AFM and CS-AFM is not related in any way to the sample conductivity, the topography information obtained by STM/CITS is directly dependent on the sample conductivity,

thus complicating the deconvolution of the obtained results and somewhat reducing the reliability of the data. Because of this factor, STM studies of organic semiconductors are largely limited to very thin films of several monolayers at best. However, as was already noted, current-imaging tunneling spectroscopy typically features a higher resolution because conducting coating makes the AFM tip less sharp and thus less sensitive to fine structural details.

While there have been several studies describing high-resolution STM imaging of various polymers and oligomers in the literature (see, e.g., [26,72–74]), in this chapter we will review only those STM investigations which specifically describe observations of the nanoscale inhomogeneity of polymer materials. Yau *et al.* [75] applied STM and STS to the study of nanoscale inhomogeneity of electrochemically deposited emeraldine salt, the protonated, conductive form of polyaniline (PANi), as well as of emeraldine base, the deprotonated, undoped form of PANi. In both cases they observed an array of conducting and insulating domains of nanometer dimensions, with the size of conducting domains for the conductive emeraldine salt being 20–80 nm and the insulating domains being a lot smaller, 5–30 nm. For the deprotonated emeraldine base material, they observed pronounced shrinking of the conducting domains down to ca. 30 nm, with the insulating regions becoming much larger and forming a continuum. The different natures of the insulating and conducting domains were also demonstrated by the shape of current-bias dependencies. While the authors did not discuss if the domain distribution is correlated to the film morphology, some correlation between the morphology and preferential locations of conducting domains can be inferred from the images presented for the conductive emeraldine salt material. The domain distribution for the undoped emeraldine base seems to be random. At the same time, it should be remembered that the STM topography information is dependent on the sample conductivity and the local density of states, so any correlation with topography should be assessed with caution.

The STS technique was also used to demonstrate the formation of conducting domains in films of another popular conducting polymer, (poly(3,4-ethylenedioxythiophene) doped with poly(4-styrenesulfonic acid) (PEDOT:PSS) [76]. Importantly, the authors were able to characterize the 3-D inhomogeneity of the films by employing an interesting procedure consisting in gradual penetration of the organic material with the STM tip and producing current (i.e., conductivity) maps at different levels of the relative tip depth. Using this approach, they were able to discover the presence of 3-D conducting islands (a typical diameter of ca. 20 nm) in spin-coated PEDOT:PSS films, as well as nonconducting areas. The relative abundance of conducting and nonconducting domains varied with the imaging depth: the sample surface was relatively nonconducting and the sample bulk featured more conducting domains. The authors attributed such variation to enrichment of the surface layers with the nonconducting PSS component. Significantly, the authors found pronounced discrepancies between STM and AFM images of the same surface, which they used to extract the surface conductivity information; however, this fact once again highlights the need to exercise caution when applying the STM technique to imaging bulk polymer films.

Grevin *et al.* [77,78] described molecular-resolution STM studies of regio-regular poly(3-hexylthiophene) (P3HT) films cast from chloroform solution onto the surface of highly oriented pyrolytic graphite (HOPG). The images clearly show ordered crystalline islands as well as disordered/amorphous areas. The ordered domains are indicated by

regular folding of the polymer chains, readily observed in the STM images. The average crystalline domain size was ca. 20 nm. Importantly, the authors observed that several chains extended between the neighboring domains, thus providing pathways for the 1-D transport widely discussed in literature, but on the basis of indirect measurements only. A chain-to-chain distance of 1.4 nm was reported for regularly folded chains, which is significantly larger than the parameters observed by molecular-resolution AFM for crystalline polybithiophene (PBT) [31]. The dimensions of the periodic motif of the ordered chains along the backbone axis were also found to be at least twice as large as the corresponding values for PBT [31]. Similar values were also reported for P3HT in papers by Mena-Osteritz *et al.* [73,74]. This is understandable in view of the presence in P3HT of large side chains necessary to produce regio-regularity; at the same time, this fact demonstrates that the degree of close packing which can be achieved with nonsubstituted polymers like PBT is significantly higher.

Payerne *et al.* [79] compared the mesoscopic organization of thin (less than a monolayer) films of regio-regular poly(3-hexylthiophene) (P3HT) and poly(3-dodecylthiophene) (P3DDT). They found the same pattern that combined the ordered and disordered domains for P3HT; however, for P3DDT, no amorphous disordered phase could be detected. Instead, with P3DDT they observed, in addition to the close-packed crystalline domains, the formation of another long-range ordered supramolecular structure with increased separation between the polymer chains. A somewhat similar pattern of the more ordered and less ordered phases was observed by Semenikhin *et al.* [31] for PBT. Parameters such as the interchain separation found for P3HT were close to those cited in previous references [77,78], while for P3DDT they were understandably larger.

Brun *et al.* [28] used STM to investigate the mesoscale inhomogeneity of an even more complex regio-regular polymer combining head-to-head coupled di-*n*-octylthiophene and fluorenone subunits, poly[(5,5′-(3,3′-di-*n*-octyl-2,2′-bithiophene))-*alt*-(2,7-fluoren-9-one)] (PDOBTF). Similar heterogeneous structures combining ordered and disordered domains were observed. However, it was noted that the presence of the rigid fluorenone subunit modified the type of supramolecular organization as compared to P3HT and P3DDT: much less chain folding was observed with PDOBFT, indicating that this polymer is more of a rigid-rod type.

Jaroch *et al.* [22] used STM to study the effect of molecular weight (MW) and polydispersity index on the local inhomogeneity of yet another regio-regular polythiophene, poly(4,4″-dioctyl-2,2′:5′,2″-terthiophene) (PDOTT). This polymer has a reduced side-chain density as compared to regio-regular P3HT and therefore is able to show even better packing and excellent charge-carrier mobilities, generally higher than that found in regio-regular P3HT. The authors were able to experimentally demonstrate the fundamental importance of polydispersity as the driving force of the nanoscale inhomogeneity. Specifically, by studying the intermolecular packing of films produced from monodisperse and polydisperse fractions of different MWs, they showed the following: the films obtained from polydisperse fractions possessed both polycrystalline and amorphous domains; the monodisperse fractions formed well-defined 2-D crystals and no amorphous/disordered domains; an increase in the MW produced notable changes in the supramolecular organization: the packing became more anisotropic showing more or less separated rows of ordered polymer chains. Perhaps this factor is related to the critical length at which a polymer chain becomes able to fold on itself. It should be noted, however,

that the MW values studied in this work were quite low: the number-average value (Mn) ranged from 1.6 to 3.6 kDa for the monodisperse fractions (6 to 15 thiophene units) and was ca. 3.9 kDa for the polydisperse sample (however, the weight-average MW of the polydisperse sample was as high as 14.3 kDa, showing the relative abundance of long chains in that sample).

3.2.5 Phase-Imaging Atomic Force Microscopy (PI-AFM) and High-Resolution Transmission Electron Microscopy (HRTEM): Studies of Local Crystallinity

Phase-imaging atomic force microscopy (PI-AFM) is a very interesting technique that is capable of characterizing the local mechanical properties of a material simultaneously and with the same nanometer resolution as topography information [80]. It is based on the analysis of the phase shift between the vibration of an AFM cantilever brought in intermittent contact with the surface, as in tapping-mode AFM, and the vibration of the same cantilever, but positioned far from the sample (a free-vibrating cantilever). As the AFM cantilever with an AFM tip mounted on it is brought closer to the sample surface, at some point an intermittent contact is established that results in partial damping of the cantilever vibration amplitude at a given frequency. This effect is well known and is used to generate topography information in the AFM tapping mode. However, at the same time the phase of the cantilever vibrations is also altered depending on whether the tip–sample contact is elastic or inelastic.

In the case of an elastic interaction, the tip 'bounces' back readily upon contact with the sample and thus the phase shift of the cantilever vibrations stays near zero or becomes positive, in the case of a strong repulsive interaction between the tip and the surface ('hard tapping'). Alternatively, in the case of an inelastic interaction, when a portion of the cantilever vibration energy is dissipated within the sample, the vibrating tip 'sticks' to the sample surface and thus retracts with a noticeable delay, which is registered under periodic vibration conditions as a negative phase shift. Overall, the magnitude of the phase shift depends on the type of the interaction (elastic/inelastic), as well as on the values of the material density and the elastic modulus [80]. Since the phase variations are measured simultaneously with the same high lateral resolution as the topography and can be easily referenced to specific locations on the sample surface, phase imaging is a very powerful technique for characterization of the nanoscale inhomogeneity of materials. Specifically, since the densities and the elastic moduli of crystalline and amorphous materials, or the crystalline and amorphous forms of the same material, are generally very different, phase imaging is an excellent tool to study the distribution of crystalline and amorphous domains. As would be expected and was confirmed by direct measurements with polymer standards [80], more crystalline domains can be recognized from relatively more positive phase values, while amorphous regions typically show a relatively negative phase in a wide range of tip–sample forces (so-called moderate tapping), where most of the practical imaging is performed.

The development of scanning probe techniques, and in particular phase-imaging AFM, created a unique opportunity for researchers to directly study the local crystallinity and inhomogeneity of conducting and semiconducting π-conjugated polymers. Early

experimental and theoretical studies of these materials all led to the conclusion that these materials consisted of small, ordered, mostly crystalline domains separated by an amorphous disordered matrix [1–20]. However, for quite long time there were no direct local studies that could confirm or disprove this conclusion on the basis of direct nanometer-scale local structural information. The phase-imaging technique allowed researchers to visualize the locations of such crystalline domains and thus not only confirmed the existing models of nanoscale inhomogeneity of conducting and semiconducting polymers, but also provided a clue to its origins. Very recently, local crystallinity studies using high-resolution transmission electron microscopy (HRTEM) started to appear in the literature as the HRTEM technique became more available. When appropriate, such results are also reviewed in this section. Two types of TEM images are generally used: bright field (BF) images that are obtained from intensities of transmitted electrons that undergo no scattering with the sample, and dark field (DF) images that are formed by electrons scattered mostly at crystalline domains. Because of this feature, DF images can be used for the identification of nanometer-size crystalline domains in conducting and semiconducting polymers [27,81–83].

The majority of PI-AFM studies have been performed with regio-regular materials, such as poly(3-alkylthiophene)s and later with other regio-regular polythiophenes, poly(3,3‴-dialkylquaterthiophene) (PQT) and poly(2,6-bis(3-alkylthiophen-2-yl)dithieno[3,2-b; 2′,3′-d]thiophene) (PBTDT). It was recognized early on that regio-regular materials can possess quite significant advantages over regio-random ones [3,4]. A subject of particular interest was the evolution of crystallinity with the MW of the polymer materials. Non-regio-regular materials are largely amorphous at low MW and become semi-crystalline only at sufficiently high values of MW [3,84,85]. Conversely, regio-regular polymers have been shown to be highly crystalline at low MW, with the degree of crystallinity and the lattice parameters of the crystalline phase, as determined by X-ray diffraction, exhibiting a complex dependence on MW [86–91]. Most results suggest that that the degree of crystallinity in regio-regular materials actually decreases with an increase in MW; however, despite this fact, all data show that the carrier mobilities in such materials invariably increase with the MW, despite this decrease in the apparent degree of crystallinity. Eventually, this paradox was related to the difference in inhomogeneity and the nanoscale structural organization of materials with low and high MW and has become one of the manifestations of the importance of the inhomogeneity factor in establishing the performance of organic materials. Very recently, the importance of a related factor, the polydispersity index (PI), which characterizes the range of MWs found in a given polymer sample, has started to be recognized [22,27,40,41].

Osawa *et al.* [84] showed as early as in 1992 that the electrical conductivity of non-regio-regular electrochemically deposited poly(3-hexylthiophene) (P3HT) greatly depended on the MW, increasing rapidly from 10^{-1} to 10^{1} S cm^{-1} with an increase in MW up to ca. 25 kDa, after which the conductivity remained approximately constant. This is readily explained by an increase in crystallinity of the polymer with increasing MW, as confirmed by wide-angle X-ray scattering.

Kline *et al.* [86,87] studied the MW dependence of the field-effect mobility in regio-regular poly(3-hexylthiophene) synthesized by different routes and prepared using different coating techniques. They found that the mobility universally increased with MW, while the degree of crystallinity as determined by X-ray diffraction considerably decreased. This

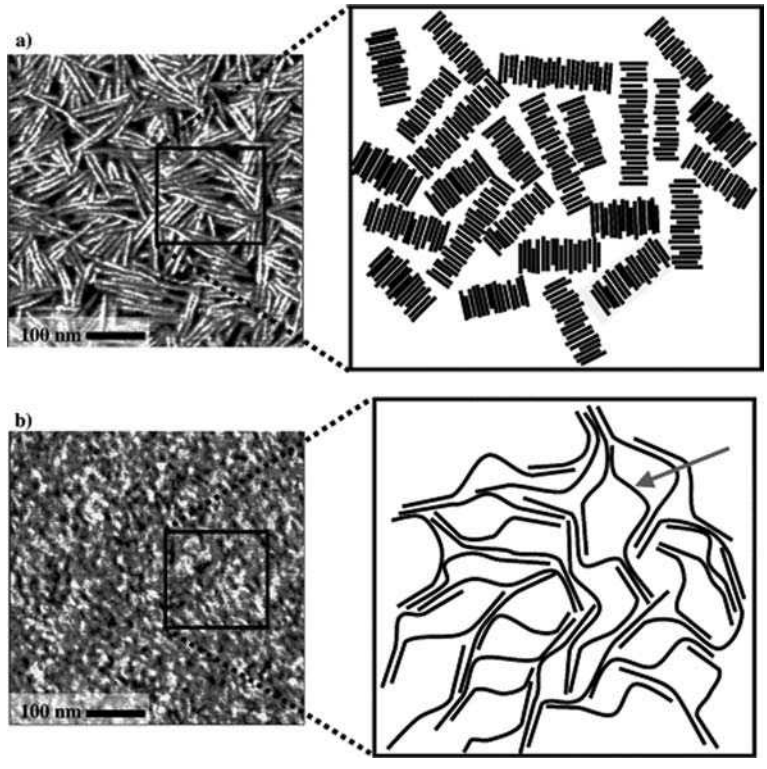

Figure 3.5 *AFM phase images and model for charge transport in (a) low MW and (b) high MW P3HT films. Charge carriers are trapped on nanorods (highlighted in grey) in the low MW case. Long chains in high MW films bridge the ordered regions and soften the boundaries (marked with an arrow). (Reprinted with permission from Macromolecules, Dependence of Regio-regular poly(3-hexythlthiophene) Film Morphology and Field-Effect Mobility on Molecular Weight by R. Joseph Kline et al., 38, 8. Copyright (2005) American Chemical Society)*

apparent inconsistency was reconciled by employing locally resolved phase-imaging AFM, which showed pronounced differences in the nanoscale morphology and local crystallinity between low and high-MW films (Figure 3.5). The low-MW material (Mn = 3.2 kDa) consisted of very distinct randomly oriented and highly anisotropic rod-like or ribbon-like crystallites (a 'haystack') with lengths of ca. 100 nm and widths of less than 10 nm, while the high-MW polymer (Mn = 31.1 kDa) showed a near isotropic nodule structure featuring small round crystallites with crystallite sizes of ca. 10–20 nm.

Zen *et al.* [88] studied the effects of MW and post-polymerization annealing on the carrier mobility and local crystallinity of regio-regular poly(3-hexylthiophene) (P3HT) materials prepared from fractions with different MWs (extracted using different solvents). X-ray data showed enhancement of crystallinity upon annealing, which was most pronounced in intermediate-MW fractions. High-MW fractions showed very little crystallinity before annealing and some after annealing. An increase in the crystallite size upon

annealing was inferred from the decreased XRD peak width. Annealing was shown to enhance considerably the mobilities observed for low-MW fractions, but the enhancement was quite limited in the high-MW materials. AFM topography and phase imaging was performed for different MW materials before and after annealing. Before annealing, the results were similar to those reported by Kline *et al.* and indicated a transition from 'haystack'-like randomly oriented crystalline nanoribbons to a network of larger and more isotropic globules with distinct crystalline cores and more amorphous material located between the crystalline cores. Upon annealing, there were very pronounced changes in the morphology and crystallinity of low-MW materials, while the changes in the high-MW materials were more limited. Specifically, annealing transformed the 'haystack' morphology of the low-MW fraction material into large anisotropic crystals with well-pronounced terraces reminiscent of crystals of annealed thiophene oligomers [92]. The changes in the higher-MW materials were generally more limited, except for the so-called hexane fraction, which showed anomalous mobility changes as well. The rest of the high-MW materials showed a better defined globular structure upon annealing, with perhaps some merging of smaller crystallites and generally reduced phase contrast between the cores and the surroundings (partial disappearance of the sharp boundaries between the crystalline and amorphous regions, as well as overall reduction in the apparent abundance of the amorphous regions). The latter fact indicates that annealing was able to reduce the degree of nanoscale inhomogeneity in these materials, thus bringing about the enhancement in carrier mobilities. This fact strongly pointed to the crucial role of inhomogeneity in defining the behavior and properties of these materials. Interestingly, in this publication Zen *et al.* adopted a different view that related the changes in carrier mobilities to variations in the degree of π-stacking in the crystallites, rather than to the mesoscopic organization of crystalline and amorphous domains, although they did support the other viewpoint in their subsequent publications [89].

Similar pronounced effects of MW were also observed with another type of regio-regular polymer, poly(thienothiophene)s [29], a new generation of regio-regular polythiophene-based materials with very high carrier mobilities. Specifically, poly(2,5-bis(3-alkylthiophen-2-yl)thieno[3,2-b]thiophene) (PBTTT) [29] featured MW dependencies very similar to those obtained with regio-regular P3HT. Films obtained from low-MW materials (8 kDa) showed highly crystalline nanoribbon haystack nanostructure, while the films with higher MW (12 and 30 kDa) showed a gradual transition, first to more tightly aligned elongated crystallites and then to the nodule-like structure of distinct large interconnected globular crystalline domains. The carrier mobility in these materials was found to increase from 0.03 to 0.2 $cm^2\ V^{-1}\ s^{-1}$ with an increase in the average MW from 8 to 30 kDa.

Brinkmann *et al.* [81] studied the properties of highly oriented P3HT films prepared using directional epitaxial solidification (directional gradual crystallization from a melt of P3HT and 1,3,5-trichlorobenzene (TCB) by slowly moving the molten mixture from a hot zone to a cold one). TEM bright-field (BF) images showed changes in morphology vs. MW similar to those revealed by AFM earlier (from rods or ribbons to a globular structure), although these observed structures were more oriented because of the directional deposition technique used. For instance, instead of randomly oriented haystack-type morphology at low MW, the authors observed the formation of relatively well-aligned nanoribbons. High-MW globular structures were also more oriented. Electron diffraction measurements

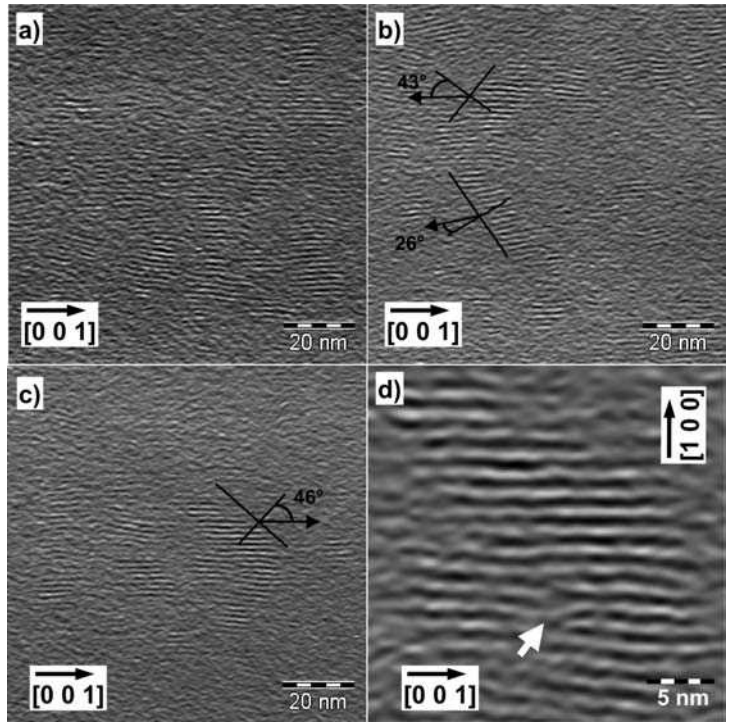

Figure 3.6 *Low-dose HR-TEM images of various representative areas showing edge-on crystalline domains in a high-MW regio-regular P3HT film prepared using directional epitaxial solidification. The polymer is characterized by an MW value of 69.6 kDa (polystyrene equivalent). In parts (b) and (c), the black arrows show the stem orientation in the crystalline lamellae and the full line depicts the edge of some crystalline domains. In part (d), the white arrow points at a structural defect at the junction between two lamellar crystals, which is likely to be a 'tying' polymer chain bridging neighboring crystalline domains. (Reprinted with permission from Macromolecules, Molecular Weight Dependence of Chain Packing and Semicrystalline Structure in Oriented Films of Regioregular Poly(3-hexylthiophene) Revealed by High-Resolution Transmission Electron Microscopy by Martin Brinkman et al., 42, 4. Copyright (2009) American Chemical Society)*

showed deterioration of the crystalline order in high-MW material, also in line with the other studies.

In their recent publication [83], Brinkmann *et al.* obtained nanoscale images of crystalline and amorphous domains in directionally solidified P3HT films using the high-resolution transmission electron microscopy (HRTEM) technique (Figure 3.6). The observed domain sizes were ca. 15–20 nm, in good agreement with the X-ray data. Additionally, the authors observed a decrease in the regularity and structural coherence of crystalline domains with an increase in MW from 7.3 kDa to 69.6 kDa (polystyrene equivalent), although the number of such domains clearly increased at high MW and they were positioned closer to each other than in low-MW films. Importantly, the authors succeeded

in direct observation of long 'tying' polymer chains bridging neighboring crystalline domains in the high-MW material, as proposed by Kline *et al.* [86,87].

Bao *et al.* [30] studied the crystallinity and microstructure of another regio-regular material, poly(2,6-bis(3-alkylthiophen-2-yl)dithieno[3,2-*b*;2′,3′-*d*]thiophene) (PBTDT). It was found that without annealing, no crystalline lamellae typical for P3HT were observed; in fact, it was noted that the surface structures were remarkably similar to the structures of polymer nanoparticles in solution, indicating that little change occurs in the structure and nanoscale organization of these materials upon deposition. Unfortunately, the authors failed to specify the MW of their material, thus hampering comparison with the results of other studies. Upon annealing, well-defined nanoribbons started to appear in the phase images. A considerable increase in the degree of stacking was also evidenced by high-resolution TEM (HRTEM) images. Before annealing, the HRTEM images showed several crystalline domains dispersed in an abundant disordered phase. Upon annealing, the domains became much more numerous and grew closer to each other, with some images showing several long chains apparently bridging neighboring domains, similar to observations by Brinkmann *et al.* [83].

Ong and coauthors [23–25] studied the degree of crystallinity and inhomogeneity of yet another regio-regular material, poly(3,3‴ dialkylquaterthiophene)s (PQT). Zhao *et al.* [23] performed extensive PI-AFM studies on thin PQT films of the same MW (Mn = 17.3 kDa, PI = 1.32). The effect of annealing at different temperatures was studied. The nonannealed films showed globular morphology similar to that observed with P3HT at much higher MWs. Upon annealing, pronounced ordering and stacking of the polymer chains occurred, as was clearly indicated by the formation of stacked lamellae in the phase images. Higher annealing temperatures (up to 148 °C) favored better stacking. Phase images also showed a considerable amount of less-ordered amorphous material between the ordered crystalline lamellae, especially at moderate annealing temperatures. Slow cooling upon annealing produced different morphology as opposed to rapid cooling, e.g., achieved by blowing nitrogen gas over the sample surface: fast-cooled samples featured considerably more amorphous disordered gaps between the crystalline lamellae compared to slowly cooled samples, thus indicating that, as in the case of P3HT deposited from various solvents and using various techniques, more rapid changes produce less-ordered structures with a greater degree of inhomogeneity. Similar results were obtained by Ong *et al.* [24]: more prolonged annealing and slower cooling resulted in an increase in the size of crystalline lamellae and their merging. As shown by Wu *et al.* [25], better ordering in such films, in particular promoted by annealing and proper preparation of the substrate before deposition, gave rise to very high mobilities of 0.18 $cm^2\ V^{-1}\ s^{-1}$.

Therefore, it was universally observed for various regio-regular materials that, despite an apparently higher degree of crystallinity in lower-MW materials, the carrier mobilities were invariably greater in high-MW materials by several orders of magnitude. An early explanation of such behavior was enhanced out-of-plane backbone conformation twisting in low-MW polymers [88]. Such a deviation from planarity was supposed to decrease the effective conjugation length and reduce the efficiency of charge hopping. However, it was soon realized [87] that the charge transport was limited by the arrangements of crystallites (i.e., mesoscopic inhomogeneity) rather than by perfection of the chain packing in individual crystallites. Therefore, it was suggested that the reason for the low mobility in more crystalline low-MW materials was the abundance of grain boundaries in the material,

which inhibited the charge transport [86,87,89]. Additionally, it was noted [89] that the average size of the crystalline domains in high-MW materials was less than the average chain length. Therefore, long chains in high-MW materials were considered to be able to bridge the crystalline domains, thus enhancing charge transport between the domains (Figure 3.5). Very recently [30,83], such 'tying' chains were directly observed by using high-resolution transmission electron microscopy (HRTEM) (Figure 3.6). While later studies suggested that there are also other reasons such as the pronounced anisotropy and misalignment of the crystallites [81,83,93,94], the fact remains that one of the main reasons for the low carrier mobility in low-MW films is the lack or inadequacy of the contact between individual crystallites, despite their relatively higher quality. Importantly, it is the increased degree of disorder and structural inhomogeneity in high-MW films that is responsible for the emergence of misaligned long chains that are able to form links between the crystalline domains. The relatively higher degree of disorder also makes the crystalline domains smaller and more close, thus again favoring interdomain charge transport. The importance of the nanoscale inhomogeneity and proper alignment of nanocrystallites has also been stressed for another important (non-regio-regular) polymer, poly(2-methoxy-5-(2′-ethylhexyloxy)-1,4-phenylene vinylene) (MEH-PPV) [95,96].

The difference in the carrier mobilities in low- and high-MW materials can be further understood if we remember that low-MW materials can form crystalline structures that are very different from those for higher-MW materials. Specifically, short-chain oligomers are known to typically form crystal structures with the neighboring chains located in different planes [92,97]. This necessarily reduces the degree of π-stacking and overlap between chains in oligomer crystals and makes charge transport highly anisotropic. As pointed out in a recent review [98], such packing gives rise to 2-D transport within the stacked organic layers, while transport between the layers is less efficient. In this connection, it is worth noting that the rod- or needle-like domains commonly found in low-MW polymeric materials are thought to comprise face-stacked polymer chains, with the width corresponding to the length of each polymer chain, and the length of the rod corresponding to the number of stacked chains [29]. This means that the most efficient transport direction in such systems would be across rather than along the length of the rod-like crystallite. This situation means that, despite the higher crystallinity, the charge transport in low-MW materials would essentially require a greater number of hops from one crystalline domain to another, compared with high-MW polymers, since the widths (not lengths) of the nanocrystallites in low-MW materials are considerably less than the size of crystallites in high-MW ones. The hopping would be further impeded by the poor 'haystack'-like alignment of the crystallites and the generally greater distances between the crystallites in low-MW materials [89].

Yet another advantage of higher-MW materials over small molecules is their smaller polaron relaxation energies [99], so that the turn-over from polaron-like to band-like transport should, in principle, occur at a lower degree of interchain order. This provides an additional explanation of the higher mobilities in higher-MW polymers, as compared to more crystalline, but lower-MW materials: longer chains tolerate more disorder.

In addition to the average MW, the importance of another factor, the polydispersity index (PI), has started to be recognized [22,27,40,41]. The PI characterizes the range of MWs that are present in a polymer sample. PI values close to unity show that most molecules have the same or similar MWs, while higher PI values indicate the presence

of fractions with different MWs distributed around the average MW. The greater the PI value, the greater the range of MWs in the sample. Therefore, PI characterizes the width of the MW distribution, while the average MW characterizes the center of such a distribution.

Pingel *et al.* [27] studied the effect of the MW and polydispersity of the starting materials on the morphology, crystallinity, and carrier mobility for thin films of P3HT and yet another regio-regular material, poly(3,3‴-dialkylquaterthiophene)s (PQT). The evolution of the morphology and crystallinity of PQT films with increasing MW was remarkably different from the pattern observed previously for regio-regular P3HT: low-MW materials formed large, flat micrometer-size crystals rather than the nanoribbon haystack structures observed with nonannealed low-MW P3HT. In fact, the structure was quite similar to those obtained for well-defined oligomers [92]. This fact was attributed to the very low polydispersity of the low-MW fraction. These observations highlight the direct relationship between polydispersity and crystallinity/degree of disorder in the resulting polymer materials. Presumably, the presence of polymer chains with variable lengths, which are absent in materials with a low polydispersity index, has the effect of impeding chain alignment and the growth of large crystallites. A similar observation was made by Jaroch *et al.* [22]. Possible mechanisms accounting for this behavior are discussed in the next section. However, the fact that unusually high mobilities can be observed with low-MW materials with low polydispersities [22,27] suggests that the effect of the MW and, specifically, the presence of 'tying' long chains extended between different domains, which have been proposed in the literature as the chief reason of the better performance of high-MW materials, may be not as important for achieving high conductivity/carrier mobility. Furthermore, these findings strongly suggest that polydispersity plays a very important role in determining the properties of the polymer materials. In fact, the same conclusion can be reached from high values of mobilities obtained with molecular crystals based on oligomers, which feature low MWs, but also no polydispersity [92]. Specifically, the presence of chains of varying lengths increases the disorder and promotes the formation of an amorphous polymer phase at the boundaries of nanocrystalline regions. This is likely to impede charge transport between these regions, which is generally accepted to be the chief reason of insufficiently high carrier mobilities in these systems. Further discussion of these effects can be found in Section 3.4.

Unlike the low-MW fraction, the high-MW fraction [27] featured significantly higher polydispersity and therefore showed behavior similar to the results described above. Specifically, dark field TEM images clearly showed, for both P3HT and PQT, the formation of nanoscale crystalline domains, supporting the results of the AFM phase imaging. A very similar domain structure was also observed by TEM for another conducting polymer, poly(*o*-ethoxyaniline) (POEA) [82].

The other important factors that were shown to affect inhomogeneity and material properties such as carrier mobilities were the deposition technique and the solvent evaporation rate. The idea was that slow deposition rates promoted crystal growth and the formation of strong interchain interactions, which led to more crystalline films, while such techniques as spin-coating restricted the crystal formation, not allowing enough time for crystallization and, especially, crystal growth to occur. Generally speaking, this helped to

control the inhomogeneity and was generally beneficial for the carrier mobilities and other device properties. The deposition rate could be also varied by controlling the evaporation rate of the solvent from which the polymer film was deposited.

Chang *et al.* [91,100] studied the carrier mobilities in polymer-based devices with P3HT active layers prepared by spin-coating from solvents with different boiling points. They found [100] that the best solvent was 1,2,4-trichlorobenzene (TCB), which showed good solubility and a high boiling point. Films spin-coated from TCB were more crystalline and showed a pronounced globular structure as compared to films coated from the regular solvent, chloroform. The effect was strikingly similar to the evolution of morphology with MW, although Chang *et al.* used polymer samples of the same average MW (37 kDa, 98% region-regular (RR)).

In a subsequent publication [91], Chang *et al.* studied the effects of both the solvent and the MW, as well as of the deposition technique. Specifically, they compared films spin-coated from chloroform (b.p. 61°C) and 1,2,4-trichlorobenzene (TCB) (b.p. 213°C), as well as films drop-cast from chloroform (drop-casting results in a slower deposition rate). They found that the effect of the MW, as described by previous studies, in fact could be very different as it was dependent on the solvent evaporation rate. While it was confirmed that the crystallinity decreased with MW, this change was more pronounced in solvents with low boiling points. Furthermore, films deposited from chloroform and TCB showed very different in-plane X-ray scattering patterns, indicating the formation of different crystalline forms or forms with very different orientation/texturing. Films deposited from chloroform showed globular morphology, while films deposited from TCB were more close to the haystack nanorod structure, even at high MWs, which was not observed with a rapid deposition technique (spin-coating from chloroform). The films obtained in the latter way showed similar evolution of morphology and crystallinity to that described in the other works. Conversely, slow deposition by spin-casting from high-boiling-point solvents allowed the polymer chains to self-organize into well-defined and highly crystalline nanoribbons, not only at low MWs, but also at high-MW values. The mobilities measured with films prepared by slow deposition were considerably higher than those obtained by rapid deposition; however, a universal increase of mobility with MW was observed for all conditions. This again demonstrates that the effect of inhomogeneity and interdomain transport dominates over the degree of order and the quality of the chain alignment in individual crystallites. When comparing the data of Chang *et al.* with the other works, it should be remembered that all films in this work [91] were annealed at 100 °C for 10 h, which certainly should have affected their morphology and crystallinity.

Yang *et al.* [101] studied the crystallinity of regio-regular poly(3-hexylthiophene) (P3HT) films deposited by drop-casting rather than the spin-coating technique. The variation in the boiling point of the solvent from which the film was cast was again found to be an important factor. All films prepared in this study showed the haystack nanoribbon morphology, which could be related to a relatively low value of MW (Mn = 11.4 kDa, PI = 2.2).

Surin *et al.* [102] studied the effect of the solvent evaporation rate and the deposition method for P3HT without varying the MW (Mn = 25.5 kDa, MW = 37.7 kDa, PI = 1.5). All films showed the haystack morphology and relatively low mobilities, which again could be related to the relatively low value of MW used. Spin-coating from chloroform suffered from severe dewetting and produced noncontinuous films.

A more comprehensive study was performed by Verilhac *et al.* [90,103] who studied the effect of both the deposition technique and the MW on the properties of the resulting materials. Furthermore, they compared the properties of P3HT films with those of another polymer with better interdigitation, poly(3,3″-dioctyl-2,2′:5′,2″-terthiophene) (PDOTT). They confirmed the strong dependence of the carrier mobilities on the MW for the two polymers and for the three deposition techniques. Films prepared from low-MW (1.9 and 5.6 kDa) polymers all showed ribbon-like haystack structures, with the structural inhomogeneity and anisotropy being more pronounced for dip-coated and drop-cast films as compared to spin-coated ones (Figure 3.7). With an increase in MW, the films started to show 'thickening' of the ribbons and formation of globules inside them, apparently due to changes in the stacking of the polymer chains, with the spin-coated ones again being the most homogeneous. Interestingly, while the morphology and crystallinity changed considerably with both the MW and the deposition technique, the mobility was dependent only on the MW and varied only insignificantly between films of the same MW, but prepared using different techniques and featuring quite different morphology. This again demonstrates that the charge transport in these materials is determined not by the properties of crystalline domains, but by the charge transport between such domains.

Therefore, it has been well established that the local crystallinity of conducting and semiconducting polymer materials, and especially the distribution of the crystalline and amorphous phases, are very important parameters that determine many of the properties of such materials. It is of considerable interest to explore how the crystallinity and distribution of crystalline and amorphous domains evolve during the process of polymer deposition specifically, in order to clarify the mechanism underlying the emergence of the nanoscale inhomogeneity and the domain structure. O'Neil *et al.* [40] used PI-AFM to study the inhomogeneity and the relationship between polymer crystallinity and surface morphology for non-regio-regular polybithiophene (PBT) films electrochemically polymerized under potentiostatic conditions. The most important finding was that the degree of crystallinity and inhomogeneity of the polymer films underwent a significant change during the process of the film growth. The deposition process began with the formation of very small (lateral dimensions of less than 20 nm and heights of ca. 1 nm) polymer nuclei, which were shown by the phase imaging to be fully crystalline. At a later stage more nuclei were formed until full coverage of the surface with the polymer globules was reached. However, film growth was achieved by further nucleation rather than growth of previously formed nuclei, since the size of the polymer globules remained quite close to that of the nuclei (the globule lateral dimensions were ca. 30 nm or less, and the height was 1–2 nm). This indicates progressive nucleation. The polymer globules remained fully crystalline at this stage. With an increase in the polymerization time, a second layer of polymer globules was formed on top of the first fully crystalline layer, and the globules of the second layer were much bigger in size (lateral dimensions of ca. 100 nm and heights of ca. 20 nm, see Figure 3.8). Furthermore, in contrast to the first layer, the second layer showed significant amorphous content. The distribution of the amorphous and crystalline phases was very definite and featured crystalline domains with sizes of ca. 50 nm located in the cores of the polymer globules, with the amorphous phase surrounding these crystalline cores and forming the periphery of the polymer globules (see Figure 3.8). Further polymer growth did not change significantly the crystallinity distribution and resulted in further layer-by-layer deposition of semicrystalline globules, all featuring crystalline cores and

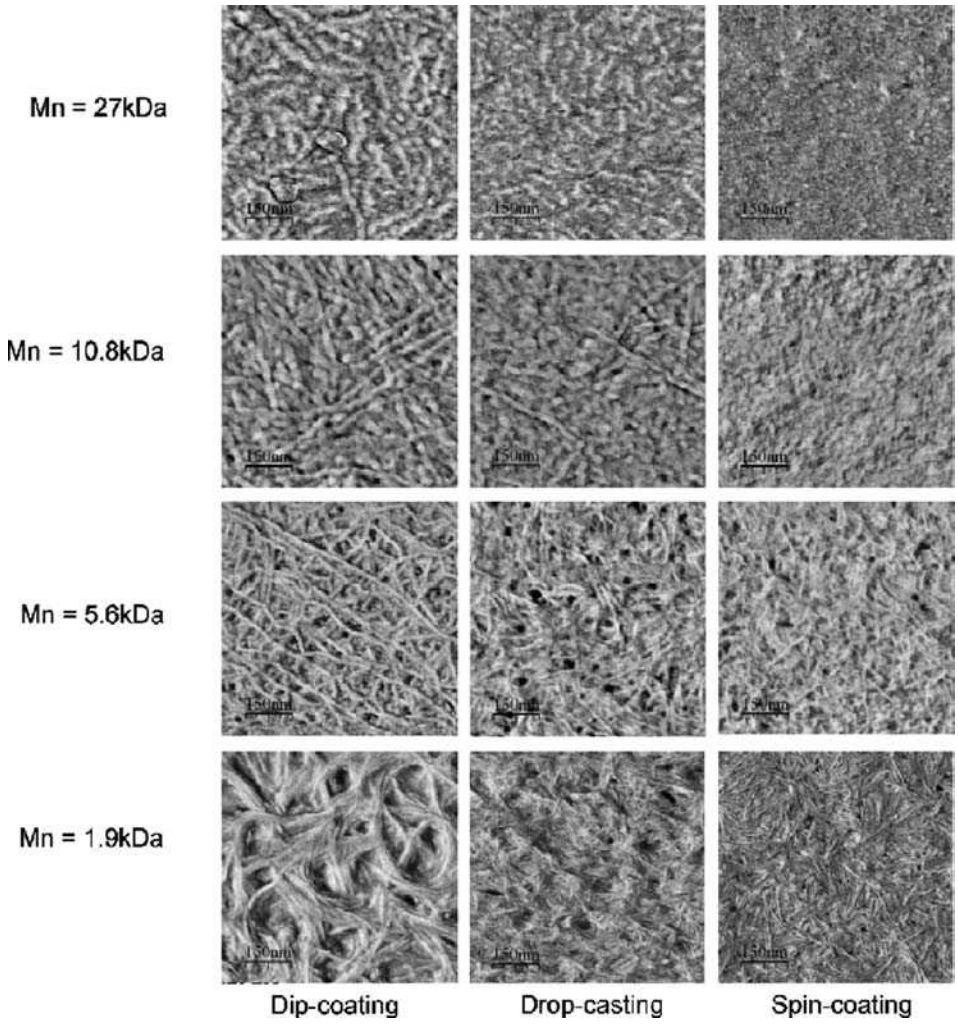

Figure 3.7 *Atomic force microscopy phase images of thin layers obtained from regio-regular P3HT fractions of different number-average molecular weight (Mn) and using different processing techniques. (Reprinted with permission from Synthetic Metals, Effect of macromolecular parameters and processing conditions on supramolecular organisation, morphology and electrical transport properties in thin layers of regioregular poly(3-hexylthiophene) by J.-M. Verilhac, G. LeBlevennec, D. Djurado et al., 156, 11–13. Copyright (2006) Elsevier Ltd)*

amorphous peripheries and resembling high-MW films of semicrystalline P3HT and other polymers described above.

Therefore, this result shows that the polymer inhomogeneity is determined by the process of polymer nucleation and growth. The inhomogeneity is directly related to the polymer morphology: the crystalline regions are located at the cores of the polymer

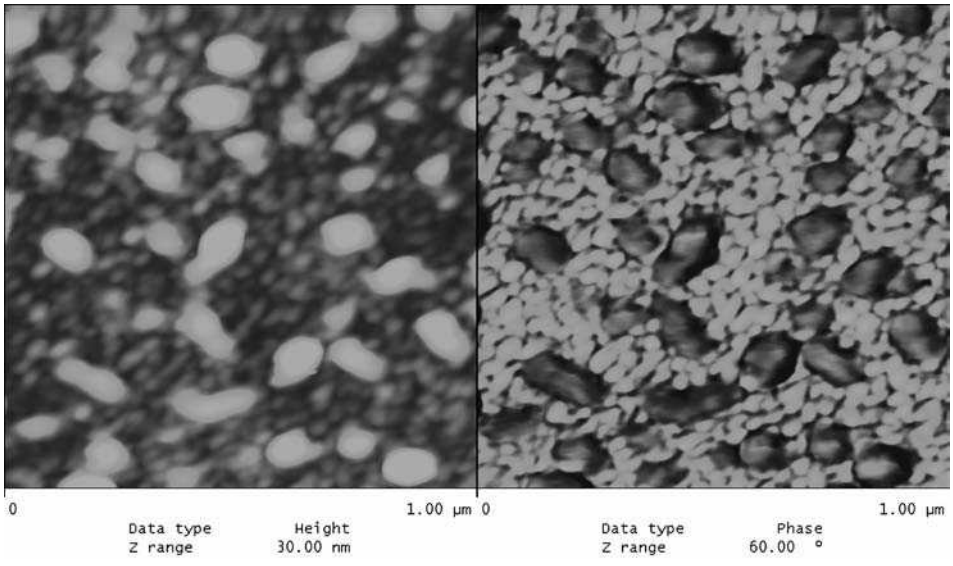

Figure 3.8 *Simultaneous 1 µm by 1 µm images of topography (left) and phase (right) for a thin electrochemically deposited polybithiophene film. The deposition charge was 5.7 mC cm^{-2}. The images show the beginning of formation of the second polymer layer. (Reprinted with permission from Journal of Physical Chemistry C, AFM Phase Imaging of Electropolymerized Polybithiophene Films at Different Stages of Their Growth by Kevin D. O'Nei et al., 111, 40. Copyright (2007) American Chemical Society)*

globules, while the amorphous polymer is situated at the peripheries of such globules, or, using the terminology adopted by other researchers, at the crystalline domain boundaries. Furthermore, the inhomogeneity is not only longitudinal (the crystallinity of the globule core differs from that of the globule periphery), but also latitudinal (there is a pronounced change in crystallinity between the inner and outer layers of the polymer films). These facts indicate that the polymer inhomogeneity originates from the polymer deposition process. At early stages of the polymer deposition, the polymer phase is almost entirely crystalline, while at the later stages there is an increase in the amorphous content; furthermore, even then, the crystalline phase is located inside the polymer globules with the amorphous phase located at the boundary of the crystalline regions, as was also found elsewhere for P3HT and other materials. Taken together, these findings indicate that, in the polymer deposition process, the crystalline phase is deposited first and the amorphous phase is formed only at later stages in the polymer film growth. These results are supported by studies of the same polymer performed earlier using CS-AFM [41,66], as well as macroscopic electrochemical data obtained for a related polymer, poly(3-methylthiophene) [36] Since the polymer studied in reference [40] was not regio-regular, only high-MW fractions could form the crystalline regions. Therefore, it was concluded that the polymer inhomogeneity was the result of preferential deposition of high-MW polymer at early stages of polymer film formation, with the low-MW fractions not able to deposit until late in the polymer deposition process.

3.2.6 Near-Field Scanning Optical Microscopy (NSOM)

Unlike traditional AFM, near-field scanning optical microscopy (NSOM, or SNOM) utilizes a sharp tip made from a specially prepared (tapered) optical fiber, which can be brought very close to the sample to either perform local illumination or collect optical signals in the near-field regime with a resolution of several tens of nanometers. The same sharpened fiber can be used to obtain topography information, although the quality and resolution of the topography images are not as high as with traditional AFM. One of the possible applications of NSOM is imaging the distribution of local photoluminescence (PL) or local photocurrents with nanometer resolution. Since the efficiency of photoluminescence or photocurrent generation is expected to be dependent on the degree of organization of the polymer chains, which affects the delocalization of the carrier wave functions, it can be a powerful tool to study the nanoscale inhomogeneity of photoluminescent polymers, such as poly(phenylene vinylene) and its derivatives, as well as photoactive polymer blends. This fact allowed Blatchford *et al.* [32] to use the local PL signal measured through an NSOM tip to detect pronounced inhomogeneity in the distribution of the PL intensity in spin-coated films of a semiconducting polymer, poly(pyridyl vinylene) (PPyV). From the PL signal imaged at various polarizations, they deduced that the emission originated from ordered domains of aggregated polymer chains, with the domain size being ca. 200 nm. Importantly, they did not detect any correlation between the distribution of the PL-active domains and the film morphology; however, they did note a pronounced difference between NSOM images taken at vertical and horizontal polarizations, which indicated a pronounced anisotropy of the fluorescence from the samples.

DeAro *et al.* [104] used the NSOM technique to study the inhomogeneity of a related semiconducting polymer, poly(*p*-phenylene vinylene) (PPV) prepared by thermal conversion as freestanding thin films. Unlike Blatchford *et al.* [32], DeAro *et al.* stressed that they observed a marked correlation between local optical properties, such as the photoluminescence intensity, and the film morphology: the luminescence seemed to be quenched at the polymer clusters observed in the topography images, thus suggesting a higher concentration of nonradiative centers in such clusters. They also showed that such a correlation could not originate from topography-induced contrast artifacts. Importantly, no such clusters were observed in spin-coated solution-processed MEH-PPV polymer films, which pointed to the importance of the preparation technique and its effect on inhomogeneity.

Wei *et al.* [105] used NSOM to study the inhomogeneity of thin films of polyaniline (PANi) plasticized with 1-methyl-2-pyrrolidone. They used the fact that oxidative doping shifts the absorption maximum of PANi to longer wavelengths. Therefore, they used monochromatic illumination at 632.8 and 543.5 nm to obtain transmission-mode NSOM images, which showed pronounced inhomogeneity. There were clearly visible domains of more-doped and less-doped polymer in the images, with the domain size being ca. 120 nm or more; however, the actual domain size could be smaller due to insufficient resolution of the NSOM technique. The optical images at 632.8 and 543.5 nm showed clearly opposite contrast, with a brighter area in one image corresponding to a darker area in the other. The topography images were also presented, but their resolution was insufficient to show the morphological features as resolved by AFM and SEM.

Teetsov and Vanden Bout [106–109] published a series of papers on NSOM studies of poly(9,9′-dialkylfluorene)s. In these papers they introduced a new procedure for

enhancing the NSOM images by exciting the polymer films with circularly polarized light and measuring simultaneously two fluorescence images, either at two different wavelengths or at two orthogonal polarizations. These images were then compared and other derivative images were generated by combining in a certain way the data of the two raw images. Specifically, one could sum up the fluorescent intensities, resulting in an addition image, use a ratio of fluorescent intensities at different wavelengths, or generate a so-called anisotropy image by using the following equation:

$$I = X - Y/X + Y, \tag{3.1}$$

where I is the resulting anisotropy signal, and X and Y are normalized fluorescence signals measured at the same location. The anisotropy signal is then +100% when all the fluorescence signal is observed in the X direction, –100% when it is all in the Y direction, and zero for isotropic fluorescence. Using these derivative data, which were acquired simultaneously with the topography information, Teetsov and Vanden Bout found that the polymer films had two different domain types. The first type was associated with small (50–150 nm) clusters, which showed strongly quenched fluorescence associated with the formation of interpolymer species, or an increase in the intermolecular interactions, in line with the results of DeAro *et al.* [104]. These clusters were attributed to insufficient solubility of the polymer in the coating solution. The fluorescence from these clusters was unpolarized, indicating their amorphous character. In addition, using the anisotropy images, they demonstrated the occurrence of larger (50–500 nm) highly polarized anisotropic domains, which did not correlate with the sample topography, in line with the results of Blatchford *et al.* [32]. Importantly, these domains were not observed in the addition fluorescent images, indicating that the difference between the domains was in their orientation rather than the overall fluorescence efficiency. Since no domains in the anisotropy images showed 100% signals, it was suggested that the real domains were smaller than the possible NSOM resolution due to the relatively large size of the aperture, and the observed patterns were due to superposition of signals from different domains. Numerical modeling gave the size of such domains as ca. 15 nm, in good agreement with X-ray data. Therefore, these domains revealed the true polymer inhomogeneity as opposed to the isotropic polymer clusters that originated from the polymer solubility during the film deposition.

In their subsequent papers [107–109], Teetsov and Vanden Bout also studied the effect of annealing on the anisotropy and inhomogeneity of poly(9,9′-dialkylfluorene)s with various lengths of alkyl side chain. Annealing was shown to result in the disappearance of the small clusters with reduced unpolarized fluorescence, and formation of polymer nanoribbons or lamellae 40–70 nm wide and more than 500 nm long, which showed a high degree of polarization anisotropy. This was accompanied by almost total quenching of the intrapolymer emission and emergence of new lower-energy states attributed to the formation of interpolymer emissive species due to an increase in the overlap of the π-electron orbitals of the neighboring polymer chains upon annealing-induced ordering. The intensity of fluorescence was found to be the highest when collected perpendicular to the lamellae's long axis. Since the fluorescence dipole was aligned with the polymer axis, this result indicated that the polymer chains in the nanoribbons are aligned across the lamellae widths, perpendicular to the lamellae's long axis. This conclusion is in remarkable

agreement with the results of crystallinity and X-ray studies of regio-regular poly(3-alkylthiophene)s discussed above. The authors also found that longer alkyl substituents increased the packing ability of pristine polymer before annealing; however, upon annealing, shorter alkyl substituents allowed for denser packing. The close packing in the case of shorter alkyl substituents produced an increased excimer emission, while films of polymers with long dodecyl substituents showed poor ordering.

Tan *et al.* and Wei *et al.* [110–112] studied the anisotropy and mesoscopic inhomogeneity of thin films of poly(*p*-phenylene vinylene) (PPV) and poly(2-methoxy-5-(2′-ethylhexyloxy)-1,4-phenylene vinylene) (MEH-PPV) using ac polarization modulation. They found that the homogeneous isotropic structure of as-coated films becomes highly anisotropic and inhomogeneous upon annealing (12 h, 210 °C, N_2 atmosphere). Transmission NSOM imaging revealed a pronounced variation in the optical density upon annealing not related to the thickness changes. This indicated the formation of a domain structure. Further insights were provided by measurements of the so-called dichroic ratio γ, which is somewhat similar to the anisotropy parameter in the papers by Teetsov and Vanden Bout:

$$\gamma = \frac{I_{/\!/} - I_{\perp}}{I_{/\!/} + I_{\perp}}, \tag{3.2}$$

where $I_{/\!/}$ and $I_{\perp}$ are the intensities of the transmitted optical signals obtained when the light is polarized in the parallel and perpendicular directions with respect to the sample. The dichroic ratio was corrected for the tip dichroism occurring due to asymmetry of the tip geometry and tip coating. The images of the corrected dichroic ratio showed a very clear domain structure indicating pronounced anisotropy of the annealed films, with the average domain size being ca. 300 nm. The domain size was independent of the film thickness. The phase images showed abrupt changes at the domain boundaries (the phase signal shows a discontinuity when there is a zero dichroism). The domain orientation was random and was averaged out to yield a zero net polarization anisotropy measured by macroscopic far-field techniques. The occurrence of the pronounced inhomogeneity upon annealing was detrimental to the carrier mobilities in these materials: time-of-flight measurements showed a change from nondispersive to dispersive charge transport and a decrease in the hole mobility by ca. one order of magnitude [112].

McNeill *et al.* [113,114] studied the near-field photoluminescence of thin-film MEH-PPV induced by a voltage bias applied between the near-field probe and the substrate. The goal was to investigate the field-induced modulation of the local carrier density. The injected carriers recombined giving rise to photoluminescence measured by the NSOM probe. The images under applied bias showed a domain structure similar to those reported by other groups. This indicates that the inhomogeneous polymer structure affects the process both with and without an electric-field-induced carrier injection.

Schaller *et al.* [115] used NSOM to collect local light emission from the surface of MEH-PPV polymer samples in contact with various solvents. The goal of this study was to identify various emissive interchain species present in annealed MEH-PPV films. The

results indicated a pronounced increase in the inhomogeneity of the local photoluminescence (PL) intensity when films were exposed to various solvents, thus indicating that inhomogeneity could be increased by solvent-induced swelling of the polymer films. This effect was more pronounced in low-MW material (ca. 60 kDa) as compared to a high-MW one (ca. 450 kDa), indicating that low-MW material is more susceptible to reorganization upon interaction with the solvent.

The same group [116] studied the formation and properties of the interchain species in more detail using a combination of the NSOM technique with third harmonic generation (THG). The goal of their study was to clarify the origin of the domains found in these materials, as described above, and separate the effects related to the excited states of the polymer molecules/aggregates, such as photoluminescence, from the effects related to the ground states of the these species, which can be probed by THG. For instance, this approach allowed the authors to confirm that the NSOM data reported previously were indeed due to formation of domains as a result of polymer chain aggregation in their ground states, as opposed to possible excimer formation, or formation of interacting species by electrons overlapping in the excited state only. The domains of ground-state interchain species were formed with high frequency in annealed films of MEH-PPV, as opposed to as-cast films, where only excited-state weakly emissive interchain species could be found. The use of the THG technique also allowed great improvements in the image quality by eliminating the background.

Pomraenke *et al.* [117,118] used spectrally broadband NSOM as a tool to obtain spatially resolved absorption spectra of local spots on the sample surface with 100 nm resolution. They used a femtosecond Ti:Sapphire laser to generate a high-intensity spatially coherent ultrabroadband light beam, which was then efficiently coupled into the NSOM probe. After passing through the sample, the light beam was collected by a microscope objective lens and analyzed using conventional optical spectrometric techniques. Using this technique, Pomraenke *et al.* studied the inhomogeneity of polycrystalline thin films of oxotitanyl phthalocyanine (TiOPc) prepared by vacuum vapor deposition. Using the difference in the absorption spectra of the crystalline and amorphous forms of this material, they detected the formation of clearly pronounced amorphous and crystalline domains several hundreds of nanometers in size.

In addition to studies of nanoscale inhomogeneity of pristine semiconducting polymers, the NSOM technique and its variations were successfully used for imaging local nanoscale photocurrents and fluorescence emission produced by various polymer blends [119–124].

Therefore, all NSOM data obtained by various groups with different polymeric organic materials suggested the same general pattern of formation of relatively large polarization anisotropic domains or interchain species, which were especially pronounced after solvent or thermal treatment. However, despite the progress achieved in this area, the fundamental problem remains of the insufficient lateral resolution of the NSOM technique and poor topography image quality. In many cases, it was inferred that the actual inhomogeneity and domain size were below the resolution limit of the NSOM imaging employed. Nevertheless, the NSOM data unanimously supported the existence of mesoscopic inhomogeneity in semiconducting and conducting polymers, evidenced by the other scanning probe techniques.

3.3 *In situ* Studies of Conducting and Semiconducting Polymers: Electrochemical Atomic Force Microscopy (EC-AFM) and Electrochemical Scanning Tunneling Microscopy (EC-STM)

3.3.1 Introduction

Traditionally, the preparation of conducting and semiconducting π-conjugated polymers was achieved by electrochemical polymerization. However, since the late 1990s, with the development of organic electronics and especially with the introduction of regio-regular materials, the electrochemical method of polymer-film preparation has been largely replaced by spin-coating and related techniques borrowed from the semiconductor industry. However, the electrochemical route of preparation of electronically conducting polymers (ECPs) still retains its importance, both from the fundamental viewpoint and for several important applications such as batteries, sensors, fuel cells, etc. In this section, we will review studies of inhomogeneity of ECPs at the early stages of formation of such materials and its evolution during the process of polymer growth. Yet another important area reviewed in this section is the change in nanoscale morphology and inhomogeneity in the process of electrochemical doping–undoping of such materials, which is of prime importance for such applications as polymer batteries and supercapacitors. These studies are best performed *in situ*, that is, without taking the polymer film from the solution, which allows one to clearly distinguish the effects of inhomogeneity from the effects of polymer drying and ageing.

Electrochemical synthesis of ECPs is usually carried out in a three-electrode electrochemical cell containing an electrolytic solution prepared from dissolution of a background salt and the monomer in a solvent (water or organic solvent). For this purpose, the working electrode is polarized at a potential allowing the electrochemical oxidation of the monomer and, thus, that of the polymer, as this latter is known to occur at lower anodic potentials than monomer oxidation [125]. The cationic character of the resulting polymer backbone therefore necessitates the entrapment of anions from the solution in the polymer structure for charge compensation. Depending on the properties and structures of these anions, the consequences are functionalization by electrochemical doping of the electrodeposited polymer film and the possible adoption of ion-exchange behavior. As a function of the properties (size, charge, etc.) of the anions, (i) those incorporated during the electrodeposition step and (ii) those present in the doping-undoping electrolytic solution, if different from the electropolymerization solution, ECP films may actually behave as cation, anion or cation/anion exchangers during electrochemically stimulated doping–undoping processes. It is well established that they can also exchange solvent molecules (these latter being either free or acting as solvating agents towards the exchanged ions) with the electrolytic medium [126,127]. Indeed, the solvent exchanges observed during the doping–undoping processes mentioned above are not always correlated, either chronologically or quantitatively, with the cation or anion exchanges.

In any case, the displacement of cations, anions, and solvent molecules through the film/electrolytic solution interface is likely to provoke a volume change in the ECP films [128]. Nevertheless, other reasons may explain such swelling/deswelling (contraction/expansion) processes. For example, it may also result from changes in conjugation length

produced by changes in the doping state. These latter may then generate modifications in the relative orientations of monomer molecules in the polymer chains due to changes in the conformational flexibility of the polymeric chains. The doping–undoping mechanisms are also expected to influence the hydrophilic character of the polymer chains and may therefore significantly alter their stacking and chemical interactions. From all these expectations, it is therefore obvious that links existing between the doping state of polymer films and their thickness are numerous, which makes it considerably harder to quantitatively predict the extent of swelling/deswelling. Obviously, the identity of the solvent and background salts used during the electrodeposition step and in the doping–undoping processes will also strongly influence this phenomenon in a rather unpredictable manner, via their role in the interactions between the polymer chains and their packing.

For all these reasons, many research groups have developed strategies allowing the accurate *in situ* measurement of the volume and topographical changes under electrochemical control of the doping state of the polymer film, either at the local or the global scale. Among the various techniques allowing such measurements, the following section will exclusively focus on techniques allowing *in situ* local investigations of the swelling/deswelling mechanisms of ECPs with nanometer lateral and vertical resolution, namely atomic force microscopy (AFM) and scanning tunneling microscopy (STM) [129]. When used in an electrolytic solution under electrochemical conditioning of the substrate, these two techniques are called EC-AFM and EC-STM, respectively. Notice that a vast set of *ex situ* AFM investigations aimed at correlating the surface topography of electrogenerated ECP films with doping ions and/or electrochemical parameters used during the synthesis is disseminated in literature. Indeed, contact-mode or acoustic-oscillating (tapping)-mode AFM images showing the topography of ECPs are disseminated in many publications, although topography is almost never the main purpose of the reported investigations. These studies revealed ultimately topography varying from a globular aspect towards various versions of the well-known cauliflower-like morphology of ECPs as the electrodeposition step lasts longer (see [38,130–134] for examples). Other *ex situ* studies allowed the determination of the nucleation and growth mechanisms taking place during the electrodeposition of ECPs as a function of the initial topography and the material of the working electrode (see [135], for example).

3.3.2 EC-AFM Investigations of the Swelling/Deswelling of ECPs

EC-AFM is a particular working mode of AFM in which contact-mode AFM imaging is performed *in situ* in an electrolytic solution so as to allow the sample to be placed under electrochemical control. When applied to conducting polymers, EC-AFM is thus used in an electrochemical cell especially dedicated to AFM studies, in which the back of the cell supports the conducting polymer sample electrodeposited at the top of the working electrode (see Figure 3.9). For electrochemical conditioning of the sample, reference and counter-electrodes are added to the cell.

Among the very first studies of this kind, EC-AFM investigations were carried out on *p*-toluene-sulfonate-doped polypyrrole films electrodeposited from aqueous solutions [137]. Such polymer films were found to be produced as highly structured materials in a gradual step-by-step process. They are made of highly ordered micrograins and of many

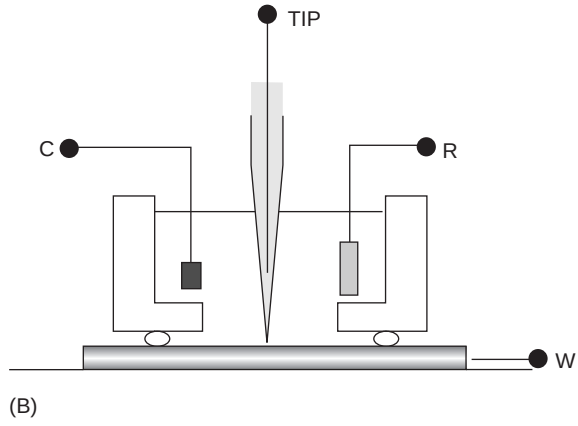

Figure 3.9 *Schematic view of the cell used for* in situ *ECAFM measurement. (Reprinted with permission from Electrochimica Acta, In situ atomic force microscopy in the study of electrogeneration of polybithiophene on Pt electrode by M. Innocenti, F. Logio, L. Pigani et al., 50, 7–8. Copyright (2005) Elsevier Ltd)*

microholes, the structural elements that were thought to play an important role in electron transport phenomena in polypyrrole films. It was also suggested that the transition from the doped to the undoped state and the subsequent holding of these films in the undoped state for more than five minutes led to substantial and irreversible topographical evolution.

Nyffenegger *et al.* compared the performances of EC-AFM and EC-STM during investigations related to the swelling/deswelling of polyaniline films [138]. Their conclusion was that AFM provides more acceptable results as they are in good agreement with those measured using other techniques, such as *in situ* ellipsometry. This technique indeed allows a clear dependence to be found between the thickness change and the initial thickness expressed from the charge of the oxidation wave of the film measured after transfer to an electrolytic solution. For a PANI film whose doping charge is 8.67 mC cm^{-2}, the thickness was found to increase by about 26.9 nm during an electrochemically stimulated doping step. Similar measurements carried out with EC-STM provided two orders of magnitude difference between the two sets of volume changes measured. Several methods used for these EC-STM measurements also led to worrying substantial differences between the results.

In an article published by Dunsch *et al.* in 1995, EC-AFM investigations were carried out on a tosylate-doped polypyrrole film electrodeposited on HOPG from aqueous solution containing tosylate anions [139]. Such investigations revealed that the surface microstructures of these films depend on the preparation method. When grown electrochemically at high current densities, the films display a significantly rougher microstructure in the submicrometric range, whereas low current density electrodeposition of PPy films produces smoother surface structures. Upon transfer to an electrolytic solution for studies of the doping–undoping process, it was also observed that the surface roughness of these films increases with the anodic potential applied to the polymer sample during imaging, and thus with the doping state. From an equilibrium potential up to 1000 mV vs. Ag/AgCl

reference electrode, a potential range that encompasses that allowing the doping–undoping of the PPy film, the mean roughness value r_a increases by a factor of about six from 4.6 up to 29.4 nm. This increase is particularly pronounced in the potential region where the oxidation peak corresponding to doping appears. After decreasing the anodic potential so as to produce undoped and thus insulating PPy films, the surface roughness also decreases, indicating thus that the observed roughness changes are reversible.

After preliminary investigations using *ex situ* AFM aimed at investigating the structure of poly(3-methylthiophene) (P3MT) layers at several stages of their electrochemical deposition, from nucleation up to 200 nm thick layers (see references cited in [140]), Chao *et al.* reported EC-AFM investigations on the structural change of P3MT films upon doping–undoping [140]. Thin polymer films (thickness below 30 nm) were deposited potentiostatically on polycrystalline platinum electrodes from acetonitrile solutions containing 3-methylthiophene (6 M) and $LiClO_4$ (0.2 M). The main conclusion was that an important time constant was observed during the doping–undoping reaction between *in situ* ellipsometry results that rather reveal rapid electronic processes, and EC-AFM imaging that rather suggest very slow structure modifications expected from the exchange of ions and solvent molecules at the film/solution interface. More precisely, these observations indicate that these films do not swell significantly upon potentiodynamically stimulated doping, as long as the potential scan rate exceeds 16 mV s^{-1}. Slower scan rates, such as 5 mV s^{-1}, allow significant swelling of the polymer film to occur essentially at the end of the electrochemically driven doping. When relaxation of the polymer in its doped state is allowed to take place between doping and undoping steps, no effect was observed on the cathodic part of the voltammogram corresponding to undoping, indicating possibly, as the authors claim, that swelling mainly results from the slow penetration of solvent molecules into polymer grains only slightly dilated by the penetration of counter-ions. When the doping reaction is performed with the help of very slow step-by-step potential programs, the transport of counter-ions controls the evolution of the polymer grain size. The polymer shrinks as a consequence of counter-ions and solvent expulsion during the initial stages of doping ($E < 0.5$ V) and swells during the later stages of doping ($E > 0.5$ V) when counter-ions penetrate back into the film. Similar behavior was shown for the doping-undoping of P3HT by electrochemical quartz microbalance (ECQM) measurements [37]. The most spectacular observation is the impressive duration of the swelling beyond the end of the potential scanning, and the end of the doping reaction, in spite of the slow scan rate.

Häring *et al.* reported the comparison of *in situ* imaging of PANI films during electrochemical doping–undoping processes using EC-STM, EC-AFM, and EC-intermittent contact-mode atomic force microscopy (IC-AFM) [141]. As Nyffenegger *et al.* a few years earlier, they concluded that EC-STM is not well-adapted to the imaging of swelling/deswelling of electronically conducting polymers, as the severe drop in the tunneling current expected to occur during the transition from the doped to the undoped state of the polymer will definitely lead either to artifacts or to damages to the polymer film during the imaging procedure. Contact-mode AFM appeared to be much better adapted for such purpose, although one can fear wear or pollution of the AFM tip on soft materials like ECPs. By the time this contribution was published, the authors have expressed their doubts about IC-AFM due to the development level of this technique in 1995, in spite of its satisfying performance in the above-mentioned imaging.

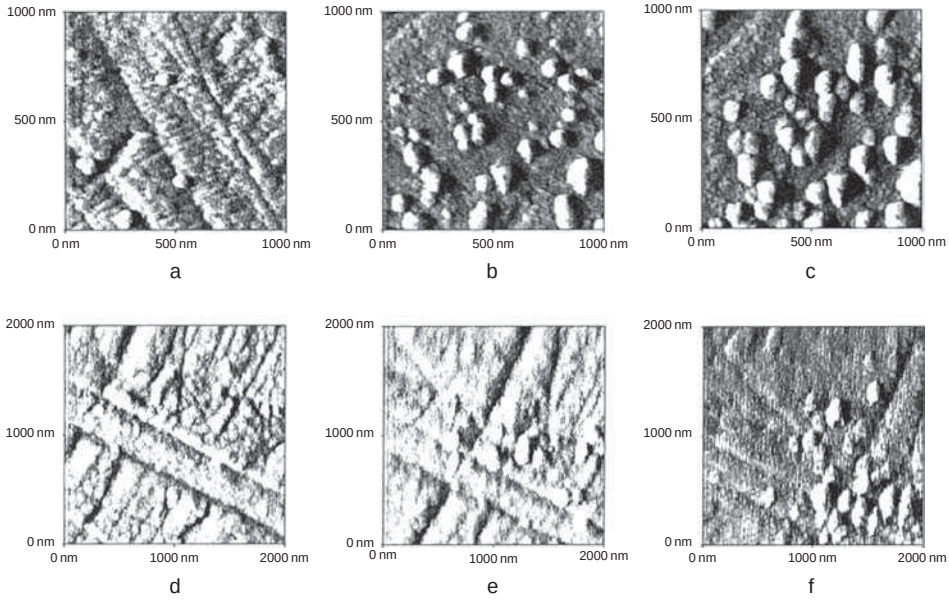

Figure 3.10 *AFM images of PPy grown on a polycrystalline platinum electrode during the first stage of growth. (Top) The sequence of PPy grown in 0.1 M NaClO4, after: (a) 20, (b) 64, and (c) 98 s of synthesis. The roughness increases from: (a) 45 to (c) 154 nm. (Bottom) The sequence of PPy grown in 0.1 M sodium* p*-toluenesulfonate, after (d) 216, (e) 396, and (f) 576 s of synthesis. The roughness increases from (d) 25 to (f) 48 nm. The pyrrole concentration was 0.005 M and the synthesis potential was 0.8 V vs. SCE. (Reprinted with permission from Journal of Electroanalytical Chemistry, In situ atomic force microscopy study of polypyrrole synthesis and the volume changes induced by oxdation and reduction of the polymer by M. F. Suarez and R. G. Compton, 462, 2. Copyright (1999) Elsevier Ltd)*

Compton and coworkers probed the morphology of polypyrrole films during the initial stages of their electrodeposition, either in sodium perchlorate or sodium *p*-toluene sulfonate aqueous solutions, on polycrystalline platinum, polycrystalline gold, or glassy carbon electrodes [142]. The authors claim from their EC-AFM observations that 2-D growth initially takes place on platinum, leading then to a thin polypyrrole layer covering the whole electrode surface (see Figure 3.10). In the second step, polypyrrole nodules start growing, with dimensions that seem to depend on the identity of the anion of the background salt. On the other hand, EC-AFM images show surprising oval shapes oriented along a single direction on gold and a set of fibrous and/or oval fibrous shapes, depending on the anion of the background salt (perchlorate or *p*-toluene sulfonate) on glassy carbon. These observations were interpreted by the authors as evidence of more-ordered PPy structures resulting potentially from the formation of flat and oriented initial layers, whereas the following layers are oriented randomly. The first growth stage is likely to correspond to deposition of a primary polymer layer resulting either from polymerization of the adsorbed monomer molecules on the electrode surface or from precipitation of

oligomers produced by electropolymerization of the dissolved monomers in the electrode vicinity, whereas the second stage corresponds to the growth of the top layers, following several possible mechanisms, such as, for example, the random deposition of polymer chains electrogenerated in solution, preferential deposition of polymer at growth centers or continued growth of polymer chains after their precipitation/deposition on the electrode surface. It is nevertheless unlikely that random precipitation can produce preferential growth of specific nuclei or ordered fibrous structures. The authors claim that only the ability of the electrogenerated polymer chains precipitating from solution to move towards a more stable and ordered polymer domain can explain the ordered structures observed on EC-AFM images. In the course of their experiments, it also appeared that these PPy films underwent a substantial topography evolution over time after their electrochemical synthesis, from an oval structure resulting from the electrodeposition step towards a rather globular and disordered structure, whatever the underlying electrode material.

They also observed that the first electrochemical reduction (undoping) of a likely anion exchanger such as a perchlorate-doped polypyrrole film at a –0.8 V/SCE reduction potential led to a rapid swelling followed by a subsequent continuous slow shrinking as soon as the potential was switched from –0.8 to +0.2 V. This behavior was observed during the first undoping–doping transition only, as the following transitions, stimulated by identical potential steps, did not produce any evident volume variation of this film, possibly indicating that continuing potential conditioning of the film allowed some structural modifications to occur. The authors observed that a one-hour-old film did not undergo significant volume changes, even during the first undoping–doping transition, confirming, thus, that ageing-induced morphological transitions may have a strong influence on the electrochemical (doping–undoping) behavior of ECPs. In contrast, a likely cation exchanger such as *p*-toluene-sulfonate-doped polypyrrole film swells when in potential conditions corresponding to reduction (–0.8 V/SCE) and then shrinks during the oxidation (doping) process.

Volume changes can be induced by various mechanisms taking place in electronically conducting polymers, for example: (i) phase relaxation probably inducing exchange of solvent molecules through the film/electrolytic solution interface, as well as simultaneous, but slow structural rearrangement, and (ii) ion transport necessary for charge compensation in the bulk of the film. This second possibility seems to be sufficient to explain the volume changes described above, as the swelling process corresponds to penetration of ions into the film in both cases.

Semenikhin and coworkers carried out EC-AFM experiments aimed at studying the initial stages of galvanostatic deposition of polybithiophene on HOPG from propylene carbonate solution [33]. The topography images were obtained under open-circuit conditions without any electrochemical treatment. In the first stage, separate nuclei with a height of about 1 nm were generated on the electrode surface. A 0.5 mC cm^{-2} grafting charge was required to get a continuous PBT film. Nanoscratching procedures were used to access the *in situ* polymer film thickness. This latter was proportional to the grafting charge Q with a coefficient of 2.6 $nm.cm^2$ mC^{-1} and, like the morphology of the films, independent of the deposition current density I in the interval $0.1 \leq I \leq 2$ mA cm^{-2}. The average grain size was found to be 54.0 ± 2.5 nm. X-ray diffraction studies revealed a substantial degree of crystallinity for these films.

EC-AFM experiments were carried out on regio-regular oligomers of 3-octylthiophene deposited by solvent casting on gold foils [143–145]. The study revealed the disappearance

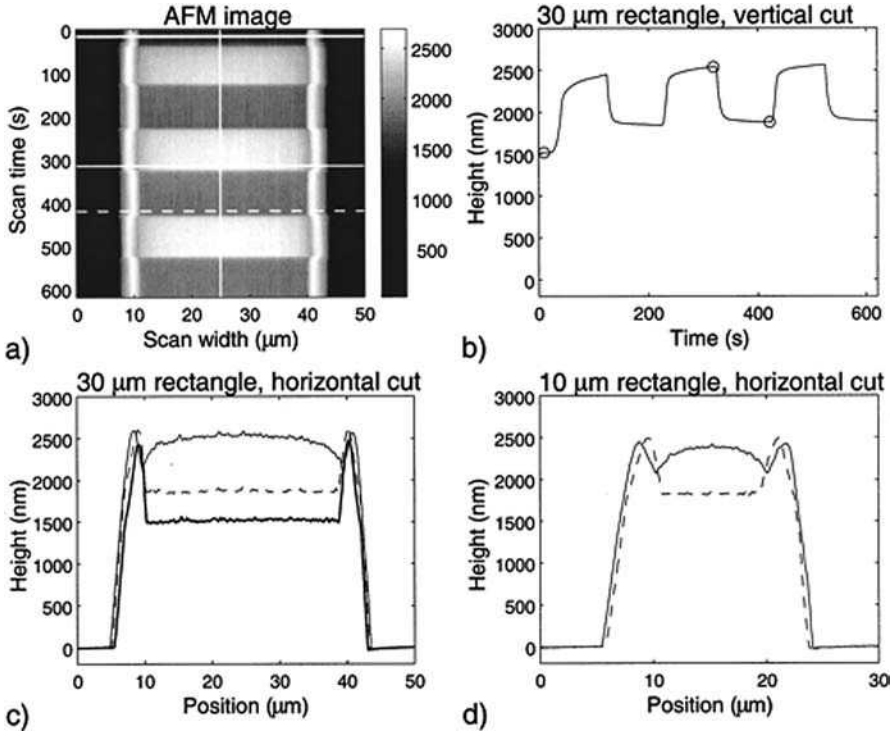

Figure 3.11 *(a) AFM image obtained from a patterned PPy rectangle nominally 30 μm wide from the voltage step sequence: 0 V for 20 sec, –1 V for 100 sec, 0 V for 100 sec, –1 V for 100 sec, 0 V for 100 sec, etc.; (b) vertical cut at the position of the vertical white line in (a) showing the change in height of the PPy over time; (c) horizontal cuts for 0 V before any cycling (heavy line) and for applied potentials of –1 V (solid line) and 0 V (dashed line) corresponding to the white lines in (a) and circles in (b); (d) horizontal cuts as for (c), but for a narrower, 10 μm wide rectangle. (Reprinted with permission from Journal of Physical Chemistry B, Volume Change in Polypyrrole Studied by Atomic Force Microscopy by Elisabeth Smela et al., 105, 39. Copyright (2001) American Chemical Society)*

of hills and valleys, existing initially on the film surface at very low potentials, during potential steps between 0 and 1.2 V in nonaqueous electrolytic solutions. These morphology changes were found to be fully reversible with approximately 1-μm-thick films. They were attributed to conformational changes and stacking occurring during potential-dependent doping processes.

In a very convincing contribution [146,147], Smela and Gadegaard used EC-AFM in an electrolytic medium to investigate the topography and to measure the expansion and contraction of dodecylbenzene-sulfonate (DBS)-doped polypyrrole films known to behave as cation exchangers. Patterned electrodeposited polymer films were used in order to measure their absolute thickness as a function of their doping state by allowing the AFM tip to scan over the whole polymer pattern (see Figure 3.11). It was confirmed that dry

films swell progressively after immersion as a consequence of water absorption, following kinetics similar to those measured for water absorption from ambient air. Such polymer patterns were also found to display the same topography, whether they were as-grown, or in the reduced or oxidized states, when their thickness is within the 0.15–4.0 μm range. In another experiment, the doping level of a polymer pattern was controlled by 100 s potential steps. The film was found to decrease in volume during oxidation, corresponding to the expulsion of cations, and to increase in volume during reduction, corresponding to the insertion of cations. The first potential step resulting in reduction of the polymer led to an anisotropic 61% increase in volume in the out-of-plane direction, whereas subsequent potential steps revealed that the thickness increased by about 35% when the polymer went from its oxidized (doped) state towards its reduced (undoped) state. In the course of these experiments, swelling and deswelling rates were found to be 57.5 and 84.3 nm s^{-1} respectively, allowing 80% of the swelling and deswelling processes to occur within 12 and 11 s, respectively. An obvious correlation was found between the swelling/deswelling events and the cyclic voltammograms. The abnormally large cathodic peak current measured during the first potential scan correlated well with the start of a 125% volume expansion. On the reverse (anodic) scan, the oxidation peak corresponding to the doping of the polymer and the contraction of the film both started as soon as the potential reached 0.7 V, but the film did not reach its initial thickness at the end of this anodic scan. Subsequent potential cycles produced roughly identical anodic and cathodic currents and a 40% expansion during the transition from the oxidized to the reduced state. Moreover, the extent of the thickness variation was found to be a function of the initial thickness. Polymer films 1.5 μm thick were found to produce the maximum thickness variation. Interestingly, the authors also suggest, from their EC-AFM observations, that their polymer patterns are softer in the reduced state than in the oxidized state.

The electrochemical doping–undoping of polymer films of regio-regular poly(3-hexylthiophene) in propylene carbonate solutions of 0.1 M $LiClO_4$ is accompanied by substantial swelling/deswelling (expansion/shrinkage) of the film [148]. The order of magnitude of the thickness variation is 1250 nm for 3–3.5 μm thick P3HT films at a 3 mV s^{-1} scan rate and only approximately 500 nm for a 20 mV s^{-1} scan rate, which corresponds to 35–40% and 15–17% of the initial film thicknesses, respectively. The comparison of the variations of thickness and current as a function of potential indicates that film thickness variation is significantly delayed with respect to formation of cations and dications along the polymer chains upon oxidation. The authors suggest that the swelling of the polymer matrix allows reconfiguration of polymer chains. They also claim that the more compact structure and spatial constraints expected to occur in the crystalline zones of the polymer may explain the smaller variation in the polymer thickness observed during the first doping step. The second oxidation step attributed to amorphous zones is thought to correspond to the penetration of significant amounts of solvent, leading then to a more rapid dilatation of the polymer film. It was also observed that the doping provokes a morphological transition from a granular to a chain-like structure. When carried out in aqueous solutions of $LiClO_4$, the electrochemical doping leads to much smaller thickness variations than those observed in propylene carbonate electrolytic solutions. In this situation, the authors' interpretation is that this weak swelling of the polymer matrix in aqueous solutions and, as a consequence, the penetration of a predictably low amount of ions from the electrolytic solution is likely to limit the reconfiguration of the polymer chains.

In a recent contribution, EC-AFM has been used to investigate the influence of the background salt ($LiClO_4$ or $TBAPF_6$) and electrochemical conditioning (potentiostatic or potentiodynamic) on the early stages of the growth of PBT films [136]. Potentiostatic growth of PBT was carried out on a platinum electrode surface in the presence of acetonitrile/$LiClO_4$ at + 0.57 V vs. the Fc^+/Fc redox couple, so as to produce very slow PBT electrodeposition. EC-AFM imaging was performed *in situ* at a potential corresponding to the undoping of the polymer, (–0.58 V vs. Fc^+/Fc redox couple), after each 1 minute growth period. AFM images collected during the first five minutes only show that the polishing scratches are progressively filled with electrodeposited polymer growing preferentially at surface defects on the platinum surface (see Figure 3.12A). Images corresponding to longer growth durations show a homogeneous distribution of globular features (grains or nodules, see Figure 3.12B–H) whose diameter (approximately 400 nm on average) increases with time, suggesting thus that the polymerization mechanism is due to the preferential growth of preformed 'active' nuclei that then merge together in a second step. From the computed R_{RMS} (the root mean square roughness) and h (the difference between the maximum and minimum z values in an image), the authors claim that the deposits grow through the simultaneous formation of new nuclei and the preferential deposition of polymer chains at nucleation centers, according to a 3-D growth mechanism.

Similar EC-AFM investigations carried out during the electrodeposition of PBT from $TBAPF_6$/acetonitrile electrolytic solutions led to slightly different conclusions. Sets of

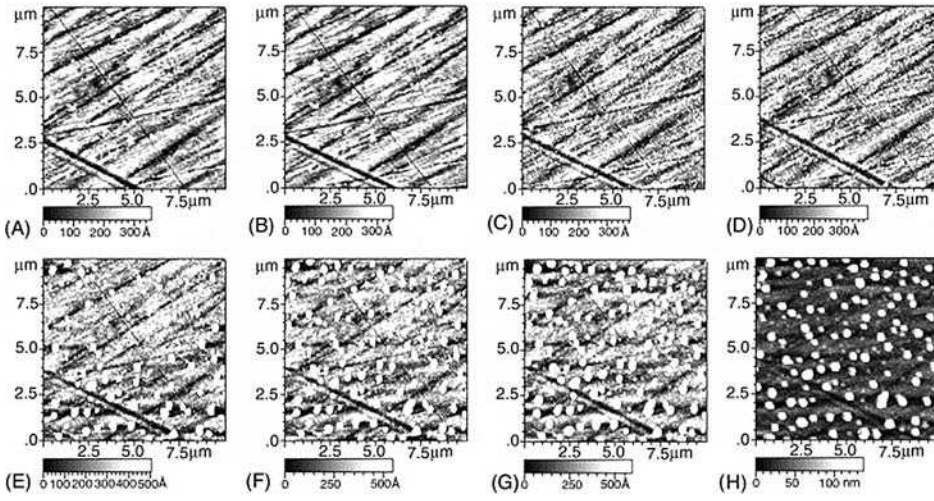

Figure 3.12 *AFM images of PBT grown on polycrystalline Pt electrode during various stages of growth at +0.58V vs. Fc^+/Fc redox couple in the presence of $LiClO_4$ supporting electrolyte. (A) bare electrode; after starting the electropolymerization by: (B) 1 min; (C) 6 min; (D) 7 min; (E) 8 min; (F) 13 min; (G) 18 min; (H) 23 min. (Reprinted with permission from Electrochimica Acta, In situ atomic force microscopy in the study of electrogeneration of polybithiophene on Pt electrode by M. Innocenti, F. Logio, L. Pigani et al., 50, 7–8. Copyright (2005) Elsevier Ltd)*

R_{RMS} and h values seem to indicate that the polymer starts growing through a 3-D growth mechanism as a first step, with a noticeable nonhomogeneous increase in the dimensions of the numerous nucleation centers leading finally to a nonuniform population of grains, and then through a bi-dimensional growth mechanism in a second step. This may indicate that both salts have significantly different impacts on the packing of oligomer chains during the formation of the polymer. The same authors observed that the background salt has generally no effect on the topography of PBT films grown using potentiodynamic conditions.

Electrodes modified by polythiophenes bearing different substituents have been prepared and the behavior of the resulting conducting polymers has been studied with respect to the structural phenomena occurring in the doping–undoping processes as functions of the supporting electrolyte, the discharge (neutralization) time, and the potential value stimulating the doping–undoping process [129]. Such studies are meaningful with respect to the possibility of charging–discharging the polymer reversibly and quickly, as well as for providing a way to optimize the performances of ion-releasing devices of technological interest, such as artificial muscles, rechargeable batteries, supercapacitors, and ion-selective membranes [129]. The steric hindrance of the substituents on the polymer chain has been demonstrated to play a fundamental role in determining the extent of compactness of the film, as induced by polarization of the electrode at potentials at which the previously charged polymer is discharged. Such a conclusion is in accordance with prediction of the electrochemically stimulated conformational relaxation (ESCR) model [128,149]. Electrochemical AFM measurements have been performed in order to acquire a direct view of the morphological modifications of the polymer coatings during the reduction.

The measurements performed with different polythiophenes point out that a proper compact structure for the neutral polymer is more and more difficult to achieve as the steric hindrance of the side chains substituents on the backbone increases. Bulkier and bulkier substituents allow the polymer to shrink to a lower and lower extent by neutralization, so that swelling by oxidation is a thermodynamically and kinetically easier and easier process. Hence, in the limiting case of 'sterically hindered' PBST, a high enough degree of compactness cannot be reached at the negative potentials at which neutralization of the previously charged and concomitantly swollen polymer occurs, even with prolonged cathodic polarization. The relaxation effects are, in this case, not evident at all; the tuning from 'compact' to open structure is consequently particularly easy, so that it does not introduce any significant thermodynamic or kinetic effects in the doping process: the relevant responses are independent of the compacting potential and time. On the other hand, in general, the EC-AFM measurements performed to date illustrate the role of time and of the discharge potential in determining the surface morphology. Moreover, the differences in morphological changes of PBT with respect to PBST at varying potentials are easily detectable, giving sound confirmation to the predictions of the ESCR model.

In the course of original investigations, Pyo *et al.* investigated the effect of pH, rather than that of an electrochemical procedure, on the ion transport at the perchlorate-doped polypyrrole film/electrolytic solution interface [150]. Preliminary EC-AFM investigations allowed them to detect a 12.6% volume increase when the solution pH varied from 1.0 to 11.3 in a 50 mM $NaClO_4$ aqueous solution.

Recently, Contractor *et al.* investigated volume changes occurring in electrodeposited polyaniline films in sulfate and chloride media, as well as PANI microtubules and

nanowires in a sulfate medium using EC-AFM [151]. Their main observation was that PANI films expand during oxidation and shrink during reduction, as a consequence of solvated anion exchange at the PANI/electrolytic solution interface. Such volume changes were found to be reversible in PANI microtubules and nanowires. In PANI nanowires doped with large anions such as poly(styrene sulfonate), swelling and deswelling were claimed to be as high as 33% and were expected to occur as a consequence of the proton exchange between the polymer and the electrolytic solution. EC-AFM investigations of volume changes occurring in PANI nanoparticles may reveal variations in the 17.5–89.8% range.

Dynamic actuation of polystyrene-sulfonate (PSS)-doped polypyrrole thin films was investigated by Wallace *et al.* using EC-AFM (see Figure 3.13) [152]. PPy/PSS films were grown from aqueous electrolytic solutions containing NaPSS (0.05 M) and Py (0.2 M) in galvanostatic conditions using a 1.3 mA cm^{-2} current density on gold working electrodes. Preliminary AFM imaging of PPy/PSS films showed that those grown with a 600 s electrodeposition time possess significantly rougher cauliflower-like morphology than those electrodeposited over 10 seconds. The root-mean-square (RMS) surface roughness was found to follow a semilogarithmic increase as the electrodeposition time increased from 10 to 600 seconds. As far as the thickness of these films is concerned, it was determined from nanoscratching tests carried out with the AFM tip (and/or mechanical scratching using a sharp scalpel), followed by AFM imaging of the height profile of the resulting print. The thickness was found to increase linearly with the electropolymerization charge from 0.09 μm up to 3.17 μm for the same electrodeposition time range at a rate of 3.91 μm C cm^{-2}. In the course of investigations related to the electrochemical behavior of these films in aqueous NaPSS solutions, it was found that five consecutive cyclic voltammograms (–500 to 500 mV at 50 mV s^{-1}) encompassing the doping–undoping processes of these films were necessary before the polymer films displayed stable electrochemical behavior. This electrochemical optimization of the doping–undoping was therefore applied to each film prior to EC-AFM imaging experiments aimed at measuring the thickness change upon doping–undoping. These latter were carried out in contact mode with the slow scan axis disabled at different potential scan rates (10, 50, 100, and 200 mV s^{-1}) in the same potential range (–500 to 500 mV) for each thickness (10, 120, 300, 600 s electrodeposition times). By doing so, the resulting AFM images showed cyclic thickness variations that correlated with triangular potential signal-type stimuli applied to the polymer films, thus giving a direct measurement of the dynamic mechanical actuation of the PPy/PSS film. By plotting a cross-section of this image with the corresponding voltage and current signals related to the electrochemical treatment, one can distinguish that the actuation height is 180° out of phase with the potential stimulus, which actually indicates that the film shrinks as it is oxidized (doped), whereas is swells as it is reduced, as a consequence of the predictable cation-exchange behavior of PPy/PSS films. Moreover, it was observed that the extent of the actuation shows a high, but not linear, decay as a function of the potential scan rate for thick films, such as those obtained at 600 s electrodeposition times.

The height profiles extracted from the EC-AFM images showed that the actuation height decreases as the scan rate increases. This observation could easily be predicted from the time-limited diffusion process of sodium cations at the film/electrolytic solution interface. The actuation dependence on the potential scan rate was found to become weaker and more linear as the film thickness (or the electrodeposition time) decreases. As an illustration, the

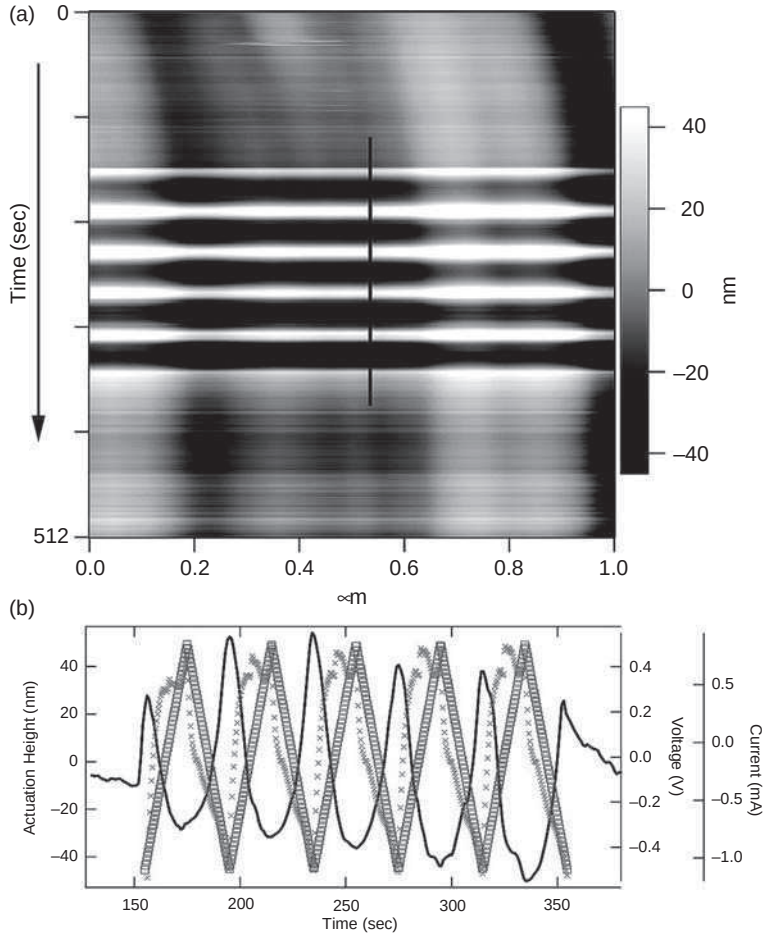

Figure 3.13 *(A) AFM height image of a PPy/PSS film grown for 10 min in 0.05 NaPSS during a cyclic voltammogram (CV) measurement initiated at ~150 s into the AFM scan. The image's vertical axis is given as time (see text for details). Lighter (higher regions) and darker (lower regions) bands in the image correspond to the cyclic displacement, or actuation of the film in response to the CV which was performed with an applied potential moving from –500 to +500 mV at 50 mV s^{-1} for five cycles. (B) Cross-sectional height profile (black line) taken through the vertical line shown in (A) as a function of the CV time(s). The height profile shows a cyclic increase and decrease in height, and an out-of-phase response with the corresponding applied voltage (square) and current (hatch) signals. (Reprinted with permission from Langmuir, Visualizing Dynamic Actuation of Ultrathin Polypyrrole Films by Michael J. Higgins et al., 25, 6. Copyright (2009) American Chemical Society)*

actuation of the thicker films (600 s electrodeposition time, 3.17 μm thickness, on average) was 18 times higher than that measured with thinner films (10 s electrodeposition time, 97 nm thickness, on average) at a 10 mV s^{-1} potential scan rate, whereas it was only eight times higher at a 200 mV s^{-1} potential scan rate. Diffusion-limited processes may explain

this nonlinear decay observed for thick films if the rate and distance of ion exchange at the film/electrolyte solution interface limits the extent of actuation. The linear dependence observed for the thin films seems to correspond to an electrochemical actuation process limited by current rather than by diffusion. One may suggest that the thickness dependence of the polymer structure may lead to variations in the diffusion coefficient of ions when thickness goes from the micrometer to the nanometer range. The usual 'cauliflower-like' structure observed for such polymer films is known to arise from the conglomeration of 50–100 nm diameter particles, thus producing higher-order fractal structures in which micropores and interstitial nanometer-size openings can be observed. It is likely that the resulting porosity allows a high mobility for large anions (such as PSS^-), and more generally speaking an increase in the diffusion coefficient of ions as the film thickness increases as a consequence of decreasing film density. In contrast, thinner and therefore denser films show a porosity essentially made of interstices and may well display shorter diffusion paths, a negative influence on the diffusion rate, and, simultaneously, easy access for the solvated ions to a greater majority of the film.

The set of investigations reported above is largely sufficient to show that EC-AFM is the relevant technique to probe, with the nanometer resolution, the topographical and thickness evolutions occurring during electrodeposition and electrochemically controlled doping–undoping processes of ECPs. Interestingly, this technique does not only allow such investigations in static electrochemical conditions, but also in dynamic ones, thus giving access to the dynamics of the above mentioned morphological changes observed in ECPs. However, such investigations are still too rare nowadays to constitute an exploitable source of information on the subject. From the AFM point of view, this whole set of results has been obtained by using contact-mode AFM imaging (except in the contribution published by Häring *et al.*, where the performances of intermittent contact mode and contact mode were compared). However, variable imaging procedures were used, which results in various representations of the obtained results and may influence their interpretation. It is obvious anyway that the AFM imaging of ECPs in contact mode in solution requires much expertise and care in order to avoid artifacts predictable from the very soft character of such materials. Another confusion comes from the various potential programs applied during the AFM imaging in order to control the variation of the doping state of ECPs with time (constant potential, potential steps, potential scans). The various combinations of AFM imaging procedure and potential programs used so far and those not suggested in the literature as yet do not facilitate the straight comparison of those observations and this is even more true due to the large spectrum of ECPs/doping ions/solvent/electrodeposition method systems that have been or could be investigated. In other words, this review demonstrates clearly that EC-AFM imaging of the dynamics of electronically conducting polymers is still in its infancy, in spite of the key information it may deliver for such promising applications of ECPs as actuators, artificial muscles, supercapacitors, etc.

3.3.3 EC-STM Investigations of the Swelling/Deswelling of ECPs

EC-STM consists in performing standard STM imaging, therefore based on a measure of the tunneling current, in an electrolytic solution so as to allow electrochemical control of the imaged substrate. When applied to an electronically conducting polymer, this

electrochemical control is aimed at fixing the doping level of the polymer film during the imaging process. By using this technique, the morphological evolution of perchlorate-doped polypyrrole films during the doping–undoping process in an aqueous lithium perchlorate solution was investigated [153]. Topography changes were found to be heterogeneous on the polymer film surface, indicating, possibly, that the insertion of ions takes place only locally in the bulk of the polymer. They actually correspond to a swelling of some of the nodules that constitute the film during the oxidation/doping process. Similar studies were carried out by the same authors in the presence of various anions, such as carbonate and trifluoromethane-sulfonic anions, in the transfer electrolytic solution [154]. The increase of the oxidation current measured during the doping process was found to be correlated with the swelling mechanism revealed by the evolution of the roughness and the surface of the film. Moreover, the authors suggest that the electroactivity of the polymer film is not limited by the topography changes. These latter, as well as the swelling processes, were found to be strongly influenced by the anions as a function of their properties (size, charge, etc.).

Poly(*N*-methylpyrrole)/poly(styrene sulfonate) films were found to undergo roughness variations in aqueous perchlorate solutions during electrochemical doping–undoping reactions [155]. EC-STM experiments indeed revealed that the roughness and the roughness difference between the doped and undoped states increases with the thickness of the polymer film when the polymer thickness is more than 2 μm. Moreover, it seems that the cation of the salt used in the transfer electrolyte solution is able to influence the roughness of these films, which sounds acceptable, as these films are expected to be cation exchangers due to the considerable size of the polystyrene sulfonate anions present in the electrodeposition solution. For example, the roughness of 4 μm thick PNMP/PSS films were found to be 2.58, 2.89 and 3.24 nm after electrochemical reduction in $LiClO_4$, $KClO_4$ and $CsClO_4$, respectively. The same author reported that PPy/PSS films underwent a volume variation, going from –0.95% to 15.5% when the thickness varied from 100 nm to 2 μm [156]. It was also observed that inside the 800-mV-wide potential range used for the doping of the polymer film, the film volume decreased during the first 650 mV and then increased during the last 150 mV, going from the reduced to the oxidized state.

The EC-STM investigations reported above have to be considered prudently. Indeed, the CS-AFM studies reported in Section 2.3 have clearly demonstrated that ECP films display a heterogeneous surface conductivity, whatever their doping level. This is, indeed, likely to result in artifacts during topography imaging using EC-STM as it is based on servo-control of the *z*-coordinate of the tip position on a constant tunneling current measured at the tip. It is therefore likely that local topography changes and surface conductivity drops will create confusion in the STM topography imaging. This general observation may explain the progressive decrease in the use of EC-STM for *in situ* measurements related to electronically conducting polymers.

3.3.4 Scanning Electrochemical Microscopy (SECM) Investigations of ECPs

Scanning electrochemical microscopy (SECM) is a scanning probe technique in which the probe is a disk ultramicroelectrode (typical radius in the 5 to 25 μm range) that scans the surface of the investigated sample facing it [157]. SECM measurements are carried out in

an electrolyte solution so as to allow the measurement of a faradaic current at the amperometric probe (also called the tip) as a function of the local surface properties of the sample. Among the properties that are able to influence the probe response, are surface conductivity, electrochemical reactivity, and distance to the probe (this latter being possibly influenced by local roughness). The feedback mode and the generation/collection mode are working modes of SECM that necessitate, respectively, a redox mediator initially added in the electrolytic medium, or a redox-active compound produced at the sample surface. Such redox species are necessary to provide the reactants for the redox reaction occurring at the tip biased at a constant potential during the imaging procedure.

The feedback mode of SECM was used to map the conductivity of a fluoroborate-doped polypyrrole film and to evaluate its potential dependence [158]. An ultramicroelectrode (UME), 12.5 μm in diameter, was used to detect the redox mediator more or less concentrated in the UME vicinity, depending on the ability of the polymer film to regenerate it, thus providing the potential region where the polypyrrole film is electronically conducting.

In a different procedure, Ag/AgCl-based potentiometric sensors used as SECM probes, 10–50 μm in diameter, have been used to identify the flux of chloride anions existing at the film–solution interface of a polyaniline film electrodeposited on a platinum electrode [159]. The tip potential was recorded during potential cycling applied to the PANI film in the anodic potential range situated after the first oxidation peak of PANI. Such measurement allowed the oxidation mechanism of PANI to be confirmed. These investigations were further developed by probing amperometrically the flux of protons at the film–solution interface as a function of the potential applied to the PANI film [160,161]. The measurements suggest that the presence or absence of NaCl as a supporting electrolyte may affect the redox mechanism of PANI. It provided proof of exchange of protons and chloride anions during the oxidation of PANI. As the SECM response was found to depend on the protonation state of PANI, it was confirmed that addition of NaCl led to proton uptake by the leucoemeraldine form of PANI.

The fluxes of anions produced by the oxidation and reduction reactions of polypyrrole films doped with various anions such as bromide, ferrocyanide and poly(p-styrenesulfonate) were investigated using SECM [162]. During control of the redox reactions occurring on the polypyrrole substrate using either cyclic voltammetry scans or chronopotentiometry potential steps, the tip was placed in close proximity to the substrate so as to measure the rate of ejection of bromide or ferrocyanide as a function of the reduction potential applied to the PPy film. Interestingly, it was shown that the identity of the cation (tetrabutylammonium TBA^+ or potassium K^+ cation) influences substantially the ion transport kinetics of ferrocyanide in a ferrocyanide-doped polypyrrole film. For example, TBA^+ cations were found to slow down the ejection of ferrocyanide during reduction, and it appeared that ferrocyanide species were also rejected during the oxidation step of the PPy film, whereas the incorporation of cations (such as hexa-ammino ruthenium cations) was confirmed during the reduction step.

SECM was also used to evaluate the conductivity changes of polybithiophene microstructures deposited by a laser-assisted microstructuring deposition technique as a function of their doping level, controlled by fixing the potential value at the polymer sample [163]. In order to achieve this purpose, the feedback mode of SECM was used in an electrolytic solution containing $[Ir(CN)_6]^{2-/3-}$.

From SECM studies of the electrochemical doping and undoping processes of poly-(didodecyl-terthiophene), the electron transfer between the polymer and a redox mediator in solution was investigated as a function of the doping state of the polymer [164]. The electron transfer was found to occur at the polymer–electrolytic-solution interface and not inside the polymer film. The investigated polymer films are not permeable to redox species when placed in the neutral state and therefore behave as completely passivating films.

Thin films of poly-(3-ethoxy-thiophene) (PEOT) and poly(ethylenedioxythiophene) (PEDOT) were bombarded with Ar^+ ions and then tested in terms of conductivity with the help of SECM in the feedback mode using ferrocene–methanol as redox mediator [165]. It was thus shown that the main consequence of bombardment is the creation of an approximately 30 nm thick layer that behaves mainly as an insulator. More precisely, SECM imaging, as well as the approach curves, actually reveals regions with different conductivities. By patterning such polymers using ion bombardment through adequate masks, it was possible to locally perform galvanic copper deposition onto conducting PEDOT so as to create miniaturized printed circuit boards. The feasibility of the process was established once the conducting polymer patterns had been tested using SECM to detect possible defects.

In an original contribution, Mandler *et al.* used SECM to investigate local injection and lateral propagation of charge in thin polyaniline films [166]. The SECM probe was positioned in the immediate vicinity of a chemically reduced PANI layer and polarized so as to generate a flux of an oxidant, $Fe(phen)_3^{3+}$ in this case, which could then diffuse towards the PANI surface and locally oxidize the polymer. The current–time transients were then simulated so as to allow the evaluation of the kinetics of lateral charge propagation, based exclusively on electron hopping.

In another approach, SECM permitted the *in situ* characterization of the insulator-to-metal transition of a Langmuir polyaniline (PANI) monolayer resulting from progressive evolution of the surface pressure [167]. In order to do so, a flux of electroactive species able to undergo a redox reaction at the polymer–electrolytic-solution interface was generated by using the polarized SECM tip. The extent of the expected reaction will depend on the surface conductivity of the film. It was demonstrated that the surface pressure strongly influences the tip current. As the tip approaches the polymer surface, low pressures led to a decrease in the steady-state current, whereas higher pressures led to an increase in the tip current. This dependence of the tip current on the surface pressure was explained by an insulator-to-metal transition resulting from the compression of the film that potentially reduces the distances between the PANI chains. This may suggest that interchain transfer is a possible rate-limiting process controlling conductivity.

Ion-transport studies carried out on ferrocyanide-doped PEDOT films with the help of SECM revealed that ferrocyanide ions can be exchanged with chloride ions present in the transfer electrolytic solution [168]. SECM also revealed that only ferrocyanide ions are released during the electrochemical reduction of these films.

In a procedure inspired by reference [162] PEDOT films doped with various anions, such as chloride, ferrocyanide and poly(*p*-styrenesulfonate), were the target of ion-transport studies using SECM [169]. The results differed in that, in this work, the identity of the cation was not found to influence the ion-transport kinetics in ferrocyanide-doped PEDOT films.

Recently, the substrate-generation/tip-collection mode of SECM was exploited to confirm the release of oligomers by PEDOT films electrogenerated from aqueous solutions

[170]. Such a study was made possible by the fact that the released oligomers were neutral and electrochemically active. The tip was placed close to the polymer sample and polarized at a well-determined potential so as to permit the collection and electrochemical detection of the oligomers and their electrochemical oxidation. The ejection of oligomers was the result of a series of potential scans applied to the polymer sample inside a potential range only slightly narrower on the anodic side than the one allowing the doping–undoping of the polymer sample. Oligomers were rejected in solution mainly inside the first half of the scanned potential range and also during the first scan and to a lesser extent during the five following scans.

The SECM investigations reported above confirm that SECM is another valuable kind of scanning probe microscopy relevant for studying inhomogeneity in electronically conducting polymers *in situ* (i.e. in an electrolytic solution). The targeted properties, i.e. mainly the roughness, the electronic conductivity, and the ion-exchange behavior of these materials, can be efficiently identified and/or mapped. On the other hand, the need for either soluble redox-active couples or electroactive ions for SECM investigations related to the electronic conductivity or the ion-exchange properties of ECPs, respectively, is the first limitation of this technique for such studies. Another and a more severe limitation of this technique is that the micrometric size usually encountered in the literature for SECM probes is too large by comparison with that required to study the nanometric size (about 10–100 nm) of domains existing in ECPs. This latter limitation is likely to be temporary only, as recent literature reveals important efforts aimed at allowing local electrochemical measurements to be carried out at nanometer resolution either with SECM or AFM by developing reproducible and controlled elaboration strategies for corresponding nanometric electrochemical probes.

3.4 The Origin of the Nanoscale Inhomogeneity of Conducting and Semiconducting Polymers

The previous sections have demonstrated that there is a considerable body of experimental evidence obtained by a variety of experimental techniques that all provide a surprisingly similar picture: π-conjugated organic polymer materials, whether in their doped conducting or undoped semiconducting state, consistently and universally feature pronounced nanoscale structural inhomogeneity. Specifically, these materials were shown to contain a complex array of more ordered, often crystalline, domains scattered in a more disordered amorphous polymer matrix. In many cases, the domain distribution was linked to the material morphology; in some cases, such a link was not obvious or not pursued, but could not be ruled out. The reported sizes of the domains were also remarkably similar, ranging in most cases from 15–20 to 100–200 nm. In the cases when smaller domains were not observed, this could be readily related to the insufficient resolution of the technique in question (such as NSOM). Corresponding variations in the doping level/conductivity were also observed.

The question of correlation between the morphology and the domain structure is very important because it allows one to understand the origins of the inhomogeneity and the

reasons for the occurrence of the domain structure. Surprisingly, this problem has not attracted any particular attention in the literature. The prevailing view has been that the domain formation is a stochastic process originating from random folding of the polymer chains. In some areas, the chains could form a more ordered structure due to various structural factors, forming crystalline domains, and in some areas the chain stacking was less perfect and more disordered, and an amorphous phase was formed. This view was implicit in early models of charge transport in conducting and semiconducting polymers, such as Bassler's Gaussian disorder model [13], and even the later models [8,12,14,17–19], while introducing a certain spatial correlation of energies and thus providing a starting point for the understanding of nanoscale inhomogeneity, were based on the concept of random active-site/energy distributions. However, this viewpoint could not adequately explain numerous well-established experimental observations, such as the role of preparation conditions (solvent, the deposition technique, annealing, polydispersity), as well as the correlation between the inhomogeneity and the material morphology.

In order to better understand this problem, let us consider in more detail the process of formation of polymer films. First of all, while there are various preparation techniques for these materials, all of them involve deposition of a solid polymer phase from either solution (spin-coating, dip-coating, drop-coating, electrochemical polymerization) or from melt (annealing/solidification) onto a solid substrate. The new phase formation always starts with nucleation, or formation on the substrate surface of small clusters of molecules, which subsequently grow to form the polymer material. The nucleation and growth of a new phase have been the subjects of numerous treatises and textbooks (see, e.g., references [171–173]). However, these studies refer to the situation when the nucleation and growth of a new phase occurs from solution or melt that contains only one type of depositing species or, in some cases, like alloy electrodeposition, of several chemically distinct species. In this section, we will examine the situation that arises in most practical preparation techniques for conducting polymer films, which involve the deposition of the polymer phase from solution or melt containing a considerable variety of species of the same polymer which, nevertheless, feature different properties, first and foremost, the MWs. Obviously, all these species will possess different Gibbs energies and entropies, as well as other properties, such as solubilities. A natural question arises: how the presence of polymer species with different MWs, or polydispersity, will affect the new phase formation, as well as the properties of the polymer films obtained. The inhomogeneity of the polymer films themselves also suggests variations in the energy and entropy of local domains found in these materials, which also should be taken into account. A very important question that arises here is if and how variation in the properties of the starting polymer materials in the solution or melt (polydispersity) is related to variation in the properties of the resulting polymer materials (inhomogeneity).

The driving force for film formation, in the most general form, is the difference in the Gibbs free energies of the polymeric species in the solid state and in the solution/melt. The entropy of a solid phase is always lower than that of a liquid or melt; therefore, for the formation process to be spontaneous, there should be a gain in the enthalpy upon solid phase formation. Such gains are usually attributed to the establishment of new strong bonds between the atoms or molecules in the solid state, which lowers the overall energy of the system. With polymer molecules, these energy gains would be more pronounced if a crystalline phase is formed, since ordered phases feature the most favorable electron

delocalization and also numerous favorable interchain interactions, such as π-stacking, side-chain interdigitation, etc. The formation of a disordered solid should result in a smaller energy gain, since there is less or no electron delocalization and the interchain interactions are much weaker (if anything, disorder results in a dramatic decrease in the number of sites where the polymer chains actually come close enough to form an intermolecular bond). However, disordered phases feature higher entropy and, thus, their formation may be favored under some circumstances. The formation of small clusters also results in a less pronounced energy gain, since a disproportionate number of molecules lie at the cluster surface and thus cannot lower their energy as efficiently as the molecules inside the cluster. This phenomenon is associated with the surface tension and the surface energy.

Thermodynamically, if there is an equilibrium between a solution and a solid state, the Gibbs free energies ΔG of a polymer species in solution and in the solid state are equal. The equilibrium concentration of the polymer species in solution is then called the saturated concentration, *Cs*. In the case of a polydisperse polymer, there will be polymer species with different MWs, both in solution and in the solid state, all of which will feature unique energies and saturated concentrations. To describe their contributions, chemical potentials of species μ_i are used, which are partial molar quantities and represent the change in the overall Gibbs energy of the system upon addition of one mole of the species in question.

In equilibrium, the rate of polymer deposition is equal to the rate of polymer dissolution. In order to form a film, the equilibrium must be shifted towards solid-state formation, which can be achieved, for instance, by increasing the concentration of polymer species in the solution above the equilibrium, saturated concentration. This is called supersaturation. Thermodynamically, supersaturation reduces the entropy of the species in solution, thus providing the driving force for solid-state formation (the entropy penalty due to polymer transfer from the liquid to the solid state is reduced, while the enthalpy gain is the same). Supersaturation can be achieved either by removing/evaporating a portion of the solvent (spin-coating, drop-coating), or by rapidly forming an excess of the polymeric species in solution well above the saturated concentration (electrochemical and chemical polymerization).

It is important to recognize that the driving force of the new phase formation will not be the same at different stages of polymer film deposition, neither it will be the same for polymer molecules with different MWs. In order to better understand the situation, let us use the usual approach adopted in nucleation and growth theory and consider formation of a spherical nucleus with a radius *r* on the surface of a foreign substrate (foreign means there is no specific interaction, like chemical bond formation, between the deposited molecules and the substrate). The work of new phase formation *W* can be expressed as follows:

$$W = -\frac{4}{3}\frac{\pi \cdot r^3}{V_M} \cdot \mu_i + 4 \cdot \pi \cdot r^2 \cdot \gamma \tag{3.3}$$

where μ_i is the chemical potential of the polymeric species *i* in the solid state with respect to that in the solution (at this time we assume, for simplicity, that only one type of polymer species is present), V_M is the molar volume, and γ is the surface tension at the solid polymer/solution interface.

The first term represents the energy gain due to the formation of a new bulk phase. This gain is proportional to the volume of the new phase formed. Both the entropy and enthalpy factors are taken into account by the chemical potential μ_i. This term is usually negative, since energy is gained (the chemical potential of a species in the solid state is more negative than that in solution). The second term is the surface energy of the growing cluster, which is proportional to the cluster surface area and the surface tension γ at the interface between the solid polymer and the solution. This term is positive; the larger the surface area, the greater the surface energy and the less energetically favorable the deposition process.

As follows from Eq. (3.3), the work of the new phase formation has a complex dependence on the radius of the nucleus r, which is illustrated in Figure 3.14. Specifically, the work first grows with r since the gain in the bulk energy does not compensate for the energy of the new surface formation. This means the formation of the new phase is not a spontaneous process. However, as r increases, the relative contribution of the surface vs. the bulk energy decreases (r^2 vs. r^3), and the work of the new phase formation starts to become negative too, making the deposition process spontaneous. The curve has a maximum at a certain critical radius r^*, which can be found from Eq. (3.3) to be:

$$r^* = V_M \frac{2\gamma}{\mu_i} \tag{3.4}$$

Mechanistically, the new phase formation starts with the formation of polymer nuclei at the substrate surface. This process can be thought of as a dynamic equilibrium between stochastic formation and dissociation of clusters of polymer molecules with various sizes. If a cluster has size less than r^*, its formation is energetically unfavorable ($W > 0$) and it will be dissolved. However, if a cluster has a size that exceeds the critical radius r^*, its formation will be energetically favorable ($W < 0$). Furthermore, such a cluster or nucleus will undergo spontaneous growth by attracting polymer material from the solution, since an increase in the cluster size maximizes the energy gain (see Eq. (3.3) and Figure 3.14). Ultimately, the cluster grows to form a polymer grain or a globule.

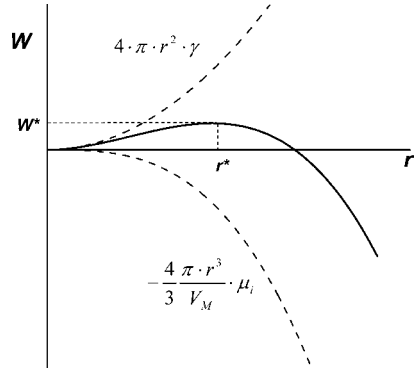

Figure 3.14 *Illustration of the dependence of the work of the new phase formation* W *on the nucleus radius* r

The value of the critical radius has a profound impact on the number of nuclei formed and thus on the morphology of the resulting material. Smaller critical radii make the formation of new nuclei easier; more nuclei survive and compete for the polymer material deposited from the solution phase. Therefore, a high driving force for deposition produces many small grains. Larger critical radii mean that only a few nuclei are formed, all other nuclei formed through local fluctuations are too small and dissolve. In this case, fewer, but larger, grains are formed.

If several polymer species are present in solution at the same time, each of the species will have its own work of nucleation determined by its own chemical potential μ_i. Overall, the deposition will be determined by the driving force of nucleation and ultimately by the maximal gain in energy as determined by the chemical potential differences. If the energy gain for a certain species is greater than for another species, the driving force of deposition will be greater for the former species. Therefore, the clusters of these species will have a smaller critical radius and thus a greater probability of surviving and becoming the cores of polymer globules. At the nucleus growth stage, the driving force required to deposit polymer molecules on the existing polymer grains becomes progressively smaller as the polymer grain grows (see Eq. (3.3)). This makes it possible for the polymer species with the lower deposition driving force (a less negative difference in the chemical potentials between the solid and liquid phases) to deposit. An additional factor here would be that the nucleation occurs at a foreign substrate surface and thus requires a specifically high energy gain to take place. The growth of already-formed nuclei occurs through polymer molecules depositing on the surface of the polymer phase, so that the depositing molecules can form much stronger bonds with the surface and thus lower their energy more efficiently. Overall, all these factors should result in a complex heterogeneous grain structure with the species with the higher driving force forming the cores of the grains and the species with the lower driving force deposited at later stages of grain growth and thus predominantly found at the grain periphery.

In the simplest case, when the only component of the driving force of nucleation is supersaturation, that is, the increase in the concentration of depositing species C over the saturated concentration C_s, Eq. (3.4) can be resolved to yield the well-known Kelvin equation:

$$r^* = \frac{2 \cdot \gamma \cdot V_{\mathrm{M}}}{R_{\mathrm{gas}} T \cdot \ln\left(\dfrac{C}{C_{\mathrm{s}}}\right)} \tag{3.5}$$

This case was discussed by O'Neil *et al.* [41]. In this treatment, the only parameter that segregates different polymer species is the MW and the resulting solubility differences expressed through different C_s values. Higher-MW fractions always have lower solubility (lower C_s) than low-MW ones and thus smaller critical radii of nucleation. Therefore, they are deposited first and form the core of the polymer grains. The low-MW fractions are deposited later and form disordered grain periphery/grain boundaries. The driving force of nucleation in this case is determined only by the decrease in the entropy of the depositing species in the solution phase at supersaturation; there is no MW-dependent variation in the way the polymer molecules of various lengths can arrange themselves in the solid state and thus there is no corresponding variation in the enthalpy component of the chemical potential difference.

However, we remember from the previous discussions that generally this is not the case. Therefore, Eq. (3.5) should be updated to reflect this fact. In general, the most enthalpy gain should be expected for materials with high MWs since longer molecules have more ways to form intermolecular bonds and to lower their energy. There is experimental evidence to support this: Zen *et al.* [88] showed that solvatochromism, that is, the difference in the light absorption spectra of polymer fractions in solution and in the solid state, is most pronounced for high-MW fractions. The red shift in the solid state indicates better alignment and better interaction of the polymer chains. Later, the same group [89] used differential scanning calorimetry (DSC) to measure the melting enthalpies of P3HT fractions with various MW. The total melting enthalpy for the high MW (chloroform, Mn = 27.05 kDa) fraction was 23.7 J g^{-1}, or 640 kJ mol^{-1}, while the enthalpy for the low-MW (ethyl acetate, Mn = 2.58 kDa) fraction was only 4.54 J g^{-1}, or 11.7 kJ mol^{-1}.

Moreover, the most pronounced enthalpy gain occurs when a crystalline or at least a more-ordered solid is formed. If some polymer fractions can form a highly ordered crystalline phase in the solid state, and some cannot, there will be a pronounced difference in the driving force for deposition of these fractions, and the molecules that are able to form the crystalline phase will be deposited first. Therefore, in the process of nucleation and growth of new solid-state polymer phase from a supersaturated solution containing polymer fractions of varying MWs (a polydisperse polymer), which is a routine situation in all major polymer deposition processes, the nuclei will be entirely crystalline. All experimental data support this conclusion (see Section 3.2 and especially Subsection 3.2.5). The chief reason is that nucleation requires a considerably higher driving force, which is achieved only if the new phase formation features a particularly high enthalpy gain, as when a crystalline highly ordered phase is formed.

With non-regio-regular materials, such as regio-random polythiophenes, only high-MW fractions can form crystalline phases (see Section 3.2). The low-MW phase will be amorphous. Therefore, non-regio-regular materials will form high-MW crystalline grain cores surrounded by a low-MW amorphous grain periphery. This has been demonstrated experimentally [40,41]. The situation with regio-regular materials, such as regio-regular poly(3-alkylthiophene)s, is a bit more complex because low-MW fractions are able to form crystalline phases due to the ordering effect of interdigitized side chains (although their structures are different from those formed by the high-MW material). Therefore, highly polydisperse samples of regio-regular polymers feature three structures: low-MW anisotropic crystallites, such as haystack nanoribbons, high-MW more isotropic crystallites (observed as round globules), and an amorphous disordered phase between them. In fact, this behavior was demonstrated as early as in 1996 by DSC and X-ray diffraction studies with various poly(3-alkylthiophene) samples with different degree of head-to-tail (HT) regularity [3]. It was shown that materials with moderate HT regularity were formally amorphous, with some quasi-ordered domains dispersed in a continuous disordered matrix, while poly(3-alkylthiophene)s with high HT regularity consisted of crystalline, quasi-ordered, and disordered phases. The melting/crystallization enthalpies were notably higher in highly regio-regular materials, indicating their better crystallinity and higher enthalpy gain upon formation of the solid polymer phase, as opposed to materials with moderate HT regularity.

Therefore, if a solution of a regio-regular polymer contains low-MW fractions, they will be deposited first and form crystallites, which will be surrounded with a more disordered material that features a lower deposition driving force and thus will be deposited later. There is abundant experimental evidence that this is indeed the case (Section 3.2): numerous studies have shown the formation of typical haystack or nanoribbons crystallites embedded in a disordered amorphous phase. If the regio-regular material is fractionated to remove the fractions which can form such nanoribbons, the morphology of the material changes dramatically, but still there are ordered domains likely formed by high-MW polymer material surrounded by the disordered polymer matrix. The same is observed for polydisperse non-regio-regular materials because they cannot form a crystalline phase at low MW. However, in all cases the same pattern is observed, that the cores of the polymer grains or globules are formed by more-crystalline/ordered material, surrounded by a less-ordered/amorphous phase forming the periphery of the globules (grain boundaries). Our analysis provides a very simple explanation for this fact: the cores are crystalline because crystalline phases feature a larger driving force of deposition and thus are deposited first. The disordered phase has a lower driving force of deposition and thus can be deposited only later when the growing grains are sufficiently large. The decrease in the degree of crystallinity in the process of polymer film growth has been confirmed experimentally [36,40]. Furthermore, the difference in the driving force of nucleation at low and high MWs can also explain the changes in the morphology and, in particular, in the grain size of materials deposited from solutions containing polymer fractions with different average MWs [27,89]: the size of the polymer grains universally decreases with an increase in MW, as is to be expected, since a higher driving force means smaller critical nuclei able to survive and form the polymer grains.

Therefore, the detail analysis presented in this chapter suggests that the random folding model is at variance with the observed experimental data. Since the long chains and short chains are not deposited at the same time, the origin of heterogeneity is not that long chains randomly form some coherent ordered domains and some disordered portions that bridge these coherent domains, as suggested previously. Rather, the origin of the inhomogeneity is spatial and temporal segregation during the deposition process of the polymer molecules according to their MW and their ability to form crystalline phases. All this points to polydispersity, that is, the presence of fractions with different MWs in the polymer sample, as the main source of the resulting inhomogeneity of the deposited polymer material. The effect of polydispersity has been little studied in the literature; however, very recently, several papers have appeared that directly relate the inhomogeneity of the polymer films to polydispersity [22,27,40,41]. At a more general level, inhomogeneity is a way for a system to avoid the entropy penalty associated with formation of large continuous homogeneous phases (such as extra-large single crystals) and boost the free energy gain upon new phase formation. From the entropy standpoint, to obtain materials with low or no inhomogeneity and thus very low entropy, one should use materials with low starting entropy, such as solutions with low polydispersity, or the process will not be spontaneous. An example of this situation is crystallization of pure oligomers that produces large well-defined crystals [92] or polymer films deposited from solutions with very low polydispersity [22,27]. Our analysis suggests that the best way to control the inhomogeneity of conducting and semiconducting polymers prepared by deposition from solutions is to control the polydispersity of the starting polymer materials.

References

[1] P. Robin, J.P. Pouget, R. Comes, H.W. Gibson, and A.J. Epstein, X-ray-diffraction studies of iodine-doped polyacetylene. *Polymer*, **24**, 1558 (1983).

[2] J.P. Pouget, M.E. Jozefowicz, A.J. Epstein, X. Tang, and A.G. MacDiarmid, X-ray structure of polyaniline. *Macromolecules*, **24**, 779 (1991).

[3] C. Yang, F.P. Orfino, and S. Holdcroft, A phenomenological model for predicting thermochromism of regioregular and nonregioregular poly(3-alkylthiophenes). *Macromolecules*, **29**, 6510 (1996).

[4] H. Sirringhaus, P.J. Brown, R.H. Friend, M.M. Nielsen, K. Bechgaard, B.M.W. Langeveld-Voss, A.J.H. Spiering, R.A.J. Janssen, E.W. Meijer, P. Herwig, and D.M. de Leeuw, Two-dimensional charge transport in self-organized, high-mobility conjugated polymers. *Nature*, **401**, 685 (1999).

[5] K.E. Aasmundtveit, E.J. Samuelsen, M. Guldstein, C. Steinsland , O. Flornes, C. Fagermo, T.M. Seeberg, L.A.A. Pettersson, O. Inganas, R. Feidenhans'l, and S. Ferrer, Structural anisotropy of poly(alkylthiophene) films. *Macromolecules*, **33**, 3120 (2000).

[6] Z.H. Wang, C. Li, E.M. Scherr, A.G. MacDiarmid, and A.J. Epstein, 3 Dimensionality of metallic states in conducting polymers – polyaniline. *Phys. Rev. Lett.*, **66**, 1745 (1991).

[7] Z.H. Wang, E.M. Scherr, A.G. MacDiarmid, and A.J. Epstein, Transport and EPR studies of polyaniline – a quasi-one-dimensional conductor with 3-dimensional metallic states. *Phys. Rev. B*, **45**, 4190 (1992).

[8] V.N. Prigodin and K.B. Efetov, Localization transition in a random network of metallic wires – a model for highly conducting polymers. *Phys. Rev. Lett.*, **70**, 2932 (1993).

[9] R.S. Kohlman, D.B. Tanner, G.G. Ihas, Y.G. Min, A.G. MacDiarmid, and A.J. Epstein, Inhomogeneous insulator-metal transition in conducting polymers. *Synth. Met.*, **84**, 709 (1997).

[10] J. Joo, S.M. Long, J.P. Pouget, E.J. Oh, A.G. MacDiarmid, and A.J. Epstein, Charge transport of the mesoscopic metallic state in partially crystalline polyanilines. *Phys. Rev. B*, **57**, 9567 (1998).

[11] J. Joo, J.K. Lee, S.Y. Lee, K.S. Jsng, E.J. Oh, and A.J. Epstein, Physical characterization of electrochemically and chemically synthesized polypyrroles. *Macromolecules*, **33**, 5131(2000).

[12] V.N. Prigodin and A.J. Epstein, Nature of insulator-metal transition and novel mechanism of charge transport in the metallic state of highly doped electronic polymers. *Synth. Met.*, **125**, 43 (2002).

[13] H. Bassler, Charge transport in disordered organic photoconductors – a Monte-Carlo simulation study. *Phys. Status Solidi B-Basic Research*, **175**, 15 (1993).

[14] Y.N. Gartstein and E.M. Conwell, High-field hopping mobility in molecular-systems with spatially correlated energetic disorder. *Chem. Phys. Lett.*, **245**, 351 (1995).

[15] S.V. Novikov and A.V. Vannikov, Cluster structure in the distribution of the electrostatic potential in a lattice of randomly oriented dipoles. *J. Phys. Chem.*, **99**, 14573 (1995).

[16] P.W.M. Blom, M.J.M. deJong and M.G. vanMunster, Electric-field and temperature dependence of the hole mobility in poly(p-phenylene vinylene). *Phys. Rev. B*, **55**, R656 (1997).

[17] S.V. Novikov, D.H. Dunlap, V.M. Kenkre, P.E. Parris, and A.V. Vannikov, Essential role of correlations in governing charge transport in disordered organic materials. *Phys. Rev. Lett.*, **81**, 4472 (1998).

[18] P.W.M. Blom and M.C.J.M. Vissenberg, Charge transport in poly(*p*-phenylene vinylene) light-emitting diodes. *Mater. Sci. Eng., R*, **27**, 53 (2000).

[19] S.V. Rakhmanova and E.M. Conwell, Electric-field dependence of mobility in conjugated polymer films. *Appl. Phys. Lett.*, **76**, 3822 (2000).

[20] S.V. Novikov and A.V. Vannikov, Charge carrier transport in nonpolar disordered organic materials: What is the reason for Poole–Frenkel behavior? *Mol. Cryst. Liq. Cryst.*, **361**, 89 (2001).

[21] M.L. Chabinyc, X-ray scattering from films of semiconducting polymers. *Polym. Rev.*, **48**, 463 (2008).

[22] T. Jaroch, M. Knor, R. Nowakowski, M. Zagorska, and A. Pron, Effect of molecular mass on supramolecular organisation of poly(4,4″-dioctyl-2,2′:5′,2″-terthiophene). *Phys. Chem. Chem. Phys.*, **10**, 6182 (2008).

[23] N. Zhao, G.A. Botton, S.P. Zhu, A. Duft, B.S. Ong, Y.L. Wu, and P. Liu, Microscopic studies on liquid crystal poly(3,3‴-dialkylquaterthiophene) semiconductor. *Macromolecules*, **37**, 8307 (2004).

[24] B.S. Ong, Y.L. Wu, P. Liu, and S. Gardner, Structurally ordered polythiophene nanoparticles for high-performance organic thin-film transistors. *Adv. Mater.*, **17**, 1141 (2005).

[25] Y.O. Wu, P. Liu, B.S. Ong, T. Srikumar, N. Zhao, G. Botton, and S.P. Zhu, Controlled orientation of liquid-crystalline polythiophene semiconductors for high-performance organic thin-film transistors. *Appl. Phys. Lett.*, **86**, 142102 (2005).

[26] P. Keg, A. Lohani, D. Fichou, Y.M. Lam, Y.L. Wu, B.S. Ong, and S.G. Mhaisalkar, Direct observation of alkyl chain interdigitation in conjugated polyquarterthiophene self-organized on graphite surfaces. *Macromol. Rapid Commun*, **29**, 1197 (2008).

[27] P. Pingel, A. Zen, D. Neher, I. Lieberwirth, G. Wegner, S. Allard, and U. Scherf, Unexpectedly high field-effect mobility of a soluble, low molecular weight oligoquaterthiophene fraction with low polydispersity. *Appl. Phys. A: Mater. Sci. Process.*, **95**, 67 (2009).

[28] M. Brun, R. Demadrille, P. Rannou, A. Pron, J.P. Travers, and B. Grevin, Multiscale scanning tunneling microscopy study of self-assembly phenomena in two-dimensional polycrystals of pi-conjugated polymers: the case of regioregular poly (dioctylbithiophene-alt-fluore-none). *Adv. Mater.*, **16**, 2087 (2004).

[29] I. McCulloch, M. Heeney, M.L. Chabinyc, D. DeLongchamp, R.J. Kline, M. Coelle, W. Duffy, D. Fischer, D. Gundlach, B. Hamadani, R. Hamilton, L. Richter, A. Salleo, M. Shkunov, D. Sporrowe, S. Tierney, and W. Zhong, Semiconducting thienothiophene copolymers: design, synthesis, morphology, and performance in thin-film organic transistors. *Adv. Mater.*, **21**, 1091 (2009).

[30] Q.L. Bao, J. Li, C.M. Li, Z.L. Dong, Z.S. Lu, F. Qin, C. Gong, and J. Guo, Direct observation and analysis of annealing-induced microstructure at interface and its effect on performance improvement of organic thin film transistors. *J. Phys. Chem. B*, **112**, 12270 (2008).

[31] O.A. Semenikhin, L. Jiang, T. Iyoda, K. Hashimoto, and A. Fujishima, Atomic force microscopy and Kelvin probe force microscopy evidence of local structural inhomogeneity and nonuniform dopant distribution in conducting polybithiophene. *J. Phys. Chem.*, **100**, 18603 (1996).

[32] J.W. Blatchford, T.L. Gustafson, A.J. Epstein, D.A. VandenBout, J. Kerimo, D.A. Higgins, P.F. Barbara, D.K. Fu, T.M. Swager, and A.G. MacDiarmid, Spatially and temporally resolved emission from aggregates in conjugated polymers. *Phys. Rev. B*, **54**, R3683 (1996).

[33] O.A. Semenikhin, L. Jiang, T. Iyoda, K. Hashimoto, and A. Fujishima, *In situ* AFM study of the electrochemical deposition of polybithiophene from propylene carbonate solution. *Synth. Met.*, **110**, 195 (2000).

[34] O.A. Semenikhin, L. Jiang, T. Iyoda, K. Hashimoto, and A. Fujishima, A Kelvin probe force microscopic study of the local dopant distribution in conducting polybithiophene. *Electrochim. Acta*, **42**, 3321 (1997).

[35] O.A. Semenikhin, L. Jiang, K. Hashimoto, and A. Fujishima, Kelvin probe force microscopic study of anodically and cathodically doped poly-3-methylthiophene. *Synth. Met.*, **110**, 115 (2000).

[36] M. Skompska, Alternative explanation of asymmetry in cyclic voltammograms for redox reaction of poly(3-methylthiophene) films in acetonitrile solutions. *Electrochim. Acta*, **44**, 357 (1998).

[37] A.R. Hillman, I. Efimov, and M. Skompska, Dynamics of regioregular conducting polymer electrodes in response to electrochemical stimuli. *Faraday Discuss.*, **121**, 423 (2002).

[38] J.N. Barisci, R. Stella, G.M. Spinks, and G.G. Wallace, Characterisation of the topography and surface potential of electrodeposited conducting polymer films using atomic force and electric force microscopies. *Electrochim. Acta*, **46**, 519 (2000).

[39] J.N. Barisci, R. Stella, G.M. Spinks, and G.G. Wallace, Study of the surface potential and photovoltage of conducting polymers using electric force microscopy. *Synth. Met.*, **124**, 407 (2001).

[40] K.D. O'Neil and O.A. Semenikhin, AFM phase imaging of electropolymerized polybithiophene films at different stages of their growth. *J. Phys. Chem. C*, **111**, 14823 (2007).

[41] K.D. O'Neil, B. Shaw, and O.A. Semenikhin, On the origin of mesoscopic inhomogeneity of conducting polymers. *J. Phys. Chem. B*, **111**, 9253 (2007).
[42] T. Hassenkam, D.R. Greve, and T. Bjornholm, Direct visualization of the nanoscale morphology of conducting polythiophene monolayers studied by electrostatic force microscopy. *Adv. Mater.*, **13**, 631 (2001).
[43] B. Bush, G.H. Xu, C. Carraro, and R. Maboudian, Layer-by-layer self-assembled conductive thin films for MEMS applications. *Sens. Actuators, A*, **126**, 194 (2006).
[44] M. Chiesa, L. Burgi, J.S. Kim, R. Shikler, R.H. Friend, and H. Sirringhaus, Correlation between surface photovoltage and blend morphology in polyfluorene-based photodiodes. *Nano Lett.*, **5**, 559 (2005).
[45] T. Glatzel, H. Hoppe, N.S. Sariciftci, M.C. Lux-Steiner, and M. Komiyama, Kelvin probe force microscopy study of conjugated polymer/fullerene organic solar cells. *Jpn. J. Appl. Phys. Part 1*, **44**, 5370 (2005).
[46] H. Hoppe, T. Glatzel, M. Niggemann, A. Hinsch, M.C. Lux-Steiner, N.S. Sariciftci, Kelvin probe force microscopy study on conjugated polymer/fullerene bulk heterojunction organic solar cells. *Nano Lett.*, **5**, 269 (2005).
[47] D.C. Coffey and D.S. Ginger, Time-resolved electrostatic force microscopy of polymer solar cells. *Nat. Mat.*, **5**, 735 (2006).
[48] H. Hoppe, T. Glatzel, M. Niggemann, W. Schwinger, F. Schaeffler, A. Hinsch, M.C. Lux-Steiner, and N.S. Sariciftci, Efficiency limiting morphological factors of MDMO-PPV: PCBM plastic solar cells. *Thin Solid Films*, **511**, 587 (2006).
[49] A.A. Alagiriswamy, C. Jager, D. Haarer, M. Thelakkat, A. Knoll, and G. Krausch, Local potential distribution of macrophase separated polymer blend domains. *J. Phys. D: Appl. Phys.*, **40**, 4855 (2007).
[50] A. Liscio, G. De Luca, F. Nolde, V. Palermo, K. Muellen, and P. Samori, Photovoltaic charge generation visualized at the nanoscale: A proof of principle. *J. Am. Chem. Soc.*, **130**, 780 (2008).
[51] K. Maturova, M. Kemerink, M.M. Wienk, D.S.H. Charrier, and R.A.J. Janssen, Scanning Kelvin probe microscopy on bulk heterojunction polymer blends. *Adv. Funct. Mater.*, **19**, 1 (2009).
[52] L.S.C. Pingree, O.G. Reid, and D.S. Ginger, Electrical scanning probe microscopy on active organic electronic devices. *Adv. Mater.*, **21**, 19 (2009).
[53] D.H. Han, H.J. Lee, and S.M. Park, Electrochemistry of conductive polymers XXXV: Electrical and morphological characteristics of polypyrrole films prepared in aqueous media studied by current sensing atomic force microscopy. *Electrochim. Acta*, **50**, 3085 (2005).
[54] H.J. Lee and S.M. Park, Electrochemistry of conductive polymers. 30. Nanoscale measurements of doping distributions and current-voltage characteristics of electrochemically deposited polypyrrole films. *J. Phys. Chem. B*, **108**, 1590 (2004).
[55] H.J. Lee and S.M. Park, Electrochemistry of conductive polymers 37. Nanoscale monitoring of electrical properties during electrochemical growth of polypyrrole and its aging. *J. Phys. Chem. B*, **109**, 13247 (2005).
[56] D.H. Han and S.M. Park, Electrochemistry of conductive polymers. 32. Nanoscopic examination of conductivities of polyaniline films. *J. Phys. Chem. B*, **108**, 13921 (2004).
[57] S.Y. Hong and S.M. Park, Electrochemistry of conductive polymers 36. pH dependence of polyaniline conductivities studied by current-sensing atomic force microscopy. *J. Phys. Chem. B*, **109**, 9305 (2005).
[58] H.J. Lee and S.M. Park, Electrochemistry of conductive polymers. 33. Electrical and optical properties of electrochemically deposited poly(3-methylthiophene) films employing current-sensing atomic force microscopy and reflectance spectroscopy. *J. Phys. Chem. B*, **108**, 16365 (2004).
[59] D.H. Han, J.W. Kim, and S.M. Park, Electrochemistry of conductive polymers 38. Electrodeposited poly(3,4-ethylenedioxy-thiophene) studied by current-sensing atomic force microscopy. *J. Phys. Chem. B*, **110**, 14874 (2006).
[60] J. Kim, S. Cho, S. Choi, S. Baek, D. Lee, O. Kim, S.M. Park, and M. Ree, Novel electrical properties of nanoscale thin films of a semiconducting polymer: Quantitative current-sensing AFM analysis. *Langmuir*, **23**, 9024 (2007).

[61] S.S. Chang and C.G. Wu, Effects of polymerization media on the nanoscale conductivity and current-voltage characteristics of chemically synthesized polyaniline films. *J. Phys. Chem. B*, **109**, 18275 (2005).
[62] C.G. Wu and S.S. Chang, Nanoscale measurements of conducting domains and current – Voltage characteristics of chemically deposited polyaniline films. *J. Phys. Chem. B*, **109**, 825 (2005).
[63] H.N. Lin, H.L. Lin, S.S. Wang, L.S. Yu, G.Y. Perng, S.A. Chen, and S.H. Chen, Nanoscale charge transport in an electroluminescent polymer investigated by conducting atomic force microscopy. *Appl. Phys. Lett.*, **81**, 2572 (2002).
[64] L.S. C. Pingree, B.A. MacLeod, and D.S. Ginger, The changing face of PEDOT: PSS films: Substrate, bias, and processing effects on vertical charge transport. *J. Phys. Chem. C*, **112**, 7922 (2008).
[65] X.D. Dang, M. Dante, and T.Q. Nguyen, Morphology and conductivity modification of poly(3,4-ethylenedioxythiophene):poly(styrene sulfonate) films induced by conductive atomic force microscopy measurements. *Appl. Phys. Lett.*, **93**, 241911 (2008).
[66] T.T. Kantzas, K.D. O'Neil, and O.A. Semenikhin, The effect of preparation conditions on the photoelectrochemical properties of polybithiophene based photoelectrodes. *Electrochim. Acta*, **53**, 1225 (2007).
[67] C. Ionescu-Zanetti, A. Mechler, S.A. Carter, and R. Lal, Semiconductive polymer blends: Correlating structure with transport properties at the nanoscale. *Adv. Mater.*, **16**, 385 (2004).
[68] A. Alexeev, J. Loos, and M.M. Koetse, Nanoscale electrical characterization of semiconducting polymer blends by conductive atomic force microscopy. *Ultramicroscopy*, **106**, 191 (2006).
[69] D.C. Coffey, O.G. Reid, D.B. Rodovsky, G.P. Bartholomew, and D.S. Ginger, Mapping local photocurrents in polymer/fullerene solar cells with photoconductive atomic force microscopy. *Nano Lett.*, **7**, 738 (2007).
[70] O. Douheret, A. Swinnen, S. Bertho, I. Haeldermans, J. D'Haen, M. D'Olieslaeger, D. Vanderzande, and J.V. Manca, High-resolution morphological and electrical characterisation of organic bulk heterojunction solar cells by scanning probe microscopy. *Prog. Photovoltaics*, **15**, 713 (2007)
[71] A. Alexeev and J. Loos, Conductive atomic force microscopy (C-AFM) analysis of photoactive layers in inert atmosphere. *Org. Electron.*, **9**, 149 (2008).
[72] E. Lacaze, K. Uvdal, P. Bodo, J. Garbarz, W.R. Salaneck, and M. Schott, Scanning tunneling microscopy of single polyalkylthiophene molecules adsorbed on graphite. *J. Polym. Sci., Part B: Polym. Phys.*, **31**, 111 (1993).
[73] E. Mena-Osteritz, A. Meyer, B.M.W. Langeveld-Voss, R.A.J. Janssen, E.W. Meijer, and P. Bauerle, Two-dimensional crystals of poly(3-alkylthiophene)s: Direct visualization of polymer folds in submolecular resolution. *Angew. Chem., Int. Ed.*, **39**, 2680 (2000).
[74] E. Mena-Osteritz, Superstructures of self-organizing thiophenes. *Adv. Mater.*, **14**, 609 (2002).
[75] S.T. Yau, J.N. Barisci, and G.M. Spinks, Tunneling spectroscopy and spectroscopic imaging of granular metallicity of polyaniline. *Appl. Phys. Lett.*, **74**, 667 (1999).
[76] M. Kemerink, S. Timpanaro, M.M. de Kok, E.A. Meulenkamp, and F.J. Touwslager, Three-dimensional inhomogeneities in PEDOT: PSS films. *J. Phys. Chem. B*, **108**, 18820 (2004).
[77] B. Grevin, P. Rannou, R. Payerne, A. Pron, and J.P. Travers, Scanning tunneling microscopy investigations of self-organized poly(3-hexylthiophene) two-dimensional polycrystals. *Adv. Mater.*, **15**, 881 (2003).
[78] B. Grevin, P. Rannou, R. Payerne, A. Pron, J.P. Travers, Multi-scale scanning tunneling microscopy imaging of self-organized regioregular poly(3-hexylthiophene) films. *J. Chem. Phys.*, **118**, 7097 (2003).
[79] R. Payerne, M. Brun, P. Rannou, R. Baptist, and B. Grevin, STM studies of poly(3-alkylthiophene)s: model systems for plastic electronics. *Synth. Met.*, **146**, 311 (2004).
[80] S.N. Magonov and D.H. Reneker, Characterization of polymer surfaces with atomic force microscopy. *Annu Rev. Mater. Sci.*, **27**, 175 (1997).
[81] M. Brinkmann and P. Rannou, Effect of molecular weight on the structure and morphology of oriented thin films of regioregular poly(3-hexylthiophene) grown by directional epitaxial solidification. *Adv. Funct. Mater.*, **17**, 101 (2007).

[82] F.L. Leite, W.F. Alves, M. Mir, Y.P. Mascarenhas, P.S.P. Herrmann, L.H.C. Mattoso, and O.N. Oliveira, TEM, XRD and AFM study of poly(*o*-ethoxyaniline) films: new evidence for the formation of conducting islands. *Appl. Phys. A: Mater. Sci. Process.*, **93**, 537 (2008).
[83] M. Brinkmann and P. Rannou, Molecular weight dependence of chain packing and semicrystalline structure in oriented films of regioregular poly(3-hexylthiophene) revealed by high-resolution transmission electron microscopy. *Macromolecules*, **42**, 1125 (2009).
[84] S. Osawa, M. Ito, S. Iwase, H. Yajima, R. Endo, and K. Tanaka, Effects of molecular-weight on the electrical-properties of electrochemically synthesized poly(3-hexylthiophene). *Polymer*, **33**, 914 (1992).
[85] M. Kobashi and H. Takeuchi, Inhomogeneity of spin-coated and cast non-regioregular poly(3-hexylthiophene) films. Structures and electrical and photophysical properties. *Macromolecules*, **31**, 7273 (1998).
[86] R.J. Kline, M.D. McGehee, E.N. Kadnikova, J.S. Liu, and J.M.J. Frechet, Controlling the field-effect mobility of regioregular polythiophene by changing the molecular weight. *Adv. Mater.*, **15**, 1519 (2003).
[87] R.J. Kline, M.D. McGehee, E.N. Kadnikova, J.S. Liu, J.M.J. Frechet, and M.F. Toney, Dependence of regioregular poly(3-hexylthiophene) film morphology and field-effect mobility on molecular weight. *Macromolecules*, **38**, 3312 (2005).
[88] A. Zen, J. Pflaum, S. Hirschmann, W. Zhuang, F. Jaiser, U. Asawapirom, J.P. Rabe, U. Scherf, and D. Neher, Effect of molecular weight and annealing of poly (3-hexylthiophene)s on the performance of organic field-effect transistors. *Adv. Funct. Mater.*, **14**, 757 (2004).
[89] A. Zen, M. Saphiannikova, D. Neher, J. Grenzer, S. Grigorian, U. Pietsch, U. Asawapirom, S. Janietz, U. Scherf, I. Lieberwirth, and G. Wegner, Effect of molecular weight on the structure and crystallinity of poly(3-hexylthiophene). *Macromolecules*, **39**, 2162 (2006).
[90] J.M. Verilhac, G. LeBlevennec, D. Djurado, F. Rieutord, M. Chouiki, J.P. Travers, and A. Pron, Effect of macromolecular parameters and processing conditions on supramolecular organisation, morphology and electrical transport properties in thin layers of regioregular poly(3-hexylthiophene). *Synth. Met.*, **156**, 815 (2006).
[91] J.F. Chang, J. Clark, N. Zhao, H. Sirringhaus, D.W. Breiby, J.W. Andreasen, M.M. Nielsen, M. Giles, M. Heeney, and I. Mcculloch, Molecular-weight dependence of interchain polaron delocalization and exciton bandwidth in high-mobility conjugated polymers. *Phys. Rev. B*, **74**, 115318 (2006).
[92] D. Fichou, Structural order in conjugated oligothiophenes and its implications on opto-electronic devices. *J. Mater. Chem.*, **10**, 571 (2000).
[93] M.L. Chabinyc, M.F. Toney, R.J. Kline, I. McCulloch, and M. Heeney, X-ray scattering study of thin films of poly(2,5-bis(3-alkylthiophen-2-yl)thieno[3,2-b]thiophene). *J. Am. Chem. Soc.*, **129**, 3226 (2007).
[94] L.H. Jimison, A. Salleo, M.L. Chabinyc, D.P. Bernstein, and M.F. Toney, Correlating the microstructure of thin films of poly[5,5-bis(3-dodecyl-2-thienyl)-2,2-bithiophene] with charge transport: Effect of dielectric surface energy and thermal annealing. *Phys. Rev. B*, **78**, 125319 (2008).
[95] A.R. Inigo, C.C. Chang, W. Fann, J.D. White, Y.S. Huang, U.S. Jeng, H.S. Sheu, K.Y. Peng, and S.A. Chen, Enhanced hole mobility in poly-(2-methoxy-5-(2′-ethylhexoxy)-1,4-phenylenevinylene) by elimination of nanometer-sized domains. *Adv. Mater.*, **17**, 1835 (2005).
[96] Y.F. Huang, A.R. Inigo, C.C. Chang, K.C. Li, C.T. Liang, C.W. Chang, T.S. Lim, S.H. Chen, J.D. White, U.S. Jeng, A.C. Su, Y.S. Huang, K.Y. Peng, S.A. Chen, W.W. Pai, C.H. Lin, L.R. Tameev, S.V. Novikov, A.V. Vannikov, and W.S. Fann, Nanostructure-dependent vertical charge transport in MEH-PPV films. *Adv. Funct. Mater.*, **17**, 2902 (2007).
[97] G. Horowitz, B. Bachet, A. Yassar, P. Lang, F. Demanze, J.L. Fave, and F. Garnier, Growth and Characterization of Sexithiophene Single-Crystals. *Chem. Mater.*, **7**, 1337 (1995).
[98] V. Coropceanu, J. Cornil, D.A. da Silva, Y. Olivier, R. Silbey, and J.L. Bredas, Charge transport in organic semiconductors. *Chem. Rev.*, **107**, 926 (2007).
[99] D. Beljonne, J. Cornil, H. Sirringhaus, P.J. Brown, M. Shkunov, R.H. Friend, and J.L. Bredas, Optical signature of delocalized polarons in conjugated polymers. *Adv. Funct. Mater.*, **11**, 229 (2001).

[100] J.F. Chang, B.Q. Sun, D.W. Breiby, M.M. Nielsen, T.I. Solling, M. Giles, I. Mcculloch, and H. Sirringhaus, Enhanced mobility of poly(3-hexylthiophene) transistors by spin-coating from high-boiling-point solvents. *Chem. Mater.*, **16**, 4772 (2004).
[101] H.C. Yang, T.J. Shin, L. Yang, K. Cho, C.Y. Ryu, and Z.N. Bao, Effect of mesoscale crystalline structure on the field-effect mobility of regioregular poly(3-hexyl thiophene) in thin-film transistors. *Adv. Funct. Mater.*, **15**, 671 (2005).
[102] M. Surin, P. Leclere, R. Lazzaroni, J.D. Yuen, G. Wang, D. Moses, A.J. Heeger, S. Cho, and K. Lee, Relationship between the microscopic morphology and the charge transport properties in poly(3-hexylthiophene) field-effect transistors. *J. Appl. Phys.*, **100**, 033712 (2006).
[103] J.M. Verilhac, R. Pokrop, G. LeBlevennec, I. Kulszewicz-Bajer, K. Buga, M. Zagorska, S. Sadki, and A. Pron, Molecular weight dependent charge carrier mobility in poly(3,3″-dioctyl-2,2′:5′,2″-terthiophene). *J. Phys. Chem. B*, **110**, 13305 (2006).
[104] J.A. Dearo, K.D. Weston, S.K. Buratto, and U. Lemmer, Mesoscale optical properties of conjugated polymers probed by near-field scanning optical microscopy. *Chem. Phys. Lett.*, **277**, 532 (1997).
[105] P.K. Wei, J.H. Hsu, W. Fann, K.R. Chuang, H.T. Lee, and S.A. Chen, Phase separation in polyaniline with near-field scanning optical microscopy. *Appl. Opt.*, **36**, 3301 (1997).
[106] J. Teetsov and D.A. Vanden Bout, Near-field scanning optical microscopy (NSOM) studies of nanoscale polymer ordering in pristine films of poly(9,9-dialkylfluorene). *J. Phys. Chem. B*, **104**, 9378 (2000).
[107] J. Teetsov and D.A. Vanden Bout, Near-field scanning optical microscopy (NSOM) study of alkyl-substituted polyfluorene films: The effect of alkyl substituent length on nanoscale polymer ordering and cluster formation. *Macromol. Symp.*, **167**, 153 (2001).
[108] J.A. Teetsov and D.A. Vanden Bout, Imaging molecular and nanoscale order in conjugated polymer thin films with near-field scanning optical microscopy. *J. Am. Chem. Soc.*, **123**, 3605 (2001).
[109] J. Teetsov and D.A. Vanden Bout, Near-field scanning optical microscopy studies of nanoscale order in thermally annealed films of poly(9,9-diakylfluorene). *Langmuir*, **18**, 897 (2002).
[110] C.H. Tan, A.R. Inigo, J.H. Hsu, W. Fann, and P.K. Wei, Mesoscale structures in luminescent conjugated polymer thin films studied by near-field scanning optical microscopy. *J. Phys. Chem. Solids*, **62**, 1643 (2001).
[111] P.K. Wei, Y.F. Lin, W. Fann, Y.Z. Lee, and S.A. Chen, Polarization anisotropy in mesoscale domains of poly(phenylene vinylene) thin films. *Phys. Rev. B*, **63**, 045417 (2001).
[112] C.H. Tan, A.R. Inigo, W. Fann, P.K. Wei, G.Y. Perng, and S.A. Chen, The morphological dependence of charge transport in a soluble luminescent conjugated polymer. *Org. Electron.*, **3**, 81 (2002).
[113] J.D. McNeill, D.B. O'Connor, D.M. Adams, P.F. Barbara, and S.B. Kammer, Field-induced photoluminescence modulation of MEH-PPV under near-field optical excitation. *J. Phys. Chem. B*, **105**, 76 (2001).
[114] J.D. McNeill and P.F. Barbara, NSOM investigation of carrier generation, recombination, and drift in a conjugated polymer. *J. Phys. Chem. B*, **106**, 4632 (2002).
[115] R.D. Schaller, L.F. Lee, J.C. Johnson, L.H. Haber, R.J. Saykally, J. Vieceli, I. Benjamin, T.Q. Nguyen, and B.J. Schwartz, The nature of interchain excitations in conjugated polymers: Spatially-varying interfacial solvatochromism of annealed MEH-PPV films studied by near-field scanning optical microscopy (NSOM). *J. Phys. Chem. B*, **106**, 9496 (2002).
[116] R.D. Schaller, P.T. Snee, J.C. Johnson, L.F. Lee, K.R. Wilson, L.H. Haber, R.J. Saykally, T.Q. Nguyen, and B.J. Schwartz, Nanoscopic interchain aggregate domain formation in conjugated polymer films studied by third harmonic generation near-field scanning optical microscopy. *J. Chem. Phys.*, **117**, 6688 (2002).
[117] R. Pomraenke, C. Ropers, J. Renard, C. Lienau, L. Luer, D. Polli, and G. Cerullo, Structural phase contrast in polycrystalline organic semiconductor films observed by broadband near-field optical spectroscopy. *Nano Lett.*, **7**, 998 (2007).
[118] R. Pomraenke, C. Ropers, J. Renard, C. Lienau, L. Lur, D. Polli, and G. Cerullo, Broadband optical near-field microscope for nanoscale absorption spectroscopy of organic materials. *J. Microscopy Oxford*, **229**, 197 (2008).

[119] J. Chappell, D.G. Lidzey, P.C. Jukes, A.M. Higgins, R.L. Thompson, S. O'Connor, I. Grizzi, R. Fletcher, J. O'Brien, M. Geoghegan, and R.A.L. Jones, Correlating structure with fluorescence emission in phase-separated conjugated-polymer blends. *Nat. Mater.*, **2**, 616 (2003).
[120] C.R. McNeill, H. Frohne, J.L. Holdsworth, and P.C. Dastoor, Direct influence of morphology on current generation in conjugated polymer: methanofullerene solar cells measured by near-field scanning photocurrent microscopy. *Synth. Met.*, **147**, 101 (2004).
[121] C.R. McNeill, H. Frohne, J.L. Holdsworth, and P.C. Dastoor, Near-field scanning photocurrent measurements of polyfluorene blend devices: Directly correlating morphology with current generation. *Nano Lett.*, **4**, 2503 (2004).
[122] C.R. McNeill, H. Frohne, J.L. Holdsworth, J.E. Furst, B.V. King, and P.C. Dastoor, Direct photocurrent mapping of organic solar cells using a near-field scanning optical microscope. *Nano Lett.*, **4**, 219 (2004).
[123] C.R. McNeill and P.C. Dastoor, Photocurrent pattern formation in polymer/methanofullerene blends imaged by near-field scanning photocurrent microscopy. *J. Appl. Phys.*, **99**, 033502 (2006).
[124] R. Riehn, R. Stevenson, D. Richards, D.J. Kang, M. Blamire, A. Downes, and F. Cacialli, Local probing of photocurrent and photoluminescence in a phase-separated conjugated-polymer blend by means of near-field excitation. *Adv. Funct. Mater.*, **16**, 469 (2006).
[125] S. Sadki, P. Schottland, N. Brodie, and G. Sabouraud, The mechanisms of pyrrole electropolymerization. *Chem. Soc. Rev.*, **29**, 283 (2000).
[126] C. Gabrielli, J.J. Garcia-Jareno, M. Keddam, H. Perrot, and F. Vicente, Ac-electrogravimetry study of electroactive thin films. I. Application to Prussian Blue. *J. Phys. Chem. B*, **106**, 3182 (2002).
[127] C. Gabrielli, J.J. Garcia-Jareno, M. Keddam, H. Perrot, and F. Vicente, Ac-electrogravimetry study of electroactive thin films. II. Application to polypyrrole. *J. Phys. Chem. B*, **106**, 3192 (2002).
[128] T.F. Otero and I. Boyano, Potentiostatic oxidation of polyaniline under conformational relaxation control: Experimental and theoretical study. *J. Phys. Chem. B*, **107**, 4269 (2003).
[129] L. Pigani, R. Seeber, F. Terzi, O. Cerri, M. Innocenti, R. Udisti, and G. Sanna, Relaxation phenomena and structural modifications of substituted polythiophenes during the p-doping processes. An electrochemical and morphological study. *Electrochim. Acta*, **51**, 2698 (2006).
[130] T. Silk, Q. Hong, J. Tamm, and R.G. Compton, AFM studies of polypyrrole film surface morphology -I. The influence of film thickness and dopant nature. *Synth. Met.*, **93**, 59 (1998).
[131] T. Silk, Q. Hong, J. Tamm, and R.G. Compton, AFM studies of polypyrrole film surface morphology - II. Roughness characterization by the fractal dimension analysis. *Synth. Met.*, **93**, 65 (1998).
[132] N.T.L. Hien, B. Garcia, A. Pailleret, and C. Deslouis, Role of doping, ions in the corrosion protection of iron by polypyrrole films. *Electrochim. Acta*, **50**, 1747 (2005).
[133] F. Chao, M. Costa, G. Jin, and C. Tian, Role of poly-3-methylthiophene structure determined by AFM on the dielectric-constant spectra. *Electrochim. Acta*, **39**, 197 (1994).
[134] F. Chao, M. Costa, and C. Tian, Different steps in electrodeposition of poly(3-methylthiophene) films on platinum-electrodes studied by ellipsometry, SEM and AFM techniques. *Synth. Met.*, **53**, 127 (1993).
[135] B.J. Hwang, R. Santhanam, and Y.L. Lin, Nucleation and growth mechanism of electroformation of polypyrrole on a heat-treated gold/highly oriented pyrolytic graphite. *Electrochim. Acta*, **46**, 2843 (2001).
[136] M. Innocenti, F. Loglio, L. Pigani, R. Seeber, F. Terzi, and R. Udisti, *In situ* atomic force microscopy in the study of electrogeneration of polybithiophene on Pt electrode. *Electrochim. Acta*, **50**, 1497 (2005).
[137] J. Li, E. Wang, M. Green, and P.E. West, *In-Situ* AFM study of the surface-morphology of polypyrrole film. *Synth. Met.*, **74**, 127 (1995).
[138] R. Nyffenegger, E. Ammann, H. Siegenthaler, R. Kotz, and O. Haas, *In-situ* scanning probe microscopy for the measurement of thickness changes in an electroactive polymer. *Electrochim. Acta*, **40**, 1411 (1995).

[139] C. Froeck, A. Bartl, and L. Dunsch, STM-investigations and AFM-investigations of one-dimensional and 2-dimensional polypyrrole structures on electrodes. *Electrochim. Acta*, **40**, 1421 (1995).
[140] F. Chao, M. Costa, and C. Tian, Modification of poly(3-methylthiophene) (PMeT) structure during electrochemical doping-undoping, studied by *in situ* atomic force microscopy (ECAFM). *Synth. Met.*, **75**, 85 (1995).
[141] P. Haring, R. Kotz, G. Repphun, O. Haas, and H. Siegenthaler, In situ scanning probe microscopy investigations of electroactive films. *Appl. Phys. A: Mater. Sci. Process.*, **66**, S481 (1998).
[142] M.F. Suarez and R.G. Compton, In situ atomic force microscopy study of polypyrrole synthesis and the volume changes induced by oxidation and reduction of the polymer. *J. Electroanal. Chem.*, **462**, 211 (1999).
[143] M. Lapkowski, J. Zak, M. Kolodziej-Sadlok, S. Guillerez, and G. Bidan, Effects of the redox state on the morphology of the regioregular sexi-3-alkylthiophene. *Electrochim. Acta*, **46**, 4001 (2001).
[144] M. Lapkowski, M. Kolodzief-Sadlok, J. Zak, S. Guillerez, and G. Bidan, Electrochemically induced, reversible morphology changes of regioregular oligo-3-alkylthiophene film. *Adv. Mater.*, **13**, 803 (2001).
[145] M. Lapkowski, J. Zak, M. Kolodziej-Sadlok, S. Guillerez, and G. Bidan, *In situ* AFM and conductivity measurements of regioregular oligoalkylthiophenes during electrochemical doping. *Synth. Met.*, **119**, 417 (2001).
[146] E. Smela and N. Gadegaard, Volume change in polypyrrole studied by atomic force microscopy. *J. Phys. Chem. B*, **105**, 9395 (2001).
[147] E. Smela and N. Gadegaard, Surprising volume change in PPy(DBS): An atomic force microscopy study. *Adv. Mater.*, **11**, 953 (1999).
[148] M. Skompska, A. Szkurlat, A. Kowal, and M. Szklarczyk, Spectroelectrochemical and AFM studies of doping-undoping of poly(3-hexylthiophene) films in propylene carbonate and aqueous solutions of $LiClO_4$. *Langmuir*, **19**, 2318 (2003).
[149] T.F. Otero and I. Boyano, Comparative study of conducting polymers by the ESCR model. *J. Phys. Chem. B*, **107**, 6730 (2003).
[150] J.H. Hwang and M. Pyo, pH-induced mass and volume changes of perchlorate-doped polypyrrole. *Synth. Met.*, **157**, 155 (2007).
[151] P.R. Singh, S. Mahajan, S. Raiwadec, and A.Q. Contractor, EC-AFM investigation of reversible volume changes with electrode potential in polyaniline. *J. Electroanal. Chem.*, **625**, 16 (2009).
[152] M.J. Higgins, S.T. McGovern, and G.G. Wallace, Visualizing dynamic actuation of ultrathin polypyrrole films. *Langmuir*, **25**, 3627 (2009).
[153] E. Chainet and M. Billon, *In situ* study of polypyrrole morphology by STM: effect of the doping state. *J. Electroanal. Chem.*, **451**, 273 (1998).
[154] E. Chainet and M. Billon, *In situ* STM study of the counterion effect on the doping stages of polypyrrole films. *Synth. Met.*, **99**, 21 (1999).
[155] M. Pyo, Surface roughness changes of poly(*N*-methylpyrrole)/poly(styrene sulfonate) with doping in perchlorate solutions of various cations. *J. Electrochem. Soc.*, **152**, E90 (2005).
[156] M. Pyo and C.H. Kwak, *In situ* scanning tunneling nuicroscopy study on volume change of polypyrrole/poly (styrene sulfonate). *Synth. Met.*, **150**, 133 (2005).
[157] M.A. Edwards, S. Martin, A.L. Whitworth, J.V. Macpherson, and P.R. Unwin, Scanning electrochemical microscopy: principles and applications to biophysical systems. *Physiol. Meas.*, **27**, R63 (2006).
[158] J.Y. Kwak, C. Lee, and A.J. Bard, Scanning electrochemical microscopy. 5. A study of the conductivity of a polypyrrole film. *J. Electrochem. Soc.*, **137**, 1481 (1990).
[159] G. Denuault, M.H.T. Frank, and L.M. Peter, Scanning electrochemical microscopy – potentiometric probing of ion fluxes. *Faraday Discuss.*, **94**, 23 (1992).
[160] M.H. T. Frank, and G. Denuault, Scanning electrochemical microscopy – probing the ingress and egress of protons from a polyaniline film. *J. Electroanal. Chem.*, **354**, 331 (1993).

[161] M.H.T. Frank and G. Denuault, Scanning electrochemical microscope (SECM) study of the relationship between proton concentration and electronic charge as a function of ionic-strength during the oxidation of polyaniline. *J. Electroanal. Chem.*, **379**, 399 (1994).
[162] M. Arca, M.V. Mirkin, and A.J. Bard, Polymer-films on electrodes .26. Study of ion-transport and electron-transfer at polypyrrole films by scanning electrochemical microscopy. *J. Phys. Chem.*, **99**, 5040 (1995).
[163] T. Morgenstern and J.W. Schultze, Laser deposition of metals and polymers in Si-microstructures *Electrochim. Acta*, **42**, 3057 (1997).
[164] M. Tsionsky, A.J. Bard, D. Dini, and F. Decker, Polymer films on electrodes. 28. Scanning electrochemical microscopy study of electron transfer at poly(alkylterthiophene) films. *Chem. Mater.*, **10**, 2120 (1998).
[165] G. Wittstock, T. Asmus, and T. Wilhelm, Investigation of ion-bombarded conducting polymer films by scanning electrochemical microscopy (SECM). *Fresenius J. Anal. Chem.*, **367**, 346 (2000).
[166] D. Mandler and P.R. Unwin, Measurement of lateral charge propagation in polyaniline layers with the scanning electrochemical microscope. *J. Phys. Chem. B*, **107**, 407 (2003).
[167] J. Zhang, A.L. Barker, D. Mandler, and P.R. Unwin, Effect of surface pressure on the insulator to metal transition of a Langmuir polyaniline monolayer. *J. Am. Chem. Soc.*, **125**, 9312 (2003).
[168] V. Syritski, R.E. Gyurcsanyi, A. Opik, and K. Toth, Synthesis and characterization of inherently conducting polymers by using scanning electrochemical microscopy and Electrochemical Quartz Crystal Microbalance. *Synth. Met.*, **152**, 133 (2005).
[169] N.J. Yang and C.G. Zoski, Polymer films on electrodes: Investigation of ion transport at poly(3,4-ethylenedioxythiophene) films by scanning electrochemical microscopy. *Langmuir*, **22**, 10338 (2006).
[170] E. Ventosa, A. Colina, A. Heras, A. Martinez, O. Orcajo, V. Ruiz, and J. Lopez-Palacios, Electrochemical spectroscopic and electrogravimetric detection of oligomers occluded in electrochemically synthesized poly (3,4-ethylenedioxythiophene) films. *Electrochim. Acta*, **53**, 4219 (2008).
[171] L.D. Landau and E.M. Lifshitz, *Landau and Lifshitz Course of Theoretical Physics*, Vol. **5**, Butterworth-Heinemann, Oxford, 1980,p. 533.
[172] D. Kashchiev, *Nucleation: Basic Theory with Applications*, Butterworth-Heinemann, Oxford, 2000.
[173] E. Ruckenstein and Y.S. Djikaev, Recent developments in the kinetic theory of nucleation. *Adv. Colloid Interface Sci.*, **118**, 51 (2005).

Part Two

4

Nanostructured Conductive Polymers by Electrospinning

Ioannis S. Chronakis

Swerea IVF, Swedish Institute for Industrial Research and Development, Mölndal, Sweden

4.1 Introduction to Electrospinning Technology

Electrospinning is a fiber-spinning technology used to produce long, three-dimensional, ultrafine fibers with diameters in the range of a few nanometers to a few microns (more typically 100 nm to 1 micron) and lengths up to kilometers (Figure 4.1). When used in products, the unique properties of nanofibers are utilized, such as extraordinarily high surface area per unit mass, very high porosity, tuneable pore size, tuneable surface properties, layer thinness, high permeability, low basis weight, ability to retain electrostatic charges, and cost effectiveness, among others [1,2].

While electrospinning technology was developed and patented by Formhals in the 1930s [3], it was only about 10 years ago that actual developments were triggered by Reneker and coworkers [4]. Interest today is greater than ever and this cost-effective technique has made its way into several scientific areas, such as electronics, sensors, biomedicine, filtration, catalysis, and composites [5,6]. Electrospinning is a continuous technique and is hence suitable for high-volume production of nanofibers. The ability to customize micronanofibers to meet the requirements of specific applications gives

Nanostructured Conductive Polymers Edited by Ali Eftekhari

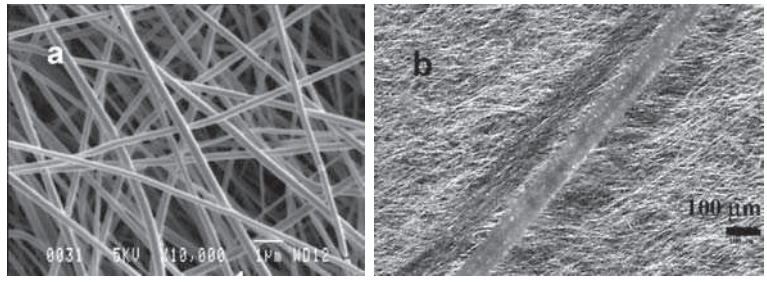

Figure 4.1 *(a) SEM image of poly(ethylene terephthalate) (PET) nanofiber web. The nanofibers were electrospun from a PET solution in THF:DMF. The diameter of the fibers is about 200 nm. (b) PET nanofiber web – comparison with human hair. (Reprinted with permission from Current Opinion in Colloid and Interface Science, Polymer nanofibers assembled by electrospinning, by A. Frenot and I. S. Chronakis, 8, 64–75. Copyright (2003) Elsevier Ltd)*

electrospinning an advantage over other, larger-scale, micronano production methods. Carbon and ceramic nanofibers made of polymeric precursors further expand the list of possible uses of electrospun nanofibers [7].

4.2 The Electrospinning Processing

Electrospinning is increasingly being used to produce ultrathin fibers from a wide range of polymer materials. This nonmechanical, electrostatic technique involves the use of a high-voltage electrostatic field to charge the surface of a polymer solution droplet, thereby inducing the ejection of a liquid jet through a spinneret (Figure 4.2). In a typical process, an electrical potential is applied between a droplet of a polymer solution held at the end of a capillary tube and a grounded target. When the electric field that is applied overcomes the surface tension of the droplet, a charged jet of polymer solution is ejected. On the way to the collector, the jet will be subjected to forces that allow it to stretch immensely. Simultaneously, the jet will partially or fully solidify through solvent evaporation or cooling, and an electrically charged fiber will remain, which can be directed or accelerated by electrical forces and then collected in sheets or other useful shapes.

A characteristic feature of the electrospinning process is the extremely rapid formation of the nanofiber structure, which occurs on a millisecond scale. Other notable features of electrospinning are a huge material elongation rate of the order of 1000 s^{-1} and a reduction of the cross-sectional area of the order of 10^5 to 10^6, which have been shown to affect the orientation of the structural elements in the fiber. Moreover, the traditional set-up for electrospinning has been modified in a number of ways during the last few years in order to be able to control the electrospinning process and tailor the structure of micronanofibers. A set-up was developed for electrospinning involving a dual syringe spinneret (Figure 4.3). The development enables spinning highly functional nanofibers, such as hollow nanofibers, nanotubes, and fibers with a core–shell structure [8].

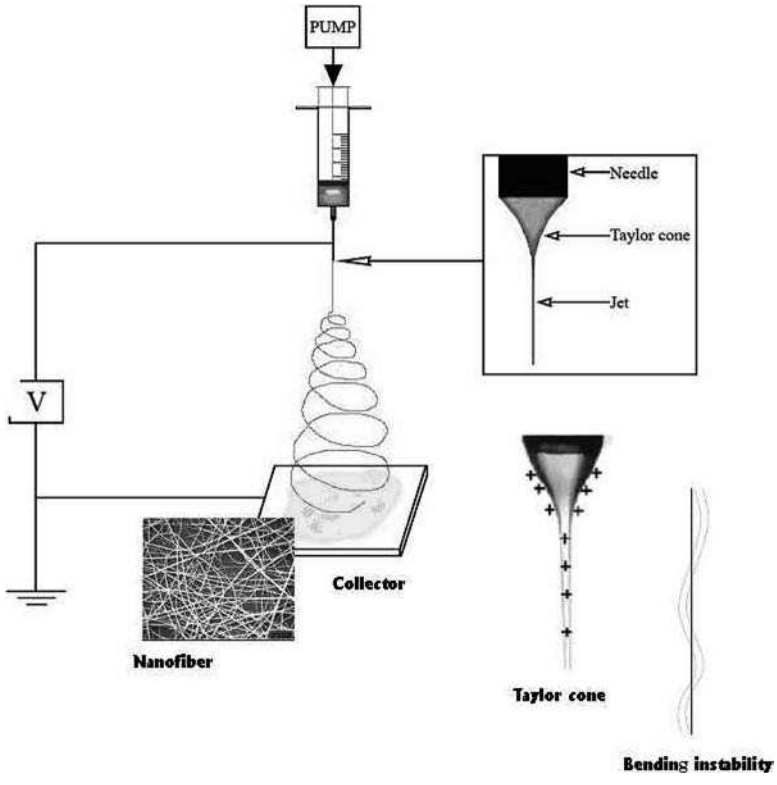

Figure 4.2 *Schematic illustration of the conventional set-up for electrospinning. The insets show a drawing of the electrified Taylor cone, bending instability, and a typical SEM image of the nonwoven mat of PET nanofibers deposited on the collector. The bending instability is a transversal vibration of the electrospinning jet. It is enhanced by electrostatic repulsion and suppressed by surface tension*

4.3 Electrospinning Processing Parameters: Control of the Nanofiber Morphology

The fiber morphology has been shown to be dependent on process parameters, namely solution properties (system parameters), process conditions (operational parameters), and ambient conditions [1,2].

4.3.1 Solution Properties

Solution properties are those such as molecular weight, molecular weight distribution, and architecture of the polymer, and properties such as viscosity, conductivity, dielectric constant, and surface tension. The polymer solution must have a concentration high

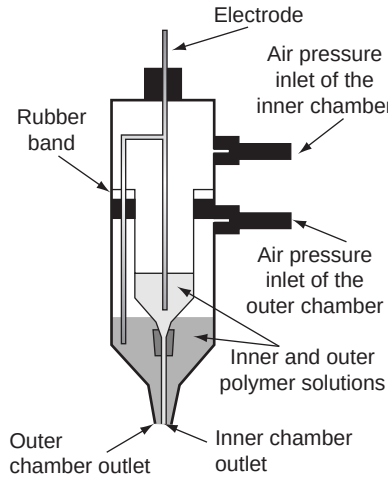

Figure 4.3 *Schematic illustration of the set-up used to coelectrospin compound core–shell nanofibers. It involves the use of a spinneret consisting of two coaxial capillaries through which two polymer solutions can simultaneously be ejected to form a compound jet. (Reprinted with permission from Advanced Materials, Compound Core-Shell Polymer Nanofibers by Co-Electrospinning by Z. Sun, E. Zussman, A. L. Yarin et al., 15, 22, 1929–1932. Copyright (2003) Wiley-VCH)*

enough to cause polymer entanglements, yet not so high that the viscosity prevents polymer motion induced by the electric field. The resulting fibers' diameters usually increase with the concentration of the solution according to a power law relationship. Decreasing the polymer concentration in the solution produces thinner fibers. Decreasing the concentration below a threshold value causes the uniform fiber morphology to change into beads [9]. The main factors affecting the formation of beads (Figure 4.4) during electrospinning have been shown to be solution viscosity, surface tension, and the net charge density carried by the electrospinning jet. Higher surface tension results in a greater number of bead structures, in contrast to the parameters of viscosity and net charge density, for which higher values favor fibers with fewer beads. This reduction in thickness is due to the solution conductivity, which reflects the charge density of the jet and thus the elongation level. The surface tension also controls the distribution and the width of the fibers, which can be decreased by adding a surfactant to the solution. Adding a surfactant or a salt to the solution is a way to increase the net charge density and thus reduce the formation of beads. Finally, the choice of solvent(s) directly affects all of the properties mentioned and is of major importance to the fiber morphology.

4.3.2 Process Conditions

The parameters in the process are spinning voltage, distance between the tip of the capillary and the collector, solution flow rate (feed rate), needle diameter, and, finally,

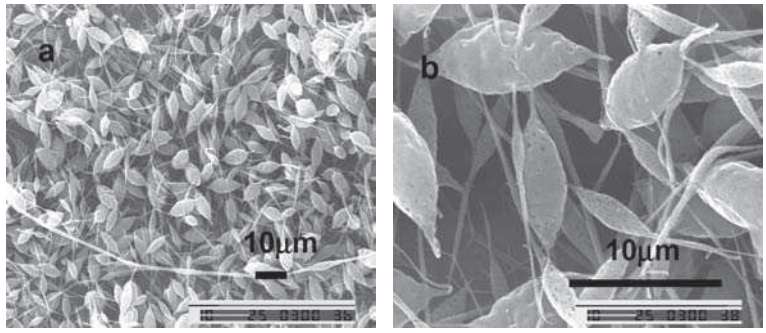

Figure 4.4 *Example of bead formation during electrospinning: SEM micrographs of poly (propyl carbonate) (PPC) beads prepared by electrospinning a PPC solution in dichloromethane. (Reprinted with permission from Biomaterials, Electrospun aliphatic polycarbonates as tailores tissue scaffold materials by A. Welle, M. Kröger et al., 28, 2211–2219. Copyright (2007) Elsevier Ltd)*

the motion of the target screen. Voltage and feed rate show different tendencies and are less effective in controlling fiber morphology as compared to the solution properties. Too high a voltage might result in splaying and irregularities in the fibers. A bead structure is evident when the voltage is either too low or too high. However, a higher voltage also leads to a higher evaporation rate of the solvent, which in turn might lead to solidification at the tip and instability in the jet. Morphological changes in the nanofibers can also occur upon changing the distance between the syringe needle and the substrate. Increasing the distance or decreasing the electrical field decreases the bead density, regardless of the concentration of the polymer in the solution.

4.3.3 Ambient Conditions

Ambient conditions include factors such as humidity and temperature, air velocity in the spinning chamber, and atmospheric pressure. Humidity primarily controls the formation of pores on the surface of the fibers. Above a certain threshold level of humidity, pores begin to appear and, as the level increases, so do the number and size of the pores.

The precise mechanism behind the formation of pores and texturing on the surface is complex and is thought to be dependent on a combination of breath figure formation and phase separation. Breath figures are imprints formed due to the evaporative cooling during evaporation of the solvent, which results in condensed solvent drops on the surface and, later, pores. Surface porosity can also be achieved by selective removal of one of the components in the polymer blend after spinning. The pores formed on the fiber surface can be used, for example, to capture nanoparticles, act as a cradle for enzymes or increase the surface area for filtration applications. Increasing the solution temperature is also a method for speeding up the process, but it might cause morphological imperfections, such as the formation of beads.

4.4 Nanostructured Conductive Polymers by Electrospinning

Among the electrospun nanostructures, multifunctionalized nanostructures of conducting polymers (CPs) have received great attention because of their unique properties and technological applications in electrical, optical, and magnetic materials and devices. Electrospinning has been successfully used to produce nanostructures of polyaniline (PANI), polypyrrole (PPy), poly(*p*-phenylene vinylenes) (PPVs), and polythiophenes (PThs). As the CPs are generally insoluble in most organic solvents and have rigid backbones, different strategies have been used to overcome their limited processability by electrospinning processing: (i) the use of more flexible polymer precursors or even monomers that can be converted into CPs in a second step, (ii) the addition of a spinable polymer to assist the formation of fibers, or (iii) the use of a core–shell coaxial electrospinning strategy, where the CP is the core and the spinable polymer is the post-removable shell or, inversely, the spinable polymer is the core and the CP is the shell [10].

4.4.1 Polyaniline (PANI)

Polyaniline (PANI) is one of the most frequently investigated conducting polymers because of its ease of synthesis, its relative environmental stability and its ability to exist in a range of intrinsic redox states. PANI exists in various oxidation states, ranging from a reduced leucoemeraldine form to the fully oxidized pernigraniline form.

Using electrospinning, Diaz-de Leon *et al.* prepared nanofibers of pure doped PANI in concentrated sulfuric acid or in blends with polystyrene (PS) or polyethylene oxide (PEO) [11]. The room temperature conductivity of pure PANI nanofibers was measured to be 0.76 S cm^{-1} and similar to the bulk value. It was found in the case of PANI blended with PS and PEO that the PS-based blend was better for achieving fibers of a thinner ($<$100 nm) diameter. The conductivity was found to be very sensitive to the morphology of the fibers (i.e. amount of defects and thickness), which is related to the initial blend properties and solvent used. Therefore, a better chain alignment in the polymer blends yields a higher overall conductivity of the blended nanofibers. It is also notable that the nanofibers obtained showed regions with polymer crosses; these polymer–polymer junctions are of interest in making nanoelectronic junction devices. Recent studies by Cárdenas *et al.* also report the formation of pure PANI submicron fibers collected on SiO_2/Si and Si wafer pieces by the electrospinning method [12]. The isolated fibers show a linear current–voltage characteristic, and the conductivity values vary in the range usually observed for partially doped PANI.

PANI is insoluble in most organic solvents and, as a result, electrospinning is mainly found for mixtures of PANI and other polymers. Ultrafine fibers of PANI doped with camphorsulfonic acid (PAn.HCSA) blended with PEO were reported by MacDiarmid and coworkers in 2000 [13,14]. The morphology and fiber diameter of electrospun PANI blend fibers revealed that both the PEO and the PAn.HCSArPEO blend fibers had a diameter ranging between 950 nm and 2.1 μm, with a generally uniform thickness along the fiber (Figure 4.5).

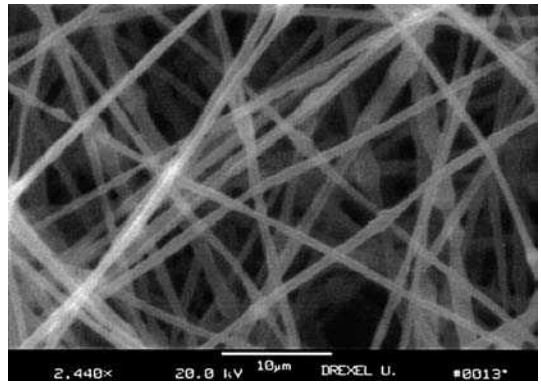

Figure 4.5 *SEM micrograph of the electrospun fibers from a 2 wt% PAn.HCSAr and 2 wt% PEO solution dissolved in chloroform at 25 kV. (Reprinted with permission from Synthetic Metals, Electrostatic fabrication of ultrafine conducting fibers: polyaniline/polyethylene oxide blends by I. D. Norris, M. M. Shaker, F. K. Ko and A. G. McDiarmid, 114, 109–114. Copyright (2000) Elsevier Ltd)*

Although the conductivity of the nonwoven fiber mat, as measured by the four-point probe method, was slightly lower than that of a cast film, owing to the high porosity of the nonwoven mat, the rate for the vapor phase dedoping redoping of the electrospun fibers is at least one order of magnitude faster than for cast films. This emphasizes the enormous effect an increase in the surface-to-volume ratio, accomplished by electrospinning the polymer material into fibers, can have on the selected chemical properties of PANI blends. The conductivity of a single fiber was 0.1 S cm^{-1}. It has been also emphasized that the four-point probe method measures the volume resistivity from which the conductivity can then be calculated, and not that of an individual fiber. The (reversible) conductivity/temperature relationship between 295 K and 77 K for a single 1.32 μm fiber (72 wt% PAn.HCSA in PEO) is shown at Figure 4.6. The conductivity ($\sim$33 S cm^{-1} at 295 K) was unexpectedly large for a blend, since the conductivity of a spun film of a pure polymer cast was only $\sim 10^{-1}$ S cm^{-1} and this suggests that there may be significant alignment of polymer chains in the fiber [14]. Moreover, in 2001, Ko and coworkers published a patent claiming a method for producing conductive polymeric fibers comprising electrospinning fibers from a blend of polymers dissolved in an organic solvent [15]. The conductive polymer involved is PANI, and it is dissolved in chloroform and electrospun together with polyethylene oxide or polyacrylonitrile. The conductive fibers produced with the patented method are claimed to be applied in a simple electronic device.

Other studies in 2000 by Drew *et al.* reported that it is very difficult to spin fibers of PANI complexed to sulfonated polystyrene (PANI/SPS), even when solutions containing sodium chloride and dodecyl benzene sulfonic acid sodium salt were used to lower the surface tension and thereby enhance electrospinning [16,17]. However, PANI/SPS nanofibers can be produced by adding a carrier polymer such as PEO, polyacrylonitrile, or polyurethane. Also reported was the use of electrostatically layered sulfonated polystyrene as a template for the surface polymerization of conjugated polymers in their conducting form. Enzymatic synthesis of PANI and a copolymer of pyrrole and PEDOT was done on electrospun nanofiber

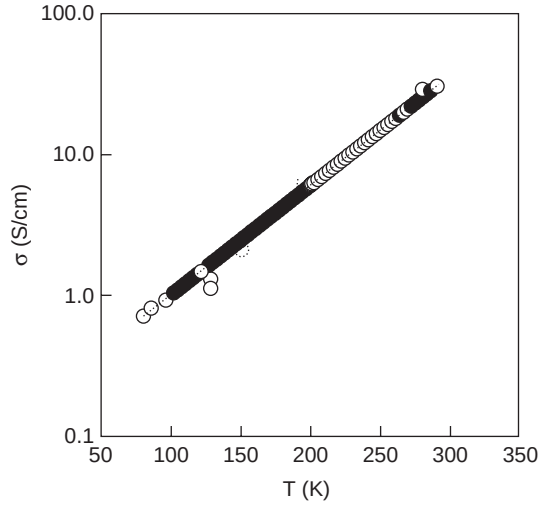

Figure 4.6 *Conductivity/temperature relationship for a 72 wt% blend fiber of Pan.HCSA in PEO. (Reprinted with permission from Synthetic Metals, Electrostatically-generated nanofibers of electronic polymers by A. G. MacDiarmid, W. E. Jones Jr., I. D. Norris et al., 119, 27–30. Copyright (2001) Elsevier Ltd)*

surfaces modified by electrostatic assembly of polyelectrolytes. The conductivity was measured and found to be on the order of 10^{-3} S cm^{-1}. Furthermore, Desai and Sung investigated the effects of electrospinning parameters on the formation of PANI/PMMA fibers and the phase morphology of the electrospun fibers [18,19]. They produced nanofibers using PANI of the emeraldine base form, doped with camphor sulfonic acid (CSA).

The Pinto research group has also studied camphor sulfonic acid-doped polyaniline/polyethylene oxide (PANI/PEO) nanofibers [20,21]. The electrical conductivity of PANI/PEO nanofibers with diameters in the 100–200 nm range showed values of 0.3–1.0 S cm^{-1}, which is higher than the values reported for thicker nanofibers, but less than the bulk value of PANI. It was suggested that the excellent adherence of the nanofibers to SiO_2 as well as gold electrodes may be useful in the design of future devices [21]. Saturation channel currents were observed at surprisingly low source-drain voltages, and the elimination or reduction of the PEO content in the fibers was expected to enhance device parameters [22]. These properties suggest then that electrospinning can be a simple method for fabricating a one-dimensional polymer field-effect transistor (FET), which forms the basic building block in logic circuits and switches for displays. Nanofibers of PANI-CSA blended with PEO were also studied in the work of Kahol and Pinto [21]. The EPR magnetic susceptibility behavior of the camphorsulfonic-acid-doped polyaniline (PANCSA) blends with PEO is reported in fibers and films. In particular, EPR investigations of electrospun $(PANCSA)_{0.72}/(PEO)_{0.28}$ nanofibers, cast films of $(PANCSA)_{0.72}/(PEO)_{0.28}$, and cast films of (PANCSA) were made to investigate differences in the mesoscopic disorder, as induced by the process of electrospinning. The changes observed in the Pauli susceptibility, EPR line shape, EPR line width, and dc conductivity are interpreted as being due to

increased chain alignment in the fibers compared with the cast films. Pinto's group also prepared micron size diameter fibers of 2-acrylamido-2-methyl-1-propanesulfonic-acid-doped polyaniline via electrospinning [22]. The conductivity of individual fibers was found to be lower than that of a cast film of the same polymer. The fibers were coated with thin films of nickel using the electroless deposition technique. The metal uniformly coated the fibers without any lateral overlap, as was evident from SEM spectroscopy, leading to a decrease in its resistance by three orders of magnitude, while retaining the large surface area that is inherent to small-diameter fibers. In that study, they combined the electrospinning and electroless deposition techniques to prepare metal-coated fibrous polymer substrates with a large surface area within minutes.

Polyaniline polyethylene (PANI/PEO)-based polymer nanofibers with diameters smaller than 30 nm were reported by Zhou *et al*. [23]. The behavior of the electronic properties of polymer nanofibers was observed by scanning conductance microscopy (SCM) and single-fiber transport experiments. SCM showed that fibers with a diameter less than 15 nm are electrically insulating, as the small diameter may allow complete dedoping in air or be smaller than phase-separated grains of PANI and PEO. The electrical contacts with nanofibers were made by shadow mask evaporation with no chemical or thermal damage to the fibers. Single fiber *I–V* characteristics showed that thin fibers conduct more poorly than thick ones, in agreement with SCM data. *I–V*s of asymmetric fibers are rectifying, consistent with the formation of Schottky barriers at the nanofiber–metal contacts.

Another study by Hong *et al.* also reports the preparation of conducting PANI/nylon-6 composites with high electrical conductivity and superior mechanical properties, such as flexibility and lightness [24]. PANI was chemically polymerized on the surface of the nylon-6 electrospun nanofiber webs. The electrical conductivity measurements showed that the conductivity of the PANI/nylon-6 composite electrospun fiber webs was superior to that of PANI/nylon-6 plain-weave fabrics because of the high surface area/volume ratios. The volume conductivities of the PANI/nylon-6 composite electrospun fiber webs increased from 0.5 to 1.5 S cm^{-1} as the diffusion time increased from 10 min to 4 h because of the even distribution of PANI in the electrospun fiber webs. However, the surface conductivities of the PANI/nylon-6 composite electrospun fiber webs somewhat decreased from 0.22 to 0.14 S cm^{-1} as the diffusion time increased, probably because PANI was contaminated with aniline monomers, aniline oligomers, and some alkyl chains, which served as electrical resistants.

Electrospinning is also used to prepare polyaniline/polystyrene films with water contact angles as high as 165° and a sliding angle of less than 5°. The superhydrophobicity and conductivity of the films were stable over a wide pH range, also in oxidizing solutions. The effect of surface morphology on these properties has also been investigated. The polystyrene content can strongly influence the morphology of the composite films, which thus display different superhydrophobicities and conductivities [25].

The development of conducting polyaniline/poly(lactic acid) nanofibers as thin as 100–200 nm by electrospinning was reported by Picciani and coworkers [26]. These fibers were visually homogeneous, and this indicated good interactions between the components of the polyaniline/poly(L-lactic acid) blend. The high interaction between the components and the rapid evaporation of the solvent during electrospinning resulted in nanofibers with a lower degree of crystallinity in comparison with cast films. The electrical conductivity of the electrospun fiber mats was lower than that of blend films produced by casting, probably

because of the lower degree of crystallinity of the polyaniline dispersion and the high porosity of the nonwoven mat. They suggested that this novel system opens new and interesting opportunities for applications in biomedical devices, biodegradable materials, and biosensors.

Oligoanilines with well-defined chain lengths are model compounds for the electronic, optical, magnetic, and structural properties of PANI with a number of potential applications. Chao *et al.* [27] report the preparation and characterization of oligoaniline derivative/polyvinylpyrrolidone nanofibers containing silver nanoparticles. PVP is used to immobilize the Ag nanoparticles, and the oligoaniline derivative (OD) is used as a reducing agent for Ag^{+} in the PVP solution. The average diameter of the OD/PVP nanofibers containing Ag nanoparticles was about 240 nm (Figure 4.7). The authors suggest that the possible formation mechanism of Ag nanoparticles appears to involve a redox reaction between Ag^{+} and the oligoaniline derivative.

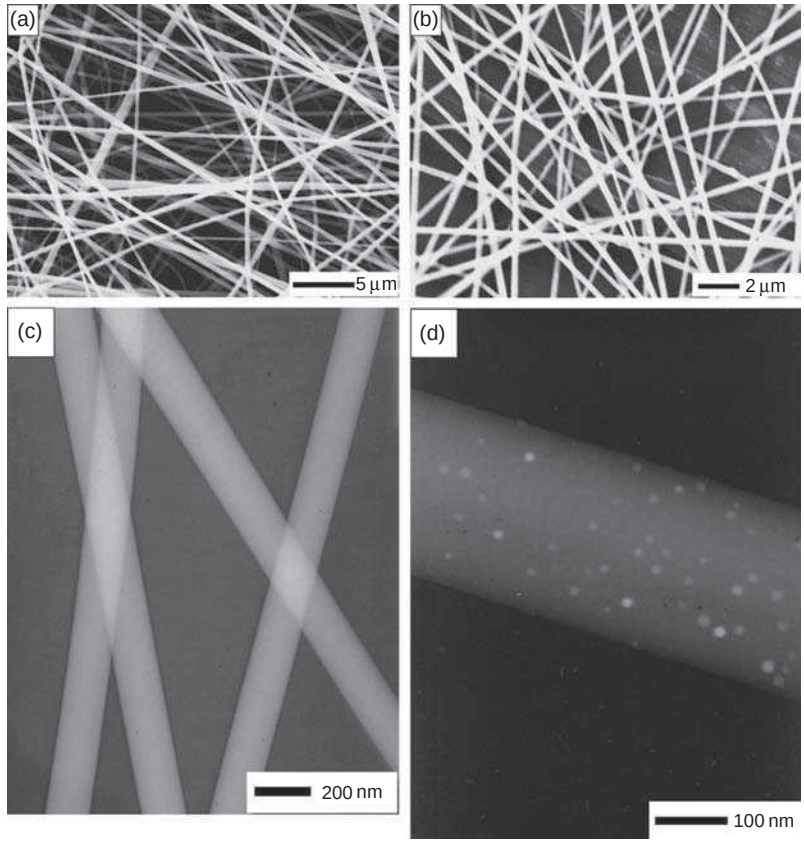

Figure 4.7 *SEM images of OD/PVP nanofibers (a) and OD/PVP with Ag nanocomposite (b), and TEM images of OD/PVP nanofibers (c) and OD/PVP with Ag nanocomposite (d). (Reprinted with permission from Synthetic Metals, Preparation of oligoaniline derivative/polyvinylpyrolidone nanofibers containing silver nanoparticels by D. Chao, L. Cui, J. Zhang et al., 159, 537–540. Copyright (2009) Elsevier Ltd)*

Conducting polyaniline-Al_2O_3 composite nanofibers with varying conductivity were also prepared by seeding with alumina nanofibers and oxidative polymerization of aniline [28]. The PANI-Al_2O_3 nanofibers had average diameters of 37–52 nm and the conductivity decreased with an increase in the Al_2O_3 that was incorporated (Figure 4.8).

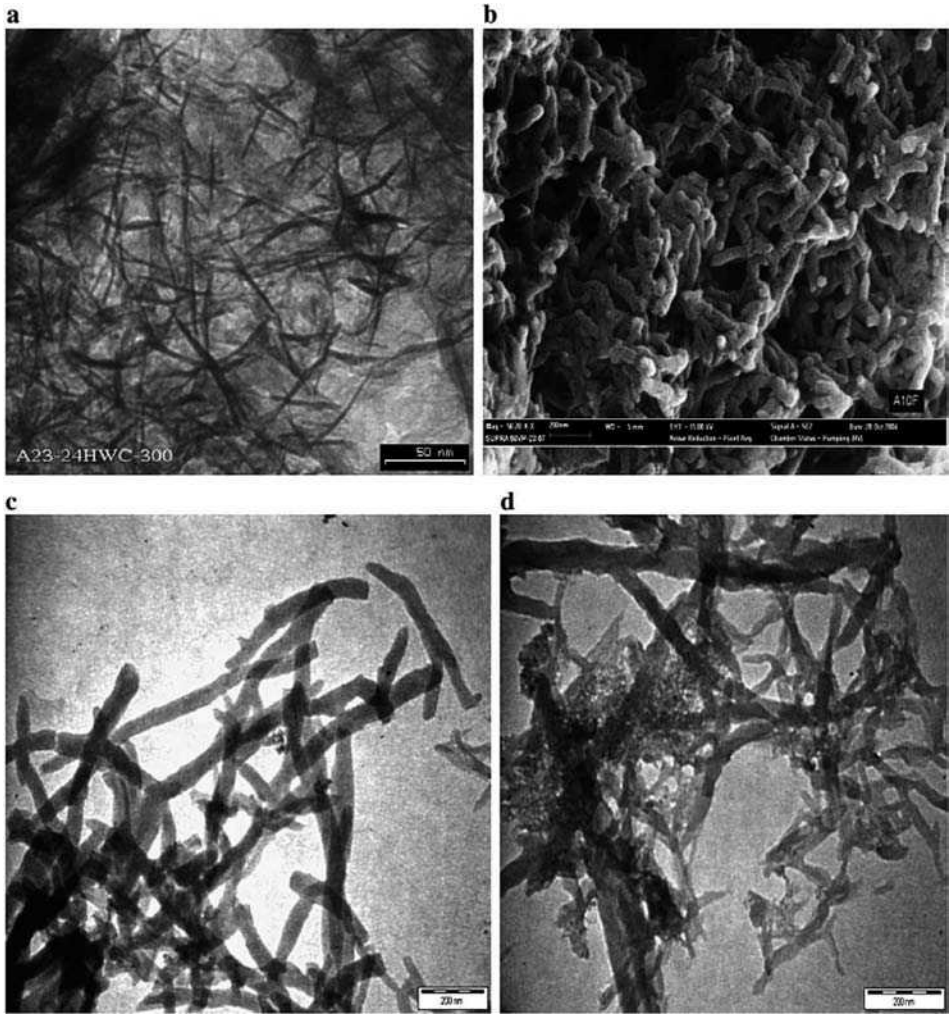

Figure 4.8 *(a) TEM micrograph of alumina nanofibers calcined at 540 °C, scale bar: 50 nm, (b) FESEM and (c) TEM micrographs of PANI-Al_2O_3 nanocomposite with 0.05 g loading of alumina nanofibers and (d) TEM micrograph of PANI-Al_2O_3 nanocomposite with 1.0 g loading of alumina nanofibers. Scale bars for (b), (c), and (d) are 200 nm. (Reprinted with permission from Materials Letters, Preparation of polyaniline-Al_2O_3 composites nanofibers with controllable conductivity by G. L. Teoh, K. Y. Liew and W. A. K. Mahmood, 61, 4947–4949. Copyright (2007) Elsevier Ltd)*

It is furthermore to be noted that the traditional set-up for electrospinning has been modified in a number of ways during the last few years in order to be able to control the electrospinning process and tailor the structure of micronanofibers. A number of set-ups have been developed that allow control of the orientation of fibers. The orientation is crucial in different applications of nanofibers and opens new opportunities for manufacturing yarn, micronanowire devices etc. Most of the set-ups are based on rotating collection devices. Another method for controlled deposition of oriented nanofibers uses a microfabricated scanned tip as an electrospinning source [29]. The tip is dipped in a polymer solution to gather a droplet as a source material. A voltage applied to the tip causes the formation of a Taylor cone and, at sufficiently high voltage, a polymer jet is extracted from the droplet. By moving the source relative to a surface, thus acting as a counter-electrode, oriented nanofibers can be deposited and integrated with microfabricated surface structures. This electrospinning technique is called a scanned electrospinning nanofiber deposition system. In addition to achieving uniform fiber deposition, the scanning tip electrospinning source can produce self-assembled composite fibers of micro- and nanoparticles aligned in a polymeric fiber. Using this method, Kameoka and coworkers deposited oriented conductive polymeric fibers of polyaniline and investigated their conductivity as components for polymeric nanoelectronics [30].

4.4.1.1 Coaxial Nanofibers and Nanotubes of PANI

Electrically conductive polyaniline (PANI)/poly(methyl methacrylate) (PMMA) coaxial fibers were prepared through the chemical deposition of PANI onto preformed PMMA fibers via *in situ* polymerization [31]. PMMA fibers were prepared as core materials via electrospinning. Spectral studies and scanning electron microscopy observations indicated the formation of PANI/PMMA coaxial fibers with a diameter of approximately 290 nm and a PANI layer thickness of approximately 30 nm. The polymer molecular weight, solution concentration, solvent dielectric constant, and addition of soluble organic salts were strongly correlated to the morphology of the electrospun fiber mat. It was concluded that the conductivity of the PANI/PMMA coaxial fibers was significantly higher than that of electrospun fibers of PANI/poly(ethylene oxide) blends and blend cast films of the same PANI composition. Moreover, core–shell nanofibers with conductive polyaniline as the core and an insulating polymer as the shell were prepared by electrospinning of blends of polyaniline with either polystyrene or polycarbonate [32]. The incompatibility of the polymers and low molecular weight of compositions played a key role in the formation of core–shell structures, as opposed to co-continuous morphologies when polyaniline was blended with the polymers. These unique core–shell structures offer a potential in a number of applications, including nanoelectronics.

Polyaniline (PANI) nanowires and nanotubes can also be developed by electrospinning. Polyaniline nanotubes have been prepared using submicrometer polymer fibers as templates [33]. The core fibers were fabricated by electrospinning and conductive polyaniline (PANI) was coated on the surface of preformed polymer nanofibers by *in situ* deposition. The removal of the core from the resulting PANI coaxial fibers by pyrolysis leads to the formation of PANI tubular materials, which undergo reversible doping between the conducting and insulating phase with acid or base. Nanowires have also been prepared using electrospun PANI/PEO and PANI/PMMA polymer blends [34]. Pure PANI

nanotubes were prepared using the electrospun PMMA nanowires as a template, and aligned on a substrate by using a simple electrostatic steering method.

Further, emulsion polymerization and electrospinning were used to prepare polyaniline-nylon-6 composite nanowires [35]. In particular, polyaniline (PANI) nanoparticles doped with dodecylbenzene sulfonic acid (DBSA) were prepared, and these nanoparticles were electrospun with nylon-6 as the matrix material into a fiber web. Depending on the contents and concentrations of PANI and nylon-6, either nylon-6 nanofibers (~96 nm) or PANI-nylon-6 composite nanofibers (~12 nm) were obtained. The electrical conductivity of PANI(DBSA)–nylon-6 electrospun fiber web was lower than that of PANI(DBSA)-nylon-6 film because of the low crystallinity of the PANI(DBSA)-nylon-6 composite electrospun fiber web. However, it was shown that the PANI-nylon-6 composite nanofibers would have applications as nanowires for connecting microelectromechanical systems (MEMS). Other studies using electrospinning developed microscale helical coils consisting of a composite of one conducting poly(aniline sulfonic acid) and one nonconducting polymer (PEO). The helical structures were formed as a result of viscoelastic contraction upon partial neutralization of the charged fibers. Such polymeric microcoils may find application sin microelectromechanical systems, advanced optical components, and drug delivery systems [36].

4.4.1.2 PANI Nanofibers with Carbon Nanotubes

A good strategy for improving the electrical properties of electrospun conducting fibers is to incorporate carbon nanotubes (CNTs), which have superior electrical conductivity, into the conducting polymer. In the work of Shin *et al.*, PANI/PEO/MWNT multiwalled carbon nanotubes nanofibers were fabricated to increase the electrical conductivity of PANI/PEO nanofibers [37]. While measuring the conductivity of the conducting composite nanofibers, they observed a new, unexpected transition in the electrical conductivity of the conducting composite nanofibers when the aligned composite fibers were exposed to a high electric field. The surprise transition is closely related to the self-heating of the CNTs inside the conducting polymer, and the transition in the electrical conductivity was attributed to a change in the localization length of the composite fibers (Figure 4.9). Such experimental data represent one example of using thermal dissipation by the self-heating of CNTs in a nanoscale structure. They state that, in the future, the self-heating method will be very helpful in enhancing the electrical properties of conducting composite fibers, combined with a method for increasing the amount of CNTs that can be incorporated into a conducting polymer.

4.4.2 Polypyrrole (PPy)

Polypyrrole (PPy) is a widely investigated conducting polymer with good electrical conductivity and good environmental stability under ambient conditions. Chronakis and coworkers prepared conductive polypyrrole nanofibers with diameters in the range of about 70–300 nm using electrospinning processes, and discussed the factors that facilitate the formation of electrical conduction paths through the electrospun nanofiber segments [38]. Two methods were employed (Figure 4.10). Electrospun nanofibers were prepared

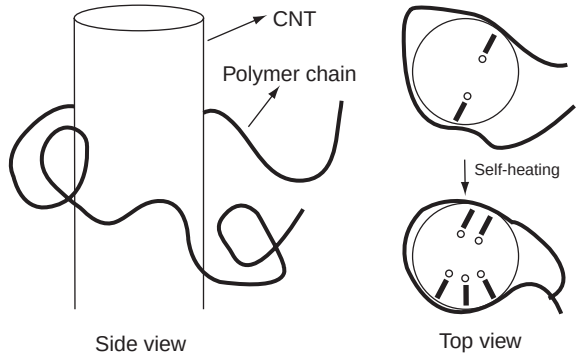

Figure 4.9 *A scheme showing the change in interactions between a CNT and a polymer chain by the self-heating of a CNT inside a conducting composite nanofiber. (Reprinted with permission from Sensors and Actuators B., Enhanced conductivity of aligned PANi/PEO/MWNT nanofibers by electrospinning by M. K. Shin, Y. J. Kim, S. I. Kim et al., 134, 122–126. Copyright (2008) Elsevier Ltd)*

from a solution mixture of PPy, and poly(ethylene oxide) (PEO) acted as a carrier in order to improve PPy processability. Both the electrical conductivity and the average diameter of PPy nanofibers can be controlled with the ratio of the PPy/PEO content. In addition, pure (without carrier) polypyrrole nanofibers could also be formed by electrospinning organic-solvent-soluble polypyrrole, [(PPy_3)C (DEHS)K]x, prepared using the functional doping agent di(2-ethylhexyl) sulfosuccinate sodium salt (NaDEHS). Electrospun blends of sulfonic acid (SO_3H)-bearing water soluble polypyrrole, [PPy(SO_3H)—DEHS], with PEO acting as a carrier, were also reported.

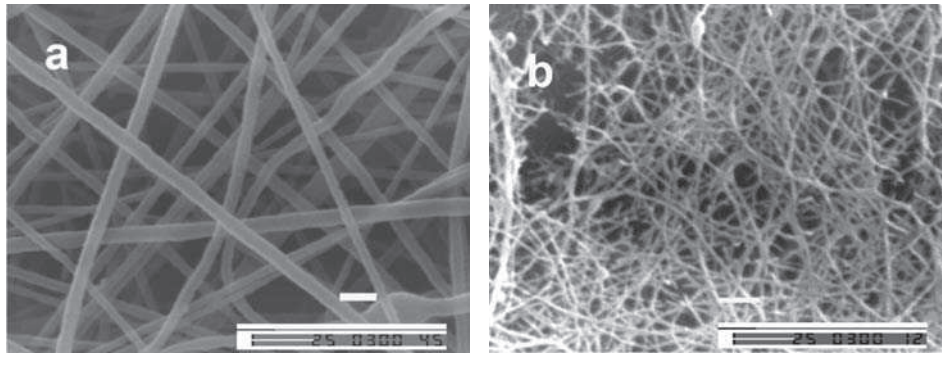

Figure 4.10 *SEM micrographs of electrospun nanofibers from (a) aqueous solutions of 1.5 wt% PEO as carrier with PPy content of 71.5 wt%, (b) 7.5wt% $[(PPy3)^{+}\ (DEHS)^{-}]_x$ solution in DMF. The scale bar is 1μm. (Reprinted with permission from Polymer, Conductive polypyrrole nanofibers via electrospinning: Electrical and morphological properties by I. S. Chronakis, S. Grapenson and A. Jakob, 47, 1597–1603. Copyright (2006) Elsevier Ltd)*

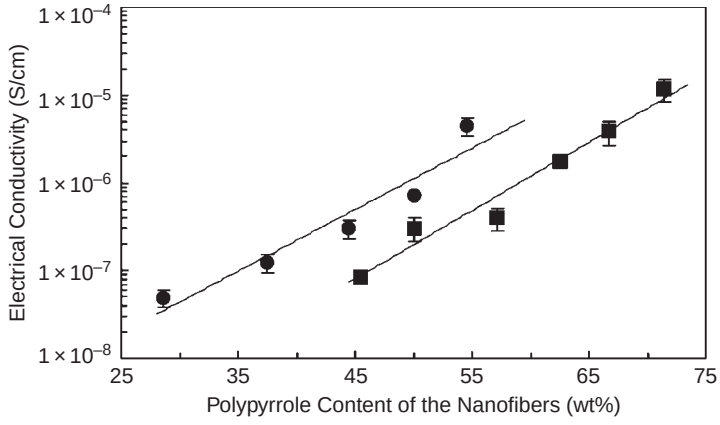

Figure 4.11 *Electrical conductivity of PPy/PEO nanofiber webs as a function of their polypyrrole content. Solutions of PPy with 2.5 wt% PEO (●) and 1.5 wt% PEO (■) as carrier were used (lines are visual guides). (Reprinted with permission from Polymer, Conductive polypyrrole nanofibers via electrospinning: Electrical and morphological properties by I. S. Chronakis, S. Grapenson and A. Jakob, 47, 1597–1603. Copyright (2006) Elsevier Ltd)*

The electrical conductivity of these nanofiber structures can be varied by controlling the ratio of PPy/PEO. As illustrated in Figure 4.11, the conductivity through the thickness of the electrospun PPy/PEO nanofibers increased by two orders of magnitude from the lowest to the highest concentration of PPy and ranged from about 4.9×10^{-8} to 1.2×10^{-5} S cm^{-1} [38].

Other studies also report electrically conducting polypyrrole-poly(ethylene oxide) (PPy-PEO) composite nanofibers. Nair *et al.* used a two-step process where, first, $FeCl_3$-containing PEO nanofibers are produced by electrospinning and the PEO-$FeCl_3$ electrospun fibers are then exposed to pyrrole vapor for the synthesis of polypyrrole [39]. The vapor-phase polymerization occurs through the diffusion of pyrrole monomer into the nanofibers. The collected nonwoven fiber mat was composed of 96 ± 30 nm diameter PPy-PEO nanofibers. Kang and coworkers prepared highly conducting soluble PPy chemically polymerized using ammonium persulfate (APS) as the oxidant and dodecylbenzene sulfonic acid (DBSA) as the dopant source [40]. The electrical conductivity and solubility of the resulting PPy powder varied significantly with the polymerization conditions, such as the concentration of the oxidant, polymerization temperature, and time. The PPy solution with the appropriate concentration in chloroform was then electrospun resulting in electrically conducting PPy fibers with a circular cross-section, a smooth surface, and a diameter of about 3 μm. It was found that the electrical conductivity of the compressed PPy nonwoven web was about 0.5 S cm^{-1}, which was slightly higher than that of the powder or the cast films, possibly because of molecular orientation induced during electrospinning.

The fabrication and characterization of conductive and aligned polymeric nanofibers using PPy and PEO were studied by Lee *et al.* [41]. Composite materials containing a conducting (PPy) polymer alloyed with a nonconducting (PEO) polymer were proposed to improve the structural and electrical properties of the aligned nanofibers. The resulting electric field between the grounded base/collector plates and the charged syringe can be

split by separating the metal target plates, and this divergence in the electric field facilitates the ordered placement of the nanofibers. In this way, ordered, continuous nanofibers with a diameter of 150 nm were developed.

A novel route to pure and composite fibers of polypyrrole was recently reported by Han and Shi [42]. An organic salt (FeAOT) was synthesized by the reaction of sodium 1,4-bis(2-ethylhexyl)sulfosuccinate (AOT) and ferric chloride. It was fabricated into nanofibers by manual drawing and electrospinning. Long PPy fibers were obtained for the first time by a vapor deposition reaction of pyrrole on the FeAOT fibers, and this technique was extended to the synthesis of PPy composite fibers with multiwalled carbon nanotubes (PPy-MWCNT fibers). The PPy and PPy-MWCNT fibers had a nanoporous morphology, a conductivity of 10–15 S cm^{-1} and a tensile strength of 12–43 MPa. Studies of the electrochemistry and current–voltage characteristics of the PPy fibers were also reported.

Conductive polyamide-6 (PA-6) nanofibers have been prepared by making a conductive polypyrrole coating obtained by a polymerization of pyrrole molecules directly on the fiber surface [43]. A solution of PA-6 added with ferric chloride in formic acid was electrospun, and the fibers obtained showed an average diameter of 260 nm with a smooth surface. The fibers were then exposed to pyrrole vapors, and a compact conductive coating of polypyrrole formed on their surface. Conducting nanofibers using a poly(dimethyl siloxane) (PDMS)-based microfluidic device were presented by Srivastava and coworkers [44]. To scale up the process and spin multicomponent systems, they designed a unique multispinnerette electrospinning device using microchannels cast in PDMS. Nanofibers of poly (vinylpyrrolidone) and its composite with polypyrrole were successfully prepared using one-step and two-step microfluidic electrospinning. The effect of processing variables on the morphology of the nanofibers formed using this device was also studied in detail.

4.4.2.1 Core-Shell Polypyrrole Nanofibers and Nanotubes

A simple method was recently introduced for preparing core–shell nanostructured conductive PPy composite [45]. The PPy core particles were first introduced in flexible shell solutions by *in situ* polymerization, and then different core–shell structures could be obtained by the electrospinning method (Figure 4.12). In that study, PPy was selected as the as-dispersed phase (cores) and polyacrylonitrile (PAN) as the continuous phase (shell); the morphology of the resulted nanostructures can be controlled by changing the concentration of the solutions. This method is very useful in the design and preparation of nanosized core–shell structures using electroconductive polymers.

In another method, the fabrication of electrically conducting nonwoven porous mats of polystyrene–polypyrrole core–shell nanofibers via electrospinning and vapor-phase polymerization was proposed [46]. PS nanofibers were produced by electrospinning PS solutions containing chemical oxidants capable of polymerizing pyrrole monomers. The electrospun (PS) nanofibers provided a robust and stable template for the growth of conducting PPy layers via a vapor-phase polymerization process. Two chemical oxidants widely used in PPy synthesis – ferric chloride and ferric tosylate – were compared. Upon exposure to pyrrole vapor, both oxidants produced PPy conducting polymers over PS nanofibers. It was found that the ferric-tosylate-containing template fibers showed much faster PPy growth kinetics than the ferric-chloride-containing fibers. The PPy growth on ferric-tosylate-containing template fibers also produced highly faceted fibers and gave a

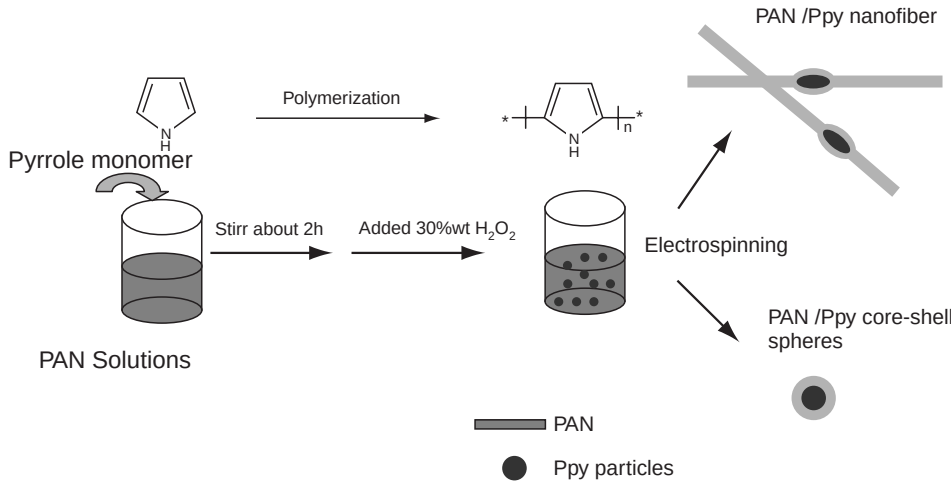

Figure 4.12 *Schematic illustration of the mechanism for preparing core–shell nanostructured conductive PPy composites. (Reprinted with permission from Materials Letters, Fabrication of Polyacrylonitrile/polypyrrole (PAN/Ppy) composite nanofibers and nanospheres with core shell structures by electrospinning by X. Li, X. Hao, H. Yu and H. Na, 62, 1155–1158. Copyright (2008) Elsevier Ltd)*

higher degree of crystallization of PPy than the PPy grown with ferric-chloride-containing templates. Moreover, the intrinsic doping of PPy was slightly higher in the PPy layers grown with ferric tosylate. Overall, it was concluded that the combination of higher degrees of crystallization and doping resulted in a higher conductivity in PS–PPy nanofiber mats produced with ferric tosylate than those produced with ferric chloride.

Dong and Jones Jr. reported on the preparation of submicron electrically conductive polypyrrole/poly(methyl methacrylate) coaxial fibers and conversion to polypyrrole tubes and carbon tubes [47]. In this study, PMMA fibers with an average diameter of 230 nm were initially fabricated by electrospinning as core materials. The PMMA fibers were subsequently coated as templates with a thin layer of PPy by *in situ* deposition of the conducting polymer from aqueous solution. Hollow PPy nanotubes were produced by dissolution of the PMMA core from PPy/PMMA coaxial fibers. Furthermore, high temperature (1000 °C) treatment under an inert atmosphere can be used to convert PPy/PMMA coaxial fibers into carbon tubes by complete decomposition of the PMMA fiber core and carbonization of the PPy wall (Figure 4.13).

4.4.3 Polythiophenes (PThs)

Polythiophene derivates are polymers of great interest, widely used in organic electronics. Thus, the utilization of polythiophene nanofibers could open the path to the development of nanostructured organic electronics with a high surface area for a range of applications. El-Aufy, in his PhD thesis, studied poly(3,4-ethylene dioxythiophene)/poly(styrenesulfonate) PEDOT/PSS nanofibers and nanocomposites using PAN as a

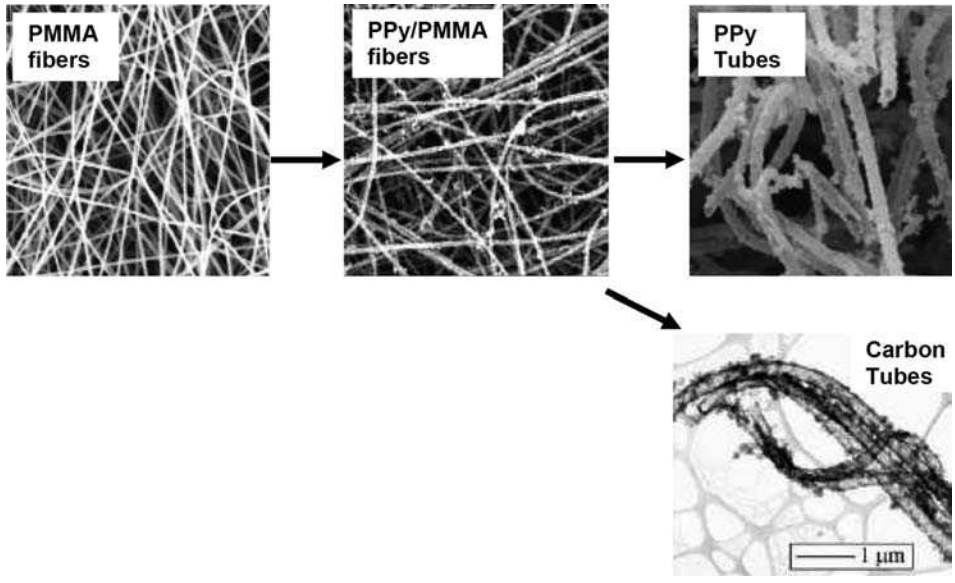

Figure 4.13 *Preparation of submicron polypyrrole/poly(methyl methacrylate) coaxial fibers and conversion to polypyrrole tubes and carbon tubes. (Reprinted with permission from Langmuir, Preparation of Submicron Polypyrrole/Poly(methyl methacrylate) coaxial fibers and conversion to polypyrrole tubes and carbon tubes by H. Dong and W. E. Jones Jr., 22, 11384–11387. Copyright (2006) American Chemical Society)*

spinnable carrier for PEDOT/PSS [48,49]. The PEDOT/PSS/PAN polymer could be electrospun into a self-assembled yarn and the self-assembled yarn was initiated by an initial deposition of the nanofibers concentrated in a small area on the target. A four-fold increase in electrical conductivity was observed as fiber diameter decreased from 260 nm to 140 nm, confirming the significant effect of fiber diameter on electrical conductivity. To introduce multiple functions to the electrospun yarn, single-walled carbon nanotubes (SWNTs) were successfully coelectrospun with a PEDOT/PAN blend. The inclusion of SWNTs showed a further increase in electrical conductivity of nanofibrous yarn, and the tensile strength was increased by 50%. The carbon-nanotube-reinforced PEDOT nanofibrous yarn was woven into a fabric to demonstrate the feasibility of the electrospun yarn as an attractive enabling material for wearable electronics.

Poly(vinyl pyrrolidone) (PVP) was used by Nguyen *et al.* as a polymer matrix to prepare electrically conducting nano(micro)poly(3,4-ethylenedioxythiophene) (PEDOT) fiber nonwoven web [50]. The electrical conductivity of the electrospun PEDOT nonwoven web was as high as 7.5 S cm^{-1} when 1-propanol was used as the solvent. An electrochemical capacitor was assembled using one pair of the PEDOT nonwoven webs as the electrodes by a simple stack method, where metal plates were used as current collectors. They observed the electrochemical charge and discharge behavior of the capacitor, confirming that the PEDOT nonwoven web can be used as an electrode for flexible electrochemical capacitors.

Further, Bianco and coworkers used the electrospinning processing to produce fibers of poly-3-dodecylthiophene (P3DDT), both as pure material and in association with PEO [51].

The role of the PEO matrix during the spinning process is of great relevance since it aids in the formation of fibers of polythiophene with good morphology. The polymer matrix can be selectively removed by using acetonitrile, with the consequence that dense fibers made only of poly-3-dodecylthiophene are produced (Figure 4.14). They further studied how the electrospinning process affects the alignment of the polymer chains and, consequently, the molecular structure. It was pointed out that the molecular structure of polythiophene in electrospun fibers is valuable in the field of molecular electronics since it is well known that the optical and electrical properties of conducting polymers are strictly related to their molecular structure and their ability to pack. Their findings support that all fibers obtained show birefringence and a strong orientation of the polythiophene chains along the fiber axes, as measured by polarized IR spectroscopy. In addition, the washing process with acetonitrile was found to affect the structure of the lateral alkyl chains and their packing.

Poly-3-hexylthiophene is also a polymer of great interest, widely used in organic electronics, especially in photovoltaic devices. Fabrication of poly-3-hexylthiophene/polyethylene oxide nanofibers (P3HT–PEO) with diameters down to 500 nm using

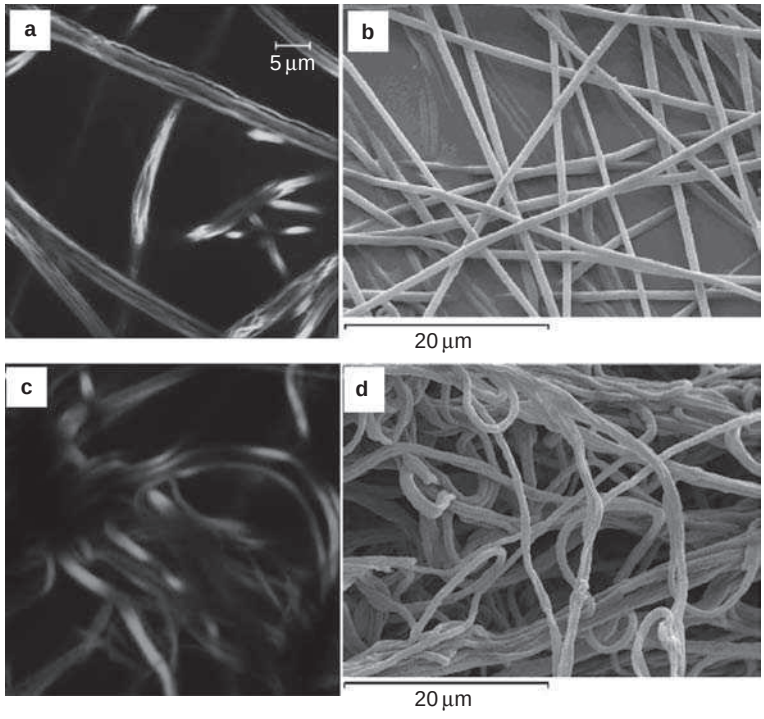

Figure 4.14 *Fluorescence confocal image of (a) P3DDT + PEO fibers; (b) SEM image of a sample of fibers; (c) fluorescence confocal image of P3DDT fibers (PEO was removed by washing with acetonitrile); (d) SEM image from the same sample of fibers. (Reprinted with permission from Synthetic Metals, Electrospun polyalkylthiophene/polyethyleneoxide fibers: Optical characterization by A. Bianco, C. Bertarelli, S. Frisk et al., 157, 276–281. Copyright (2007) Elsevier Ltd)*

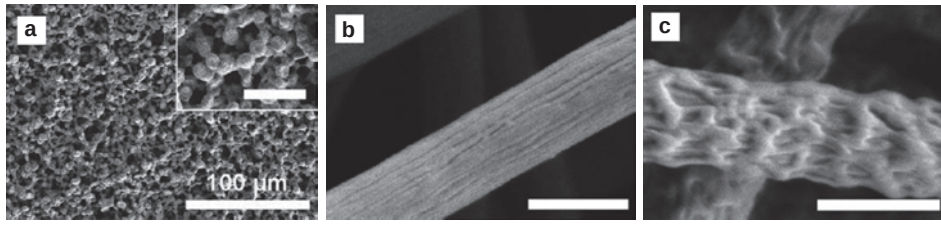

Figure 4.15 *(a) SEM micrograph of electrosprayed 3wt% P3HT solutions in THF; inset is closer view of the surface structures. Scale bar in the inset represents 10 μm; (b) high resolution SEM image of nanofibers with 75 wt% P3HT content; scale bar represents 500 nm; (c) SEM image of nanofibers with 50 wt% P3HT content (RH 39%, T = 21–23 °C); scale bar represents 1 μm. (Reprinted with permission from Synthetic Metals, Fabrication of poly-3-hexylthiophene/polyethylene oxide nanofibers using electrospinning by A. Laforgue and L. Robitaille, 158, 577–584. Copyright (2008) Elsevier Ltd)*

electrospinning (Figure 4.15) was reported by Laforgue and Robitaille [10]. The morphological study using SEM and TEM revealed that the polymer domains are aligned along the nanofiber axis, and the structural arrangement of the polymers inside the fibers was observed to change according to the ratio of the two polymers. Moreover, the conductivity was found to increase with decreasing nanofiber diameter, which could be related to an improvement in the interchain interactions caused by the compaction of the polymer chains inside the fibers and/or to the increase in the fibers' packing density in the mat. The maximum conductivity measured for unaligned fiber mats was $0.16\,S\ cm^{-1}$ and increased twice to $0.3\,S\ cm^{-1}$ when the nanofibers were aligned in one preferential direction. As discussed, this result indicates that the electrical conductivities measured by the four-point probe method are related not only to the intrinsic properties of the material, but also to the geometric structure of the sample. Consequently, the authors discussed the electrical conductivity values obtained for the mats being only apparent conductivities, and not applicable to single fibers, which present significantly higher conductivities. It is suggested that two phenomena could explain this observation [10]. The first occurs at the fiber level, and the second at the mat level. In the first case, the increased fiber stretching and related decrease in fiber diameter are believed to be directly related to a more significant polymer compaction in the fiber: when more highly stretched, the polymer chains are more compacted in the fibers, leading to a decrease in diameter. The chains within the fibers would then have better interactions with their neighbors, the lack of which is known to be the main limiting parameter to electrical conductivity. The polymer chain compaction should then lead to a better charge transport inside the fibers. Alternatively, given that the measured conductivity is a volumic one, the observed increase in conductivity could also be explained by the increase in the packing density of the mat: the decrease in fiber diameter allows the deposition of more fibers in a given volume, resulting in a larger number of electronic paths usable for the conduction.

The Sotzing group has proposed an original and elegant synthetic method for electrospinning otherwise unprocessable polythiophenes. Conducting polymer nanofibers with average diameters as low as 119 nm that exhibit electrochromism were prepared via

electrospinning of a soluble precursor polymer followed by solid/swollen-state oxidative cross-linking. During the solid/swollen-state oxidative cross-linking, the fibers welded together without significant perturbation of the morphology, thus maintaining the quality and shape of nanofibers while apparently establishing an interconnected network. The nanofibers were found to exhibit switching times between 2 and 3 s, which was approximately 20-fold faster than 1-μm-thick electrochemically prepared films of PEDOT using the same electrochemical conditions. They suggested alignment of the pendant terthiophenes during the electrospinning process resulted in an increased effective conjugation length [52]. The same group also reported the patterning of large conducting polymer nanofiber mats of the polyterthiophene precursor into regular micron-scale arrays of smaller mats, each of which has the potential of being independently addressed. These fiber grids (micro mats of conducting polymer fibers) were prepared by the combined techniques of electrospinning, soft photolithography, and solid-state electrochemical cross-linking and were shown to retain their electrochromic behavior [53,54].

Further, Lee *et al.* used electrospinning to develop uniform regio-regular poly (3-hexylthiophene) nanofibers and their blend nanofibers with poly (ε-caprolactone) [55]. This was achieved by restricting the precipitation of P3HT at the nozzle tip, therefore preventing the nozzle from becoming clogged. The field-effect mobility of pure P3HT fibers was 0.017 $cm^2\ V^{-1}\ s^{-1}$, which is acceptable for device fabrication.

In work by Kuo *et al.,* electrospun sensory fibers (diameters of 500–700 nm) consisting of a PMMA core and a poly(3-hexylthiophene-2,5-diyl) (P3HT) shell were prepared using a two-fluid coaxial electrospinning process [56]. Red emission fibers were exhibited from the laser confocal microscope and upon exposure to air and light for two weeks, significant blue-shifting was found on both absorption and luminescence spectra. As they suggested, this was probably due to chain scission occurring in the P3HT that led to reduced conjugated length. The nanofibers were more sensitive than the spin-coated P3HT film, by comparing the variation of their photophysical properties. Besides, the EPR results indicated the formation of the $P3HT{\cdot}O_2$ charge-transfer complex, leading to the fiber conductivity of 10^{-6} S cm^{-1} achieved without an external doping. This study demonstrated that conjugated polymer-based electrospun core–shell nanofibers may have potential applications in oxygen-sensing devices [56].

4.4.4 Poly(*p*-phenylene vinylenes) (PPVs)

Poly(phenylene vinylene) (PPV) is another valuable conjugated polymer, as the synthetic process of PPV is simple and low cost. PPV possesses excellent photoluminescent (PL) and electroluminescent (EL) properties, as well as photovoltaic (PV) and nonlinear optical properties [57]. These properties have led to its being used in broad applications, in such areas as light-emitting diodes (LEDs) and flat-panel displays and photonics applications such as wave-guiding and all-optical switching.

PPV nanofibers that retain their photoluminescent properties were fabricated by electrospinning PPV precursor solution in solvent mixtures of ethanol/water [57–59]. The luminescent nanofibers were obtained by electrospinning a solution of PMO-PPV, $Eu(ODBM)_3$phen and PMMA. The electrospun fibers, with diameters ranging from 70 nm to 200 nm and having a parallel orientation, show strong green and red

photoluminescence properties. The peak fluorescence positions of fibers were at 515 and 550 nm, which were the same as those of PPV film. This kind of eletrospun nanofiber is a promising candidate for optical and electrical nanomaterials for nanoscale electrical or photoelectronic nanodevices such as LEDs and flat-panel displays.

Tan *et al.* published an approach for fabricating nanofibers containing luminescent conjugated polymer, poly(2-methoxy-5-octoxy)-1,4-phenylene vinylene)-alt-1,4-(phenylene vinylene) (PMO-PPV), and rare earth complex, $Eu(ODBM)_3phen$ (ODBM: 4-*n*-octyloxydibenzoylmethanato; phen: 1,10-phenanthroline) via an electrospinning technique [60]. The electrospun fibers, with diameters ranging from 70 nm to 200 nm and having a parallel orientation, show strong green and red photoluminescence (Figure 4.16).

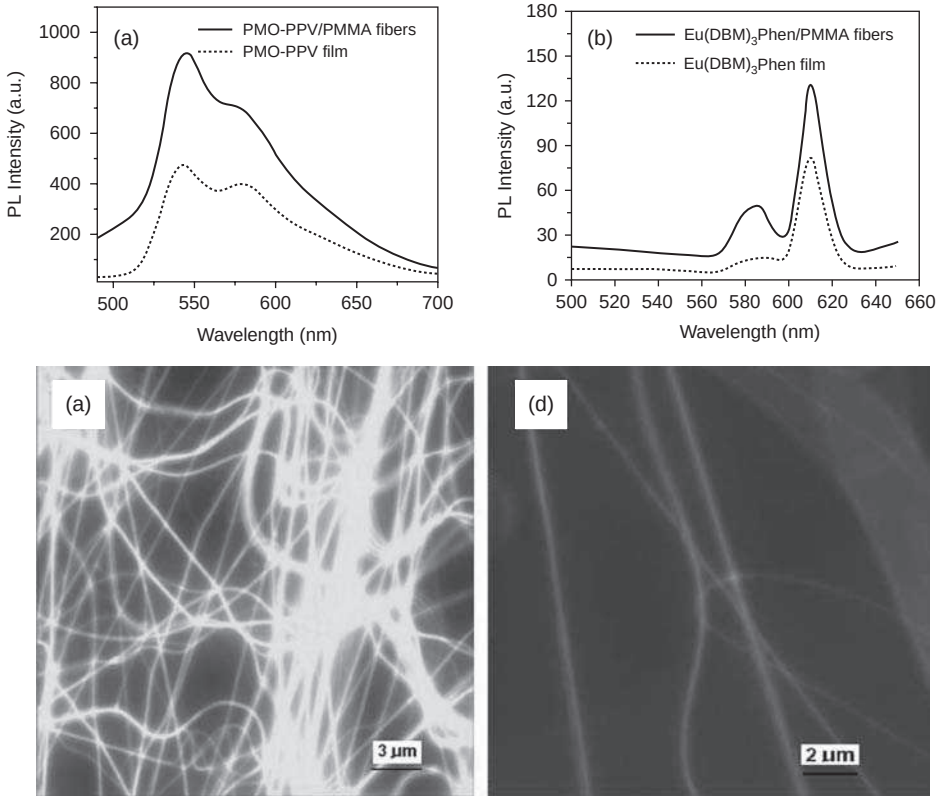

Figure 4.16 *PL spectra of (a) 20 wt% PMO-PPV/PMMA eletrospun fibers and net PMO-PPV films, and (b) 20 wt% $Eu(ODBM)_3phen$/PMMA eletrospun fibers and net $Eu(ODBM)_3phen$ films; (c) fluorescent optical microscope images of 20 wt% PMO-PPV/PMMA and (d) 20 wt% $Eu(ODBM)_3phen$/PMMA eletrospun fibers on a quartz flake. (Reprinted with permission from Materials Letters, Preparation and photoluminescence properties of electrospun nanofibers containing PMO-PPV and $Eu(ODBM)_3phen$ by S. Tan, X. Feng, B. Zhao et al., 62, 2419–2421. Copyright (2008) Elsevier Ltd)*

A drawback of PPV is its poor solubility and decomposition before melt, making it difficult to process and thus limiting its application. One strategy for solving this problem is to process the soluble sulfonium precursor of PPV, and then convert it into the conjugated form by a thermal elimination reaction, as reported by Xin *et al.* [61–63]. In that work, the neutral polymer poly(vinyl pyrrolidone) (PVP) was introduced into PPV cationic polyelectrolyte precursor solution to increase the degree of bending instability during electrospinning. Well-aligned nanofibers with outstanding emission properties were successfully prepared, and this was followed by thermal conversion. The PL spectrum of PPV/PVP nanofibers exhibited a blue shift and a change in the intensity of vibrant components relative to PPV nanofibers. It was mentioned that these PPV/PVP nanofiber arrays can be conveniently transferred onto various surfaces for many applications, including the fabrication of electronic and photonic nanodevices.

Poly[2-methoxy-5-(2′-ethyl-hexyloxy)-1,4-phenylene vinylene] (MEH-PPV) is an excellent conjugated polymer and broadly used in polymer photoelectron devices, but is difficult to electronspin directly. In the work by Zhao *et al.*, core–shell structured nanofibers were fabricated by coaxial electrospinning MEH-PPV (shell) in chlorobenzene and PVP (core) in 1,2-dichloroethane [64]. MEH-PPV was soluble in the above two solvents, which prevented the precipitation of MEH-PPV and enhanced the adhering action between the two polymers in the coaxial electrospinning process. It should be noted that this is an unusual example of core–shell nanofibers where (a nonprocessable) PPV was spun as the shell and not in the core. These uniform core/shell PVP/MEH-PPV nanofibers with a highly fluorescent property can have potential applications in the fabrication of polymer nanophotoelectron devices.

Other studies support the formation of poly(*p*-phenylenevinylene) nanofiber yarns through electrospinning a precursor [65], and ultrafine poly[2-methoxy-5-(2′-ethylhexyloxy)-1,4-phenylene-vinylene] (MEH-PPV) nanofibers using polystyrene or poly(vinyl pyrrolidone) (PVP) as polymer carries [66,67]. Pure MEH-PPV fibers obtained after the removal of PVP by Soxhlet extraction showed a remarkable blue shift of the photoluminescence (PL) peak. Moreover, Madhugiri *et al.* employed a dual-syringe electrospinning set-up to produce a composite fiber web of semi-conducting electroluminescent poly(2-methoxy-5-(2′-ethyl-hexyloxy)-1,4-phenylenevinylene) (MEH-PPV) and mesoporous SBA-15 silica, a surfactant-templated mesoporous material usually used as a molecular sieve [68]. Such a sieve can find applications in catalysis, separation, chemical sensors, dielectric coatings etc.

As shown in the study by Chen *et al.*, the morphology and photophysical properties of 2,3-dibutoxy-1,4-poly-(phenylene vinylene)/poly(methyl methacrylate) (DB-PPVDB-PPV/PMMA)-blend luminescence electrospun nanofibers could be efficiently tuned by the choice of solvent type and conjugated moiety content [69]. The blend fiber prepared from solvents with different boiling points (chloroform, tetrahydrofuran, chlorobenzene) led to various aggregated morphology of DB-PPV, such as core–shell or wire-like structures. The absorption and luminescence peak maxima were red-shifted with larger DB-PPV aggregation size or increasing blend content, but the luminescence quantum efficiency showed a decreasing trend. In addition, highly aligned DB-PPV/PMMA-blend electrospun fibers with polarized emissions were successfully prepared from chlorobenzene using a modified collector design. This led to polarized green emissions with a dichroic ratio of 1.58–3.20 as the DB-PPV/PMMA ratio was increased from 1 to 30 wt%. These studies propose that such

luminescence fibers could have potential applications as new light sources, smart textiles, and optoelectronic devices.

4.4.5 Electrospun Nanofibers from Other Conductive Polymers

The work of Chen's team [70,71] on light-emitting polyfluorenes demonstrates that full color light-emitting electrospun nanofibers (diameters of 250–750 nm) could be produced from binary blends of polyfluorene derivative/PMMA. They studied poly(fluorene)s, including poly(9,9-dioctylfluoreny-2,7-diyl) (PFO), poly[2,7-(9,9-dihexylfluorene)-*alt*-5,8-quinoxaline] (PFQ), poly[2,7-(9,9-dihexylfluorene)-*alt*-4,7-(2,1,3-benzothiadiazole)] (PFBT), and poly[2,7-(9,9-dihexylfluorene)-*alt*-5,7-(thieno[3,4-b]pyrazine)] (PFTP). Uniform electrospun fibers produced from the binary blends of PFO/PMMA, PFQ/PMMA, PFBT/PMMA, and PFTP/PMMA exhibited the following luminescence characteristics (peak maximum (nm); color): 443, blue; 483, green; 539, yellow; 628, red. The same group also studied luminescence electrospun nanofibers based on ternary blends of poly(9,9-dioctylfluoreny-2,7-diyl) (PFO)/poly[2-methoxy-5-(2-ethylhexyloxy)-1,4-phenylenevinylene] (MEH-PPV)/PMMA [72]. The emission colors of the PFO/MEH-PPV/PMMA blend nanofibers changed through blue, white, yellowish-green, greenish-yellow, orange to yellow, as the MEH-PPV composition increased. In contrast, the emission colors of the corresponding spin-coated films were blue, orange, pink-red, red and deep red. Based on the values of solubility parameters, the PFO and MEH-PPV were miscible with each other and trapped in the PMMA matrix. Hence, energy transfer between these two polymers is possible. The smaller aggregated domains in the nanofiber compared to those of spin-coated films possibly reduce the efficiency of energy transfer, leading to different emission colors. The prepared electrospun fibers also had higher photoluminescence efficiencies than those of the spin-coated films. Pure white-light-emitting fibers prepared from the PFO/MEH-PPV/PMMA blend ratio of 9.5/0.5/90 had a Commission Internationale de L'Eclairage (CIE) coordinate of (0.33, 0.31). Overall, these studies showed that light-emitting electrospun nanofibers of different colors were produced through optimizing the composition of the semiconducting polymer in the transparent polymer matrix, which could have potential applications as new light sources or sensory materials for smart textiles, for instance.

Kim and coworkers used the electrospinning technique to prepare polydiacetylene (PDA) microfibers for colorimetric sensor applications [73,74]. Randomly distributed diacetylene monomers were found to self-assemble during fiber formation and enable the generation of blue-colored PDA-containing polymer fibers upon UV irradiation. Micropatterned images with a single fiber and the feasibility of a fiber-based sensor were demonstrated. Other innovative studies include the work of Choi *et al.* [75] on colorimetric sensing using new conjugated polymers comprising *o*-phenylazonaphthols linked with a phenylene or fluorene repeat unit, and the studies of Bhaskar and Lahann [76] on multicompartmental light-emitting fibers using conductive polymers. The latter work demonstrated the fabrication of novel multicompartmental biodegradable microstructures via electrohydrodynamic cospinning of two or more polymer solutions. Thus, under optimized processing conditions, the interface between the solutions can be sustained continuously for long time intervals, yielding fibers with multiple chemically distinct

compartments. It was suggested that simultaneous control over internal fiber architecture and the spatial arrangement of individual compartments combined with precise long-range fiber alignment make these fibers potential candidates for applications such as tissue engineering or cell-culture studies.

One-dimensional polymer nanostructures, such as polymer nanofibers, are compatible with a submicrometer patterning capability and electromagnetic confinement within subwavelength volumes, and they can offer the benefits of organic light sources to nanoscale optics. In this approach, Pisignano's team studied the optical properties of fully conjugated electrospun polymer nanofibers [77]. They assessed their wave-guiding performance and emission tuneability in the whole visible range. They also demonstrated the enhancement of the fiber forward emission through imprinting periodic nanostructures using room-temperature nanoimprint lithography, and investigated the angular dispersion of differently polarized emitted light. Kotaki and coworkers also studied the effect of electrospinning processes on the optical properties of conducting polymer nanofibers in terms of their diameter (100 nm and 1 μm) and molecular orientation [78]. Using a rotating disc collector, aligned nanofibers were prepared in order to induce molecular orientation in the electrospun fibers.

4.5 Applications of Electrospun Nanostructured Conductive Polymers

4.5.1 Biomedical Applications

The electrospinning process affords the opportunity to engineer scaffolds with micro- to nanoscale topography and high porosity, similar to the natural extracellular matrix (ECM). The inherently high surface-to-volume ratio of electrospun scaffolds can enhance cell attachment, drug loading, and mass-transfer properties. Electrospun fibers can be oriented or arranged randomly, giving control over both the bulk mechanical properties and the biological response to the scaffold. Drugs ranging from antibiotics and anticancer agents to proteins, DNA, and RNA can be incorporated into electrospun scaffolds. Suspensions containing living cells have even been electrospun successfully [79]. Conducting polymers are of considerable interest for a variety of biomedical applications. Their response to electrochemical oxidation or reduction can produce a change in conductivity, color, and volume. A change in the electronic charge is accompanied by an equivalent change in the ionic charge, which requires mass transport between the polymer and electrolyte [80].

Li and coworkers blended polyaniline (PANI), with a natural protein, gelatin, and coelectrospun the blend into nanofibers to investigate its potential application as a conductive scaffold for tissue-engineering purposes [81,82]. They found that the doping of gelatin with a few % of PANI (from 0 to 5%w/w) leads to an alteration of the physicochemical properties of gelatin. To test the usefulness of PANI-gelatin blends as a fibrous matrix for supporting cell growth, H9c2 rat cardiac myoblast cells were cultured on fiber-coated glass cover slips (Figure 4.17). Cell cultures were evaluated in terms of cell proliferation and morphology. Their results indicate that all PANI-gelatin blend fibers supported H9c2 cell attachment and proliferation to a similar degree as the control tissue culture-treated plastic (TCP) and smooth glass substrates. Depending on the concentrations

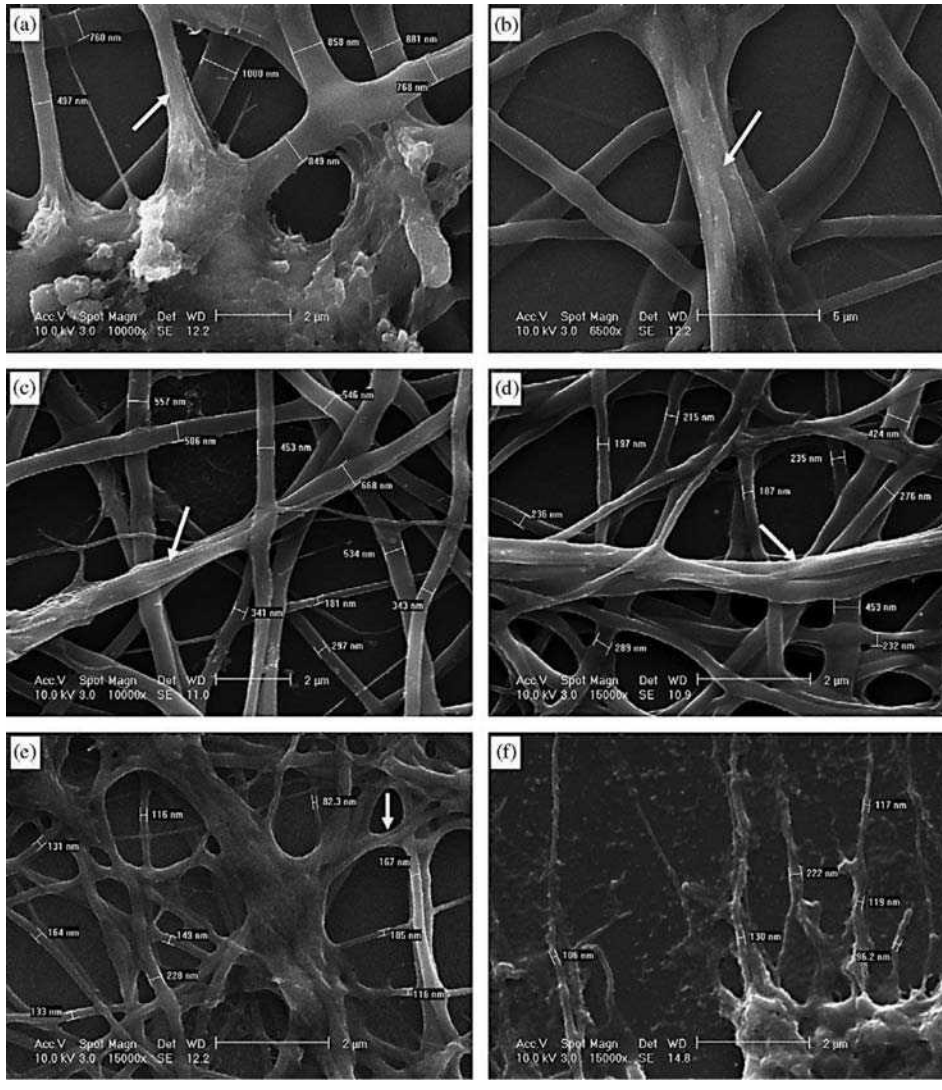

Figure 4.17 *SEM micrographs of H9c2 cells cultured on fibrous substrates: (a) cell pseudopodia on gelatin fibers; cell pseudopodia grew along; (b) gelatine fibers; (c) 15:85; (d) 30:70; (e) 45:55 PANI-gelatin blend fibers; and (f) cell pseudopodia on glass flat surface. (Reprinted with permission from Biomaterials, Electrospinning polyaniline-contained gelatin nanofibers for tissue engineering applications by M. Li, Y. Guo, Y. Wei et al., 27, 2705–2715. Copyright (2006) Elsevier Ltd)*

of PANI, the cells initially displayed different morphologies on the fibrous substrates, but all the cultures reached confluence of similar densities and morphologies after one week. Overall, they demonstrated that the electrospun C-PANI-gelatin blend fibers are biocompatible, supporting the attachment, migration, and proliferation of H9c2 rat cardiac myoblasts,

and that they might provide a novel conductive material well suited as biocompatible scaffolds for tissue engineering.

The same group also studied the conducting polymer, polyaniline (PANI), as a novel electrically conductive material for neuronal and cardiac tissue-engineering applications. It was suggested that the biocompatibility of the conductive polymer can be improved by: (i) covalently grafting various adhesive peptides onto the surface of prefabricated conducting polymer films or into the polymer structures during the synthesis, (ii) coelectrospinning or blending with natural proteins to form conducting nanofibers or films, and (iii) preparing conducting polymers using biopolymers, such as collagen, as templates. The work of Li *et al*. describes the approaches of covalently attaching oligopeptides to PANI and electrospinning PANI-gelatin blend nanofibers [82]. The employment of such modified conducting polymers as substrates for enhanced cell attachment, proliferation, and differentiation was investigated with neuronal PC-12 cells and H9c2 cardiac myoblasts. Furthermore, they observed that conductive PANI, when maintained in an aqueous physiologic environment, retained a significant level of electrical conductivity for at least 100 h, even though this conductivity decreased over time. Their preliminary data also show that the application of microcurrent stimulates the differentiation of PC-12 cells. These studies demonstrate the potential for using PANI as an electroactive polymer in the culture of excitable cells and open the possibility of using this material as an electroactive scaffold for cardiac and/or neuronal tissue-engineering applications that require biocompatibility of conductive polymers.

Jun and coworkers studied the stimulation of myoblast differentiation by electrically conductive submicron fibers [83]. As known, myotubes assemble with bundles of myofibers to form the structural units in skeletal muscle. Myotube formation therefore plays an important role in restoring muscular functions, and there is a need to develop substrates to promote the differentiation of myoblasts to myotubes for muscle tissue engineering. In that study, they first developed electrically conductive composite fibers of poly(L-lactide-*co*-ε-caprolactone) (PLCL) blended with polyaniline (PANI) using an electrospinning method and then investigated the effect of these composite fibers on the differentiation of myoblasts. The prepared PLCL/PANI fibers showed no significant difference in fiber diameter or contact angle, regardless of the incorporation of PANI. The fibers containing 30% PANI maintained elastic properties of maximum elongation at break ($160 \pm 14.4\%$). The composite fibers were cytocompatible, as the DNA content on each fiber was similar for up to eight days of C2C12 myoblast culture. After four days of culture, the number of cells positive for sarcomeric myosin was 3.6 times greater on the electrically conductive fibers than on the PLCL fibers without PANI. Furthermore, the level of *myogenin* expression detected on day 8 of culture on PLCL/PANI (with 15% PANI) was approximately 1.6-fold greater than the PLCL fibers without PANI. Similar results were observed for the expression of other genes, including *troponin T* (2-fold greater) and the *myosin heavy chain gene* (threefold greater). As discussed, these results indicate that electrically conductive substrates can modulate the induction of myoblasts into myotube formation without additional electrical stimulation, suggesting that these fibers may have potential as a temporary substrate for skeletal tissue engineering.

In another work, electrically conductive PANI doped with camphorsulfonic acid (CPSA) was also blended with poly(L-lactide-*co*-ε-caprolactone) (PLCL) and then electrospun to prepare uniform nanofibers [84]. The CPSA-PANI/PLCL nanofibers show a

smooth fiber structure and consistent fiber diameters (that range from 100 to 700 nm), even with an increase in the amount of CPSA-PANI (from 0 to 30 wt%). The four-point probe analysis revealed that electrical properties are maintained in the nanofibers, where the conductivity significantly increases from 0.0015 to 0.0138 S cm^{-1} when the nanofibers are prepared with 30% CPSA-PANI. The cell adhesion tests using human dermal fibroblasts, NIH-3T3 fibroblasts and C2C12 myoblasts demonstrate significantly higher adhesion on the CPSA-PANI/PLCL nanofibers than pure PLCL nanofibers. In addition, the growth of NIH-3T3 fibroblasts is enhanced under the stimulation of various direct current flows. Obviously, the CPSA-PANI/PLCL nanofibers with electrical conductive properties may potentially be used as a platform substrate to study the effect of electrical signals on cell activities and to direct desirable cell function for tissue-engineering applications.

Electrospinning is a promising approach to the creation of nanofiber structures that are capable of supporting adhesion and guiding extension of neurons for nerve regeneration. Electrical stimulation of neurons in the absence of topographical features has been shown to guide axonal extension. In the study of Schmidt and coworkers, conductive meshes were produced by growing PPy on random and aligned electrospun poly(lactic-*co*-glycolic acid) (PLGA) nanofibers [85]. PPy-PLGA electrospun meshes supported the growth and differentiation of rat pheochromocytoma 12 (PC12) cells and hippocampal neurons comparable to noncoated PLGA control meshes, suggesting that PPy-PLGA may be suitable as conductive nanofibers for neuronal tissue scaffolds. Electrical stimulation studies showed that PC12 cells, stimulated with a potential of 10 mV cm^{-1} on PPy-PLGA scaffolds, exhibited 40–50% longer neurites and 40–90% more neurite formation than unstimulated cells on the same scaffolds. In addition, stimulation of the cells on aligned PPy-PLGA fibers resulted in longer neurites and more neurite-bearing cells than stimulation on random PPy-PLGA fibers, suggesting a combined effect of electrical stimulation and topographical guidance and the potential use of these scaffolds for neural tissue applications. Conductive core–shell nanofibers prepared by a combination of electrospinning and aqueous polymerization, and their potential application also in neural tissue engineering, were studied by Xia and coworkers [86]. Particularly, nanofibers electrospun from poly(ε–caprolactone) (PCL) and poly(L-lactide) (PLA) were employed as templates to generate uniform shells of PPy by *in situ* polymerization. These conductive core–shell nanofibers offer a unique system to study the synergistic effect of different cues on neurite outgrowth *in vitro*. It was found that explanted dorsal root ganglia (DRG) adhere well to the conductive core–shell nanofibers and generate neurites across the surface when there is a nerve growth factor in the medium. Furthermore, the neurites can be oriented along one direction and enhanced by 82% in terms of maximum length in a comparison of uniaxially aligned conductive core–shell nanofibers with their random counterparts. Electrical stimulation, when applied through the mats of conductive core–shell nanofibers, is found to further increase the maximum length of neurites for random and aligned samples by 83% and 47%, respectively, relative to the controls without electrical stimulation.

Futhermore, nanofiber scaffold electrodes based on PEDOT for cell stimulation were recently reported by Bolin *et al.* [87]. Electronically conductive and electrochemically active three-dimensional scaffolds based on electrospun poly(ethylene terephthalate) (PET) nanofibers were prepared. Vapor-phase polymerization was employed to achieve a uniform and conformal coating of poly(3,4-ethylenedioxythiophene) doped with tosylate (PEDOT:tosylate) on the nanofibers. The PEDOT coatings had a large impact on the

wettability, making the hydrophobic PET fibers super-hydrophilic. SH-SY5Y neuroblastoma cells were grown on the PEDOT-coated fibers. The SH-SY5Y cells adhered well and showed a healthy morphology. These electrically active scaffolds were used to induce Ca^{2+} signalling in SH-SY5Y neuroblastoma cells (Figure 4.18). It was concluded that the PEDOT:tosylate-coated nanofibers represent a class of three-dimensional host environments that combines excellent adhesion and proliferation for neuronal cells with the possibility of regulating their signalling.

A method for preparing conducting polymer nanotubes that can be used for precisely controlled drug release was reported by Abidian *et al.* [80]. The fabrication process

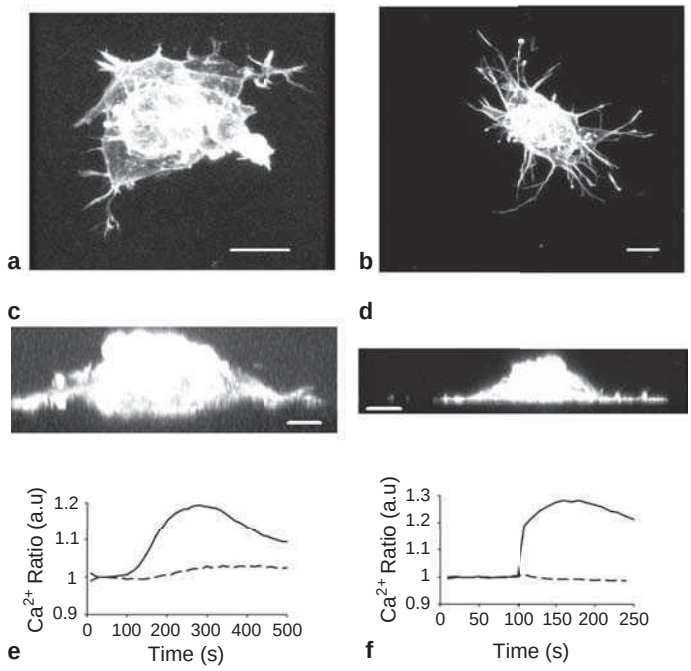

Figure 4.18 *Confocal micrograph top view Y-axis projection of Tritc-phalloidin stained cluster of SH-SY5Y cells growing on: (a) VPP-PEDOT coated nano-fiber surface; (b) cell culture treated glass. Scale bar = 20 μm. Confocal micrograph side view Z-projection of Tritc-phalloidin stained cluster of SH-SY5Y cells growing on: (c) VPP-PEDOT coated nanofiber surface (Scale bare = 10 μm) and (d) cell culture treated glass. Scale bar = 20 μm. Arrows indicate the direction of neurites. (e) Solid line shows intracellular Ca^{2+} flux in FURA-2-AM loaded SH-SY5Y cells cultured on nano-fiber surface. A potential of –3.0 V is applied at 100 s. The potential is turned off at 250 s and turned on again at 500 s. Dashed line shows cell treated with 50 μM nifedipine in order to block the VOCCs and stimulated with –3.0 V at 100 s until 380 s. (f) Solid line shows intracellular Ca^{2+} flux in FURA-2-AM loaded SH-SY5Y cells cultured in cell culture dish 50 mM KCl was added at 100 s. Dashed line shows cell treated with 50 μM nifedipine in order to block the VOCCs and stimulated in the same way. (Reprinted with permission from Sensors and Actuators B: Chemical, Nano-fiber scaffold electrodes based on PEDOT for cell stimulation by M. H. Bolin, K. Svennersten, X. Wang, I. S. Chronakis et al. 142, 451–456 (2009) Elsevier Ltd)*

involves electrospinning of a biodegradable polymer such as poly(L-lactide) (PLLA) or poly(lactide-*co*-glycolide) (PLGA), into which a drug has been incorporated, followed by electrochemical deposition of a conducting polymer (PPy or PEDOT) around the drug-loaded electrospun polymer (Figures 4.19, 4.20). They demonstrated that the impedance of

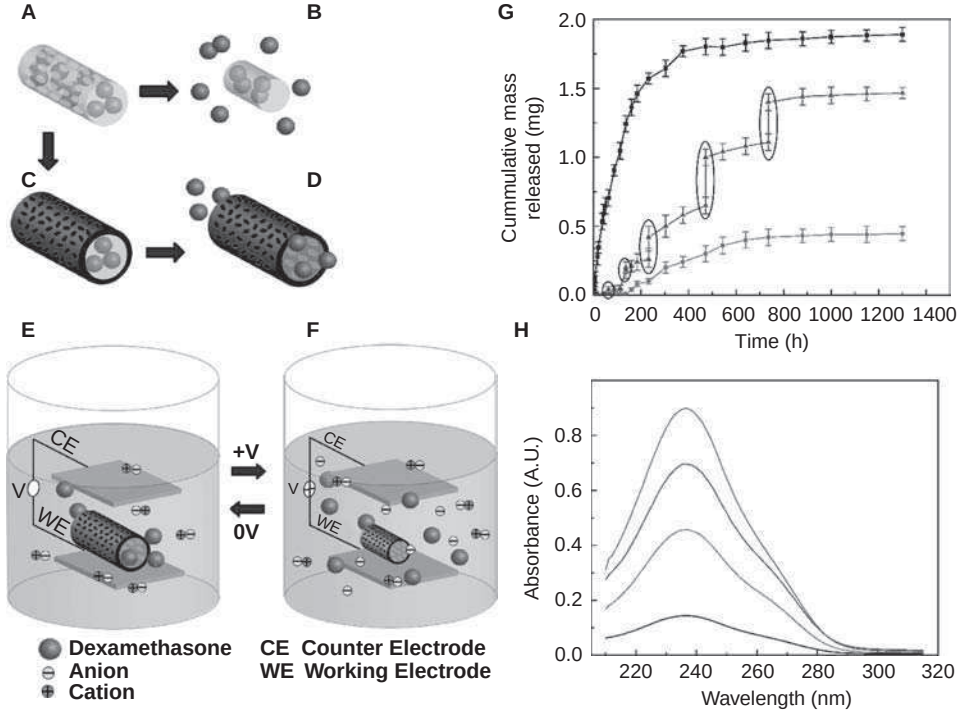

Figure 4.19 *Schematic illustration of the controlled release of dexamethasone: (A) dexamethasone-loaded electrospun PLGA, (B) hydrolytic degradation of PLGA fibers leading to release of the drug, and (C) electrochemical deposition of PEDOT around the dexamethasone-loaded electrospun PLGA fiber slows down the release of dexamethasone (D). (E) PEDOT nanotubes in a neutral electrical condition. (F) External electrical stimulation controls the release of dexamethasone from the PEDOT nanotubes due to contraction or expansion of the PEDOT. By applying a positive voltage, electrons are injected into the chains and positive charges in the polymer chains are compensated. To maintain overall charge neutrality, counter-ions are expelled towards the solution and the nanotubes contract. This shrinkage causes the drugs to come out of the ends of tubes. (G) Cumulative mass release of dexamethasone from: PLGA nanoscale fibers (black squares), PEDOT-coated PLGA nanoscale fibers (red circles) without electrical stimulation, and PEDOT-coated PLGA nanoscale fibers with electrical stimulation of 1 V applied at the five specific times indicated by the circled data points (blue triangles). (H) UV absorption of dexamethasone-loaded PEDOT nanotubes after 16 h (black), 87 h (red), 160 h (blue), and 730 h (green). The UV spectra of dexamethasone have peaks at a wavelength of 237 nm. Data are shown with a ± standard deviation (*n = 15 for each case). *(Reprinted with permission from Advanced Materials, Conducting-Polymer Nanotubes for Controlled Drug Release by M. R. Abidian, D.-H. Kim and D. C. Martin, 18, 4, 405–409. Copyright (2006) Wiley-VCH) (See colour Plate 2)*

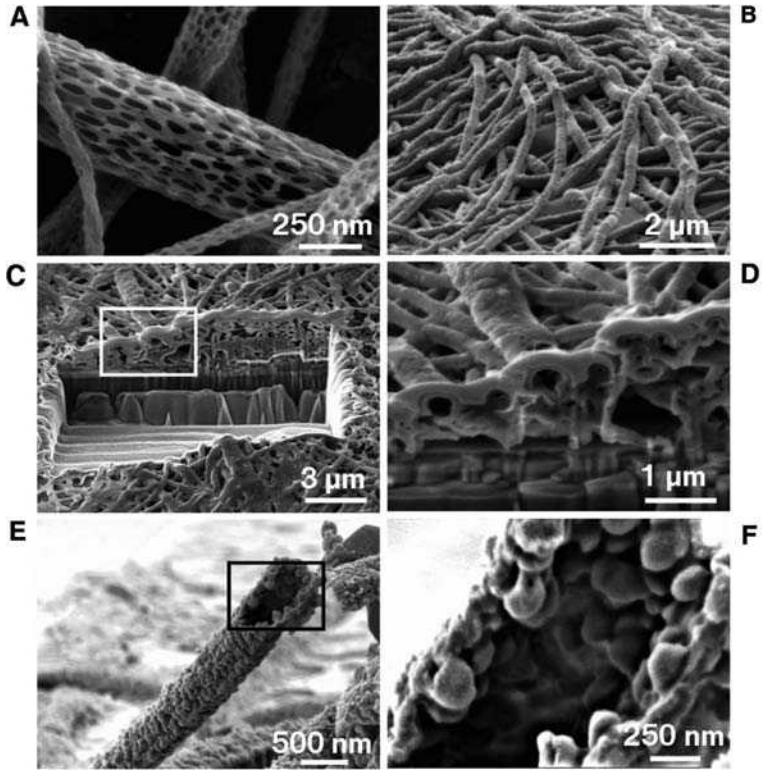

Figure 4.20 *Scanning electron micrographs of PLGA nanoscale fibers and PEDOT nanotubes: (A) diameters of the PLGA fibers were distributed over the range 40–500 nm with the majority being between 100–200 nm. (B) Electropolymerized PEDOT nanotubes on the electrode site of an acute neural probe tip after removing the PLGA core fibers. (C) A section of (B) cut with a FIB showing the silicon substrate layer and PEDOT nanoscale fiber coating. (D) Higher-magnification image of (C) showing the PEDOT nanotubes crossing each other. (E) A single PEDOT nanotube which was polymerized around a PLGA nanoscale fiber, followed by dissolution of the PLGA core fiber. This image shows the external texture at the surface of the nanotube. (F) Higher-magnification image of a single PEDOT nanotube demonstrating the textured morphology that has been directly replicated from the external surface of the electrospun PLGA fiber templates. The average wall thickness of PEDOT nanotubes varied from 50–100 nm, with the nanotube diameters ranging from 100 to 600 nm. (Reprinted with permission from Advanced Materials, Conducting-Polymer Nanotubes for Controlled Drug Release by M. R. Abidian, D.-H. Kim and D. C. Martin, 18, 4, 405–409. Copyright (2006) Wiley-VCH)*

the neural microelectrodes can be significantly decreased (by about two orders of magnitude) and the charge-transfer capacity significantly increased (about three orders of magnitude) by creating conducting polymer nanotubes on a gold electrode surface. They can precisely release individual drugs and bioactive molecules at desired points in time by using electrical stimulation of the nanotubes. It was suggested that this method provides a generally useful means for creating low-impedance, biologically active polymer coatings,

which will facilitate integration of electronically active devices with living tissues. In a final step, the fiber templates can be removed or allowed to slowly degrade, providing additional means of controlled delivery of biologically active agents incorporated into the fibers themselves. These molecule-eluting, electrically active polymer nanotubes are of interest for guidance for tissue regeneration, controlled drug delivery for ablation of specific cell populations, and for a range of biomedical engineering and pharmacological applications.

The same group also designed neural electrodes to interface with the nervous system and provide control signals for neural prostheses [88]. A novel method is reported for the fabrication of soft, low impedance, high charge density, and controlled-release nanobiomaterials that can be used for the surface modification of neural microelectrodes to stabilize the electrode/tissue interface. The fabrication process includes electrospinning of anti-inflammatory, drug-incorporated biodegradable nanofibers, encapsulation of these nanofibers by an alginate hydrogel layer, followed by electrochemical polymerization of conducting polymers around the electrospun drug-loaded nanofibers to form nanotubes and within the alginate hydrogel scaffold to form cloud-like nanostructures. The three-dimensional conducting polymer nanostructures significantly decrease the electrode impedance and increase the charge-capacity density. Dexamethasone release profiles show that the alginate hydrogel coating slows the release of the drug, significantly reducing the burst effect. These multifunctional materials are expected to be of interest for a variety of electrode/tissue interfaces in biomedical devices.

4.5.2 Sensors

Electrospun nanofibers have been proven to be excellent candidates for use as ultrasensitive sensors since they can provide large surface-area-to-volume ratios (high sensitivity and faster response time), tailored pore sizes to various dimensions, and surfaces that can be functionalized. The ability to selectively deposit isolated nanofibers via electrospinning also makes this technique attractive in the fabrication of low cost and low power consumption rapid-response sensors. Conducting electroactive polymers with tunable conductivity have also been demonstrated by Sadik [89] to have remarkable sensing applications through their ability to be reversibly oxidized or reduced by applying electrical potentials. Excellent reviews of sensors developed using electrospun nanofibers and their applications are reported [90–92]. These sensors may find applications in medical diagnosis and environmental and bioindustrial analysis.

Electrospun conductive polymers have been studied for the possibility of developing attractive sensors whose electrical properties change upon interaction with the analytes. PANI is a promising material for sensors, since its conductivity is highly sensitive to chemical vapors. PANI and/or its composites have been extensively investigated as sensitive materials for the detection of a wide spectrum of analytes, ranging from acids, bases, organic vapors, and reducing agents, to alcohols. The sensing mechanisms are different, depending on the nature of PANI and the targeting analytes. An early study at this field was the work of MacDiarmid *et al.*, which studied electrospun polyaniline-based chemical transducers with submicron dimensions [93]. Chemical sensing of NH_3 with PMMA coaxial nanofibers was also reported in the studies of Dong *et al*. [94] and Huang

et al. [95]. Nanofibers of PANI were found to have superior performance relative to conventional materials because of their much greater exposed surface area. Resistive-type sensors made from undoped or doped polyaniline nanofibers outperform conventional polyaniline on exposure to acid or base vapors, respectively. The nanofibers show essentially no dependency on thickness for their sensitivity [95]. Further, in the work of Liu *et al.* PANI nanowires oriented by electrospinning were deposited on gold electrodes [96]. The electrical resistance of this device showed a rapid and reversible change when exposed to ammonia (NH_3) at concentrations as low as 0.5 ppm. The response time of the sensors was found to be dependent on the nanowire diameter, which corresponds to the radius dependency of the diffusion time of NH_3 gas into the wires.

Using the electrospinning technique, Aussawasathiena and coworkers prepared lithium perchlorate ($LiClO_4$)-doped PEO electrospun nanofibers for humidity sensing and camphosulfonic acid (HCSA)-doped PANI/PS electrospun nanofibers for sensing hydrogen peroxide (H_2O_2) and glucose [97]. The diameters of these as-prepared polymeric nanofibers were in the range of 400–1000 nm. Owing to the large surface area and good electrical properties intrinsically associated with these nanoscale functional polymer fibers, they have achieved significantly enhanced sensitivity for the nanofiber sensors with respect to their corresponding film-type counterparts.

Conducting polymer hybrid sensors for pathogen detection were developed by Haynes and Gouma [98,99]. Using the electrospinning technique, polyaniline hybrids were developed for the detection of NO_2 gas and to monitor pH in order to determine the suitability of these sensors for exhaled human breath analyses. Their results showed that electrospun hybrids based on leucoemeraldine-based polyaniline exhibit sensitivity to NO_2 down to 1 ppm and, for the first time, using emeraldine salt polyaniline, demonstrated a conductimetric response to changes in the headspace of aqueous solutions of varying pH.

Electrospinning is a simple technique for making long (typically several centimeters long) nanowires that can easily be isolated and is therefore a promising method for the fabrication of low cost, rapid-response sensors. Pinto and coworkers prepared electrospun nanowires of PANI with tunable conductivity and used them in the fabrication of gas sensors [100,101]. Because of the large surface-to-volume ratio and the small amount of active material used, these sensors were faster and more reliable than conventional sensors based on thin films. The same group has also fabricated sensors from isolated electrospun HCSA-doped polyaniline nanofibers and from cast nanofiber mats and tested them in the presence of various aliphatic alcohol vapors. They observed that the individual nanofiber sensors also have larger responses, especially for large molecule alcohols, and exhibit true saturation over a given time interval in the presence of the control gas and small alcohol vapors compared to nanofiber mat sensors. The response of individual nanofiber sensors to small alcohols is opposite to that observed in sensors made of nanofiber mats (Figure 4.21). It was suggested that this could result from the solid-state doping process used in the electrospun polymer, which leaves behind some unreacted dopant acid that is hygroscopic, leads to adsorbed moisture, and results in reduced crystallinity and incomplete doping. However, the rapid response times suggested that electronic changes also influence the sensing mechanism.

Coaxial PMMA/PANI composite nanofibers have also been fabricated using the electrospinning technique and an *in situ* polymerization method and were then transferred to the surface of a gold interdigitated electrode to construct a gas sensor (Figure 4.22) [102]. It was

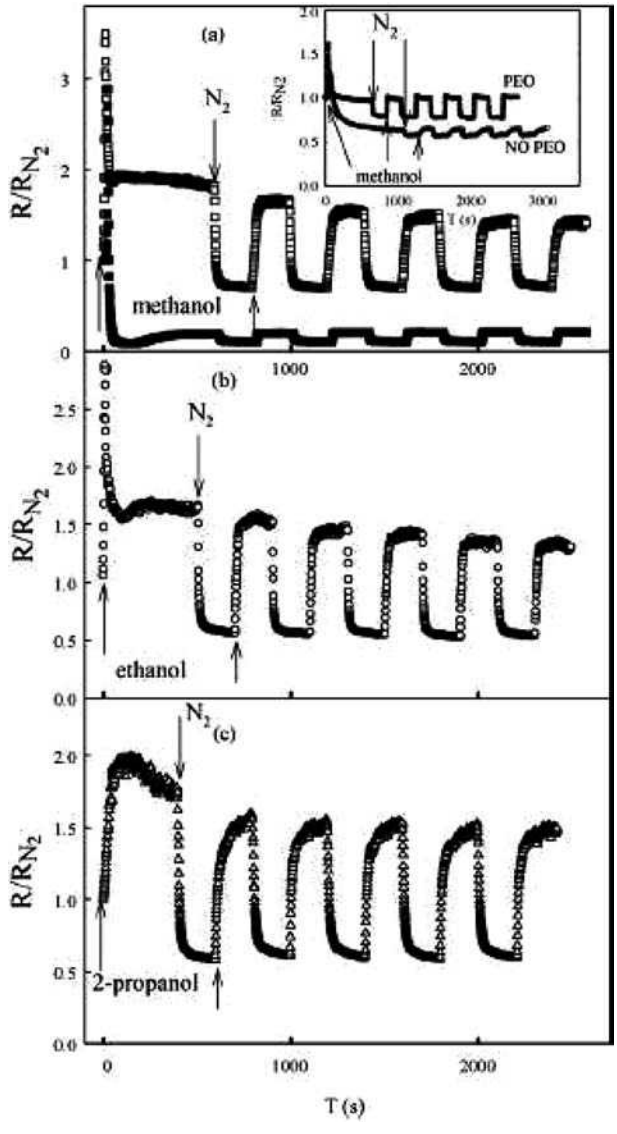

Figure 4.21 *Normalized resistance of individual electrospun HCSA-doped polyaniline nanofibers to various alcohols: (a) methanol (□), (b) ethanol (○) and (c) 2-propanol (Δ). The response of a sensor made from several nanofibers to methanol (■) is also indicated in (a) and shows lower magnitude changes when compared to the response from individual nanofibers. The inset to (a) shows the normalized resistance of a cast film of the same polymer with and without the addition of PEO. The films have a slower response time, but similar overall behavior compared to that of the nanofiber indicating that PEO has no effect on the response to methanol. (Reprinted with permission from Sensors and Actuators B., Electric response of isolated electrospun polyaniline nanofibers to vapors of aliphatic alcohols by N. J. Pinto, I. Ramos, R. Rojas et al., 129, 621–627. Copyright (2008) Elsevier Ltd)*

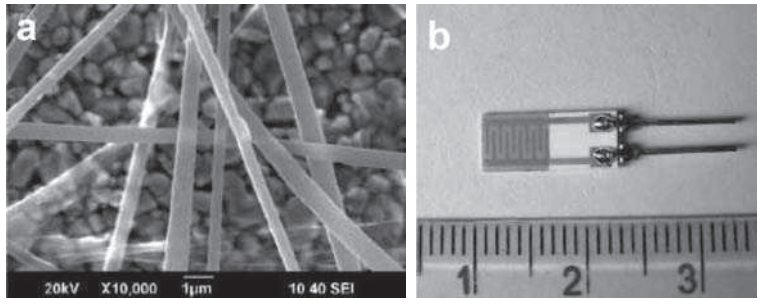

Figure 4.22 *(a) SEM photograph PANI/PMMA coaxial nanofibers (electrospun PMMA solution: 0.18 g ml^{-1}). (b) Photograph of a gas sensor based on PANI/PMMA coaxial nanofibers. (Reprinted with permission from Sensors and Actuators B., Gas sensing properties of a composite composed of electrospun poly(methyl methacrylate) nanofibers and in situ polymerized polyaniline by S. Ji, Y. Li and M. Yang, 133, 644–649. Copyright (2008) Elsevier Ltd)*

found that these nanofibers exhibited a high sensing magnitude towards triethylamine (TEA) vapors in the range 20–500 ppm (Figure 4.23). The electrical responses of the gas sensor were linear, reversible, and reproducible, suggesting their potential as a sensitive material for the detection of low-concentration amine vapors. Both the diameters of nanofibers and the doping acids have a great effect on the sensing characteristics of the composite. The effect of the diameters on the sensing magnitude of the gas sensor is proposed to be related to the difference in the surface-to-volume ratio of the fibers. In addition, the concentration of doping acids led to changes in the resistance of the sensor, but could not affect its sensing characteristics; however, the nature of the doping acids was determinative for the sensing magnitude of the sensor. The sensing mechanism of PANI and the interactions of doping acids with TEA vapor were proposed to be a deprotonation/protonation process, similar to its sensing of ammonia, and were discussed in detail. Briefly, PANI was protonated by the doping acids during the *in situ* polymerization process and exhibited a high conductivity. Upon interaction with TEA vapor, the protons in the –N+H– sites in the conjugated PANI were withdrawn by adsorbed TEA molecules, and PANI in the form of emeraldine salt was reduced to emeraldine base. As a result, the whole density in the PANI main chain was lowered, resulting in decreased conductivity. When TEA was replaced with air, the process was reversed and the conductivity returned to the original value.

4.5.3 Conductive Nanofibers in Electric and Electronic Applications

Electrospun nanofibers with electrical and electro-optical activities have received a great deal of interest in recent years because of their potential applications in nanoscale electronic and optoelectronic devices, for example nanowires, LEDs, photocells etc. Besides, one-dimensional (1-D) nanostructures are the smallest dimensional structures for efficient transport of electrons and optical excitations. One of the potential future applications of conducting polymer nanofibers is as molecular wires, which are required to connect molecular devices to electrodes. For molecular devices, it is necessary to make nanowires with diameters in the order of the size of the molecular device.

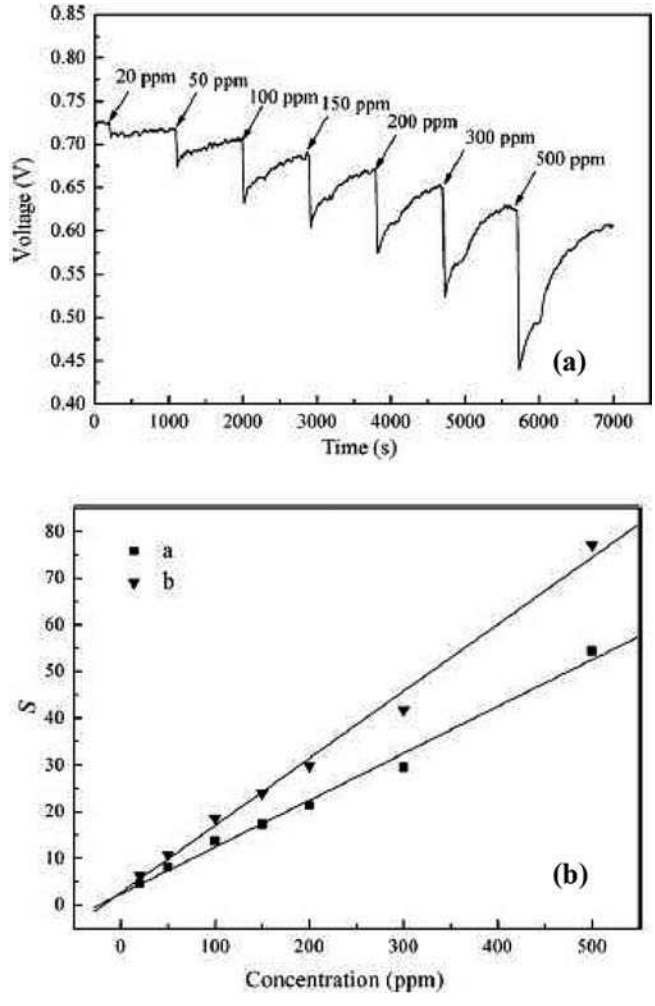

Figure 4.23 *(a) Typical electrical responses of PANI/PMMA composite nanofibers to TEA vapors of different concentrations (doping acid: TSA). (b) Sensing magnitude of PANI/PMMA composite nanofibers with different diameters as a function of the concentration of TEA vapor. Concentration of electrospun PMMA solution: (a) 0.32 g ml^{-1} and (b) 0.18 g ml^{-1}. (Reprinted with permission from Sensors and Actuators B., Gas sensing properties of a composite composed of electrospun poly(methyl methacrylate) nanofibers and in situ polymerized polyaniline by S. Ji, Y. Li and M. Yang, 133, 644–649. Copyright (2008) Elsevier Ltd)*

Extremely low-dimensional conducting nanowires (as small as 3 nm in diameter) for use in nanoelectronics can be produced with the electrospinning technique [103]. Using template methods, insulating PLA fibers with an average diameter of 200–700 nm as core materials were electrospun and subsequently coated with thin 50–100 nm films of polyaniline or polypyrrole by *in situ* polymer deposition methods. The PLA core fibers decompose upon relatively mild thermal treatment under inert atmosphere, leaving

conducting nanotubes. The greatly enhanced surface-to-volume ratio of these materials and the nanometer scale structures are predicted to yield enhanced physical properties compared with thin films prepared on traditional substrates.

As discussed above, orientation of the conducting nanowires can be achieved with the help of the scanned electrospinning technique [104]. Kameoka and coworkers used a blend of poly(*m*-phenylenevinylene)-co-(2,5-dioctoxy-*p*-phenylenevinylene) copolymer (PmPV) and PEO, and scanned electrospinning for the deposition of the nanowires on lithographically patterned gold electrodes. The metal semiconductor contact caused rectifying current–voltage characteristics. This technique represents a good opportunity for the manufacture of nanowire electronic devices thanks to its ease of production and high throughput.

A simple way to reduce the size and increase the component density in circuits is via the fabrication of devices based on semiconductor nanofibers. Thus, electrospinning is proposed as an easy, one-step process to fabricate one-dimensional polymer FETs using PThs [105]. The fabrication of an electrospun regio-regular poly(3-hexylthiophene-2,5-diyl) FET was studied, and the hole mobility of the device was calculated to be $4 \times 10^{-4} cm^2 (V.s)^{-1}$; the on/off ratio was ~7. In another study, Liu *et al*. used electrospun regioregular poly(3-hexylthiophene) to develop a single nanofiber FET [106]. Nanofibers with diameters of 100–500 nm deposited by electrospinning onto electrodes on a SiO_2/Si substrate were used, and the transistor exhibited a hole field-effect mobility of 0.03 $cm^2 (V.s)^{-1}$in the saturation regime and a current on/off ratio of 10^3 in the accumulation mode.

Xia and coworkers prepared nanofibers from conjugated polymers, such as poly [2-methoxy-5-(2-ethylhexyloxy)-1,4-phenylenevinylene] (MEH-PPV) and its blends with poly(3-hexylthiophene) (PHT) or poly(9,9-dioctylfluorene) (PFO) using the electrospinning technique. They investigated the effect of one-dimensional confinement on the optical and electronic properties of conjugated polymer nanofibers [107]. Morphological and photophysical studies showed that the phase-separated domains in the MEH-PPV/PHT nanofibers (30–50 nm) are much smaller than in the blend thin films (100–150 nm), and efficient energy transfer was observed in these blend nanofibers. The MEH-PPV/PFO blend nanofibers had cocontinuous or core–shell structures, and significant energy transfer was absent in these blend nanofibers as compared to the bulk thin films. Field-effect transistors based on the MEH-PPV/PHT blend nanofibers exhibited p-channel transistor characteristics with a hole mobility in the range of $(0.05–1) \times 10^{-4}$ $cm^2 (V.s)^{-1}$.

Furthermore, the microelectronics industry extensively uses wire bonding as a means of interconnecting bond pads on the die to the bond pads on a substrate using thin wires. Wire bonding of gold is primarily used in small signal devices because of the ability of gold to be drawn into small-diameter wires (25.4 μm). However, the next generation of wires will need to interface with smaller bond pad structures and provide the required performance and compatibility with 'molecular devices.' Lithographically made nanowires can be used as an interface, but doing so would be very expensive. A novel wire-bonding technology using electrospun conductive polymers has been reported. The work of Ruiz *et al.* addresses this next generation of nonlithographically made nanowire formation and bonding, which will provide a low-cost option for dealing with the current trend towards increased I/O and higher reliability [108]. The key point is the development of a so called 'meet-in-the-middle' technology, where functionalized electrospun polymer nanofibers deposited directly on die bond pads may substitute or complement future wire-bonding

techniques. They demonstrate the manipulation of single nonconductive nanofibers functionalized as conductive nanowires to interconnect nanoscale bond pads on the die to the bond pads on a substrate. Two general schemes for the manipulation of single nanowires were presented for diameters from 50 nm to 500 nm, and both schemes were based on the electrospinning technique (near-field electrospinning and micro-bead electrospinning) of nanofibers and their subsequent post-processing.

It is known that the rate of electrochemical reactions is proportional to the surface area of the electrode, and thus conductive nanofibrous membranes are also quite suitable for use as porous electrodes in developing high-performance batteries [13,109,110]. The electrochemical behavior of electrospun PPy/sulfonated-poly(styrene-ethylene-butylenes-styrene) (S-SEBS) composite nanofibers (about 300nm in average diameter) was investigated by Young-Wan Ju *et al*. [111,112]. The effect of both electrospinning and sulfonation results in a higher electrochemical capacity (up to 80 mAh g^{-1}) owing to the increase in doping level, high electrical conductivity, low interfacial resistance, and high reversibility by easy intercalation of the Li ion as compared to PPy/poly(styrene-ethylene-butylene-styrene) (SEBS) fibers prepared by a casting method. The same group also studied the electrochemical properties of electrospun PAN/MWCNT carbon nanofiber electrodes coated with polypyrrole by *in situ* chemical polymerization in order to improve the electrochemical performance. The capacitances of the activated carbon nanofibers (ACNF) and PPy/ACNF electrodes were 141 and 261 F g^{-1} at 1mA cm^{-2}, respectively, whereas that of PPy/ACNF/CNT was 333 F g^{-1}. The improvement in capacitance was attributed to: (i) the preparation of aligned nanosized ACNF/CNT by electrospinning and the addition of CNT that leads to superior properties (higher surface area, formation of mesopores) and an increase in electrical conductivity and (ii) the formation of a good charge-transfer complex by the PPy coating on the surface of the aligned nanosized ACNF/CNT, which offers a refined three-dimensional network due to the highly porous structure between ACNF/CNT and PPy.

Conductive (in terms of electrical, ionic and photoelectric) membranes also have a potential for applications, including electrostatic dissipation, corrosion protection, electromagnetic interference shielding, photovoltaic devices etc. [113,114]. Waters *et al.* reported the use of electrospun nanofibers in developing a liquid-crystal, optical shutter device that is switchable under an electric field between a state in which it is substantially transparent to incident light and a state in which it is substantially opaque [115]. The main part of this liquid-crystal device consisted of a layer of nanofibers permeated with a liquid-crystal material, with a thickness of only few tens of microns. The layer was located between two electrodes, by means of which an electric field could be applied across the layer to vary the transmissivity of the liquid-crystal/nanofiber composite. It is the nanoscale polymer fiber size used that determines the sensitivities of the refractive index differences between the liquid-crystal material and the fibers, and consequently governs the transmissivity in this kind of device. Moreover, the Korea Institute of Science and Technology owns a patent on the fabrication of a lithium secondary battery comprising a fibrous film made by electrospinning [116]. Other interesting progress is the development of a hybrid solar cell utilizing electrospun conductive polymers 'doped' with photovoltaic dyes and nanocrystalline semiconductor particles. Ziegler *et al.* prepared a flexible photovoltaic membrane by utilizing electrospun PAN nanofiber dyed with copper phthalocyanine, while nanocrystalline TiO_2 semiconductor particles can also be embedded within the nanofibers [117].

4.6 Conclusions

This review covers the active research area of processing functional conductive nanofibers and nanostructures with various compositions and properties by means of the electrospinning method. It is also focuses on the unique properties of electrospun conductive nanostructures that can be utilized to improve existing applications of conductive materials and on the various possibilities to meet the requirements of a number of novel applications.

Encouraged by the simplicity of the electrospinning processes and early demonstration of unique properties of nanofibers, there is an explosion of research activities in this area worldwide. Electrospinning is a simple and versatile method for creating conducting polymer-based highly functional high-performance nanostructures. The process is versatile in that there is a wide range of materials that can be spun to conductive nanostructures with unique features. The ability to customize the conductive nanostructures to meet the requirements of specific applications gives electrospinning an advantage over other production methods.

Despite the existence of some commercial electrospun nanofiber products, it is accepted that an upscaling of the electrospinning process and productivity improvements are essential and merit more effort to ensure full success of the process in socioeconomic terms. Also, regardless of the large market potential of conductive electrospun nanofibers, it is clear that this area is still in the research stage, and commercial products of conductive nanofibers are not available. Therefore, instead of focusing on extending the range of electrospun conductive polymers that could be applied, researchers should turn their attention to controlled ways of processing them towards marketable applications. The interface behavior between these nanostructures and surrounding materials is furthermore crucial and must be understood and controlled in order to converge them into concrete applications. A great deal of development work is required before the use of electrospun conductive nanostructures will become a profitable reality in any of the applications described above. Moreover, every new technology is accompanied by potential risks, which must be evaluated as carefully and as early as possible. Specific aspects and impacts on human health, the environment, and the safety of these nanomaterials should be identified.

Overall, combining well-established technologies of today with the emerging field of electrospun conductive nanostructures can potentially lead to the development of new technologies and new micro- and nanostructured smart assemblies, and stimulate opportunities for an enormous number of creative applications. In the next few years, we can expect to see many more commercial applications of electrospun conductive polymers that will have a large impact on the innovations and technologies of the future.

References

[1] A. Frenot and I. S. Chronakis, Polymer nanofibers assembled by electrospinning, *Curr. Opin. Colloid Interface Sci.*, **8**, 64–75 (2003).

[2] D. Li and Y. Xia, Electrospinning of Nanofibers: Reinventing the Wheel?, *Adv. Mater.*, **16**, 1151–1170 (2004).

[3] Formhals, Process and apparatus for preparing artificial threads. *US Patent,* 1-975-504 (1934).

[4] D. H. Reneker and I. Chun, Nanometre diameter fibres of polymer produced by electrospinning, *Nanotechnol.*, **7**, 216–223 (1996).
[5] R. Dersch, M. Steinhart, U. Boudriot, A. Greiner, and J. H. Wendorff, Nanoprocessing of polymers: applications in medicine, sensors, catalysis, photonics, *Polymers Adv. Technol.*, **16**, 276–282 (2005).
[6] W. E. Teo and S. Ramakrishna, A review on electrospinning design and nanofibre assemblies, *Nanotechnol.*, **17**, R89–R106 (2006).
[7] I. S. Chronakis, Novel nanocomposites and nanoceramics based on polymer nanofibers using electrospinning process – A review, *J. Mater. Proc. Technol.*, **167**, 283–293 (2005).
[8] Z. Sun, E. Zussman, A. L. Yarin, J. H. Wendorff, and A. Greiner, Compound core-shell polymer nanofibers by co-electrospinning, *Adv. Mater.*, **15**, 1929–1932 (2003).
[9] A. Welle, M. Kröger, M. Döring, K. Niederer, E. Pindel, and I. S. Chronakis, Electrospun aliphatic poly(carbonate)s nanofibers as tailored tissue scaffold materials, *Biomater.*, **28**, 2211–2219 (2007).
[10] A. Laforgue and L. Robitaille, Fabrication of poly-3-hexylthiophene/polyethylene oxide nanofibers using electrospinning, *Synth. Metals*, **158**, 577–584 (2008).
[11] M. Díaz, N.J. Pinto, J. Gao, and A. G. MacDiarmid, *Electrospinning nanofibers of polyaniline and polyaniline/(polystyrene and polyethylene oxide) blends, National Conference of Undergraduate Research*, University of Kentucky, Lexington (2001).
[12] J. R. Cárdenas, M. G. O. de França, E. A. de Vasconcelos, W. M. de Azevedo, and E. F. da Silva, Growth of sub-micron fibres of pure polyaniline using the electrospinning technique, *J. Phys. D: Appl. Phys.*, **40**, 1068–1071 (2007).
[13] I.D. Norris, M. M. Shaker, F. K. Ko, and A.G. MacDiarmid, Electrostatic fabrication of ultrafine conducting fibers: polyaniline/polyethylene oxide blends, *Synth. Metals*, **114**, 109–114 (2000).
[14] G. MacDiarmid, W. E. Jones Jr., I. D. Norris, J. Gao, A. T. Johnson Jr., N. J. Pinto, J. Hone, B. Han, F. K. Ko, H. Okuzaki and M. Llaguno, Electrostatically-generated nanofibers of electronic polymers, *Synth. Metals*, **119**, 27–30 (2001).
[15] F. K. Ko, A. G. MacDiarmid, I. D. Norris, M. Shaker, and R. Lec, Electrospinning ultrafine conductive polymeric fibers, *Patent* 20030137083 (2001).
[16] P. Drew, X. Wang, K. Senecal, H. Gibson-Schreuder, J. He. S. Tripathy, and L. Samuelson, Electrospun nanofibers of electronic and photonic polymer systems, *ANTEC Proc.* 1477–1481 (2000).
[17] P. Drew, *PhD Thesis, Nanoscale Composites Assembled on Electrospun Fibrous Membranes*, University of Massachusetts, Lowell MA (2004).
[18] K. Desai and C. Sung. Electrospinning nanofibers of PANI/PMMA blends, *Materials Research Society Symposium Proceedings, 736* (*Electronics on Unconventional Substrates—Electrotextiles and Giant-Area Flexible Circuits*), Boston, 121–126 (2002).
[19] K. Desai and C. Sung. DOE optimization and phase morphology of electrospun nanofibers of PANI/PMMA blends. NSTI Nanotechnology Conference and Trade Show, Boston, 429–432 (2004).
[20] N. J. Pinto, A. T. Johnson, A. G. Macdiarmid, C. H. Mueller, N. Theofylaktos, D. C. Robinson, and F. A. Miranda, Electrospun polyaniline/polyethylene oxide nanofiber field-effect transistor, *Appl. Phys. Lett.*, **83**, 4244–4246 (2003).
[21] P. K. Kahol and N. J. Pinto, An EPR investigation of electrospun polyaniline-polyethylene oxide blends, *Synth. Met.*, **140**, 269–272 (2004).
[22] N. J. Pinto, P. Carrión, and J. X. Quiñones, Electroless deposition of nickel on electrospun fibers of 2-acrylamido-2-methyl-1-propanesulfonic acid doped polyaniline, *Mater. Sci. Eng. A*, **366**, 1–5 (2004).
[23] Y. Zhou, M. Freitag, J. Hone, C. Staii, A. T. Johnson Jr., N. J. Pinto, and A. G. MacDiarmid, Fabrication and electrical characterization of polyaniline-based nanofibers with diameter below 30 nm, *Appl. Phys. Lett.*, **83**, 3800–3802 (2003).
[24] K. H. Hong, K. W. Oh, and T. J. Kang, Preparation of conducting nylon-6 electrospun fiber webs by the *in situ* polymerization of polyaniline, *J. Appl. Polymer Sci.*, **96**, 983–991 (2005).

[25] Y. Zhu, J. Zhang, Y. Zheng, Z. Huang, L. Feng, and L. Jiang, Stable, superhydrophobic, and conductive polyaniline/polystyrene films for corrosive environments, *Adv. Funct. Mater.*, **16**, 568–574 (2006).
[26] P. H. S. Picciani, E. S. Medeiros, Z. Pan, W. J. Orts, L. H. C. Mattoso, and B. G. Soares, Development of conducting polyaniline/poly(lactic acid) nanofibers by electrospinning, *J. Appl. Polymer Sci.*, **112**, 744–753 (2009).
[27] D. Chao, L. Cui, J. Zhang, X. Liu, Y. Li, W. Zhang, and C. Wang, Preparation of oligoaniline derivative/polyvinylpyrrolidone nanofibers containing silver nanoparticles *Synth. Metals*, **159**, 537–540 (2009).
[28] G. L. Teoh, K. Y. Liew, and W. A. K. Mahmood, Preparation of polyaniline-Al_2O_3 composites nanofibers with controllable conductivity, *Mater. Lett.*, **61**, 4947–4949 (2007).
[29] D. Czaplewski, J. Kameoka, and H. G. Craighead, Nonlithographic approach to nanostructure fabrication using a scanned electrospinning source, *J. Vac. Sci. Technol. B (Microelect. Nanometer Struct.)*, **21**, 2994–2997 (2003).
[30] J. Kameoka, R. Orth, Y. Yang, D. Czaplewski, R. Mathers, G. W. Coates, and H. G. Craighead, A scanning tip electrospinning source for deposition of oriented nanofibres, *Nanotechnol.*, **14**, 1124–1129 (2003).
[31] H. Dong, V. Nyame, A. G. MacDiarmid, and W. E. Jones Jr., Polyaniline/poly(methyl methacrylate) coaxial fibers: the fabrication and effects of the solution properties on the morphology of electrospun core fibers, *J. Polymer Sci. B: Polymer Phys.*, **42**, 3934–3942 (2004).
[32] M. Wei, J. Lee, B. Kang, and J. Mead, Preparation of core-sheath nanofibers from conducting polymer blends, *Macromolec. Rapid Commun.*, **26**, 1127–1132 (2005).
[33] H. Dong, S. Prasad, V. Nyame, and W. E. Jones Jr., Sub-micrometer Conducting Polyaniline Tubes Prepared from Polymer Fiber Templates, *Chem. Mater.*, **16**, 371–373 (2004).
[34] A. Attout, S. Yunus, and P. Bertrand, Electrospinning and alignment of polyaniline-based nanowires and nanotubes, *Polymer Eng. Sci.*, **48**, 1661–1666 (2008).
[35] K. H. Hong and T. J. Kang, Polyaniline–nylon-6 composite nanowires prepared by emulsion polymerization and electrospinning process, *J. Appl. Polymer Sci.*, **99**, 1277–1286 (2006).
[36] R. Kessick and G. Tepper, Microscale polymeric helical structures produced by electrospinning, *Appl. Phys. Lett.*, **84**, 4807–4809 (2004).
[37] M. K. Shin, Y. J. Kim, S. I. Kim, S-K. Kim, H. Lee, G. M. Spinks, and S. J. Kima, Enhanced conductivity of aligned PANI/PEO/MWNT nanofibers by electrospinning, *Sensors Actuat. B*, **134**, 122–126 (2008).
[38] I. S. Chronakis, S. Grapenson, and A. Jakob, Conductive polypyrrole nanofibers via electrospinning: electrical and morphological properties, *Polymer*, **47**, 1597–1603 (2006).
[39] S. Nair, S. Natarajan, and S. H. Kim, Fabrication of electrically conducting polypyrrole-poly(ethylene oxide) composite nanofibers, *Macromolec. Rapid Commun.*, **26**, 1599–1603 (2005).
[40] T. S. Kang, S. W. Lee, J. Joo, and J. Y. Lee, Electrically conducting polypyrrole fibers spun by electrospinning, *Synth. Met.*, **153**, 61–64 (2005).
[41] J. H. Lee, J. Castracane, and A. Gadre, Structural and electrical properties of conductive polymeric aligned nanofibers via electrospinning, *Proc. SPIE*, 6465, 64650Q (2007).
[42] G. Han and G. Shi, Novel route to pure and composite fibers of polypyrrole, *J. Appl. Polymer Sci.*, **103**, 1490–1494 (2007).
[43] F. Granato, A. Bianco, C. Bertarelli, and G. Zerbi, Composite polyamide 6/polypyrrole conductive nanofibers, *Macromolec. Rapid Commun.*, **30**, 453–458 (2009).
[44] Y. Srivastava, M. Marquez, and T. Thorsen, Multijet electrospinning of conducting nanofibers from microfluidic manifolds, *J. Appl. Polymer Sci.*, **106**, 3171–3178 (2007).
[45] X. Li, X. Hao, H. Yu, and H. Na, Fabrication of polyacrylonitrile/polypyrrole (PAN/PPy) composite nanofibres and nanospheres with core–shell structures by electrospinning, *Mater. Lett.*, **62**, 1155–1158 (2008).
[46] S. Nair, E. Hsiao, and S. H. Kim Fabrication of electrically-conducting nonwoven porous mats of polystyrene–polypyrrole core–shell nanofibers *via* electrospinning and vapor phase polymerization, *J. Mater. Chem.*, **18**, 5155–5161 (2008).

[47] H. Dong and W. E. Jones Jr., Preparation of submicron polypyrrole/poly(methyl methacrylate) coaxial fibers and conversion to polypyrrole tubes and carbon tubes, *Langmuir*, **22**, 11384–11387 (2006).
[48] A. K. El-Aufy, *PhD Thesis, Nanofibers and Nanocomposites Poly(3,4-Ethylene Dioxythiophene) / Poly (Styrene Sulfonate) by Electrospinning*, Drexel University, Philadelphia PA (2004).
[49] A. K. El-Aufy, B. Naber, and F. K. Ko, Carbon nanotube reinforced (PEDT/PAN) nanocomposite for wearable electronics, *Polymer Preprints*, **44**, 134–135 (2003).
[50] H. D. Nguyen, J. M. Ko, H. J. Kim, S. K. Kim, S. H. Cho, J. D. Nam, and J. Y. Lee, Electrochemical properties of poly(3,4-ethylenedioxythiophene) nanofiber non-woven web formed by electrospinning, *J. Nanosci. Nanotechnol.*, **8**, 4718–4721 (2008).
[51] A. Bianco, C. Bertarelli, S. Frisk, J. F. Rabolt, M. C. Gallazzi, and G. Zerbi Electrospun polyalkylthiophene/polyethyleneoxide fibers: Optical characterization, *Synth. Metals*, **157**, 276–281 (2007).
[52] S-Y Jang, V. Seshadri, M-S. Khil, A. Kumar, M. Marquez, P. T. Mather, and G. A. Sotzing, Welded electrochromic conductive polymer nanofibers by electrostatic spinning, *Adv. Mater.*, **17**, 2177–2180 (2005).
[53] S. Jang, M. Khil, V. Seshadri, M. Marquez, P. T. Mather, and G. A. Sotzing, Electrospinning of electrochromic conductive polymeric nanofibers, *Polymer Preprints*, **46**, 513–514 (2005).
[54] A. Kumar, C. Asemota, J. Padilla, M. Invernale, T. F. Otero, and G. A. Sotzing, Photopatterned conjugated polymer electrochromic nanofibers on paper, *J. Phys.: Conf. Ser.*, **127**, 012014 (2008) (doi:10.1088/1742-6596/127/1/012014).
[55] S. Lee, G. D. Moon, and U. Jeong, Continuous production of uniform poly(3-hexylthiophene) (P3HT) nanofibers by electrospinning and their electrical properties *J. Mater. Chem.*, **19**, 743–748 (2009).
[56] C-C. Kuo, C-T. Wang, and W-C. Chen, Poly(3-hexylthiophene)/Poly(methyl methacrylate) core-shell electrospun fibers for sensory applications. *Macromolec. Symp.*, **279**, 41–47 (2009).
[57] W. Zhang, Z. Huang, E. Yan, C. Wang, Y. Xin, Q. Zhao, and Y. Tong, Preparation of poly(phenylene vinylene) nanofibers by electrospinning, *Mater. Sci. Eng. A*, **443**, 292–295 (2007).
[58] Z.-H. Huang, J.-H. Yang, L.-C. Chen, X.-J. Wang, W.-L. Li, Y.-Q. Qiu, J.-T. Zhang, and R.-S. Wang, Study on EL emission region of polymer thin film in PPV LED, *Synth. Met.*, **91**, 315–316 (1997).
[59] W. Zhang, E. Yan, Z. Huang, C. Wang, Y. Xin, Q. Zhao, and Y. Tong, Preparation and study of PPV/PVA nanofibers via electrospinning PPV precursor alcohol solution *Eur. Polymer J.*, **43**, 802–807 (2007).
[60] S. Tan, X. Feng, B. Zhao, Y. Zou, and X. Huang, Preparation and photoluminescence properties of electrospun nanofibers containing PMO-PPV and $Eu(ODBM)_3$phen, *Mater. Lett.*, **62**, 2419–2421 (2008).
[61] Y. Xin, Z. Huang, J. Chen, C. Wang, Y. Tong, and S. Liu, Fabrication of well-aligned PPV/PVP nanofibers by electrospinning, *Mater. Lett.*, **62**, 991–993 (2008).
[62] Y. Xin, Z. H. Huang, E. Y. Yan, W. Zhang, and Q. Zhao, Controlling poly(*p*-phenylene vinylene)/poly(vinyl pyrrolidone) composite nanofibers in different morphologies by electrospinning, *Appl. Phys. Lett.*, **89**, 053101 (2006).
[63] C. Wang, E. Yan, Z. Huang, Q. Zhao, and Y. Xin, Fabrication of highly photoluminescent TiO_2/PPV hybrid nanoparticle-polymer fibers by electrospinning, *Macromolec. Rapid Commun.*, **28**, 205–209 (2007).
[64] Q. Zhao, Y. Xin, Z. Huang, S. Liu, C. Yang, and Y. Li, Using poly[2-methoxy-5-(2′-ethylhexyloxy)-1,4-phenylene vinylene] as shell to fabricate the highly fluorescent nanofibers by coaxial electrospinning, *Polymer*, **48**, 4311–4315 (2007).
[65] H. Okuzaki, T. Takahashi, N. Miyajima, Y. Suzuki, and T. Kuwabara, Spontaneous formation of poly(*p*-phenylenevinylene) nanofiber yarns through electrospinning of a precursor, *Macromolecules*, **39**, 4276–4278 (2006).
[66] S. Chuangchote, T. Srikhirin, and P. Supaphol, Color change of electrospun polystyrene/MEH-PPV fibers from orange to yellow through partial decomposition of MEH side groups, *Macromolec. Rapid Commun.*, **28**, 651–659 (2007).

[67] S. Chuangchote, T. Sagawa, and S. Yoshikawa, Fabrication and optical properties of electrospun conductive polymer nanofibers from blended polymer solution, *Jap. J. Appl. Phys.*, **47**, 787–793 (2008).
[68] S. Madhugiri, A. Dalton, J. Gutierrez, J. P. Ferraris, and K. J. Balkus, Electrospun MEH-PPV/SBA-15 composite nanofibers using a dual syringe method, *J. Am. Chem. Soc.*, **125**, 14531–14538 (2003).
[69] H-C. Chen, C-L. Liu, C-C. Bai, N-H. Wang, C-S Tuan, and W-C. Chen, Morphology and photophysical properties of DB-PPV/PMMA luminescent electrospun fibers. *Macromolec. Chem. Phys.*, **210**, 918–925 (2009).
[70] C-C. Kuo, C-H. Lin, and W-C. Chen, Morphology and photophysical properties of light-emitting electrospun nanofibers prepared from poly(fluorene) derivative/PMMA blends. *Macromolecules*, **40**, 6959–6966 (2007).
[71] C-C. Kuo, Y-C. Tung, C-H. Lin, and W-C. Chen, Novel luminescent electrospun fibers prepared from conjugated rod-coil block copolymer of poly[2,7-(9,9-dihexylfluorene)]-block-poly(methyl methacrylate), *Macromolec. Rapid Commun.*, **29**, 1711–1715 (2008).
[72] H-C. Chen, C-T. Wang, C-L Liu, Y-C. Liu, and W-C Chen, Full color light-emitting electrospun nanofibers prepared from PFO/MEH-PPV/PMMA ternary blends, *J. Polymer Sci. B: Polymer Phys.*, **47**, 463–470 (2009).
[73] S. K. Chae, H. Park, J. Yoon, C. H. Lee, D. J. Ahn, and J.-M. Kim, Polydiacetylene supramolecules in electrospun microfibers: fabrication, micropatterning, and sensor applications, *Adv. Mater.*, **19**, 521–524 (2007).
[74] J. Yoon, Y.-S. Jung, and J.-M. Kim, A combinatorial approach for colorimetric differentiation of organic solvents based on conjugated polymer-embedded electrospun fibers, *Adv. Funct. Mater.*, **19**, 209–214 (2009).
[75] M. S. Choi, J. H. Lee, D. W. Kim, and T. S. Lee, New conjugated polymers comprising *ortho*-phenylazonaphthols: Synthesis and chromogenic behaviors, *J. Polymer Sci. A: Polymer Chem.*, **45**, 4430–4440 (2007).
[76] S. Bhaskar and J. Lahann, Microstructured materials based on multicompartmental fibers. *J. Am. Chem. Soc.*, **131**, 6650–6651 (2009).
[77] F. Di Benedetto, A. Camposeo, S. Pagliara, E. Mele, L. Persano, R. Stabile, R. Cingolani, and D. Pisignano, Patterning of light-emitting conjugated polymer nanofibres, *Nature Nanotechnol.*, **3**, 614–619 (2008).
[78] M. Kotaki, X-M. Liu, and C. He, Optical properties of electrospun nanofibers of conducting polymer-based blends, *J. Nanosci. Nanotechnol.*, **6**, 3997–4000 (2006).
[79] T. J. Sill and H. A. von Recum, Electrospinning: Applications in drug delivery and tissue engineering, *Biomaterials*, **29**, 1989–2006 (2008).
[80] M. R. Abidian, D.-H. Kim, and D. C. Martin, Conducting-polymer nanotubes for controlled drug release, *Adv. Mater.*, **18**, 405–409 (2006).
[81] M. Li, Y. Guo, Y. Wei, A. G. MacDiarmid, and P. I. Lelkes, Electrospinning polyaniline-contained gelatin nanofibers for tissue engineering applications, *Biomater.*, **27**, 2705–2715 (2006).
[82] M.-Y. Li, P. Bidez, E. Guterman-Tretter, Y. Guo, A. G. MacDiarmid, P. I. Lelkes, X.-B. Yuan, X.-Y. Yuan, J. D. Sheng, H. Li, C.-X Song, and Y. Wei, Electroactive and nanostructured polymers as scaffold materials for neuronal and cardiac tissue engineering, *Chin. J. Polymer Sci. (Engl. Ed.)*, **25**, 331–339 (2007).
[83] I. Jun, S. Jeong, and H. Shin, The stimulation of myoblast differentiation by electrically conductive sub-micron fibers, *Biomaterials*, **30**, 2038–2047 (2009).
[84] S. I. Jeong, I. D. Jun, M. J. Choi, Y. C. Nho, Y. M. Lee, and H. Shin, Development of electroactive and elastic nanofibers that contain polyaniline and poly(L-lactide-*co*-ε-caprolactone) for the control of cell adhesion, *Macromolec. Biosci.*, **8**, 627–637 (2008).
[85] J. Y. Lee, C. A. Bashur, A. S. Goldstein, and C. E. Schmidt, Polypyrrole-coated electrospun PLGA nanofibers for neural tissue applications, *Biomaterials*, **30**, 4325–4335, (2009).
[86] J. Xie, M. R. MacEwan, S. M. Willerth, X. Li, D. W. Moran, S. E. Sakiyama-Elbert, and Y. Xia, Conductive core-sheath nanofibers and their potential application in neural tissue engineering, *Adv. Funct. Mater.*, **19**, 1–7 (2009).

[87] M. H. Bolin, K. Svennersten, X. Wang, I. S. Chronakis, A. Richter-Dahlfors, E. W.H. Jager, and M. Berggren, Nano-fiber scaffold electrodes based on PEDOT for cell stimulation. *Sensors Actuat. B: Chem.*, **142**, 451–456 (2009).
[88] M. R. Abidian and D. C. Martin, Multifunctional nanobiomaterials for neural interfaces, *Adv. Funct. Mater.*, **19**, 573–585 (2009).
[89] O. A. Sadik, Bioaffinity sensors based on conducting polymers: a short review, *Electroanalysis*, **11**, 839–844 (1999).
[90] B. Ding, M. Wang, J. Yu, and G. Sun, Gas sensors based on electrospun nanofibers. *Sensors*, **9**, 1609–1624 (2009).
[91] J. Jang, Conducting polymer nanomaterials and their applications, *Adv. Polymer Sci.*, **199**, 189–259 (2006).
[92] A. Greiner and J. Wendorff, Electrospinning: A fascinating method for the preparation of ultrathin fibers, *Angew. Chem. Int. Ed.*, **46**, 5670–5703 (2007).
[93] A. G. MacDiarmid, I. D. Norris, W. E. Jones Jr., M. A. El-Sherif, J. Yuan, B. Han, and F. K. Ko, Polyaniline based chemical transducers with sub-micron dimensions, *Polymer Mater. Sci. Eng.*, **83**, 544–554 (2000).
[94] H. Dong, U. Megalamane, and W. Jones Jr. Conductive polyaniline/PMMA coaxial nanofibers: fabrication and chemical sensing, *Polymer Mater. Sci. Eng.*, **44**(2), 124–125 (2003).
[95] J. Huang, S. Virji, B. H. Weiller, and R. B. Kaner, Polyaniline nanofiber sensors, *Chem. Eur. J.*, **10**, 1314–1319 (2004).
[96] H. Liu, J. Kameoka, D. A. Czaplewski, and H. G. Craighead, Polymeric nanowire chemical sensor, *Nanoletters*, **4**, 671–675 (2004).
[97] D. Aussawasathien, J.-H. Dong and L. Dai, Electrospun polymer nanofiber sensors, *Synth. Met.*, **154**, 37–40 (2005).
[98] A. S. Haynes and P. I. Gouma, Electrospun conducting polymer-based sensors for advanced pathogen detection, *Sens. J., IEEE*, **8**, 701–705 (2008).
[99] A. Bishop-Haynes and P. Gouma, Electrospun polyaniline composites for NO_2 detection, *Mater. Manufact. Proc.*, **22**, 764–767 (2007).
[100] N. J. Pinto, I. Ramos, R. Rojas, P.-C. Wang, and A. T. Johnson Jr., Electric response of isolated electrospun polyaniline nanofibers to vapors of aliphatic alcohols, *Sensors Actuat. B*, **129**, 621–627 (2008).
[101] R. Rojas and N. J. Pinto, Using electrospinning for the fabrication of rapid response gas sensors based on conducting polymer nanowires, *Sens. J., IEEE*, **8**, 951–953 (2008).
[102] S. Ji, Y. Li, and M. Yang, Gas sensing properties of a composite composed of electrospun poly(methyl methacrylate) nanofibers and in situ polymerized polyaniline, *Sensors Actuat. B*, **133**, 644–649 (2008).
[103] W. E. Jones, H. Dong, F. Ochanda, and V. Nyame, Conducting molecular wires: nanofibers and nanotubes for electronics applications, 61st Annual Technical Conference ANTEC, Nashville, TN, 1948–1950 (2003).
[104] J. Kameoka, B. Ilic, D. Czaplewski, R. T. Mathers, G. W. Coates, and H. G. Craighead, Fabrication of blended polyphenylenevinylene nanowires by scanned electrospinning, *J. Photopolymer Sci. Technol.*, **17**, 421–425 (2004).
[105] R. Gonzalez, and N. J. Pinto, Electrospun poly(3-hexylthiophene-2,5-diyl) fiber field effect transistor, *Synth. Met.*, **151**, 275–278 (2005).
[106] H. Liu, C. H. Reccius, and H. G. Craighead, Single electrospun regioregular poly (3-hexylthiophene) nanofiber field-effect transistor, *Appl. Phys. Lett.*, **87**, 253106 (2005).
[107] D. Li, A. Babel, S. A. Jenekhe, and Y. Xia, Nanofibers of conjugated polymers prepared by electrospinning with a two-capillary spinneret, *Adv. Mater.*, **16**, 2062–2066 (2004).
[108] A. Ruiz, E. Vega, R. Katiyar, and R. Valentin, Novel enabling wire bonding technology, *Proceedings – Electronic Components and Technology Conference*, ECTC '07, art. no. 4249923, 458–462 (2007).
[109] Z.-M. Huang, Y.-Z. Zhang, M. Kotaki, and S. Ramakrishna, A review on polymer nanofibers by electrospinning and their applications in nanocomposites, *Composites Sci. Technol.*, **63**, 2223–2253 (2003).

[110] K. S. Yun, B. W. Cho, S. M. Jo, W. I. Lee, K. Y. Park, H. S. Kim, U. S. Kim, S. K. Ko, S. W. Chun, and S.W. Choi, Lithium secondary battery comprising a super fine fibrous polymer separator film and its fabrication method, *US Patent* PCT/KR00/0050 (2001) (7-279-251 B1).

[111] Y-W. Ju, J-H. Park, H-R. Jung, and W-J. Lee, Electrochemical properties of polypyrrole/sulfonted SEBS composite nanofibers prepared by electrospinning, *Electrochim. Acta*, **52**, 4841–4847 (2007).

[112] Y-W. Ju, G-R. Choi, H-R. Jung, and W-J. Lee, Electrochemical properties of electrospun PAN/MWCNT carbon nanofibers electrodes coated with polypyrrole, *Electrochim. Acta*, **53**, 5796–5803 (2008).

[113] K. J. Senecal, L. Samuelson, M. Sennett, and G. H. Schreuder-Gibson, Conductive (electrical, ionic and photoelectric) membrane articlers, and method for producing same, *US Patent Application*, 0045547 (2001).

[114] K. J. Senecal, D. P. Ziegler, J. He, J. R. Mosurkal, H. Schreuder-Gibson, and L. A. Samuelson, Photoelectric response from nanofibrous membranes, *Mater. Res. Soc. Symp. Proc.*, **708**, 285–289 (2002).

[115] C. M. Waters, T. J. Noakes, and I. Pavery, C. Hitomi, Liquid crystal devices, *US Patent,* 5-088-807 (1992).

[116] W. B. Cho, S. W. Choi, J. S. Mu, H. S. Kim, U. S. Kim, and W. I. Cho, A Lithium secondary battery comprising a super fine fibrous polymer separator film and its fabrication method. *Patent* WO0189022 and WO0189023 (2001).

[117] D. P. Ziegler, K. J. Senecal, C. Dew, and L. Samuelson, Electrospun fibrous membranes of photovoltaic and conductive polymers, *J. Textile Apparel Technol. Manag.*, **1**, Special issue: The Fiber Society Spring Conference, Raleigh, NC (2001).

5

Composites Based on Conducting Polymers and Carbon Nanotubes

M. Baibarac[a]*, I. Baltog*[a]*, and S. Lefrant*[b]

[a]*National Institute of Materials Physics, Bucharest Romania*
[b]*Institut des Matériaux Jean Rouxel, Nantes, France*

5.1 Introduction

In the nanotechnology field, carbon-based materials and associated composites have received special attention both for fundamental and applicative research. In the first kind, carbon compounds may be included, often taking the form of a hollow spheres, ellipsoids, or tubes. Spherical and ellipsoidal carbon nanomaterials are referred to as fullerenes, while cylindrical ones are called nanotubes and nanofibers. In the second class, one includes composite materials that combine carbon nanoparticles with other nanoparticles, or nanoparticles with large bulk-type materials. The unique properties of these various types of nanomaterials provide novel electrical, catalytic, magnetic, mechanical, thermal, and other features that are desirable for applications in commercial, medical, military, and environmental sectors. This is the case for conducting polymers (CPs) and carbon nanotubes (CNTs) [1–5].

Besides the expected improvements in the mechanical and electronic properties of polymers, the preparation of carbon nanotube/polymer composites has been and is still explored for effective incorporation of CNTs into devices. Nevertheless, the use of CNTs as a rough material in different applications has been largely limited by their poor processability, insolubility, and infusibility. To bypass this disadvantage, an efficient

Nanostructured Conductive Polymers Edited by Ali Eftekhari

key is the functionalization of CNTs with polymers, leading to soluble composite materials. Researchers have then focused their attention on two types of materials: on one hand, composites based on insulating polymers (IPs) as polystyrene (PSt) or poly (methyl metacrylate) (PMMA), and on the other hand, those made with conducting polymers (CPs), such as polyaniline (PANI), polypyrrole (PPy), poly(*p*-phenylene vinylene) (PPV), poly(*m*-phenylene vinylene-co-2,5-dioctoxy-*p*-phenylene) (PmPV), poly(*N*-vinyl carbazole) (PVK), poly(3,4-ethylenedioxy thiophene) (PEDOT), polythiophene (PTh), and 2,2′- polybithiophene (PBTh) and polyacetylene (PA).

The combination of single-walled carbon nanotubes (SWNTs), double-walled carbon nanotubes (DWNTs), and multiwalled carbon nanotubes (MWNTs) with insulating or conducting polymers offers an attractive route to reinforce the macromolecular compounds, as well as to introduce new electronic properties based on morphological modifications or electronic interactions between the two constituents [6–10]. Usual methods for the preparation of polymer/CNT composites consist in the direct mixing of components in the melt or in solution, the production of bilayer structures by deposition of a polymer film onto a CNT layer, and chemical and electrochemical polymerization. The presentation of the background to and the state of the art for the production of new CNT-based materials, as well as CNT composites are among the main objectives of this section.

In the section devoted to CNTs, some details concerning synthesis and purification methods, as well as separation techniques for metallic and semiconducting nanotubes will be reviewed. Some aspects concerning the interactions of CNTs with reactants used in the synthesis of different composites based on conducting polymers, such as PANI, PPy, PEDOT, PBTh, PNVK, PPV, and polyfluorene (PF) will be discussed in the section devoted to the synthesis of the CP/CNT composites. Preparing a composite with the desired properties requires knowledge of the interaction between the host matrix and the guest carbon nanoparticles.

Among the most-used experimental methods to prove the functionalization of carbon nanotubes with different functional groups, molecules, or polymers are studies of X-ray diffraction, conductivity and photoconductivity, photoluminescence, thermogravimetric analysis, mechanical properties, absorption in the UV-VIS-NIR range, IR spectroscopy, and obviously Raman scattering. This chapter focuses on IR spectroscopy and Raman light scattering as methods currently used in the characterization of composites based on CPs and CNTs. As is well known, Raman scattering is often used for qualitative identification of organic and macromolecular compounds by observing the group frequencies and the scattering intensities. Because selection rules and relative intensities of IR and Raman peaks are dissimilar, Raman scattering and IR spectroscopy are often viewed as complementary. For quantitative analyses, Raman scattering intensity is linearly proportional to the analyte concentration. Potentially, this feature conveys two significant advantages in analysis, particularly with respect to IR absorption techniques: (a) an increased linear dynamic range and (b) the addition of signals from multiple analytes. The most important advantages of Raman spectroscopy are the ease of preparation of samples and the rich content of information. In this sense, we note that there are few concerns with sample thickness (as in transmission analyses) and little contribution from the ambient atmosphere, so there is no need for high-vacuum or desiccated sample holders. Glass, water, and plastic packaging have very weak Raman spectra, a fact which makes the technique even

easier to use. Often, samples can be analyzed directly inside the glass bottle without opening the package and risking contamination. Aqueous samples are readily analyzed without the need to remove water, and because ambient humidity is not a problem, there is no need to purge the instrument. This reveals an important advantage of Raman scattering spectroscopy over IR absorption spectroscopy for biomedical applications [11,12].

Traditionally, Raman analysis has been viewed as a relatively insensitive technique. Indeed, the probability of a molecule producing Raman light scattering is much less than the probability of absorption in the IR region. However, advances in instrumentation have narrowed considerably the gap to the point where, in some optimal cases, the sensitivity of normal (i.e. nonenhanced) Raman scattering compares favorably with IR absorption. It must be noted that Raman spectroscopy has an inherently small cross-section, reducing the possibility of analyte detection at low concentration levels without special enhancement processes. Nevertheless, there has been renewed interest in Raman techniques in the past two decades owing to the discovery of the surface-enhanced Raman scattering (SERS) effect, which results from a supplementary excitation of the adsorbed molecules on nanotextured metallic surfaces. Although some details of the SERS process still remain unclear, it is accepted that the enhancement process has a twofold origin: electromagnetic and chemical [13,14], the electromagnetic enhancement being the dominant mechanism. It consists in the excitation of localized and delocalized surface plasmons (SPs) [15] and is effective in silver, gold, and copper as a result of the dielectric constant and its variation with the wavelength of the excitation light [16]. The delocalized surface plasmons are surface evanescent waves that propagate along the interface between the metal and surrounding dielectric medium. Owing to the resonant excitation of surface plasmons [13–15], it induces enhanced Raman signals ($>$1000-fold). A p-polarized incident beam can be coupled to these surface waves through an optical coupler, which can be a prism or a diffraction grating under a certain angle of incidence corresponding to the minimum of reflectivity, in other words, the well-known phenomenon of attenuated total reflection (ATR). Principles and experimental details of SERS spectroscopy have been the subject of many reviews and books [13,14,17–19].

In the field of conducting polymers, the most important contribution of IR spectroscopy and Raman scattering has consisted in the demonstration of the doping process [20,21]. For CNTs, the two experimental techniques have definitely contributed to the characterization of SWNTs, DWNTs, and MWNTs, as well as to evidence of n- or p-doping processes, oxidation or reduction reactions, breaking of the SWNT bundles into individual tubes and, more recently, to the separation of metallic and semiconducting CNTs [17,22–24]. In the case of composites based on CNTs and CPs, the two methods have often been used to elucidate the interactions of CNTs with CPs [25,26]. In the case of CP/CNT composites, a detailed analysis of the literature indicates two main processes: either the polymer functionalizes the CNTs [6–10] or CPs are doped with CNTs, the latter resulting from a charge transfer between the two constituents [25–32]. Depending on the synthesis method, the functionalization of CNTs with CPs can be covalent or noncovalent [26,33].

Another goal of this chapter is to review the main contributions of IR absorption and Raman light scattering with regard to the interactions between the two constituents, as well as to determine the molecular structure of the above-mentioned composites. In fact, we wish to illustrate the usefulness of Raman scattering and IR spectroscopy as valuable tools to characterize different types of composite materials. There exists a large range of results

and we review here only particular cases regarding the vibrational properties of composites based on SWNTs and polymers such as PANI, PPy, PEDOT, PPV, and PVK. The choice of these particular cases proves the ability of IR spectroscopy and Raman scattering as valuable tools for detecting the four composites currently obtained from the interactions between CPs and CNTs: CP/CNT bilayers, CNTs covalently functionalized with CPs, CNTs noncovalently functionalized with CPs, and CPs doped with CNTs.

5.2 Carbon Nanotubes

CNTs were discovered by Sumio Iijima in 1991 [34]. The CNT structure can be clearly illustrated by considering the two 'archetypal' CNTs which can be formed by cutting a fullerene (C_{60}) molecule in half and placing a graphene cylinder between the two halves. Dividing C_{60} along one of the fivefold axes produces the 'armchair' nanotube shown in Figure 5.1a, while bisecting C_{60} parallel to one of the threefold axes results in the 'zigzag' nanotube shown in Figure 5.1b [3]. The terms 'zigzag' and 'armchair' refer to the arrangement of carbon atom hexagons around the circumference. There is a third class of structure, 'chiral', in which the hexagons are arranged helically around the tube axis, as shown in Figure 5.1c. Depending on the 'chiral' angle at which the hexagons are arranged, CNTs have either metallic or semiconducting properties. Experimentally, the tubes are generally less perfect than the idealized versions shown in Figure 5.1 and may be either multiwalled (MWNTs) or single-walled (SWNTs) [35].

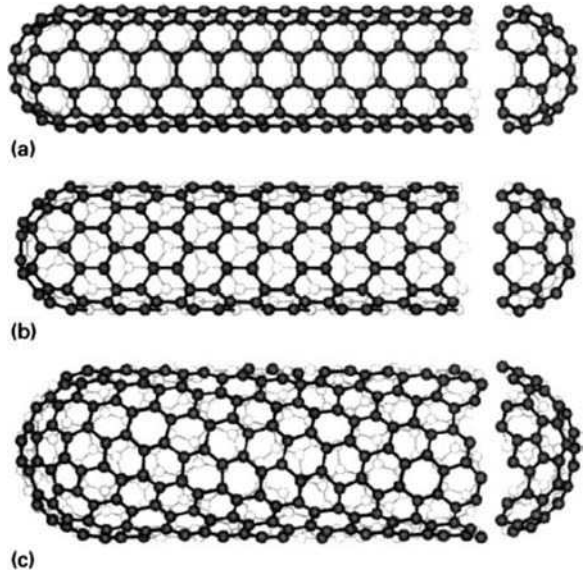

Figure 5.1 *The three types of CNT structures: (a) armchair, (b) zigzag, (c) chiral. (Reprinted with permission from International Materials Review, Carbon Nanotube Composites by P. J. F. Harris, 49, 1, 31–43. Copyright (2004) Maney Publishing www.maney.co.uk/journals/imr)*

SWNTs (Figure 5.2a) comprise a cylindrical graphite sheet of nanoscale diameter capped by hemispherical ends. The closure of the cylinder is a result of a pentagonal inclusion into the hexagonal carbon network of the nanotube walls during the growth process. Typically, SWNTs have diameters around 1 nm, with the smallest diameter reported to date being 0.4 nm. This corresponds to the theoretically predicted lower limit for stable SWNT formation based on considering the stress energy built into the cylindrical structure of the SWNTs.

MWNTs (Figure 5.2b) comprise from several to tens of concentric cylinders of these graphitic shells with an interlayer spacing of 0.3–0.4 nm. MWNTs tend to have diameters in the range 2–100 nm. MWNTs can be considered to be a mesoscale graphite system, whereas SWNTs are truly single large molecules [36].

Theoretical calculations have predicted that the electronic properties of SWNTs depend on the tube diameter d and on the helicity of the hexagonal carbon ring alignment on the nanotube surface, defined by a chiral angle θ, which in turn depends on the n and m integers, which denote the number of unit vectors $n\boldsymbol{a_1}$ and $m\boldsymbol{a_2}$ in the hexagonal lattice of the graphite:

$$\begin{aligned} d(n,m) &= C_h/\pi = 3^{1/2}a_{C-C}(m^2+mn+n^2)^{1/2}/\pi \\ \theta &= tan^{-1}\left[3^{1/2}m(m+2n)\right] \end{aligned} \tag{5.1}$$

where C_h is the length of the chiral vector $\boldsymbol{C_h}$, and $a_{C—C} = 1.42\text{Å}$ is the nearest-neighbor C—C distance. The single-walled carbon nanotube is metallic if $n - m = 3k$, $k = 1,2,3\ldots$, and semiconducting otherwise [36].

A slight variation in these parameters causes a shift from a metallic state to a semiconducting state. Regardless of the synthesis method, microscopic studies have revealed that samples consist of bundles of 20 to 100 individual nanotubes aligned in a two-dimensional crystal-packing arrangement over essentially their entire length [37,38]. The bundles, also

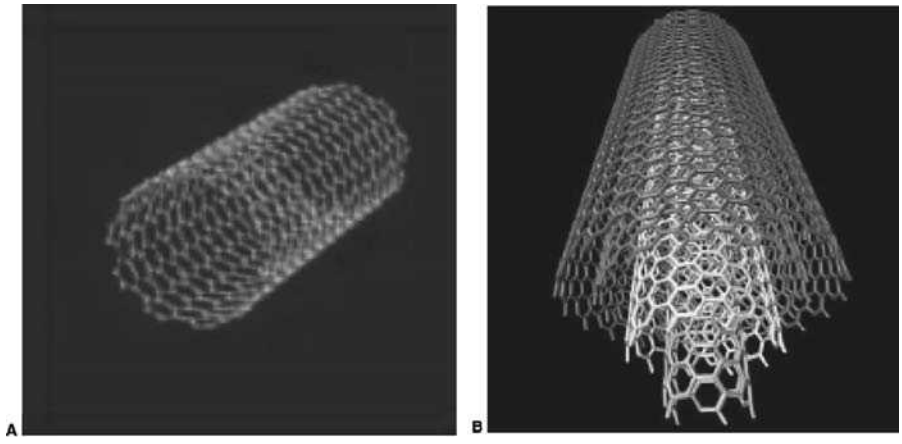

Figure 5.2 *Structures of (A) SWNTs and (B) MWNTs. (Reprinted with permission from TrAC, Trends in Analytical Chemistry, New materials for electrochemical sensing VI: Carbon nanotubes by A. Merkoci, M. Pumera, X. Llopis et al., 24, 9, 826–838. Copyright (2005) Elsevier Ltd)*

known as nanoropes, contain both metallic and semiconducting tubes. Together with transmission electron microscopy (TEM) and scanning tunneling microscopy (STM), Raman spectroscopy is one of the most widely used techniques for characterizing and understanding of the properties of the carbon tubes [36].

5.2.1 Synthesis of CNTs: Arc Discharge, Laser Ablation, Chemical Vapor Deposition

5.2.1.1 Arc-Discharge Method

The first papers to have reported the production of CNTs using the arc-discharge method are from 1992 [39] and 1993 [40]. CNTs were produced by evaporation of graphite, as for fullerene synthesis. This method creates MWNTs through an arc vaporization of two graphite rods placed end to end, separated by approximately 1 mm, in an enclosure usually filled at low pressure (between 50 and 700 mbar) with an inert gas (helium, argon). Applying a direct current (dc) arc voltage between the two separated graphite rods, CNTs ranging from 4 to 30 nm in diameter and up to 1 mm length are obtained. When a graphite rod containing a metal catalyst (for example Fe and Co) is used as the anode, the cathode being pure graphite, SWNTs [41] are generated instead of MWNTs. In this synthesis, Iijima used an arc-discharge chamber filled with a gas mixture of 10 Torr of methane and 40 Torr of argon [41]. Two vertical thin electrodes were installed in the center of the chamber. The lower electrode, the cathode, had a shallow dip to hold a small piece of iron during the evaporation. The arc-discharge was generated by running a dc current of 200 A at 20 V between the electrodes. The CNTs had diameters of 1 nm with a broad diameter distribution between 0.7 and 1.65 nm. In the arc-discharge synthesis of CNTs, Berthune *et al.* [42] used as anodes thin electrodes with bored holes, which were filled with a mixture of pure powdered metals (Fe, Ni or Co) and graphite. The electrodes were vaporized with a current of 95–105 A in 100–500 Torr of He. Large quantities of SWNTs were also generated by the arc technique by Journet *et al.* [38]. The arc was generated between two graphite electrodes in a reactor under a helium atmosphere (660 mbar), with an optimized mixture of catalyst, namely 1 at% of Y and 4.2 at% of Ni.

Large-scale synthesis of MWNTs by arc discharge was achieved [43] in a helium atmosphere. The arc-discharge evaporation of pure graphite rods has been carried out in not only ambient gases, such as helium or argon, but in methane, too [44]. It was found that methane is the best gas for the synthesis of MWNTs. This is due to the thermal decomposition of methane producing hydrogen, which achieves high temperature and activity compared to inert gases, such as He or Ar. The effectiveness of hydrogen in the synthesis of MWNTs has been reported [45].

A disadvantage of this method is the low purity of the CNTs. To use CNTs in different applications, a purification method to remove metallic catalytic material is therefore necessary. The yield for this method is about 30% and as noted above, it results in both SWNTs and MWNTs with lengths of up to 50 μm. The development of more efficient synthesis techniques is vital to the future of carbon nanotechnology.

5.2.1.2 Laser-Ablation Method

The laser-furnace or laser-ablation method [46] has been developed for the synthesis of fullerenes and CNTs. This method is widely used for the production of SWNTs. Thus, in 1996, Smalley *et al.* [37] produced high yields (ca. 70%) of SWNTs by laser ablation of graphite rods with a small amount of Ni and Co at 1200 °C. The laser is suitable for use with materials with a high boiling temperature, such as carbon, the energy density of lasers being much higher than that of other vaporization devices. The basic principle of this method is as follows: (i) a CO_2 laser beam is introduced onto the target (carbon composite doped with catalytic metals) located in the center of a quartz tube furnace; (ii) the target is vaporized in a high-temperature argon atmosphere and SWNTs are formed; (iii) the SWNTs produced are conveyed by the gas to a special collector. This method has several advantages, such as the high yields of production, the small range of diameters, and controlled growth of the SWNTs. The change of the furnace temperature, catalytic metals, and flow rate directly affect the SWNTs' diameter distribution [47,48]. The yield of this method is greater, about 70%, and produces primarily SWNTs, with a controllable diameter determined by the reaction temperateure. In comparison with arc discharge or chemical-vapor deposition, this method is more expensive.

5.2.1.3 Chemical Vapor Deposition

A major disadvantage of the above methods, i.e. arc discharge and laser ablation, is that : (i) they do not allow control of the location and the alignment of the synthesized CNTs; (ii) they rely on the evaporation of carbon atoms from solid targets at temperature >3000 °C; and (iii) the nanotubes are tangled making purification difficult and their use in some applications impossible. This can be avoided using chemical-vapor deposition (CVD), which was first used in 1996 and is widely used nowadays in CNT production [49]. The method is also known as thermal or catalytic CVD. CVD is a versatile process in which gas-phase molecules are decomposed into reactive species, leading to a film or particle growth [50]. In a typical procedure, a mixture of a hydrocarbon gas, acetylene, methane, or ethylene, and nitrogen is introduced into the reaction chamber. During the reaction, CNTs are formed on the substrate by the decomposition of the hydrocarbon at temperatures of 700–900 °C and atmospheric pressure [51]. CVD is a simple and economic technique for the synthesis of CNTs at low temperature and ambient pressure [52]. CNTs grow over the catalyst and are collected on cooling the system to room temperature. The substrate preparation and the use of the catalyst require special attention, because they determine the tubes' structure. Often, the substrate used is silicon, glass, or alumina. An ideal substrate for growing self-oriented CNTs on large surfaces is porous silicon [53]; it has been proven that CNTs grow at a higher ratio (length per minute) and they are better aligned than on plain silicon [54]. The catalysts are metallic nanoparticles, like Fe, Co, and Ni, which can be deposited on Si substrates either from solution, by electron-beam evaporation, or by physical sputtering [54]. The diameter of the CNTs depends on the catalyst particle size. A new method to grow highly aligned CNTs was reported by Xie *et al*. in 2000 [51]. Using Xie's method, the substrate can be reused after depositing new catalyst particles on the surface and the length of the nanotube arrays increases with growth time, and reaches about 2 mm after 48 h [51].

Other procedures for the synthesis of CNTs use a gas phase for introducing the catalyst, in which both the catalyst and the hydrocarbon gas are fed into a furnace, followed by a catalytic reaction in the gas phase. The method is suitable for large-scale synthesis, because nanotubes are free from catalytic supports and the reaction can be operated continuously. A high-pressure carbon monoxide reaction method, in which the CO gas reacts with iron pentacarbonyl to form SWNTs, has been developed [38]. SWNTs have been synthesized from a mixture of benzene and ferrocene in a hydrogen gas flow [55]. In both methods, catalyst nanoparticles are formed through thermal decomposition of organometallic compounds, such as iron pentacarbonyl and ferrocene.

E. Kirsten and J.L. Spencer [56] synthesized CNTs from an aerosol precursor. Solutions of transition-metal cluster compounds were atomized by electrohyrodynamic means and the resultant aerosol was reacted with ethylene in the gas phase to catalyse the formation of CNTs. The use of an aerosol of iron pentacarbonyl resulted in the formation of MWNTs, mostly 6–9 nm in diameter, whereas the use of iron dodecacarbonyl gave results that were dependent on the concentration. High concentrations resulted in a wide diameter range (30–200 nm), whereas lower concentrations gave MWNTs with diameters of 19–23 nm.

L.A. Montoro *et al.*'s [57] synthesis of high quality SWNTs and MWNTs through arc discharge in H_3VO_4 aqueous solution from pure graphite electrodes used the VO group as a nucleation agent promoting the growth of more ordered carbon structure.

J. Qiu *et al.* [58] prepared CNTs by electrically arcing carbon rods in He (99.99%) in a stainless-steel chamber with an inner diameter of 600 mm and a height of 350 mm. The anode was a coal-derived carbon rod (10 mm in diameter, 100–200 mm in length); the cathode was a high-purity graphite electrode (16 mm in diameter, 30 mm in length). He was used as a buffer gas and its pressure was varied in the 0.033–0.076 MPa range. The voltage and current for the electric arc were 30–40 V and 50–70 A, respectively.

M. Shao *et al.* [59] have synthesized CNTs in a new way using an iron catalyst at the extremely low temperature of 180 °C. In this process, carbon suboxide was used as carbon source, which changed to freshly formed free carbon clusters through disproportionation. The carbon clusters grow into nanotubes in the presence of Fe catalyst, which was obtained by the decomposition in iron carbonyl at 250 °C under a nitrogen atmosphere.

SWNTs have been successfully synthesized using a fluidized-bed method [60] that involves fluidization of a catalyst/support at high temperatures by a hydrocarbon flow.

A new method, which combines a nonequilibrium plasma reaction [61] with template-controlled growth technology, has been developed for synthesizing aligned CNTs at atmospheric pressure and low temperature. MWNTs with diameters of ca. 40 nm were synthesized in the channels of anodic aluminum oxide template from a methane hydrogen mixture gas by an alternating current (ac) corona discharge plasma reaction at a temperature below 200 °C.

The recent technique of nebulized spray pyrolysis (NSP) has been used to prepare aligned MWNTs bundles [62]. This technique consists in a spray generated by an ultrasonic atomizer. MWNTs with fairly uniform diameters, as well as aligned MWNT bundles, have been obtained by using solutions of organometallic compounds, such as ferrocine, in benzene, toluene, and other hydrocarbon solvents. The advantage of NSP is the ease of scaling up to an industrial process where the reactants are fed into the furnace continuously.

New experimental details were reported in 2006 for laser chemical-vapor deposition (LCVD), which is a derivative of CVD whereby the global heat source of a furnace is

replaced with a localized spot heated by a laser [63]. There are two types of laser CVD, pyrolytic and photolytic [64]. In the case of pyrolytic laser CVD, the chemical and physical phenomena that lead to deposition of CNTs are similar to those of conventional CVD. That is, the transfer of thermal energy to the reagent from the spot heated by the laser is responsible for the dissociation of the reagent molecules and the deposition process [64]. Laser CVD differs from conventional CVD in that the area of growth can be limited to the pass of the laser beam. Thus, one maintains the capability to deposit most materials on a larger variety of substrates than with conventional CVD. There is very little documented work using the LCVD process to deposit CNTs [63,65].

Other variations on the CVD method, such as hot-wire CVD (HWCVD) [66], rapid thermal CVD (RTCVD) [67], microwave plasma CVD (MPCVD) [68], and the floating catalyst technique [69,70] have led to improvements in product controllability, yield, and cost.

Other technological aspects of carbon nanotube synthesis currently under scrutiny include study of the growth mechanism [67,71], attempts to control the diameter [72–74], processes which yield very long CNTs [70,75], optimization of the catalyst composition [76], and improvements in purity [77]. A major area of focus is the production of CNTs at selected sites on a substrate (micropatterning) [78–81]. Other synthetic methods investigated have been: (i) a solvothermal route, in which reactants are heated in solution in a sealed autoclave [82,83]; (ii) a solid-state metathesis process [84]; (iii) a hydrothermal process which produces MWNTs from amorphous carbon [85]; and (iv) low-temperature processes [59].

Summarizing these data one may conclude that CVD is still the most widely used method for the growth of high-quality CNTs. This statement is supported by the high number of publications devoted to this subject, about 600 articles in only the first six months of 2009. Despite the high cost of CNTs, at present this method is used by several suppliers, such as NanoLab, Aldrich-Sigma, Nanocyl, etc. Increasing the yield and length of grown tubes needs futher investigation.

5.2.2 Purification

In general, CNTs produced by various synthetic methods also contain amorphous carbon, carbon nanoparticles, and catalyst residues. Although many advances have been made in terms of scaling up the synthesis, a number of obstacles regarding the purification of nanotubes still exist. The tubes have a wide range of lengths, many defects, and a variety of twists to them. Therefore, the main concern is how to separate them from the worthless soot and how to purify the tubes. For this purpose, various post-growth treatment methods to purify the nanotubes and eliminate the defects in the tubes have been developed. The material can be treated in an ultrasonic bath to free many tubes from particles that were originally stuck together [40]. The larger contaminants can be easily removed due to their relatively high weight, for example by dispersing the powder in a solvent and subsequent centrifugation. The smaller particles are more difficult to eliminate. Purification is not trivial, as any treatment designed to remove metal-catalyst particles and amorphous carbon can often result in the functionalization of the tubes and/or the introduction of new defects into the CNT structure. The most commonly used purification methods include oxidation

in the presence of acid [86] or gas [87], filtration [88,89], and chromatographic separation [90–92]. Less common methods include capillary electrophoresis [93] and ultrasonication in the presence of inorganic nanoparticles [94]. Hydrothermal treatment has also been found to be effective in the purification of SWNTs [95]. Many researchers employ a multistep process to purify CNTs.

The most prevalent method, acid oxidation, generally oxidizes metals and carbon impurities, but can also functionalize the surface of the nanotubes. Depending on the oxidizing strength of the acid or acid mixture, the damage to the CNTs ranges from functionalization of defects extant from the growth process to more severe damages. The introduction of additional oxidation defect sites can result in the tube breaking [96]. In addition to the functionalization and tube breaking, acid oxidation has also been found to degrade SWNTs and MWNTs, forming onion-like carbon structures upon refluxing in nitric acid (HNO_3) [97]. A mild acid, such as dilute HCl, has been found to react only with the end caps, which are more reactive due to curvature strain [98]. In 2002, C.M. Yang *et al.* showed that purification of CNTs in the presence of highly concentrated HCl solutions affects the pore structures of SWNTs aggregates [99].

A process known as annealing, which involves heating in an inert atmosphere [86] or under vacuum [86,100,101], eliminates some of the structural defects, such as surface functionalization (resulting from acid treatment), and can also oxidize residual catalyst particles [102]. Heating SWNTs in air has also been found to be effective in eliminating amorphous carbon, due to the relative thermal stability of the CNTs [103–105].

Although CNTs exhibit ideal characteristics when they are in an ultrahigh vacuum environment, samples in more ordinary conditions, where they are exposed to air or water vapor, show properties that are different. CNTs are very sensitive to contaminants, such as oxygen, attached to them. They severely affect the electrical properties, which is an important problem for devices made from CNTs. The soot of fabricated CNTs is often dispersed in ethanol, in which it can be preserved without damaging the tubes. The tubes themselves are stable, maintaining their shapes, regardless of the contamination mentioned above, up to 2800 °C in vacuum, and to 750 °C in air.

After purification of CNTs, pretreatment of the nanotubes that creates active sites for binding of polymers is often carried out. In the case of the PANI/MWNTs composite, significant active binding sites for polymers on CNTs are generated by the appearance of carboxylic acid groups on the surface of the tubes. As reported in Ref. [106], this is obtained by the interaction of CNTs with a 3:1 mixture of concentrated H_2SO_4 and HNO_3 at 50 °C for 24h. By the formation of active sites, one increases the solubility of MWNTs in aniline monomer [107]. In the case of composites based on MWNTs and polythiophene, the COOH groups formed on the nanotube surface were converted to COCl using thionyl chloride and followed by condensation with the polythiophene at high temperature in anhydrous DMF [108]. Other common methods to create active sites are *in situ* polymerization reactions initiated with radicals [109], and anionic polymerization after formation of CNT-polyanions using alkyal lithium [110]. To create active sites on CNTs, electrochemical methods have also been used. Thus, in the case of the PPy/SWNTs composite [111], electropolymerizable SWNTs were synthesized by chemical binding of pyrrole alcohol to oxidized nanotubes via ester formation, or functionalized by noncovalent interactions with a pyrene-pyrrole derivate. It should be noted that for CP/SWNT composites, pretreatment resulting in the appearance of COOH groups on the nanotube surface is

not often used. Generally, the interaction of SWNTs with strongly oxidizing media leads to an irreversible transformation of nanotubes, where defects and nanotube fragments of shorter lengths, such as closed-shell fullerenes, appear as final reaction products [25]. This has resulted in the composites based on CPs and fragments of nanotubes, as reported in Ref. [25]. Inhibition of this irreversible transformation was reported to occur by the reaction of aromatic monomers such as aniline [25] or *N*-vinyl carbazole [33] with CNTs, where the formation of charge-transfer complexes between the two constitutents was demonstrated by Raman spectroscopy. Despite the fact that SWNTs exhibit complicated spectroelectrochemical behavior in aqueous and nonaqueous acid solutions that is dependent on the sweep potential range, the interaction of SWNTs with HCl or HF is more attractive, because the covalent attachement of F or Cl atoms onto the nanotube surface takes place without their shortening [112,113].

Four methods have been used for the grafting of polymers onto CNTs : (i) the 'grafting-onto' method involves the termination of growing polymer radicals, cations, or anions, formed during the polymerization of different monomers initiated by conventional initiators in the presence of CNTs, or the deactivation of living polymer chain ends with functional groups on these surfaces; (ii) in the case of the 'polymer-reaction' method, the polymers are grafted onto CNTs by reactions of the surface with functional groups of polymers, such as hydroxyl, carboxyl, and amino groups; (iii) the 'grafting-from' method involves the initiation of graft polymerization of various monomers from radical and ionic initiating groups previously introduced onto the CNT surface; and (iv) the 'stepwise-growth' method uses grafted polymer chains grown from surface functional groups on CNTs by repeated reaction with low-molecular-weight compounds [114]. For the CP/CNT composites, a significant role is played by the first method. In the following, we note some examples. Wu *et al.* [115] reported the grafting of PVK and poly(butadiene) onto SWNTs by nucleophilic reaction of polymeric carbanions generated from organometallic reactents, such as sodium hydride or butyllithium. Photoinduced electron transfer was observed in PVK-grafted SWNT systems to give large optical limiting effects [115]. Feng *et al.* [29] and Wu *et al.* [116] have reported the preparation of PANI/MWNTs composite via *in situ* chemical oxidation polymerization of aniline. Grafting of PANI onto SWNTs by electrochemical polymerization was reported by Baibarac *et al.* in 2004 [26] as taking place in aqueous HCl solutions. More details concerning some aspects of the synthesis of CP/CNT composites are given in Section 5.3.

5.2.3 Separation Techniques for Metallic and Semiconducting Carbon Nanotubes

For most electronic applications preferential growth of only metallic or only semiconducting SWNTs would be highly desirable. Li *et al.* have concluded from their data that the ratio of metallic to semiconducting tubes depends on the production method, which might indicate that chirally controlled growth could be achieved in the future [117]. However, in practice, SWNTs are grown as a mixture of the two tube types, which makes separation schemes inevitable. A precondition for efficient separation is that tubes are individualized within mixture of metallic and semiconducting tubes, meaning that they do not form bundles, as generally observed. This can be achieved by suspending SWNTs in an aqueous surfactant solution under sonication, where bundles split up and the individualized tubes

are then hindered from reforming bundles by the surfactant [22,118,119]. The remaining bundles can be removed by ultracentrifugation [120]. The scheme of O'Connell *et al.* involves the use of various surfactants, such as sodium benzene sulfonate [120]. The fingerprints of surfactant-stabilized individual SWNT suspensions are sharp absorption peaks in optical absorption spectra, in contrast to the broad bands of suspended bundles. Furthermore, surfactant-stabilized SWNT suspensions show fluorescence in the near-infrared region, emitted by semiconducting tubes, which is otherwise quenched by nearby metallic tubes in bundles. It should be noted that the observation of sharp absorption and fluorescence peaks indicates a rather large fraction of individualized SWNTs in the suspension. Nevertheless, it is not sensitive enough to exclude the presence of a small fraction of bundles, information which can be given by atomic force microscopy or transmission electron microscopy after transferring the tubes onto a surface.

The main separation techniques are: (i) separation via dielectrophoresis; (ii) chemical selectivity for metallic tubes; (iii) selection via ion-exchange chromatography; and (iv) selective destabilization of the tube suspension. Separating metallic from semiconducting SWNTs, starting from individual tube suspensions, was first achieved via alternating current dielectrophoresis [24]. This physical method makes use of the different polarisabilities of metallic SWNTs and semiconducting SWNTs induced by an electrical field. Theoretically, it is expected that the dielectric constant of semiconducting SWNTs is of the order of $5\varepsilon_0$ compared to $80\varepsilon_0$ for aqueous surfactant solution. For metallic SWNTs the dielectric constant should be at least of the order of $1000\varepsilon_0$. The dielectric constant of semiconducting SWNTs and metallic SWNTs being smaller and larger than that of water gives access to separation of the two tube types by exposing them to a strong and inhomogeneous electrical field. The interaction of the induced dipole moment with the inhomogeneous external field leads to displacement of the metallic SWNTs towards the high-field region, whereas the semiconducting SWNTs move in the opposite direction towards the low-field region [24].

Chemical separation of metallic SWNTs from semiconducting SWNT would be more scalable. In this sense, M. Strano *et al.* reported that diazonium reagents, under carefully controlled conditions, primarily react with metallic SWNTs [121]. Confirmation of the selective reaction is given by optical absorption spectroscopy, where the absorption peaks associated with metallic SWNTs initially decay following addition of the diazonium reagents. Further confirmation is given by the evolution of the Raman spectra with increasing diazonium agent concentration, which shows that small metallic SWNTs are the most reactive species.

A selective electrochemical modification of metallic SWNTs that have been wired to electrodes on a surface, has been achieved by Balasubramanian *et al.* [122]. The authors used, similarly to Strano *et al.*, a diazonium agent to functionalize metallic SWNTs. Here, the reaction is driven by an electrical potential applied between electrodes in contact with tubes and a counter-electrode. The authors found conditions in which primarily metallic SWNTs react, once the semiconducting SWNTs are driven into the nonconducting state by an appropriate gate voltage. An experimental verification of the selective modification is given by transport measurements in which the signature of metallic SWNTs disappears after treatment.

Another chemical approach is to separate SWNTs by anion-exchange chromatography. M. Zheng *et al.* found out that single-stranded DNA interacts strongly with SWNTs to

form a stable DNA–SWNT hybrid material that effectively disperses SWNTs in aqueous solution under sonication [123]. Such DNA–SWNT suspensions do show similar sharp optical absorption peaks and photoluminescence to surfactant-stabilized individual tube suspensions. Since the phosphate groups on a DNA–SWNT hybrid material provide negative charge density on the surface of CNTs, the authors anticipated that a DNA–metallic-SWNT hybrid will have less surface charge than a DNA–semiconducting-SWNT hybrid due to charge screening by metallic SWNTs. To take advantage of this difference for SWNT separation, an ion-exchange liquid chromatography experiment was performed, where the difference in surface charge was expected to modify the interaction of the hybrid with the resin and hence the propagation speed through the column.

More recently, the authors conducted a systematic study of whether the formation of the DNA–SWNT hybrid material is sequence dependent [124]. The result was that DNA sequences rich in guanine and thymidine amino acids are particularly used for the formation of stable aqueous suspensions. These suspensions were then split up into various fractions by anion-exchange liquid chromatography. Optical absorption spectra revealed enrichment in metallic SWNTs in the early fractions, but complicated by variation in diameter. SWNTs with a smaller diameter pass the column faster than SWNTs with a large diameter. Recently, the group of M. Strano *et al.* performed an extensive analysis on the very same samples combining photoluminescence and Raman spectroscopy [125]. The result was that separation of the suspensions by anion-exchange liquid chromatography is primarily according to the diameter of the SWNTs, independent of the metallic or semiconducting nature of the SWNTs. The results show that ion-exchange chromatography allows the separation of DNA–SWNT hybrids at least according to their diameter.

The separation of metallic and semiconducting SWNTs cannot be achieved if bundles are of a heterogeneous composition. However, for small bundles, some degree of enrichment is possible. For instance, Chattopadhyay *et al.* reported an increase in solubility of semiconducting SWNTs when these were dispersed with ocatadecylamine (ODA) in tetrahydrofuran (THF) [126]. The authors assume that ODA is physically absorbed along the SWNT side walls, with the amino group having a stronger affinity for semiconducting SWNTs than metallic SWNTs, thereby providing additional stability to the physisorbed ODA. In contrast, metallic SWNTs are more likely to precipitate.

Recently, a quantitative analysis of the Raman spectra of such samples, carried out by G. Samsonidze *et al.*, revealed that the separation efficiency is complicated by variations in the tube diameter [127]. In particular, poor enrichment is observed for large-diameter tubes, becoming more efficient towards smaller tube diameters. The origin of this diameter dependence on the enrichment is not yet understood, but the authors point to electronic amine–SWNT interactions or curvature-induced stabilization.

In another work, Z. Chen *et al.* have added dropwise diluted bromine to Triton X-100 suspended SWNTs and SWNT bundles and observed sedimentation of tube material enriched in metallic SWNTs [128]. No enrichment was observed for experiments using sodium dodecyl sulfonate as surfactant. The authors take this experimental fact as evidence that the enrichment mechanism involves bromine-induced destabilization of the Triton X-100 surfactant shell, with greater specificity for metallic SWNTs.

By correlated studies of resonant Raman scattering, including the SERS technique and UV–VIS–NIR absorption spectroscopic measurements, the dispersion of SWNTs as

isolated entities was performed using sodium dodecyl sulfate (SDS), polyvinylpyrrolidone (PVP), and cetyl trimethyl ammonium bromide (CTMAB) solutions as chemical dispersing agents [129]. After intense ultrasonication treatment of the SWNTs suspended in surfactant solutions, the G band profile changes, and only the sharp G^+ component, located at 1592 cm^{-1} with a full-width at half-maximum (FWHM) of 8–10 cm^{-1}, remains. The sharpening of the G band, which corroborated with the $I_{isolated}/I_{bundled}$ ratio changes in the RBM region, gives the signature of isolated nanotubes.

Additionally, UV–VIS–NIR absorption spectra show that the electronic transitions associated with different individual nanotubes reveal the isolation state by the appearance of a fine structure in the absorption band, associated with $E_{11}{}^S$ and $E_{22}{}^S$ transitions [129].

5.2.4 Vibrational Properties of Carbon Nanotubes

For SWNTs, it is well known that, regardless of the synthesis method, microscopic studies have revealed that samples consist of bundles of 20–100 individual nanotubes aligned in a two-dimensional crystal-packing arrangement over essentially their entire length [38,39]. Bundles, also known as nanoropes, contain both metallic and semiconducting tubes. The coexistence of the two types of CNTs, metallic and semiconducting, for which Raman spectra differ as a function of excitation wavelength, offers the opportunity of studying bundles and individual nanotubes, but also their transformation. According to the first vibrational calculations regarding the Raman active modes in SWNTs, three spectral ranges are significant, i.e. 100–350, 1000–1700 and 1700–3000 cm^{-1} [130]. Raman spectra of SWNTs at different excitations of 1064, 676.4 and 514.5 nm are shown in Figure 5.3. In the first range, one finds the Raman bands associated with the radial breathing modes (RBM), which do not exist in graphite. Their peak position is related to the tube diameter according to a relation of the type $\nu\,(cm^{-1}) = 223.75/d$ (nm) [131]. Bands belonging to this group are very sensitive to the excitation wavelength. The intensity of each band is enhanced when the photon energy of the excitation radiation corresponds to a transition between the van Hove singularities (E_{ii}) in the valence and conduction bands of all possible nanotubes [132]. According to the theory, the two strongest bands at 164 and 176 cm^{-1}, observed for excitation wavelengths of 1064 and 676 nm, indicate that the resonance occurs over a narrow range of diameters around 1.36 and 1.27 nm, respectively [133]. Often, at an excitation wavelength of 1064 nm, the shoulder at about 178 cm^{-1} is indicative of bundled tubes whose diameter can be estimated from the RBM frequency by several expressions, one of these being $\Omega\,(cm^{-1}) = 223.75(nm.cm^{-1})\,/\,d\,(nm) + \Delta\Omega\,(cm^{-1})$, where $\Delta\Omega = 14\ cm^{-1}$denotes the up-shift due to tube–tube interactions [134,135]. The second group, consisting of G and D bands, covers the interval from 1000 to 1700 cm^{-1}. These bands are not only related to the nanotube structure: the former, peaking at about 1595 cm^{-1}, usually called the 'G' band, is complex and attributed to tangential vibration modes (TM) [135]. Recent data describe the G band as being formed of two components denoted G^+ and G^-, which in the case of the metallic SWNTs are attributed to the transversal optic (TO) circumferential and longitudinal optic (LO) axial vibrational modes, respectively [136]. The 'D' band, whose peak position varies with the excitation wavelength, is normally not active in the first-order Raman spectra of graphitic compounds. It originates from a double-resonance process induced by disorder or defects [137]. Another

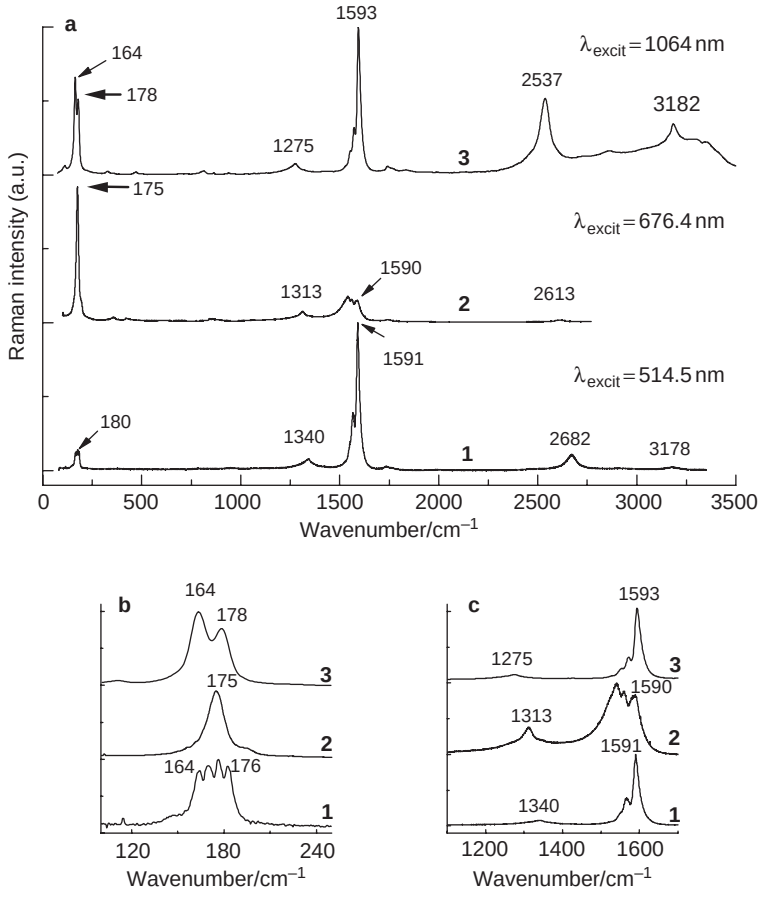

Figure 5.3 *(a) SERS spectra at $\lambda_{exc} = 514.5$ nm (1), 676 nm (2), and 1064 nm (3) of carbon nanotubes films of ca. 150 nm thickness deposited on rough Au supports. (b), (c) same as (a) with extended wavenumber ranges. (Reprinted with permission from Journal of Raman Spectroscopy, Surface-enhanced Raman scattering studies on chemically transformed carbon nanotube thin films by S. Lefrant, I. Baltog and M. Baibarac, 36, 6–7, 676–698. Copyright (2005) John Wiley & Sons Ltd)*

group, located in the high-wavenumber range from 1700 to 3500 cm^{-1}, corresponds to the second-order Raman spectrum. The most intense bands are those detected at approximately twice the wavenumbers of the D and G bands. Like their first-order counterparts, they behave resonantly when the excitation wavelength is changed.

In comparison with SWNTs, DWNTs show some RBM bands in the low-frequency 170–350 cm^{-1} region due to the inner wall tube breathing modes, and bands below 170 cm^{-1} due to the outer tubes [138]. J.M.Benoit *et al.* have presented a detailed low-frequency Raman study of arc-discharge MWNTs. A comprehensive simulation of the Raman spectrum shows that the low-frequency spectrum of MWNTs is very sensitive to their internal diameter [139].

The first vibrational calculations concerning the IR active modes in SWNTs reported that the main absorption bands are localized at ca. 682, 806, 854, 956, 1033, 1095–1164, 1262, 1443, 1541, 1585, and 1730 cm^{-1} and were all assigned [140]. According to the authors knowledge, until now, additional IR vibrations modes for the DWNTs and MWNTs have not been reported.

5.3 Synthesis of Composites Based on Conducting Polymers and Carbon Nanotubes

Many efforts have been made to combine CPs and CNTs in producing functional composite materials with improved properties able to be used in different applications in the field of supercapacitors, sensors, photovoltaic cells and photodiodes, optical limiting devices, solar cells, high-resolution printable conductor, electromagnetic absorbers, and advanced transistors. A detailed inspection of the literature devoted to composites based on CPs and CNTs shows that, depending on the synthesis method, different interface reactions between the two constituents have been proposed. The most used synthesis methods for the preparation of CP/CNT composites have been: (i) direct mixing of the CPs with CNTs; (ii) chemical polymerization of the corresponding monomer in the presence of CNTs; and (iii) electrochemical synthesis of CPs on a CNT electrode. The three routes have been supposed to give similar compounds. However, it has been shown recently that, for example, in the case of the PANI/SWNT composite, the first two routes, namely the direct mixing of CNTs with CP solution and the chemical polymerization of monomers in the presence of CNTs, lead to different materials [25]. While the former route does not affect drastically the CNTs, as SWNTs, the latter leads to a breaking of SWNTs into small fragments when the polymerization of monomers is carried out in an oxidizing medium such as $K_2Cr_2O_7$ and H_2SO_4 [25,26]. Thus, in the case of the chemical polymerization of aniline, one obtains both PANI doped with CNT fragments and CNT fragments covalently functionalized with PANI. Taking into account this example, a better understanding of the interaction of CNTs with the oxidizing medium and the monomer, respectively, is needed. Until now, different types of composites have been reported, such as blends, depositions of polymer onto CNTs, CPs doped with CNTs, and CNTs covalently functionalized with CPs. In the last two cases, i.e. when the polymer functionalizes CNTs [7,9,141] and when CPs are doped with CNTs, charge transfer is thought to occur between the two constituents [10,25,27–31]. In addition, in some cases, depending on the synthesis method, a covalent functionalization of CNTs with CPs has also been reported (for example [25,32]). An analysis of the literature devoted to CP/CNT composites indicates that: (i) direct mixing of CPs with CNTs is often reported to produce composites of CNTs noncovalently functionalized with CPs and/or CPs doped with CNTs; (ii) chemical polymerization of monomer in the presence of CNTs results in CNTs covalently functionlized with CPs and/or CPs doped with CNTs; and (iii) electrochemical synthesis of CPs on a CNT electrode leads to bilayer structures or CNTs covalently functionalized with CPs. The homogeneity of composite materials is a significant parameter in the applications field. In this context, we note that a good CP/CNT interface is not achieved when composites with a bilayer

structure are obtained. A review of the main synthesis routes of the CP/CNT composites is shown below for the each material type.

5.3.1 Polyaniline/Carbon Nanotubes

PANI/CNT composites were first prepared in 1999 [142] and since then have been the subject of intensive research and considerable progress has been made in their synthesis. Some examples include PANI/MWNT composites, prepared by the chemical oxidation of aniline in acidic aqueous environments with an oxidizing agent such as ammonium persulfate, that exhibit site-selective interactions between the quinoid ring of the repeating units of PANI emeraldine salt and MWNTs [143], a coaxial nanowire of a PANI/MWNT composite prepared by electrochemical oxidation of aniline on a CNT electrode [144], and a PANI/MWNT composite with high electrocatalytic activity for formic acid oxidation, synthesized by microemulsion polymerization of aniline in the presence of CNTs [145,146]. The first studies concerning the synthesis of PANI/SWNT composites are from 2003 [28,147,112]. In the case of SWNTs, different compounds are obtained depending on the synthesis route and reactive agents used. Thus, in the case of the chemical polymerization of aniline in the presence of SWNTs, PANI doped with CNT fragments are obtained as a result of the breaking of the SWNTs into small fragments when the oxidizing agent is $K_2Cr_2O_7$ and H_2SO_4. We note that, although the same concentration of monomer and oxidizing agent are used for the preparation of the PANI/SWNT composite and the PANI polymer, a greater reaction yield is observed in the first case. Baibarac *et al.* [25] explained this experimental fact by considering that the polymerization of aniline is controlled by the relationship between the monomer and the oxidizing agent defined by the K parameter [148], $K = (2.5n_{an})/(n_{ox}n_e)$, in which n_{an} and n_{ox} are the number of moles of aniline and oxidizing agent, respectively; n_e is the number of electrons necessary to oxidize one molecule of aniline to polyemeraldine. By decreasing the K parameter value, one increases the polymerization reaction yield [149] and this can be achieved either by increasing the concentration of the oxidizing agent in relation to the monomer concentration or by reducing the aniline concentration with regard to the concentration of oxidizing agent. A reduction of the aniline concentration can take place as a result of the interaction of the CNTs with both aniline and anilinium bisulfate. In the first case, a charge-transfer complex is obtained, while in the second case, association of the CNTs is initiated with aniline as a binding agent. The organic compound obtained from this last interaction is a tertiary amine, which, as well as triphenylamine, needs a different chemical polymerization procedure [150]. In comparison with the chemical polymerization of aniline in the presence of CNTs, composites of polymer-functionalized SWNTs having PANI in the leucoemeraldine base (LB) state are also obtained by the direct mixing route [25].

Another route for the preparation of composites based on PANI and SWNTs is electrochemical synthesis [26,30,144]. A common method for the electrochemical polymerization of aniline is cyclic voltammetry. The aqueous acidic medium frequently used is HCl or H_2SO_4. It is well known that cyclic voltammograms of polyaniline recorded in aqueous acidic media usually show two redox couples associated with the interconversion between leucoemeraldine and emeraldine (first couple) and between emeraldine and pernigraniline (the second couple) [151]. At the potential of the second oxidation peak, PANI is unstable in

aqueous solution and undergoes degradation of a hydrolytic nature [152]. SWNTs exhibit a complicated spectroelectrochemical behavior because, depending on the potential and the electrolyte used, they can exist as a variety of particles, in the reduced or oxidized state, and as neutral fragments, like closed-shell fullerenes, which distinctly differ in their spectral features [153,154]. Recently, Raman studies on the electrochemical oxidation of SWNTs in H_2SO_4 solution have shown the presence of both H_2SO_4 molecules and HSO_4^- ions in the interstitial channels between the tubes, an up-shift in the tangential G-band of 320 cm^{-1} per hole per C atom for semiconducting SWNTs [155], as well as other significant modifications in the main vibrational features of SWNT bundles, depending on the applied oxidation potential [153]. For an oxidation potential of + 600 mV vs. SCE applied to an SWNT film immersed in H_2SO_4 solution, a strong decrease in the asymmetric profile of the G band is also reported [153,154]. In an early paper, S. Lefrant *et al.* showed that the oxidoreduction process of SWNTs, deposited on Au support, carried out in H_2SO_4 solution in potential ranges larger than (0; +500) mV, is not reversible [154]. This nonreversibility is due on the one hand to the formation of a salt of the hydrogen sulfate type, similar to that resulting from the graphite–sulfuric acid interaction, and on the other hand to the breaking of SWNTs, which leads to the formation of CNT fragments of different sizes, both in the neutral and the charged state, the latter appearing as cation and anion radicals [154]. As a result of this behavior, CNT-fragment-doped PANI is obtained by the electrochemical polymerization of aniline on an SWNT film using an aqueous H_2SO_4 solution.

In the field of CP/CNT composites, a basic post-treatment, is often used to make the difference between a molecular structure which involves a doping or a functionalization process, and a blend or a bilayer structure. In the case of CNT-fragment-doped PANI, NH_4OH post-treatment leads to a partial dedopage of the CP. The FTIR spectra of these composites display a band at ca. 1144 cm^{-1} that grows with increasing cycle number for SWNT film in a solution of aniline and H_2SO_4. It indicates charge transfer between the CP and the CNT fragments. With the use of an acidic medium, such as an HCl solution, the electrochemical polymerization of aniline on SWNT film leads to a covalent functionalization of CNTs with CPs. According to Ref. [26], PANI-leucoemeraldine salt (LS)-functionalized SWNTs and PANI-emeraldine salt (ES)-functionalized SWNTs are obtained. The NH_4OH post-treatment on PANI-(LS or ES)-functionalized SWNTs involves an internal redox reaction between PANI-EB and SWNTs, which transforms the polymer chain from a semioxidized state into a reduced one.

In 2005, composite fibers consisting of a PANI host reinforced by CNTs were reported by V. Mottaghitablab *et al.* [156]. The preparation of highly dispersed CNTs in the PANI solution and the control of the nature of the PANI/CNT interface reaction ensuring both the charge transport and the transfer of mechanical load are developed in Ref. [156]. Size-distribution studies demonstrated that the quality of the dispersion could be improved by the addition of PANI to CNTs in dimethyl propylene urea. In the same year, Guo *et al.* refluxed MWNTs in aniline to obtain a good dispersion followed by electropolymerization of aniline leading to PANI/MWNT composites [157]. This synthesis method allows the monomer to interact with the CNT surface producing an enclosed nanotube wrapped and stabilized by PANI. In 2006, R.Sainz *et al.* reported PANI/MWNT composites prepared by *in situ* chemical polymerization, with a 'compact coil' conformation in DMSO and 'extended coil' conformation in *m*-cresol [158]. T.M. Wu *et al.* proposed that the chemical functionalization of CNTs results from an increase in the interface binding between

MWNTs and PANI [159]. When the functionalized CNTs are dispersed in an organic solvent and water [160,161], an improvement in the dispersion and homogeneity of the MWNTs within the polymer matrix is observed. Consequently, if the as-prepared MWNTs are treated with a 3:1 mixture of concentrated H_2SO_4:HNO_3 [161], one produces carboxylic acid groups at the defect sites (abbreviated as c-MWNTs), which in turn improve the solubility of the c-MWNTs in HCl solution. T.M. Wu *et al.* proposed that conversion of the carboxylic acid groups into acylchloride groups (abbreviated as a-MWNTs) takes place in the presence of $SOCl_2$ [162,163]. In the final stage, MWNTs that contain carboxylic acid and acylchloride groups are used as a core in the formation of tubular shells of PANI-ES/c-MWNT and PANI-ES/a-MWNT composites.

In order to obtain PANI/MWNTs, Ginic-Markovic *et al.* initiated the emulsion polymerization ultrasonically [164]. Other synthesis techniques have been reported by: (i) Ma *et al.* who produced a PANI/SWMT nanocomposite by *in situ* polymerization of 3-aminophenylboronic acid monomers in the presence of DNA-functionalized SWNTs [165]; (ii) Ramamurthy *et al.* who reported the introduction of SWNTs and MWNTs into a PANI matrix using a solution-mixing technique and used a specific gravimetric measurement to illustrate the degree of CNT dispersion [166]; and (iii) E. Zelikman *et al.* who prepared nanocomposites consisting of MWNTs dispersed in PANI doped with DBSA as the matrix [167]. In this case, MWNTs were dispersed in a water/DBSA solution by ultrasonication and then mixed either with PANI, or with aniline followed by polymerization. In light of the rheological data of the MWNT/PANI/DBSA dispersions, it was suggested that CNTs act as PANI interparticle bridges.

Depending on the application type, the main composites result from three synthesis methods, i.e. mixing of the two constituents, and chemical and electrochemical polymerization, and are summarized in Table 5.1.

Table 5.1 *Composites based on PANI and CNTs*

CNTs	Synthesis method	Synthesis medium	Composites
SWNTs	Mixing of PANI and CNTs	Organic solvents such as *N*-methyl pyrroli dinone	PANI doped with large CNT fragments and CNTs covalently functionalized with PANI
SWNTs	Chemical polymerization	Aniline, acide (HCl, H_2SO_4) , $K_2Cr_2O_7$	PANI doped with small CNT fragments, closed-shell C_{60}
SWNTs	Electrochemical polymerization	Aniline + H_2SO_4 Aniline + HCl	PANI doped with small CNT fragments, closed-shell C_{60} PANI covalent functionalized CNTs
MWNTs	Mixing of PANI and CNs	Organic solvents of PANI	PANI doped with MWNTs
MWNTs	Chemical polymerization	Aniline+HCl+$(NH_4)_2S_2O_8$	PANI doped with MWNTs
MWNTs	Electrochemical polymerization	Aniline + HCl	Coaxial wire of PANI and MWNTs

5.3.2 Polypyrrole/Carbon Nanotubes

Since 2002, a variety of methods for producing composites based on PPy and CNTs have been reported [168–170]. The most used have been the chemical and electrochemical polymerization of pyrrole in the presence of CNTs. In the context of the first technique, MWNTs have been incorporated into PPy matrices by the functionalization of nanotubes, consisting of the oxidation of nanotube side walls by the bonding of carboxylic acid groups, dispersion of nanotubes in pyrrole monomer mixtures, and subsequent electropolymerization [171] or enzyme-initiated polymerization [172]. Other methods that should be mentioned are polymerizations initialized *in situ* using radicals [173,174], anionic polymerization following the formation of CNT-polyanions when an alkyl lithium is used [110], and the covalent attachment of functional polymers to carboxylic acid groups of oxidized CNTs [175]. In 2004, using an *in situ* chemical oxidative polymerization method, Long *et al.* synthesized PPy/CNT nanocables [176]. Additional data have been reported by X. Zhang *et al.* for the preparation of size-controlled nanocables by *in situ* chemical oxidative polymerization in the presence of a cetyl trimethyl ammonium bromide (CTAB) cationic surfactant or polyethylene glycol mono-*p*-nonphenyl ether (PGME) as a nonionic surfactant [177]. Thus, when CNTs are dispersed in a solution containing a certain concentration of CTAB or PGME, the surfactant molecules are adsorbed and arranged regularly on the CNT surface. Addition of pyrrole takes place by an adsorption process at the surface of CNTs and/or wedged between the arranged CTAB or PGME molecules. As a result of adding ammonium persulfate, pyrrole is polymerized *in situ* on the surface of the CNTs (core layer) and ultimately forms the outer shell of the nanocables. Addional information concerning the *in situ* chemical polymerization of pyrrole on CNTs using ferric chloride as an oxidant has been reported by N.G. Sahoo *et al.* [178]. By changing the pyrrole/MWNT mass ratio, control of the layer thickness of PPy in a PPy/MWNT composite was demonstrated by Raman and FTIR spectroscopy [178]. In 2007, M.R. Karim *et al.* reported a new route for the synthesis of a PPy/MWNT composite by a gamma-radiation-induced *in situ* chemical polymerization method [179]. In 2009, the interfacial polymerization of pyrrole was applied in the synthesis of composite materials with MWNTs [180]. The polymerization of pyrrole was performed at the interface of two immiscible solvents in the presence of CNTs incorporated in various submicron assembled structures. The main advantage of interfacial polymerization in the synthesis of nanocomposite materials is the very low reaction rate, which enables controlled entrapment of nanostructures, CNTs in this case, metallic nanoparticles, and quantum dots, and, subsequently, their better dispersion in the polymer matrix [180].

Electrochemical polymerization of pyrrole on an SWNT electrode using an aqueous HCl 0.5 M solution as electrolyte, resulted in deposition of a PPy film onto the SWNT layer leading to a composite with a bilayer structure, as demonstrated by Raman spectroscopy [112]. A new method was developed by S. Cosner *et al.* in 2008 [111]; SWNTs were functionalized by electropolymerizable pyrrole groups following covalent and noncovalent strategies. The covalent pyrrole grafting was carried out by ester formation between pyrrole alcohol and chemically oxidized SWNTs. The strong π-interactions between pyrene and SWNTs were exploited for the noncovalent adsorption of a new pyrene-pyrrole derivative on the pristine CNT surface. The pyrrole-ester-SWNTs were solubilized in THF and electropolymerized by controlled potential electrolysis at 0.95 V. The PPy/SWNT

composites thus obtained were shown to be promising candidates for sensor devices due to their highly specific surface [111].

To summarize these data : (i) both chemical and electrochemical polymerization of pyrrole in the presence of nongrafting CNTs results in bilayer-type composites and (ii) the appearance of an active site on the CNT surface plays a significant role in covalent functionalization of CNTs with PPy.

5.3.3 Poly(3,4-ethylenedioxythiophene)/Carbon Nanotubes

New composite PEDOT/CNT materials were prepared by chemical or electrochemical polymerization of 3,4-ethylene dioxythiophene (EDOT) directly on CNTs or from an homogeneous mixture of PEDOT and CNTs in 2004 [181]. Despite of the number of applications envisaged for PEDOT/CNT composites, few articles are devoted to the molecular structures of these materials. Covalent functionalization of SWNTs with PEDOT has been reported in: (i) the electropolymerization of EDOT on a SWNT film, where a benzyl dimethyl hexadecyl ammonium chloride electrolyte was used [182] and (ii) the chemical polymerization of EDOT in the presence SWNTs and $FeCl_3$ [183]. In the case of the chemical polymerization of EDOT in the presence of CNTs, a chemical interaction of SWNTs with $FeCl_3$ involving a doping reaction accompanied by a cointercalation process, was shown by I. Baltog *et al.* [183]. Differences were noted between composites based on CPs of the poly(3,4-ethylenedioxytiophene)/polystyrene sulfonate (PEDOT/PSS) type and CNTs. Simple mixing of pristine SWNTs or DWNTs with PEDOT/PSS resulted in a partial doping process [184,185]. Until 2006, all synthesis routes reported for the PEDOT/CNT composite preparation were based on the direct functionalization of CNTs with CPs. In 2008, a new route was proposed by H.T. Ham *et al.* for the synthesis of PEDOT/PSS/CNT composites [186]. Three types of surface-modified SWNTs were obtained: (i) labeled carboxylated SWNTs, obtained by the reaction of nitric acid and CNTs with carboxylic acid groups attached on the surface; (ii) 1-pyrenebutyric-acid-wrapped SWNTs; and (iii) 1-pyrenebutyric acid lithium-salt-wrapped SWNTs [186]. The surface modifiers influenced the dispersion state of CNTs which in turn were influenced by the surface aggregate concentrations. Thus, in the polymer matrix, there was a lower aggregate concentration for the carboxylated SWNTs than for the other surface-modified SWNTs [186].

At present, it can be concluded from the data reported in literature that: (i) chemical and electrochemical polymerization of EDOT in the presence of CNTs results in covalent functionalization of the tube wall and (ii) the mixing of CNTs with PEDOT-type polymers involves a partial doping process.

5.3.4 Poly(2,2′-bithiophene)/Carbon Nanotubes

The literature devoted to PBTh/CNT composites reveals only four published articles. Three of them deal with the electrochemical properties [187,188] and the use of this composite material in the fabrication of photovoltaic devices with a high open-circuit voltage [189]. The last article, dated 2009, is devoted to the molecular structure of the composite resulting from the electrochemical polymerization of 2,2′-bithiophene on

SWNTs in the presence of $TBABF_4$ [190]. It is shown that: (i) the electrochemical polymerization of BTh on SWNT films leads to the formation of two reaction products, doped PBTh-functionalized SWNTs and undoped PBTh-functionalized SWNTs; and (ii) the functionalization process of SWNTs with PBTh involves the formation of new covalent C–S bonds between the two constituents, which induce steric hindrance effects in macromolecular chains [190].

5.3.5 Poly(*N*-vinylcarbazole)/Carbon Nanotubes

Recently, increased attention has been devoted to poly(*N*-vinylcarbazole)/carbon nanotube (PVK/CNT) composites [115,191–198], due to a number of interesting physical and chemical properties, such as optical limiting performance [192,198], a good photoconductivity [115,198], potential use as an active material in rechargeable batteries and supercapacitors [194,195], the fabrication of light-emitting devices based on PVK/SWNT composites [196], and the use of MWNTs as a mechanical reinforcement agent in PVK [198]. For PVK/CNT composites, three synthesis methods have been reported so far: (i) direct mixing of the polymer with CNTs in chloroform; (ii) chemical polymerization of the monomer in the presence of CNTs and butyl lithium; and (iii) electropolymerization of *N*-vinylcarbazole (VK) on a CNT film via cyclic voltammetry in $LiClO_4$/acetonitrile solution [115,191–197].

The first method leads to the wrapping of the CNTs with PVK [191], in other words to noncovalent functionalization. By chemical and electrochemical polymerization of VK in the presence of CNTs, the covalent functionalization of nanotubes with PVK in the undoped [33] and the doped state [194,195], respectively, is produced. Two ways have been reported for the chemical polymerization of VK in the presence of CNTs: the bulk method [33] and synthesis via direct free-radical reaction [199].

The bulk polymerization reaction of VK at 70 °C in the presence of SWNTs leads to the covalent functionalization of CNTs with PVK in an undoped state [33]. The mechanism proposed for the bulk polymerization of VK in the presence of SWNTs involves in two steps: an addition reaction between SWNTs and VK followed by the polymerization reaction. Thus, one obtains a PVK/SWNT composite in which the polymer is in an undoped state. A year later [200], homogeneous wrapping of the outer surface of CNTs by a PVK chain was observed in the case of PVK/MWNT composites. For PVK/SWNT composites, a dense and robust network of very long and highly entangled CNTs has been shown. This originates in the different degree of surface reactivity between SWNTs and MWNTs. It is well known how difficult it is to obtain good dispersion of SWNTs in the polymer matrix, due to their high tendency to agglomerate into thick ropes or bundles and their inherent insolubility in most solvents. When a mixture of VK and SWNTs is heated above the melting point of VK, the melted VK monomers are first inserted into the SWNT bundles and the polymerization starts from the SWNT surface. The separation of some tubes from the bundles and the formation of network structures occurs during the precipitation of PVK onto the SWNT bundles in methanol solution. In the case of PVK/SWNT composites, some PVK is grafted onto the SWNT surface. This may be due to the very high degree of activation of the SWNT surface, which promotes VK polymerization, and is actually related to the huge surface area of individual SWNTs.

In comparison with bulk polymerization, for the free radical reaction of VK in the presence CNTs, PVK was reacted directly with MWNTs at 70 °C in DCB with azo-bis-izobutyronitrile (AIBN) as the radical initiator [199]. After purification, deep-grey products, which can be dissolved in common solvents such as chloroform and 1,2-dichlorobenzene (DCB), were obtained. It was confirmed that PVK was grafted onto the surface of CNTs by FTIR and Raman spectroscopy, CPS, TGA, TEM, and UV-VIS spectra [199].

The electrochemical polymerization of PVK in $LiClO_4$/acetonitrile solution on an SWNT electrode was studied by cyclic voltammetry [194,195]. The mechanism of the electropolymerization reaction of VK on the SWNT film was characterized by three stages, chemical–electrochemical–chemical [194]. The main difference between the mechanism of electropolymerization of VK on a Pt electrode only, and an electrode covered with a SWNT film consists in the fact that during the first stage, the formation of a charge-transfer complex results in the formation of VK radical cations and the SWNT radical anions.

From these results, it can be seen that the direct mixing of PVK with CNTs results in PVK noncovalently functionalized CNTs, while chemical and electrochemical polymerization lead to covalent functionalization of CNTs with PVK in the undoped and doped states, respectively.

5.3.6 Polyfluorenes/Carbon Nanotubes

In the last two years, special attention has been given to polyfluorene/carbon nanotube (PF/CNT) composites from both the point of view of basic research and of applications. Until now the main applications of PF/CNT composites have been focused on nonvolatile plastic memory devices and field-effect transistors [200,201]. Two synthesis routes have been used at the present time: mixing two constituents [202] and chemical polymerization [203]. In the first case, i.e. CNT powders, using poly-9,9-di-*n*-octyl-fluorenyl-2,7-diyl (PFO) as an extracting agent in toluene, selective extraction of semiconducting SWNTs, without detectable traces of metallic SWNTs and impurities was reported [202]. G. Xu *et al.* reported functionalization of MWNTs with 7-bromo-9,9-dioctylfluorene-2-carbaldehyde by using 1,3-dipolar cycloaddition of azomethine to introduce bromo functional groups on the surface of MWNTs [203]. These bromo functional groups could be modified by Suzuki polycondensation to afford PF-functionalized MWNTs with a cable-like structure [203]. The covalent functionalization of MWNTs with PF is promising for new applications in the photovoltaic field.

5.3.7 Poly(*p*-phenylene) Vinylene/Carbon Nanotubes

As mentioned before, the incorporation of carbon nanotubes in conjugated polymers can lead to improved properties of such composites, one of them being great enhancement of the transport characteristics, which is of primary importance in organic light-emitting diodes (OLEDs) for example. Due to their solubility, which allows easy preparation, composites based on PPV (poly(phenylene vinylene)) derivatives have been extensively studied. Detailed investigation of PmPV (poly(*m*-phenylene

vinylene-co-2,5-dioctyloxy-*p*-phenylene vinylene)) has been performed by different spectroscopic techniques, showing that the interaction between the two constituents leads to a significant reduction in the electron delocalization, as well as less freedom of movement for the polymer. This is a consequence of a structured wrapping of the polymer onto the nanotube lattice, and a signature of strong noncovalent binding [204,205]. Another method of preparation of composites based on SWNTs and PPV was reported by S. Lefrant's group [206,207]. The materials were prepared by mixing SWNTs at different weight concentrations in the soluble sulfonium polyelectrolyte precursor of PPV, with sonication. The solutions were then deposited onto quartz substrates and heated under vacuum at 300 °C to convert the precursor into PPV. The objective of these studies was primarily to investigate the influence of the presence of SWNTs in the precursor polymer on the optical properties of PPV. It was demonstrated in particular that SWNTs interact with the precursor, leading to the incomplete removal of the sulfonium salt. This was shown by a decrease in absorbance of the main π–π^* band of PPV, accompanied by a blue shift of this band. In addition, photoluminescence spectra were strongly modified, in both intensity and shape, with the appearance of new bands in the blue range. This was interpreted as the formation of short conjugated segments that dominate long segments in composite materials [206,207].

Finally, we note that for composites based on PPV-type polymers and CNTs, a noncovalent functionalization of the tube surface with CPs is systematically reported. Unlike other composites, the PPV/CNT hybrid material can be obtained only in the thin-film form.

5.3.8 Polyacetylene/Carbon Nanotubes

A new composite based on CNTs and polyacetylene (PA) using Ziegler–Natta polymerization of acetylene inside CNTs was reported in 2007 by J. Steinmetz *et al.* [208]. This approach consists in filling nanotubes with a large variety of different organic compounds using supercritical CO_2. Supercritical CO_2 exhibits a very low viscosity and surface tension, enabling it to enter easily into opened CNTs. Thus, CNTs filled with toluene let the Ziegler–Natta catalyst diffuse into the nanotubes, allowing removal of the catalyst outside, and exposure to acetylene gas. Only one study has been devoted to the synthesis of PA/CNT composites following this procedure. Briefly, the CNTs were filled with toluene using supercritical CO_2; the CNT powder and 10 ml of toluene were placed in a 30 ml high pressure vessel equipped with a pressure gauge, a thermometer, and a magnetic stirrer. The vessel was heated to 42–44 °C and then filled with CO_2 at 105 bar. The CNTs were stirred under these conditions for 1 h. Then the vessel was cooled down to below the critical temperature of CO_2 and the pressure was released slowly. Since the Ziegler–Natta catalyst is sensitive to air and water, the following steps were carried out under Argon using Schlenk techniques. The toluene-filled nanotubes were stirred overnight with the Ziegler–Natta catalyst, and a solution of triethyl aluminum and tetrabuthyl titanate in toluene. The solution was then filtered using a PTFE membrane with 1 μm pore size and washed several times with dry toluene in order to remove the catalyst outside the CNTs. The CNTs were again transferred into a Schlenk flask which was then filled with 0.5 bar of acetylene gas and left to react overnight. The approach of using supercritical fluids to transport organic molecules inside CNTs seems to be very promising. The inherent insolubility and infusibility of PA coupled with its sensitivity to air imposes a barrier to the processability of the polymer.

5.4 Vibrational Properties of Composites Based on Conducting Polymers and Carbon Nanotubes

Concerning the vibrational properties of the CPs/CNT composites, there exists a large range of results. Therefore we will review here only some particular cases regarding the vibrational properties of composites based on SWNTs and polymers such as polypyrrole, polyaniline, poly(3,4-ethylene dioxytiophene), poly(*N*-vinyl carbazole), and poly(*p*-phenylene vinylene). The choice of these particular cases has been made to prove the ability of IR spectroscopy and Raman light scattering as valuable tools to investigate the four types of composites currently obtained from the interactions between CPs and CNTs, i.e., bilayers, CNTs covalently functionalized with CPs, CNTs noncovalently functionalized with CPs, and CPs doped with CNTs.

5.4.1 Conducting Polymer/Carbon Nanotube Bilayer Structures

Generally, for blends or bilayer structures formed from CPs and CNTs, when there is no interaction between constituents, the Raman spectrum of composites is a weight-modulated sum of CNT and polymer spectra. This is shown in Figure 5.4, where one observes in curves 2–6 the appearance and a gradual increase in intensity of the Raman lines of PPy in the doped state, when electrochemical polymerization of pyrrole on a SWNT film immersed in HCl 0.5 M solution has taken place [112]. The main Raman lines of doped PPy are observed at 937, 1107, 1301, 1371, 1477, and 1589 cm^{-1}. They are attributed to the following vibrational modes: ring deformation, the symmetrical C_β-H in-plane associated with the dication, the $C_{\beta'}$-H bending, the anti-symmetrical N-C_α stretching, the skeletal band, and the $C_\alpha = C_\beta$ stretching + $C_\alpha = C_\beta$ in-ring + C_α-;$C_{\alpha'}$ inter-ring stretching, respectively [209–211]. As mentioned above, in CNT chemistry, post-treatment with NH_4OH solution is often used as a defunctionalization procedure. The proof that the electrochemical polymerization of pyrrole on SWNTs corresponds to a successive deposition of polymer layers on nanotubes film is obtained by post-treatment with NH_4OH, when the Raman spectrum (curve 7, Figure 5.4) again reveals bands of PPy in its undoped state. The main peaks of undoped PPy are recorded at 923, 1040, 1215, 1310, 1403, 1496, and 1608 cm^{-1}, being attributed to the following vibrations modes: ring deformation, symmetrical C_β-H in-plane, C_α-$C_{\alpha'}$ stretching + C_β-H bending, C_β-$C_{\beta'}$ in ring + C_α-$C_{\alpha'}$ inter-ring stretching, C_α=N-$C_{\alpha'}$ stretching, skeletal band, and C_α= $C_{\beta'}$ stretching [209–211].

In conclusion, one can see that the Raman features of composites of blends or bilayers correspond to a modulated sum of the Raman spectra of the two constituents.

5.4.2 Covalently Functionalized Carbon Nanotubes with Conducting Polymers

Covalently functionalization of SWNTs with CPs is a reliable method to produce soluble materials containing such nanoparticles. The following three composites: (i) PANI/CNTs; (ii) PEDOT/CNTs; and (iii) PVK/CNTs, are discussed in this section. In the first two cases the covalent functionalization involves covalent bonding of macromolecular chains both

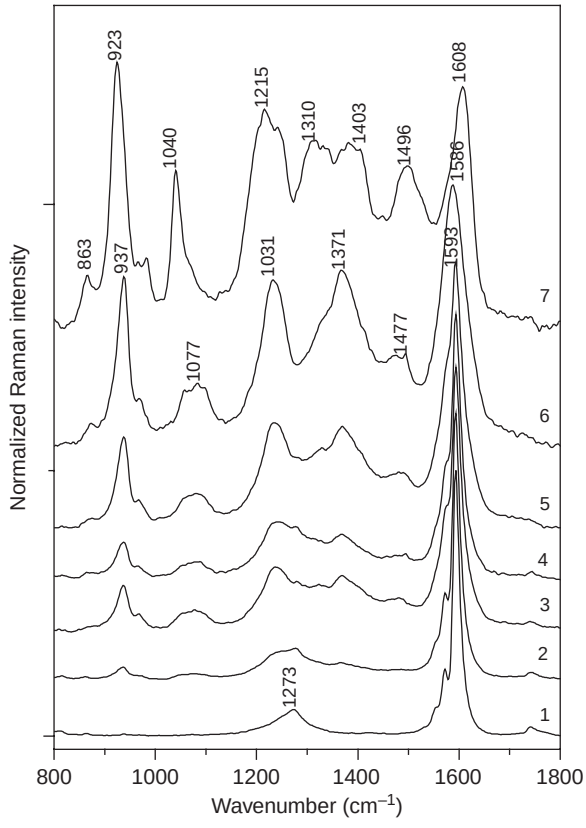

Figure 5.4 *Raman spectra ($\lambda_{exc} = 1064$ nm) of PPY/SWNT composites obtained by electropolymerization of pyrrole on a SWNT film in HCl 0.5 M. Curve 1 corresponds to the SWNT film Raman spectrum. Curves 2–6 show the evolution of the Raman spectrum after 6, 12, 25, 50, and 100 cycles, respectively, carried out in the potential range (+100; +800) mV vs. SCE with a sweep rate of 100 mV s^{-1}. Curve 7 corresponds to the composites described by curve 6 after interaction with NH_4OH 1 M solution. (Reprinted with permission from Diamond and Related Materials, Electrochemical and vibrational properties of single-walled carbon nanotubes in hydrochloric acid solutions by S. Lefrant, M. Baibarac, I. Baltog et al., 14, 3–7, 873–880. Copyright (2005) Elsevier Ltd)*

chemically and electrochemically, which results in an additional roping of CNTs [25,26]. In the third case covalent attachment of two or more macromolecular chains to the CNTs takes place and a 'flagellene'-type molecular structure, which favors the breaking of the CNT bundle into individual tubes, is obtained [33,56].

As was mentioned above, in 2007, it was shown that SWNT covalently functionalized with a polymer may be obtained by a bulk polymerization [33]. The reaction mechanisms that occur in the polymerization processes can be understood by Raman light scattering and FTIR spectroscopic studies, which prove the functionalization of CNTs both with monomers (e.g. *N*-vinyl carbazole (VK)) and polymer molecules (e.g. PVK) [33].

Figures 5.5–5.7 present SERS spectra of PVK/SWNT composites, prepared by bulk polymerization of VK in the presence of CNTs and VK/SWNT blends obtained by mechanico-chemical interactions. The main Raman lines of PVK, at ca. 297, 434–529, 722, 1022, 1129, 1235, 1320, 1452, 1491, 1578, and 1626 cm^{-1}, are attributed to the

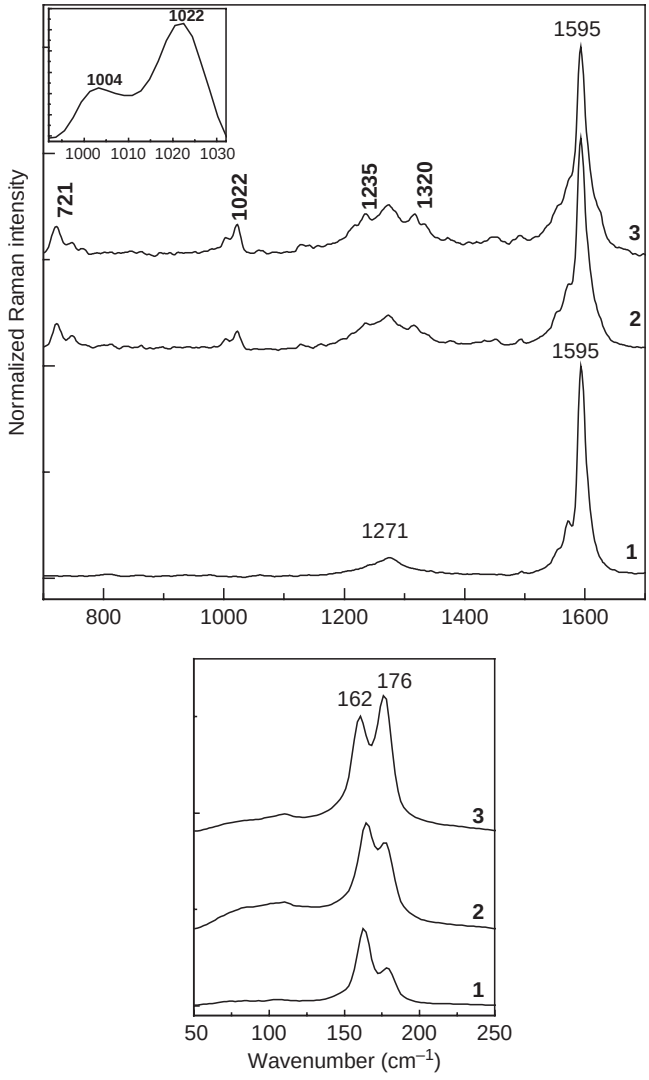

Figure 5.5 *SERS spectra at $\lambda_{exc} = 1064$ nm of a SWNT film of about 100 nm thickness deposited on a rough Au support (curve 1) and composites obtained by the bulk polymerization of VK (0.5 g) in the presence of different amounts of SWNTs: 0.01 g (curve 2) and 0.1 g (curve 3). (Reprinted with permission from Polymer, Spectroscopic evidence for the bulk polymerization of N-vinyl carbozole in the presence of single-walled carbon nanotubes by M. Baibarac, I. Baltog, S. Lefrant and P. Gomez-Romero, 48, 18, 5279. Copyright (2007) Elsevier Ltd)*

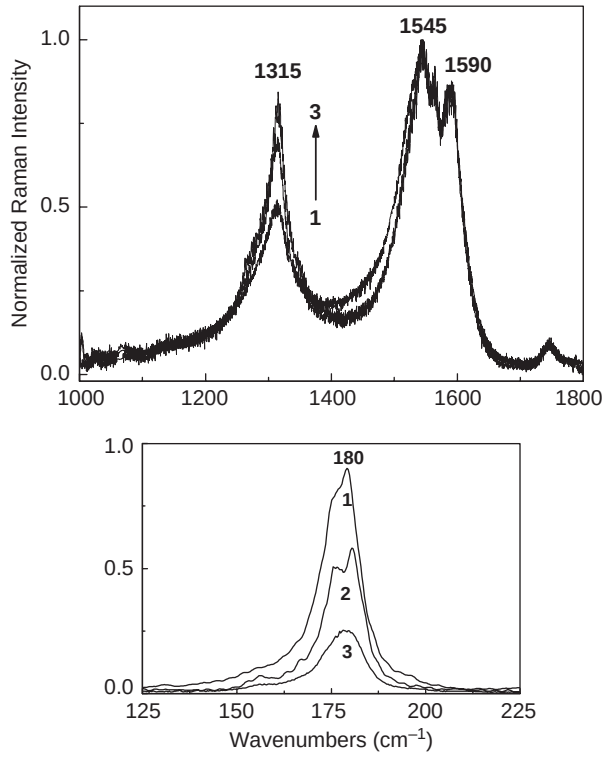

Figure 5.6 *SERS spectra at $\lambda_{exc} = 676$ nm of SWNT films of about 100 nm thickness deposited on a rough Au support (curve 1) and composites obtained by the bulk polymerization of VK (0.5 g) in the presence of different amounts of SWNTs: 0.01 g (curve 2) and 0.1 g (curve 3). (Reprinted with permission from Polymer, Spectroscopic evidence for the bulk polymerization of N-vinyl carbozole in the presence of single-walled carbon nanotubes by M. Baibarac, I. Baltog, S. Lefrant and P. Gomez-Romero, 48, 18, 5279. Copyright (2007) Elsevier Ltd)*

following vibration modes: C—C deformation in polyvinyl, benzene ring deformation, rocking-wagging of methylene in polyvinyl, rocking-twisting of methylene in polyvinyl, wagging of methylene in polyvinyl, C—H deformation of the benzene ring, C-H in the hetero-five-membered ring, stretching of the hetero-five-membered ring, C=C stretching in the benzene ring and C—C stretching in the benzene ring, respectively [212]. The main changes in the Raman spectra observed in Figures 5.5 and 5.6 consist in: (i) a strong decrease in intensity of the Raman bands situated in the 125–225 cm^{-1} spectral range, accompanied by an increase of the D band intensity without modification in the G band profile when the excitation wavelength is 676 nm (Figure 5.6); (ii) at the excitation wavelength of 1064 nm, besides the increase in the D band, one observes also a change in the intensity ratio of the Raman lines situated at 162 and 176 cm^{-1}, the latter becoming more intense (Figure 5.5). These facts indicate a decrease in the relative content of isolated tubes as a result of their interaction with the polymer. In this case, the appearance of new Raman peaks at ca. 721, 1022, 1235, and 1320 cm^{-1} seen on spectra 2 and 3 of

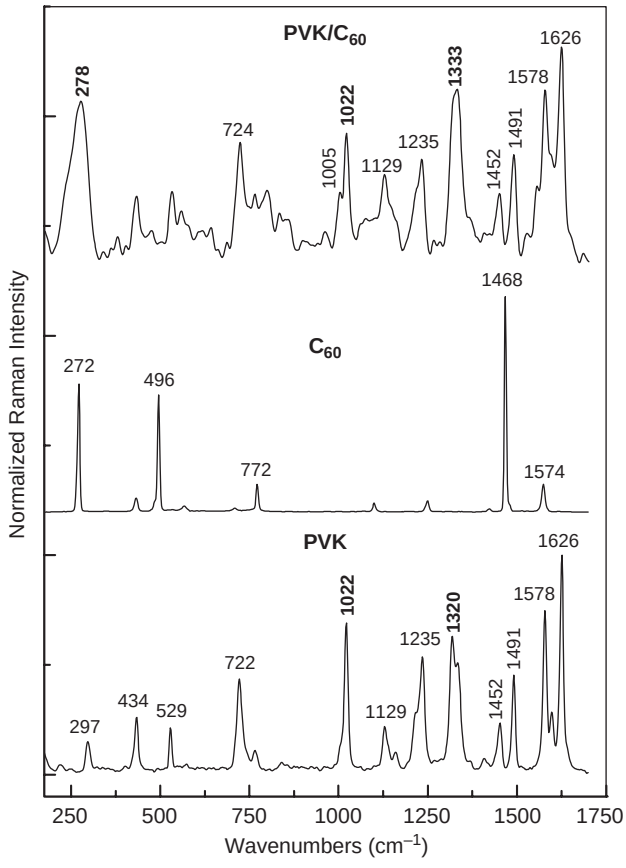

Figure 5.7 *SERS spectrum at $\lambda_{exc} = 1064$ nm of PVK, C_{60} and PVK/C_{60} films of about 150 nm thickness deposited on the rough Au support. (Reprinted with permission from Polymer, Spectroscopic evidence for the bulk polymerization of N-vinyl carbozole in the presence of single-walled carbon nanotubes by M. Baibarac, I. Baltog, S. Lefrant and P. Gomez-Romero, 48, 18, 5279. Copyright (2007) Elsevier Ltd)*

Figure 5.5, belonging to PVK, are also observed in Figure 5.7. For composites prepared by the bulk polymerization of VK in the presence of SWNTs, one observes in the 1000–1030 cm^{-1} spectral range, the appearance of a new band with a maximum at ~1004 cm^{-1}, almost equal in intensity to the Raman line at 1022 cm^{-1} (Figure 5.5, curves 2 and 3). The Raman line at 1022 cm^{-1} is present in the SERS spectrum of PVK/C_{60} composites (Figure 5.7) and has been interpreted by M. Baibarac *et al.* [33] as a signature of the chemical interaction between methylene groups and different carbon nanoparticles such as SWNTs and C_{60}.

A better understanding of the chemical interaction between compounds based on VK units and carbon nanoparticles and the structural modifications induced on CNTs during the mechanico-chemical reaction of VK with SWNTs has been obtained [31]. These results are summarized in Figure 5.8. According to an early paper, the main Raman lines of VK

are situated at: 220, 431, 569, 743, 1015, 1107, 1291, 1314, 1455, 1576, 1629, and 1640 cm^{-1} [213], the line at 1640 cm^{-1} is attributed to the vinyl group [214]. The transition from the monomer (VK) to the polymer (PVK) is characterized by: (i) a down-shift of the Raman line from 743 to 722 cm^{-1}; (ii) an up-shift of the Raman lines from 1107 and 1314 cm^{-1} to 1129–1138 and 1320 cm^{-1}, respectively; and (iii) the disappearance of the Raman line peaked at 1640 cm^{-1}. In the case of VK alone mixed with SWNTs and compressed nonhydrostatically for 5 min at 0.58 GPa, the SERS spectrum in Figure 5.8

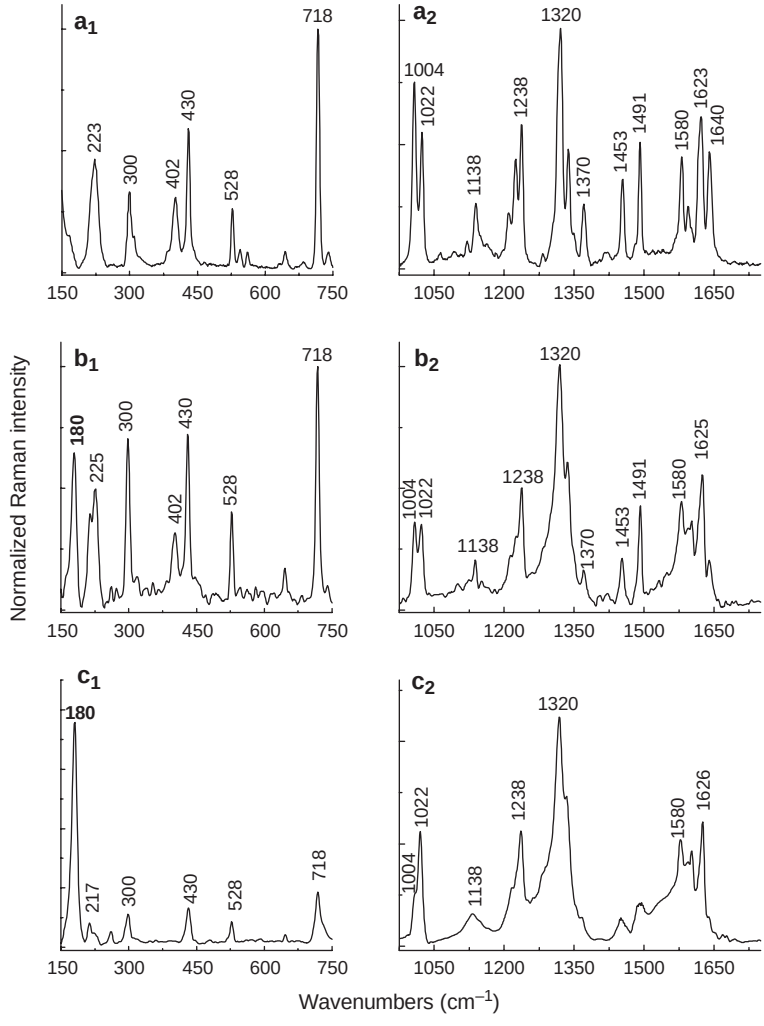

Figure 5.8 *SERS spectra at $\lambda_{exc} = 1064$ nm of VK after its compression at 0.58 GPa alone (a_1, a_2) and in the presence SWNTs with 1 wt% (b_1, b_2) and 10 wt% (c_1, c_2). (Reprinted with permission from Polymer, Spectroscopic evidence for the bulk polymerization of N-vinyl carbozole in the presence of single-walled carbon nanotubes by M. Baibarac, I. Baltog, S. Lefrant and P. Gomez-Romero, 48, 18, 5279. Copyright (2007) Elsevier Ltd)*

reveals the following features: (i) an intense Raman band at 718 cm^{-1} associated to the rocking-wagging vibrational mode of methylene in polyvinyl; (ii) a well-developed Raman band at 1320 cm^{-1} attributed to the C—H deformation of the benzene ring; (iii) a new Raman line appearing at 1370 cm^{-1}; and (iv) a complex Raman band having two components at about 1004 and 1022 cm^{-1}. The Raman line at 1004 cm^{-1} is associated with the ring-breathing vibration mode of cyclobutane [214].

Taking into account the above changes, as well as the FTIR spectra (Figure 5.9) of samples prepared by the bulk polymerization of VK in the presence of CNTs [33], covalent functionalization of SWNTs with undoped PVK via the vinyl group is expected to be taking place. A short comment concerning Figure 5.9 is necessary. The main FTIR bands of PVK, at 718, 742, 1122–1156, 1220, 1324, 1404, 1452, 1597, and 1624 cm^{-1} are attributed to the following vibrations: ring deformation of substituted aromatic structure, CH_2 rocking vibration due to tail-to-tail addition, C—H in-plane deformation of the aromatic ring, C—N stretching of VK, C—H in-plane deformation of vinylidene group, CH_2 deformation of vinylidene group, ring vibration of VK moiety, C—C + C=C stretching in benzene (B) ring and C—C stretching (B), respectively [141,215,216]. The covalent functionalization of SWNTs with undoped PVK via the vinyl group is supported by a careful analysis of the variations observed on Figure 5.9. This indicates that the main perturbations induced in the chemical structure of PVK by adding SWNTs during the bulk synthesis are in the following vibrations: CH_2 rocking in to tail-to-tail addition, CH_2 deformation of the vinylidene group, C—H in-plane deformation of the vinylidene group, ring vibration of VK moiety and C—C stretching (B). All these permit the conclusion that a covalent attachment of PVK in the undoped state to SWNTs takes place via the vinyl group as, shown in Scheme 5.1, a fact that explains the steric hindrance effects reviewed above.

Similarly, perturbations such as those described above have also been reported in the case of PANI covalently functionalized SWNT samples prepared by electrochemical polymerization of aniline on a CNT film deposited on a Pt electrode. The covalent functionalization of SWNTs with PANI was explained, on the basis of the Raman and FTIR spectra shown in Figures 5.10 and 5.11, respectively, as taking place in two successive steps [26]. The first corresponds to the electrochemical polymerization of aniline on a SWNT film from which one obtains a composite of PANI-leucoemeraldine salt (LS)-functionalized

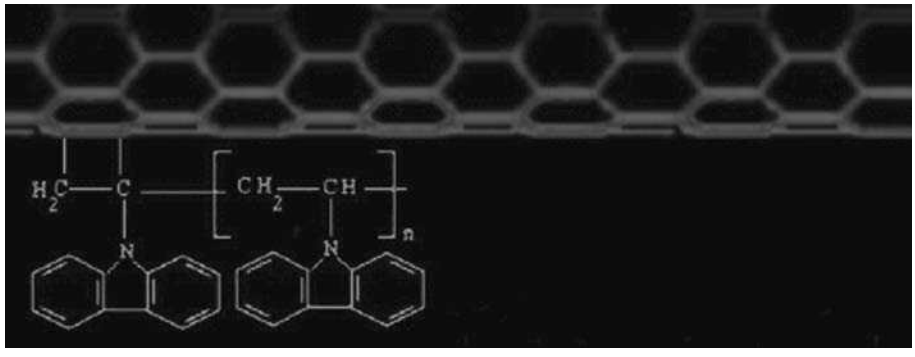

Scheme 5.1

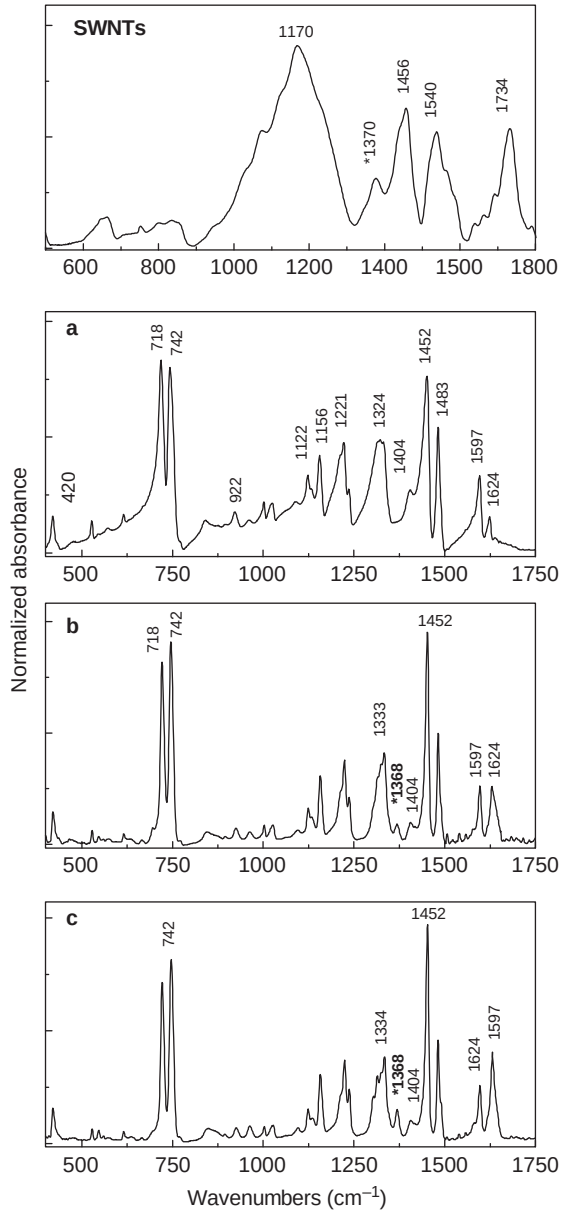

Figure 5.9 *FTIR spectra of SWNTs, undoped PVK (a) and the undoped PVK/SWNT composite obtained by bulk polymerization of VK (0.5 g) in the presence of different CNT weights: 0.01 g (b) and 0.1 g (a). (Reprinted with permission from Polymer, Spectroscopic evidence for the bulk polymerization of N-vinyl carbozole in the presence of single-walled carbon nanotubes by M. Baibarac, I. Baltog, S. Lefrant and P. Gomez-Romero, 48, 18, 5279. Copyright (2007) Elsevier Ltd)*

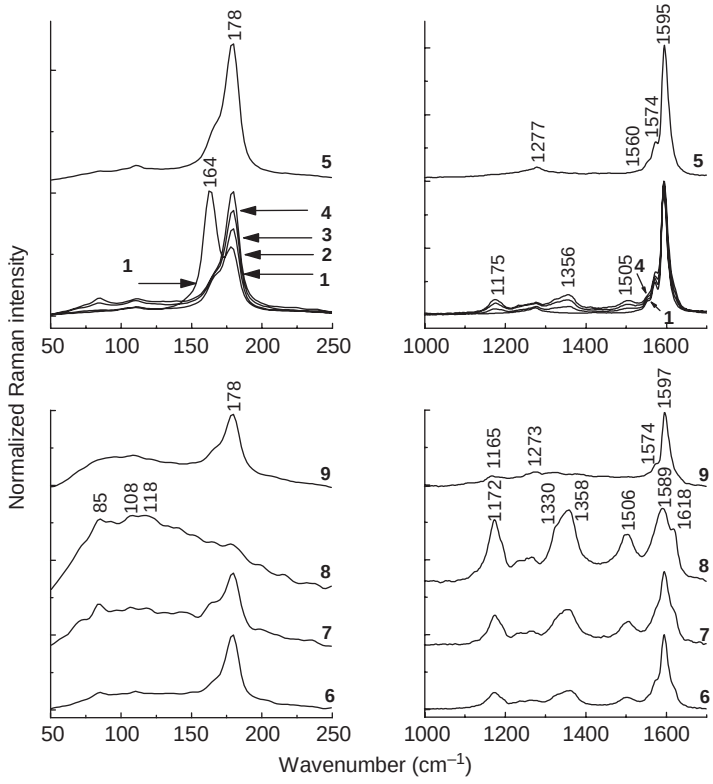

Figure 5.10 *Raman spectra ($\lambda_{exc} = 1064$ nm) of PANI/SWNT composites obtained by electrochemical polymerization of aniline on a SWNT film in HCl 0.5 M. Curve 1 corresponds to the SWNT film Raman spectrum. Curves 2–4 and 6–8 show the evolution of the Raman spectrum after 25, 50, 75, 100, 150, and 300 cycles, respectively, carried out in the potential range (–200; +700) mV vs. SCE with a sweep rate of 100 mV s^{-1}. The dedoping of the PANI-salt-functionalized SWNT films (curves 4 and 8), as a result of the chemical reaction with NH_4OH 1M solution, is illustrated in curves 5 and 9. (Reprinted with permission from Carbon, Covalent functionalization of single-walled carbon nanotubes by aniline electrochemical polymerization by M. Baibarac, I. Baltog, S. Lefrant et al., 42, 15, 3143–3152. Copyright (2004) Elsevier Ltd)*

SWNTs and PANI-emeraldine salt (ES)-functionalized SWNTs. The second step is a consequence of NH_4OH post-treatment of PANI-(LS or ES)-functionalized SWNTs. It is associated with an internal redox reaction between PANI-emeraldine base (EB) and SWNTs, which transforms the polymer chain from a semioxidized state into a reduced one. The increase in the intensity of the Raman band at 178 cm^{-1} (Figure 5.10), associated with the RBM of SWNT bundles, during the electrochemical polymerization of aniline on a CNT film immersed into an HCl solution, indicates an additional roping of nanotubes with PANI as a binding agent. The binding of SWNTs as whole units on the polymer chain induces strong steric hindrance effects observed in the FTIR spectra in Figure 5.11 by the enhancement of bands at ca. 740, 750 and 772 cm^{-1}.

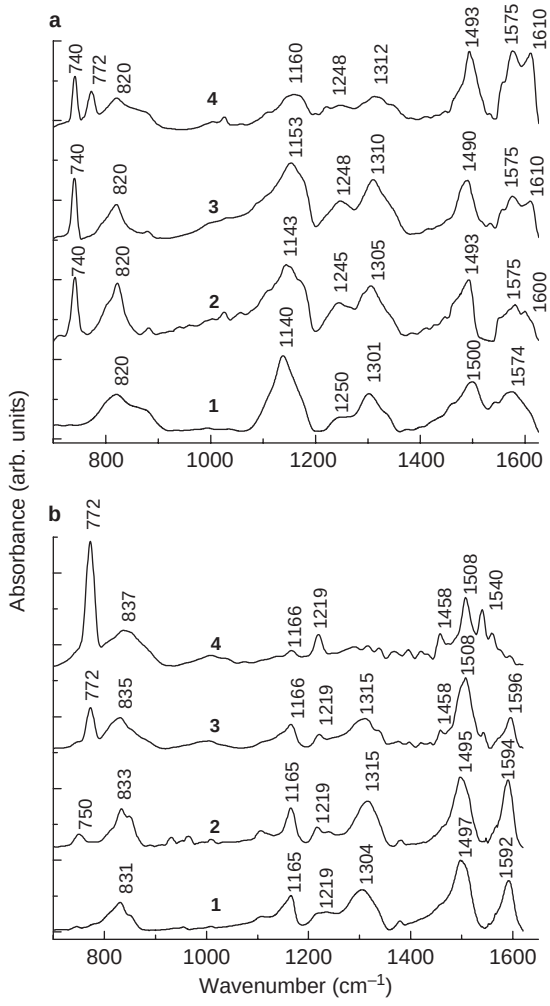

Figure 5.11 *FTIR spectra of PANI-ES (curve 1, a) and PANI-salt functionalized SWNT composites (curves 2–4, a). These composites were electrochemically prepared by the achievement of 75, 150, and 300 cycles (curves 4, 3, and 2, respectively) with the SWNT film immersed in the solution of aniline and HCl 0.5 M, in the potential range (–200; +700) mV vs. SCE with a sweep rate of 100 mV s^{-1}. FTIR spectra of PANI-EB (curve 1, b) and PANI-base-functionalized SWNT composites (curves 2–4, b) obtained by a subsequent reaction of PANI-salt-functionalized SWNTs (curve 2 4, a) with NH_4OH 1M solution. (Reprinted with permission from Carbon, Covalent functionalization of single-walled carbon nanotubes by aniline electrochemical polymerization by M. Baibarac, I. Baltog, S. Lefrant et al., 42, 15, 3143–3152. Copyright (2004) Elsevier Ltd)*

In the CP/CNT composite field, special attention has been given to the functionalization of the side wall of SWNTs with CPs having repeating units such as thiophene rings [112]. An example is SWNTs electrochemically functionalized with PEDOT. For covalent functionalization, a significant change is observed in the structure of the G band, which

consists of four Raman lines found at ca. 1555, 1573, 1595, and 1610 cm^{-1} [217]. Cyclic voltammetry was used for the electropolymerization of 3,4-ethylenedioxythiophene (EDOT) on a SWNT film immersed in aqueous benzyl dimethyl hexadecylammonium chloride solution (BDHAC). It was observed that the increase of the number of cycles from 100 to 300 (curves 3-6, Figure 5.12) leads to: (i) a progressive increase in the relative intensity of the Raman line found at 1570 cm^{-1} and after 300 cycles (curve 6, Figure 5.12), the intensity ratio of Raman lines from 1573 and 1595 cm^{-1} approaching unity; (ii) the up-shift of the D band from 1275 to 1300 cm^{-1}; and (iii) the appearance and increase in intensity of the main Raman lines of PEDOT. Other convincing proofs for the functionalization of the side wall of CNTs with PEDOT are given by transmission electron

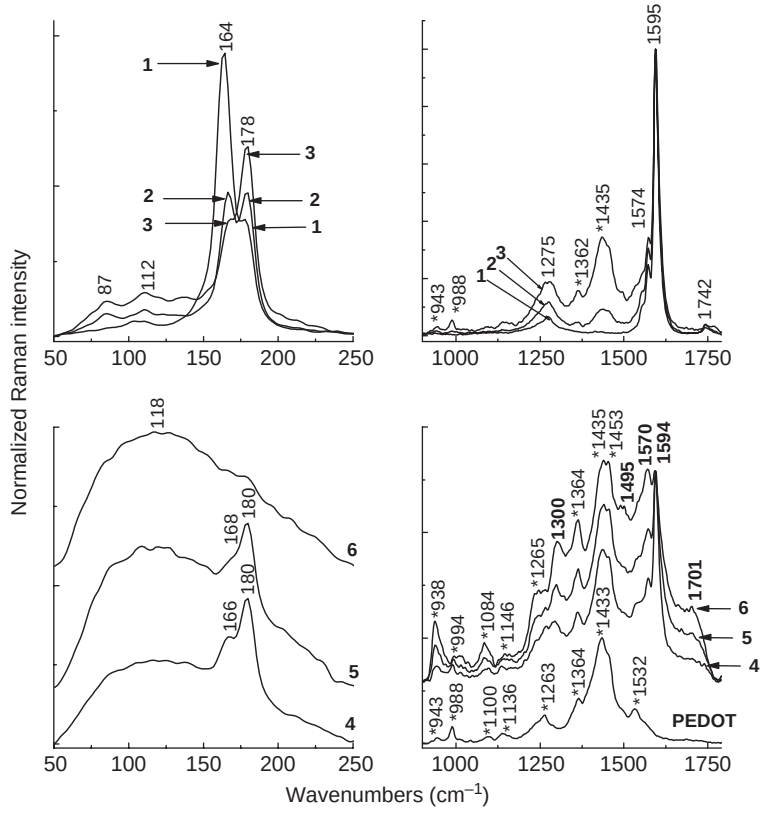

Figure 5.12 *Raman spectra at $\lambda_{exc} = 1064$ nm of PEDOT/SWNT composites obtained by electrochemical polymerization of EDOT on a SWNT film in BDHAC solution. Curve 1 corresponds to the SWNT film Raman spectrum. Curves 2–6 show the evolution of the Raman spectrum after 50, 100, 150, 200, and 300 cycles, respectively, carried out in the potential range (–800; +800) mV vs. SCE with a sweep rate of 100 mV s^{-1}. Raman spectra of the PEDOT film deposited on Au support in the same conditions after 200 cycles. (Reprinted with permission from Diamond and Related Materials, Functionalization of single-walled carbon nanotubes with conducting polymers evidenced by Raman and FTIR spectroscopy by S. Lefrant, M. Baibarac, I. Baltog et al., 14, 3–7, 867. Copyright (2005) Elsevier Ltd)*

microscopy (TEM) studies [115] and Raman measurements carried out at the 676 nm excitation wavelength [183]. In Ref. [178], it has also been demonstrated that an additional enhancement of the Raman signal of PEDOT occurs, as a result of a resonant excitation of plasmons in metallic nanotubes. In 2009, a detailed Raman study concerning the excitation of plasmons in metallic SWNTs was evidenced by an abnormal anti-Stokes Raman scattering of poly (2,2′-bithiophene) [190]. In this last case, significant steric hindrance effects were reported using ATR-IR spectroscopy, as a result of the bonding of thiophene ring onto the CNT surface, with new C-S covalent bonds being formed.

A final remark regarding the vibrational spectra of CNTs covalently functionalized with CPs, is that depending on the type of covalent bond formed between the two constituents (CP and CNT), e.g. C-C, and C-N or C-S, composites with flagellene- and bracelet-type molecular structures, respectively, are obtained. All composites involving covalent functionalization of CNTs with CPs are characterized by steric hindrance effects.

5.4.3 Conducting Polymers Doped with Carbon Nanotubes

In this section, the ability of IR spectroscopy and Raman scattering to detect CPs doped with CNT composites is shown in the particular case of PANI doped with SWNTs. Until now, PANI doped with CNTs has been produced as a result of either the chemical polymerization of aniline in the presence of SWNTs, $K_2Cr_2O_7$, and an acidic solution (e.g. HCl, H_2SO_4, etc.) [25] or the electrochemical polymerization of aniline on an SWNT film deposited on a Pt electrode immersed in an H_2SO_4 solution [26]. An explanation for the formation of PANI doped with CNTs originates in the breaking of SWNTs into small fragments, neutral or radical anions and radical cations. In fact, a significant role in the formation of the PANI doped CNT composite is played by radical anion and radical cation SWNT fragments. The attachment of these two SWNT fragment types explains the differences observed in the SERS spectra of composites prepared by the two methods, as well as the similarity between FTIR spectra of PANI/SWNT and PANI/C_{60} composites prepared chemically. In this context, SERS spectra of the composites M_1, M_2, and M_3 presented in Figure 5.13 (see caption for labels) appear to be a sum of PANI-EB and SWNT Raman spectra, each one with its specific characteristics. The relative decrease in the second-order of the D band observed in Figure 5.13 indicates a less perfect structure for the nanotubes embedded in or bound to the polymer. The formation of a new composite material was noticed in the Raman spectrum by a decrease in the RBM bands and a G band that remains as strong as before, regardless of the weight ratio of the two components in the composite. The G band, associated with tangential vibrational modes, reveals, in this case, the sum of contributions coming from SWNTs, nanotube fragments, and polymer/CNT (whole units and fragments) composites. The differences between SERS spectra of PANI deposited on Au and Ag substrates originates in the different reducing properties of the metal substrates [218]. A significant change in shape and Raman line positions is noted in the SERS spectra of composites of the S type in Figure 5.14. These are quite similar to SERS spectra of fullerene-doped PANI compounds [219]. Both groups of spectra recorded on Ag and Au substrates exhibit two bands at 1330 and 1370 cm^{-1} that grow with the SWNT content. As was noticed in early papers, this is the Raman signature of the PANI salt [218]. Great similarities are observed in Figure 5.15 between FTIR spectra of PANI/

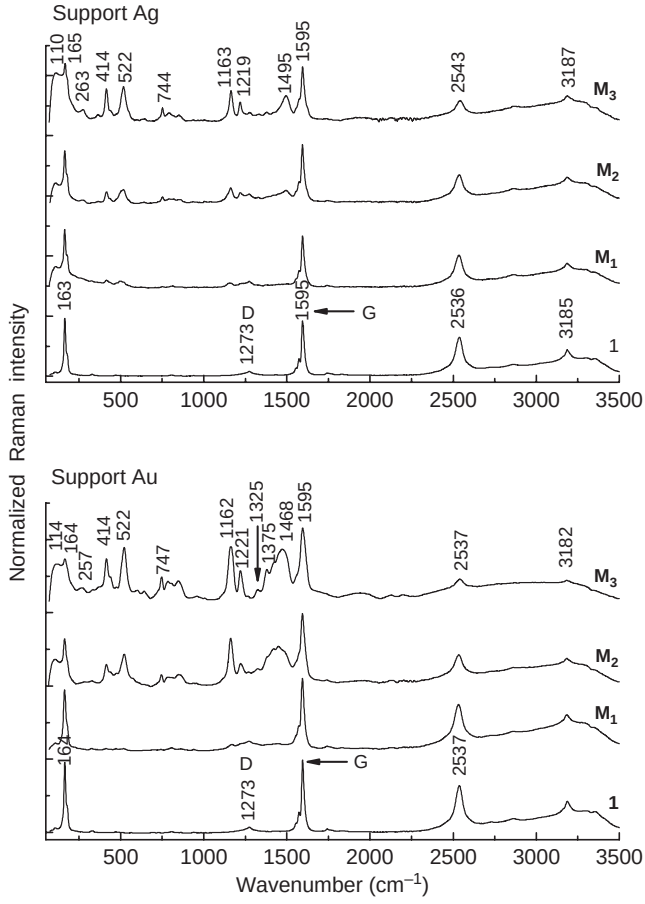

Figure 5.13 *SERS spectra, at $\lambda_{exc} = 1064$ nm, of PANI-EB/SWNT composites obtained by mixing of PANI-EB and CNTs. M_3, M_2, and M_1 spectra correspond to compounds with PANI-EB/SWNT mass ratios of 3.33, 1, and 0.33, respectively. Spectrum 1 is of SWNTs. (Reprinted with permission from Chemistry of Materials, Polyaniline and Carbon Nanotubes Based Composites Containing Whole Units and Fragments of Nanotubes by M. Baibarac, S. Lefrant, I. Baltog et al., 15, 21, 4149. Copyright (2003) American Chemical Society)*

SWNTs (curves S_1–S_3) and PANI/C_{60} composites (F_1–F_3), and those of the polyaniline-emeraldine salt (PANI-ES). This result indicates that composites of the types S and F correspond to PANI doped with CNTs and PANI doped with C_{60}, respectively; in other words, to a PANI salt. As a general remark concerning Figure 5.15, we note that all composites exhibit in their FTIR spectra an absorption band at 1144 cm^{-1}, increasing with the carbon nanoparticle content, which suggests a charge transfer between the two constituents. In addition, the FTIR spectra of compounds obtained by adding SWNTs to the polymer solution display an intense absorption band with two components at 773 and 755 cm^{-1}, which are associated with the deformation vibration of the benzene and the quinoid ring, respectively [220]. This indicates a strong hindrance effect produced by the

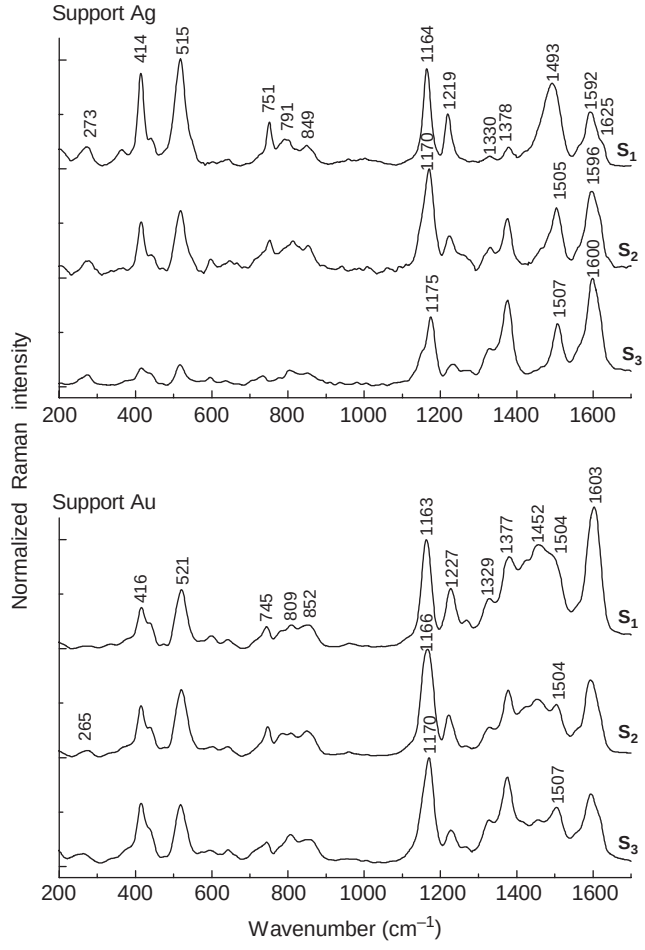

Figure 5.14 *SERS spectra, at $\lambda_{exc} = 1064$ nm, of PANI-EB/SWNT composites obtained by chemical synthesis. S_1, S_2, and S_3 spectra correspond to compounds with PANI-EB/SWNT mass ratios of 56.5, 9.2, and 4.4, respectively. (Reprinted with permission from Chemistry of Materials, Polyaniline and Carbon Nanotubes Based Composites Containing Whole Units and Fragments of Nanotubes by M. Baibarac, S. Lefrant, I. Baltog et al., 15, 21, 4149. Copyright (2003) American Chemical Society)*

binding of voluminous carbon particles as nanotubes and large fragments of nanotubes to the polymer chain. Such composites based on PANI doped with CNT fragments have been reported to be obtained by the electrochemical polymerization of aniline on a SWNT film using an aqueous H_2SO_4 solution [26]. The NH_4OH post-treatment of PANI doped with CNTs fragments, leads to a partial dedoping of the CP. The FTIR spectra of these composites display at ca. 1144 cm^{-1} a band that increases in intensity with the cycle number carried out on the SWNT film in a solution of aniline and H_2SO_4. It indicates a charge transfer between the CP and CNT fragments [26].

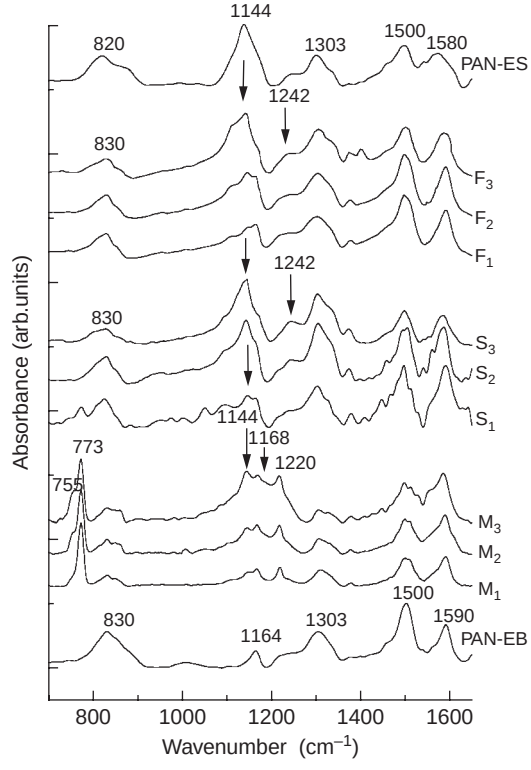

Figure 5.15 *FTIR spectra of PANI-LB, PANI-ES, and PANI-EB/SWNT composites obtained by mixing of compounds (spectra M_1, M_2, and M_3, respectively) and chemical synthesis (spectra S_1, S_2, and S_3, respectively). Spectra F_1, F_2, and F_3 correspond to the fullerene-doped PANI composite prepared similarly to composites of the S series. (Reprinted with permission from Chemistry of Materials, Polyaniline and Carbon Nanotubes Based Composites Containing Whole Units and Fragments of Nanotubes by M. Baibarac, S. Lefrant, I. Baltog et al., 15, 21, 4149. Copyright (2003) American Chemical Society)*

From the results presented above, to diagnose the type of interaction, a good knowledge of the properties of each component of the composite is needed. In the case of the CP doped with CNT composite, CNTs have the role of a doping agent, which removes or adds electrons to or from the polymer backbone, resulting in n or p doping, respectively. In the case of PANI doped with CNTs, a p doping process was reviewed above.

5.4.4 Noncovalent Functionalization of Carbon Nanotubes with Conducting Polymers

At the present time in Raman spectroscopy studies, noncovalent functionalization of CNTs with CPs has been seen to induce only variations in the RBM range. An example is the case of SWNTs noncovalently functionalized with PPV. Thus, in Figure 5.16, Raman spectra

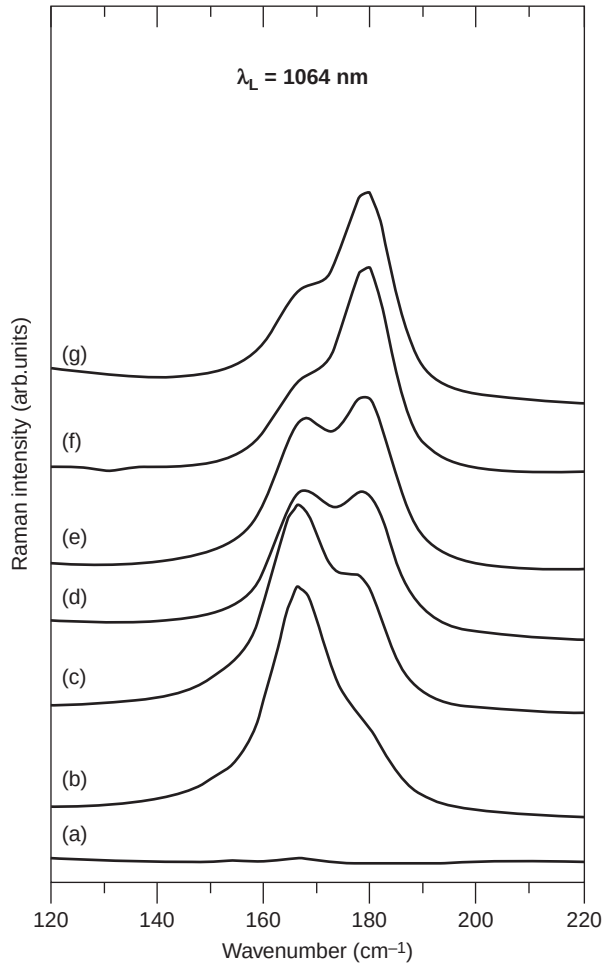

Figure 5.16 *Raman scattering spectra of the composite films at room temperature taken with* $\lambda_L = 1064$ *nm in the frequency region 120–220* cm^{-1}. *(a)* $x = 0$, *(b)* $x = 1\%$, *(c)* $x = 2\%$, *(d)* $x = 8\%$, *(e)* $x = 16\%$, *(f)* $x = 32\%$, *and (g)* $x = 64\%$. *(Reprinted with permission from Phys Rev B., Photoconductivity and optical properties in composites of poly(paraphenylene vinylene) and single-walled carbon nanotubes by E. Mulazzo, R. Perego, H. Aarab et al., 70, 15, 155206. Copyright (2004) American Physical Society)*

recorded in the low-frequency range where RBM of nanotubes are observed reveal specific features at $\lambda_{exc} = 1064$ nm [207]. Two components are present at 160 and 180 cm^{-1}, assigned to tubes in isolated and in bundled forms, respectively [113]. The evolution of these bands confirms the aggregation of SWNTs by an increase in their concentration. The whole spectra of PPV/SWNT composites recorded at $\lambda_{exc} = 676.4$ nm (Figure 5.17) show also that, even at high concentration of SWNTs (64%) the asymmetric G^- band is still present [207]. This is proof that SWNTs have been neither covalently bonded to nor doped with the PPV polymer.

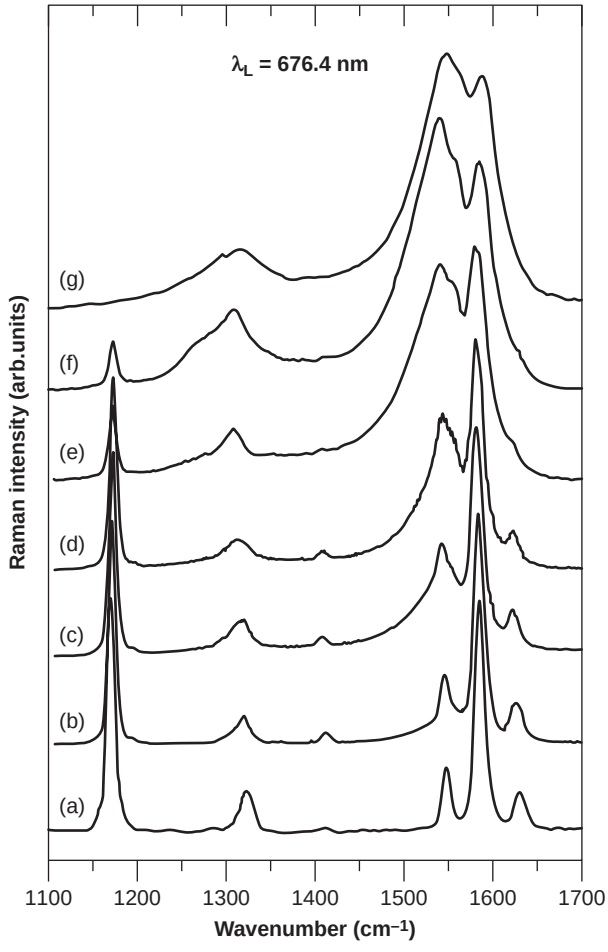

Figure 5.17 *Raman scattering spectra of the composite films at room temperature for* $\lambda_L = 676.4$ *nm in the frequency region 1100–1700* cm^{-1}. *(a)* $x = 0$, *(b)* $x = 1\%$, *(c)* $x = 2\%$, *(d)* $x = 8\%$, *(e)* $x = 32\%$, *(f)* $x = 64\%$, *and (g) SWNT powder. (Reprinted with permission from Phys Rev B., Photoconductivity and optical properties in composites of poly(paraphenylene vinylene) and single-walled carbon nanotubes by E. Mulazzo, R. Perego, H. Aarab et al., 70, 15, 155206. Copyright (2004) American Physical Society)*

5.5 Conclusions

Rapid progress in the polymer/carbon nanotube composite research field has demonstrated a large potential for the discovery of new materials and phenomena, as well as the development of new technologies. The transition from fundamental to applied research involves a good knowledge of the physico-chemical properties of the studied materials, and their vibrational characteristics provide primary information. Therefore, in this chapter, we have reviewed recent progress in the CP/CNT composites field from the point of view

of both synthesis and the ability of Raman light scattering and IR spectroscopy to distinguish between different types of composites: CP/CNT bilayer structures, CNTs covalently functionalized with CPs, CNTs noncovalently functionalized with CPs, and CPs doped with CNTs. In the last few years, new applications have been reported for CP/CNT composites [183]. However, using Raman spectroscopy in the anti-Stokes branch, new opportunities for CP/CNT composites have emerged in the nonlinear optics field. Such an example has been recently published [190]. Therefore, an extension of Raman spectroscopy studies in the anti-Stokes branch is expected in the cases of both conducting polymers, and composites based on polymers and carbon nanoparticles, in view of new applications.

Acknowledgments

This work was performed in the framework of the Scientific Cooperation between the Institute of Materials, Jean Rouxel, Nantes and the Laboratory of Optics and Spectroscopy of the National Institute of Materials Physics, Bucharest. A part of this work was supported by the Romanian research projects IDEI 39, IDEI 41, PN II 62081 and PN II72182.

References

[1] P.M. Ajayan, O. Stephan, C. Colliex, and D. Trauth, Aligned carbon nanotube arrays formed by cutting a polymer resin–nanotube composite, *Science*, **265**, 1212–1214 (1994).
[2] P. J. F. Harris, Carbon nanotube composites, *Int. Mater. Rev.*, **49**, 31–43 (2004).
[3] D. Tasis, N. Tagmatarchis, A. Bianco, and M. Prato, Chemistry of carbon nanotubes, *Chem. Rev.*, **106**, 1105–1136 (2006).
[4] F. Hussain, M. Hojjati, M. Okamoto, and R. E. Gorga, Polymer-matrix nanocomposites, processing, manufacturing, and application: an overview, *J. Composite Mater.*, **40**, 1511–1575 (2006).
[5] M. Baibarac and P. Gomez-Romero, Nanocomposites based on conducting polymers and carbon nanotubes: from fancy materials to functional applications *J. Nanosci. Nanotech.*, **6**, 289–302 (2006).
[6] J. Dai, Advanced syntheses and microfabrications of conjugated polymers, C_{60}-containing polymers and carbon nanotubes for optoelectronic applications, *Polym. Adv. Technol.*, **10**, 357–420 (1999).
[7] G. Z. Chen, M.S.P. Shaffer, D. Coleby, G. Dioxan, W. Zhou, D. J. Fray, and A. H. Windle, Carbon nanotube and polypyrrole composites: coating and doping, *Adv. Mater.*, **12**, 522–526 (2000).
[8] Y. Saito, S. Uemura, and K. Hamaguchi, Cathode ray tube lighting elements with carbon nanotube field emitter, *Jpn. J. Appl. Phys.*, **37**, L 346–348 (1998).
[9] S. A. Curran, P. M. Ajayan, W. J. Blau, D. L. Carroll, J. N. Coleman, A. B. Dalton, A. P. Davey, B. McCarthy, S. Maier, and A. Strevens, A Composite from poly(*m*-phenylenevinylene-*co*-2,5-dioctoxy-*p*-phenylenevinylene) and carbon nanotubes: a novel material for molecular optoelectronics, *Adv. Mater.*, **10**, 1091–1093 (1998).
[10] H. Ago, K. Petritch, M. S. P. Shaffer, A. H. Windle, and R. H. Friend, Composites of carbon nanotubes and conjugated polymers for photovoltaic devices, *Adv. Mater.*, **11**, 1281–1285 (1999).
[11] D. Naumann, Chapter 9, FT-Infrared and FT-Raman spectroscopy in biomedical research in *Infrared and Raman Spectroscopy of Biological Materials* ed. H. Ulrich and G.B. Yan, Practical Spectroscopy Series, Vol. **24**, Taylor & Francis Group, London, 337–350, 2000.
[12] E. Smith and G. Dent, *Modern Raman Spectroscopy*, John Wiley & Sons Inc., New York, 2005.

[13] A. Otto, *Surface enhanced raman scattering* in *Light Scattering in Solids* IV, ed. R.K. Chang and T.E. Furtak, Topics in Applied Physics, Vol. **54**, Spinger, Berlin, 1984.
[14] M. Moskovits, Surface-enhanced spectroscopy, *Rev. Mod. Phys.*, **57**, 783–826 (1985).
[15] H. Raether, *Surface Plasmons on Smooth and Rough Surface and Gratings*, Springer Tracts in Modern Physics, Springer, Berlin, 1988.
[16] M. A. Ordal, L. Long, R. J. Bell, R. W. Alexander, and C. L. Ward, Optical properties of the metals Al, Co, Cu, Au, Fe, Pb, Ni, Pd, Pt, Ag, Ti, and W in the infrared and far infrared *Appl. Opt.*, **22**, 1099–1119 (1983).
[17] S. Lefrant, I. Baltog, and M. Baibarac, Surface-enhanced Raman scattering studies on chemically transformed carbon nanotube thin films, *J. Raman Spectrosc*, **36**, 676–698 (2005).
[18] K. Kneipp, M. Moskovits, and H. Kneipp (Eds.) *Surface-Enhanced Raman Scattering Physics and Applications*, Topics in Applied Physics, Vol. **103**, Springer, Berlin, 2006.
[19] J. J. Laserna (Ed.), *Modern Techniques in Raman Spectroscopy*, John Wiley & Sons Ltd., Chichester, 1996.
[20] N. J. Everall, J. M. Chalmers, and P. R. Griffiths (Eds.), *Vibrational Spectroscopy of Polymers: Principles and Practice*, John Wiley & Sons Ltd., Chichester, 2007.
[21] H. S. Nalwa (Ed.), *Conductive Polymers: Spectroscopy and Physical Properties*, Handbook of Organic Conductive Molecules and Polymers, Vol. **3**, John Wiley & Sons Ltd, Chichester, 1997.
[22] Z. B. Zhang and S. L. Zhang, Photon-Induced Selective Interaction between Small-Diameter Metallic Carbon Nanotubes and Triton X-100, *J. Am. Chem. Soc*, **129**, 666–671 (2007).
[23] M. S. Arnold, A. A. Green, J. F. Hulvat, S. I. Stupp, and M. C. Hersam, Sorting carbon nanotubes by electronic structure using density differentiation, *Nature Nanotechnology*, **1**, 60–65 (2006).
[24] R. Krupke, F. Hennrich, H. V. Lohneysen, and M. M. Kappes, Separation of metallic from semiconducting single-walled carbon nanotubes, *Science*, **301**, 344–347 (2003).
[25] M. Baibarac, I. Baltog, S. Lefrant, J.Y. Mevellec, and O. Chauvet, Polyaniline and carbon nanotubes based composites containing whole units and fragments of nanotubes, *Chem. Mater.*, **15**, 4149–4156 (2003).
[26] M. Baibarac, I. Baltog, C. Godon, S. Lefrant, and O. Chauvet, Covalent functionalization of single-walled carbon nanotubes by aniline electrochemical polymerization *Carbon*, **42**, 3143–3152 (2004).
[27] H. Zengin, W. Zhou, J. Jin, R. Czerw, D. W. Smith, L. Echegoyen, D. L. Carroll, S. H. Foulger, and J. Ballato, Carbon nanotube doped polyaniline, *Adv. Mater.*, **14**, 1480–1483 (2002).
[28] J. E. Huang, X. H. Li, J. C. Xu, and H. L. Li, Well-dispersed single-walled carbon nanotube/polyaniline composite films, *Carbon*, **41**, 2731–2736 (2003).
[29] W. Feng, X. D. Bai, Y. Q. Lian, J. Liang, X. G. Wang, and K. Yoshino, Well-aligned polyaniline/carbon-nanotube composite films grown by in-situ aniline polymerization *Carbon*, **41**, 1551–1557 (2003).
[30] Y. K. Zhou, B. L. He, W. J. Zhou, J. Huang, X. H. Li, B. Wu, and H. L. Li, Electrochemical capacitance of well-coated single-walled carbon nanotube with polyaniline composites *Electrochim. Acta*, **49**, 257–262 (2004).
[31] V. Bavastrello, S. Carrara, M. K. Ram, and C. Nicolini, Optical and electrochemical properties of poly(*o*-toluidine) multiwalled carbon nanotubes composite Langmuir–Schaefer films, *Langmuir*, **20**, 969–973 (2004).
[32] X.H. Li, B. Wu, J.E. Huang, J. Zhang, Z.F. Liu, and H.L. Li, Fabrication and characterization of well-dispersed single-walled carbon nanotube/polyaniline composites, *Carbon*, **41**, 1670–1673 (2003).
[33] M. Baibarac, I. Baltog, S. Lefrant, and P. Gomez-Romero, Spectroscopic evidence for the bulk polymerization of N-vinyl carbazole in the presence of single-walled carbon nanotubes, *Polymer*, **48**, 5279–5288 (2007).
[34] S. Iijima, Helical microtubules of graphitic carbon, *Nature*, **354**, 56–58 (1991).
[35] A. Merkoci, M. Pumera, X. Llopis, B. Perez, M. Del Valle, and S. Alegret, New materials for electrochemical sensing VI: Carbon nanotubes, *Trends Anal. Chem.*, **24**, 826–838 (2005).

[36] A. Jorio, G. Dresselhaus, and M. Dresselhaus (Eds.), *Carbon Nanotubes*, *Advanced Topics in the Synthesis, Structure, Properties and Applications*, Topics in Applied Physics, Vol. **111**, Springer, Berlin, 2008.
[37] A. Thess, R. Lee, P. Nikolaev, H. Dai, P. Petit, J. Robert, C. Xu, Y.H. Lee, S.G. Kim, A.G. Rinzler, D.T. Colbert, G.E. Scuseria, D. Tomanek, J.E. Fischer, and R.E Smaley, Crystalline ropes of metallic carbon nanotubes, *Science* **273**, 483–487 (1996).
[38] C. Journet, W.K. Maser, P. Bernier, A. Loiseau, M. Lamy de la Chapelle, S. Lefrant, R. Lee, and J.E. Fischer, Large-scale production of single-walled carbon nanotubes by the electric-arc technique, *Nature*, **388**, 756–758 (1997).
[39] T.W. Ebbesen and P. M. Ajayan, Large-scale synthesis of carbon nanotubes, *Nature*, **358**, 220–222 (1992).
[40] Y. Ando and S. Iijima, Preparation of carbon nanotubes by arc-discharge evaporation, *Jpn. J. Appl. Phys.*, **32**, 107–109 (1993).
[41] S. Iijima and T. Ichihashi, Single-shell carbon nanotubes of 1-nm diameter, *Nature*, **363**, 603–605 (1993).
[42] D.S. Bethune, C.H. Kiang, M.S. De Vries, G. Gorman, R. Savoy, J. Vazquez, and R. Beyers, Cobalt-catalysed growth of carbon nanotubes with single-atomic-layer walls, *Nature*, **363**, 605–607 (1993).
[43] J. Guo, S. Goasguen, M. Lundstrom, and S. Datta, Metal–insulator–semiconductor electrostatics of carbon nanotubes, *Appl. Phys. Lett*. **81**, 1486–1489 (2002).
[44] D.T. Colbert, J. Zhang, S.M. McClure, P. Nikolaev, Z. Chen, J.H. Hafner, D.W. Owens, P.G. Kotula, C.B. Carter, J.H. Weaver, A.G. Rinzler, and R.E. Smalley, Growth and sintering of fullerene nanotubes, *Science*, **266**, 1218–1222 (1994).
[45] X. Zhao, M. Ohkohchi, M. Wang, S. Iijima, T. Ichihashi, and Y. Ando, Preparation of high-grade carbon nanotubes by hydrogen arc discharge, *Carbon*, **35**, 775–781 (1997).
[46] X. Zhao, M. Ohkohchi, M. Wang, S. Iijima, T. Ichihashi, and Y. Anod, Preparation of high-grade carbon nanotubes by hydrogen arc discharge, *Carbon*, **35**, 775–781, (1997).
[47] T. Guo, P. Nikolaev, A. Thess, D. T. Colbert, and R. E. Smalley, Catalytic growth of single-walled manotubes by laser vaporization, *Chem. Phs. Lett.*, **243**, 49–54 (1995).
[48] R. Sen, Y. Ohtsuka, T. Ishigaki, D. Kasuya, S. Suzuki, H. Kataura, and Y. Achiba, Time period for the growth of single-wall carbon nanotubes in the laser ablation process: evidence from gas dynamic studies and time resolved imaging *Chem. Phys. Lett*. **332**, 467–473 (2000).
[49] W.Z. Li, S.S. Xie, L.X. Qian, B.H. Chang, B.S. Zhou, and W.Y. Zhou, Large-scale synthesis of aligned carbon nanotubes, *Science*, **274**, 1701–1703 (1996).
[50] G. Che, B.B. Lakshmi, C.R. Martin, and E.R. Fisher, Chemical vapor deposition based synthesis of carbon nanotubes and nanofibers using a template method, *Chem. Mater.*, **10**, 260–267 (1998).
[51] S. Xie, W. Li, Z. Pan, B. Chang, and L. Sun, Carbon nanotube arrays, *Mater. Sci. Eng. A* **286**, 11–15 (2000).
[52] V. Ivanov, J. B. Nagy, P. Lambin, A. Lucas, X. B. Zhang, X. F. Zhang, D. Bernaerts, G. VanTendeloo, S. Amelincks, and J. Van Landuyt, The study of carbon nanotubules produced by catalytic method, *Chem. Phys. Lett*. **223**, 329–335 (1994).
[53] S. Fan, W. Liang, H. Dang, N. Franklin, T. Tombler, and M. Chapline, Carbon nanotube arrays on silicon substrates and their possible application, *Phys. E: Low Dimensional Syst. Nanostructures* **8**, 179–183 (2000).
[54] R. Wang, H. Xu, L. Guo, and J. Liang, Growth of single-walled carbon nanotubes on porous silicon, *Appl. Surf. Sci.*, **252**, 7347–7351 (2006).
[55] Z.K. Tang, L. Zhnag, N. Wang, X.X. Zhang, G.H. Wen, and G.D. Li, Superconductivity in 4 Angstrom single-walled carbon nanotubes, *Science*, **292**, 2462–2465 (2001).
[56] K. Edgar and J.L. Spencer, Aerosol-based synthesis of carbon nanotubes, *Curr. Appl. Phys.*, **4**, 121–124 (2004).
[57] L. A. Montoro, R. C. Z. Lofrano, and J. M. Rosolen, Synthesis of single-walled and multi-walled carbon nanotubes by arc-water method, *Carbon*, **43**, 200–203, (2005).
[58] J. Qiu, Y. Li, Y. Wang, and W. Li. Production of carbon nanotubes from coal, *Fuel Proc. Technol.*, **85**, 1663–1670 (2004).

[59] M. Shao, D. Wang, G. Yu, B. Hu, W. Yu, and Y. Qian, The synthesis of carbon nanotubes at low temperature via carbon suboxide disproportionation, *Carbon*, **42**, 183–185 (2004).
[60] Y. L. Li, I. A. Kinloch, M. S. P. Shaffer, J. Geng, B. Johnson, and A. H. Windle, Synthesis of single-walled carbon nanotubes by a fluidized-bed method, *Chem. Phys. Lett.*, **384**, 98–102 (2004).
[61] M.W. Li, Z. Hu, X.Z. Wang, Q. Wu, Y. Chen, and Y.L. Tian, Low-temperature synthesis of carbon nanotubes using corona discharge plasma at atmospheric pressure, *Diamond Rel. Mater.*, **113**, 111–115 (2004).
[62] C.N. R. Rao, A. Govindaraj, G. Gundiah, and S.R.C. Vivekchand, Nanotubes and nanowires, *Chem. Eng. Sci.*, **59**, 4665–4671 (2004).
[63] S.N. Bondi, W.J. Lackey, R.W. Johnson, X. Wang, and Z.L. Wang, Laser assisted chemical vapor deposition synthesis of carbon nanotubes and their characterization, *Carbon*, **44**, 1393–1403 (2006).
[64] C. Duty, D. Jena, and W.J. Lackey, Laser chemical vapour deposition: materials, modelling, and process control, *Int. Mater. Rev.*, **46**, 271–287 (2001).
[65] K. Kwok and W.S. Chiu, Growth of carbon nanotubes by open-air laser-induced chemical vapor deposition, *Carbon*, **43**, 437–446 (2005).
[66] A.C. Dillon, A.H. Mahan, P.A. Parilla, J.L. Alleman, M.J. Heben, K.M. Jones, and K.E.H. Gilbert, Continuous hot wire chemical vapor deposition of high-density carbon multi-wall nanotubes, *Nano Lett.*, **3**, 1425–1429 (2003).
[67] Y.H. Mo, A.K.M.F. Kibria, and K.S. Nahm, The growth mechanism of carbon nanotubes from thermal cracking of acetylene over nickel catalyst supported on alumina, *Synth. Met.*, **122**, 443–447 (2001).
[68] M. Chen, C.M. Chen, and C.F. Chen, Preparation of high yield multi-walled carbon nanotubes by microwave plasma chemical vapor deposition at low temperature, *J. Mat. Sci.*, **37**, 3561–3567 (2002).
[69] H. Hou, A.K. Schaper, Z. Jun, F. Weller, and A. Greiner, Large-scale synthesis of aligned carbon nanotubes using $FeCl_3$ as floating catalyst precursor, *Chem. Mater.*, **15**, 580–585 (2003).
[70] H.N. Zhu, C.L. Xu, D.H. Wu, B.Q. Wei, R. Vajtai, and P.M. Ajayan, Direct synthesis of long single-walled carbon nanotube strands, *Science*, **296**, 884–886 (2002).
[71] Y. Tian, Z. Hu, Y. Yang, X. Wang, X. Chen, H. Xu, Q. Wu, W. Ji, and Y. Chen, *In situ* TA-MS study of the six-membered-ring-based growth of carbon nanotubes with benzene precursor, *J. Am. Chem. Soc.*, **126**, 1180–1183 (2004).
[72] J.M. Bonard, P. Chauvin, and C. Klinke, Monodisperse multiwall carbon nanotubes, *Nano Lett.*, **2**, 665–667 (2002).
[73] C.L. Cheung, A. Kurtz, H. Park, and C.M. Lieber, Diameter-controlled synthesis of carbon nanotubes, *J. Phys. Chem. B*, **106**, 2429–2433 (2002).
[74] C.H. Kiang, J. S. Choi, T.T. Tran, and A.D. Bacher, Molecular nanowires of 1 nm diameter from capillary filling of single-walled carbon nanotubes, *J. Phys. Chem. B*, **103**, 7449–7451 (2000).
[75] Z.W. Pan, S.S. Xie, B.H. Chang, C.Y. Wang, L. Lu, W. Liu, W.Y. Zhou, W.Z. Li, and L.X. Qian, Very long carbon nanotubes, *Nature*, **394**, 631–632 (1998).
[76] I.A. Kinloch, M.S.P. Shaffer, Y.M. Lam, and A.H. Windles, High-throughput screening for carbon nanotube production, *Carbon*, **42**, 101–110 (2004).
[77] B.C. Liu, S.C. Lyu, S.I. Jung, H.K. Kang, C.-W. Yang, J.W. Park, C.Y. Park, and C.J. Lee, Single-walled carbon nanotubes produced by catalytic chemical vapor deposition of acetylene over Fe–Mo/MgO catalyst, *Chem. Phys. Lett.*, **383**, 104–108 (2004).
[78] L. Dai, Functionalized carbon nanotubes: properties and applications, *Acc. Chem. Res.* **35**, 1035–1044 (2002).
[79] K. Kempa, B. Kimball, J. Rybczynski, Z. P. Huang, P. F. Wu, D. Steeves, M. Sennett, M. Giersig, D.V.G.L.N. Rao, D.L. Carnahan, D.Z. Wang, J.Y. Lao, W.Z. Li, and Z.F. Ren, Photonic crystals based on periodic arrays of aligned carbon nanotubes, *Nano Lett.*, **3**, 13–18 (2003).
[80] Y. Tu, Y. Lin, and Z.F. Ren, Nanoelectrode arrays based on low site density aligned carbon nanotubes, *Nano Lett.*, **3**, 107–109 (2003).

[81] H.T. Ng, M.L. Foo, A. Fang, J. Li, G. Xu, S. Jaenicke, L. Chan, and S.F.Y. Li, Soft-lithography-mediated chemical vapor deposition of architectured carbon nanotube networks on elastomeric polymer, *Langmuir*, **18**, 1–5 (2002).
[82] Y. Jiang, Y. Wu, S. Zhang, C. Xu, W. Yu, Y. Xie, and Y. Qian, A catalytic-assembly solvothermal route to multiwall carbon nanotubes at a moderate temperature, *J. Am. Chem. Soc.*, **122**, 12383–12384 (2000).
[83] X. Wang, J. Lu, Y. Xie, G. Du, Q. Guo, and S. Zhang, A novel route to multi-walled carbon nanotubes and carbon nanorods at low temperature, *J. Phys. Chem. B*, **106**, 933–937 (2002).
[84] J.L. O'Loughlin, C.H. Kiang, C.H. Wallace, T.K. Reynolds, L. Rao, and R.B. Kaner, Rapid synthesis of carbon nanotubes by solid-state metathesis reactions, *J. Phys. Chem. B*, **105**, 1921–1924 (2001).
[85] J.M. Calderon Moreno and M. Yoshimura, Hydrothermal processing of high-quality multi-wall nanotubes from amorphous carbon, *J. Am. Chem. Soc.*, **123**, 741742 (2001).
[86] D. Chattopadhyay, I.Galeska, and F. Papadimitrakopoulos, Complete elimination of metal catalysts from single-wall carbon nanotubes, *Carbon*, **40**, 985–988 (2002).
[87] I.W. Chiang, B.E. Brinson, R.E. Smalley, J.L. Margrave, and H.R. Hauge, Purification and characterization of single-wall carbon nanotubes, *J. Phys. Chem. B*, **105**, 1157–1161 (2001).
[88] S. Bandow, A.M. Rao, K.A. Williams, A. Thess, R.E. Smalley, and P.C. Eklund, Purification of single-wall carbon nanotubes by microfiltration, *J. Phys. Chem. B*, **101**, 8839–8842 (1997).
[89] K.B. Shelimov, R.O. Esenaliev, A.G. Rinzler, C.B. Huffman, and R.E. Smalley, Purification of single-wall carbon nanotubes by ultrasonically assisted filtration, *Chem. Phys. Lett.*, **282**, 429–434 (1998).
[90] S. Niyogi, H. Hu, M.A. Hamon, P. Bhownik, B. Zhao, S.M. Rozenshak, J. Chen, M.E. Itkis, M.S. Meier, and R.C. Haddon, Chromatographic purification and properties of soluble single-walled carbon nanotubes, *J. Am. Chem. Soc.*, **123**, 733–734 (2001).
[91] B. Zhoa, H. Hu, S. Niyogi, M.E. Itkis, M.A. Hamon, P. Bhowmik, M.S. Meier, and R.C. Haddon, Chromatographic purification and properties of soluble single-walled carbon nanotubes, *J. Am. Chem. Soc.*, **123**, 11673–11677 (2001).
[92] G.S. Duesberg, M. Burghard, J. Munster, G. Philip, and S. Roth, Separation of carbon nanotubes by size exclusion chromatography, *Chem. Commun.*, 435–437 (1998).
[93] S.K. Doorn, R.E. Fields III, H. Hu, M.A. Hamon, R.C. Haddon, J.P. Selegue, and V. Majidi, High resolution capillary electrophoresis of carbon nanotubes, *J. Am. Chem. Soc.*, **124**, 3169–3174 (2002).
[94] L. Thien-Nga, K. Hernadi, E. Ljubovic, S. Garaj, and L. Forro, Mechanical purification of single-walled carbon nanotube bundles from catalytic particles, *Nano Lett.*, **2**, 1349 (2002).
[95] G.S. Duesberg, S. Roth, P. Downes, A. Minett, R. Graupner, L. Ley, and N. Nicoloso, Modification of single-walled carbon nanotubes by hydrothermal treatment, *Chem. Mater.*, **15**, 3314–3319 (2003).
[96] Y. Zhang, H. Zou, Q. Qing, Y. Yang, Q. Li, Z. Liu, X. Guo, and Z. Du, Effect of chemical oxidation on the structure of single-walled carbon nanotubes, *J. Phys. Chem. B*, **107**, 3712–3718, (2003).
[97] K.H. An, K.K. Jeon, J.M. Moon, S.J. Eum, C.W. Yang, G.S. Park, C.Y. Park, and Y.H. Lee, Transformation of singlewalled carbon nanotubes to multiwalled carbon nanotubes and onion-like structures by nitric acid treatment, *Synth. Met.*, **140**, 1–8 (2004).
[98] J. Sloan, J. Hammer, M. Zwiefka-Sibley, and M.L.H. Green, The opening and filling of single walled carbon nanotubes, *Chem. Commun*. 347–349 (1998).
[99] C.M. Yang, K. Kaneko, M. Yudasaka, and S. Iijima, Effect of purification on pore structure of hipco single-walled carbon nanotube aggregates, *Nano Lett.*, **2**, 385–388 (2002).
[100] L. Valentine, I. Armentano, D. Puglia, and J.M. Kenny, Dynamics of amine functionalized nanotubes/epoxy composites by dielectric relaxation spectroscopy, *Carbon*, **42**, 323–329 (2004).
[101] O. Zhou, H. Shimoda, B. Gao, S. Oh, L. Fleming, and G. Yue, Materials science of carbon nanotubes: fabrication, integration, and properties of macroscopic carbon nanotubes, *Acc. Chem. Res.*, **35**, 1045–1053 (2002).

[102] R. Andrews, D. Jacques, M. Minot, and T. Rantell, Fabrication of carbon multi-wall nanotube/polymer composites by shear mixing, *Macromol. Mater. Eng.*, **287**, 395–403 (2002).
[103] B.P. Grady, F. Pompeo, R.L. Shambaugh, and D.E. Resasco, Nucleation of polypropylene crystallization by single-walled carbon nanotubes, *J. Phys. Chem. B*, **106**, 5852–5858 (2002).
[104] M. Zhang, M. Yudasaka, A. Koshio, and S. Iijima, Effect of polymer and solvent on purification and cutting of single-wall carbon nanotubes, *Chem. Phys. Lett.*, **349**, 25–30 (2001).
[105] J.W.G. Wildoer, L.C. Venema, A.G. Rinzler, R.E. Smalley, and C. Dekker, Electronic structure of atomically resolved carbon nanotubes, *Nature*, **391**, 59–62 (1998).
[106] T.M. Wu and J.Y. Lin, Doped polyaniline/multi-walled carbon nanotube composites: preparation, characterization and properties, *Polymer*, **47**, 3576–3582 (2006).
[107] L.B. Kong, J. Zhang, J.J. An, Y.C. Luo, and L. Kang, MWNTs/PANI composite materials prepared by in-situ chemical oxidative polymerization for supercapacitor electrode, *J. Mater. Sci.*, **43**, 3664–3669 (2008).
[108] B. Philip, J. Xie, A. Chandrasekhar, J. Abraham, and V.K. Varadan, A novel nanocomposite from multi-walled carbon nanotubes functionalized with a conducting polymer, *Smart Mater. Struct.*, **13**, 295–298 (2004).
[109] H.T. Ham, Y.S. Choi, N., Jeons, and I.J. Chung, Single wall carbon nanotubes covered with polypyrrole nanoparticles by the miniemulsion polymerization, *Polymer*, **46**, 6308–6315 (2005).
[110] R. Blake, Y.K. Gun'ko, J. Coleman, M. Cadek, A. Fonseca, J.B. Nagy, and W.J. Blau, A generic organometallic approach toward ultra-strong carbon nanotube polymer composites, *J. Am. Chem. Soc.*, **126**, 10226–10227 (2004).
[111] S. Cosnier and M. Holzinger, Design of carbon nanotube-polymer frameworks by electropolymerization of SWCNT-pyrrole derivatives, *Electrochim. Acta*, **53**, 3948–3954 (2008).
[112] S. Lefrant, M. Baibarac, I. Baltog, J. Y. Mevellec, C. Godon, and O. Chauvet, Electrochemical and vibrational properties of single-walled carbon nanotubes in hydrochloric acid solutions, *Diamond Rel. Mater.*, **14**, 873–880 (2005).
[113] P.R. Marcoux, J. Schreiber, P. Batail, S. Lefrant, J. Renouard, G. Jacob, D. Albertini, and J.Y. Mevellec, A spectroscopic study of the fluorination and defluorination reactions on single-walled carbon nanotubes, *Phys. Chem. Chem. Phys.*, **4**, 2278–2285 (2002).
[114] N. Tsubokawa, Preparation and properties of polymer-grafted carbon nanotubes and nanofibers, *Polymer J.*, **37**, 637–655 (2005).
[115] W. Wu, X. Zhang, J. Li, J. Li, L. Liu, Y. Qin, Z.X. Guo, L. Dai, C. Ye, and D. Zhu, PVK-modified single-walled carbon nanotubes with effective photoinduced electron transfer, *Macromolecules*, **36**, 6286–6288 (2003).
[116] T.M. Wu, Y.W. Lin, and C.S. Liao, Preparation and characterization of polyaniline/multi-walled carbon nanotube composites, *Carbon*, **43**, 734–70, (2004).
[117] Y. Li, D. Mann, M. Rolandi, W. Kim, A. Ural, S. Hung, A. Javey, J. Cao, D. Wang, E. Yenilmez, Q. Wang, J.F. Gibbons, Y. Nishi, and H. Dai, Preferential growth of semiconducting single-walled carbon nanotubes by a plasma enhanced CVD method, *Nano Lett.*, **4**, 317–321 (2004).
[118] Y. Maeda, S. Kimura, M. Kanda, Y. Hirashima, T. Hasegawa, T. Wakahara, Y. Lian, T. Nakahodo, T. Tsuchiya, T. Akasaka, J. Lu, X. Zhang, Z. Gao, Y. Yu, S. Nagase, S. Kazaoui, N. Minami, T. Shimizu, H. Tokumoto, and R. Saito, Large-scale separation of metallic and semiconducting single-walled carbon nanotubes, *J. Am. Chem. Soc.*, **127**, 10287–10290 (2005).
[119] A.A. Green and M.C. Hersam, Processing and properties of highly enriched double-wall carbon nanotubes, *Nature Nanotechnol.*, **1**, 64–70 (2006).
[120] M.J. O'Connell, S.M. Bachilo, C.B. Huffman, V.C. Moore, M.S. Strano, E.H. Haroz, K.L. Rialon, P.J. Boul, W.H. Noon, C. Kittrell, J. Ma, R.H. Hauge, R.B. Weisman, and R.E. Smalley, Band gap fluorescence from individual single-walled carbon nanotubes, *Science*, **297**, 593–596 (2002).
[121] M.S. Strano, C.A. Dyke, M.L. Usrey, P.W. Barone, M.J. Allen, H.W. Shan, C. Kittrell, R.H. Hauge, J.M. Tour, and R.E. Smalley, Electronic structure control of single-walled carbon nanotube functionalization, *Science*, **301**, 1519–1522 (2003).

[122] K. Balasubramanian, R. Sordan, M. Burghard, and K. Kern, A selective electrochemical approach to carbon nanotube field-effect transistors, *Nano Lett.*, **4**, 827–830 (2004).
[123] M. Zheng, A. Jagota, E.D. Semke, B.A. Diner, R.S. McLean, S.R. Lustig, R.E. Richardson, and N.G. Tassi, DNA-assisted dispersion and separation of carbon nanotubes, *Nature Mater.*, **2**, 338–342 (2003).
[124] M. Zheng, A. Jagota, M.S. Strano, A.P. Santos, P. Barone, S.G. Chou, B.A. Diner, M.S. Dresselhaus, R.S. McLean, G.B. Onoa, G.G. Samsonidze, E.D. Semke, M. Usrey, and D.J. Walls, Structure-based carbon nanotube sorting by sequence-dependent dna assembly, *Science*, **302**, 1545–1548 (2003).
[125] M.S. Strano, M. Zheng, A. Jagota, B.B. Onoa, D.A. Heller, P.W. Barone, and M.L. Usrey, Understanding the nature of the DNA-assisted separation of single-walled carbon nanotubes using fluorescence and Raman spectroscopy, *Nano Lett.*, **4**, 543–550 (2004).
[126] D. Chattophadhyay, I. Galescka, and F. Papadimitrakopoulos, A route for bulk separation of semiconducting from metallic single-wall carbon nanotubes, *J. Am. Chem. Soc.*, **125**, 3370–3375 (2003).
[127] G.G. Samsonidze, S.G. Chou, A.P. Santos, V.W. Brar, G. Dresselhaus, M.S. Dresselhaus, A. Selbst, A.K. Swan, M.S. Unlu, B.B. Goldberg, D. Chattopadhyay, S.N. Kim, and F. Papadimitrakopoulos, Quantitative evaluation of the octadecylamine-assisted bulk separation of semiconducting and metallic single-wall carbon nanotubes by resonance Raman spectroscopy, *Appl. Phys. Lett.*, **85**, 1006–1009 (2004).
[128] Z. Chen, X. Du, M.H. Du, C.D. Rancken, H.P. Cheng, and A.G. Rinzler, Bulk separative enrichment in metallic or semiconducting single-walled carbon nanotubes, *Nano Lett.*, **3**, 1245–1249 (2003).
[129] M. Husanu, M. Baibarac, and I. Baltog, Non-covalent functionalization of carbon nanotubes: Experimental evidence for isolated and bundled tubes, *Physica E*, **41**, 66–69 (2008).
[130] H. Hiura, T.W. Ebbensen, K. Tanigaki, and H. Takahashi, Raman studies of carbon nanotubes, *Chem. Phys. Lett.*, **202**, 509–512 (1993).
[131] A.M. Rao, S. Bandow, E. Richter, and P.C. Eklund, Raman spectroscopy of pristine and doped single wall carbon nanotubes, *Thin Solid Films*, **331**, 141–147 (1998).
[132] E. Richter and K.R. Subbaswamy, Theory of size-dependent resonance Raman scattering from carbon nanotubes, *Phys. Rev. Lett.*, **79**, 2738–2741 (1997).
[133] S. Bandow, S. Asaka, Y. Saito, A.M. Rao, L. Grigorian, E. Richter, and P.C. Eklund, Effect of the growth temperature on the diameter distribution and chirality of single-wall carbon nanotubes, *Phys. Rev. Lett.*, **80**, 3779–3782 (1998).
[134] A.M. Rao, J. Chen, E. Richter, U. Schlecht, P.C. Eklund, R.C. Haddon, U.D. Venkateswaran, Y.K. Kwon, and D. Tomanek, Effect of van der Waals interactions on the Raman modes in single walled carbon nanotubes, *Phys. Rev. Lett.*, **86**, 3895–3898 (2001).
[135] R. Saito, G. Dresselhaus, and M.S. Dresselhaus, *Physical Properties of Carbon Nanotubes*, Imperial College Press, London, 1998.
[136] S. Piscanec, M. Lazzeri, J. Robertson, A.C. Ferrari, and F. Mauri, Optical phonons in carbon nanotubes: Kohn anomalies, Peierls distortions, and dynamic effects, *Phys. Rev. B*, **75**, 035427 1–22 (2007).
[137] C. Thomsen and S. Reich, Double resonant Raman scattering in graphite, *Phys. Rev. Lett.*, **85**, 5214–5217 (2007).
[138] E.B. Barros, H. Son, Ge.G. Samsonidze, A.G. Souza Filho, R. Saito, Y.A. Kim, H. Muramatsu, T. Hayashi, M. Endo, J. Kong, and M.S. Dresselhaus, Raman spectroscopy of double-walled carbon nanotubes treated with H_2SO_4, *Phys. Rev. B*, **76**, 045425 (2007).
[139] J.M. Benoit, J.P. Buisson, O. Chauvet, C. Godon, and S. Lefrant, Low-frequency Raman studies of multiwalled carbon nanotubes: Experiments and theory, *Phys. Rev. B*, **66**, 073417 (2002).
[140] U.J. Kim, X.M. Liu, C.A Furtado, G. Chen, R. Saito, J. Jiang, M.S. Dresselhaus, and P.C. Eklund, Infrared-active vibrational modes of single-walled carbon nanotubes, *Phys. Rev. Lett.*, **95**, 157402 (2005).
[141] J. Dai, Advanced syntheses and microfabrications of conjugated polymers, C_{60}-containing polymers and carbon nanotubes for optoelectronic applications, *Polym. Adv. Technol.*, **10**, 357–420 (1999).

[142] C. Downs, J. Nugent, P.M. Ajayan, D.J. Duquette, and K.S.V. Santhanam, Efficient polymerization of aniline at carbon nanotube electrodes, *Adv. Mater.*, **11**, 1028–1031 (1999).
[143] M. Cochet, W.K. Maser, A.M. Benito, M.A. Callejas, M.T. Martinez, J.M. Benoit, J. Schreiber, and O. Chauvet, Synthesis of a new polyaniline/nanotube composite: *'in-situ'* polymerisation and charge transfer through site-selective interaction *Chem. Commun.*, 1450 (2001).
[144] M. Gao, S.M. Huang, L.M. Dai, G. Wallace, and R. Gao, Aligned coaxial nanowires of carbon nanotubes sheathed with conducting polymers, *Angew. Chem. Int. Ed.*, **39**, 3664–3667 (2000).
[145] H.J. Barraza, F. Pompeo, E.A. O'Rear, and D.E. Resasco, SWNT-filled thermoplastic and elastomeric composites prepared by miniemulsion polymerization, *Nano Lett.*, **2**, 797–802 (2002).
[146] Z.Z. Zhu, Z. Wang, and H.L. Li, Functional multi-walled carbon nanotube/polyaniline composite films as supports of platinum for formic acid electrooxidation *Appl. Surf. Sci.*, **254**, 2934–2940 (2008).
[147] W.K. Maser, A.M. Benito, M.A. Callejas, T. Seeger, M.T. Martinez, J. Schreiber, J. Muszynski, O. Chauvet, Z. Osvath, A.H. Koos, and L.P. Biro, Synthesis and characterization of new polyaniline/nanotube composites, *Mat. Sci. Eng. C, Biomim. Supermolec. Syst.*, **23**, 87–91 (2003).
[148] A. Pron, F. Genoud, C. Menardo, and M. Nechtschein, The effect of the oxidation conditions on the chemical polymerization of polyaniline, *Synth. Met.*, **24**, 193–201 (1988).
[149] M.A. Rodrigues and M.A. de Paoli, Electrochemical properties of chemically prepared poly(aniline), *Synth. Met.*, **41–43**, 2957–2962 (1991).
[150] M. Ishikawa, M. Hawai, and Y. Ohsawa, Synthesis and properties of electrically conducting polytriphenylamines, *Synth. Met.*, **40**, 231–238 (1991).
[151] W.S. Huang, B.D. Humphrey, and A.G. MacDiarmid, A general chemical route to polyaniline nanofibers, *J. Chem. Soc. Faraday Trans.*, **82**, 2385–2390 (1986).
[152] M. Lapkowski, K. Berrada, S. Quillard, G. Louarn, S. Lefrant, and A. Pron, Electrochemical oxidation of polyaniline in nonaqueous electrolytes: '*in situ*' Raman spectroscopic studies, *Macromolecules*, **28**, 1233–1238 (1995).
[153] P. Corio, P.S. Santos, V.W. Brar, G.G. Samsonidze, S.G. Chou, and M.S. Dresselhaus, Potential dependent surface Raman spectroscopy of single wall carbon nanotube films on platinum electrodes, *Chem. Phys. Lett.*, **370**, 675–682 (2003).
[154] S. Lefrant, M. Baibarac, I. Baltog, J.Y. Mevellec, L. Mihut, and O. Chauvet, SERS spectroscopy studies on the electrochemical oxidation of single-walled carbon nanotubes in sulfuric acid solutions, *Synth. Met.*, **144**,133–142 (2004).
[155] G.U. Sumanasekera, J.L. Allen, S.L. Fang, A.L.Loper, A.M. Rao, and P.C. Eklund, Electrochemical oxidation of single-wall carbon nanotube bundles in sulfuric acid, *J. Phys. Chem. B*, **103**, 4292–4297 (1999).
[156] V. Mottaghitalab, G.M. Spinks, and G.G. Wallace, The influence of carbon nanotubes on mechanical and electrical properties of polyaniline fibers, *Synth. Met.*, **152**, 77–80 (2005).
[157] D. Guo and H. Li, Well-dispersed multi-walled carbon nanotube/polyaniline composite films, *J. Solid State Electrochem.*, **9**, 445–449 (2005).
[158] R. Sainz, W.R. Small, N.A. Young, C. Valles, A.M. Benito, W.K. Maser, and M. in het Panhuis, Synthesis and properties of optically active polyaniline carbon nanotube composites, *Macromolecules*, **39**, 7324–7332 (2006).
[159] T. Ming Wu and Y.W. Lin, Doped polyaniline/multi-walled carbon nanotube composites: Preparation, characterization and properties, *Polymer*, **47**, 3576–3582 (2006).
[160] Y.P. Sun, W.J. Huang, Y. Lin, K.F. Fu, A. Kitaygorodskiy, L.A. Riddle, J. Yu, and D.L. Carroll, Soluble dendron-functionalized carbon nanotubes: preparation, characterization, and properties, *Chem. Mater.*, **13**, 2864–2869 (2001).
[161] J. Liu, A.G. Rinzler, H.J. Dai, J.H. Hafner, R.K. Bradley, P.J. Boul, A. Lu, T. Iverson, K. Shelimov, C.B. Huffman, F. Rodriguez-Macias, Y.-S. Shon, T.R. Lee, D.T. Colbert, and R.E. Smalley, Fullerene pipes, *Science*, **280**, 1253–1256 (1998).

[162] J. Chen, M.A. Hamon, H. Hu, Y. Chen, A.M. Rao, P.C. Eklund, and R.C. Haddon, Solution properties of single-walled carbon nanotubes, *Science*, **282**, 95–98 (1998).
[163] M.A. Hamon, J. Chen, H. Hu, Y. Chen, M.E. Itkis, A.M. Rao, P.C. Eklund, and R.C. Haddon, Dissolution of single-walled carbon nanotubes, *Adv. Mater.*, **11**, 834–840 (1999).
[164] M. Ginic-Markovic, J.G. Matisons, R. Cervini, G.P. Simon, and P.M. Fredericks, Synthesis of new polyaniline/nanotube composites using ultrasonically initiated emulsion polymerization, *Chem. Mater.*, **18**, 6258–6265 (2006).
[165] Y. Ma, S.R. Ali, L. Wang, P.L. Chiu, R. Mendelsohn, and H. He, *In situ* fabrication of a water-soluble, self-doped polyaniline nanocomposite: the unique role of DNA functionalized single-walled carbon nanotubes, *J. Am. Chem. Soc.*, **128**, 12064–12065 (2006).
[166] P.C. Ramamurthy, W.R. Harrell, R.V. Gregory, and A.M. Rao, Integration and distribution of carbon nanotubes in solution-processed polyaniline/carbon nanotube composites, *J. Electrochem. Soc.*, **154**, H495–H498 (2007).
[167] E. Zelikman, M. Narkis, A. Siegmann, L. Valentini, and J.M. Kenny, Polyaniline/multiwalled carbon nanotube systems: dispersion of CNT and CNT/PANI interaction, *Polym. Eng. Sci.*, **48**, 1872–1877 (2008).
[168] Q. Xiao and X. Zhou, The study of multi-walled carbon nanotube deposited with conducting polymer for supercapacitor, *Electrochim. Acta*, **48**, 575–580 (2003).
[169] M. Hughes, G.Z. Chen, M.S.P. Shaffer, D.J. Fray, and A.H. Windle, Electrochemical capacitance of a nanoporous composite of carbon nanotubes and polypyrrole, *Chem. Mater.*, **14**, 1610–1613 (2002).
[170] G. Han, J. Yuan, G. Shi, and F. Wei, Electrodeposition of polypyrrole/multi-walled carbon nanotube composite films, *Thin Solid Films*, **474**, 64–69 (2005).
[171] R. Turcu, A. Darabont, A. Nan, N. Aldea, D. Macovei, D. Bica, L. Vekas, O. Pana, M.L. Soran, A.A. Koos, and L.P. Biro, New polypyrrole-multi-wall carbon nanotubes hybrid materials, *J. Optoelectron. Adv. Mater.*, **8**, 643–647 (2006).
[172] X. Cui, C. M. Li, J. Zhang, Q. Zhou, Y. Gan, H. Beo, J. Guo, V.S. Lee, and S.M. Moochhala, Biocatalytic generation of Ppy-enzyme-CNT nanocomposite: from network assembly to film growth, *J. Phys. Chem. C*, **111**, 2025–2031 (2007).
[173] H.T. Han, Y.S. Choi, N. Jeong, and I.J. Cheng, Single-wall carbon nanotubes covered with polypyrrole nanoparticles by the miniemulsion polymerization, *Polymer*, **46**, 6308–6315 (2005).
[174] M.S.P. Shaffer and K. Koziol, Polystyrene grafted multi-walled carbon nanotubes, *Chem. Commun.*, 2074–2076 (2002).
[175] D.H. Jung, Y.K. Ko, and H.T. Jung, Aggregation behavior of chemically attached poly(ethylene glycol) to single-walled carbon nanotubes (SWNTs) ropes, *Mater. Sci. Eng. C*, **24**, 117–121 (2004).
[176] Y. Long, Z. Chen, X. Zhang, J. Zhang, and Z. Liu, Electrical properties of multi-walled carbon nanotube/polypyrrole nanocables: percolation-dominated conductivity, *J. Phys. D: Appl. Phys.*, **37**, 1965–1970 (2004).
[177] X. Zhang, J. Zhang, R. Wang, T. Zhu, and Z. Liu, Surfactant-directed polypyrrole/CNT nanocables: synthesis, characterization, and enhanced electrical properties, *Chem. Phys. Chem.*, **5**, 998–1002 (2004).
[178] N. Gopal Sahoo, Y.C. Jung, H.H. So, and J.W. Cho, Polypyrrole coated carbon nanotubes: Synthesis, characterization, and enhanced electrical properties, *Synth. Met.*, **157**, 374–379 (2007).
[179] M.R. Karim, C.J. Lee, A.M.S. Chowdhury, N. Nahar, and M.S. Lee, Radiolytic synthesis of conducting polypyrrole/carbon nanotube composites, *Mat. Lett.*, **61**, 1688–1692 (2007).
[180] V. Georgakilas, P. Dallas, D. Niarchos, N. Boukos, and C. Trapalis, Polypyrrole/MWNT nanocomposites synthesized through interfacial polymerization, *Synth. Met.*, **159**, 632–636 (2009).
[181] K. Lota, V. Khomenko, and E. Frackoviak, Capacitance properties of poly(3,4-ethylene dioxythiophene)/carbon nanotubes composites, *J. Phys. Chem. Solids*, **65**, 295–301 (2004).
[182] S. Lefrant, M. Baibarac, I. Baltog, J.Y. Mevellec, C. Godon, and O. Chauvet, Functionalization of single-walled carbon nanotubes with conducting polymers evidenced by Raman and FTIR spectroscopy, *Diamond and Rel. Mater.*, **14**, 867–872 (2005).

[183] I. Baltog, M. Baibarac, S. Lefrant, and P. Gomez Romero, SERS studies on poly(3,4-ethylene dioxythiophene)/SWNTs composites and their application to rechargeable lithium batteries, *J. Nanosci. Nanotech.*, **9**, 6204–6209 (2009).
[184] M. Kalbac, L. Kavan, M. Zukalova, and L. Dunsch, An *in situ* Raman spectroelectrochemical study of the controlled doping of single walled carbon nanotubes in a conducting polymer matrix, *Carbon*, **45**, 1463–1470 (2007).
[185] M. Kalbac, L. Kavan, and L. Dunsch, Controlled doping of double walled carbon nanotubes and conducting polymers in a composite: An in situ Raman spectroelectrochemical study, *Comp. Sci. Technol.*, **69**, 1553–1557 (2008).
[186] H.T. Ham, Y.S. Choi, M.G. Chee, M.H. Cha, and I.J. Chung, PEDOT-PSS/singlewall carbon nanotubes composites, *Polym. Eng. Sci.*, **48**, 1–10 (2008).
[187] E.V. Ovsyannikova, O.N. Efimov, A.P. Moravsky, R.O. Loutfy, E.P. Krinichnaya, and N.M. Alpatova, Electrochemical properties of thin-layered composites formed by carbon nanotubes and polybithiophene, *Rus. J. Electrochem.*, **41**, 439–446 (2005).
[188] E.V. Ovsyannikova, O.N. Efimov, E.P. Krinichnaya, and N.M. Alpatova, Cathodic doping of thin-layered composites. Formed by electroactive polymers and rubbed single-walled carbon nanotubes, *Rus. J. Electrochem.*, **43**, 1064–1068 (2007).
[189] R.L. Patyk, B.S. Lomba, A.F. Nogueira, C.A. Furtado, A.P. Santos, R.M.Q. Mello, L. Micaroni, and I.A. Hümmelgen, Carbon nanotube-polybithiophene photovoltaic devices with high open-circuit voltage, *Phys. Stat. Solidi – Rapid Res. Lett.*, **1**, R43–R45 (2007).
[190] M. Baibarac, I. Baltog, and S. Lefrant, Raman spectroscopic evidence for interfacial interactions in poly(bithiophene)/single-walled carbon nanotube composites, *Carbon*, **47**, 1389–1398 (2009).
[191] W. Wu, J. Li, L. Liu, L. Yanga, Z.X. Guo, L. Dai, and D. Zhu, The photoconductivity of PVK-carbon nanotube blend, *Chem. Phys. Lett.*, **364**, 196–199 (2002).
[192] C. Li, C. Liu, F. Li, and Q. Gond, Optical limiting performance of two soluble multi-walled carbon nanotubes, *Chem. Phys. Lett.*, **380**, 201–205 (2003).
[193] W. Wang, Y. Li, and Y.P. Sun, Poly(N-vinyl carbazole)-functionalized single-walled carbon nanotubes: Synthesis, characterization, and nanocomposite thin films, *Polymer*, **46**, 8634–8640 (2005).
[194] M. Baibarac, M. Lira Cantu, J. Oro Sole, N. Casan Pastor, and P. Gomez Romero, Electrochemically functionalized carbon nanotubes and their application to rechargeable lithium batteries, *Small*, **2**, 1075–1082 (2006).
[195] M. Baibarac, P. Gomez Romero, M. Lira Cantu, N. Casan Pastor, N. Mestres, and S. Lefrant, Electrosynthesis of the poly(*N*-vinyl carbazole)/carbon nanotubes composite for applications in the supercapacitors field, *Eur. Polym. J.*, **42**, 2302–2312 (2006).
[196] J.Y. Kim, M. Kim, and J.H. Choi, Characterization of light emitting devices based on a single-walled carbon nanotube–polymer composite, *Synth. Met.*, **139**, 565–568 (2003).
[197] P. Bertoncello, A. Natargiacomo, V. Erokhin, and C. Nicolini, Functionalization and photoelectrochemical characterization of poly[3-3'(vinylcarbazole)] multi-walled carbon nanotube (PVK-MWNT) Langmuir–Schaefer films, *Nanotechnology*, **17**, 699–705 (2006).
[198] M. Cadek, J.N. Coleman, V. Barron, K. Hedicke, and W.J. Blau, Morphological and mechanical properties of carbon-nanotube-reinforced semicrystalline and amorphous polymer composites, *Appl. Phys. Lett.*, **81**, 5123–5126 (2002).
[199] H.X. Wu, X.Q. Qiu, R.F. Cai, and S.X. Qian, Poly(N-vinyl carbazole)-grafted multi-walled carbon nanotubes: Synthesis via direct free radical reaction and optical limiting properties, *Appl. Surf. Sci.*, **253**, 5122–5128 (2007).
[200] A. Maity, S.S. Ray, and M.J. Hato, The bulk polymerisation of N-vinylcarbazole in the presence of both multi- and single-walled carbon nanotubes: A comparative study *Polymer*, **49**, 2857–2865 (2008).
[201] C.H. Yang, Z.A. Tan, B.H. Fan, Q.J. Sun, J.F. Li, X.H. Zohou, J. Pei, J.Y. Qin, and Z.X. Guo, An electrogenerated chemical-oxidation-driving nonvolatile plastic memory device with the conjugated polymer/carbon nanotube blend, *Electrochem. Solid State Lett.*, **10**, P19–P22 (2007).

[202] N. Izard, S. Kazaoui, K. Hata, T. Okazaki, T. Saito, S. Iijima, and N. Minami, Semiconductor-enriched single wall carbon nanotube networks applied to field effect transistors, *Appl. Phys. Lett.*, **92**, 243112 (2008).
[203] G. Xu, B. Zhu, Y. Han, and Z. Bo, Covalent functionalization of multi-walled carbon nanotube surfaces by conjugated polyfluorenes, *Polymer*, **48**, 7510–7515 (2007).
[204] B. McCarthy, J.N. Coleman, R. Czerw, A.B. Dalton, M. in het Panhuis, A. Maiti, A. Drury, P. Bernier, J.B. Nagy, B. Lahr, J. Byrne, D.L. Carroll, and W.J. Blau, A microscopic and spectroscopic study of interactions between carbon nanotubes and a conjugated polymer, *J. Phys. Chem B*, **106**, 2210–2216 (2002).
[205] M. in het Panhuis, A. Maiti, A.B. Dalton, A. van den Noort, J.N. Coleman, B. McCarthy, and W. Blau, Selective interaction in a polymer–single-wall carbon nanotube composite, *J. Phys. Chem. B*, **107**, 478–482 (2003).
[206] J. Wéry, H. Aarab, S. Lefrant, E. Faulques, E. Mulazzi, and R. Perego, Photoexcitations in composites of poly(paraphenylene vinylene) and single-walled carbon nanotubes, *Phys. Rev. B*, **67**, 115202 (2003).
[207] E. Mulazzi, R. Perego, H. Aarab, L. Mihut, S. Lefrant, E. Faulques, and J. Wéry, Photoconductivity and optical properties in composites of poly(paraphenylene vinylene) and single-walled carbon nanotubes, *Phys. Rev B*, **70**, 155206 (2004).
[208] J. Steinmetz, H.J. Lee, S. Kwon, D.S. Lee, C. Goze-Bac, E. Aboul-Hamad, H. Kim, Y.W. Park, J.Y. Choi, Routes to the synthesis of carbon nanotube–polyacetylene composites by Ziegler–Natta polymerization of acetylene inside carbon nanotubes, *Curr. Appl. Phys.*, **7**, 39–41 (2007).
[209] E. Faulques, W. Wallnofer, and H. Kuzmany, Vibrational analysis of heterocyclic polymers-study of polythiophene, polypyrrole and polyisothianaphthene, *J. Chem. Phys.*, **90**, 7585–7593 (1989).
[210] Y.C. Liu and B.J. Hwang, Identification of oxidized polypyrrole on Raman spectrum *Synth. Met.*, **113**, 203–207 (2000).
[211] R. Kostic, D. Rakovic, S.A. Stepanyan, I.E. Davidova, and L.A. Gribov, Vibrational spectroscopy of polypyrrole, theoretical studies, *J. Chem. Phys.*, **102**, 3104–3109 (1995).
[212] N. Pei, X.T. Zhang, Y.C. Li, Y.B. Huang, and Y.J. Mo, A study of poly (*N*-vinylcarbazole) adsorbed on silver surface by SERS, *Vibr. Spectrosc.*, **21**, 39–43 (1999).
[213] R. Anandhi and S. Umapathy, Resonance Raman spectroscopic studies on the conducting state of polyvinylcarbazole and its model compound, *J. Raman Spectrosc.*, **29**, 901–906 (1998).
[214] D. Lin–Vien, N.B. Colthyp, W.G. Fateley, and J.G. Grasseli, The Handbook of Infrared and Raman Characteristic Frequencies of Organic Molecules, Academic Press, London, 1991.
[215] P. Bertoncello, A. Notargiacomo, and C. Nicolini, Synthesis, fabrication and characterization of poly[3-3′(vinylcarbazole)] (PVK) Langmuir–Schaefer films, *Polymer*, **45**, 1659–1664 (2004).
[216] N. Ballav and M. Biswas, A conducting composite of polyN-vinylcarbazole and polythiophene, *Synth. Met.*, **132**, 213–218 (2003).
[217] S. Lefrant, I. Baltog, M. Baibarac, J. Schreiber, and O. Chauvet, Modification of surface-enhanced Raman scattering spectra of single-walled carbon nanotubes as a function of nanotube film thickness, *Phys. Rev. B.*, **65**, 235401 (2002).
[218] M. Baibarac, L. Mihut, G. Louarn, S. Lefrant, and I. Baltog, Doping and metallic-support effect evidenced on SERS spectra of polyaniline thin films, *J. Polym. Sci., Part B: Polym. Phys.*, **38**, 2599–2609 (2000).
[219] M. Giusca, M. Baibarac, S. Lefrant, O. Chauvet, I. Baltog, A. Devenyi, and R. Manaila, C60–polymer nanocomposites: evidence for interface interaction, *Carbon*, **40**, 1565–1574 (2002).
[220] S. Quillard, G. Louarn, S. Lefrant, and A.G. MacDiarmid, Vibrational analysis of polyaniline: A comparative study of leucoemeraldine, emeraldine, and pernigraniline bases, *Phys. Rev. B.*, **50**, 12496–12508 (1994).

6

Inorganic-Based Nanocomposites of Conductive Polymers

Rabin Bissessur

Department of Chemistry, University of Prince Edward Island, Charlottetown, PEI, Canada

6.1 Introduction

The term intercalation literally refers to the act of inserting some extra interval of time into the calendar, such as February 29 in a leap year. In chemistry it means the reversible insertion of guest species into lamellar host structures, where the structural integrity of the hosts is maintained [1]. However, in today's chemical literature the use of the term 'intercalation' is rather loose and broad. The term has also been applied to three-dimensional solids such as zeolites [2,3], and one-dimensional materials such as carbolite [4], as well as zero-dimensional structures such as fullerenes [5]. Interestingly enough the term 'intercalation' has also been adopted for cases where complete structural integrity of the host is not preserved, as in the case of MoO_3 intercalated with pyridine [6]. The reversibility of the insertion reaction is no longer a prerequisite either. For instance, the introduction of electrically conductive polypyrrole in the gallery space of layered FeOCl [7,8], which is an irreversible process, has been referred to as an intercalation reaction.

The first intercalation chemistry was reported in 1841 by Schaffautl, who successfully intercalated sulfate ions into graphite. After this pioneering work, fascination with intercalation chemistry did not start until the 1960s. The synthesis and study of intercalation compounds are both useful and rewarding. Intercalated phases have found applications as electrodes in high-energy-density batteries [9] and as catalytic materials [10]. Since the

Nanostructured Conductive Polymers Edited by Ali Eftekhari

first report of Schaffautl and until the mid-1980s, intercalation had been involved exclusively with small molecules. From the mid-1980s onwards, there has been a considerable amount of interest in the insertion of polymers, especially those that are electrically conductive and ionically conductive into layered structures. These intercalated systems have been referred to as intercalated nanocomposites or nanomaterials, since the two components are intimately mixed at the molecular level. In principle, enhanced properties can be synergistically derived from these hybrid materials that cannot be displayed by the components on their own [11,12]. The choice of layered structures is rather wide, ranging from a plethora of clay minerals, transition-metal dichalcogenides, oxides, and halides, to phosphates and phosphonates. This article will review the work that have been done on layered transition-metal oxides, phosphates and phosphonates, rutiles, perovskites, titantes, and graphite oxide.

6.2 FeOCl

While FeOCl is referred to as an oxyhalide, it could also be considered as an oxide since the layered material consists of oxygen atoms. From a historical perspective, it is worthwhile to review the work than has been done on this lamellar host system. The structure of FeOCl can be described as edge-sharing FeO_4Cl_2 octahedra, forming infinite 2-D sheets that are held together by weak van der Waals forces. In 1987, Marks and Kanatzidis reported the insertion of polypyrrole, an electrically conductive polymer into FeOCl, by treatment of the latter with pyrrole monomer [7]. This is a truly remarkable reaction. At first sight, one would predict that this intercalation reaction would be kinetically slow. However, the feasibility of this reaction lies in its driving force. FeOCl is highly oxidizing, the potential of which is believed to be similar to that of $FeCl_3$, which is about 1.1 V. Therefore, FeOCl is capable of oxidizing the pyrrole monomer, which oxidatively inserts into the layered host as the polymer (Figure 6.1). This reaction has been referred to as an *in situ* intercalation/polymerization reaction, or redox intercalative polymerization (RIP), with both polymerization and intercalation occurring at the same time. The exact mechanism of this reaction is not fully understood. However, it is believed that the initial step may be coordination of pyrrole to a Fe^{3+} site on the edge of the FeOCl crystal, followed by electron transfer. Since then, other electrically conductive polymers have been encapsulated into FeOCl, such as polyaniline and polythiophene [13,14]. For all of these nanomaterials, powder X-ray diffraction data show that the polymer chain inserts with the phenyl groups oriented perpendicular with respect to the layered sheets. Table 6.1 summarizes the XRD data on the FeOCl system.

It is interesting to note that the intercalation of polyaniline into FeOCl was revisited by Matsuo *et al*. [15]. This was achieved via an exchange reaction, a completely different method from the early reports on the FeOCl system. *N*-hexadecylamine was first intercalated into FeOCl through a solid–solid reaction by intimately mixing the two components, followed by heating at 60 °C overnight. The stoichiometry of the resulting intercalate was $(C_{16}H_{33}NH_2)_{0.5}FeOCl$. $(PANI)_{0.42}FeOCl$ was then obtained by adding polyaniline ($MW > 15\,000$, emeraldine salt) to an NMP suspension of $(C_{16}H_{33}NH_2)_{0.5}FeOCl$. Powder X-ray diffraction confirmed successful formation of the

Table 6.1 *Summary of data on the FeOCl system*

Polymer	Stoichiometry	Interlayer expansion (Å)
Polypyrrole	$(Ppy)_{0.34}FeOCl$	5.30
Polyaniline	$(PANI)_{0.20}FeOCl$	6.54
Polythiophene	$(Pth)_{0.27}FeOCl$	5.33

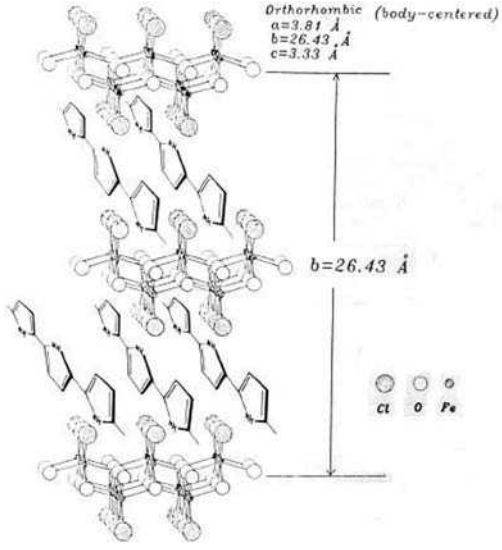

Figure 6.1 *Structural model for the intercalated polypyrrole chains within the van der Waals gap of FeOCl. (Reprinted with permission from Solid State Ionics, In situ intercalative polymerization chemistry of FeOCl. Generation and properties of novel, highly conductive inorganic/organic polymer microlaminates by M. G. Kanatzidis, H. O. Marcy, W. J. McCarthy et al., 594–608, 1–3. Copyright (1989) Elsevier Ltd)*

intercalated phases (Figure 6.2). Compared to the RIP method, the exchange method produced an intercalated phase with a higher polymer content, and in principle higher molecular weights can be intercalated. For instance, gel permeation chromatography on the extracted PANI from $(PANI)_{0.16}FeOCl$, synthesized via the RIP method, showed a lower molecular weight of the intercalated polymer (MW 6100) [16].

6.3 V_2O_5 Systems

Though vanadium pentoxide gels ($V_2O_5.nH_2O$) have been known from as early as 1885 [17], it was actually Livage and coworkers who revived this amazing material. The synthesis, structure, and electrical properties, as well as electrochemical and spectroscopic data on $V_2O_5.nH_2O$ have been thoroughly reported by Livage *et al*. [18–22].

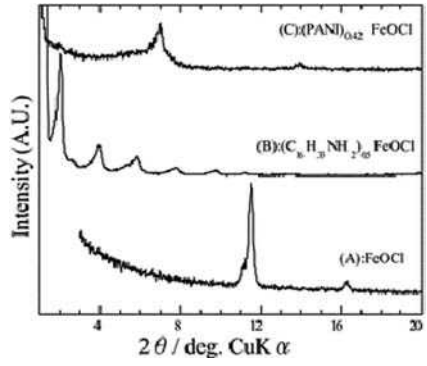

Figure 6.2 *XRD of (A) FeOCl; (B) $(C_{16}H_{33}NH_2)_{0.5}$FeOCl; (C) $(PANI)_{0.42}$FeOCl. (Reprinted with permission from Journal of Materials Chemistry, Synthesis of polyaniline-intercalated layered materialsvia exchange reaction by Y. Matsuo, S. Hihashika, Y. Miyamoto et al., 12, 1592–1596. Copyright (2002) Royal Society of Chemistry)*

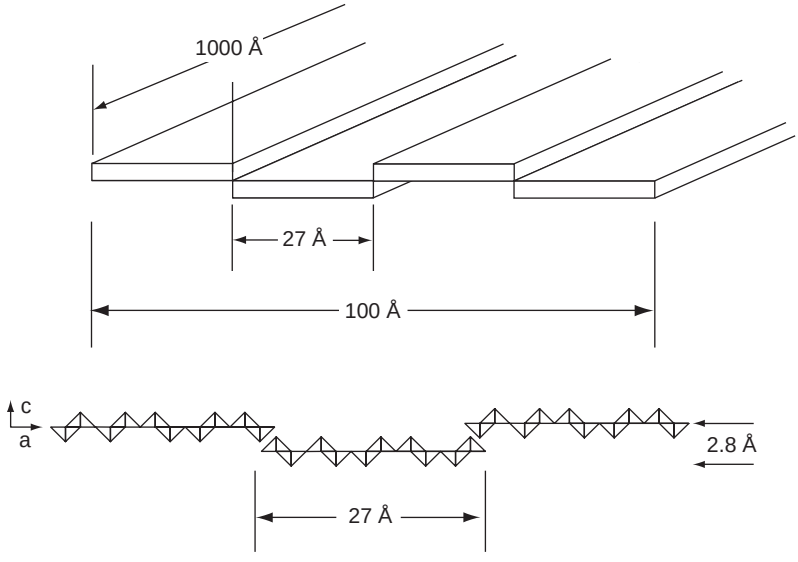

Figure 6.3 *Representation of the V_2O_5 fibril with approximate dimensions. (Reprinted with permission from Mat. Res. Proc., Vol. 210, Pittsburgh, PA, Layered V_2O_5 Xerogels: Host-Guest Chemistry and Conductive Polymers by C.-G. Wu and M. G. Kanatzidis, 429–442. Copyright (1991) Materials Research Society)*

V_2O_5 xerogels are layered in nature with an interlayer spacing value of 11.55 Å [23]. X-ray, neutron, and transmission electron microscopic studies show that V_2O_5 xerogels consist of corrugated ribbons with an average planar dimension of 1000×100 Å (Figure 6.3). The intraribbon structure is closely related to orthorhombic V_2O_5, with the vanadium atom in a square pyramidal geometry (Figure 6.4). It is interesting to note that

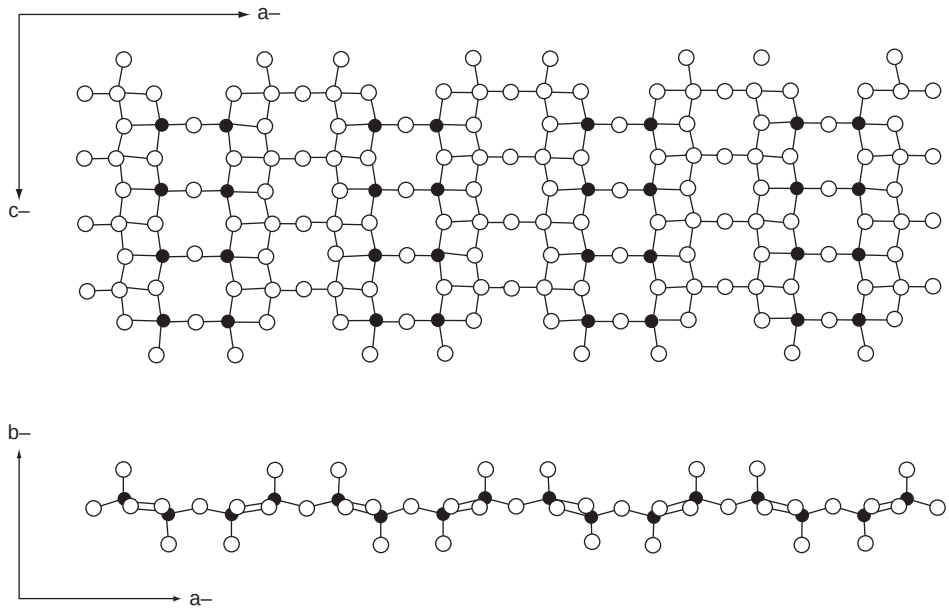

Figure 6.4 *Two views of the structure of a V_2O_5 layer in orthorhombic V_2O_5. Open circles: oxygens; solid circles: vanadium. (Reprinted with permission from Mat. Res. Proc., Vol. 210, Pittsburgh, PA, Layered V_2O_5 Xerogels: Host-Guest Chemistry and Conductive Polymers by C.-G. Wu and M. G. Kanatzidis, 429–442. Copyright (1991) Materials Research Society)*

the axial V—O bond is a double bond. In V_2O_5 xerogels, about half of the vanadium centers are coordinated with water molecules. In addition, there is a layer of water loosely bound via hydrogen bonding to the coordinated water molecules.

The structure of $V_2O_5.nH_2O$ as shown in Figures 6.3 and 6.4 are actually based on the work performed by Livage *et al*. It should, however, be pointed out that the structure of $V_2O_5.nH_2O$ (d-spacing = 11.5 Å at room temperature) was also re-explored by Yamamoto *et al*. using the Rietveld method [24]. To sum up, it was found that 1-D Patterson maps hinted that a V_2O_5 layer consists of two V_2O_5 sheets facing each other at a distance of 2.8 Å. The calculated pattern from a structure of double-sheet V_2O_5 layers and bilayer arrangements of interlayer water molecules was in good agreement with the observed pattern, and the structure agreed well with the 1-D Fourier map. Further, the observed sample density confirmed the structure of a double-sheet V_2O_5 layer (Figure 6.5).

V_2O_5 xerogels are generally prepared from polyvanadic acid solutions, obtained by the cation exchange of $NaVO_3$ with an acid solution. The polyvanadic precursor solution is gradually converted into a polyvanadic acid gel. The slow evaporation of water at room temperature results in the formation of $V_2O_5.nH_2O$. It is interesting to note that long-term aging of the polyvanadic acid gel affects the structure and electrochemical properties of the xerogels [25].

Similarly to FeOCl, $V_2O_5.nH_2O$ is also capable of undergoing *in situ* intercalation/polymerization. The intercalation of polyaniline, polypyrrole, and polythiophene into

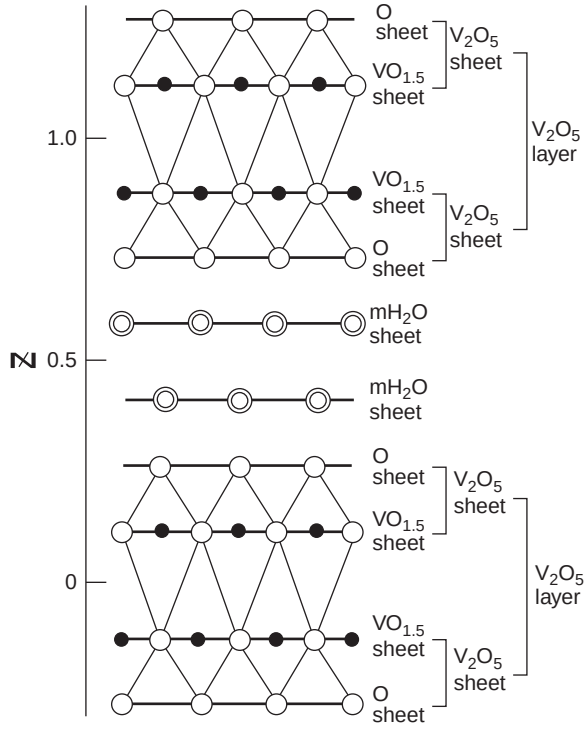

Figure 6.5 *Model structure of V_2O_5 gels represented by atomic sheets: $VO_{1.5}$, O and mH_2O sheets. Closed, open and double circles denote vanadium, oxygen and water, respectively. (Reprinted with permission from Materials Research Bulletin, Layered structures of vanadum pentoxide gels by T. Yao, Y. Oka and N. Yamamoto, 27, 6, 669–675. Copyright (1992) Elsevier Ltd)*

$V_2O_5.nH_2O$ has been reported [26,27,28]. This can be achieved by refluxing the xerogel in acetonitrile solutions of the monomers. A range of loading of the intercalated polymer has been reported, as summarized in Table 6.2. It should be noted that the polythiophene/xerogel phase can only be obtained by treatment of the dimer (2,2′-bithiophene) with the xerogel. The oxidation potential of thiophene itself is not high enough to lead to the desired product. It is interesting to note that strong electric fields promote oriented intercalative polymerization of pyrrole inside the lamellar matrices of V_2O_5 xerogels. The resulting nanocomposites show electric anisotropy in the 100 and 010 crystallographic directions [29].

The interlayer expansions shown in Table 6.2 take into account the removal of the loosely bound layer of water from the gallery space of the host, upon intercalation of the polymer.

Murugan *et al*. reported on the intercalation of electrically conductive poly(3,4-ethylene dioxythiophene) (PEDOT) into crystalline V_2O_5. PEDOT is a stable, environmentally friendly polymer with potential applications in supercapacitors and lithium ion batteries. PEDOT was encapsulated into V_2O_5 by treatment of the latter with the monomer (3,4-ethylene dioxythiophene). The reaction is essentially an *in situ*

Table 6.2 *Polymer/intercalated phases of $V_2O_5.nH_2O$*

Intercalate	d-Spacing (Å)	Net interlayer expansion (Å)
$(PANI)_{0.06}V_2O_5 1.0H_2O$	13.92	5.17
$(PANI)_{0.21}V_2O_5 0.56H_2O$	13.92	5.17
$(PANI)_{0.37}V_2O_5 0.62H_2O$	13.94	5.19
$(PANI)_{0.44}V_2O_5 0.5H_2O$	13.94	5.19
$(Ppy)_{0.22}V_2O_5.0.68H_2O$	11.44	2.69
$(Ppy)_{0.26}V_2O_5.0.36H_2O$	16.60	7.85
$(Ppy)_{0.32}V_2O_5.0.48H_2O$	14.56	5.81
$(Ppy)_{0.44}V_2O_5.\ nH_2O$	11.44	2.69
$(Ppy)_{0.64}V_2O_5.0.50H_2O$	14.55	2.8
$(C_8H_4S_2)_{0.08}V_2O_5{\cdot}0.60H_2O$	14.55	5.8
$(C_8H_4S_2)_{0.20}V_2O_5{\cdot}0.65H_2O$	14.57	5.82
$(C_8H_4S_2)_{0.44}V_2O_5{\cdot}0.60H_2O$	14.70	5.95

Data derived from Reference [28].

intercalation/polymerization process and can be carried out in water under reflux condition for 12 hours [30] or for a much shorter reaction time of 8 min under microwave irradiation [31].

The direct intercalation of polyaniline doped with 12-phosphormolibdic acid (PANI-PMA) into V_2O_5 xerogels was reported by Posudievsky *et al*. Treatment of an aqueous solution of the xerogel or its lithium bronze with a solution of PANI-PMA in *m*-cresol, in equal amounts, led to the formation of $(PANI\text{-}PMA_{0.07})_{0.34}V_2O_5$. The conductivity of the nanocomposite was found to be 5.0×10^{-2} S cm^{-1} [32].

Li and Ruckenstein. reported on the intercalation of conductive polyaniline into mesostructured V_2O_5 containing a small amount of Mg. The mesoporous structure was synthesized by starting with the dissolution of V_2O_5 into a dilute solution of sodium hydroxide. The resulting solution was then added to a dilute hydrochloric acid solution, containing a mixture of surfactants, cetyltrimethylammonium bromide (CTAB) and hexadecylamine (HDA) in a 1:1 mole ratio, in the presence of magnesium chloride, which served as the structure stabilizer. The mixture was stirred at room temperature for 24 hours and then allowed to age at room temperature for a week. The solid mesoporous material was recovered by filtration, washed with distilled water until neutral, and dried at 100 °C. To allow for complete removal of surfactants, the mesostructured material was heated at 450 K, followed by extraction with a mixture of ethanol and water, and then dried. Aniline was then allowed to diffuse into the pores of the nanostructured material, in the presence of dilute hydrochloric acid. The insertion reaction was done under a nitrogen blanket. The resulting solution was then exposed to air to allow for the oxidation of aniline to polyaniline. The externally lying polymer chains were removed by washing with acetone and ethanol. It was found that the V_2O_5/PANI system showed an increase in electrical conductivity when allowed to age at room temperature in air, and this has been ascribed as the head-to-tail coupling of the short PANI chains into longer chains [33].

The hydrothermal synthesis of polyaniline-V_2O_5 nanocomposites with nanosheet morphology has been reported by Zhang and coworkers [34]. Reacting V_2O_5 powder with aniline, in the presence of water and hydrochloric acid, in an autoclave at 120 °C for 24 hours resulted in the formation of polyaniline-V_2O_5 intercalated

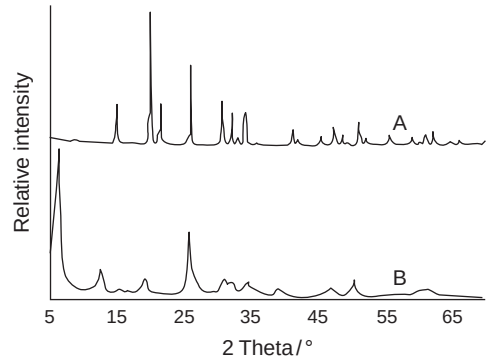

Figure 6.6 *XRD pattern of: (A) V_2O_5 precursor; (B) PANI/V_2O_5 nanocomposite nanosheets. (Reprinted with permission from Macromolecular Rapid Communications, Synthesis of polyaniline-vanadium oxide nanocomposite nanosheets by S. Pang, G. Li and Z. Zhang, 26, 1262–1265. Copyright (2005) Wiley-VCH)*

nanosheets. Evidence of intercalation was obtained from powder X-ray diffraction (Figure 6.6), and FTIR studies confirmed the identity of the entrapped polymer. Scanning electron microscopy revealed that the morphology of the composite materials was affected by the reaction conditions. An increase in aniline concentration from 0.008 M to 0.032 M resulted in a decrease of the thickness of the nanosheets from 40–50 nm to 10–20 nm. It was also observed that it was difficult to obtain thickness less than 10 nm by controlling the concentration of aniline. Temperature also played an important role in the synthesis, as it affected the resulting morphology of the nanosheets. Nanosheets could be obtained by performing the reaction with 0.016 M aniline at 80 °C for 24 hours; however, lowering the temperature of the reaction to room temperature resulted in the formation of rod-like PANI-V_2O_5 composites.

Luca and coworkers reported on the electrosynthesis of macroporous polyaniline-V_2O_5 nanocomposites [35]. This is a novel two-step electrochemical method. The electropolymerization of macroporous PANI films was first carried out from 0.25 M aniline solution in 1M $HClO_4$. The PANI films were grown on the surface of a titanium plate for 1 hour using a current density of 0.08 mA cm^{-2}. The polymer-coated electrode was washed with 1 M $HClO_4$ to remove oligomeric PANI and excess aniline. After drying in air, it was used as the working electrode for the electrodeposition of V_2O_5 from a 1 M aqueous $VOSO_4$ solution under a constant current density of 1–5 mA cm^{-2} for 30 min, at room temperature. SEM and TEM characterization on the PANI-V_2O_5 film revealed a macroporous fibrous network structure consisting of interconnecting fibrils with an average diameter of 100–150 nm (Figure 6.7). The thickness of the film was typically 3–5 μm. It was found that experimental conditions such as current density and deposition time affected the morphology of the electrodeposited PANI-V_2O_5 film. When a low current density of 1 mA cm^{-2} was used, the fibrillar structure of the PANI-V_2O_5 nanocomposite was similar to that of the parent polyaniline. Increasing the current density to 3 mA cm^{-2} coarsened the fibrils, thereby reducing the void space in the

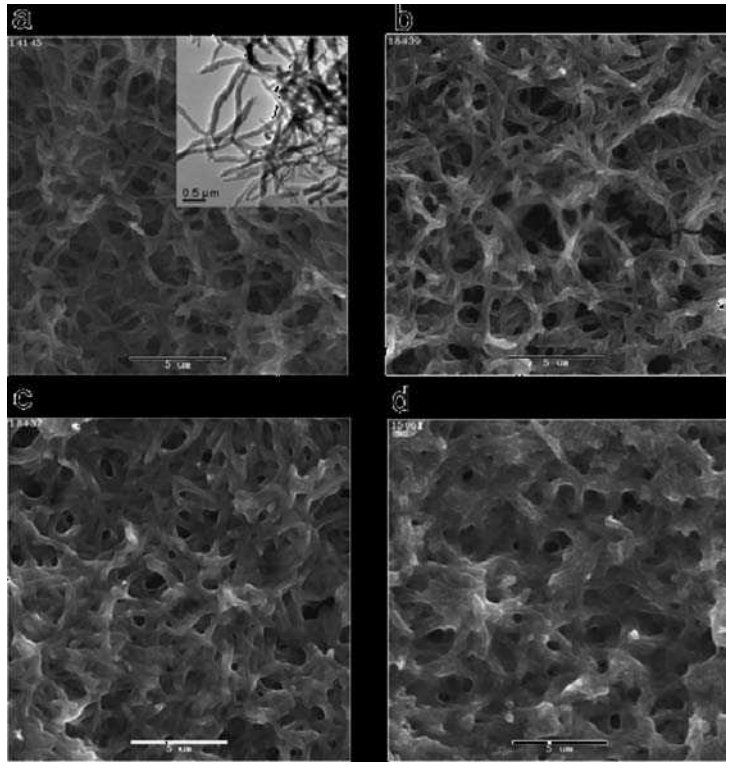

Figure 6.7 *SEM and TEM (a, inset) images of as-prepared PANI and PANI-V_2O_5 nanocomposites deposited for 30 min as a function of current densities of (mA cm^{-2}): (b) 1, (c) 3, and (d) 5. (Reprinted with permission from Chemistry of Materials, Electrosynthesis of Macroporous Polyaniline-V_2O_5 Nanocomposites and Their Unusual Magnetic Properties by I. Karatchevtseva, Z. Zhang, J. Hanna and V. Luca, 18, 20. Copyright (2006) American Chemical Society)*

structure. Further increase in current density produced a denser structure, with reduced void spaces.

Oliveira *et al*. prepared PANI-V_2O_5 nanocomposite films via a layer-by-layer (LBL) technique [36]. V_2O_5 was synthesized by a sol-gel method, by adding vanadyl tri-(isopropoxide) ($VC_9H_{21}O_4$) to water, and evaporating the resulting solution under vacuum at 70 °C in order to achieve a V_2O_5 concentration of 0.02 M. The emeraldine base form of PANI was dissolved in dimethyl acetamide (DMAc). The PANI solution was filtered, and HCl was slowly added until a pH of 2.0 was attained. An indium–tin-oxide sheet (1 cm^2) was alternately immersed for 3 min into the polycationic solution (PANI) and polyanion (V_2O_5) dispersions. Following each deposition the substrate was rinsed for 1 min with HCl solution (pH = 2). This procedure led to the formation of LBL V_2O_5/PANI films. LBL films were also deposited on quartz crystals. V_2O_5/PANI films produced via the LBL technique were shown to promote enhancement of charge storage capability, new electrochromic effects, and control of ionic flux.

Torresi and coworkers reported on the intercalation of polyaniline into V_2O_5 nanotubes. The nanotubes were prepared by treating crystalline V_2O_5 with an ethanolic solution of hexadecylamine. The mixture was vigorously stirred for a couple of hours, and to the mixture was added a limited amount of ultrapure water. The reaction mixture was aged for 48 hours, followed by hydrothermal treatment at 180 °C for a week. It was washed with water followed by absolute ethanol, and then dried under vacuum. The final product, V_2O_5 nanotubes, intercalated with the protonated from of hexadecylamine, were cation-exchanged with protonated PANI (doped with camphor sulfonic acid), to afford PANI/V_2O_5 nanotubes [37].

Wu *et al*. reported on the fabrication of a conductive polyaniline/V_2O_5 composite by simply mixing water-soluble poly-aniline-propane sulfonic acid (PAPSA) with wet V_2O_5 xerogel [38]. The nanomaterial was isolated as a thin film on glass or silicon wafer, by using the dip-coating method. XRD provided evidence for the intercalation of a monolayer of PAPSA in the gallery space of the layered host system. It is interesting to note that the XRD pattern of the nanocomposite reveals six distinguishable (00*l*) reflections (Figure 6.8), attributed to the structure-directing ability of the PAPSA guest species, to construct a well-ordered V_2O_5 framework.

Polypyrrole-vanadium pentoxide hybrid aerogels were prepared by Dunn and coworkers [39]. Two sol-gel routes were employed. The first method involved simultaneous polymerization of pyrrole and vanadyl alkoxide precursors. Hydrolysis of $VO(OC_3H_7)_3$ with mixtures consisting of pyrrole, water, and acetone, over a range of compositions, resulted in green-black gels, which upon supercritical drying afforded polypyrrole/V_2O_5 aerogels composites. These composites were shown to display high surface areas. The second method involved oxide gel formation in the presence of a colloidal suspension of

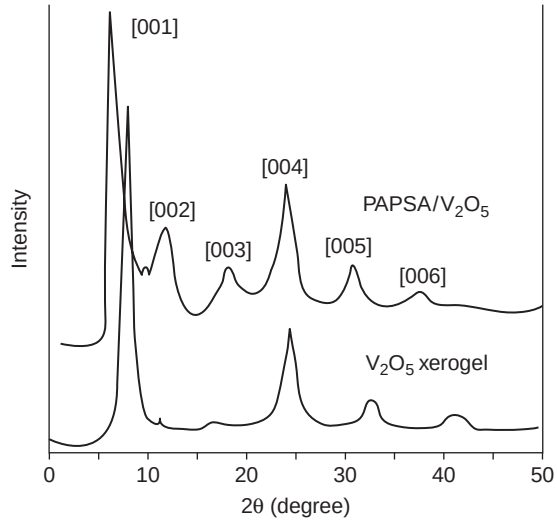

Figure 6.8 *XRD patterns of PAPSA/V_2O_5 and V_2O_5. (Reprinted with permission from Synthetic Metals, Assembly of conducting polymer/metal oxide multlayer in one step by C.-O. Wu, Y.-C. Liu and S.-S. Hsu, 102, 1–3. Copyright (1999) Elsevier Ltd)*

polypyrrole. In this synthetic route, the polymer colloids are poured into vanadyl alkoxide solutions, shaken quickly, and then allowed to form gels upon drying and aging. Supercritical drying of these gels produced V_2O_5 aerogels intercalated with polypyrrole.

The intercalation of polyethylene oxide (PEO) into V_2O_5 xerogels was also explored. Interest in PEO lies in the fact that this polymer exhibits ionic conductivity when complexed with salts, in particular those of lithium. Hence, PEO could potentially be used as a solid electrolyte in solid-state lithium batteries. The intercalation of PEO or of its salt complex into layered structures can produce nanomaterials for battery applications where the diffusion of lithium ions from the lithium anode to the nanomaterials could be enhanced because of the lowered activation energy of the process. The intercalation of PEO into V_2O_5 xerogels was easily accomplished by simply mixing aqueous solutions of PEO with aqueous gels of V_2O_5 in varying ratios, as demonstrated by Kanatzidis *et al*. [40]. The interlayer spacing of the PEO/V_2O_5.nH_2O phase was shown to be 13.2 Å, corresponding to a net interlayer expansion of 4.5 Å. This is consistent with having a single layer of the polymer chain sandwiched in between the V_2O_5 slabs (Figure 6.9). It was also demonstrated that PEO/V_2O_5.nH_2O can be intercalated with lithium ions by reacting with lithium iodide through a redox process.

Using a similar synthetic methodology, other water soluble polymers, such as poly(vinylpyrrolidinone) (PVP), poly(propylene glycol) (PPG), and methyl cellulose (MCel) were intercalated into V_2O_5.nH_2O xerogels [41]. The ratio of intercalated polymer to the layered host could be synthetically manipulated. Similarly to PEO, PVP, PPG, and MCel could also function as solid electrolytes when complexed with lithium salts, and hence their relevance in lithium battery applications. The intercalation of PEO into V_2O_5nH_2O was also reported by Ruiz-Hitzky *et al*. [42].

PEO is a semicrystalline material, and it has been demonstrated that ions move much better in the amorphous part of the polymer. Thus, there has been a focus towards solid polymer electrolytes (SPEs) that are completely amorphous, and therefore display higher

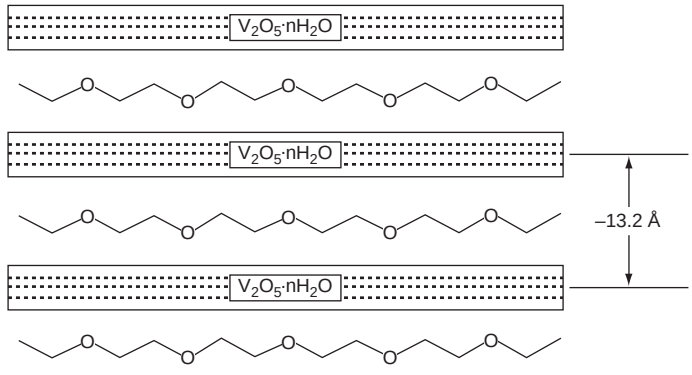

Figure 6.9 *Lamellar arrangement of PEO/V_2O_5.nH_2O composite. (Reprinted with permission from Chemistry of Materials, Intercalation of poly(ethylene oxide) in vanadium pentoxide (V_2O_5) xerogel by Y. J. Liu, D. C. DeGroot, J. L. Schindler et al., 3, 6. Copyright (1991) American Chemical Society)*

ionic conductivity values. One such polymer is poly[oxymethylene-(oxyethylene)], a derivative of PEO which has been referred to as amorphous PEO (a-PEO) or POMOE. POMOE displays high ionic conductivity when complexed with lithium salts, such as lithium triflate ($LiCF_3SO_3$). For instance, the room-temperature ionic conductivity of $(POMOE)_{25}LiCF_3SO_3$ is $3 \times 10^{-5}\,S\,cm^{-1}$ [43]. The intercalation of POMOE into $V_2O_5.nH_2O$ was reported by Shriver *et al*. $V_2O_5[(a\text{-}PEO)_n\ LiCF_3SO_3]_x$ ($n = 10-24$, $x = 0.01 - 0.05$) were prepared by passing an aqueous solution of NH_4VO_3 through a proton exchange resin (Dowex 50-W, 50X-100) and then adding aqueous solutions of a-PEO and $LiCF_3SO_3$ in appropriate concentrations. The resulting composites were isolated as thin films. Evidence of intercalation was provided from powder X-ray diffraction [44].

Posudievsky and coworkers prepared ternary composites consisting of both PANI and PEO intercalated between V_2O_5 xerogels [45]. Two different strategies were used. $PANI_{0.29}PEO_{0.86}V_2O_50.57H_2O$ was synthesized by treating the intercalation compound of PEO into V_2O_5 (PEO-V_2O_5) with aniline into order to induce *in situ* intercalative polymerization of the latter. On the other hand, $(PANICSA_{0.12})_{0.62}.PEO_{0.85}V_2O_5.0.85H_2O$ was prepared by adding an *m*-cresol solution of polyaniline doped with camphor sulfonic acid ($PANICSA_{0.5}$) to an aqueous solution of PEO-V_2O_5 nanocomposite. The interlayer gallery height for these two ternary phases was 5.6 Å, and based on this observation it was suggested that the PANI inserts between PEO macromolecules, but not between PEO macromolecules and V_2O_5 sheets. The performance of the ternary nanocomposites as cathode materials in lithium electrochemical cells were investigated, and it was found that the after five cycles, the charge capacity was 150 (mAh) g^{-1}, which was approximately 1.2 times larger than that of PANI-V_2O_5, and 1.5 times larger than that of pristine V_2O_5 xerogel.

A ternary composite consisting of polyaniline, the clay mineral bentonite, and $V_2O_5.nH_2O$ was reported by Toma *et al*. [46]. The nanocomposite material (BV) was first prepared as an aqueous suspension, by combining an aqueous solution of polyvanadic acid (precursor of $V_2O_5.nH_2O$) with an aqueous suspension of bentonite. The excess water was decanted and the residue was treated with dry acetonitrile in order to obtain an organic suspension of the material; the latter procedure was repeated several times in order to obtain a water-free BV sample. Treatment of the acetonitrile BV suspension with acetonitrile solutions of aniline (of varying concentrations) resulted in the formation of $(PANI)_xBV$ ternary composites, with values of x ranging from 0.7 to 1.8. XRD confirmed the formation of lamellar materials, and it is interesting to observe an increase in interlayer spacing value of the ternary phase as a function of polymer content. Along similar lines, ternary composites consisting of BV and polypyrrole have also been reported by the same group of researchers [47].

Ternary composites with electroactive components were also discussed by Gomez-Romero and coworkers in one of their recent publications [48]. The ternary composites consisted of doped-polyaniline (PANI) or doped-polypyrrole (Ppy) intercalated into V_2O_5 xerogels. The dopant anion for the conducting polymers was $[Fe(CN)_6]^{3-}$ (HCF), derived from $H_3Fe(CN)_6$. More specifically, the synthesis of Ppy/HCF/V_2O_5 and PANI/HCF/V_2O_5 was carried out by treating the monomer (aniline or pyrrole)

with V_2O_5 gel solutions in the presence of $H_3Fe(CN)_6$. The electrochemical performance of Ppy/HCF/V_2O_5 was evaluated in lithium rechargeable batteries, and it was shown to demonstrate a high initial specific charge value of 160 Ah kg^{-1}, despite poor cyclability.

6.4 $VOPO_4.2H_2O$

Similarly to FeOCl and V_2O_5 xerogels, $VOPO_4.2H_2O$ is a layered material capable of undergoing redox intercalative polymerization. It is synthesized by refluxing a mixture of V_2O_5, H_3PO_4, and water for 16 hours. The structure of $VOPO_4.2H_2O$ can be described as consisting of $VOPO_4$ sheets which are made up of VO_6 octahedra and PO_4 tetrahedra linked through the corners (Figure 6.10). In addition, there is a water molecule bound to each of the vanadium centers, with interlamellar water hydrogen bonded to the coordinated water [49].

$VOPO_4.2H_2O$ is capable of undergoing *in situ* intercalation/polymerization with molecules such as aniline [50, 51], substituted anilines [52, 53, 54], and pyrroles [55]. Evidence of intercalation was obtained from powder X-ray diffraction. As an example, the powder pattern of poly(*N*-methylaniline) (PMA) intercalated into $VOPO_4$ is illustrated in Figure 6.11. The identity of the intercalated polymer was confirmed by Fourier-transform infrared studies.

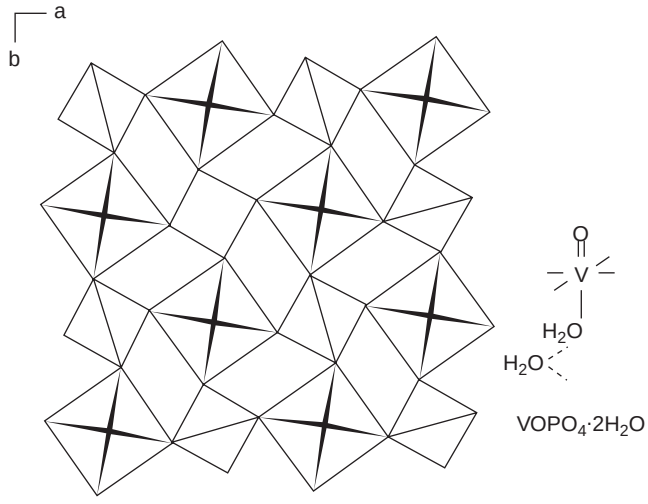

Figure 6.10 *Structure of $VOPO_4.2H_2O$. (Reprinted with permission from Inorganic Chemistry, Coordination intercalation reactions of the layered compounds vanadyl phosphate ($VOPO_4$) and vanadyl arsenate ($VOAsO_4$) with pyridine by J. W. Johnson, A. J. Jacobson, J. F. Brody and S. M. Rich, 21, 10. Copyright (1982) American Chemical Society)*

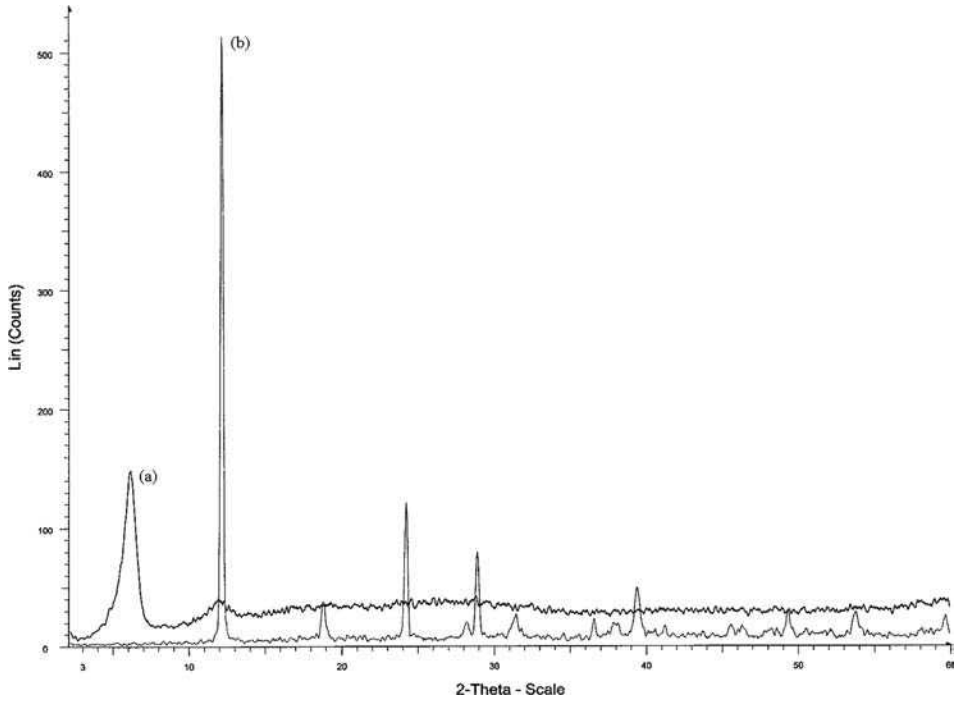

Figure 6.11 *XRD of: (a) PMA/$VOPO_4$ and (b) $VOPO_4.2H_2O$. (Reprinted with permission from Solid State Sciences, Novel alkyl substituted polyanilines/$VOPO_4$ nanocomposites by R. Bissessur and J. MacDonald, 8, 5, 531–536. Copyright (2006) Elsevier Ltd)*

6.5 MoO_3

MoO_3 is an interesting compound with a unique layered structure consisting of 7.0 Å thick double layers of edge- and corner-sharing MoO_6 octahedra [56] (see Figure 6.12). It is an important component of many industrial catalysts. The intercalation of MoO_3 has been explored to an appreciable extent in recent years, owing to its high crystallinity, its potential applications in lithium high-energy-density batteries and in electrochromic devices.

However, of particular interest has been the intercalation of electrically conductive polymers into this layered structure. The intercalation of polyaniline into MoO_3 has been performed by using different methodologies. It should be pointed out that, unlike FeOCl, $V_2O_5.nH_2O$, and $VOPO_4.nH_2O$, MoO_3 is not oxidizing enough to undergo *in situ* intercalation/polymerization. The insertion of aniline into MoO_3 formed $(C_6H_5NH_3^+)_x(C_6H_5NH_2)_yMoO_3$, where $x + y = 0.4$, as determined by thermogravimetric analysis. Treatment of the resulting intercalate with two equivalents of an aqueous solution 0.4 M solution of $(NH_4)_2S_2O_8$ led to the formation of $(PANI)_{0.7}MoO_3$ [57].

The intercalation of polyaniline into MoO_3 was also reported by Nazar [58]. This was achieved by reacting mixed alkali hydrated bronze of MoO_3

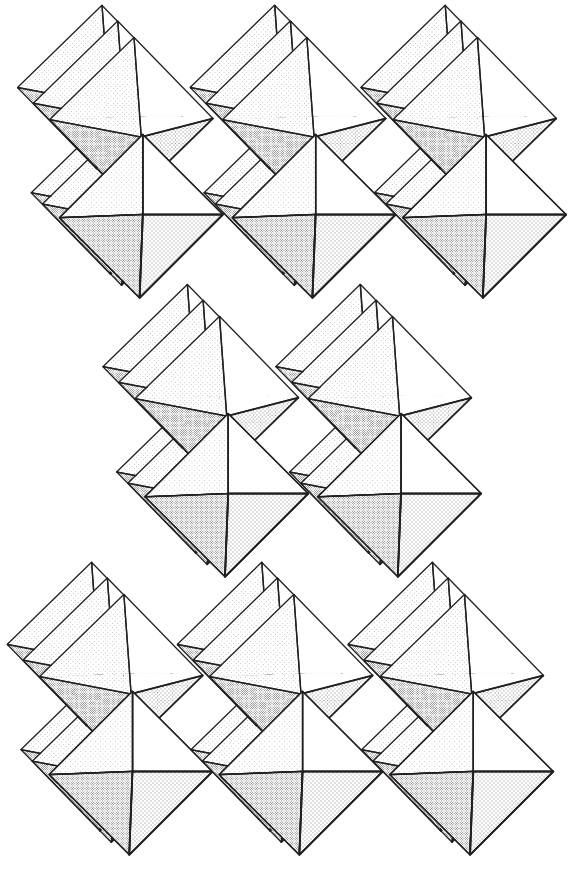

Figure 6.12 *Structure of MoO_3. (Reprinted with permission from Materials Chemistry and Physics, Preparation and characterization of layered molybdenum trioxide pillared with chromia by X. Wang, W. Hou, X. Guo and Q. Yan, 73, 1. Copyright (2002) Elsevier Ltd)*

($[Li^+]_{0.09}[Na^+]_{0.15}(H_2O)_n[MoO_3]^{-0.25}$) with excess aniline, followed by addition of two equivalents of $FeCl_3$. The composition of the resulting material was $[PANI]_{0.24}MoO_3$.

It is also interesting to note that polyaniline doped with camphor sulfonic acid (PANI-CSA) was intercalated into MoO_3. This was achieved by adding PANI-CSA dissolved in *m*-cresol to an aqueous sol of Li_xMoO_3. The stoichiometry of the intercalate as determined from elemental analysis was $(PANI\text{-}CSA_{0.124})_{1.06}MoO_3$. Evidence of intercalation was obtained from powder X-ray diffraction [59].

Using a one-pot reaction design, an intercalated compound of polyaniline into MoO_3 was prepared by Shao *et al*. [60]. This particular method of synthesis uses a coprecipitation route to fabricate the layered structure. An excess of aniline was acidified to a pH of 0.5, to which was added ammonium molybdate $[(NH_4)_6Mo_7O_{24}.7H_2O]$ and $FeCl_3$. The powder pattern of the isolated product revealed the formation of an intercalated phase of polyaniline into MoO_3. The identity of the entrapped polymer was confirmed by FTIR

spectroscopy. The composition of the material as determined by TGA was $[PANI]_{0.35}MoO_3(H_2O)_{1.11}$. This one-pot coprecipitation route can be exploited to synthesize a wide range of novel nanocomposite materials based on MoO_3.

Hill and coworkers also reported on the intercalation of polyaniline into MoO_3 [61]. The reduction of MoO_3 was, first and foremost, achieved by treatment with an excess of a saturated solution of $Na_2S_2O_4$. This yielded a hydrated sodium bronze of MoO_3, i.e., $Na_x(H_2O)_yMoO_3$. The sodium ions in the bronze were then exchanged with a mixture of aniline and anilinium ions to give an intercalated material, formulated as $(C_6H_5NH_2)_x(C_6H_5NH_3^+)_zMoO_3$; the value of x + z as determined from TGA was found to be 0.4. Powder X-ray diffraction measurements on $(C_6H_5NH_2)_x(C_6H_5NH_3^+)_zMoO_3$, revealed an interlayer spacing value of 13.56 Å, suggesting a bilayer arrangement of the monomers in the gallery space of the layered host. Treatment of the monomer/MoO_3 phase with iodine vapour was shown to initiate polymerization. It should be noted that iodine is a mild oxidizing agent, and it is most likely that oligomeric species of PANI were formed in between the MoO_3 slabs. The interlayer spacing of the PANI/MoO_3 phase was 13.26 Å, a decrease of only 0.3 Å compared to the monomer intercalated phase.

Polyaniline was intercalated into MoO_3 by an *ex situ* three-step process [62]. Using $Mo(CO)_6$ at 40 °C, a thin film of MoO_3 was deposited by chemical vapor deposition on a $LaAlO_3$ (100) substrate at 500 °C for 15 min. The pressure of oxygen was kept at around 106 Pa, with a rate of flow of 100 ml min^{-1}. The MoO_3 thin film was then immersed for 80 s in an aqueous solution consisting of $Na_2MoO_4.2H_2O$ and $Na_2S_2O_4$, purged with argon gas. This caused reduction of the MoO_3 thin film into a blue Na_xMoO_3 thin film. The Na_xMoO_3 thin film was air-dried at 80 °C for 30 min, and then immersed for 30 s into a polyaniline suspension, previously prepared by reacting an acidified solution of aniline with ammonium peroxydisulfate for 30 min, under an argon blanket. Evidence of intercalation was provided by powder X-ray diffraction. The interlayer spacing of the $(PANI)_xMoO_3$ thin film was 13.6 Å, consistent with having a single layer of the polymer chain sandwiched in between the MoO_3 sheets. The $(PANI)_xMoO_3$ thin film was shown to exhibit an increase in electrical conductivity in response to volatile organic compounds, with good sensitivity and selectivity towards formaldehyde and acetaldehyde vapors.

As noted above, the intercalation of conductive polyaniline into MoO_3 has been a major focus of attention. However, it is worthwhile to note the intercalation of conducting poly(*p*-phenylenevinylene) (PPV) in layered MoO_3 [63]. PPV displays high electronic conductivity and a large nonlinear optical susceptibility, both of which properties are dependent on the orientation and alignment of the polymer chains. An intercalated nanomaterial of PPV into MoO_3 was obtained by using a series of steps. Mixed alkali hydrated bronzes of MoO_3, $Na_xLi_y(H_2O)_zMoO_3$ were first cation-exchanged with the precursor of PPV, poly(*p*-xylylene-α-dimethyl sulfonium chloride, MW 10^5 Da). The resulting polymer intercalated phase was then heated in air or under nitrogen to yield $(PPV)_xMoO_3$.

With MoO_3 as a host system, the intercalation of polymers with solid electrolyte properties has also been reported. For instance, Nazar and coworkers were able to introduce PEO between the layers of MoO_3 [64]. Sodium ions were first intercalated into MoO_3 by treatment with an aqueous solution of $Na_2S_2O_4$ to produce the hydrated metal bronze, $Na_{0.25}(H_2O)_nMoO_3$. Treatment of an aqueous suspension of $Na_{0.25}(H_2O)_nMoO_3$ with an aqueous solution of PEO (MW: 100 000) resulted in the

incorporation of a monolayer of PEO between the MoO_3 layers. The composition of the resulting intercalated phase, as determined by chemical and thermogravimetric analysis, was $(PEO)_{0.4}[Na(H_2O)_{1.0}]_{0.25}MoO_3$. The authors found that bilayer composites were more readily achievable from $Na_{0.25}(H_2O)_nMoO_3$ that were ion-exchanged with Li. During the preparation of the bronze, Li_2MoO_4 was used as a buffer, resulting in a mixed-metal bronze formation, i.e. $[Li,Na]_{0.25}MoO_3$. The resulting material was ion-exchanged with LiCl to yield '$LiMoO_3$'. Treatment of '$LiMoO_3$' with a water–methanol mixture of PEO resulted in an intercalated nanocomposite whose composition was determined to be $(PEO)_{0.9}[Li_{0.6}Na_{0.4}(H_2O)_{0.5}]_{0.25}MoO_3$. Powder X-ray diffraction data support the formation a bilayer arrangement of the polymer chains in between the MoO_3 sheets.

Kanatzidis and coworkers reported on the intercalation of poly(ethylene oxide) (PEO), poly(ethylene glycol) (PEG), poly(propylene glycol) (PPG), poly(vinylpyrrolidinone) (PVP), and methyl cellulose (MCel) into MoO_3 [65]. Commercially available MoO_3 was heated in an open quartz vial in air at 600 °C for almost two days. A dramatic increase in the crystallite size of the MoO_3 was observed. The material was then reacted with $LiBH_4$ in a 1:0.4 molar ratio for a day, under nitrogen atmosphere. This method of lithiation produced a quantitative yield of the lithium molybdenum bronze (Li_xMoO_3). The value of x ranged from 0.3 to 0.4, as shown by elemental analyses and thermogravimetric analysis. Li_xMoO_3 exfoliates readily in water and addition of the suspension to an excess solution of the polymer in water, followed by stirring under nitrogen for two days resulted in the formation of polymer-MoO_3 nanocomposite. It is interesting to note that the nanocomposite of MCel was isolated as a precipitate, whereas the others remained as colloidal suspensions and were isolated to dryness by pumping off the water. It was found that the MW of the PEO had no effect on the interlayer spacing of the composite. PEO (MW: 5 000 000 and 100 000) gave a similar interlayer spacing value of 16.6 Å. For PEO of lower MW, i.e. PEG, the observed interlayer spacing value was found to be dependant on the MW value of the polymer. In general, it was established that the lower MW of the polymer (PEG), the smaller is the observed interlayer spacing value.

Chen and coworkers also reported the intercalation of PEO into MoO_3 xerogel ($MoO_3.nH_2O$) [66]. Similar to MoO_3, MoO_3 xerogel is also layered. The xerogel was prepared by the ion exchange of $(NH_4)_4Mo_7O_{24}.4H_2O$ through a proton-exchange resin. After ion-exchange a clear light blue $MoO_3.nH_2O$ sol (pH: 2.0) was observed. Addition of an aqueous solution of PEO (MW: 400 000) to the sol produced a mixed sol. The ratio of polymer to the MoO_3 sol was varied to produce composites with composition $(PEO)_xMoO_3.nH_2O$ (where $x = 0.5$, 1, and 2). The composites were isolated as thin membranes on glass substrates using a dip-coating method. Thin films were then obtained by heating the composite membranes for 36 hours at 380 °C in a nitrogen atmosphere.

6.6 Layered Phosphates and Phosphonates

The intercalation of polyaniline into hydrogen uranyl phosphate $HUO_2PO_4.4H_2O$ (HUP) was reported by Liu and Kanatzidis [67]. HUP is a layered material with an interlayer-spacing value of 8.69 Å. The layers consist of dumb-bell-shaped UO_2^{+} ions with uranium further coordinated to four equatorial oxygen atoms of four PO_4^{3-} tetrahedra. The van der

Waals gap of the host consists of two layers of water molecules, which are hydrogen-bonded to each other. Reaction of HUP with an excess of aniline in water resulted in the formation of an intercalated phase $(C_6H_5NH_3)UO_2PO_4 0.5H_2O$ (AUP), with an interlayer spacing value of 10.49 Å. Heating AUP in air at 130 °C resulted in the formation of $(PANI)_{0.94}UO_2PO_4 0.4H_2O$ (PUP), with an interlayer-spacing value of 11.8 Å. Pressed pellets of PUP did not show any electrical conductivity, due to the fact that the polymer was embedded inside an insulating host matrix. The intercalated polymer was extracted by dissolution of the host in dilute HCl solution, and a low room-temperature conductivity of 10^{-5} S cm^{-1} was observed. The low conductivity of the polyaniline was attributed to cross-linking, due to the relatively high temperature of the solid-state polymerization. As an extension to their previous report, Liu and Kanatzidis investigated the intercalation of aniline, as well as its dimer, *N*-phenyl-1,4-phenylenediamine (PPDA) into α-$Ti(HOPO_3)_2.2H_2O$ and α-$Zr(HOPO_3)_2.2H_2O$ [68]. For the case of α-$Zr(HOPO_3)_2.2H_2O$, it was experimentally observed from powder X-ray diffraction that both aniline and its dimer intercalated in a somewhat tilted bilayer configuration. Subsequent heating of the intercalates at 130 °C resulted in the formation of a bilayer arrangement of PANI chains in the gallery space of the layered host. On the other hand, it was found that only aniline molecules were capable of intercalating into α-$Ti(HOPO_3)_2.2H_2O$ in a bilayer arrangement. Heating the resulting material in air at 130 °C resulted in the formation of a monolayer arrangement of PANI in the layered host matrix.

The intercalation of PANI in zirconium phosphate (ZrP) was also reported by Chang *et al*. [69]. Different phases of zirconium phosphate, such as γ-ZrP, the dihydrogen form of α-ZrP [α-ZrP(HH)], and α-ZrP(NaNa), were intercalated with aniline by either ion-exchange or adsorption, and then polymerized by oxidizing agents such as ammonium peroxydisulfate and iron (III) chloride. The resulting polyaniline nanocomposites showed measurable electrical conductivities, as listed in Table 6.3.

Chang *et al*. also reported on the intercalation of aniline into zirconium phosphate sulfophenylphosphonate (ZPS), an organo derivative of α-zirconium phosphate [70]. The hydrophilic ($-SO_3H$) groups in ZPS promote swelling of ZPS, which served as a template for aniline. The aniline-ZPS system was then oxidized with ammonium peroxydisulfate to yield a polyaniline-ZPS composite. However, there is no X-ray evidence that has been provided to support the formation of an intercalated phase.

The intercalation of PANI into α- and γ-zirconium hydrogen phosphates was also reported by Bonnet *et al*. [71]. These layered structures were partially exchanged with Cu^{2+} ions, resulting in the formation of phases with compositions, α-$ZrCu_{0.6}H_{0.8}(PO_4)_2.4H_2O$ and γ-$ZrCu_{0.7}H_{0.6}(PO_4)_2.4H_2O$. Treatment of these bi-phasic

Table 6.3 *Conductivity data for PANI samples*

Sample	Conductivity (S cm^{-1})
PANI-α-ZrP(HH)	1×10^{-3}
PANI extracted from PANI-α-ZrP(HH)	1×10^{-1}
PANI-α-ZrP(NaNa)	3×10^{-6}
PANI-γ-ZrP	3×10^{-4}

From reference [69].

phases with aniline guest species resulted in their intercalation as anilinium ions due to proton transfer from the acidic hosts. The interlayer anilinium was subsequently oxidized by the Cu^{2+}, which behaved as the oxidizing agent. The formation of interlamellar polyaniline was confirmed by FTIR spectroscopy.

The intercalation of polyaniline into a layered tin(IV) phosphonate was described by De Paoli *et al*. [72]. The layered host system was synthesized by reacting organophosphonic acid ($HOOCH_2CH_2PO_3H_2$) with $SnCl_4$ in the presence of dilute HNO_3. The protons of the carboxylic acid groups in the layered host system were then exchanged with different amounts of Fe^{3+} ions, and then treated with an acidic solution of aniline to yield polyaniline intercalated phases. The materials were characterized by powder X-ray diffraction to support intercalation of the polymer. Electrical conductivity measurements on these materials were low (10^{-9} Scm^{-1}), providing supporting evidence that the polyaniline is, in fact, intercalated, since externally lying PANI would show a pronounced increase in electrical conductivity.

6.7 Layered Rutiles

Koene and Nazar intercalated aniline into the trirutile-like layered oxides, $HMWO_6.nH_2O$ (M = Ta, Nb) by making use of the strong Brønsted acidity of the layered hosts [73]. The resulting intercalated phase, $[Aniline]_{0.68}HMWO_6$, displayed an interlayer spacing value of 20.02 Å, a 11.1 Å interlayer expansion with respect to the pristine layered hosts. This is consistent with a bilayer arrangement of the aniline molecules in the gallery space of the inorganic host matrices. Thermal treatment of $[Aniline]_{0.68}HMWO_6$ in air resulted in evaporation of half of the aniline molecules, along with polymerization of the remaining half within the layers of the host. The stoichiometry of the polyaniline nanocomposite was $PANI_{0.34}HMWO_6$, with an interlayer spacing value of 14.5 Å, which was consistent with a single layer of the polymer chain trapped in between the lamellae of the host system. $PANI_{0.34}HMWO_6$ was shown to possess an electrical conductivity value of 1×10^{-6} S cm^{-1}, a 10^7 fold increase with respect to $[Aniline]_{0.68}HMWO_6$.

By using an exfoliation and flocculation technique, Prasad *et al*. were able to prepare a polyaniline/$NbWO_6$ hybrid material [74]. Dispersed nanosheets of $HNbWO_6$ were obtained by treating $HNbWO_6$ with tetrabutyl ammonium hydroxide. The suspension of the exfoliated layers was then added to an alcoholic solution of aniline, followed by addition of a few drops of 1 M HCl, and overnight sonication in order to induce flocculation of the aniline-$NbWO_6$ nanocomposite. The nanocomposite was isolated by centrifugation, and dried. Treatment of the nanocomposite with O_2 at 130 °C for several weeks resulted in the formation of intercalated PANI.

The polymerization of aniline in layered $HMMoO_6.H_2O$ (M = Nb, Ta) was reported by Bhuvanesh and Gopalakrishnan [75]. These layered systems, possessing the rutile-related structure, behave as Brønsted acids, and were found to readily intercalate aniline, producing intercalated phases with composition, $(C_6H_5NH_3)_xH_{1-x}MMoO_6.H_2O$ ($x \sim 0.35$). The interlayer spacing of the intercalate was 17.6 Å, corresponding to a monolayer arrangement of anilinium inside the layered host system. Oxidation of the latter in air polymerized the interlayer aniline to yield a polyaniline intercalated phase with

stoichiometry $(PANI)_xH_{1-x}MMoO_6$. The observed interlayer spacing value of $(PANI)_xH_{1-x}MMoO_6$ was 15.7 Å, also corresponding to a monolayer of the polymer sandwiched in between the layered sheets.

The polymerization of aniline in the galleries of layered $HNbMoO_6$ was also reported by Byeon *et al*. Aniline was first inserted into the structure via an acid–base reaction to produce $(anilinium)_xNbMoO_6$, which upon treatment with $FeCl_3$ as an oxidizing agent resulted in the formation of $(PANI)_xNbMoO_6$ [76].

6.8 Layered perovskites

Uma and Gopalakrishnan reported the insertion of aniline into $HCa_2Nb_3O_{10}$ and $HCa_2Nb_2MO_9$ (M = Al, Fe) [77]. The driving force of the intercalation reaction is through an acid–base reaction, with the layered perovskites behaving as solid acids. Subsequent treatment of these intercalates with $(NH_4)_2S_2O_8$ led to the formation of PANI-layered perovskite composites. It was found that pressed pellets of $(PANI)_{0.80}Ca_2Nb_3O_{10}$ showed no measurable conductivity ($<10^{-10}$ S cm^{-1}), suggesting that the polymer was intercalated, with no polymer residing on the outside of the layered host. This also corroborated well with the fact that the morphology of $(PANI)_{0.80}Ca_2Nb_3O_{10}$, as viewed under a scanning electron microscope, showed clean and smooth crystal surfaces, with no obvious signs of externally lying polymer chains. The measured electrical conductivity of the extracted polymer from $(PANI)_{0.80}Ca_2Nb_3O_{10}$ is around 10^{-5} S cm^{-1}, a rather low value, implying considerable cross-linking of the polymer.

6.9 Layered Titanates

While it is worthy to note that polyaniline-TiO_2 nanocomposites have been synthesized and characterized [78–83], it should, however, be emphasized that these nanocomposites are not intercalated, but rather consist of TiO_2 nanoparticles, in either the anatase or rutile phase, mixed with the polymer.

The protonated form of layered titanate exhibits acid-like properties and is therefore amenable to the intercalation of aniline. The synthesis of the protonated titanate is performed by mixing and grinding anatase TiO_2 with 0.2 equivalents of Cs_2CO_3 in an alumina crucible, heating the solid mixture briefly to 800 °C, regrinding and reheating the solid for a longer period of time at 800 °C. This results in the formation of a white powder with composition, $Cs_xTi_{2-x/4}\square_{x/4}O_4{\bullet}yH_2O$ where □ is a vacancy. The protonated form of the titanate ($H_xTi_{2-x/4}\square_{x/4}O_4{\bullet}yH_2O$ where $x \sim 0.7$ and $y \sim 1$) is afforded via ion exchange with 1 M HCl [84]. For simplicity, the layered titanate is simply denoted as $HTiO_2$.

Treating $HTiO_2$ with an excess of freshly distilled aniline in the presence of water resulted in the formation of a sandwiched compound whose composition is $(aniline)_{0.1}HTiO_2$, as determined by thermogravimetric analysis. Heating $(aniline)_{0.1}HTiO_2$ in air at 140 °C resulted in the oxidation of the interlamellar aniline/anilinium to produce a dark-green product, an intercalated compound of polyaniline into titanate. FTIR spectroscopy confirmed

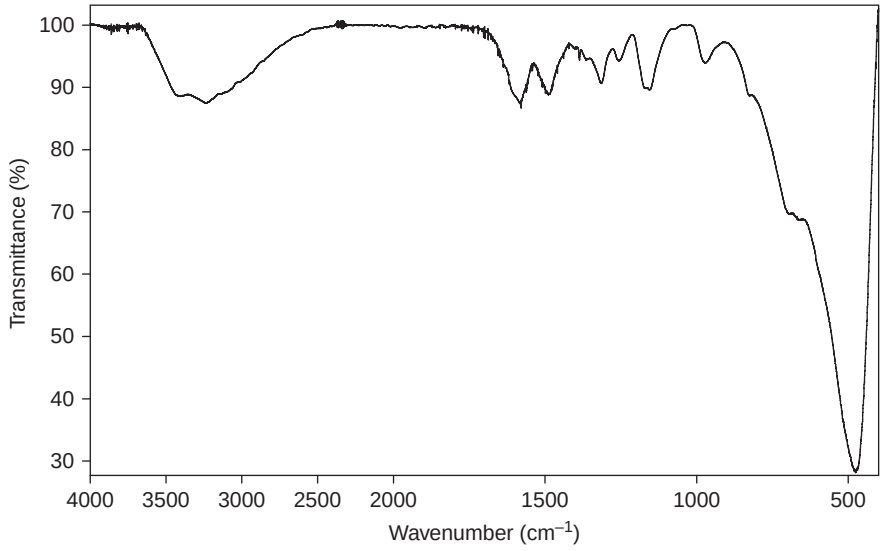

Figure 6.13 *FTIR of (polyaniline)$_{0.1}$HTiO$_2$. (Reprinted with permission from Synthetic Metals, An intercalated polyaniline-titanate nanomaterial by S. F. Scully and R. Bissessur, 159, 7–8 637–641. Copyright (2009) Elsevier Ltd)*

the characteristic signature of polyaniline (Figure 6.13). This technique also confirmed that the structure of the layered system was maintained, as depicted by the broad band between 400 and 800 cm^{-1}. It is interesting to note that when compared to chemically synthesized bulk polyaniline, all the peaks corresponding to the intercalated polyaniline are shifted to higher wavenumbers. This indicates that there is some interaction between the polymer and the layered host. This interaction is more likely to be due to hydrogen bonding between the N—H group of the intercalated polymer and the acidic proton of the layered structure. TGA data confirmed a stoichiometry of (polyaniline)$_{0.1}$HTiO$_2$, which was similar to the stoichiometry of the precursor intercalate. It is interesting to note that the aerial method of oxidation does not result in loss of monomer units [85].

Sukpirom and Lerner encapsulated PEO and PVP into HTiO$_2$ [84]. This was achieved by adding aqueous solutions of the polymers to suspensions of exfoliated HTiO$_2$ layers, followed by acidification to obtain gel-like materials. Exfoliation of the HTiO$_2$ was achieved by adding to an aqueous solution of tetrabutylammonium hydroxide, followed by ultrasonication. XRD data showed strong evidence of intercalation. The interlayer-spacing value of the PEO/HTiO$_2$ intercalate was 14.9 Å, whereas that of PVP/HTiO$_2$ was 28.8 Å.

6.10 Graphite Oxide

Graphite oxide (GO) is a layered structure that has recently attracted a considerable amount of interest in the scientific community. It can be prepared by Hummers' method through its harsh oxidation with KMnO$_4$ in concentrated sulfuric acid [86]. While the

precise structure of graphite oxide is not known, FTIR studies confirm that it contains functional groups such as COC, COOH, C═O, and OH. It has generally been accepted from ^{13}C solid-state NMR spectroscopy that the carboxyl and carbonyl functionalities tend to be located near the edges, while other functionalities such as epoxides and hydroxyl groups tend to be located on the basal planes of the layered structure. It has been found that GO exfoliates readily in water, or in dilute alkaline solution, due to deprotonation of the acidic functionalities, creating negatively charged nanoplatelets that repel each other. The colloidal suspension of GO can be reconstructed to yield restacked GO upon addition of an acidic solution. However, in the presence of foreign species the GO layers restack to form sandwiched compounds.

The intercalation of polyaniline into GO was reported by several researchers. For instance, the intercalation of polyaniline (PANI) into GO had been reported by both the Matsuo [87] and Gong [88] groups, using similar methods. A colloidal suspension of GO was first obtained by treatment with a dilute solution of sodium hydroxide. Aniline monomer was then added to the colloidal suspension followed by addition of an aqueous solution of an oxidizing agent (ammonium peroxydisulfate or iron(III) chloride). The product obtained by the Matsuo group showed evidence of intercalation from powder X-ray diffraction studies, whereas Gong's product did not. Gong *et al*. reinvestigated the intercalation of PANI into GO [89] and used a modification of their previously reported procedure. Aniline was first intercalated into GO and the resulting phase treated with ammonium peroxydisulfate to yield an intercalated compound of PANI into GO.

The Matsuo group also re-explored the intercalation of PANI into GO, by using a different synthetic route [15]. This time, an intercalation compound of *n*-hexylamine into GO was prepared. Further treatment of this compound with an NMP solution of PANI afforded $(PANI)_xGO$ through an ion-exchange reaction.

Bissessur and coworkers explored the inclusion of poly(2-ethylaniline) (PEA) and poly(2-propylaniline) (PPA) into GO, in addition to polyaniline [90]. The technique of intercalation differed from previously reported methods. They showed that polyanilines can be directly inserted into GO without the preparation of precursor phases. The polymers were first prepared from the monomers by oxidation with ammonium peroxydisulfate in acidic medium. GO, synthesized by using the Hummers' method, was dispersed in deionized water with the aid of sonication. Colloidal suspensions of the polymers in NMF were then added to the aqueous GO suspensions. The reaction mixtures were then acidified and heated at 60 °C for 90 min. The intercalated phases were isolated via freeze-drying. A similar process was used to intercalate polypyrrole into GO [91].

Bissessur and Scully reported on the intercalation of solid electrolyte precursors, polyethylene oxide (PEO), polyvinylpyrrolidone (PVP), methyl cellulose (MCel), poly[oxymethylene-(oxyethylene)] (POMOE), and poly[oligo(ethylene glycol oxalate)] (POEGO) into layered graphite oxide [92]. This was achieved by mixing aqueous suspensions of GO with aqueous solutions of the polymers. A small amount of dilute NaOH was added to complete the exfoliation process of the GO. Following acidification and heating as described above, the polymer intercalates were finally isolated through freeze-drying. It is important to note that the intercalation of PEO into GO was also reported by Matsuo and coworkers [93].

Bissessur *et al*. recently reported on the inclusion of poly[bis(methoxyethoxyethoxy)-phosphazene] (MEEP) complexed with lithium triflate into the gallery space of GO [94].

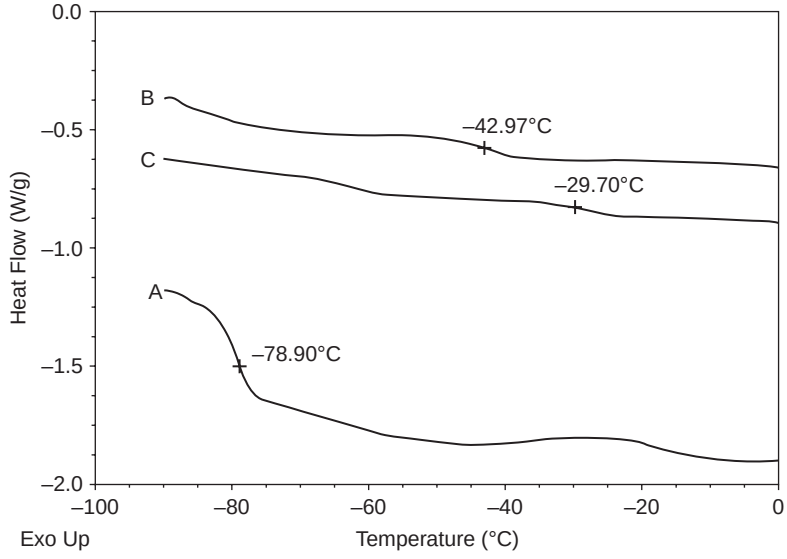

Figure 6.14 *DSC of (A) pure MEEP, (B) $(MEEP)_{4.0}LiCF_3SO_3$, and (C) $(MEEP)_{4.0}LiCF_3SO_3$/GO. (Reprinted with pemission from Solid State Ionics, Inclusion of poly[bis(methoxyethoxyethoxy) phosphazene] into layered graphite oxide by S. F. Scully, R. Bissessur, K. W. MacLean and D. C. Dahn, 180, 2–3. Copyright (2009) Elsevier Ltd)*

MEEP is an amorphous polymer that displays high ionic conductivity when complexed with lithium salts. The composition of the salt complex used in the study was $(MEEP)_{4.0}LiCF_3SO_3$. Powder X-ray diffraction supported the intercalation of $(MEEP)_{4.0}LiCF_3SO_3$ into GO. Differential scanning calorimetry provided supporting evidence. Pure MEEP displayed a low glass transition temperature (T_g) at –78.90 °C, which shifted to –42.97 °C upon complexation with the triflate salt. A further shift in T_g to –29.70 °C was observed for the composite material, $(MEEP)_{4.0}LiCF_3SO_3$/GO (Figure 6.14). The composite was also characterized by AC impedance spectroscopy, and it was shown to possess significant ionic conductivity.

6.11 Conclusions

The insertion of polymers, with electrical and ionic conductivity, into two-dimensional host structures continues to be a growing field of research in materials science/chemistry. As seen in this review, the technique of intercalation depends on the layered structure that is being investigated. It should also be pointed out that there is a huge repertoire of layered systems that is at the disposal of the researcher, providing the opportunity to create a wide range of nanostructured materials with specific applications.

Acknowledgements

The author is grateful to the Natural Sciences and Engineering Research Council of Canada (NSERC), Canada Foundation for Innovation (CFI), Atlantic Innovation Fund of Canada (AIF), and UPEI for financial support.

References

[1] M. S. Whittingham and A.J. Jacobson, *Intercalation Chemistry*, Academic Press, New York, 1982.
[2] (a) M. Zendehdel, A. Babaei, and Sh. Alami, Intercalation of xylenol orange, morin and calmagite into NaY zeolite and their application in dye/zeolite modified electrode, *J. Incl. Phenom. Macrocycl. Chem*., **59**, 345–349 (2007).
[3] M. A. Zanjanchi and Sh. Sohrabnejad, Intercalation of methylene blue into modernites: role of zeolite acidity, *J. Incl. Phenom. Macrocycl. Chem.*, **46**, 43–49 (2003).
[4] S. Tanuma and K. Kusano, Synthesis of intercalation compounds of alkali metal atoms and a halogen molecule with quasi one dimensional carbon crystal 'carbolite'. *Synth. Met.*, **86**, 1875–1876 (1997).
[5] Z-H. Yang and H-Q Wu, Electrochemical intercalation of lithium into fullerene soot, *Mater. Lett.*, **50**, 108–114 (2001).
[6] J. W. Johnson, A. J. Jacobson, S. M. Rich, and J. F. Brody, New layered compounds with transition-metal oxide separated by covalently bound organic ligands. Molybdenum and tungsten trioxide-pyridine, *J. Am. Chem. Soc.*, **103**, 5246–5247 (1981).
[7] M. G. Kanatzidis, L. M. Tonge, T. J. Marks, H. O. Marcy, and C. R. Kannewurf, *In situ* intercalative polymerization of pyrrole in FeOCl: A new class of layered, conducting polymer-inorganic hybrid materials, *J. Am. Chem. Soc.*, **109**, 3797–3799 (1987).
[8] M. G. Kanatzidis, H.O. Marcy, W. J. McCarthy, C. R. Kannewurf, and T. J. Marks, *In situ* intercalative polymerization chemistry of FeOCl. Generation and properties of novel, highly conductive inorganic/organic polymer microlaminates, *Solid State Ionics*, **32/33**, 594–608 (1989).
[9] M. Armand, Intercalation electrodes. In *Materials for Advanced Batteries*, ed. D. W. Murphy, J. Broadhead, and B. C. H. Steele, Plenum, New York, 1980.
[10] K. E. Dungey, M. D. Curtis, and J. E. Penner-Hahn, Behaviour of MoS_2 intercalation compounds in HDS catalysis, *J. of Catal.*, **175**, 129–134 (1998).
[11] S-H. Wu, F-Y. Wang, C-C.M. Ma, W-C. Chang, C-T. Kuo, H-C. Kuan, and W-J. Chen, Mechanical, thermal and morphological properties of glass fiber and carbon fiber reinforced polyamide-6 and polyamide-6/clay nanocomposites, *Mater. Lett.*, **49**, 327–333 (2001).
[12] J. C. Hutchison, R. Bissessur, and D. F. Shriver, Conductivity anisotropy of polyphosphazene-montmorillonite composite electrolytes, *Chem. Mater.*, **8**, 1597–1599 (1996).
[13] M. G. Kanatzidis, C-G. Wu, H. O. Marcy, D. C. DeGroot, C. R. Kannewurf, A. Kostikas, and V. Papaefthymiou, Intercalation chemistry of conducting polymers: New crystalline microlaminate phases in polyaniline/FeOCl system, *Adv. Mater.*, **2**, 364–366 (1990).
[14] M. G. Kanatzidis, M. Hubbard, L. M. Tonge, T. J. Marks, H. O. Marcy, and C. R. Kannewurf, In situ intercalative polymerization as a route to layered conducting polymer-inorganic matrix microlaminates. Polypyrrole and polythiophene in FeOCl, *Synth. Met.*, **28**, C89–C95 (1989).
[15] Y. Matsuo, S. Higashika, K. Kimura, Y. Miyamoto, T. Fukutsuka, and Y. Sugie, Synthesis of polyaniline-intercalated layered materials via exchange reaction. *J. Mater. Chem.*, **12**, 1592–1596 (2002).
[16] C.-G. Wu, D. C. DeGroot, H. O. Marcy, J. L. Schindler, C. R. Kannewurf, T. Bakas, V. Papaefthymiou, W. Hirpo, J. P. Yesinowski, Y.-J. Liu, and M. G. Kanatzidis, Reaction of

aniline with FeOCl. Formation and ordering of conducting polyaniline in a crystalline layered host, *J. Am. Chem. Soc.*, **117**, 9229–9242 (1995).
[17] A. Ditte, Recherches sur le vanadium; propriétés de l'acide vanadique. *C. R. Hebd. Seances Acad. Sci.*, **101**, 698–702 (1885).
[18] N. Gharbi, C. Sanchez, J. Livage, J. Lemerle, L. Néjem, and J. Lefebvre, Mixed-valence polyvanadic acid gels, *Inorg. Chem.*, **21**, 2758–2765 (1982).
[19] P. Aldebert, N. Baffier, N. Gharbi, and J. Livage, Layered structure of vanadium pentoxide gels, *Mat. Res. Bull.*, **16**, 669–676 (1981).
[20] J. J. Legendre and J. Livage, Vanadium pentoxide gels: I. Structural study by electron diffraction, *J. Colloid Interface Sci.*, **94**, 75–83 (1983).
[21] J. Livage, Sol-gel chemistry and electrochemical properties of vanadium oxide gels, *Solid State Ionics*, **86–88**, 935–942 (1996).
[22] J. Livage, Synthesis of polyoxovanadates via 'chimie douce', *Coord. Chem. Rev.*, **178–180**, 999–1018 (1998).
[23] C.-G. Wu and M. G. Kanatzidis, Layered V_2O_5 xerogels: Host-guest chemistry and conductive polymers, *Mat. Res. Soc. Symp. Proc.*, **210**, 429–442 (1991).
[24] T. Yao, Y. Oka, and N. Yamamoto, Layered structures of vanadium pentoxide gels, *Mat. Res. Bull.*, **27**, 669–675 (1992).
[25] F. J. Anaissi, G. J.-F. Demets, E. B. Alvarez, M. J. Politi, and H. E. Toma, Long-term aging of vanadium (V) oxide xerogel precursor solutions: structural and electrochemical implications, *Electrochim. Acta*, **47**, 441–450 (2001).
[26] M. G. Kanatzidis, C-G. Wu, H. O. Marcy, and C. R. Kannewurf, Conductive polymer bronzes. Intercalated polyaniline in. V_2O_5 xerogels, *J. Am. Chem. Soc.*, **111**, 4139–4141 (1989).
[27] M. G. Kanatzidis, C-G. Wu, H. O. Marcy, D. C. DeGroot, and C. R. Kannewurf, Conductive polymer/oxide bronze nanocomposites. Intercalated polythiophene in V_2O_5 xerogels, *Chem. Mater.*, **2**, 222–224 (1990).
[28] C-G. Wu, H. O. Marcy, D. C. DeGroot, C. R. Kannewurf, and M. G. Kanatzidis, V_2O_5 xerogels as hosts for conductive polymers. Intercalative polymerization of aniline, pyrrole and 2,2′-bithiophene, *Mat. Res. Soc. Symp. Proc.*, **173**, 317–322 (1990).
[29] G. J.-F. Demets and H. E. Toma, Strong electric fields promote oriented intercalative polymerization of pyrrole inside the lamellar matrices of vanadium pentoxide, *Electrochim. Comm.*, **5**, 73–77 (2003).
[30] A. V. Murugan, B. B. Kale, C. W. Kwon, G. Campet, and K. Vijayamohanan, Synthesis and characterization of a new organic-inorganic poly(3,4-ethylene dioxythiophene) PEDOT/V_2O_5 nanocomposite by intercalation, *J. Mater. Chem.*, **11**, 2470–2475 (2001).
[31] A. V. Murugan, C.W. Kwon, G. Campet, B. B. Kale, A. B. Mandale, S. R. Sainker, C. S. Gopinath, and K. Vijayamohanan, A novel approach to prepare poly(3,4-ethylenedioxythiophene) nanoribbons between V_2O_5 layers by microwave irradiation, *J. Phys. Chem. B*, **108**, 10736–10742 (2004).
[32] O.Y. Posudievsky, Y. I. Kurys, and V. D. Pokhodenko, 12-Phosphormolibdic acid doped polyaniline-V_2O_5 composite, *Synth. Met.*, **144**, 107–111 (2004).
[33] Z. F. Li and E. Ruckenstein, Intercalation of conductive polyaniline in the mesostructured V_2O_5, *Langmuir*, **18**, 6956–6961 (2002).
[34] S. Pang, G. Li, and Z. Zhang, Synthesis of polyaniline-vanadium oxide nanocomposite nanosheets, *Macromol. Rapid Commun.*, **26**, 1262–1265 (2005).
[35] I. Karatchevtseva, Z. Zhang, J. Hanna, and V. Luca, Electrosynthesis of macroporous polyaniline-V_2O_5 nanocomposites and their unsual magnetic properties, *Chem. Mater.*, **18**, 4908–4916 (2006).
[36] F. Huguenin, M. Ferreira, V. Zucolotto, F. C. Nart, R. M. Torresi, and O. N. Oliveira, Jr., Molecular-level manipulation of V_2O_5/polyaniline layer-by-layer films to control electrochromogenic and electrical properties, *Chem. Mater.*, **16**, 2293–2299 (2004).
[37] M. Malta, G. Louarn, N. Errien, and R. M. Torresi, Redox behaviour of nanohybrid material with defined morphology: vanadium oxide nanotubes intercalated with polyaniline, *J. Power Sources*, **156**, 533–540 (2006).

[38] C-G. Wu, Y-C Liu, and S.-S Hsu, Assembly of conducting polymer/metal oxide multilayer in one step, *Synth. Met.*, **102**, 1268–1269 (1999).
[39] J. Harreld, H. P. Wong, B. C. Dave, B. Dunn, and L. F. Nazar, Synthesis and properties of polypyrrole-vanadium oxide hybrid aerogels. *J. Non-Cryst. Solids*, **225**, 319–324 (1998).
[40] Y.-J. Liu, D. C. DeGroot, J. L. Schindler, C. R. Kannewurf, and M. G. Kanatzidis, Intercalation of poly(ethylene oxide) into V_2O_5 xerogel, *Chem. Mater.*, **3**, 992–994 (1991).
[41] Y.-J. Liu, D. C. DeGroot, J. L. Schindler, C. R. Kannewurf, and M. G. Kanatzidis, Intercalation of water-soluble polymers in V_2O_5 xerogel. *Adv. Mater.*, **5**, 369–372 (1993).
[42] E. Ruiz-Hitzky, P. Aranda, and B. Casal, New polyoxyethylene intercalation materials in vanadium oxide xerogel, *J. Mater. Chem.*, **2**, 581–582 (1992).
[43] C. V. Nicholas, D. J. Wilson, C. Booth, and J. R. M. Giles, Improved synthesis of oxymethylene-linked poly(oxyethylene), *Brit. Polym. J.*, **20**, 289–292 (1988).
[44] G. M. Kloster, J. A. Thomas, P. W. Brazis, C. R. Kannewurf, and D. F. Shriver, Synthesis, characterization, and transport properties of new mixed ionic-electronic conducting V_2O_5 – polymer electrolyte xerogel nanocomposites, *Chem. Mater.*, **8**, 2418–2420 (1996).
[45] O. Y. Posudievsky, S. A. Biskulova, and V. D. Pokhodenko, New hybrid guest-host nanocomposites based on polyaniline, poly(ethylene oxide) and V_2O_5, *J. Mater. Chem.*, **14**, 1419–1423 (2004).
[46] F. J. Anaissi, G.J.-F. Demets, R. A. Timm, and H. E. Toma, Hybrid polyaniline/bentonite-vanadium (v) oxide nanocomposites, *Mater. Sci. Eng. A*, **347**, 374–381 (2003).
[47] G.J.-F. Demets, F. J. Anaissi, H. E. Toma, and M. B. A. Fontes, Preparation and properties of polypyrrole/bentonite/vanadium (v) oxide ternary composites, *Mater. Res. Bull.*, **37**, 683–695 (2002).
[48] A. K. Cuentas-Gallegos and P. Gomez-Romero, Triple hybrid materials: A novel concept within the field of organic-inorganic hybrids, *J. Power Sources*, **161**, 580–586 (2006).
[49] J. W. Johnson, A. J. Jacobson, J. F. Brody, and S. M. Rich, Coordination intercalation reactions of the layered compounds $VOPO_4$ and $VOAsO_4$ with pyridine. *Inorg. Chem.*, **21**, 3820–3825 (1982).
[50] H. Nakajima and G. Matsubayashi, Intercation/polymerization of the anilinium cation in the $VOPO_4$ interlayer space, *Chem. Lett.*, **22**, 423–426 (1993).
[51] R. F. de Farias and C. Airoldi, Synthesis and characterization of an$VOPO_4$-polyaniline lamellar hybrid compound, *Solid State Sci.*, **5**, 611–613 (2003).
[52] E. C. Zampronio and H. P. Oliveira, Synthesis, spectroscopic and structural characterization of poly-*o*-methoxyaniline and poly-*o*-methylaniline intercalated into layered vanadyl phosphate, *Mater. Res. Bull.*, **39**, 1525–1538 (2004).
[53] R. Bissessur and J. MacDonald, Novel alkyl substituted polyanilines/$VOPO_4$ nanocomposites, *Solid State Sci.*, **8**, 531–536 (2006).
[54] R. Bissessur and J. MacDonald, Synthesis and characterization of halo-substituted polyanilines/$VOPO_4$ nanocomposites, *Mater. Chem. Phys.*, **106**, 256–259 (2007).
[55] G. Matsbayashi and H. Nakajima, Intercalative polymerization of 3-methyl- and 3,4-dimethylpyrrole in the$VOPO_4$ interlayer space, *Chem. Lett.*, **22**, 31–34 (1993).
[56] X. Wang, W. Hou, X. Guo, and Q. Yan, Preparation and characterization of layered molybdenum trioxide pillared with chromia, *Mater. Chem. Phys.*, **73**, 13–18 (2002).
[57] R. Bissessur, D. C. DeGroot, J. L. Schindler, C. R. Kannewurf, and M. G. Kanatzidis, Inclusion of poly(aniline) into MoO_3, *J. Chem. Soc. Chem. Commun*., 687–689 (1993).
[58] T. A. Kerr, H. Wu, and L. F. Nazar, Concurrent polymerization and insertion of aniline in molybdenum trioxide: Formation and properties of a $[polyaniline]_{0.24}MoO_3$ nanocomposite, *Chem. Mater.*, **8**, 2005–2015 (1996).
[59] O. Y. Posudievsky, S. A. Biskulova, and V. D. Pokhodenko, New polyaniline-MoO_3 nanocomposite as a result of direct polymer intercalation, *J. Mater. Chem.*, **12**, 1446–1449 (2002).
[60] K. Shao, Y. Ma, Z-H. Chen, X-H. Ji, W-S. Yang, and J-N. Yao, In situ insertion of poly(aniline) into molybdenum oxide layers, *Chem. Lett.*, **31**, 322–323 (2002).
[61] P. G. Hill, P. J. S. Foot, and R. Davis, Novel inorganic/conjugated polymer nano-composites, *Synth. Met.*, **76**, 289–292 (1996).

[62] J. Wang, I. Matsubara, N. Murayama, S. Woosuck, and N. Izu, The preparation of polyaniline intercalated MoO_3, thin film and its sensitivity to volatile organic compounds. *Thin Solid Films*, **514**, 329–333 (2006).
[63] L. F. Nazar, Z. Zhang, and D. Zinkweg, Insertion of poly(p-phenylenevinylene) in layered MoO_3, *J. Am. Chem. Soc.*, **114**, 6239–6240 (1992).
[64] L. F. Nazar, H. Wu, and W. P. Power, Synthesis and properties of a new $(PEO)_x[Na(H_2O)]_{0.25}MoO_3$, *J. Mater. Chem.*, **5**, 1985–1993 (1995).
[65] L. Wang, J. Schindler, C. R. Kannewurf, and M. G. Kanatzidis, Lamellar polymer-Li_xMoO_3 nanocomposites via encapsulative precipitation, *J. Mater. Chem.*, **7**, 1277–1283 (1997).
[66] Y. Hu, W. Chen, Q. Xu, and R. Yuan, Nanocomposite films of MoO_3 xerogel with poly(ethylene oxide) (PEO) intercalation, *J. Mater. Sci. Technol.*, **17**, S124–S126 (2001).
[67] Y-J. Liu and M. G. Kanatzidis, Topotactic polymerization of aniline in layered uranyl phosphate, *Inorg. Chem.*, **32**, 2989–2991 (1993).
[68] Y-J. Liu and M. G. Kanatzidis, Postintercalative polymerization of aniline and its derivatives in layered metal phosphates, *Chem. Mater.*, **7**, 1525–1533 (1995).
[69] K. J. Chao, T. C. Chang, and S. Y. Ho, Intercalation and oxidative polymerization of aniline in zirconium phosphates, *J. Mater. Chem.*, **3**, 427–428 (1993).
[70] T. C. Chang, W. Y. Shen, and S. Y. Ho, Oxidative polymerization of aniline in zirconium phosphate sulfophenylphosphonate, *Microporous Mater.*, **4**, 335–343 (1995).
[71] B. Bonnet, R. El Mejjad, M.-H. Herzog, D. J. Jones, and J. Rozière, Protonation and oxidative intercalation of aniline in two-dimensional inorganic substrates, *Mater. Sci. Forum*, **91–93**, 177–182 (1992).
[72] D. J. Maia, O. L. Alves, and M.-A. De Paoli, Growth of linear polyaniline chains in a layered tin (IV) phosphonate host, *Synth. Met.*, **90**, 37–40 (1997).
[73] B. E. Koene and L.F. Nazar, Synthesis and electrochemical lithium insertion in polyaniline/$HMWO_6$ (M = Ta, Nb) nanocomposites, *Solid State Ionics*, **89**, 147–157 (1996).
[74] G. K. Prasad, T. Takei, Y. Yonesaki, N. Kumada, and N. Kinomura, Hybrid nanocomposite based on $NbWO_6$ nanosheets and polyaniline, *Mater. Lett.*, **60**, 3727–3730 (2006).
[75] N. S. P. Bhuvanesh and J. Gopalakrishnan, Polymerization of aniline in layered $HMMoO_6.H_2O$, *Mat. Sci. Eng. B*, **53**, 267–271 (1998).
[76] H-J. Nam, H. Kim, S. H. Chang, S-G. Kang, and S-H. Byeon, Polymerization of aniline in the galleries of layered $HNbMoO_6$, *Solid State Ionics*, **120**, 189–195 (1999).
[77] S. Uma and J. Gopalakrishnan, Polymerization of aniline in layered perovskites, *Mat. Sci. Eng. B*, **34**, 175–179 (1995).
[78] X. Li, G. Wang, X. Li, and D. Lu, Surface properties of polyaniline/nano-TiO_2 composites, *Appl. Surf. Sci.*, **229**, 395–401 (2004).
[79] L. Zhang, P. Liu, and Z. Su, Preparation of PANI-TiO_2 nanocomposites and their solid-phase photocatalytic degradation, *Polym. Degrad. Stab.*, **91**, 2213–2219 (2006).
[80] J-C. Xu, W-M. Liu, and H-L. Li, Titanium dioxide doped polyaniline, *Mater. Sci. Eng. C*, **25**, 444–447 (2005).
[81] S-J. Su and N. Kuramoto, Processable polyaniline-titanium dioxide nanocomposites: effect of titanium dioxide on conductivity, *Synth. Met.*, **114**, 147–153 (2000).
[82] X. Li, W. Chen, C. Bian, J. He, N. Xu and G. Xue, *Appl. Surf. Sci.*, **217**, 16–22 (2003).
[83] X. Ma, M. Wang, G. Li, H. Chen, and R. Bai, *Mater. Chem. Phys.*, **98**, 241–247 (2006).
[84] N. Sukpirom and M. M. Lerner, Preparation of organic-inorganic nanocomposites with a layered titanate, *Chem. Mater.,***13**, 2179–2185 (2001).
[85] S. F. Scully and R. Bissessur, An intercalated polyaniline-titanate nanomaterial, *Synth. Met.*, **159**, 637–641 (2009).
[86] W. S. Hummers Jr. and R. E. Offeman, Preparation of graphitic oxide, *J. Am. Chem. Soc.*, **80**, 1339 (1958).
[87] S. Higashika, K. Kimura, Y. Matsuo, and Y. Sugie, Synthesis of polyaniline-intercalated graphite oxide, *Carbon*, **37**, 354–356 (1999).
[88] P. Liu and K. Gong, Synthesis of polyaniline-intercalated graphite oxide by an *in situ* oxidative polymerization reaction, *Carbon*, **37**, 706–707 (1999).

[89] P. Xiao, M. Xiao, P. Liu, and K. Gong, Direct synthesis of a polyaniline-intercalated graphite oxide nanocomposite, *Carbon*, **38**, 626–641 (2000).
[90] R. Bissessur, P. K. Y. Liu, W. White, and S. F. Scully, Encapsulation of polyanilines into graphite oxide, *Langmuir*, **22**, 1729–1734 (2006).
[91] R. Bissessur, P. K. Y. Liu, and S. F. Scully, Intercalation of polypyrrole into graphite oxide, *Synth. Met.*, **156**, 1023–1027 (2006).
[92] R. Bissessur and S. F. Scully, Intercalation of solid polymer electrolytes into graphite oxide, *Solid State Ionics,* **178**, 877–882 (2007).
[93] Y. Matsuo, K. Tahara, and Y. Sugie, Structure and thermal properties of poly(ethylene oxide)-intercalated graphite oxide, *Carbon*, **35** 113–120 (1997).
[94] S. F. Scully, R. Bissessur, K. W. MacLean, and D. C. Dahn, Inclusion of poly[bis(methoxyethoxyethoxy)phosphazene] into layered graphite oxide, *Solid State Ionics*, **180**, 216–221 (2009).

7

Metallic-Based Nanocomposites of Conductive Polymers

Vessela Tsakova

Institute of Physical Chemistry, Bulgarian Academy of Sciences, Sofia, Bulgaria

7.1 Introduction

Since the remarkable discovery of high electrical conductivity in polymer materials in 1977 [1], studies on conductive polymers (CP[1]) have developed into interdisciplinary research expanding in various directions. A significant impetus to the field was given by materials scientists in their attempts to combine the unique properties of conductive polymers with those of other inorganic and organic materials. Thus, in the last two decades, research on the synthesis of CP-based composite materials has flourished and resulted in the development of a great variety of new materials with interesting specifically designed properties. The accumulation of a great number of studies on nanocomposite materials has provoked the recent appearance of several review articles [2–7] attempting to summarize, from different specific points of view, the advances made in the field. Thus, electrochemical aspects [2,7] of CP-based composites, optical and electronic properties [3], polyaniline(PANI)-based nanocomposites [4], the involvement of composites of CPs in chemical sensing [5], and the incorporation of metallocenes in CPs [6] have been extensively discussed.

[1] All acronyms used throughout the text are summarized in the List of Acronyms at the end of the chapter.

Nanostructured Conductive Polymers Edited by Ali Eftekhari

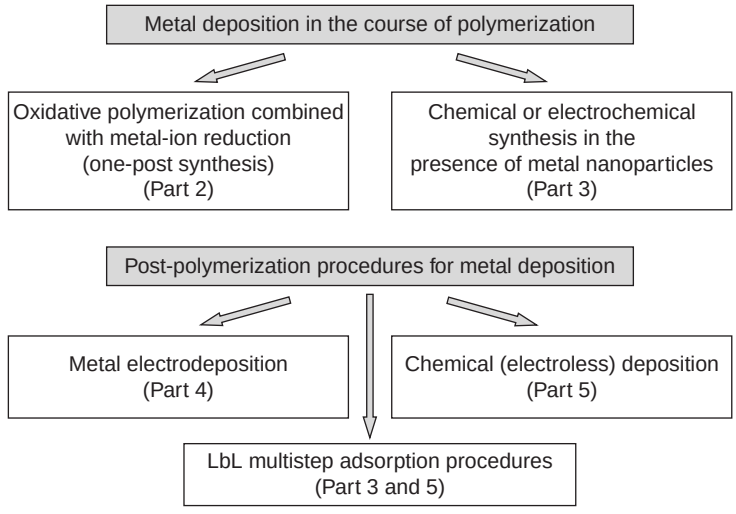

Figure 7.1 *Organization of the topics addressed in the chapter*

It is the aim of this chapter to give an overview on both chemical and electrochemical techniques for producing metallic-particle-based CP nanocomposite materials and to outline the progress made in this field. The various synthetic approaches are organized in such a way as to present first those involving metal particle deposition in the course of polymerization, and subsequently post-polymerisation procedures that involve chemical, electrochemical, or adsorption processes (Figure 7.1). Well-established approaches, along with some newly developed techniques will be discussed, with special emphasis on those that are still underdeveloped. Synthesis of metal oxide particle-based CP composites (see e.g. [8]), as well as modification of CPs with transition-metal complexes (see e.g. [5]) remain outside the scope of this chapter.

Metallic-particle-based CP nanocomposites are explored in view of a great variety of applications, including electrocatalysis, electroanalytics, sensorics, corrosion protection etc. The discussion in this chapter concerning applications will address the relationship between synthetic conditions and mainly electrocatalytic and electroanalytic performance, without going into the specific topic of mechanisms of electrochemical reactions. The latter research area (see e.g. [9]) requires extensive presentation and remains outside the scope of this overview.

Finally, this chapter aims to present a snapshot of the state of the art by extensively covering the otherwise widely spread literature on metallic-based CP nanocomposites (including microcomposites that are at the nanocoscale limit). This attempt is launched with the hope that not much work has been left unnoticed.

7.2 Oxidative Polymerization Combined with Metal-Ion Reduction (One-Pot Synthesis)

Studies on one-pot chemical syntheses of metallic-particle-based CP nanocomposites [10–45] rely on the direct oxidation of the monomer by metal ions present in the solution,

in the absence of additional oxidants. This approach has been explored for the formation of Au-, Pt- and Ag-based composites of PANI, polypyrrole (PPY), poly(3,4-etylenedioxythiophene) (PEDOT) and some of their derivatives (Table 7.1). The performed investigations show that one-pot chemical synthesis, carried out in aqueous solution and in the absence of stabilizers, fails in most cases to give small enough metal particles [20–22,37]. According to a detailed study on the synthesis of Au-PPY colloids [11], however, the size and shape of the obtained metal particles vary significantly depending on the synthesis solution composition. By keeping the metal (Au)-to-monomer (pyrrole) ratio as low as 0.1, spherical nanoparticles (NPs) with a narrow size distribution and a mean diameter of 7 nm have been obtained. Thus, thorough experimentation is needed in order to achieve the formation of nanocomposites with small enough and possibly monodisperse metal NPs.

The involvement of bulky sulfonate anions, e.g. dodecylbenzenesulfonate (DBS), polysterenesulfonate (PSS), or camphorsulphonate, that act both as dopants and stabilizers for the metal NPs results usually in the formation of metal particles on the nanometer scale. In the studies performed so far, the role of parameters such as monomer, stabilizer, and metal ion concentration on the characteristics of the produced nanocomposites are rarely assessed. A detailed investigation on the formation of Ag- poly(2,5-dimethoxyaniline(PDMA)-PSS nanocomposites obtained at various concentrations of DMA, PSS, and Ag anions [36] shows that the dopant concentration determines the composite properties, e.g. doping level, growth rate and Ag NP size distribution. The role of the type of the stabilizing agent (PSS, dodecylsulfate, or poly(vinyl alcohol)-PVA) has been investigated in the case of Au-PEDOT nanocomposite formation [39]. Use of various ionic and nonionic compounds as stabilizing species in the course of the chemical synthesis offers undoubtedly multiple opportunities to influence the formation of metallic-particle-based CP nanocomposites.

Attempts to use organic solutions for the one-pot synthesis of aniline-based nanocomposites resulted in the formation of Au-NPs in PANI [42,43], Au-NP-decorated PANI nanoballs [24], and a uniform distribution of Pd NPs in poly(3,5-dimethylaniline) [25]. An interesting approach for a two-phase interfacial synthesis of Pt-PANI nanocomposite was suggested by Liu [35] using aniline dissolved in chloroform as the lower organic phase and aqueous solution of chloroplatinic acid and PSS as the upper phase. The Pt NPs were found to be uniformly dispersed in the PANI-PSS nanocomposite.

One-pot synthesis approaches have also been developed, involving sonication [23,26], and UV- [15,28] or γ-irradiation [27,32,41]. It was found that sonication and γ-irradiation resulted in acceleration of the nanocomposite formation by inducing radical formation (i.e. $H_2O \rightarrow H^{\bullet} + OH^{\bullet}$). The hydrogen and hydroxyl radicals drive both metal-ion reduction and monomer oxidation. The role of H_2O_2, either available in the solution or generated through radical recombination, for the enhancement of the rate of polymerization was extensively discussed [23,26].

Finally, apart from the chemical oxidation-reduction one-pot approach, electrochemical one-pot synthesis routes based on the application of cyclic voltammetry or unsymmetrical square-wave current procedures have been used for the formation of Pd-, Pt-, and Ag-nanocomposites [10,14,34] supported on conducting substrates (Table 7.1). The monomer oxidation proceeds at the positive potentials of the voltammetric cycle or during the oxidative galvanostatic pulse. Metal nucleation and growth is initiated at the more negative potentials of the voltammetric cycle or during the reductive galvanostatic pulse, correspondingly. Thus, both oxidative polymerization and metal ions reduction are time-resolved, but occur in the same solution.

Table 7.1 *Overview of systems investigated for one-pot synthesis of metallic-based CP nanocomposites*

Monomer	Metal-ion source	Method	Counter-ion, solvent	Metal particle size	Ref.
Aniline	$KAuCl_4$	Direct oxidation-reduction	BF_4^-, H_2O	1 μm	20, 21
Aniline	$HAuCl_4$	Direct oxidation-reduction	Cl^- and SDS, H_2O	50–300 nm	31
Aniline	$HAuCl_4$	Direct oxidation-reduction	Cl^-, H_2O (various pH and *T*)	10 nm–1 μm (depending on pH and *T*)	37
Aniline	$HAuCl_4$	Direct oxidation-reduction	Camphorsulfonate, H_2O	50–60 nm diameter of coaxial nanocables	33
Aniline	$HAuCl_4$	Direct oxidation-reduction	acetate, H_2O, Tween 40	<1 μm, core-shell	38
Aniline	$HAuCl_4$	Direct oxidation-reduction	No additional anions, toluene	Au-decorated PANI nanoballs	24
Aniline	$HAuCl_4$ or $PdCl_2$	Direct oxidation-reduction	Cl^- and DBS, hexane and butanol	2–5 nm	43
Aniline	$HAuCl_4$	Direct oxidation-reduction with or without carbon nanotubes (CNT)	Cl^-, ethanol	3 nm (PANI-CNT), 6 nm (PANI)	42
Methoxyaniline	$HAuCl_4$	Direct oxidation-reduction	Camphorsulfonate, H_2O or organic solvent	3.0–4.9 nm (H_2O) 1.4–13.3 nm (org.)	17
Methoxyaniline	$HAuCl_4$	Direct oxidation-reduction	DBS, H_2O	<10 nm, filaments of NPs	18
3-Aminophenyl boronic acid	$HAuCl_4$	Direct oxidation-reduction	Cl^-, H_2O PVA as disperser	15.5–39.4 nm (depending on PVA concentration)	29
Aniline	K_2PtCl_6	Direct oxidation-reduction	BF_4^-, H_2O	1 μm	22
Aniline	H_2PtCl_6	Direct oxidation-reduction; interfacial synthesis in two-phase system	PSS, H_2O-Me salt; chloroform-aniline	90–100 nm	35
Aniline, DMA, aniline-DMA	$AgNO_3$	Direct oxidation-reduction	PSS, H_2O	19 nm (PANI), 22 nm (PDMA), 20 nm (PANI-DMA)	40
DMA	$AgNO_3$	Direct oxidation-reduction	PSS, H_2O	~10 to ~100 nm (depending on DMA, PSS and Ag^+ concentrations)	30, 36
2,3-Dimethyl-aniline	Pd-acetate	Direct oxidation-reduction	Acetate, toluene	2 nm	25

Pyrrole	$HAuCl_4$	Direct oxidation-reduction	DBS, Cl^-, H_2O	12.8 nm	16
Pyrrole	$HAuCl_4$	Direct oxidation-reduction	Cl^-, H_2O	3–10 nm; 20–50 nm; 50–100 nm; 120–130 nm (depending on Au/pyrrole ratio)	11–13
Pyrrole	Pd-acetate	Direct oxidation-reduction	Acetate, acetonitrile	2.0–2.5 nm	44
EDOT	$HAuCl_4$	Direct oxidation-reduction	Cl^-, H_2O or PSS, SDS or PVP, H_2O	26.3 nm* (PSS), 45.3 nm* (SDS), 220.0 nm* (PVP) *hydrodynamic diameters of the nanocomposite particles	39
EDOT	$PdCl_2$	Direct oxidation-reduction	Cl^-, H_2O or PSS + Cl^-, H_2O	1–9 nm	45
EDOT	$CuCl_2$	Direct oxidation-reduction		–	19
Aniline	$HAuCl_4$	Sonication; H_2O_2	Cl^-	–	23
Aniline	$HAuCl_4$ $AgNO_3$	γ-Irradiation with or without add. oxidant	Cl^-, NO_3^-, H_2O	10–100 nm (Au) (no add. oxidant), 2–25 nm (Ag) (add. oxidant), PANI decorated nanofibers	27
Aniline	$AgNO_3$	Sonication or γ-irradiation	NO_3^-, H_2O	40 nm (sonication), 60 nm (γ-irradiation)	41
aniline	$AgNO_3$	UV-Vis irradiation at 254 and 365 nm	NO_3^-, H_2O	<50 nm	28
Pyrrole	$AuCl_3$, $AgNO_3$, $CuSO_4$	UV irradiation	DS, H_2O	–	15
Pyrrole	$HAuCl_4$, K_2PtCl_6	Sonication	DS, H_2O	15 nm (Au), 40 nm (Pt) core-shell	26
N-vinyl-carbazole	$AgNO_3$, $PdNO_3$, H_2PtCl_6, $RuCl_3$	γ–irradiation	PVP, (and acrylic acid), mixed org./H_2O, H_2O	Aggregates	32
Aniline	$PdSO_4$	Cyclic voltammetry	SO_4^{2-}, H_2O		10
Aniline	Na_2PtCl_6, $PdSO_4$	Cyclic voltammetry	SO_4^{2-}, H_2O	~40 nm (Pt), 8–10 nm (Pd)	14
Aniline	$AgNO_3$	Unsymmetric square-wave current method	NO_3^-, H_2O	<50 nm	34

Most of the investigations of one-pot synthesis of metallic-based CP nanocomposites remain focused on the synthesis itself and mainly present information on the metal particle size and dispersion in the polymer phase alone. In a few cases materials properties such as electrical conductivity and thermal stability have been explored and compared to those of the corresponding pristine polymer materials. For instance, in the case of Ag-PANI-PSS and Ag-PDMA-PSS nanocomposites, an improved thermal stability has been established [40]. Concerning the electrical conductivity, there are differing data showing increased [15,23,27,43] or preserved [20,40] conductivity of the composites in comparison with the corresponding pristine polymers, synthesized under identical conditions. In general, the problem with the influence of the metal NPs on the conductivity of the nanocomposite material is not easily handled. The electrical conductivity depends on the amount of metal content in the nanocomposite, but also on the CP structure and oxidation state, which in turn might be influenced by the synthetic procedure. Thus, detailed studies are needed to differentiate between the roles of various factors influencing the nanocomposite material properties.

7.3 Nanocomposite Formation by Means of Pre-Synthesized Metal Nanoparticles

The involvement of pre-synthesized metal NPs in the formation of CP-based nanocomposites offers the possibility to incorporate metallic species with defined characteristics, e.g. size and stabilization shell, in the polymer material. An additional important advantage is the opportunity to achieve a homogeneous distribution of the metal particles in three dimensions that is usually not the case for metal deposition in pre-synthesized supported CPs. The synthesis of nanocomposites by means of pre-synthesized metal NPs [46–87] has been approached in several ways: by carrying out electrochemical [46–59,70,71] or chemical [60–69] polymerization in their presence; by simple mixing with dissolved CPs [73–76]; by NPs adsorption on pre-synthesized CP layers [77–83]; by layer-by-layer (LbL) adsorption using dissolved CPs [84–87] (Table 7.2, A and B).

The metal colloid preparations are mostly based on reduction of metal ions in the presence of bulky anions (e.g. citrate and mercaptoethanesulfonate), but also quaternary ammonium salts (e.g. tetraoctylammonium bromide) or polymers (e.g. poly(*N*-vinylpyrrolidone (PVP)) are used as stabilizers (Figure 7.2). Ionic species involved in the NP synthesis play a dual role of stabilizers for the metal particles and dopants for the polymer material. In some cases the synthesis of the metal NPs occurs under γ-irradiation in the presence of the monomer, which stabilizes the metal particles [64–66,68]. A two-phase approach for the preparation of the monomer or eventually oligomer-stabilized metal particles has been also suggested in the case of octylthiophen [57] and 3,4-ethylenedioxythiophene (EDOT) [70,71].

Electrochemical polymerization in the presence of a platinum colloid was first investigated as early as 1992 by Rajeshwar *et al*. [46,47] for PPY. These studies were followed by investigations on the incorporation of various metal colloids in the course of

Table 7.2 *Overview on systems investigated for the preparation of metallic-based CP nanocomposites by using pre-synthesized metal NPs*

A Polymerization in the presence of NPs

Monomer	Metal NPs	NP stabilizer/reductant	Polymerization method	Ref.
Aniline	Au	Mercaptoethane sulfonate	Electrochemical	48
Aniline	Pt	Citrate or mercaptoethane sulfonate	Electrochemical	49, 50
Aniline	Pt	Polyoxometallates	Adsorption of anilinium and electrochem. polymerization without monomer	80, 81
Aniline	Au	H_2O_2	Chemical	60
Aniline	Au	10-Bromodecyl peroxide	Surface-initiated chemical oxidation by peroxide groups	63
Aniline	Cu	BH_4^-	Chemical	61, 62
Aniline	Au	Monomer	Chemical	64
Aniline	Ag	Monomer	Chemical	65
Aniline	Ag	PVP or Monomer	Chemical	68
Aniline	Pd	Monomer	Chemical	66
Aniline	Ag	PVP	Chemical	67
O-toluidine	Ag	Citrate	Chemical	69
Aniline	Ag	Electrochem. reduction	Oxidation-reduction process	72
Pyrrole	Pt	Citrate	Electrochemical	46, 47
Pyrrole	Pt	Citrate	Electrochemical	51–53
Pyrrole	Pd	Tetraoctylammonium-bromide	Electrochemical	54
Pyrrole	Au	Citrate	Electrochemical	55
Thiophene	Pt, Pt-Pd	Citrate	Electrochemical	56
Octylthiophene	Au	Monomer	Electrochemical	57
EDOT	Au	Monomer	Electrochemical	70, 71
EDOT	Au	Bulky anions	Electrochemical	58, 59

B Use of pre-polymerized CP materials

Polymer	Metal NPs	NP stabilizer	Method of nanocomposite formation	Ref.
PANI	Pd	PVP	Mixing	73, 74
PANI	Au	Citrate	Mixing	76
PEDOT-PSS	Au, Ag	No data	Mixing	75
PANI	Au	Citrate	Adsorption	78
PANI	Ag	PVA	Drop-coating	83
P3MET	Au, Ag	BH_4^-(Ag)	Adsorption	79
PEDOT	Au, Ag	BH_4^-(Ag)	Adsorption	79
PPY	Pd	Tetraoctylammonium-bromide	Adsorption and electrochemical treatment	77
PPY	Ag	None	Electrochemical treatment	82
PANI	Au	Mercaptosuccinate	LbL adsorption	84, 85
PANI	Au, Ag	Mercaptoethane sulfonate	LbL adsorption	86
PANI	Au	Citrate	LbL adsorption	87

electropolymerization of aniline [48–50], pyrrole [46,47,51–55], thiophene [56], octylthiophene [57], and EDOT [58,59] (Table 7.2). The electrochemical polymerization occurs under potentiostatic or potentiodynamic conditions in the presence of the metal colloid. It is interesting to note that despite several attempts to use this approach for the synthesis of metallic-based CP nanocomposites, there are almost no data on the spatial distribution of the metal NPs in the electrosynthesized polymer layer. A homogeneous distribution of the metallic particles within the CP layer is presumed, but direct evidence is obtained only in the case of the Pt-PPY nanocomposite studied in [51].

The all-chemical synthesis approach, based on pre-synthesized metal NPs has been used for aniline and involves chemical polymerization by hydrogen peroxide or ammonium persulfate in the presence of gold [60] or copper [61,62] colloids, respectively. Surface-initiated chemical oxidation of aniline by peroxide groups that are part of the protective shell (10-bromodecylperoxide) of Au NPs has also been suggested [63]. The interesting possibility of using the monomer as a stabilizing agent for the metal particles has been explored for mercapto-octylthiophene [57], aniline [64–68], and EDOT [70,71]. The metal-CP nanocomposites were obtained in a subsequent step, either by chemical or electrochemical polymerization of the NP stabilization shells (Figure 7.2). γ-Irradiation has been used for the synthesis of aniline-protected NPs [64–67], whereas a two-phase synthetic approach was followed to produce thiol- and EDOT-protected Au NPs. The comparison of aniline- and PVP-protected Ag NPs, both produced through γ-irradiation, showed that the size and shape of the NPs depend on the weight ratios of aniline to Ag ions and the type of stabilizing agent used in the preparation [67]. Finally, direct oxidation reduction has been used to oxidize the monomer (pyrrole) at the expense of metal reduction by using Ag NPs having positively charged Ag species [72].

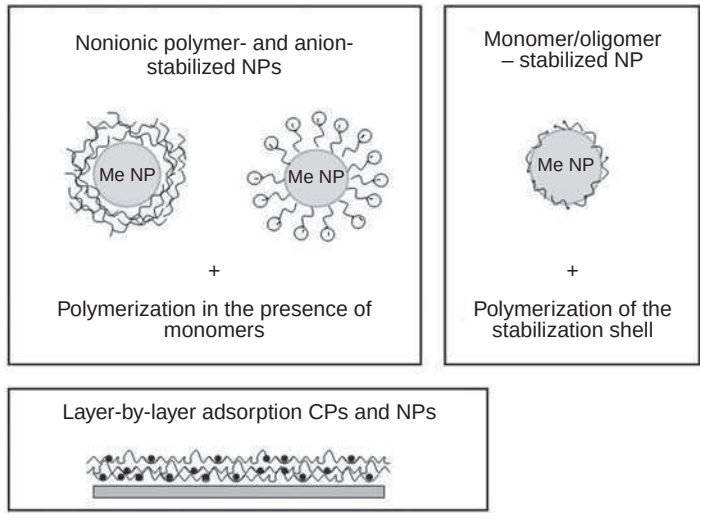

Figure 7.2 *Involvement of pre-synthesized metallic nanoparticles in the formation of CP-based composites*

Another way of introducing pre-synthesized metal NPs into nanocomposite materials is mixing with pre-synthesized CPs. It has been shown that simple mixing of PANI with a Pd suspension [73,74] and PEDOT-PSS with Au and Ag dispersions [75] results in the formation of the corresponding metal particle-CP nanocomposites in solution. The encapsulation of pre-synthesized Au NPs in pre-prepared water-soluble poly(aniline-2-carboxylic acid) was found to result in the formation of a composite nanocolloid that remains stable in aqueous solution [76].

Several approaches have been designed that involve metal NP adsorption on supported polymer surfaces with (or without) subsequent treatments aimed at better stabilization of the adsorbed NPs. Thus, electropolymerized PPY layers were immersed in Pd NP solution and subsequently treated by square-wave cathodic pulses [77]. Electrosynthesized PANI layers were immersed in a Au-colloid solution [78] and used to build a sandwich structure by repeated electropolymerization after Au NP adsorption. The adsorption of Au NPs was evidenced by UV-Vis spectroscopy showing the characteristic gold plasmonic peak in the adsorbed Au NPs-PANI layer. CP layers of the polythiophene (PTHI)-type (i.e. poly (3-methylthiophene) (P3MET) and PEDOT) were decorated by Au and Ag nanopraticles after immersion in the corresponding colloids [79]. Evidence was obtained for ohmic contact between the adsorbed NPs and the polymer surface. A repeatedly applied immersion procedure involving adsorption of polyoxometalte-protected Pt NPs and anilinium ions followed by electrochemical polymerization of the monomer species was designed to produce a Pt-PANI nanocomposites [80,81].

A true layer-by-layer adsorption approach has been developed for producing multilayered structures of PANI and Au or Ag NPs by repeatedly immersing a supporting substrate in solutions containing dissolved polyaniline and Au or Ag colloids [84–87]. This approach seems to be extremely useful for the deposition of ultrathin composite layers with homogeneous metal distributions that are well suited for applications requiring the avoidance of the otherwise large intrinsic charge capacity of CPs.

As already shown, there have been various simple or more sophisticated attempts to involve pre-synthesized metal NPs in the preparation of CP nanocomposite materials. There is, however, little known about the influence of the metal NPs on the bulk properties of the obtained nanocomposites. Indications of increased conductivity have been obtained in the cases of Au NPs-PPY [55], Pd NPs-PPY [77], and Ag NPs-PPY. Enhanced absorbance in the visible range, which depends on the amount of incorporated metal particles was observed for the Ag NPs-PEDOT composite [75]. A shift in the Au absorption peak with applied potential was found for Au NPs immobilized between two PANI electrosynthesized layers [78]. It was suggested that this effect could be used in electroactive plasmonic devices.

7.4 Metal Electrodeposition in Pre-Synthesized CPs

Not long after the discovery of CP materials, the electrochemical community realized the ease of electrochemical deposition of CP layers on conducting substrates and the promising prospect of producing new electrocatalytic materials by dispersing (in an electrochemical way) metallic particles in the CP matrix. Thus, starting with the early works of Tourillon and Garnier [88] and Chandler and Pletcher [89], interest in this area has continuously grown and has resulted in a large number of experimental studies. The electrodeposition of various metals of practical interest, such as Pt [51,79,90–141], Au [20,142–147], Pd [148–158],

Ag [159–163], Cu [165–189], Ni [159,190–193], Pb [89,138,159] etc. and also of Pt-based bimetallic systems [95,102,103,111,112,126,135] has been extensively studied (Table 7.3). The majority of investigations address the various possibilities of dispersing Pt particles in PANI [90–127] and PPY [51,79,128–137]. What follows is an outline of the developments in this field of research with emphasis on experimental techniques that provide nanosized metallic particles in electrosynthesized CP layers and on approaches that influence their spatial distribution in a pre-defined way.

The use of CP-coated electrodes for metal electrodeposition, instead of the typical conducting (metal, glassy carbon etc.) substrates, results in the interference in this process of various specific factors that closely relate to the intrinsic propertiesof CPs. Among them are the initial oxidation state of the CP material, its surface morphology and surface chemical state, and also bulk characteristics, such as porosity and metal–polymer chemical interactions. These factors are often inter-related and therefore it is difficult to differentiate clearly their effect on the characteristics of the obtained metal deposit.

Another complication arises from the fact that, in contrast to conventional electrodes, CP-coated electrodes often undergo changes in their oxidation state and structure in the course of metal electrodeposition. This is usually the case when driving metal-ion reduction by means of the most frequently applied electrochemical techniques – cyclic voltammetry, multistep potential procedures, repetitive square-wave potential (or pulse potentiostatic) techniques, and galvanostatic reduction (Figure 7.3). In spite of the difficulty in

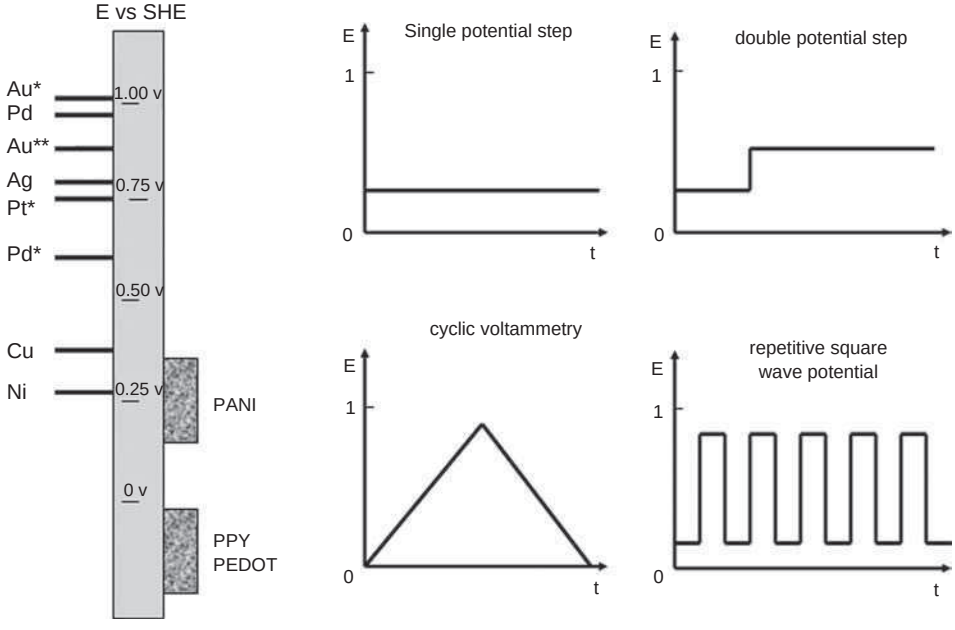

Figure 7.3 *Potential scale showing the standard equilibrium potentials of various metal ions and the potential intervals for CP reduction. Electrochemical techniques used to initiate metal electrodeposition in CPs. The asterisk (*) denotes the standard potentials of the respective tetrachloride metal ions and Au** indicates for* $AuBr_4^-$.

Table 7.3 *Overview of systems investigated for electrochemical deposition of Pt, Au, Pd, and Cu particles in CPs*

Pt

Metal-ion source (concentration)	Conductive polymer	Metal deposition method	Me particle size (for Me loading) and/or Me deposit location	Ref.
K_2PtCl_6 (5 mM)	PANI	Single-, double-potential steps or exhaustive electrolysis, pre-soaking with Me ions	100 nm (for 2 μg cm^{-2}), 20–100 nm (for 4 μg cm^{-2}), particle agglomerates (20 μg cm^{-2})	90
H_2PtCl_6 (0.24–1 mM)	PANI	Cyclic voltammetry	50–700 nm (dep. on PANI synthesis *T*), 50–100 nm	91, 92, 96, 117
H_2PtCl_6 (3.9 mM)	PANI	Cyclic voltammetry in absence of Me ions, after pre-soaking	<100 nm (for 200 μg cm^{-2})	93, 94
K_2PtCl_6 (3 mM), $SnCl_4$ (7 mM), K_2RuCl_5 (1.3 mM)	PANI	Cyclic voltammetry (Pt-Ru and Pt-Sn)	300–500 nm (Pt-Ru) (for 0.25–1.0 mg cm^{-2})	95
K_2PtCl_6 (1 mM)	PANI-camphorsulfonate	Cyclic voltammetry	Enrichment at the CP/solution interface	97
H_2PtCl_6 (0.24 mM)	PANI	Single potential step		98
K_2PtCl_6 (0.2 mM), $RuCl_3$ (0.1 mM), NH_4SnCl_3(0.15 mM)	PANI	Single potential step	50–200 nm (Pt)	102
H_2PtCl_6 (0.5 mM)	PANI-DABS	Single potential step	Pt depth profile dep. on potential	101
K_2PtCl_6 (1 mM)	PANI	Single potential step	9–62 nm (for 11–155 μg cm^{-2})	99, 100
H_2PtCl_6 (1 mM)	PANI	RSWP (0.05 Hz)	50–100 nm (for 25 μg cm^{-2})	104

(*continued overleaf*)

Table 7.3 (*continued*)

Pt				
Metal-ion source (concentration)	Conductive polymer	Metal deposition method	Me particle size (for Me loading) and/or Me deposit location	Ref.
H_2PtCl_6 (5 mM)	PANI	Single potential step after pre-soaking	15.5–44.6 nm (for 26–357 μg cm^{-2})	106
H_2PtCl_6 (3.7 mM)	PANI	Single potential step or RSWP (1 Hz)	50–200 nm, Pt depth profile dep. on method	109
K_2PtCl_6 (0.2 mM)	PANI	Single potential step (several successive steps)	<150 nm	110
H_2PtCl_6 (2–50 mM), $RuCl_3$ (13–100 mM)	PANI	RSWP	90 nm (Pt and Pt-Ru)	111, 112
K_2PtCl_6 (0.2 mM), K_2RuCl_5 (0.2 mM), $MoCl_5$ (0.04 mM)	PANI	Single potential step (5 successive steps)		107, 108
H_2PtCl_6 (3 mM)	PANI	Cyclic voltammetry, single potential step or RSWP (0.1 Hz)	100–400 nm (dep. on method)	113–115
H_2PtCl_6 (7 mM)	PANI	Cyclic voltammetry or RGP	100–400 nm or 50–100 nm (dep. on method)	116
K_2PtCl_4 (20 mM), K_2PtCl_6 (20 mM)	PANI	Cyclic voltammetry	200 nm–1 μm (dep. on Me ion source)	22, 120
H_2PtCl_6 (3.68 mM)	PANI	Single potential step	200 nm	121
H_2PtCl_6 (3 mM) also Pt-Ru	PANI and PANI–CNT	Single potential step	20 nm (PANI-CNT), 80 nm (PANI)	118, 119
H_2PtCl_6 (24.4 mM)	PANI	Double potential step after complete CP reduction	~200 nm	122
H_2PtCl_6 (5 mM)	PANI-PSS and PANI	Single potential step	Pt depth profile dep. on PANI-type	123, 127

H_2PtCl_6 (no data), $RuCl_3$ (no data)	PANI-PSS	Cyclic voltammetry, subsequent deposition of Pt-Ru or Ru-Pt	Pt and Ru depth profiles depend on Me deposition sequence	126
K_2PtCl_4 (10 mM)	PANI (PANI/Pt sandwich structure)	RSWP (0.25 Hz – few pulses)	210 nm	124
H_2PtCl_6 (5 mM)	PANI (400 nm)	Single or double potential steps	16–17 nm	125
H_2PtCl_6 (5 mM)	poly(*o*-aminophenol)	Single or double potential steps	17–19 nm	125
H_2PtCl_6 (70 mM)	PPY	Galvanostatic reduction	50–150 nm	128
K_2PtCl_4 (1 mM), (10 mM pre-soaking)	PPY	Single potential step; reduction after pre-soaking in reduced or oxidized CP	Pt depth profile dep. on deposition method	129
H_2PtCl_6 (1 mM)	PPY	Single potential step or RSWP (1 Hz) after pre-soaking		130
H_2PtCl_6 (1 mM)	PPY	Single potential step, RSWP (0.1 Hz), galvanostatic reduction or cyclic voltammetry after PPY synthesis in presence of Me ions	Pt depth profile dep. on deposition method	51, 52, 132
K_2PtCl_4 (10 mM), K_2PdCl_4 (10 mM)	PPY-substitited	Single potential step in absence of Me ions, after pre-soaking		136, 137
K_2PtCl_4 (2–10 mM)	PPY synthesized in the presence of $PtCl_4^{2-}$	Cyclic voltammetry for Me–ions reduction	10 nm [117]	131, 133
H_2PtCl_6 (5 mM), $IrCl_6$ (5 mM), $RuCl_3$	(1) PPY- synthesis in the presence of Me ions (2) PPY	(1) Reduction of Me ions – galvanostatically or by cyclic voltammetry (2) Galvanostatic	(1) 3-D distribution (2) Me particles enriched at the polymer/solution interface	134
K_2PtCl_6 (1 mM)	PPY	Single potential step	20–60 nm	79
H_2PtCl_6 (1 mM), $Pb(NO_3)_2$ (3 mM)	PTHI	Potential cycle followed by potential step	Pt and Pt-Pb	103

(*continued overleaf*)

Table 7.3 (*continued*)

Pt				
Metal-ion source (concentration)	Conductive polymer	Metal deposition method	Me particle size (for Me loading) and/or Me deposit location	Ref.
K_2PtCl_4 (50 mM), K_2PtBr_4 (50 mM) or $AgClO_4$ (100 mM)	PTHI	Single potential step or RGP	30 nm–several μm (single pot. step) 3–200 nm (RGP)	88
H_2PtCl_6 (3 mM), $Pb(NO_3)_2$ (3 mM)	PTHI	Single potential step	–	138
H_2PtCl_6 (5 mM), $SnCl_2$ (50 mM)	P3MET	Single potential step	Pt-Sn	135
H_2PtCl_6 (5 mM)	PEDOT-PSS	Cyclic voltammetry	60–300 nm	141
Au				
$KAu(CN)_2$ (1 mM)	PPY	Single potential step	100 nm	143
$KAuCl_4$ (25 mM)	PANI	Cyclic voltammetry	150–300 nm	20
thin Au-sub layer	PANI	Galvanostatic stripping of Au-sublayer, reduction of Au-anion complexes	3–15 nm (dep. on stripping conditions)	144, 145
$HAuCl_4$ (0.5 mM)	PPY	Cyclic voltammetry	15 nm	147
Pd				
$PdCl_2$ (10 mM)	PANI, PPY	Single potential step		150
$PdSO_4$ (2 mM)	PANI	Single potential step or cyclic voltammetry	Me content depth profile dep. on method	10
$PdSO_4$ (2 mM)	PANI	Single potential step	<100 nm	153

$PdCl_2$ (60 mM)	PANI-RVC	Single potential step	5 nm (aggregates)	155
$PdSO_4$ (1 mM)	PANI	Single potential step	9–39 nm (dep. on loading.)	156, 157
K_2PdCl_4 (10 mM), Na_3RhCl_6 (10 mM)	PPY-substituted	Single potential step or cyclic voltammetry in absence of me ions, after pre-soaking	100–200 nm (Pd), 1–2 μm (Rh)	137, 149
$Pd(OAc)_2$ (10 mM)	PPY (0.5–1 μm)	RSWP or cyclic voltammetry (0.2–0.02 Hz)	Homogeneous distribution at the surface	154
K_2PdCl_4 (50 mM)	PTHI	RSWP (1–10 kHz)	6–10 nm (10 kHz), 300–600 nm (1 Hz)	148
$PdSO_4$ (2 mM)	PEDOT	Single potential step	Pd particles within the CP layer	152
Ag				
$AgClO_4$(10, 100 mM)	PANI	Single potential step	>1 μm	160, 162, 163
$AgNO_3$ (1 mM)	poly(*o*-aminophenol)	Single potential step	>1 μm	161
$AgClO_4$ (100 mM)	P3MET	Single potential step, RGP	30 nm–1 μm, 3–200 nm	88
Cu				
$CuSO_4$ (10 or 33 mM)	PANI	Single potential step or galvanostatic reduction	~50–350 nm and ~1 μm (bi-modal size distribution)	179–181
Cu-citrate (20 mM), Cu-oxalate (20 mM)	PANI	Single potential step or galvanostatic reduction	300 nm–1.5 μm (citrate), 150 nm (oxalate)	182, 183
$CuSO_4$ (33 mM)	POMA	Galvanostatic reduction	–	189
$Cu(ClO_4)_2$ (35 mM)	poly(*o*-aminophenol)	Single potential step	~1 μm	171
$CuSO_4$ (1 mM)	PPY	Single potential step	~1 μm	166
$CuSO_4$ (10 mM)	PPY, PPY-PSS	Single potential step or cyclic voltammetry	400 nm (PPY-PSS), 400 nm–1 μm (PPY)	168
Cu-oxalate (1 mM)	PPY-functionalized	Single potential step or single potential step in absence of Me ions, after pre-soaking	100–200 nm, 10–100 nm (after pre-soaking)	170
$CuCl_2$ (100 mM)	PPY	RSWP	160 nm and large crystal agglomerates	173

(*continued overleaf*)

Table 7.3 (*continued*)

Cu				
Metal-ion source (concentration)	Conductive polymer	Metal deposition method	Me particle size (for Me loading) and/or Me deposit location	Ref.
$CuSO_4$ (10 mM)	PPY	Single potential step or galvanostatic reduction	90–105 nm	175, 176
$CuSO_4$ (50 mM)	PPY	Single potential step	25–150 nm (dep. on potential and CP layer thickness)	177
$CuSO_4$ (100 mM)	PPY (fully reduced)	Single potential step	Dendrites covering uniformly the CP surface	178
$CuSO_4$ (10 mM)	PPY-SDS	Single potential step or galvanostatic reduction	Dendrites	184
$CuCl_2$ (50 mM)	P3MET	RSWP	350–685 nm (CuCl or Cu_2O) (dep. on pulse width)	151, 169
$Cu(NO_3)_2$ (200 mM)	P3MET	Single potential step	–	167
$CuSO_4$	PEDOT	Galvanostatic reduction or single potential step	100–600 nm or ~1 μm (dep. on deposition method)	186–188

differentiating between the various factors influencing the characteristics (e.g. size, location, number) of electrodeposited metal particles in CPs, some illustrative examples may be used to outline the general trends.

7.4.1 Size and Size Distribution of Electrodeposited Metal Particles

The electrochemical technique used to deposit metal particles in CPs is one of the major factors influencing the characteristics of the metal deposit. Cyclic voltammetry within fixed potential limits is usually carried out in the potential range where the CP undergoes reduction/reoxidation and the equilibrium potential E_0 of the depositing metal is close to or higher than the high potential limit (Figure 7.3). Under these conditions the overpotential for metal deposition, $\eta = |E - E_0|$ (E is the actual potential applied to the electrode) that drives the metal nucleation and also controls the growth of the nucleated metal particles is continuously changing. Thus, in the framework of this experimental technique, due to both the continuously changing oxidation state of the CP layer and the overpotential for nucleation and growth, it is difficult to study the process. Nevertheless, by appropriate choice of potential limits, number of voltammteric cycles, and metal-ion concentration, this technique can provide metal particles with sizes in the several 10ths of a nanometer range (Table 7.3). In some cases, however, cyclic voltammetry results in a degradation of the CP material, e.g. PANI [117]. Therefore, directed experiments for elucidation of CP structural changes induced by the deposition technique are needed in order to assess correctly its role in the characteristics of the obtained metal–polymer composites.

The technique that is most commonly used for metal electrodeposition is the potential-step technique. It is suitable for studying the kinetics of the process as far as the metal nucleation and growth occur at constant overpotential. In spite of this seeming advantage, the situation often remains complicated due to the fact that the potential step gives rise to both metal-ion and CP reduction. For that reason the current transients measured during the potential step reflect both processes and could not be directly interpreted by means of the existing theoretical models for electrochemical nucleation and growth. Additional experimentation in metal-ion-free solutions may help to account for the CP reductive behavior and thus to fit the experimental current transients in a more adequate way [162]. The size of the metal particles deposited in single-step potential experiments depends on the duration of the potential pulse. It has been demonstrated for various systems that by keeping the metal loading low, metal particles in the 15–20 nm range can be obtained (Table 7.3). Double-step potential procedures for metal electrocrystallization have been employed with the aim of controlling the growth process by combining a strongly reductive potential (first step) necessary to drive the nucleation of the metal particles and a more positive, but still reductive potential (second step) that is sufficient to sustain growth of the metal clusters without allowing for the appearance of new ones. The duration of the second pulse is used to control the size of the deposited metal particles.

Galvanostatic reduction is another alternative for metal electrocrystallization in CPs. The metal nucleation and growth occurs at a continuously varying overpotential and therefore it is not suitable for gaining insight into the kinetics of the metal electrodeposition. Nevertheless, this approach provides a helpful opportunity to assess the involvement of CP reduction in the overall process, and to explore fine differences in the reductive behavior of CP materials synthesized under various electrochemical conditions [180–183,185,189].

Repetitive square-wave potential techniques switch the potential continuously between the strongly reductive value necessary for the nucleation of the metal particles and a more positive one that is chosen to promote reoxidation of the CP material and thus recuperation of its conducting state, and/or improved penetration of metal complex anions in the CP layer. Metal complex anions that are used as sources of metal reduction become partially consumed, but also expulsed as doping anions in the course of the reductive dedoping pulse. The size of the electrodeposited metal particles has been found to depend essentially on the frequency of the potential pulses [37,169] (Table 7.3). In fact, the data summarized in Table 7.3 show that by appropriate adjustment of the corresponding parameters, all of the currently exploited electrochemical techniques may result in the deposition of metal NPs in CPs.

Apart from the size, a further important characteristic of the metal particles electrodeposited in CPs is their size distribution. The size distribution of the metal particles – narrow (close to monodisperse) or broad – depends basically on the type of nucleation kinetics – instantaneous or progressive. Instantaneous nucleation, i.e. 'simultaneous' appearance of all irreversibly growing nuclei, occurs, as a rule, at high overpotentials, whereas progressive nucleation is observed for lower overpotentials, but also for strongly inhomogeneous substrates. Thus CP surface homogeneity, which is known to depend on several parameters, e.g. type of electrochemical or chemical synthetic procedures, doping anion, CP layer thickness etc., may play a crucial role in the size distribution of the electrodeposited metal particles. In fact, the inhomogeneity of the polymer layer seems to be in the origin of the production of metal particles with sizes of very different scales (e.g. nm-sized and μm-sized) (Figure 7.4), which are sometimes simultaneously observed on the polymer surface [173,180,181]. The appearance of rather large metal crystals can be related to the existence of microdefects, e.g. large pores in the CP layer where the metal particles are in direct contact with the underlying foreign conducting substrate or to a much thinner CP substrate. The amount of microdefects has been extensively studied in the case of PANI (synthesized through potential-step, cyclic-voltammetry or repetitive square-wave potential (RSWP) experiments) [180].

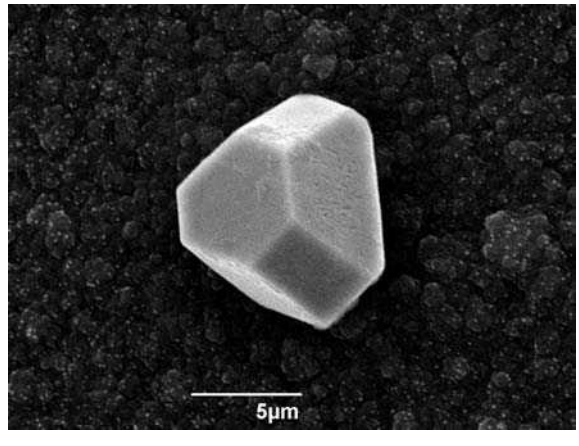

Figure 7.4 *Micrometer-sized copper crystal coexisting with a large number of much smaller copper particles on PEDOT.*

The observation of metal crystals at two different size scales has been used to identify microdefects in the polymer structure. Thus the largest amount of defects ($5 \times 10^5\,cm^{-2}$) is found in PANI layers synthesized at constant potential, whereas use of the RSWP procedure results in PANI with the lowest amount of microdefects ($2.6 \times 10^4\,cm^{-2}$). An interesting example demonstrating clearly the inhomogeneity of the polymer surface was recently obtained in studies on copper galvanostatic electrodeposition on thick PEDOT layers [195].

Large crystals surrounded by circular nucleation exclusion zones have been observed with the whole remaining PEDOT surface densely packed with much smaller Cu crystals (Figure 7.5). To explain this microscopic picture it should be assumed that a small number of nuclei have appeared much earlier than the remainder and have grown (without further nucleation events in their vicinity) to an extent large enough to deplete the diffusion field in their surroundings. The depleted diffusion field, corresponding to a lower local overpotential, entirely prohibits further nucleation. Such a situation can arise only with a highly inhomogeneous surface. The use of galvanostatic conditions for metal reduction that provide a gradual increase in the metal deposition overpotential favors the manifestation of such an effect.

The role of the CP surface structure in the characteristics of the metal deposit was demonstrated in the comparative study of Pd particle electrodeposition in two types of PANI layers differing in their surface morphology and porosity [157]. The elctrodeposition in both samples was carried out by single-step potential experiments at the same potential. AFM observations revealed the presence of nanometer-sized (50–90 nm) particles with a relatively narrow size distribution located on top of a more compact PANI layer. The use of layers with a rougher porous structure resulted in Pd particles with a larger size distribution (50–180 nm) located on the globular PANI surface. The possible formation of metal clusters inside the polymer matrix has also been suggested in the latter

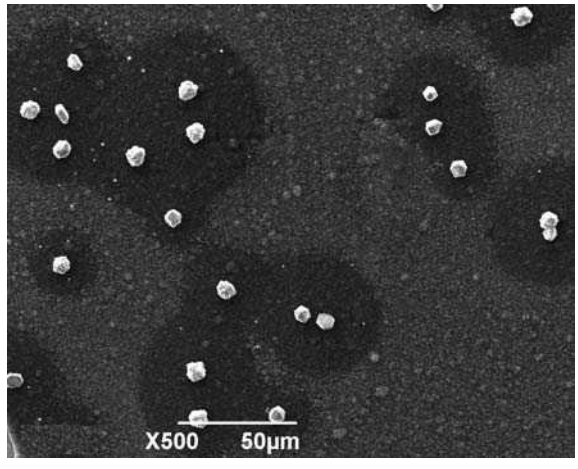

Figure 7.5 *Copper crystals electrodeposited through galvanostatic reduction of Cu^{2+} on PEDOT. Dark areas – nucleation exclusion zones; bright areas – nanoscale fine copper deposits.*

case. Further demonstrations of the role of polymer structure of chemically and electrochemically synthesized layers of PANI and poly(*o*-methoxynailine) (POMA) in the type of metal deposit are shown in [185,189].

7.4.2 Spatial Distribution of Electrodeposited Metal Particles

For most of the applications of metal-based CP nanocomposites a crucial point is the spatial distribution of the metal particles across the CP layer, which may depend essentially on the deposition technique (Figure 7.6). Thus, there is evidence that pre-saoking of the CP layer with metal-anion complexes and subsequent reduction in the absence of metal ions results in a homogeneous distribution of the metal particles inside the CP layer [51,131,134,170] (Figure 7.6a). Enrichment with metal particles close to the polymer layer/solution interface is expected to occur in the case of single-step potential deposition techniques applied to CP layers in their conducting state (Figure 7.6b). This is due to the fact that the external polymer surface will first take part in the metal nucleation process and the formed nuclei will gradually begin consuming the whole diffusive flux without allowing for metal-ion diffusion inside the CP layer. Repetitive square-wave potential techniques partially eliminate this problem by favoring the diffusion of metal ions inside the CP layer in the course of the more positive potential pulse of each pulse sequence. The porosity of the CP layer may also play a determining role in the location of the metal particles, for metals with negative enough equilibrium potentials to deposit in completely reduced CP layers. Experiments on Cd [194] and Cu [170,171,181] depositions carried out under these conditions have been interpreted by assuming that the metal nucleation occurs at the underlying substrate–CP-layer interface, and growth continuous throughout the polymer layer (Figure 7.6c). Direct evidence for the availability of copper inside the PANI layer was obtained through the study of the Cu-content depth profile obtained through XPS analysis [181].

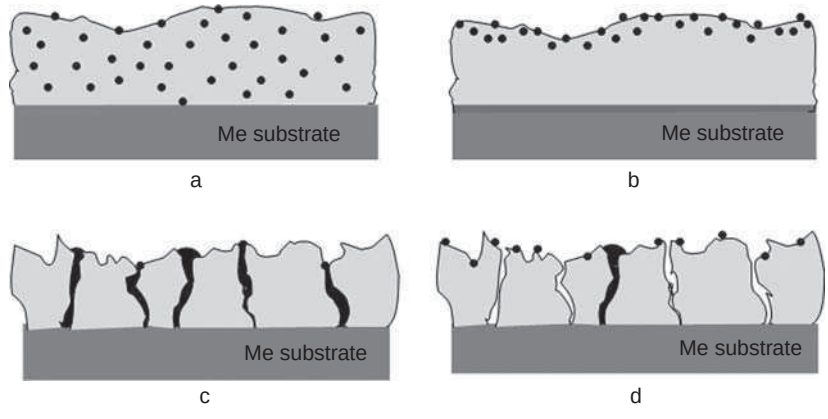

Figure 7.6 *Spatial distribution of metallic particles electrodeposited in CPs. (Adapted with permission from V. Tsakova, How to affect number, size and location of metal particles deposited in conducting polymer layers, J. Solid State Electrochem., 12, 1421–1434 (2008). Copyright (2008) Springer)*

An illustration of the role of the oxidation state in the distribution of the metal particles across the CP layer was presented in single-step potential deposition experiments on platinum in sulfonated PANI that were carried out at two values of the potential (–0.2 and +0.2 V vs. Ag/AgCl reference electrode), corresponding to the reduced and oxidized states of PANI [101]. In the first case a homogeneous distribution of Pt across the entire CP layer up to the underlying carrying substrate was observed, whereas in the second case (oxidized PANI) the Pt content decreased steeply within a narrow region close to the polymer/solution interface [101].

In general, most of the direct evidence for the spatial distribution of the metallic particles after single-potential-step experiments starting at initially oxidized CPs, supports the presence of enriched metal-containing regions close to the outer polymer surface. This has been found to occur for the deposition of Pt in PPY [129,132], PANI [109], and PTHI [88], of Pd in PPY [149] and PANI [10], and of Cu in PPY [168]. If, however, sulfonated PPY is involved in the metal reduction of cationic species (Cu^{2+}) (instead of pristine PPY), a more uniform distribution of the metal phase inside the PPY-PSS layer is found due to the doping role that the metal cations take in this situation [168]. There are few examples showing comparisons of the spatial distribution of the metal component when using alternative metal-deposition techniques. Thus, Pt deposited in PANI by a RSWP technique resulted in a more homogeneous metal distribution in the depth of the sample in comparison to single-potential-step-deposited Pt [109]. Obviously the RSWP approach allows for continuous relaxation of the PANI layer and for retention of its oxidation state throughout the experiment. A comparative study of Pd/PANI composite layers obtained by one-pot electrochemical synthesis and by a single-step potential experiment in pre-synthesized CP showed a major difference in the metal distribution [10]. The maximum Pd content was found to be close to the conducting substrate/polymer interface for the one-pot synthesis case and close to the polymer/solution interface for the single-step deposition case.

The design of subtle specific methods for depositing metal NPs, e.g. [144,145] is another way to control the location of the metal deposit within the CP layer. One proposed approach involves the deposition of a thin, sacrificial Au layer on a Pt substrate, electropolymerization of PANI on the Au-plated substrate, gold oxidation in chloride solution, and finally reduction of the $AuCl_4^-$ complexes entrapped in the PANI structure. Thus gold/polyaniline free-standing composite films are produced [144,145].

Thin CP layers present a specific problem with respect to the metal particle location due to their porous and also highly defective micromorphology. For such layers, along with the CP oxidation state (which controls the extent of conductivity), porosity, and defectiveness, become highly relevant for metal nucleation by providing the opportunity for fast transport of metal ions directly to the supporting electrode substrate (Figure 7.6c,d). In fact, there is always competition between the reduction of metal ions on the outer and inner polymer surface and on the underlying conducting substrate. The outcome of this competition depends on the specific combination of morphology and conducting properties occurring under any given experimental conditions. This is demonstrated in the case of Ag electrodeposition in PANI layers with various thicknesses [162]. Bearing in mind that Ag electrodeposition is driven in the oxidized state of PANI and according to the discussion presented above, it is expected that Ag crystals will nucleate at the outer polymer surface. Detailed kinetic studies based on the interpretation of single-potential-step current transients show that for thin PANI layers with thickness below 0.3 μm, the metal nucleation

occurs most probably on the underlying metal electrode through defects in the polymer structure. For thicker PANI layers, exceeding the 0.3 μm thickness limit, the microdefects seem to be leveled out and the Ag crystals are formed preferentially at the polymer/electrolyte interface. There are also experimental findings in other systems, e.g. Cu-PPY [175] showing a strong dependence of the number, size, and size distribution of electrodeposited metal particles on the CP layer thickness.

7.4.3 Number Density of Electrodeposited Metal Particles

The number density of metal particles deposited in the CP material is an important parameter for metal-based CP nanocomposites, especially in view of electrocatalytic and electroanalytic applications. In general, in the case of heterogeneous nucleation the number of emerging metal nuclei depends on the number of so-called active sites. Active sites for nucleation are energetically favored spots on the surface that provide the lowest energetic barrier to random nucleation events. For single-crystal substrates these are, for instance, steps and kinks at the crystalline surface. Unfortunately, in most practical cases the physical nature of the active sites cannot be exactly revealed and this also the case for CPs when used as heterogeneous substrates for electrodeposition. Nevertheless, there are experimental findings showing several practical approaches for influencing the number of deposited metal particles. Among them are use of metal-anion complexes instead of metal cations, involvement of metal–CP chemical interactions, and CP surface laser treatment.

The involvement of metal-anion complexes instead of the corresponding metal cation in metal electrocrystallization is a well-known approach in the practice of galvanic electroplating, used for improving the characteristics of the metal coatings. As a rule the use of metal-anion complexes shifts the potential window for metal deposition in the negative direction in comparison to that used for the corresponding cation. Thus, metal electrodeposition may be initiated in different oxidation states of the CP material. This approach has been demonstrated in a series of studies on Cu and Ag electrodeposition using various metal-anion complexes (Cu-citrate, Cu-oxalate, Ag-thiosulfate and Ag-EDTA) without allowing for preliminary exchange of the doping anion in the CP material [182,183,163]. (As already discussed, in the case of CP materials, metal-anion complexes may become involved in the doping of CP materials by replacing the pre-existing anions or by polymer synthesis in presence of these species.) It was found that the investigated metal-anion complexes provoke the expected shift of the potential window for metal deposition in a negative direction. In some cases, e.g. Cu-citrate and Ag-thiosulfate, this potential shift is large enough to separate the potential windows for CP and metal-ion reductions. In this situation, metal nucleation and growth occurs in reduced PANI layers, becomes inhibited, and results, in both cases, in the appearance of small numbers ($10^6\,cm^{-2}$) of crystals on the polymer surface. On the other hand, in the Cu-oxalate solution, the potential windows for metal-ion and CP reduction overlap, and both processes proceed in parallel. In this situation, a homogeneous surface distribution of a large number ($10^8\,cm^{-2}$) of smaller copper particles is obtained. One of the interesting points in these types of studies is to identify the role of the various ligands in the kinetics of metal nucleation and growth, and thus in the number and growth shape of the metal crystals. This point has so far barely been

addressed in the literature and needs to be elucidated in the future. Investigations involving, preferably, CP layers with pH-independent oxidation state and conductivity would be most useful.

Studies on metal electrodeposition in CP-coated electrodes show that electrochemical reduction of metal ions does not always result in crystallization alone, but also in chemical stabilization of metal species in the volume of the polymer layer. This effect and metal–CP interactions in general have been observed in several systems [186,187,196–207,223,238,246]. Evidence was obtained for the interaction of partially reduced metal ions, e.g. Cu(I) or Au(I), with specific (nitrogen or sulfur) sites in the polymer chains, resulting in the formation of metal–polymer complexes. Investigations into copper electroreduction in PEDOT [186,187] have shown that by driving the process at low constant overpotential it is possible to introduce reduced copper atoms in the polymer layer without building copper crystals. The copper atoms are reversibly oxidized to the Cu(I) state, the Cu(I) species remaining captured inside the PEDOT layer. This effect was further used to influence the copper-crystal formation by carrying out double-potential-step experiments involving stabilization at low overpotential, and subsequent crystallization at high overpotential [188]. The comparison of the microscopic pictures obtained after applying a crystallization overpotential directly and after a two-step copper electroreduction (partial reduction at low overpotential followed by high nucleation overpotential) is shown in Figure 7.7 (a and b). It is evident that the presence of stabilized species favors the copper electrocrystallization process and results in an increase in the crystal numbers. It is difficult to specify whether the stabilized copper atoms act directly as additional active sites for copper crystallization, or rather affect the polymer electronic structure. Nevertheless, it is clear that in all cases when metal

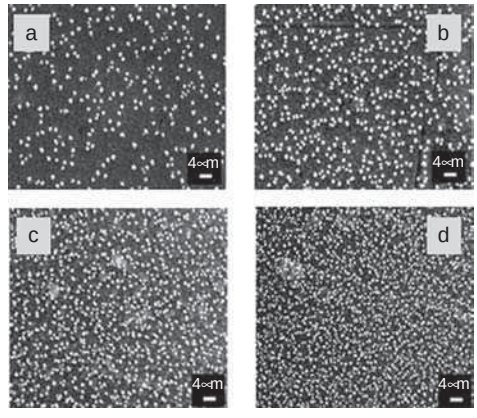

Figure 7.7 *Copper crystals electrodeposited on PEDOT layers by means of single-potential-step experiments (a, c) and double-potential-step experiments involving copper stabilization (b, d) before (a, b) and after (c, d) UV-irradiation of the CP surface. (Micrographs a and b adapted with permission from M. Ilieva, V. Tsakova, N.K. Vuchkov, K.A. Temelkov, N.V. Sabotinov, UV copper ion laser treatment of poly-3,4- ethylenedioxythiophene,* J. Optoelectron. Adv. Mat.*, **9**, 303–306 (2007). Copyright 2007 Nartional Institute of Research and Development for Optoelectronics.)*

stabilization in CPs is expected to occur, this effect provides an additional, still relatively unexplored tool for influencing the characteristics of the deposited metal particles.

Finally, recent investigations on mild UV-laser surface treatment of PEDOT layers [208,209] have shown that the surface chemical state of the polymer can become modified without any appreciable effect on the CP bulk properties. It was found [208] that UV-laser treatment results in activation of the surface with respect to metal nucleation and an increase in the number of deposited crystals by preserving a mono-disperse size distribution (Figure 7.7 c and d).

Metal electrodeposition provides a variety of techniques for introducing metal NPs into CPs and also effective means for control of the size distribution and spatial location of the metal NPs. There have been a great number of investigations in this field that are mostly directed to practical applications concerning mainly electrocatalysis and electronalytics (see Section 7.6). Nevertheless, there has been a significant effort to elucidate the specifics of the metal electrodeposition process in CPs, based on the traditional concepts of electrochemical nucleation and growth. One of the important issues in this field concerns the physical nature of the active sites that serve to initiate the metal nucleation process. To get some insight in this subject, the local properties of the CP layers (e.g. morphology, chemical and physical structure, conductivity etc.) should be studied and correlated with the nucleation stage of metal-particle formation.

7.5 Chemical Reduction of Metal Ions in Pre-Polymerized CP Suspensions or Layers

7.5.1 Use of the Polymer Material as Reductant

Conducting polymers may take different interconvertable oxidation states and therefore provide the possibility for chemical (electroless) deposition of metals. Metal ion reduction occurs at the expense of the transition from lower to higher oxidation state of the CP material:

$$\mathrm{Me}^{n+} + n\mathrm{e}^- \rightarrow \mathrm{Me}^0 \tag{7.1}$$

$$\mathrm{CP}^{m+} \rightarrow \mathrm{CP}^{(m+n)+} + \mathrm{ne}^-$$

where n is the number of electrons necessary to reduce a single metal ion and m denotes the extent of initial oxidation of the CP material. The CP initial oxidation state may be controlled either through acid–base or doping/dedoping processes. As an example the various oxidation states of PANI are shown in Figure 7.8.

Most of the studies in this field concern the deposition of noble metals Au [16,210–222], Ag [223–235], Pd [156,158,236–248], Pt [249,250] and Hg [251,252], with equilibrium potentials that are positive enough with respect to the potentials of oxidation transitions in most CPs, e.g. PANI, PPY etc. (Figure 7.3). Investigations have been carried out in both homogeneous (chemically produced suspensions) and heterogeneous (electrodeposited or

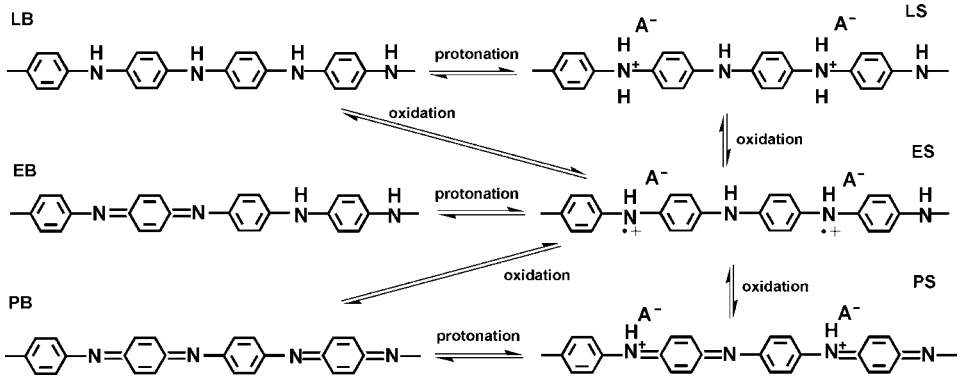

Figure 7.8 *Interconvertable oxidation states of PANI*

solution-cast CP layers and membranes) systems. An overview on the metal–CP couples that have been studied in view of CP-driven chemical deposition of metal particles is presented in Table 7.4.

In spite of the great number of investigations on CP-driven chemical deposition of metal particles there have been almost no attempts to address the mechanism of this process, either in homogeneous or heterogeneous cases. In a homogeneous system with dispersed metal ions and CP species, the process most probably includes continuous formation of metal nuclei that provide a catalytic surface for further reduction of metal ions and give rise to autocatalytic growth [254].

In the heterogeneous case the process may be treated in a way similar to electrodriven metal deposition. Thus, the 'electroless' chemical metal deposition should involve an initial nucleation step that occurs through electron transfer from the CP layer to the metal ions, followed by growth of the metallic nuclei, which remain fixed at the CP surface. Both stages are controlled through the potential difference between the two phases – metal ions in solution and bulk metal deposited on the polymer surface. The electrochemical potential of the deposited metal depends on the actual potential of the CP-layer substrate. Therefore, the potential difference driving the phase formation process, and thus the probability of metal particle nucleation, will be larger for CP materials with a lower initial extent of oxidation. In the course of metal deposition the potential difference is constantly changing due to both gradual oxidation of the CP material and depletion of the metal ion concentration in solution (which occurs in the case of low concentrations and small reactive volumes). The decrease in metal ion concentration in the reacting solution is frequently used as one of the few measurable quantities indicating the progress of the metal-deposition process. Another quantity that is relevant for CP-driven metal deposition is the open-circuit potential (OCP), i.e. the self-established electrical potential of the bulk CP. Measurement of this quantity in the course of CP-driven metal deposition shows a gradual shift of the CP state from lower to higher oxidation state [163,226,232,248] and indicates clearly the timescale of substantial changes in the driving force of the process (Figure 7.9).

Table 7.4 *Overview of the systems involved in CP-driven chemical reduction of metal ions*

Metal-ion source (concentration)	Polymer type (method of synthesis)	Reductant (initial oxidation state of the CP material)	Me particle size	Ref.
Au				
$AuCl_4^-$ (0.1–0.5 mM)	PANI films (chem.)	EB, ES, LB, NA	About 20 nm (NMP), 50–200 nm (H_2O)	210, 211, 213, 216
n.d.	PANI-PAA (chem.)	EB, ES	7–12 nm	233
$KAuBr_4$ (0.5 mM)	PANI (electrochem.)	ES	25–400 nm	219
$AuCl^-_4$ (0.01 mM)	PANI membranes	EB, ES	Depending on the doping	220
$AuCl^-_4$ (1 mM)	PANI (electrochem.)	LS	A few nm–300 nm	221, 222
$HAuCl_4$ (0.3 mM)	PPY films (chem.)	25% Deprotonated	–	212, 213
$AuCl_3$ (10 mM)	PPY, PANI, PEDOT (chem.)	Doped and base-treated	1000 or 100–400 nm (PPY) (depending on pH)	217
$AuCl_3$ (10 mM)	Poly(3-alkylthiophene)	Dedoped	–	214, 215
$HAuCl_4$ (1 mM)	Poly(dithiafulvene)	Reduced	6 nm	218
Ag				
$AgNO_3$ (0.01 mM)	PANI membranes	ES, EB	~μm structures (depending on dopant type)	220
$AgNO_3$(100 ppm)	PANI- powder, membranes or coated RVC and fabrics	ES	Silver recovery	231
$AgNO_3$ (30 mM)	PANI-PAA colloid	EB, ES	3 nm	233
$AgNO_3$ (various Ag:PANI ratios)	PANI – granular, nanotubular, oligomers (chem.)	ES	20–40 nm	235
$AgNO_3$ (0.1 M)	PANI (electrochem.)	LM	μm-Sized dendrites	223
Ag^+ (0.93 mM)	PANI (electrochem.)	ES	Silver recovery	226
$AgClO_4$ (10 mM), Ag-EDTA (0.4 –10 mM)	PANI (electrochem.)	LS	1–2 μm (ClO_4^-), 70–250 nm (EDTA) (depending on Ag ions concentration)	163
Ag NO_3 (0.5–2.0 mM)	PPY (chem.)	Doped	10 nm	228, 229
$AgNO_3$ (0.5–25 ppm)	PPY (electrochem.)	Doped and base-treated	Silver recovery	225
$AgNO_3$ (0.1 mM)	PPY (electrochem.)	Various oxidation states	–	227
$AgNO_3$ (100 mM)	PPY (electrochem.)	Base-treated	–	230

$AgNO_3$ (0.01–10 mM)	PPY, PEDOT (electrochem.)	Doped	–	232
Ag-triflate (3.5 mM)	Poly(3-alkylthiophenes) films (chem.)	De-doped	60–250 nm	224
$AgClO_4$ (0.5–2.0 mM)	Poly(3-octylthiophene) (chem.)	Doped	3 and 17 nm (bi-modal size distribution)	234
Pd				
$PdCl_2$ (2.3 mM)	PANI (chem.)	EB		237, 238, 241
$Pd(NO_3)_2$ (1 mM)	PANI (chem.)	LM	110–160 nm	216
$PdCl_2$ (0.9 mM), $Pd(NO_3)_2$ (0.9 mM)	PANI (chem.)	EB, LM	–	239
$Pd(NO_3)_2$ (0.9 mM)	PANI films (chem.)	EB, LM, NA	–	243
Pd in HCl (25 ppm)	PANI (electrochem.)	LM, PN	100 nm–1 μm	236
$PdCl_2$ (20 mM), Pd-acetate (20 mM)	PANI, poly(*o*-toluidene), poly (o-chloroamine)	EB		245
Pd in HCl (100 ppm)	PANI (electrochem.)	LS	15 nm or 20 and 80–200 nm (depending on synthetic conditions)	156, 248
$PdCl_2$ (2.3 mM)	POMA (chem.)	EB and ES	200–1000 nm	246, 247
$PdCl_2$ (0.9 mM), $Pd(NO_3)_2$ (0.9 mM)	PPY (chem.)	Fully reduced	n.d.	239
$PdCl_2$ (0.9 mM), $Pd(NO_3)_2$ (0.9 mM)	PPY (electrochem.)	Fully reduced, protonated and deprotonated	n.d.	244
$PdSO_4$ (2 mM)	PEDOT (electrochem.)	Dedoped	20–40 nm	158
Pd-acetate (5 mM)	Poly(dithiafulvene) (chem.)	Reduced	6 nm	218
Pt				
K_2PtCl_4 (0.01 mM)	PANI membranes	EB, ES	100–300 nm agglomerates	220
n.d.	PANI-PAA (chem.)	EB, ES	2 nm	233
K_2PtCl_4 (10 mM)	PANI (chem.)	EMS	30–90 nm	249, 250
H_2PtCl_6 (10 mM)	Poly(dithiafulvene)	Reduced	6 nm	218
Hg				
$HgNO_3$ (1–2 mM)	PANI (chem.) – powder	EB, LM		252
$HgCl_2$ (2 mM)	PANI (electrochem.)	EMS	–	251

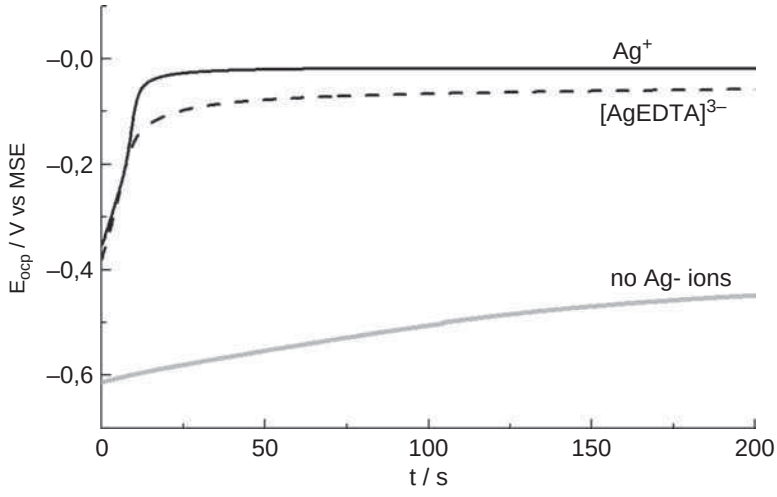

Figure 7.9 *Open-circuit potentials measured when immersing electrochemically reduced PANI layers in Ag ion-containing solutions. The grey reference line shows the OCP of PANI in the absence of metal ions. (Adapted with permission from S. Ivanov and V. Tsakova, Electroless versus electrodriven deposition of silver crystals in polyaniline: Role of silver anion complexes,* Electrochim. Acta*, **50**, 5616–5623 (2005). Copyright 2005 Elsevier.)*

It is known that the nucleation of metal particles may occur as an instantaneous (at high supersaturations) or a progressive (at low supersaturations) process. A particle size distribution of a delta-type is characteristic for the first case, whereas a broad size distribution is observed in the second one. An illustration of the occurrence of these two situations is found in the study of Ag electroless deposition in electrodeposited PANI layers [7,163]. By keeping the amount of deposited Ag the same, and using different concentrations of the Ag ion solution it is possible to affect the number density and size distribution of the metal particles. At higher concentration, a lower number of almost equally sized Ag articles is formed (Figure 7.10a), a situation corresponding to instantaneous nucleation of the metal particles. Reducing the concentration of the metal-ion species present in the solution results in the appearance of a higher number of Ag particles with a broader size distribution (Figure 7.10b).

An intensive nucleation process provokes a fast shift to a higher oxidation state for the CP material and therefore a steep decrease in the supersaturation and the probability of metal nucleation. Therefore, it is only particle growth that occurs further with time. Such an example is provided by the investigation of Au deposition in CH_3COO^--doped PANI [191]. An increase in the Au NP size was found with immersion time (4 to 20 min) at roughly preserved particle numbers. On the other hand, sluggish nucleation occurring at lower metal ion concentrations, or a higher extent of initial CP oxidation lets the system remain at the initial supersaturation for a longer time and results in the progressive appearance of new metallic nuclei.

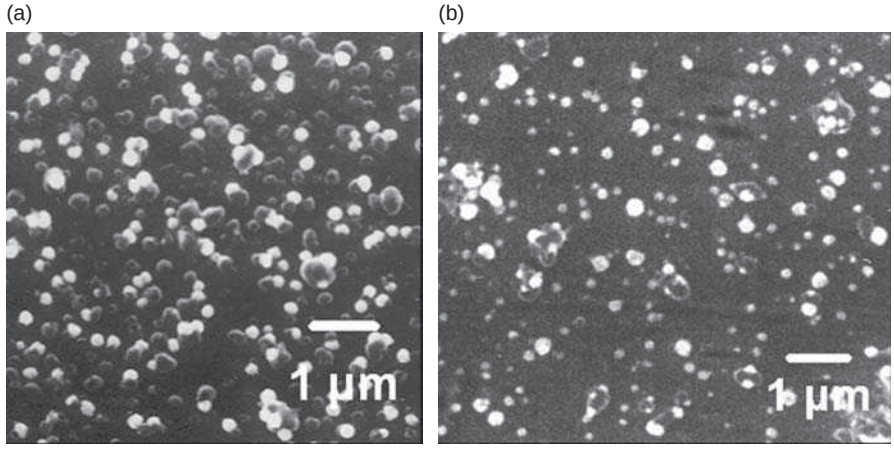

Figure 7.10 *Silver crystals obtained after immersion of electrochemically reduced PANI in Ag-EDTA solution with two different concentrations: (a) 10 mM and (b) 2 mM. (Reproduced with permission from V. Tsakova, How to affect number, size and location of metal particles deposited in conducting polymer layer,* J. Solid State Electrochem.*, **12**, 1421–1434 (2008). Copyright 2008 Springer.)*

Quantitative studies of CP-driven metal deposition in homogeneous systems are usually based on measurements of the depletion of the metal ion solution as a result of metal deposition. In heterogeneous systems the amount of reduced metal obtained at various deposition conditions may be determined by electrochemical oxidative dissolution of the metal phase [163,227]. An example showing the correlation between the deposited amount of Ag (obtained by oxidative dissolution) and the thickness of the PANI layer is presented in Figure 7.11 [163]. The data are obtained at two concentrations of Ag ions. All PANI layers are electrochemically reduced at the same extent before immersion in the Ag ion solution, but due to the different amount of CP material they differ in their oxidation charge, i.e. oxidative capacity. The oxidation charge is taken as an indirect measure of the PANI layer thickness. The deposited amount of Ag obtained at the higher concentration increases with increasing PANI oxidation charge. This means that the amount of the Ag deposited can be easily controlled by monitoring the thickness and thus the oxidation charge of the polymer layer. The results obtained at the lower concentration (0.4 mM) show a different trend. In this case electroless deposition occurs very slowly and the short immersion time used in this series of experiments is apparently not enough to consume the whole oxidative capacity of the polymer layer. Increasing the immersion time allows the amount of deposited silver to increase up to values limited by the oxidative capacity of the PANI layer. Therefore a proper choice of the two parameters – Ag-ion concentration and immersion time allows a switch between oxidation-charge limited and time-limited electroless metal deposition. Using low concentrations and short immersion times results in deposition of the same amount of metal, irrespective of the oxidative capacity of the PANI layer.

The interplay between rates of nucleation and growth (both depending on supersaturation) is not the only factor that determines the number, shape, and size distribution of the deposited metal particles. In addition, there are several specific factors, such as the surface

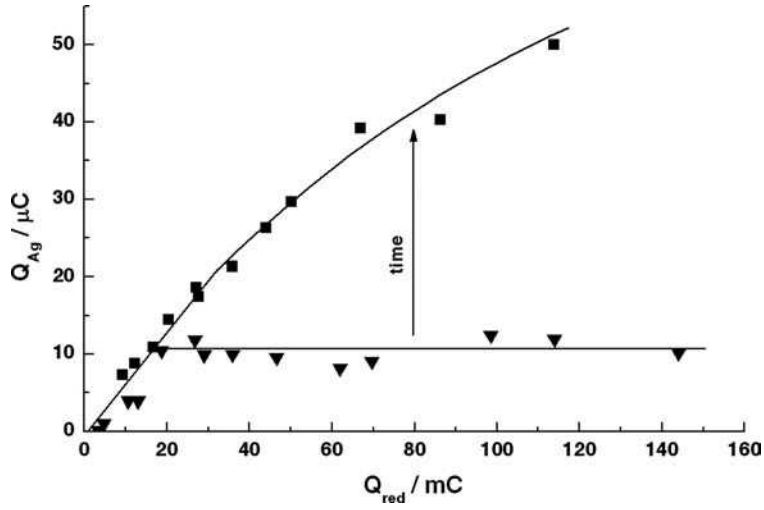

Figure 7.11 *Dependence of the amount of deposited silver (measured through the charge of oxidative dissolution) on the amount of PANI (measured through the PANI intrinsic oxidation state) at two different concentration of Ag-EDTA solution: 10 mM (■) and 0.4 mM (▼). (Adapted with permission from S. Ivanov and V. Tsakova, Electroless versus electrodriven deposition of silver crystals in polyaniline: Role of silver anion complexes,* Electrochim. Acta*, **50**, 5616–5623 (2005). Copyright 2005 Elsevier.)*

morphology and surface state, the type of dopant, the investigated timescale of the process, and the solution pH, that may strongly affect the CP-driven metal deposition process. Examples illustrating the involvement of such factors are given below.

The role of the surface morphology on CP-driven Pd deposition on electrochemically synthesized PANI layers was studied by Mourato *et al*. [248]. The surface structure was intentionally modified by using two different potentiodynamic polymerization regimes. Thus, it was found that for the more compact PANI surface, Pd clusters with an average size of 20 nm and also larger particles with a size distribution between 80 and 200 nm are formed. In the case of a more porous surface morphology, smaller clusters (15 nm) with very narrow size distribution were observed, together with larger particles in the 100–200 nm range. The role of the surface chemical state of electrochemically deposited layers was demonstrated in the case of PEDOT by studying CP-driven deposition of Ag and Pd particles on nonirradiated and UV-laser-irradiated samples [209]. Irradiated and subsequently electrochemically reduced PEDOT samples were immersed in metal-ion containing solutions. The irradiated samples turned out to be highly active for metal deposition in comparison to their nonirradiated counterparts (Figure 7.12). It was argued that new surface states that favor the metal-ion-reduction process appear after irradiation at the CP surface [209]. A further example in this direction is provided by recent investigations of a Ag/PANI homogeneous system [235] showing a strong effect of the type of PANI (granular or nanotubular) used for the electroless deposition on the properties of the obtained Ag-PANI nanocomposites. PANI-Ag samples with comparable silver content were found to differ in conductivity by several orders of magnitude.

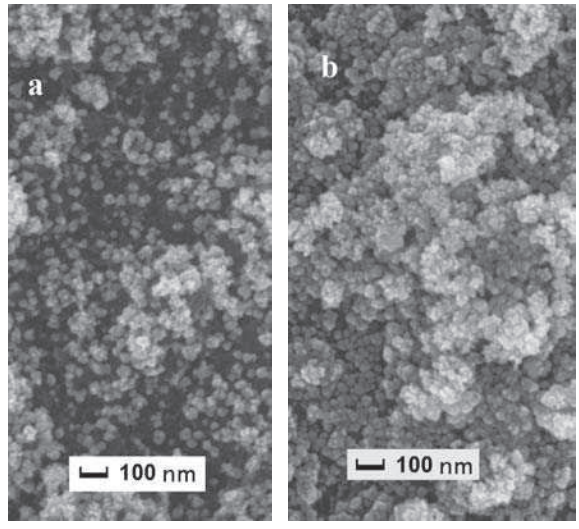

Figure 7.12 *Chemical deposition of Pd NPs in electrochemically reduced PEDOT layers (a) before and (b) after UV-irradiation of the CP surface*

The effect of the type of doping anion available in the CP layer on the characteristics of the obtained metal deposit has been demonstrated in the case of PANI-driven deposition of Ag [220]. Investigations were carried out by doping PANI membranes with six different acids – hydrochloric, mandelic, citric, *p*-toluenesulfonic, trifluoroacetic, and phosphoric – and immersing the membranes in 0.01 M $AgNO_3$ solution. Silver crystals with a large variety of growth shapes (yarn-balls, nanowires, leaf-like structures) and sizes (from nanometers to several microns) were observed. It is expected that PANI-doping by various acids will result in different extents of PANI protonation. In general acidity is a further important parameter of the CP-driven electroless process. It is argued that strongly acidic solutions do not favor electroless metal deposition due to the competition of hydrogen and metal ions for the same specific sites on the polymer backbone [227]. Further systematic studies under precise control of the oxidation state and the degree of protonation of the CP materials are needed in order to assess the roles of the type of doping anion and acidity on CP-driven metal-deposition processes.

In the various investigations on CP-driven metal deposition the timescale of the experiments has varied over a wide range starting from a few seconds to few minutes [163,219], hours [210–212,216], or even days [213]. Whereas short-timescale experiments in heterogeneous systems rely basically on the leveling off of the initial potential difference between the CP material and the metal ions in solution, long-timescale experiments involve additionally so-called self-sustained deposition. Starting with the very first studies on the chemical deposition of Au in PPY and PANI [210–212] it has been established that in some particular cases chemical metal deposition in CPs may proceed for hours as a self-sustained process. This was found to occur in acidic solutions where spontaneous reprotonation of the deprotonated (in the course of metal ions reduction) CP (e.g. PANI or PPY)

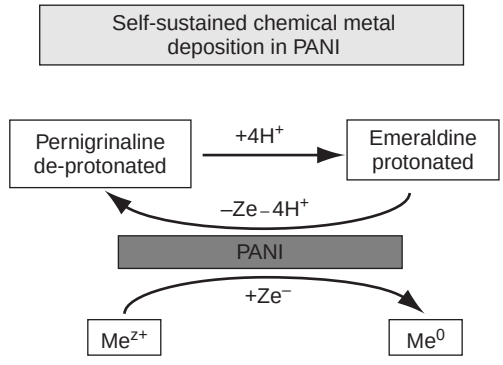

Figure 7.13 *Reactions taking place in the course of the self-sustained metal deposition in PANI*

takes place. The recuperated reduced state of the CP material further enables the self-sustained process, as illustrated for PANI in Figure 7.13.

Later investigations [217] have shown the occurrence of this process in neutral solutions and also for polymers of the thiophene type that are not expected to undergo protonation/deprotonation reactions. The self-sustained metal-deposition process has been suggested as tool for recovery of precious metals from waste solutions by using CP powders, membranes, supported layers, coated fabrics, or reticulated vitreous carbon (RVC) [210–212,225,226,236,253]. However, very long-term exposure to the metal-ion-containing solution may result in degradation (decrease in electrical conductivity and gradual loss of material) of the CP layer, as evidenced with the exposure of PANI to chloraureate solution [213].

CP-driven chemical metal deposition is a useful and generally easily performed process for producing metallic-based CP nanocomposite materials. Nevertheless, it requires strict control over several parameters in order to achieve the deposition of nanosized metal particles. In supported CP layers, chemically deposited metal particles are predominantly located at the polymer/solution interface. For heterogeneous systems the basic advantage of chemical over electrochemical metal deposition seems to be the possibility of eliminating the role of structural microdefects in the CP layer. The most favorable sites for metal-particle deposition are those where the polymer structure becomes readily oxidized. Thus, the polymer morphology is of prime importance, but instead of defects, the active sites for nucleation are most probably polymer chains with a higher extent of conjugation and order. Further comparative investigations involving studies on the local properties at the nanoscale are needed in order to identify the active sites for chemical deposition and the means to influence them in a pre-defined way.

7.5.2 Use of Additional Reductant

Apart from the extensively studied opportunity to reduce metal ions in pre-polymerized suspensions or layers by involving the reducing capacities of the polymers themselves, the possibility to use additional reductants has been also explored in few

cases [255–262]. Thus, formaldehyde was introduced to reduce Pt [255,257,260–262], Pt-Ru [260,262], and Pt-Pd [261] in PPY, PTHI, and PEDOT, and sodium tetrahydroborate for reducing Au [258] and Pd [259] in PEDOT and PANI, respectively. In all these cases nanometer-sized metal particles were obtained. A loss in electrical conductivity compared to the corresponding polymer was established in the Pt-PPY [255] and Au-PEDOT [258] cases. The use of another reductant (hydrogen) in the Pt-PPY system resulted in the formation of large and agglomerated platinum particles [256]. Chemical deposition of Ni in PPY, PANI, and P3MET has also been investigated [190,263,264].

Finally, the possibility of involving γ-irradiation in reduction of Fe and Pd ions was demonstrated for the preparation of nanocopmposite materials containing sulfonated PANI, multiwall carbon nanotubes, and Fe, Pd, or Fe-Pd alloy NPs [265]. Recently, UV-induced photoreduction was used for the formation of Pt particle-modified PANI and TiO_2-PANI composite layers [266]. This turned out to be an effective approach for achieving a homogeneous distribution of small enough metal particles on the CP surface.

7.6 Metallic-Based CP Composites for Electrocatalytic and Electroanalytic Applications

The overview presented so far has shown the manifold activities of synthetic chemists and electrochemists to produce various metallic-based CP nanocomposite materials. These efforts have been directed to a diversity of applications, e.g. electrocatalysis, electroanalytics, chemical and electrochemical sensing etc. To outline these areas of research is a separate task that remains outside the scope of this chapter. Nevertheless, for the prevailing number of investigations, where the synthetic work has been combined with applications-related measurements, a brief outline will be presented here.

Most of the applications-oriented investigations address the possibility of using metallic-based CP nanocomposites as electrocatalytic materials for a number of reactions summarized in Table 7.5 [267–310] (and references cited therein). Electro-oxidation of methanol, formic acid, and formaldehyde, as well as reduction of dioxygen have been intensively studied in view of the development of new electrocatalysts suitable for fuel cells. (The development of metal/polymer composites as electrode materials for low-temperature fuel cells has been recently reviewed [311].) In these cases the CP material is used as a suitable conducting matrix for dispersing the metal catalyst. Electro-oxidation of several organic compounds of biological interest (e.g. ascorbic acid, dopamine, glucose, NADH, uric acid) has been explored with regard to prospective electroanalytical applications (Table 7.5). It was established that CPs show electrocatalytic activity for these reactions [312] and thus suitable combinations with electrocatalytic metals that could provide increased sensitivity or selectivity for detection of specific analytes have been sought. Finally, gas sensing using various metallic-based CP nanocomposites has been also intensively investigated [61,151,313,314].

The development of nanostructured composite materials suitable for electrocatalytic and electroanalytic purposes is based on expectations of increasing the surface-to-volume

Table 7.5 *Electrocatalytic reactions studied on various metallic based CP composite materials*

Oxidation reactions			
Substance	Polymer	Me particles	References
Methanol	PANI	Pt	90, 106, 108, 113–116, 118–120, 123–125, 127, 267–271
		Pt-Ru; Pt-Ru-Mo	95, 108, 111, 126; 108, 112, 272
		Pt-Sn; Pt-Os, Pt-Ru-Os	95; 112
		Pt, Pt-H_xMoO_3	273
		Au	274
	Poly(*o*-phenylenediamine)	Pt	275, 276
	Poly(diphenylamine)	Pt	277
	PPY	Pt; Pt-Ru	130–132, 278, 279; 260
	P3MET	Pt; Pt-Sn	280; 135
	PEDOT	Pt, Pt-Ru	141, 281–283
Ethanol	PANI	Pt-Ru, Pt-Sn	95
Hydrogen	PANI	Pt	99
	PPY	Pt	51, 128, 133
Co	PANI	Pt; Pt-Ru, Pt-Os, Pt-Mo	121, 267; 112
Ethylene glycol	PANI	Pt; Pt-Ru, Pt-Sn	98; 102
	PTHI	Pt, Pt-Ru	262
Formaldehyde	PANI	Pt; Pt-H_xMoO_3	117; 118
	PPY	Pt; Ag	261; 230
Formic acid	PANI	Pt; Pt-Pb; Pt-H_xMoO_3	92, 267; 118, 286; 118
		Pd	153, 267
	PPY	Pt, Pt-Pb	103, 261, 286
	PTHI	Pt, Pb, Pt-Pd	138, 286, 287
Glycerol	PANI	Pt	110
Hydrazine	PANI	Pt	249
	PPY	Au	147
Hydroxylamine	PPY	Au	147
Ascorbic acid	PANI	Au	48
	POMA, PANI	Cu	288
	PEDOT	Au	59, 70, 71
Ascorbic acid and dopamine	Poly(4-aminothiophenol)	Au	289
Dopamine, serotonin	PPY – overoxidized	Au	290
Dopamine	PEDOT	Au; Pd	59, 70, 71; 291
Glucose	PANI	Cu	292, 293
	PANI	Au	29, 294
	PPY	Pd, Pt, Pt-Pb, Pt-Sn, Pt-Bi, Pt-Ru	295–298

Table 7.5 (*continued*)

Oxidation reactions			
Substance	Polymer	Me particles	References
	PEDOT	Pd	299
NADH	PANI	Au	84
	P3MET	Cu	300
	PEDOT	Au	301
Uric acid	PEDOT	Au; Pd	59, 71; 291
Reduction reactions			
O_2	PANI	Pt	80, 97, 100
	PANI	Pd	150
	Poly(*o*-phenylenediamine)	Pt	302
	Poly(aminothiophenol)	Au	303
	PPY	Pt	5, 129, 284
	PTHI	Pt	304
	PEDOT	Pt	305
H_2O_2	PANI	Pt	306
	PPY	Cu	307
Hydrogenation reactions			
C=C and C≡C bonds conjugated with aromatic ring	Substituted PPY	Pd, Rh	136, 149, 308
Limonene, carvone	Substituted PPY	Pt, Pd, Rh; Pd+Pt, Pd+Rh	137
2-Eethylanthraquinone	PANI	Pd	237, 241
Nitrobenzene	PANI	Pd	239
	PPY	Cu	170
4-Nitrobenzaldehyde	PANI	Pd	156
4-Nitrophenol	PEDOT	Au, Pd	39, 45
2-Ethylanthraquinone	POMA	Pd	247
Maleic acid	POMA	Pd	247
Other reactions			
Chloro-, bromo- and iodobenzenes (Heck reaction)	PPY	Pd	154
Aryl chlorides (Suzuki coupling)	PANI	Pd	309
Substituted aryl alkynes (hydrosilylation)	PANI	Pt	310

ratio of the catalytic material, to improve the electron transfer, to prevent adsorption of reaction products, and eventually achieve a synergistic effect due to the combination of the electrocatalytic performances of the composite constituents. In addition, reducing the size of the metallic particles results in the formation of crystals exposing new crystallographic

facets at the surface and thus the opportunity to involve crystallographic anisotropy effects in the electrocatalytic reactions. Finally, the properties of small enough metal NPs ($d < 10$ nm) become shape and size sensitive, and significant changes in electrocatalytic activity might be expected [315–318].

Despite the great number and diversity of studies in the field of metallic-based conducting polymer composites, most of the above-mentioned aspects have not been clearly identified. There are still several open questions concerning the roles of the metal deposit characteristics, i.e. spatial distribution, size and number of metallic particles, and of the polymer matrix properties in the electrocatalytic performance. One of these questions addresses specifically the spatial distribution of the metallic phase. The problem is whether the metallic particles incorporated in the bulk of the polymer layer are effective as catalytic centers or whether the reactions of interest occur mainly at the polymer/solution interface. Investigations on methanol oxidation in Pt-PPY systems [132] by varying the method of metal-particle deposition have shown that Pt particles obtained by electrosynthesis in the presence of the corresponding metal complex (with subsequent reduction) or incorporated pre-synthesized NPs have no electrocatalytic activity. A comparative study of PPY layers modified with noble metallic particles for hydrogen evolution reactions showed better performance for composite materials obtained through electrodeposition on pre-synthesized layers in comparison to those obtained by CP synthesis in the presence of metal complex anions and subsequent reduction [134]. Metallic particles located mainly near the CP/solution interface (as usually obtained by means of electrodeposition on pre-synthesized CP layers) were also found to exhibit better electrocatalytic activity in other cases [51,128,154]. The various ways of producing metallic-based CP nanocomposites offers wide possibilities for influencing the surface distribution of the metallic NPs at the CP/solution interface. The role of this factor in electrocatalytic performance has been demonstrated in a Pt-PANI system [120]. The electrodeposition of Pt metallic particles from $PtCl_4^{2-}$ and alternatively from $PtCl_6^{2-}$ solutions resulted in a difference in the shape and surface distribution of the Pt particles. This was found to affect markedly the methanol oxidation current. The role of the properties of the polymer matrix (e.g. morphology, conductivity etc.) in electrocatalytic performance itself has rarely been assessed in electrocatalytic studies of metallic-based CP materials. For instance, a comparison between Pt-PANI and Pt-PANI-PSS for methanol oxidation [123] showed better performance for the Pt-PANI-PSS case, although it is not clear whether this was due to the different spatial distribution of the metallic particles in the CP layer or to the different bulk properties of the CP material. In general, the fact that the electrocatalytic performance depends on a number of inter-related factors concerning both the metal particles and the polymer matrix, which are not easy to assess due to their complexity, leads to controversial conclusions regarding the electrocatalytic activity of given nanocomposite systems.

Studies concerning the involvement of metallic-based CP nanocomposites in electroanalytical applications in general have not addressed issues concerning the specifics of the material in terms of metal-particle characteristics and CP bulk properties. The main focus has remained on showing possibilities for electroanalytical applications without going into the various possibilities to influence the properties of the nanocomposite materials and thus of the electroanalytic response. This seems to be an area that requires further concerted efforts by chemists specializing in the synthesis of metallic-based CP nanocomposites and those aiming at specific applications.

List of Acronyms

AFM	atomic force microscopy
CNT	carbon nanotubes
CP	conductive polymer
DABS	2,5-diaminobenzenesulfonate
DBS	dodecylbenzenesulfonate
DMA	2,5-dimethoxyaniline
DS	dodecyl sulfonate
EB	emeraldine base
EDOT	3,4-etylenedioxythiophene
EDTA	ethylenediaminetetraacetic acid
ES	emeraldine salt
LbL	layer-by-layer
LB	leucemeraldine base
LS	leucoemeraldine salt
NA	nigraniline
NMP	*N*-methylpyrrolidinone
NP	nanoparticle
OCP	open-circuit potential
PAA	polyaclilic acid
PANI	polyaniline
PB	pernigraniline base
PDMA	poly(2,5-dimethoxyaniline)
PEDOT	poly(3,4-etylenedioxythiophene)
POMA	poly(*o*-methoxynailine)
PPY	polypyrrole
PS	pernigraniline salt
PSS	polysterenesulfonate
PTHI	polythiophene
P3MET	poly(3-methylthiophene)
PVA	poly(vinyl alcohol)
PVP	poly(*N*-vinylpyrrolidone)
RGP	repetitive galvanostatic pulses
RSWP	repetitive square wave potential
RVC	reticulated vitreous carbon
SDS	sodium dodecylsulfate
XPS	X-ray photoelectron spectroscopy

References

[1] H. Shirakawa, E.J. Louis, A.G. MacDiarmid, C.K. Chiang, and A.J. Heeger, Synthesis of electrically conducting organic polymers: Halogen derivatives of polyacetylene, (CH)x, *J. Chem. Soc. Chem. Commun.*, **16**, 578–580 (1977).

[2] A. Malinauskas, J. Malinauskiene, and A. Ramanavicius, Conducting polymer-based nanostructurized materials: electrochemical aspects, *Nanotechnology*, **16**, R51–R62 (2005).

[3] B.C. Sih and M.O. Wolf, Metal nanoparticle-conjugated polymer nanocomposites, *Chem. Commun*., 3375–3384 (2005).
[4] X. Li, J. Sun, and M. Huang, Preparation and properties of nanocomposites of polyaniline and metal nanoparticles, *Progr. Chemistry*, **19**, 787–795 (2007).
[5] D.W. Hatchett and M. Josowicz, Composites of intrinsically conducting polymers as sensing nanomaterials, *Chem. Reviews*, **108**, 746–769 (2008).
[6] M.A. Vorotyntsev and S.V. Vasilyeva, Metallocene-containing conjugated polymers, *Adv. Colloid Interf. Sci*., **139**, 97–149 (2008).
[7] V. Tsakova, How to affect number, size and location of metal particles deposited in conducting polymer layer, *J. Solid State Electrochem*., **12**, 1421–1434 (2008).
[8] R. Gangopadhyay and A. De, Conducting polymer nanocomposites: A brief overview. *Chem. Mater*., **12**, 608–622 (2000).
[9] C. Lamy and J.M. Leger, Electrocatalysis with electron conducting polymers modified by noble metal nanoparticles. In *Catlysis and Electrocatalysis at Nanoparticle Surfaces*, ed. A. Vieckowski, E. Saviniva, and C. Vayenas, Marcell Dekker, New York, 2003.
[10] H.S. Li, M. Josowicz, D.R. Baer, M. Engelhardt, and J. Janata, Preparation and characterization of polyaniline-palladium composite films, *J. Electrochem. Soc*., **142**, 798–805 (1995).
[11] S.T. Selvan and M. Nogami, Novel gold-polypyrrole anisotropic colloids: a TEM investigation, *J. Mater. Sci. Lett*., **17**, 1385–1388 (1998).
[12] S.T. Selvan, J.P. Spatz, H.A. Klok, and M. Möller, Gold-polypyrrole core-shell particles in diblock copolymer micelles, *Adv. Mater*., **10**, 132–134 (1998).
[13] S.T. Selvan, T. Hayakawa, M. Nogami, and M. Möller, Block copolymer mediated synthesis of gold quantum dots and novel gold-polypyrrole nanocomposites, *J. Phys. Chem. B*, **103**, 7441–7448 (1999).
[14] Y.M. Maksimov, B.I. Podlovchenko,T.D. Gladysheva, and E.A. Kolyadko, Structural and sorptive properties of platinum-polyaniline and palladium-polyaniline systems obtained by cycling the electrode potential, *Russ. J. Electrochem*., **35**, 1225–1232 (1999).
[15] M.A. Breimer, G. Yevgeny, S. Sy, and O.A. Sadik, Incorporation of metal nanoparticles in photopolymerized organic conducting polymers: A mechanistic insight, *Nano Lett*., **1**, 305–308 (2001).
[16] M.V. Henry, C.C. Hsueh, B. P. Timko, and M.S. Freund, Reaction of pyrrole and chlorauric acid. A new route to composite colloids, *J. Electrochem. Soc*., **148**, D155–D162 (2001).
[17] X. Dai, Y. Tan, and J. Xu, Formation of gold nanoparticles in the presence of *o*-anisidine and the dependence of the structure of poly(*o*-anisidine) on synthetic conditions, *Langmuir*, **18**, 9010–9016 (2002).
[18] Y. Tan, Y. Li,and D. Zhu, Synthesis of poly(2-methoxyaniline)/Au nanoparticles in aqueous solution with chlorauric acid as the oxidant, *Synth. Met*., **135–136**, 847–848 (2003).
[19] M.S. Cho, S.Y. Kim, J.D. Nam, and Y. Lee, Preparation of PEDOT/Cu composite film by in-situ redox reaction between EDOT and copper (II) chloride, *Synth. Met*., **158**, 865–869 (2008).
[20] J.M. Kinyanjui, J. Hanks, D.W. Hatchett, A.J. Smith, and M. Josowicz, Chemical and electrochemical synthesis of polyaniline/gold composites, *J. Electrochem. Soc*., **151**, D113–D120 (2004).
[21] J.M. Kinyanjui, D.W. Hatchett, A.J. Smith, and M. Josowicz, Chemical synthesis of a polyaniline/gold composite using tetrachloroaurate, *Chem. Mater*., **6**, 3390–3398 (2004).
[22] J.M. Kinyanjui, N.R. Wijeratne, J. Hanks, and D.W. Hatchett, Chemical and electrochemical synthesis of polyaniline/platinum composites, *Electrochim. Acta*, **51**, 2825–2835 (2006).
[23] M. Sivakumar and A. Gedanken, A sonochemical method for the synthesis of polyaniline and Au-polyaniline composites using H_2O_2 for enhancing rate and yield, *Synth. Met*., **148**, 301–306 (2005).
[24] K. Mallick, M.J. Witcomb, A. Dinsmore, and M.S. Scurrell, Polymerization of aniline by auric acid: Formation of gold decorated polyaniline nanoballs, *Macromol. Rapid Commun*., **26**, 232–235 (2005).
[25] K. Mallick, M.J. Witcomb, A. Dinsmore, and M.S. Scurrell, Fabrication of a metal nanoparticles and polymer nanofibers composite material by in situ chemical synthetic route, *Langmuir*, **21**, 7964–7967 (2005).
[26] J.E. Park, M. Atobe, and T. Fuchigami, Sonochemical synthesis of conducting polymer-metal nanoparticles nanocomposite, *Electrochim. Acta*, **51**, 849–854 (2005).

[27] S. Pillalamarri, F.D. Blum, A.T. Touhiro, and M.F. Bertino, One-pot synthesis of polyaniline-metal nanocomposites, *Chem. Mater*., **17**, 5941–5944 (2005).
[28] P.K. Khanna, N. Singh, S. Charan, and A. Viswanath, Synthesis of Ag/polyaniline nanocomposite via an in situ photo redox mechanism, *Mat. Chem. Phys*., **92**, 214–219 (2005).
[29] Y. Ma, N. Li, C. Yang, and X. Yang, One-step synthesis of water-soluble gold nanoparticles/polyaniline composite an dits application in glucose sensing, *Colloids Surf. A*, **269**, 1–6 (2005).
[30] L.M. Huang, C.C. Tsai, T.C. Wen, and A. Gopalan, Simultaneous synthesis of silver nanoparticles and poly(2,5-dimethoxyaniline) in poly(sterene sulfonic acid), *J. Polym. Sci. A*, **44**, 3843–3852 (2006).
[31] Z. Peng, L. Guo, Z. Zhang, B. Tesche, T. Wilke, D. Ogermann, S. Hu, and K. Kleinermanns, Micelle-assisted one-pot synthesis of water-soluble polyaniline-gold composite particles, *Langmuir*, **22**, 10915–10918 (2006).
[32] Y.O. Kang, S.H. Choi, A. Gopalan, K.P. Lee, H.D. Kang, and Y.S. Song, One-pot synthesis of a few nanocomposites with poly(N-vinylcarbazole) and CdS, Ag, Pd_{50}-Ag_{50}, and Pt_{50}-Ru_{50} nanoparticles with γ-irradiation, *J. Appl. Polym. Sci*., **100**, 1809–1815 (2006).
[33] K. Huang, Y. Zhang, Y. Long, J. Yuan, D. Han, Z. Wang, L. Niu, and Z. Chen, Preparation of highly conductive, self-assembled gold/polyaniline nanocables and polyaniline nanotubes, *Chem. Eur. J*., **12**, 5314–5319 (2006).
[34] H.H. Zhou, X.H. Ning, S.L. Li, J.H. Chen, and Y.F. Kuang, Synthesis of polyaniline-silver nanocomposite film by unsymmetrical square wave current method, *Thin Solid Films*, **510**, 164–168 (2006).
[35] F.-J. Liu, L.-M. Huang, T.-C. Wen, A. Gopalan, and J.-S. Hung, Interfacial synthesis of platinum loaded polyaniline nanowires in poly(sterene sulfonic acid), *Mater. Letters*, **61**, 4400–4405 (2007).
[36] L.M. Huang and T.C. Wen, One-step synthesis of silver nanoparticles and poly(2,5-dimethoxyaniline) in poly(sterenesulfonic acid), *Mat. Sci. Engin. A*, **445–446**, 7–13 (2007).
[37] Z. Guo, Y. Zhang, L. Huang, M. Wang, J. Wang, J. Sun, L. Xu, and N. Gu, One-step controlled synthesis of anisotropic gold nanostructures with aniline as the reductant in aqueous solution, *J. Colloid Interface Sci*., **309**, 518–523 (2007).
[38] Z. Wang, J. Yuan, D. Han, and A. Iwaska, One-step synthesis of gold-polyaniline core-shell particles, *Nanotechnology*, **18**, 115610 (2007).
[39] S.S. Kumar, C.S. Kumar, J. Mathiyarasu, and K.L. Phani, Stabilized gold nanoparticles by reduction using 3,4-ethylenedioxythiophene-polysterenesulfonate in aqueous solutions: nanocomposite formation, stability, and application in catalysis, *Langmuir*, **23**, 3401–3408 (2007).
[40] G. Neelgund, E. Hrehorova, M. Joyce, and V. Bliznyuk, Synthesis and characterization of polyaniline derivative and silver nanoparticle composites, *Polym. Int.*, **57**, 1083–1089 (2008).
[41] R.A. De Barros and W.M. De Azevedo, Polyaniline/silver nanocomposite preparation under extreme or non-classical conditions, *Synth. Met*., **158**, 922–926 (2008).
[42] L. Guo and Z. Peng, One-pot synthesis of carbon nanotube-polyaniline-gold nanoparticle and carbon nanotube-gold nanoparticle composites by using aromatic amine chemistry, *Langmuir*, **24**, 8971–8975 (2008).
[43] L. Li, G. Yan, J. Wu, X. Yu, and Q. Guo, Preparation of polyaniline-metal composite nanospheres by in situ microemulsion polymerization, *J. Colloid. Interface Sci*., **326**, 72–75 (2008).
[44] S.V. Vasilyeva, M.A. Vorotyntsev, I. Bezverkhyy, E. Lesniewska, O. Heintz, and R. Chassagnon, Synthesis and characterization of palladium nanoparticle/polypyrrole composites, *J. Phys. Chem. C*, **112**, 19878–19885 (2008).
[45] S. Harish, J. Mathiyarasu, K.L.N. Phani, and V. Yegnaraman, Synthesis of conducting polymer supported Pd nanoparticles in aqueous medium and catalytic activity towards 4-nitrophenol reduction, *Catal. Lett*., **128**, 197–202 (2009).
[46] C.S.C. Bose and K. Rajeshwar, Efficient electrocatalyst assemblies for proton and oxygen reduction: the electrosynthesis and characterization of polypyrrole films containing nanodispersed platinum particles, *J Electroanal. Chem*., **333**, 235–256 (1992).
[47] C.C. Chen, C.S.C. Bose, and K. Rajeshwar, The reduction of dioxygen and the oxidation of hydrogen at polypyrrole film electrodes containin nanodispersed platinum particles, *J. Electroanal. Chem*., **350**, 161–176 (1993).

[48] E. Granot, E. Katz, B. Basnar, and I. Willner, Enhanced bioelectrocatalysis using Au-nanoparticle/polyaniline hybrid systems in thin films and microstructured rods assembled on electrodes, *Chem. Mater*., **17**, 4600–4609 (2005).
[49] M. Grzeszczuk and P. Poks, The HER performance of colloidal Pt nanoparticles incorporated in polyaniline, *Electrochim. Acta*, **45**, 4171–4177 (2000).
[50] A. Nirmala Grace and K. Pandian, Pt, Pt-Pd and Pt-Pd/Ru nanoparticles entrapped polyaniline electrodes – a potent electrocatalyst towards the oxidation of glycerol, *Electrochem. Commun*., **8**, 1340–1348 (2006).
[51] K. Bouzek, K.M. Mangold, and K. Jüttner, Platinum distribution and electrocatalytic properties of modified polypyrrole films, *Electrochim. Acta*, **46**, 661–670 (2000).
[52] K. Jüttner, K.M. Mangold, M. Lange, and K. Bouzek, Preparation and properties of composite catalytic systems polypyrrole-Pt, *Russian J. Electrochem*., **40**, 317–325 (2004).
[53] V. Selvaraj, M. Alagar, and I. Hamerton, Electrocatalytic properties of monometallic and bimetallic nanoparticles-incorporated polypyrrole films for electro-oxidation of methanol, *J. Power Sources*, **160**, 940–948 (2006).
[54] N. Cioffi, L. Torsi, L. Sabbatini, P.G. Zambonin, and T. Bleve-Zacheo, Electrosynthesis and characterization of nanostructured palladium-polypyrrole composites, *J. Electroanal. Chem.*, **488**, 42–47 (2000).
[55] W. Chen, C.M. Li, P. Chen, and C.Q. Sun, Electrosynthesis and characterization of polypyrrole/Au nanocomposite, *Electrochim. Acta*, **52**, 2845–2849 (2007).
[56] V. Selvaraj, M. Alagar, and I. Hamerton, Nanocatalysts impregnated polythiophene electrodes for the electrooxidation of formic acid, *Appl. Catalysis B*, **73**, 172–179 (2007).
[57] Z. Peng, E. Wang, and S. Dong, Incorporation of surface-derivatized gold nanoparticles into electrochemically generated polymer films, *Electrochem. Commun*., **4**, 210–213 (2002).
[58] C. Zanardi, F. Terzi, L. Pigani, A. Heras, A. Collina, J. Lopez-Pallacios, and R. Seeber, Development and characterization of a novel composite electrode material consisting of poly (3,4-ethylenedioxythiophene) including Au nanoparticles, *Electrochim. Acta*, **53**, 3916–3923 (2008).
[59] F. Terzi, C. Zanardi, V. Martina, L. Pigani, and R. Seeber, Electrochemical, spectroscopic and microscopic characterization of novel poly(3,4-ethylenedioxythiophene)/gold nanoparticles composite materials, *J. Electroanal. Chem.*, **619–620**, 75–82 (2008).
[60] T. K. Sarma, D. Chowdhury, A. Paul, and A. Chattopadhyay, Synthesis of Au nanoparticle-conductive polyaniline composite using H_2O_2 as oxidizing as well as reducing agent, *Chem. Commun*., 1048–1049 (2002).
[61] S. Sharma, C. Nirkhe, S. Pethkar, and A. Athawale, Chloroform vapour sensor based on copper/polyaniline nanocomposite, *Sens. Actuators* B, **85**, 131–136 (2002).
[62] A.A. Athawale and S.V. Bhagwat, Synthesis and characterization of novel copper/polyaniline nanocomposite and application as a catalyst in the Wacker oxidation reaction, *J. Appl. Polym. Sci*., **89**, 2412–2417 (2003).
[63] S. K. Pillalamarri, F.D. Blum, and M.F. Bertino, Synthesis of polyaniline-gold nanocomposites using 'grafting from' approach, *Chem. Commun*., 4584–4585 (2005).
[64] A.A. Athawale, S.V. Bhagwat, P. P. Katre, A. J. Chandwadkar, and P. Karandikar, Aniline as a stabilizer for metal nanoparticles, *Mat. Lett*., **57**, 3889–3894 (2003).
[65] A.A. Athawaleand and P. P. Katre, Ag dispersed conducting polyaniline nanocomposite as a selective sensor for ammonia, *J. Metast. Non-cryst. Mat*., **23**, 323–326 (2005).
[66] P.P. Katre and A.A. Athawale, Au-polyaniline nanocomposite synthesized using γ-ray induced Au nanoparticles, *Synth. Reactivity Inorg. Met.-Organic Nano-Met. Chem*., **37**, 363–366 (2007).
[67] Y.O. Kang, S.H. Choi, A. Gopalan, K.P. Lee, H.D. Kang, and Y.S. Song, Tuning of morphology of Ag nanoparticles in the Ag/polyaniline nanocomposites prepared by γ–ray irradiation, *J. Non-Cryst. Solids*, **352**, 463–468 (2006).
[68] Y.O. Kang, S.H. Choi, A. Gopalan, K.P. Lee, H.D. Kang, and Y.S. Song, Tuning of morphology of Ag nanoparticles in the Ag/polyaniline nanocomposites prepared by γ-ray irradiation, *J. Non Cryst. Solids*, **352**, 463–468 (2006).
[69] K.R. Reddy, K.P. Lee, Y. Lee, and A.I. Gopalan, Facile synthesis of conducting polymer-metal hybrid nanocomposite by *in situ* chemical oxidative polymerization with negatively charged metal nanoparticles, *Mat. Letters*, **62**, 1815–1818 (2008).

[70] S.S. Kumar, J. Mathiyarasu, and K. L. Phani, Exploration of synergism between polymer matrix and gold nanoparticles for selective determination of dopamine, *J. Electroanal. Chem*., **578**, 95–103 (2005).
[71] J. Mathiyarasu, S. Senthilkumar, K.L.N. Phani, and V. Yegnaraman, PEDOT-Au nanocomposite film for electrochemical sensing, *Mater. Lett.*, **62**, 571–573. (2008).
[72] Y.C. Liu, H. Lee, and S.J. Yang, Strategy for the synthesis of isolated fine silver nanoparticles and polypyrrole/silver nanocomposites on gold substrates, *Electrochim. Acta*, **51**, 3441–3445 (2006).
[73] J.E. Park, S.G. Park, A. Koukitu, O. Hatozaki, and N. Oyama, Effect of adding Pd nanoparticles to dimercaptan-polyaniline cathodes for lithium polymer battery, *Synth. Met*., **140**, 121–126 (2004).
[74] J.E. Park, S.G. Park, A. Koukitu, O. Hatozaki, and N. Oyama, Electrochemical and chemical interactions between polyaniline and palladium nanoparticles, *Synth. Met*., **141**, 265–269 (2004).
[75] M.A.G. Namboothiry, T. Zimmerman, F. M. Coldren, J. Liu, K. Kim, and D.L. Carroll, Electrochromic properties of conducting polymer metal nanoparticles composites, *Synth. Met.*, **157**, 580–584 (2007).
[76] P. Englebienne and A. Van Hoonacker, Gold-conductive polymer nanoparticles: A hybrid material with enhanced photonic reactivity to environmental stimuli, *J. Colloid Interface Sci*., **292**, 445–454 (2005).
[77] N. Cioffi, L. Torsi, I. Losito, L. Sabbatini, P.G. Zambonin, and T. Bleve-Zacheo, Nanostructured palladium-polypyrrole composites electrosynthesised from organic solvents, *Electrochim. Acta*, **46**, 4205–4211 (2001).
[78] Y. Leroux, E. Eang, C. Fave, G. Trippe, and J.C. Lacroix, Conducting polymer/gold nanoparticle hybrid materials: A step toward electroactive plasmonic devices, *Electrochem. Commun*., **9**, 1258–1262 (2007).
[79] S. Cho and S.-M. Park, Electrochemistry of conductive polymers 39. Contacts between conducting polymers and noble metal nanoparticles studied by current-sensing atomic force microscopy, *J. Phys. Chem. B*, **110**, 25656 (2006).
[80] P.J. Kulesza, M. Chojak, K. Karnicka, K. Miecznikowski, B. Palys, and A. Lewera, Network films composed of conducting polymer-linked and polyoxometallate-stabilized platinum nanoparticles *Chem. Mater*., **16**, 4128–4134 (2004).
[81] P.J. Kulesza, K. Karnicka, K. Miecznikowski, M. Chojak, A. Kolary, P. Barczuk, G. Tsirlina, and W. Czerwinski, Network electrocatalytic films of conducting polymer-linked polyoxometallate-stabilized platinum nanoparticles, *Electrochim. Acta*, **50**, 5155–5162 (2005).
[82] A. Alqudami, S. Annapoorni, P. Sen, and R.S. Rawat, The inciorporation of silver nanoparticles into polypyrrole: Conductivity changes, *Synth. Met*., **157**, 53–59 (2007).
[83] F.N. Crespilho, R.M. Iost, S.A. Travain, O.N. Oliveira Jr., and V. Zucolotto, Enzyme immobilization on Ag nanoparticles/polyaniline nanocomposites, *Biosens. Bioelectronics*, **24**, 3073–3077 (2009).
[84] S. Tian, J. Liu, T. Zhu, and W. Knoll, Polyaniline doped with modified gold nanoparticles and its electrochemical properties in neutral aqueous solution, *Chem. Commun*., 2738–2739 (2003).
[85] S. Tian, J. Liu, T. Zhu, and W. Knoll, Polyaniline/gold nanoparticle multilayer films: Assembly, properties, and biological applications, *Chem. Mater*., **16**, 4103 (2004).
[86] X. Zou, H. Bao, H. Guo, L. Zhang, L. Qi, J. Jiang, L. Niu, and S. Dong, Mercaptoethane sulfonate protected, water-soluble gold and silver nanoparticles: Syntheses, characterization and their building multilayer films with polyaniline via ion-dipole interactions, *J. Colloid Interface Sci*., **295**, 401–408 (2006).
[87] U. Lange, S. Ivanov, V. Lyutov, V. Tsakova, and V. Mirsky, Voltammetric and conductometric behaviour of nanocomposites of polyaniline and gold nanoparticles prepared by layer-by-layer technique, *J. Solid State Electrochem*., doi 10.1007/s10008-009-0922-2 (2009).
[88] G. Tourillon and F. Garnier, Inclusion of metallic aggregates in organic conducting polymers. A new catalytic system, [poly93-methylthiophene)-Ag-Pt], for proton electrochemical reaction, *J. Phys. Chem*., **88**, 5281–5285 (1984).
[89] G.K. Chandler and D. Pletcher, The electrodeposition of metals onto polypyrrole films from aqueous solution, *J. Appl. Electrochem*., **16**, 62–68 (1986).
[90] K. Kost, D. Bartak, B. Kazee, and Th. Kuwana, Electrodeposition of platinum microparticles into polyaniline films with electrocatalytic applications, *Anal. Chem*., **60**, 2379–2384 (1988).

[91] P.O. Esteban, J.M. Leger, C. Lamy, and E. Genies, Electrocatalytic oxidation of methanol on platinum dispersed in polyaniline conducting polymers, *J. Appl. Electrochem.*, **19**, 462–464 (1989).
[92] M. Gholamian and A.Q. Contractor, oxidation of formic acid at platinum microparticles dispersed in a polyaniline matrix Influence of long-range order and metal-polymer interaction, *J. Electroanal. Chem.*, **289**, 69–83 (1990).
[93] M. Ulmann, R. Kostecki, J. Augustynski, D.J. Strike, and M. Koudelka-Hep, Modification des polymers conducteurs avec de petites particules metalliques; proprietes des films de polypyrrole et de polyaniline platines, *Chimia*, **46**, 138–140 (1992).
[94] R. Kostecki, M. Ulmann, J. Augustynski, D.J. Strike, and M. Koudelka-Hep, Enhanced rate of redox conversion of polyaniline films induced by the incorporation of platinum microparticles, *J. Phys. Chem.*, **97**, 8113–8115 (1993).
[95] C.T. Hable and M.S. Wrighton, electrocatalytic oxidation of methanol and ethanol: A comparison of platinum-tin, and platinum-ruthenium catalyst particles in a conducting polyaniline matrix, *Langmuir*, **9**, 3284–3290 (1993).
[96] M. Grzeszczuk, Electrochemical study of polyaniline film electrodes and their modifications – impedance spectroscopy measurements on hydrogen evolution reaction, *Electrochim. Acta*, **39**, 1809–1816 (1994).
[97] E.K.W. Lai, P.D. Beattie, and S. Holdcroft, Electrocatalytic reduction of oxygen by platinum microparticles deposited on polyaniline films, *Synth. Met.*, **84**, 87–88 (1997).
[98] F. Ficicioglu and F. Kadirgan, Electrooxidation of ethylene glycol on a platinum doped polyaniline electrode, *J. Electroanal. Chem.*, **451**, 95–99 (1998).
[99] M.J. Croissant, T. Napporn, J.M. Leger, and C. Lamy, Electrocatalytic oxidation of hydrogen at platinum-modified polyaniline electrodes, *Electrochim. Acta*, **43**, 2447–2457 (1998).
[100] C. Coutanceau, M.J. Croissant, T. Napporn, and C. Lamy, Electrocatalytic reduction of dioxygen at platinum particles dispersed in a polyaniline film, *Electrochim. Acta*, **46**, 579–588 (2000).
[101] C.H. Yang and T.C. Wen, Electrodeposited platinum microparticles in a sulfobnate-polyaniline film for the electrosorption of metahnol and sorbitol, *Electrochim. Acta*, **44**, 207–218 (1998).
[102] A. Kelaidopoulou, E. Abelidou, A. Papoutsis, E.K. Polychromiadis, and G. Kokkinidis, Electrooxidation of ethylene glycol on Pt-based catalysts dispersed in polyaniline, *J. Appl. Electrochem.*, **28**, 1101–1106 (1998).
[103] R. Schrebler, M.A. Del Valle, H. Gomez, C. Veas, and R. Cordova, Preparation of polythiophene-modied electrodes by electrodeposition of Pt and Pt+Pb. Application to formic acid electro-oxidation, *J. Electroanal. Chem.*, **380**, 219–227 (1995).
[104] M. Malik, M. Galkowski, H. Bala, B. Grzybowska, and P. Kulesza, Evaluation of polyaniline films containing traces of dispersed platinum for protection of stainless steel against corrosion, *Electrochim. Acta*, **44**, 2157–2163 (1999).
[105] A.M. Castro-Luna, Novel electrocatalytic polyaniline electrode for methanol oxidation, *J. Appl. Electrochem.*, **30**, 1137–1142 (2000).
[106] A.A. Mikhaylova, E.B. Molodkina, O.A. Khazova, and V.S. Bagotzky, Electrocatalytic and adsorption properties of platinum microparticles electrodeposited into polyaniline films, *J. Electroanal. Chem.*, **509**, 119–127 (2001).
[107] A. Lima, C. Coutanceau, J.M. Leger, and C. Lamy, Investigation of ternary catalysts for methanol electrooxidation, *J. Appl. Electrochem.*, **31**, 379–386 (2001).
[108] A. Lima, F. Hahn, and J.M. Leger, Oxidation of metahnol on Pt, Pt-Ru, and Pt-Ru-Mo electrocatalysts dipsersed in polyaniline: An *in situ* infrared reflectance spectroscopy study, *Russ. J. Electrochem.*, **40**, 369–379 (2004).
[109] C.C. Hu, E. Chen, and J.Y. Lin, Capacitive and textural characteristics of polyaniline-platinum composite films, *Electrochim. Acta*, **47**, 2741–2749 (2002).
[110] E.C. Venancio, W.T. Napporn, and A. Motheo, Electro-oxidation of glycerol on platinum dispersed in polyaniline matrices, *Electrochim. Acta*, **47**, 1495–1501 (2002).
[111] T. Kessler and A.M. Castro Luna, A catalytic platinum-ruthenium-polyaniline electrode for methanol oxidation, *J. Appl. Electrochem.*, **32**, 825–830 (2002).

[112] T. Kessler and A.M. Castro Luna, Catalytic polyaniline-supported electrodes for application in electrocatalysis, *J. Solid State Electrochem*., **7**, 593–598 (2003).
[113] L. Niu, Q. Li, F. Wei, X. Chen, and H. Wang, Formation optimization of platinum-modified polyaniline films for the electrocatlytic oxidation of methanol, *Synth. Met*., **139**, 271–276 (2003).
[114] L. Niu, Q. Li, F. Wei, X. Chen, and H. Wang, Electrochemical impedance and morphological characterization of platinum-modified polyaniline film electrodes and their electrocatalytic activity for methanol oxidation, *J. Electroanal. Chem*., **544**, 121–128 (2003).
[115] L. Niu, Q. Li, F. Wei, S. Wu, P. Liu, and X. Cao, Electrocatalytic behavior of Pt-modified polyaniline electrode for methanol oxidation: Effect of Pt deposition modes *J. Electroanal. Chem*., **578**, 331–337 (2005).
[116] H.H. Zhou, S.Q. Jiao, J.H. Chen, W.Z. Wei, and J.F. Kuang, Effects of conductive polyaniline (PANI) preparation and platinum electrodeposition on electroactivity of metahnol oxidation, *J. Appl. Electrochem*., **34**, 455–459 (2004).
[117] L.H. Mascaro, D. Goncalves, and L.O.S. Bulhoes, Electrocatalytic propereties and electrochemical stability of polyaniline and polyaniline modified with platinum nanoparticles in formaldehyde medium, *Thin Solid Films*, **461**, 243–249 (2004).
[118] G. Wu, L. Li, J.H. Li, and B.Q. Xu, Polyaniline-carbon composite films as supports of Pt and PtRu particles for methanol electrooxidation, *Carbon*, **43**, 2579–2587 (2005).
[119] G. Wu, L. Li, J.H. Li, and B.Q. Xu, Methanol electrooxidation on Pt particles dispersed into PANI/SWNT composite films, *J. Power Sources*, **155**, 118–127 (2006).
[120] D.W. Hatchett, R. Wijeratne, and J.M. Kinyanjui, reduction of $PtCl_6^{2-}$ and $PtCl_4^{2-}$ in polyaniline: Catalytic oxidation of methanol at morphologically different composites, *J. Electroanal. Chem*., **593**, 203–210 (2006).
[121] Z. Tang, D. Geng, and G. Lu, Electrocatalytic oxidation of carbon monoxide on platinum-modified polyaniline film electrode, *Thin Solid Films*, **497**, 309–314 (2006).
[122] N. Atta, A. Galal, and F. Khalifa, Electrodeposited metals at conducting polymer electrodes I - Effect of particle size and film thickness on electrochemical response, *Appl. Surf. Sci*., **253**, 4273–4282 (2007).
[123] L. M. Huang, W. R. Tang, and T.C. Wen, Spatially electrodeposited platinum in polyaniline doped with poly(styrene sulfonic acid) for methanol oxidation, *J. Power Sources*, **164**, 519–526 (2007).
[124] S. Palmero, A. Colina, E. Munoz, A. Heras, V. Ruiz, and J. Lopez-Palacios, layer-by-layer electrosynthesis of Pt-polyaniline nanocomposites for the catalytic oxidation of methanol, *Electrochem. Commun*., **11**, 122–125 (2009)
[125] S. Dominguez-Dominguez, J. Arias-Pardilla, A. Berenguer-Murcia, E. Murallon, and D. Cazorla-Amoros, Electrochemiical deposition of platinum nanoparticles on different carbon supports and conducting polymers, *J. Appl. Electrochem*., **38**, 259–268 (2008).
[126] F.J. Liu, L.M. Huang, T.C. Wen, C.F. Li, S.L. Huang, and A. Gopalan, Effect of deposition sequence of platinum and ruthenium particles into nanofibrous network of polyaniline-poly (styrene sulfonic acid) on electrocatalytic oxidation of methanol, *Synth. Met*., **158**, 603–609 (2008).
[127] F.J. Liu, L.M. Huang, T.C. Wen, C.F. Li, S.L. Huang, and A. Gopalan, Platinum particles dispersed polyaniline-modified electrodes containing sulfonated polyelectrolyte for methanol oxidation, *Synth. Met*., **158**, 767–774 (2008).
[128] F.T.A. Vork, L.J.J. Janssen, and E. Barendrecht, Oxidation of hydrogen at platinum-polypyrrole electrodes, *Electrochim. Acta*, **31**, 1569–1575 (1986).
[129] S. Holdcroft, and B.L. Funt, Preparation and electrocatalytic properties of conducting films of polypyrrole containing platinum microparticulates, *J. Electroanal. Chem*., **240**, 89–103 (1988).
[130] D.J. Strike, N.F. De Rooij, M. Koudelka-Hep, M. Ulmann, and J. Augustynski, Electrocatalytic oxidation of methanol on platinum microparticles in polypyrrole, *J. Appl. Electrochem*., **22**, 922–926 (1992).
[131] M. Hepel, The electrocatalytic oxidation of methanol at finely dispersed platinum nanoparticles in polypyrrole films, *J. Electrochem. Soc*., **145**, 124–134 (1998).

[132] K. Bouzek, K.M. Mangold, and K. Jüttner, Electrocatalytic activity of platinum modified polypyrrole films for the methanol oxidation reaction, *J. Appl. Electrochem*., **31**, 501–507 (2001).
[133] P. Holzhauser, K. Bouzek, and Z. Bastl, Electrocatalytic properties of polypyrrole films prepared with palatinate(II) counter-ions, *Synth. Met*., **155**, 501–508 (2005).
[134] M. Trueba, S.P. Trasatti, and S. Trasatti, Electrocatalytic activity of hydrogen evolution of polypyrrole films modified with noble metal particles, *Mat. Chem. Phys*., **98**, 165–171 (2006).
[135] S. Swathirajan and Y.M. Mikhail, Methanol oxidation on platinum-tin catalysts dispersed on poly(3-methylthiophene) conducting polymer, *J. Electrochem. Soc*., **139**, 2105–2110 (1992).
[136] J.C. Moutet, A. Ourari, and A. Zouaoui, Electrocatalytic hydrogenation of azides using precious metal microparticles dispersed in polymer films, *Electrochim. Acta*, **37**, 1261–1263 (1992).
[137] J.C. Moutet, Y. Ouennoughi, A. Ourari, and S. Hamar-Thibault, Electrocatalytic hydrogenation on noble metal particles dispersed in polymer films. Enhanced catalytic activity induced by the incorporation of bimetallic catalysts, *Electrochim. Acta*, **40**, 1827–1833 (1995).
[138] P. Ocon, P. Herrasti, and S. Rojas, Galvanostatic and pulse potential synthesis of poly-3-methylthiophene. Polymer as catalytic support, *Polymer*, **42**, 2439–2448 (2001).
[139] S. Biallozor, A. Kupniewska, and V. Jasulajtene, Properties of electrodes modified with poly(3,4-ethylenedioxythiophene) and Pt particles – Part I, *Bull. Electrochem*., **20**, 231–236 (2004).
[140] S. Biallozor and A. Kupniewska, Properties of electrodes modified with poly(3,4-ethylenedioxythiophene) and Pt particles – Part II, *Bull. Electrochem*., **20**, 241–246 (2004).
[141] C.W. Kuo, L.M. Huang, T.C. Wen, and A. Gopalan, Enhanced electrocatalytic performance fro methanol oxidation of a novel Pt-dispersed poly(3,4-ethylenedioxythiophene)-poly (styrene sulfonic acid) electrode, *J. Power Sources*, **160**, 65–72 (2006).
[142] D.W. Hatchett, M. Josowicz, J. Janata, and D.R. Baer, Electrochemical formation of Au clusters in polyaniline, *Chem. Mater*., **11**, 2989–2994 (1999).
[143] B.J. Hwang, R. Santhanam, and Y.L. Lin, Electrochemical deposition of gold metal particles into 3-dimensional polypyrrole film deposited on a highly oriented pyrolytic graphite, *Electroanalysis*, **15**, 1667–1676 (2003).
[144] J.A. Smith, M. Josowicz, and J. Janata, Gold-polyaniline composite Part I. Moving electrochemical interface, *Phys. Chem. Chem. Phys*., **7**, 3614–3618 (2005).
[145] J.A. Smith, M. Josowicz, M. Engelhard, D.R. Baer, and J. Janata, Gold-polyaniline composites Part II. Effects of nanometer sized particles, *Phys. Chem. Chem. Phys*., **7**, 3619–3625 (2005).
[146] Z. Wang, J. Yuan, M. Li, D. Han, Y. Zhang, Y. Shen, L. Niu, and A. Ivaska, Electropolymerization and catalysis of well-dispersed polyaniline/carbon nanotube/gold composite, *J. Electroanal. Chem*., **599**, 121–126 (2007).
[147] J. Li and X. Lin, Electrocatalytic oxidation of hydrazine and hydroxylamine at gold nanoparticle-polypyrrole nanowire modified electrode, *Sensors Act. B*, **126**, 527–535 (2007).
[148] A. Yassar, J. Roncali, and F. Garnier, Preparation and electroactivity of poly(thiophene) electrodes modified by electrodeposition of palladium particles, *J. Electroanal. Chem*., **255**, 53–69 (1988).
[149] I.M.F. De Oliveira, J.C. Moutet, and S. Hamar-Thibault, Electrocatalytic hydrogenation activity of palladium and rhodium microparticles dispersed in alkylammonium- and pyridinium-substituted polypyrrole films, *J. Mater. Chem*., **2**,167–173 (1992).
[150] A. Leone, W. Marino, and B. Scharifker, Electrodeposition and electrochemical behavior of palladium particles at polyaniline and polypyrrole films, *J. Electrochem. Soc*., **139**, 438–443 (1992).
[151] L. Torsi, M. Pezzuto, P. Siciliano, R. Rella, L. Sabbatini, L. Valli, and P.G. Zambonin, Conducting polymers doped with metallic inclusions: New materials for gas sensors, *Sens. Actuators B*, **48**, 362–367 (1998).
[152] V. Tsakova, S. Winkels, and J.W. Schultze, Crystallization kinetics of Pd in composite films of PEDT, *J. Electroanal. Chem*., **500**, 574–583 (2001).
[153] Yu.M. Maksimov, E.A. Kolyadko, A.B. Shishilova, and B.I. Podlovchenko, Electrocatalytic behavior of a palladium-polyaniline system obtained by electrodepositing palladium into a preliminarily formed polyaniline film, *Russ. J. Electrochem*., **37**, 777–781 (2001).

[154] K.-M. Mangold, F. Meik, and K. Jüttner, Polypyrrole/palladium composites for the electrocatalyzed heck reaction, *Synth. Met*., **144**, 221–227 (2004).
[155] A. Frydrychewicz, S.Y. Vassilev, G.A. Tsirlina, and K. Jackowska, Reticulated vitreous carbon-polyaniline-palladium composite electrodes, *Electrochim. Acta*, **50**, 1885–1893 (2005).
[156] A. Mourato, S.M. Wong, H. Siegenthaler, and L.M. Abrantes, Polyaniline films containing palladium microparticles for electrocatalytic purposes, *J. Solid State Electrochem*., **10**,140–147 (2006).
[157] A. Mourato, J.P. Correia, H. Siegenthaler, and L.M. Abrantes, Palladium electrodeposition on polyaniline films, *Electrochim. Acta*, **53**, 664–672 (2007).
[158] M. Ilieva, V. Tsakova, and W. Erfurth, Electrochemical formation of bi-metal (copper-palladium) electrocatalyst supported on poly-3,4-ethyelenedioxythiophene, *Electrochim. Acta*, **52**, 816–824 (2006).
[159] J.Y. Lee and T.C. Tan, Cyclic voltammetry of electrodeposition of metal on electrosynthesized polypyrrole film, *J. Electrochem. Soc*., **137**, 1402–1408 (1990).
[160] V. Tsakova and A. Milchev, Nucleation of silver on a polyaniline coated platinum electrode, *Electrochim. Acta*, **36**, 1151–1155 (1991).
[161] N. Hernandez, J.M. Ortega, M. Choy, and R. Ortiz, Electrodeposition of silver on a poly (*o*-aminophenol) modified platinum electrode, *J. Electroanal. Chem*., **515**, 123–128 (2001).
[162] S. Ivanov and V. Tsakova, Silver electrocrystallization at polyaniline-coated electrodes, *Electrochim. Acta*, **49**, 913–921 (2004).
[163] S. Ivanov and V. Tsakova, Electroless versus electrodriven deposition of silver crystals in polyaniline: Role of silver anion complexes, *Electrochim. Acta*, **50**, 5616–5623 (2005).
[164] H.H. Zhou, S.Q. Jiao, J.H. Chen, W.Z. Wei, and Y.F. Kuang, Effects of conductive polyaniline (PANI) preparation and platinum electrodeposition on electroactivity of methanol oxidation, *J. Appl. Electrochem*., **34**, 455–459 (2004).
[165] D.M. Leeuw, P.A. Kraakman, P.F.G. Bongaerts, C.M.J. Mutsaers, and D.B.M. Klaassen, Electroplating of conductive polymers for the metallization of insulators, *Synth. Met*., **66**, 263–273 (1994).
[166] R.J. Nichols, D. Schröer, and H. Meyer, An *in situ* scanning probe microscopy study of copper electrodeposition on conductive polypyrrole, *Electrochim. Acta*, **40**, 1479–1485 (1995).
[167] L.M. Abrantes and J.P. Correia, Photoelectrochemical studies of polymer films: Poly (3-methylthiophene) and poly(3-methylthiophene)/Cu systems, *Electrochim. Acta*, **42**, 1747–1755 (1996).
[168] M. Hepel, Y.M. Chen, and R. Stephenson, Effect of the composition of polypyrrole substrate on the electrodeposition of copper and nickel, *J. Electrochem. Soc*., **143**, 498–505 (1996).
[169] M.R. Guascito, P. Boffi, C. Malitesta, L. Sabbatini, and P.G. Zambonin, Conducting polymer electrodes modified by metallic species for electrocatalytic purposes – spectroscopic and microscopic characterization, *Mater. Chem. Phys*., **44**, 17–24 (1996).
[170] A. Zouaoui, O. Stephan, M. Carrier, and J.C. Moutet, Electrodeposition of copper into functionalized polypyrrole films, *J. Electroanal. Chem*., **474**, 113–122 (1999).
[171] J.M. Ortega, Electrodeposition of copper on poly(*o*-aminophenol) modified platinum electrode, *Thin Solid Films*, **360**, 159–165 (2000).
[172] L. Martinot, D. Leroy, H. Zhan, C. Licour, C. Jerome, G. Chapelle, C. Calberg, and R. Jerome, The use of conducting polymers as cathodes for the electrochemical deposition of magnetic transition metal/rare earth alloys, *J. Mater. Chem*., **10**, 729–735 (2000).
[173] N. Cioffi, L. Torsi, I. Losito, C. Di Franco, I. De Bari, L. Chiavarone, G. Scamarcio, V. Tsakova, L. Sabbatini, and P.G. Zambonin, Electrosynthesis and analytical characterisation of polypyrrole thin films modified with copper nanoparticles, *J. Mater. Chem.*, **11**, 1434–1440 (2001).
[174] Y.C. Liu, K.H. Yang, and M.D. Ger, Mechanism of underpotential deposition of metal on conducting polymer, *Synth. Met*., **126**, 337–345 (2002).
[175] D.K. Sarkar, X.J. Zhou, A. Tannous, M. Louie, and K.T. Leung, Growth of self-assembled copper nanostructure on conducting polymer by electrodeposition, *Solid State Commun*., **125**, 365–368 (2003).

[176] D.K. Sarkar, X.J. Zhou, A. Tannous, and K.T. Leung, Growth mechanisms of copper nanocrystals on thin polypyrrole films by electrochemistry, *J. Phys. B*, **107**, 2879–2881 (2003).
[177] X.J. Zhou, A.J. Harmer, N.F. Heinig, and K.T. Leung, Parametric study on electrochemical deposition of copper nanoparticles on an ultrathin polypyrrole film deposited on a gold film electrode, *Langmuir*, **20**, 5109–5113 (2004).
[178] T.F. Otero, S.O. Costa, M.J. Ariza, and M. Marquez, Electrodeposition of Cu on deeply reduced polypyrrole electrodes at very high cathodic potentials, *J. Mater. Chem*., **15**, 1662 (2005).
[179] V. Tsakova and D. Borissov, Electrochemical deposition of copper in polyaniline films – number density and spatial distribution of deposited metal crystals, *Electrochem. Commun*., **2**, 511–515 (2000).
[180] V. Tsakova, D. Borissov, and S. Ivanov, Role of the polymer synthesis conditions for the copper electrodeposition in polyaniline, *Electrochem. Commun*., **3**, 312–316 (2001).
[181] V. Tsakova, D. Borissov, B. Ranguelov, Ch. Stromberg, and J.W. Schultze, Electrochemical incorporation of copper in polyaniline layers, *Electrochim. Acta*, **46**, 4213–4222 (2001).
[182] S. Ivanov and V. Tsakova, Influence of copper anion complexes on the incorporation of metal particles in polyaniline. Part. I. The copper citrate complex, *J. Appl. Electrochem.*, **32**, 701–707 (2002).
[183] S. Ivanov and V. Tsakova, Influence of copper anion complexes on the incorporation of metal particles in polyaniline. Part. II. The copper oxalate complex, *J. Appl. Electrochem*., **32**, 709–715 (2002).
[184] N. Watanabe, J. Morais, and M.C.M. Alves, Chemical environment of copper aggregates embedded in polypyrrole films: the nature of the copper-polypyrrole interaction, *J. Phys. Chem. B*, **106**, 1102–1107 (2002).
[185] S. Ivanov, P. Mokreva, V. Tsakova, and L. Terlemezyan, Electrochemical and surface structural characterization of chemically and electrochemically synthesized polymer layers – a comparison, *Thin Solid Films*, **441**, 44–49 (2003).
[186] M. Ilieva and V. Tsakova, Copper modified poly(3,4-ethylenedioxythiophene): Part I. Galvanostatic experiments, *Synth. Met*., **141**, 281–285 (2004).
[187] M. Ilieva and V. Tsakova, Copper modified poly(3,4-ethylenedioxythiophene): Part I. Potentiostatic experiments, *Synth. Met.*, **141**, 287–292 (2004).
[188] M. Ilieva and V. Tsakova, Copper electrocrystallization in PEDOT in presence and absence of copper-polymer stabilized species, *Electrochim. Acta*, **50**, 1669–1674 (2005).
[189] L. Komsiyska, Ts. Tsacheva, and V. Tsakova, Electrochemical formation and copper modification of poly-o-methoxyaniline, *Thin Solid Films*, **493**, 88–95 (2005).
[190] L.M. Abrantes and J.P. Correia, Metal incorporation in conducting polymers by electroless deposition, *Portug. Electrochim. Acta*, **16**, 85–91 (1998).
[191] A. Zaoui, O. Stephan, A. Ourari, and J.C. Moutet, Electrocatalytic hydrogenation of ketones and enones at nickel microparticles dispersed into poly(pyrrole-alkylammonium) films *Electrochim. Acta*, **46**, 49–58 (2000).
[192] J.M. Ko, D.Y. Park, N.V. Myung, J.S. Chung, and K. Nobe, Electrodeposited conducting polymer-magnetic metal composite films, *Synth. Met*., **128**, 47–50 (2002).
[193] T. Trung, T. H. Trung, and C.-S. Ha, Preparation and cyclic voltammetry studies on nickel-nanoclusters containing polyaniline composites having layer-by-layer structures, *Electrochim. Acta*, **51**, 984–990 (2005).
[194] V.D. Jovic, T. Trisovic, B.M. Jovic, and M. Vojnovic, The morphology of different metals electrodeposited onto polyaniline films, *J. Electroanal. Chem*., **408**, 149–155 (1996).
[195] A. Stoyanova and V. Tsakova, Copper-modified poly(3,4-ethylenedioxythiophene) layers for selective determination of dopamine in the presence of ascorbic acid: II Role of the characteristics of the metal deposit. *J. Solid State Electrochem*. (2010), in press.
[196] J. Rau, J. Lee, and S. Chen, Study of Au(I)-polypyrrole interaction, *Synth. Met*., **79**, 69–74 (1996).
[197] M.B. Inoue, K.W. Nebesny, and Q. Fernando, Complexation of electroconducting polypyrrole with copper, *Synth. Met*., **38**, 205–212 (1990).

[198] Y.C. Liu and B.J. Hwang, Interaction of copper(I)-polypyrrole complexes prepared by depositing-dissolving copper onto and from polypyrroles, *Thin Solid Films*, **339**, 233–239 (1999).
[199] Y.C. Liu and B.J. Hwang, Mechanism of conductivity decay of polypyrrole exposed to water and enhancement of conductivity stability of copper(I)-modified polypyrrole, *J. Electroanal. Chem*., **501**, 100–106 (2001).
[200] G. Tourillon, E. Dartyge, H. Dexpert, A. Fontaine, A. Jucha, P. Lagarde, and D.E. Sayers, Electrochemical inclusion of metallic clusters in organic conducting polymers: an *in-situ* dispersive X-ray absorption study *J. Electroanal. Chem*., **178**, 357–366 (1984).
[201] G. Tourillon, E. Dartyge, H. Dexpert, A. Fontaine, A. Jucha, P. Lagarde, and D.E. Sayers, Electrochemical inclusion of metallic clusters in organic conducting polymers: an *in-situ* dispersive X-ray absorption study, *Surf. Sci*., **156**, 536–547 (1985).
[202] G. Tourillon, E. Dartyge, A. Fontaine, and A. Jucha, Dispersive X-ray spectroscopy for time-resolved *in situ* observation of electrochemical inclusion of metallic clusters within a conducting polymer, *Phys. Rev. Letters*, **57**, 603–606 (1986).
[203] D. Gourier and G. Tourillon, production of highly ordered organic conducting polymers (poly(3-methylthiophene)) under electrochemical inclusion of Cu^{2+} ions: an ESR study, *J. Phys. Chem*., **90**, 5561–5565 (1986).
[204] D. Guay, G. Tourillon, and A. Fontaine, Electrochemical inclusion of copper and iron species ina conducting polymer observed *in situ* using time-resolved X-ray absorption spectroscopy, *Fraday Discuss. Chem*., **89**, 41–50 (1990).
[205] D. Guay, G. Tourillon, E. Dartyge, A. Fontaine, and H. Tolentino, *In-situ* observations of electrochemical inclusion of copper and iron species in a conducting organic polymer by using time-resolved X-ray absorption spectroscopy, *J. Electrochem. Soc*., **138**, 399–405 (1991).
[206] J.W. Sobczak, E. Sobczak, A. Kosinski, and A. Bilinski, XANES investigations of Pd-doped polyaniline, *J. Alloys Comp*., **328**, 132–134 (2001).
[207] J. Posdorfer and B. Wessling, Oxidation of copper in the presence of the organic metal polyaniline, *Synth. Met*., **119**, 363–364 (2001).
[208] M. Ilieva, V. Tsakova, N.K. Vuchkov, K.A. Temelkov, and N.V. Sabotinov, UV copper ion laser treatment of poly-3,4- ethylenedioxythiophene, *J. Optoelectron. Adv. Mat*., **9**, 303–306 (2007).
[209] M. Ilieva, A. Stoyanova, V. Tsakova, N.K. Vuchkov, K.A. Temelkov, W. Erfurth, and N.V. Sabotinov, Effect of deep UV laser treatment on electroless silver precipitation in supported poly-3,4-ethylenedioxythiophene layers, *J. Optoelectron. Adv. Mat*., **11**, 1444–1447 (2009).
[210] E.T. Kang, Y.P. Ting, KG. Neoh, and K.L Tan, Spontaneous and sustained gold reduction by polyaniline in acid solution, *Polymer*, **34**, 4494–4496 (1993).
[211] Y.P. Ting, K.G. Neoh, E.T. Kang, and K.L. Tan, recovery of gold by electroless precipitation from aci solutions using polyaniline, *J. Chem. Tech. Biotechnol*., **59**, 31–36 (1994).
[212] E.T. Kang, Y.P. Ting, K.G. Neoh, and K.L. Tan, Electroless recovery of precious metals from acid solutions by N-containing electroactive polymers, *Synth. Met*., **69**, 477–478 (1995).
[213] K.G. Neoh, T.T. Young, N.T. Looi, and E.T. Kang, Oxidation-reduction interactions between electroactive polymer thin films and Au(III) ions in acid solutions, *Chem. Mater*., **9**, 2906–2912 (1997).
[214] M.S.A. Abdou and S. Holdcroft, Oxidation of π-conjugated polymers with gold trichloride: enhanced stability of the electronically conducting state and electroless deposition of Au^{o}, *Synth. Met*., **60**, 93–96 (1993).
[215] M.S.A. Abdou and S. Holdcroft, Gold-decorated poly(3-alkylthiophenes) *Chem. Mater*., **8**, 26–31 (1996).
[216] J. Wang, K.G. Neoh, and E. T. Kang, Preparation of nanosized metallic particles in polyaniline, *J. Colloid Interface Sci*., **239**, 78–86 (2001).
[217] M.A. Khan, C. Perruchot, S.P. Armes, and D.P. Randall, Synthesis of gold-decorated latexes *via* conducting polymer redox templates, *J. Mater. Chem*., **11**, 2631–2372 (2001).
[218] Y. Zhou, H. Itoh, T. Uemura, K. Naka, and Y. Chujo, Synthesis of novel stable nanometer-sized metal (M=Pd, Au, Pt) colloids protected by a π-conjugated polymer, *Langmuir*, **18**, 277–283 (2002).

[219] J.A. Smith, M. Josowicz, and J. Janata, Polyaniline-gold nanocomposite system, *J. Electrochem. Soc*., **150**, E384–E388 (2003).
[220] H.L. Wang, W. Li, Q.X. Jia, and E. Akhadov, Tailoring conducting polymer chemistry for the chemical deposition of metal particles and clusters, *Chem. Mater*., **19**, 520–525 (2007).
[221] M. Scheffer, V. Martina, R. Seeber, and D. Mandler, Deposition of gold nanoparticles on thin polyaniline films, *Israel J. Chem*., **48**, 349–357 (2008).
[222] M. Sheffer and D. Mandler, Control of locally deposited gold nanoparticles on polyaniline films, *Electrochim. Acta*, **54**, 2951–2956 (2009).
[223] A.Q. Zhang, C.Q. Cui, J.Y. Lee, and F.C. Loh, Interactions between polyaniline and silver cations, *J. Electrochem. Soc*., **142**, 1097–1104 (1995).
[224] M.Y. Lebedev, M.V. Lauritzen, A.E. Curzon, and S. Holdcroft, Solvato-controlled doping of conducting polymers, *Chem. Mater*., **10**, 156–163 (1998).
[225] N.L. Pickup, J.S. Shapiro, and D.K.Y. Wong, Extraction of silver by polypyrrole films upon a base-acid treatment, *Anal. Chim. Acta*, **364**, 41–51 (1998).
[226] L.M. Abrantes, A.C. Cascalheira, and M. Savic, Performance of polyaniline coatings on stainless steel for silver recovery, *Portug. Electrochim. Acta*, **17**, 157–164 (1999).
[227] F.Y. Song and K.K. Shiu, Preconcentration and electroanalysis of silver species at polypyrrole film modified glassy carbon electrodes, *J. Electroanal. Chem*., **498**, 161–170 (2001).
[228] C. Visy, E. Pinter, T. Fullei, and R. Patakfalvi, Characterization of electronically conducting polypyrrole based composite materials, *Synth. Met*., **152**, 13–16 (2005).
[229] E. Pinter, R. Patakfalvi, T. Fiilei, Z. Gingl, I. Dekany, and C. Visy, Characterization of polypyrrole-silver nanocomposites prepared in the presence of different dopants, *J. Phys. Chem. B*, **109**, 17474–17478 (2005).
[230] V.M. Jovanovic, S. Terzic, and A. Dekanski, Characterization and electrocatalytic application of silver modified polypyrrole electrodes, *J. Serb. Chem. Soc*., **70**, 41–49 (2005).
[231] R. Dimeska, P.S. Murray, S.F. Ralph, and G.G. Wallace, Electroless recovery of silver by inherently conducting polymer powders, membranes and composite materials, *Polymer*, **47**, 4520–4530 (2006).
[232] M. Ocypa, M. Ptasinska, A. Michalska, K. Maksymiuk, and E.A.H. Hall, Electroless silver deposition on polypyrrole and poly(3,4-ethylenedioxythiophene): The reaction/diffusion balance, *J. Electroanal. Chem*., **596**, 157–168 (2006).
[233] W. Li, Q. X. Jia, and H.L. Wang, Facile synthesis of metal nanoparticles using conducting polymer colloids, *Polymer*, **47**, 23–26 (2006).
[234] E. Pinter, Z.A. Fekete, O. Berkesi, P. Makre, A. Patzko, and C. Visy, Characterization of poly(3-octylthiophene)/silver nanocomposites prepared by solution doping, *J. Phys. Chem. C*, **111**, 11872–11878 (2007).
[235] J. Stejskal, J. Prokes, and I. Sapurina, The reduction of silver ions with polyaniline: The effect of the type of polyaniline and the mole ratio of the reagents, *Mater. Lett*., **63**, 709–711 (2009).
[236] L.M. Abrantes and J.P. Correia, Polymer films containing metal particles – noble metals in polyaniline, *Mater. Sci. Forum*, **191**, 235–340 (1995).
[237] M. Hasik, A. Derlinkiewicz, M. Choczynski, S. Quillard, and A. Pron, Polyaniline containing palladium – new conjugated polymer supported catalysts, *Synth. Met*., **84**, 93–94 (1997).
[238] A. Derlinkiewicz, M. Hasik, and M. Choczynski, Preparation and properties of polyaniline containing palladium, *Mater. Res. Bull*., **33**, 739–762 (1998).
[239] S.W. Huang, K.G. Neoh, C.W. Shih, D.S. Lim, E.T. Kang, H.S. Han, and K.L. Tan, Synthesis, characterization and catalytic properties of palladium-containing electroactive polymers, *Synth. Met*., **96**, 117–122 (1998).
[240] M. Josowicz, H.S. Li, K. Domansky, and D.R. Baer, Effect of oxidation state of palladium in polyaniline layers on sensitivity to hydrogen, *Electroanalysis*, **11**, 774–781 (1999).
[241] A. Derlinkiewicz, M. Hasik, and M. Kloc, Pd-PANI: preparation and catalytic properties, *Synth. Met*., **102**, 1307–1308 (1999).
[242] A. Derlinkiewicz, M. Hasik, and M. Kloc, Pd/polyaniline as the catalysts for 2-ethylantraquinone hydrogenation. The effect of palladium dispersion, *Catalysis Lett.*, **64**, 41–47 (2000).

[243] Z.H. Ma, K.L. Tan, and E.T. Kang, Electroless plating of palladium and copper on polyaniline films, *Synth. Met*., **114**, 17–25 (2000).
[244] V.W.L. Lim, E.T. Kang, and K.G. Neoh, Electroless plating of palladium and copper on polypyrrole films, *Synth. Met*., **123**, 107–115 (2001).
[245] M. Hasik, A. Derlinkiewicz, and E. Wenda, Interactions between polyaniline and palladium ions: similarities and differences, *Synth. Met*., **119**, 335–336 (2001).
[246] M. Hasik, E. Wenda, C. Paluskiewicz, A. Bernasik, and J. Camra, *Synth. Met*., *Poly(o-methoxyaniline)- palladium systems: effect of preparation conditions on physico-chemical properties*, **143**, 341–350 (2004).
[247] A. Derlinkiewicz, M. Hasik, J.W. Sobczak, E. Sobczak, A. Bernasik, and E. Bielanska, Physicochemical and catalytic properties of palladium supported on poly(*o*-methoxyaniline), *Mater. Res. Bull*, **40**, 869–889 (2005).
[248] A. Mourato, A.S. Viana, J.P. Correia, H. Siegenthaler, and L.M. Abrantes, Polyaniline films containing electrolessly precipitated palladium, *Electrochim. Acta*, **49**, 2249–2257 (2004).
[249] A.P. O'Mullane, S.E. Dale, J.V. Macpherson, and P.R. Unwin, Fabrication and electrocatalytic properties of polyaniline/Pt nanoparticle composites, *Chem. Commun*., 1606–1607 (2004).
[250] A.P. O'Mullane, S.E. Dale, T.M. Day, N.R. Wilson, J.V. Macpherson, and P.R. Unwin, Formation of polyaniline/Pt composite films and their electrocatalytic properties, *J. Solid State Electrochem*., **10**, 792–807 (2006).
[251] J. Langmaier and J. Janata, Sensitive layer for electrochemical detection of hydrogen cyanide, *Anal. Chem*., **64**, 523–527 (1992).
[252] B. Sofiane, H. Didier, and L.P. Laurent, Synthesis and characterization of composite Hg-polyaniline powder material, *Electrochim. Acta*, **52**, 62–67 (2006).
[253] J. Ding, W.E. Price, S.F. Ralph, and G.G. Wallace, Electroless recovery of gold chloride using inherently conducting polymers, *Polym. Int*., **53**, 681–687 (2004).
[254] M. A. Watzky and R.G. Finke, Nanocluster size-control and "magic number" investigations. Experimental tests of the "living-metal polymer" concept and of mechanism-based size-control predictions leading to the syntheses of iridium(0) nanoclusters centering about four sequential magic numbers, *Chem. Mater*., **9**, 3083–3095 (1997).
[255] Z. Qi and P.G. Pickup, Novel supported catalysts: platinum and platinum oxide nanoparticles dispersed on polypyrrole/polysterenesulfonate particles, *Chem. Commun*., 15–16 (1998).
[256] Z. Qi, M.C. Lefebvre, and P.G. Pickup, Electron and proton transport in gas diffusion electrodes containing electronically conductive proton-exchange polymers, *J. Electroanal. Chem*., **459**, 9–14 (1998).
[257] Z. Qi and P.G. Pickup, High performance conducting polymer supported oxygen reduction catalysts, *Chem. Commun*., 2299–2300 (1998).
[258] B.Y. Kim, M.S. Cho, Y.S. Kim, Y. Son, and Y. Lee, Fabrication and characterization of poly(3,4-ethylenedioxythiophene)/gold nanocomposite via *in-situ* redox cycle system, *Synth. Met*., **153**, 149–152 (2005).
[259] T. Amaya, D. Saio, and T. Hirao, Template synthesis of polyaniline/Pd nanoparticle and its catalytic application, *Tet. Lett*., **48**, 2729–2732 (2007).
[260] V. Selvaraj and M. Alagar, Pt and Pt-Ru nanoparticles decorated polypyrrole/multiwalled carbon nanotubes and their catalytic activity towards methanol oxidation, *Electrochem. Commun.*, **9**, 1145–1153 (2007).
[261] V. Selvaraj, M. Alagar, and K. S. Kumar, Synthesis and characterization of metal nanoparticles-decorated PPY-CNT composite and their electrocatalytic oxidation of formic acid and formaldehyde for fuel cell applications, *Appl. Catalysis B*, **75**, 129–138 (2007).
[262] V. Selvaraj and M. Alagar, Ethylene glycol oxidation on Pt and Pt-Ru nanoparticle decorated polythiophene/multiwalled carbon nanotube composites for fuel cell applications, *Nanotechnology*, **19**, 045504 (2008).
[263] L.M. Abrantes and J.P. Correia, Poly(3-methylthiophene) incorporating electrolessly deposited Ni-P particles, *Surf. Coat. Technol*., **107**, 142–148 (1998).
[264] L.M. Abrantes and J.P. Correia, Polypyrrole incorporating electroless nickel, *Electrochim. Acta*, **45**, 4179–4185 (2000).

[265] K.R. Reddy, K.P. Lee, A.I. Gopalan, M.S. Kim, A.M. Showkat, and Y.C. Nho, Synthesis of metal (Fe or Pd)/alloy(Fe-Pd) – nanoparticles embedded multiwall carbon nanotube/sulfonated polyaniline composites by γ–irradiation, *J. Polym. Sci. A*, **44**, 3355–3364 (2006).
[266] M. Ilieva, S. Ivanov, and V. Tsakova, Electrochemical synthesis and characterization of TiO2-polyaniline composite layers, *J. Appl. Electrochem*., **38**, 63–69 (2008).
[267] B.I. Podlovchenko, Y.M. Maksimov, T.D. Gladysheva, and E.A. Kolyadko, Electrocatalytic activity of platinum-polyaniline and palladium-polyaniline systems obtained by cycling the electrode potential, *Russ. J. Electrochem*., **36**, 731–735 (2000).
[268] A. Kitani, T. Akashi, K. Sugimoto, and S. Ito, Electrocatalytic oxidation of methanol on platinum modified polyaniline electrodes, *Synth. Met*., **121**, 1301–1302 (2001).
[269] F.J. Liu, L.M. Huang, T.C. Wen, and A. Gopalan, Large-area network of polyaniline nanowires supported platinum nanocatalysts for methanol oxidation, *Synth. Met*., **157**, 651–658 (2007).
[270] F.J. Liu, L.M. Huang, T.C. Wen, K.C. Yin, J.S. Hung, and A. Gopalan, Composite electrodes consisting of platinum particles and polyaniline nanowires as electrocatalysts for methanol oxidation, *Polym. Composites*, 650–656 (2007).
[271] J. Yano, T. Shiraga, and A. Kitani, Dispersed platinum and tin polyaniline film electrodes for the anodes of the direct methanol fuel cell, *J. Solid State Electrochem*., **12**, 1179–1182 (2008).
[272] A. Lima, C. Coutanceau, J.M. Leger, and C. Lamy, Investigation of ternary catalysts for methanol electrooxidation, *J. Appl. Electrochem*., **31**, 379–386 (2001).
[273] Y.M. Wu, W.S. Li, J. Lu, J.H. Du, D.S. Lu, and J.M. Fu, *J. Power Sources*, **145**, 286–291 (2005).
[274] P. Santhosh, A. Gopalan, and K.P. Lee, Gold nanoparticles dispersed polyaniline grafted multiwall carbon nanotubes as newer electrocatalysts: Preparation and performances for methanol oxidation, *J. Catal*., **238**, 177–185 (2006).
[275] S.M. Golabi and A. Nozad, Electrocatalytic oxidation of methanol on electrodes modified by platinum microparticles dispersed into poly(*o*-phenylenediamine), *J. Electroanal. Chem*., **521**, 161–167 (2002).
[276] T. Maiyalagan, Electrochemical synthesis, characterization and electro-oxidation of methanol on platinum nanoparticles supported poly(*o*-phenylenediamine) nanotubes, *J. Power Sources*, **179**, 443–450 (2008).
[277] P. Santhosh, A. Gopalan, T. Vasudevan, and K.P. Lee, Platinum particles dispersed poly (diphenylamine) modified electrode for methanol oxidation, *Appl. Surf. Sci*., **252**, 7964–7969 (2006).
[278] H. Yang, T. Lu, K. Xue, S. Sun, G. Lu, and S. Chen, Electrrocatalytic oxidation of methanol on polypyrrole film modified with platinum microparticles, *J. Electrochem. Soc*., **144**, 2302–2306 (1997).
[279] J. Li and X. Lin, A composite of polypyrrole nanowire platinum modified electrode for oxygen reduction and methanol oxidation reactions, *J. Electrochem. Soc*., **154**, B1074–B1079 (2007).
[280] B. Rajesh, K. R. Thampi, J.M. Bonard, A.J. McEvoy, N. Xanthopoulos, H.C. Mathieu, and B. Viswanathan, Pt particles supported on conducting polymeric nanocones as electro-catalysts for methanol oxidation, *J. Power Sources*, **133**, 155–161 (2004).
[281] M.C. Lefebvre, Z. Qi, and P.G. Pickup, Electronically conducting proton exchange polymers as catalyst supports for proton exchange membrane fuel cells, *J. Electrochem. Soc*., **146**, 2054–2058 (1999).
[282] C. Arbizzani, M. Biso, E. Manferrari, and M. Mastragostino, methanol oxidation by pEDOT-pSS/PtRu in DMFC, *J. Power Sources*, **178**, 584–590 (2008).
[283] C. Arbizzani, M. Biso, E. Manferrari, and M. Mastragostino, Passive DMFCs with PtRu catalyst on poly(3,4-ethylenedioxythiophene)-polysterene-4-sulphonate support, *J. Power Sources*, **180**, 41–45 (2008).
[284] F.T.A. Vork and E. Barendrecht, The reduction of dioxygen at polypyrrole-modified electrodes with incorporated Pt particles, *Electrochim. Acta*, **35**, 135–139 (1990).
[285] Y.M. Maksimov, T.D. Gladysheva, and B.I. Podlovchenko, Electrochemical behavior of platinum-modified polyaniline films in sulfuric acid solutions of carbon monoxide *Russ. J. Electrochem*., **37**, 554–558 (2001).

[286] M.A. Del Valle, F.R. Diaz, M.E. Bodini, T. Pizarro, R. Cordova, H. Gomez, and R. Schrebler, Polythiophene, polyaniline and polypyrrole electrodes modified by electrodeposition of Pt and Pt+Pb for formic acid electrooxidation, *J. Appl. Electrochem*., **28**, 943–946 (1998).
[287] V. Selvaraj, M. Alagar, and I. Hamerton, Nanocatalysts impregnated polythiophene electrodes for the electrooxidation of formic acid, *Appl. Catalysis B*, **73**, 172–179 (2007).
[288] L. Komsiyska and V. Tsakova, Ascorbic acid oxidation at non-modified and copper-modified polyaniline and poly-ortho-methoxyaniline coated electrodes, *Electroanalysis*, **18**, 807–813 (2006).
[289] A.I. Gopalan, K.P. Lee, K.M. Manesh, P. Santhosh, J.H. Kim, and J.S. Kang, Electrochemical determination of dopamine and ascorbic acid at a novel gold nanoparticles distributed poly (4-aminothiophenol) modified electrode, *Talanta*, **71**, 1774–1781 (2007).
[290] J. Li and X. Lin, Simultaneous determination of dopamine and serotonin on gold nanocluster/overoxidized-polypyrrole composite modified glassy carbon electrode, *Sens. Actuators B*, **124**, 486–493 (2007).
[291] S. Harish, J. Mathiyarasu, K.L.N. Phani, and V. Yegnaraman, PEDOT/palladium composite material: synthesis, characterization and application to simultaneous determination of dopamine and uric acid, *J. Appl. Electrochem*., **38**, 1583–1588 (2008).
[292] G. Casella, T.R.I. Cataldi, A. Guerrieri, and E. Desimoni, Copper dispersed into polyaniline films as an amperometric sensor in alkaline solutions of amino acids and polyhydric compounds, *Analyt. Chim. Acta*, **335**, 217–225 (1996).
[293] S.T. Farrel and C.B. Breslin, Oxidation and photo-induced oxidation of glucose at a polyaniline film modified by copper particles, *Electrochim. Acta*, **49**, 4497–4503 (2004).
[294] I. Becerik and F. Kadirgan, Electrocatalytic properties of platinum particles incorporated with polypyrrole films in D-glucose oxidation in phosphate media, *J. Electroanal. Chem*., **436**, 189–193 (1997).
[295] S. Komathi, A.I. Gopalan, and K.P. Lee, Fabrication of a novel layer-by-layer film based glucose biosensor with compact arrangement of multi-components and glucose oxidase, *Biosens. Bioelectronics*, **24**, 3131–3134 (2009).
[296] H. Yamato, T. Koshiba, M. Ohwa, W. Wernet, and M. Matsumara, A new method for dispersing palladium microparticles in conducting polymer films and its application to biosensors, *Synth. Met*., **87**, 231–236 (1997).
[297] I. Becerik, S. Suzer, and F. Kadirgan, Platinum-palladium loaded polypyrrole film electrodes for the electrooxidation of D-glucose in neutral media, *J. Electroanal. Chem*., **476**, 171–176 (1999).
[298] I. Becerik and F. Kadirgan, Glucose sensitivity of platinum-based alloys incorporated in polypyrrole films at neutral media, *Synth. Met*., **124**, 379–384 (2001).
[299] P. Santhosh, K.M. Manesh, S. Uthayakumar, S. Komathi, A.I. Goplana, and K.P. Lee, Fabrication of enzymatic glucose biosensor based on palladium nanoparticles dispersed into poly(3,4-ethylenedioxythiophene) nanofibers, *Bioelectrochem*., **75**, 61–66 (2009).
[300] M.R. Guascito, P. Boffi, C. Malitesta, L. Sabbatni, and P.G. Zambonin, Conducting polymer electrodes modified by metallic species for electrocatalytic purposes – Spectroscopic and microscopic characterization, *Mater. Chem. Phys*., **44**, 17–24 (1996).
[301] K.M. Manesh, P. Santhosh, A. Gopalan, and K.P. Lee, Electrocatalytic oxidation of NADH at gold nanoparticles loaded poly(3,4-ethylenedioxythiophene)-poly(sterene sulfonic acid) film modofoed electrode and integration of alcohol dehydrogenase for alcohol sensing, *Talanta*, **75**, 1307–1314 (2008).
[302] Y. Li, R. Lenigk, X. Wu, B. Gruendig, S. Dong, and R. Renneberg, Investigation of oxygen- and hydrogen peroxide-reduction on platinum particles dispersed on poly (*o*-phenylenediamine) film modified glassy carbon electrodes, *Electroanalysis*, **10**, 671–676 (1998).
[303] A.I. Gopalan, K.P. Lee, K.M. Manesh, P. Santhosh, and J.H. Kim, Gold nanoparticles dispersed into poly(aminophenol) as a novel electrocatalyst- Fabrication of modified electrode and evaluation of electrocatalytic activities for dioxygen reduction, *J. Mol. Catalysis A*, **256**, 335–345 (2006).
[304] M.T. Giacomini, E.A. Ticianelli, J. McBreen, and M. Balasubramanian, Oxygen reduction on supported platinum/polythiophene electrocatalysts, *J. Electrochem. Soc*., **148**, A323–A329 (2001).

[305] J. Shan and P.G. Pickup, Characterization of polymer supported catalyst by cyclic voltammetry and rotating disk voltammetry, *Electrochim. Acta*, **46**, 119–125 (2000).
[306] Y. Wang, J. Huang, C. Zhang, J. Wei, and X. Zhou, Determination of hydrogen peroxide in rainwater by using a polyaniline film and platinum particles co-modified carbon fiber microelectrode, *Electroanalysis*, **10**, 776–778 (1998).
[307] T. Zhang, R. Yuan, Y. Chai, W. Li, and S. Ling, A novel nonenzymatic hydrogen peroxide sensor based on a polypyrrole nanowire-copper nanocomposite modified gold electrode, *Sensors*, **8**, 5141–5152 (2008).
[308] L. Coche and J.C. Moutet, Electrocatalytic hydrogenation of organic compounds on carbon electrodes modified by precious metal microparticles in redix active polymer films, *J. Am. Chem. Soc*., **109**, 6887–6889 (1987).
[309] B.J. Gallon, R.W. Kojima, R.B. Kaner, and P.L. Diaconescu, Palladium nanoparticles supported on polyaniline nanofibers as a semi-heterogeneous catalyst in water, *Angew. Chem., Int. Edition*, **46**, 7251–7254 (2007).
[310] H.H. Shih, D. Williams, N.H. Mack, and H.L. Wang, Condusctng polymer-based electrodeless deposition of Pt nanoparticles and its catalytic properties regioselective hydrosilylation reactions, *Macromolecules*, **42**, 14–16 (2009).
[311] E. Antolini and E.R. Gonzalez, Polymer supports for low-temperature fuel cell catalysts, *Appl. Catal. A*, **365**, 1–19 (2009).
[312] H.B. Mark Jr., N. Atta, Y.L. Ma, K.L. Petticrew, H. Zimmer, Y. Shi, S.K. Lunsford, J.F. Rubinson, and A. Galal, The electrochemistry of neurotransmitters at conducting organic polymer electrodes: electrocatalysis and electroanalytical applications, *Bioelectrochem. Bioenerget*., **38**, 229–245 (1995).
[313] A.A. Athawale, S.V. Bhagwat, and P.P. Katre, Nanocomposite of Pd-polyaniline as a selective methanol sensor, *Sens. Actuators B*, **114**, 263–267 (2006).
[314] S. Jiang, J. Chen, J. Tang, E. Jin, L. Kong, W. Zhang, and C. Wang, Au nanoparticles-functionalized two-dimensional patterned conducting PANI nanobowl monolayer for gas sensor, *Sens. Actuators B*, **140**, 520–524 (2009).
[315] M.A. El-Sayed, Some interesting properties of metals confined in time and nanometer space of different shapes, *Acc. Chem. Res*., **34**, 257–264 (2001).
[316] R. Narayanan and M.A. El-Sayed, Shape-dependent catalytic activity of platinum nanoparticles in colloidal solutions, *Nano Letters*, **4**, 1343–1348 (2004).
[317] R. Narayanan and M.A. El-Sayed, Catalysis with transition metal nanoparticles in colloidal solutions: nanoparticle shape dependence and stability, *J. Phys. Chem. B*, **109**, 12663–12676 (2005).
[318] C. Burda, X. Chen, R. Narayanan, and M.A. El-Sayed, Chemistry and properties of nanocrystals of different shapes, *Chem. Rev*., **105**, 1025–1102 (2005).

8

Spectroscopy of Nanostructured Conducting Polymers

Gustavo M. do Nascimento[a,b] *and Marcelo A. de Souza*[b]

[a]*Universidade Federal de Minas Gerais (UFMG)*
[b]*Universidade de São Paulo (USP)*

8.1 Synthetic Metals

Intrinsically conducting polymers (ICPs), more commonly known as 'synthetic metals,' form one of the largest classes of molecular conductors [1]. The study of conjugated polymers has been hampered by their insolubility, infusibility, and instability in air. In the early 1970s, Shirakawa and Ikeda [2] showed the possibility of preparing more stable films of semiconducting poly(acetylene) (PA). This discovery did not generate much interest until 1977, when MacDiarmid *et al.* [3] found that, when PA is doped with a Lewis acid (or base), the conductivity increases by 13 orders of magnitude. Since this initial discovery, the development of the conducting polymer field has continued to accelerate at an unexpectedly rapid rate. This has been stimulated not only by the fundamental synthetic novelty and importance, but mainly because this field is a cross-disciplinary section of many areas.

The concept of doping is unique and has central importance, because it is what differentiates the conducting polymers from all other kinds of polymers [4–6]. During the process of doping, an insulating or semiconducting organic polymer with low conductivity, typically ranging from 10^{-10} to $10^{-5}\,\mathrm{S\,cm^{-1}}$, is converted into a polymer which shows 'metallic' conductivity (ca. $1–10^{4}\,\mathrm{S\,cm^{-1}}$). The addition

Nanostructured Conductive Polymers Edited by Ali Eftekhari

of nonstoichiometric chemical species in commonly low quantities (≤10%), results in dramatic changes in the electronic, electrical, magnetic, optical, and structural properties of the polymer. The doping is reversible, and the polymer can return to its original state without major changes in its structure. In the doped state, the presence of counter-ions stabilizes the doped state. All conductive polymers (and their derivatives, see Scheme 8.1), for example, poly(*p*-phenylene) (1), poly(*p*-phenylene-vinylene) (2), poly(pyrrole) (3), poly(thiophene) (4), poly(furan) (5), poly (heteroaromatic vinylene) (6, where Y = NH, NR, S, O), poly(*p*-phenylenediamine) (7) and poly(aniline) (8), among others, may be doped by p (oxidation) or n (reduction) through chemical and/or electrochemical process.

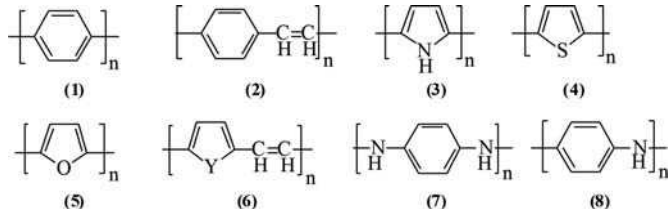

Scheme 8.1 *Schematic representation of the structures of the most representative conducting polymers: Poly(*p*-phenylene) (**1**), poly(*p*-phenylene-vinylene) (**2**), poly(pyrrole) (**3**), poly(thiophene) (**4**), poly(furan) (**5**), poly(heteroaromatic vinylene) (**6**, where Y = NH, NR, S, O), poly (*p*-phenylenediamine) (**7**), and poly(aniline) (8)*

8.2 Nanostructured Conducting Polymers

Nowadays a promising way to control the bulk polymer properties, such as conductivity, processability, thermal, and mechanical stabilities, is through the organization of the polymeric chains on the nanometer scale [7–9]. The first approach used to achieve this goal was the synthesis of conducting polymers in cavities of porous hosts. Commonly named nanocomposites, these materials have two or more different components on the nanoscale, and can show catalytic, electronic, magnetic, and optical properties better than those of the individual phases. The basic reason for this synergism is still not fully understood, but it is considered that confinement and electrostatic interactions between the components play an important role.

The host structure must provide an environment of restricted geometry, sometimes preventing the reticulation of the polymeric chains. Chains of poly(aniline), poly(pyrrole) and poly(thiophene) and others have been encapsulated by many forms of host [10–13] (see Table 8.1). Two routes are commonly used for this: (i) the monomer is dissolved in an organic solvent (or in aqueous solution in its protonated form), and by diffusion and/or charge-exchange processes, the monomer is encapsulated in the cavities of a host, followed by oxidation with ammonium persulfate or another oxidant (*in situ* polymerization), (ii) a host having oxidant ions, such as Cu(II) or Fe(III) is exposed to monomer vapors and then acid vapors [10–11].

Table 8.1 *Hosts used for formation of nanostructured conducting polymers*

Pores	Host Structure	Examples	Ref.
3-D	Zeolites	Zeolite MFI (ZSM-5)	[162,163]
		Zeolite Y	[10,11,75]
		Zeolite LTL (L)	[163]
		Zeolite FAU (Faujasita)	[10,11]
		Porous Vycor Glass (PVG)	[48]
2-D	Silicates and Clays	Hectorite, Montmorillonite	[83], [57–75]
	Metallic Oxides	MoO_3, V_2O_5	[49], [50]
	Layered Uranyl	$HUO_2PO_4.4H_20$ (HUP)	[52]
	Phosphate	$HMMoO_6{\cdot}H_2O$ (M= Nb, Ta)	[56]
	Layered Brönsted acids	MoS_2	[55]
	Layered double hydroxide	$Cu_2Cr(OH)_6Cl.nH_2O$	[54]
1-D		Track-etched membranes and porous alumina	[8,9]
	Zeolites	Zeolite MOR (Mordenite)	[10,11,75]
	Nanotubes	Carbon Nanotubes	[141,142]
	Mesoporous	MCM-41	[86–88]
0-D	Cyclodextrins	α-, β- and γ-ciclodextrins	[91–93]

The host structures can be classified by the dimensionality of their pores or cavities; hosts with cavities extending and connecting in three dimensions (3-D), such as some zeolites and mesopore materials (see Figure 8.1 and Table 8.1); cavities which extend in two directions (2-D), as is the case with all lamelar materials, such as clays; materials with cavities in a single direction (1-D), for example, carbon nanotubes; and finally there are materials with small cavities or with closed cavities (0-D), such as fullerenes and cyclodextrins.

Martin *et al.* [8,9] developed one of the best methods for synthesis of polymers with hosts, using porous polycarbonate membranes (track-etched membranes) and porous alumina. Track-etched membranes are available commercially (Poretics, Nuclepore, etc.) with various sizes of pores from 10 nm upwards and a density of approximately 10^9 pores cm^{-2} [8,9]. The membranes of porous alumina are prepared electrochemically from Al foil, and can have pore densities of up to 10^{11} pores cm^{-2}. Polymerization within

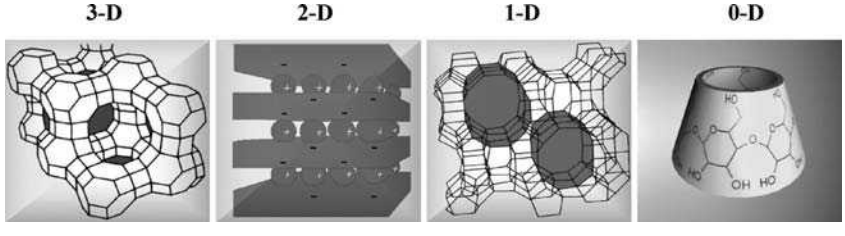

Figure 8.1 *Schematic representation of the structures of: zeolite Y (3-D), montmorillonite clay (2-D), zeolite mordenite (1-D) and α-cyclodextrin (0-D)*

the pores of these membranes can be performed chemically or electrochemically. By controlling the duration of polymerization, it is possible to obtain tubes or filaments of conductive polymers. The polymers can be isolated by dissolving the membranes with an appropriate solvent, and separated by filtration. The polymer chains obtained after this treatment are much more conductive than polymers obtained in the conventional manner, and the authors attribute this behavior to greater alignment of the chains [8].

Recently, great efforts have been made to produce nanostructured polymer chains without the use of rigid hosts. Generally, the conventional synthesis of conducting polymers produces a polymer with irregular morphology that is accompanied by a very small percentage of nanoscale fibers [14,15]. To circumvent this behavior, several approaches have been developed by which nanofibers can be obtained as the dominant nanostructure. For instance, in the absence of an external physical or chemical template, nanofibers/tubes of several conducting polymers can be obtained by making use of large organic acids. These acids form micelles upon which the monomer can be polymerized and doped. Fiber diameters are observed to be as low as 30–60 nm and are highly influenced by reagent ratios [16–20].

Ionic liquids, organic salts that are liquid at low temperature, have also been used as synthetic media for the preparation of nanostructured conducting polymers [21,22]. Uniform nanofibers have also been prepared by polymerization at an aqueous–organic interface [14,15]. It is hypothesized that migration of the product into the aqueous phase can suppress uncontrolled polymer growth by isolating the fibers from the excess of reagents. Interfacial polymerization can therefore be regarded as a nontemplate approach in which high local concentrations of both monomer and dopant anions at the liquid–liquid interface might be expected to promote the formation of monomer–anion (or oligomer–anion) aggregates. These aggregates can act as nucleation sites for polymerization, resulting in powders with fibrillar morphology. It has recently been demonstrated that the addition of certain surfactants to such an interfacial system grants further control over the diameter of the nanofibers. 'Seeding' with various nanomaterials has also been used with great effect to initiate polymer nanofiber formation in single-phase polymerizations [23,24]. Thus, the template-free methods, such as interfacial, seeding, and micellar, can be employed as different 'bottom-up' approaches to obtain pure conducting polymer nanofibers. The possibility to prepare nanostructured conducting polymers by self-assembly with reduced post-synthesis processing warrants further study and application of these materials, especially in the field of electronic nanomaterials.

8.3 Spectroscopic Techniques

Different characterization techniques have been employed in determination of the structure and also the behavior of nanostructured conducting polymers. Among these, the spectroscopic techniques have been essential in understanding the molecular structure and interactions resultant from the arrangment at the nanometric level. In this section, a description of the main characteristics of the spectroscopic techniques that have been broadly used in the structural investigation of nanostructured conducting polymers will be given. Results obtained using spectroscopic techniques that have not been largely used for the cases discussed here (such as solid-state nuclear magnetic resonance, etc.) have also

been considered in the discussion of the spectroscopic data of the nanostructured conducting polymers (Section 7.4) where appropriate.

8.3.1 Vibronic Techniques (UV-vis-NIR, FTIR, Raman, Resonance Raman)

Among the different techniques that can be applied for the investigation of the structure of conducting polymers, the vibronic techniques are the most frequently used [25–27]. The eletronic spectra of conjugated polymers are very dependent on their oxidation and/or doping state. The doping process leads to dramatic changes in the electronic structure of the polymer. The formation of charged species (solitons, radical cations, dications, etc.) promotes a local distortion in the polymeric backbone. If this distortion is high enough the charge will be localized in the polymeric structure [28–30]. The association of this distortion with a localized charge is known as polaron in solid-state terminology. This process can be visualized as the formation of a localized state in the band gap, associated with the appearance of a broad electronic band in the visible region. For example, Figure 8.2 shows the UV-vis-NIR spectra of PANI before (in its semiconductor emeraldine base form, PANI-EB) and after doping with choridric acid (in its metallic emeraldine salt

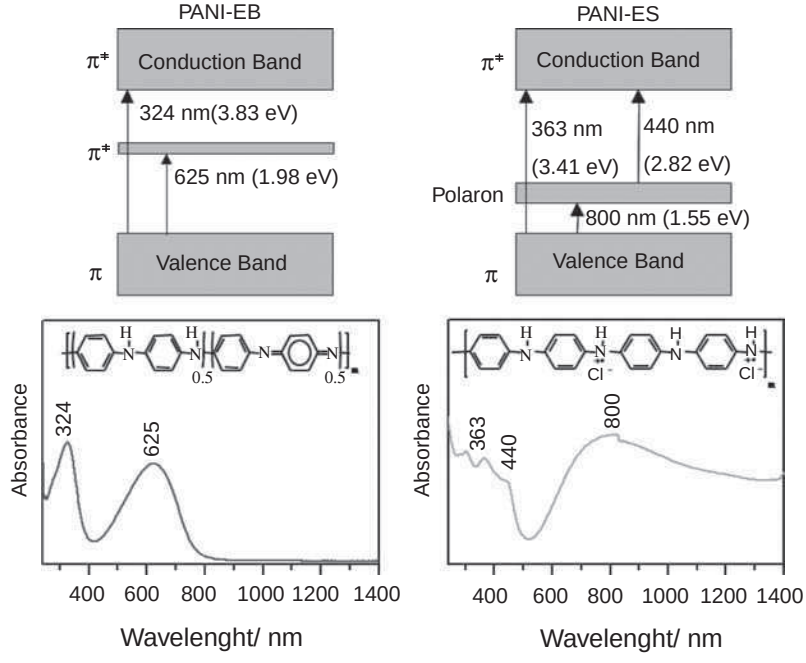

Figure 8.2 *The UV-vis-NIR spectra observed for PANI in its emeraldine base (EB) and salt (ES) forms (see the schematic structure). Above the spectra are presented the energy diagram for PANI-EB and PANI-ES. The UV-vis-NIR spectra were acquired using a Shimadzu UVPC-3101 scanning spectrophotometer in transmission mode with 1 mm quartz cell; PANI-EB was dissolved in* N*-methyl-pyrrolidone and PANI-ES was dissolved in concentrated HCl*

form, PANI-ES). For PANI-EB the band at 324 nm corresponds to a $\pi \rightarrow \pi^*$ transition and the band at 625 nm has been assigned to the electron transition from a benzenoid to a quinoid ring [31]. After doping, a rearrangement of the charges owing mainly to the protonation of quinoid nitrogens leads to the formation of polarons or radical cations. For PANI-ES, the peak at ca. 440 nm and the broad band starting at ca. 600 nm are assigned to electronic absorptions of radical cation segments [32].

UV-vis-NIR spectroscopy is also a powerful tool in the investigation of the organization of the polymeric backbone. When the chains of conducting polymer are well organized in an extended conformation, the respective electronic absorption spectrum shows a very intense and broad polaronic band starting from ca. 900 nm and extending to the NIR region [33]. Further, UV-vis-NIR data have been employed in the study of the polymerization mechanism of conducting polymers prepared in different synthetic condictions [34]. For instance, UV-vis spectra obtained in the initial steps of aniline polymerization show that the formation of *N*-phenyl-1,4-benzequinonediimine (PBQ, the oxidated form of the aniline dimer, which absorbs at ca. 420 nm) is the first main step and afterwards, propagation occurs by addition of monomer in the PBQ chains. However, many doubts remain, and more recently it has been suggested that the formation of phenazine-like rings also occurs in aniline polymerization [35,36], while for polypyrrole and poly(thiophene) the formation of radical species is the main step in the polymerization mechanism.

The oxidation, doping, and nanostructuring of the polymeric chains also provoke a dramatic change in the vibrational levels of the conducting polymers. Over the years, infrared and Raman spectroscopies have been the techniques *par excellence* for the investigation of the vibrational structure of conducting polymers. In Raman spectroscopy the radiation source has much more energy than the vibrational transitions, but through the scattering of incident light (laser source) by the vibrational modes, it is possible to see the vibrational levels. Conversely, in IR spectroscopy, the incident radiation has the same magnitude as the vibrational transitions, being absorbed when its value is similar to a permitted transition (see diagram in Figure 8.3). When the laser source has energy of very different magnitude to a permitted electronic transition in the molecule, the scattering light is almost independent of the incident light, thus the intensity of the Raman bands are proportional to λ_s^4 [27]. However, when the energy of the incident light is near to an available eletronic transition of the molecule, the process changes drastically. The intensities of vibrational Raman modes that are associated with a excited eletronic state that is in resonance can be greatly increased, typically 10^5 times. For conducting polymers, which are a typical multichromophoric system, it is possible to search the different chromophoric segments, just by changing the incident laser line energy.

8.3.2 X-Ray Techniques (XANES, EXAFS AND XPS)

Spectroscopic techniques that employ electromagnetic radiation between vacuum UV energy ($\sim$10–40 eV, 125–31 nm) and soft X-rays (40–1500 eV, 31–0.8 nm) and going on to hard X-rays (1500–105 eV, 0.8–0.01 nm) have also been of great importance in elucidating the electronic structure of complex materials [34]. It is well known that an electromagnetic wave can be scattered and/or absorbed when interacted with the surface of material. In the case of absorption, the X-ray beam intensity (I) is attenuated by the solid

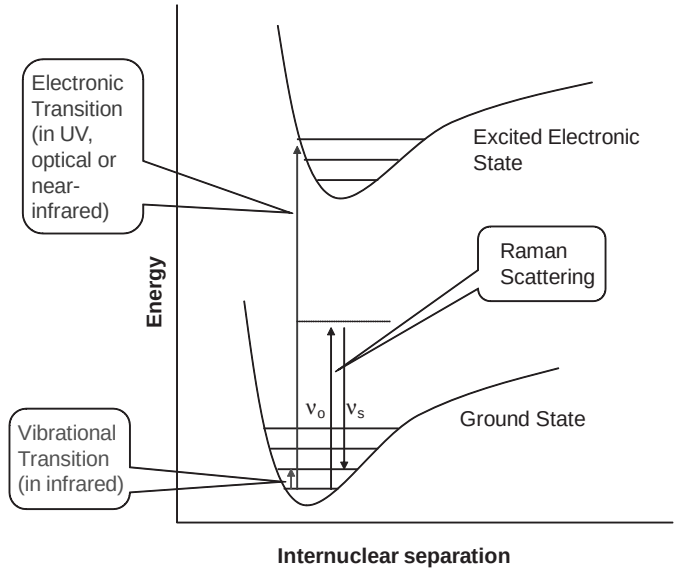

Figure 8.3 *Schematic representation of two eletronic states (ground and excited) and their respective vibrational levels (the eletronic and vibrational levels are not represented on the same scale). The arrows indicate the types of transitions that can occur among the different levels. It is important to say that in the case of Raman scattering, if the laser line (λ_o) used has energy similar to one electronic transition of the molecule, the signal can be intensified by a resonance process, know as the resonance Raman effect. In the figure, ν_o and ν_s are laser line and scattering frequencies, respectively (just the Stokes, $\nu_s < \nu_o$, component is shown in the diagram)*

material, following the Beer–Lambert law; i.e. $I(x) = I_o\exp(-\alpha x)$ shows that the intensity decreases according to the penetration of the material (x) as the argument ($-\alpha x$) of the function is negative. The value of α is a function of the material and the wavelength. The absorption coefficient decreases with increasing photon energy, but there are sudden changes, so that the spectrum exhibits a characteristic saw-tooth pattern. These variations correspond to different edges of absorption in the material. The absorption of X-rays occurs when the energy of the incident photon is transferred to an electron strongly connected to the atom [37,38].

Figure 8.4A schematically displays the absorption of an electron in the K shell (1s level) of an atom of a solid material. Photons with energies lower than the ionization threshold ($h\nu_1$) are poorly absorbed by the material because there are no unoccupied energy states below this energy. However, when the energy of the photon reaches the value $h\nu_2$, a sudden increase in absorption is observed, which corresponds to the absorption edge of the K shell. This energy is called the ionization threshold of the 1s electron. If the photon energy of the incident power source continues to increase ($h\nu_3$), the electron can leave the atom, leaving it ionized. This fact explains why the absorption coefficient is very similar to the cross-section of the photoelectric effect, i.e., there is a probability of ejection of electrons of the atom due to absorption of photons [37–39]. If the value of the photon

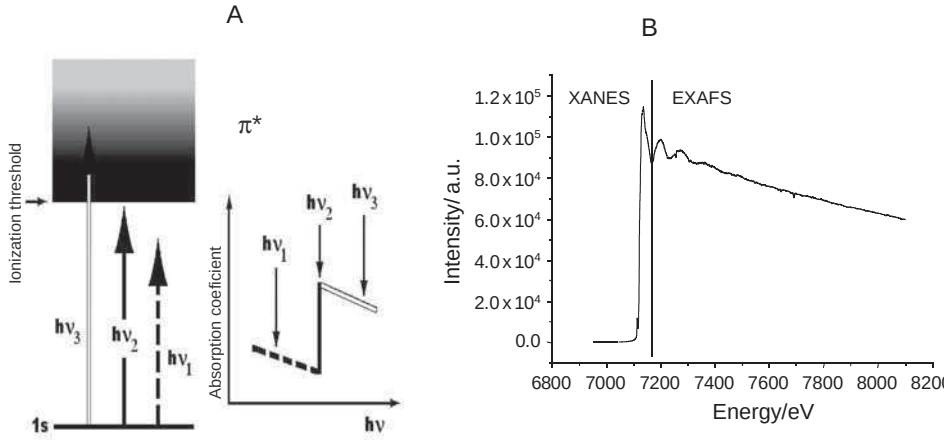

Figure 8.4 *(A) Squematic representation of the X-ray absorption process for K edge excitation. The energy of photons are $h\nu_3 > h\nu_2 > h\nu_1$. (B) X-ray absorption spectrum of poly(aniline) doped with Fe(III) at Fe K-edge. (Data acquired at EXAFS beam line of the Brazilian National Synchrotron Lab, Brazil.) Generally, it is considered that the EXAFS region starts after ~50 eV of the edge, as represented in the figure*

energy continues to rise, the absorption begins to decrease gradually, but further sudden jumps may occur, if there are other absorption edges in the material. The identification of a chemical element in a material is only one item of the chemical information that it is possible to obtain in the X-ray absorption spectrum. Indeed, the phenomenon of absorption is much more complex than it appears, and therefore carries more information than our approach suggests. As can be seen in Figure 8.4B a typical absorption spectrum is formed by a series of oscillations that extends over a large range of energy values (tens of units of eV) and loses intensity as it gets further from the edge of absorption. This set of changes is divided into two regions, one near to the edge of absorption, and another that goes beyond the edge. The structure near the edge is called NEXAFS (Near-Edge X-ray Absorption Fine Structure), better known as XANES (X-ray Absorption Near-Edge Structure); the second region comprises the so-called EXAFS (Extended X-ray Absorption Fine Structure).

More commonly, the electronic structure of solids has been studied by X-ray photoelectron spectroscopy (XPS). Through measurements of the kinetic energy of the photoelectron that leaves the material, the chemical element can be identified, and in addition its oxidation level determined and the electronic states involved in the chemical bonds studied. The XPS technique is very sensitive to the surface owing to the higher signal contribution from the photoelectrons of the first atomic layers, making it a powerful tool to study surfaces. For conducting polymers, XPS spectroscopy has been widely employed with the goal of determining their oxidation states and doping degree. For instance, the different molecular segments present in the PANI chains are known to have different atomic potentials, creating different chemical shifts in the XPS spectrum at N 1s and C 1s. For instance, several authors have investigated the XPS spectra of PANI samples in order

to identify the different nitrogen bonding states [40–44]. Two N 1s peaks of nearly equal intensity were obtained for the emeraldine base, which were ascribed to imine (—N═) 398.1 eV and amine (—NH—) 399.3 eV groups, respectively. After doping, the emeraldine salt gives an N 1s spectrum with an additional shoulder at the high-energy side in the binding energy region 400–403 eV. Many authors decompose the N 1s signal into four peaks, ascribing the two additional components at higher energies to positively charged amine and imine species. The assignments and the quantification of different nitrogen sites are difficult tasks, because the degree of localization of the partial electronic charges and their influence on the binding energy values [42,43] are not exactly known. The close similarities of the N 1s binding energies of amine and protonated imine groups [44] and the possible weak contributions of shake-up processes may further complicate the analysis of the N ls data. The high-energy shoulder of the N 1s photoelectron peak gives no indication of how many bonding states appear. Additional information on the counter-ions from XPS data and from core excitation, including the antibonding π^* states from N 1s XANES might be useful to characterize the polymers. Energies and probabilities of inner-shell excitation processes can be derived from XANES, giving the energy differences between the N ls→2p π^* resonances complementary to the N 1s ionization energies from the XPS.

8.4 Spectroscopy of Nanostructured Conducting Polymers

In the following sections, the main spectroscopic results obtained in the literature for nanostructured conducting polymers will be described. The major results are concerned with six classes of conducting polymers, poly(aniline), poly(pyrrole), poly(thiophene), poly(*p*-phenylene-vinylene), poly(acetylene), and poly(diacetylene). For each section, the results are divided in two subsections: (i) nanocomposites, systems where the nanostructured polymers chains were acquired by using rigid hosts, such as clays, zeolites, and carbon nanotubes, among others, and where the physical properties are derived from the combination of the guest–host interactions; and (ii) nanostructures, systems where the nanostructured polymers were obtained through self-assembly or by using surfactants, and also systems where the polymer can be separated from the template without loss of the nanostructured properties are considered in this section.

8.4.1 Nanostructured Polyaniline and its Derivates

8.4.1.1 Nanocomposites

Polyaniline (PANI) and its derivates represent a very important class of conducting polymers, in which the electronic structure can be modulated by changing the oxidation and/or protonation levels [5]. The half-oxidized forms of PANI have more environmental stability than the others, and can be changed from the semiconductor state (called the emeraldine base, PANI-EB, see Scheme 8.2 for $y = 0.5$), to the highly conducting form (called the emeraldine salt, PANI-ES, see Scheme 8.1) just by changing the protonation degree of the polymeric backbone [5].

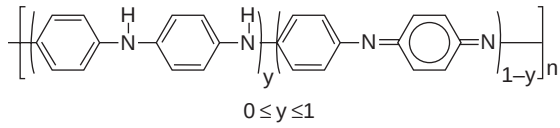

Scheme 8.2 *Schematic representation of the PANI structure*

One of the pioneering studies showed the preparation of nanostructured PANI chains in the cavities of zeolites Y and Mordenite [45]. The aniline was included in the structure of acidic zeolites by adsorption of aniline, followed by its oxidation with persulfate ions. The electronic absorption spectra of both samples showed absorption bands comparable to bulk PANI. The bands at ca. 560 nm (2.2 eV) were associated with quinone diimine structures, [—N═(C_6H_4)═N—], similar to those observed for free PANI-EB or PANI-PB. The shoulders at approximately 400 nm (3.1 eV) and the broad features in the visible and near-IR (<1.8 eV) were associated with polarons. PANI obtained in zeolite Mordenite displayed less protonation (less intense polaron bands) than that prepared in Zeolite Y. The IR spectrum of samples showed typical vibrations of PANI-ES [46,47] at 1583, 1497, 1315, and 1246 (sh) cm^{-1} and a characteristic tail of the electronic excitation corresponding to free carrier absorption. Small shifts between IR frequencies of the zeolite/PANI inclusions and bulk PANI suggested some interaction of the polymer with the host. By means of XPS it was possible to verify the homogeneous distribution of nitrogen in all the zeolite crystals. Porous Vycor glass (PVG), another type of 3-D host, was also used as a host to PANI. PVG is a highly transparent glass to visible light, consisting basically of SiO_2, with a random network of interconnected 3-D pores [48]. The nanocomposites obtained were highly transparent and green. Analysis by UV-vis-NIR and Raman indicated the formation of PANI-ES. It was found that the nanocomposites change color with pH (from dark green at pH = 1 to dark blue at pH = 13).

Among the different types of hosts used in the formation of nanocomposites with PANI, undoubtedly lamelar materials are the most employed. One reason is that the distance between the layers can be modified, facilitating the intercalation of various chemical species. Hosts, such as MoO_3 [49], V_2O_5 [50], α-$Zr(HPO_4)_2H_2O$ [51], $HUO_2PO_4.4H_2O$ [52], FeOCl [53], layered double hydroxide (LDH) [54], MoS_2 [55], $HMMoO_6{\cdot}H_2O$ (M = Nb, Ta) [56], and more frequently clays are used for intercalation of PANI [57–75]. Mainly smectite clays are used, whose structure consists of a central sheet containing $MO_4(OH)_2$ groups of octahedral symmetry associated with two tetrahedral sheets (MO_4) producing layers designated T:O:T [76]. The octahedral sites are occupied by ions of aluminum, iron, and magnesium, while the centers accommodate tetrahedrons of silicon and aluminum ions. The individual layers of negative T:O:T assume a mutually parallel orientation and the electric charge is neutralized by the presence of hydrated positive ions that are in the interlayer region and can be modulated by ion exchange [76]. These clays show large surface adsorption and catalytic activity in organic reactions. Montmorillonite (MMT) is the most common smectite clay, and the negative charge of the lamellae arises mainly in the layers of octahedral substitution of aluminum by magnesium ions.

It is well known that clays have the property to generate colored species by the adsorption of aromatic amines. The most remarkable case is the blue color generated by the adsorption of benzidine (4,4′-diaminobiphenyl) in clay [77]. Among the earliest

studies, Yariv *et al*. [78], Brindley *et al*. [79], and Cloos *et al*. [80] reported that MMT clay containing oxidant ions (such as Cu^{2+} ions) become black after adsorption of aniline. Electron paramagnetic resonance (EPR) and infrared (FTIR) data show that copper ions oxidize aniline to produce polymeric species through the formation of radical cations, generating monovalent copper. Soma and Soma [81,82] used resonance Raman spectroscopy (RR) in the study of the oxidation of aromatic compounds (benzene and derivatives) adsorbed on clay, and showed that when vapors of aniline were adsorbed on MMT containing Cu^{2+}, benzidine was formed as a dication. However, when aniline was absorbed on Cu^{2+} or Fe^{3+}-MMT, a polymer formed in the liquid phase. Soma and Soma proposed, by the analysis of the RR spectrum, that the polymer formed was equal to that generated electrochemically (PANI-ES), but the observation of an additional band at 1432 cm^{-1} in the RR spectrum of the polymer-MMT excited at 457.9 nm, led the authors to consider the presence of azo linkages (—N═N—) in the polymer structure. Although the study of the interaction of amines with clay is relatively old, just recently (a little over a decade) amine-clay research moved to trying to produce conducting polymer-clay nanocomposites.

Thus, in 1991, Giannelis *et al*. [83] synthesized PANI intercalated in a synthetic hectorite containing Cu^{2+} ions, the formation of PANI being confirmed by UV-vis-NIR data. In 1992 Chao *et al*. [57] reported the polymerization of PANI in MMT clay galleries. Absoprtion bands were observed at 420 and 800 nm, which are characteristic of the PANI-ES form. Furthermore, the FTIR spectrum of PANI-MMT showed bands at 1568, 1505, 1311, and 1246 cm^{-1} characteristic of the emeraldine salt, but the bands were shifted to higher frequencies in relation to the FTIR spectrum of PANI-ES. According to the authors this displacement is a consequence of geometric restriction imposed on the aromatic rings. In other work, Wu *et al*. [58,59] also obtained PANI-MMT using ammonium persulfate as an oxidizing agent, the electronic spectrum of the composite is very similar to that obtained for PANI in an extended conformation. The formation of PANI-ES was confirmed by the presence of bands at 1489, 1562, and 1311 cm^{-1} in the FTIR spectrum of the material. Later, many authors reported the synthesis of PANI in MMT clay by intercalation of anilinium ions, followed by oxidation with ammonium persulfate [60–70]. In common was the use of the FTIR spectroscopy to confirm the formation of PANI.

Using resonance Raman (RR) spectroscopy it was possible to show that the structure of intercalated PANI is different from the PANI-ES structure [71–75], contrary to previously observed using only FTIR spectroscopy. Figure 8.5 shows the RR spectra of two PANI-MMT samples and PANI-ES, using two exciting wavelengths. The RR spectrum of PANI-MMT prepared by *in situ* polymerization and excited at 632.8 nm is very different from the PANI-ES spectrum. The bands at 984, 1179, 1201, 1264, 1349, 1395, and 1630 cm^{-1} cannot be associated with any form of PANI, strongly indicating the formation of another kind of chromophoric segment in the intercalated PANI chains. This resonance is corroborated by the presence of an electronic absorption at 620–670 nm observed in the intercalated PANI-MMT composites [58,59,71–75]. At 488.0 nm exciting radiation the RR spectrum of PANI-MMT prepared by *in situ* polymerization shows bands at 1195 and 1618 cm^{-1} that can be assigned to reduced benzenoid segments of PANI-ES. In addition, a band at ca. 1449 cm^{-1} was assigned to νN═N of azo segments. This assignment was further proved by extensive study of the adsorption, intercalation, and polymerization of benzidine (4,4′-diaminobiphenyl) in MMT clay [84,85]. Another important result was displayed

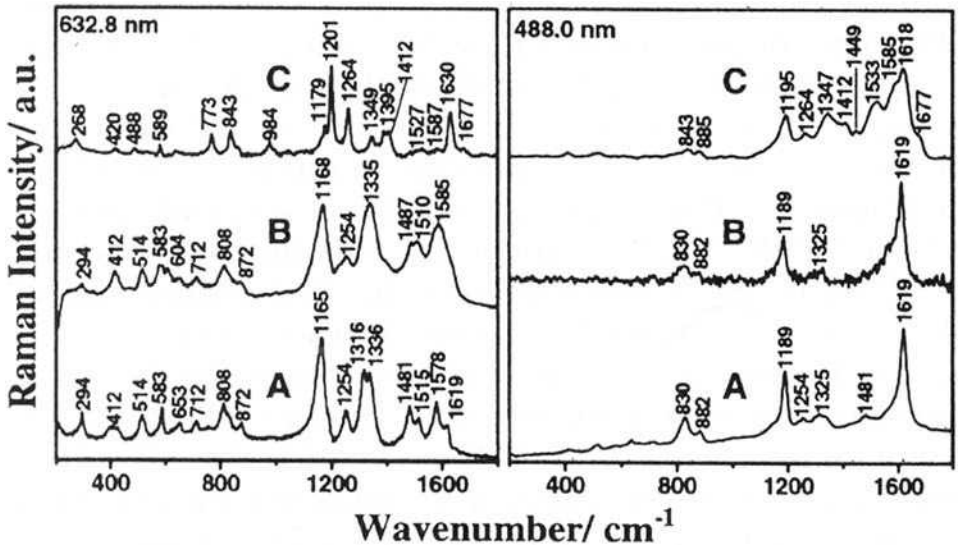

Figure 8.5 *Resonance Raman spectra excited at 632.8 nm and 488.0 nm of powdered samples of: PANI-ES (A), PANI-MMT samples prepared from:* ex situ *polymerization (B) and* in situ *polymerization (C). (Reprinted with permission from Macromolecules, Spectroscopic Characterization of a New Type of Conducting Polymer-Clay Nanocomposite by G. M. do Nascimento, V. R. L. Constantino and M. L. A. Temperini, 35, 20. Copyright (2002) ACS)*

by the RR spectra of PANI-MMT obtained by *ex situ* polymerization (without previous intercalation of anilinium ions), which are very similar to those of PANI-ES for both exciting wavelengths (see Figure 8.5). In addition, the FTIR spectra of PANI-MMT, obtained by *in situ* polymerization, is dominated by clay bands at 1100 cm^{-1}, at 3700–3000 cm^{-1}, and at 1630 cm^{-1}, assigned to νSi-O, adsorbed water, and structural OH clay groups [71,72]. There is no significant difference between the IR bands of the polymers obtained by the two routes and these spectra are similar to the PANI-ES spectrum. Hence, the use of the IR information and the observation of a green color of the PANI-MMT nanocomposites led to a partial view of the structure of intercalated PANI, because only segments similar to those of PANI-ES were observed.

Using several techniques to follow the polymerization of intercalated aniline it was possible to elucidade the structure of the nanostructured PANI chains [71]. The RR spectra obtained at early stages of the polymerization of intercalated anilium ions show the presence of bands of radical cations of PANI-ES (at 1167, 1318/1339, and 1625 cm^{-1}) and dications (at 1481 and 1582 cm^{-1}) and also bands due to benzidine dications at 1211, 1370, 1455, and 1608 cm^{-1}, confirming that head-to-tail and also tail-to-tail couplings between the aniline monomers occur in the clay galleries. In the final stages of the polymerization, the RR spectra obtained at 632.8 nm resembles neither the spectrum of radical cation of PANI-ES nor the spectrum of benzidine dication, indicating that another type of chromophore is also formed. At this point, the use of XANES spectroscopy was

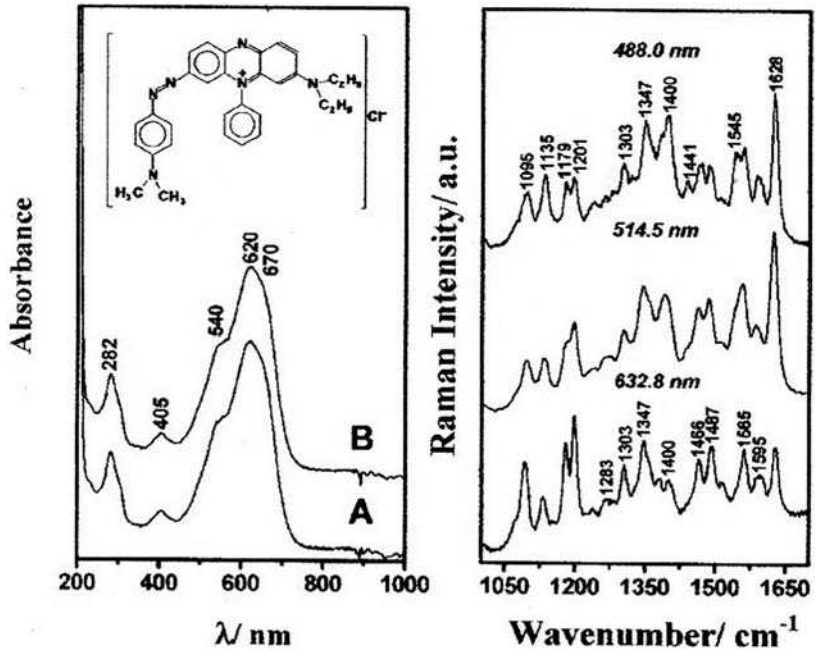

Figure 8.6 *UV-vis-NIR spectra of solutions of Janus Green B azo dye in NMP (A), and aqueous acidic solution (B), and resonance Raman spectra of Janus Green B azo dye in the solid state obtained at the indicated exciting radiations. The dye molecular structure is also shown. (Reprinted with permission from Macromolecules, Aniline Polymerization into Montmorillonite Clay: A Spectroscopic Investigation of the Intercalated Conducting Polymer by G. M. do Nascimento, V. R. L. Constantino, R. Landers and M. L. A. Temperini, 37, 25. Copyright (2004) American Chemical Society)*

very important. Through the analysis of several dyes, with structures possibly present in the structure of PANI-MMT, it was found that the structure of intercalated PANI also has phenazine rings. Taking all these considerations into account, the best standard compound, having an azo group together with phenazine or oxazine-like rings in the structure, which give out vibrational and electronic signatures similar to those of the PANI-MMT nanocomposites was Janus Green B (JGB). Figure 8.6 displays the UV-vis-NIR spectra of JGB in solution and also the RR spectra at different excitations. The bands at 620 and 670 nm are similar to those observed for PANI-MMT. Also, the frequencies and relative intensities of the dye bands at 1179, 1201, 1347, 1400, and 1628 cm^{-1} in the RR spectrum at 632.8 nm exciting radiation (Figure 8.6) are in good agreement with those of PANI-MMT nanocomposites at the same radiation (Figure 8.5). Therefore, this result indicates that a phenazine-type ring is another kind of segment present in the polymeric structure.

The formation of filaments of PANI was also achieved using MCM-41 as a template [86,87]. MCM-41 is a synthetic aluminosilicate, with hexagonal arrays of holes ca. 3.0 nm in size. Nanocomposites of PANI-MCM-41 were synthesized by exposure of MCM-41 containing ions of Cu (II) or Fe (III) to vapors of aniline [88]. The adsorption of aniline

vapors into the dehydrated host containing these metals produces radical cations or oligomers of aniline. But just by putting this material in an aqueous medium containing HCl acid and persulfate ions, PANI is formed. The electronic spectrum of the composite shows typical bands due to polaron transitions (3.4 and 1.6 eV). The encapsulated polymer also showns a fairly broad EPR signal (8–19 G), suggesting a lower doping degree or dipolar interactions with the MCM-41 walls or metal cations inside.

Cyclodextrins (CDs) can also be used for inclusion of monomers and polymers. The α-, β-, γ-, and δ-CDs are made up of six to nine units of glucose, respectively [89,90]. The diameters of CDs range from 0.47 to 083 nm for α- to δ-CDs. Shimomura *et al.* [91,92] reported that many β-CDs may include polymer chains of PANI-EB in solution. The authors report that in the inclusion compound, the PANI chains are completely covered by CD molecules, preventing doping with iodine. The formation of this 'molecular necklace' was confirmed by frequency domain electric birefringence spectroscopy (FEB), which showed that the polymer changes from a coil to an extended conformation after inclusion. Do Nascimento *et al.* [93] also synthesized β-CD and PANI-EB. The preparation of the 'molecular necklace' was confirmed by measures of X-ray diffraction, FTIR spectroscopy, and resonance Raman (RR). Using the RR spectra it was possible to monitor both PANI and the β-CDs, using different exciting radiation, and the doping of the polymer after exposure to vapors of HCl and iodine, could be verified by the appearance of the νC—N radical cation band at ca. 1333 cm^{-1}, characteristic of PANI-ES. The observation of the doping of PANI led Do Nascimento *et al.* [93] to propose that the chains of PANI are not fully covered by the CDs.

8.4.1.2 Nanostructures

One of the first examples of PANI nanofibers/tubes came from aniline polymerization in a medium containing large organic acids [5–8]. These acids form micelles upon which aniline is polymerized and doped. Fiber diameters are observed to be as low as 30–60 nm and are highly influenced by reagent ratios [17–20,94–96]. The FTIR spectra of PANI doped with various organic acids, containing sulfo groups (SO_3H^-), show broad absorbances at about 3430 cm^{-1}, 1560 cm^{-1}, 1480 cm^{-1}, 1130 cm^{-1}, and 800 cm^{-1}, which are related to the PANI-ES structure [95]. UV-vis spectra of all doped PANI samples show two major absorptions around 400 and 800 nm that are attributed to polarons. The position of the polaron absorption peak shifts to a long wavelength when the size of the dopant increases. For example, the polaron absorption for PANI doped with a smaller dopant is located at 800–900 nm. On the other hand, the polaron absorption for PANI doped with a larger dopant is shifted to 1060–1118 nm. The RR spectra (1000 to 1800 cm^{-1}) of PANI doped with β-naphthalenesulfonic acid (β-NSA) fibers with different diameters show similar behavior [19]. The RR spectra of PANI-NSA fibers show bands at 1163 and 1330 cm^{-1} and these can be assigned to βC—H and νC—N of polaronic segments, respectively. Their relative intensities in PANI-NSA spectra increase as the molar ratio of β-NSA/aniline increases. The high relative intensities of bands at 1490 and 1585 cm^{-1} in PANI-NSA spectra indicate a lower protonation degree of PANI-NSA fibers than that of PANI-ES. The PANI-NSA fibers can acquire the emeraldine doped state after treatment with HCl solution. However, SEM images show a loss of fibrous morphology, indicating great morphological instability of the fibers during the doping process.

Further studies have revealed that submitting the PANI-NSA to heat treatment at 200 °C, results in the formation of cross-linking structures, proved by the appearance of characteristic RR bands at 578, 1398, and 1644 cm^{-1}, hence the fibrous morphology is retained after the doping process [20]. In fact, it was observed that the formation of cross-linking structures is a general feature of PANI chains prepared in micellar media and it has been proposed that these structures are responsible for the formation of the nanofiber PANI morphology [96]. The structure of PANI-CSA (CSA is 1*R*-(−)10-camphorsulfonic acid) nanofibers was also investigated by solid-state ^{13}C and ^{15}N nuclear magnetic resonance (NMR) [97]. The results (compared to the unstructured, granular form of PANI) revealed a slight variation in the structural features of the polymer that led to some differences in the chemical environments of the respective nuclei. The presence of two extra-sharp peaks at 96.5 and 179.8 ppm is a distinct feature found exclusively in the nanofiber spectra and the presence of a complete set of sharp NMR peaks is a consequence of the more ordered morphology in the PANI nanofibers.

More recently, uniform nanofibers of pure metallic PANI (30–120 nm diameter, depending on the dopant) have also been prepared by polymerization at an aqueous–organic interface [14,15]. However, it has often been observed that the quality of the products, such as the shape and stability of their dispersions, varies with different synthetic conditions, such as stirring, temperature, and pH, among others. For instance, RR spectra at low wavenumbers (from 200 to 500 cm^{-1}) of PANI nanofibers prepared in different pH conditions show a decrease in the intensities of the bands at 200 and 296 cm^{-1}, and also a shift of the bands from 393–427 cm^{-1} to 422–451 cm^{-1} with an increase in the pH of the synthetic medium. It is possible to correlate the changes in the intensities of the bands with an increase in the torsion angles of $C_{ring}—N—C_{ring}$ segments [98–100], owing to the formation of bipolarons (protonated, spinless units) in the PANI backbone higher than the PANI samples prepared by the conventional route. The nanostructured surface of PANI permits major diffusion of the ions inside the polymeric matrix leading to a more effective protonation of the polymeric chain than PANI prepared in the conventional way, leading to the reduction of crystallinity of PANI, and a decrease in the amount of nanofibers.

8.4.2 Nanostructured Poly(Pyrrole)

8.4.2.1 Nanocomposites

Polypyrrole (PPy) is a promising conducting polymeric material for various electronic applications because of its environmental stability to oxygen and water, high conductivity, and ease of synthesis. Generally, PPys are brittle, insoluble, and infusible, and hence unprocessible. In order to improve these properties, several approaches have been used in the literature with the aim of producing Ppy nanocomposites, preferably using clay as host. One of the fisrt examples of intercalation of PPy in MMT clay was made by the interaction of colloidal nanoparticles of the polymers with exfoliated clay [101]. The FTIR spectra of the PPy/clay composites, showed peaks associated with PPy at 1550 and 1460 cm^{-1}, and in the region of 800–900 cm^{-1}, and clay peaks were observed at 1040, 590, and 480 cm^{-l}. PPy-MMT nanocomposites were also prepared using dodecylbenzenesulfonic acid (DBSA) as both an emulsifier and as a dopant [102,103]. Similarly to Ref. [102], the FTIR spectra of

PPy/clay composites showed bands owing to PPy at 1560 cm^{-1} (2,5-substituted pyrrole), 1050 cm^{-1} (C—H vibration of 2,5-substituted pyrrole), and 920 and 800 cm^{-1} (C—H deformation of 2,5-substituted pyrrole); those of MMT clay were shown at 1040 cm^{-1} (νSi—O), 600 cm^{-1} (νAl—O) [103]. In addition, the electron paramagnetic resonance (EPR) data showed a sharp signal with 1-D characteristics [104], which originates from the weak spin–orbit interaction of the intercalated and well-ordered PPy–DBSA nanolayers between the clay layers. Coulomb interactions between the positively charged polymer backbone of the intercalated PPy–DBSA nanolayers and the negatively charged surface of the clay play an important role in enhancing the thermal stability in the PPy–DBSA/clay samples. It was interesting to find that the peak position of π–π* absorption is 430 nm for free PPy solution and at 421 nm for the PPy-MMT composites. This blue shift is related to the decreasing of the conjugated chain length of PPy into MMT galleries.

High conductive PPy-expanded vermiculite (EVMT, conductivity of 67 S cm^{-1}) clay nanocomposite was prepared using sodium dodecylbenzene sulfate (SDBS) as dopant and surfactant, and $FeCl_3$ as oxidant.[105] The FTIR spectrum of PPy-EVMT nanocomposite showed peaks at 3457 and 1641 cm^{-1} that were attributed to the stretching and bending modes of adsorbed water, respectively. The bands at 990 and 450 cm^{-1} were assigned to νSi—O of EVMT. PPy ring vibrations were located between 800 and 1600 cm^{-1}[106]. The bands at 1300, 1470, and 1551 cm^{-1} were attributed to νC—N, νC—C, νC=C modes, respectively, while the band at 1178 cm^{-1} was assigned to ring breathing stretching [107,108]. Thereby, the characteristic peaks of PPy in the EVMT system showed the intercalation of PPy in the EVMT interlayers.

The effect of iron present in the clay structure, as well as present in the interlayer spaces on the adsorption of pyrrole during its polymerization has been thoroughly investigated [109,110]. It was found that high amounts of structural iron in the clay prevent the formation of intercalated PPy because of the fast spontaneous polymerization of the adsorbed pyrrole. Structural iron located in the tetrahedral sheet (synthetic saponites) disfavors pyrrole adsorption. PPy-clay nanocomposites are easily formed in smectites with none or moderate (0–6%) iron content in the octahedral sheet, but containing a redox ion, such as Fe^{3+}, as an exchangeable cation. Pyrrole also intercalates in the organo clays, but the formation of PPy-organoclay nanocomposites requires further treatment with an oxidizingt agent, such as I_2, to induce its polymerization. Using Mössbauer spectroscopy [110], the influence of iron on the formation of PPy-MMT composites was investigated; it was found that the formation of PPy by the oxidative action of Fe^{3+} is independent of the intercalation of pyrrole.

PPy-MMT nanocomposites have also been prepared using ammonium persulfate as oxidant [111,112]. Similar to the other cases, the FTIR spectrum of PPy-MMT show bands that can be related to both PPy and Clay. Peaks at ca. 1041, 523, and 468 cm^{-1} corresponding to $\nu_{Si\text{-}O\text{-}Si}$, $\nu_{Si\text{-}O}$, and $\delta_{Si\text{-}O}$, respectively, are characteristic of MMT [113]. The bands at ca. 1554, 1468, 1294, and 1189 cm^{-1} have been attributed to the PPy chain [114,115], displaying small shifts in comparison to the bands of pristine PPy. For example, the band at 1454 cm^{-1} in the spectrum of pure PPy occurs at 1442 cm^{-1} for PPy-MMT (1 wt% of MMT) and at 1440 cm^{-1} for PPy-MMT (10 wt% of MMT) nanocomposites. A higher band situated at 3434 cm^{-1} (N—H stretching vibration) in the PPy spectrum is shifted to 3440 and 3446 cm^{-1} for PPy-MMT (1 wt% of MMT) and for PPy-MMT (10 wt% of MMT) nanocomposites, respectively. Thus, the FTIR spectroscopy supplies

evidences of possible interactions between PPy and MMT clay, which were suggested earlier. The UV-vis spectra show that the characteristic π–π^* transition [116] at ca. 467nm of PPy shifts gradually toward the higher wavelength region in the range 550–565 nm as the MMT content increases. This is contrary to the usual blue shifts observed for PPy-MMT clay by other groups [116,103]. Probably, the interfacial interactions of PPy on the intercalated MMT clay surface uncoil the PPy chain, increasing its conjugation length. This interaction therefore causes a red shift in the UV-vis absorption spectra.

The XPS spectrum of PPy-MMT is dominated by the main MMT features O 1s (531 eV), Si 2p (103 eV), and Al 2p (74 eV), a qualitative indication that the nanocomposite surface is MMT-rich. The contributions of the major elements characteristic of PPy, i.e. C and N, increase with PPy loading, and simultaneously those of Si, Al, and O (the major ones in the clay) decrease. PPy is thus gradually loaded at the surface of the nanocomposites as the initial pyrrole concentration increases. However, the surface N/Si ratios 0.04, 0.05, 0.06, and 0.11 determined for PPy mass loadings of 2.8, 10.8, 13.3, and 21.4%, respectively, are lower than those determined for the bulk of the nanocomposites by elemental analysis.

8.4.2.2 Nanostructures

PPy nanofibers and nanotubes have been synthesized by electrochemical and chemical polymerization with a scanning microneedle electrode or by using a microporous membrane or porous alumina as a template [117–123]. Compared to the electrochemical method, *in situ* chemical polymerization is simpler and cheaper for producing large quantities of nanostructural PPy, because it overcomes the limitation of the area of electrode. PPy nanotubes present interesting mechanical and conductivity properties. Cuenot *et al*. [121] found that the elastic modulus strongly increases when the thickness or outer diameter of PPy nanotubes decreases. Martin *et al*. [8,9] found that the conductivity enhances when the diameter of PPy nanotubes decreases, the maximum value of conductivity being over 2.10^3 S cm^{-1}.

Duchet *et al.* [122] used track-etched membranes as templates to prepare PPy nanotubes and nanofibers. From the intensity ratio between a Raman band sensitive to the oxidation state of the polymer (i.e., 1596 cm^{-1}) and a skeletal band (i.e., 1500 cm^{-1}) a qualitative measurement of the conjugation length can be obtained. It was observed the ratio increases as the tube diameter decreases. That means that the polarizability of the system is higher for smaller PPy tubes, or, in other words, that the conjugation length increases. Liu and Wan [124] have also synthesized PPy nanotubes, using β-naphthalenesulfonic acid (β-NSA) as surfactant and dopant. The FTIR spectra of PPy-NSA showed no great differences when the morphology of PPy-NSA was changed. The characteristic bands of PPy at 1538 and 1455 cm^{-1} (pyrrole ring vibration), the =C—H in-plane vibration at 1290, 1100, and 1030 cm^{-1}, and the N-H stretching vibration at 3400 cm^{-1}, were observed in tubular PPy-NSA. All of these were consistent with previous reports [124,125]. These results indicated that the polymer main chain of PPy-NSA with different morphology was identical to that of PPy synthesized by a well-known method.

Coral-like nanowires and nanowire networks of conducting PPy have been synthesized by chemical oxidation polymerization of pyrrole monomers in a dodecyl-benzene sulfonic acid (DBSA) aqueous solution with $FeCl_3$ as oxidant and poly(vinyl-alcohol) (PVA) as

additive [126]. FTIR spectra of PPy with different morphologies showed no obvious difference. The characteristic bands of the PPy samples were consistent with those in [127]: the pyrrole ring fundamental vibration at 1544 and 1457 cm^{-1}, the =C—H in-plane vibration at 1303 and 1040 cm^{-1}, and the C—N stretching vibration at 1175 cm^{-1}. The results indicate that the molecular structure of the PPy chain is identical to that of PPy synthesized by a common method.

Nanostructured PPy has also been obtained with bowl-, cup- and bottle-like morphologies; these were generated electrochemically by direct oxidation of pyrrole in an aqueous solution of camphorsulfonic acid (HCSA) [128]. Well-ordered microstructures were found to stand upright on the working electrode surface in a high density. Raman spectra of the PPy structures excited at 633 nm showed strong bands at ca. 1370 and 1085 cm^{-1} which were attributed to the ring stretching and the N–H in-plane deformation of the oxidized (doped) species, respectively [129]. The Raman band at ca. 1600 cm^{-1} represent the backbone stretching mode of C—C bonds. The FTIR spectra of the PPy microstructures display the bands commonly assigned to PPy in addition to the dopant bands at 1035 (SO_3^- group), 1735 (carbonyl group), 2800 (CH_3 group), and 2900 cm^{-1} (CH_2 group). In the FTIR spectrum of dedoped PPy bands of the carboxyl group at around 1700 cm^{-1} were not observed, indicating that the polymer is not overoxidized in the growth process.

8.4.3 Nanostructured Poly(Thiophenes)

8.4.3.1 Nanocomposites

Poly(thiophenes) (PThs) have attracted significant research interest in the last decade because they can be solubilized by appropriate substitution by an alkyl [130] or alkoxy group [131,132], and also, unlike the majority of conjugated polymers, they retain their electroactivity upon ring substitution. In the neutral (undoped) state they exhibit extremely interesting optical properties, such as, for example, strong electroluminescence. Similar to those observed above for PANI and PPy, the first examples of nanostructured PTh came from intercalation in layered materials. Structurally better-defined PTh chains, with a minimal degree of cross-linking and thus improved charge-transport properties, were obtained in V_2O_5 galleries by M. G. Kanatzidis *et al*. [133]. FTIR spectroscopy clearly showed the presence of PTh with no evidence of free 2,2′-bithiophene (the characteristic intense peaks at 823 and 809 cm^{-1} were absent). EPR spectra (recorded at 273 and 77 K) showed a broad signal observed at g∼1.963, which arises from interacting V^{4+} centers, formed by reduction of the V^{5+} sites. The typical signal observed from PTh was absent, suggesting the presence of antiferromagnetic exchange between the unpaired density on the polymer backbone and that in the V_2O_5. PTh displays an EPR signal only after dissolution of the host. These data show that there is no phase separation between the PTh and the inorganic host. The polymerization of thiophene was also carried out in the galleries of MMT clay [134]. The FTIR data confirm polymerization of the monomer in the MMT galleries due to the appearance of peaks at 469, 525, 695, 797, and 1046 cm^{-1} in the FTIR spectrum of the composite.

Nanocomposites consisting of a TiO_2 core with a grain size of 25–250 nm and a PTh shell between 1 and 2 nm in thickness have been produced [135]. The presence of two

sulfur peaks (S 2p3/2) were found, at 163.8 and 165.2 eV in the XPS spectra of composite, and were assigned to neutral and oxidized thiophene units in the polymer chain, respectively [136]. In the investigated example, 20% of the thiophene units were in the oxidized form, meaning that, on average, every fifth PTh unit was oxidized. Q.-T. Vu *et al*. [137] also prepared PTh/TiO_2 nanocomposites composed of nanoparticles with a TiO_2 core and a thin PTh shell (2–3 nm). The chemical structure of the composite was investigated by Raman spectroscopy. In the oxidized state (black color), the Raman peak at 1420 cm^{-1} was attributed to the C_α═C_β ring stretching of quinoid units (radical cations). On the other hand, in the reduced state this peak disappeared and a new peak at 1455 cm^{-1} has arose, attributed to the C_α═C_β ring stretching of the neutral PTh (red color) [138]. The bipolaron band, proposed to be at 1400 cm^{-1} in the oxidized state was not observed, supporting the view that the oxidized PTh chains have mainly radical cations. The doping level measured by XPS was analogous to the PTh/TiO_2 composite (20%) shown in Ref. [135]. Nanostructured PThs around nanoparticles of gold have also been investigated [139]. The UV-vis spectrum of PTh-stabilized nanoparticles showed a main absorption band at 450 nm that was attributed to the absorption of free PTh in solution [140]. The presence of a broad absorption from 500 to 600 nm in the UV-vis spectrum of PTh stabilized nanoparticles was due to the long-range order of the PTh caused by self-assembly of polymers on nanoparticles, and there was also a peak from the gold surface plasmon resonance observed around 530 nm.

PTh/single-wall carbon nanotubes (SWNTs) nanocomposites have been prepared [141,142]. The FTIR spectrum of nanocomposites is nearly identical to the IR spectrum of the free PTh in the range 600–3200 cm^{-1}. The IR spectrum of PTh has several low-intensity peaks in the range 2800–3100 cm^{-1} that can be attributed to the aromatic νC—H [143]. The peak at 786 cm^{-1} is usually ascribed to the βC—H out-of-plane, whereas other peaks in this region are attributed to the ring stretching and C—H in-plane deformation modes [128,144]. The Raman spectra for the SWNT–PTh composites show bands that can be related to free PTh and pristine SWNTs. The G band of SWNTs is observed at 1581 cm^{-1} and the radial-breathing modes at 163 and 177 cm^{-1}[145]. Peaks at 1451, 1044, and 697 cm^{-1}, are related to the PTh chains, which are assigned to νC═C, νC—C plus a C—H wagging component, and C—S—C ring deformation, respectively [146,147]. The UV-vis spectra of SWNT–PTh composites exhibit a broadening and a red-shifting of the characteristic polaron (π–π*-type) band of PTh at approximately 441 nm [148], revealing some interactions between the quinoid rings of PTh and the carbonic surface of the SWNTs. The S-2p XPS spectrum of the SWNT–PTh can be deconvoluted into at least two spin-orbit-split doublet (S-2p3/2 and S-2p1/2) peaks at approximately 163.6 and 163.7 eV, respectively, which are attributed to the neutral sulfur atoms [149]. This means that the chemical environment of the S element, in pure PTh and SWNT-PTh, is almost identical, supporting the idea that the SWNTs serve merely as templates in the formation of a coaxial nanostructure for the composites.

8.4.3.2 Nanostructures

Poly(terthiophene) and poly(3,4-ethylenedioxythiophene) (PEDOT) with fibrillar (50–100 nm) morphologies have been achieved by chemical polymerization in a biphasic

ionic liquid/water system [150]. The formation of the polymers was confirmed by UV-vis, Raman and other techniques, which suggested that the physical properties of these materials are similar to those of the bulk polymer material. For instance, the UV-vis spectrum of the poly(terthiophene) shows significant absorption over the range 365–600 nm, but only a weak bipolaron band at 400–600 nm. This spectrum indicates the presence of predominantly short-chained or undoped polymer, which is consistent with the suggested difficulties in forming long-chain poly(terthiophene) [151]. Raman analysis of the poly(terthiophene) is consistent with the formation of the polymer, with bands assigned to antisymmetric νC=C (1512 cm^{-1}), symmetric νC=C (1451 cm^{-1}), inter-ring νC—C (1220 cm^{-1}), C—H in-plane bending (1049 cm^{-1}), and inter-ring νC—C (1179 and 1154 cm^{-1}). XPS analysis of poly(terthiophene) samples synthesized in this way indicated an average doping level of ca. 0.27 charges per terthiophene unit for the majority (ca. 75%) of the dopant anions. PEDOT displays a small absorption band at 600 nm, which corresponds to the π–π* transition [152], plus a strong, broad free-carrier tail, indicating the presence of delocalized charges on the polymer chains. The intensity at low wavelengths may be due to the presence of some ionic liquid, either incorporated into or coating the polymer, which absorbs at wavelengths below 400 nm. The Raman spectrum is typical of PEDOT, dominated by the strong symmetric νC=C vibration at 1426 cm^{-1}, whose position indicates significant doping, and a weaker νC_β—C_β band at 1364 cm^{-1} [152]. PEDOT nanofibers have also been obtained using liquid-crystal templating [153]. The UV-vis absorption spectrum shows an absorption at 520 nm, confirming the formation of PEDOT. At the same time, an absorption at 520 nm as a function of polarization angle was measured, revealing a sinusoidal variation in absorption with a period of 180° and thus confirming the the uniaxial orientation of the polymer.

NEXAFS spectroscopy has also been employed to elucidate the conformation of poly(3-hexylthiophene) (P3HT) chains in nanowires [154]. Figure 8.7 shows a series of NEXAFS spectra obtained at two different incident angles, 90 and 20°. The spectra are dominated by four resonances, originating from the 1s states to C=C π* (285.5 eV), C—H/Rydberg (288.1 eV), C—C σ* (293.5 eV), and C—C σ* (303.7 eV) orbitals [155,156]. The intensities of the 285.5 and 288.1 eV components at normal X-ray incidence ($\theta = 90°$) are stronger than those obtained at grazing incidence ($\theta = 20°$). The two other transitions show the opposite polarization dependence with changing incident angle. These results demonstrate that the side chains in the surface layer are oriented almost perpendicular to the surface [157,158], in which the CH_3 groups are exposed at the surface. Moreover, the backbone (thienyl group) chains in P3HT 1-D nanowires are oriented parallel to the insulator substrate, demonstrating the opposite polarization dependence with changing incident angle for transitions to C=C π* orbitals and C=C σ* orbitals.

Thin films of poly(3-hexylthiophene-2,5-diyl) and poly(3-octylthiophene-2,5-diyl) mixed with two electron-accepting polyquinolines [159] show quenching of the steady-state photoluminescence and a shortening of the fluorescence lifetime of the polyquinolines, suggesting photoinduced electron transfer from polythiophene to polyquinoline at the polyquinoline/polythiophene interface. A new, weak and red-shifted emission band centered at 630 nm and reduced lifetimes show the formation of intermolecular exciplexes at the polyquinoline/polythiophene interface. Exciton diffusion lengths in the polyquinolines have been estimated to be 17–22 nm.

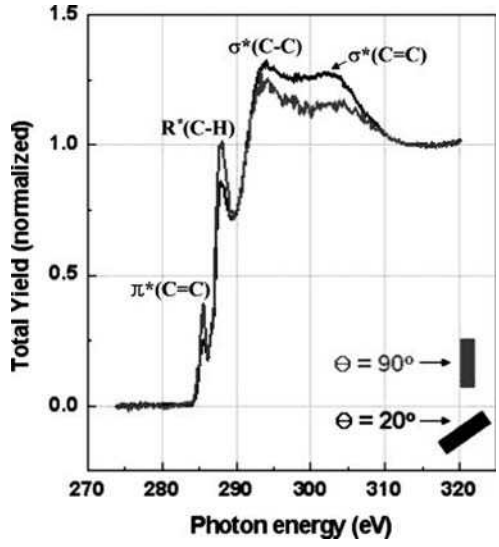

Figure 8.7 *NEXAFS spectra of the C 1s edge of P3HT 1-D nanowires deposited on an insulator substrate recorded for different angles of incidence (θ) of incoming photons. (Reprinted with permission from Journal of Physical Chemistry B., Controlled One-Dimensional Nanostructures in Poly(3-hexylthiophene) Thin Film for High-Performance Organic Field-Effect Transistors by D. H. Kim, Y. Jang, Y.D. Park and K. Cho, 110, 32. Copyright (2006) American Chemical Society)*

8.4.4 Nanostructured Poly(Acetylene) and Poly(Diacetylene) and their Derivates

8.4.4.1 Poly(acetylene) Nanocomposites

The best-known member within the family of linear polymers is poly(acetylene) (PA) (denoted $(CH)_n$). Its properties are highly dependent on the synthetic conditions and the post-synthesis treatment. Although PA exhibits high electrical conductivities in the doped state, its utility as a conducting polymer is greatly limited by its instability in air. PA has a dimerized structure, as a result of Peierls instability with two carbon atoms in the repeat unit, $(-CH{=}CH)_n$. In recent years, several groups have reported the polymerization of acetylene in zeolites in an attempt to form well-oriented, isolated chains [160–162]. The included PA may be very useful as a model for understanding the physical properties of conducting polymers. However, these first studies only produced oligomeric products inside the zeolite cavities. Nowadays, by using the layer-by-layer technique, ordered multilayer nanocomposites have been prepared by electrostatic assembly between exfoliated aluminosilicate (saponite) nanoplatelets (averaging from 170 to 30 nm) and substituted ionic polyacetylenes, poly(*N*-octadodecyl-2-ethynylpyridinium bromide, (PEPy-C18) [163].

Polarized absorption spectroscopy was used to assess the orientation of PEPy-C18 polymer molecules on ordered saponite layers. Figure 8.8 shows the polarized absorption spectra of PEPy-C18/saponite 32-bilayer films. The relatively large difference in optical

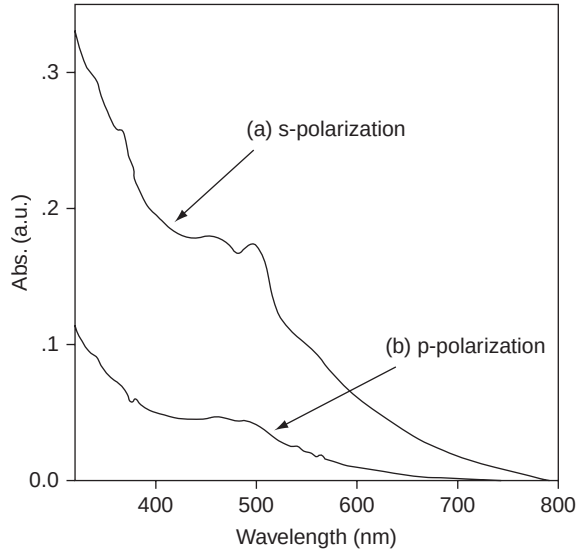

Figure 8.8 *Polarized absorption spectra of PEPy-C18/saponite 32-bilayer films obtained by irradiating: (a) s-polarized light and (b) p-polarized light (incidence angle $\theta = 80°$). (Reprinted with permission from Chemistry of Materials, Ordered Multilayer Nanocomposites Prepared by Electrostatic Layer-by-Layer Assembly between Aluminosilicate Nanoplatelets and Susbtituted Ionic Polyacetylenes by D. W. Kim, A. Blumstein, J. Kumar et al., 14, 9. Copyright (2002) ACS)*

absorption with the direction of polarization of the incident light reveals the molecular orientation of the polymer chains. The absorption peaks at 471 and 502 nm are much more intense when observed in s-polarized light than in p-polarized light. This suggests that the polymer chains are oriented parallel to the plane of the film [164]. Similar results were obtained with other ionic poly(acetylene), poly(2-ethynylpyridine) [165].

The linear UV-vis absorption spectra of multilayer films show red-shifted peaks at 471 and 502 nm, when compared to the 'free' polymer, which was correlated with an increase in the effective conjugation length or an increase in the π–π contact (π-stacking) between the double bonds of neighboring conjugated polymer chains as a result of chain orientation [166]. The same group also prepared nanocomposite films consisting of amphiphilic ionic PAs, poly(*N*-octadecyl-2-ethynylpyridinium bromide) (P2EPy-C18), and layered aluminosilicates (saponite) [167]. UV-vis spectra of the nanocomposites indicate that the maximum absorbance of the polymers increased linearly with deposition cycles. UV-vis absorption spectroscopy of the (P2EPy-R/saponite) nanocomposite films showed that the absorption maximum of P2EPy-R at 450 nm was red-shifted to 471 and 502 nm as the alkyl chain length increased. This indicates that the polyacetylenes tend to be more ordered with increasing alkyl side chains, resulting in increased π–π interaction of the conjugated polymer chains on the flat surface of the aluminosilicate nanoplates.

Another PA derivative, poly(2-ethynylpyridine) (P2Epy), has also been intercalated into MMT clay [168]. Studies on the extracted polymer by FTIR and UV-vis absorption

spectroscopies provide some useful information concerning the inserted polymer, such as, for example, an increase in conjugation with adsorption yield (red shift of the absorption maximum at 440 and 500 nm) or a clear evidence for the absence of the triple bond (disappearance of $\equiv$C—H and —C$\equiv$C— stretching bands at 3290 and 2110 cm^{-1}, respectively) after polymerization [169,170]. The solid-state NMR data show that at low adsorption yield the polymers are more tightly bound to the MMT surface, and as the adsorption yield increases, the fraction of loosely bound polymer increases. The solid-state NMR chemical shifts together with FTIR data can be used as an indicator of the extension of protonation in the *in situ* polymerized P2EPy/MMT nanocomposites. The NMR spectral features of intercalated P2EPy-bulk polymers appear to be similar to the *in situ* polymerized sample, and the positive charge on the nitrogen of the protonated P2EPy-bulk appears to be partially neutralized by interaction with the negative charge on the surface of the MMT. The polymer extracted from the nanocomposite P2EPy/MMT complex is in the uncharged state. It displays similar NMR spectral features to that of a synthesized bulk polymer in the deprotonated state. The solid-state NMR spectrum of the remaining residual nanocomposite (after the extraction process) shows the presence of polymer bound to the MMT surface. The features of this spectrum are similar to that of *in situ* polymerized nanocomposite with a low polymer yield.

8.4.4.2 Nanostructured Poly(acetylene)

Recently [171], using a novel polymerization method, it has been possible to produce helical PA film with a spiral morphology, in which bundles consisting of nanofibrils with diameters $<$100 nm are twisted and concentrically curled. These films can be further transformed after carbonization into carbon nanofibers. It has been considered difficult to prepare a freestanding carbon thin film through the carbonization of an organic polymer film. This is because carbonization at high temperature causes thermal decomposition and volatilization of hydrocarbon gases, destroying the morphology of the original film. However, it was found that helical PA films doped with iodine can retain their morphology after carbonization. The Raman spectrum of the carbon film shows a strong, broad peak at 1350 cm^{-1} attributed to the disordered structure (D-band), together with a comparable peak at 1580 cm^{-1} corresponding to the structure of the sp^2 hexagonal carbon-bond network (G-band). It is apparent that the iodine doping prevents the PA film from thermally decomposing at high temperature. According to the structural model of the iodine-doped PA film, polyiodide ions such as I_3^- and I_5^- are situated between the PA chains, forming a charge-transfer complex. [171]

8.4.4.3 Poly(diacetylene) Nanocomposites and Nanostructures

Among the conjugated polymers reported here, poly(diacetylenes) (PDAs) are unique in several regards [172–175]. First, unlike most of other conjugated polymers, PDAs are prepared from UV or γ-irradiation of supramolecularly assembled crystalline or semicrystalline diacetylene (DA) monomers. PDA materials in the forms of vesicles, liposomes, films, and nanocomposites have been synthesized, and their chromatic responses to various stimuli, including temperature, pH, ions, solvent, stress, and ligand interactions, have been demonstrated. However, most of the chromatic responses are irreversible, limiting their application in colorimetric sensing. PDAs undergo color (typically

blue-to-red) and fluorescence (non-to-red) transitions in response to various environmental perturbations. The colorimetric and fluorogenic properties of PDAs have attracted great attention in chemosensors [175]. Owing to their self-assembly properties, PDAs have been used as building blocks in the formation of nanostructures and nanocomposites; for this reason, all cases presented here are discussed in one section.

PDA/Silica nanocomposites with tunable molecular architecture provide nanocomposites with adjustable thermochromatic properties [176]. The UV-vis absorption spectra of the nanocomposites, subjected to a heating–cooling cycle, show the main excitonic peak of the blue form at 640 nm with a vibronic maximum at 590 nm, whereas for the red form, the excitonic peak appears at 540 nm associated with a broad vibronic peak at 490 nm. Once heated from room temperature to 90 °C, all of the nanocomposites demonstrate a chromatic transition from blue to red. It is widely accepted that this color transition is caused by a reduction in the effective conjugation length resulting from distortions imposed by the backbone conformation. The distortions can be induced by fluctuations within the side-chain layers, activated by external stimuli [177]. In fact, all successful colorimetric reversibilities reported so far, are based on enhanced hydrogen bonding among the head-groups of the side chains [178]. In contrast, the most recent PDA assemblies have been produced by covalent bonds formed through the hydrolysis and condensation reactions of the ethoxysilane groups. The complete thermochromatic reversibility suggests that the stable covalent interactions between the PDA side chains and the inorganic silica network help restore the original chain confirmations upon removal of the thermal stimuli.

Periodic mesoporous organosilica (PMO), with a hybrid pore wall, was prepared embedded with PDA chains [179]. Such a hierarchical molecular design endows the PDA-PMO with thermochromatic reversibility, mechanical robustness, enhanced thermal stability, and rapid chemochromatic response. The reversible chromatic responses to external stimuli were demonstrated by subjecting PDA-PMO to thermal cycles between 20 and 103 °C. PDA-PMO rapidly changes its color reversibly between blue and red, the chromatic response can be quantitatively defined using the colorimetric response (CR), which is defined as the percentage of blue-to-red transition calculated from the corresponding UV-vis spectra [180]. Consistent chromatic responses (14% at 103 °C and 0.2 % at 20 °C) are achieved over 15 thermal cycles. While the high CR value at high temperatures may provide fine thermochromatic sensing ability, the near-zero CR values at low temperatures imply a complete red-to-blue reversibility and a potentially reusable device.

8.5 Concluding Remarks

The studies of the electronic and vibrational features of the nanostructured conducting polymers using several spectroscopies has been decisive in the determination of their structures and the types of interactions between the polymeric chains and the hosts. Polymerization inside the pores of a rigid host has been commonly employed to acquire nanostructured conducting polymer chains; shifts in the vibrational frequencies and changes in the UV-vis-NIR spectra of the confined conducting polymer are generally observed. Hence, there is a clear indication of the electrostatic interactions between the nanostructured chains and the walls of the hosts, and also the restricted geometry imposed

on the aromatic rings. The force of these interactions is responsible for the increases in thermal stability, conjugation length (as observed for poly(acetylene) derivates), and chromatic reversibity in the case of poly(diacetylene). Another peculiar effect is the formation of a polymeric backbone with a distinct structure from that observed in the free polymer, as observed for poly(aniline). Conducting polymers with nanofiber and nanotube structures have been largely obtained without the use of rigid hosts. However, the morphology is more susceptible to synthetic conditions (such as pH) and also post-synthesis procedures. It has been observed through changes in the vibrational spectra that the conjugation of the chains increases with reduction of the diameter of the nanofibers/nanotubes.

Acknowledgements

First, the authors would like to thanks the editor for the invitation to write this chapter. In addition, the authors would like to thank the LNLS and Mr. Paulo de Tarso for XANES measurements at the SGM beam line.

References

[1] R. Liepins and C.C. Ku, *Electrical Properties of Polymers*, C. H. Verlag, Munich, 1987.
[2] H. Shirakawa and S. Ikeda, Cyclotrimerization of acetylene by the tris (acetylacetonato)titanium(III)-diethylaluminum chloride system, *J. Poylm. Sci. Polym. Chem.*, **12**, 929–937 (1974).
[3] C.K. Chiang, C.R. Fincher Jr, Y.W. Park, A.J. Heeger, H. Shirakawa, E.J. Louis, and A.G. MacDiarmid, Electrical conductivity in doped polyacetylene, *Phys. Rev. Lett.*, **39**, 1098–1101 (1977).
[4] H. Shirakawa, The discovery of polyacetylene film: the dawning of an era of conducting polymers (Nobel Lecture), *Angew. Chem. Int. Ed.*, **40**, 2574–2580 (2001).
[5] A.G. MacDiarmid, 'Synthetic Metals': a novel role for organic polymers (Nobel Lecture), *Angew. Chem. Int. Ed.*, **40**, 2581–2590 (2001).
[6] A.J. Heeger, Semiconducting and Metallic Polymers: the fourth generation of polymeric materials (Nobel Lecture), *Angew. Chem. Int. Ed.*, **40**, 2591–2611 (2001).
[7] G.A. Ozin, Nanochemistry – synthesis in diminishing dimensions, *Adv. Mater.*, **4**, 612–649 (1992).
[8] C.R. Martin, Template synthesis of electronically conductive polymer nanostructures, *Acc. Chem. Res.*, **28**, 61–68 (1995).
[9] C.R. Martin, Nanomaterials – A membrane-based synthetic approach, *Science*, **266**, 1961–1966 (1994).
[10] T. Bein, Conjugated and conducting nanostructures in zeolites. In *Recent Advances and New Horizons in Zeolite Science and Technology Studies in Surfaces Science and Catalysis*, ed. H. Chan, and S.-E. Woo, Elsevier Science, Amsterdam, 1996.
[11] T. Bein, Zeolite inclusion chemistry. In *Supramolecular Architecture, Synthetic Control in Thin Films and Solids*, ed. T. Bein, ACS Symposium Series, ACS, Washington-DC, 1992.
[12] E. Ruiz-Hitzky and P. Aranda, Confinement of conductive polymers into inorganic solids, *Anales de Química Int. Ed.*, **93**, 197–212 (1997).
[13] D.J. Cardin, Encapsulated conducting polymers, *Adv. Mater.*, **8**, 553–563 (2002).
[14] J. Huang and R.B. Kaner, Nanofiber Formation in the chemical polymerization of aniline: a mechanistic study, *Angew. Chem., Int. Ed.*, **43**, 5817–5821 (2004).

[15] J. Huang and R.B. Kaner, A general chemical route to polyaniline nanofibers, *J. Am. Chem. Soc.*, **126**, 851–855 (2004).
[16] Z. Zhang, Z. Wei, and M. Wan, Nanostructures of polyaniline doped with inorganic acids, *Macromolecules*, **35**, 5937–5942 (2002).
[17] H. Qiu, M. Wan, B. Matthews, and L. Dai, Conducting polyaniline nanotubes by template-free polymerization, *Macromolecules*, **34**, 675–677 (2001).
[18] Z. Wei, Z. Zhang, and M. Wan, Formation mechanism of self-assembled polyaniline micro/nanotubes, *Langmuir*, **18**, 917–921 (2002).
[19] G.M. Do Nascimento, C.H.B. Silva, and M.L.A. Temperini, Electronic structure and doping behavior of PANI-NSA nanofibers investigated by resonance Raman spectroscopy, *Macromol. Rapid Commun.* **27**, 255–259 (2006).
[20] G.M. Do Nascimento, C.H.B. Silva, and M.L.A. Temperini, Spectroscopic characterization of the structural changes of polyaniline nanofibers after heating, *Polym. Degrad. Stab.*, **92**, 1–7 (2007).
[21] H. Gao, T. Jiang, B. Han, Y. Wang, J. Du, Z. Liu, and J. Zhang, Aqueous/ionic liquid interfacial polymerization for preparing polyaniline nanoparticles, *Polymer*, **45**, 3017–3019 (2004).
[22] F. Rodrigues, G.M. Do Nascimento, and P.S. Santos, Dissolution and doping of polyaniline emeraldine base in imidazolium ionic liquids investigated by spectroscopic techniques, *Macromol. Rapid Commun.*, **28**, 666–669 (2007).
[23] X. Zhang, W.J. Goux, and S.K. Manohar, Synthesis of Polyaniline Nanofibers by 'Nanofiber Seeding', *J. Am. Chem. Soc.*, **126**, 4502–4503 (2004).
[24] X. Zhang and S.K. Manohar, Polyaniline nanofibers: chemical synthesis using surfactants, *Chem. Commun.*, **4**, 2360–2361 (2004).
[25] D.N. Batchelder, Resonance Raman spectroscopy of conjugated polymers. In *Optical Techniques to Characterize Polymer Systems*, ed. H. Brässler, Elsevier, Amsterdam, 1987.
[26] D.N. Batchelder and D. Bloor, Resonance Raman spectroscopy of conjugated macromolecules. In *Advances in Infrared and Raman Spectroscopy*, Wiley-Heyden, London, 1984.
[27] J.H. Clark and T.J. Dines, Resonance Raman spectroscopy, and its application to inorganic chemistry. New analytical methods, *Angew. Chem. Int. Ed. Engl.*, **25**, 131–158 (1986).
[28] J.L. Brédas and G.B. Street, Polarons, bipolarons, and solitons in conducting polymers, *Acc. Chem. Res.*, **18**, 309–315 (1985).
[29] J.L. Brédas, R.R. Chance, and R. Silbey, Comparative theoretical study of the doping of conjugated polymers: Polarons in polyacetylene and polyparaphenylene, *Phys. Rev. B.: Condens. Matter.*, **26**, 5843–5854 (1982).
[30] J.L. Brédas, J.C. Scott, K. Yakushi, and G.B. Street, Polarons and bipolarons in polypyrrole: evolution of the band structure and optical spectrum upon doping, *Phys. Rev. B.: Condens. Matter.*, **30**, 1023–1025 (1984).
[31] J. Libert, J. Cornil, D.A. Dos Santos, and J.L. Brédas, From neutral oligoanilines to polyanilines: a theoretical investigation of the chain-length dependence of the electronic and optical properties, *Phys. Rev. B*, **56**, 8638–8650 (1997).
[32] W.S. Huang and A.G. MacDiarmid, Optical properties of polyaniline, *Polymer*, **34**, 1833–1845 (1993).
[33] A.G. MacDiarmid and A.J. Epstein, The concept of secondary doping as applied to polyaniline, *Synth. Met.*, **65**, 103–116 (1994).
[34] N. Gospodinova and L. Terlemezyan, Conducting polymers prepared by oxidative polymerization: polyaniline, *Prog. Polym. Sci.*, **23**, 1443–1484 (1998).
[35] G. Čirič-Marjanovič, N.V. Blinova, M. Trchová, J. Stejskal, and P. Holler. Chemical oxidative polymerization of safranines, *J. Phys. Chem. B.*, **111**, 2188–2199 (2007).
[36] G. Čirič-Marjanovič, M. Trchová, and J. Stejskal, MNDO-PM3 study of the early stages of the chemical oxidative polymerization of aniline, *Collect. Czech. Chem. Commun.*, **71**, 1407–1426 (2006).
[37] G. Margaritondo, *Introduction to Synchrotron Radiation*, Oxford University Press, New York, 1988.
[38] D.H. Bilderback, P. Elleaume, and E. Weckert, Review of third and next generation synchrotron light sources, *J. Phys. B: At., Mol. Opt.Phys.*, **38**, S773–S798 (2005).

[39] S.M. Heald, Design of an EXAFS experiment. In *X-ray Absorption*, ed. D.C. Koningsberger and R. Prins, John Wiley & Sons, Inc., New York, 1988.
[40] K.L. Tan, B.T.G. Tan, E.T. Kang, and K.G. Neoh, X-ray photoelectron-spectroscopy studies of the chemical strutucture of polyaniline, *Phys. Rev. B*, **39**, 8070–8073 (1989).
[41] E.T. Kang, K.G. Neoh, K.L. Tan, and B.T.G. Tan, Structural studies of halogen-substituted polyanilines by X-ray photoelectron spectroscopy, *Synth. Met.*, **35**, 345–355 (1990).
[42] P. Snauwaert, R. Lazzaroni, J. Riga, J.J. Verbist, and D. Gonbeau, A photoelectron spectroscopic study of the electrochemical processes in polyaniline, *J. Chem. Phys.*, **92**, 2187–2193 (1990).
[43] S.N. Kumar, F. Gaillard, G. Bouyssoux, and A. Sartre, High-resolution XPS studies of electrochemically synthesized conducting polyaniline films, *Synth. Met.*, **36**, 111–127 (1990).
[44] X. Demaret, G. Cristallo, P. Snauwaert, J, Riga, and J.J. Verbist, XPS study of polyaniline treated in pH decreasing solutions: Charges distribution along polymer chains, *Synth. Met.*, **55**, 1051–1056 (1993).
[45] P. Enzel and T. Bein Inclusion of polyanlline filaments in zeolite molecular sieves, *J. Phys. Chem.*, **93**, 6270–6272 (1989).
[46] N.S. Sariciftci, M. Bartonek, H. Kuzmany, H. Neugebauer, and A. Neckel, Analysis of various doping mechanisms in polyaniline by optical, FTIR and Raman spectroscopy, *Synth. Mer.*, **29**, 193–202 (1989).
[47] Y. Furukawa, F. Ueda, Y. Hydo, I. Harada, T. Nakajima, and T. Kawagoe, Vibrational spectra and structure of polyaniline, *Macromolecules*, **21**, 1297–1305 (1988).
[48] A.J.G. Zarbin, M.A. De Paoli, and O.L. Alves, Nanocomposites glass/conductive polymers, *Synth. Met.*, **99**, 227–235 (1999).
[49] R. Bissessur, D.C. DeGroot, J.L. Schindler, C.R. Kannewurf, and M.G. Kanatzidis, Inclusion of poly(aniline) into MoO_3, *J. Chem. Soc.: Chem. Comumm.*, 687–689 (1993).
[50] C.-G. Wu, D.C. DeGroot, H.O. Marcy, J.L. Schindler, C.R. Kannewurf, Y.-J. Liu, W. Hirpo, and M.G. Kanatzidis, Redox intercalative polymerization of aniline in V_2O_5 xerogel. The postintercalative intralamellar polymer growth in polyaniline/metal oxide nanocomposites is facilitated by molecular oxygen, *Chem. Mater.*, **8**, 1992–2004 (1996).
[51] T. Chang, S. Ho, and K. Chao, Polyaniline intercalated into zeolites, zirconium phosphate and zirconium arsenate, *J. Phys. Org. Chem.*, **7**, 371–376 (1994).
[52] M.G. Kanatzidis and Y. Liu, Topotactic polymerization of aniline in layered uranyl phosphate, *Inorg. Chem.*, **32**, 2989–2991 (1993).
[53] C.-G. Wu, D.C. DeGroot, H.O. Marcy, J.L. Schindler, C.R. Kannewurf, T. Bakas, V. Papaefthymiou, W. Hirpo, J.P. Yesinowski, Y.-J. Liu, and M.G. Kanatzidis, Reaction of aniline with FeOCl. Formation and ordering of conducting polyaniline in a crystalline layered host, *J. Am. Chem. Soc.*, **117**, 9229–9242 (1995).
[54] E.M. Moujahid, M. Dubois, J.-P. Besse, and F. Leroux, Role of atmospheric oxygen for the polymerization of interleaved aniline sulfonic acid in LDH, *Chem. Mater.*, **14**, 3799–3807 (2002).
[55] F. Wypych, N. Seefeld, and I. Denicoló, Preparation of nanocomposites based on the encapsulation of conducting polymers into 2H-MoS_2 and 1T-TiS_2, *Quimica Nova*, **20**, 356–360 (1997).
[56] N.S.P. Bhuvanesh and J. Gopalakrishnan, Polymerization of aniline in layered $HMMoO_6{\cdot}H_2O$ (M = Nb, Ta), *Mater. Sci. Eng. B*, **53**, 267–271 (1998).
[57] Te-C. Chang, S.-Y. Ho, and K.-J. Chao, Intercalation of polyaniline in montmorillonite and zeolite, *J. Chin. Chem. Soc.*, **39**, 209–212 (1992).
[58] Q. Wu, Z. Xue, Z. Qi, and F. Wang, Synthesis and characterization of PAn/clay nanocomposite with extended chain conformation of polyaniline, *Polymer*, **41**, 2029–2032 (2000).
[59] Q. Wu, Z. Xue, Z. Qi, and F. Wang, Synthesis and characterization of PAN/clay hybrid with extended chain conformation of polyaniline, *Acta Polym. Sin.*, **10**, 551–556 (1999).
[60] M. Biswas and S.S. Ray, Water-dispersible nanocomposites of polyaniline and montmorillonite, *J. Appl. Polym. Sci.*, **77**, 2948–2956 (2000).
[61] J.-M. Yeh, S.-J. Liou, C.-Y. Lai, and P.-C.W -Y. Tsai, Enhancement of corrosion protection effect in polyaniline via the formation of polyaniline-clay nanocomposite materials, *Chem. Mater.*, **13**, 1131–1136 (2001).

[62] Q.H. Zeng, D.Z. Wang, A.B. Yu, and G.Q. Lu, Synthesis of polymer-montmorillonite nanocomposites by *in situ* intercalative polymerization, *Nanotechnology*, **13**, 549–554 (2002).
[63] D. Lee, K. Char, S.W. Lee, and Y.W. Park, Structural changes of polyaniline/montmorillonite nanocomposites and their effects on physical properties, *J. Mater. Chem.*, **13**, 2942–2947 (2003).
[64] B.H. Kim, J.H. Jung, J.W. Kim, H.J. Choi, and J. Joo, Physical characterization of polyaniline-Na^+-montmorillonite nanocomposite intercalated by emulsion polymerization *Synth. Met.*, **117**, 115–118 (2001).
[65] B.H. Kim, J.H. Jung, J.W. Kim, H.J. Choi, and J. Joo, Effect of dopant and clay on nanocomposites of polyaniline (PAN) intercalated into Na^+-montmorillonite (Na^+-MMT), *Synth. Met.*, **121**, 1311–1312 (2001).
[66] B.H. Kim, J.H. Jung, J. Joo, J.W. Kim, and H.J. Choi, Charge transport and structure of nanocomposites of polyaniline and inorganic clay, *J. Korean Phys. Soc.*, **36**, 366–370 (2000).
[67] H. Inoue and H. Yoneyama, Electropolymerization of aniline intercalated in montmorillonite, *J. Electroanal. Chem.*, **233**, 291–294 (1987).
[68] D. Orata and F. Segar, Electrodeposition of polyaniline on acidified clay montmorillonite modified electrode, *React. Funct. Polym.*, **43**, 305–314 (2000).
[69] B. Feng, Y. Su, J. Sang, and K. Kang, Electropolymerization of polyaniline/montmorillonite nanocomposite, *J. Mater. Sci. Lett.*, **20**, 293–94 (2001).
[70] K.H. Chen and S.M. Yang, Polyaniline-montmorillonite composite synthesized by electrochemical method, *Synth. Met.*, **135**, 151–152 (2003).
[71] G.M. Do Nascimento, V.R.L. Constantino, and M.L.A. Temperini, Spectroscopic characterization of a new type of conducting polymer-clay nanocomposite *Macromolecules*, **35**, 7535–7537 (2002).
[72] G.M. Do Nascimento, V.R.L. Constantino, R. Landers, and M.L.A. Temperini, Aniline polymerization into montmorillonite clay: a spectroscopic investigation of the intercalated conducting polymer, *Macromolecules*, **37**, 9373–9385 (2004).
[73] G.M. Do Nascimento, V.R.L. Constantino, R. Landers, and M.L.A. Temperini, Spectroscopic characterization of polyaniline formed in the presence of montmorillonite clay, *Polymer*, **47**, 6131–6139 (2006).
[74] G.M. Do Nascimento, A.C.M. Padilha, V.R.L. Constantino, and M.L.A. Temperini, Oxidation of anilinium ions intercalated in montmorillonite clay by electrochemical route, *Coll. Surf. A: Physicochem. Eng. Aspects*, **318**, 245–253 (2008).
[75] G.M. Do Nascimento and M.L.A. Temperini, Structure of polyaniline formed in different inorganic porous materials: A spectroscopic study, *Eur. Polym. J.*, **44**, 3501–3511 (2008).
[76] S. Yariv and K.H. Michaelian, Structure and Surface Acidity of Clay Minerals. In *Organo-Clay Complexes and Interactions*, ed. S. Yariv and H. Cross, Marcel Dekker, New York, 2002.
[77] E.A. Hauser and M.B. Leggett, Color Reactions between Clays and Amines, *J. Am. Chem. Soc.*, **62**, 1811–1814 (1940).
[78] S. Yariv, L. Heller, and Z. Safer, Sorption of aniline by montmorillonite, *Israel J. Chem.*, **6**, 741–756 (1968).
[79] T. Furukawa and G.W. Brindley, Adsorption and oxidation of benzidine and aniline by montmorillonite and hectorite, *Clay Clay Miner.*, **21**, 279–288 (1973).
[80] P. Cloos, A. Morale, C. Broers, and C. Badat, Adsorption and oxidation of aniline and p-chloroaniline by montmorillonite, *Clay Miner.*, **14**, 307–321 (1979).
[81] Y. Soma and M. Soma, Adsorption of benzidines and anilines on Cu- and Fe-montmorillonites studied by resonance Raman spectroscopy, *Clay Miner.*, **23**, 1–12 (1988).
[82] Y. Soma and M. Soma, Chemical reactions of organic compounds on clay surfaces, *Environmental Health Perspectives*, **83**, 205–214 (1989).
[83] V. Mehrotra and E.P. Giannelis, Metal-insulator molecular multilayers of electroactive polymers: intercalation of polyaniline in mica-type layered silicates, *Solid State Commun.*, **77**, 155–158 (1991).
[84] G.M. Do Nascimento, P.S.M. Barbosa, V.R.L. Constantino, and M.L.A. Temperini, Benzidine oxidation on cationic clay surfaces in aqueous suspension monitored by in situ resonance Raman spectroscopy, *Coll. Surf. A: Physicochem. Eng. Aspects*, **289**, 39–46 (2006).

[85] G.M. Do Nascimento, V.R.L. Constantino, and M.L.A. Temperini, Spectroscopic characterization of doped poly(benzidine) and its nanocomposite with cationic clay, *J. Phys. Chem. B*, **108**, 5564–5571 (2004).
[86] C.-G. Wu and T. Bein, Conducting polyaniline filaments in a mesoporous channel host, *Science*, **264**, 1757–1759 (1994).
[87] C.-G. Wu and T. Bein, Conducting polymer wires in mesopore hosts. In *Zeolites and related microporous materials: state of the art 1994*, ed. J. Weitkamp, H. G. Karge, H. Pfeifer, W. Hölderich, Studies in Surface Science and Catalysis, Vol. 84, Elsevier Science, BV, Amsterdam,1994.
[88] C.-G. Wu and T. Bein, Polyaniline wires in oxidant-containing mesoporous channel hosts *Chem. Mater.*, **6**, 1109-1112 (1994).
[89] G. Wenz, Cyclodextrins as building blocks for supramolecular structures and functional units, *Angew. Chem. Int. Ed. Engl.*, **33**, 803–822 (1994).
[90] A. Harada, Construction of supramolecular structures from cyclodextrins and polymers, *Carbohyd. Polym.*, **34**, 183–188 (1997).
[91] T. Shimomura, K. Yoshida, K. Ito, and R. Hayakawa, Insulation effect of an inclusion complex formed by polyaniline and β-cyclodextrin in solution, *Polym. Adv. Technol.*, **11**, 837–839 (2000).
[92] T. Shimomura, K. Yoshida, and R. Hayakawa, Inclusion complex formation of cyclodextrin and polyaniline, *Langmuir*, **15**, 910–913 (1999).
[93] G.M. Do Nascimento, J.E.P. da Silva, S.I.C. de Torresi, P.S. Santos, and M.L.A. Temperini, Spectroscopic characterization of the inclusion compound formed by polyaniline and β-cyclodextrin, *Mol. Cryst. Liq. Cryst.*, **374**, 53–58 (2002).
[94] Z. Wei and M. Wan, Hollow microspheres of polyaniline synthesized with an aniline emulsion template, *Adv. Mater.*, **14**, 1314–1317 (2002).
[95] J. Huang and M. Wan, Polyaniline doped with different sulfonic acids by in situ doping polymerization, *J. Polym. Sci.: Part A: Polym. Chem.*, **37**, 1277–1284 (1999)
[96] G.M. do Nascimento, C.H. B. Silva, C.M.S. Izumi, and M.L.A. Temperini, The role of cross-linking structures to the formation of one-dimensional nano-organized polyaniline and their Raman fingerprint, *Spectrochim. Acta Part A*, **71**, 869–875 (2008).
[97] A.R. Hopkins, R.A. Lipeles, and S.-J. Hwang, Morphology characterization of polyaniline nano- and microstructures, *Synth. Met.* **158**, 594–601 (2008).
[98] G.M. do Nascimento, P.Y.G. Kobata, and M.L.A. Temperini, Structural and vibrational characterization of polyaniline nanofibers prepared from interfacial polymerization, *J. Phys. Chem. B*, **112**, 11551–11557 (2008).
[99] M. Cochet, G. Louarn, S. Quillard, M. I. Boyer, J.P. Buisson, and S. Lefrant, Theoretical and experimental vibrational study of polyaniline in base forms: non-planar analysis. Part I, *J. Raman Spectrosc.*, **31**, 1029–1039 (2000).
[100] M. Cochet, G. Louarn, S. Quillard, J.P. Buisson, and S. Lefrant, Theoretical and experimental vibrational study of emeraldine in salt form. Part II, *J. Raman Spectrosc.*, **31**, 1041–1049 (2000).
[101] C.O. Oriakhi and M.M. Lerner, Poly(pyrrole) and poly(thiophene)/clay nanocomposites via latex-colloid interaction, *Materials Research Bulletin*, **30**, 723–729 (1995).
[102] J.W. Kim, F. Liu, F,H.J. Choi, S.H. Hong, and J. Joo, Intercalated polypyrrole/Na^+ montmorillonite nanocomposite via an inverted emulsion pathway method, *Polymer*, **44**, 289–293 (2003).
[103] J.-M. Yeh, C.-P. Chin, and S. Chang, Enhanced corrosion protection coatings prepared from soluble electronically conductive polypyrrole-clay nanocomposite materials, *J. Appl. Polym. Sci.*, **88**, 3264–3272 (2003).
[104] B.H. Kim, S.H. Hong, J. Joo, I.-W. Park, A.J. Epstein, J.W. Kim and H.J. Choi, Electron spin resonance signal of nanocomposite of conducting polypyrrole with inorganic clay, *J. A. Phys.*, **95**, 2697 (2004).
[105] J. Lin, Q. Tang, J. Wu, and H. Sun, Synthesis, characterization, and properties of polypyrrole/expanded vermiculite intercalated nanocomposite, *Polymer*,**110**, 2862–2866 (2008).
[106] P.W. Faguy, R.A. Lucas, and W.L. Ma, FT-IR-ATR spectroscopy study of the spontaneous polymerization of pyrrole in iron-exchanged montmorillonite, *Colloid Surf A*, **105**, 105–112 (1995).

[107] D.M.M. Krishantha, R.M.G. Rajapakse, D.T.B. Tennakoon, and H.V.R. Dias, Polypyrrole-montmorillonite nanocomposite: a composite fast ion conductor, *J. Compos. Mater.*, **40**, 1009–1021 (2006).
[108] A.U. Ranaweera, H.M.N. Bandara, and R.M.G. Rajapakse, Electronically conducting montmorillonite-Cu_2S and montmorillonite Cu2S-polypyrrole nanocomposites, *Electrochim Acta*, **52**, 7203–7209 (2007).
[109] S. Letaïef, P. Aranda, and E. Ruiz-Hitzky, Influence of iron in the forniation of conductive polypyrrole-clay nanocomposites, *Appl. Clay Sci.*, **28**, 183–198 (2005).
[110] V. Ramirez-Valle, A. Lerf, F. E. Wagner, J. Poyato, and J.L. Pérez-Rodriguez, Fe3+ intercalation/depositon on vermiculites and interaction with pyrrole: a mossbauer spectroscopic investigation, *Clay Miner.*, **43**, 487–499 (2008).
[111] K. Boukerma, J-Y. Piquemal, M.M. Chehimi, M. Mravcákova, M. Omastova, and P. Beaunier, Synthesis and interfacial properties of montmorillonite/polypyrrole nanocomposites, *Polymer*, **47**, 569–576 (2006).
[112] M.R. Karim and J.H. Yeum, In situ intercalative polymerization of conducting polypyrrole/montmorillonite nanocomposites, *J. Polym. Sci. B*, **46**, 2279–2285 (2008).
[113] B.K. Kuila and A.K. Nandi, Physical, mechanical and conductivity properties of poly(3-hexylthiophene)-montmorillonite clay nanocomposites produced by the solvent casting method, *Macromolecules*, **37**, 8577–8584 (2004).
[114] J. Liu and M. Wan, Synthesis, characterization and electrical properties of microtubules of polypyrrole synthesized by a template-free method, *J. Mater. Chem.*, **11**, 404–407 (2001).
[115] T. Wang, W. Liu, J. Tian, X. Shao, and D. Sun, Sctructure characterization and conductive performance of polypyrrol-molybdenum disulfide intercalation materials, *Polym Compos.*, **25**, 111–117 (2004).
[116] W.J. Bae, K.H. Kim, W.H. Jo, and Y.H. Park, Fully exfoliated nanocomposite from polypyrrole graft copolymer, *Polymer*, **46**, 10085–10091 (2005).
[117] S. Shirator, S. Mori, and K. Ikeyaki, Wire bonding over insulating substrates by electropolymerization of polypyrrole using a scanning micro-needle, *Sens. Actuators B*, **49**, 30–33 (1998).
[118] J. Mansouri and R.P. Burford, Novel membranes from conducting polymers, *J. Membr. Sci.*, **87**, 23–34 (1994).
[119] M. Granström and O. Inganäs, Electrically conductive polymer fibres with mesoscopic diameters: 1. Studies of structure and electrical properties, *Polymer*, **36**, 2867–2872 (1995).
[120] M. Granström, J.C. Carlberg, and O. Inganäs, Electrically conductive polymer fibres with mesoscopic diameters: 2. Studies of polymerization behaviour, *Polymer*, **36**, 3191–3196 (1995).
[121] S. Cuenot, S. Demoustier-Champagne, and B. Nysten, Elastic modulus of polypyrrole nanotubes, *Phys. Rev. Lett.*, **85**, 1690–1693 (2000).
[122] J. Duchet, R. Legras, and S. Demoustier-champagne, Chemical synthesis of polypyrrole: structure-properties relationship, *Synth. Met.*, **98**, 113–122 (1998).
[123] J. Liu and M. Wan, Synthesis, characterization and electrical properties of microtubules of polypyrrole synthesized by a template-free method, *J. Mater. Chem.*, **11**, 404–407 (2001).
[124] W.R. Salanak, R. Erlandssom, J. Priza, I. Lundatrom, and O. Inganas, X-ray photoelectron spectroscopy of boron fluoride doped polypyrrole, *Synth. Met.*, **5**, 125–139 (1983).
[125] A. Watanabe, M. Tanaka, and J. Tanak, Electrical and optical properties of a stable synthetic metallic polymer: polypyrrole, *Bull. Chem. Soc. Jpn.*, **54**, 2278–2281 (1981).
[126] H. Chang, Y. Chunhe, and L. Yongfang, Chemical synthesis of coral-like nanowires and nanowire networks of conducting polypyrrole, *Synthetic Metals*, **139**, 539–545 (2003).
[127] J. Lei and W. Liang, and C.R. Martin, Infrared investigations of pristine, doped and partially doped polypyrrole, *Synth. Met.*, **48**, 301–312 (1992).
[128] L. Qu, G. Shi, J. Yuan, G. Han, and F. Chen., Preparation of polypyrrole microstructures by direct electrochemical oxidation of pyrrole in an aqueous solution of camphorsulfonic acid , *J. Elect. Chem.*, **561**, 149–156 (2004).
[129] Y.C. Liu, B.J. Hwang, W.J. Jian, and R. Santhanan, In situ cyclic voltammetry-surface-enhanced Raman spectroscopy: studies on the doping–undoping of polypyrrole film, *Thin Solid Films*, **374**, 85–91 (2000).

[130] J. Roncali, Conjugated poly(thiophenes): synthesis, functionalization, and applications, *Chem. Rev.*, **92**, 711–738 (1992).
[131] J. Heinze and M. Dietrich, Poly (4,4′-dimethoxybithiophene)-a neuw conducting polymer with extraordinary redox and optical-properties, *Synth. Met.*, **41**, 503–506 (1991).
[132] M. Granstrom, M. Berggren, and O. Inganas, Micrometer-sized and nanometer-sized polymeric light-emitting-diodes, *Science*, **267**, 1478–1481 (1995).
[133] M.G. Kanatzidis, C.-G. Wu, H.O. Marcy, D.C. DeGroot, and C.R. Kannewurfi, Conductive polymer/oxide bronze nanocomposites. Intercalated polythiophene in vanadium pentoxide (V2O5) xerogels, *Chem. Mater.*, **2**, 222–224 (1990).
[134] N. Ballav and M. Biswas, A conducting nanocomposite via intercalative polymerisation of thiophene in montmorillonite clay, *Synth. Metals.*, **142**, 309–315 (2004).
[135] N. Hebestreit, J. Hofmann, U. Rammelt, and W. Plieth, Physical and electrochemical characterization of nanocomposites formed from polythiophene and titanium dioxide, *Electrochim. Acta*, **48**, 1779–1788 (2003).
[136] E.T. Kang, K.G. Neoh, and K.L. Tang, Surface modifications of poly(3-alkylthiophene) films by graft copolymerization, Macromolecules, **25**, 6842–6848 (1992).
[137] Q.-T. Vu, M. Pavlik, N. Hebestreit, U. Rammelt, W. Plieth, and J. Pfleger, Nanocomposites based on titanium dioxide and polythiophene: Structure and properties, *React. Func. Polym.*, **65**, 69–77 (2005).
[138] G. Shi, J. Xu, and M. Fu, raman spectroscopic and electrochemical studies on the doping level changes of polythiophene films during their electrochemical growth processes, *J. Phys. Chem. B*, **106**, 288–292 (2002).
[139] L. Zhai and R. D. McCullough, Regioregular polythiophene/gold nanoparticle hybrid materials. *J. Mat. Chem.*, **14**, 141–143 (2004).
[140] R.D. McCullough, R.D. Lowe, M. Jayaraman, and D.L. Anderson, Design, synthesis, and control of conducting polymer architectures: structurally homogeneous poly(3-alkylthiophenes), *J. Org. Chem.*, **58**, 904–912 (1993).
[141] M.R. Karim, C.J. Lee, and M.S. Lee, Synthesis and characterization of conducting polythiophenie/carbon nanotubes composites, *J. Polym. Sci. A*, **44**, 5283–5290 (2006).
[142] G.M.A. Rahman, D.M. Guldi, R. Cagnoli, A. Mucci, L. Schenetti, L. Vaccari, and M. Prato, Combining single wall carbon nanotubes and photoactive polymers for photoconversion, *J. Am. Chem. Soc.*, **127**, 10051–10057 (2005).
[143] Y.D. Wang and M.F. Rubner, Stability studies of the electrical-conducitivity of various poly(3-alkylthiophenes), *Synth. Met.*, **39**, 153–175 (1990).
[144] N. Toshima and S. Hara, Direct synthesis of conducting polymers from simple monomers, *Prog. Polym. Sci.*, **20**, 155–183 (1995).
[145] A. Rao, E. Richter, S. Bandow, B. Chase, P. Eklund, K. Williams, S. Fang, K. Subbaswamy, M. Menon, A. Thess, R. Smalley, G. Dresselhaus, and M. S. Dresselhaus, Diameter-selective Raman scattering from vibrational modes in carbon nanotubes, *Science*, **275**, 187–191 (1997).
[146] A. Pron, G. Louran, M. Lapkowsky, M. Zagorska, J. Glowczyk-Zubek, and S. Lefrant, 'In situ' Raman spectroelectrochemical studies of poly(3,3′-dibutoxy-2,2′-bithiophene), *Macromolecules*, **28**, 4644–4649 (1995).
[147] Y. Furukawa, M. Akimoto, and I. Harada, Vibrational key bands and electrical conductivity of polythiophene, *Synth. Met.*, **18**, 151–156 (1987).
[148] A. Patil, A.J. Heeger, and F. Wudl, Optical-properties of conducting polymers, *Chem. Rev.*, **88**, 183–200 (1988).
[149] E.T. Kang, K.G. Neoh, and K.L. Tan, X-RAY photoelectron spectroscopic studies of poly(2,2'-bithiophene) and its complexes, *Phys. Rev. B*, **44**, 10461–10469 (1991).
[150] J.M. Pringle, O. Ngamna, C. Lynam, G.G. Wallace, M. Forsyth, and D.R. MacFarlane, Conducting polymers with fibrillar morphology synthesized in a biphasic ionic liquid/water system, *Macromolecules*, **40**, 2702–2711 (2007).
[151] J. Roncali, F. Garnier, M. Lemaire, and R. Garreau, Poly mono-, bi- and trithiophene: Effect of oligomer chain length on the polymer properties, *Synth. Met.*, **15**, 323–331 (1986).
[152] S. Garreau, G. Louarn, J.P. Buisson, G. Froyer, and S. Lefrant, Packing length influence in linear polymer melts on the entanglement, critical, and reptation molecular weights, *Macromolecules*, **32**, 6807–6812 (1999).

[153] J.F. Hulvat and S.I. Stupp, Anisotropic properties of conducting polymers prepared by liquid crystal templating, *Adv. Mater.*, **16**, 589 (2004).
[154] D.H. Kim, Y. Jang, Y.D. Park, and K. Cho, Controlled one-dimensional nanostructures in poly(3-hexylthiophene) thin film for high-performance organic field-effect transistors, *J. Phys. Chem. B*, **110**, 15763–15768 (2006).
[155] G. Tourillon, A. Fontaine, R. Garrett, M. Sagurton, P. Xu, and G.P. Williams, Near-edge x-ray-absorption fine-structure observations of odering and metallic-like behavior in organic conducting polymers grafted on a pt surface, *Phys. Rev. B*, **35**, 9863–9866 (1987).
[156] D.A. Outka, J. Stöhr, J.P. Rabe, and J.D. Swalen, *J. Chem. Phys.*,The orientation of langmuir-blodgett monolayers using nexafs, **88**, 4076–4087 (1988).
[157] H. Sirringhaus, P.J. Brown, R.H. Friend, M.M. Nielsen, K. Bechgaard, B.M.W. Langeveld-Voss, A.J.H. Spiering, R.A. Janssen, E.W. Meijer, P. Herwig, and D.M. de Leeuw, Two-dimensional charge transport in self-organized, high-mobility conjugated polymers, *Nature*, **401**, 685–688 (1999).
[158] R.J. Kline, M.D. McGehee, E.N. Kadnikova, J. Liu, J.M.J. Frechet, and M.F. Toney, Dependence of regioregular poly(3-hexylthiophene) film morphology and field-effect mobility on molecular weight, *Macromolecules*, **38**, 3312–3319 (2005).
[159] M.M. Alam and S.A. Jenekhe, Nanolayered heterojunctions of donor and acceptor conjugated polymers of interest in light emitting and photovoltaic devices: Photoinduced electron transfer at polythiophene/polyquinoline interfaces, *J. Phys. Chem. B*, **105**, 2479–2482 (2001).
[160] C. Pereira, G.T. Kokotailo, and R.J. Gorte, Acetylene polymerization in a H-ZSM-5 zeolite, *J. Phys. Chem.*, **95**, 705–709 (1991).
[161] D.C. Sherman and D.S. Galen, Polymerization of methylacetylene in hydrogen zeolites, *J. Phys. Chem.*, **95**, 710–720 (1991).
[162] A.R. Lewis, G.J. Millar, R.P. Cooney, and G.A. Bowmaker, Trans-polyacetylene on sodium and cesium mordenites: A resonance raman spectroscopic study, *Chem. Mater*, **5**, 1509–1517 (1993).
[163] D.W. Kim, A. Blumstein, J. Kumar, L.A. Samuelson, B. Kang, and C. Sung. Ordered multilayer nanocomposites prepared by electrostatic layer-by-layer assembly between aluminosilicate nanoplatelets and substituted ionic polyacetylenes, *Chem. Mater.*, **14**, 3925–3929 (2002).
[164] M. Hasegawa, T. Matano, Y. Shindo, and T. Sugimura, Spontaneous molecular orientation of polyimides induced by thermal imidization .2. In-plane orientation, *Macromolecules*, **29**, 7897–7909 (1996).
[165] D.W. Kim, J. Kumar, and A. Blumstein, Ordered assembly of conjugated ionic polyacetylenes within clay nanoplatelets: Layer-by-layer assembly and intercalative polymerization, *Applied Clay Science*, **30**, 134–140 (2005).
[166] J.-H. Liao, M. Benz, E. LeGoff, and M.G. Kanatzidis, Oligothiophenes as models for polythiophenes-the crystal and molecular-structures of 3″,4″-dibutylpentathiophene and 3′3(′x4),4′,4(′x4)-tetrabutylhexathiophene, *Adv. Mater.*, **6**, 135–138 (1994).
[167] B.-C. Ku, D.W. Kim, D. Steeves, R. Nagarajan, A. Blumstein, J. Kumar, P.W. Gibson, J.A. Ratto, and L.A. Samuelson, Molecularly ordered structure and permeability properties of amphiphilic polyacetylene-multilayer nanocomposites, *Comp. Sc. and Tech.*, **68**, 3215–3219 (2008).
[168] S.K. Sahoo, D.W. Kim, J. Kumar, A. Blumstein, and A.L. Cholli, Nanocomposites from in-Situ polymerization of substituted polyacetylene within lamellar surface of the montmorillonite: a solid-state NMR study, *Macromolecules*, **36**, 2777–2784 (2003).
[169] H. Liu, D.W. Kim, A. Blumstein, J. Kumar, and S.K. Tripathy, Nanocomposite derived from intercalative spontaneous polymerization of 2-ethynylpyridine within layered aluminosilicate: montmorillonite, *Chem. Mater.*, **13**, 2756–2758 (2001).
[170] D.W. Kim, A. Blumstein, H. Liu, M.J. Downey, J. Kumar, and S.K.J. Tripathy, Organc/inorganic nanocomposites prepared by spontaneous polymerization of ethynylpyridine within montmorillonite, *Macromol. Sci., Pure Appl. Chem. A*, **38**, 1405–1415 (2001).
[171] M. Kyotani, S. Matsushita, T. Nagai, Y. Matsui, M. Shimomura, A. Kaito, and K. Akagi, Helical carbon and graphitic films were prepared from iodine-doped helical Poly(acetylene)

film using morphology-retaining carbonization., *J. Am. Chem. Soc.*, **130** (33), 10880–10881 (2008).
[172] J. Song, J.S. Cisar, and C.R. Bertozzi, Functional self-assembling bolaamphiphilic polydiacetylenes as colorimetric sensor scaffolds, *J. Am. Chem. Soc.*, **126**, 8459–8465 (2004).
[173] B.N. Thomas, C.M. Lindemann, R.C. Corcoran, C.L. Cotant, J.E. Kirsch, and P.J. Persichini, Phosphonate lipid tubules II, *J. Am. Chem. Soc.*, **124**, 1227–1233 (2002).
[174] G. Wang and R.I. Hollingsworth, Offsetting the tubule-forming tendency of chiral diacetylene-containing lipids: Planar strips, ribbons, and liposomes from a diacetylenic lipid analog of a thermophilic bacterium, *Adv. Mater.*, **12**, 871–874 (2000).
[175] D.H. Charych, J.O. Nagy, W. Spevak, and M.D. Bednarski, Direct colorimetric detection of a receptor-ligand interaction by a polymerized bilayer assembly, *Science*, **261**, 585–588 (1993).
[176] H. Peng, J. Tang, J. Pang, D. Chen, L. Yang, H.S. Ashbaugh, C.J. Brinker, Z. Yang, and Y. Lu, Polydiacetylene/Silica nanocomposites with tunable mesostructure and thermochromatism from diacetylenic assembling molecules, *J. Am. Chem. Soc.*, **127** (37), 12782–12783 (2005).
[177] Y. Lu, Y. Yang, A. Sellinger, M. Lu, J. Huang, H. Fan, R. Haddad, G. Lopez, A. R. Burns, D. Y. Sasaki, J. Shelnutt, and C. J. Brinker, Self-assembly of mesoscopically ordered chromatic polydiacetylene/silica nanocomposites, *Nature*, **410**, 913–917 (2001).
[178] J. Song, J.S. Cisar, and C.R. Bertozzi, Functional self-assembling bolaamphiphilic polydiacetylenes as colorimetric sensor scaffolds, *J. Am. Chem. Soc.*, **126**, 8459–8465 (2004).
[179] T. Asefa, M.J. MacLachan, N. Coombs, and G.A. Ozin, Periodic mesoporous organosilicas with organic groups inside the channel walls, *Nature*, **402**, 867–871 (1999).
[180] M. Rangin and A. Basu, Lipopolysaccharide identification with functionalized polydiacetylene liposome sensors, *J. Am. Chem. Soc.*, **126**, 5038–5039 (2004).

9

Atomic Force Microscopy Study of Conductive Polymers

Edgar Ap. Sanches[1], Osvaldo N. Oliveira Jr[1], and Fabio Lima Leite[2]

[1]University of São Paulo (USP), Institute of Physics of São Carlos (IFSC), São Carlos, Brazil
[2]Federal University of São Carlos (UFSCar), Rodovia João Leme dos Santos, Sorocaba, Brazil

9.1 Introduction

Atomic force microscopy (AFM) has been widely used for studying conducting polymers as it is capable of providing information that is not possible with scanning electron microscopy (SEM). Surface images can be taken of materials under the most varied conditions (air, vacuum, and liquid medium). With conducting polymers, AFM has been used to investigate many features. These include surface morphology, conformation and packing of the polymer chains, tribology, phase segregation, porosity, roughness, mapping the distribution of electric charges, and chemical interactions. The images obtained with the different types of AFM are related to the nature of the involved forces: coulombic repulsion (AFM contact mode), Van der Waals (AFM noncontact mode) [1], magnetic force (MFM), and electric force (EFM). Though AFM is advantageous for many studies, it cannot replace electron microscopy completely, and should be seen as complementary.

This chapter aims to explore the major studies using AFM for conductive polymers, focusing on the application of images and force spectroscopy for nanostructured films, nanostructures, and sensors.

Nanostructured Conductive Polymers Edited by Ali Eftekhari

9.2 AFM Fundamentals and Applications

9.2.1 Basic Principles

This topic briefly introduces the basic elements of AFM and its principle of operation, which serves as a background for further discussion of image collection and interpretation. The microscope scans over the sample surface with a sharp probe (tip) situated at the apex of a flexible cantilever that is often diving-board-shaped or V-shaped and normally made of silicon or silicon nitride (Si_3N_4). A sample is mounted on a piezoelectric tube, which allows the sample to be precisely scanned, i.e., AFM utilizes a scanner that moves the sample with a sub-nanometer displacement (stable motion on a scale of less than 1.0 Å) when a voltage is applied. To form an image, the tip is brought into contact with or close to the sample and raster-scanned over the surface, causing the cantilever to deflect because of a change in surface topography or in probe–sample forces. A line-by-line image of the sample is formed as a result of this deflection, which is detected using a variety of mechanisms, the most common of which is an 'optical lever', consisting of a laser light reflected off the back surface of the cantilever onto a position-sensitive photodetector. Forces acting between the sharp probe (tip) placed in close contact with the sample result in a measurable deformation of the cantilever (console) to which the probe is attached (see Figure 9.1). The cantilever bends vertically upwards or downwards because of a repulsive

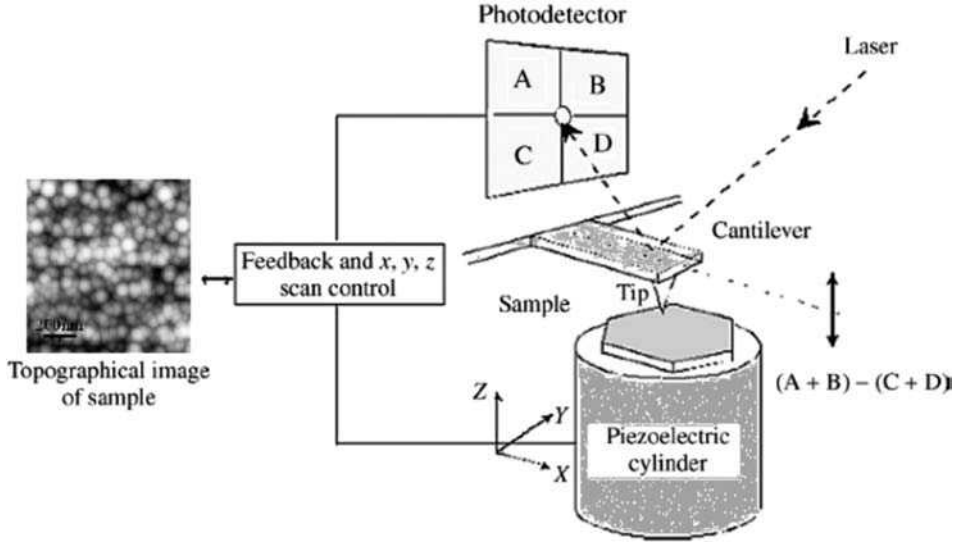

Figure 9.1 *A schematic drawing of an AFM. A detector consisting of four photodiodes is shown. Scanning perpendicular to the long cantilever axis, the (A+B) − (C+D) signal gives topographical data, while the (A+C) − (B+D) signal responds to friction due to torsion of the cantilever, providing lateral force information. (Reprinted with permission from Journal of Adehsion Science and Technology, Application of atomic force spectroscopy (AFS) to studies of adhesion phenomena: a review by F. L. Leite, P. S. P. Herrmann et al., 19, 3–5, 365–405. Copyright (2005) Brill)*

or attractive interactions. The forces acting on the tip vary, depending on the operating mode and the conditions used for imaging.

9.2.2 Imaging Modes

A force sensor in an AFM can only work if the probe interacts with the force field associated with a surface. The interaction force between the probe and the surface in ambient air is illustrated in Figure 9.2. The total intermolecular pair potential is obtained by assuming one attractive ($-C_1/z^6$) and another repulsive potential (C_2/z^{12}). Superimposing the two gives an expression for the well-known Lennard–Jones potential, where C_1 and C_2 are the corresponding coefficients for the attractive and repulsive interactions, respectively, and z is the distance between the sample surface and rest position of the cantilever.

There are three basic regions of interaction between the probe and surface: (i) free space, (ii) attractive region, and (iii) repulsive region. At short distances, the cantilever mainly senses interatomic forces: the very short range (≈ 0.1 nm) repulsive forces, and the longer-range (up to 10 nm) van der Waals forces. Attractive forces near the surface can arise from a layer of contamination present on all surfaces in ambient air. The contamination is typically an aerosol composed of water vapor and hydrocarbons. On the other hand, the repulsive force occurs between any two atoms or molecules that approach so closely that

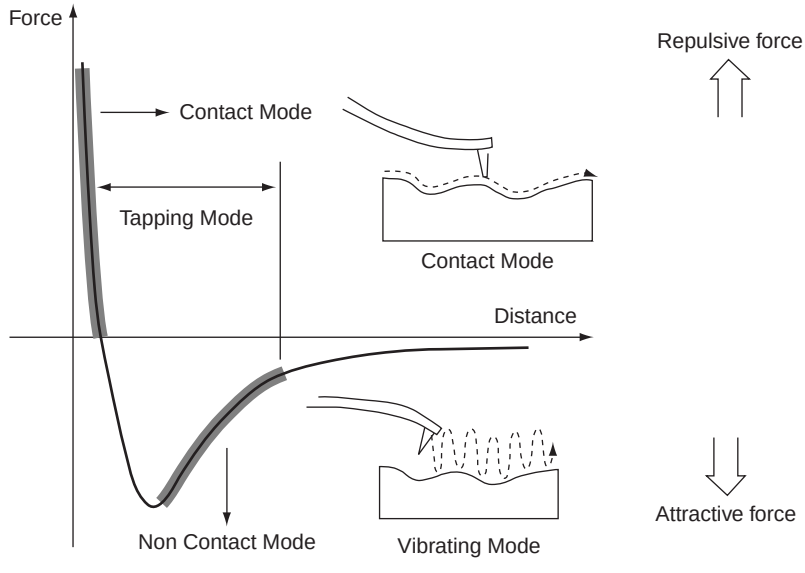

Figure 9.2 *Empirical force vs. distance (z) curve that reflects the type of interaction between the AFM tip and the sample during measurements using distinct imaging modes. (Reprinted with permission from Journal of Adehsion Science and Technology, Application of atomic force spectroscopy (AFS) to studies of adhesion phenomena: a review by F. L. Leite, P. S. P. Herrmann et al., 19, 3–5, 365–405. Copyright (2005) Brill)*

their electronic orbitals begin to overlap. It is thus a result of the Pauli exclusion principle. When this repulsive force is predominant in an AFM, the tip and the sample are considered to be in 'contact'. There are two primary methods for establishing the forces between a probe and a sample when an AFM is operated. In the contact mode, the deflection of the cantilever is measured, and in the vibrating mode the changes in frequency and amplitude are used to measure the force interaction. Every AFM system is used for topography, i.e., to reproduce a surface landscape as an image. There are three basic modes in AFM in which topography can be obtained: contact mode, noncontact mode, and tapping mode (vibrating modes). The contact mode represents the region of strong repulsive forces between the tip and the surface (see Figure 9.2), while in the noncontact mode weak attractive forces are measured. For the tapping mode one uses the region in between, i.e., the interaction between the tip and the surface is in the contact region for a short time (a 'tap'), but it is in the noncontact region most of the time [3].

9.2.2.1 Contact Mode

In the contact mode, there are static modes (dc-modes), and dynamic modes (ac-modes). In the former, a cantilever-type spring bends in response to the force which acts on the probing tip until a static equilibrium is established [1]. In the dynamic mode, the lever oscillates close to its resonance frequency. A distance-dependence force shifts the resonance curve. Another technique is to modulate the position of the sample at a frequency below the cantilever resonance but above the feedback-response frequency and send the response signal to a lock-in amplifier to measure the signal's amplitude and phase [4]. The lock-in output is connected to the auxiliary data acquisition channels to form an image – this approach is popularly known as force modulation (FM-mode). FM-mode imaging or force curve is an AFM technique that identifies and maps differences in surface stiffness or elasticity.

The dc-mode or topography mode with quasi-static probe contact [5] is the most used, in which the AFM tip is in intimate repulsive contact with a surface, as shown in Figure 9.2. The contact mode is typically used for scanning hard samples and when a resolution of greater than 20 nm is required. The cantilevers are usually silicon (Si) or silicon nitride (Si_3N_4), with typical resonant frequencies of 50 kHz and force constants below 1 N m^{-1}.

Scanning can be carried out in two ways:

(i) In the 'constant-force mode' (constant-deflection mode) the cantilever deflection is kept constant by extending and retracting the piezoelectric scanner; in this method, a feedback loop adjusts the height of the sample (to maintain constant deflection) by varying the voltage applied to the *z* portion of the *xyz* piezoelectric scanner (see Figure 9.3a). The vertical displacement of the scanner under scanning reflects the sample topography under investigation.

(ii) In the 'variable-deflection mode' or 'constant-height mode' (free deflection mode) the piezotube extension is constant and the cantilever deflection is recorded; the feedback loop is open, so that the cantilever undergoes a deflection proportional to the change in the tip–sample interaction (see Figure 9.3b). In this mode the scanner of the microscope maintains the fixed end of the cantilever at a constant height value (*H*), so the deflection of the cantilever during scanning reflects the sample topography.

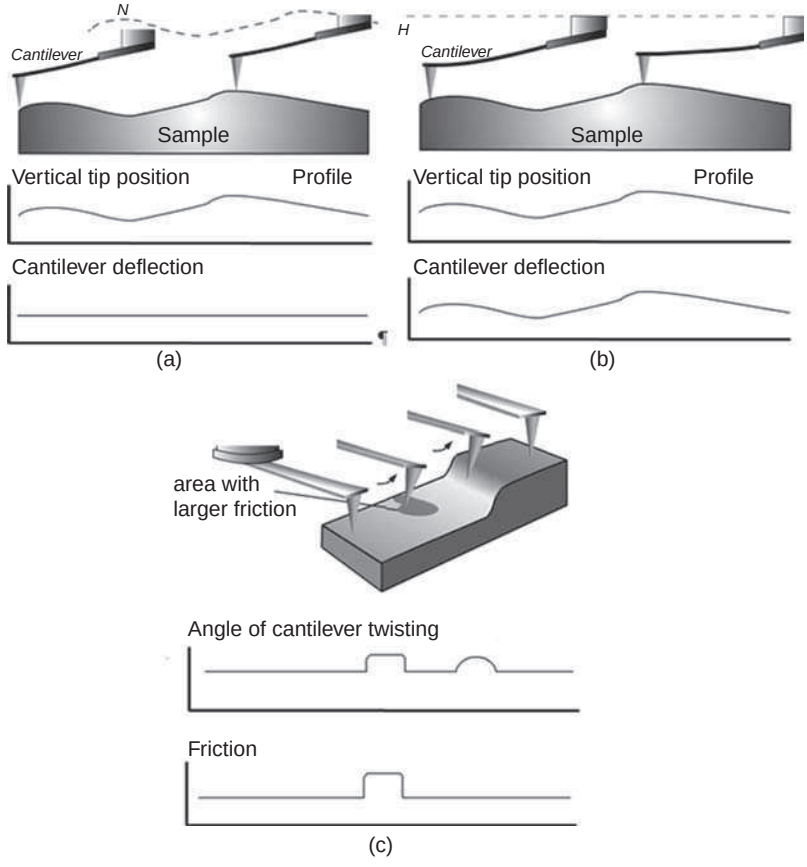

Figure 9.3 *Contact mode techniques: (a) constant-force, (b) constant-height, and (c) lateral force mode. (Reproduced with kind permission from Denis Andreyuk, NT-MDT Co. www.ntmdt.com)*

The main advantage of the constant force mode is the possibility to measure with high resolution the topography in addition to other characteristics such as friction forces and spreading resistance, while the variable-deflection mode has the advantage of operating at high scanning speeds (it is restricted only by the resonant frequency of the cantilever). The variable-force mode is a contact mode for presumably atomic resolution and should be used in very small scanned areas because the tip and/or the sample could be damaged with large changes in height on the surface that will produce a large deflection on the cantilever [3].

The AFM tip in the contact mode makes soft 'physical contact' with the sample, with a cantilever with a low spring constant. As the scanner gently traces the tip across the sample (or the sample under the tip), the contact force causes the cantilever to bend to accommodate changes in topography. For example, nanostructured films of conducting polymers have been investigated using the AFM contact mode. These films may be obtained with techniques such as the Langmuir–Blodgett (LB) [6] or the layer-by-layer methods (LbL) [7], which offer precise control of thickness and molecular architecture. For studies of

conducting conjugated polymers, e.g., polyaniline (PANI) and derivatives, interface properties may vary extensively due to the interplay of the adsorption mechanisms, and therefore a systematic analysis of the capabilities of LbL films requires use of surface characterization techniques. Because LbL films are essentially surface films, AFM [8–9] is suitable for characterizing the initial nucleation and growth, and the final surface structure, from which a number of features could be captured not only in terms of the film properties, but also of the adsorption mechanisms.

Leite *et al.* 2005 [11] analyzed the morphology and adsorption processes for poly (*o*-ethoxyaniline) (POEA), a derivative of PANI, layer using the dc contact mode. Parameters such as roughness, relative surface coverage, and fractal dimension were used to interpret the data. Figure 9.4 displays AFM images of a POEA layer adsorbed at different time intervals at pH 3 on a glass substrate. In general, the morphology of a POEA film is characterized by small globules, ranging from 20 to 100 nm in diameter. The number of globules increases with the time of immersion and then reaches saturation as the substrate is entirely coated. Since pH 3 was used for the POEA solution, there should be considerable repulsion as POEA is positively charged. The surface of POEA is expected to reflect both the long-range morphology due to the existence of globules, and the short-range morphology corresponding to the region inside the globules. The last term may be dominant for thicker films (two or more layers) [12].

The morphological features of nanostructured films have been correlated with the chain conformations in solution [13], for which a dummy atom model (DAM) was used. The AFM images in Figure 9.5 represented an 'off print' of the solution conformation when molecules of emeraldine base POEA (POEA-EB) were adsorbed on the substrate. The size of the globules is comparable to the aggregates of polymer molecules in solution. Significantly, the adsorption mechanisms and film properties for polyanilines are altered by a mere change in pH [14], which has been exploited in sensors and other applications [15].

Conducting LB and Langmuir–Schaefer (LS) films have also been studied with AFM [16–17]. Riul *et al.,* [18] characterized LB films of parent PANI to optimize experimental conditions for the formation of stable Langmuir monolayers and their subsequent transfer onto solid substrates. PANI LB films displayed a fibrillar structure with the fibril width ranging from 60 to 160 nm, depending on the region of the sample analyzed. Similar results were obtained by Mazur and Krysinski [19] for PANI chemically deposited *in situ* on gold electrodes coated with thiol monolayers containing methyl, hydroxy, and carboxy terminal groups. The surface of the synthesized polymer was relatively smooth and regular, consisting of small protrusions with diameters of approximately 200 nm.

Contact-AFM has been used for characterizing nanoparticles [20], nanowires [21], and nanofibers [22]. Polypyrrole nanoparticles synthesized in an enzymatic medium and deposited onto SiO_2 and Pt surfaces had the shape and size monitored by contact mode AFM [23]. Borato *et al.* [24] studied LbL films of POEA, chitosan, and chitosan-poly (methacrylic acid) (CS-PMMA) nanoparticles. The authors used this system to detect copper ions in aqueous solutions. Figure 9.6 shows that films obtained with CS-PMAA – with no alternating layers – are already thick, which clearly points to the importance of the nanoparticles for strong adsorption. The roughness was extremely high, almost two orders of magnitude larger than for a chitosan film. The films with CS-PMMA are also thicker

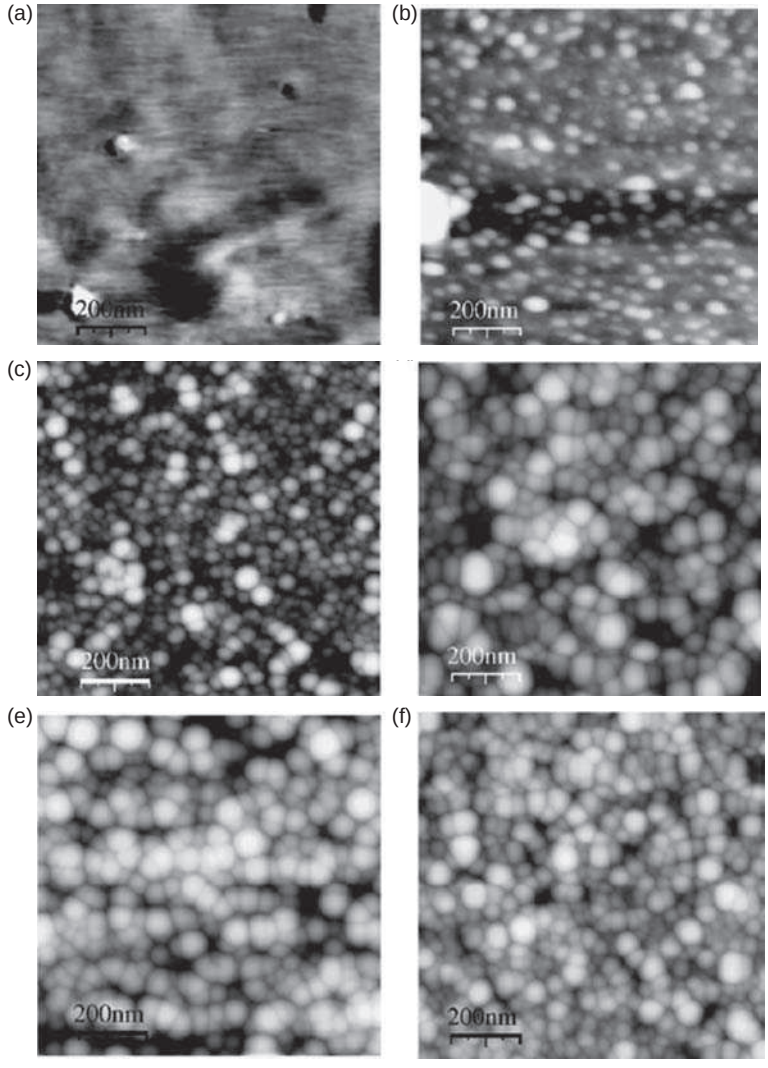

Figure 9.4 *AFM images (contact mode) of POEA films produced from a pH 3 solution for distinct immersion times: (a) 0.0 min (i.e. bare glass), (b) 0.5 min, (c) 1.0 min, (d) 3.0 min, (e) 10.0 min, and (f) 30.0 min. (Reprinted with permission from Polymer, Study on the adsorption of poly(o-ethoxyaniline) nanostructyred films using atomic force miscroscopy by F. L. Leite, L. G. Paterno, C. E. Borato et al., 46, 26. Copyright (2005) Elsevier Ltd)*

and rougher than POEA films alternated with any other polyanion reported in the literature.

Lateral force microscopy (LFM) is a variant of the dc-contact mode, specifically the constant-force mode, in which the laser-beam detector is arranged so as to allow monitoring not only of the vertical component of the tip deflection (topography), but also the

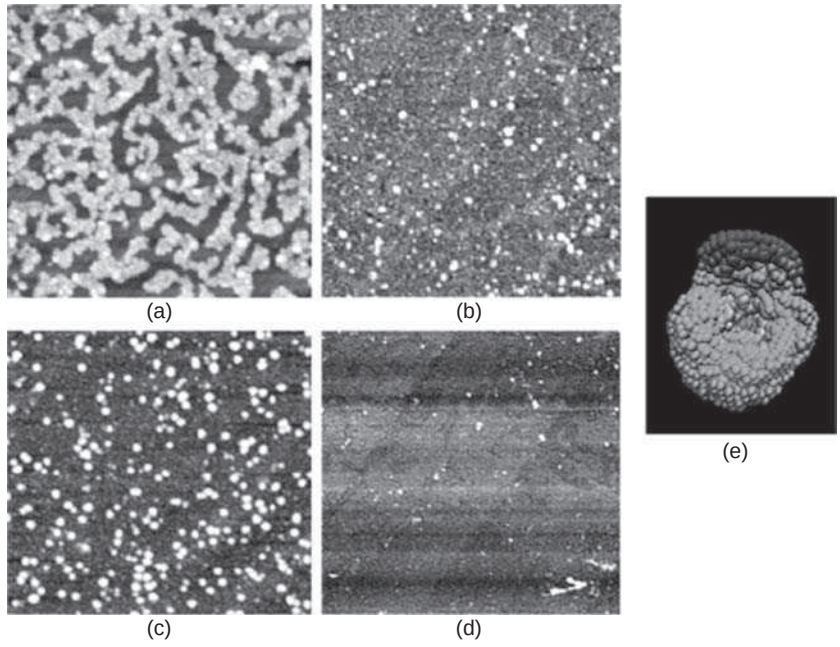

Figure 9.5 *AFM images (10 × 10 μm) of POEA-EB (pH 10.0) for immersion times of (a) 1s, (b) 3s, (c) 5s, (d) 180s, and (e) average DAM for POEA-EB. (Reprinted with permission from Journal of Colloid and Interface Science, Nanoscale conformational ordering in polyanilines inestigated by SAXS and AFM by F. L. Leite, M. de Oliveira Neto, L. G. Paterno et al., 316, 2. Copyright (2007) Elsevier Ltd) (See colour Plate 3)*

torsion deformation exerted by the lateral forces acting on the tip [25] (see Figure 9.3c). With small deflections, the angle of torsion is proportional to the side (lateral) force. This mode allows imaging of surfaces that exhibit only minor topographic changes, but pronounced variations in the chemical composition of the surface. As depicted in Figure 9.3c, lateral deflections of the cantilever usually arise from two sources: changes in surface friction and changes in slope. In the first case, the tip may experience greater friction as it traverses some areas, causing the cantilever to twist more strongly. In the second case, the cantilever may twist when it encounters a steep slope. To separate one effect from the other, LFM and AFM images should be collected simultaneously.

LFM images of composite Langmuir–Blodgett (LB) films containing different weight percentages of cadmium stearate and 16-mer PANI were investigated by Riul *et al.,* [26]. Upon increasing the amount of 16-mer PANI content in the composite, large globular structures with higher average roughness were observed. The results indicated a phase separation of 16-mer and cadmium stearate in the composite, with the roughness increasing considerably when higher contents of 16- mer were employed. Asmus and Wolf [27], studied the changes in surface properties of polymer materials induced by ion irradiation and on reproducing hexagonal and square patterns in the micrometre scale. Effects were studied on thin films of doped polyethoxithiophene (PEOT) and polyethylenedioxithiophene (PEDT)

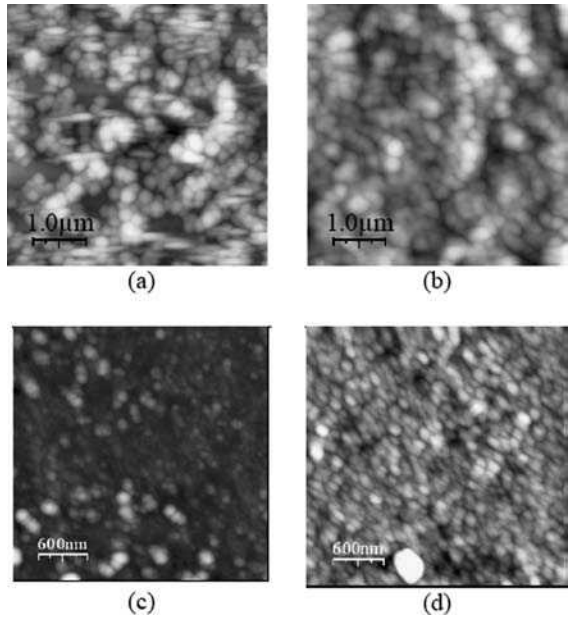

Figure 9.6 *AFM images of: (a) doped POEA alternated with CS-PMMA nanoparticles (pH 3), (b) dedoped POEA alternated with CS-PMMA nanoparticles pH 3, (c) doped POEA with chitosan pH 3 and (d) dedoped POEA alternated with chitosan pH 3. (Reprinted with permission from IEEE Transactions on Dielectrics and Electrical Insulation, Layer-by-layer films of poly(o-ethoxyaniline), chitosan and chitosan-poly(methacrylic acid) nanoparticles and their application in an electronic tongue by C. E. Borato, F. L. Leite et al, 13, 5, 1101–1109. Copyright (2006) IEEE)*

deposited on an insulating substrate of polyethersulfone (PES), caused by bombardment of 14 keV Ar^+ within a fluence range from 10^{14} to 10^{17} ions cm^{-2}. AFM/LFM images of PEOT irradiated with 10^{15} ions cm^{-2} on copper substrates are shown in Figure 9.7. The irradiated area does not differ from the shaded region according to AFM-topology (Figure 9.7a), but shows a significant contrast according to the LFM surface energy (Figure 9.7b). In Figure 9.7c, a hexagonal honeycomb pattern is visible with positive contrast in the LFM scanning mode from left to right.

In 1997, Hayes *et al*. [28] reported the physical and electrochemical properties of two-component self-assembled monolayers (SAMs) composed of both electroactive (4-aminothiophenol, 4-ATP) and electroinactive (*n*-octadecanethiol, ODT) species. LFM images obtained at three points near the critical region of the isotherm indicated that these two-component SAMs display complex phase behavior: at relatively low 4-ATP coverage, the surface consists of small islands of 4-ATP embedded in an ordered film of ODT; at higher coverage of 4-ATP, however, evidence was found for both separation into distinct phases and mixing of the two components.

Guan *et al.*, [29], used LFM to examine the topography of patterned PANI films. The topographic images in Figure 9.8a show the line patterns with relatively clear boundaries,

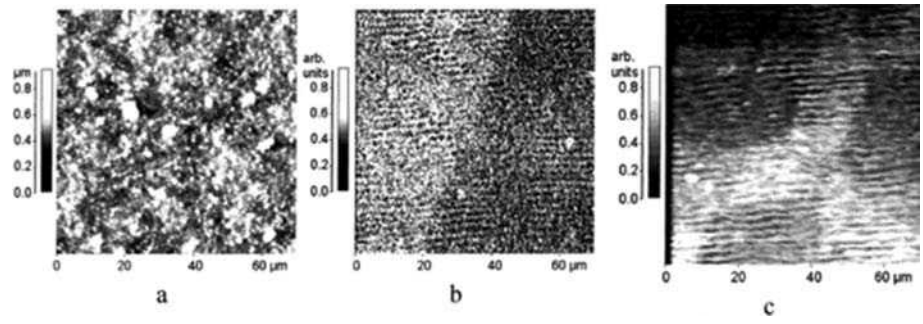

Figure 9.7 *PEOT on copper substrate, the right half of the sector irradiated with 10^{15} ions cm^{-12}: (a) AFM surface topology shows no differences between irradiated and shaded area, (b) LFM surface characterization of the same sector shows a significant contrast of irradiated and shaded area, (c) irradiated hexagonal honeycomb pattern of the same sample in the LFM-mode, scanning direction from left to right. (Reprinted with permission from Nuclear instruments and Methods in physics Research Section B: Beam Interactions with Materials and Atoms, Modification and structuring of conducting polymer films on insulating substrates by ion beam treatment by T. Asmus and G. K. Wolf, 166–167. Copyright (2000) Elsevier ltd)*

where the bright stripes represent the higher areas, and the dark stripes the lower areas. The LFM images in Figure 9.8b point to a smooth surface, which suggests that monoaniline is polymerized on both octadecyltrichorosilane (OTS)-modified ITO surfaces and bare ITO surfaces. This implies that the rate of polymerization is different in distinct patterned areas.

Another tool for conducting polymers is scanning thermal microscopy (SThM), with thermal probing of micro- and nanostructured materials and devices. SThM research is divided into three main categories: those that use (i) thermovoltage-based measurements, (ii) electrical resistance techniques, and (iii) thermal expansion measurements. SThM maps the local temperature and thermal conductivity of an interface. The probe in a scanning thermal microscope is sensitive to local temperatures, providing a nanoscale thermometer. Thermal measurements at the nanometer scale are of both scientific and industrial interest. SThM has been used by Dutta, [30], for the visualization of an ultrathin plasma polymer film of perfluoro(methylcyclohexane) at a submicrometer level. The growth of the plasma polymer film on a silicon wafer (Si-wafer) was determined using a new hole-burning technique.

The SThM technique has been used for examining the surface thermal properties of conducting polymers using microthermal analysis (μTA) [31]. The approaching-retracting mode was used to collect force–distance data concurrently with the thermal signal (see Figure 9.9), which is the current measured through the thermal probe. The authors discussed μTA results in comparison with the data collected from conventional methods of thermal analysis and concluded that the thermomechanical contribution, which is due to a variable physical contact area for a 'sinking' tip, was dominant in the microthermal response of polymers. Studies have been performed on conducting polymers and semiconductor or metal surfaces [32–33]. Nelson and King [34], used heated silicon AFM probes to perform local thermal analysis (LTA) on a polystyrene film with nanoscale spatial resolution.

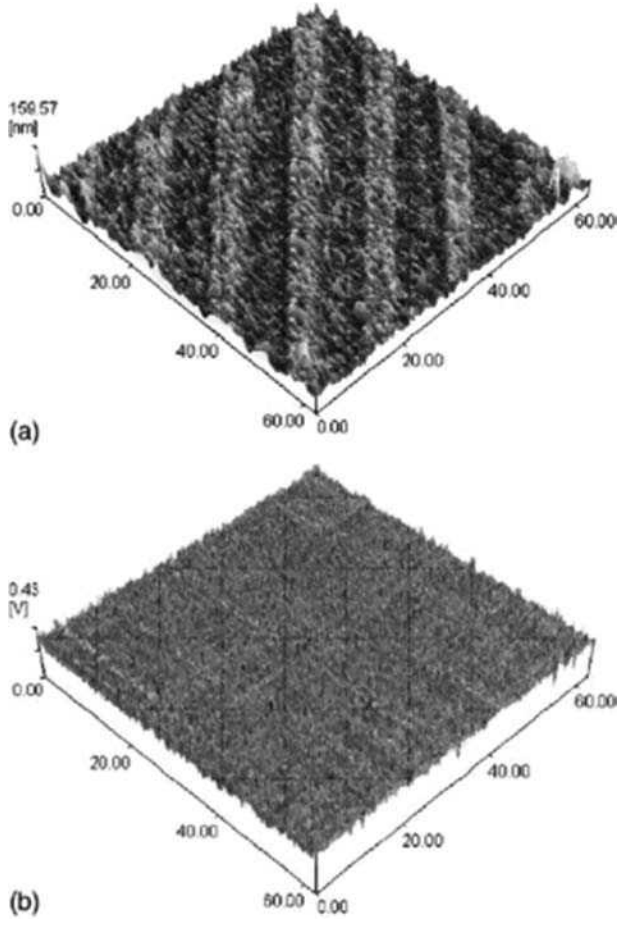

Figure 9.8 *(a) AFM and (b) LFM image of patterned PANI films (Reprinted with permission from Applied Surface Science, Fabrication of patterned polyaniline microstructure through microcontact printing and electrochemistry by Fei Guan, Miao Chen, Wu Yang et al., 230, 1–4, 131–137. Copyright (2004) Elsevier ltd)*

Hammiche *et al.*, [35], studied the thermal mapping of immiscible polymer blends, e.g. poly(vinyl chloride) (PVC)/polybutadiene (PB) and poly(methyl methacrylate) (PMMA)/chlorinated polyethylene (CPE) blends. Figure 9.10 shows a zero-frequency mode thermal image of a PVC/PB film. The image contrast is a representation of thermal conductivity variations across the sample within a depth of a few microns. The two phases are clearly apparent: brighter island-like domains identified as PB of higher thermal conductivity (0.24 J s^{-1} m^1 K^{-1}) than PVC (0.14 J s^{-1} m^1 K^{-1}), which forms the matrix. In the PMMA/CPE system, PMMA has a higher thermal conductivity than CPE (0.193 against 0.144 J s^{-1} m^1 K^{-1}) and segregates into island-like domains in a matrix of CPE. The imaging of a subsurface of metallic particles embedded in a polymer matrix was also made possible using a probe that acted as both an Ohmic heater and a thermometer [32].

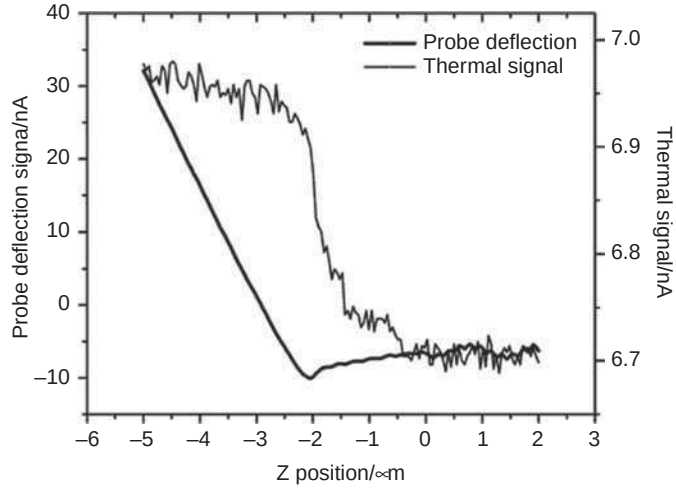

Figure 9.9 *Thermal signal and cantilever deflection vs. tip/surface during the approaching cycle for a polyethylene sample. The approaching velocity is 5 μm s^{-1} and the initial probe temperature is 50 °C. (Reprinted with permission from thermochimica Acta, Microthermal analysis of polymeric materials by V. V. Tsukruk, V. V. Gorbunov and N. Fuchigami, 395, 1–2, 151–158. Copyright (2002) Elsevier Ltd)*

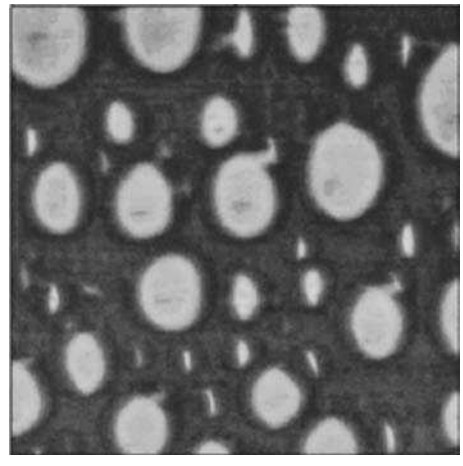

Figure 9.10 *Thermal images of a PVC/PB immiscible blend. (Reprinted with permission from Journal Of Vacuum Science and Technology B., Scanning thermal microscopy: Subsurface imaging, thermal mapping of polymer blends, and localized calorimetry by A. Hammiche, D. J. Hourston, H. M. Pollock et al., 14, 2, 1486–1491. Copyright (1996) American Institute of Physics)*

The latter authors concluded that this method could be used quantitatively to map changes in thermal conductivity in heterogeneous samples. Furthermore, the depth at which inclusions are located could be determined in cases where the thermal conductivities of the inclusions and the enclosing material are known.

Alternating current, thermal microscopy, and microthermal analysis have been utilized by Kuo and Chen, [36] for imaging the surface thermal conductivity and obtaining a local thermal analysis of polybutadiene–polyaniline core-shell microparticles. The significant changes in thermal conductivity and stiffness between rubber and the conducting polymer revealed the remarkable responses in the microthermal analysis. The depth-dependent thermal microscopy controlled by the heating frequency distinguished the rubber core, which was buried under a few-micron thick polyaniline outer layer. Local thermal analysis also demonstrated the heat penetration-dependent sensor response from the rigid polyaniline shell to the soft polybutadiene core. These experimental results confirmed the core-shell structure of the microparticles, as well as the continuous conducting phase of polyaniline. The sensor responses of PSS–PANI and PSSB4–PANi1 are shown in Figure 9.11a, while Figure 9.11b displays the responses for PSS–PANI and PSSB4–PANI7. Three selected locations are shown in the topographic images before and after the three LTA measurements.

AFM measurements with an oscillating cantilever can be performed in C-AFM modes, using the ac-contact mode. In contrast to vibrating modes, in which the amplitude of the vibrating cantilever is in the 20–100 nm range, in the ac-contact mode the amplitude is smaller to prevent tip–sample disconnection [37]. A peculiarity of the ac-contact mode is that the sample area nearest the cantilever also oscillates, not only on the normal (out-of-plane), but also on the lateral directions. Moreover, the cantilever can oscillate in higher harmonics. Measurements in ac-contact modes are carried out simultaneously with topography measurements and allow determining contact stiffness, Young's modulus (force-modulation mode, atomic force acoustic microscopy) and other sample parameters, e.g., electric forces (contact-electric-force microscopy) and magnetic properties (magnetic sample modulation). Force modulation microscopy (FMM) [38] allows recording of the local mechanical compliance and maps differences in surface stiffness or elasticity, but has rarely been used to measure the local viscoelasticity of conducting polymers.

Daniels *et al.* [39] investigated the magnetic properties of ferritin, a spherical iron-storage protein with a hollow shell enclosing a cavity containing iron atoms, using an AFM with magnetic sample modulation (MSM), as the iron cores of ferritin are ferromagnetic, thus providing a well-defined reference sample for magnetic imaging. Figure 9.12 shows baseline reference images without the influence of a magnetic field (Figure 9.12A–C) and the same sample with an applied AC field (0.2 T, 96 kHz) to acquire the MSM images (Figure 12D–L). The MSM amplitude and phase images clearly distinguish the locations of ferritin, with good contrast for the rings and for the individual proteins located between rings.

The shell of ferritin may act as an electron conductor [40–42], which has motivated studies of ferritin adsorption on gold surfaces [42]. Xu and Davis [43] used the conductive-AFM technique (c-AFM) [44] to measure the conductivity of single ferritin molecules on flat gold surfaces. C-AFM was used to measure the local conductivity of thin molecule layers by positioning the conductive tip on the top of the thin film layer.

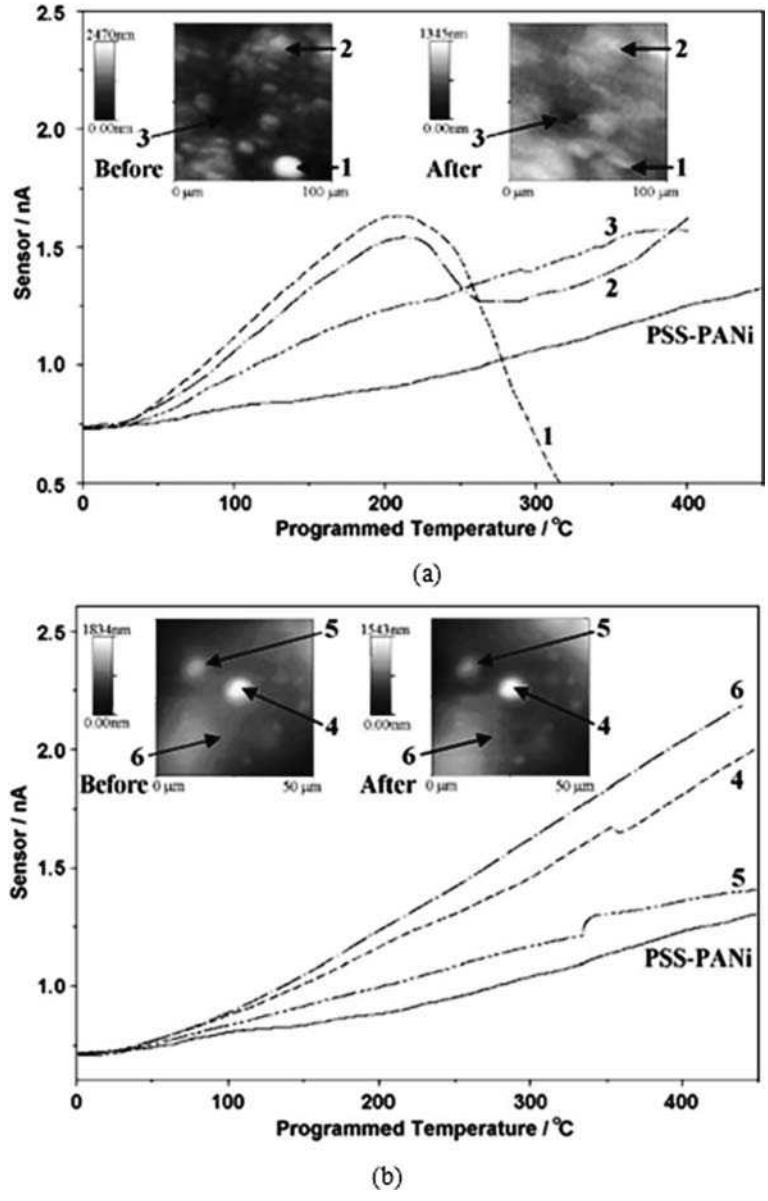

Figure 9.11 *(a) Sensor responses of PSS–PANI and PSSB4–PANI1 with three selected locations, as shown in the two topographic images in the inset, before and after the measurements. (b) Sensor responses of PSS–PANI and PSSB4–PANI7 with three selected locations, as shown in the two topographic images in the inset, before and after the measurements. (Reprinted with permission from Thermochimica Acta, Microthermal analysis of rubber-polyaniline core-shell microparticles using frequency-dependent thermal responses by Changshu Kuo, Chien-Chung Chen and William Bannister. 403, 1, 115–127. Copyright (2002) Elsevier Ltd)*

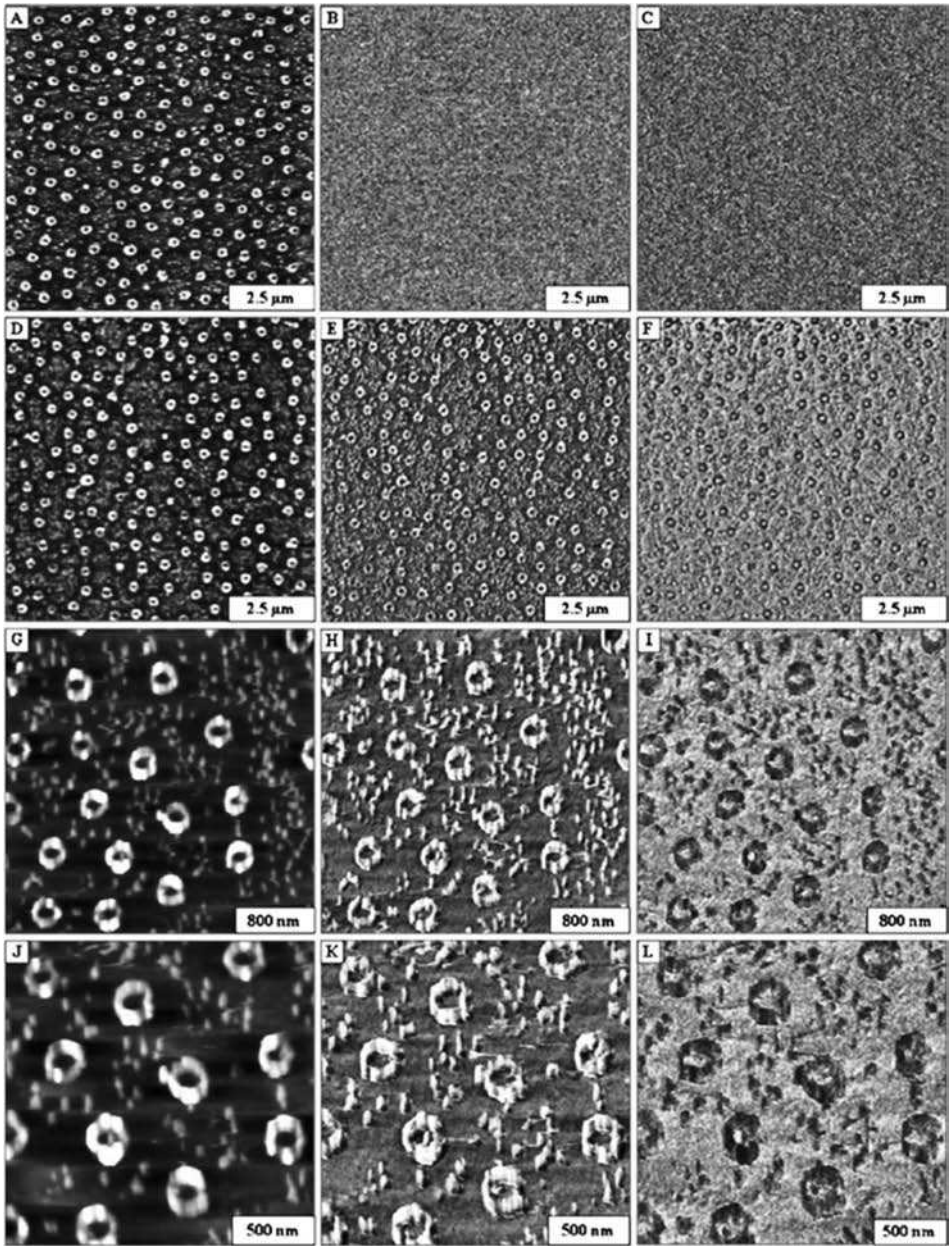

Figure 9.12 *AFM images of ferritin ring structure acquired with MSM: (A, B, C) topography images acquired with contact mode; (D, E, F) topography acquired using MSM; (G–L) zoom-in MSM topography. (Reprinted with permission from Analytical and Bioanalytical Chemistry, Investigation of the magnetic properties of ferritin by AFM imaging with magnetic sample modulation by S. L. Daniels, 394, 1, 215–223. Copyright (2009) Springer Science + Business Media)*

9.2.2.2 Vibrating Modes

There are two main types of vibrating mode: the first is often known as the tapping or intermittent-contact mode (IC–AFM) [45], whilst the second is usually called the non-contact mode (NC–AFM) [46]. In the IC-AFM depicted in Figure 9.13a, the cantilever is deliberately excited by an electrical oscillator to amplitudes of up to 100 nm, so that it effectively bounces up and down (or taps) as it travels over the sample [11]. The oscillation amplitude is measured as a root mean square (RMS) value of the deflection signal. The feedback system is set to detect the perturbation of the oscillation amplitude caused by the intermittent contact with the surface [47]. A relatively small shift in the oscillating frequency with sensing repulsive forces means that the contact of the cantilever tip with the sample surface under oscillation is not constant. Only during a small part of the oscillating period does the tip 'feel' the contact repulsive force. When the tapping mode is carried out in liquids, the tip of the cantilever taps the sample gently during part of the force curve; this mode is similar to the tapping mode operating in air, except that the sample is tapped against the tip instead of the cantilever being driven at resonance to tap the sample [48].

The IC mode has some advantages over the dc-contact mode. The pressure of the cantilever on the surface is lower, which allows one to work with softer and easy-to-damage materials such as conducting polymers. The IC mode is also more sensitive to the interaction with the surface; hence, surface characteristics, such as distribution of magnetic and electric domains, elasticity and viscosity, are investigated more precisely. When the vibrating probe tip touches the sample surface it experiences not only repulsive, but also adhesive, capillary, and other forces. So the interaction between the tip and the sample surface yields changes in frequency as well as in the phase. If the sample surface is not homogeneous, phase shifts will be measured upon scanning the surface. This mode of operation is referred to as phase contrast imaging mode.

In the NC mode depicted in Figure 9.13b, the oscillating cantilever never actually touches the sample surface. The spacing between the tip and sample is of the order of tens to hundreds of angstroms, with an oscillation amplitude of only about 5 nm. The NC mode usually involves a sinusoidal excitation of the cantilever with a frequency close to its main resonant frequency. In this mode, van der Waals (vdW) forces are in effect. Some

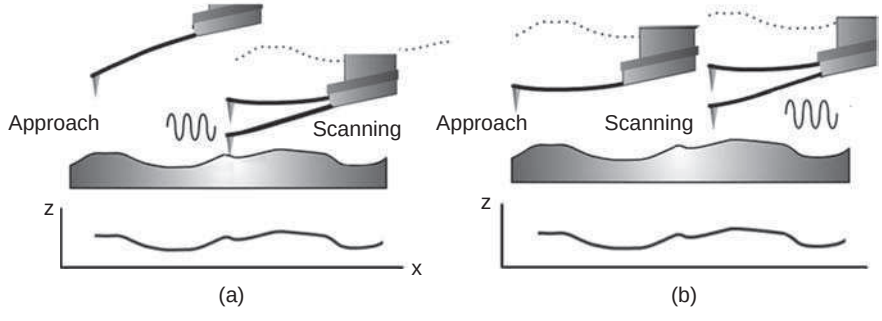

Figure 9.13 *Vibrating modes: (a) tapping or intermittent contact mode (~100 nm amplitude) and (b) noncontact mode (~1 nm amplitude). (Reproduced with kind permission from Denis Andreyuk, NT-MDT Co. www.ntmdt.com)*

other forces could be in action, such as electrical and magnetic forces; however, if the surface is not charged and if the surface and tip are not ferromagnetic, the predominant forces are vdW. A schematic representation of the noncontact mode is given in Figure 9.13b. When the tip is away from the surface, the cantilever is made to oscillate close to its resonance frequency with a given amplitude. The oscillation of the deflection signal is measured by a lock-in amplifier, where the reference is the driving frequency of oscillation to obtain the topography.

Mattoso *et al.* [49] observed that adsorption of POEA chains is faster and more effective for pH 1, which is due to an increase in the electrostatic attraction of the polymeric molecules to the substrate (glass). This result was confirmed by Paterno and Mattoso, [50] using self-assembled films of POEA doped with HCl alternated with sulfonated lignin (SL) at different pH values. The adsorption at lower pH is faster owing to the greater electrostatic attraction between the POEA and the SL-covered substrate, but a lower amount of POEA is deposited due to charge repulsion of the additional POEA chains and conformational steric hindrance. At higher pH the adsorption of POEA takes longer, but it is more effective for three reasons: stronger contribution from hydrogen bonding, lower charge repulsion between POEA chains, and a more compact polymer conformation. AFM was employed to investigate the morphology of the alternating layers, in which POEA layers were granular and rough, while SL layers were much smoother. Figure 9.14 shows an AFM image of a five-bilayer POEA/SL film prepared at pH 3, with POEA at the uppermost layer exhibiting a granular structure. This is better illustrated in Figure 9.14b, where a rough granular surface appears for the POEA layer, whereas a significantly flatter one is seen for the SL surface.

Souza *et al.* [51–52] studied adsorption processes in LbL films of poly(*o*-methoxyaniline)/poly(vinyl sulfonic acid) (POMA)/PVS, particularly the role of aggregation and the influence of solution treatment on the adsorption and morphology of the films. Figure 9.15 shows a sequence of AFM images for POMA/PVS films prepared with solution 1 (1.202 g of POMA was swollen in 20 ml of acetonitrile, which was then diluted with 980 ml of ultrapure water). The images correspond to a POEA layer deposited on 10 bilayers of POMA/PVS, where each layer was adsorbed for 3 min. The structure is globular, similar to that for PANI films obtained with other techniques, with the size of the grains increasing and decreasing as the time of adsorption increases.

The adsorption processes to form films with conducting polypyrroles (PPy) have also been studied [53–55]. Taranekar *et al.* [56] produced electropolymerized films of polysiloxane-functionalized pyrrole or poly(methyl-(undec-pyrrole-1-yldecyl)- siloxane), whose topography and phase images are shown in Figure 9.16. Unique 'nanoscale' morphologies were formed because of phase-segregation of polysiloxane domains and cross-linked PPy, depending on the thickness and electrochemical conditions. From the AFM images, one infers that relatively smooth films were formed together with the appearance of phase-separated 'dot' structures, which change in size and distribution with composition.

Other studies exist involving conducting polymer films using the static (contact) and dynamic modes (noncontact and tapping) [8,50,57–68].

Pruneanu *et al.* [69], studied self-assembly of DNA-template PPy nanowires using the noncontact mode, whose images are shown in Figure 9.17. The thickness of the nanowires appears to increase after a reaction time of 24 h, with thicker nanowires being entangled

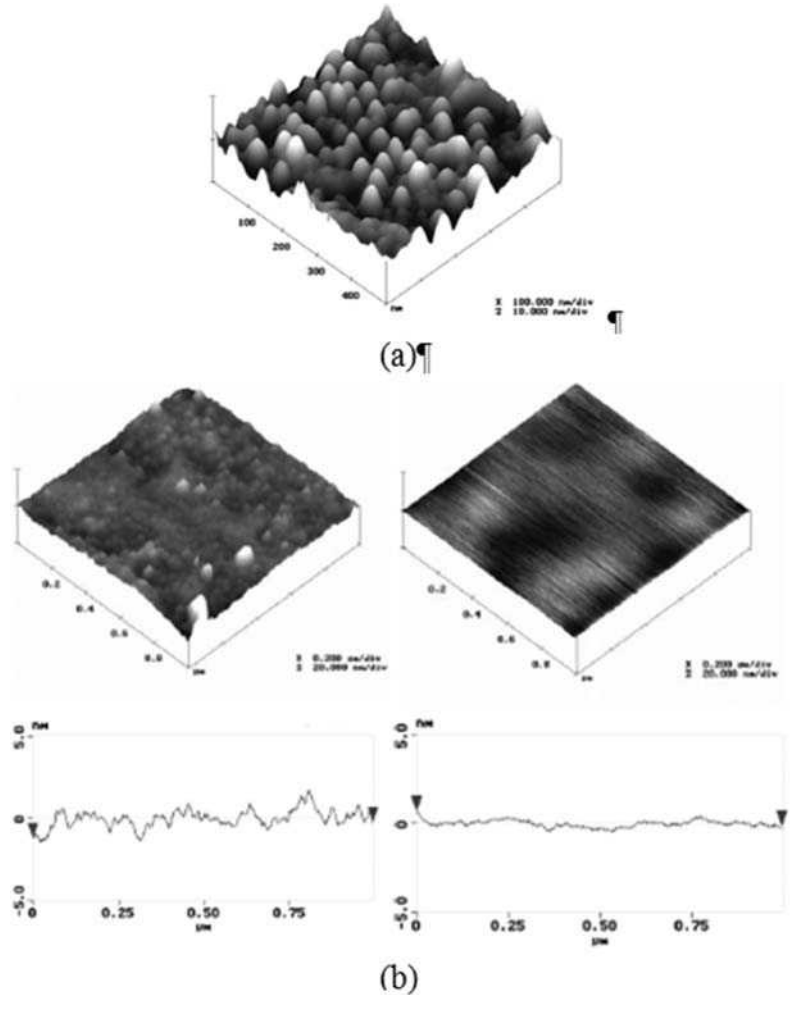

Figure 9.14 *AFM images (tapping mode) of a five-bilayer film of HCl-doped POEA layers alternated with SL layers, showing the surface of the fifth layer of POEA (500 nm × 500 nm 3-D image): (a) 1mu × 1 mu image of a film containing only one layer of POEA and its cross-section profile; (b) 1mu × 1 mu image of a film containing one bilayer of POEA/SL and its cross-section profile. (Reprinted with permission from Polymer, Effect of pH on the preparation of self-assembled films of poly(o-ethoxyaniline) and sulfonated lignin by Leonardo G. Paterno and Luiz H. C. Mattoso, 42, 12, 5239–5245. Copyright (2001) Elsvier Ltd)*

bundles, as seen in Figure 9.17b and 9.17c. Over longer periods of times, a self-assembly process occurs, with conducting polymer/DNA nanowires forming nanopores.

Another widely used application of dynamic modes is the investigation of surface electrical characteristics. Electrical force microscopy (EFM) comprises a set of related techniques [70], and provides the possibility of probing localized charge distribution,

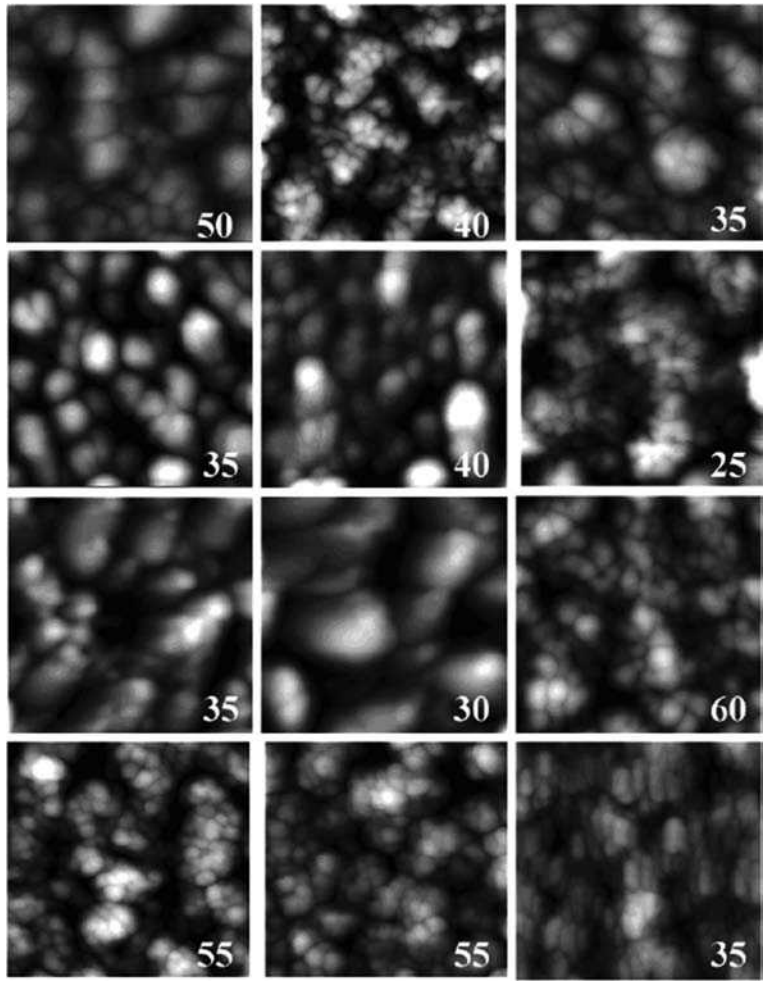

Figure 9.15 *AFM images (tapping mode) of LbL films with a POMA layer adsorbed on top of 10 bilayers of POMA/PVS, obtained using solution 1. The time periods of adsorption for the 11th layer were 0, 10, 30 s; 1, 2, 10, 15, 30 min; 1, 2, 3, and 12 h (starting from the top left corner and moving to the right and down). The scanned length was* $L = 500$ *nm. The number annotated in each image refers to the surface height (z axis). (Reprinted with permission from Journal of Physical Chemistry B., Influence of Solution Treatment on the Adsorption and Morphology of Poly(o-methoxyaniline) Layer-by-Layer Films by N. C. de Souza, J. R. Silva, R. Di Thommazo et al., 108, 36, 13599–13606. Copyright (2004) American Chemical Society)*

surface potential, and doping profiles at the surface [71]. The scanning Kelvin probe microscope (KPM), which detects the local surface potential, can be used to investigate structural properties of Langmuir–Blodgett (LB) and self-assembled films, since the surface potential depends on the orientation and packing of the chains.

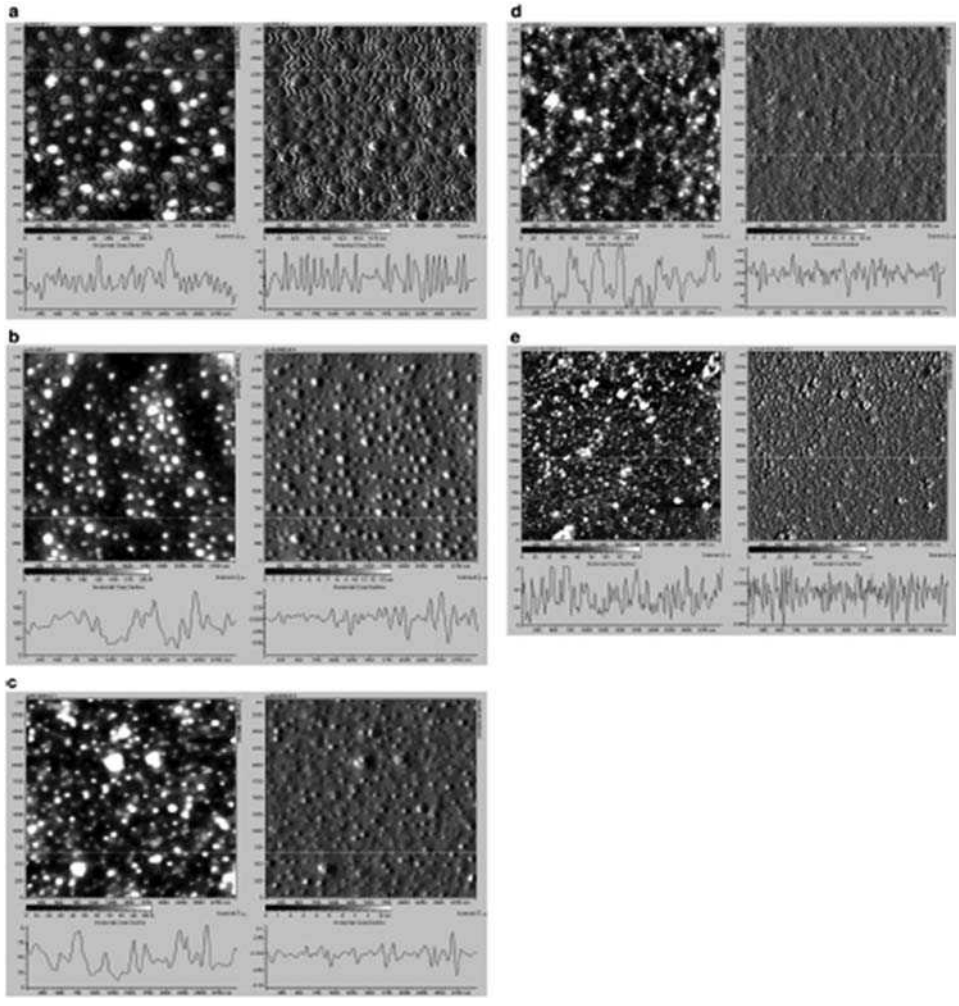

Figure 9.16 *AFM images (noncontact mode) of (a) pure precursor polymer, (b) 10% pyrrole copolymer, (c) 50% pyrrole copolymer, (d) pure polypyrrole, and (e) precursor 1 on an Au electrode. (Reprinted with permission from Langmuir, Distinct Surface Morphologies of Electropolymerized Polymethylsiloxane Network Polypyrrole and Comonomer Films by P. Taranekar, X. Fan, and R. Advincula, 18, 21, 7943–7952. Copyright (2002) American Chemical Society)*

EFM has been used by Barisci *et al.* [72] to characterize the surface morphology and the surface potential (SP) of conducting polymer films. The AFM/EFM images in Figure 9.18 exhibit the following features: (i) the film morphology is globular, typical of conducting polymers [11], with grains ranging from 50 to 100 nm; (ii) the EFM map shows that the SP distribution is not uniform, i.e. the material is heterogeneous; (iii) the top of the grains is more doped than the peripheral regions. Significantly, in electrochemically prepared films

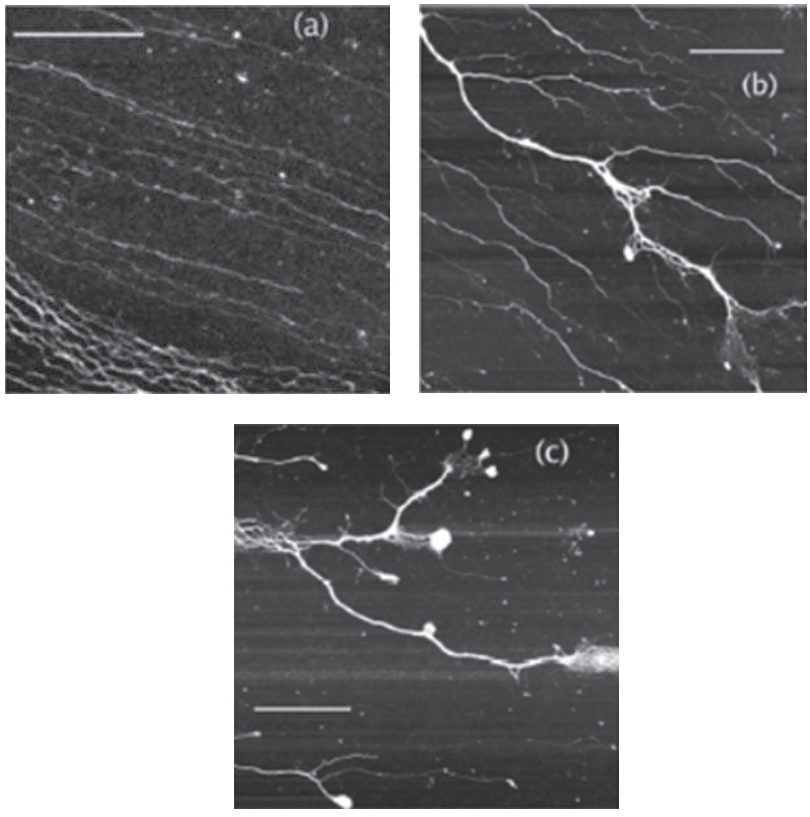

Figure 9.17 *AFM images of PPy-DNA nanowires and nanopores on a SiO_2/Si surface: (a) nanowires observed 3 h after preparation; (b) and (c) two representative images of 'nanorope' samples observed after standing for 24 h. (Reprinted with permission from Advanced Functional Materials, Self-Assembly of DNA-Templated Polypyrrole Nanowires: Spontaneous Formation of Conductive Nanoropes by S. Pruneanu, S. A. Farha Al-Said, L. Dong et al., 18, 16, 2444–2454. Copyright (2008) Wiley-VCH)*

the work function in the grains was higher than in the surrounding areas, suggesting a higher dopant concentration in the grains [73–74].

Barisci *et al.* [75] also used EFM to verify the effect of the polymer composition, preparation method, and nature of the substrate on the surface potential (SP). Both the average value and the distribution of the SP across the polymer surface are influenced by these factors. Polythiophene (PTh) polymers, potentially useful for solar energy conversion, were used to examine the generation of light-induced changes in SP. Bush and Maboudian [76] studied the influence of $FeCl_3$ oxidant concentration on the electric and morphological properties of LbL films, with a polyanion (polystyrene) and a polycation (PPy). Using EFM, the film morphology was found to exhibit globular structures with an approximate grain size of 28 nm and 60 mV surface potential distribution

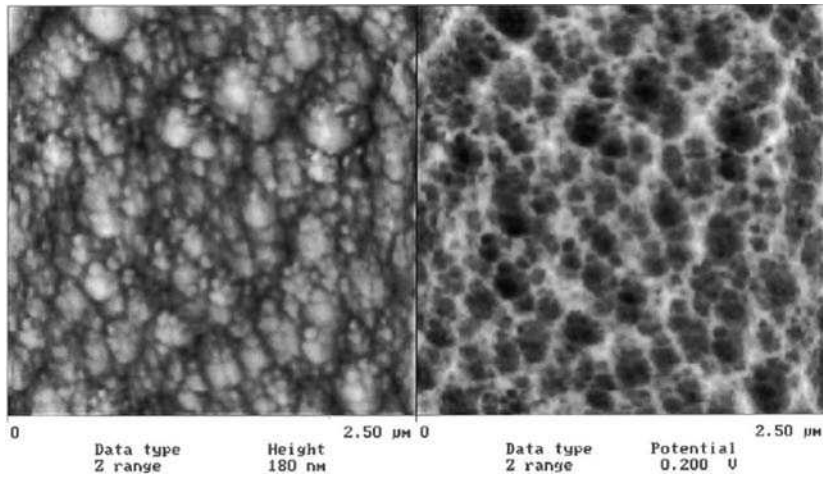

Figure 9.18 *Topography image (left), and SP image (right), of a PPy/*p*-toluene sulphonate (PTS) film grown potentiostatically at 0.6 V for 5 min, thickness 150 nm. (Reprinted with permission from Electrochimica Acta, Characterisation of the topography and surface potential of electrodeposited conducting polymer films using atomic force and electric force microscopies by J. N. Barisci, R. Stella, G. M. Spinks and G. G. Wallace, 46, 4. Copyright (2000) Elsevier Ltd)*

(see Figure 19.9). The top of the grains displays the higher surface potential, corroborating Barisci *et al.* [72] and Semenikhin *et al.* [77].

With EFM, Jespersen [78] was able to map individual single-wall carbon nanotubes (SWCNTs) in spin-cast polymer/SWCNT composites. By correlating the measured EFM amplitude with its dependence on the SWCNT length and tip–tube separation they showed that the technique can be used for mapping the three-dimensional position of the SWCNTs in the polymer matrix. The technique provided important information about the homogeneity of the incorporated SWCNT; because individual nanotubes can be identified, the distribution of lengths and orientation could be measured. Such 3-D mapping is promising for optimizing nanotube distributions in nanocomposite materials.

EFM was employed by Patricio *et al.* [79] in the electrical characterization of a blend of thermoplastic polyurethane (TPU) and poly(2-methoxy-5-(20-ethyl-hexyloxy)-1, 4-phenylenevinylene) (MEH-PPV)-conjugated polymer. Although a qualitative EFM interpretation is straightforward, its quantitative analysis always relies on approximated models. The extraction of physically reasonable parameters is normally assumed as a proof of validity of the theoretical model employed. In order to gather information about the electrical properties of this blend and to test the EFM technique itself, two distinct models were developed to fit the experimental EFM data. Even though MEH-PPV was regarded as a conductor in one model and as a dielectric in the other, both models yielded coherent and reasonable electrical properties for this blend. Such unexpected results were used to discuss the robustness of EFM in the analysis of complex materials. Figure 9.20 shows the AFM (a) and EFM (b through g) images of the MEH-PPV/TPU blend. It was concluded that: (i) the sole fact that an EFM model fits a data set should not be used as a certification

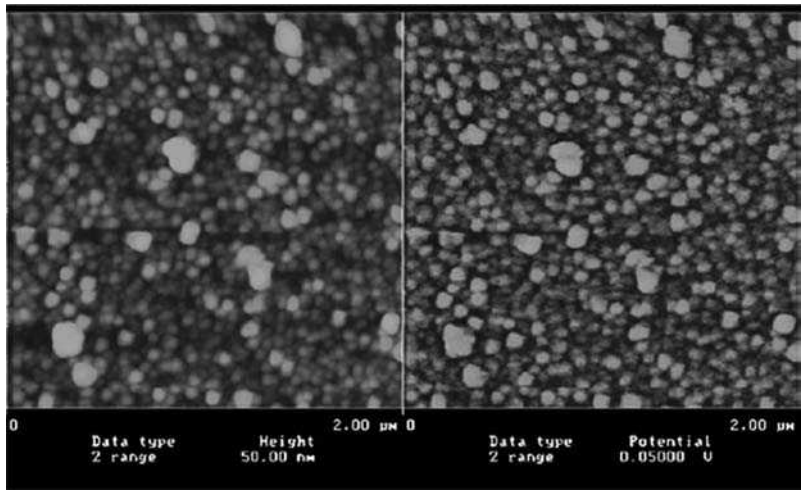

Figure 9.19 *Simultaneous 2 μm × 2 μm image of film topography (left) and surface potential (right) of a seven-bilayer, 30 nm $MFeCl_3$, Ppy/SPS bilayer films. The Z-scale ranges are 50 nm for the topography and 50 mV for the surface potential. (Reprinted with permission from Sensors and Actuators A: Physical, Layer-by-layer self-assembled conductive thin films for MEMS applications by B. Bush, G. Xu, C. Carraro and R. Maboudian, 126, 1, 194–200. Copyright (2006) Elsevier Ltd)*

of its physical meaningfulness; and (ii) the concomitant use of additional, or even dissonant, models might prove to be useful as a route for a thorough EFM analysis of multicomponent complex materials.

In a magnetic force microscope (MFM), a probe coated with a magnetic film is vibrated slightly above a surface while scanning. As with EFM, the resolution achievable with MFM depends on the thickness and quality of the coating at the apex of the probe. This is often very difficult to control so the results from MFM are fairly inconsistent. Also, when trying to measure the magnetic domains on a soft magnetic material, the domains on the probe can cause a change in the domain structure on the surface. Santa Maria *et al.* [80] used AFM to investigate the morphology and the phase difference of composite materials based on styrene (STY) and divinylbenzene (DVB), containing iron particles. MFM images were obtained in order to evaluate the magnetic character of the iron particles. Figures 9.21b and 9.21d indicate that the magnetic phases are located not on the center of the palettes, but on the interface between palette layers, as well as in small microspheres and valleys on the bead surface.

Modified poly(methacrylic acid) microparticles complexed with gadolinium(III) (Gd^{3+}) ions were prepared at 100 nm by Michinobu [81]. The emulsion terpolymerization of methacrylic acid, ethyl acrylate, and allyl methacrylate and the following complexation with Gd^{3+} ions yielded the polymer particles with different Gd^{3+} ion contents. Potentiometric titration of the complexation of the particle with Gd^{3+} ions indicated the formation of a very stable tris-carboxylate coordinate complex with the Gd^{3+} ion. The microparticles dispersed on a mica substrate were subjected to AFM, followed by MFM. AFM showed 100-nm-sized and monodispersed spherical images. The following MFM

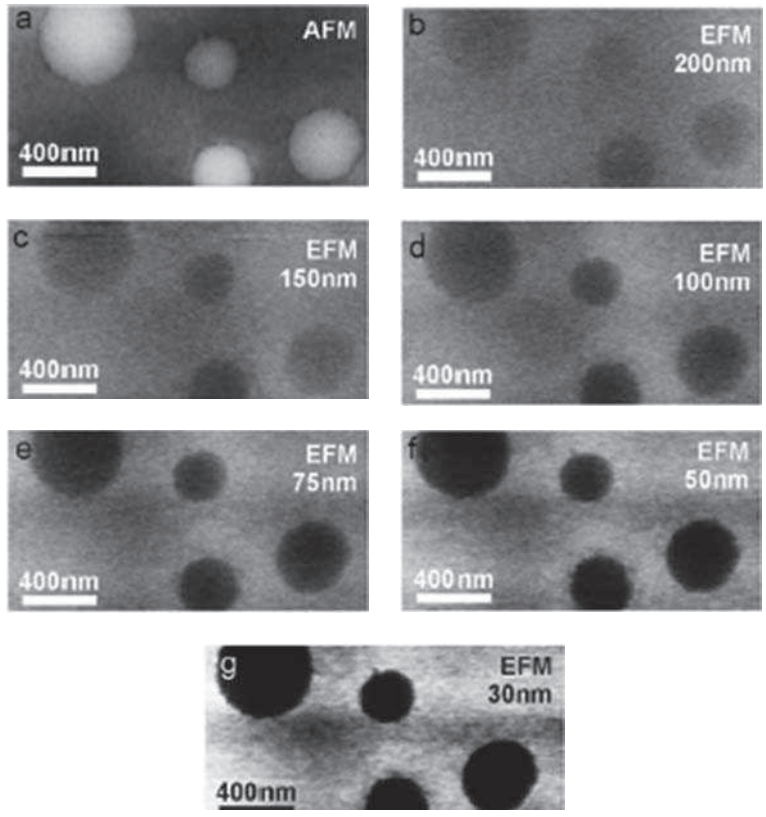

Figure 9.20 *AFM (a) and EFM (b through g) images of the MEH-PPV/TPU blend. The scale bar at the bottom left of each image indicates its dimension. Images (b), (c), (d), (e), (f), and (g) were acquired with at a bias* $\vee_T = 5$ *V and tip–sample distance* z *equal to 200, 150, 100, 75, 50, and 30 nm, respectively. The grayscale in image (a) corresponds to a height variation of 50 nm, and in images (b) through (g), to a frequency variation of 20 Hz. (Reprinted with permission from Ultramicroscopy, Electric force microscopy investigation of a MEH-PPV conjugated polymer blend: Robustness or frailty? by P.S.O. Patrício, L.A. Cury, G.G. Silva, B.R.A. Neves, 108, 4, 302–308. Copyright (2008) Elsevier Ltd)*

clearly provided strong magnetic responses at exactly the same particle positions, of which the images were also dependent on the Gd^{3+} ion content in the particle.

The use of magnetic nanoparticles in the development of ultra-high-density recording media is the subject of intense research. Much of the attention of this research is devoted to the stability of magnetic moments, often neglecting the influence of dipolar interactions.

AFM also provides information on the lateral distribution of the surface potential over a sample. The term surface potential in this context means the potential difference between the sample and a conducting probe that is positioned close to the sample. This is so-called Kelvin probe force microscopy (KFM) [46], which offers a possibility of distinguishing between regions with different chemical natures or compositions. For example,

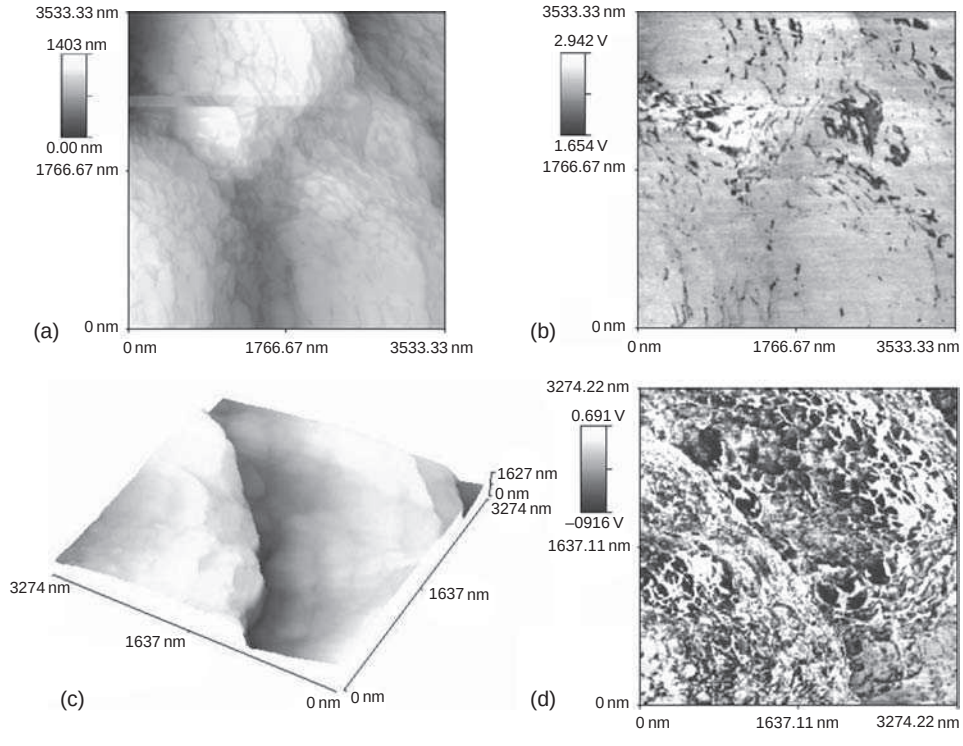

Figure 9.21 *MFM images of a poly(styrene-co-divinylbenzene) bead containing iron: (a) topographic image; (b) out of phase MFM image – 15 nm apart from the surface of one region of one bead; and (c) topographic 3D image and (d) out of phase MFM image – 15 nm apart from the surface of one region of another bead. (Reprinted with permission from Microscopy and Microanalysis, AFM Characterization of Composite Materials Containing Iron in a Resin Host Based on Styrene and Divinylbenzene by L. C. de Santa Maria, M. A. S. Costa, L. F. Senna et al., 11, S3, 166–169. Copyright (2005) Cambridge University Press)*

Semenikhin *et al.* [77], studied evidence of local structural inhomogeneity and nonuniform dopant distribution in conducting polybithiophene (PBT). The KFM data suggested that the polymer consists of grains that differ in work function and thus in the dopant concentration from the peripheral regions (see Figure 9.22). For the as-grown polymer, most of the doping charge is located at the grain tops. The origin and characterization of the structural inhomogeneity and local potential distribution of conducting polymer have been studied by other groups using KFM [82–84].

9.2.3 Force Spectroscopy

AFM can be used to determine the dependence of the interaction on the probe–sample distance at a given location [85], in so-called atomic force spectroscopy (AFS). Both the

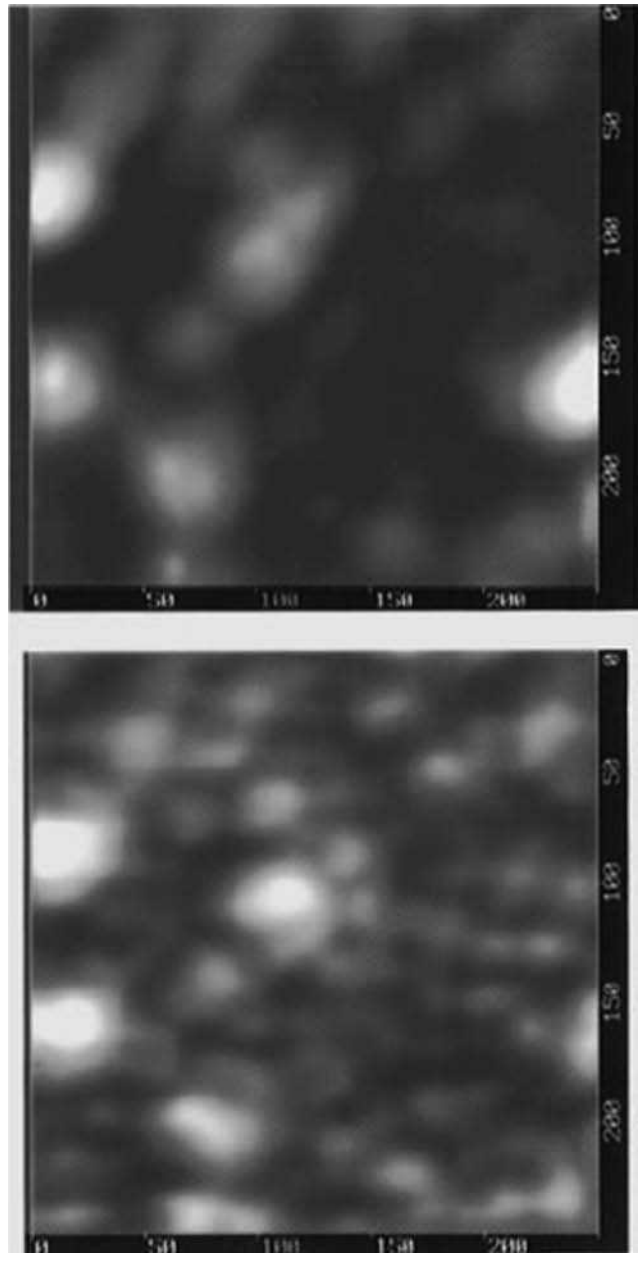

Figure 9.22 *Simultaneous images of (a, top) topography and (b, bottom) surface potential acquired with an as-grown PBT film in the KFM feedback mode. (Reprinted with permission from Journal of Physical Chemistry B., On the origin of Mesoscopic Inhomogenity of Conducting Polymers by K. D. O'Neil et al., 111, 31. Copyright (2007) American Chemical Society)*

dynamic and static modes can be used to locally detect forces, thus comprising a local probe for studying the mechanical properties of the sample. The type of information one may infer from a force curve is depicted in Figure 9.23. AFS may be performed in two ways: local force (LFS) and force imaging spectroscopy (FIS). In LFS, the force curve is determined at a particular location on the sample surface. Force curves are plots of the deflection of the cantilever (force) vs. the extension of the piezoelectric scanner (sample displacement); if the cantilever spring constant is known, then the deflection can be converted into force. These curves can be used to measure the vertical force that the tip applies to the sample surface and to study the surface properties of the sample, including the elastic deformation of soft samples. They can also be used to monitor the unfolding of protein molecules as the latter are pulled from the sample surface by the AFM tip.

Segment a–d represents the first half cycle (approach curve) while segment d–h is the second half cycle (withdrawal curve) of the curve. These cycles can be divided roughly into three regions: the contact line, the noncontact region, and the zero line. The zero line is obtained when the tip is far from the sample and the cantilever deflection is close to zero. When the sample is pressed against the tip, the corresponding cantilever deflection plot is referred to as the contact line, which can provide information on sample stiffness. The most interesting regions of the force curve are two noncontact regions, containing the JTC and the JOC. The noncontact region in the approach curve provides information about attractive (vdW or Coulombic forces) or repulsive forces (vdW in some liquids, double-layer, hydration, and steric forces) before contact; this discontinuity occurs when the

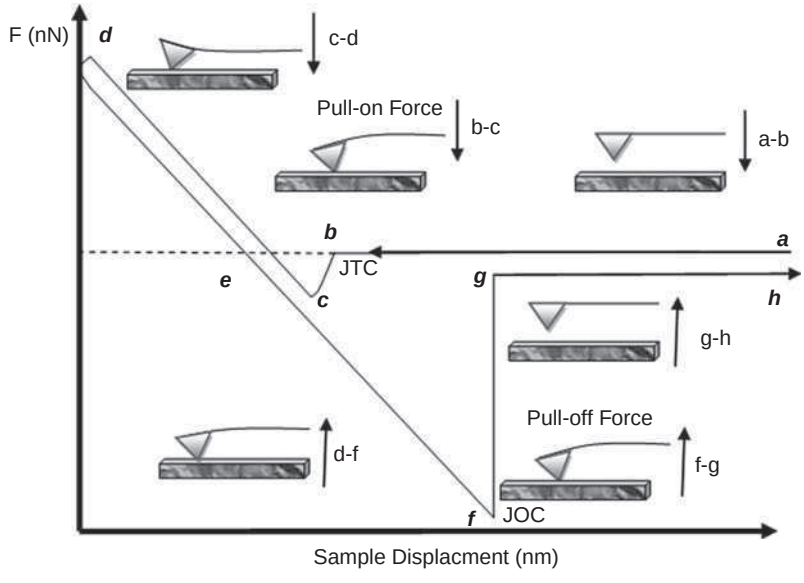

Figure 9.23 *Force curve on wood surface illustrating the points where jump-to-contact (JTC) (approach) and jump-off-contact (JOC) (withdrawal) occur and the maximum values of the attractive force (pull-on force and pull-off force)*

gradient of the tip–sample force exceeds the spring constant of the cantilever. The maximum forward deflection of the cantilever multiplied by the effective spring constant of the cantilever is the pull-on force [86]. The noncontact region in the withdrawal curve contains the jump-off-contact, a discontinuity that occurs when the cantilever's spring constant is greater than the gradient of the tip–sample adhesion forces. The maximum backward deflection of the cantilever multiplied by the effective spring constant of the cantilever is the pull-off force [86].

In the mid-1990s, the idea of collecting data from force–distance curves obtained from many points on a sample was introduced, effectively to produce a map of the tip–surface interactions [87]. Layered imaging is an SPM technique in which several measurements of cantilever deflection are made at each image pixel. Each measurement of a deflection at a given displacement is recorded. When all measurements for the current pixel are completed, the process is repeated at the next pixel and so on through the scan area. The resulting spatial maps represent the lateral variation of adhesion force due to material inhomogeneities and the surface topography [11]. The resulting three-dimensional data set can be thought of as a stack of 'layers' of images. Each horizontal layer is an image which represents measurements taken throughout the scanned area at a specified height z. Since several measurements are made at each pixel, the data set can also be processed vertically to yield the force–distance curve at each pixel. This force imaging spectroscopy (FIS) mode of AFM can thus be used to measure adhesion, hardness, or deformability of samples [11].

AFS was used by Leite *et al.* [88] to measure interaction forces between the tip and nanostructured layers of POEA in pure water and $CuSO_4$ solutions. When the tip approach and retraction were carried out at low speeds, POEA chains could be physisorbed onto the Si_3N_4 tip via nonspecific interactions. The authors conjectured that while detaching POEA chains were stretched and the estimated chain lengths were consistent with the expected values from the measured POEA molecular weight (see Figure 9.24). The effects from POEA doping can be investigated directly by performing AFS measurements in a liquid cell, with the POEA film exposed to liquids of distinct pH values. For pH $\geq$6.0, the force curves normally display an attractive region for POEA, but at lower pH values – where POEA is protonated – the repulsive double-layer forces dominate. Measurements in the liquid cell can be further exploited to investigate how the film morphology and the force curve are affected when impurities are deliberately introduced in the liquid. The shape of the force curves and the film morphology depend on the concentration of heavy metal in the liquid cell. AFS may therefore be used to study the interaction between the film and the analyte, with important implications for the understanding of mechanisms governing the sensing ability of taste sensors. The interaction forces and interface phenomena in conducting polymers have also been studied by Franceschini and Corti [89] and Zheng *et al.* [90].

AFS has been used in the investigation of conductivity in polymers, namely PANI and its derivatives (POEA and POMA). The degree of protonation and the conductivity vary within the PANI class, which is attributed to differences in conformation of the polymer chains and packing in a film. The mechanisms of charge conduction are still not completely understood, precisely because of the diversity of factors affecting conductivity. It is, nevertheless, widely accepted that in the PANI structure the doped molecules are not uniformly distributed, but rather agglomerated into conducting islands. In a systematic

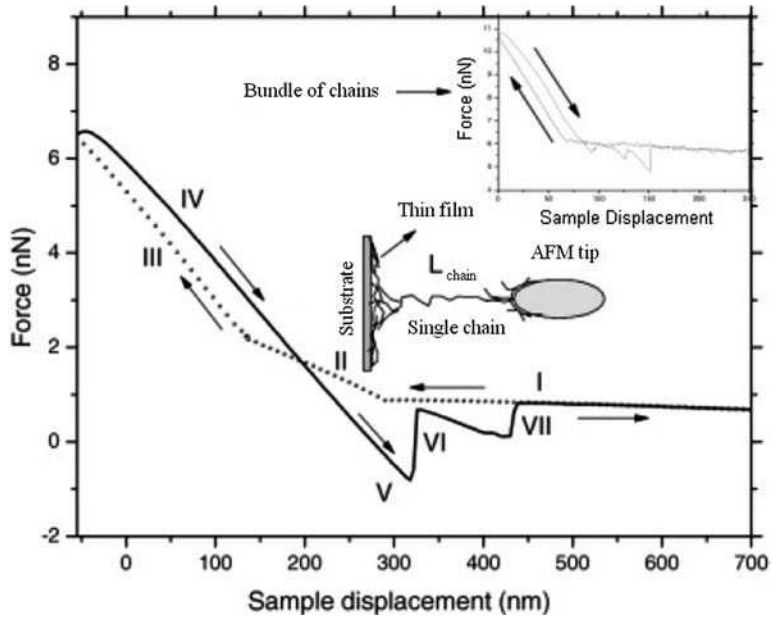

Figure 9.24 *Force curve obtained when extending chains of POEA from the chrome surface in water with frequency of jumps $< 1\,\mu m\ s^{-1}$: I: no tip-POEA interactions; II: film being compressed; III/IV: repulsive contact with the substrate; V: pull-of force due to surface adhesion; VI: cantilever 'pulls off' the surface; VII: attractive peak due to stretching of POEA chains. (Reprinted with permission from Microscopy and Microanalysis, Atomic Force Spectroscopy on Poly(o-ethoxyaniline) Nanostructured Films: Sensing Nonspecific Interactions by F.L. Leite, C.E. Borato, W.T.L. da Silva, P.S.P. Herrmann, O.N. Oliveira Jr., L.H.C. Mattoso, 13, 304 (Copyright 2007).*

study by Leite *et al.* [88] using adhesion maps, POEA films were prepared at different pH values, with the doping level and fabrication conditions affecting the POEA film morphology and the interactions of the atomic force microscopy (AFM) tip with the polymer molecules. For example, mapping of the forces indicated the presence of conducting islands surrounded by a less conductive matrix in POEA and PANI films, with the conducting islands being characterized by the presence of double-layer forces (see Figure 9.25).

The study of intermolecular interactions at interfaces is essential for a number of applications, in addition to the understanding of mechanisms involved in sensing and biosensing with liquid samples. There are, however, only a few methods to probe such interfacial phenomena, one of which is AFS. Leite *et al*. [92] used force curve measurements to estimate adhesion forces for a nanostructured film of POEA doped with various acids, in measurements performed in air. The adhesion force was lower for POEA doped with inorganic acids, such as HCl and H_2SO_4, than with organic acids, because the counterions were screened by the ethoxy groups. Significantly, the morphology of POEA both in the film and in solution depends on the doping acid. In AFS measurements in a liquid cell,

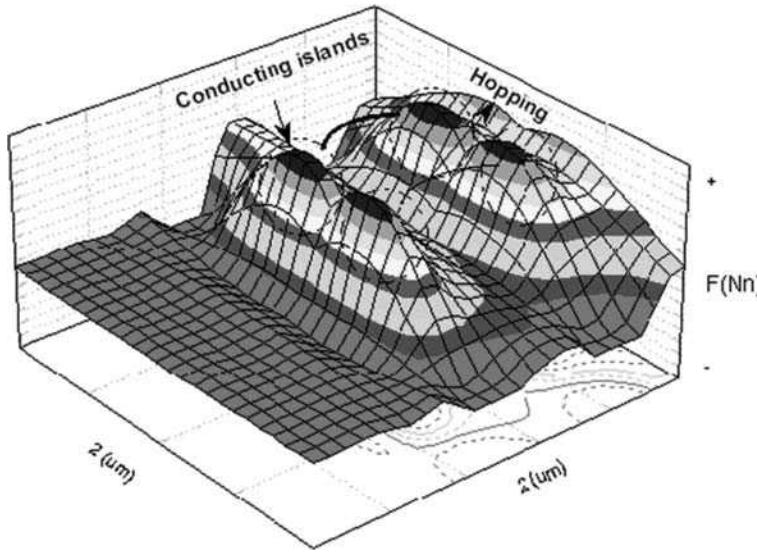

Figure 9.25 *Map of forces obtained with AFS showing regions of repulsive (conducting islands) and attractive interactions on POEA films in solution (pH 3). (Reprinted with permission from Applied Physics A, TEM, XRD and AFM study of poly(o-ethoxyaniline) films: new evidence for the formation of conducting islands by F. L. Leite, Applied Physics A, 93, 2. Copyright (2008) Springer Science + Business Media)*

the force curves for a POEA layer displayed an attractive region for pH $\geq$5 due to van der Waals interactions, with no contribution from a double-layer since POEA was dedoped. In contrast, for pH $\leq$3, POEA was doped and the repulsive double-layer force dominated. With AFS one is therefore able to correlate molecular-level interactions with doping and morphology of semiconducting polymers.

The mechanical properties of conducting polymers may also be investigated with AFS, e.g., nanoindentation [13,93], elastic and viscoelastic properties [94–95], softening transitions [96], and adhesion [91]. Tivanski *et al.* [97] examined how the adhesion force between a conducting probe and a conductive surface influences the electrical properties of conductive polymers. The authors used conducting probe AFM (CP-AFM) and AFS, in which an attractive electrostatic capacitance force is added to the adhesion force after a voltage was applied. The results for the adhesion force measurements as a function of applied bias (see Figure 9.26) show good agreement with the theoretical predictions. To calculate the adhesion force the authors used the equation

$$F_{\mathrm{adh}} = -V\sqrt{\pi R \varepsilon_o \varepsilon_r k_c}$$

where R is the tip radius, ε_{r} is an effective dielectric constant of the polymer solvent system, and k_{c} is the elastic constant of the cantilever. According to this equation the adhesion force depends linearly on the applied bias.

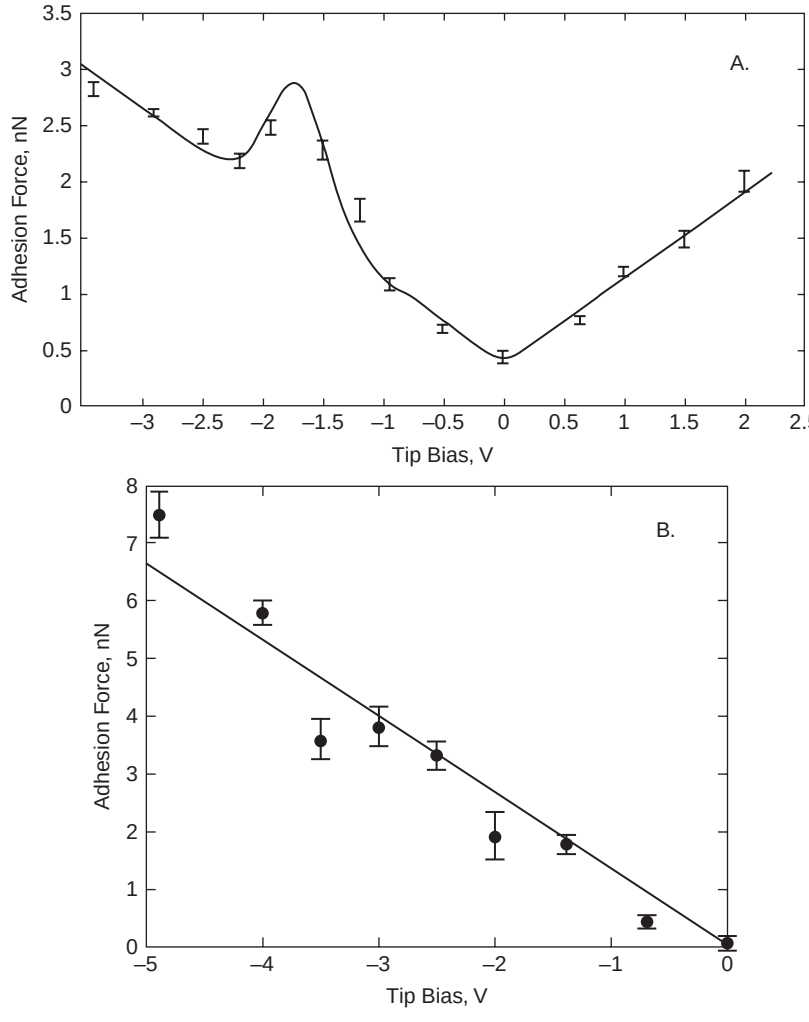

Figure 9.26 *Upper panel (A): Adhesion force as a function of applied bias. Lower panel (B): Adhesion force (symbols) and the best fit line for the 1,4-benzene dimethanethiol sample. (Reprinted with permission from Langmuir, Adhesion Forces in Conducting Probe Atomic Force Microscopy by A. V. Tivanski et al., 19, 6. Copyright (2003) American Chemical Society)*

9.3 Concluding Remarks

Atomic force microscopy is now perhaps the most versatile tool to investigate surface morphologies for a very wide variety of materials, including the conducting polymers analyzed in this chapter. In addition to morphology, other surface properties may be interrogated with the various types of AFM methods, with which mechanical, electrical,

and magnetic properties may be studied. Overall, the data acquired with AFM measurements are analyzed only qualitatively owing to the difficulties in establishing models that allow one to obtain a quantitative treatment, especially because the data depend on molecular-level interactions. There is now the need to improve the experimental methods to provide data with increasing resolution, not only in terms of spatial resolution, but also accuracy in the forces measured. Furthermore, molecular modeling is now becoming popular, which is promising for the quantitative analysis.

Acknowledgments

This work was supported by FAPESP and CNPq (Brazil).

References

[1] E. Meyer, Atomic force microscopy, *Prog. Surf. Sci.*, **41**, 3–49 (1992).
[2] F.L. Leite and P.S.P Herrmann, Application of atomic force spectroscopy (AFS) to studies of adhesion phenomena: a review, *J. Adhesion Sci. Technol.*, **19**(3), 365–405 (2005).
[3] G. Zavala, Atomic force microscopy, a tool for characterization, synthesis and chemical processes, *Colloid Polym. Sci.*, **286**(1), 85–95 (2008).
[4] N.A. Burnham, G. Gremaud, A.J. Kulik, P.J. Gallo, and F, Oulevey, Materials' properties measurements: Choosing the optimal scanning probe microscope configuration, *J. Vac. Sci. Technol. B: Microelectr. Nanometer Structures*, **14**(2), 1308–1312 (1996).
[5] G. Binnig, C.F. Quate, and C. Gerber, Atomic force microscope, *Phys. Rev. Lett.*, **56**, 930–933 (1986).
[6] G.G. Roberts, Langmuir–Blodgett Films, New York, Plenum Press, 1990.
[7] G. Decher, J.D. Hong, and J. Schmitt, Buildup of ultrathin multilayer films by a self-assembly process: III. Consecutively alternating adsorption of anionic and cationic polyelectrolytes on charged surfaces, *Thin Solid Films*, **210**, 831–835 (1992).
[8] L.K. Xie, L.J. Buckley, and J.Y. Josefowicz, Observations of polyaniline surface morphology modification during doping and de-doping using atomic force microscopy, *J. Mater. Sci.*, **29**(16), 4200–4204 (1994).
[9] S.A. Chen and H.T. Lee, Structure and properties of poly(acrylic acid)-doped polyaniline structure and properties of poly(acrylic acid)-doped polyaniline, *Macromolecules*, **28**, 2858–2866 (1995).
[10] *Nt-Mdt*, **2002**, www.ntmdt.com.
[11] F.L. Leite, L.G. Paterno, C.E. Borato, P.S.P. Herrmann, O.N. Oliveira Jr, and L.H.C. Mattoso, Study on the adsorption of poly(*o*-ethoxyaniline) nanostructured films using atomic force microscopy, *Polymer*, **46**(26), 12503–12510 (2005).
[12] T. Silk, Q. Hong, J. Tamm, and R.G. Compton, AFM studies of polypyrrole film surface morphology I. The influence of film thickness and dopant nature. *Synth. Met.*, **93**(1), 59–64 (1998).
[13] F.L. Leite, M. Oliveira Neto, L.G. Paterno, M.R.M Ballestero, I. Polikarpov, Y.P. Mascarenhas, P.S.P Herrmann, L.H.C. Mattoso, and O.N. Oliveira Jr., Nanoscale conformational ordering in polyanilines investigated by SAXS and AFM, *J. Colloid. Interface Sci.*, **316**(2), 376–387 (2007).
[14] E.C. Venâncio, N. Consolin Filho, C.J.L Constantino, L. Martin-Neto, and L.H.C Mattoso, Studies on the interaction between humic substances and conducting polymers for sensor application, *J. Braz. Chem. Soc.*, **16**, 24–30 (2005).

[15] K. Xu, L.H. Zhu, and H.Q. Tang, Effects of dopants on percolation behaviors and gas sensing characteristics of polyaniline film, *Electrochim. Acta*, **52**(2), 723–727 (2006).
[16] M.K. Ram, M. Adami, M. Sartore, M. Salerno, S. Paddeu, and C. Nicolini, Comparative studies on Langmuir–Schaefer films of polyanilines, *Synth. Met.*, **100**(3), 249–259 (1999).
[17] S. Choudhury, V. Saxena, S.K. Gupta, and J.V. Yakhmi, A study on Langmuir–Blodgett films of conducting polycarbazole, *Thin Solid Films*, **493**(1–2), 267–272 (2005).
[18] A. Riul Jr, L.H.C. Mattoso, G.D. Telles, P.S.P. Herrmann, L.A. Colnago, N.A. Parizotto, V. Baranauskas, R.M Faria, O.N. Oliveira Jr, Characterization of Langmuir–Blodgett films of parent polyaniline, *Thin Solid Films*, **284–285**, 177–180 (1996).
[19] M. Mazur and P. Krysinski, Polymer sandwiches: polyaniline films deposited on thiol-coated gold by chemical *in situ* method, *Thin Solid Films*, **396**(1–2), 131–137 (2001).
[20] M.B. Fritzen-Garcia, B.G. Zanetti-Ramos, C.S. De Oliveira, V. Soldi, A. Pasa, and T.B. Creczynski-Pasa, Atomic force microscopy imaging of polyurethane nanoparticles onto different solid substrates, *Mat. Sci. Eng. C.*, **29**(2), 405–409 (2009).
[21] J.H. Song, X.D. Wang, E. Riedo, and Z.L. Wang, Elastic property of vertically aligned nanowires, *Nano Lett.*, **5**(10), 1954–1958 (2005).
[22] M.G. Xavier, E.C. Venâncio, E.C. Pereira, F.L. Leite, E.R. Leite, A.G. MacDiarmid, and L.H.C. Mattoso, Synthesis of nanoparticles and nanofibers of polyaniline by potentiodynamic electrochemical polymerization, *J. Nanosci. Nanotechnol.*, **9**(3), 2169–2172 (2009).
[23] A. Ramanaviciene, W. Schuhmann, and R. Ramanavicius, AFM study of conducting polymer polypyrrole nanoparticles formed by redox enzyme – glucose oxidase – initiated polymerisation, *Colloid Surf. B.*, **48**(2), 159–166 (2006).
[24] C.E. Borato, F.L. Leite, L.H.C. Mattoso, R.C. Goy, S.P. Campana Filho, C.L. De Vasconcelos, C.G. Da Trindade Neto, M.R. Pereira, and J.L.C. Fonseca, Layer-by-layer films of poly (*o*-ethoxyaniline), chitosan and chitosan-poly(methacrylic acid) nanoparticles and their application in an electronic tongue. *IEEE Trans. Dielect. Electr. Insul.*, **13**(5), 1101–1109 (2006).
[25] C.M. Mate, G.M. McClelland, R. Erlandsson, and S. Chiang, Atomic-scale friction of a tungsten tip on a graphite surface, *Phys. Rev. Lett.*, **59**, 1942–1945 (1987).
[26] A. Riul Jr, A. Dhanabalan, M.A. Cotta, P.S.P Herrmann, L.H.C. Mattoso, A.G. Macdiarmid, and O.N. Oliveira Jr., AFM studies of composite 16-mer polyaniline Langmuir-Blodgett (LB) films, *Synth. Met.*, **101**(1–3), 830–831 (1999).
[27] T. Asmus and G.K. Wolf, Modification and structuring of conducting polymer films on insulating substrates by ion beam treatment, *Nucl. Instrum. Meth. Phys. Res. B*, 166–167, 732–736 (2000).
[28] W.A Hayes, H. Kim, X. Yue, S. Perry, and C. Shannon, Nanometer-scale patterning of surfaces using self-assembly chemistry. 2. Preparation, characterization, and electrochemical behavior of two-component organothiol monolayers on gold surfaces, *Langmuir*, **13**(9), 2511–2518 (1997).
[29] F. Guan, M. Chen, W. Yang, J. Wang, R. Zhang, S. Yang, and Q. Xue, Fabrication of patterned polyaniline microstructure through microcontact printing and electrochemistry, *App. Surface Sci.*, **230**(1–4), 131–137 (2004).
[30] N.K. Dutta, N.D. Tran, and N.R. Choudhury, Perfluoro(methylcyclohexane) plasma polymer thin film: Growth, surface morphology, and properties investigated by scanning thermal microscopy, *J. Polym. Sci. B.*, **43**, 1392–1400 (2005).
[31] V.V. Tsukruk, V.V Gorbunov, and N. Fuchigami, Microthermal analysis of polymeric materials, *Thermochim. Acta*, **395**, 151–158 (2003).
[32] A. Hammiche, M. Reading, H.M. Pollock, M. Song, and D.J. Hourston, Localized thermal analysis using a miniaturized resistive probe. *Rev. Sci. Instrum.*, **67**, 4268–4274 (1996).
[33] V.V. Gorbunov, N. Fuchigami, J.L. Hazel, and V.V. Tsukruk, Probing surface microthermal properties by scanning thermal microscopy, *Langmuir*, **15**, 8340–8343 (1999).
[34] B.A. Nelson and W.P. King, Measuring material softening with nanoscale spatial resolution using heated silicon probes, *Rev. Sci. Instrum.*, **78**: 023702–023708 (2007).
[35] A. Hammiche, D.J. Hourston, H.M Pollock, M. Reading, and M. Song, Scanning thermal microscopy: Subsurface imaging, thermal mapping of polymer blends, and localized calorimetry, *J. Vac. Sci. Technol. B*, **14**, 1486–1491 (1996).

[36] C. Kuo, C.C. Chen, and W. Bannister, Microthermal analysis of rubber-polyaniline core-shell microparticles using frequency-dependent thermal responses. *Thermochim. Acta*, **403**(1), 115–127 (2003).
[37] S.N. Magonov and M.H. Whangbo, *Surface Analysis with STM and AFM: Experimental and Theoretical Aspects of Image Analysis*, VCH, New York, 1996.
[38] H.J. Maivald, H.J. Butt, S.A.C. Gould, C.B. Prater, B. Drake, J.A. Gurley, V.B. Elings, and P.K. Hansma, Using force modulation to image surface elasticities with the atomic force microscope, *Nanotechnol.*, **2**, 103–106 (1991).
[39] S.L. Daniel, J.N. Ngunjiri, and J.C. Garno, Investigation of the magnetic properties of ferritin by AFM imaging with magnetic sample modulation. *Anal. Bioanal. Chem.*, **394**, 215–223 (2009).
[40] R.K. Watt, R.B. Frankel, and G.D. Watt, Redox reactions of apo mammalian ferritin, *Biochem.*, **31**(40), 9673–9679 (1992).
[41] D.C. Zapien and M.A. Johnson, Direct electron transfer of ferritin adsorbed at bare gold electrodes, *J. Electroanal. Chem.*, **494**, 114–120 (2000).
[42] F. Caruso, D.N. Furlong, and P.J. Kingshot, Characterization of ferritin adsorption onto gold, *J. Colloid Interf. Sci.*, **186**(1), 129–140 (1997).
[43] D. Xu and R. Davis, Atomic force microscope conductivity measurements of single ferritin molecules, Thesis, Brigham Young University, 2004.
[44] Y. Okada, M. Miyagi, K. Akahane, Y. Iuchi, and M. Kawabe, Self-organized InGaAs quantum dots on GaAs (311)B studied by conductive atomic force microscope tip, *J. App. Phys.*, **90**, 192–196 (2001).
[45] Q. Zhong, D. Inniss, K. Kjoller, and V.B. Elings, Fractured polymer/silica fiber surface studied by tapping mode atomic force microscopy, *Surf. Sci. Lett.*, **290**(1–2), L688–L692 (1993).
[46] Y. Martin, D.W. Abraham, and H.L. Wickramasinghe, High-resolution capacitance measurement and potentiometry by force microscopy, *App. Phys. Lett.*, **52**, 1103–1105 (1998).
[47] R.G. Winkler, J.P. Spatz, S. Sheiko, M. Moller, P. Reineker, and O. Marti, Imaging material properties by resonant tapping-force microscopy: A model investigation, *Phys. Rev. B.*, **54**, 8908–8912 (1996).
[48] P.K. Hansma, J.P. Cleveland, M. Radmacher, D.A. Walters, P.E. Hilner, M. Bezanilla, M. Fritz, D. Vie, H.G. Hansma, C.B. Prater, J. Massie, J. Fukunaga, J. Gurley, V. Elings, Tapping mode atomic force microscopy in liquids, *Appl. Phys. Lett.*, **64**(13), 1738–1740 (1994).
[49] L.H.C. Mattoso, L.G. Paterno, S.P. Campana, and O.N. Oliveira Jr, Kinetics of adsorption of self-assembled films from doped poly(o-ethoxyaniline), *Synth. Met.*, **84**(1–3), 123–124 (1997).
[50] L.G. Paterno and L.H.C. Mattoso, Effect of pH on the preparation of self-assembled films of poly(*o*-ethoxyaniline) and sulfonated lignin, *Polymer*, **42**(12), 5239–5245 (2001).
[51] N.C. Souza, J.R. Silva, C.A. Rodrigues, L.F. Costa, J.A. Giacometti, and O.N. Oliveira Jr, Adsorption processes in layer-by-layer films of poly(*o*-methoxyaniline): the role of aggregation, *Thin Solid Films*, **428**, 232–236 (2003).
[52] N.C. Souza, J.R. Silva, R. Di Thommazo, M. Raposo, D.T. Balogh, J.A. Giacometti, and O.N. Oliveira Jr, Influence of solution treatment on the adsorption and morphology of poly (*o*-methoxyaniline) layer-by-layer films, *J. Phys. Chem. B.*, **108**, 13599–13606 (2004).
[53] J. Li, E. Wang, M. Green, and P.E. West, *In situ* AFM study of the surface morphology of polypyrrole film, *Synth. Met.*, **74**(2), 127–131 (1995).
[54] M.L. Abel, J.L. Camalet, M.M. Chehimi, J.F. Watts, and P.A. Zhdan, A solvent effect on the morphology of PMMA-coated polypyrrole surfaces, *Synth. Met.*, **81**(1), 23–31 (1996).
[55] A.C. Cascalheira, A.S. Viana, and L.M. Abrantes, Effect of substrate preparation conditions on the morphology of polypyrrole coatings on copper – an AFM study, *Adv. Mater. Forum*, 455–456, 661–664 (2004).
[56] P. Taranekar, X. Fan, and R. Advincula, Distinct surface morphologies of electropolymerized polymethylsiloxane network polypyrrole and comonomer films, *Langmuir*, **18**(21), 7943–7952 (2002).
[57] C. Kranz, H.E. Gaub, and W. Schuhmann, Polypyrrole towers grown with the scanning electrochemical microscope, *Adv. Mater.*, **8**, 634–637 (1996).

[58] M.D Levi, C. Lopez, E. Vieil, and M.A. Vorotyntsev, Influence of ionic size on the mechanism of electrochemical doping of polypyrrole films studied by cyclic voltammetry, *Electrochim. Acta*, **42**, 757–769 (1997).
[59] A.O. Semenikhin, L. Jiang, T. Iyoda, K. Hashimoto, and A. Fujishima, A Kelvin probe force microscopic study of the local dopant distribution in conducting polybithiophene, *Electrochim. Acta*, **42**, 3321–3326 (1997).
[60] M. Elkaoutit, A.H. Naggar, I. Naranjo-Rodriguez, M. Dominguez, and J.L.H.H. de Cisneros, Electrochemical AFM investigation of horseradish peroxidase enzyme electro-immobilization with polypyrrole conducting polymer, *Synth. Met.*, **159**, 541–545 (2009).
[61] R.F.M. Lobo, M.A. Pereira da Silva, M. Raposo, R.M. Faria, O.N. Oliveira Jr, *In situ* thickness measurements of ultra-thin multilayer polymer films by atomic force microscopy, *Nanotechnology*, **10**, 389–393 (1999).
[62] J. Mattsson, J.A. Forrest, A. Krozer, U. Doddervall, A. Wennerberg, and L.M. Torell, Characterisation of sub micron salt-doped polymer electrolyte films. *Electrochim. Acta*, **45**, 1453–1461 (2000).
[63] C. Miron and D. Nedelcu, Atomic force microscopy on thin layers of polyaniline (PANI) obtained by plasma polymerization technique, *Materiale Plastice*, **41**, 215–218 (2004).
[64] R. Shao and D.A. Bonnell, Scanning probes of nonlinear properties in complex materials, *Jpn. J. App. Phys. Part 1*, **43**, 4471–4476 (2004).
[65] E.C. Venancio, L.G. Paterno, C.E. Borato, A. Firmino, and L.H.C. Mattoso, Influence of the pH and substrate immersion time on the adsorption of poly(*o*-ethoxyaniline) in self-assembled films, *J. Braz. Chem. Soc.*, **16**, 558–564 (2005).
[66] A.L. Morales-Cruz, E.R. Fachini, F.A. Miranda, and C.R. Cabrera, Surface analysis monitoring of polyelectrolyte deposition on $Ba_{0.5}Sr_{0.5}TiO_3$ thin films, *App. Surface Sci.*, **253**, 8846–8857 (2007).
[67] D.C. Paine, B. Yaglioglu, Z. Beiley, and S. Lee, Amorphous IZO-based transparent thin film transistors, *Thin Solid Films*, **516**, 5894–5898 (2008).
[68] T.V. Shishkanova, P. Matejka, V. Kral, I. Sedenkova, M. Trchova, and J. Stejskal Optimization of the thickness of a conducting polymer, polyaniline, deposited on the surface of poly(vinyl chloride) membranes: A new way to improve their potentiometric response, *Anal. Chim. Acta*, **624**, 238–246 (2008).
[69] S. Pruneanu, S.A.F Al-Said, L. Dong, T.A. Hollis, M.A. Galindo, N.G. Wright, A. Houton, and B.R. Horrocks, Self-assembly of DNA-templated polypyrrole nanowires: spontaneous formation of conductive nanoropes, *Adv. Func. Mater.*, **18**, 2444–2454 (2008).
[70] W.R. Silveira, E.M. Muller, T.N. Ng, D.H. Dunlap, and J.A. Marohn, High sensitivity electric force microscopy of organic electronic materials and devices. In *Scanning Probe Microscopy Electrical and Electrochemical Phenomena at the Nanoscale* ed. S. Kalinin and A. Gruverman, Springer, New York, 2006.
[71] S.R. Cohen, and A. Bitler, Use of AFM in bio-related systems, *Curr. Op. Colloid Inter. Sci.*, **13**, 316–325 (2008).
[72] J.N. Barisci, R. Stella, G.M. Spinks, and G.G Wallace, Characterisation of the topography and surface potential of electrodeposited conducting polymer films using atomic force and electric force microscopies, *Electrochim. Acta.*, **46**, 519–531 (2000).
[73] R. Yang, D.F. Evans, L. Christensen, and W.A. Hendrickson, Scanning tunneling microscopy (STM) evidence of semicrystalline and helical conducting polymer structures, *J. Phys. Chem.*, **94**, 6117–6122 (1990).
[74] D. Jeon, J. Kim, M.C. Gallagher, R.F. Willis, and Y.T. Kim, Morphology of inicial growth stages and tunneling spectroscopy of electropolymerized polyaniline thin films, *J. Vac. Sci. Technol. B*, **9**, 1154–1158 (1991).
[75] J.N. Barisci, R. Stella, G.M. Spinks, and G.G. Wallace, Study of the surface potential and photovoltage of conducting polymers using electric force microscopy. *Synth. Met.*, **124**(2–3), 407–414 (2001).
[76] B. Bush and C.C.R. Maboudian, Layer-by-layer self-assembled conductive thin films for MEMS applications, *Sensors Act. A*, **126**, 194–200 (2006).
[77] O.A. Semenikhin, L. Jiang, T. Iyoda, K. Hashimoto, and A. Fujishima, Atomic force microscopy and kelvin probe force microscopy evidence of local structural inhomogeneity and

nonuniform dopant distribution in conducting polybithiophene, *J. Phys. Chem.*, **100**, 18603–18606 (1996).
[78] T.S. Jespersen and J. Nygard, Mapping of individual carbon nanotubes in polymer/nanotube composites using electrostatic force microscopy, *App. Phys. Lett.*, **90**, 183108–183110 (2007).
[79] P.S.O. Patrício, L.A. Cury, G.G. Silva, and B.R.A. Neves, Electric force microscopy investigation of a MEH-PPV conjugated polymer blend: Robustness or frailty?, *Ultramicroscopy*, **108**(4), 302–308 (2008).
[80] L.C. Santa Maria, M.A.S. Costa, L.F. Senna, M.R. Silva, and R.A. Simão, AFM characterization of composite materials containing iron in a resin host based on styrene and divinylbenzene, *Microsc. Microanal.*, **11**, 166–169 (2005).
[81] T. Michinobu, N. Sasao, and H. Nishide, Microparticles of poly(methacrylic acid)-gadolinium ion complex and their magnetic force microscopic images, *J. Polymer Sci. A*, **42**, 1912–1918 (2004).
[82] K.D. O'Neil, B. Shaw, and O.A. Semenikhin, On the origin of mesoscopic inhomogeneity of conducting polymers, *J. Phys. Chem. B.*, **111**(31), 9253–9269 (2007).
[83] A.A. Alagiriswamy, C. Jager, D. Haarer, M. Thelakkat, A. Knoll, and G. Krausch, Local potential distribution of macrophase separated polymer blend domains, *J. Phys. D – App. Phys.*, **40**, 4855–4865 (2007).
[84] L.S.C. Pingree, O.G. Reid, and D.S. Ginger, Electrical scanning probe microscopy on active organic electronic devices, *Adv. Mater.*, **21**, 19–28 (2009).
[85] K. Cooper, A. Gupta, and S. Beaudoin, Substrate morphology and particle adhesion in reacting systems, *J. Colloid Interf. Sci.*, **228**, 213–219 (2000).
[86] N.A. Burnham, R.J. Colton, and H.M. Pollock, Interpretation of force curves in force microscopy, *Nanotechnology*, **4**, 64–80 (1993).
[87] C. Rotsch and M. Radmacher, Mapping local electrostatic forces with the atomic force microscope, *Langmuir*, **13**(10), 2825–2832 (1997).
[88] F.L. Leite, C.E. Borato, W.T.L Silva, P.S.P Herrmann, O.N. Oliveira Jr, and L.H.C. Mattoso, Atomic force spectroscopy on poly(*o*-ethoxyaniline) nanostructured films: sensing nonspecific interactions, *Microsc. Microanal.*, **13**, 304–312 (2007).
[89] E.A. Franceschini and H.R. Corti, Elastic properties of Nafion, polybenzimidazole and poly [2,5-benzimidazole] membranes determined by AFM tip nano-indentation, *J. Power Sources*, **188**, 379–386 (2009).
[90] X.Z. Zheng, J.B. Weng, Q.M. Huang, B.H. Hu, T. Qiao, and P. Deng, Fabrication of a stable poly(vinylpyrrolidone)/poly(urushiol) multilayer ultrathin film through layer-by-layer assembly and photo-induced polymerization, *Colloid Surf. A*, **337**, 15–20 (2009).
[91] F.L. Leite, W.F. Alves, M. Mir, Y.P. Mascarenhas, P.S.P Herrmann, L.H.C. Mattoso, and O.N. Oliveira Jr, TEM, XRD and AFM study of poly(*o*-ethoxyaniline) films: new evidence for the formation of conducting islands, *Appl. Phys. A.*, **93**(2), 537–542 (2008).
[92] F.L. Leite, W.F. Alves, M. Oliveira Neto, I. Polikarpo, P.S.P Herrmann, L.H.C. Mattoso, O.N. Oliveira Jr, Doping in poly(*o*-ethoxyaniline) nanostructured films studied with atomic force spectroscopy (AFS). *Mícron.*, **39**, 1119–1125 (2008).
[93] J.Y. He, Z.I. Zhang, M. Midttun, G. Fonnum, G.I. Modahl, H. Kristiansen, and K. Redford, Size effect on mechanical properties of micron-sized PS–DVB polymer particles, *Polymer*, **49**(18), 3993–3999 (2008).
[94] S. Cuenot, C. Frétigny, S. Demoustier-Champagne, and B. Nysten, Measurement of elastic modulus of nanotubes by resonant contact atomic force microscopy, *J. Appl. Phys.*, **93**(9), 5650–5655 (2003).
[95] X.D. Li, H.S. Gao, W.A. Scrivens, D.L. Fei, X.Y. Xu, M.A. Sutton, A.P. Reynolds, and M.L. Myrick, Nanomechanical characterization of single-walled carbon nanotube reinforced epoxy composites, *Nanotechnology*, **15**(11), 1416–1423 (2004).
[96] J. Zhou, B. Berry, J.F. Douglas, A. Karim, C. Snyder, and C. Soles, Nanoscale thermal–mechanical probe determination of 'softening transitions' in thin polymer films, *Nanotechnol.*, **19**, 495703–495703 (2008).
[97] A.V. Tivanski, J.E Bemis, B.B. Akhremitchev, H. Liu, and G.C. Walker, Adhesion forces in conducting probe atomic force microscopy, *Langmuir*, **19**(6), 1929–1934 (2003).

10

Single Conducting-Polymer Nanowires

Yixuan Chen and Yi Luo

Department of Electrical and Computer Engineering, Carnegie Mellon University, 5000 Forbes Ave, Pittsburgh, PA

10.1 Introduction

In the past decade, we have experienced tremendous development in science and technology on nanometer scales. Substantial advances in material synthesis and nanofabrication techniques have led to the successful preparation of a wide variety nanoscale materials and structures; fundamental studies have broadened and deepened our scientific understanding of nature on nanometer scales; phenomena and functionalities that are unique to nanomaterials and nanodevices have introduced numerous potential applications, and further driven the extremely broad and diversified studies on material systems at such length scales.

Among various types of novel nanoscale materials, nanowires made of different conducting polymers have drawn considerable attention. Compared to other materials, conducting polymers (CP) have some unique electrical, chemical, and mechanical properties. For example, they can be flexible, transparent, and conductive, there exists a very large collection of different CP materials, and chemical modification of CP materials is relatively easy. They have been widely used for applications in many different areas, e.g. electronics, optoelectronics, MEMS, and chemical sensing, etc. One-dimension and quasi-one-dimension conducting polymer nanowires (CPNWs) made of this category of materials have introduced even more potential attraction.

Nanostructured Conductive Polymers Edited by Ali Eftekhari

Due to the unique nature of CPs, preparation methods and physical properties of CPNWs differ considerably from those of many inorganic nanoscale materials. In this chapter, we intend to review the studies on this important category of materials. The review focuses on the following aspects: (i) preparation of CPNWs, (ii) transport properties and electrical characterization, and (iii) potential applications. The primary concentration of this chapter will be on individual CPNWs.

10.2 Fabrication of Single Conducting-Polymer Nanowires (CPNWs)

Since the discovery of conducting polymers (CPs) in the 1970s, tremendous efforts have been made trying to create miniature features in this category of materials. Particularly in the last decade, we have experienced significant progresses in preparing nanoscale CP materials and structures resulting from general advances in chemical synthesis and nanofabrication technology. Various conducting polymer nanowires (CPNWs) and nanotubes (CPNTs) have been demonstrated using several different types of approach. These new materials have brought numerous novel physical phenomena and introduced various potential applications.

To date, many different approaches have been applied towards making well-ordered individual CPNWs and CPNTs. In this section, we will introduce and discuss some of the most important developments in the preparation of 1-D CPNWs and CPNTs. While general background information will be provided, primarily, as we have mentioned in the introduction, we will focus our discussion on those methods that have been demonstrated to be capable of or have shown potential to produce ordered, single, and individually addressable CPNWs or CPNTs. Some techniques which are able to produce ordered arrays of parallel single CPNWs are also included. Generally, the approaches can be characterized into the following categories: (i) lithography based, (ii) template based, (iii) scanning probe based, and so on. The advantages, limitations, and future development potential of each approach will be provided.

10.2.1 Lithographical Methods

Advances in conventional lithography approaches, e.g. photolithography and electron-beam lithography, etc. have allowed deep submicron patterning for many different kinds of materials. Arbitrarily designed nanoscale features of inorganic semiconductors, dielectrics, and metals, etc. can be fabricated with these lithography technologies. However, many of these methods cannot be directly used to pattern CP materials. A typical issue is the incompatibility between a processible CP and the organic solvents (i.e. photoresist solvent, developer, and photoresist remover, etc.) involved in the lithographic and follow-up processes. Therefore, modification of existing methods and development of novel lithographic methods that are suitable for nanoscale patterning of CP materials are required. In the following, we will review some of the most representative methods in this category. They include direct electron-beam lithography on CP, nanoimprint lithography, soft lithography, and block-copolymer lithography, etc.

10.2.1.1 Direct Electron-Beam Patterning of CP Thin Films

While using photo- or electron-beam-resist on top of CP thin films has some difficulties, Persson *et al.* explored the possibility of using electron beams to pattern CP thin films directly. It was found that when a spin-cast poly(3-octylthiophene) (P3OT) film was selectively exposed to a 50 KeV e-beam with dosages up to 800 nC cm^{-2}, the polymer became insoluble in chlorobenzene, while the unexposed portion was still soluble [1]. The authors suggested that the e-beam irradiation causes the polymer chains to partially cross-link and consequently reduces the solubility of the polymer in chlorobenzene. This phenomenon introduces a mechanism for direct e-beam patterning of a CP thin film which responds similarly to electron-beam irradiation to a negative e-beam resist. With this approach, P3OT lines as narrow as 50 nm have been produced by the authors. Similarly, microscale features have also been made with optical irradiation (Refs. 11 and 12 in [1]).

Dong *et al.* used a copolymer strategy, in which other components are incorporated into the CP to improve its properties, such as adhesion, solubility, conductivity, and coated film thickness. The copolymer was processed by e-beam lithography followed by a lift-off process to produce individual sub-100 nm nanowires (Figure 10.1) [2].

10.2.1.2 Nanoimprint Lithography

Nanoimprint lithography (NIL) is a relatively new technique designed to produce precisely defined nanoscale features in a parallel, efficient, and cost-effective manner [3,4]. In a typical NIL process, a prepatterned mold is used to press against a resist layer which can go through a thermal plastic transition at an elevated temperature or can be permanently

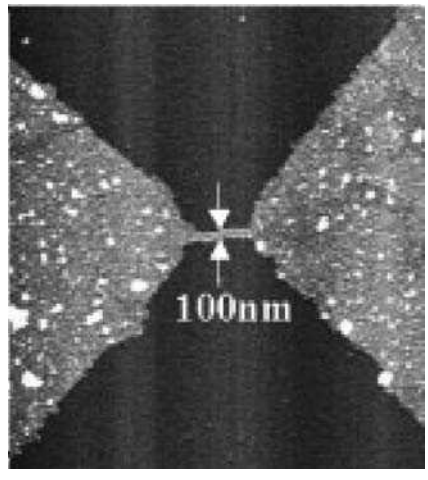

Figure 10.1 *Atomic force microscopy (AFM) image of one 100-nm-wide polypyrrole wire that bridges the ends of two polypyrrole microelectrodes (size: 9 μm × 10 μm). (Reprinted with permission from Advanced Materials, Patterning of Conducting Polymers Based on a Random Copolymer Strategy: Toward the Facile Fabrication of Nanosensors Exclusively Based on Polymers by B. Dong, D. Y. Zhong, L. F. Chi and H. Fuchs, 17, 22, 2736–2741. Copyright (2005) Wiley-VCH)*

cross-linked by heating or optical irradiation. As a general lithographic technique, NIL has tremendous potential in nanofabrication. In recent years, NIL has also been applied for the preparation of CP nanowires. Usually, a prefabricated mold bearing indented nanofeatures is used in the process to transfer patterns on the mold directly onto a CP layer or through an imprint resist layer. For example, this method was used by Guo and colleagues to produce nanostructures directly on thin CP layers for organic photovoltaic applications [5]. It has also been shown that poly(9,9-di-*n*-octyl-2,7-fluorene) (PFO), poly (3,3‴-didodecyl-quaterthiophene) (PQT), and polypyrrole (PPY) nanowires could be made by pressing the mold into a thin film of the corresponding CPs in a fluidic state followed by cooling or solvent evaporation while the mold is in place [6]. In a separate study, Behl *et al.* fabricated CP nanostructures by imprinting a mixture of CP precursor and photo-initiator with subsequent UV exposure to cure the polymer. CP nanowires of $\sim$ 300 nm in width were demonstrated [7].

Clearly, NIL-based techniques are capable of producing well-ordered and precisely designed nanoscale CP structures. They are parallel and efficient approaches. A major concern regarding to these methods is shorting between neighboring features. This is because quite frequently with NIL it is extremely difficult to completely squeeze out the material (i.e. polymer or polymer precursor) between two adjacent features. There likely exists a thin layer of residual CP that creates an electrical short between the adjacent features. Usually, in order to remove the residual layer, an etching step is required, which can introduce undesired damage to the prepared features.

On the other hand, with a somewhat different approach, Dong, *et al.*, showed that it is also possible to fabricate CPNWs using a lift-off method following CP layer deposition on patterns in a resist layer created by NIL (Figures 10.2 and 10.3) [8].

10.2.1.3 Soft Lithography

Soft lithography includes a collection of lithographic methods in which a soft mold or template is used to create patterned structures in the subjected materials. These methods offer attractive solutions for producing well-ordered CP nanowires. For example, Beh *et al.* have developed a micromolding in capillaries (MIMIC) process in which a poly(dimethylsiloxane) (PDMS) mold with embedded channels can be used for the

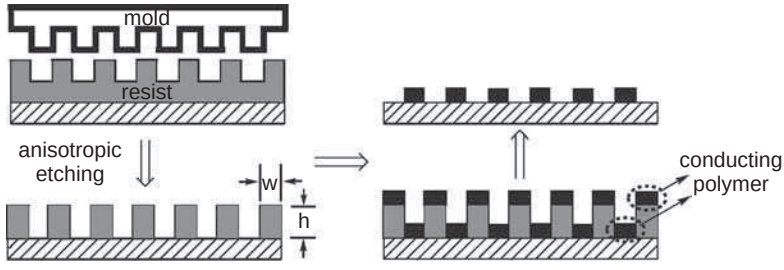

Figure 10.2 *Schematic illustration of the fabrication process. (Reprinted with permission from Advanced Functional Materials, Fabrication of High-Density, Large-Area Conducting-Polymer Nanostructures by B. Dong, N. Lu, M. Zelsmann et al., 16, 15, 1937–1942. Copyright (2006) Wiley-VCH)*

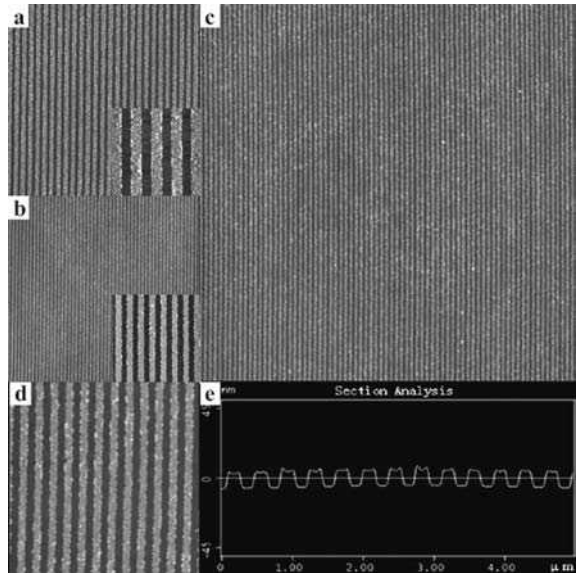

Figure 10.3 *A series of AFM images showing the high-density polypyrrole nanowires fabricated using NIL and a lift-off process, with the polypyrrole layer deposited for 1 h in a solution containing $FeCl_3$ (0.08 g), pyrrole (300 µl), py-silane (30 µl), and purified water (126 ml): (a) 600 nm wide polypyrrole nanowires with a separation of 540 nm (size: 30 µm × 30 µm). Inset: enlarged AFM image of (a) showing one 5 µm × 5 µm area; (b) 300 nm wide polypyrrole nanowires with a separation of 300 nm (size: 30 µm × 30 µm). Inset: enlarged AFM image showing one 5 µm × 5 µm area; (c) 150 nm wide polypyrrole nanowires with a separation of 150 nm (size: 30 µm × 30 µm); (d) enlarged AFM image of (c) showing one 5 µm × 5 µm area; (e) average section analysis of (d). (Reprinted with permission from Advanced Functional Materials, Fabrication of High-Density, Large-Area Conducting-Polymer Nanostructures by B. Dong, N. Lu, M. Zelsmann et al., 16, 15, 1937–1942. Copyright (2006) Wiley-VCH)*

formation of nanoscale CP structures. In this approach, CP solution is applied and drawn into the micro- and nanoscale channels formed between indented features on a PDMS mold and a substrate by capillary force. Well-ordered CP nanostructures remain on the substrate after the removal of the PDMS mold. Nanowires of down to ~350 nm in width have been demonstrated with this method (Figure 10.4) [9]. In a separate study, Zhang *et al.* also reported that CP nanowires ~ 278 nm wide had been made by the MIMIC process as well as the liquid embossing technique in which the PDMS stamp is placed a on surface which is already covered with a liquid containing the CP (Figure 10.5) [10].

Single CP nanowires may also be prepared by other forms of lithography. Lipomi *et al.* reported a method termed 'edge lithography'. In their study, alternating layers of two different CPs, poly(2-methoxy-5-(2′-ethylhexyloxy)-1,4-phenylenevinylene) (MEH-PPV) and poly(benzimidazobenzophenanthroline ladder) (BBL), were spin-coated on a substrate to form a composite multilayer film from their respective solutions. This film was then embedded in thermally curable epoxy and was subsequently sliced by an ultramicrotome. As a result, each slice contained multiple parallel alternating MEH-PPV and BBL

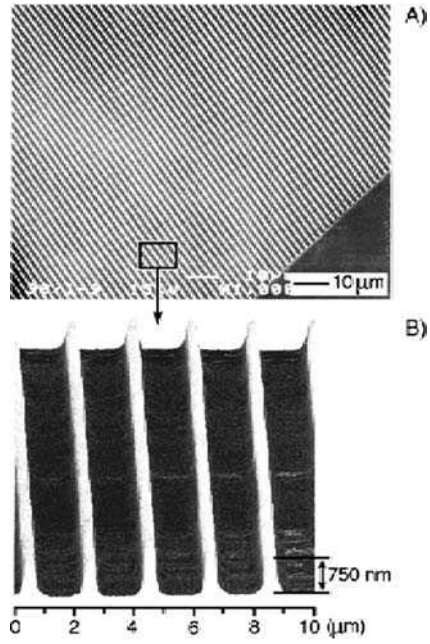

Figure 10.4 *(A) SEM and (B) AFM images of parallel lines of PANI that were fabricated on a polyester film by MIMIC. (Reprinted with permission from Advanced Materials, Formation of Patterned Microstructures of Conducting Polymers by Soft Lithography, and Applications in Microelectronic Device Fabrication by W. S. Beh, I. T. Kim, D. Qin et al., 11, 12, 1038–1041. Copyright (1999) Wiley-VCH)*

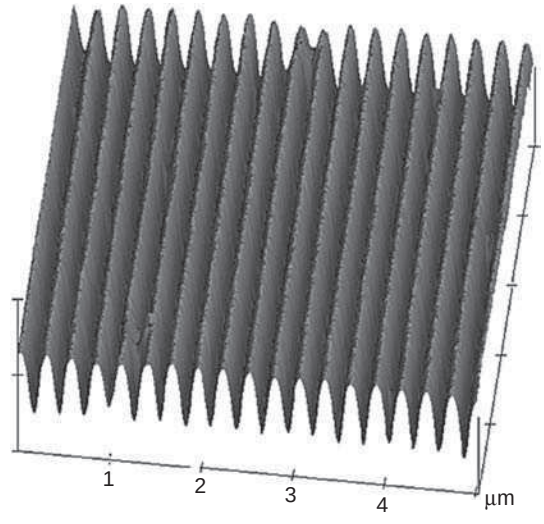

Figure 10.5 *SFM images of narrow nanowires (278 nm) of semiconducting polymer poly(3-(2′-methoxy-5′-octyphenyl)thiophene) (POMeOPT) by soft-embossing. (Reprinted with permission from Nano Letters, Conducting Polymer Nanowires and Nanodots made with Soft Lithography by Fengling Zhang et al., 2, 12. Copyright (2002) American Chemical Society)*

nanowires. Either MEH-PPV or BBL wires could be selectively etched leaving behind an array of desired polymer nanowires with their width controlled by the thickness of the corresponding layers in the initial composite film [11].

More recently, Jung *et al.* demonstrated 'block-copolymer lithography' (Figure 10.6) in which, using an etch mask consisting of self-assembled patterns of cylinder-forming poly(styrene-b-dimethylsiloxane) (PS-PDMS) diblock copolymer confined in topographic templates, a pattern of an array of 15nm wide nanowires was transferred to the underlying spin-coated CP (PEDOT:PSS) film (Figure 10.7) [12].

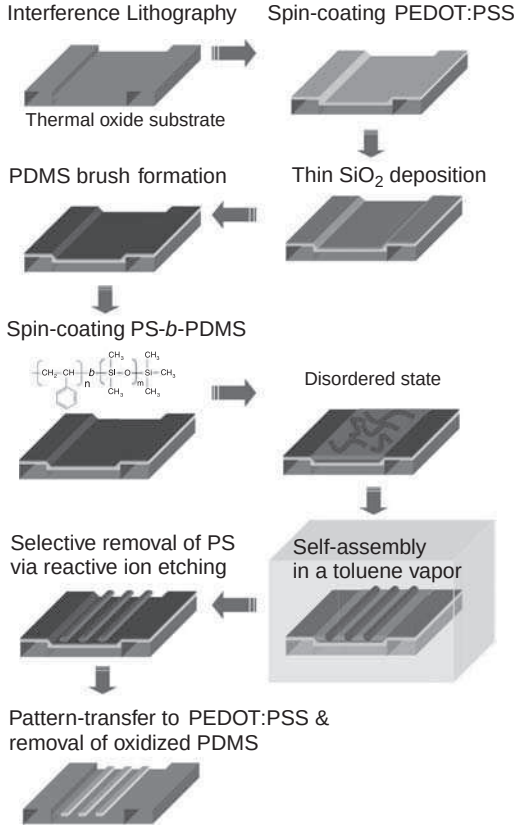

Figure 10.6 *Procedure for polymer nanowire fabrication. An aqueous PEDOT:PSS solution was spin-coated on a substrate patterned with a 1.3 μm period grating, then coated with a thin SiO_2 layer and a PDMS homopolymer brush. A PS-PDMS block-copolymer thin film was then spin-coated and solvent-annealed. The self-assembled block-copolymer patterns were transferred into the underlying PEDOT:PSS film through a series of reactive ion etching steps employing CF_4 and O_2 plasmas. (Reprinted with permission from Nano Letters, Nanowire Conductive Polymer Gas Sensor Patterned Using Self-Assembled Block Copolymer Lithography by Y. S. Jung et al., 8, 11. Copyright (2008) American Chemical Society)*

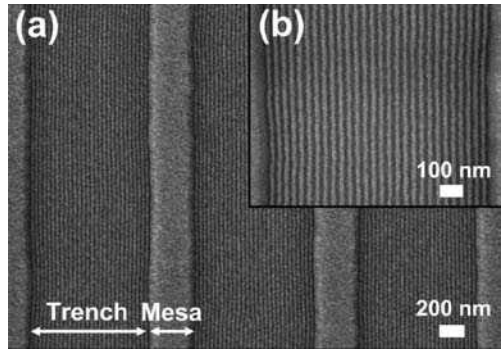

Figure 10.7 *Self-assembled block copolymer patterns after two-step reactive ion etching composed of a 5 s, 50 W, CF_4 etch followed by a 30 s 90 W, O_2 etch. (Reprinted with permission from Nano Letters, Nanowire Conductive Polymer Gas Sensor Patterned Using Self-Assembled Block Copolymer Lithography by Y. S. Jung et al., 8, 11. Copyright (2008) American Chemical Society)*

10.2.1.4 Lift-Off Process Following Standard Lithography with Enhanced CP Adhesion to Substrate

There have also been reports on ways to improve adhesion of the CP layer to the substrate so that more general lithographic methods can be applied to produce high-quality CPNWs. Im *et al.* showed a process called oxidative chemical-vapor deposition (oCVD) in which a thin layer of CP is grafted onto a polymer substrate containing aromatic groups to achieve better adhesion between the CP and the substrate. Different lithographical processes can then be applied to pattern the CP layer into CP nanofeatures down to 60 nm [13].

It has also been shown that a self-assembled monolayer (SAM) with proper functional groups can significantly improve the adhesion of CP thin film on a substrate. Based on this concept, Jung and Lee have demonstrated the fabrication of CP nanostructures via a lift-off process. In their study, 16-mercaptohexadecanolc acid and 3-aminopropyltriethoxy silane SAM were used on Au and SiO2/Si surfaces to promote the adhesion of PPY and PEDOT:PSS, respectively. This allowed nanostructures of these CP materials to be fabricated using standard e-beam lithography followed by a lift-off process [14].

10.2.2 Scanning-Probe-Based Techniques

Scanning-probe-based lithographic techniques have been successfully used for patterning and delivering material on nanometer scales in many different applications. These versatile techniques have also been applied to patterning and grafting CP nanostructures. In this section, we will review important studies and progresses in this area.

It is rather clear that the width of a CPNW produced by a scanning probe is closely related to the dimension of the tip which can have a radius smaller than 2 nm. In general, the shape and pattern of a CPNW can be defined by the scan path and speed, along with other growth and deposition parameters. It has been demonstrated that a scanning-probe-based technique can easily produce sub-100-nm-wide single CPNWs. On the other hand, a clear drawback of

this approach is that, since a scanning probe can only produce one CPNW at a time as it moves along, it is generally a slow process. However, please note that recent developments using multiple tips on a scan head provide a potential solution to this issue [15,16].

In the following, we introduce a few representative examples in which scanning tips are used to pattern, deliver, or grow nanoscale CP features. Based on the functionality of the probe, the approaches in this category include electrochemical polymerization, dip-pen, and nanomechanical scratching.

10.2.2.1 Electrochemical Polymerization with Scanning Probe

The most common approach based on a scanning-probe technique is the electrochemical polymerization of the corresponding monomer. In such an approach CP patterns are electrochemically grown by applying an electrical potential between the scanning probe and the substrate in the present of monomer solution. There are two slightly different types of setup within this approach.

In the first case, the tip serves both as monomer (and electrolyte) delivery tool and as the cathode for the electrochemical polymerization, while the conductive substrate is the anode. The polymerized material with a well-defined pattern and shape is subsequently deposited on the substrate. Many kinds of CPNWs, e.g. PPY, PANI, and PEDOT nanowires have been prepared with this approach on (semi-)conducting substrates e.g. silicon, graphite, or gold, using STM or conductive AFM tips [17–21]. Figure 10.8 is an AFM

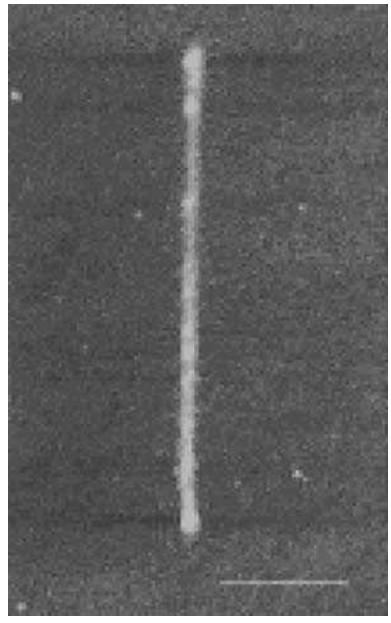

Figure 10.8 *Polymer line fabricated at 10 nm s^{-1}, 48% humidity, –12 V. Polymer line width: 30 nm; scale bar: 250 nm. (Reprinted with permission from Journal of the American Chemical Society, Direct-Writing of Polymer Nanostructures: Poly(thiophene) Nanowires on Semiconducting and Insulating Surfaces by Benjamin W. Maynor et al., 124, 4. Copyright (2002) American Chemical Society)*

image of a 30-nm-wide PEDOT nanowire produced by such a method [21]. The nanoscale feature size could be attributed to the small effective surface area of the STM tip. As the tip scans following a preprogrammed route, CPNWs in desired patterns can then be grown and deposited on the substrate.

In the second case, a slightly different tip-based electrochemical method involves the attachment of the monomers to an insulating polymer (precursor polymer) backbone as side chains, and localized cross-linking of the monomer side units by the biased AFM tip to produce CPNWs in or on the precursor polymer. For example, Jang *et al.* reported that using a voltage-biased AFM tip which functioned as the working electrode, sub-100 nm nanowires of poly(terthiophene) were patterned by electric-field-induced cross-linking on a substrate coated with an insulating film of a polymer containing terthiophene side chains [22].

With the AFM tip as the cathode, nanowires of polycarbazole were also patterned by electric-field-induced cross-linking and polymerization of carbazole units on an Au/mica or Si substrate (anode) spin-coated with insulating poly(vinylcarbazole) film [23,24]. Figure 10.9 shows a schematic of the experimental setup and Figure 10.10 shows an AFM image of the patterned CP nanostructures [24]. Similarly, electrochemical oxidation and cross-linking of carbazole and thiophene due to the flow of electrons from the conductive AFM tip to the polymer (polystyrene functionalized with carbazole and thiophene groups) precursor film on an Si substrate produced CP nanofeatures in the precursor polymer film [25].

In a well-controlled situation, CP features with molecular-level accuracy can be achieved. An excellent demonstration of such molecular-level manipulation and the potential of this approach were given by Okawa and Aono [26,27]. In their study, the authors were able to induce and guide the polymerization of single molecule chain on a graphite substrate (Figure 10.11) [26]. Atomically ordered polydiacetylene molecular lines and monolayer can be created using the STM tip from a monolayer of a diacetylene compound absorbed on a graphite surface (Figure 10.12) [27].

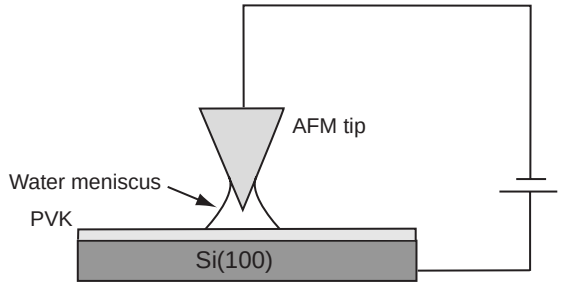

Figure 10.9 *Schematic diagram of electrochemical nanolithography. (Reprinted with permission from Langmuir, Direct Electrochemical Nanopatterning of Polycarbazole Monomer and Precursor Polymer Films: Ambient Formation of Thermally Stable Conducting Nanopatterns by S. Jegadesan et al., 22, 2. Copyright (2006) American Chemical Society)*

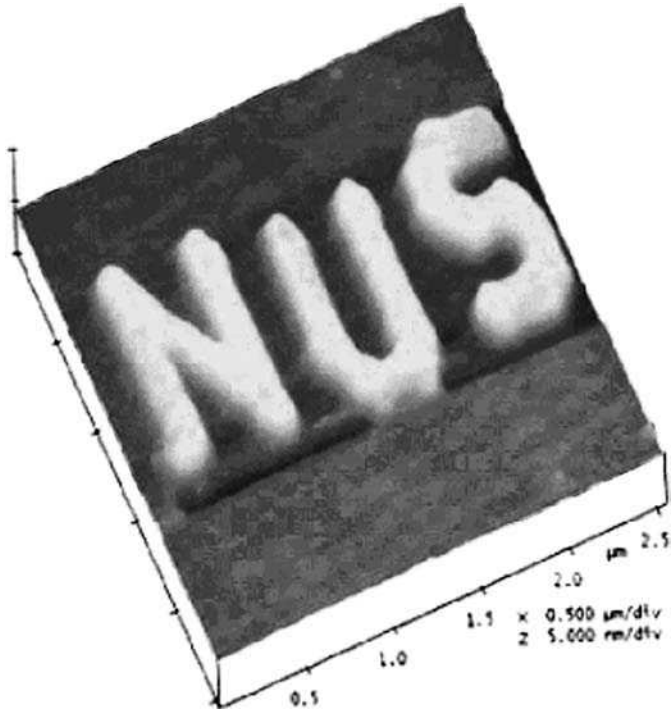

Figure 10.10 *AFM image of patterned CP characters 'NUS'. (Reprinted with permission from Langmuir, Direct Electrochemical Nanopatterning of Polycarbazole Monomer and Precursor Polymer Films: Ambient Formation of Thermally Stable Conducting Nanopatterns by S. Jegadesan et al., 22, 2. Copyright (2006) American Chemical Society)*

10.2.2.2 Dip-Pen

With a different setup, a scanning probe can also be used in 'dip-pen' lithography for the preparation of CP nanofeatures. In this case, the probe delivers a soluble CP ink onto a substrate following a programmed route to create CPNWs with the desired pattern and shape.

A few variations to the original dip-pen lithography have been applied in separate studies. The results have fully demonstrated the potential of this technique [28,29]. For instance, Lim and Mirkin reported a patterning method in which the AFM tip was coated with a water-soluble CP by thermal evaporation or dip-coating and the charged water-soluble polymer was transported from the AFM tip to the pretreated oppositely charged substrate by electrostatic interactions (Figure 10.13 and 10.14) [28].

Su *et al.* reported a slightly different method in which a monomer ink was transported from the AFM tip to the substrate while polymerizing chemically with an acid promoter to form CPNWs [30]. Another modification of such a dip-pen nanolithography method is called 'thermal dip-pen nanolithography', where a tip

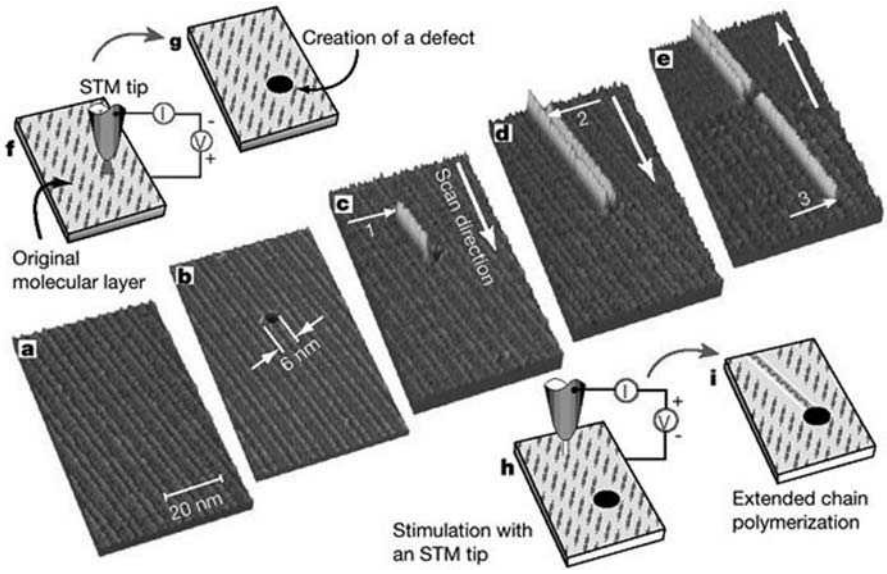

Figure 10.11 *Scanning tunneling microscope (STM) images and diagrams showing the process of controlling the initiation and termination of linear-chain polymerization with an STM tip. STM images were obtained in air at room temperature in constant-current mode. (a) STM image of the original monomolecular layer of 10,12-nonacosadiynoic acid. (b) Creation of an artificial defect in advance in the monomolecular layer using an STM tip. (c) First chain polymerization, initiated at the point indicated by arrow (1) using an STM tip, and terminated at the artificial defect. (d) Second chain polymerization, initiated at arrow (2). (e) Third chain polymerization, initiated at arrow (3). (f), (g) Creation of an artificial defect in advance with an STM tip. (h), (i) Initiation of chain polymerization with an STM tip, and termination of the polymerization at the artificial defect. (Reprinted with permission from Nature, Materials science Nanoscale control of chain polymerization by Yuji Okawa and Masakazu Aono, 409, 6821, 683–684. Copyright (2001) Macmillan Publishers Ltd)*

heater was integrated with an AFM cantilever coated with a CP which is solid at room temperature and melts at an elevated temperature and is deposited onto the substrate surface as nanowires [31].

Cai *et al.* showed that local enhancement of electrochemical polymerization of PPY and PANI on a graphite substrate can be achieved by a scanning AFM tip [32]. In their study, graphite substrate and a platinum wire were used as the working and counter-electrodes, respectively. A Si_3N_4 AFM tip was used to manipulate the electrochemical polymerization and deposition processes of pyrrole and aniline on the substrate. It is found that at a proper stage of growth, AFM tip can significantly enhance the local polymer deposition rate, leading to a potential mechanism for the selective growth of desired PPY and PANI nanostructures. Figure 10.15 shows an AFM image of CPNWs grown by this method. The minimum feature size obtained by this approach was limited by the grain size of polymers to $\sim$60 nm or larger [32].

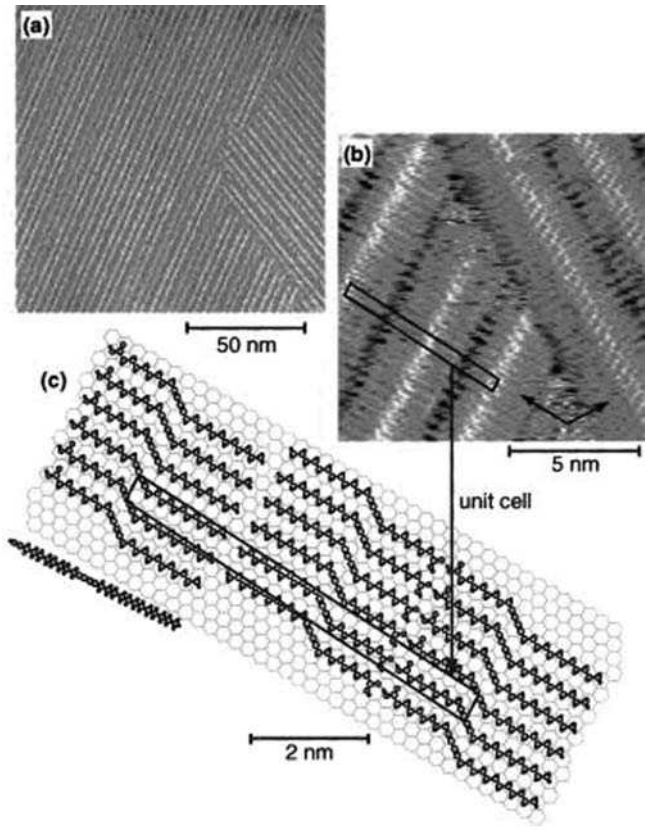

Figure 10.12 *(a) STM image of 10,12-pentacosadiynoic acid layer on graphite (sample bias voltage $V_s = -1.0$ V and tunneling current $I_t = 0.07$ nA). (b) Magnified STM image of the layer ($V_s = +0.5$ V, $I_t = 1.0$ nA). The arrows in the image indicate the main crystal axes of graphite, $\langle 1 \ \bar{\frac{1}{2}} \ \bar{\frac{1}{2}} \ 0 \rangle$. (c) Top and side views of a model of the molecular arrangement. Parallelograms in (b) and (c) represent the unit cell. (Reprinted with permission from Journal of Chemical Physics, Linear chain polymerization initiated by a scanning tunneling microscope tip at designated positions by Y. Okawa and M. Aono, 115, 5. Copyright (2001) American Institute of Physics)*

10.2.2.3 Nanomechanical Scratching with Tip

There have been efforts to put scanning tips to different uses in which the scanning probe is employed neither as an electrode nor as a monomer/CP delivery mechanism, but as a nanomechanical tip to create 'scratches' on a substrate to guide the growth or promote selective adhesion of CP nanofeatures. For example, it has been shown that a tip can be used to scratch the poly(methyl methacrylate) (PMMA) layer on top of electrolyte and catalyst underlayers to achieve selective chemical polymerization of pyrrole monomer on

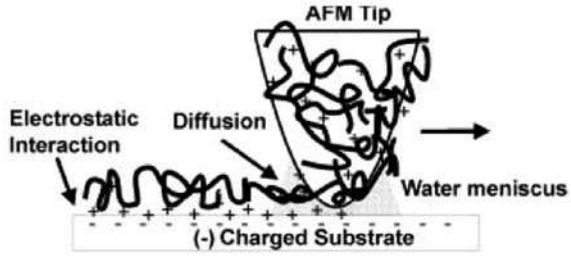

Figure 10.13 *Schematic representation of dip-pen nanolithography for charged comducting polymers. (Reprinted with permission from Advanced Materials, Electrostatically Driven Dip-Pen Nanolithography of Conducting Polymers by J.-H. Lim and C. A. Mirkin, 14, 20, 1474–1477. Copyright (2002) Wiley-VCH)*

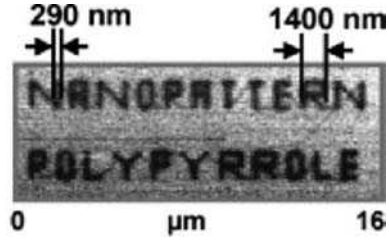

Figure 10.14 *Lateral force microscopy (LFM) image of PPY nanopattern written at 0.8 μm* s^{-1}*. (Reprinted with permission from Advanced Materials, Electrostatically Driven Dip-Pen Nanolithography of Conducting Polymers by J.-H. Lim and C. A. Mirkin, 14, 20, 1474–1477. Copyright (2002) Wiley-VCH)*

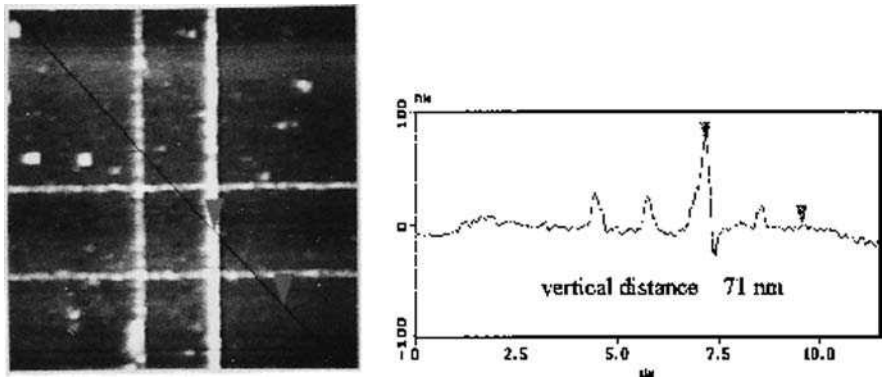

Figure 10.15 *AFM image of cross-lines obtained by disabling the* y *scanning at different positions or by rotating the scanning by 90°. The cross-lines show different heights (20–70 nm) due to different scanning times (0.5–2 min). (Reprinted with permission from Langmuir, Nanomodification of Polypyrrole and Polyaniline on Highly Oriented Pyrolytic Graphite Electrodes by Atomic Force Microscopy by X. W. Cai et al., 14, 9. Copyright (1998) American Chemical Society)*

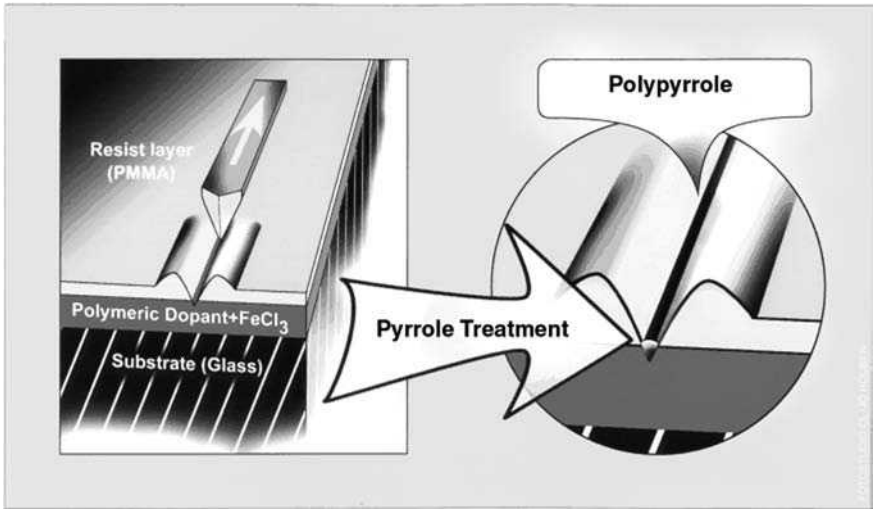

Figure 10.16 *A general concept for the production of nanowires: an AFM is used as a nanomechanical tool for scratching a resist layer, to result in selective exposure of the underlying polymeric dopant surface containing the catalyst for polymerization. Treatment with the pyrrole monomer results in polymerization in the nanochannels. (Reprinted with permission from ChemPhysChem, In Situ Polymerisation of Pyrrole in Nanochannels Produced by Means of AFM Lithography by S. Jahromi, J. Dijkstra, E. van der Vegte and B. Mostert, 3, 8, 693–696. Copyright (2002) Wiley-VCH)*

a glass substrate (Figure 10.16) [33]. Similarly, Woodson and Liu in a separate study used an AFM tip as a nanoscratching tool to define nanochannels in a hexamethyldisilazane (HMDS) self-assembled monolayer (SAM) on thermal oxide (Figure 10.17) [34]. While the hydrophobic HMDS functionalization prevented polymer growth from aqueous monomer solution, CP nanowires can be electrochemically polymerized between gold electrodes inside the hydrophilic nanochannel created by the AFM tip.

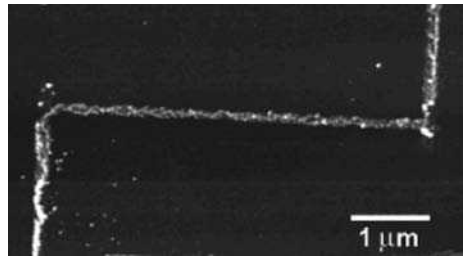

Figure 10.17 *AFM image of a PPY nanowire created by guided growth. (Reprinted with permission from Journal of the American Chemical Society, Guided Growth of Nanoscale Conducting Polymer Structures on Surface-Functionalized Nanopatterns by M. Woodson et al., 128, 11. Copyright (2006) American Chemical Society)*

In summary, tip-based lithography approaches have proved to be extremely flexible in producing very narrow CPNWs of various materials. A major disadvantage of this type of method is its relatively low pattering speed. Also, it has been reported that the process can be very sensitive to the size and scanning speed of the tip, as well as environmental conditions, e.g. temperature, humidity, substrate condition, etc.

10.2.3 Template-Guided Growth or Patterning

Owing to the linear molecular chain nature, the persistent length of most CPs is very short. As a result, unlike some of the inorganic conducting polymer nanowires, of which the persistent length is usually long, e.g. many microns, CPNWs tend to bend and curve easily as they are grown/synthesized in free space. Without any form of guidance, it is extremely difficult to grow long CPNWs with acceptable directionality. In this section, we discuss another important category of preparation methods – template-guided approaches for precisely controlled CPNW growth. To date, many different templates have been used in the studies. In this section, we will introduce the following representative examples, i.e. anodic alumina, nanoporous polycarbonate (PC), lithographically patterned nanotrenches and nano-channels, etc.

10.2.3.1 Alumina, Polycarbonate and Block-Copolymer Templates

Anodic alumina (Al_2O_3) nanoporous templates have been the most widely used to guide the growth of CPNWs. The very narrow and ordered alumina nanopores provide excellent templates for the formation of CPNWs. The dimensions of the CPNWs can be accurately controlled by the diameter and length of the nanopores. Typical pore diameters range from tens to hundreds of nanometers. Typically, alumina nanopores are used to provide templates for either polymerization of corresponding precursors or molding of soluble/molten polymers directly. A few examples of these methods will be introduced in the following.

Electrochemical Polymerization Inside Alumina Nanopores

CPNWs and CPNTs can be grown inside alumina nanopores with electrochemical polymerization. A thin layer of metal (e.g. gold, etc.) that serves as the anode for the growth of CPNW in the pores is usually deposited on one side of the alumina template. Electrochemical polymerization is carried out in the solution phase with a monomer and electrolyte mixture that can diffuse from the open end into a nanopore, resulting in polymer deposition on the anode. Subsequently, the grown nanowire serves as the anode for the continuous growth of well-defined CPNWs inside the nanoporous template.

To isolate one single nanowire for individual electrical connection, additional processes are required after releasing the CPNWs by dissolving the alumina template. This section will give only a brief overview of the preparation of CPNWs by this method, and the focus will be on the processes to isolate and use a single CPNW. For more details of the experimental setup, growth mechanism, CPNW formation, and template dissolution, please follow references [30–40]. Figure 10.18 shows a schematic of CPNW preparation using a nanoporous alumina template [35]. After CPNW growth, the metallic anode layer and the alumina template can be dissolved so that CPNWs are released.

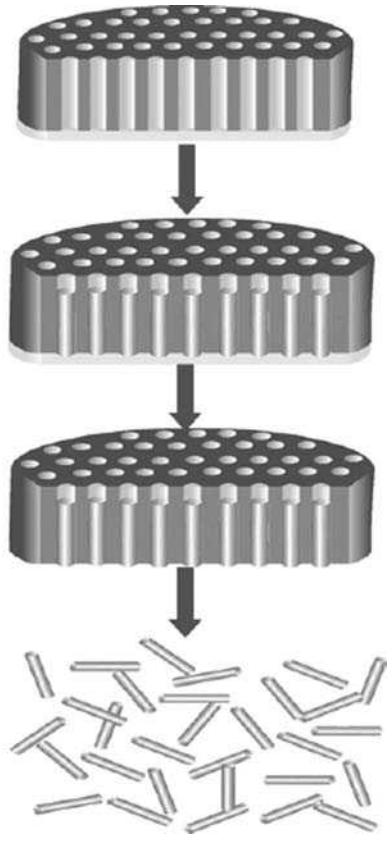

Figure 10.18 *Protocol for CPNW fabrication. (Reprinted with permission from Biosensors and Bioelectronics, Label-free detection of cupric ions and histidine-tagged proteins using single poly(pyrrole)-NTA chelator conducting polymer nanotube chemiresistive sensor by C. L. Aravinda, S. Cosnier, W. Chen et al., 24, 5. Copyright (2009) Elsevier Ltd)*

Figure 10.19 shows SEM and TEM images of PPY nanowires after the removal of the alumina template [36]. The CPNWs are then rinsed, ultrasonicated, and dispersed in a solvent. CPNWs prepared with this method have been featured in many fundamental investigations of CPNW properties [35,37–39]. A typical way to obtain individual nanowires on a substrate is by drop-casting of a very dilute suspension of the CPNWs in solution [35–45]. An SEM image of a single CPNW placed across four metal electrodes for four-point measurement is shown in Figure 10.20 [38].

Besides CP nanowires, heterogeneous CP-metal nanowires can also be synthesized in alumina templates. Nanowires that contain segments of different materials can be grown electrochemically inside the alumina nanopores via sequential deposition of the materials using different precursors and electrolytes [46–52]. Figure 10.21 shows SEM images of gold-PPY nanowires prepared using alumina templates [46]. The incorporated metal

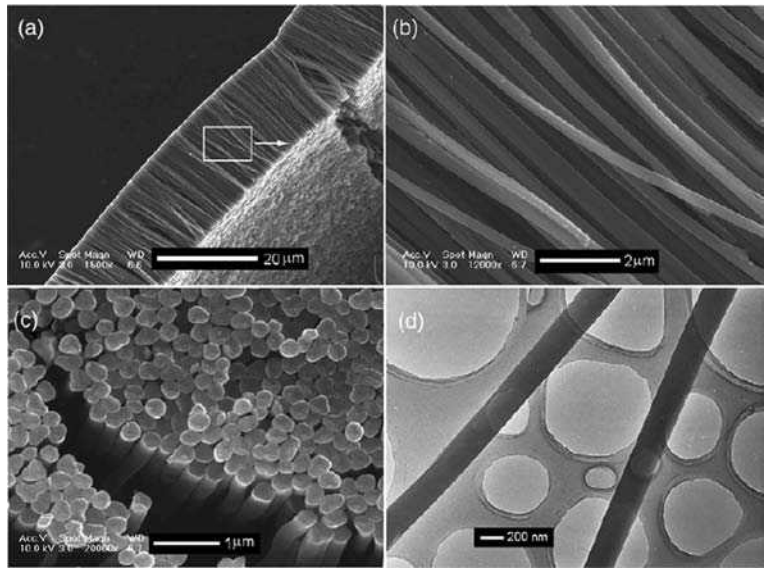

Figure 10.19 *(a–c) SEM images and (d) TEM image of the PPY nanowires. (Reprinted with permission from Nanotechnology, Synthesis, property and field-emission behaviour of amorphous polypyrrole nanowires by H. L. Yan, L. Zhang, J. Y. Shen et al., 17, 14, 3446–3450. Copyright (2006) Institute of Physics Inc.)*

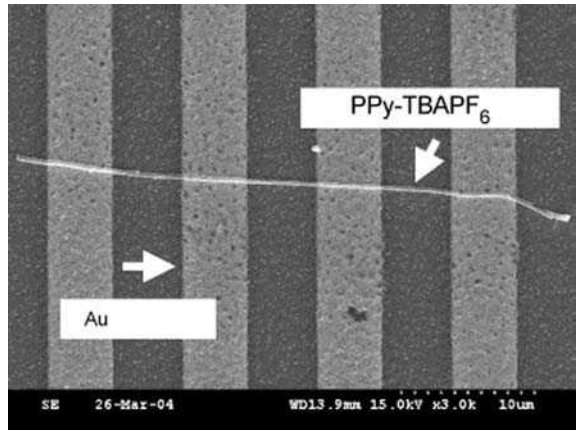

Figure 10.20 *SEM photograph of a single strand PPy-TBAPF6 (tetrabutylammonium-hexafluorophosphate) nanowire on a four-probe photolithography pattern. (Reprinted with permission from Synthetic Metals, Synthesis, characteristics, and field emission of doped and de-doped polypyrrole, polyaniline, poly(3,4-ethylenedioxythiophene) nanotubes and nanowires by B. H. Kim, D. H. Park, J. Joo et al., 150, 3, 279–284. Copyright (2005) Elsevier Ltd)*

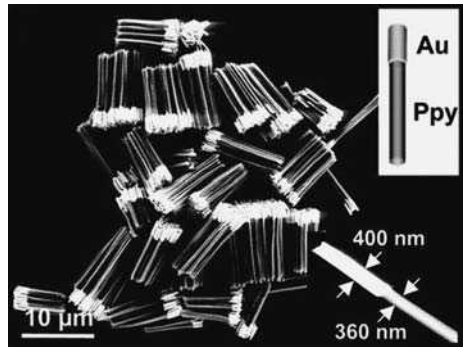

Figure 10.21 *SEM images of Au-PPY rods. The bright segments are gold, and the dark domains are polypyrrole, corresponding to the diagram in the upper right inset. Lower right inset: A zoom-in image of a single rod, showing the difference in diameter for the two different blocks. (Reprinted with permission from Science, Self-Assembly of Mesoscopic Metal-Polymer Amphiphiles by S. Park, J.-H. Lim, S.-W. Chung and C. A. Mirkin, 303, 5656, 348–351. Copyright (2004) American Association for the Advancement of Science)*

segments introduce some desirable properties as they can be utilized in making electrical contact with the nanowires, and provide a special handle in manipulating the nanowires [46–48,50–52]. For instance, gold and cobalt terminating segments have yielded excellent contacts for metal-polymer-metal nanowires [49,51], while gold and cadmium (Cd) segments in a single Au-PPY-Cd-Au nanowire gave rise to the application of the nanowire as a nanodiode [47], and nickel (Ni) segments in single Au-PPY-Ni-Au nanowires was used to manipulate and assemble single nanowires by magnetic dipole interactions between the ferromagnetic nickel segment and the ferromagnetic electrodes in the present of an external magnetic field (Figure 10.22) [52].

Chemical Oxidation Polymerization

Other than electrochemistry, single CP nanowires may also be polymerized from the corresponding monomers by chemical oxidation in an alumina nanoporous template. For example, PPY nanowires have been synthesized in an alumina template using chemical oxidative polymerization by immersing the template in a solution of pyrrole monomer and an oxidizing agent. With this approach, pyrrole monomer is oxidized and cross-linked into polymer filling the nanopores thus forming very well-defined PPY nanowires [53].

Alumina nanoporous templates have also been used in gas-phase growth of CPNTs. It has been reported that isolated nanotubes consisting of poly(*p*-phenylenevinylene) (PPV) and carbonized-PPV bilayers can be synthesized in an alumina template by chemical-vapor deposition (CVD) polymerization. In a study done by Kim and colleagues, CVD polymerization of PPV was carried out by passing monomer vapor through a pyrolysis zone at 625 °C to form precursor polymer nanotubes on the inner surface of the alumina nanochannels. The nanotubes were further thermally treated in vacuum at 270 °C for an extended time (14 h) to be converted into PPV nanotubes. In order to create PPV/carbonized PPV bilayer nanotubes, the PPV nanotubes were then carbonized at 850 °C

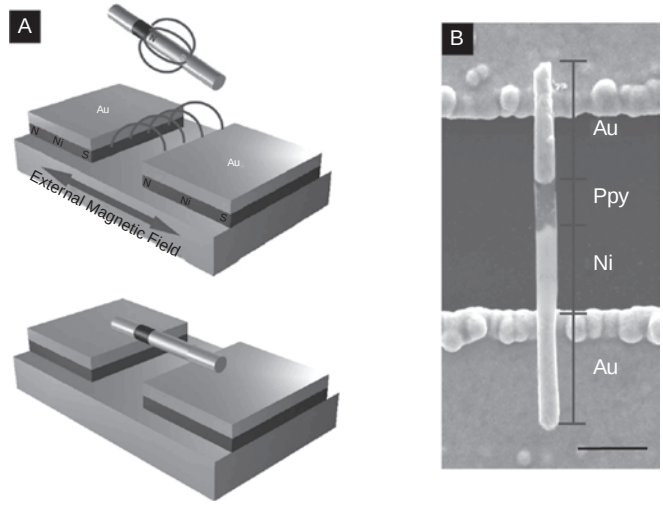

Figure 10.22 *(A) Schematic illustration of the magnetic assembly of multisegmented nanowires. The lines represents the magnetic field of the nanowire and the ferromagnetic electrodes. The bottom figure shows the placement of different segments of the nanowire on the contact electrodes. (B) SEM image of single nanowire device assembled using magnetic assembly on prefabricated electrodes; scale bar: 1 μm). (Reprinted with permission from Electroanalysis, Magnetically Assembled Multisegmented Nanowires and Their Applications by M. A. Bangar, C. M. Hangarter, B. Yoo et al., 21, 1, 61–67. Copyright (2009) Wiley-VCH)*

in an argon environment followed by a second growth of PPV nanotubes inside these carbonized nanotubes using the above-described procedure [54,55]. As will be discussed in the following section, these PPV/carbonized PPV nanotubes are reported to yield significant higher photocurrents than single-layer PPV nanotubes.

Polymer Filling

Instead of polymerizing monomers, single CP nanowires can also be prepared in an alumina template directly using molten or solution-phase polymers. For example, O'Brien, *et al*. reported that single poly(3-hexylthiophene) (P3HT) nanowires can be prepared by a 'melt-assisted template wetting method' [56]. By heating a P3HT layer on the alumina template above its melting temperature, the molten polymer and drawn into the nanopore due to the high surface energy of the alumina membrane and continues to fill the entire pores. P3HT nanowires can be obtained this way after slowly cooling to room temperature. Similarly, single poly[(9,9-dioctylfluorenyl-2,7-diyl)-co-(bithiophene)] (F8T2) nanowires were prepared by a 'solution-assisted template wetting method'. In this case, F8T2 solution fills the nanopores of the alumina template by capillary force [57].

Besides nanoporous alumina template, nanoporous polycarbonate (PC) is another popular choice for the growth of CPNWs. PPV and PEDOT nanowires of a few hundred nanometers have been prepared by CVD and electrochemical methods, respectively, using PC templates [55,58].

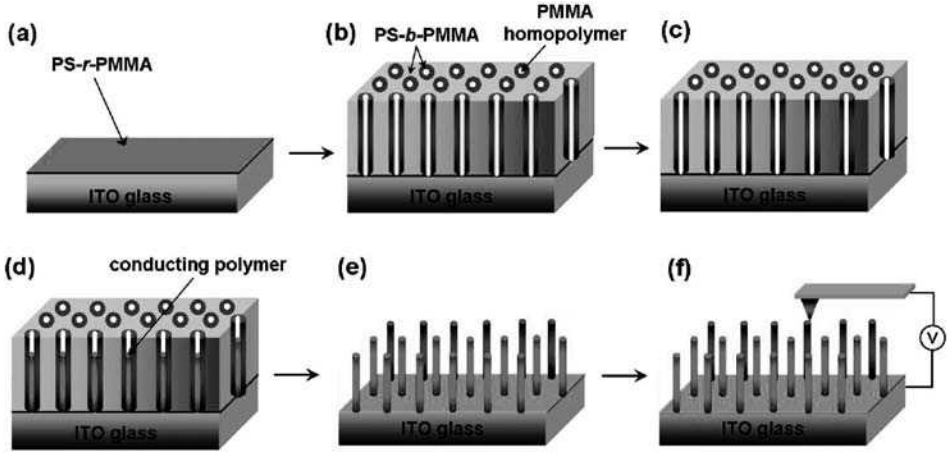

Figure 10.23 *Fabrication of ultrahigh density array of conducting polymer nanorods with block-copolymer nanoporous templates. (Reprinted with permission from Nano Letters, Highly Aligned Ultrahigh Density Arrays of Conducting Polymer Nanorods using Block Copolymer Templates by J. I. Lee et al., 8, 8. Copyright (2008) American Chemical Society)*

In addition, block copolymer has also been used as a nanoporous template for the growth of CPNWs. Figure 10.23 schematically illustrates an example of CPNW preparation using a block-copolymer template [59]. A random copolymer of styrene and methyl methacrylate (PS-r-PMMA) was spin-coated and anchored to the ITO-coated glass to orient the poly(methyl methacrylate) (PMMA) microdomains normal to the substrate. A mixture of PMMA homopolymer and PS-b-PMMA was then spin-coated on top of the random copolymer and the PMMA homopolymer was selectively removed by acetic acid to produce an array of nanochannels in the PS-b-PMMA matrix. PPY nanowires were then prepared in these nanochannels from the base by electropolymerization. Finally, the PS-b-PMMA template was removed by toluene, leaving behind an array of single PPY nanowires of ~25 nm diameter standing normal to the substrate surface (Figure 10.24) [59].

10.2.3.2 DNA Templates

Recently, taking advantage of the ordered nanoscale size of DNA molecules, a few research groups have explored the possibility of using DNA molecules as templates for the growth of CPNWs. It was found that a CPNW can be prepared on or around a DNA strand to produce a nanowire of the DNA/CP complex. Single CPNWs of sub-10-nm diameter or width are easily produced on DNA templates due to the extremely small size of the template. In this approach, DNA molecules act as template for precursors to adsorb and subsequently polymerize to form very narrow nanowires. Figure 10.25 schematically illustrates how a PANI nanowire is grown by the horseradish peroxidase (HRP) enzymatic approach on a DNA template [60].

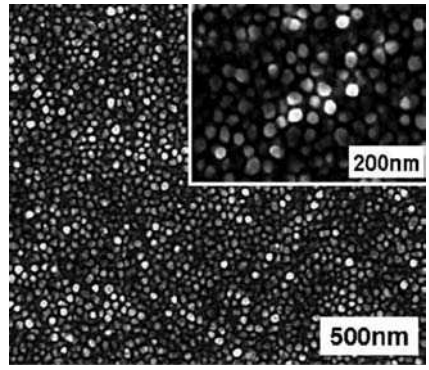

Figure 10.24 *Top-view SEM image of PPY nanorods after removing the template. (Reprinted with permission from Nano Letters, Highly Aligned Ultrahigh Density Arrays of Conducting Polymer Nanorods using Block Copolymer Templates by J. I. Lee et al., 8, 8. Copyright (2008) American Chemical Society)*

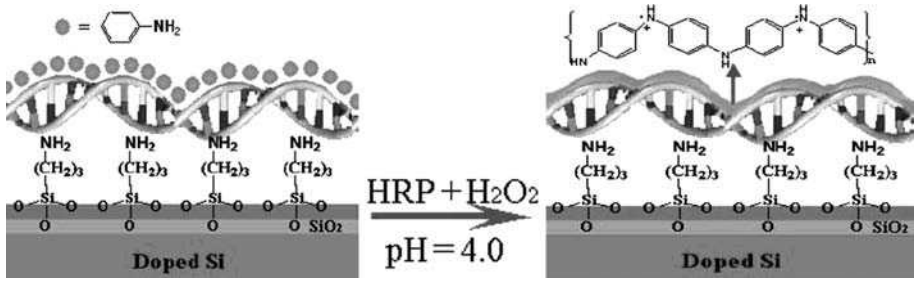

Figure 10.25 *Fabrication of a polyaniline nanowire immobilized on a Si surface with stretched double-stranded DNA as a guiding template. (Reprinted with permission from Journal of the American Chemical Society, Polyaniline nanowires on Si Surfaces Fabricated with DNA Templates by Y. Ma et al., 126, 22. Copyright (2004) American Chemical Society)*

With this method, single poly(*p*-phenylene vinylene) (PPV), PANI, and PPY nanowires have been synthesized and very narrow CPNWs with diameters as small as ~5 nm have been demonstrated using DNA templates [60–63].

10.2.3.3 Lithographically Defined Nanochannels/Templates

CP patterning techniques based on a lithographically defined nanochannel in the substrate are a more engineered approach for the creation of a single CPNW. In such approaches, a nanochannel/template is created in the substrate by a nanolithographical method, such as e-beam lithography and nanoimprinting to physically confine the formation of the CP. Thus in a fully enclosed channel, the channel shape and dimension dictate the pattern and scale of the CPNW. The width of a single CPNW produced by such methods can be down to the smallest scale that the current lithography technology permits. For example, e-beam

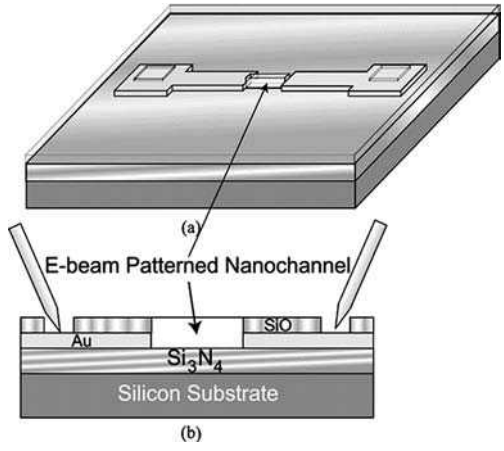

Figure 10.26 *Schematic diagram of a structure used for electrochemical wire growth: (a) electrodeposited wire connected between electrodes; (b) cross-sectional view of the Si substrate, silicon nitride (1 μm), Au contacts, and thermally evaporated SiO. Channels for the electrolyte solution are formed between electrodes by e-beam patterning of the SiO. (Reprinted with permission from Nano Letters, Electrochemically grown Wires for Individually Addressable Sensor Arrays by M. Yun et al., 4, 3. Copyright (2004) American Chemical Society)*

lithography can easily create a channel of sub-100-nm width in a substrate. Typically, nanoscale open trenchs or completely enclosed channels are used as templates for the electrochemical growth of CPNWs with corresponding monomers. For example, Myung and colleagues have shown that single CPNWs of ∼100 nm in width can be electrochemically grown in a lithographically patterned trench in an insulating substrate (Figure 10.26 and 10.27) [64–66]. In their study, a pair of gold electrodes served as

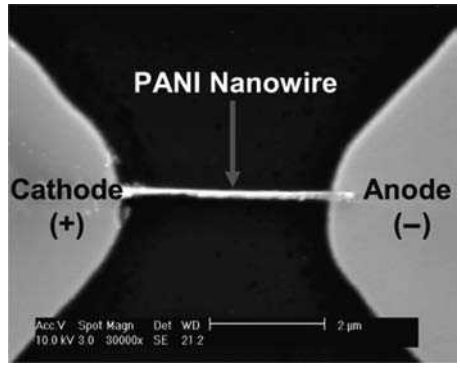

Figure 10.27 *SEM image of a 100 nm wide by 4 μm long PANI nanowire; scale bar: 2 μm. (Reprinted with permission from Nano Letters, Individually Addressable Conducting Polymer Nanowires Array by Kumaran Ramanathan et al., 4, 7. Copyright (2004) American Chemical Society)*

anode and cathode electrodes located at opposite ends of the trench. Monomer was electrochemically polymerized inside the open trench between the gold electrodes. Since the top side of the channel was not covered, variation of nanowire size and cross-section did occur along the length of the trench.

Peng *et al.* used fully enclosed nanochannels for the formation of single CPNWs [67,68]. Sub-100-nm silicon nitride nanochannels on a SiO_2/Si substrate were fabricated (Figure 10.28) [68]. PT and PANI nanowires (Figure 10.29) were prepared inside the nanochannels through chemical and electrochemical polymerization of the

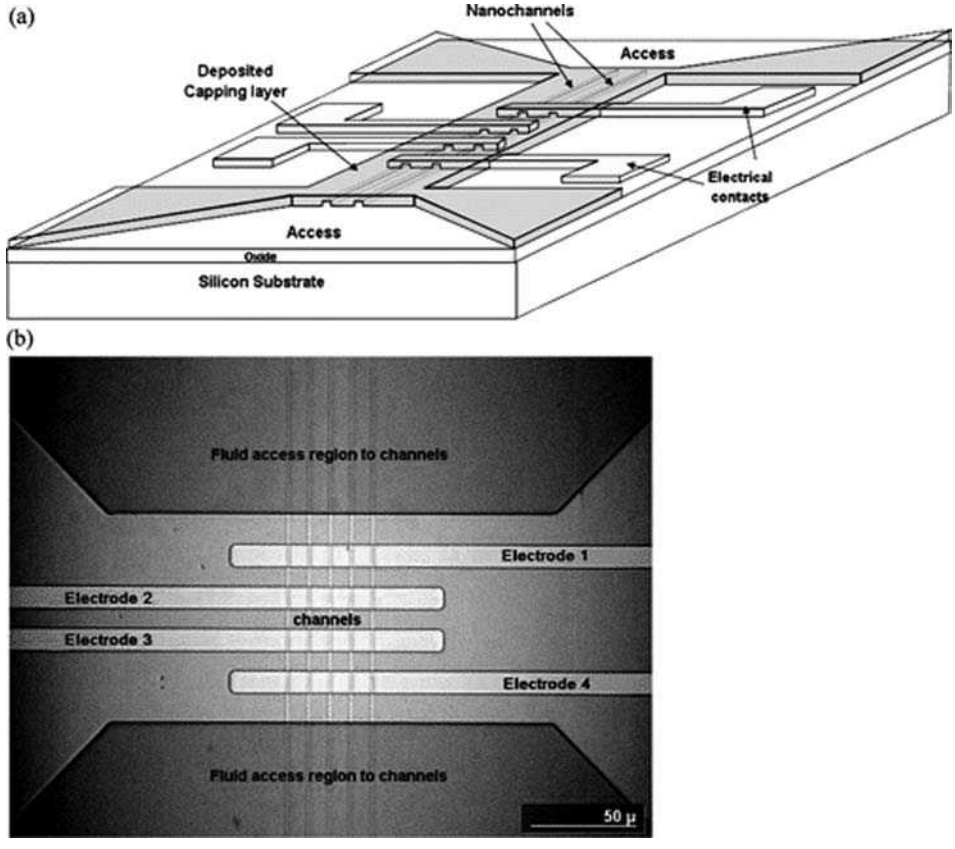

Figure 10.28 *(a) Schematic concept diagram showing two nanochannel templates with built-in electrodes for electrochemical polymerization and electrical contacting. (b) Optical image of an actual nanochannel template region with built-in contacts. Shown are fluid access regions, electrical connections, and a group of five empty channels. (Reprinted with permission from Nano Letters, A "Grow-in-Place" Architecture and Methodology for Electrochemical Sythesis of Conducting Polymer Nanoribbon Device Arrays by C.-Y. Peng et al., 5, 3. Copyright (2005) American Chemical Society)*

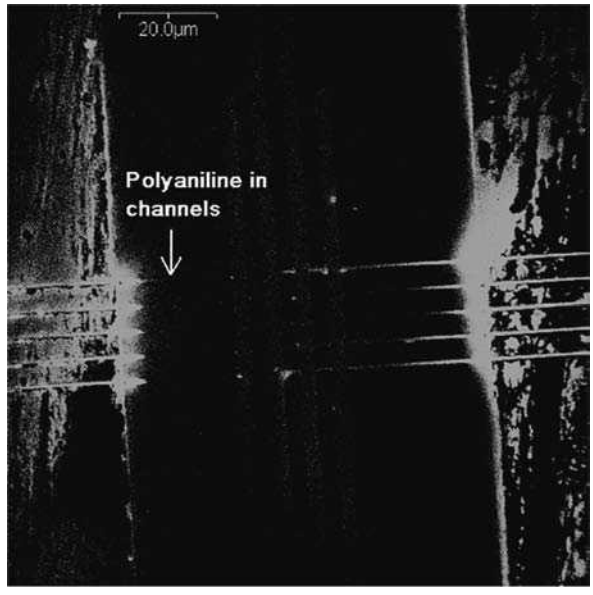

Figure 10.29 *Fluorescent image of five 200 nm wide, 55 nm high template channels with polyaniline grown chemically. (Reprinted with permission from Nano Letters, A "Grow-in-Place" Architecture and Methodology for Electrochemical Sythesis of Conducting Polymer Nanoribbon Device Arrays by C.-Y. Peng et al., 5, 3. Copyright (2005) American Chemical Society)*

corresponding monomers [67,68]. A clear advantage of using the fully enclosed nanochannels is that the shape of CPNWs is very well defined. However, it may not be used directly in some applications such as chemical sensing as the analytes cannot reach the enclosed CPNW.

Chen and Luo have introduced a technique which is capable of creating precisely defined individually addressable parallel sub-100-nm nanowires of multiple CP materials side by side on a rigid or flexible substrate in a parallel way [69]. As illustrated in Figure 10.30, this method consists of electrochemical growth of CPNWs on an e-beam lithography patterned mold with metal (e.g. Pt and Au) electrode template in enclosed nanochannels, followed by transfer of the CP structures onto a desired substrate. The growth of single CPNWs is templated by the metal electrodes and is further confined in enclosed nanochannels. As it is made, each individual CPNW is electrically connected with leads and contact pads of the same CP material via the same growth step (Figure 10.31). No cross-talk leakage between adjacent CP structures was observed. This approach has offered a method for the fabrication of completely deterministic heterogeneous CP nano- and microscale devices and circuitries. It has can be readily applied in many polymer nanoelectronic and optoelectronic applications.

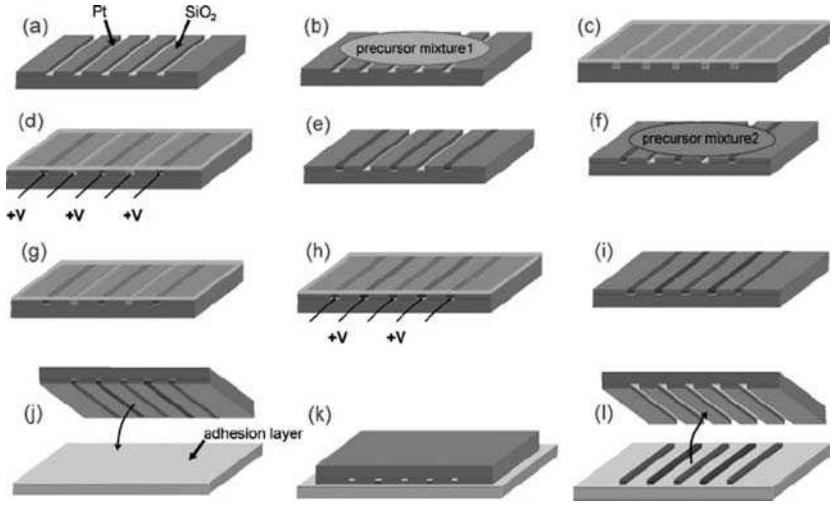

Figure 10.30 *Schematic procedure for preparing CP nanofeatures: (a) prefabricated electrode template with fluoroalkane termination on both SiO_2 and Pt surfaces; (b) the first fluidic polymer precursor mixed with a small percentage of alcohol electrolyte (e.g., $LiClO_4$) solution is applied to the mold; (c) a flexible planar sheet with low surface energy (e.g., PDMS) is pressed against the template to remove excessive precursor that is not inside the indented electrode features on the template; (d) The precursor is electrochemically polymerized on specific electrodes by applying bias to those electrodes; (e) after the removal of the surface cover sheet, the template is rinsed with isopropyl alcohol and water to remove 'uncured' precursor while insoluble polymer features remain on the indented electrodes; (f–i) following steps (b–e), features of another CP are prepared on different electrodes using the corresponding precursor; (j–l) CP structures are transferred from the growth template to a desired substrate by means of an adhesion layer. (Reprinted with permission from Advanced Materials, Precisely Defined Heterogeneous Conducting Polymer Nanowire Arrays – Fabrication and Chemical Sensing Applications by Y. Chen and Y. Luo, 21, 20, 2040–2044. Copyright (2009) Wiley-VCH)*

10.2.4 Other Methods

10.2.4.1 Hydrodynamically Focused Channels

Tseng and colleagues have developed a unique approach for the fabrication of individually addressable CPNWs. In their study, a precisely confined fluidic stream of monomer and electrolyte solution is hydrodynamically focused by multiple fluidic jets into a nanometer scale using PDMS-based microfluidic circuits. PPY and PANI nanowires have been successfully prepared with this approach. One attractive aspect of this method is that it conveniently integrates electronic and microfluidic circuits, which has been proven to be advantageous for gas- and especially solution-phase chemical and biological sensing with the prepared CPNWs [70] (see Figures 10.32 and 10.33).

10.2.4.2 Growth from Grafted SAM Surface

Jerome *et al.* demonstrated that a single PPY nanowire with a diameter of a few hundred nanometers could be prepared from a polyethylacrylate (PEA)-coated conducting

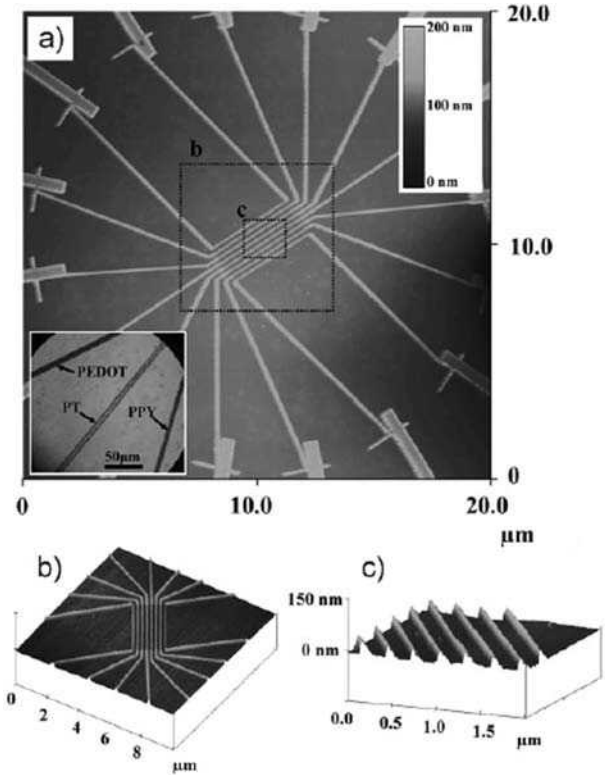

Figure 10.31 *(a) 2-D AFM image of a parallel array of sub-100-nm CP nanowires consisting of different CP materials with connecting micrometer-scale CP wires. The inset is an optical image of PPY, PEDOT, and PT peripheral fan-out lines. (b,c) Higher resolution 3-D AFM images of parts of the same structure as in (a). (Reprinted with permission from Advanced Materials, Precisely Defined Heterogeneous Conducting Polymer Nanowire Arrays – Fabrication and Chemical Sensing Applications by Y. Chen and Y. Luo, 21, 20, 2040–2044. Copyright (2009) Wiley-VCH)*

substrate [71,72]. Figure 10.34 shows a schematic of PPY nanowire growth by this method [72]. An insulating polymer PEA was first electrografted onto the conducting substrate. Then the substrate was used as anode for electropolymerization of PPY nanowires in a solution containing pyrrole monomers and dopants. Monomers could diffuse through the solvent swollen PEA layer, start nucleation and PPY growth on the electrode surface beneath the insulating layer, laterally displacing PEA chains, and forming a small channel for PPY growth. Figure 10.35 shows a SEM image of a grown PPY nanowire [72].

A single PANI nanowire of ~100 nm diameter was produced by electrochemical growth on gold electrodes modified with SAMs of thiolated cyclodextrins or 4-aminothiophenol (molecular templates) in alkanethiol [73,74]. Monomers were seeded to the surface within the isolated hydrophobic cyclodextrin cavities and initiated polymerization. While in these studies, the shape and directionality of the nanowires were not well controlled, they have demonstrated the possibility of growing individual CPNWs in selected locations using molecular templates.

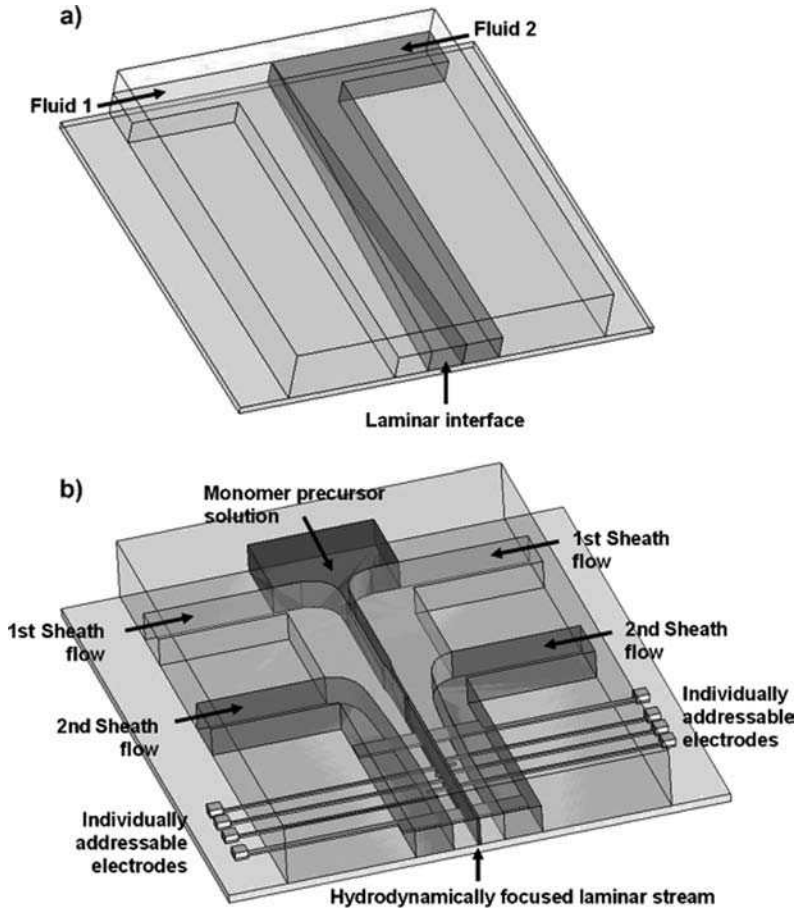

Figure 10.32 *(a) A laminar interface generated between two miscible fluid streams can serve as a flowing template for continuous micropatterning in a fluidic channel. (b) A hydrodynamically focused laminar stream produced in a new type of microfluidic setup can be employed as a dynamic template for site-specific electrochemical deposition of sizecontrollable CP micropatterns across individually addressable electrode junction pairs. (Reprinted with permission from Angewandte Chemie Int. Ed., A Hydrodynamically Focused Stream as a Dynamic Template for Site-Specific Electrochemical Micropatterning of Conducting Polymers by S. Hou, S. Wang, Z. T. F. Yu et al., 47, 6, 1072–1075. Copyright (2008) Wiley-VCH)*

10.2.4.3 Electrospinning

Electrospinning is an attractive method that is rather unique to the preparation of polymer/organic nanofibril materials. Figure 10.36 shows an exemplary schematic setup for CPNW fabrication by electrospinning [75]. By applying an electric field between a CP solution droplet held at a tip and a conductive substrate, thin polymer fibrils can be extracted from

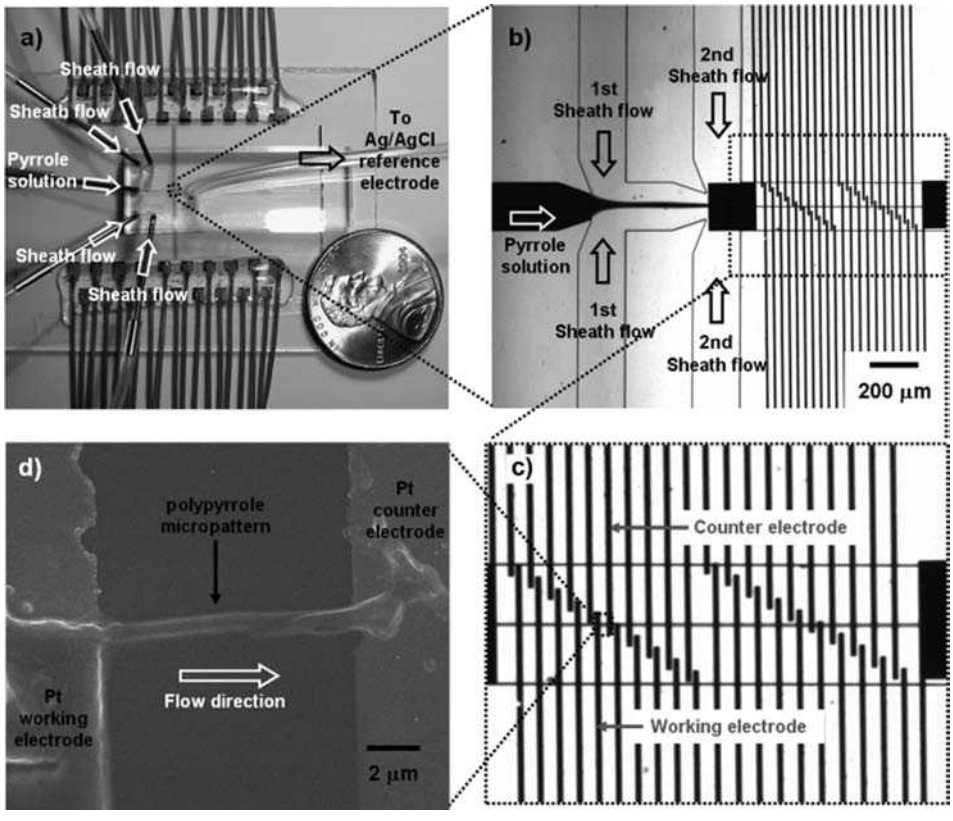

Figure 10.33 *(a) Photograph of the actual microfluidic device. (b) Micrograph of the device in action. A pyrrole solution (flow rate: 1.0 ml min^{-1}) was first injected into the device, and two pairs of sheath streams (flow rate: 30 ml min^{-1}) were employed to compress the pyrrole solution in sequence to generate a 2-mm-wide hydrodynamically focused laminar stream. To help visualize the flow characteristics, food dye was dissolved in the pyrrole solution. (c) The 2-mm-wide focused laminar steam served as a dynamic template for deposition of a 1-mm-wide PPY micropattern across a 10 mm microelectrode junction gap where a constant current (200 nA) was applied. (d) Scanning electron microscopy (SEM) image of the 1-mm-wide PPY micropattern across a Pt electrode pair. (Reprinted with permission from Angewandte Chemie Int. Ed., A Hydrodynamically Focused Stream as a Dynamic Template for Site-Specific Electrochemical Micropatterning of Conducting Polymers by S. Hou, S. Wang, Z. T. F. Yu et al., 47, 6, 1072–1075. Copyright (2008) Wiley-VCH)*

the polymer solution droplet and deposited on the substrate. A high electrical bias is required to create the necessary field. It is common to apply a voltage of several to tens of kilovolts across a gap that is typically in the range 5–50 cm between the tip and the substrate. The diameter of the wires can be controlled by the concentration of polymer solution and the relative speed of the tip against the substrate laterally. Electrospinning is a

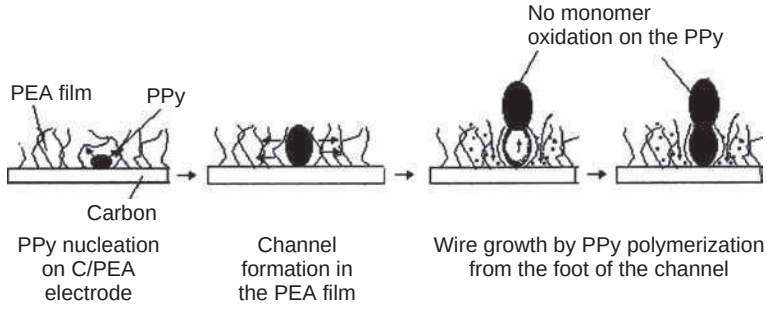

Figure 10.34 *Schematic growth mechanism for PPY wires from a PEA grafted carbon anode. (Reprinted with permission from Chemistry: A European Journal, Electrochemical Synthesis of Conjugated Polymer Wires and Nanotubules by C. Jérôme, S. Demoustier-Champagne, R. Legras and R. Jérôme, 6, 17, 3089–3093. Copyright (2000) Wiley-VCH)*

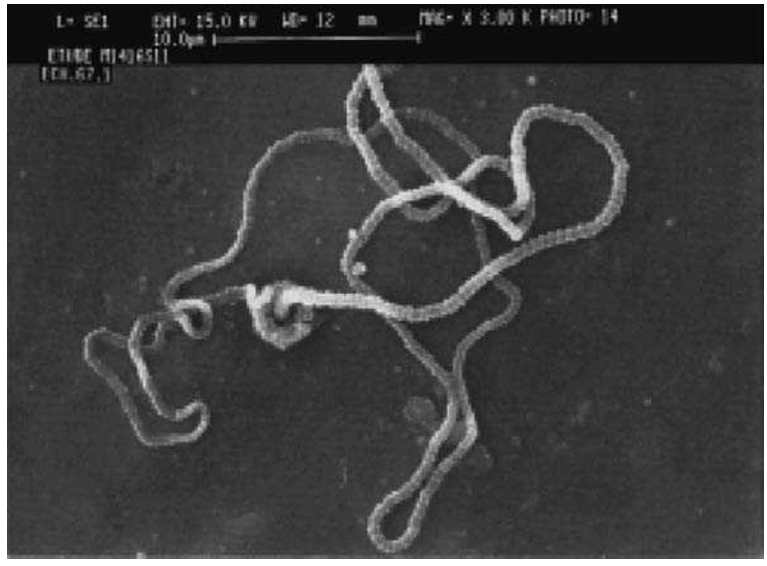

Figure 10.35 *SEM image of PPY/ClO_4 wires grown from a PEA grafted carbon electrode; scale bar: 10 μm. (Reprinted with permission from Chemistry: A European Journal, Electrochemical Synthesis of Conjugated Polymer Wires and Nanotubules by C. Jèrôme, S. Demoustier-Champagne, R. Legras and R. Jérôme, 6, 17, 3089–3093. Copyright (2000) Wiley-VCH)*

serial method for generation of a single CPNW from a droplet of a solution of the CP. PANI and P3HT nanowires with diameters ranging from 30 nm down to microns have been demonstrated [75–81]. Figure 10.37 shows the SEM image of a electrospinning-produced PANI nanowire [80]. The orientation of the CPNWs was controlled by the relative speed of the tip with respect to the substrate.

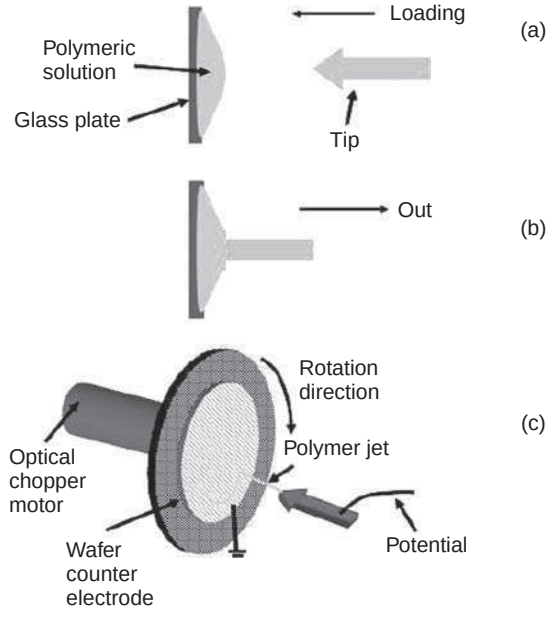

Figure 10.36 *Polymeric nanofibre fabrication process: (a) scanning tip was dipped in a polymeric solution; (b) scanning tip was taken out of the polymeric solution and a liquid droplet was formed on the scanning tip; (c) the potential was applied to a gold wire connected to the scanning tip and the liquid jet was extracted. The fiber jet was deposited on a counter-electrode that was attached to an optical chopper motor for controlling nanofibre orientation. (Reprinted with permission from Nanotechnology, A scanning tip electrospinning source for deposition of oriented nanofibres by J. Kameoka, R. Orth, Y. N. Yang et al., 14, 10, 1124–1129. Copyright (2003) IOP Publishing Inc.)*

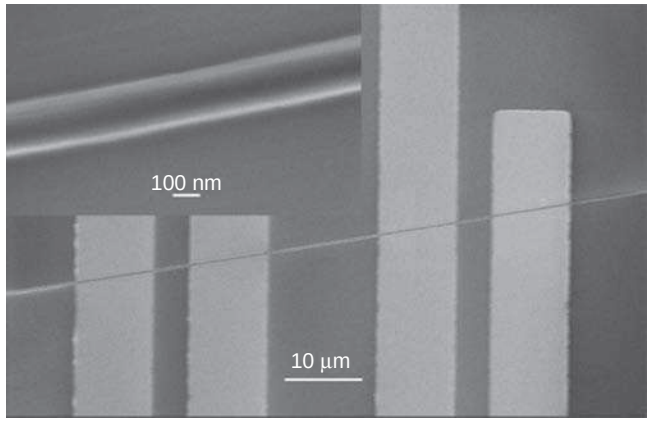

Figure 10.37 *Scanning electron micrograph of a single PANI nanowire lying across four-terminal gold electrodes used for conductivity measurements. (Inset) Higher-magnification view of the CPNW of diameter 180 nm. (Reprinted with permission from Nano Letters, Polymeric Nanowire Chemical Sensor by H. Liu et al., 4, 4. Copyright (2004) American Chemical Society)*

10.2.4.4 Template-Free Controlled Electrochemical Growth between Electrodes

While a template can effectively produce very well-controlled growth of CPNWs, there have been some efforts trying to achieve directional growth of CPNWs without a template. The most common approach is to grow a bridging wire across a pair of metal electrodes by electrochemical polymerization of monomer in a controlled manner. Usually the electrodes used in this approach are defined by lithography, and contain narrow tips facing each other. Different electrochemical growth configurations have been reported to produce satisfactory CPNW growth: (i) the two facing electrodes each serving as working electrode and counter-electrode, respectively ; and (ii) both electrodes serving as working electrodes while a third counter-electrode is employed [82–85]. Figures 10.38 and 10.39 show images of CPNWs produced by such methods.

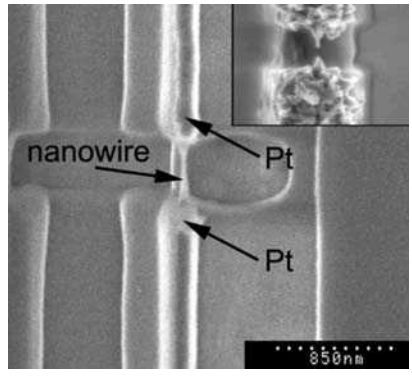

Figure 10.38 *SEM image of a single nanowire between the nanoelectrodes. The inset, an SEM image of a device with incomplete nanowire growth, shows the two-nanowire approach to bridging the gap. (Reprinted with permission from Advanced Materials, Bridging the Gap: Polymer Nanowire Devices by N. T. Kemp, D, McGrouther, J. W. Cochrane and R. Newbury, 19, 18, 2634–2638. Copyright (2007) Wiley-VCH)*

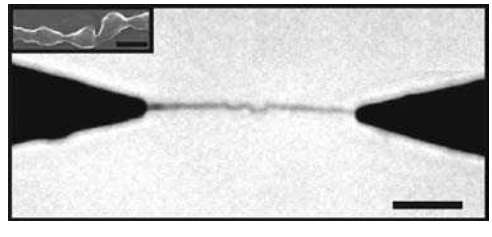

Figure 10.39 *An optical micrograph of a wire grown from aqueous EDOT/PSS solution. Inset: a scanning electron micrograph of a PEDOT nanowire. The scale bars represent 10 μm except for those in the insets, which denote 500 nm. (Reprinted with permission from Applied Physics Letters, Directional growth of polypyrrole and polythiophene wires by P. S. Thapa, D. J. Yu, J. P. Wicksted et al., 94, 3 (2009) American Institute of Physics)*

It has been reported that the size and directionality of the nanowire is very sensitive to synthetic conditions such as electrode size, the gap between the electrodes, and magnitude and frequency of the voltage/current, as well as the concentrations of the monomers and electrolyte, etc. However, even if precautions are taken, control over the dimensions and directionality of the grown single nanowire is limited. Variation of the wire size is common, and the wires can be knobbly.

10.3 Transport Properties and Electrical Characterization

10.3.1 Background

Charge transport plays an essential role in electronic and optoelectronic applications of nanoscale conducting-polymer materials. Understanding the fundamental transport physics of CPNWs is of significant importance for potential application of these materials as FET, chemical and biological sensors, and organic photovoltaic devices. Over the last two decades, following the development of nanomaterial synthesis and nanofabrication technology, major advances in characterization methodology for low-dimensional material systems, as well as fundamental physical understanding have been achieved. There have been numerous studies on the electronic transport of nanowires, nanotubes, nanoparticles, and single molecules, etc. For example, ballistic electronic transport has been found in highly ordered inorganic nanowires and carbon nanotubes, the Luttinger model has been used to explain charge injection into1-D CNTs, and the Coulomb blockade has been found to be the dominating mechanism for electronic transport between electrodes separated by a miniature material, e.g. nanoparticles and molecules. On the other hand, however, while great progress has been made, complete understanding of charge transport in nanoscale conducting-polymer wires has proved to be much more challenging. This is largely due to the differences in physical nature between the CP material and other materials, as well as the enormous structural variation as a result of their different physical and chemical natures at the atomic and molecular levels.

At the basic atomic and molecular levels, most CPs are constituted of linear chains of conjugated organic molecules. Compared to inorganic nanowires and carbon nanotubes, in which 3-D and 2-D chemical bonding constructs very rigid atomic networks, in CPs 1-D bonding along the linear-shaped molecules makes bending and rotation of the polymer chain inevitable. This is true even in cases when π–π stacking between neighboring polymer chains introduces molecular order and stiffness on a localized scale. However, due to the limited strength of π–π stacking relative to the large configuration entropy of the system, unlike oligomers or small molecules, most CP materials are either amorphous or polycrystalline, with the exception of very limited examples where single crystalline materials, e.g. P3HT self-organized crystals, have been demonstrated [86,87.]

On one hand, the flexibility of the polymer introduces some very attractive properties, e.g. flexible, solution processible, easy to functionalize, and so on, to this category of materials; on the other hand, the structure variation causes tremendous variation in the electronic transport properties of CPs. The overall structure of a CP nanowire is determined by material organization at several length scales. Therefore, unlike some of the

inorganic single-crystal nanowires and nanotubes, electronic transport in CPNWs is collectively determined by a few characteristic charge-transport processes at different levels, i.e. intramolecule, intermolecule, and intergrain-domain, etc. Depending on the size of polymer molecule, side-chain modification, and detailed preparation methods, conducting-polymer nanowires exhibit quite different morphologies, which can lead to significant disparity in electronic transport.

As discussed previously, significant advances have been made in the preparation of CP nanowires and nanotubes over the past decade. Various potential applications with nanoscale CP materials have been proposed or even demonstrated. As critical factors that govern the performance of CP nanowires in electronic and optoelectronic applications, electronic conductance and underlying fundamental transport physics have been a focal point for many of the studies. While studies on bulk, thin films and the assembly of nanowires are of importance, electrical characterization and fundamental transport investigation on single nanowires can provide detailed understanding of the materials with less ambiguity. This is in contrast to collective results obtained from multiple nanowires that have distributed properties; and single nanowire study also eliminates the potentially complicated transport process across wire boundaries. Studies on individually addressable CP nanowires can thus presumably yield more detailed transport physics. Substantial numbers of investigation have been carried out on single PAC, PPY, PANI, and PEDOT nanowires and nanotubes [38,51,79,88–105]. These investigations have significantly improved our understanding of electrical conductivity in this category of materials. In this section, we will review and discuss recent progress made in the characterization of electronic transport properties of single conducting-polymer nanowires.

10.3.2 Brief Summary of Transport in 3-D CP Materials

Before we continue to discuss charge transport in nanoscale CP materials, it is important to briefly introduce the progress and current understanding of transport physics in bulk CP materials. Also, it is important to point out that, governed by the material nature, many nanoscale CP materials exhibit very similar electronic and optical properties to their 3-D counterparts. Significant deviation between nano and bulk materials occurs only when the size of nanomaterials reach $\sim$10 nm – the typical charge delocalization length scale in a CP material [106]. However, please also note that enhanced structural order in a CPNW much wider than 10 nm is suggested to be the cause of noticeable improvement of the conductance of a CPNW [68].

Since the discovery of CPs in the 1970s, there has been intensive study of the electrical properties of these materials. Fundamental understanding of electronic energy band structures, carrier doping, and transport in 3-D CP materials has been developed to the extent that theories and models are now readily available to predict and interpret the electrical conductivity of the materials, and provide guidelines for the design and performance analysis of electronic and optoelectronic devices made from this category of materials. The award of the Nobel Prize in Chemistry in 2000 to Alan Heeger, Alan MacMiarmid, and Hideki Shirakawa for the discovery and development of CPs indicates the importance and establishment of this field.

In contrast to single crystalline materials, the heterogeneity in CP structures introduces remarkable complexity in the electronic transport on different material levels and different

length scales. The conductivity of a material is determined at least by intramolecular, intermolecular (within a crystalline grain), and intergrain electronic transport. Depending on the doping concentration and extent of order (or disorder), each of these factors may contribute/influence more or less towards the total conductivity of the material. In a simple way, the underlying causes for different materials yielding similar conductivities can be fundamentally different as the total conductance is collectively dictated by several factors at different length levels. Typically, a careful temperature dependence study of conductivity can reveal much more detailed information on the transport properties of a material, as the transport in each of the above length scales exhibits different characteristic temperature dependence.

Based on the doping concentration, in their early studies of PAc and PPY materials, Heeger and colleagues observed the transition from insulator to metallic as the dopant, (e.g. AsF_5^-, PF_6^-, I_3^-, etc.) concentration increases. The conductivity of these materials can be characterized under three distinct categories, i.e. insulating, critical, and metallic [107–109]. These three cases can be summarized as follows.

First, at low dopant concentrations, both PPY and PAc act as insulators. At a relatively high temperature, electronic transport can be described by Mott variable-range-hopping (VRH) model. Resistivity is a function of temperature that follows:

$$\rho(T) \propto \exp\left(T_{\text{Mott}}/T\right)^{1/(d+1)} \tag{10.1}$$

where d is the dimensionality. In particular, for 3-D and 1-D systems, the corresponding temperature dependence of the resistivity are $\rho(T) \propto \exp\left(T_{\text{Mott}}/T\right)^{1/4}$ and $\rho(T) \propto \exp\left(T_{\text{Mott}}/T\right)^{1/2}$, respectively. However, at low temperatures, as the Coulomb interaction between electrons becomes significant, a crossover from Mott VRH to Efros–Shklovskii VRH conduction occurs. In the Efros–Shklovskii 3-D VRH model, resistivity is expected to follow $\rho(T) \propto \exp\left(T_{\text{ES}}/T\right)^{1/2}$. Recently, such a crossover has been observed in individual PANI and PPY submicron tubes as well, indicating the 3-D transport nature of these materials (Figure 10.40) [105]. Since resistivity in 3-D E-S VRH has a similar temperature dependence as 1-D Mott VRH, care should be taken when interpreting the results.

Second, as the dopant concentration increases, the conductivity is in the critical regime when the metal–insulator transition occurs. For a 3-D system, the temperature dependence of the resistivity follows a power law [110]:

$$\rho(T) \propto T^{-\beta}$$

where $0.33 < \beta < 1.0$.

Third, at high a dopant concentrations the materials become metallic. The total resistivity is a combination of the resistance from the doped metallic islands and resistance rising from the fluctuation-induced-tunneling (FIT) between metallic islands. The latter part has a temperature dependence that follows [111]:

$$\rho(T) \propto \exp\left(T_{\text{t}}/(T + T_{\text{s}})\right)$$

where T_{t} and T_{s} are characteristic temperature parameters in the tunneling process.

In reality, due to the polymer and amorphous nature of many CP materials, the overall resistance of the materials is the sum of resistances of inhomogeneous elements along a

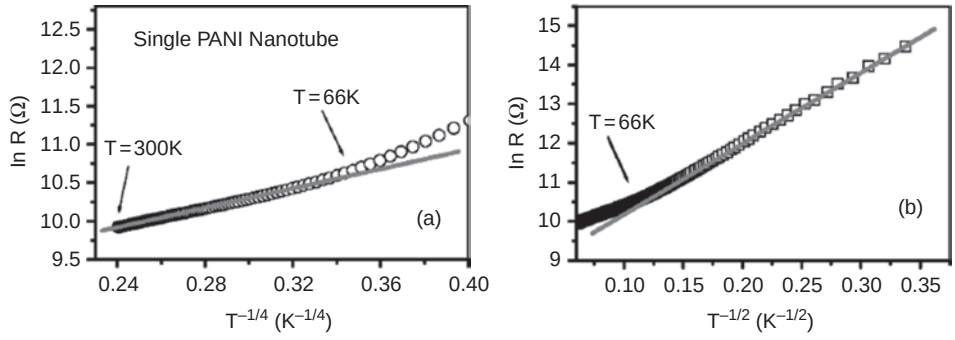

Figure 10.40 *Temperature dependence of resistance of the single polyaniline-CSA tube: (a) plotted as ln* $R(T) \sim T^{-1/4}$*; (b) plotted as ln* $R(T) \sim T^{-1/2}$*. (Reprinted with permission from Phys. Rev. B., Electronic transport in single polyaniline and polypyrrole microtubes by Y. Long, L. Zhang, Z. Chen et al., 71, 16, 165412. Copyright (2005) American Physical Society)*

carrier-transport route. Temperature dependence of the resistance can potentially be rather complicated. In recent articles, Kaiser further rationalized the overall conductivity of several CPs with a model of the heterogeneous transport process originating from the heterogeneous disorder of the materials [112–114]. Capturing the heterogeneous nature of the materials, this model produces a good agreement with experimentally observed temperature dependence of conductivity for several CPs.

10.3.3 Conductivity of CP Nanowires, Nanofibers, and Nanotubes

As we discussed in the previous section, in recent years, there has been significant progress in the preparation of various nanoscale CP materials. Nanowires, nanotubes, and nanofibers of a considerable number of materials have been demonstrated. In many studies, individually addressable nanomaterials have been successfully prepared. These advances have provided tremendous opportunities for transport studies of individual linear nanomaterials. In the following, we will review and discuss some of the recent efforts in conductivity studies of this category of materials.

Determined by their molecular nature, most CP nanoscale materials are either amorphous or polycrystalline. In the latter case, the size of the ordered crystalline grain/island is typically less than 10 nm [106]. This limits the electron and hole delocalization length to a similar scale. Therefore, based on this argument, unless the cross-section of a CP nanowire is comparable to the delocalization length, electron and hole transport in such a nanowire should follow their behavior in a 3-D bulk material. As we have discussed in the previous section, many nanowires and nanotubes prepared so far are indeed larger than the characteristic electronic localization length, and it is, in general, valid to treat these nanowires and nanotubes with the already established electronic-transport theories and models for 3-D CP materials.

Although consistently preparing sub-10-nm CPNWs is still very challenging, Samitsu and colleagues measured the conductance of a very narrow (~3.7 nm wide) section of a

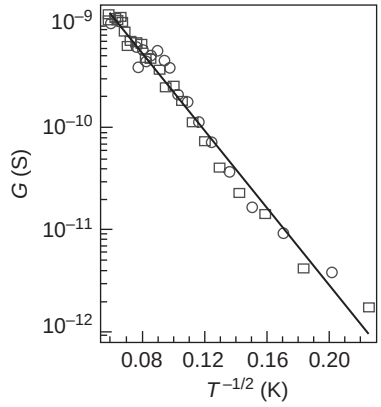

Figure 10.41 *Semilogarithmic plot of* G *vs* $T^{-1/2}$ *for PEDOT nanowires. The square and circle symbols show the conductance values with decreasing and increasing temperatures, respectively. The solid line shows the fitting curve based on the quasi-one-dimensional VRH model. (Reprinted with permission from Applied Physics Letters, Conductivity measurements of individual poly(3,4 ethylenedioxythiophene)/poly(styrenesulfonate) nanowires on nanoelectrodes using manipulation with an atomic force microscope by S. Samitsu, T. Shimomura, K. Ito et al., 86, 23. Copyright (2005) American institute of Physics)*

PEDOT:PSS nanowire (Figure 10.41) [101,102]. The temperature dependence of the resistance indeed followed Mott VRH for a 1-D system, i.e., $\rho(T) \propto \exp\left(T_{\text{Mott}}/T\right)^{1/2}$. T_{Mott} was determined to be 1900 K, which is similar to that of PEDOT:PSS thin films.

On the other hand, several studies have found out that reduction of the cross-section of nanowires can induce the morphology of the material to change. According to these studies, such effects typically become noticeable as the size of the wire approaches the order of ~100–200 nm (Figure 10.42) [68]. However, based on the above analysis, significant alternation of transport physics will not occur until the size of nanowire reaches around 10 nm. Therefore, the increase of conductivity observed is possibly due to more ordered structures within a narrower nanowire, which lead to significant enhancement of the electrical conductivity of the nanowires.

Similar to bulk or thin film samples, CPNWs doped with different species exhibit dramatic differences in conductance and temperature dependence. Cao *et al*. have shown that the conductance of PEDOT:PPS and PEDOT/(ClO_4) nanowires differ qualitatively from each other and their temperature dependence (in the higher temperature ranges, 30–300 K) show that PEDOT:PSS and PEDOT/(ClO_4) nanowires are on the insulating and metallic sides of the metal–insulator transition, following Mott VRH and a power law, respectively. At lower temperatures however, the measured data appear to follow a different relationship for both nanowires. The authors suggested that tunneling plays a more important role than thermally activated hopping at a lower temperature [51].

Park, Aleshin and colleagues have conducted detailed studies of conductivities of PAc and PPY nanofibers [91–94,104]. In these studies, the authors tried to take the quasi-1-D nature of the polymer molecules into consideration to explain the observed conductivity as a function of sample temperature – $\sigma(T)$. Experimental results were

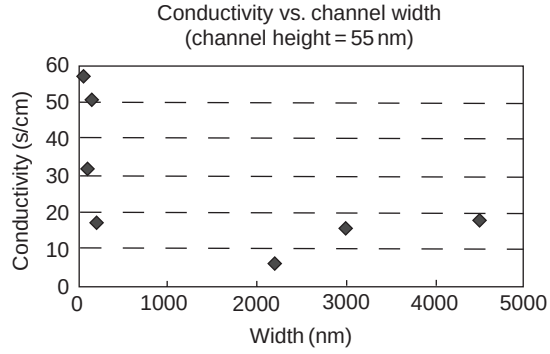

Figure 10.42 *Relationship between conductivity and channel width obtained by four-point measurements. (Reprinted with permission from Nano Letters, Polymeric Nanowire Chemical Sensor by H. Liu et al., 4, 4 671–675. Copyright (2004) American Chemical Society)*

compared with the Luttinger liquid (LL), VRH, environmental Coulomb blockade, and Wigner crystal models. It was found that each of the above theoretical models alone cannot explain the data observed. It was suggested that a combination of these models may be needed to reflect the heterogeneous conductivity of the materials. Such a consideration is consistent with the inhomogeneous material structure of CPNWs, i.e. the overall conductance of a CPNW is governed by a few transport processes at different length scales. Furthermore, the authors proposed a physical possibility that involves multiple kinks in the LL model. For a more complete description, readers are directed to later reviews by some of the authors [95,106].

While the temperature dependence of conductance can reveal fundamental transport mechanisms in CPNWs, current–voltage characteristics provide direct information on the electrical properties of CP materials. Kaiser and Park introduced an expression with which the nonlinear *I–V* characteristics of highly conductive CP materials can be treated as conduction through small barriers between metallic regions [100]:

$$G = \frac{I}{V} = \frac{G_0 \exp(V/V_0)}{1 + h[\exp(V/V_0) - 1]}$$

where G_0 is the temperature-dependent low-field conductance; V_0 is a scale factor; $h = G_0/G_h$, and G_h is the high-field saturating conductance. It has been shown that this expression describes the *I–V* characteristics of various types of nanoscale materials very well, including CPs, carbon nanotubes, and V_2O_5 nanofibres, etc. at different temperatures (Figure 10.43) [100].

Very recently, Yin *et al.* applied this expression in a transport study of individual PPY, PANI nanotubes, and PEDOT nanowires [99]. The authors also found that the temperature- and field-dependent *I–V* characteristics of these nanoscale materials can be fitted very well with the expression.

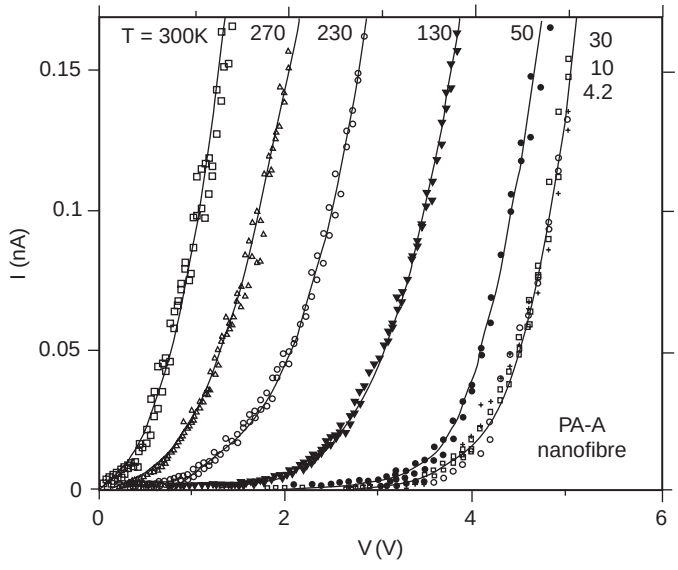

Figure 10.43 *Current–voltage characteristics of individual polyacetylene nanofibers. (Reprinted with permission from Synthetic Metals, Current-voltage characteristics of conducting polymers and carbon nanotubes by A. B. Kaiser and Y. W. Park, 152, 1–3. Copyright (2005) Elsevier Ltd)*

10.3.4 Summary

We have briefly reviewed fundamental studies and recent progress in charge transport and electrical conductivity of nanoscale CP materials. It is found that in most situations, as the sizes of CPNWs or CPNTs are larger than the carrier delocalization length (usually <10 nm), the transport behavior of nanoscale materials can still be described well with theories developed for bulk CP materials. When the size of a nanowire gets down to $\sim$10 nm, a 1-D model can indeed be used to better describe the transport process. Given the inhomogeneous structures of most CP materials, the overall conductivity of a CPNW can best be rationalized with heterogeneous carrier transport though different regions of the materials. This concept has been successfully applied to describe both the temperature and the field dependence of conductivity of various types of CPNWs.

10.4 Applications of Single Conducting Polymer Nanowires (CPNWs)

After nearly 30 years of research and development, CPs have become a very important category of materials. Compared to other materials, CPs possess some distinctive chemical, electrical, and mechanical properties which lead to unique applications in electronics, optoelectronics, and chemical/biological sensing, etc. They are being widely applied in many different areas. However, compared to bulk materials, applications of nanoscale CP materials are still at a relatively early stage. Obviously, whether these nanoscale materials

can find their way into particular applications is mainly determined by whether they can introduce novel properties and physical phenomena. Quite often, properties of a material depend heavily on the quality of the material. As we have discussed in the previous section, in recent years there has been tremendous effort in developing synthesis and fabrication methodology for the preparation of high-quality nanoscale CP materials. In this section, we will review some of the important recent progress towards potential applications of novel nanoscale CP materials. In particular, we will dedicate the discussion mainly to, again, those individually addressable CPNWs and CPNTs. The applications of an array of parallel CPNWs which are connected to common electrodes are also included. The general applications of CP materials in other forms and scales are not a topic of this section and are addressed in another chapter.

10.4.1 CPNW Chemical and Biological Sensors

One of the most investigated applications of single CPNWs is chemical/biological sensing [2,8,11,12,35,39,50–53,64,69,70,80,82,84,115,116]. There are several different device configurations. Among them, chemoresistors are the most common and popular type of CPNW-based sensor. Primarily, the interaction between the CPNW and analytes results in changes in the charge transport properties of the CPNW; therefore electrical conductance of such a device varies accordingly with a change in the chemical or biological environments.

CPNW sensors have attracted tremendous attention due to the following main reasons: (i) quasi-one-dimensional CPNWs have very large surface-to-volume ratio so that their conductance can response sensitively to environmental changes; (ii) CPs can be modified and functionalized easily so that they can be sensitive to specific analytes; (iii) CPs can interact with a wide range of analytes via various chemical and physical interactions; and (iv) there are a variety of CP materials available.

It has been demonstrated that CPNWs are promising materials for the fabrication of a wide range of chemical and biological sensors. For example, a single PANI nanowire was reported to be able to detect ammonia gas at concentrations as low as 0.5 ppm with short response and recovery times (Figure 10.44) [80]. In another case, a single PANI nanowire detected ammonia gas down to a pressure of 10^{-7} bar (Figure 10.45) [84].

A glucose sensor which was made by immobilizing glucose oxidase on a single PANI nanowire showed a short response time of less than 200 ms and a high sensitivity of less than 2 mM (Figure 10.46) [82]. Functional biological molecules, avidin-conjugated ZnSe/CdSe quantum dots (Aqd), were incorpoarted into a PPY nanowire during electropolymerization for bioaffinity sensing, and 1 nM of biotin conjugated to a 20-mer DNA (biotin-DNA) could be detected by the functionalized nanowire due to the binding of biotin-DNA with avidin in the nanowire [115]. A chemical and biological chemiresistive sensor based on a single polypyrrole-nitrilotriacetic (PPY-NTA) nanotube was used as for detection of as low as 1 ng ml^{-1} histidine-tagged protein and 0.6 ppt cupric ions (Figure 10.47) [35]. A chemiresistive sensor for a cancer biomarker, which was able to detect 1 to 1000 U ml^{-1} CA 125 in phosphate buffer and in spiked human blood plasma, was made by functionalizing a single PPY nanowire with antibodies towards the cancer antigen (CA 125) using glutaraldehyde (GA) and *N*-(3-dimethylaminopropyl)-*N′*-ethylcarbodiimide hydrochloride (EDC) chemistry (Figure 10.48) [116].

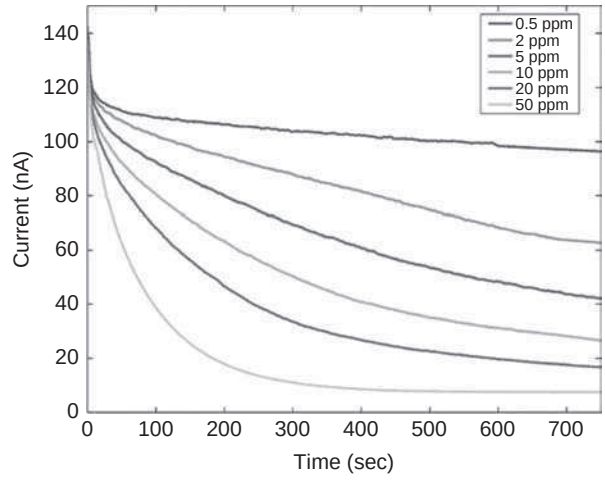

Figure 10.44 *Measured time-dependent current through an individual CPNW sensor upon exposure to NH_3 gas. The nanowire device being tested was about 335 nm in diameter. (Reprinted with permission from Nano Letters, Polymeric Nanowire Chemical Sensor by H. Liu et al., 4, 4, 671–675. Copyright (2004) American Chemical Society) (See colour Plate 4)*

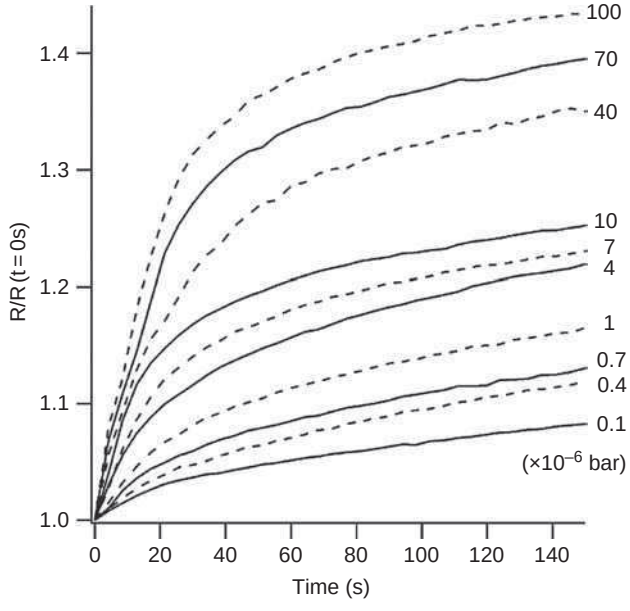

Figure 10.45 *Real-time CP nanowire device response to ammonia gas for pressures ranging from 0.1 to 100 × 10^{-6} bar. The data is normalized by the resistance* $R/R(t = 0)$ *of the device prior to each exposure. (Reprinted with permission from Advanced Materials, Bridging the Gap: Polymer Nanowire Devices by N. T. Kemp, D, McGrouther, J. W. Cochrane and R. Newbury, 19, 18, 2634–2638. Copyright (2007) Wiley-VCH)*

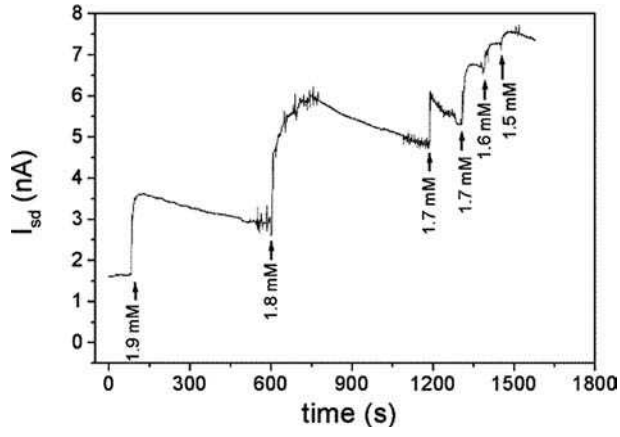

Figure 10.46 *Time course of drain current at* $E_g = 35$ *mV vs. SCE* ($V_{sd} = -20$ *mV) for a PANI-PAA/PANI-bisulfite/GOx-PDAB nanojunction (20–60 nm) in 20 µl McIlvaine buffer, 0.5 M* Na_2SO_4 *pH 5 upon 1 µl successive additions of 40 mM glucose. (Reprinted with permission from Nano Letters, A Conducting Polymer Nanojunction Sensor for Glucose Detection by Erica S. Forzani et al., 4, 9. Copyright (2004) American Chemical Society)*

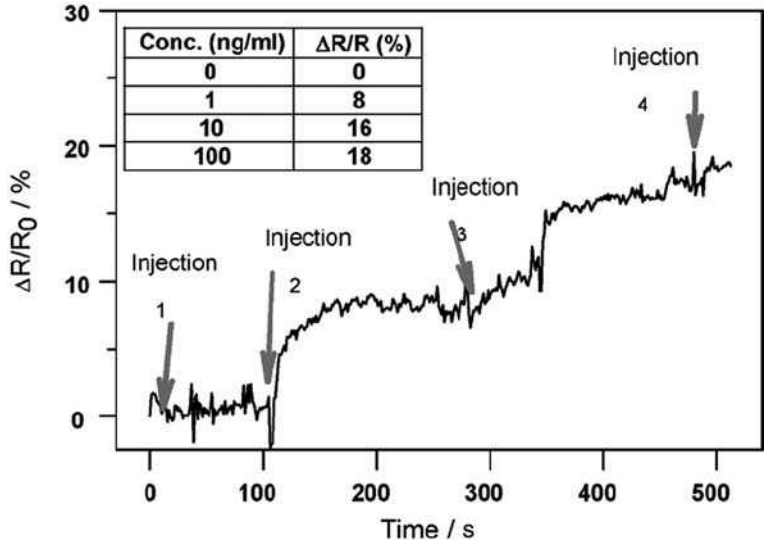

Figure 10.47 *Real-time detection of* His_5*-syntaxin with a PPY-NTA single nanotube saturated with* Cu^{2+} *ions. 5 µl injections of: (1) water, (2) 1 ng* ml^{-1}*, (3) 10 ng* ml^{-1}*, and (4) 100 ng* ml^{-1}*. (Reprinted with permission from Biosensors and Bioelectronics, Label-free detection of cupric ions and histidine-tagged proteins using single poly(pyrrole)-NTA chelator conducting polymer nanotube chemiresistive sensor by C. L. Aravinda, S. Cosnier, W. Chen et al., 24, 5. Copyright (2009) Elsevier Ltd)*

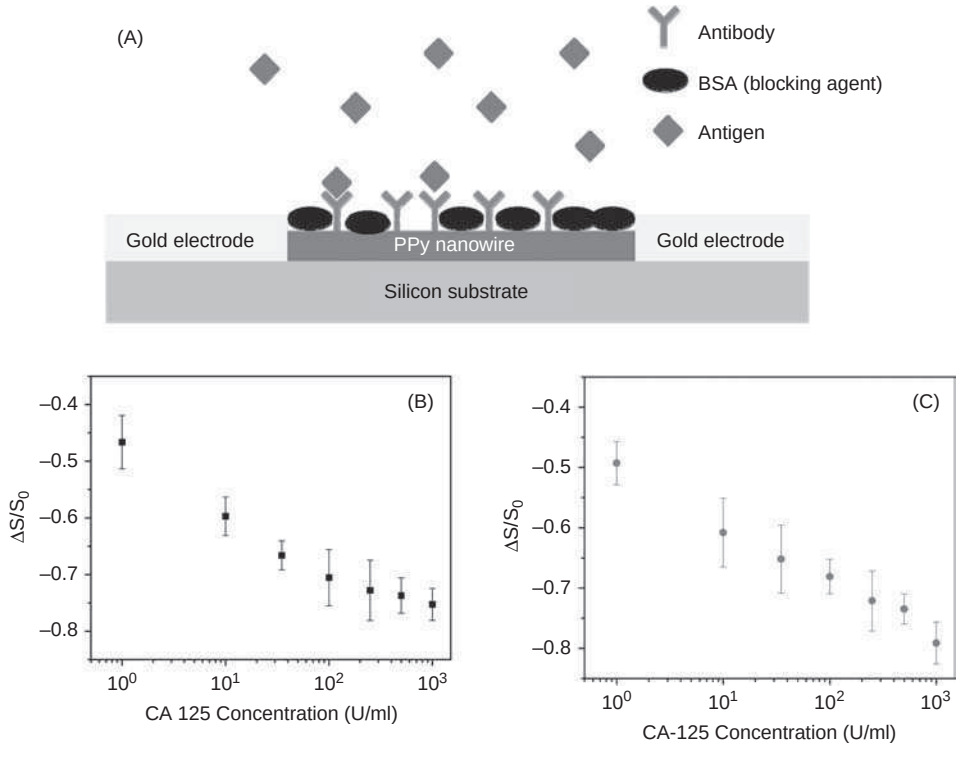

Figure 10.48 *(A) Schematic of a single PPy nanowire sensor covalently modified with anti-CA 125 using EDC chemistry and blocked by BSA to reduce nonspecific binding. Calibration curve in terms of normalized conductance change of a single PPy nanowire biosensor for CA 125 detection in 10 mM phosphate buffer (B) and spiked human blood plasma (C). Each point represents an average of three (B) or four (C) measurements, and the error bars represent ±1 standard deviation. (Reprinted with permission from Analytical Chemistry, Single Conducting Polymer Nanowire Chemiresistive Label-Free Immunosensor for Cancer Biomarker by M. A. Bangar et al., 81, 6. Copyright (2009) American Chemical Society)*

Chen and Luo demonstrated a multi-CPNW sensor approach which includes multiple precisely defined and individually addressable heterogeneous CPNWs. A collection of PPY, PEDOT, and CPs based on their variations were used to prepare multimodality chemical-sensor systems, which showed different responses to different gases or vapors with high sensitivities (Figure 10.49) [69]. Such a combinatorial approach can potentially provide 'finger-printing' for different species for accurate and reliable detection of various chemical analytes.

10.4.2 CPNW Field-Effect Transistors

As an important potential application, single CPNW field-effect transistors (FET) have also been demonstrated by a few research groups [34,38,49,81,117–119]. Figure 10.50 shows a schematic of CPNW FET [81]. In general, limited by their low carrier mobility,

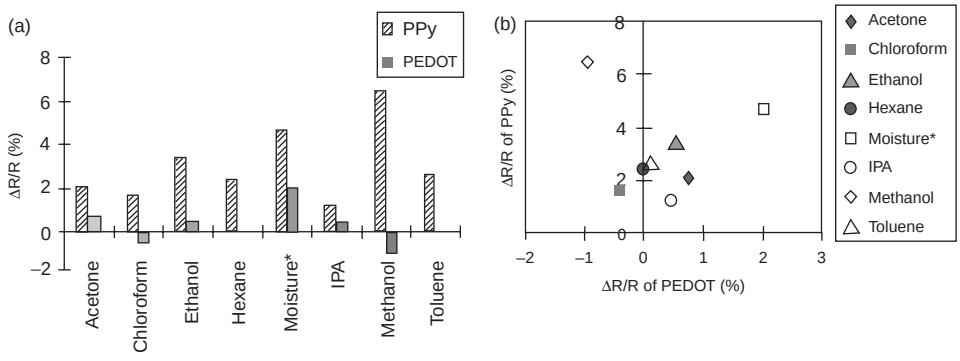

Figure 10.49 *(a) Resistance response of 80-nm-wide PPY and PEDOT nanowires to analytes at 1000 ppm concentration. (b) Sensing responses from the two nanowires presented on a 2-D scatter plot. Moisture corresponds to 8% relative humidity at 23 °C. IPA stands for isopropyl alcohol. (Reprinted with permission from Advanced Materials, Precisely Defined Heterogeneous Conducting Polymer Nanowire Arrays – Fabrication and Chemical Sensing Applications by Y. Chen and Y. Luo, 21, 20, 2040–2044. Copyright (2009) Wiley-VCH)*

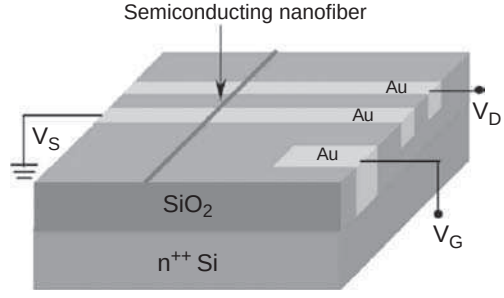

Figure 10.50 *Schematic of the nanofiber field effect transistor structure. (Reprinted with permission from Applied Physics Letters, Single electrospun regioregular poly(3-hexylthiophene) nanofiber field-effect transistor by H. Liu, C. H. Reccius and H. G. Craighead, 87, 25. Copyright (2005) American Institute of Physics)*

the switching speed of various CP-based FETs does not come close to that of a silicon FET. This is true for CPNW FETs as well. However, with advantages such as ease of fabrication and low manufacturing cost, CP-based FETs, especially those based on a single CPNW, have been a focus of intensive studies (see Figure 10.50).

Since most of the CPNWs are p-type (or undoped), an FET made from such a CPNW also has a p-channel operating in either the depleted or the enhanced mode depending on the doping level and work function of the metal electrodes. For example, in a depleted-mode FET, a positive gate bias against the source, above a threshold voltage, is required to turn off the conductance of holes in the channel. However, quite often, the gating response is rather poor due to a thick gate dielectric layer and more importantly, a very shallow carrier depletion depth in CP materials (Figure 10.51) [81,120]. Nevertheless, FETs based on a single CPNW have shown promising electrical performance. A single CPNW FET with an

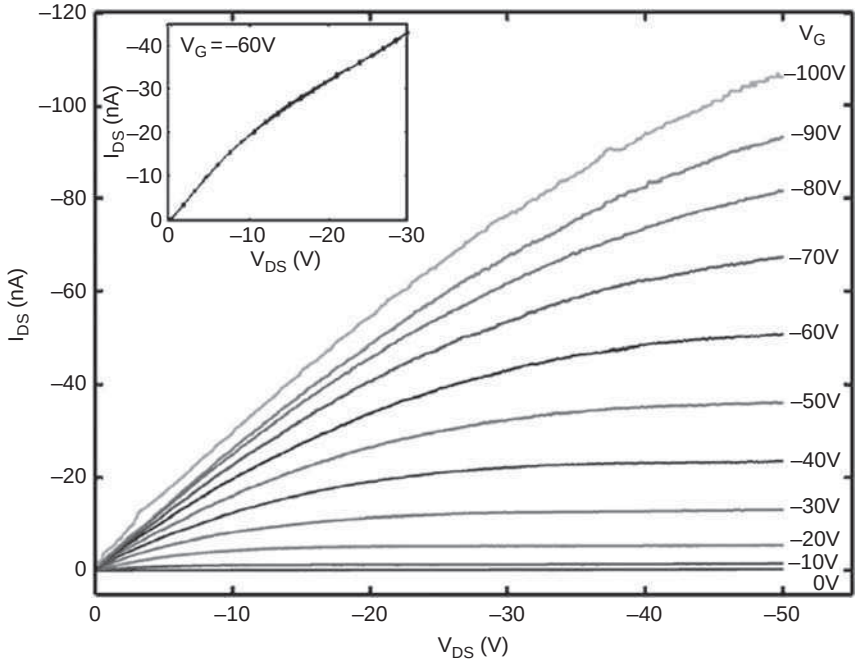

Figure 10.51 *I_{DS} vs. V_{DS} characteristics of a regio-regular P3HT nanofiber FET, with an effective channel length of 10 μm and diameter of 180 nm, showing accumulation mode operation when a different negative gate bias is applied. Inset: The forward and reverse sweeps exhibit negligible hysteresis of the device. (Reprinted with permission from Applied Physics Letters, Single electrospun regioregular poly(3-hexylthiophene) nanofiber field-effect transistor by H. Liu, C. H. Reccius and H. G. Craighead, 87, 25. Copyright (2005) American Institute of Physics) (See colour Plate 5)*

electrolyte solution gate was demonstrated to have better electrical performance than CP thin-film-based FETs in terms of transconductance and on/off current ratio [117]. Though not as common as a p-channel FET, an n-channel single CPNW FET may also be fabricated from a limited pool of CP materials. An FET made from a single poly(benzobisimidazobenzophenanthroline) (BBL) nanobelt was measured to be of the n-type with electron mobility of 7×10^{-3} cm^2 V^{-1} s^{-1} and on/off current ratio of $\sim 10^4$. (Figure 10.52) [118].

10.4.3 CPNW Optoelectronic Devices

CPs have been proven to be excellent materials for optoelectronic applications, e.g. polymer light-emitting diodes and solar cells etc. [106,121]. Numerous studies have been devoted to this area with the primary focus on thin-film or bulk materials. For CPNWs in particular, recent studies have shown that these materials are very promising candidates for efficient nanoscale photovoltaic devices [30,52,54,57]. Figure 10.53 shows the optical response of a single CPNW in terms of photocurrent towards light exposure [52].

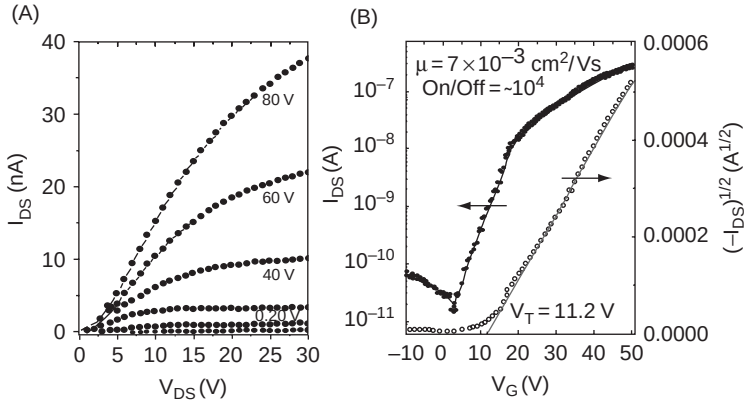

Figure 10.52 *Electrical characterization of a single BBL nanobelt transistor with the nanobelt bridging the source-drain electrodes: (A) output characteristics showing well-resolved current–voltage saturation; (B) corresponding transfer and square root of current characteristics. (Reprinted with permission from Chemistry of Materials, Self-Assembly, Molecular Packing and Electron Transport in n-Type Polymer Semiconductor Nanobelts by A. L. Briseno et al., 20, 14. Copyright (2008) American Chemical Society)*

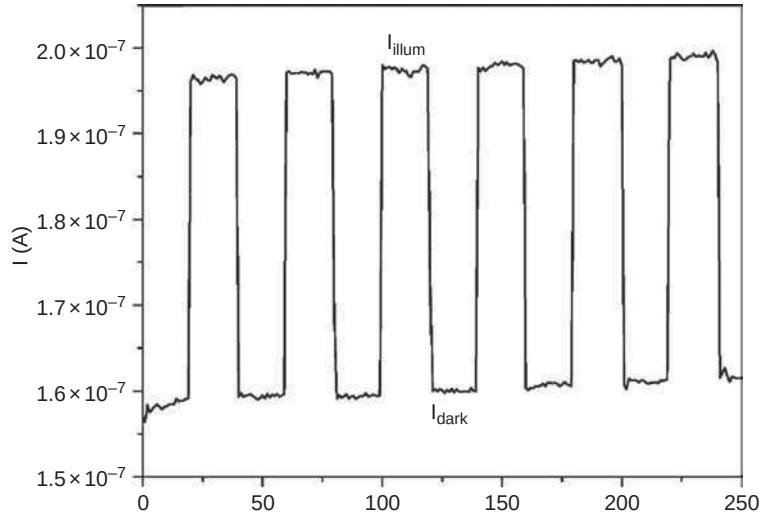

Figure 10.53 *Optoelectronic response of a multisegmented nanowire towards multiple exposure to light (550 nm) at 0.5 V bias.* I_{illum} *and* I_{dark} *correspond to current flowing through the nanowire under light illumination and dark conditions, respectively. (Reprinted with permission from Electroanalysis, Magnetically Assembled Multisegmented Nanowires and Their Applications by M. A. Bangar, C. M. Hangarter, B. Yoo et al., 21, 1, 61–67. Copyright (2009) Wiley-VCH)*

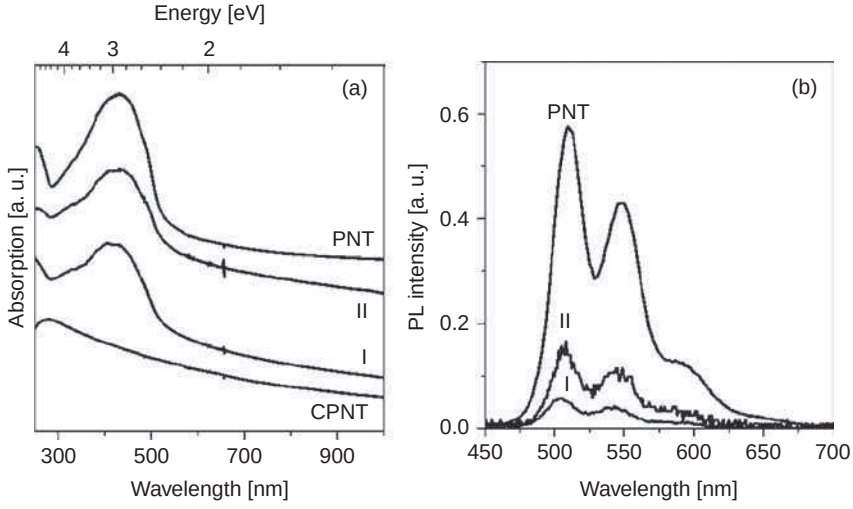

Figure 10.54 *Comparison of: (a) UV-vis absorption and (b) photoluminescence (PL) spectra ($\lambda_{ex} = 360$ nm) of CPNT, bilayer nanotube I (~4 nm thick PPV layer), bilayer nanotube II (~18 nm thick PPV layer), and PPV nanotube (PNT). The samples (1.0 mg) were dispersed in chloroform (5 ml) by ultrasonication. The PL intensities were normalized against the corresponding absorption value at an excitation wavelength of 360 nm. (Reprinted with permission from Advanced Materials, Photoconductivity of Single-Bilayer Nanotubes Consisting of Poly(p-phenylenevinylene) (PPV) and Carbonized-PPV Layers by K. Kim, B. H. Kim, S.-H. Joo et al., 17, 4, 464–468. Copyright (2005) Wiley-VCH)*

For example, Kim *et al.* showed a single bilayer PPV nanotube photoconducting device that yielded high photoconductivity efficiencies under light illumination (Figures 10.54 and 10.55) [54]. In comparison, a single-layer PPV yields much lower photoconductivity. The significant enhancement of photoconductance is a result of effective charge separation of excitons at the interface between PPV and carbonized PPV, whereas in a single-layer PPV nanowire, electrons and holes in excitons are tightly bound and cannot split into separate charge carriers. This is consistent with the observation of efficient quenching of the photoluminescence (PL) of the PPV layer by the carbonized PPV layer.

A single poly[(9,9-dioctylfluorenyl-2,7-diyl)-co-(bithiophene)] (F8T2) nanowire was made into a photodetector with responsitivity of about 0.4 mA W^{-1} and quantum efficiency of about 0.1% under monochromatic illumination (Figure 10.56) [57].

On the other hand, single CPNWs may be use as nano light emitters [45], which can have potential applications in field-emission displays 36–38, electrochromic displays [42–44,58] and multicolor fluorescent labeling in bioscience [40]. It has been reported that a dedoping process can improve the photoluminescence (PL) intensity of a CPNW as the measured PL intensity of a dedoped single PEDOT nanowire was 2–3 times higher than that of a doped one, due to the reduction of PL quenching during the dedoping process (Figure 10.57) [45]. Cho *et al.* demonstrated the potential application of single CPNWs in low-power fast electrochomic displays. Alternating square potentials from 1 V to –1 V were applied to switch the redox state of the single PEDOT nanotubes. The color switching

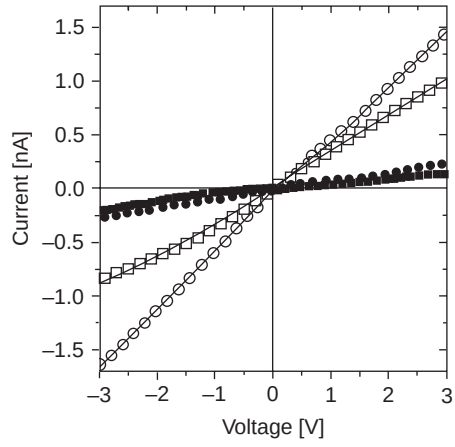

Figure 10.55 *Voltage dependence of current with light (□: bilayer nanotube I, ○: bilayer nanotube II) and without light (■: bilayer nanotube I, ●: bilayer nanotube II). (Reprinted with permission from Advanced Materials, Photoconductivity of Single-Bilayer Nanotubes Consisting of Poly(p-phenylenevinylene) (PPV) and Carbonized-PPV Layers by K. Kim, B. H. Kim, S.-H. Joo et al., 17, 4, 464–468. Copyright (2005) Wiley-VCH)*

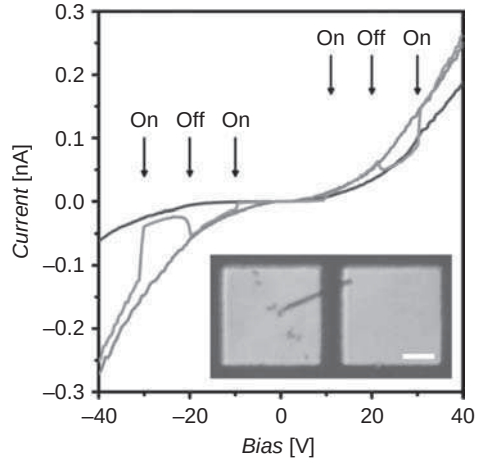

Figure 10.56 *I–V characteristics of a top-contacted F8T2 nanowire acquired in the dark (blue line) and under 405 nm illumination (red line). Reversible switching in I–V data measured under manually chopped 405 nm illumination is also shown (green line). Inset: optical microscopy image of a typical top-contacted F8T2 nanowire device. Scale bar: 10 μm. (Reprinted with permission from Advanced Materials, A Single Polymer Nanowire Photodetector by G. A. O'Brien, A. J. Quinn, D. A. Tanner and G. Redmond, 18, 18, 2379–2383. Copyright (2006) Wiley-VCH) (See colour Plate 6)*

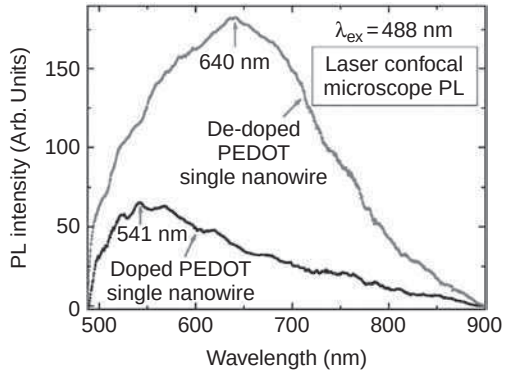

Figure 10.57 *Comparison of laser confocal microscope (LCM) PL spectra of an isolated single strand of doped and dedoped PEDOT nanowires without Raman modes. (Reprinted with permission from Synthetic Metals, ight emission of a single strand of poly(3,4-ethylenedioxythiophene) (PEDOT) nanowire by D. H. Park, H. S. Kim, Y. B. Lee et al., 158, 3–4. Copyright (2008) Elsevier Ltd)*

(oxidation for decoloring and reduction for coloring) time for induvidual nanotubes with 200 nm diameter and 20 nm wall thickness was less than 10 ms [42].

Other applications of single CPNWs include nanodiodes and nanoactuators. For example, a single Au-PPY-Cd-Au nanowire could be formed as a nanodiode after a Schottky junction was formed at the PPY/Cd interface and an ohmic junction was formed at the PPY/Au interface (Figure 10.58) [47]. An array of parallel PPY nanowires was used as a nanoactuator as the mechanical function was derived from the expansion and contraction of the PPY nanowires caused by the movement of ions into and out of the polymer matrix in an aqueous eletrolyte during electrically controlled reversible reduction and oxidation [122].

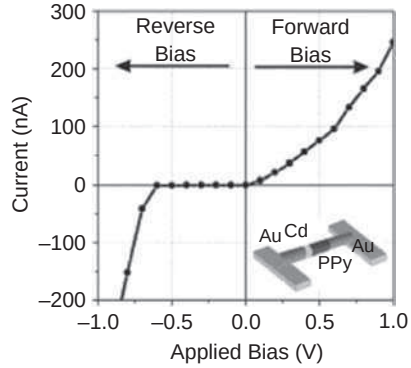

Figure 10.58 *I–V characteristics for a single Au-Ppy-Cd-Au rod at room temperature. (Reprinted with permission from Journal of the American Chemical Society, Hybrid Organic-Inorganic, Rod-Shaped Nanoresistors and Diodes by S. Park et al., 126, 38. Copyright (2004) American Chemical Society)*

10.5 Summary and Outlook

This chapter has focused on important issues in preparation, transport, and potential applications of individually addressable single CPNWs. Comprehensive reviews are given in each of the categories, especially in nanomaterial preparation, transport, and electrical properties. This review has covered the significant progress made in these areas in the past two decades. During the same period of time, tremendous advances have occurred in broad areas of nanoscale science and technology. Numerous fabrication and synthesis techniques have been developed; fundamental understanding of nanoscale materials and structures has now become available. Studies on CPs have substantially benefited from the general advance in our knowledge base, and material processing and handling capabilities. There have been demonstrations of nanoscale CP materials in chemical/biological sensing, as well as electronic and optoelectronic applications. However, looking into the future, several major issues still need to be addressed before nanoscale CP materials can find their way into major, especially single-wire-based, applications. The challenges are mainly in the consistent preparation of high-quality materials that have predictable and reliable chemical, electrical, and optical properties, and furthermore, similar to an outstanding problem faced by other types of nanoscale materials, accurately delivering CPNWs to designated locations and arranging them into ordered structures. Nevertheless, as we have seen in several recent studies, these issues have been addressed. Nanoscale CP materials and structures with complete deterministic dimensions and patterns can now be fabricated by a few different approaches.

References

[1] S.H.M. Persson, P. Dyreklev, and O. Inganas, Patterning of poly(3-octylthiophene) conducting polymer films by electron beam exposure, *Adv. Mater.*, **8**, 405–408 (1996).
[2] B. Dong, D.Y. Zhong, L.F. Chi, and H. Fuchs, Patterning of conducting polymers based on a random copolymer strategy: Toward the facile fabrication of nanosensors exclusively based on polymers, *Adv. Mater.*, **17**, 2736–2741 (2005).
[3] S.Y. Chou, P.R. Krauss, and P.J. Renstrom, Imprint lithography with 25-nanometer resolution, *Science*, **272**, 85–87 (1996).
[4] L.J. Guo, Nanoimprint lithography: Methods and material requirements, *Adv. Mater.*, **19**, 495–513 (2007).
[5] M.S. Kim, J.S. Kim, J.C. Cho, M. Shtein, L.J. Guo, and J. Kim, Flexible conjugated polymer photovoltaic cells with controlled heterojunctions fabricated using nanoimprint lithography, *Appl. Phys. Lett.*, **90**, 123113 (2007).
[6] Z.J. Hu, B. Muls, L. Gence, D.A. Serban, J. Hofkens, S. Melinte, B. Nysten, S. Demoustier-Champagne, and A.M. Jonas, High-throughput fabrication of organic nanowire devices with preferential internal alignment and improved performance, *Nano Lett.*, **7**, 3639–3644 (2007).
[7] M. Behl, J. Seekamp, S. Zankovych, C.M.S. Torres, R. Zentel, and J. Ahopelto, Towards plastic electronics: Patterning semiconducting polymers by nanoimprint lithography, *Adv. Mater.*, **14**, 588–591 (2002).
[8] B. Dong, N. Lu, M. Zelsmann, N. Kehagias, H. Fuchs, C.M.S. Torres, and L.F. Chi, Fabrication of high-density large-area conducting-polymer nanostructures, *Adv. Funct. Mater.*, **16**, 1937–1942 (2006).

[9] W.S. Beh, I T. Kim, D. Qin, Y.N. Xia, and G.M. Whitesides, Formation of patterned microstructures of conducting polymers by soft lithography, and applications in microelectronic device fabrication, *Adv. Mater.*, **11**, 1038–1041 (1999).
[10] F.L. Zhang, T. Nyberg, and O. Inganas, Conducting polymer nanowires and nanodots made with soft lithography, *Nano Lett.*, **2**, 1373–1377 (2002).
[11] D.J. Lipomi, R.C. Chiechi, M.D. Dickey, and G.M. Whitesides, Fabrication of conjugated polymer nanowires by edge lithography, *Nano Lett.*, **8**, 2100–2105 (2008).
[12] Y.S. Jung, W. Jung, H.L. Tuller, and C.A. Ross, Nanowire conductive polymer gas sensor patterned using self-assembled block copolymer lithography, *Nano Lett.*, **8**, 3776–3780 (2008).
[13] S.G. Im, P.J. Yoo, P.T. Hammond, and K.K. Gleason, Grafted conducting polymer films for nano-patterning onto various organic and inorganic substrates by oxidative chemical vapor deposition, *Adv. Mater.*, **19**, 2863–2867 (2007).
[14] M.H. Jung and H. Lee, Patterning of conducting polymers using charged self-assembled monolayers, *Langmuir*, **24**, 9825–9831 (2008).
[15] D. Bullen, S.W. Chung, X.F. Wang, J. Zou, C.A. Mirkin, and C. Liu, Parallel dip-pen nanolithography with arrays of individually addressable cantilevers, *Appl. Phys. Lett.*, **84**, 789–791 (2004).
[16] K. Salaita, S.W. Lee, X.F. Wang, L. Huang, T.M. Dellinger, C. Liu, and C.A. Mirkin, Sub-100 nm, centimeter-scale, parallel dip-pen nanolithography, *Small*, **1**, 940–945 (2005).
[17] D.R. Yaniv and L.D. Mccormick, Polypyrrole nanoplating on HOPG utilizing an STM tip, *Nanotechnology*, **3**, 44–47 (1992).
[18] K. Sasano, K. Nakamura, and K. Kaneto, *In Situ* observation and selective electrochemical deposition of polypyrrole by scanning tunneling microscope, *Jpn. J. Appl. Phys.*, **32**, L863–L865 (1993).
[19] R. Yang, D.F. Evans, and W.A. Hendrickson, Writing and reading at nanoscale with a scanning tunneling microscope, *Langmuir*, **11**, 211–213 (1995).
[20] R.M. Nyffenegger and R.M. Penner, Nanometer-scale electropolymerization of aniline using the scanning tunneling microscope, *J. Phys. Chem.*, **100**, 17041–17049 (1996).
[21] B.W. Maynor, S.F. Filocamo, M.W. Grinstaff, and J. Liu, Direct-writing of polymer nanostructures: Poly(thiophene) nanowires on semiconducting and insulating surfaces, *J. Am. Chem. Soc.*, **124**, 522–523 (2002).
[22] S.Y. Jang, M. Marquez, and G.A. Sotzing, Rapid direct nanowriting of conductive polymer via electrochemical oxidative nanolithography, *J. Am. Chem. Soc.*, **126**, 9476–9477 (2004).
[23] S. Jagadesan, R.C. Advincula, and S. Valiyaveettil, Nanolithographic electropolymerization of a precursor polymer film to form conducting nanopatterns, *Adv. Mater.*, **17**, 1282–1285 (2005).
[24] S. Jegadesan, S. Sindhu, R.C. Advincula, and S. Valiyaveettil, Direct electrochemical nanopatterning of polycarbazole monomer and precursor polymer films: Ambient formation of thermally stable conducting nanopatterns, *Langmuir*, **22**, 780–786 (2006).
[25] S. Jegadesan, P. Taranekar, S. Sindhu, R.C. Advincula, and S. Valiyaveettil, Electrochemically nanopatterned conducting coronas of a conjugated polymer precursor: SPM parameters and polymer composition, *Langmuir*, **22**, 3807–3811 (2006).
[26] Y. Okawa and M. Aono, Materials science – Nanoscale control of chain polymerization, *Nature*, **409**, 683–684 (2001).
[27] Y. Okawa and M. Aono, Linear chain polymerization initiated by a scanning tunneling microscope tip at designated positions, *J. Chem. Phys.*, **115**, 2317–2322 (2001).
[28] J.H. Lim and C.A. Mirkin, Electrostatically driven dip-pen nanolithography of conducting polymers, *Adv. Mater.*, **14**, 1474–1477 (2002).
[29] A. Noy, A.E. Miller, J.E. Klare, B.L. Weeks, B.W. Woods, and J.J. DeYoreo, Fabrication of luminescent nanostructures and polymer nanowires using dip-pen nanolithography, *Nano Lett.*, **2**, 109–112 (2002).
[30] M. Su, M. Aslam, L. Fu, N.Q. Wu, and V.P. Dravid, Dip-pen nanopatterning of photosensitive conducting polymer using a monomer ink, *Appl. Phys. Lett.*, **84**, 4200–4202 (2004).
[31] M. Yang, P.E. Sheehan, W.P. King, and L.J. Whitman, Direct writing of a conducting polymer with molecular-level control of physical dimensions and orientation, *J. Am. Chem. Soc.*, **128**, 6774–6775 (2006).

[32] X.W. Cai, J.S. Gao, Z.X. Xie, Y. Xie, Z.Q. Tian, and B.W. Mao, Nanomodification of polypyrrole and polyaniline on highly oriented pyrolytic graphite electrodes by atomic force microscopy, *Langmuir*, **14**, 2508–2514 (1998).
[33] S. Jahromi, J. Dijkstra, E. van der Vegte, and B. Mostert, In situ polymerisation of pyrrole in nanochannels produced by means of AFM lithography, *Chemphyschem*, **3**, 693–696 (2002).
[34] M. Woodson and J. Liu, Guided growth of nanoscale conducting polymer structures on surface-functionalized nanopatterns, *J. Am. Chem. Soc.*, **128**, 3760–3763 (2006).
[35] C.L. Aravinda, S. Cosnier, W. Chen, N.V. Myung, and A. Mulchandani, Label-free detection of cupric ions and histidine-tagged proteins using single poly(pyrrole)-NTA chelator conducting polymer nanotube chemiresistive sensor, *Biosens. Bioelectr.*, **24**, 1451–1455 (2009).
[36] H.L. Yan, L. Zhang, J.Y. Shen, Z.J. Chen, G.Q. Shi, and B.L. Zhang, Synthesis, property and field-emission behaviour of amorphous polypyrrole nanowires, *Nanotechnology*, **17**, 3446–3450 (2006).
[37] J. Joo, K.T. Park, B.H. Kim, M.S. Kim, S.Y. Lee, C.K. Jeong, J.K. Lee, D.H. Park, W.K. Yi, S.H. Lee, and K.S. Ryu, Conducting polymer nanotube and nanowire synthesized by using nanoporous template: Synthesis, characteristics, and applications, *Synth. Met.*, **135**, 7–9 (2003).
[38] B.H. Kim, D.H. Park, J. Joo, S.G. Yu, and S.H. Lee, Synthesis, characteristics, and field emission of doped and de-doped polypyrrole, polyaniline, poly (3,4-ethylenedioxythiophene) nanotubes and nanowires, *Synth. Met.*, **150**, 279–284 (2005).
[39] S.B. Tolani, M. Craig, R.K. DeLong, K. Ghosh, and A.K. Wanekaya, Towards biosensors based on conducting polymer nanowires, *Anal. Bioanal. Chem.*, **393**, 1225–1231 (2009).
[40] L.T. Qu and G.Q. Shi, Crystalline oligopyrene nanowires with multicolored emission, *Chem. Commun.*, 2800–2801 (2004).
[41] J. Joo, B.H. Kim, D.H. Park, H.S. Kim, D.S. Seo, J.H. Shim, S.J. Lee, K.S. Ryu, K. Kim, J.I. Jin, T.J. Lee, and C.J. Lee, Fabrication and applications of conducting polymer nanotube, nanowire, nanohole, and double wall nanotube, *Synth. Met.*, **153**, 313–316 (2005).
[42] S.I. Cho, W.J. Kwon, S.J. Choi, P. Kim, S.A. Park, J. Kim, S.J. Son, R. Xiao, S.H. Kim, and S.B. Lee, Nanotube-based ultrafast electrochromic display, *Adv. Mater.*, **17**, 171–175 (2005).
[43] R. Xiao, S. Il Cho, R. Liu, and S.B. Lee, Controlled electrochemical synthesis of conductive polymer nanotube structures, *J. Am. Chem. Soc.*, **129**, 4483–4489 (2007).
[44] S.I. Cho, R. Xiao, and S.B. Lee, Electrochemical synthesis of poly(3,4-ethylenedioxythiophene) nanotubes towards fast window-type electrochromic devices, *Nanotechnology* **18**, 405705 (2007).
[45] D.H. Park, H.S. Kim, Y.B. Lee, J.M. Ko, J.Y. Lee, H.J. Kim, D.C. Kim, J. Kim, and J. Joo, Light emission of a single strand of poly(3,4-ethylenedioxythiophene) (PEDOT) nanowire, *Synth. Met.*, **158**, 90–94 (2008).
[46] S. Park, J.H. Lim, S.W. Chung, and C.A. Mirkin, Self-assembly of mesoscopic metal-polymer amphiphiles, *Science*, **303**, 348–351 (2004).
[47] S. Park, S.W. Chung, and C.A. Mirkin, Hybrid organic-inorganic, rod-shaped nanoresistors and diodes, *J. Am. Chem. Soc.*, **126**, 11772–11773 (2004).
[48] Y. Berdichevsky and Y.H. Lo, Fabrication and evaluation of conducting polymer nanowire heterostructures, *Mater. Res. Soc. Symp. Proc.* **872**, J13.14 (2005).
[49] H.J. Chung, H.H. Jung, Y.S. Cho, S. Lee, J.H. Ha, J.H. Choi, and Y. Kuk, Cobalt-polypyrrole-cobalt nanowire field-effect transistors, *Appl. Phys. Lett.*, **86**, 213113 (2005).
[50] Y.P. Dan, Y.Y. Cao, T.E. Mallouk, A.T. Johnson, and S. Evoy, Dielectrophoretically assembled polymer nanowires for gas sensing, *Sens. Actuat. B Chem.*, **125**, 55–59 (2007).
[51] Y. Cao, A.E. Kovalev, R. Xiao, J. Kim, T.S. Mayer, and T.E. Mallouk, Electrical transport and chemical sensing properties of individual conducting polymer nanowires, *Nano Lett.*, **8**, 4653–4658 (2008).
[52] M.A. Bangar, C.M. Hangarter, B. Yoo, Y. Rheem, W. Chen, A. Mulchandani, and N.V. Myung, Magnetically assembled multisegmented nanowires and their applications, *Electroanalysis*, **21**, 61–67 (2009).
[53] S.C. Hernandez, D. Chaudhuri, W. Chen, N.V. Myung, and A. Mulchandani, Single polypyrrole nanowire ammonia gas sensor, *Electroanalysis* **19**, 2125–2130 (2007).

[54] K. Kim, B.H. Kim, S.H. Joo, J.S. Park, J. Joo, and J.I. Jin, Photoconductivity of single-bilayer nanotubes consisting of poly(*p*-phenylenevinylene) (PPV) and carbonized-PPV layers, *Adv. Mater.*, **17**, 464–468 (2005).
[55] K. Kim and J.I. Jin, Preparation of PPV nanotubes and nanorods and carbonized products derived therefrom, *Nano Lett.*, **1**, 631–636 (2001).
[56] G.A. O'Brien, A.J. Quinn, D. Iacopino, N. Pauget, and G. Redmond, Polythiophene mesowires: synthesis by template wetting and local electrical characterisation of single wires, *J. Mater. Chem.*, **16**, 3237–3241 (2006).
[57] G.A. O'Brien, A.J. Quinn, D.A. Tanner, and G. Redmond, A single polymer nanowire photodetector, *Adv. Mater.*, **18**, 2379–2383 (2006).
[58] S.I. Cho, D.H. Choi, S.H. Kim, and S.B. Lee, Electrochemical synthesis and fast electrochromics of poly(3,4-ethylenedioxythiophene) nanotubes in flexible substrate, *Chem. Mater.*, **17**, 4564–4566 (2005).
[59] J.I. Lee, S.H. Cho, S.M. Park, J.K. Kim, J.K. Kim, J.W. Yu, Y.C. Kim, and T.P. Russell, Highly aligned ultrahigh density arrays of conducting polymer nanorods using block copolymer templates, *Nano Lett.*, **8**, 2315–2320 (2008).
[60] Y.F. Ma, J.M. Zhang, G.J. Zhang, and H.X. He, Polyaniline nanowires on Si surfaces fabricated with DNA templates, *J. Am. Chem. Soc.*, **126**, 7097–7101 (2004).
[61] Y. Eichen, E. Braun, U. Sivan, and G. Ben-Yoseph, Self-assembly of nanoelectronic components and circuits using biological templates, *Acta Polymer.*, **49**, 663–670 (1998).
[62] P. Nickels, W.U. Dittmer, S. Beyer, J.P. Kotthaus, and F.C. Simmel, Polyaniline nanowire synthesis templated by DNA, *Nanotechnology* **15**, 1524–1529 (2004).
[63] L. Q. Dong, T. Hollis, S. Fishwick, B.A. Connolly, N.G. Wright, B.R. Horrocks, and A. Houlton, Synthesis, manipulation and conductivity of supramolecular polymer nanowires, *Chem. Eur. J.*, **13**, 822–828 (2007).
[64] M.H. Yun, N.V. Myung, R.P. Vasquez, C.S. Lee, E. Menke, and R.M. Penner, Electrochemically grown wires for individually addressable sensor arrays, *Nano Lett.*, **4**, 419–422 (2004).
[65] K. Ramanathan, M.A. Bangar, M.H. Yun, W.F. Chen, A. Mulchandani, and N.V. Myung, Individually addressable conducting polymer nanowires array, *Nano Lett.*, **4**, 1237–1239 (2004).
[66] K. Ramanathan, M.A. Bangar, M.H. Yin, W. Chen, A. Mulchandani, and N.V. Myung, *In situ* fabrication of single poly(methyl pyrrole) nanowire, *Electroanalysis* **19**, 793–797 (2007).
[67] C.Y. Peng, W.J. Nam, S.J. Fonash, B. Gu, A. Sen, K. Strawhecker, S. Natarajan, H.C. Foley, and S.H. Kim, Formation of nanostructured polymer filaments in nanochannels, *J. Am. Chem. Soc.*, **125**, 9298–9299 (2003).
[68] C.Y. Peng, A.K. Kalkan, S.J. Fonash, B. Gu, and A. Sen, A 'grow-in-place' architecture and methodology for electrochemical synthesis of conducting polymer nanoribbon device arrays, *Nano Lett.*, **5**, 439–444 (2005).
[69] Y. Chen and Y. Luo, Precisely defined heterogeneous conducting polymer nanowire arrays – fabrication and chemical sensing applications, *Adv. Mater.*, **21**, 2040–2044 (2009).
[70] S. Hou, S. Wang, Z.T.F. Yu, N.Q.M. Zhu, K. Liu, J. Sun, W.Y. Lin, C.K.F. Shen, X. Fang, and H.R. Tseng, A hydrodynamically focused stream as a dynamic template for site-specific electrochemical micropatterning of conducting polymers, *Angew, Chem. Int. Ed.*, **47**, 1072–1075 (2008).
[71] C. Jerome and R. Jerome, Electrochemical synthesis of polypyrrole nanowires, *Angew. Chem. Int. Ed.*, **37**, 2488–2490 (1998).
[72] C. Jerome, S. Demoustier-Champagne, R. Legras, and R. Jerome, Electrochemical synthesis of conjugated polymer wires and nanotubules, *Chem. Eur. J.*, **6**, 3089–3093 (2000).
[73] S.J. Choi and S.M. Park, Electrochemical growth of nanosized conducting polymer wires on gold using molecular templates, *Adv. Mater.*, **12**, 1547–1549 (2000).
[74] S.M. Park, J.Y. Lee, and S.J. Choi, Growth and characterization of nanosized structures of conducting polymers, *Synth. Met.*, **121**, 1297–1298 (2001).
[75] J. Kameoka, R. Orth, Y.N. Yang, D. Czaplewski, R. Mathers, G.W. Coates, and H.G. Craighead, A scanning tip electrospinning source for deposition of oriented nanofibres, *Nanotechnology*, **14**, 1124–1129 (2003).

[76] D.H. Reneker and I. Chun, Nanometre diameter fibres of polymer, produced by electrospinning, *Nanotechnology*, **7**, 216–223 (1996).
[77] D.H. Reneker, A.L. Yarin, H. Fong, and S. Koombhongse, Bending instability of electrically charged liquid jets of polymer solutions in electrospinning, *J. Appl. Phys.*, **87**, 4531–4547 (2000).
[78] A.G. MacDiarmid, W.E. Jones, I.D. Norris, J. Gao, A.T. Johnson, N.J. Pinto, J. Hone, B. Han, F.K. Ko, H. Okuzaki, and M. Llaguno, Electrostatically-generated nanofibers of electronic polymers, *Synth. Met.*, **119**, 27–30 (2001).
[79] Y.X. Zhou, M. Freitag, J. Hone, C. Staii, A.T. Johnson, N.J. Pinto, and A.G. MacDiarmid, Fabrication and electrical characterization of polyaniline-based nanofibers with diameter below 30 nm, *Appl. Phys. Lett.*, **83**, 3800–3802 (2003).
[80] H.Q. Liu, J. Kameoka, D.A. Czaplewski, and H.G. Craighead, Polymeric nanowire chemical sensor, *Nano Lett.*, **4**, 671–675 (2004).
[81] H.Q. Liu, C.H. Reccius, and H.G. Craighead, Single electrospun regioregular poly(3-hexylthiophene) nanofiber field-effect transistor, *Appl. Phys. Lett.*, **87**, 253106 (2005).
[82] E.S. Forzani, H.Q. Zhang, L.A. Nagahara, I. Amlani, R. Tsui, and N.J. Tao, A conducting polymer nanojunction sensor for glucose detection, *Nano Lett.*, **4**, 1785–1788 (2004).
[83] A. Das, C.H. Lei, M. Elliott, J.E. Macdonald, and M. L. Turner, Non-lithographic fabrication of PEDOT nano-wires between fixed Au electrodes, *Org. Electron.*, **7**, 181–187 (2006).
[84] N.T. Kemp, D. McGrouther, J.W. Cochrane, and R. Newbury, Bridging the gap: Polymer nanowire devices, *Adv. Mater.*, **19**, 2634–2638 (2007).
[85] P.S. Thapa, D.J. Yu, J.P. Wicksted, J.A. Hadwiger, J.N. Barisci, R.H. Baughman, and B.N. Flanders, Directional growth of polypyrrole and polythiophene wires, *Appl. Phys. Lett.*, **94**, 033104 (2009).
[86] H. Sirringhaus, P.J. Brown, R.H. Friend, M.M. Nielsen, K. Bechgaard, B.M.W. Langeveld-Voss, A.J.H. Spiering, R.A.J. Janssen, E.W. Meijer, P. Herwig, and D.M. de Leeuw, Two-dimensional charge transport in self-organized, high-mobility conjugated polymers, *Nature*, **401**, 685–688 (1999).
[87] D.H. Kim, J.T. Han, Y.D. Park, Y. Jang, J.H. Cho, M. Hwang, and K. Cho, Single-crystal polythiophene microwires grown by self-assembly, *Adv. Mater.*, **18**, 719–723 (2006).
[88] J.G. Park, B. Kim, S.H. Lee, A.B. Kaiser, S. Roth, and Y.W. Park, Tunneling conduction in polyacetylene nanofiber, *Synth. Met.*, **135**, 299–300 (2003).
[89] J.G. Park, S.H. Lee, B. Kim, and Y.W. Park, Electrical resistivity of polypyrrole nanotube measured by conductive scanning probe microscope: The role of contact force, *Appl. Phys. Lett.*, **81**, 4625–4627 (2002).
[90] H.X. He, C.Z. Li, and N.J. Tao, Conductance of polymer nanowires fabricated by a combined electrodeposition and mechanical break junction method, *Appl. Phys. Lett.*, **78**, 811–813 (2001).
[91] J.G. Park, G.T. Kim, V. Krstic, B. Kim, S.H. Lee, S. Roth, M. Burghard, and Y.W. Park, Nanotransport in polyacetylene single fiber: Toward the intrinsic properties, *Synth. Met.*, **119**, 53–56 (2001).
[92] A.N. Aleshin, H.J. Lee, Y.W. Park, and K. Akagi, One-dimensional transport in polymer nanofibers, *Phys. Rev. Lett.*, **93**, 196601 (2004).
[93] A.N. Aleshin, H.J. Lee, K. Akagi, and Y.W. Park, One-dimensional transport in polymer nanowires, *Microelectron. Eng.*, **81**, 420–427 (2005).
[94] J.G. Park, B. Kim, S.H. Lee, and Y.W. Park, Current-voltage characteristics of polypyrrole nanotube in both vertical and lateral electrodes configuration, *Thin Solid Films*, **438**, 118–122 (2003).
[95] A.N. Aleshin, Quasi-one-dimensional transport in conducting polymer nanowires, *Phys. Solid State*, **49**, 2015–2033 (2007).
[96] Y. Long, Z.J. Chen, N.L. Wang, Y.J. Ma, Z. Zhang, L.J. Zhang, and M.X. Wan, Electrical conductivity of a single conducting polyaniline nanotube, *Appl. Phys. Lett.*, **83**, 1863–1865 (2003).

[97] Y.Z. Long, L.J. Zhang, X.J. Ma, Z.J. Chen, N.L. Wang, Z. Zhang, and M.X. Wan, Electrical conductivity of an individual polyaniline nanotube synthesized by a self-assembly method, *Macromol. Rapid Commun.*, **24**, 938–942 (2003).
[98] Y.Z. Long, J.L. Duvail, Z.J. Chen, A.Z. Jin, and C.Z. Gu, Electrical conductivity and current-voltage characteristics of individual conducting polymer PEDOT nanowires, *Chin. Phys. Lett.*, **25**, 3474–3477 (2008).
[99] Z.H. Yin, Y.Z. Long, C.Z. Gu, M.X. Wan, and J.L. Duvail, Current-voltage characteristics in individual polypyrrole nanotube, poly(3,4-ethylenedioxythiophene) nanowire, polyaniline nanotube, and CdS nanorope, *Nanoscale Res. Lett.*, **4**, 63–69 (2009).
[100] A.B. Kaiser and Y.W. Park, Current–voltage characteristics of conducting polymers and carbon nanotubes, *Synth. Met.*, **152**, 181–184 (2005).
[101] S. Samitsu, T. Iida, M. Fujimori, S. Heike, T. Hashizume, T. Shimomura, and K. Ito, Conductivity measurements of PEDOT nanowires on nanoelectrodes, *Synth. Met.*, **152**, 497–500 (2005).
[102] S. Samitsu, T. Shimomura, K. Ito, M. Fujimori, S. Heike, and T. Hashizume, Conductivity measurements of individual poly(3,4-ethylenedioxythiophene) /poly(styrenesulfonate) nanowires on nanoelectrodes using manipulation with an atomic force microscope, *Appl. Phys. Lett.*, **86**, 233103 (2005).
[103] N.A. Zimbovskaya, A.T. Johnson, and N.J. Pinto, Electronic transport mechanism in conducting polymer nanofibers, *Phys. Rev. B*, **72**, 024213 (2005).
[104] A.N. Aleshin, H.J. Lee, S.H. Jhang, H.S. Kim, K. Akagi, and Y.W. Park, Coulomb-blockade transport in quasi-one-dimensional polymer nanofibers, *Phys. Rev. B*, **72**, 153202 (2005).
[105] Y.Z. Long, L.J. Zhang, Z.J. Chen, K. Huang, Y.S. Yang, H.M. Xiao, M.X. Wan, A.Z. Jin, and C.Z. Gu, Electronic transport in single polyaniline and polypyrrole microtubes, *Phys. Rev. B*, **71**, 165412 (2005).
[106] Terje A. Skotheim and John R. Reynolds, Handbook of Conducting Polymers. *Conjugated Polymers: Theory, Synthesis, Properties, and Characterization*, 3rd edn. CRC Press, Boca Raton, 2007, p.1 v. (various pages).
[107] Y.W. Park, A.J. Heeger, M.A. Druy, and A.G. Macdiarmid, Electrical transport in doped polyacetylene, *J. Chem. Phys.*, **73**, 946–957 (1980).
[108] C.O. Yoon, M. Reghu, D. Moses, and A.J. Heeger, Transport near the Metal-Insulator-Transition - Polypyrrole Doped with Pf(6), *Phys. Rev. B*, **49**, 10851–10863 (1994).
[109] A. Aleshin, R. Kiebooms, R. Menon, and A.J. Heeger, Electronic transport in doped poly(3,4-ethylenedioxythiophene) near the metal-insulator transition, *Synth. Met.*, **90**, 61–68 (1997).
[110] D.E. Khmelnitskii and A.I. Larkin, Mobility edge shift in external magnetic-field, *Solid State Commun.*, **39**, 1069–1070 (1981).
[111] P. Sheng, Fluctuation-induced tunneling conduction in disordered materials, *Phys. Rev. B*, **21**, 2180–2195 (1980).
[112] A.B. Kaiser, Systematic conductivity behavior in conducting polymers: Effects of heterogeneous disorder, *Adv. Mater.*, **13**, 927–941 (2001).
[113] A.B. Kaiser, G.U. Flanagan, D.M. Stewart, and D. Beaglehole, Heterogeneous model for conduction in conducting polymers and carbon nanotubes, *Synth. Met.*, **117**, 67–73 (2001).
[114] A.B. Kaiser, Electronic transport properties of conducting polymers and carbon nanotubes, *Rep. Progr. Phys.*, **64**, 1–49 (2001).
[115] K. Ramanathan, M.A. Bangar, M. Yun, W. Chen, N.V. Myung, and A. Mulchandani, Bioaffinity sensing using biologically functionalized conducting-polymer nanowire, *J. Am. Chem. Soc.*, **127**, 496–497 (2005).
[116] M.A. Bangar, D.J. Shirale, W. Chen, N.V. Myung, and A. Mulchandani, Single conducting polymer nanowire chemiresistive label-free immunosensor for cancer biomarker, *Anal. Chem.*, **81**, 2168–2175 (2009).
[117] A.K. Wanekaya, M.A. Bangar, M. Yun, W. Chen, N.V. Myung, and A. Mulchandani, Field-effect transistors based on single nanowires of conducting polymers, *J. Phys. Chem. C*, **111**, 5218–5221 (2007).

[118] A.L. Briseno, S.C.B. Mannsfeld, P.J. Shamberger, F.S. Ohuchi, Z.N. Bao, S.A. Jenekhe, and Y.N. Xia, Self-assembly, molecular packing, and electron transport in n-type polymer semiconductor nanobelts, *Chem. Mater.*, **20**, 4712–4719 (2008).
[119] J.P. Hong, M.C. Um, S.R. Nam, J.I. Hong, and S. Lee, Organic single-nanofiber transistors from organogels, *Chem. Commun.*, 310–312 (2009).
[120] G. Horowitz, Organic thin film transistors: From theory to real devices, *J. Mater. Res.*, **19**, 1946–1962 (2004).
[121] T.A. Skotheim and J.R. Reynolds, Handbook of Conducting Polymers. *Conjugated Polymers: Processing and Applications*, 3rd edn., CRC Press, Boca Raton, 2007, p.1 v. (various pages).
[122] Y. Berdichevsky and Y.H. Lo, Polypyrrole nanowire actuators, *Adv. Mater.*, **18**, 122–125 (2006).

11

Conductive Polymer Micro- and Nanocontainers

Jiyong Huang and Zhixiang Wei

National Center for Nanoscience and Technology, Beijing, P. R. China

11.1 Introduction

Micro- and nanostructured materials, often characterized by a significant amount of surfaces and interfaces, have been attracting intensive interest because of their demonstrated or anticipated unique properties compared to conventional materials. As an important type of carrier for foreign species, micro- and nanocontainers are common in nature, for example, the vesicles in living cells. A vesicle is a small, intracellular, membrane-enclosed container that stores or transports substances within a cell.

In recent years, laboratorially available micro- and nanocontainers have been obtained with the advancement of nanotechnology resulting from the scientific exploration of nature. Particularly, conducting-polymer micro- and nanocontainers (CPCs) have roused great attention because of their special inherent properties. Noticeably, the biggest advantage of nanostructured conducting polymers is that their structure and properties can be adjusted reversibly by the doping–dedoping process. Therefore, conducting polymers have been widely studied as actuators in aqueous solution. The polymer matrix expands and contracts with the flux of counter-ions during the electrochemically controlled reversible doping and dedoping.

So far, various structures of conductive-polymer containers have been produced by chemical or electrochemical approaches, including porous films, hollow spheres, tube-like

Nanostructured Conductive Polymers Edited by Ali Eftekhari

structures, etc. Numerous novel methods have been introduced to fabricate CPCs. Among them, hard templates, soft templates, and nanofabrication are usual and typical routes. Meanwhile, the formation mechanisms of these CPCs have been investigated. Based on the comprehensive understanding of their chemical, electrical, and mechanical properties, CPCs are considered to be competitive potential candidates for applications in encapsulation, drug delivery, and controlled release. A great deal of such examples are available in recent reports, reviews, and books. However, there are seldom systematic summaries, including the methods, corresponding mechanisms, and applications of these containers. Because of their significant possibilities for the future, the current state of knowledge concerning the aspects mentioned above is reviewed in this chapter with a systematic perspective.

11.2 Structures of Micro- and Nanocontainers

Conducting polymers (CPs) are typical smart electrode materials with an actuating property, which is based on the expansion and contraction of the polymer matrix with the movement of ions during electrically controlled doping and dedoping processes. This unique property makes them attractive for laboratories-on-a-chip and applications under physiological conditions. Targeted delivery and controlled release of the encapsulated material have a high priority for further development in modern medicine, material science, and biochemistry [1]. In particular, this research work is important for curing dangerous diseases, for example, cancer. To date, polymer and polyelectrolyte capsules, fluoroalcane microemulsions, micelles, hydrogels, and porous hydroxyapatites have been developed to encapsulate and transfer various materials dispersed at the micro- and nanolevel [2–10]. A number of conductinge polymers (CPs) have been developed as prospective electrode materials. Their good conductivity, chemical stability, and mechanical properties allow their use as hosts to encapsulate desirable content. In this short section, various micro- and nanostructured CPCs are presented.

11.2.1 Hollow Spheres

Hollow spheres are a typical structure of CPCs, which in particular have a wide number of potential applications, including stationary phases for separation science, biomedical devices, coating additives, controlled-release reservoirs, and encapsulation. In fact, the multifunctionality of hollow spheres of CPs is an important subject in the field of materials science.

In order to give a comprehensive review of micro- and nanocontainers, it is necessary to introduce lipid-based or lipophilic hollow-sphere containers, which have been intensively investigated, before starting the discussion of conducting-polymer hollow spheres. Many studies on pharmaceutical delivery systems have been carried out to develop drug carriers that are suitable for delivering a drug to specific site. Among them, numerous efforts have been paid to polymeric micelles, lipid nanocapsules, liposomes, or lipid microspheres [2,11–15]. Emulsion delivery systems have been widely used to encapsulate drugs.

However, the use of high quantities of surfactants and cosurfactants (such as butanol), used to improve the solubility of the shell material (for example, polymers or lipids) in both organic solvents and water, increases the potential toxicity of the drug carriers. Currently, lipid microspheres (LM), usually including soybean oil and lecithin, are widely used in clinical medicine for parenteral nutrition since they are very stable and have no adverse effects. The lipid microspheres formed by dispersion of the LM particles in aqueous solution appear to be safe and efficient drug carriers because they avoid any harmful organic solvents or toxic products [12]. Unfortunately, the preparation of lipid microspheres usually needs a special high-pressure setup to emulsify oil solutions, which increases the difficulty of preparation and leads to higher processing costs.

To address the problems mentioned above, Dmitry G. Shchukin and his coworkers developed a simple method to fabricate a novel drug-carrier system by combining an ultrasonic technique and a layer-by-layer (LBL) assembly protocol (Figure 11.1) [1,16,17]. They used a lipophilic drug (rifampicin) and vegetable oil to fabricate a new type of biofriendly drug carrier. The core of the presented drug carrier contained lipophilic

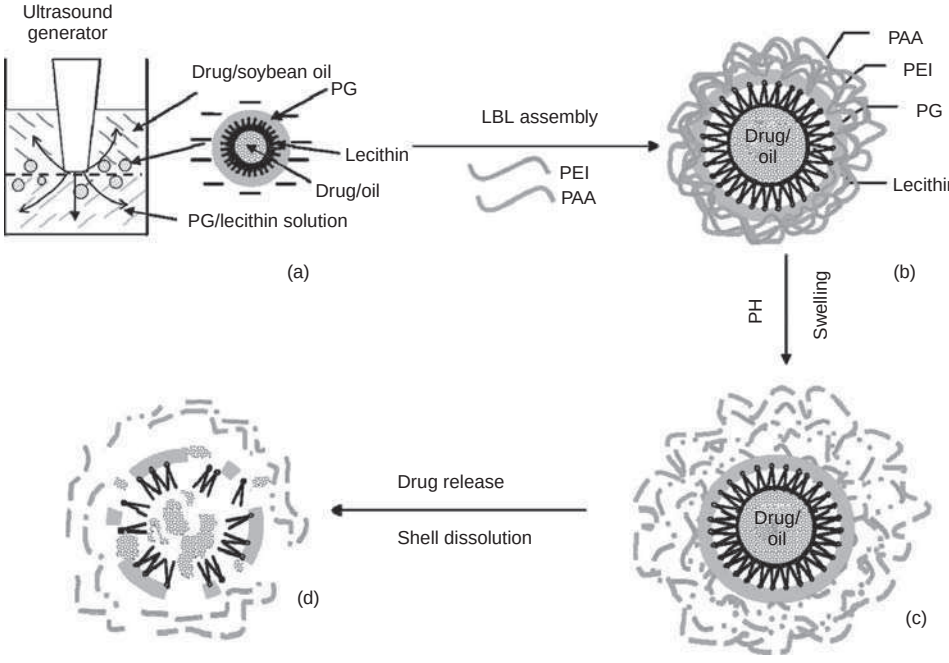

Figure 11.1 *Schematic illustration of the formation of LBL-synthesized containers and drug release after pH changes (PG, polyglutamate; PEI, polyethyleneimine; PAA, poly(acrylic acid); LBL, layer-by-layer): (a) Formation of oil-loaded polyglutamate containers in an ultrasonic field; (b) LBL assembly of a PEI/PAA shell; (c), (d) swelling and dissolution of the container shell by changing the pH value of the surrounding circumstance. (Reprinted with permission from Langmuir, A Novel Drug Carrier: Lipophilic Drug-Loaded Polyglutamate/Polyelectrolyte Nanocontainers by X. Rong Teng, D.G. Shchukin, and H. Mohwald, 24, 2, 383–389. Copyright (2008) American Chemical Society) (See colour Plate 7)*

drug and vegetable oil, as well as lecithin as an emulsifier, which is similar to lipid microspheres. The shells of the containers were made of polyglutamate/polyethyleneimine (PEI)/poly(acrylic acid) (PAA) multilayers. The hydrophobic drug could be released by switching the polyglutamate/polyelectrolyte shell permeability through variation of environmental conditions, such as pH value and ionic strength [18–20]. The polyelectrolyte shell can also be modified to have some additional functionality.

Furthermore, porous CPs (e.g., polypyrrole, polyaniline) films have been used as host matrices for polyelectrolyte capsules developed from composite material, which can combine electric conductivity of the polymer with controlled permeability of polyelectrolyte shell to form controllable micro- and nanocontainers. A recent example was reported by D.G. Schchukin and his co-workers [21]. They introduced a novel application of polyelectrolyte microcapsules as microcontainers with a electrochemically reversible flux of redox-active materials into and out of the capsule volume. Incorporation of the capsules inside a polypyrrole (PPy) film resulted in a new composite electrode. This electrode combined the electrocatalytic and conducting properties of the PPy with the storage and release properties of the capsules, and if loaded with electrochemical fuels, this film possessed electrochemically controlled switching between 'open' and 'closed' states of the capsule shell. This approach could also be of practical interest for chemically rechargeable batteries or fuel cells operating on an absolutely new concept. However, in this case, PPy was just utilized as support for the polyelectrolyte microcapsules.

Compared with the methods mentioned above, the direct fabrication of conducting-polymer hollow spheres was investigated intensively. Up to now, several publications have reported on the synthesis of polystyrene (PS) cores coated with CPs such as PPy, polyaniline (PANI), and polyethylenedioxythiophene (PEDOT) [22–27]. Conducting-polymer hollow spheres can be further created by removing the PS core (Figure 11.2). This colloidal approach was extensively investigated not only because it allows improvement of the processability of conducting-polymer materials, but also because of the attractive properties of these materials, for example, well-defined colloidal dimensions or morphologies [23], intense coloration, biocompatibility [28], high surface area, efficient radiation absorption, wide spectrum of surface

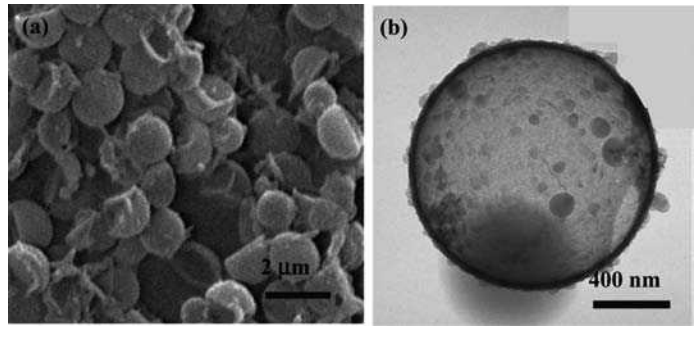

Figure 11.2 *Micrographs of PPy hollow nanocontainers after etching of the PS core in THF, obtained by: (a) SEM and (b) TEM. (Reprinted with permission from Langmuir, Latex and Hollow Particles of Reactive Polypyrrole: Preparation , Properties, and Decoration by Gold Nanospheres by Claire Mangeney et al., 22, 24, 10163–10169. Copyright (2006) American Chemical Society)*

functionalization, good film-forming properties, and so forth [26,29–32]. There has been a massive amount of work on the synthesis, characterization, and use of latex particles coated with conducting-polymer shells in solution.

Wei *et al.* [33,34] utilized emulsion templates to prepare hollow PANI miscrospheres since the emulsion template can be easily removed through dissolution or evaporation after polymerization. Bajpai *et al.* [35] prepared semiclosed PPy containers in the presence of fluorescein cadaverin in solution. Furthermore, oil microdroplets were used in the template polymerization of pyrrole into semispherical containers deposited on glass or quartz surfaces, reported by M. Mazur [36,37]. In the report by Wan *et al.*, a novel route utilizing organic acid acting as both surfactant and dopant to fabricate conductive polymer micro- and nanospheres, as well as composites, was developed [38,39]. They indicated that hollow microspheres of PANI doped with salicylic acid (SA) could be prepared by this simple method (Figure 11.3) [40]. In fact, they found that this method is essentially a self-assembly process because micelles formed by SA and aniline act as templates for the formation of the microspheres. This result further inspired them to use the self-assembly process to prepare the PANI-SA/TiO_2 composite microspheres. They also reported PANI-SA composite

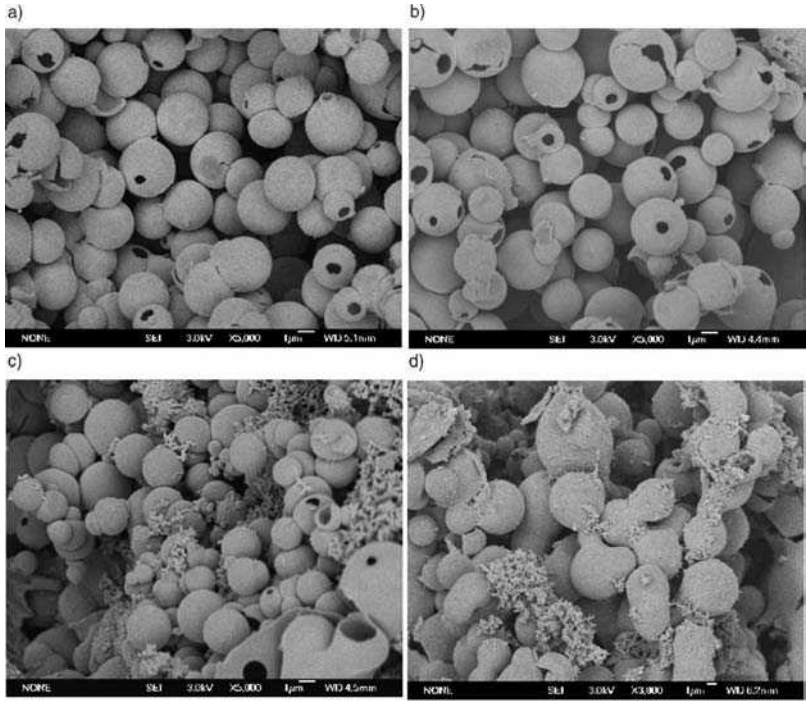

Figure 11.3 *SEM images of PANI-SA/RhB synthesized using different concentrations of RhB: (a) 0 M, (b) 1 mM, (c) 5 mM, and (d) 10 mM. Synthetic conditions: [An] = 0.2 M, [An]/[SA] = 1:1, and [An]/[APS] = 1:1. (Reprinted with permission from Macromol. Rapid Commun., Hollow Polyaniline Microspheres with Conductive and Fluorescent Function by Lijuan Zhang, Meixiang Wan and Yen Wei, 27, 11, 888–893. Copyright (2006) Wiley-VCH)*

hollow microspheres with a high conductivity and a strong fluorescence constructed with rhodamine B (RhB) as the fluorescent material via a self-assembly process.

11.2.2 Tubes

It is common in human daily life to utilize tube-like receptacles to hold and transport items or matter, for example, the water pipe that is used to conduct water, the glass test tube to keep samples. Similar to these well-known commodities, the large inner space of micro- and nanotubes allows them to be promising candidates for micro- and nanocontainers. Since Foulds *et al.* first introduced the incorporation of enzymes in active PPy matrices in 1986 [41], their approach to enzyme immobilization has been widely adopted. This method has several advantages [42]. However, it also has several drawbacks that need to be overcome to improve its performance. One critical problem is that the monomer needs to be soluble in the enzyme-soluble aqueous environment and be polymerized at a moderate pH. The second is that the enzyme immobilized in the layers of conducting polymer is not in an independent state, and its activity degrades with time. To confine the enzyme in a hollow micro- and nanostructured CP would be a solution. Many strategies for preparing various micro- and nanostructured polymers for novel applications have been studied. Biosensors and bioreactors, nanoelectrodes, molecular filtration, and ion-channel mimetic sensing are examples of such applications [43–46]. Martin *et al.* utilized a commercially available track-etched membrane to prepare metal, semiconductor, and conducting-polymer nanofibers and nanotubes [47–49]. Applications of these nanostructured materials in bioencapsulation and biosensors have also been reported [50–52]. One involved sealing the opening of the structure with a nonconducting sealing agent that contained the enzyme within the structure. However, no report focused on separating the membrane and electrochemical signal transducer by sealing the opening of the tubule directly with a conducting composite. In a report by Son *et al.*, microscale conducting-polymer cylinders were synthesized by electrochemical polymerization [53]. According to a conventional procedure, the microtubes were prepared first, and microcapping was carried out on the opening of the tubes with a commercially available PEDOT/PSS aqueous dispersion. This final structure was able to host the electroactive material safely inside and behaved as a current collector for the redox reaction of the guest agents. With the aid of the PEDOT layer on the cap, the cap structure was insoluble in an aqueous environment. The interior free space in the final cylindrical microstructure could be used to load various materials. Since many types of guest material can be used, this strategy may be a good choice for enzyme immobilization. Because the enzyme will be in a perturbation-free state in the pore of the structure, it may also reduce the rate of degradation in the enzyme activity during the immobilization process.

Based on the work on template-synthesized nano-test-tubes, which are closed at one end and open at the other, Martin *et al.* explored an alternative payload-release strategy (Figure 11.4) [54,55]. They supposed that if these nano-test-tubes could be filled with a payload and then the open end ‘corked’ with a chemically labile cap, they might function as a universal delivery vehicle. The long-range objective would be to have the bonds holding the ‘corks’ on the nano-test-tubes be labile only when a specific chemical signal is encountered (for example, the lower local pH surrounding certain tumor cells). Actually,

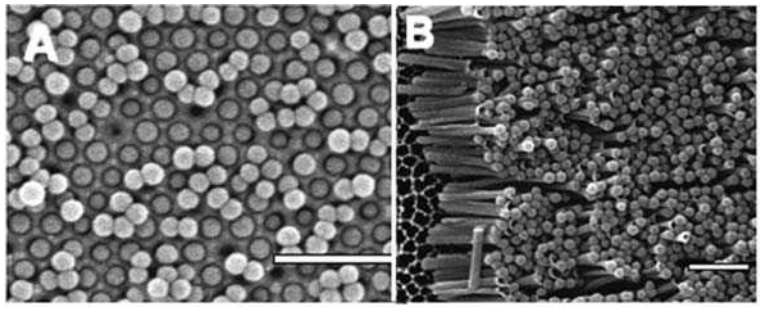

Figure 11.4 *SEM images of anion-aldehyde-corked nano-test-tubes: (A) template embedded; (B) after template removal. Scale bar = 500 nm. (Reprinted with permission from Journal of the American Chemical Society, Corking Nano Test Tubes by Chemical Self Assembly by H. Hillebrenner et al., 128,13. Copyright (2006) American Chemical Society)*

they achieved the first step toward this corked-nano-test-tube strategy by proving that template-synthesized silica nano-test-tubes functionalized on the upper rim with amino groups could be spontaneously corked with appropriately sized aldehyde-functionalized latex nanoparticles, which involved a Schiff-base reaction to form imine linkages between the test tubes and the nanoparticle corks. This pioneering work provides a powerful strategy for the preparation of conducting-polymer nanotubes.

Conductive polymer nanotubes with opening ends have also been investigated for precisely controlled drug release. The response of CPs to electrochemical oxidation or reduction can produce a change in their conductivity, color, and volume [56–58]. A change in the electronic charge is accompanied by an equivalent change in the ionic charge, which includes mass transport between the polymer and the electrolyte [59]. The polymer expands when counter-ions enter it and the contracts when they exit. The extent of expansion or contraction depends on the number and size of ions involved [60]. Based on this principle, electrochemical actuators using CPs have been developed by several investigators [61,62]. They can be doped with bioactive drugs, and can be applied in actuators such as microfluidic pumps [63,64]. The precisely controlled local release of drugs at desired points in time is important for clinical therapy [65]. In previous work, D. Martin and coworkers have prepared CPs such as PPy and PEDOT in nanostructured templates for neural prosthesis applications, and shown that PPy and PEDOT can decrease the impedance of the recording sites [66–68]. They then used biodegradable poly(L-lactide) (PLLA) or poly(lactide-*co*-glycolide) (PLGA) nanofibers as templates to fabricate tube-like CPCs (Figure 11.5) [69]. Their porous structures can be used directly as containers for drugs. Minimizing the electrode impedance is an important requirement for obtaining high-quality signals [70], so they prepared PEDOT nanotubes that have a well-defined internal and external surface texture and further showed that this nanostructure decreases the electrode impedance by increasing the effective surface area for ionic-to-electronic charge transfer occurring at the interface between brain tissue and the recording site. They also demonstrated that dexamethasone can be released from the nanotubes in a desired fashion by electrical stimulation of the nanotubes.

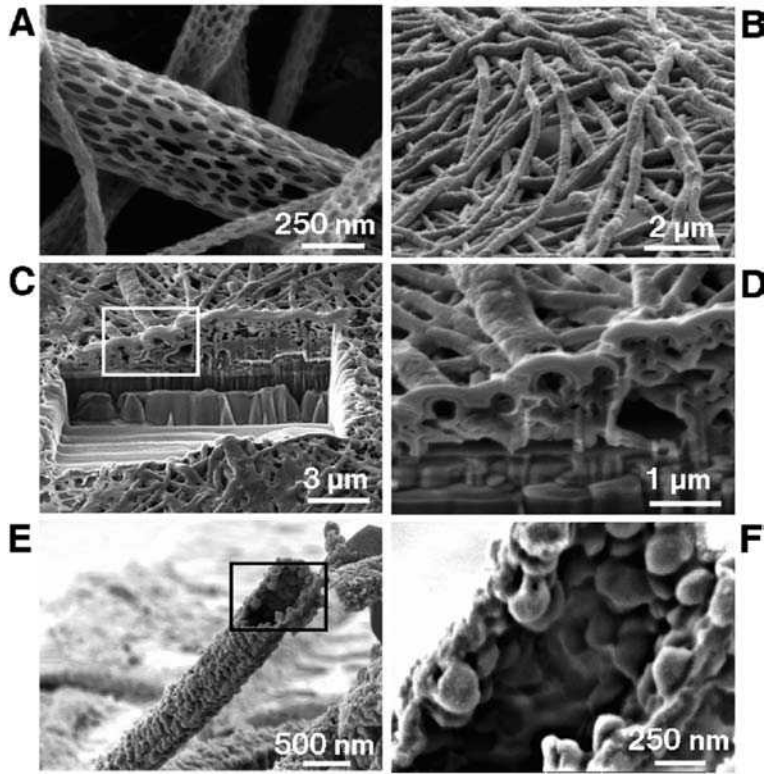

Figure 11.5 *SEM images of PLGA nanoscale fibers and PEDOT nanotubes: (A) PLGA nanofibers with the diameter mainly ranging between 100 and 200 nm; (B) PEDOT nanotubes on the electrode after removal of the PLGA core fibers; (C) section view of PEDOT nanotubes cut with an FIB showing the silicon substrate layer and PEDOT nanoscale fiber coating; (D) higher-magnification image of (C) showing the PEDOT nanotubes crossing each other; (E) single PEDOT nanotube which was polymerized around a PLGA nanoscale fiber, followed by dissolution of the PLGA core fiber; (F) higher-magnification image of a single PEDOT nanotube demonstrating the textured morphology that has been directly replicated from the external surface of the electrospun PLGA fiber templates. (Reprinted with permission from Advanced Materials, Conducting-Polymer Nanotubes for Controlled Drug Release by M. R. Abidian, D.-H. Kim, D. C. Martin, 18, 4, 405–409. Copyright (2006) Wiley-VCH)*

11.2.3 Others

To date, beside the conventional micro- and nanostructures that have been mentioned previously, there are numerous reports concerning other micro- and nanoarchitectured CPCs, such as mesoporous, bowl-like, goblet-like, pipette-like structures, and so forth. Features such as high pore volume and high surface area allow mesoporous materials to serve as containers for foreign species [71]. A recent example of porous CPCs was reported by Cui [72]. In their experiment, nanoporous PPy films were synthesized using a

polystyrene (PS) nanobead template. PPy was synthesized on a PS-modified electrode and the film grew within the interstitial spaces among the closely packed PS nanobeads. A nanoporous PPy film was formed after the removal of the PS nanobeads. In addition, the release efficiency of this nanoporous PPy film was found to be higher than non-nanostructured films by electrochemically controlled drug-release measurements. However, electrochemical deposition using a solution composed of a biological entity and pyrrole monomers restricted homogeneous drug distribution throughout the PPy surface and interfered with electrochemical control of various parameters such as film thickness, loading concentration, and diffusion of the biomolecules of interest. In order to improve the performance of mesoporous CPCs, Cho's group proposed an alternative method [73]. As reservoirs of single or multiple substances, nanoparticles are capable of delivering highly concentrated chemical agents in a controlled-release manner [74–78]. In Cho's report, mesoporous silica nanoparticles (MSNs) were first synthesized and then were embedded into a polypyrrole film by electrochemical deposition. The PPy/MSNs composite had several potential advantages. For example, efficient loading of nanoparticles due to the large surface area of the conducting polymer, and a spontaneous and reversible oxidation/reduction reaction would promote release of the contents of the MSNs in the presence of electrical stimulation.

Moreover, Shi and his group reported electrochemical deposition of PPy microcontainers onto 'soap bubbles' associated with O_2 gas released from the electrolysis of H_2O in an aqueous solution of β-naphthalenesulfonic acid (β-NSA), camphorsulfonic acid (CSA), or poly(styrene sulfonic acid) (PSSA), which act both the surfactant and dopant [79–81]. Morphologies such as bowls, cups, and bottles could be controlled by electrochemical conditions (Figure 11.6). However, the microcontainers were randomly located on the electrode surface, which limited further applications, Shi and coworkers reported a linear arrangement of PPy microcontainers by self-assembly with gas bubbles acting as templates on a silicon electrode surface patterned by photolithography [82]. They found that capillary interactions between the gas bubbles and the polymer photoresist walls led the microcontainers to be arranged linearly.

In view of the fact that the direct generation of O_2 gas on the working electrode under a relatively high positive potential ($>$0.8 V) could result a detrimental overoxidation effect, Dai *et al.* introduced the electrochemical polymerization of PPy microcotainers by releasing H_2 (electrolysis of H_2O) around the working electrode under a negative potential (Figure 11.7) [35]. Unlike the previous method with which it is hard to obtain PPy microcotainers below 0.8 V, the modified method should allow the formation of conducting-polymer microtainers on the working electrode even at a relatively low potentials. What is more, patented and nonpatented PPy microcontainers with an open-and-close mouth were also investigated.

To obtain nanocontainers, Wei *et al.* employed micelles as soft templates to assist the polymerization [83]. Hollow conical nanostructures are produced by a slow polymerization process (Figure 11.8). Microcontainers could be produced in the open or closed state by changing the polymerization time. However, as far as we are aware, most of the reported actuators were based on bulk materials or synergistic properties of nanostructure bundles instead of single nanostructure. Wei *et al.* realized the manipulation of separated nanocontainers by an electrochemical approach to control of the state of the nanocontainer '*in situ*'. Studying the switching of single nanostructured CPs will open potential

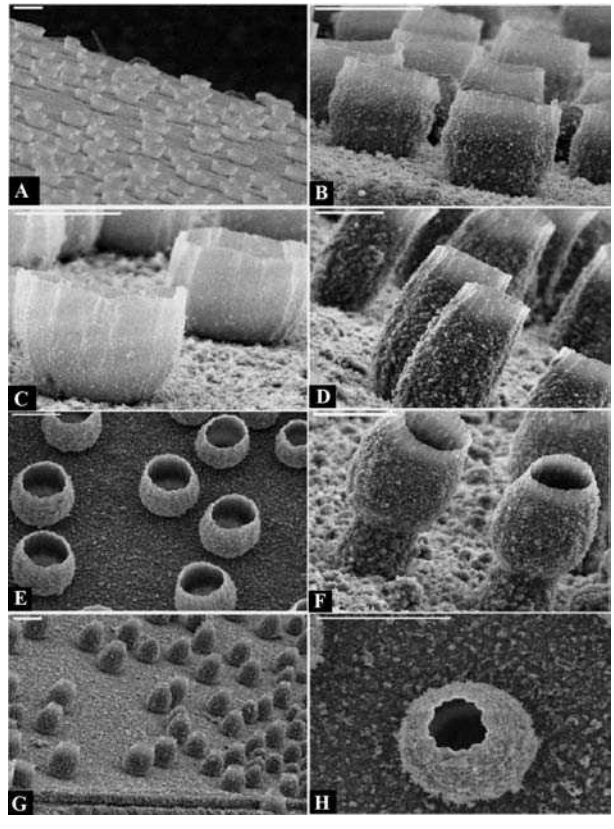

Figure 11.6 *SEM images of polypyrrole microcontainers synthesized electrochemically using a 'soap bubble'-assisted soft-template method. (Reprinted with permission from Chemical Communications, Electrochemical synthesis of novel polypyrrole microstructures by L. T. Qu and G. Q. Shi, 2003, 2, 206–207. Copyright (2003) Royal Society of Chemistry)*

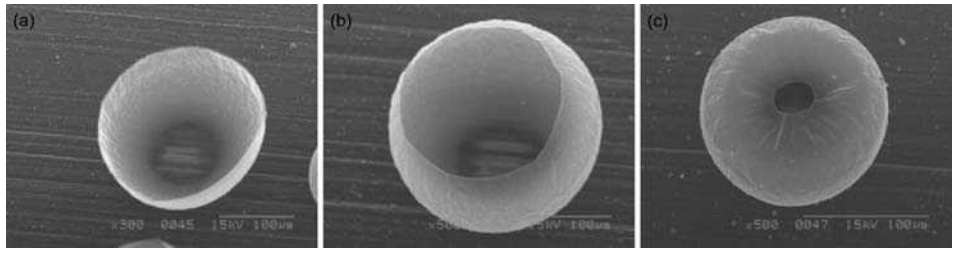

Figure 11.7 *SEM images of polypyrrole microcontainers formed by soft-template polymerization under different electropolymerization conditions. (Reprinted with permission from Advanced Functional Materials, Conducting-polymer microcontainers: Controlled syntheses and potential applications by V. Bajpai, P. G. He and L. M. Dai, 14, 2, 145–151. Copyright (2004) Wiley-VCH)*

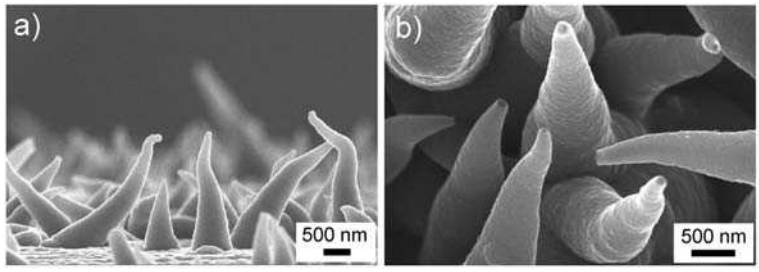

Figure 11.8 *SEM images of polypyrrole conical nanocontainers produced on a platinum substrate. (Reprinted with permission from Macromol. Rapid Commun., Conducting Polypyrrole Conical Nanocontainers: Formation Mechanism and Voltage Switchable Property by J. Huang, B. Quan, M. Liu et al., 29, 15, 1335–1340. Copyright (2008) Wiley-VCH)*

applications of this kind of smart nanostructure, such as controllable transfer and the delivery of extremely small volumes of liquid [83].

As is well known, CPs like PPy and PANI are excellent materials for actuators. Both macro- and microactuators based on these materials have been presented in previous literature [56, 57, 60–62, 84–86]. These actuators are based on the reversible volume change of the CPs upon oxidation and reduction. For instance, microactuators based on PPy-Au bilayers fabricated by E. Jager, *et al.* [87–89] enable large movements of structures attached to these actuators and are of particular interest for the manipulation of biological objects, such as single cells. Moreover, a kind of self-assembled microcontainer has been obtained recently (Figure 11.9) [90,91]. The self-folding is based on an on-demand, thin-film stress-driven mechanism, by utilizing hinges composed of a metallic bilayer (Cr/Cu), which, coupled with a polymer layer, serves as the motion trigger. The successes of these two cases suggest the possibility of fabricating low-cost, electric-driven

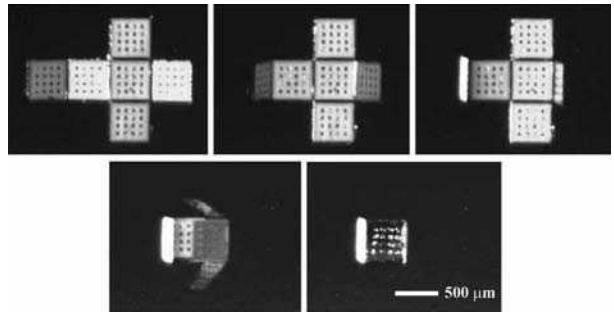

Figure 11.9 *Folding sequence of a 500 mm microcontainer with opposite hinge layer configurations. (Reprinted with permission from Small, Thin Film Stress Driven Self-Folding of Microstructured Container by T.G. Leong et al., 4, 10, 1605–1609. Copyright (2008) Wiley-VCH)*

microcontainers which use electroactive CP films to serve as the hinge, to compensate for the lack of precise control shown in the previous example.

11.3 Preparation Methods and Formation Mechanisms

The preparation method is a fundamental topic in the field of conducting polymer nanostructures, thus numerous efforts have been focused on this issue [34,38,46,92–101]. Nowadays, hard templates and soft templates, as well as the nanofabrication approach have been used to obtain CPCs. The hard-template method, like its literal meaning, requires a hard template, such as a porous membrane, or a polystyrene sphere, to guide the growth of the containers, leading to complete control of the morphology and diameter of the conducting-polymer containers. In order to obtain pure containers, the hard template is often removed after polymerization, resulting in a complex preparation procedure. In the soft-template method, supermolecules are self-assembled via hydrogen bonds, Van der Waals forces, and electrostatic interactions as the driving forces instead of a hard template to form the desired structures. Therefore, the soft-template method is simpler one of the two due to omission of the hard template and its post-treatment removal. However, the soft-template method often suffers from a lack of controllability compared with the hard-template method, because the formation of supermolecules is often affected by the reaction conditions. Moreover, with the advancement of nanotechnology, nanofabrication techniques have become a competitive option for preparing CPCs. Although nanofabrication is a precise controllable approach, it is still too limited by a expensive cost and complicated procedures for wide application. In the previous section, CPCs with diverse structures were introduced. However, details of the preparation methods and formation mechanisms were not included. For this reason, this section mainly focuses on the methodology and mechanisms regarding the fabrication of these containers.

11.3.1 Hard-Template Method

Many strategies for preparing various CPCs for novel applications have been devised (Figure 11.10). In particular, tube-like structures have been synthesized in the pores of membrane filters (Figure 11.10a). Martin *et al.* explored a template synthesis method for the first time to prepare nanotubes or nanowires of CPs using commercially available porous membranes as templates [47,102,103]. This hard-template method has several advantages: first of all, it is a general tool to prepare nanostructured materials including metals, semiconductors and conducting polymers; secondly, the diameter of the nanostructures is controlled by the size of the pores in the membrane; thirdly, the nanostructures are able to be chemically or electrochemically prepared by a hard-template method. This is in particular useful for CPs because almost all can be synthesized by either a chemical or an electrochemical approach. Furthermore, the templates are removable and thus the free nanostructured materials can be obtained.

Typically, sealed tube-like CPCs can be prepared by the approach introduced by Son and coworkers [53]. An ITO electrode was used as a substrate electrode, with a conducting

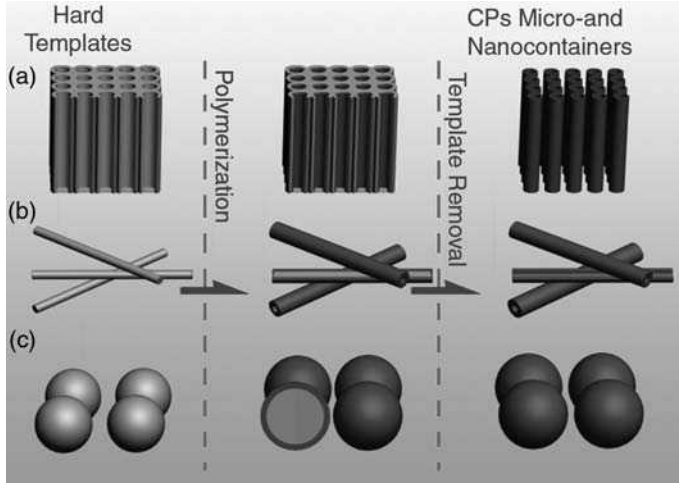

Figure 11.10 *A schematic representation of the hard-template method used to prepare CPCs: (a) porous membrane, (b) colloidal particles, (c) nanowires*

polymer paste spin-coated onto the surface of ITO glass. The conducting composite paste has two functions: to glue the template onto the ITO electrode and to provide an electrical connection between the ITO electrode and the electrolytic solution. PVA and PEDOT/PSS were used to prepare a conducting-paste composite to achieve this purpose. The porous template was then fixed onto the ITO glass. After that, electrochemical polymerization of EDOT was carried out by applying a potential directly to the ITO electrode. The lengths and thicknesses of the tubes were determined by the conditions of the electrochemical polymerization. In a subsequent procedure, the guest substance $K_3Fe(CN)_6$ was loaded into the tubes, and the tubes were shaken for several minutes to allow the material to flow into their hollow inner part. After filling the tubes with the electroactive species, a capping procedure was completed by performing two different steps. The first was spin-casting of the conducting composite on top of the filled tubes, followed by placement of a membrane with nanopores on the composite coating before drying. The conducting composite itself would not form a capping film during the course of drying without this membrane. This thick film could hinder the transport of electrolytes, solvents, etc., from the exterior solution to the tube interior. Since the composite was prepared in an aqueous environment, there was potentially less harm to the contents than if organic solvents had been used. The capping procedure was completed by electrochemical deposition a layer of PEDOT to reinforce the dried composite in order to prevent dissolution in the aqueous solution.

Martin *et al.* also introduced another method to seal the open end of the tubes [54,55]. They proved that silica nano-test-tubes could be covalently corked by chemical self-assembly of nanoparticles, which remained attached to the mouths of the nano-test-tubes after liberation from the alumina template. What is more, the caps were present only at the mouth and not within the tubes. Commonly, applications in drug delivery may require modified outer surfaces of tubes carrying specific moieties to direct the carriers to their

targets, and this template-based synthesis approach makes it possible to add these modifications after release from the alumina template. Significantly, this approach suggests the possibility of fabricating conductive polymer nano-test-tubes which could also be corked by other techniques, since polymers are more easily modified than silica.

As mentioned above, D.C. Martin *et al.* used biodegradable poly(L-lactide) (PLLA) or poly(lactide-co-glycolide) (PLGA) nanofibers as templates to fabricate tube-like CPCs (see also Figure 11.10b) [69]. PLLA and PLGA were considered to be suitable polymers for the template because firstly, they can be readily processed into nanofibers; secondly, they are stable during electrochemical deposition of the conducting polymer coating; and thirdly, they can be easily removed under conditions that leave the wall material intact. In their experiment, PLLA/PLGA nanofibers and dexamethasone-incorporated PLGA nanofibers were collected on microfabricated electrode tips and gold-coated silicon wafers, respectively. The diameters of the nanofibers were mainly in the range 100 to 200 nm. The nanofibers were distributed randomly on the surface of the probe. This rough surface morphology was useful for molding a similar structure in the subsequently deposited PEDOT coating. After PEDOT deposition, the PLGA fibers were removed by soaking in dichloromethane for 5 min and finally the PEDOT containers were obtained.

Unlike the porous membrane, colloidal particles (such as PS or silica particle) are another type of template for the preparation of CPCs (Figure 11.10c). In previous work, core/shell PS/PANI composite particles were prepared by chemical oxidative seeded dispersion polymerization. A conventional coating protocol was employed as follows. The aniline monomer was dissolved in a strongly acidic solution in the presence of the PS seed latex (an alternative method involves using a miscible aniline hydrochloride monomer without external acid). Then polymerization was initiated by the addition of oxidant aqueous solution. The suspended PS particles were coated with PANI by *in situ* deposition of the formed conducting polymer or oligomer from the aqueous phase.

The deposition of thin PANI and PPy coatings onto monodisperse silica particles had already been reported in 1991. To date, a massive amount of work on the synthesis, characterization, and use of colloidal particles coated with conducting polymer shells in solution has been reported. In addition, great efforts have been made on the surface functionalization and modification of PS seed particles to improve the adhesion of PANI and further form a smooth and uniform PANI overlayer. Reynaud and coworkers [104] introduced a relatively high coverage of PANI based on cross-linked PS particles stabilized by a surfactant bearing an amide group, which allows the formation of hydrogen bonds with the PANI backbone. Yamamoto *et al.* [105] synthesized PANI on carboxylated styrene-butadiene- methacrylate latex particles. Similarly, Aoki and Lei [106] employed a copolymeric PS latex with sulfonate groups, which could act as a chemical dopant for the growing conducting polymer. Wang *et al.* [107] reported cationic PS latex and equilibrated it with a negatively charged sulfate surfactant prior to the coating process, which was apparently adopted to take advantage of the electrostatic interaction with the positively charged PANI oligomer. In work by Mangeney's group, PPy-coated PS particles were synthesized. In order to improve the colloidal stability of the conducting polymer-coated PS particles, the PS was pretreated. Armes *et al.* [22,108] mainly dealt with polyvinylpyrrolidone (PVP)-stabilized PS latexes and invented various surface modification strategies. However, they claimed that these PANI overlayers still suffered from the shortcoming of

nonuniform, inhomogeneous morphologies, in contrast to the relatively smooth morphologies obtained from the deposition of PPy onto the same sterically stabilized PS latexes [109–111]. It was also emphasized that nonuniform conducting-polymer deposits would be obtained if the latex was less hydrophobic [24,112,113]. Even though surface modification could generally optimize the deposition architecture of the PANI overlayer, it obviously complicates the synthetic procedure. Moreover, it is noteworthy that the chemical groups available at the latex seed surface to monitor the deposition of the PANI component are nonuniformly distributed [114]. Therefore, this widely used synthetic strategy has its own disadvantages in achieving a perfect conducing polymer shell. Efforts have been directed to address this phenomenon. A distinctly novel strategy to fabricate PANI-coated PS microspheres was proposed by Wang and coworkers [115]. In their system, a PANI overlayer was formed by diffusion-interface polymerization of aniline preabsorbed on PS seed latex without any surface modification. The resulting structure and morphology were well controlled by simply changing the initial amount of aniline or the rate of addition of the doping agent.

Although the preparation of core/shell conducting polymer spheres using nanoscale-sized latex particles or silica spheres has been widely studied [22,23,108,116–118], there are a few reports concentrated on using metal-oxide nanoparticles as templates to fabricate CPCs. Since the polymerization is required to be performed in strong acidic conditions in general, the core of the metal-oxide nanoparticles are usually etched away during the polymerization process. Chen *et al.* developed a new synthetic route employing metal-oxide nanoparticles to obtain PANI hollow spheres [119]. A double-surfactant-layer (DSL)-assisted polymerization method was designed to control the polymerization of PANI onto the surface of various metal oxide nanoparticles, including copper oxide, hematite, and indium oxide. The prepared metal-oxide nanoparticles were modified by PVP to improve their dispersibility in solution. The modified metal-oxide nanoparticles were dispersed in aqueous solution. Sodium dodecyl sulfate (SDS) was subsequently added to the solution before the polymerization reaction. A double-surfactant PVP-SDS layer was formed surrounded by the polar amide groups of PVP on the surface of the metal-oxide core, and the negative side of the SDS molecule facing out into the solution. Afterwards, aniline monomers were added and adsorbed onto the surface of the metal oxides due to static interaction. The adsorption resulted in a great increase in the local concentration of aniline monomer near the core surface. This was favorable for the initial polymerization of aniline at low monomer concentrations. Once aniline nucleation has been intitiated, the polymerization predominately and continuously took place in close proximity to the existing PANI [120]. Eventually, a homogeneous, continuous, and uniform PANI shell was coated onto the surface of the metal-oxide core. Hollow PANI capsules were obtained by the subsequent removal of the template. The hollow sphere-like CPs were evaluated for various applications, such as encapsulation materials. An interesting characteristic of the CPCs is that transport rates of small molecules into the capsule core are affected by the oxidation state of the conductive polymer, which has potential utility in many molecular uptake and release scenarios. Wan *et al.* found that Cu_2O can be oxidized by ammonium persulfate (APS) in an acid solution [121], suggesting that PANI microstructures could be prepared using octahedral Cu_2O crystals as templates. Consequently, they prepared hollow octahedral PANI by using octahedral Cu_2O as template in the presence of H_3PO_4 and APS as dopant and oxidant, respectively.

Compared with a conventional template, octahedral Cu_2O was not only a new type of template (in both shape and quality), but also omitted the need for subsequent template-removal treatment.

Hard-template synthesis can provide micro- and nanocontainers with a controlled geometric shape. However, this approach requires complicated synthetic steps, including the dissolution of the template in corrosive media. Collapse of the hollow structure after template removal is also a critical problem. Therefore, the potential drawback of using hard templates forced scientists to search for more efficient and facile routes to prepare CPCs. Among these newly developed approaches, the soft-template method is considered a powerful tool as an alternative strategy to hard-template synthesis.

11.3.2 Soft-Template Method

The advantage of using soft-template materials is that they can be removed easily after synthesis, leaving micro- and nanostructures of the resulting polymer. So far, new types of soft template, such as surfactant micelles, oil droplets, liquid-crystalline phases, 'soap bubble' templates, and so on, have been reported for the fabrication of CPCs via self-assembly processes (Figure 11.11). For example, emulsion polymerization has been employed to prepare containers of PPy and PANI [33,34,38,39,83]. Liquid droplets have also been used for template growth of polymeric nano- or microspheres. Gaseous bubbles were electrochemically generated at the electrode surface and coated with PPy, forming microcontainers with various, such as bottles, whiskers, and cups [35,79–82]. The synthetic process and the formation mechanism of these methods are briefly reviewed in detail below.

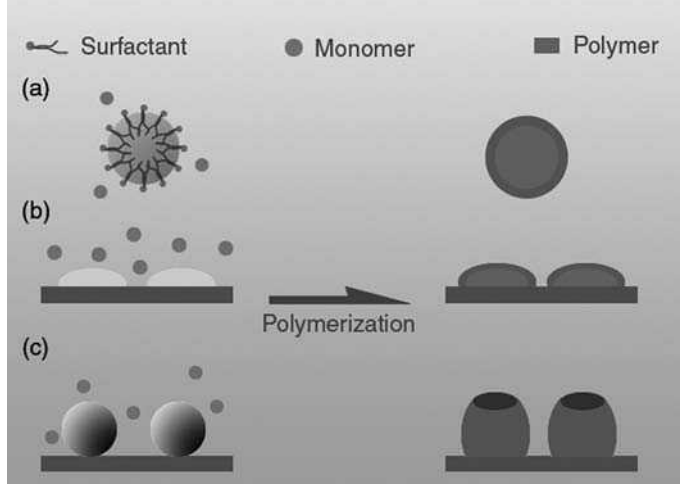

Figure 11.11 *A schematic representation of the soft-template method used to prepare CPCs: (a) micelles, (b) oil droplets, (c) gaseous bubbles*

As is well known, surfactants are a common 'soft-template' because they easily form thermodynamically stable, and controllable nanometer-scale micelles in solution or at interfaces. Anionic surfactants like sodium dodeyl sulfate (SDS) and cationic surfactants such as cetyltrimethylammonium bromide (CTAB) were widely used to form micelles. Surfactants can assemble into aggregates in the bulk solution. The favored aggregate morphologies of the surfactant in solution for the preparation of CPCs include spherical and cylindrical. In general, monomer in the solution can be diffused into these spherical or cylindrical micelles to serve as a 'soft template' for forming micro- and nanocontainers. Once oxidant is added (chemical approach), or oxidative potential is applied (electrochemical approach), polymerization will initially take place at the water/micelle interface. Hollow-structured CPs can then be obtained by stopping the polymerization at the appropriate time. In a report by Zhang *et al.*, wire-, ribbon-, and sphere-like PPy nanostructures were synthesized by a solution chemistry method in the presence of various surfactants (anionic, cationic, or nonionic surfactant) with various oxidizing agents [122]. The effects of surfactant concentration, surfactant chain length, monomer concentration, etc. on the morphologies of the resulting PPy have been investigated in detail. The mechanisms of templates during polymerization have also been discussed. Among surfactants used as soft-templates, reverse-emulsion templates are considered to be an efficient tool for the fabrication of hollow conducting-polymer structures. The most widely used surfactant to form reverse micelles is sodium bis(2-ethylhexyl) sulfosuccinate (AOT), which is an anionic surfactant and has two hydrophobic tailgroups.

Based on the characteristics of the surfactants, Wan *et al.* proposed that the micelles formed by dopant, dopant/monomer salt, or supermolecules, and even by the monomer itself might serve as soft-templates in the self-assembled nanostructures [34,38]. The micelle model was confirmed by dynamic light scattering (DLS) [123] and direct measurement of the micelle morphology by freeze-fracture transmission electronic microscopy (FFTEM) imaging. Based on the above ideas, conductive and superhydrophobic 3-D microstructures assembled from 1-D nanofibers of PANI, such as hollow rambutan-like spheres, and hollow dandelion-like and cube-like 3-D microstructures, have been obtained by Wan *et al.* [39], with perfluorooctane sulfonic acid (PFOSA) and perfluorosebacic acid (PFSEA) as the dopant, respectively. The hydrophilic —SO_3H group in PFOSA or the two hydrophilic —COOH end groups in PFSEA serve both as the dopant and the template at the same time, while the perfluorinated carbon chain in both PFOSA and PFSEA contributes to the hydrophobic properties of the micro- and nanostructures. When PFSEA is used as the dopant with a high molar ratio of PFSEA to aniline, a hollow dandelion-like structure is obtained, whereas hollow cube-like 3-D microstructures are synthesized at a low concentrations of aniline and a low molar ratio of PFSEA to aniline.

By investigating different contact angles for monomer droplets on different substrates, unique hollow PPy nanostructured arrays with conical shapes have been produced via stepwise electrochemical polymerization by Wei *et al.* [83]. In order to investigate the formation mechanism of the PPy conical nanocontainers, they measured the contact angles of pyrrole monomer droplets on different substrates. The contact angle of a pyrrole droplet on a platinum plate was measured as 126.1° (in the aqueous solution of the reaction system), while the contact angle on an Au/Pt plate was 43.3° under the same conditions. In the case of electrochemical polymerization, they suggested that the micelles adsorbed on the surface of substrate acted as a soft template at the beginning of the polymerization.

Since pyrrole droplets have a contact angle higher than 90° on platinum substrates, pyrrole-filled micelles were anchored firstly on the substrate by the polymerization of pyrrole along the contact interface between the micelles and substrate. After that, pyrrole monomer was predominately polymerized on the edge of anchored micelles due to the higher electric field originating from edge effects. Therefore, hollow conical nanostructures were produced by a slow polymerization process. In contrast, in the case of using an oleophilic Au/Pt substrate as the working electrode, initial nucleation occurred on the surface of the micelles. Because pyrrole droplets only have a contact angle of 43.3° on the Au/Pt substrate, each individual nucleus has a diffusion zone depending on the size and age of the nucleus. The overlap of these diffusion zones joined the growing nuclei in a bulk film on the substrate during the consequent incorporation process. Therefore, a cauliflower-like PPy film was finally produced. The existence of pyrrole-filled micelles was proven by TEM investigation of a replica film prepared by freeze-fracture replication. The pyrrole-filled micelles showed a spherical shape with diameters ranging from 30 to 100 nm. When a high current was applied, pyrrole-filled micelles were polymerized together with the free pyrrole on the electrode. A crater-like structure with an approximate diameter of 150 nm was observed if polymerization was stopped after the first stage. The diameter of the crater-like structures was even bigger than the largest micelles observed. Obviously, the crater-like structure was an intermediate structure in the formation of the nanocontainers.

Oil micro- and nanodroplets can also sevrve as templates for preparing CPCs. M. Mazur employed mineral oil droplets as templates directing polymer growth in the form of 3-D containers on glass or quartz surfaces [36]. The dissolution of fluorescent dyes within the droplets prior to polymer deposition allowed their entrapment within the containers. Because of the use of glass or quartz as substrates, the encapsulated dyes were easily observed from the transparent substrate side, wherein emitted light could be used to track phenomena occurring within the capsules. In this work, PPy microcontainers were deposited on transparent substrates in two steps. Firstly, liquid emulsion microdroplets were adsorbed onto the solid substrate, and then coated with a thin adlayer of polymeric material. An oil-in-water emulsion was prepared by sonication, and then subsequently used as a dipping solution for glass slides for pretreatment. The immersion of the glass slides resulted in a rapid adsorption of oil droplets onto the surface. Because no emulsion stabilizer was used, the adsorption of oil droplets onto the glass surface was relatively easy. Consequently, the emulsion was relatively unstable, permitting fusion of the droplets onto the glass surface. The droplets are randomly distributed on the surface, with their sizes ranging over several micrometers. After oil-droplet adsorption, the next step in preparing the microcontainer was the deposition of PPy. PPy was easily prepared in the form of a thin film adjacent to the substrate by *in situ* polymerization. Polymer layers were grown by immersing glass slides in a polymerization bath containing monomer and oxidant, finally forming microcontainers filled with fluorescent dyes.

In addition to the above-mentioned soft templates, 'soup bubbles' have been also used as templates to fabricate CPCs. PPy microcontainers with bowl-, cup-, and bottle-like morphologies have been electrochemically generated by direct oxidation of pyrrole in an aqueous solution of β-naphthalenesulfonic acid (β-NSA), first reported by Shi *et al.* [79–82]. The bubbles were produced by the decomposition of water. The gas bubbles and the aqueous solution containing the monomer and β-NSA led to the formation of 'soap

bubbles'. The growth of PPy around these bubbles resulted in the PPy microcontainers. The 'soap bubble' size and generation rate and the growth rate of PPy film depended strongly on the experimental conditions. Thus, changing the electrolysis conditions could modulate the shape, size, and caliber of the PPy microstructures. They also found that no microstructures were formed at potentials lower than 0.8 V. However, in view of the fact that the direct generation of O_2 gas on the working electrode under a relatively high positive potential could have a detrimental overoxidation effect, Dai *et al.* started the electrochemical polymerization of PPy microcontainers by releasing H_2 around the working electrode under a negative potential [35]. The newly released H_2 gas bubbles were stabilized by the anionic surfactant molecules in the solution and assembled onto the working electrode under a positive potential. The mechanism in the case of H_2 gas bubbles is similar to the O_2 gas bubbles, although the former allows the formation of PPy microcontainers on the working electrode at a relatively low potential. Based on their previous work, Shi *et al.* reported linear arrangement of PPy microcontainers by self-assembling gas bubbles to act as a template on a silicon electrode surface patterned by photolithography [82]. This was mainly due to the surface tension of the gas bubbles being decreased by interactions between the walls of the polymeric photoresist and the gas bubbles (capillary interaction), which led the gas bubbles to self-assemble linearly along the two edges of the silicon electrode.

11.3.3 Micro- and Nanofabrication Techniques

However, each currently developed method has its own disadvantages. Hard-template methods, for instance, are a universal and controlled approach to obtaining conducting-polymer nanostructures, but the requirement of a template and the post-treatment for template removal not only results in a complex preparation process, but can also destroy the formed structures. Moreover, the size and morphology of available templates is limited. The soft-template method is another relatively simple, cheap, and powerful approach to obtain CPCs via a self-assembly process. However, the morphology and size control of the self-assembled nanostructures obtained is poor. Therefore, finding a facile, efficient, and controlled route to prepare CPs nanostructures is desirable.

Despite the fact that a number of porous structures containing polymers have been reported [124–131], few systematic efforts have been made to correlate the patterning of CPCs by nanofabrication techniquea. Zhou *et al.* developed a methodology to deposit PANI in the free volume existing at the patterned surface [132]. Nanosphere lithography (NSL) has been demonstrated by several research groups to be a simple, reproducible, and versatile technique for fabricating well-ordered 2-D nanoparticle and metal arrays [48,133–136]. A periodic 2-D array of colloidal particles has been shown by Van Duyne and coworkers to be better ordered and more defect-free than a 3-D multilayered particle network [48,135–137]. Because the upper layers of colloidal particles in a 3-D network may impose a possible hindrance to the aniline monomer diffusion from the solution to the underlying electrode surface, the use of a 2-D array should allow a better patterned PANI film to be formed. Therefore, they predeposited the PS particles with alternating layers of polyelectrolyte and applied the NSL procedure. By electrochemical polymerization of PANI within the interstitial voids in a preformed PE-coated colloidal particle assembly and

extraction of the PS particles using toluene, a PANI honeycomb film with pores containing PE layers was finally formed.

As discussed previously, it is possible to obtain stimuli-responsive CPCs when combining the nanofabrication methods reported by E. Jager and D. Gracias. Standard microfabrication procedures, including surface and bulk micromachining methods, which involve sequential deposition and removal steps, were used to fabricate PPy actuators in a report by E. Jager *et al.* Two methods, differential adhesion and sacrificial layer, were investigated. The differential adhesion method was based on the poor adhesion between Au and Si. A Cr layer was patterned on a Si surface, resulting in adhesive and nonadhesive areas. Then an Au layer was deposited over this surface, and PPy was electrochemically deposited on it. The PPy was patterned; thus a minor part of the Au/PPy bilayer was in contact with the adhesive Cr layer, and this part functioned as an anchor holding the actuator to the surface. The major part of the bilayer was in contact with the Si, to which the Au did not adhere. Activating the bilayer caused it to pull itself free. Although the differential adhesion method is easy and fast, the author suggested that this technique would not be suited to all designs, for example it could not be used to fabricate some individually controlled microactuators. Therefore, they used the well-known sacrificial layer technique to fabricate micro robot arms. A support layer of Ti (the sacrificial layer) was patterned onto a SiO_2-covered wafer. Then they deposited Cr, Au, and PPy layers. The microactuators were patterned with a small part overlapping the Si as the anchor point and the rest overlapping the sacrificial layer. A free-hanging bilayer that could be activated was achieved by removing the sacrificial layer. Although the sacrificial-layer method suffers disadvantages, including a long underetching time and potential damage to the PPy, depending on the etchant, it is advantageous for building more complex microactuator devices. Later, D. Gracias *et al.* reported stress-driven self-folding microstructured containers, accomplished by using trilayer hinges. The hinge was composed of a bimetallic component containing chromium and copper and a trigger made of photoresist polymer. Notably, it is possible to use intelligent CPs serving as the hinges to connect each nickel wall and then form stimuli-responsive containers. It is worthwhile to combine these two techniques together to prepare novel micro- and nanocontainers because of the advantages of lower cost, more precise control, wider applicable conditions, and so forth.

11.4 Properties and Applications of Micro- and Nanocontainers

Generally, the application of certain materials is based on a comprehensive understanding of their properties, including physical, chemical, and electrical aspects, etc. Therefore, it is necessary to summarize the properties of CPs in the first place. So far, a great deal of research work has been focused on the characterization of CPs. A great number of articles, reviews, and books about this issue are available in science libraries and digital databases. For example, CPs are sensitive to numerous stimuli and can be made to respond. They can store foreign species and are capable of performing intelligent functions. Because of these inherent properties, containers made from CPs are considered excellent candidates for encapsulation, drug delivery, and controlled release. As is well known, effective, but

highly toxic, drugs are usually employed for cancer therapy. To decrease their toxicity and avoid the negative influence of the toxic drugs on the rest of the body, it is desirable to treat only the damaged part of the organism. The most promising approach to solving this problem is to entrap toxic drugs in the inner volume of the micro- and nanocontainers. The shell of micro- and nano containers will interdict any contact with healthy tissue during the targeted delivery of drugs before they reach damaged cells. To date, the encapsulation of chemical species within cavities of conducting-polymer structures can be understood by using three methods. Furthermore, efforts have focused on the investigation of drug delivery and controlled release, another important potential application of CPCs. The ability to recognize particular stimuli and respond, and good biocompatibility allow these CPCs to be competitive drug-delivery and release systems. More details about the chemical and electrical properties of CPs and their potential applications are reviewed in this section.

11.4.1 Chemical and Electrical Properties

CPs are considered to be intelligent materials because of their unique physical and chemical properties. For example, their chemical properties can be manipulated to produce materials capable of trapping simple anions or rendering them bioactive. Their electrical properties can also be controlled to produce materials with different conductivities and different electrochemical properties. After synthesis, the properties of these fascinating structures can be manipulated further through processes cycling between oxidation and reduction states. The application of electrical stimuli can result in drastic changes in the chemical, electrical, and mechanical properties of CPs. However, these complex properties can be controlled only if they are completely understood: first of all, the nature of the processes which control them during the synthesis of the CPs, and the second, the extent to which these properties are changed by the application of an applied stimulus such as electrical signal. As defined by G. Wallace, an intelligent material is capable of recognizing appropriate environmental stimuli, processing the information arising from the stimuli, and responding in an appropriate manner and timeframe. What is particularly important is that the responses obtained are appropriate [138]. In other words, they must result in desirable behavior that enhances the performance of the material or structure. To function as intelligent materials, CPs must be able to recognize the stimulus, process the information, and respond with actuation. As a result, they must have appropriate chemical properties that can change in response to stimuli, as well as appropriate electrical properties that allow information to be transported within the structure and switches to be actuated. The mechanical properties must also be considered, because it will be of questionable value to create materials with ideal chemical and electrical properties, but with inappropriate mechanical properties.

The ability of CPs to recognize particular stimuli and respond is determined by the chemical properties of the resultant structure. Moreover, these properties determine how the conducting polymer interacts with other materials in the construction of composite intelligent material structures. The dynamic nature of these chemical properties is important. For example, G. Wallace and coworkers have shown that the affinity for particular antibody molecules can be altered by the application of electrical stimuli [138]. In

addition, the activity of incorporated functional molecules such as proteins can be altered by application of appropriate electrical stimuli. That the application of an electrical potential influences the antigen and antibody interaction was demonstrated in previous work. Although the mechanism is not absolutely clear, the same principles as sensing technology proved to be applicable [138].

The electrical properties of intelligent materials are important because they determine the abilities of those materials to transport information from one part to another, to trigger responses. Electrical conductivity in CPs is a complex issue. The experimental parameters applied during synthesis have a significant effect on the polymer conductivity. Particularly, the electrochemical conditions, and the solvent, dopant, and monomers used during synthesis influence the electronic properties of the resulting polymer. The electrochemical conditions during synthesis can be manipulated to vary the concentration of electrons removed per unit time, which will have a dramatic effect on the resulting polymer. Charge can be reversibly added to or removed from a conducting polymer by cycling the material through the oxidation and reduction states. For example, as the polymer is reduced, anions are encouraged to leave the polymer; however, if it is hard to accomplish, charge compensation may be achieved by incorporation of cations from the electrolyte. In some cases, where the anion incorporated during synthesis is bulky or has a bulky hydrophobic component, the cation-incorporation process will predominate and the polymer mass will increase upon reduction. The change in resistance is much less when cation rather than anion movement predominates in the polymer oxidation/reduction process.

Clearly, the way CPs are assembled has a dramatic effect on their chemical, electrical, and mechanical properties. This information can be used to guide attempts in material design at the molecular level. Fully understanding the importance of the properties of CPs for their successful application requires that the properties of these materials be further investigated. This, however, requires a greater understanding of their structure, both at the molecular and the supramolecular level. Fortunately, scientists already have made great efforts in this aspect to satisfy the requirement of novel applications such as programmable encapsulation, intelligent delivery, and controllable release.

11.4.2 Encapsulation

The encapsulation of chemical species within cavities of CPCs can be realized using three methods. In the first method, a small opening is left within the shell of a container during its synthesis process to allow subsequent loading of the empty cavity with guest molecules. The opening is sealed using an additional polymerization step after the empty cavity is loaded (Figure 11.12a). Using this method, polymeric nanotubes have been used to entrap several enzymes. The tube-like containers were prepared within a porous membrane, which was then immersed in a solution of the enzyme, and then finally subjected to a second polymerization step to seal the open ends of the nanotubes [51,103]. In a report by Son *et al.*, the PEDOT nanotubes were used as containers retaining water-soluble electroactive materials and to play the role of a current collector for electrochemical reaction of the species retained inside [53]. In this study, $K_3Fe(CN)_6$ was employed as the probe material stored in the cylinders. The current collector exhibited a fine current response due

to the redox reaction of the interior species. These results indicate that guest materials can be stored in these capped nanotubes without the problems associated with the use of organic solvents during the preparation process.

Bajpai *et al.* prepared PPy containers in the presence of fluorescein cadaverin in solution [35]. The containers were loaded with the dye molecules, and the openings of the capsules were sealed after electrochemical polymerization. To verify that the foreign species were encapsulated in the containers, they rinsed the sealed microcontainers thoroughly with distilled water until there was no fluorescence in the rinsing liquid, and then these closed microcontainers were mechanically broken in distilled water, after which a fluorescence signal was detected. This phenomenon indicated that the conducting-polymer microcontainers are capable of encapsulating foreign species.

The second encapsulation method uses the permeation of chemical species through the walls of the container (Figure 11.12b). Using this method, Jang *et al.* loaded PPy nanospheres with pyrene, a photochromic dye material [139]. Green emissions of pyrene molecules were observed in the form of solid spheres, indicating that pyrene molecules were introduced into the inner cavity of the polymer containers owing to hydrophobic interactions. The mesochannels in the polymer capsule wall could act as a passage for the introduction of pyrene molecules into the pores. They observed that the size of emission spot was slightly larger than the average pore size of the PPy capsules. This was considered to show that some portion of pyrene molecules was adsorbed on the outer surface of the polymer capsule.

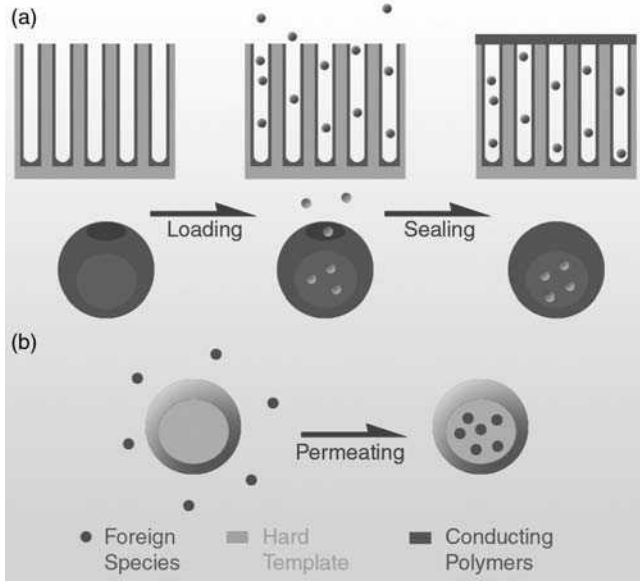

Figure 11.12 *A schematic illustration of the encapsulation approaches: (a) loading the content after the synthesis process and then sealing the open ends of the CPCs by a further polymerization; (b) entrapping the chemical species by their permeation phenomenon (See colour Plate 8)*

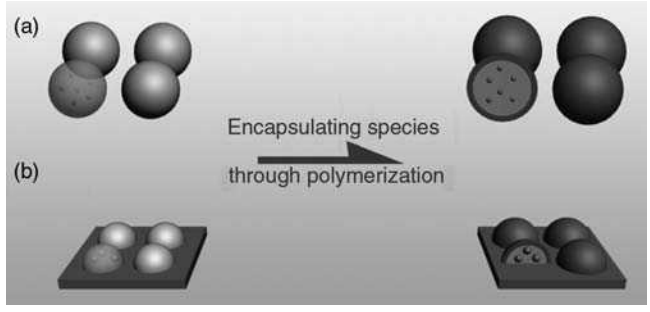

Figure 11.13 *A schematic illustration of the encapsulation approach encapsulating the foreign species via a polymerization procedure*

In the third encapsulation method, the chemical species are entrapped through the polymerization process (Figure 11.13). Feldheim *et al.* covalently attached rhodamine B to gold nanoparticles, which were then subsequently coated with PPy. The gold cores were then etched in a KCN solution, leaving the dye molecules entrapped in the containers. A method for guest molecule encapsulation inside the cavities of polymeric structures grown on droplet templates was recently introduced by M. Mazur [36,37]. Target molecules were dissolved in the oil droplets prior to polymer deposition, and were then entrapped in the cavity of the polymer after polymerization. To demonstrate the encapsulation of molecules within PPy containers, two fluorescent dyes, pyrene and perylene, were employed. Their presence inside the containers could be easily detected with spectrofluorometry, providing evidence of the successful encapsulation of guest species. The release of the microcontainer content could be achieved by controlling the hydration of the polymeric shell. When the containers were placed in an aqueous or humid environment, the dye molecules stayed entrapped. When the PPy was dried, oil containing the fluorophore permeated through the polymeric walls and flowed away from the containers. However, it was confirmed that subsequent rehydration of the sample in water did not result in uptake of the oil content back into the capsule.

11.4.3 Drug Delivery and Controlled Release

Current drug-delivery methods pose specific problems that scientists are endeavoring to address. For example, many drug potencies and therapeutic effects are limited or reduced because the drugs partially degrade before they reach the target in the body. Further, injectable medications could be made more cheaply and administered more easily if they were dosed orally [140]. However, this improvement cannot take place until methods are developed for the safe delivery of drugs through specific areas of the body or through an area where healthy bone and tissue are badly affected. The goal of all drug-delivery systems is to transport medications intact to specifically targeted parts of the body through a medium that can control the release of the drugs by means of either a physiological a or chemical trigger. To achieve this, researchers have put enormous effort into the fields of micro- and nanotechnology. During past decades, polymeric microspheres, polymer

micelles, and hydrogel-type materials have all been proven to be effective in enhancing drug targeting specificity, lowering systemic drug toxicity, improving treatment absorption rates, and providing protection for pharmaceuticals against biochemical degradation. So far, many sophisticated and potent drugs have been developed. However, conventional dosage forms such as oral delivery and injection have been found to be unsuitable for many of these new protein- and DNA-based drugs. Failing to target a specific area, these delivery routes often require frequent administration of drugs in high dosages. Consequently, the body experiences a rapid release of the drug, which renders these dosage forms unsuitable for many of the new drugs, because their toxicity requires observation for concentration spikes. Therefore, the blood concentrations and target areas of these drugs must be carefully controlled. Furthermore, since the efficacy of many new and traditional drugs is strongly influenced by their temporal administration, it is necessary to deliver drugs at a controlled rate. For example, many therapeutic agents are most effective when delivered in a pulsatile release profile. For these reasons, new cost-effective technology for controlled drug delivery is demanded for the administration of the new drugs. Progress has been made in recent years following advances in nanotechnology, such as microparticles, biocapsules, microneedles, and micropumps. The ideal drug-delivery system that can self-regulate the delivery rate in response to the patient's physiological condition to obtain the optimal therapeutic effect has yet to be attained.

The reasons why CPs are the ideal materials for biomedical actuators and relevant applications have been summarized by Smela [59]. These lightweight materials have large strain and high strength. They are able to work at room or body temperature and in body fluids, and they only require low voltages for actuation. Many CPs are also biocompatible and suitable for processing by microfabrication with existing technology. CPs have been chosen as the material for micropump drug-delivery systems. Experiments were conducted to choose the polymer or polymer composites most suitable for the application. Numerous articles have indicated that PPy is a good candidate because of its *in vivo* stability and biocompatibility. Different micropump designs were also modeled by computer simulation. CPs possess reversible electrochemical responses, where they expand upon oxidation and contract on reduction. The volume change originates from the insertion or expulsion of counter-ions from an electrolyte for charge balancing, together with the movement of solvent molecules. When conducting electroactive polymers expand, they generate force and movement in a particular direction. This electrochemically controlled actuation has been investigated for a wide range of applications, including artificial muscles, microrobotics, and microfluidics. Electrochemical switching of an electronically conducting polymer is accompanied by charge compensation through ion flux into or out of a membrane formed from such a polymer, which can be made to work as an ion gate.

PPy functions very well as an ion-gate membrane, which is positively charged in its oxidized state and neutral in its reduced state. The ion-gate membrane can be used to control the delivery of drugs, which can be accumulated in the membrane, e.g. during oxidation, and then released by electrochemically controlled reduction of the membrane. PPy is particularly suitable for this purpose because the monomer is nontoxic and the electrochemical synthesis of the polymer membrane can be done in aqueous solution. Glutamate and dopamine can be released from a PPy membrane using potential control. Pyo *et al.* have shown that controlled release of adenosine 5′-triphosphate (ATP) can be achieved using the same polymer membrane [141]. Hepel and Mahdavi have used a

composite PPy film as an ion-gate membrane for the potential-controlled release of a cationic drug, chlorpromazine [142]. The electrochemical synthesis conditions have a great influence on the redox properties of the PPy membrane and these determine the ion-gate function of the membrane. In a recent study, efforts were made towards the electrochemical polymerization of PPy conductive polymer in order to find the optimum conditions for producing a PPy membrane which could exchange anions [143]. Furthermore, Iseki *et al.* evaluated the efficiency of a PPy membrane as a device for drug delivery using model compounds, which in aqueous solution produce anions with therapeutic activity. The selected anions were salicylate, nicoside, and naproxen. These anions have an aromatic structure and are of medium size [144]. The delivery of anions from the membrane was studied by using an electrochemical quartz crystal microbalance (EQCM), as well as high-pressure liquid chromatography (HPLC) as an analytical tool.

In a report by D.G. Shchukin, the release and reloading cycles of a PPy microcontainer system were visualized by fluorescence microscopy, employing FITC-labeled dextran as a probe (Figure 11.14). The initial dextran-loaded PPy microcontainer electrode demonstrated a high uptake yield in solution without applied potential bias. Changing to a reductive potential resulted in the release of the encapsulated material. Further, hollow polyelectrolyte capsules could be reloaded with new portions of FITC-dextran at a positive potential bias. Twenty minutes of incubation at an oxidative potential were sufficient to reload the capsules inside the PPy microcontainer electrode. The incubation time or release time could be reduced by increasing the potential bias.

D. Martin *et al.* demonstrated that PEDOT nanotubes can precisely release individual drugs and bioactive molecules at desired points in time by using electrical stimulation (Figure 11.15) [69]. In their research, PEDOT nanotubes were placed in a neutral electrical condition to stimulate the body environment. External electrical stimulation controlled the

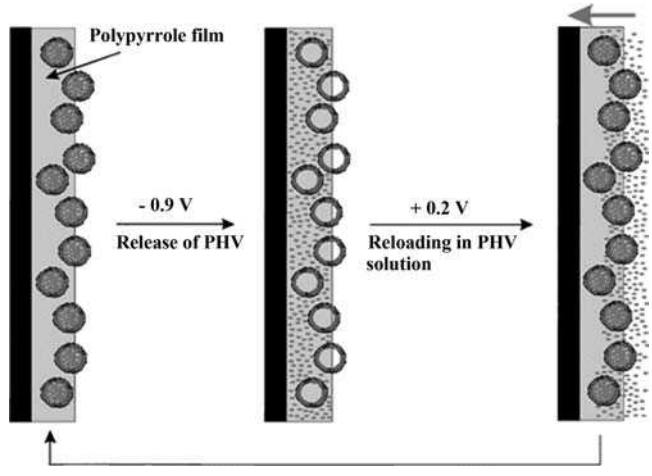

Figure 11.14 *Schematic representation of the functioning of a polypyrrole microcontainer electrochemical system. (Reprinted with permission from Journal of the American Chemical Society, Microcontainers with Electrochemically Reversible Permeability by Dmitry G. Shchukin et al., 128, 14. Copyright (2006) American Chemical Society)*

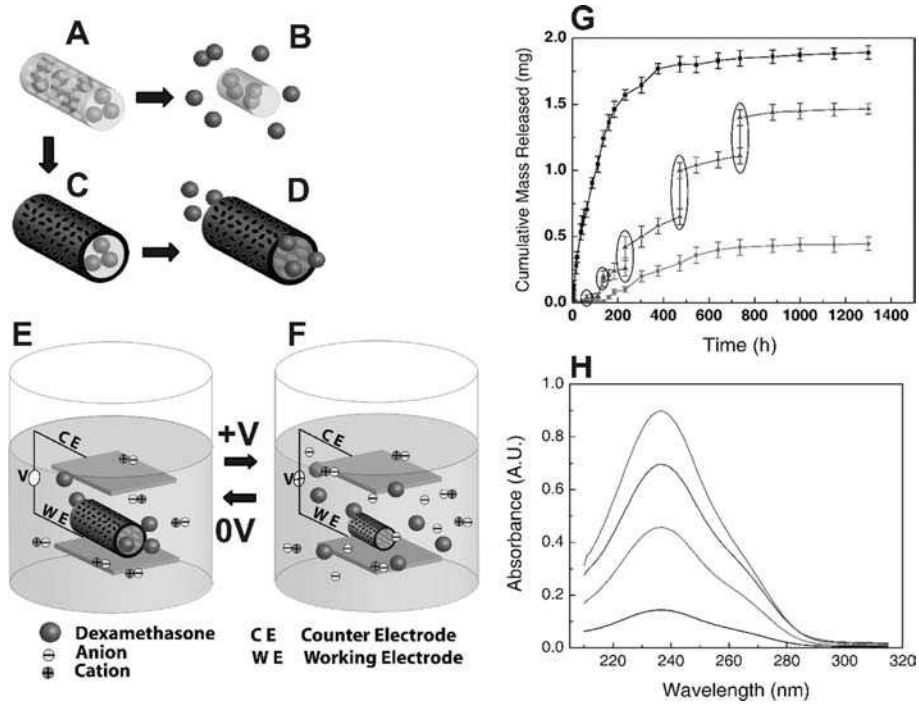

Figure 11.15 *Schematic illustration of the controlled release of dexamethasone: (A) dexamethasone-loaded electrospun PLGA; (B) hydrolytic degradation of PLGA fibers results in the release of the loaded drug; (C) electrochemical deposition of PEDOT around the dexamethasone-loaded PLGA fiber; (D) the PEDOT shell slows down the release of dexamethasone; (E) PEDOT nanocontainers in a neutral electrical condition; (F) external electrical stimulation controls the release of dexamethasone from the PEDOT nanocontainers due to contraction or expansion of the PEDOT; (G) cumulative mass release of dexamethasone from: PLGA fibers (black), PEDOT-coated PLGA nanocontainers (red) without electrical stimulation, and PEDOT-coated PLGA nanocontainers with electrical stimulation of 1 V applied at the five specific times indicated by the circled data points (blue); (H) UV absorption of dexamethasone-loaded PEDOT nanocontainers after 16 h (black), 87 h (red), 160 h (blue), and 730 h (green). The UV spectra of dexamethasone have peaks at a wavelength of 237 nm. (Reprinted with permission from Advanced Materials, Conducting-Polymer Nanotubes for Controlled Drug Release by M. R. Abidian, D.-H. Kim, D. C. Martin, 18, 4, 405–409. Copyright (2006) Wiley-VCH)*

release of dexamethasone from the PEDOT nanotubes due to contraction or expansion of the PEDOT. By applying a positive voltage, electrons were injected into the chains and then positive charges in the polymer chains were compensated. To maintain overall charge neutrality, counter-ions were expelled towards the solution and the nanotubes contracted. PEDOT contraction then produced a mechanical force creating pressure within the nanotubes. The hydrodynamic force inside the nanotubes thus caused expulsion of PLGA degradation products and dexamethasone, presumably either through the ends of PEDOT nanotubes or though openings or cracks on the surface of the nanotubes created

by actuation. This research provided a general method capable of facilitating integration of electronically active devices into living tissues.

Encapsulation, drug delivery, and controlled release are the main goal of scientists in preparing CPCs. Considering their special structures and unique properties, CPCs could also applied to other aspects. For example, because of the high specific area, conducting-polymer microcontainers are considered to be good candidates for sensing applications. Dai *et al.* found that the response current for PPy microcontainers is roughly double that of the corresponding PPy film when using them to detect glucose [35]. Furthermore, CPCs are capable of serving as a catalyst support due to their hollow structures and high surface-to-volume ratios. Despite their potential applications in other fields, encapsulation of certain foreign species, and delivery and release of contents continue to be the focus of research.

11.5 Conclusions

In this chapter, various micro- and nanostructured CPCs have been reviewed. Conventional structures (such as hollow spheres and tubes) and novel structures (for example, goblet- and pipette-like structures) have been presented. The methods developed so far to prepare CPCs have also been discussed. The hard-template-assisted method, which employs commercial available porous membranes or removable colloidal particles and nanowires as the template is a powerful tool to obtain CPCs. However, the template-removal process often cause structural damage to the CPCs. Therefore, the soft-template method was proposed as another way to fabricate CPCs. In this method, the desired structures are formed by driving forces such as supermolecular self-assembly via hydrogen bonds, Van der Waals forces, and electrostatic interactions. Because the formation of supermolecules is often affected by the reaction conditions, the soft-template method has the disadvantage of lacking controllability compared with the hard-template method. Furthermore, with the advancement of nanotechnology, the nanofabrication technique has become a competitive option for the preparation of CPCs. However, this technique is still limited by the expensive cost and the complicated procedure.

CPs have attracted intensive attention because of their inherent properties, such as stimuli recognition, information processing, response actuation, and good biocompatibility. They can store foreign species and are capable of performing intelligent functions. Therefore, CPCs are considered to be promising candidates for applications in encapsulation and controlled drug delivery and release. Three kinds of approach have been used to encapsulate foreign species in the empty cavities of CPCs. Individual drugs and bioactive molecules were precisely released at desired points in time by using electrical stimulation of the CPCs. Detailed evidence has proven that CPCs are particularly applicable for controlled delivery in some circumstances. We envision that CPs can be further optimized with the assistance of developed or developing techniques to form micro- and nanocontainers for applications such as the construction of ‘smart’ containers with enhanced functionality and those with on-demand, reversible opening and closing capabilities.

References

[1] D.G. Shchukin, D.A. Gorin, and H. Moehwald, Ultrasonically induced opening of polyelectrolyte microcontainers, *Langmuir*, **22**(17), 7400–7404 (2006).

[2] Y. Mizushima, Lipid microspheres (lipid emulsions) as a drug carrier – An overview, *Adv. Drug Deliv. Rev.*, **20**(2–3), 113–115 (1996).

[3] G.B. Sukhorukov, E. Donath, S. Davis, H. Lichtenfeld, F. Caruso, V.I. Popov, and H. Möhwald, Stepwise polyelectrolyte assembly on particle surfaces: a novel approach to colloid design, *Polym. Adv. Technol.*, **9**(10–11), 759–767 (1998).

[4] L.M. Croll, and H.D.H. Stover. Composite tectocapsules via the self-assembly of functionalized poly(divinylbenzene) microspheres. In *39th IUPAC Congress/86th Conference of the Canadian Society for Chemistry*, International Union for Pure and Applied Chemistry Ottawa, Canada, 2003.

[5] H. Ai, S.A. Jones, M.M. de Villiers, and Y.M. Lvov, Nano-encapsulation of furosemide microcrystals for controlled drug release, *J. Contr. Rel.*, **86**(1), 59–68 (2003).

[6] Z.G. Cui, W. Fountain, M. Clerk, M. Jay, and R.J. Mumper, Novel ethanol-in-fluorocarbon microemulsions for topical genetic immunization, *Pharm. Res.*, **20**(1), 16–23 (2003).

[7] T. Uchiyama, Y. Kiritoshi, J. Watanabe, and K. Ishihara, Degradation of phospholipid polymer hydrogel by hydrogen peroxide aiming at insulin release device, *Biomaterials*, **24**(28), 5183–5190 (2003).

[8] R. Ideta, Y. Yanagi, Y Tamaki, F. Tasaka, A. Harada and K. Kataoka, Effective accumulation of polyion complex micelle to experimental choroidal neovascularization in rats, *FEBS Lett.*, **557**(1–3), 21–25 (2004).

[9] D. Lee, M.F. Rubner, and R.E. Cohen, Formation of nanoparticle-loaded microcapsules based on hydrogen-bonded multilayers, *Chem. Mater.*, **17**(5), 1099–1105 (2005).

[10] Y. Mizushima, T. Ikoma, J. Tanaka, K. Hoshi, T. Ishihara, Y. Ogawa, and A. Ueno, Injectable porous hydroxyapatite microparticles as a new carrier for protein and lipophilic drugs, *J. Contr. Rel.*, **110**(2), 260–265 (2006).

[11] T. Yamaguchi, Lipid microspheres as drug carriers: A pharmaceutical point of view, *Adv. Drug Deliv. Rev.*, **20**(2–3), 117–130 (1996).

[12] R. Igarashi, M. Takenaga, and T. Matsuda, Distribution of lipid microsphere preparations, *Adv. Drug Deliv. Rev.*, **20**(2–3), 147–154 (1996).

[13] M.C. Jones, and J.C. Leroux, Polymeric micelles – a new generation of colloidal drug carriers, *Eur. J. Pharm. Biopharm.*, **48**(2), 101–111 (1999).

[14] A. Lamprecht, Y. Bouligand, and J.P. Benoit, New lipid nanocapsules exhibit sustained release properties for amiodarone, *J. Contr. Rel.*, **84**(1–2), 59–68 (2002).

[15] A. Malzert-Freon, S. Vrignaud, P. Saulnier, V. Lisowski, J.P. Benoit, and S. Rault, Formulation of sustained release nanoparticles loaded with a tripentone, a new anticancer agent, *Int. J. Pharm.*, **320**(1–2), 157–164 (2006).

[16] D.G. Shchukin, I.L. Radtchenko, and G.B. Sukhorukov, Synthesis of nanosized magnetic ferrite particles inside hollow polyelectrolyte capsules, *J. Phys. Chem. B*, **107**(1), 86–90 (2003).

[17] X.R. Teng, D.G. Shchukin, and H. Mohwald, A novel drug carrier: Lipophilic drug-loaded polyglutamate/polyelectrolyte nanocontainers, *Langmuir*, **24**(2), 383–389 (2008).

[18] A.A. Antipov, G.B. Sukhorukov, S. Leporatti, I.L. Radtchenko, E. Donath and H. Möhwald, Polyelectrolyte multilayer capsule permeability control. In *9th International Conference on Organized Molecular Films (LB9)*, Elsevier Science BV, Potsdam, Germany, 2000.

[19] G. Ibarz, L. Dähne, E. Donath, and H. Möhwald, Smart micro- and nanocontainers for storage, transport, and release, *Adv. Mater.*, **13**(17), 1324–1327 (2001).

[20] C. Dejugnat and G.B. Sukhorukov, PH-responsive properties of hollow polyelectrolyte microcapsules templated on various cores, *Langmuir*, **20**(17), 7265–7269 (2004).

[21] D.G. Shchukin, K. Kohler, and H. Mohwald, Microcontainers with electrochemically reversible permeability, *J. Am. Chem. Soc.*, **128**(14), 4560–4561 (2006).

[22] C. Barthet, S.P. Armes, S.F. Lascelles, S.Y. Luk, and H.M.E. Stanley, Synthesis and characterization of micrometer-sized, polyaniline-coated polystyrene latexes, *Langmuir*, **14**(8), 2032–2041 (1998).
[23] M.A. Khan and S.P. Armes, Conducting polymer-coated latex particles, *Adv. Mater.*, **12**(9), 671–674 (2000).
[24] D.B. Cairns, M.A. Khan, C. Perruchot, A. Riede, and S.P. Armes, Synthesis and characterization of polypyrrole-coated poly(alkyl methacrylate) latex particles, *Chem. Mater.*, **15**(1), 233–239 (2003).
[25] M.G. Han and S.P. Armes, Synthesis of poly(3,4-ethylenedioxythiophene)/silica colloidal nanocomposites, *Langmuir*, **19**(11), 4523–4526 (2003).
[26] C. Mangeney, S. Bousalem, C. Connan, M.-J. Vaulay, S. Bernard, and M.M. Chehimi, Latex and hollow particles of reactive polypyrrole: Preparation, properties, and decoration by gold nanospheres, *Langmuir*, **22**(24), 10163–10169 (2006).
[27] C. Mangeney, M. Fertani, S. Bousalem, M. Zhicai, S. Ammar, F. Herst, P. Beaunier, A. Elaissari, and M.M. Chehimi, Magnetic Fe_2O_3-polystyrene/PPy core/shell particles: bioreactivity and self-assembly, *Langmuir*, **23**(22), 10940–10949 (2007).
[28] Y.L. Li, K.G. Neoh, and E.T. Kang, Plasma protein adsorption and thrombus formation on surface functionalized polypyrrole with and without electrical stimulation, *J. Coll. Interf. Sci.*, **275**(2), 488–495 (2004).
[29] M.D. Butterworth, R. Corradi, J. Johal, S.F. Lascelles, S. Maeda, and S.P. Armes, Zeta-poential measurements on conducting polymer-inorganic oxide nanocomposite particles, *J. Coll. Interf. Sci.*, **174**(2), 510–517 (1995).
[30] S. Slomkowski, Polyacrolein containing microspheres: Synthesis, properties and possible medical applications, *Prog. Polym. Sci.*, **23**(5), 815–874 (1998).
[31] A. Azioune, A.B. Slimane, L.A. Hamou, A. Pleuvy, M.M. Chehimi, C. Perruchot, and S.P. Armes, Synthesis and characterization of active ester-functionalized polypyrrole-silica nanoparticles: Application to the covalent attachment of proteins, *Langmuir*, **20**(8), 3350–3356 (2004).
[32] K. Boukerma, M. Mičušik, M. Mravčákova, M. Omastova, M.-J. Vaulay, P. Beaunier, and M.M. Chehimi, Surfactant-assisted control of the surface energy and interfacial molecular interactions of polypyrrole, *Coll. Surf. A, Physicochem. Eng. Asp.*, **293**(1–3), 28–38 (2007).
[33] Z.X. Wei and M.X. Wan, Hollow microspheres of polyaniline synthesized with an aniline emulsion template, *Adv. Mater.*, **14**(18), 1314–1317 (2002).
[34] Z.X. Wei, Z.M. Zhang, and M.X. Wan, Formation mechanism of self-assembled polyaniline micro/nanotubes, *Langmuir*, **18**(3), 917–921 (2002).
[35] V. Bajpai, P.G. He, and L.M. Dai, Conducting-polymer microcontainers: Controlled syntheses and potential applications, *Adv. Funct. Mater.*, **14**(2), 145–151 (2004).
[36] M. Mazur, Polypyrrole containers grown on oil microdroplets: Encapsulation of fluorescent dyes, *Langmuir*, **24**(18), 10414–10420 (2008).
[37] M. Mazur, Preparation of three-dimensional polymeric structures using gas bubbles as templates, *J. Phys. Chem. C*, **112**(35), 13528–13534 (2008).
[38] M.X. Wan, A template-free method towards conducting polymer nanostructures, *Adv. Mater.*, **20**(15), 2926–2932 (2008).
[39] Y. Zhu, H. He, M. Wan, and L. Jiang, Rose-like microstructures of polyaniline by using a simplified template-free method under a high relative humidity, *Macromol. Rapid Commun.*, **29**(21), 1705–1710 (2008).
[40] L.J. Zhang, M. Wang, and Y. Wei, Hollow polyaniline microspheres with conductive and fluorescent function, *Macromol. Rapid Commun.*, **27**(11), 888–893 (2006).
[41] N.C. Foulds and C.R. Lowe, Enzyme entrapment in electrically conducting polymers – immobilization of glucose-oxidase in polypyrrole and its application in amperometric glucose sensors. *J. Chem. Soc. Faraday Trans. 1*, **82**, 1259–1264 (1986).
[42] M.A. Rahman, N.-H. Kwon, M.-S. Won, E.S. Choe, and Y.-B. Shim, Functionalized conducting polymer as an enzyme-immobilizing substrate: An amperometric glutamate microbiosensor for *in vivo* measurements, *Anal. Chem.*, **77**(15), 4854–4860 (2005).

[43] K.B. Jirage, J.C. Hulteen, and C.R. Martin, Nanotubule-based molecular-filtration membranes, *Science*, **278**(5338), 655–658 (1997).
[44] A. Kros, S.W.F.M. van Hövell, N.A.J.M. Sommerdijk, and R.J.M Nolte, Poly(3,4-ethylenedioxythiophene)-based glucose biosensors, *Adv. Mater.*, **13**(20), 1555–1557 (2001).
[45] C.Y. Peng, W.J. Nam, S.J. Fonash, B. Gu, A. Sen, K. Strawhecker, S. Natarajan, H.C. Foley, and S.H. Kim, Formation of nanostructured polymer filaments in nanochannels, *J. Am. Chem. Soc.*, **125**(31), 9298–9299 (2003).
[46] A. Eftekhari, M. Harati, and M. Pazouki, Electrochemical synthesis of polypyrrole macro-tubes on aluminum substrate, *Synth. Met.*, **156**(9–10), 643–647 (2006).
[47] C.R. Martin, Membrane-based synthesis of nanomaterials, *Chem. Mater.*, **8**(8), 1739–1746 (1996).
[48] J.C. Hulteen and C.R. Martin, A general template-based method for the preparation of nanomaterials, *J. Mater. Chem.*, **7**(7), 1075–1087 (1997).
[49] C.R. Martin, M. Nishizawa, K. Jirage, and M. Kang, Investigations of the transport properties of gold nanotubule membranes, *J. Phys. Chem. B*, **105**(10), 1925–1934 (2001).
[50] R.V. Parthasarathy and C.R. Martin, Synthesis of polymeric microcapsule arrays and their use for enzyme immobilization, *Nature*, **369**(6478), 298–301 (1994).
[51] R.V. Parthasarathy and C.R. Martin, Enzyme and chemical encapsulation in polymeric microcapsules, *J. Appl. Polym. Sci.*, **62**(6), 875–886 (1996).
[52] L.M. Moretto, P. Ugo, M. Zanata, P. Guerriero, and C.R. Martin, Nitrate biosensor based on the ultrathin-film composite membrane concept, *Anal. Chem.*, **70**(10), 2163–2166 (1998).
[53] J. Park, J. Kim, and Y. Son, Conducting polymer micro-tubules hosting electroactive species without guest modification, *Synth. Met.*, **156**(9–10), 714–720 (2006).
[54] R. Gasparac, P. Kohli, M.O. Mota, L. Trofin and C.R. Martin, Template synthesis of nano test tubes, *Nano Lett.*, **4**(3), 513–516 (2004).
[55] H. Hillebrenner, F. Buyukserin, M. Kang, M.O. Mota, J.D. Stewart, and C.R. Martin, Corking nano test tubes by chemical self-assembly, *J. Am. Chem. Soc.*, **128**(13), 4236–4237 (2006).
[56] E. Smela, O. Inganas, and I. Lundstrom, Controlled folding of micrometer-size structures, *Science*, **268**(5218), 1735–1738 (1995).
[57] E. Smela, A microfabricated movable electrochromic 'pixel' based on polypyrrole, *Adv. Mater.*, **11**(16), 1343–1345 (1999).
[58] B.L. Groenendaal, F. Jonas, D. freitag, H. Pielartzik, and J.R. Reynolds, Poly(3,4-ethylenedioxythiophene) and its derivatives: Past, present, and future, *Adv. Mater.*, **12**(7), 481–494 (2000).
[59] E. Smela, Conjugated polymer actuators for biomedical applications, *Adv. Mater.*, **15**(6), 481–494 (2003).
[60] G.G. Wallace, M.R. Gandhi, P. Murray, G.M. Spinks, Mechanism of electromechanical actuation in polypyrrole, *Synth. Met.*, **73**(3), 247–256 (1995).
[61] Q.B. Pei and O. Inganas, Conjugated polymers and the bending cantilever method – electrical muscles and smart devices, *Adv. Mater.*, **4**(4), 277–278 (1992).
[62] T.F. Otero and M.T. Cortes, Artificial muscles with tactile sensitivity, *Adv. Mater.*, **15**(4), 279–282 (2003).
[63] S.B. Adeloju, S.J. Shaw, and G.G. Wallace, Pulsed-amperometric detection of urea in blood samples on a conducting polypyrrole-urease biosensor, *Anal. Chim. Acta*, **341**(2–3), 155–160 (1997).
[64] J.M. Pernaut and J.R. Reynolds, Use of conducting electroactive polymers for drug delivery and sensing of bioactive molecules: A redox chemistry approach, *J. Phys. Chem. B*, **104**(17), 4080–4090 (2000).
[65] C.S. Reinhard, M.L. Radomsky, W.M. Saltzman, J. Hilton, H. Brem, Polymeric controlled release of dexamethasone in normal rat-brain, *J. Contr. Rel.*, **16**(3), 331–340 (1991).
[66] D.H. Kim, M. Abidian, and D.C. Martin, Conducting polymers grown in hydrogel scaffolds coated on neural prosthetic devices, *J. Biomed. Mater. Res. A*, **71A**(4), 577–585 (2004).
[67] J.Y. Yang and D.C. Martin, Microporous conducting polymers on neural microelectrode arrays – I – Electrochemical deposition, *Sens. Actuat. B Chem.*, **101**(1–2), 133–142 (2004).

[68] X.Y. Cui, J.F. Hetke, J.A. Wiler, D.J. Anderson, and D.C. Martin, Electrochemical deposition and characterization of conducting polymer polypyrrole/PSS on multichannel neural probes, *Sens. Actuat. A Phys.*, **93**(1), 8–18 (2001).
[69] M.R. Abidian, D.H. Kim, and D.C. Martin, Conducting-polymer nanotubes for controlled drug release, *Adv. Mater.*, **18**(4), 405–409 (2006).
[70] D.R. Kipke, R.J. Vetter, J.C. Williams, and J.F. Hetke, Silicon-substrate intracortical microelectrode arrays for long-term recording of neuronal spike activity in cerebral cortex. In *2nd International Meeting on the Brain-Computer Interfaces for Communication and Control.* Rensselaerville, Institute of Electrical and Electronics Engineers Inc., New York, 2002.
[71] M. Vallet-Regi, F. Balas, and D. Arcos, Mesoporous materials for drug delivery, *Angew. Chem. Int. Ed.*, **46**(40), 7548–7558 (2007).
[72] X.L. Luo and X.T. Cui, Electrochemically controlled release based on nanoporous conducting polymers, *Electrochem. Commun.*, **11**(2), 402–404 (2009).
[73] Y. Cho, A mesoporous silica nanosphere-based drug delivery system using an electrically conducting polymer, *Nanotechnology*, **20**(27) (2009).
[74] L. Brannon-Peppas and J.O. Blanchette, Nanoparticle and targeted systems for cancer therapy, *Adv. Drug Del. Rev.*, **56**(11), 1649–1659 (2004).
[75] D.F. Emerich and C.G. Thanos, The pinpoint promise of nanoparticle-based drug delivery and molecular diagnosis, *Biomol. Eng.*, **23**(4), 171–184 (2006).
[76] M.N. Rhyner, A.M. Smith, X. Gao, H. mao, L. Yang and S. Nie, Quantum dots and multifunctional nanoparticles: new contrast agents for tumor imaging, *Nanomedicine*, **1**(2), 209–217 (2006).
[77] S. Jin and K.M. Ye, Nanoparticle-mediated drug delivery and gene therapy, *Biotechnology Prog.*, **23**(1), 32–41 (2007).
[78] Y.Y. Liu, H. Miyoshi, and M. Nakamura, Nanomedicine for drug delivery and imaging: A promising avenue for cancer therapy and diagnosis using targeted functional nanoparticles, *Int. J. Cancer*, **120**(12), 2527–2537 (2007).
[79] L.T. Qu, and G.Q. Shi, Electrochemical synthesis of novel polypyrrole microstructures, *Chem. Commun.*, 206–207 (2003).
[80] L.T. Qu, G. Shi, F. Chen and J. Zhang, Electrochemical growth of polypyrrole microcontainers, *Macromolecules*, **36**(4), 1063–1067 (2003).
[81] J.Y. Yuan, D. Zhang, L. Qu, G. Shi, and X. Hong, Direct electrochemical generation of conducting polymer microcontainers on silicon substrate, *Polym. Int.*, **53**(12), 2125–2129 (2004).
[82] J.Y. Yuan, L. Qu, D. Zhang, and G. Shi, Linear arrangements of polypyrrole microcontainers, *Chem. Commun.*, 994–995 (2004).
[83] J.Y. Huang, B. Quan, M. Liu, Z. Wei and L. Jiang, Conducting polypyrrole conical nanocontainers: Formation mechanism and voltage switchable property, *Macromol. Rapid Commun.*, **29**(15) 1335–1340 (2008).
[84] E. Smela, O. Inganäa, Q Pei, and I Lundström, Electrochemical muscles-micromachining fingers and corkscrews, *Adv. Mater.*, **5**(9), 630–632 (1993).
[85] A. DellaSanta, D. DeRossi, and A. Mazzoldi, Characterization and modelling of a conducting polymer muscle-like linear actuator, *Smart Mater. Struct.*, **6**(1), 23–34 (1997).
[86] E.W.H. Jager, E. Smela, O. Inganäs and I Lundström, Applications of polypyrrole microactuators. In *Smart Structures and Materials 1999 Conference.* International Socirty of Optical Engineering, Newport Beach, CA, 1999.
[87] E.W.H. Jager, E. Smela, and O. Inganäs, On-chip microelectrodes for electrochemistry with moveable PPy bilayer actuators as working electrodes, *Sens. Actuat. B Chem.*, **56**(1–2), 73–78 (1999).
[88] E.W.H. Jager, E. Smela, and O. Inganäs, Microfabricating conjugated polymer actuators, *Science*, **290**(5496), 1540–1545 (2000).
[89] E.W.H. Jager, O. Inganäs, and I. Lundström, Microrobots for micrometer-size objects in aqueous media: Potential tools for single-cell manipulation, *Science*, **288**(5475), 2335–2338 (2000).
[90] T.G. Leong, B.R. Benson, E.K. Call and D.H. Gracias, Thin film stress driven self-folding of microstructured containers, *Small*, **4**(10), 1605–1609 (2008).

[91] T.G. Leong, C.L. Randall, B.R. Benson, A.M. Zarafshar, D.H. Gracias, Self-loading lithographically structured microcontainers: 3D patterned, mobile microwells, *Lab on a Chip*, **8**(10), 1621–1624 (2008).
[92] C.R. Martin, Nanomaterials – A membrane-based synthetic approach, *Science*, **266**(5193), 1961–1966 (1994).
[93] R. Gangopadhyay and A. De, Conducting polymer nanocomposites: A brief overview, *Chem. Mater.*, **12**(3), 608–622 (2000).
[94] Z.X. Wei, Self-assembling sub-micrometer-sized tube junctions and dendrites of conducting polymers, *Adv. Mater.*, **15**(16), 1382–1385 (2003).
[95] A. Eftekhari, Enhanced stability and conductivity of polypyrrole film prepared electrochemically in the presence of centrifugal forces, *Synth. Met.*, **142**(1–3), 305–308 (2004).
[96] J.X. Huang and R.B. Kaner, A general chemical route to polyaniline nanofibers, *J. Am. Chem. Soc.*, **126**(3), 851–855 (2004).
[97] D.M. Cheng, X. Zhou, H. Xia, and H.S.O. Chan, Novel method for the preparation of polymeric hollow nanospheres containing silver cores with different sizes, *Chem. Mater.*, **17**(14), 3578–3581 (2005).
[98] A. Eftekhari, Synthesis of nanostructured large particles of polyaniline, *J. Appl. Polym. Sci.*, **102**(6), 6060–6063 (2006).
[99] A. Eftekhari and I. Ahmadi, Electrodeposition of smooth and adherent film of polypyrrole on lead electrode, *Progr. Org. Coatings*, **57**(4), 371–375 (2006).
[100] A. Eftekhari and P. Jafarkhani, Polymerization of aniline through simultaneous chemical and electrochemical routes, *Polym. J.*, **38**(7), 651–658 (2006).
[101] A. Eftekhari, M. Kazemzad, and M. Keyanpour-Rad, Electropolymerization of aniline on plastically deformed Pd surface: Structure at micro- and nano-scale, *Polym. J.*, **38**(4), 329–334 (2006).
[102] C.R. Martin, Template synthesis of electronically conductive polymer nanostructures, *Acc. Chem. Res.*, **28**(2), 61–68 (1995).
[103] C.R. Martin and R.V. Parthasarathy, Polymeric microcapsule arrays, *Adv. Mater.*, **7**(5), 487–488 (1995).
[104] N. Kohut-Svelko, S. Reynaud, R. Dedryvère, H. Martinez, D. Gonbeau, and J. François Study of a nanocomposite based on a conducting polymer: Polyaniline, *Langmuir*, **21**(4), 1575–1583 (2005).
[105] C.F. Liu, T. Maruyama, and T. Yamamoto, Conductive blends of pi-conjugated polymers and thermoplastic polymers in latex form, *Polym. J.*, **25**(4), 363–372 (1993).
[106] T. Lei and K. Aoki, Monodispersed redox submicrometer particles created by polyaniline-coated polystyrene latex, *J. Electroanal. Chem.*, **482**(2), 149–155 (2000).
[107] L.Y. Wang, Y.J. Lin, and W.Y. Chiu. Synthesis and properties of monodisperse conductive core-shell latexes. In *16th International Conference on Science and Technology of Synthetic Metals (ICSM 2000).* Elsevier Science, Gastein, Austria, 2000.
[108] C. Barthet, S.P. Armes, M.M. Chehimi, C. Bilem, and M. Omastova, Surface characterization of polyaniline-coated polystyrene latexes, *Langmuir*, **14**(18), 5032–5038 (1998).
[109] S.F. Lascelles and S.P. Armes, Sythesis and characterization of micrometer-sized polypyrrole-coated polystyrene latexes, *Adv. Mater.*, **7**(10), 864 (1995).
[110] S.F. Lascelles and S.P. Armes, Synthesis and characterization of micrometre-sized, polypyrrole-coated polystyrene latexes, *J. Mater. Chem.*, **7**(8), 1339–1347 (1997).
[111] S.F. Lascelles, S.P. Armes, P.A. Zhdan, S.J. Greaves, A.M. brown, J.F. Watts, S.R. Leadley, and S.Y. Luk, Surface characterization of micrometre-sized, polypyrrole-coated polystyrene latexes: verification of a 'core-shell' morphology, *J. Mater. Chem.*, **7**(8), 1349–1355 (1997).
[112] D.B. Cairns, S.P. Armes, and L.G.B. Bremer, Synthesis and characterization of submicrometer-sized polypyrrole-polystyrene composite particles, *Langmuir*, **15**(23), 8052–8058 (1999).
[113] D.B. Cairns, S.P Armes, M.M. Chehimi, C. Perruchot, and M. Delamar, X-ray photoelectron spectroscopy characterization of submicrometer-sized polypyrrole – Polystyrene composites, *Langmuir*, **15**(23), 8059–8066 (1999).
[114] Y. Deslandes, D.F. Mitchell, and A.J. Paine, X-ray photoelectron-spectroscopy and static time-of-flight secondary-ion mass-spectrometry study of dispersion polymerized polystyrene latexes, *Langmuir*, **9**(6), 1468–1472 (1993).

[115] Q. Wu, Z.Q. Wang, and G. Xue, Controlling the structure and morphology of monodisperse polystyrene/polyaniline composite particles, *Adv. Funct. Mater.*, **17**(11), 1784–1789 (2007).
[116] J.S. Jang, J. Ja, and B. Lim, Synthesis and characterization of monodisperse silica-polyaniline core-shell nanoparticles, *Chem. Commun.*, 1622–1624 (2006).
[117] Z.W. Niu, Z. Yang, Z. Hu, Y. Lu, and C.C. Han, Polyaniline-silica composite conductive capsules and hollow spheres, *Adv. Funct. Mater.*, **13**(12), 949–954 (2003).
[118] M.K. Park, K. Onishi, J. Locklin, F. Caruse, and R.C. Advincula, Self-assembly and characterization of polyaniline and sulfonated polystyrene multilayer-coated colloidal particles and hollow shells, *Langmuir*, **19**(20), 8550–8554 (2003).
[119] C.L. Zhu, SS.W. Chou, S.F. He, W.N. Liao, and C.C. Chen, Synthesis of core/shell metal oxide/polyaniline nanocomposites and hollow polyaniline capsules, *Nanotechnology*, **18**(27), 275604 (2007).
[120] A. Riede, M. Helmstedt, V. Riede, and J. Stejskal, Polyaniline dispersions .7. Dynamic light scattering study of particle formation, *Coll. Polym. Sci.*, **275**(9), 814–820 (1997).
[121] Z.M. Zhang, J. Sui, L. ZXhang, M. Wan, Y. Wei, and L. Yu, Synthesis of polyaniline with a hollow, octahedral morphology by using a cuprous oxide template, *Adv. Mater.*, **17**(23), 2854–2857 (2005).
[122] X.T. Zhang, J. Zhang, W. Song, and Z. Liu, Controllable synthesis of conducting polypyrrole nanostructures, *J. Phys. Chem. B*, **110**(3), 1158–1165 (2006).
[123] J.N. Israelachvili, D.J. Mitchell, and B.W. Ninham, Theory of self-assembly of hydrocarbon amphiphilies into micelles and bilayers, *J. Chem. Soc. Faraday Trans. 2*, **72**, 1525–1568 (1976).
[124] O.D. Velev and E.W. Kaler, Structured porous materials via colloidal crystal templating: From inorganic oxides to metals, *Adv. Mater.*, **12**(7), 531–534 (2000).
[125] O.D. Velev, A.M. Lenhoff, and E.W. Kaler, A class of microstructured particles through colloidal crystallization, *Science*, **287**(5461), 2240–2243 (2000).
[126] S.A. Johnson, P.J. Ollivier, and T.E. Mallouk, Ordered mesoporous polymers of tunable pore size from colloidal silica templates, *Science*, **283**(5404), 963–965 (1999).
[127] S.H. Park and Y.N. Xia, Fabrication of three-dimensional macroporous membranes with assemblies of microspheres as templates, *Chem. Mater.*, **10**(7), 1745–1747 (1998).
[128] J.F. Bertone, P. Jiang, K.S. Hwang, D.M. Mittleman, and V.L. Colvin, Thickness dependence of the optical properties of ordered silica-air and air-polymer photonic crystals, *Phys. Rev. Lett.*, **83**(2), 300–303 (1999).
[129] T. Sumida, Y. Wada, T. Kitamura, and S. Yaagida, Electrochemical preparation of macroporous polypyrrole films with regular arrays of interconnected spherical voids, *Chem. Commun.*, 1613–1614 (2000).
[130] T. Cassagneau and F. Caruso, Semiconducting polymer inverse opals prepared by electropolymerization, *Adv. Mater.*, **14**(1), 34–38 (2002).
[131] P.N. Bartlett, P.R. Birkin, and M.A. Ghanem, Electrochemical deposition of macroporous platinum, palladium and cobalt films using polystyrene latex sphere templates, *Chem. Commun.*, 1671–1672 (2000).
[132] S.B. Han, A.L. Briseno, X. Shi, D.A. Mah, F. Zhou, Polyelectrolyte-coated nanosphere lithographic patterning of surfaces: Fabrication and characterization of electropolymerized thin polyaniline honeycomb films, *J. Phys. Chem. B*, **106**(25), 6465–6472 (2002).
[133] T.R. Jensen, G.C. Schatz, and R.P. Van Duyne, Nanosphere lithography: Surface plasmon resonance spectrum of a periodic array of silver nanoparticles by ultraviolet-visible extinction spectroscopy and electrodynamic modeling, *J. Phys. Chem. B*, **103**(13), 2394–2401 (1999).
[134] T.R. Jensen, M.D. Malinsky, C.L. Hayes and R.P. Van Duyne, Nanosphere lithography: Tunable localized surface plasmon resonance spectra of silver nanoparticles, *J. Phys. Chem. B*, **104**(45), 10549–10556 (2000).
[135] J.C. Hulteen and R.P. Vanduyne, Nanosphere lithography – a meterials genral fabrication process for periodic particle array surfaces, *J. Vac. Sci. Tech. A Vac. Surf. Films*, **13**(3), 1553–1558 (1995).
[136] J.C. Hulteen, D.A. Treichel, M.T. Smith, M.L. Duval, T.R. Jensen, and R.P Van Duyne, Nanosphere lithography: Size-tunable silver nanoparticle and surface cluster arrays, *J. Phys. Chem. B*, **103**(19), 3854–3863 (1999).

[137] C.L. Haynes, Ad. McFarland, M.T. Smith, J.C. Hulteen, and R.P. Van Duyne, Angle-resolved nanosphere lithography: Manipulation of nanoparticle size, shape, and interparticle spacing, *J. Phys. Chem. B*, **106**(8), 1898–1902 (2002).
[138] G.G. Wallace, G.M. Spinks, L.A.P. Kane-Maguire, and P.R. Teasdale, *Conductive Electroactive Polymers: Intelligent Materials Systems*, 2nd Edn., CRC Press LLC, Boca Raton, 2003.
[139] J. Jang, J.H. Oh, and X.L. Li, A novel synthesis of nanocapsules using identical polymer core/shell nanospheres, *J. Mater. Chem.*, **14**(19), 2872–2880 (2004).
[140] S. Geetha, C.R.K. Rao, M. Vijayan, and D.C. Trivedi, Biosensing and drug delivery by polypyrrole, *Anal. Chim. Acta*, **568**(1–2), 119–125 (2006).
[141] M. Pyo, Controlled-release of biological molecules from conducting polymer-modified electrodes – the potential-dependent release of adenosine 5′-triphosphate from poly(pyrrole adenosine 5′-triphosphate) films, *J. Electroanal. Chem.*, **368**(1–2), 329–332 (1994).
[142] M. Hepel and F. Mahdavi, Application of the electrochemical quartz crystal microbalance for electrochemically controlled binding and release of chlorpromazine from conductive polymer matrix, *Microchem. J.*, **56**(1), 54–64 (1997).
[143] K. Kontturi, L. Murtomaki, P. Pentti, and G. Sundholm, Preparation and properties of a pyrrole-based ion-gate membrane as studied by the EQCM, *Synth. Met.*, **92**(2), 179–185 (1998).
[144] M. Iseki, Effect of cations on the electrochemical-behavior of p-toluenesulfonate-doped polypyrrole in various aqueous-solutions, *J. Electroanal. Chem.*, **358**(1–2), 221–233 (1993).

12

Magnetic and Electron Transport Behaviors of Conductive-Polymer Nanocomposites

Zhanhu Guo[1], Suying Wei[2], David Cocke[1], and Di Zhang[1]

[1] Integrated Composites Laboratory (ICL), Dan F. Smith Department of Chemical Engineering, Lamar University, Beaumont, Texas, USA

[2] Department of Chemistry and Physics, Lamar University, Beaumont, USA

12.1 Introduction

Conductive conjugated polymers belonging to polyenes or polyaromatics, such as polyacetylene, polyaniline (PANI), polypyrrole (PPy), polythiophene, poly(*p*-phenylene), and poly(phenylene vinylene) classes, have been investigated extensively [1–3]. PANI and PPy families of conjugated polymers are of much interest due to their low cost, easy synthesis, unique conduction mechanism, good stability and environmentally benign performance [4,5].

The conductivity of a conductive polymer is strongly dependent on the doping agent (dopant) with electron donor or acceptor ability. The doping process can even transform an intrinsically insulating conjugated polymer to a near-metallic conductor [6,7]. Conductive-polymer thin films doped with different species have been reported to serve as polymeric rechargeable batteries for energy-storage purposes [8], electrode materials used in electrochemical supercapacitors [9,10], metal-corrosion protection coating materials [11,12], matrices for structural composite materials [13], electromagnetic

Nanostructured Conductive Polymers Edited by Ali Eftekhari

interference (EMI) shielding, electro-chemomechanical devices [14], and sensors for pH [15], gas, and humidity testing [16,17].

Composites are engineered materials made from two or more constituent materials with significantly different physical or chemical properties which remain separate and distinct on a macroscopic level within the finished structure. Nanocomposites can be defined [18] as multiphase solid materials, in which at least one of the phases has a dimension of less than 100 nanometers (nm). In other words, the structures have nanometer-scale dimensional repeat distances between the different phases that make up the unity. In the broadest sense this definition can include colloids, porous (mesoporous) media, gels, and copolymers, but is more usually taken to mean the solid combination of nanodimensional phases differing in properties due to dissimilarities in structure and chemistry. The properties of the nanocomposites are different from the bulk composites.

From the mechanical point of view, nanocomposites differ from conventional composite materials due to the exceptionally high specific surface area (surface-to-volume ratio) of the reinforcing phase. The reinforcing nanosized material can have a range of shapes and morphologies, such as nanoparticles, nanotubes, nanoflakes, and long and short nanodiameter fibers. These are exemplified by oxide nanoparticles, carbon nanotubes, exfoliated clay particles, short carbon fibers, and long electrospun fibers, respectively. The area of the interface between the matrix and reinforcement phases is typically an order of magnitude greater than that in conventional composites. The matrix material is significantly affected by proximity to the reinforcement. This large reinforcement surface area means that the effect of a relatively small amount of nanoscale fillers can have an observable effect on the macroscale properties of the composites. For example, adding carbon nanotubes improves the electrical and thermal conductivity. Other kinds of nanoparticles may result in enhanced optical, electronic, dielectric properties, or mechanical properties, such as stiffness and strength. In general, the nanofillers are dispersed into the matrix during processing. The percentage (weight/mass fraction) of the nanoparticles introduced can remain very low (on the order of 0.5% to 5%) due to the low filler percolation threshold, especially for the most commonly used nonspherical, high aspect-ratio fillers (such as thin nanoplatelets, nanoflakes, or carbon nanotubes).

Polymer-based nanocomposites reinforced with nanoparticles (NPs) have attracted much interest due to their homogeneity, relatively easy processability, and tunable physicochemical properties, such as mechanical, magnetic, electric, thermoelectric, and electronic properties [2,19–36]. High particle loading is required for certain industrial applications, such as electromagnetic-wave absorbers [37,38], photovoltaic cells (solar cells) [39,40], photo detectors, and smart structures [41–43]. A nanoparticle core with a polymer shell renders many industrial applications possible, such as nanofluids and magnetic resonance imaging (MRI).

Magnetic nanoparticles, due to their unique magnetic and electronic properties, are used in various applications, such as biomedical drug delivery, specific site targeting, magnetic data storage, and sensors [43–47]. The magnetic nanoparticles include metals such as iron, cobalt, nickel, and their alloys among them or with others (such as FePt), oxides (γ-Fe_2O_3 [48–51], Fe_3O_4 [5,52,53], cobalt oxide [54]), iron cobalt oxide ferrite [55], manganese-zinc ferrite ($Mn_{0.68}Zn_{0.25}Fe_{2.07}O_3$) [56], and barium ferrite ($BaFe_{12}O_{19}$) [57]. Compared with the metallic magnetic materials, ferrite materials can have higher resistivity and still have larger saturation magnetization, which allows them to obtain a good

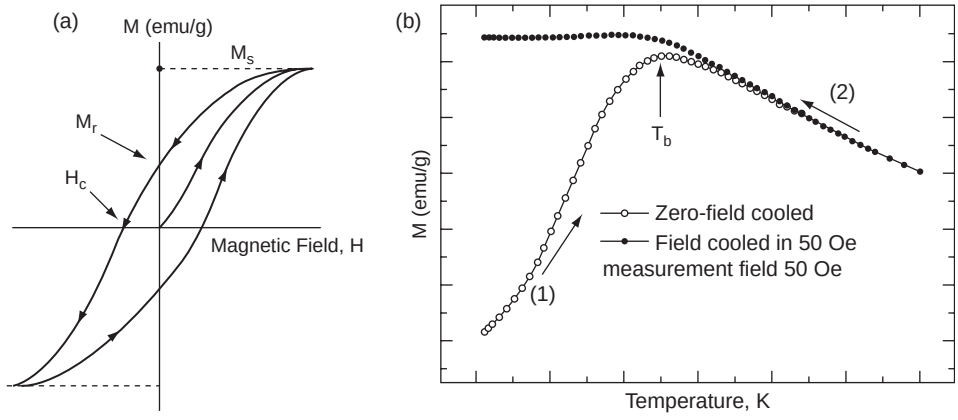

Figure 12.1 *Schematic of the magnetic properties: (a) hysteresis loop and (b) ZFC and FC temperature-dependent magnetization curves*

frequency-permeability responses for high frequency applications [55,58]. By combining in a single material the electrical conductivity of the polymer and the magnetic properties of the nanoparticles, magnetopolymeric materials can be built and have many potential applications [55]. The insulating properties of the ferrites have the advantage of reducing the eddy current losses and some of the soft ferrites have been extensively investigated for RF applications such as AC/DC converters, wide-band transformers, antennas, and electromagnetic interference (EMI) shielding.

There are four important physical parameters, as shown in Figure 12.1, used to describe the magnetic properties of a nanomaterial, i.e., saturation magnetization (M_s, emu g^{-1}), remanent magnetization (M_r, emu g^{-1}, a material's ability to retain a certain amount of residual magnetic field when the magnetizing force is removed after achieving saturation), coercivity (coercive force, H_c, Oe, the amount of reverse magnetic field which must be applied to a magnetic material to make the magnetization return to zero), and blocking temperature (T_b, K, characteristic of the transition temperature between the superparamagnetic state and the ferromagnetic state).

According to the magnetic properties, materials can be classified into soft and hard categories. Materials, with coercivity (coercive force) larger than 200 Oe, are called hard materials and smaller than 200 Oe are called soft materials. In the soft materials, a unique category is called superparamagnetic materials. Superparamagnetic material consists of small ferromagnetic clusters (e.g. crystallites), but where the clusters are so small that they can randomly flip direction under thermal fluctuations. As a result, the material as a whole is not magnetized (coercivity and remanent magnetization equal to zero) except in an externally applied magnetic field (in that respect, it is like paramagnetism).

Successful incorporation of magnetic nanoparticles into a conductive polymer matrix will definitely widen their applicability in the fields of electronics, biomedical drug delivery, and optics. These doubly functionalized nanocomposites will exhibit the magnetic properties of the magnetic particles and the conducting properties of the conductive-polymer matrices. However, one of the challenges so far is the ability to integrate a high

fraction of nanoparticles into the polymer matrix in a strong acidic environment. The acidic environment, which is normally required for conductive-polymer synthesis, will etch away the nanoparticles in an aqueous solution. A balance between the polymerization requirement in an acidic solution and the prevention of dissolution of reactive iron oxide nanoparticles will be a determining factor for high-quality nanocomposite fabrication.

Polypyrrole nanocomposites with iron oxide and other nanoparticles have been prepared by several methods. For example, *in situ* chemical oxidative polymerization approach with either ultrasonication [59] or mechanical stirring [60] was reported. The nanocomposites showed particle-loading-dependent magnetic properties and electric conductivity. In addition, a supercritical fluid approach, implemented because of green chemistry, was also reported to be used as a medium in *in situ* chemical oxidative polymerization for the fabrication of conductive-polymer magnetic nanocomposites [61].

The stirring method (ultrasonication or mechanical stirring) is believed to have a significant effect on the formed nanocomposites and the subsequent physicochemical properties. However, there are few papers reported in the literature. In this chapter, the synthetic methods for making magnetic conductive-polymer nanocomposites are summarized. The effect of nanoparticle addition on the morphology of the polymer matrix, the magnetic properties, and the electrical conductivity of the resulting nanocomposite are addressed. The conductive mechanisms within the magnetic conducting-polymer nanocomposites are also discussed.

12.2 Magnetic Polymer Nanocomposite Preparation

Several methods have been reported for the preparation of magnetic-nanoparticle-reinforced conductive-polymer nanocomposites, including the oxidation in solution method, the electrochemical method, sequential deposition approaches, the irradiation method, etc.

12.2.1 Solution-Based Oxidation Method

Polypyrrole nanocomposites filled with γ-Fe_2O_3 nanoparticles were fabricated by the oxidation method in aqueous solution [49]. A dispersion of γ-Fe_2O_3 nanoparticles (5–25 nm) was made by adding the desired amount of γ-Fe_2O_3 in 20 ml deionized water under sonication. *p*-Toluenesulfonic acid ($CH_3C_6H_4SO_3H$, *p*-TSA, 6.0 mmol) and pyrrole (7.3 mmol, Aldrich) were added to the above suspended nanoparticle solution under sonication. Ammonium persulfate (APS, oxidant, 3.6 mmol) was rapidly mixed into the above solution at room temperature, and the resulting solution was kept under sonication for one hour. In addition, the effect of reaction time was investigated by using a seven-hour sonication, as used previously in the study of micron-size iron oxide particles [60]. Both mechanical stirring and ultrasonic stirring were used to produce nanocomposites. All the products were washed thoroughly with deionized water (to remove the unreacted APS and *p*-TSA) and methanol (to remove oligomers). The precipitated powder was dried at 50 °C. A similar solution-based oxidation method has been used to prepare polyaniline-barium ferrite nanocomposites [57].

A microemulsion polymerization method [62,63] was also reported to produce magnetic polypyrrole nanocomposites filled with γ-Fe_2O_3. The nanoparticles were dispersed in the oil phase. $FeCl_3$ was used as an oxidizing agent. Sodium dodecylbenzenesulfonic acid (SDBA) and butanol were used as the surfactant and cosurfactant, respectively. $FeCl_3$ (0.97 g) was dissolved in a mixture of 15 mol deionized water, SDBA (6 g), and butanol (1.6 ml). A specific amount of γ-Fe_2O_3 suspended nanoparticle solution was added to the above solution for dispersion. Pyrrole was added for nanocomposite polymer fabrication in the microemulsion system. The polymerization was continued for 24 hours and quenched by acetone.

12.2.2 Electropolymerization Method

Compared to an inorganic substrate, a conductive polymer has the advantages of light weight, flexibility, and easy synthesis. The conductive polymer needs be very stable at a negative potential during electropolymerization in order to serve as an electrode. A PPy thin film doped with *m*-sulfobenzoic acid has high conductivity in the order of 100 S cm^{-1} in air, at relatively high temperatures, in a reductive agent and with negative potential, which provides the opportunity for electrodeposition applications [64]. The electrochemical synthetic approach has been used to produce a multilayered structure with a conductive polymer as the substrate [65]. Yan *et al.* used a heavily doped PPy film as a substrate for subsequent multilayered Co and Cu formation and observed magnetic-field-dependent electron-transport behavior [65]. Abe *et al.* [66,67] reported an Fe_3O_4 film formation by using electroplating (anodic oxidization) or electroless plating (air oxidation) in aqueous solution at low temperature ($T < 80\,°C$) and this approach promoted the formation of oxides on various substrates or in matrices. The nanoparticles used in the polypyrrole nanocomposite fabrication included γ-Fe_2O_3 [68] and Fe_3O_4 [69].

Jarjayes *et al.* have fabricated PPy-Fe_2O_3 nanocomposites in one single electrochemical step [68], rather than the two-step deposition process [70]. The anionic ferrofluid, a stable liquid solution containing magnetic nanocrystals coated with anionic chelating agents (surfactant), rendered the neccessary compatability between the nanoparticles and the polymer chains. The ferrofluid-containing PPy films were electrodeposited in a single compartment cell on an ITO anode (2×3 cm) by electrolysis at 0.7 V/SCE of a nonstirred aqueous solution of 0.5 mol l^{-1} pyrrole and ferrofluid (0.1 mol l^{-1} in Fe). The deposition charge is typically 5 C cm^{-2} for a current density of around 1 mA cm^{-2}. The films were purified by washing with deionized water and acetonitrile. The films were stripped from the electrode substrate after one night free standing and dried under vacuum at 60 °C for 12 hours.

Yan *et al.* [69] have further extended the electrodeposition method to prepare multilayered PPy and magnetite (Fe_3O_4). The conductive polymer layer was electropolymerized in a one-compartment three-electrode cell with a computer-controllable EG&G potentiostat Model M273. The electrolyte was 0.1 mol l^{-1} *p*-toluenesulfonate and 0.1 mol l^{-1} pyrrole aqueous solution. Stainless steel (4×2 cm), Pt sheet and Ag/AgCl (0.1 M KCl) electrodes were used as the working electrode, the counter-electrode and the reference electrode for the PPy film formation, respectively. A galvanostatic method (consisting of placing a constant current pulse upon an electrode and measuring the variation of the

resulting current through the solution; a way to measure the rate of an electrochemical reaction) was used for electrochemical polymerization of PPy in a current density of 1 mA cm^{-2} and the thickness of the deposited film was controlled by the passed electric charge during the electropolymerization thin-film growth. A working electrode covered with PPy film was washed thoroughly with distilled water and acetone, and used as the working electrode for magnetite (Fe_3O_4) film electrodeposition. The galvanostatic method was employed again with a current density of 0.5 mA cm^{-1}. The electrolyte contained 0.03 mol l^{-1} $FeSO_4$ with a pH value of 7 (adjusted with NaOH solution) at 75 °C. A sandwich structure with different alternating layers was obtained by repeating the above process. The maximum thickness of magnetite is about 0.2 μm. Zhang *et al.* [71] and Long *et al.* [72] reported nanostructures (nanorods and nanotubes) of PANI composites containing Fe_3O_4 nanoparticles synthesized by a self-assembly process in the presence of β-naphthalene sulfonic acid (NSA) as a dopant for the first time in 2003. Briefly, 0.2 ml of aniline monomer and a quantitative amount of Fe_3O_4 nanoparticles were mixed with NSA (0.26 g) dissolved in 10 ml of deionized water under supersonic stirring for 10 min to form an emulsion of an aniline/NSA complex containing Fe_3O_4 nanoparticles. An aqueous solution of $(NH_4)_2S_2O_8$ (APS, oxidant, 0.46 g in 5 ml deionized water) was then added to the above reaction mixture with supersonic stirring. The mixture was left overnight. The product was washed with deionized water, methanol, and ether, and then dried in vacuum for 24 h to obtain a green-black powder of PANI-NSA/ Fe_3O_4 nanocomposites. It was found that the conductivity and magnetic properties of the PANI-NSA/Fe_3O_4 nanostructures could be adjusted by changing the content of Fe_3O_4 NPs in the composites.

12.2.3 Two-Step Deposition Method

Forder *et al.* [70] have successfully prepared superparamagnetic conductive polyester textile composites (polypyrrole and magnetite on polyester textile fiber substrate) by a two-step deposition method, i.e., magnetite deposition and PPy deposition.

Preparation of magnetite-textile fiber composites is described as follows. The cleaned and dried polymer textile substrate (average fiber diameter 10–20 μm) was immersed in the magnetite dispersion for about half an hour and air-dried for several hours. The coated textile was further dried at 60 °C. The magnetite-impregnated textile was further used for conductive-polymer coating. The solution for immersion of the treated textile fibers was 1,5-napthalenedisulfonic acid (0.27 g), 5-sulfosalicylic acid (1.71 g), and $FeCl_3$ $6H_2O$ (1.82 g) in 150 ml deionized water. The magnetite-treated textile fibers (2.75 g) were immersed in the above solution and then pyrrole (0.20 cm^3) was added for the polymerization. The polymerization was quenched with excess deionized water and the product was washed and dried.

12.2.4 UV-Irradiation Technique

Poddar *et al.* [56] successfully extended the UV-irradiation technique [73] for PPy formation to composite fabrication. In this technique, silver nitrate (10–5 mol%) was added to the pyrrole monomer as the electron acceptor for pyrrole photopolymerization. A photoinitiator was used to increase the polymerization rate and uniformity. A cationic

photoinitiator (CYRACURE UV 16992 from DOW Inc.) was added to the pyrrole/salt solution at 0.3%. A specific amount of ferrite nanoparticles were dispersed in the above solution and spin-coated onto a glass substrate. The nanocomposite thin films were formed by overnight polymerization under UV light (365 nm) irradiation.

12.3 Physicochemical Property Characterization

A Fourier-transform infrared (FT-IR) spectrometer in transmission mode under dry nitrogen flow (10 cubic centimeters per minute, ccpm) was used to test the physicochemical interactions between PPy and Fe_2O_3 nanoparticles. The dried PPy powder was mixed with powdered KBr, ground and compressed into a pellet. Its spectrum was recorded as a reference for comparison with that of the Fe_2O_3/PPy nanocomposites.

The dispersion quality of the nanoparticles within the conductive polymer matrix, and the nanostructures of the polymer and nanocomposites were normally investigated by scanning electron microscopy (SEM). SEM specimens were prepared by spreading a thin layer of powder onto a double-sided carbon tape. The microstructure and crystallinity were investigated with a transmission electron microscope with an accelerating voltage of 100 keV. The samples were prepared by dispersing the powder in anhydrous ethanol, dropping some suspended solution onto a carbon-coated copper grid and drying naturally in ambient conditions.

The magnetic properties of the nanocomposite were measured in a 9 tesla physical properties measurement system (PPMS) by Quantum Design. Two different measurements were normally carried out. The temperature-dependent magnetization was investigated using zero-field-cooled (ZFC) and field-cooled (FC) conditions at an applied field (for example,100 Oe). ZFC was done by cooling the sample first to 5 K without a field, then magnetization changes were recorded with the temperature increasing from 5 to 300 K with an applied field of 100 Oe. FC was recorded immediately after ZFC by decreasing the temperature from 300 to 5 K with a constant field of 100 Oe. Field-dependent magnetization (hysteresis loop) was tested for certain temperatures.

The electrical conductivities were measured using a standard four-probe method to minimize the surface contact resistance.

12.4 Microstructure of the Conductive Polymer Nanocomposites

Figure 12.2 shows the SEM microstructures of pure PPy and Fe_2O_3/PPy nanocomposites synthsized by the conventional method, as used for micron-size iron oxide particle-filled PPy composite fabrication [60]. The conventional method is based on mechanical stirring. In contrast to the network structure of pure PPy, as shown in Figures 12.2(a) and (b), discrete spherical nanoparticles with uniform size distribution are observed in the nanocomposite counterparts fabricated by the conventional method, as shown in Figures 12.2(c) and (d). However, no attraction was observed when a permanent magnet was placed nearby, and further quantitative magnetic characterization did not show any sign of magnetization in the nanocomposites. The disappearance of the magnetic nanoparticles is

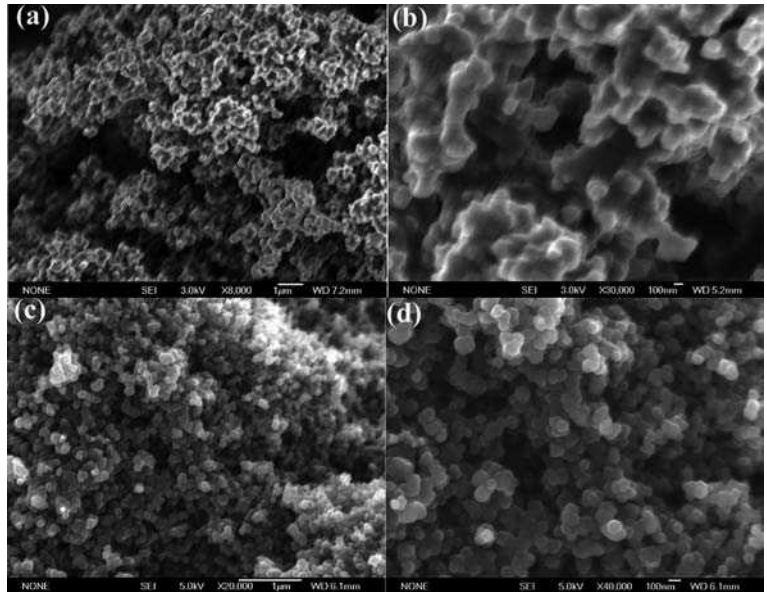

Figure 12.2 *(Reprinted with permission from Journal of Nanoparticle Research, Fabrication and Characterization of Iron Oxide Nanoparticles Reinforced Polypyrrole Nanocomposites, by Z. Guo, K. Shin, A. B. Karki et al., 11 (6) 1441–1452. Copyright (2009) Springer Science + Business Media")*

due to slow dissolution over time caused by the acidic solution used in the pyrrole polymerization. This observation also suggests the formation of a porous polypyrrole shell rather than a solid one that can protect the magnetic nanoparticles from dissolution.

For *in situ* formation of the conductive magnetic nanocomposite, a short reaction time (1 hour) was used to balance the PPy polymerization and the nanoparticle dissolution. Ultrasonic stirring was used rather than mechanical stirring to minimize contamination and achieve better particle dispersion. The red particles turned black after the polymerization, indicating the formation of PPy. Unlike the network structure observed in pure PPy, the SEM micrographs (shown in Figure 12.3) of nanocomposites with different initial particle loadings show discrete nanoparticles without any obvious agglomeration. In stark contrast to the obvious loss of magnetic particles when mechanical stirring was used for seven-hour polymerization, the dried nanocomposite powder in Figure 12.3 was attracted to a permanent magnet, indicating the presence of the magnetic nanoparticles.

12.5 Interaction between the Nanoparticles and the Conductive-Polymer Matrix

Figure 12.4 shows the FT-IR spectra of pure PPy and Fe_2O_3/PPy nanocomposites. The characteristic peaks of PPy are observed in all the samples, indicating the formation of

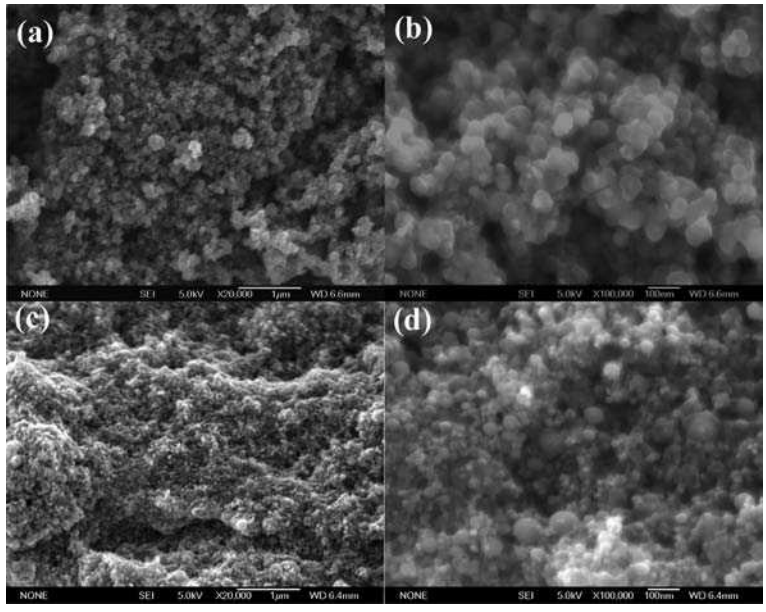

Figure 12.3 *(Reprinted with permission from Journal of Nanoparticle Research, Fabrication and Characterization of Iron Oxide Nanoparticles Reinforced PolypyrroleNanocomposites, by Z. Guo, K. Shin, A. B. Karki et al., 11 (6) 1441–1452. Copyright (2009) Springer Science + Business Media)*

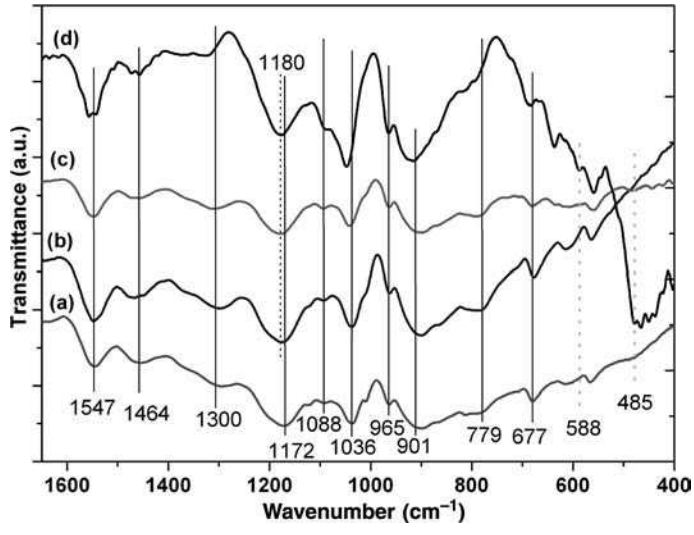

Figure 12.4 *(Reprinted with permission from Journal of Nanoparticle Research, Fabrication and Characterization of Iron Oxide Nanoparticles Reinforced Polypyrrole Nanocomposites, by Z. Guo, K. Shin, A. B. Karki et al., 11 (6) 1441–1452. Copyright (2009) Springer Science + Business Media)*

PPy. The peaks at 1547 and 1464 cm^{-1} can be assigned to C=C and C–N stretching vibrations, respectively. The peaks at 1164 and 901 cm^{-1} are due to the C–H in-plane bending and ring deformation, respectively. Similar patterns were also observed in PPy-Fe[OH] microcomposites [60]. The obvious spectral differences between pure PPy and the composites indicate that PPy exhibits a different chain structure, and there are physico-chemical interactions between the nanoparticles and PPy. The presence of iron oxide nanoparticles in the composite is strongly supported by the new peaks at 485 cm^{-1} and 588 cm^{-1} as shown in Figures 12.4c and d, which are due to the stretching vibrations of iron oxide [74]. This observation indicates that a magnetic nanocomposite can be synthesized with PPy if polymerization is achieved in a short period of time. Pprolonged polymerization is characterized by the disappearance of the characteristic IR peaks of iron oxide, Figure 12.4b. The small differences between the spectra of PPy and the nanocomposites with prolonged polymerization also indicates the loss of iron oxide nanoparticles.

The thermal stabilities of the pure PPy and Fe_2O_3/PPy nanocomposites were investigated by TGA measurements and the results are shown in Figure 12.5. Figure 12.5(a) shows the thermogravimetric profiles of nanocomposites with particle loadings of 0, 20, and 50 wt%, respectively. The black nanocomposites were observed to turn red upon test completion, characteristic of iron oxide rather than the black carbon, indicating complete loss of PPy. The weight loss at temperatures lower than 120 °C was due to loss of moisture, and the major loss at temperatures higher than 240 °C was due to the decomposition of PPy. The differences in the residues reflected the different amounts of iron oxide nanoparticles present. In addition, the nanocomposites showed better thermal stability than that of the pure PPy. The thermal stability increased slightly with increasing nanoparticle loading, which is believed to be due to the lower mobility of the polymer chains when the polymer chains are bound onto the nanoparticles with strong chemical interactions [75].

The only peak at 254.5 °C observed in the as-received nanoparticles, as shown in Figure 12.5(b), is due to the decomposition of the iron oxide-hydroxide (goethite, FeOOH as proved by the FT-IR spectra) [31,76]. Similar to the TGA observation, a higher decomposition temperature (308.0 °C) was observed in PPy formed with the aid of nanoparticles than that of pure PPy formed without them (298.4 °C). Whereas only one peak was observed in the pure PPy samples, two exothermic peaks were observed in the DTA curves of the nanocomposites. These were due to the decomposition of PPy at 307 °C and the possible phase transition of iron oxide at 480 °C, as reported for the Fe_2O_3/PPy nanocomposites fabricated by the simultaneous gelation and polymerization (sol-gel) method [77,78] respectively. As compared with no obvious phase transition in the pure iron oxide nanoparticles, the observed phase transition was due to the intermediate product of PPy [77,78].

12.6 Magnetic Properties of Conductive-Polymer Nanocomposites

Figure 12.6 shows the magnetic hysteresis loops of nanocomposites with an initial particle loading of 20 wt% and 50 wt%, respectively. There was no hysteresis observed in the sample formed from the seven-hour reaction due to the dissolution of the magnetic nanoparticles in the acidic solution. The saturation magnetizatiosn (M_s) were 29.4 emu g^{-1} and 45.1 emu g^{-1}

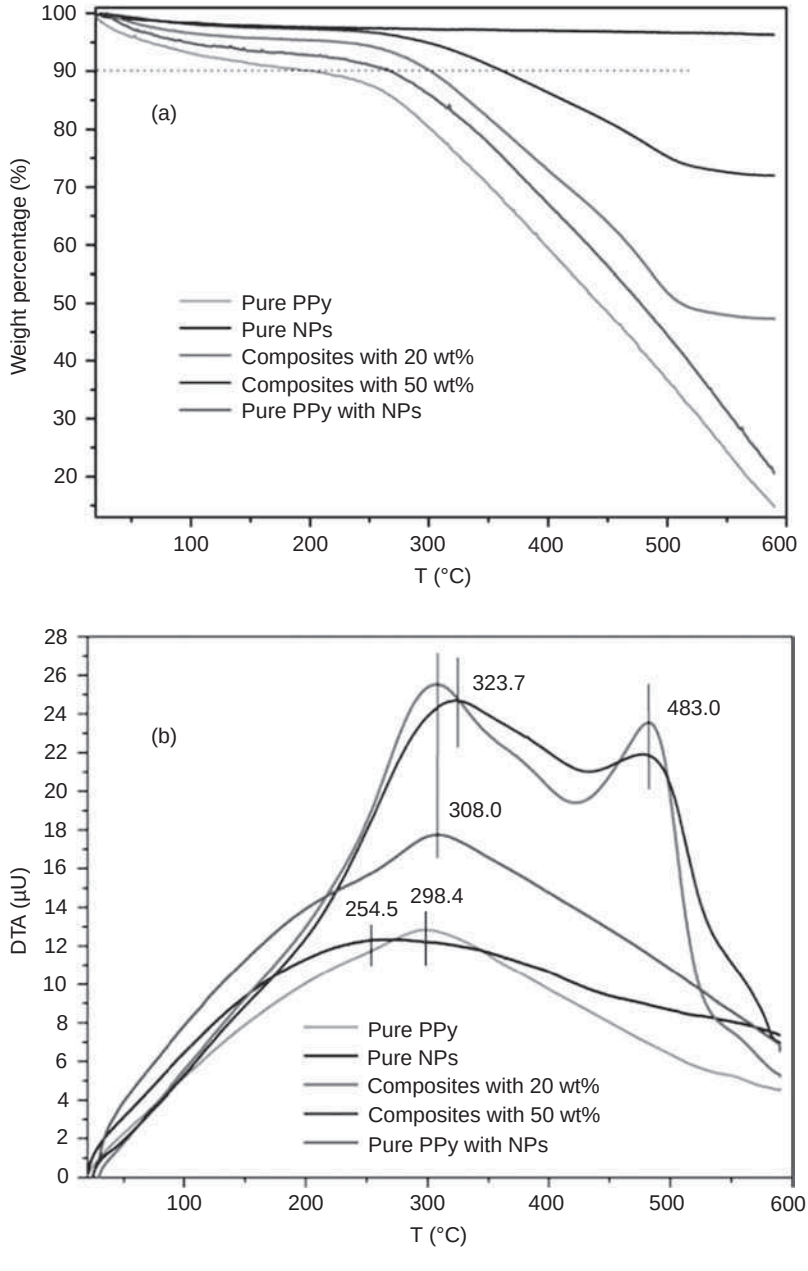

Figure 12.5 *(Reprinted with permission from Journal of Nanoparticle Research, Fabrication and Characterization of Iron Oxide Nanoparticles Reinforced Polypyrrole Nanocomposites, by Z. Guo, K. Shin, A. B. Karki et al., 11 (6) 1441–1452. Copyright (2009) Springer Science + Business Media (See colour Plate 9))*

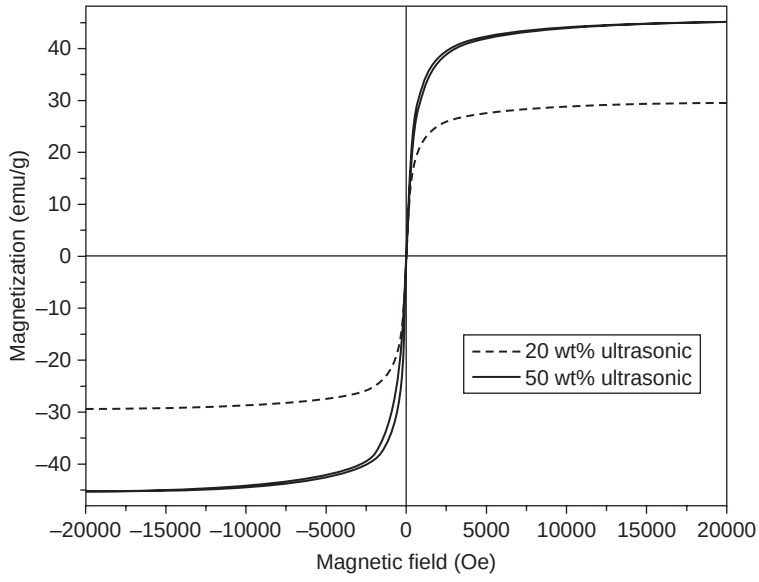

Figure 12.6 *(Reprinted with permission from Journal of Nanoparticle Research, Fabrication and Characterization of Iron Oxide Nanoparticles Reinforced Polypyrrole Nanocomposites, by Z. Guo, K. Shin, A. B. Karki et al., 11 (6) 1441–1452. Copyright (2009) Springer Science + Business Media)*

based on the total weight of the nanocomposites with initial loadings of 20 wt% and 50 wt%, respectively. The saturation magnetization of iron oxide was reported to be 74 emu g^{-1} and independent of the surface chemistry of the nanoparticles. Thus, the real nanoparticle loadings in nanocomposites with initial loadings of 20 wt% and 50 wt% were calculated to be 27 wt% and 68 wt%, respectively. The calculated particle loading based on the magnetic data is much higher than the initial particle loading considering the partial particle loss from dissolution during the nanocomposite fabrication. This indicates that the yield of PPy was lower. In other words, the pyrroles were partially polymerized into PPy, which led to the higher particle loading. In addition, the polymer yield was observed to be lower at the higher initial particle loading than that at the lower initial particle loading.

The effect of the stirring method, i.e., mechanical or ultrasonic stirring, was investigated by polymerizing for seven hours, as used with mechanical stirring. The final product exhibited a strong tendency to be attracted onto a permanent magnet, indicating the presence of iron oxide nanoparticles. Figure 12.7 shows the hysteresis loop of as-received nanoparticles and nanocomposite synthesized with ultrasonic stirring over seven hours and an initial particle loading of 50 wt%. The weight percentage of the iron oxide nanoparticles in the nanocomposite was estimated to be 20.2%, based on the saturation magnetizations of the nanocomposite and the as-received nanoparticles. This weight percentage is much lower than the initial particle loading and the composite sample formed with one hour of ultrasonic stirring. This indicated that more particles were lost due to dissolution with a longer reaction time between the nanoparticles and the protons. The coercivity was

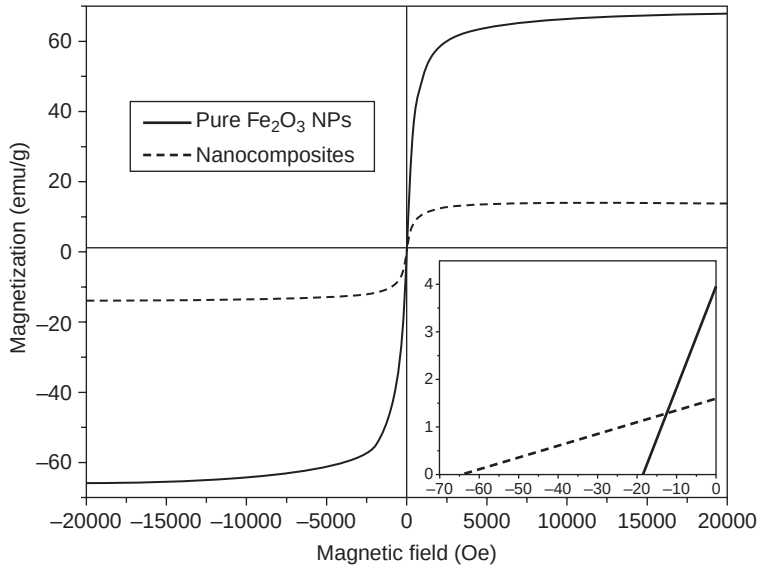

Figure 12.7 *(Reprinted with permission from Journal of Nanoparticle Research, Fabrication and Characterization of Iron Oxide Nanoparticles Reinforced Polypyrrole Nanocomposites, by Z. Guo, K. Shin, A. B. Karki et al., 11 (6) 1441–1452. Copyright (2009) Springer Science + Business Media)*

observed to be much larger in the nanocomposite (65 Oe) than for the as-received samples (18 Oe), due to the dispersion of the single-domain-size nanoparticles.

12.7 Electron Transport in Conductive-Polymer Nanocomposites

The electrical conductivity was measured by a standard four-probe method. Figure 12.8a shows the temperature-dependent resistivity of pure PPy and nanocomposites with different particle loadings. The PPy, synthesized in the presence of the nanoparticles with a long reaction time, was observed to have large resistance beyond the capability of the utilized equipment. This was due to poor contact between small particles [79] and the amorphous structure which will be discussed later. At lower temperatures the resistance was too large to be measured by the available equipment. The much lower resistivity in pure PPy prepared by the conventional method was due to the formation of a network structure, as shown in the SEM image in Figure 12.2(b), which favors electron transport. The resistivity change was not due to the doping extent, based on the fact that all the samples were washed and doped with the same solution (species) [80]. The resistance was observed to decrease dramatically in the Fe_2O_3/PPy nanocomposites, which was due to a crystalline structure change and will be discussed later. Nanocomposite with an initial particle loading of 50 wt% was observed to have a higher resistivity, which was due to the known insulating effect of iron oxide [81,82] and consistent with silicon carbide/polypyrrole [83], silica/polypyrrole [84], and titanium dioxide/polyaniline nanocomposites [85].

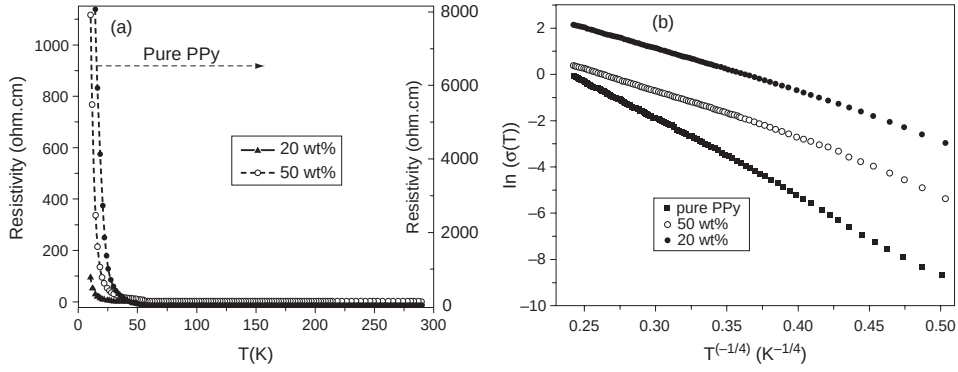

Figure 12.8 *(Reprinted with permission from Journal of Nanoparticle Research, Fabrication and Characterization of Iron Oxide Nanoparticles Reinforced Polypyrrole Nanocomposites, by Z. Guo, K. Shin, A. B. Karki et al., 11 (6) 1441–1452. Copyright (2009) Springer Science + Business Media)*

Figure 12.8b shows the temperature-dependent conductivity (σ). The conductivity of pure PPy and nanocomposites with two different particle loadings can be linearly correlated to temperature with the quasi-three-dimensional variable-range hopping (quasi-3D-VRH) model. The variable-range hopping theory analysis indicates that three-dimensional hopping dominates in these samples, and the correlation between conductivity and temperature can be expressed by Equation (12.1),

$$\sigma(T)=\sigma_0 \exp\left[-\left(\frac{T_0}{T}\right)^{1/4}\right] \tag{12.1}$$

where T_0 is the characteristic Mott temperature and the pre-exponential factor σ_0 is the conductivity at infinite temperature. σ_0 was calculated to be 3000.1 S cm^{-1} for pure PPy, and 978.4 S cm^{-1} and 298.8 S cm^{-1} for nanocomposites with initial particle loadings of 20 wt% and 50 wt%, respectively. T_0 was calculated to be 1204137 K for pure PPy, and 138346 K and 212010 K for nanocomposites with initial particle loadings of 20 wt% and 50 wt%, respectively. The parameter T_0 is inversely proportional to the localization length of the charge carriers. A larger T_0 implies a strong localization of the charge carriers, which results in an increase in resistance at low temperatures; whereas a small T_0 implies a weak localization [2]. The observed T_0 variation for the component is consistent with the observed resistivity change in the synthesized PPy and Fe_2O_3/PPy systems.

It has been reported that the electrical conductivity strongly depends on the ordered states of the conductive polymer [86]. In other words, the structural and electronic properties of PPy can be easily modified due to the soft lattices, which are reflected in the crystalline structure of the nanomaterials. Iron oxide nanoparticles were thought to serve as a template for the subsequent PPy matrix formation. Ultrasonic energy has been reported to have a strong capability to alter the electronic structure of the polymer or even produce various nanoparticles. Here, the crystalline structure change with the nanocomposite formation was investigated by selected-area electron diffraction (SAED) and dark-field TEM microstructures.

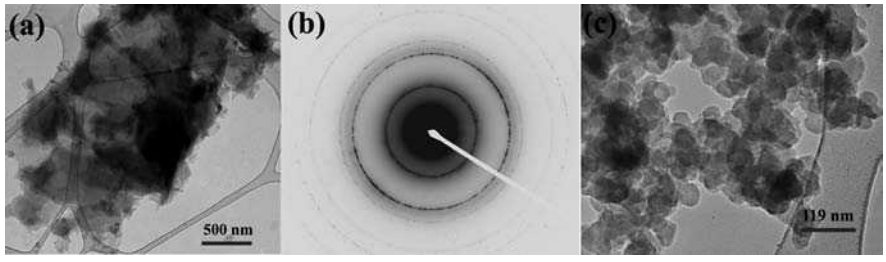

Figure 12.9 *(Reprinted with permission from Journal of Nanoparticle Research, Fabrication and Characterization of Iron Oxide Nanoparticles Reinforced Polypyrrole Nanocomposites, by Z. Guo, K. Shin, A. B. Karki et al., 11 (6) 1441–1452. Copyright (2009) Springer Science + Business Media)*

Figure 12.9a and b show the bright-field TEM microstructure of pure PPy and the corresponding selected-area electron diffraction (SAED). Similar to the SEM observation, linked nanoparticles were observed in the bright-field TEM images, as shown in Figure 12.9a. The clear ring pattern shown in Figure 12.9b indicates the crystalline structure of the formed polypyrrole. Conductive polymer is reported to have a homogeneously disordered structure, i.e., partially crystalline, especially in nanostructures such as nanotubes (15%) [87]. Higher crystallinity is reported to render higher conductivity [88,89]. The calculated lattice distance (the lattice constant of PPy refers to the constant distance between unit cells in a PPy crystal lattice) indicates partial crystallinity for PPy nancomposites. The lattice distances and crystalline planes (from the inner to the outer) of pure PPy calculated from the electron diffraction patterns are 0.117 nm (100), 0.0666 nm (111), 0.0577 nm (200), 0.0434 nm (220), and 0.0386 nm (300). However, no ring pattern was observed in PPy formed in the presence of iron oxide nanoparticles over a long reaction time, indicating an amorphous or disordered structure. The observed discrete spherical structure shown in Figure 12.9c is consistent with the SEM observation, which leads to the poor contact and high resistivity.

Figures 12.10 and 12.11a, b and c show bright-field microstructures, selected-area electron diffraction, and dark-field micrographs of prepared nanocomposites with initial particle loadings of 20 wt% and 50 wt%, respectively. Discrete nanoparticles observed in the nanocomposites were consistent with the SEM observations. The image

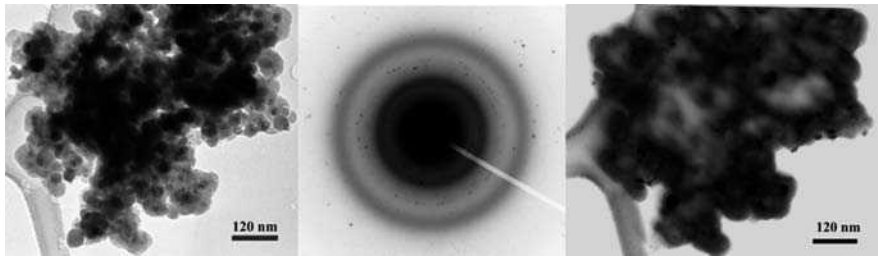

Figure 12.10 *(Reprinted with permission from Journal of Nanoparticle Research, Fabrication and Characterization of Iron Oxide Nanoparticles Reinforced Polypyrrole Nanocomposites, by Z. Guo, K. Shin, A. B. Karki et al., 11 (6) 1441–1452. Copyright (2009) Springer Science + Business Media)*

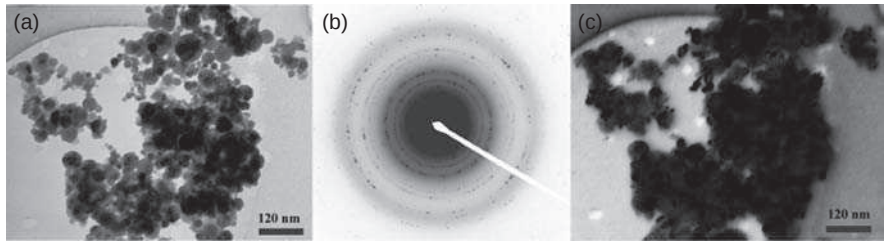

Figure 12.11 *(Reprinted with permission from Journal of Nanoparticle Research, Fabrication and Characterization of Iron Oxide Nanoparticles Reinforced Polypyrrole Nanocomposites, by Z. Guo, K. Shin, A. B. Karki et al., 11 (6) 1441–1452. Copyright (2009) Springer Science + Business Media)*

contrast arose from the molecular weight of PPy and iron oxide. The dark and grey regions corresponded to the iron oxide and PPy, respectively. The lattice distance of the related SAED of nanocomposite with an initial particle loading of 20 wt% shown in Figure 12.9b was indexed to be 0.167 nm (2 1 1, Fe_2O_3), 0.137 nm (2 0 8, Fe_2O_3), 0.114 nm (100. PPy), 0.086 nm (2 3 8, Fe_2O_3), and 0.0804 nm (2 4 4, Fe_2O_3). The SAED pattern of the nanocomposite with an initial particle loading of 50 wt% was calculated and indexed to be 0. 167 nm (2 1 1, Fe_2O_3), 0.137 nm (2 0 8, Fe_2O_3), 0.111 nm (100, PPy), 0.0863 nm (2 3 8, Fe_2O_3), 0.0804 nm (2 4 4, Fe_2O_3), 0.0648 nm (111, PPy), 0.0569 nm (200, PPy), and 0.0376 nm (300, PPy). All the calculated numbers in the reflection planes were all even or odd, indicating face-centered-cubic structures [90].

The dark-field micrographs of the nanocomposites corresponding to the bright-field image shown in Figures 12.10 and 12.11c also indicate a crystalline structure. The high crystallinity observed in the nanocomposites is most likely responsible for the increased conductivity. In addition, the lattice distance of PPy was observed to be smaller in the nanocomposite with the higher particle loading, indicating that the nanoparticles favor a compact PPy structure with a lower resistivity. However, the high resistivity in the higher particle-loaded nanocomposites is due to the insulating nature of the iron oxide nanoparticles, which dominate the electron transport. T_0 is the characteristic Mott temperature, i.e. the energy needed for hopping conduction of charge carriers. A smaller value of T_0 indicates higher conductivity of the sample. The value of T_0 can be obtained from the slop of $\ln \rho(T) \sim T^{-1/2}$ plot. This explains the phenomenon of the characteristic Mott temperature of nanocomposite with a 20 wt% particle loading decreasing and then increasing again with 50 wt% loading.

The effect of the stirring method, i.e., mechanical or ultrasonic stirring, on the conductivity was investigated by polymerizing for seven hours. Figure 12.12 shows the temperature-dependent resistivity and conductivity (σ) of nanocomposite with an initial particle loading of 50 wt% and ultrasonically stirred for seven hours. In comparison to the high resistivity of the nanoproduct (pure PPy, complete loss of the nanoparticles), the lower resistivity and the presence of magnetic hysteresis indicates that the stirring method has a significant effect on the composite preparation. Ultrasonic stirring favors protection of nanoparticles from dissolution. The

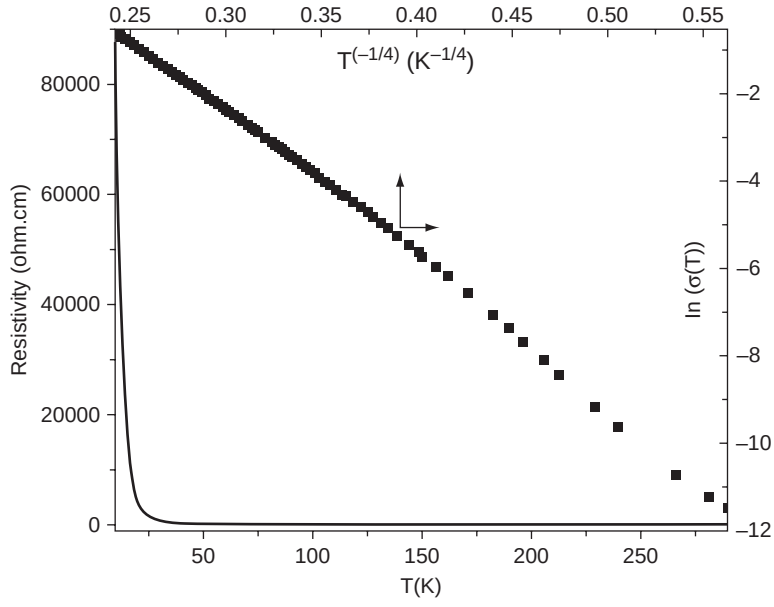

Figure 12.12 *(Reprinted with permission from Journal of Nanoparticle Research, Fabrication and Characterization of Iron Oxide Nanoparticles Reinforced Polypyrrole Nanocomposites, by Z. Guo, K. Shin, A. B. Karki et al., 11 (6) 1441–1452. Copyright (2009) Springer Science + Business Media)*

linear relation between $\ln(\sigma)$ and $T^{-1/4}$ indicates a quasi-three-dimensional variable-range hopping (quasi-3D-VRH) mechanism.

Figure 12.13a–c shows the bright-field microstructures, the corresponded selected-area electron diffraction, and dark-field microstructures of nanocomposites with ultrasonic stirring, respectively. The contrast shown in Figure 12.13a represents iron oxide nanoparticles (black region) and PPy polymer (gray region). The nanoparticles were observed to be enclosed and protected from complete dissolution by the polymer matrix. The ring patterns with clear spots shown in Figure 12.13b

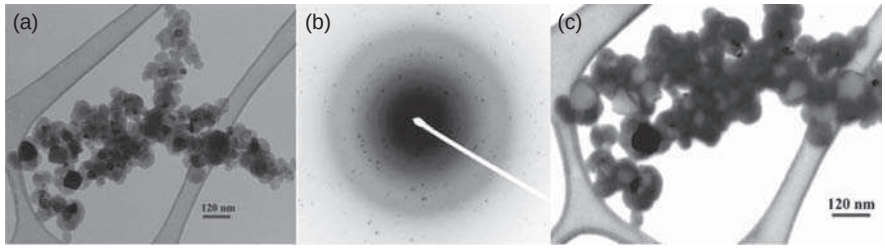

Figure 12.13 *(Reprinted with permission from Journal of Nanoparticle Research, Fabrication and Characterization of Iron Oxide Nanoparticles Reinforced Polypyrrole Nanocomposites, by Z. Guo, K. Shin, A. B. Karki et al., 11 (6) 1441–1452. Copyright (2009) Springer Science + Business Media)*

Table 12.1 *Physical properties of pure PPy and Fe_2O_3/PPy nanocomposites*

Material name	Resistivity at 10 K (ohm.cm)	Resistivity at 290 K(ohm.cm)	Lattice constant of PPy(nm)	Final particle loading(wt %)[d]
Pure PPy[a]	8058.60	1.10	0.117	0
Nanocomposite 20 wt%[b] (1 hour ultrasonic stirring)	94.90	0.12	0.114	27.0
Nanocomposite 50 wt% (1 hour ultrasonic stirring)	1117.00	0.69	0.111	68.0
Nanocomposite 50 wt% (seven hour ultrasonic stirring)	96424.20	1.82	0.117	20.2
Nanocomposite 50 wt%[c] (seven hour mechanical stirring)	Infinite	Infinite	Amorphous	0

[a] Pure PPy formed without iron oxide nanoparticles.
[b] The weight percentage was the initial particle loading before polymerization and calculated based on the total mass of monomers and the nanoparticles
[c] This is pure PPy and the nanoparticles were completely dissolved due to the reaction between the nanoparticles and the protons
[d] Particle loading was estimated from the saturation magnetization.

indicate the highly crystalline structure of the nanocomposites, which can be indexed to the iron oxide nanoparticles and the formed PPy. The dark-field microstructures of the nanocomposites also indicate a crystalline structure.

The crystalline structural parameter and electrical resitivity of pure PPy and the nanocomposites are summarized in Table 12.1. The crystalline structure parameter was observed to be larger in nanocomposites with seven-hour ultrasonic stirring and an initial particle loading of 50 wt%, which is due to the majority being PPy matrix, as observed in the TEM (Figure 12.13a), and also the lower final particle loading. With a similar crystalline structural parameter, the presence of iron oxide nanoparticles made the nanomaterials less conductive. With an amorphous structure, PPy formed with the presence of the iron oxide nanoparticles, and mechanical stirring for a long time produced insulating materials.

12.8 Giant Magnetoresistance in Conductive-Polymer Nanocomposites

A giant magnetoresistance (GMR) effect indicates a significant change in resistance in response to an external magnetic field. With zero external field, the magnetization directions of adjacent ferromagnetic layers in a GMR material are antiparallel due to a weak antiferromagnetic coupling between the layers. When an applied external field aligns the magnetization in adjacent layers, a low level of resistance is observed. Since

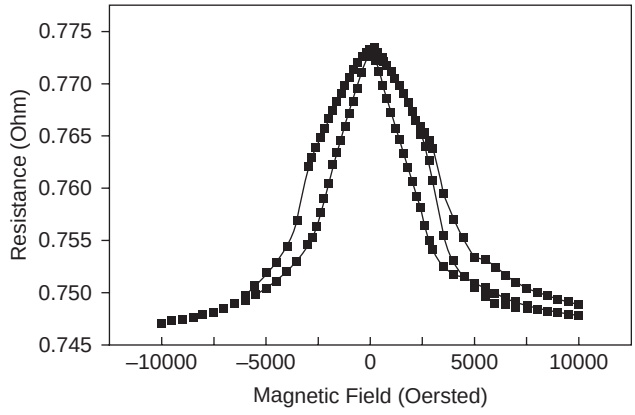

Figure 12.14 *Resistance vs. in-plane magnetic field curves at room temperature for electrodeposited (30 repeats) Co (2 nm)/Cu (3 nm) on conductive polypyrrole film (thickness 5 mm).*[65] *(Reprinted with permission from Journal of Materials Chemistry, A flexible giant magnetoresistance sensor prepared completely by electrochemical synthesis by F. Yan, G. Xue and F. Wan, 12, 2606–2608. Copyright (2002) Royal Society of Chemistry)*

the discovery of GMR in thin-film structures composed of alternating ferromagnetic and nonmagnetic metal layers in 1988 [91], GMR sensors have spurred many commercial applications, such as magnetic storage (read heads in modern hard drives) [92], magnetic random access memory (MRAM), and biological detection [93,94]. Compared with traditional metal matrix composites, polymer nanocomposites containing magnetic nanoparticles are more attractive because of their high flexibility, easy processing, and low cost.

With PPy as the substrate, Yan *et al*. noticed interesting GMR behavior with a value of 4% in cobalt and copper multilayers, as shown in Figure 12.14 [65]. The copper layer serves as a spacer for cobalt layers, similar to a conventional metal electrode system. However, there is no report regarding conductive polymer layers as ferromagnetic layer spacers. The reported value is lower than that of the pure metal system. There were three proposed reasons for the difference: the quality of the cobalt layer (with more copper in the ferromagnetic cobalt layers with a PPy substrate); the roughness of the PPy thin film (rougher compared than conventional metal); and the low conductivity of the PPy film used.

The flexibility of a plastic substrate-based GMR is shown in Figure 12.15a,b and the observed GMR values in polyester are lower than those in silicon and kapton substrates, as seen in Figure 12.15c [95]. By minimizing the roughness of the plastic substrate with a suitable buffer layer (2 μm photoresist), Chen *et al.* [95] improved the roughness of the plastic, which was comparable to that of the conventional Si substrate, as seen in Figure 12.16a. The number of bilayers was found to have a significant effect on the GMR values (Figure 12.16b,c).

Granular polymer nanocomposites have also been investigated for possible GMR applications [43,96]. Conductive iron nanoparticle-reinforced vinyl ester resin nanocomposites are observed to possess MRs of only 0.9%, which increase to 1.7% after

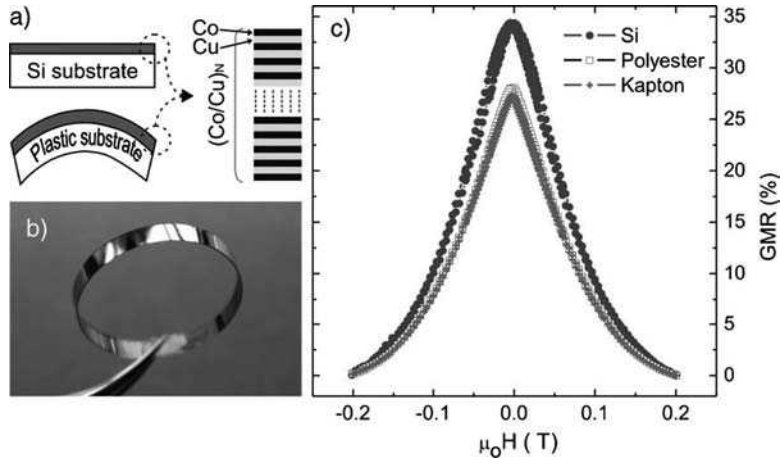

Figure 12.15 *(a) Schematic illustration of $(Co/Cu)_N$ multilayers deposited on Si and flexible substrates. (b) A photographic image of circularly bent $(Co/Cu)_{20}$ MLs deposited on a polyester substrate. (c) GMR curves for $(Co/Cu)_{20}$ MLs deposited on polyester, kapton, and thermally oxidized Si substrates. (Reprinted with permission from Advanced Materials, Towards Flexible Magnetoelectronics: Buffer-Enhanced and Mechanically Tunable GMR of Co/Cu Multilayers on Plastic Substrates by Y. M. Yuan-fu Chen, Rainer Kaltofen, Jens Ingolf Mönch et al., 20, 3224–3228. Copyright (2008) Wiley-VCH)*

carbonization (Figure 12.17a). The particle loading was found to have a significant effect on the GMR values (Figure 12.17b). Optimizing the particle loading has great potential to achieve further increases in GMR.

12.9 Summary

The effect of iron oxide nanoparticles on the chemical polymerization of pyrroles in acidic solution has been investigated and found to significantly influence the morphology (size and shape) and other physicochemical properties of PPy. Pure discrete PPy nanoparticles with a much higher resistivity were formed over a long reaction time in the presence of iron oxide nanoparticles. Similar to pure PPy formed with nanoparticles and different from the network structure of pure PPy formed without nanoparticles, discrete nanoparticles were observed in all nanocomposites with initial particle loadings of 20 wt% and 50 wt%. Subsequent nanocomposites were observed to have improved thermal stabilities with higher decomposition temperatures. FT-IR, TGA/DTG and TEM/SAED analyses indicated a strong interaction between the nanoparticles and polymer matrix. PPy was observed to have a lower yield of nanocomposite with a higher initial particle loading. Saturation magnetization in

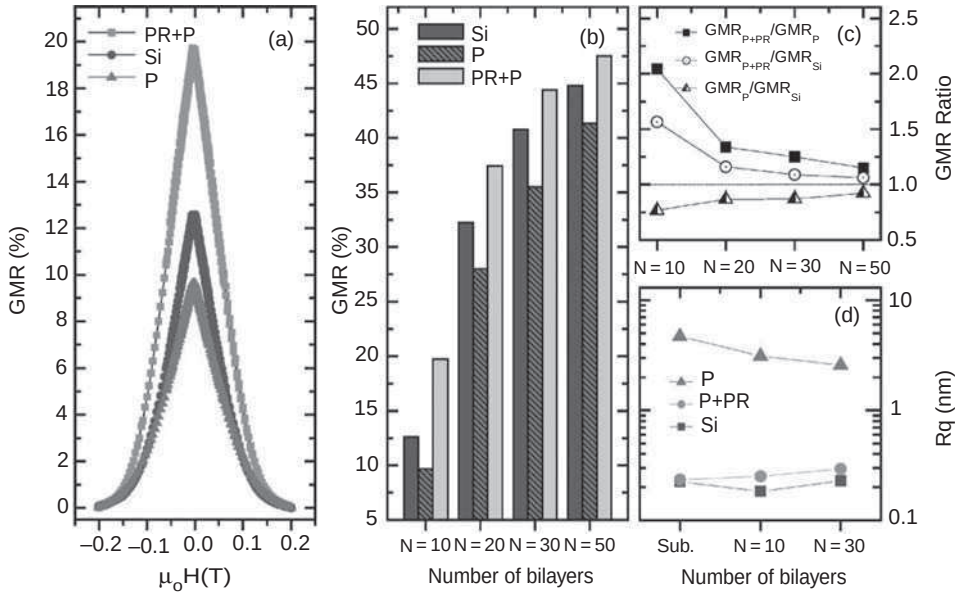

Figure 12.16 *(a) GMR curves of $(Co/Cu)_{10}$ multilayers deposited on Si, polyester (P), and photoresist-buffered polyester (PR+R) substrates. (b) GMR comparison of $(Co/Cu)_N$ MLs on various substrates with different numbers of bilayers. (c) GMR ratio of $(Co/Cu)_N$ multilayers deposited on Si, P, and PR+P substrates. (d) Root mean square roughness, R_q, of Si, P, PR+P bare substrates and Co/Cu films on the corresponding substrates. (Reprinted with permission from Advanced Materials, Towards Flexible Magnetoelectronics: Buffer-Enhanced and Mechanically Tunable GMR of Co/Cu Multilayers on Plastic Substrates by Y. M. Yuan-fu Chen, Rainer Kaltofen, Jens Ingolf Mönch et al., 20, 3224–3228. Copyright (2008) Wiley-VCH)*

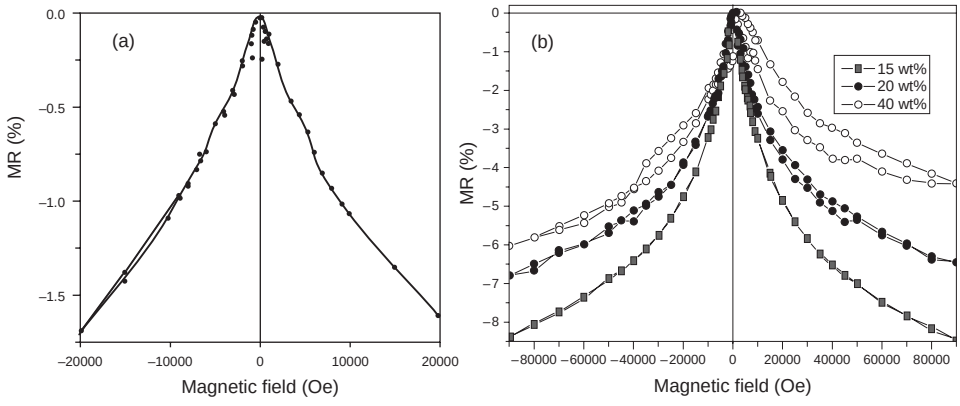

Figure 12.17 *(Reprinted with permission from Journal of Applied Physics, Magnetic and magnetoresistance behaviors of particulate iron/vinyl ester resin nanocomposites by Z. Guo, H. T. Hahn, H. Lin et al., J. Appl.Phys., 104, 014314. Copyright (2008) American Institute of Physics)*

nanocomposite with a high particle loading was larger, and the conductive behavior followed the three-dimensional variable-range hopping mechanism. The presence of nanoparticles in the nanocomposites was observed to produce a more condensed structure of PPy. The decreased conductivity with high particle loading was due to the insulating behavior of the iron oxide. Compared to mechanical stirring, ultrasonic stirring played a critical role in iron oxide-PPy nanocomposite formation and provided protection from proton dissolution for nanoparticles, arising from a tight PPy matrix formed around the iron oxide nanoparticles.

12.9.1 Materials Design Perspective

The importance of hierarchical theories and models bridging multiple length- and time-scales, working in conjunction with experiments, was recognized in 1987 with the publication of the book *Design of New Materials* [97]. Recent theoretical and modeling work on nanocomposites confirms the earlier predictions [98,99]. Nanocomposite experimentation in synthesis and fabrication represents a case-in-point scenario design challenge which covers the micro-, meso-, and macro-size scales, as illustrated in the current work. This brings into perspective several experimentally derived concepts for which theory and modeling must account:

- Nanoparticles in relatively small amounts, through their high surface area, affect not only the mesoscale and macroscale physical properties, but electrical properties and magnetic properties as well.
- Nanoparticles, through their higher surface energies, are more reactive and this must be controlled during synthesis since it can influence meso- and macroscale structures, as well as physical chemical and physical properties.
- Nanoparticles dispersed in a matrix bring their own properties to bear on the system, as seen with the reduced electrical conductivity with increasing concentration and the changes in magnetic properties.

References

[1] D. Kumar and R.C. Sharma, Advances in conductive polymers, *Eur. Polym. J.*, **34**, 1053–1060 (1998).
[2] R. Gangopadhyay, A. De, and S. Das, Transport properties of polypyrrole-ferric oxide conducting nanocomposites, *J. Appl. Phys.*, **87**, 2363 (2000).
[3] R. Gangopadhyay and A. De, Conducting polymer nanocomposites: A brief overview, *Chem. Mater*, **12**, 608–622 (2000).
[4] J.-M. Yeh, C.-P. Chin and S. Chang, Enhanced corrosion protection coatings prepared from soluble electronically conductive polypyrrole-clay nanocomposite material, *J. Appl. Polym. Sci*, **88**, 3264–3272 (2003).
[5] J. Deng, X. Ding, W. Zhang, Y. Peng, J. Wang, X. Long, P. Li, and A.S.C. Chan, Magnetic and conducting Fe3O4-cross-linked polyaniline nanoparticles with core-shell structure, *Polymer*, **43**, 2179–2184 (2002).
[6] K. Lee, S. Cho, S.H. Park, A.J. Heeger, C.-W. Lee, and S.-H. Lee, Metallic transport in polyaniline, *Nature*, **44**, 65–68 (2006).

[7] K. Huang, H. Qiu, and M. Wan, Synthesis of highly conducting polyaniline with photochromic azobenzene side groups, *Macromolecules*, **35**, 8653–8655 (2002).
[8] H.-K. Song and G.T.R. Palmore, Redox-active polypyrrole: toward polymer-based batteries, *Adv. Mater.*, **18**, 1764–1768 (2006).
[9] M.D. Ingram, H. Staesche, and K.S. Ryder, 'Ladder-doped' polypyrrole: a possible electrode material for inclusion in electrochemical supercapacitors?, *J. Power Sources*, **129**, 107–112 (2004).
[10] K.A. Noh, D.-W. Kim, C.-S. Jin, K.-H. Shin, J.H. Kim and J.M. Ko, Synthesis and pseudo-capacitance of chemically-prepared polypyrrole powder, *J. Power Sources*, **124**, 593–595 (2003).
[11] B. Zaid, S. Aeiyach, and P.C. Lacaze, Electropolymerization of pyrrole in propylene carbonate on zinc electrodes modified by heteropolyanions, *Synth. Met.*, **65**, 27–34 (1994).
[12] C.A. Ferreira, S. Aeiyach, M. Delamar, and P.C. Lacaze, Electropolymerization of pyrrole on iron electrodes Influence of solvent and electrolyte on the nature of the deposits, *J. Electroanal. Chem.*, **284**, 351–369 (1990).
[13] G. Han, J. Yuan, G. Shi, and F. Wei. Electrodeposition of polypyrrole/multiwalled carbon nanotube composite films, *Thin Solid Films*, **474**, 64–69 (2005).
[14] S. Asavapiriyanont, G.K. Chandler, G.A. Gunawardena, and D. Pletcher, The electrodeposition of polypyrrole films from aqueous solutions, *J. Electroanal. Chem.*, **177**, 229–244 (1984).
[15] B. Lakard, O. Segut, S. Lakard, G. Herlem, and T. Gharbi, Potentiometric miniaturized pH sensors based on polypyrrole films, *Sens. Actua. B*, **122**, 101–108 (2007).
[16] R.P. Tandon, M.R. Tripathy, A.K. Arora, and S. Hotchandani, Gas and humidity response of iron oxide-polypyrrole nanocomposites, *Sens. Actuat. B Chem.*, **114**, 768–773 (2006).
[17] K.H. An, S.Y. Jeong, H.R. Hwang, and Y.H. Lee. Gas and humidity response of iron oxide-polypyrrole nanocomposites, *Adv. Mater.*, **16**, 1005–1009 (2004).
[18] P.M. Ajayan, L.S. Schadler, and P.V. Braun, *Nanocomposite Science and Technolgoy*, Wiley VCH, Weinheim, 2003.
[19] C. Castro, J. Ramos, A. Millan, J. Gonzalez-Calbet, and F. Palacio, Production of magnetic nanoparticles in imine polymer matrixes, *Chem. Mater.*, **12**, 3681–3688 (2000).
[20] M.K. Corbierre, N.S. Cameron, M. Sutton, S.G.J. Mochrie, L.B. Lurio, A. Ruehm and R.B. Lennox, Polymer-stabilized gold nanoparticles and their incorporation into polymer matrices, *J. Am. Chem. Soc.*, **123**, 10411–10412 (2001).
[21] V. Yong and H.T. Hahn, Processing and properties of SiC/vinyl ester nanocomposites, *Nanotechnology*, **15**, 1338–1343 (2004).
[22] J.J. Mack, L.M. Viculis, A. Ali, R. Luoh, G. Yang, H.T. Hahn, F.K. Ko, and R.B. Kaner, Graphite nanoplatelet reinforcement of electrospun polyacrylonitrile nanofibers, *Adv. Mater.*, **17**, 77–80 (2005).
[23] G. Sandi, H. Joachin, R. Kizilel, S. Seifert, and K.A. Carrado, *In situ* SAXS studies of the structural *changes* of polymer nanocomposites used in battery applications, *Chem. Mater.*, **15**, 838–843 (2003).
[24] G. Sandi, R. Kizilel, K.A. Carrado, R. Fernandez-Saavedra, and N. Castagnola, Effect of the silica precursor on the conductivity of hectorite-derived polymer nanocomposites, *Electrochim. Acta*, **50**, 3891–3896 (2005).
[25] Z. Guo, L.L. Henry, V. Palshin and E.J. Podlaha, Synthesis of poly(methyl methacrylate) stabilized colloidal zero-valence metallic nanoparticles, *J. Mater. Chem.*, **16**, 1772–1777 (2006).
[26] J.M. Brown, D.P. Anderson, R.S. Justice, K. Lafdi, M. Belfor, K.L. Strong and D.W. Schaefer, Hierarchical morphology of carbon single-walled nanotubes during sonication in an aliphatic diamine, *Polymer*, **46**, 10854–10865 (2005).
[27] Y. Chen, L. Sun, O. Chiparus, I. Negulescu, V. Yachmenev, and M. Warnock, Kenaf/Ramie composite for automotive headliner, *J. Polym. Environ.*, **13**, 107–114 (2005).
[28] B. Wetzel, F. Haupert, and M.Q. Zhang, Epoxy nanocomposites with high mechanical and tribological performance, *Comp. Sci. Tech.*, **63**, 2055–2067 (2003).
[29] Z. Guo, T. Pereira, O. Choi, Y. Wang, and H.T. Hahn, Surface functionalized alumina nanoparticle filled polymer nanocomposites with enhanced mechanical properties, *J. Mater. Chem.*, **16**, 2800–2808 (2006).

[30] Z. Guo, S. Park, S. Wei, T. Pereira, M. Moldovan, A.B. Karki, D.P. Young, and H.T. Hahn, Flexible high-loading particle-reinforced polyurethane magnetic nanocomposite fabrication through particle-surface-initiated polymerization, *Nanotechnology*, **18**, 335704 (2007).
[31] R.M. Cornell and U. Schwertmann, *The Iron Oxide*, 2n Edn. Wiley-VCH, Weinheim, 2003.
[32] L. Wang, M. Rocci-Lane, P. Brazis, C.R. Kannewurf, Y.-I. Kim, W. Lee, J.-H. Choy, and M.G. Kanatzidis, R-$RuCl_3$/polymer nanocomposites: The first group of intercalative nanocomposites with transition metal halides, *J. Am. Chem. Soc.*, **122**, 6629–6640 (2000).
[33] S.R.C. Vivekchand, K.C. Kam, G. Gundiah, A. Govindaraj, A.K. Cheetham and C.N.R. Rao, Electric properties of inorganic nonowire-polymer composites, *J. Mater. Chem.*, **15**, 4922–4927 (2005).
[34] S. Lee, H.-J. Shin, S.-M. Yoon, D.K. Yi, J.-Y. Choi, and U. Paik, Refractive index engineering of transparent ZrO_2-polydimethyldiloxane nanocomposites, *J. Mater. Chem.*, **18**, 1751–1755 (2008).
[35] Y. Li, G.-X. Wei, and H.-J. Sue, Morphology and toughening mechanisms in clay-modified styrene-tutadiene-styrene rubber-toughened polypropylene, *J. Mater. Sci.*, **37**, 2447–2459 (2002).
[36] F. Mammeri, E. Le Bourhis, L. Rozes, and C. Sanchez, Mechanical properties of hybrid organic-inorganic materials, *J. Mater. Chem.*, **15**, 3787–3811 (2005).
[37] C. Brosseau and P. Talbot, Effective magnetic permeability of Ni and Co Micro- and nanoparticles embedded in a ZnO matrix, *J. Appl. Phys.*, **97**, 104325–1/11 (2005).
[38] Z. Guo, S. Park, H.T. Hahn, S. Wei, M. Moldovan, A.B. Karki, and D.P. Young, Magnetic and electromagnetic evaluation of the magnetic nanoparticle filled polyurethane nanocompositesm, *J. Appl. Phys.*, **101**, 09M511 (2007).
[39] J.-D. Kwon, P.-H. Kim, J.-H. Keum, and J.S. Kim, Polypyrrole/titania hybrids: synthetic variation and test for the photovoltaic materials, *Sol. Energy Mater. Sol. Cells*, **83**, 311–321 (2004).
[40] W.J.E. Beek, M.M. Wienk, and R.A.J. Jassen, Efficient hybrid solar cells from zinc oxide nanoparticles and a conjugated polymer, *Adv. Mater.*, **16**, 1009–1013 (2004).
[41] K. Gall, M.L. Dunn, Y. Liu, G. Stefanic, and D. Balzar, Internal stress storage in shape memory polymer nanocomposites, *Appl. Phys. Lett*, **85**, 290–292 (2004).
[42] R. Mohr, K. Kratz, T. Weigel, M. Lucka-Gabor, M. Moneke, and A. Lendlein, Initiation of shape-memory effect by inductive heating of magnetic nanoparticles in thermoplastic polymers, *PNAS*, **103**, 3540–3545 (2006).
[43] Z. Guo, S. Park, H.T. Hahn, S. Wei, M. Moldovan, A.B. Karki, and D.P. Young, Giant magnetoresistance behavior of an iron/carbonized polyurethane nanocomposite, *Appl. Phys. Letts*, **90**, 053111 (2007).
[44] S.J. Toal and W.C. Trogler, Polymer sensors for nitroaromatic explosives detection, *J. Mater. Chem.*, **16**, 2871–2883 (2006).
[45] E.J. Podlaha, Y. Li, J. Zhang, Q. Huang, A. Panda, A. Lozano-Morales, D. Davis, and Z. Guo, Electrochemical deposition of nanostructured metals. In *Nanomaterials Handbook*, ed. Y. Gogotsi, CRC Press, New York, 475–495 (2006).
[46] Z. Lei and S. Bi, Preparation of polymer nanocomposites of core-shell structure via surface-initiated atom transfer radical polymerizations, *Mater. Lett.*, **61**, 3531–3534 (2007).
[47] S. Bi, X. Wei, N. Li, and Z. Lei, *In situ* formation of Fe_3O_4 nanoparticles within the thermosensitive hairy hybrid particles, *Mater. Lett.* **62**, 2963–2966 (2008).
[48] S.R. Dhage, Y.B. Khollam, H.S. Potdar, S.B. Deshpande, P.P. Bakare, S.R. Sainkar, and S.K. Date, Effect of variation of molar ratio (pH) on the crystallization of iron oxide phases in microwave hydrothermal synthesis, *Mater. Lett*, **57**, 457–462 (2002).
[49] Z. Guo, K. Shin, A.B. Karki, D.P. Young, and H.T. Hahn, Fabrication and characterization of iron oxide nanoparticles reinforced polypyrrole nanocomposites, *J. Nanopar. Res.* **11**(6), 1441–1452 (2009).
[50] B.Z. Tang, Y. Geng, J.W.Y. Lam, B. Li, X. Jing, X. Wang, F. Wang, A.B. Pakhomow, and X.X. Zhang, Processible nanostructured materials with electrical conductivity and magnetic susceptibility: preparation and properties fo maghemite/polyaniline nanocomposite films, *Chem. Mater.*, **11**, 1581–1589 (1999).

[51] B.Z. Tang, Y. Geng, Q. Sun, X.X. Zhang, and X. Jing, Processible nanomaterials with high conductivity and magnetization. preparation and properties of maghemite/polyaniline nanocomposite films, *Pure Appl. Chem.*, **72**, 157–162 (2000).
[52] Y.B. Khollam, S.R. Dhage, H.S. Potdar, S.B. Deshpande, P.P. Bakare, S.D. Kulkarni, and S.K. Date, Microwave hydrothermal preparation of submicron-sized spherical magnetite (Fe_3O_4) powders, *Mater. Lett.*, **56**, 571–577 (2002).
[53] O.Y. Posudievskii and V.D. Pokhodenko, Superparamagnetic polyaniline/magnetite nanocomposite, *Theor. Exper. Chem.*, **32**, 213–216 (1996).
[54] I.L. Radtchenko, G.B. Sukhorukov, and H. Mohwald, A novel method for encapsulation of poorly water-soluble drugs: precipitation in polyelectrolyte multilayer shells, *Int. J. Pharm.*, **242**, 219–223 (2002).
[55] N. Murillo, E. Ochoteco, Y. Alesanco, J.A. Pomposo, J. Rodriguez, J. Gonzalez, J.J. del. Val, J.M. Gonzalez, M.R. Britel, F.M. Varela-Feria, and A.R. de. Arellano-Lopez, $CoFe_2O_4$–polypyrrole (PPy) nanocomposites: new multifunctional materials, *Nanotechnology*, **15**, S322–S327 (2004).
[56] P. Poddar, J.L. Wilson, H. Srikanth, S.A. Morrison, and E.E. Carpenter, Magnetic properties of conducting polymer doped with magnanese-zinc ferrite nanoparticles, *Nanotechnology*, **15**, S570–S574 (2004).
[57] Y. Li, H. Zhang, Y. Liu, Q. Wen, and J. Li, Rod-shape polyaniline-barium ferrite nanocomposite: preparation, characterization and properties, *Nanotechnology*, **19**, 105605 (2008).
[58] V.R. Inturi and J.A. Barnard, Studies of laminated and single layer high moment soft FeTaN films, *J. Appl. Phys.*, **81**, 4504 (1997).
[59] S.J. Yen, E.C. Chen, R.K. Chiang, and T.M. Wu, Preparation and characteriztion of polypyrrole/magnetite nanocomposites synthesized by *in situ* chemical oxidative polymerization, *J. Polym. Sci. B, Polym. Phys.*, **46**, 1291–1300 (2008).
[60] X. Li, M. Wan, Y. Wei, J. Shen, and Z. Chen, Electromagnetic functionalized and core-shell micro/nanostructured polypyrrole composites, *J. Phys. Chem. B*, **110**, 14623–14626 (2006).
[61] H. Yuvaraj, M.H. Woo, E.J. Park, Y.T. Jeong, and K.T. Lim, Polypyrrole/r-Fe2O3 magnetic nanocomposites synthesized in supercritical fluid, *Eur. Poly. J.*, **44**, 637–644 (2008).
[62] X. Yang, L. Xu, S.C. Ng, and S.O.H. Chan, Magnetic and electrical properties of polypyrrole-coated γ-Fe_2O_3 nanocomposite particles, *Nanotechnology*, **14**, 624–629 (2003).
[63] K. Sunderland, P. Brundetti, L. Spinu, J. Fang, Z. Wang, and W. Lu, Synthesis of γ-Fe_2O_3/polypyrrole nanocomposite materials, *Mater. Lett.*, **58**, 3136–3140 (2004).
[64] S. Takeoka, T. Hara, K. Yamamoto, and E. Tsuchida, Thermal stabilization of polypyrrole by incorporation of aromatic sulfonate derivatives as dopants, *Chem. Lett.*, **25**, 253 (1996).
[65] F. Yan, G. Xue, and F. Wan, A flexible giant magnetoresistance sensor prepared completely by electrochemical synthesis, *J. Mater. Chem.*, **12**, 2606–2608 (2002).
[66] M. Abe and Y. Tamaura, Ferrite plating in aqueous solution: New technique for preparing magnetic thin film, *J. Appl. Phys.*, **55**, 2614–2616 (1984).
[67] M. Abe, T. Itoh, Y. Tamaura, Y. Gotoh, and M. Gomi, Ferrite plating on GaAs for microwave monolithic integrated circuit, *IEEE Trans. Magn.*, **23**, 3736–3738 (1987).
[68] O. Jarjayes, P.H. Fries, and C. Bidan, New nanocomposites of polypyrrole including [gamma]-Fe_2O_3 particles: electrical and magnetic characterizations, *Synth. Met.*, **69**, 343–344 (1995).
[69] F. Yan, G. Xue, J. Chen, and Y. Lu, Preparation of a conducting polymer/ferromagnet composite film by anodic-oxidation method, *Synth. Met.*, **123**, 17–20 (2001).
[70] C. Forder, S.P. Armes, A.W. Simpson, C. Maggiore, and M. Hawley, Preparation and characterisation of superparamagnetic conductive polyester textile composites, *J. Mater. Chem*, **3**, 563–569 (1993).
[71] Z. Zhang and M. Wan, Nanostructures of polyaniline composites containing nano-magnet, *Synth. Met.*, **132**, 205–212 (2003).
[72] Y. Long, Z. Chen, J.L. Duvail, Z. Zhang, and M. Wan, Electrical and magnetic properties of polyaniline/Fe_3O_4 nanostructures, *Physica B: Cond. Matter* **370**, 121–130 (2005).

[73] O.J. Murphy, G.D. Hitchens, D. Hodko, E.T. Clarke, D.L. Miller, and D.L. Parker, Method of manufacturing passive elements using conductive polypyrrole formulations, United States Patent 5855755 (1999).
[74] S. Sepulveda-Guzman, L. Lara, O. Perez-Camacho, O. Rodriguez-Fernandez, A. Olivas, and R. Escudero, Synthesis and characterization of an iron oxide poly(styrene-co-carboxybutylmaleimide) ferrimagnetic composite, *Polymer*, **48**, 720–727 (2007).
[75] W. Chen, X. Li, G. Xue, Z. Wang, and W. Zou, Magnetic and conducting particles: preparation of polypyrrole layer on Fe_3O_4 nanospheres, *Appl. Surf. Sci.*, **218**, 215–221 (2003).
[76] M. Pregelj, P. Umek, B. Drolc, B. Jancar, Z. Jaglicic, R. Dominko, and D. Arcon, Synthesis, structure, and magnetic properties of iron-oxide nanowires, *J. Mater. Res.*, **21**, 2955–2962 (2006).
[77] K. Suri, S. Annapoorni, and R.P. Tandon, Bull. Phase change induced by polypyrrole in iron-oxide polypyrrole nanocomposite, *Mater. Sci.*, **24**, 563–567 (2001).
[78] K. Suri, A. Annapoorni, R.P. Tandon, C. Rath, and V.K. Aggrawal, Thermal transition behavior of iron oxide-polypyrrole nanocomposites, *Curr. Appl. Phys.*, **3**, 209–213 (2003).
[79] A. Dey, A. De, and S.K. De, Electrical transport and dielectric relaxation in Fe3O4-polypyrrole hybrid nanocomposites, *J. Phys. Cond. Matter*, **17**, 5895–5910 (2005).
[80] K. Huang, M. Wan, Y. Long, Z. Chen, and Y. Wei, Multi-functional polypyrrole nanofibers via a functional dopant-introduced process, *Synth. Met.*, **155**, 495–500 (2005).
[81] C. Ortiz, G. Lim, M.M. Chen, and G. Castillo, Physical properties of spinel iron oxide thin films, *J. Mater. Res.*, **3**, 344–350 (1988).
[82] Y. Mei, Z.-J. Zhou, and H.L. Luo, Electrical resistivity of RF-sputtered iron oxide thin films, *J. Appl. Phys.*, **61**, 4388–4389 (1987).
[83] M. Omastova, K. Boukerma, M.M. Chehimi, and M. Trchova, Novel silicon carbide/polypyrrole composite; preparation and physicochemical properties, *Mater. Res. Bull.*, **40**, 749–765 (2005).
[84] K. Dutta and S.K. De, Transport and optical properties of SiO2-polypyrrole nanocomposites *Solid State Commun.*, **140**, 167–171 (2006).
[85] S.-J. Su and N. Kuramoto, Processable polyaniline-titanium dioxide nanocomposites: effect of titanium dioxide on the conductivity, *Synth. Met.*, **114**, 147–153 (2000).
[86] P.S. Abthagir and R. Saraswathi, Thermal stability of polypyrrole prepared from a ternary eutectic melt, *Mater. Chem. Phys.*, **92**, 21–26 (2005).
[87] Y. Long, J. Luo, J. Xu, Z. Chen, L. Zhang, J. Li, and M. Wan, Specific heat and magnetic susceptibility of polyaniline nanotubes: inhomogeneous disorder, *J. Phys. Cond. Matter*, **16**, 1123–1130 (2004).
[88] A.B. Kaiser, Electronic transport properties of conducting polymers and carbon nanotubes, *Rep. Prog. Phys.*, **64**, 1–49 (2001).
[89] A.B. Kaiser, Systematic conductivity behavior in conducting polymers: effects of heterogeneous disorder, *Adv. Mater.*, **13**, 927–941 (2001).
[90] P.E. Champness, *Electron Diffraction in the Transmission Electron Microscope*, Bios Scientific, Oxford, 2001.
[91] M.N. Baibich, J.M. Broto, A. Fert, F. Nguyen Van Dau, F. Petroff, P. Eitenne, G. Creuzet, A. Friederich, and J. Chazelas, Giant magnetoresistance of (001)iron/(001)chromium magnetic superlattices, *Phys. Rev. Lett.*, **61**, 2472–2475 (1988).
[92] A. Moser, K. Takano, D.T. Margulies, M. Albrecht, Y. Sonobe, Y. Ikeda, S. H. Sun, and E.E. Fullerton, Magnetic recording: advancing into the future, *J. Phys. D, Appl. Phys.*, **35**, R157–R167 (2002).
[93] R.L. Edelstein, C.R. Tamanaha, P.E. Sheehan, M.M. Miller, D.R. Baselt, L.J. Whitman, and R.J. Colton, The BARC biosensor applied to the detection of biological warfare agents, *Biosens. Bioelectron.*, **14**, 805–813 (2000).
[94] M.M. Miller, P.E. Sheehan, R.L. Edelstein, C.R. Tamanaha, L. Zhong, S. Bounnak, L.J. Whitman, and R.J. Colton, A DNA array sensor utilizing magnetic microbeads and magnetoelectronic detection, *J. Magn. Magn. Mater.*, **225**, 138–144 (2001).
[95] Y.F. Chen, R. Kaltofen, J.I. Mönch, J. Schumann, J. Freudenberger, H.-J. Klauß, O.G. Schmidt, Towards flexible magnetoelectronics: buffer-enhanced and mechanically tunable GMR of Co/Cu multilayers on plastic substrates, *Adv. Maters.*, **20**, 3224–3228 (2008).

[96] Z. Guo, H.T. Hahn, H. Lin, A.B. Karki, and D.P. Young, Magnetic and magnetoresistance behavior of particulate iron/vinyl ester resin nanocomposites, *J. Appl. Phys.*, **104**, 014314 (2008).
[97] D.L. Cocke and A. Clearfield, *Design of New Materials*, Plenum Press, New York, 1987.
[98] T.E. Karakasidis and C.A. Charitidis, Multiscale modeling in nanomaterials science, *Mater. Sci. Eng. C*, **27**, 1082–1089 (2007).
[99] Q.H. Zeng, A.B. Yu, and G.Q. Lu, Multiscale modeling and simulation of polymer nanocomposites, *Prog. Polym. Sci.*, **33**, 191–269 (2008).

13

Charge Transfer and Charge Separation in Conjugated Polymer Solar Cells

Ian A. Howard,[1,2] *Neil C. Greenham,*[1] *Agnese Abrusci,*[1]
Richard H. Friend,[1] *and Sebastian Westenhoff*[3]

[1] *OE-Group, Cavendish Laboratory, JJ Thomson Avenue, Cambridge UK*
[2] *Current Affiliation: Max Planck Institute for Polymer Research, Mainz, Germany*
[3] *Department of Chemistry, Biochemistry and Biophysics, University of Gothenburg, Sweden*

13.1 Introduction

Until the early 1970s polymers were considered to be insulating materials. This view was revolutionalized by the demonstration of metal-like conductivity in iodine-doped poly (acetylene) by Heeger and coworkers, which ignited research into the use of polymers as active components in electronic devices [1]. Another important breakthrough was achieved in 1990 when Friend and coworkers discovered electroluminescence in the semiconducting polymer poly(*p*-phenylenevinylene) (PPV) [2]. After only a few decades of development the optoelectronic properties of conjugated polymers are now of commercial as well as scientific interest, with organic light-emitting diode displays (OLEDs) and polymer transistor backplanes currently competing against their inorganic counterparts in the marketplace.

One large potential impact for conjugated polymers lies in the field of solar energy. Polymer solar-cell devices can be manufactured cheaply and with low embodied energy.

Nanostructured Conductive Polymers Edited by Ali Eftekhari

Furthermore, the production is expected to be easily scalable. This technology is currently developed by many researchers around the world, but has not yet reached the marketplace. In order for polymer solar cells to become economic their efficiency must be improved. The power conversion efficiency of a solar cell is dictated by three factors: (i) the fraction of sunlight that can be absorbed, (ii) the fraction of absorbed photons that lead to extracted charges ('internal quantum efficiency'), and (iii) the energy that is retained by the extracted charges (ideally close to the 'open-circuit voltage'). In this review we will refer often to factors (ii) and (iii). Their interplay is not well understood and at present these have not both been optimized simultaneously even in state-of-the-art organic solar cells.

Photon absorption in conjugated polymers results in formation of a bound electron–hole pair, termed an exciton, which must be split into charges to achieve photovoltaic energy conversion. This excited state has a Coulombic binding energy of around 0.5 eV. Therefore, separating the electron and hole directly from it requires impractically high electric fields. A much more promising approach is to form nanocomposites by blending electron donating and accepting organic materials. Excitons created close to the heterojunction may undergo a charge-transfer reaction at the interface and the charges can be further separated and transported to the electrodes by weak electric fields [3–5]. The active layer of the devices can be conveniently fabricated by mixing the two materials in organic solvents and spin-casting them onto a substrate. This creates partially demixed blends of the two materials with a large interfacial area, which is termed the 'bulk heterojunction'. We focus our review on the understanding of charge transfer in various blends used in organic solar cells. We will review how the overall device efficiency of polymer:polymer solar cells is related to the photophysical processes that occur at the heterojunction.

13.1.1 Polymer: PCBM Solar Cells

Organic solar-cell devices using regioregular poly(3-hexylthiophene) (P3HT) as a light absorber and electron donor and the soluble C-60 derivative [6,6]-phenyl-C_{61}-butyric acid methyl ester (PCBM) as an electron acceptor (PCBM is a weak absorber in the visible spectral region so its role in absorption is minimal) have power conversion efficiencies exceeding 5% [3,6]. For further detailed information about device physics, characterization, and fabrication the reader is referred to other recent reviews [7,8]. The power-conversion efficiency can be increased by stacking two or more active layers in a tandem cell configuration wherein each of the active layers is tailored to efficiently absorb a specific region of the solar spectrum. Using this approach a power conversion efficiency of 6.5% has been reached [9]. One advantage of PCBM/polymer solar cells is that the internal quantum efficiency, which is the ratio of charge carriers collected at the electrodes per absorbed photon, is high [6]. The main disadvantage is that PCBM is a very strong electron acceptor (see Figure 13.1), which implies that a significant amount of energy is lost in the charge-transfer reaction. This leads to a moderate open-circuit voltage of approximately 0.7 V in the best cases and imposes a significant constraint on the further optimization of this material system [10].

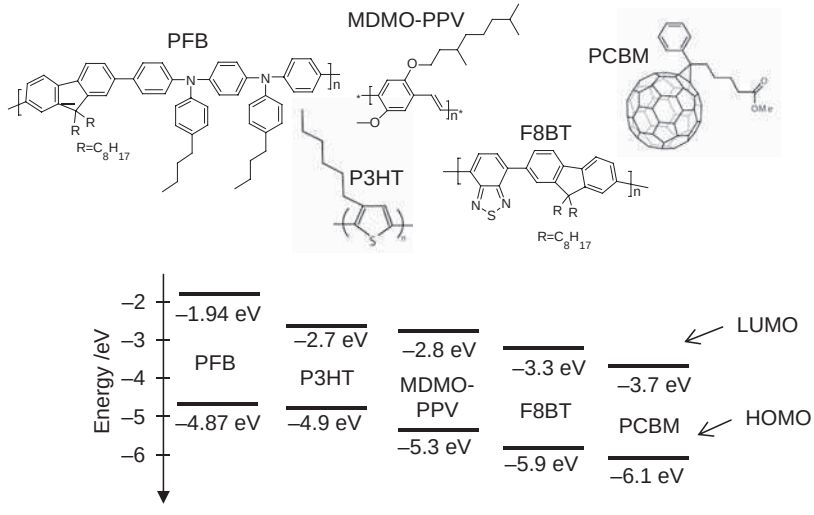

Figure 13.1 *Some popular materials for organic solar cells together with HOMO and LUMO values, all taken from the literature [12,84,114]. The HOMO levels were deduced by cyclic voltammetry and the LUMO level was calculated based on the HOMO level and the π–π* gap*

13.1.2 Polymer: Polymer Solar Cells

Solar cells based on two conjugated polymers can have smaller band-edge offsets than PCBM-based solar cells and therefore reach higher open-circuit voltages of around 1.3 V (see Figure 13.1). However, the internal quantum efficiencies of such systems are, in general, poor. This indicates that a significant amount of charges recombine before they are collected at the electrodes. The highest power-conversion efficiencies achieved in single-active-layer polymer:polymer solar cells are approaching 2% [11–13]. This is considerable lower than the efficiencies for polymer:PCBM solar cells. However, if the loss mechanisms that reduce the quantum efficiency in these devices can be reduced or circumvented, high power-conversion efficiencies, surpassing those of devices using PCBM as an electron acceptor, could be obtained.

Polymer:polymer solar cells have further potential advantages relative to PCBM-containing blends such as enhanced optical absorption and techniques to control mesoscale morphology. Increasing the fraction of solar photons absorbed, while maintaining the open-circuit voltage and quantum efficiency, is one approach to better power-conversion efficiency. Selecting two polymers that strongly absorb visible light in complimentary portions of the solar spectrum increases the fraction of absorbed photons and consequently raises the maximum achievable power-conversion efficiency [12,14]. The development of polymers that absorb in the near infrared will provide opportunities to utilize material combinations with very broad-band optical absorption [15]. In terms of control of the mesoscale morphology, which is a parameter critical in determining the quantum efficiency of the solar cell, polymer brushes, which are grown from one of the electrodes [16,17], and block copolymers, which can be used to form a wide variety of mesophases,

are attractive options. The use of a block copolymer to form a bicontinuous double-gyroid template that is selectively dissolved and replicated in titanium dioxide has been demonstrated in a dye-sensitized solar cell of the Grätzel type [18]. Manufacturing such ordered phases directly from a block copolymer made from two conjugated materials would provide a greater control of domain morphology compared to that currently achieved by partial demixing of two component solutions during film formation. This control might be used to address quantum-efficiency loss mechanisms by a more precise control of domain size and interfacial area.

13.1.3 Polymer: Inorganic Nanoparticle Solar Cells

Various types of colloidal inorganic nanoparticles can be used as electron donors or acceptors in polymer-based solution-processed solar cells. Colloidal nanocrystals consist of a roughly spherical core of an inorganic material with a diameter of less than 10 nm, surrounded by a coating of an organic ligand that passivates the nanocrystal surface and also stabilizes the nanocrystals in solution by preventing aggregation [19,20]. The optical and electronic properties of nanoparticles can be tuned by the particle size. The first report on polymer:nanoparticle solar cells used cadmium selenide nanoparticles as an electron acceptor [21]. Volatile ligands were used that could be removed from the surfaces of the nanoparticles after a blend film was formed. This facilitated charge transfer by allowing nanoparticle and polymer to come into direct contact. Subsequently, nanoparticles with more exotic shapes, including high-aspect-ratio rods and tetrapods, have been developed in the attempt to improve charge transport in solar-cell device structures [22–25]. Also, devices utilizing nanoparticles that extend the absorption of the solar cell into the infrared [26,27] and devices made from less toxic and environmentally damaging materials have been developed [28]. The best power-conversion efficiencies achieved to date are in the region of 2–3% [28–30]. The mechanism and rate of charge transfer between polymer and nanoparticle are still not well understood, and are complicated by the possible influences of organic ligands and nanoparticle surface states. Furthermore, in many cases energy transfer from a polymer exciton to a nanocrystal exciton could precede or compete with charge transfer. Recent studies of charge transfer between nanoparticles and surface-adsorbed ligands are beginning to address these issues and provide estimates for charge-transfer rates in the solid-state blend [31,32].

13.2 Charge Transfer in Conjugated Polymers

In this section we review theoretical and experimental results important for understanding the photophysics of polymer solar cells. We examine the states that are involved in the processes of photoinduced charge generation, and present a theoretical framework that describes the separation and recombination of charge-transfer states. Finally, we review the mechanisms for charge formation that operate in a film of a single conjugated polymer and the additional mechanisms, relevant to solar cell devices, that occur in binary donor:acceptor blends.

13.2.1 Excitons as the Primary Photoexcitations

In the early literature there was significant debate regarding the singlet exciton binding energy, and therefore the ease with which dissociated polarons could be created in a conjugated polymer following photoexcitation. Some interpretations of transient optical absorption and transient photoconductivity measurements suggested that free charges could be directly produced by photoexcitation with a yield of up to 90% [33,34]. Other experiments suggested that optical excitation exclusively led to singlet excitons with significant binding energies [35]. Although charge generation in conjugated polymers depends strongly on the disorder, morphology, and purity of the sample, the early discrepancies were later attributed to experimental artifacts caused by the high photon fluxes used in the initial optical-spectroscopy experiments [36]. It is now widely accepted that the primary photoexcitation is singlet excitons with a significant Coulombic binding energy of approximately 0.5 eV. As the exciton binding energy is around 20 times higher than thermal energy at room temperature, charges do not spontaneously form. The high binding energy is a fundamental property of organic oligomers and polymers, and arises from the weak screening of charges in organic materials, substantial electron–electron correlation and geometric relaxation effects [37].

Excitons are localized on a small number of repeat units (few nanometers) and do not extend over the whole polymer chain. An exciton in a conjugated polymer is thus very similar to its counterpart in a photoactive small molecule, but has little in common with extended, weakly bound excitons in inorganic semiconductors.

13.2.2 Charge Transfer at Semiconductor Heterojunctions

In order to facilitate efficient ionization of the exciton, bulk heterojunction structures are used, at which the excitons can undergo a charge-transfer reaction at the interface between an electron-donating and an electron-accepting material. Depending on the relative alignment of the HOMOs (highest occupied molecular orbitals) and LUMOs (lowest unoccupied molecular orbital) of the two semiconductors, two regimes are distinguished, as sketched in Figure 13.2. A ‘type I’ heterojunction does not lead to charge transfer, but rather exciton transfer at the heterojunction. In case of a ‘type II’ heterojunction, charge transfer is supported and it is therefore the alignment regime of choice for organic photovoltaics. Once an exciton is photogenerated in the electron-donating material, electron transfer can occur if there is a favorable difference in LUMO energy levels of the two materials. Likewise, an exciton generated in the electron-accepting material can ionize and a hole is transferred to the electron-donating material. The offsets in between the HOMOs and LUMOs, respectively, have to be larger than exciton binding energy minus the binding energy of the charge-transfer state that is formed. As a rule of thumb, band offsets of >0.4 eV are sufficient for charge generation to occur.

After ionization of the excitons, the spatial separation of electrons and holes is small, i.e. <10 nm. Therefore, the charges attract each other by Coulomb interaction, and cannot be thought of as two independent freely moving species (Figure 13.2b). In the literature on organic solar cells this situation is described as ‘bound electron–hole pairs’, or ‘geminate electron–hole pairs’. The separation of electron and hole can be so small that their

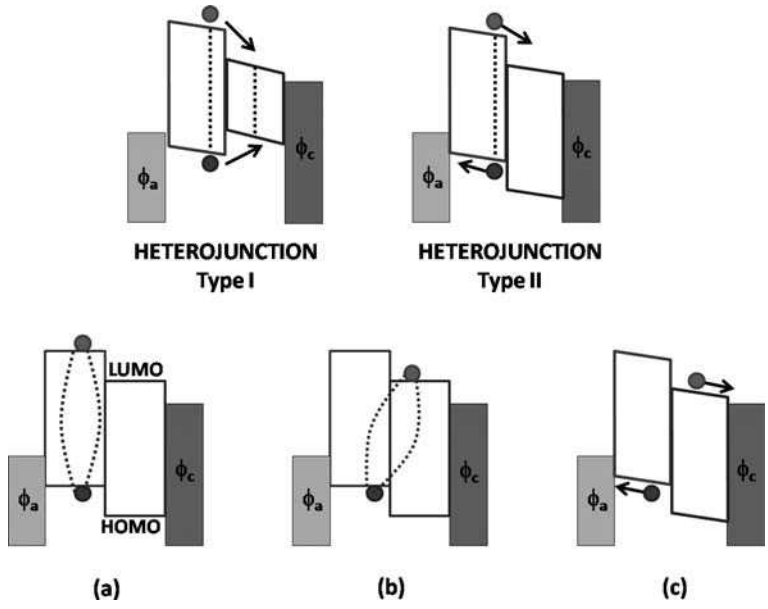

Figure 13.2 *Schematic energy-level diagram for 'type I' and 'type II' organic semiconductor heterojunctions where Φ_a and Φ_c, the electrodes' work function are also indicated. For type II, panel (a) shows a tightly bound exciton on the hole-transporting material and panel (b) shows a weakly bound charge-transfer state at the interface after exciton ionization. Both cases are in the flat-band regime. Figure (c) shows the device under short-circuit conditions. The separation of the charge-transfer state at the interface is assisted by the internal electric field*

wavefunctions overlap [38], allowing absorption and/or photoluminescence from these states to be observed [39–41]. The states were initially identified by their photoluminescence in polymer:polymer blends and termed 'exciplex' [40], because an associated absorption was not observed. However, more recently it was demonstrated in PCBM: polythiophene blends, that corresponding states may absorb photons, and accordingly they were classed as 'charge-transfer states' [39]. In order to simplify the nomenclature we will use the term 'charge-transfer state' in this chapter to describe all states where the two charges are placed directly at the heterojunction. Charge-transfer states are closely bound and are characterized by wavefunction overlap. This is not a requirement for classification as geminate charge pairs, where significant Coulomb interaction is characteristic.

Charge-transfer states play a key role in organic solar cells as they dictate the rates for charge separation and recombination. A 'free' charge can be transported to the electrodes and may contribute to the photocurrent, whereas a charge trapped by its counter-charge in a charge-transfer state may not. The internal electric field will assist the separation of charge-transfer states and help the charges to move away from each other, in the appropriate direction for charge collection in the external circuit (Figure 13.2c). The competition between charge-transfer state separation and recombination can account for the major quantum efficiency loss mechanism in various classes of organic solar cell (see below) [42–44].

We also note that charge-transfer states play a central role in OLEDs. Whereas recombination of charge-transfer states is an unwanted loss mechanism in organic solar cells, it is vital for the operation of OLEDs. Indeed, blends of conjugated polymers with type II band alignment and metastable interfacial charge-transfer states can be used to fabricate highly efficient OLEDs [40]. In this case, the charge-transfer state acts as a weakly emissive, but long-lived, energy reservoir that can endothermically transfer into a highly emissive singlet exciton on one blend component.

13.2.3 Charge Transport

After splitting of the exciton at the heterojunction and further separation of the charge-transfer state, the charges (or polarons) need to be transported within the semiconductor materials network to the respective electrodes. Despite the recognition that it is mainly the separation of the charge-transfer states that limits current polymer:polymer solar-cell devices, charge transport also has to be considered, because it is another potential loss mechanism. We will briefly cover this topic; the interested reader is referred to a recent review by Blom *et al.* [7].

In amorphous films of conjugated polymers, the lack of crystalline lattice structure prevents the charge-transport mechanism from being considered band-like; instead the charge-transport process has to be regarded in terms of a hopping of carriers between localized states [45]. Moreover, defects, kinks, and twists disrupt the polymer backbone conjugation giving mobility in the range of 10^{-12}–10^{-10} m^2 Vs^{-1} for polymer LEDs and photovoltaics. Three main models have been developed to justify such low mobilities in disordered polymer semiconductors. The polaron model accounts for the strong electron–phonon coupling in conjugated polymers, which leads to relaxation of the polymer backbone around the charge. If enough thermal energy is available, the polarons may hop between adjacent sites. In this representation, which is theoretically described by Marcus theory [46], the hopping probability for a carrier increases with the electric field. Although the activation energy varies considerably between materials, it has been estimated to range between 25 and75 meV by using this model [47].

Bässler's Gaussian disorder model for disordered conjugated systems introduces energetic and positional disorder [48]. Energetic disorder is approximated by a Gaussian density of states (DOS), which is motivated by the Gaussian profile of the polymer's excitonic absorption spectra and the recognition that the polarization energy is determined by a large number of internal coordinates, so the central limit theorem of statistics holds. The charge transport using the Gaussian disorder model cannot be solved analytically, hence Monte Carlo simulations are used [48,49]. Using the hopping rate described by the Miller–Abrahams formalism, Monte Carlo simulations reveal that the charge-carrier mobility is temperature and field dependent. The Gaussian disorder model agrees with experimental data only at high electric fields, a problem that has been attributed to the absence of correlation of energies of adjacent sites in the original model [50].

An alternative model to account for low mobilities in organic semiconductors is the multitrapping and release model. Traps are localized levels as lattice defects or impurities in which charge carriers are immobilized. The ones localized near the center of the bandgap are called deep traps, while the ones close to the conduction or valence band

are called shallow traps. The model considers all charges below a certain energy as trapped, and all those above, as free. A thermally assisted process releases the charges, which can move through the lattice until they meet another trap site. Transport of charge carriers in this model depends on the energy levels of the trap states and the applied voltage [51]. Although the temperature dependences of the mobility extracted by using the disorder, polaronic, or multitrapping models are different, none of them has been universally approved or disapproved. This may be because it is difficult to correctly interpret the experimental data, as the accessible temperature range is small. There has been intense research effort to refine the transport models, as well as try a unified interpretation of the experimental data [52]. For a disordered organic system, it is most likely that charge transport will be a superposition of the three effects: trapping, disorder (more important at low temperature), and polaronic (more important at high temperatures).

With respect to organic photovoltaic devices, it is important that the electron and hole mobilities in the electron- and hole-accepting materials, respectively, are high and that they are balanced. This is due to two reasons: (i) The charge carriers have a higher probability to escape geminate recombination if their initial mobility is high and (ii) afterwards, high and balanced mobilities are important to efficiently sweep the charge carriers out of the device with a high quantum efficiency. However, it is not straightforward to determine the mobilities in the devices, because the intimate mixing in a bulk heterojunction cell prohibits extrapolation of mobilities obtained from pristine polymer films. Therefore the mobilities have to be measured *in situ* [7]. Furthermore, the small domain size used in bulk heterojunction cells may cause electrons and/or holes to be trapped in domains, which have to be connected to the matching electrode. This issue is particularly problematic, because increasing the domain size will decrease the exciton ionization efficiency (see below) and it is at present not possible to reliably control the shape and relative alignment of the domains.

13.2.4 Photoinduced Charge Transfer

We now discuss in greater detail how charges can be created after photoexcitation, first in the case of pristine polymers and then in donor:acceptor blends with type II heterojunctions. In general, we consider a two-step mechanism: first, the singlet exciton is transformed into a charge-transfer state. This state is intermediate between exciton and 'free' charges. It is characterized by a larger charge separation than the exciton, but the electron and hole are still bound by their mutual Coulomb attraction and have a varying degree of wavefunction overlap [38]. In pristine materials this charge-transfer state may be either intra- or intermolecular, with the electron and hole wavefunctions centered on the same or different polymer chains. Once the charge-transfer state is created, the electron and hole may either recombine with each other (geminate recombination) or, with the assistance of a field or thermal energy, hop apart and escape their mutual attraction. The three cases of charge generation that we will consider are schematically illustrated in Figure 13.3. Panel (a) shows charge generation via highly excited singlet state in a pristine conjugated polymer. Panel (b) depicts the process of charge generation via a singlet state assisted by thermal activation or an applied electric field in a pristine conjugated polymer. Finally, panel (c) shows the case relevant to organic solar cells under solar illumination, where

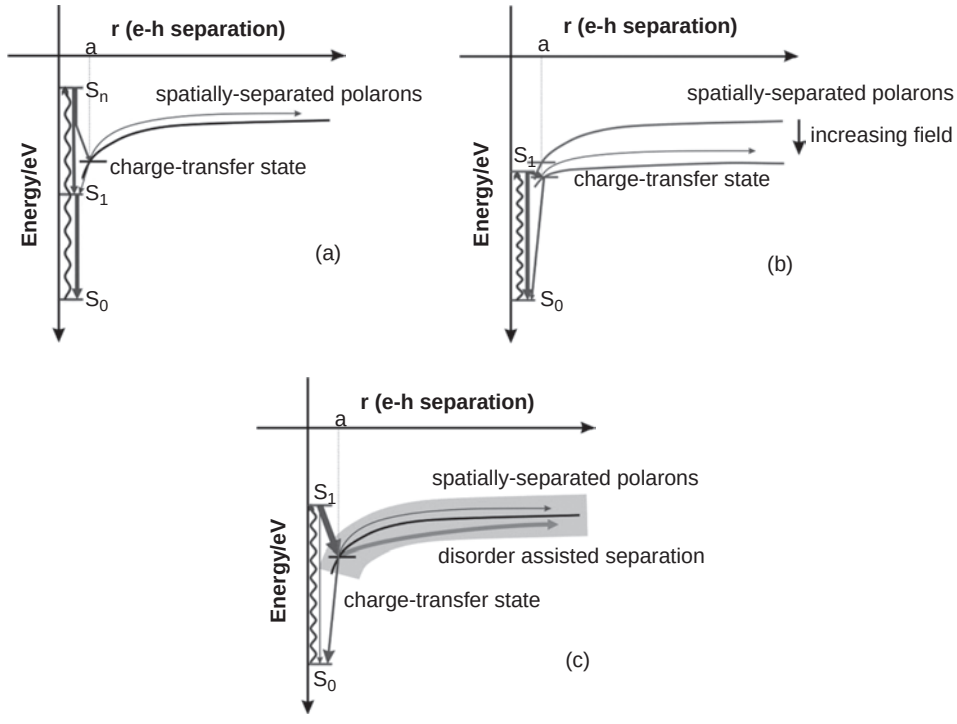

Figure 13.3 *Charge-transfer state generation and separation. The energetics of charge-transfer state generation and subsequent separation are shown for (a) a highly excited singlet state in a pristine material, (b) thermal excitation or electric field assistance in a pristine material, and (c) a donor-acceptor blend*

charge generation occurs by exciton ionization at an interface between two materials with appropriately aligned band offsets (the type II heterojunction, introduced above).

We note at this point that the concepts and language used to describe the photophysics of organic electronics very much reflect the different backgrounds of the researchers participating in this field. Initially, physicists developed models based on band theories. However, motivated by the insight that the device physics are significantly affected by localized states, a more chemistry-oriented theoretical framework based on molecular excitations has been established in recent years. Each of these approaches has merits, it is easy to rationalize the energetics of semiconductor heterojunctions (see Figure 13.2) using a sketch that is inspired by 'physical' band theories. On the other hand, it is more intuitive to address the question of charge-transfer state recombination and separation, which we will discuss in the following, using a 'chemical' framework based on molecular excitations. We therefore, use either the 'physical' or 'chemical' framework as simplicity and convenience of understanding dictate while discussing the photophysics of organic bulk heterojunction solar cells. With reference to continuity (and terminology), this situation may be undesirable, but we believe this deficit is justified in order to present the concepts most intuitively case to case.

13.2.5 Onsager–Braun Model of Charge-Transfer State Dissociation

Before we discuss the various cases for charge-transfer state generation and recombination, we will briefly review Onsager–Braun theory [53], which is commonly used to describe the charge-transfer state separation into free and mobile charge carriers. Onsager–Braun theory is based on Onsager's model of charge dissociation in organic crystals [54], and is similar to a special case in the more general model developed by Tachiya and Sano [55]. An alternative description that considers the role of interfacial dipoles at the heterojunction has been proposed by Arkhipov [56]. Onsager theory determines the probability that an electron and hole in a charge-transfer state escape from each other. It considers that the electron and hole both move in the same material. The electron and hole in the charge transfer are assumed to have some initial degree of spatial separation. Subsequently, the electron and hole may diffuse, but are somewhat bound to each other by their mutual Coulomb attraction. If their separation ever becomes zero they instantly recombine. If they hop apart far enough that their Coulomb attraction becomes negligible, they become considered free (spatially separated). This model was modified by Braun to better represent systems in which the charge-transfer state was relatively stable, as is the case in donor–acceptor blends. He assumed that the charges would not instantly recombine if they met, but instead considered that their decay could be described with a finite rate constant [53]. The fraction of charge-transfer states that separates can then be calculated from the kinetic competition between separation and relaxation as:

$$P(F,T) = \frac{k_{dis}(F,T)}{k_{dis}(F,T) + k_r}, \tag{13.1}$$

where $k_{dis}(F, T)$ is the field and temperature dependent dissociation rate. The expression for $k_{dis}(F, T)$ is given by

$$k_{dis}(F,T) = \nu \exp\left(-\Delta E/kT\right)(1 + b + b^2/3 + b^3/18 + \ldots). \tag{13.2}$$

where

$$\nu = \frac{3\langle\mu\rangle e}{4\pi\langle\varepsilon\rangle/\varepsilon_0\, a^3}, \tag{13.3}$$

$$b = \frac{e^3 F}{8\pi\langle\varepsilon\rangle\varepsilon_0 k_b^2 T^2}, \tag{13.4}$$

The barrier to dissociation is given by the Coulomb energy of the initial pair as $\Delta E = e^2/\left(4\pi\ \langle\varepsilon\rangle\ \varepsilon_0 a\right)$, and the summation is an approximation of the Bessel function of order one. Here the dielectric constant and mobility, $\langle\varepsilon\rangle$ and $\langle\mu\rangle$ represent the spatially averaged values accounting for both materials in a blend. This averaging of the properties of the materials is the only way in which a blend of donor and acceptor material is accounted for in Braun–Onsager theory. No explicit consideration of the mesoscale morphology is included. This problem can be overcome by using Monte-Carlo schemes in which charge-carrier migration is modeled in realistic blend morphologies [57,58]. Nevertheless, the Onsager–Braun model provides a qualitative view of charge-transfer state separation that

is very useful. The separation of charge-transfer states is temperature activated and enhanced by the application of an external electric field. Furthermore, the efficiency of separation scales with the spatially averaged mobility of the two materials. We will consider that this general picture of charge-transfer state separation applies to all the cases below, and examine how the formation and relaxation of the charge-transfer state varies from case to case.

13.2.6 Charge Formation from High-Lying Singlet States in a Pristine Polymer

Excitons in high-lying states can directly form charge-transfer states, as shown in Figure 13.3a. For example, when the singlet exciton is in a high-lying singlet exciton state S_n, with energy greater than the charge-transfer state energy, it can either relax via internal conversion to the S_1 state or form an intra- or interchain charge-transfer state. The formation of the charge-transfer state in this way is assisted by the greater electron–hole separation in the wavefunctions of high-lying excitons 59. The scheme as drawn in Figure 13.3a is supported by a wide range of experimental evidence. First, examination of the steady-state photocurrent in pristine materials as a function of incident photon energy shows that photocurrent is only generated from photons with at least 1 eV of energy in excess of the optical bandgap [59–61]. Ultrafast laser experiments, in which highly excited excitons can be created by sequential absorption of photons, by exciton–exciton annihilation, or by excitation with photons much higher in energy than the band gap, provide also evidence for this route of charge-transfer state generation [62–66]. Recently it was reported that charge-transfer states may also be generated from excited triplet states in a polyfluorene [67]. The rate of charge-transfer state formation must compete with internal conversion from the S_n to S_1 level, which occurs on the order of 100 fs. In order to generate spatially separated charges from the charge-transfer state, it has to separate, which competes with the relaxation of the charge-transfer state either back to an exciton (which is in this case exothermic) or its direct recombination to the ground state. Recent work on the photophysics of poly(phenylenevinylene) show that only around 1% of the S_n states create charge-transfer states, and of these only around 10% become spatially separated [68,69]. Thus, the total yield of extractable charges generated by such a method is very low. Exceedingly little photocurrent can be created in an organic solar cell by this mechanism, because the mechanism is inefficient and also because extreme excitation conditions are needed to generate a significant quantity of S_n states.

13.2.7 Field-Assisted Charge Generation in Pristine Materials

The generation of a charge-transfer state from an S_1 singlet exciton can occur in the presence of a sufficiently large external electric field. The external field alters both the energy of the charge-transfer state and the potential barrier it needs to overcome in order to further separate into spatially separate polarons, as shown in Figure 13.3b. Studies using bias-dependent transient absorption spectroscopy on ladder-type PPV and poly (9,9-dioctylfluorene) have shown that charges can be created from excitons over their entire lifetime [70,71]. These findings show that exciton splitting and generation of a charge-transfer state can itself be field dependent. When this is the case, Onsager–Braun

theory will not correctly predict the number of photoexcitations that separate because the model considers only the bias dependence of charge-transfer state separation and neglects any bias dependence of the initial charge-transfer state generation. We note that in solar cells the built-in field from the work-function difference of the metallic contacts is too weak to dissociate a sufficient amount of excitons within their lifetime. Therefore organic solar cells based on pristine material are very inefficient, and the rate of exciton splitting and charge-transfer state generation can be considered field independent.

13.2.8 Charge Generation in Donor: Acceptor Blends

The inability to efficiently create charges from excitons in a pristine conjugated polymer has led to the use of blends of electron-donating and -accepting materials to energetically stabilize charge-separated states with respect to excitonic states in organic solar cells [3,5,34]. The energy levels of the various states in the blend are summarized in Figure 13.3c. If the alignment of the HOMOs and LUMOs is appropriate (a type II heterojunction), the charge-transfer state has a lower energy than the singlet excitons on both materials (as indicated in Figure 13.3c). Thus, it will form spontaneously when the exciton approaches the interface between the electron donor and acceptor. The ionization efficiencies of excitons in blends depend on the natural lifetime of the excitons and the time it takes for an exciton to travel to the nearest interface. This in turn depends on how far the exciton has to travel to reach a heterojunction (ie. the sample morphology) and how quickly the exciton moves. To achieve high yields of exciton ionization, the domain size of each component within the blend should not be greater than an exciton diffusion length, which is typically assumed to be on the order of 10 nm.

In order to uncover the photophysical processes and the loss mechanism in polymeric solar cells, two main approaches can be distinguished: electrical measurements and time-resolved optical spectroscopy. Electrical measurements have the fundamental disadvantage that they lack time and spatial resolution to probe the processes that occur directly after exciton ionization. To investigate these dynamics, time-resolved spectroscopy is a much more promising approach, because ultrafast laser systems allow observing these processes directly with subpicosecond time resolution.

Figure 13.4 shows a summary of the photophysical processes in polyhtiophene:PCBM blends, as presented in recent work by Durrant and coworkers [10]. The generation of charge-transfer states (which are labeled in Figure 13.4 as BRP: 'bound radical pairs') from excitons can be observed in real time by using femtosecond transient absorption spectroscopy [72–74]. A consensus in the literature has been reached with regard to the timescales of initial charge-transfer state generation, which was found to be 45 fs in a study where sub-10-fs pulses were used [72]. This time constant was measured at a high concentration of electron-accepting PCBM molecules, where exciton diffusion within the polymer domains can be neglected. Theoretical studies highlight the importance of phonon modes in this ultrafast reaction [75,76]. It was also found that the charge-transfer time and efficiency depend on the blend composition [72,73], which was assigned to exciton migration prior to charge transfer. Interestingly, the maximum charge-generation efficiency was found for PCBM contents from 20 wt% to 50 wt%, whereas the maximum short-circuit current density, which is indicative of the most efficient solar cells, is found

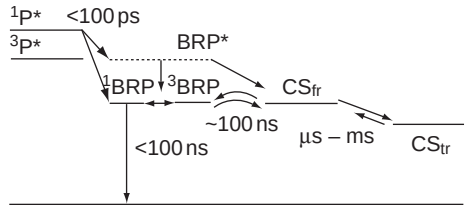

Figure 13.4 *Charge generation in PCBM:polyhtiophene solar cells. Charge-transfer state generation, separation, and recombination rates for P3HT:PCBM are shown. (Reprinted with permission from Journal of the American Chemical Society, Charge Carrier Formation in Polythiophene/Fullerene Blend Films Studied by Transient Absorption Spectroscopy by H. Ohkita, S. Cook, Y. Astuti et al., 130, 10, 3030–3042. Copyright (2008) American Chemical Society)*

for 80 wt% PCMB content [73]. The discrepancy must be related to a more efficient charge transport out of the device and/or a lower nongeminate charge-recombination rate in blends with higher PCBM contents. This reflects a general tradeoff that research into bulk heterojunction solar cells faces: if the polymer or PCBM domains get too big (as in the case of 80 wt% PCBM content), the exciton ionization efficiency is not optimal and if the domains are two small, the charge-transfer states will not separate and/or the charge transport to the electrodes is inhibited.

It seems intuitive to also follow processes subsequent to exciton ionization, i.e. charge separation and transport, with transient absorption spectroscopy. Unfortunately, this is made challenging by the fact that charge-transfer states and free charges both show broad and unstructured photoinduced absorption in amorphous polymers. P3HT:PCBM blends, however, are a fortunate case, because the absorption of charges in the polycrystalline P3HT changes significantly depending on their confinement. The spectral signature of a charge localized on a single P3HT chain is very different to that of a charge delocalized over several P3HT chains in a crystalline domain [77]. This signature can be used to detect spatially separated charge carriers that have migrated away from the interface into a crystalline polymer region [74].

The rates of charge-transfer state separation and geminate and nongeminate recombination of charges have been examined using transient absorption spectroscopy on nanosecond to microsecond timescales in PCBM:polythiophene blends [10,74,78–80]. The charge-transfer state (labeled 'BRP' in Figure 13.4) may recombine geminately or further separate into spatially separated charges (labeled 'CS' in Figure 13.4). The timescale for both of these processes are on the order of 100 ns [10]. Hwang *et al.* report a much faster charge separation time (picoseconds) [74]. Despite this discrepancy, it is agreed that the rates vary with material system and morphology, and have been shown to limit the efficiency of organic solar cells [80,81]. For example, the ratio of charge-transfer state recombination to separation depends strongly on the annealing conditions and associated morphological changes [42,74,82]. Finally, the separated charges can recapture an opposite charge and undergo bimolecular recombination, become trapped in a low mobility state leading to trap-assisted recombination ('CS$_{tr}$' in Figure 13.4), or be extracted from the solar cell. It has been suggested that 'hot' charge-transfer states ('BRP' in Figure 13.4)

transform faster into spatially separated charges than cooled charge-transfer states, which is also indicated in Figure 13.3 [10]. This would mean that charge-transfer states created with significant excess energy (for example those created from excitons) would be more likely to separate than charge-transfer states created with little excess energy (for example those that are reformed due to bimolecular charge capture).

The work on PCBM:polythiophene blends underlines that, in order to increase the efficiency of organic solar cells, the kinetics of the charge-transfer state are a key factor. To improve device efficiency the rate of charge-transfer state recombination should be reduced and the rate of separation of charges from the charge-transfer state should be increased. In order to modify these rates the mechanisms by which the processes occur must be understood in greater detail.

13.2.9 Mechanisms of Charge-Transfer State Recombination

In the previous section we discussed that the solar-cell quantum efficiency is affected by the ratio of charge-transfer states that separate to those that recombine. In order to gain

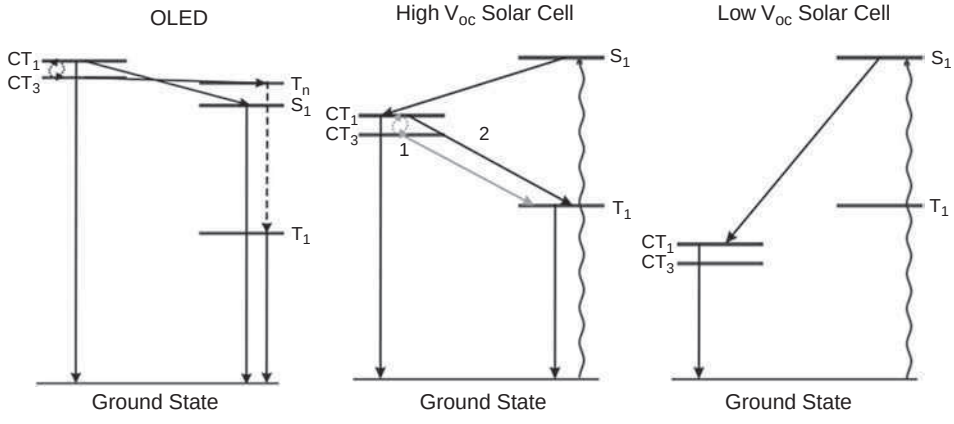

Figure 13.5 *Energy diagrams of charge-transfer state recombination. Panel (a) shows that in OLEDs the charge-transfer state can recombine into a singlet or a triplet exciton. Transfer from the charge-transfer triplet (CT^3) to T_1 is in the Marcus inverted region, so transfer proceeds via a higher lying triplet state (T_n). Depending on the relative energy of the T_n with respect to the CT^3 and S_1 states, this may lead to slower recombination of the triplet charge-transfer state than the singlet charge-transfer state (CT^1) [115], which helps explain the high electroluminescent efficiencies found for OLEDS made from some conjugated polymer blends. Panel (b) shows the possible recombination pathways in a high open-circuit voltage (V_{OC}) solar cell. The charge-transfer states can directly recombine into the ground state (for example by exciplex emission [40]), and also into lower-lying triplet exciton states. The mechanism for recombination into the triplet exciton could involve: (i) intersystem crossing within the charge-transfer state manifold, followed by electron transfer, or by (ii) electron transfer from the singlet charge-transfer state to the triplet manifold by spin–orbit coupling. Panel (c) shows the simple case of recombination in a low-V_{OC} solar cell, such as for PCBM:P3HT, wherein the T_1 state is thermodynamically inaccessible and the charge-transfer states recombine directly to the ground state*

more insight into what limits the rate of charge-transfer state recombination we now examine more closely the specific pathways and mechanisms involved in it. We agree with the recent statement of Brédas *et al.* that 'it is remarkable to realize that, at this point in time, our understanding of the charge generation and recombination processes is still rather limited' [83]. One theme that we examine is the role of triplet states in charge recombination.

The possible relaxation pathways for charge-transfer states of varying energy are shown in Figure 13.5. The relative energy of the charge-transfer state with respect to the excitonic levels is correlated with the band offsets between HOMOs and LUMOs of the electron-donor and -acceptor molecules. Larger band offsets, which imply lower open-circuit voltages, lead to charge-transfer states with lower energies. As the charge-transfer state varies in energy from the highest excited state (as in OLEDs), to the lowest excited state (as in photovoltaic blends with a very strong electron acceptor like PCBM) we see that the energetic channels available for charge recombination vary. As the energy drop in the charge-transfer reaction increases, the open-circuit voltage of the solar cell decreases. We note that in photovoltaic blends with a high open-circuit voltage, the role of triplet states could clearly play a role in relaxation. This has only recently been realized [79] and we present in the following a detailed discussion of this situation.

13.3 Charge Generation and Recombination in Organic Solar Cells with High Open-Circuit Voltages

In this section we will discuss spectroscopic studies of the energy flow in a model blend of two conjugated polyfluorenes that exhibits a high open-circuit voltage ($\sim$1.3 V) in solar cells (see Figure 13.1) [84]. The band-edge offsets (see Figure 13.1) are optimized for exciton ionization at the heterojunction, but are small enough so that a high open-circuit voltage of 1.3 V is achieved. The polymers are poly(9,9-dioctylfluorene-*alt*-benzothiadiazole) (F8BT) and poly(9,9-dioctylfluorene-co-bis-*N,N′*-(4,butylphenyl)-bis-*N,N′*-phenyl-1,4-phenylene-diamine) (PFB) with molecular weights $M_p = 135$ kg mol^{-1} and $M_p = 150$ kg mol^{-1}, respectively (see Figure 13.1). When mixed in organic solvents, such as chloroform, toluene etc., and spin-coated onto a substrate, the blend partially demixes, which is a general property of polymeric materials [85]. The degree of demixing can be controlled by changing the drying time, in order to form domains with characteristic sizes ranging from less than 10 nm to micrometers. The boiling point of the solvent is a convenient way to control the drying time [8]. Alternatively, the blends can be annealed above the glass transition temperature of the polymers to facilitate phase separation [84]. If not noted otherwise, all the experiments summarized in the following are performed on PFB:F8BT blends spin-cast from chloroform. Atomic force microsocopy (AFM) cannot resolve distinct features on the surface of these films, which suggests a domain size of less than 10 nm [84]. In solar cells, this blend gives a moderate power-conversion efficiency, which is due to its low quantum efficiency of roughly 3.4% [84]. We will argue that this poor quantum efficiency is due to substantial geminate recombination of charge-transfer states.

13.3.1 Exciton Ionization at Polymer: Polymer Heterojunctions

Figure 13.6 shows femtosecond to picosecond transient optical absorption data for F8BT:PFB blends in the visible region. The lower-band-gap polymer, F8BT ($\lambda_{max} =$ 475 nm), is excited selectively at 490 nm, so that no excitons are generated in the higher-optical-gap material PFB ($\lambda_{max} = 390$ nm). In pure F8BT, positive and negative differential transmission signals ($\Delta T/T$) are observed due to the stimulated emission and photoinduced absorption of excitons at wavelengths shorter than and longer than 620 nm, respectively (see Figure 13.6a) [63,84]. The transient absorption spectra of the blends show the same features at early times, which then rapidly evolve into a secondary broad and long-lived absorption. The latter band is a typical signature of equal populations of PFB cations and F8BT anions [63,80,84,86]. Figure 13.6c shows the time evolution of the signal, spectrally averaged from 530 nm to 600 nm. In this wavelength region a positive signal corresponds to stimulated emission of singlet excitons and a negative signal is due to photoinduced absorption of the charge-transfer state. Thus it is a convenient monitor of the

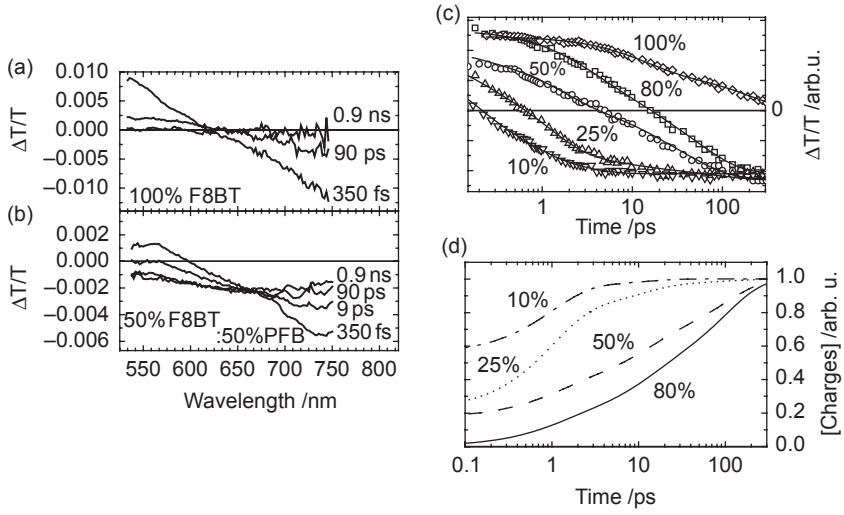

Figure 13.6 *Exciton ionization in PFB:F8BT blends measured by femtosecond transient absorption spectroscopy. Panels (a) and (b) show differential transmission spectra of pure F8BT and a 50 wt%:50 wt% blend, respectively, at delay times as indicated in the figure. The markers in panel (c) show the kinetics spectrally integrated from 530 nm to 600 nm. The F8BT content is indicated and was controlled by manipulating the ratio of F8BT and PFB in solution. The traces are normalized to the number of absorbed photons. The excitation photon flux was* $< 1 \times 10^{14}$ *photons* cm^{-2} *for all samples and low enough to avoid charge generation by multiphoton interaction [63]. The lines are a global fit to a generic kinetic model to deconvolve the time dependence of charge and exciton species (see [87] for details). Panel (d) shows the concentration of charges reconstructed from the fits. (Reprinted with permission from Physical Review Letters, Probing the morphology and energy landscape of blends of conjugated polymers with sub-10 nm resolution by S. Westenhoff, I. A. Howard and R. H. Friend, Physical Review Letters, 101, art.no. 016102. Copyright (2008) American Physical Society)*

charge-transfer dynamics. Similar experimental data sets collected for PFB:F8BT films under different annealing conditions were used to assess the efficiency of charge generation as a function of annealing temperature [84]. In Figure 13.6c it is observed that the time for the evolution from the positive 'singlet exciton' to the negative 'charge' signal increases with increasing concentration of F8BT. This indicates that the charge generation is limited by diffusion of excitons to the heterojunction. This is also highlighted in panel (d), where the concentration of charges is plotted as a function of time, with the data extracted from panel (c) by a fit to a generic kinetic model [87]. The initial amplitude in the data in Figure 13.6d corresponds to charges formed by excitons that are generated at the heterojunction. The charge transfer from excitons that do not have to migrate to the heterojunction is ultrafast (<100 fs), which is consistent with charge-transfer times in PCBM:P3HT blends and with theory [72,75]. The larger the polymer domains, the longer the excitons have to diffuse before they arrive at the heterojunction to ionize. This data can therefore be used to extract information about the phase size of the polymer blends on a length scale of less than 10 nm, which is not accessible by other techniques.

Two methods to determine the morphology of the blends were recently demonstrated by us based on data shown in Figure 13.6 [87]. The first method relies on initially measuring and modeling the kinetics of exciton diffusion in a pristine film. Exciton diffusion is modeled as hopping of Frenkel excitons, which are thought to be localized on extended segments of the conjugated backbones. This method yields the maximum displacement , R_{max}, of excitons as a function of time due to diffusion. With the knowledge of R_{max}, the charge generation time (see Figure 13.6d) can be translated into the distribution of distances that excitons have travelled prior to reaching the heterojunction. This spatial information reflects the distribution of phase sizes within the blend and can measure the distribution of phase sizes with characteristic dimensions smaller than the resolution of the most advanced force microscopy techniques, i.e. sub-10 nm [87]. The second method is to solve the Fokker–Planck equation for exciton diffusion in spherical symmetry, which yields the time-dependent exciton population as a function of domain size, exciton diffusion, and exciton drift. The model in [87] takes into account the time-dependence of the exciton diffusion coefficient, which can be determined rigorously from R_{max}. Immediate charge transfer at the heterojunction is included as one of the boundary definitions. It can be seen in Figure 13.7 that the experimental data is only well reproduced when a drift component towards the heterojunction is included. This is because excitons on polymer chains at the heterojunction have a lower energy than bulk excitons [88], i.e. they form energy sinks and excitations transfer to these sites preferentially. Such a 'drift' component would enhance the rate of charge transfer in polymer solar cells, which provides a framework for understanding the high efficiencies of exciton ionization that are usually observed for solar-cell polymer blends. It is in agreement with a recent model by Beljonne, Herz, and coworkers that is described in the next section [88].

13.3.2 Photoluminescence from Charge-Transfer States

The recent discovery of emission from interfacial charge-transfer states in blends of conjugated polymers has challenged the assumption that exciton ionization at the heterojunction leads to pairs of charges without any wavefunction overlap between electrons and

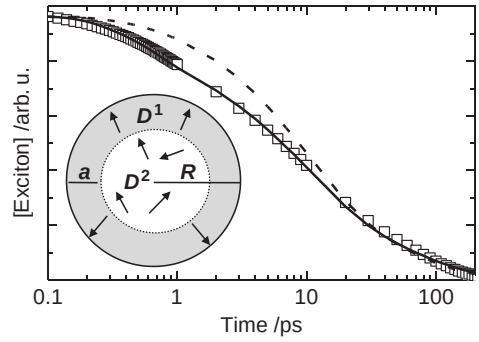

Figure 13.7 *Exciton diffusion to the heterojunction. Experimental (symbols) and modeled (lines) diffusion-limited exciton populations are compared. The experimental data show the exciton population recovered from femtosecond transient absorption measurements of charge generation in PFB:F8BT polymer blends. The modeled data are a fit using a modified Fokker–Planck equation, with (dashed line) and without (solid line) the drift component close to the interface. The inset shows a cartoon of the diffusion (D^2) in the bulk of the domain and the additional drift towards the heterojunction (D^1) in the interface region. (Reprinted with permission from Physical Review Letters, Probing the morphology and energy landscape of blends of conjugated polymers with sub-10 nm resolution by S. Westenhoff, I. A. Howard and R. H. Friend, Physical Review Letters, 101, art.no. 016102. Copyright (2008) American Physical Society)*

holes [40]. The emission is red-shifted from that of the lower-band-gap polymer and has a lifetime on the order of tens of nanoseconds, which is significantly longer than that of an exciton. The emissive states in polymer:polymer blends were initially termed exciplex, because of the absence of direct absorption from the ground state in blends of polyfluorenes and poly(*p*-phenylenevinylene) derivatives [40,79,89]. Recently, an emissive charge-transfer state was also reported for the popular P3HT:PCBM blend system [39]. In the same study it was also described that this state has a direct absorption from the ground state and it has therefore been classified as a charge-transfer exciton [39]. Further studies to clarify the exact nature (exciplex or charge-transfer state) of this state and its role in organic solar cells will be of interest. However, in both cases, the existence of luminescence implies that the interfacial states have some excitonic character and that the charge separation is small. Herein, we refer to both such species as charge-transfer states.

Interfacial charge-transfer states are characterized by a weaker Coulombic exciton binding energy compared to bulk excitons in conjugated polymers. Making use of their emissive properties, this quantity can be conveniently measured by recording the change of photoluminescence with electric field. Such studies yield a binding energy on the order of 100 meV for the charge-transfer state [39]. This is reasonable, considering that these states are intermediates between tightly bound excitons with a Coulombic binding energy of $\sim$500 meV and free charges with a binding energy of $\sim$0 eV. By observing exciplex emission from a number of polymer blends, it was found that the energy of emission is correlated with the band-edge offsets and the open-circuit voltage of the polymer blends [79,90]. This is expected from basic theory of exciplexes [91].

The discovery of emissions from interfacial charge-transfer states has already contributed significantly to the current understanding of photophysics at polymer heterojunctions. Offermans *et al.* have reported that an exciplex in a conjugated polymer blend can decay into a triplet exciton localized to the lower band-gap material, and suggest this may be a loss mechanism in organic solar cells [79]. Morteani *et al.* describe how singlet excitons are endothermically regenerated at the heterojunction [89] and provide an elegant explanation for the high brightness of OLEDS made of polyfluorene blends with minimal band-edge offsets [40,92]. Electronic-structure calculations support this finding [93]. The emissive charge-transfer states have also been studied as a function of hydrostatic pressure [94]. However, because all these studies rely on luminescence measurements of states with unknown oscillator strength, it is difficult to quantitatively account for all excitations. Quantitative treatment is especially relevant when one wants to characterize the major loss mechanism in organic solar cells. To achieve this, time-resolved photoluminescence and absorption measurements can be combined (see Section 13.3.4).

13.3.3 The Nature of the Charge-Transfer States

The electronic structure of interfacial excitations was recently described by Beljonne, Herz, Friend, and coworkers [38,88]. Static dipoles in the ground state of one polymer chain are considered to modulate the exciton energy on the neighboring polymer chains by Coulomb interactions across the heterojunction. Depending on the relative position of the chains, attractive or repulsive interaction were found, which respectively stabilize or obstruct charge-transfer state formation [88]. This implies that the density of states of interfacial excitons is broader than that for bulk excitons. Indeed, this was experimentally observed by femtosecond time-resolved photoluminescence spectroscopy in the same study [88]. The broader density of states at the heterojunction is consistent with the fast directional motion toward the interface described above (see Section 13.3.1) [87]). Excitons could transfer quickly into lower energy interfacial sites when they approach the interfacial region.

In a second study, the same collaboration also characterized the electronic structure of excited states at the heterojunction [38]. Using semiempirical quantum-chemical calculations it was found that the excited states at the heterojunction can have very different radiative lifetimes, charge-transfer characters (which reflects the degree of charge separation), and absorption oscillator strengths, all of which again depend on the relative orientation and position of the polymer chains [38]. With slight variations in relative positions of the chains, the most stable excited state could change from an exciton that is fully localized on the lower band-gap polymer to a charge-transfer state with electron and hole localized on polymer chains across the polymer heterojunction (see Figure 13.8). The calculations agreed directly with the lifetime and polarization anisotropy of the photoluminescence observed from these states [38,90]. The surprising variety of interface states shows that the local arrangement of polymer chains at the heterojunction can be equally important as the band offset of the bulk materials when charge transfer is evaluated. It is at present not possible to control the arrangement of polymer chains across the heterojunction on a molecular level; research in this direction, however, could present interesting possibilities for the design of OLEDs and photovoltaic devices.

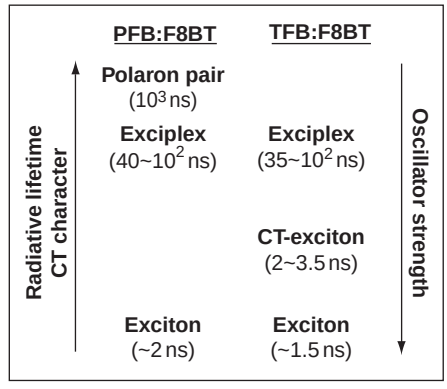

Figure 13.8 *Interfacial excitations. Schematic of the lowest excitonic excitations at the heterojunction of the PFB:F8BT and the TFB:F8BT systems. TFB abbreviates poly(9,9-dioctylfluorene-co-N-(4-butylphenyl)diphenylamine) and can be used to fabricate highly efficient OLEDs when blended with F8BT. (Reprinted with permission from Nature Materials, Electronic structures of interfacial states formed at polymeric semiconductor heterojunctions, Nature Materials by Y.-s. Huang, S. Westenhoff, I. Avilov et al., 7, 483–489. Copyright (2008) Macmillan Publishers Ltd)*

13.3.4 Probing the Major Loss Mechanism in Organic Solar Cells with High Open-Circuit Voltages

It is clear from photoluminescence quenching studies and from spectroscopic measurements, such as those shown in Figure 13.6, that the ionization of excitons at the heterojunction is highly efficient, even in polymer blends with small band-edge offsets [42,84,87]. Thus, the loss mechanism that limits the efficiency of polymer solar cells with high open-circuit voltages has to be a process that follows the initial charge-transfer reaction. Indirect evidence about possible loss mechanisms can be obtained by electrical measurements. However, these studies have not reached agreement, also because electrical measurements lack time resolution to probe the early (ns) timescales. Electrical and optical studies probing long ($> \mu s$) timescales have proposed that inefficient bulk charge transport and the convoluted nature of charge-collection pathways in bulk heterojunction cells lead to (trap-limited) *nongeminate* recombination as the dominant loss channel [92,95–97]. However, significant charge extraction and recombination should occur on the nanosecond timescale. Indeed, a number of studies quantitatively account for all photogenerated charges with nanosecond or better time resolution and suggest that intensity-independent *geminate* recombination may significantly deplete the number of long-lived and extractable charges [79–81,84,98]. None of the methods used was able to satisfactorily determine the reason for the poor charge-collection efficiency in polymer solar cells with high open-circuit voltages.

With the objective to characterize the performance-limiting recombination process in photovoltaics with high open-circuit voltages, we have recently introduced polarization-resolved transient absorption (TA) spectroscopy to directly track the movement of

photogenerated charges. The polarization anisotropy of photoinduced absorption signals is commonly used to track exciton diffusion in organic semiconductors on picosecond timescales [99–102]. In order to resolve the fate of the charge pairs on longer (nanosecond to microsecond) timescales, we augmented our femtosecond TA spectrometer with a nanosecond Nd:YVO4 laser, which was synchronized and electronically delayed with respect to the femtosecond pulses. With this setup, transient absorption spectroscopy can be performed on all timescales from femtoseconds to milliseconds. To measure the polarization anisotropy with a high signal-to-noise ratio, it is advisable to simultaneously measure differential transmission signals ($\Delta T/T$) for parallel and perpendicular polarizations of each probe pulse [99]. This yields both time-resolved polarization anisotropy ($r = (\Delta T/T^{\text{para}} - \Delta T/T^{\text{perp}})/(\Delta T/T^{\text{para}} + 2\,\Delta T/T^{\text{perp}})$) and magic angle (population) decays ($\Delta T/T^{\text{para}} + 2\,\Delta T/T^{\text{perp}}$).

Figure 13.9b shows the population decay kinetics of PFB:F8BT blends on a nanosecond timescale, spin-cast from chloroform, containing 50 wt% (circles) and 10 wt% F8BT (squares). The photoinduced absorption at the probe wavelength (532 nm) is due to charge pairs, and after ~40 ns triplet excitons also contribute to the decay (see Section 13.4.5). The photoinduced absorption decays quickly, with 75% of the signal disappearing within 40 ns. The polarization anisotropy, on the other hand, is roughly constant over this 40 ns period. This indicates that the charge-transfer states, which are initially formed at the

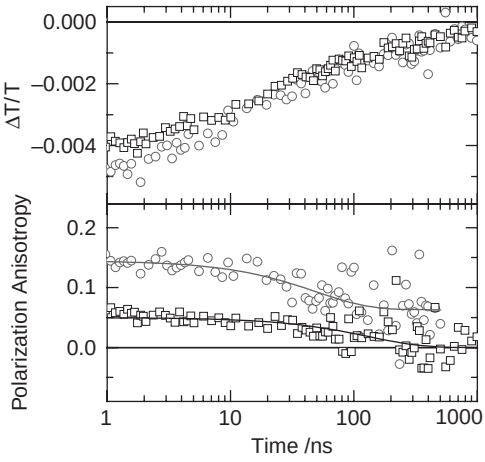

Figure 13.9 *Polarization-resolved transient absorption spectroscopy on nanosecond timescale. Panel (a) shows the differential transmission kinetics recorded at 532 nm probe wavelength for two F8BT:PFB blends. The polarization was set to the magic angle to measure the population dynamics. Open circles and squares correspond to blends containing 10 wt% and 50 wt% F8BT, respectively. The excitation fluence was 1×10^{14} and 1×10^{13} at 490 nm, respectively. Panel (b) shows the corresponding polarization anisotropy decays with markers as in panel (a). The lines are monoexponential fits to guide to the eye. (Reprinted with permission from Journal of the American Chemical Society, S. Westenhoff, I. A. Howard, J. M. Hodgkiss, K. R. Kirov, H. A. Bronstein, C. K. Williams, N. C. Greenham and R. H. Friend, Charge recombination in organic photovoltaic devices with high open-circuit voltages, 130, 13653–13658. Copyright (2008) American Chemical Society)*

heterojunction, are predominantly immobile. The similarity of the decay kinetics of the polarization anisotropy for the two blend compositions in Figure 13.9b suggests that the decay dynamics are sensitive to the domain size. The differences in amplitudes of the same traces are related to the blend morphology and caused by differences in the average distance travelled by an exciton prior to charge transfer in the two different blends [87]. The fact that the 40 ns timescale of the limited polarization anisotropy loss approaches or exceeds the lifetime of the photoinduced absorption shows directly that most charge pairs recombine geminately at their site of generation.

These measurements show very directly that the charge-transfer state is located at the heterojunction and no significant amount of charge separation occurs within 40 ns. This finding is in agreement with the observation of exciplex emission in the same blends [40]. That the charge-transfer state is immobile is in stark contrast to singlet and triplet excitons, which are generally found to be highly mobile in disordered organic semiconductors, with elementary hoping times of 1–10 ps and 1–10 ns, respectively. Hence, the charge-transfer state does not sample many different sites in the films. This emphasizes that the local arrangement of chains at the heterojunction, as predicted by electronic-structure calculations [38], plays an important role for the overall device physics.

13.3.5 Geminate Recombination of Interfacial Charge-Transfer States into Triplet Excitons

At this stage, we have seen how excitons ionize at the heterojunction (Section13.3.1), reviewed the properties of the interfacial charge transfer states (Sections 13.3.2 and 13.3.3) and learned that the majority of charge-transfer states recombine geminately (Section 13.3.4). It remains to clarify the mechanism of charge recombination. Figure 13.10 summarizes nanosecond transient absorption spectra with a broad-band probe pulse (spanning from 530 to 780 nm). Figure 13.10a shows that the photoinduced absorption spectra shift on a nanosecond timescale. After 5 ns the broad charge absorption ($\lambda_{max} = 670$ nm) is observed, whereas after 75 ns a new component absorbing in the > 700 nm region has arisen ($\lambda_{max} =$ 740 nm). The latter spectral shape is characteristic of F8BT triplet excitons [43,103].

The recombination of charge-transfer states into triplet excitons represents a potential limitation to photovoltaic efficiencies in polymer solar cells. However, the yield of free charge carriers is dependent on the competitive kinetics of long-range charge separation vs. recombination. The branching ratio was quantified using the data that are displayed in Figure 13.10c [43]. The signal at 475 nm is due to the ground-state bleach of F8BT and thus the total number of excited states is probed; the signal at 625 nm is mainly due to photoinduced absorption of polarons; at 780 nm photoinduced absorption of polarons and F8BT triplets contribute; and at 2200 nm, which is below the band gap of triplet excitons, charges are probed exclusively [104]. The data at the infrared (IR) wavelength show directly that most of the charges decay on a nanosecond timescale. Triplets are generated on the same timescale as highlighted by the dotted line in Figure 13.10c. This confirms that triplet excitons are formed directly from the charge-transfer state. However, $\sim$10% of the IR signal prevails beyond 500 ns, which are those that do not undergo conversion into triplets. As the polarization anisotropy has decayed to zero in the 50% blend at 500 ns delay time (see Figure 13.9b), these charge pairs must have migrated away from the heterojunction.

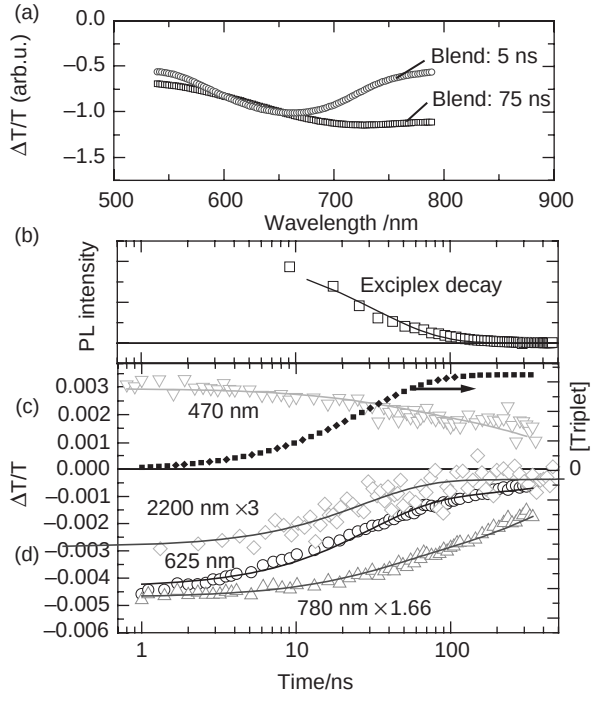

Figure 13.10 *Triplet generation in F8BT:PFB polymer blends. Panel (a) shows time-resolved spectra of a PFB:F8BT (50:50 wt%) blend at delay times as indicated in the figure. The spectra are smoothed using a fast Fourier-transform filter (Origin 6.0, Originlabs Inc). Panel (b) shows the photoluminescence decay of the exciplex as measured by time-correlated single photon counting at 650 nm (symbols) together with a monoexponential fit (line). Panel (c) shows TA kinetics with magic-angle polarization between pump and probe at wavelengths as indicated in the figure. Excitation was at 355 nm with fluences of* $\sim 5 \times 10^{13}$ *photons* cm^{-2} *(at 650, 775, and 2200 nm), and* $\sim 2.5 \times 10^{13}$ *photons* cm^{-2} *(at 475 nm). The dashed black line is the triplet density reconstructed from the global fit. (Reprinted with permission from Journal of the American Chemical Society, S. Westenhoff, I. A. Howard, J. M. Hodgkiss, K. R. Kirov, H. A. Bronstein, C. K. Williams, N. C. Greenham and R. H. Friend, Charge recombination in organic photovoltaic devices with high open-circuit voltages, 130, 13653–13658. Copyright (2008) American Chemical Society)*

A kinetic model summarizing these findings is presented in Figure 13.11 (see [43] for details of the model). Primary interfacial charge-transfer states (marked 'charge pairs' in Figure 13.11) are generated on a picosecond timescale with near unity efficiency (see Section13.3.1; Fig 13.6). These charge-transfer states may be emissive exciplexes [40] that can decay directly to the ground state, or nonemissive polaron pairs [38]. All interfacial charge-transfer states may recombine into triplet excitons, which are thermodynamically available in blend systems with a small band-edge offsets and the high exchange energies typical of conjugated polymers [105], or they can recombine directly into the ground state nonradiatively or radiatively (exciplex emission). Charge separation

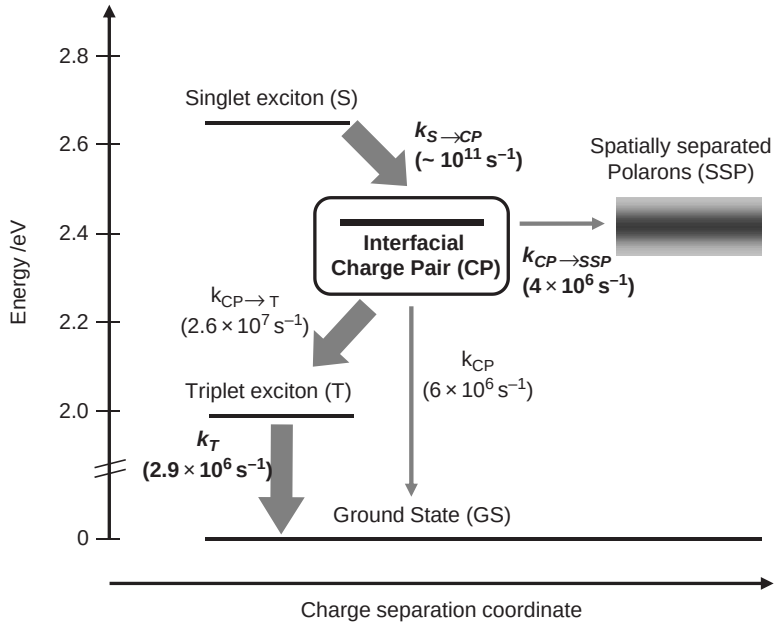

Figure 13.11 *Charge recombination mechanism at the polymer-polymer heterojunction. The energy of the interfacial charge pair and F8BT triplet exciton were taken to be respectively 200 meV [40] and 700 meV [105] below the F8BT singlet-exciton energy level. The bold arrows summarize the main flow of energy. (Reprinted with permission from Journal of the American Chemical Society, S. Westenhoff, I. A. Howard, J. M. Hodgkiss, K. R. Kirov, H. A. Bronstein, C. K. Williams, N. C. Greenham and R. H. Friend, Charge recombination in organic photovoltaic devices with high open-circuit voltages, 130, 13653–13658. Copyright (2008) American Chemical Society)*

kinetically competes with these recombination reactions. The rate constants are presented in Figure 13.11 and the bold arrows schematically highlight the major decay pathway. It is clear that geminate recombination of the metastable interfacial charge-transfer states are the bottleneck for device efficiency in blends of F8BT and PFB. Furthermore, the main mechanism of charge recombination is the formation of a triplet exciton on the F8BT, with 75% of the charge-transfer state population recombining into triplet excitons on a time-scale of 40 ns. During this time the charges in the charge-transfer states do not move significantly. The fraction of charge-transfer states that form spatially separated, 'free' charges is limited to a modest 10%, which readily explains the low external quantum efficiency of 3.4% measured in solar cells under short-circuit conditions made from this material system [84].

Currently the best-performing heterojunction photovoltaic devices are made from blends of polythiophenes and PCBM [6,106]. Here, the charge-transfer states are stable with respect to triplet excitons, which comes at the cost of modest open-circuit voltages of ~0.6 V. Recent experimental evidence suggests that the high performance of PCBM: polymer solar cells could also be attributed to the kinetic advantage in charge-transfer state separation that these cells have over those made from amorphous polymers. It is

suggested that the high local charge mobility allows charges to readily escape the interface region on a picosecond-to-nanosecond timescale with minimal applied field [74,81,107]. This consideration suggests that electron acceptors with lower electron affinities than PCBM ought still to be considered for photovoltaic devices, as long as they exhibit high local electron mobility. The geminate recombination time of roughly 40 ns sets a general benchmark against which the kinetics of long-range charge separation must be favorable for efficient charge extraction in the next generation of photovoltaic materials.

13.3.6 The Exchange Energy of Interfacial Charge-Transfer States in Semiconducting Polymer Blends

In the previous section we have seen that intersystem crossing from the singlet to the triplet charge-transfer state is the dominant loss mechanism in PFB:F8BT blends, which serves as a model organic solar cell with high open-circuit voltage. It is notable that this intersystem crossing rate (2.6×10^7 s^{-1}, see Figure 13.11) is similar to the rate of triplet formation from singlet excitons in pristine F8BT (1.2×10^7 s^{-1}) [103]. Thus, the increased triplet population in blends is due to the increased lifetime of the charge-transfer state, rather than a change in the triplet formation rate. Currently, the mechanism of intersystem crossing involving the charge-transfer state is not clear.

Intersystem crossing can occur by spin–orbit coupling, hyperfine interaction, or spin–lattice relaxation. The timescale for spin–lattice relaxation in PPV was recently measured to be $\sim$30 μs [108]. This is much longer than the lifetimes of the singlet exciton and charge-transfer state, so it can be neglected in polymer blends. The other two mechanisms are only efficient when the energy gap between the triplet and singlet charge-transfer states is small. The exchange energy of charge-transfer states in organic blends has been measured by Segal *et al*., who electrically excited an OLED containing small organic molecules to obtain a negative exchange energy of -7 meV [109]. Kadashchuk *et al*. used temperature-dependent photoluminescence measurements on PPV to measure a value of 3–6 meV [110]. The negative exchange energy determined by Segal *et al*. is interesting, because it means that the triplet charge-transfer state lies above the corresponding singlet state. This has recently been rationalized in a theoretical study [111], where it was also found that the sign of the exchange energy can change depending on the orientation of the two molecules on which the charge-transfer state resides. These studies indicate that it might be possible to engineer the magnitude and sign of exchange energy by choosing appropriate materials or controlling the molecular orientation. This is certainly an interesting option which may suppress intersystem crossing within the charge-transfer state and consequently lead to enhanced charge-collection efficiencies in organic solar cells with high open-circuit voltages.

13.4 Conclusions and Outlook

Charge-transfer states are formed efficiently at heterojunctions in polymer blends, provided that the band-edge offsets are appropriate and that the domain size is smaller

than an exciton diffusion length. Their formation rate provides detailed insight into the morphology of the solar-cell blend. This domain-size information is of great importance for charge transport and has hitherto eluded the resolution of force microscopy. Following the efficient formation of the charge-transfer states, it is the kinetic competition between geminate recombination and further spatial separation that places the major limitation on solar-cell quantum efficiency. The pathways available for charge-transfer state recombination vary. In low open-circuit voltage blends, such as those that employ PCBM as an electron acceptor, the charge-transfer states can only recombine directly into the ground state. The absence of any other recombination channels, coupled with the fast kinetics of charge separation due to high carrier mobilities, may explain the high quantum efficiency observed in P3HT:PCBM solar cells. In high open-circuit voltage solar cells, further recombination mechanisms arise, because the triplet excitons on the lower-band-gap polymer are now thermodynamically available. Thus, charge-transfer states can recombine to form a triplet exciton and this also is the fundamental loss channel that reduces the solar-cell quantum efficiency.

Control over the kinetics of the various recombination mechanisms is needed to optimize the efficiency of future generation of solar cells. An elegant solution would be to direct the charges away from the heterojunction with energy cascades. This is realized in dye-sensitized solar cells and photosynthetic reaction centers. A third material separating the electron donor and acceptor materials could fulfill this proposition. The energy levels should be aligned such that stepwise electron/hole transport occurs. The manufacturing of such blends is a demanding task as the current solution-based manufacturing methods offer only little control over the molecular arrangements of the components in the films. However, recent advances in the chemistry of self-assembled large supramolecular structures using hydrogen bonding [112], or the use of polymer brushes [113] may open up perspectives for the design of such materials.

Acknowledgements

Sebastian Westenhoff acknowledges a Post Doc stipend from the Swedish Research Council and an Intraeuropean Fellowship from the European Commission. Ian Howard acknowledges funding from the EPSRC and the Cambridge Commonwealth Trust.

References

[1] C.K. Chiang, C.R.J. Fincher, Y.W. Park, A.J. Heeger, H. Shirakawa, E.J. Louis, S.C. Gau, and A.G. MacDiarmid, Electrical conductivity in doped polyacetylene, *Phys. Rev. Lett.*, **39**, 1098–1101 (1977).

[2] J.H. Burroughes, D.D.C. Bradley, A.R. Brown, R.N. Marks, K. Mackay, R.H. Friend, P.L. Burns, and A.B. Holmes, Light-emitting-diodes based on conjugated polymers, *Nature*, **347**, 539–541 (1990).

[3] N.S. Sariciftci, L. Smilowitz, A.J. Heeger, and F. Wudl, Photoinduced electron-transfer from a conducting polymer to buckminsterfullerene, *Science*, **258**, 1474–1476 (1992).

[4] G. Yu, J. Gao, J.C. Hummelen, F. Wudl, and A.J. Heeger, Polymer photovoltaic cells – enhanced efficiencies via a network of internal donor-acceptor heterojunctions, *Science*, **270**, 1789–1791 (1995).
[5] J.J.M. Halls, C.A. Walsh, N.C. Greenham, E.A. Marseglia, R.H. Friend, S.C. Moratti, and A.B. Holmes, Efficient photodiodes from interpenetrating polymer networks, *Nature*, **376**, 498–500 (1995).
[6] M. Reyes-Reyes, K. Kim, and D.L. Carroll, High-efficiency photovoltaic devices based on annealed poly(3-hexylthiophene) and 1-(3-methoxycarbonyl)-propyl-1-phenyl-(6,6)C-61 blends, *Appl. Phys. Lett.*, **87**, 083506 (2005).
[7] P.W.M. Blom, V.D. Mihailetchi, L.J.A. Koster, and D.E. Markov, Device physics of polymer : fullerene bulk heterojunction solar cells, *Adv. Mater.*, **19**, 1551–1566 (2007).
[8] S. Gunes, H. Neugebauer, and N.S. Sariciftci, Conjugated polymer-based organic solar cells, *Chem. Rev.*, **107**, 1324–1338 (2007).
[9] J.Y. Kim, K. Lee, N.E. Coates, D. Moses, T.Q. Nguyen, M. Dante, and A.J. Heeger, Efficient tandem polymer solar cells fabricated by all-solution processing, *Science*, **317**, 222–225 (2007).
[10] H. Ohkita, S. Cook, Y. Astuti, W. Duffy, S. Tierney, W. Zhang, M. Heeney, I. McCulloch, J. Nelson, D.D.C. Bradley, and J.R. Durrant, Charge carrier formation in polythiophene/fullerene blend films studied by transient absorption spectroscopy, *J. Am. Chem. Soc.*, **130**, 3030–3042 (2008).
[11] T. Kietzke, H.H. Horhold, and D. Neher, Efficient polymer solar cells based on M3EH-PPV, *Chem. Mater.*, **17**, 6532–6537 (2005).
[12] C.R. McNeill, A. Abrusci, J. Zaumseil, R. Wilson, M.J. McKiernan, J.H. Burroughes, J.J.M. Halls, N.C. Greenham, and R.H. Friend, Dual electron donor/electron acceptor character of a conjugated polymer in efficient photovoltaic diodes, *Appl. Phys. Lett.*, **90**, 193506 (2007).
[13] M.M. Koetse, J. Sweelssen, K.T. Hoekerd, H.F.M. Schoo, S.C. Veenstra, J.M. Kroon, X.N. Yang, and J. Loos, Efficient polymer: polymer bulk heterojunction solar cells, *Appl. Phys. Lett.*, **88**, 083504 (2006).
[14] F.L. Zhang, E. Perzon, X.J. Wang, W. Mammo, M.R. Andersson, and O. Inganas, Polymer solar cells based on a low-bandgap fluorene copolymer and a fullerene derivative with photocurrent extended to 850 nm, *Adv. Funct. Mater.*, **15**, 745–750 (2005).
[15] M.M. Wienk, M.P. Struijk, and R.A.J. Janssen, Low band gap polymer bulk heterojunction solar cells, *Chem. Phys. Lett.*, **422**, 488–491 (2006).
[16] H.J. Snaith, G.L. Whiting, B.Q. Sun, N.C. Greenham, W.T.S. Huck, and R.H. Friend, Self-organization of nanocrystals in polymer brushes. Application in heterojunction photovoltaic diodes, *Nano Lett.*, **5**, 1653–1657 (2005).
[17] G.L. Whiting, H.J. Snaith, S. Khodabakhsh, J.W. Andreasen, D. Breiby, M.M. Nielsen, N.C. Greenham, P.H. Friend, and W.T.S. Huck, Enhancement of charge-transport characteristics in polymeric films using polymer brushes, *Nano Lett.*, **6**, 573–578 (2006).
[18] M. Nedelcu, J. Lee, E.J.W. Crossland, S.C. Warren, M.C. Orilall, S. Guldin, S. Huttner, C. Ducati, D. Eder, U. Wiesner, U. Steiner, and H.J. Snaith, Block copolymer directed synthesis of mesoporous TiO2 for dye-sensitized solar cells, *Soft Matter*, **5**, 134–139 (2009).
[19] C.B. Murray, S.H. Sun, W. Gaschler, H. Doyle, T.A. Betley, and C.R. Kagan, Colloidal synthesis of nanocrystals and nanocrystal superlattices, *IBM J. Res. Devel.*, **45**, 47–56 (2001).
[20] Y. Yin and A.P. Alivisatos, Colloidal nanocrystal synthesis and the organic-inorganic interface, *Nature*, **437**, 664–670 (2005).
[21] N.C. Greenham, X.G. Peng, and A.P. Alivisatos, Charge separation and transport in conjugated polymer/semiconductor nanocrystal composites studied by photoluminescence quenching and photoconductivity, *Phys. Rev. B*, **54**, 17628–17637 (1996).
[22] X.G. Peng, L. Manna, W.D. Yang, J. Wickham, E. Scher, A. Kadavanich, and A.P. Alivisatos, Shape control of CdSe nanocrystals, *Nature*, **404**, 59–61 (2000).
[23] L. Manna, D.J. Milliron, A. Meisel, E.C. Scher, and A.P. Alivisatos, Controlled growth of tetrapod-branched inorganic nanocrystals, *Nature Mater.*, **2**, 382–385 (2003).
[24] L. Manna, E.C. Scher, and A.P. Alivisatos, Synthesis of soluble and processable rod-, arrow-, teardrop-, and tetrapod-shaped CdSe nanocrystals, *J. Am. Chem. Soc.*, **122**, 12700–12706 (2000).

[25] Y. Wang, Luminescent CdTe and CdSe semiconductor nanocrystals: Preparation, optical properties and applications, *J. Nanosci. Nanotech.*, **8**, 1068–1091 (2008).
[26] S.A. McDonald, G. Konstantatos, S.G. Zhang, P.W. Cyr, E.J.D. Klem, L. Levina, and E.H. Sargent, Solution-processed PbS quantum dot infrared photodetectors and photovoltaics, *Nature Mater.*, **4**, 138–U14 (2005).
[27] E.H. Sargent, Solution-processed infrared optoelectronics: Photovoltaics, sensors, and sources, *IEEE J. Sel. Top. Quant. Electr.*, **14**, 1223–1229 (2008).
[28] W.J.E. Beek, M.M. Wienk, and R.A.J. Janssen, Hybrid polymer solar cells based on zinc oxide, *J. Mater. Chem.*, **15**, 2985–2988 (2005).
[29] B.Q. Sun, H.J. Snaith, A.S. Dhoot, S. Westenhoff, and N.C. Greenham, Vertically segregated hybrid blends for photovoltaic devices with improved efficiency, *J. Appl. Phys.*, **97**, 014914 (2005).
[30] S. Kumar and G.D. Scholes, Colloidal nanocrystal solar cells, *Microchim. Acta*, **160**, 315–325 (2008).
[31] J.Y. Huang, L.S. Li, and M.C. Chen, Probing molecular binding effect from zinc oxide nanocrystal doping in surface-stabilized ferroelectric liquid crystal with two-dimensional infrared correlation technique, *J. Phys. Chem. C*, **112**, 5410–5415 (2008).
[32] M. Sykora, M.A. Petruska, J. Alstrum-Acevedo, I. Bezel, T.J. Meyer, and V.I. Klimov, Photoinduced charge transfer between CdSe nanocrystal quantum dots and Ru-polypyridine complexes, *J. Am. Chem. Soc.*, **128**, 9984–9985 (2006).
[33] J.W.P. Hsu, M. Yan, T.M. Jedju, L.J. Rothberg, and B.R. Hsieh, Assignment of the picosecond photoinduced absorption in phenylene vinylene polymers, *Phys. Rev. B*, **49**, 712–715 (1994).
[34] C.H. Lee, G. Yu, D. Moses, and A.J. Heeger, Picosecond transient photoconductivity in poly (p-phenylenevinylene), *Phys. Rev. B*, **49**, 2396–2407 (1994).
[35] J.W. Blatchford, S.W. Jessen, L.B. Lin, J.J. Lih, T.L. Gustafson, A.J. Epstein, D.K. Fu, M.J. Marsella, T.M. Swager, A.G. MacDiarmid, S. Yamaguchi, and H. Hamaguchi, Exciton dynamics in poly(p-pyridyl vinylene), *Phys. Rev. Lett.*, **76**, 1513–1516 (1996).
[36] C. Silva, A.S. Dhoot, D.M. Russell, M.A. Stevens, A.C. Arias, J.D. MacKenzie, N.C. Greenham, R.H. Friend, S. Setayesh, and K. Mullen, Efficient exciton dissociation via two-step photoexcitation in polymeric semiconductors, *Phys. Rev. B*, **64**, 125211 (2001).
[37] J.L. Bredas and R. Silbey, Excitons surf along conjugated polymer chains, *Science*, **323**, 348–349 (2009).
[38] Y.-S. Huang, S. Westenhoff, I. Avilov, P. Sreearunothai, J.M. Hodgkiss, C. Deleener, R.H. Friend, and D. Beljonne, Electronic structures of interfacial states formed at polymeric semiconductor heterojunctions, *Nature Mater.*, **7**, 483–489 (2008).
[39] M. Hallermann, S. Haneder, and E. Da Como, Charge-transfer states in conjugated polymer/fullerene blends: Below-gap weakly bound excitons for polymer photovoltaics, *Appl. Phys. Lett.*, **93**, 053307 (2008).
[40] A.C. Morteani, A.S. Dhoot, J.S. Kim, C. Silva, N.C. Greenham, C. Murphy, E. Moons, S. Cina, J.H. Burroughes, and R.H. Friend, Barrier-free electron-hole capture in polymer blend heterojunction light-emitting diodes, *Adv. Mater.*, **15**, 1708–1712 (2003).
[41] S.A. Jenekhe and J.A. Osaheni, Excimers and exciplexes of conjugated polymers, *Science*, **265**, 765–768 (1994).
[42] D. Veldman, O. Ipek, S.C.J. Meskers, J. Sweelssen, M.M. Koetse, S.C. Veenstra, J.M. Kroon, S.S. Van Bavel, J. Loos, and R.A.J. Janssen, Compositional and electric field dependence of the dissociation of charge transfer excitons in alternating polyfluorene copolymer/fullerene blends, *J. Am. Chem. Soc.*, **130**, 7721–7735 (2008).
[43] S. Westenhoff, I.A. Howard, J.M. Hodgkiss, K.R. Kirov, H.A. Bronstein, C.K. Williams, N.C. Greenham, and R.H. Friend, Charge recombination in organic photovoltaic devices with high open-circuit voltages, *J. Am. Chem. Soc.*, **130**, 13653–13658 (2008).
[44] L.J.A. Koster, E.C.P. Smits, V.D. Mihailetchi, and P.W.M. Blom, Device model for the operation of polymer/fullerene bulk heterojunction solar cells, *Phys. Rev. B*, **72**, 085205 (2005).
[45] A. Miller and E. Abrahams, Impurity conduction at low concentrations, *Phys. Rev.*, **120**, 745 (1960).

[46] R.A. Marcus, Nonadiabatic processes involving quantum-like and classical-like coordinates with applications to nonadiabatic electron transfers, *J. Chem. Phys.*, **81**, 4494–4500 (1984).
[47] K. Seki and M. Tachiya, Electric field dependence of charge mobility in energetically disordered materials: Polaron aspects, *Phys. Rev. B (Condens. Matter Mater. Phys.)*, **65**, 014305 (2001).
[48] H. Bässler, Charge transport in disordered organic photoconductors a monte carlo simulation study, *Phys. Status Solidi B*, **175**, 15–56 (1993).
[49] P.M. Borsenberger, L. Pautmeier, and H. Bassler, Charge transport in disordered molecular-solids, *J. Chem. Phys.*, **94**, 5447–5454 (1991).
[50] S.V. Novikov, D.H. Dunlap, V.M. Kenkre, P.E. Parris, and A.V. Vannikov, Essential role of correlations in governing charge transport in disordered organic materials, *Phys. Rev. Lett.*, **81**, 4472–4475 (1998).
[51] G. Horowitz, R. Hajlaoui, and P. Delannoy, Temperature-dependence of the field-effect mobility of sexithiophene – determination of the density of traps, *J. Phys. III*, **5**, 355–371 (1995).
[52] P.W.M. Blom and M. Vissenberg, Charge transport in poly(p-phenylene vinylene) light-emitting diodes, *Mater. Sci. Eng. Rep.*, **27**, 53–94 (2000).
[53] C.L. Braun, Electric field assisted dissociation of charge transfer states as a mechanism of photocarrier production, *J. Chem. Phys.*, **80**, 4157–4161 (1984).
[54] L. Onsager, Initial recombination of ions, *Phys. Rev.*, **54**, 554–557 (1938).
[55] H. Sano and M. Tachiya, Partially diffusion-controlled recombination, *J. Chem. Phys.*, **71**, 1276–1282 (1979).
[56] V.I. Arkhipov, P. Heremans, and H. Bassler, Why is exciton dissociation so efficient at the interface between a conjugated polymer and an electron acceptor?, *Appl. Phys. Lett.*, **82**, 4605–4607 (2003).
[57] C. Groves, R.A. Marsh and N.C. Greenham, Monte Carlo modeling of geminate recombination in polymer-polymer photovoltaic devices, *J. Chem. Phys.*, **129**, 114903 (2008).
[58] P.K. Watkins, A.B. Walker, and G.L.B. Verschoor, Dynamical Monte Carlo modelling of organic solar cells: The dependence of internal quantum efficiency on morphology, *Nano Lett.*, **5**, 1814–1818 (2005).
[59] A. Kohler, D.A. dos Santos, D. Beljonne, Z. Shuai, J.L. Brédas, A.B. Holmes, A. Kraus, K. Mullen, and R.H. Friend, Charge separation in localized and delocalized electronic states in polymeric semiconductors, *Nature*, **392**, 903–906 (1998).
[60] M. Chandross, S. Mazumdar, S. Jeglinski, X. Wei, Z.V. Vardeny, E.W. Kwock, and T.M. Miller, Excitons in poly(para-phenylenevinylene), *Phys. Rev. B*, **50**, 14702 (1994).
[61] S. Barth, H. Bassler, T. Wehrmeister, and K. Mullen, Photoconduction in oligo-para-phenylenevinylene films, *J. Chem. Phys.*, **106**, 321–327 (1997).
[62] V. Gulbinas, Y. Zaushitsyn, H. Bässler, A. Yartsev, and V. Sundström, Dynamics of charge pair generation in ladder-type poly(para-phenylene) at different excitation photon energies, *Phys. Rev. B*, **70**, 035215 (2004).
[63] M.A. Stevens, C. Silva, D.M. Russell, and R.H. Friend, Exciton dissociation mechanisms in the polymeric semiconductors poly(9,9-dioctylfluorene) and poly(9, 9-dioctylfluorene-co-benzothiadiazole), *Phys. Rev. B*, **63**, 165213 (2001).
[64] X. Zhang, Y. Xia, R.H. Friend, and C. Silva, Sequential absorption processes in two-photon-excitation transient absorption spectroscopy in a semiconductor polymer, *Phys. Rev. B (Condens. Matter Mater. Phys.)*, **73**, 245201 (2006).
[65] X. Zhang, Y. Xia, and R.H. Friend, Multiphoton excited photoconductivity in polyfluorene, *Phys. Rev. B (Condens. Matter Mater. Phys.)*, **75**, 245128 (2007).
[66] C. Gadermaier, G. Cerullo, G. Sansone, G. Leising, U. Scherf, and G. Lanzani, Time-resolved charge carrier generation from higher lying excited states in conjugated polymers, *Phys. Rev. Lett.*, **89**, 117402 (2002).
[67] X.D. Yang, C.L. Lee, S. Westenhoff, X.P. Zhang, and N.C. Greenham, Saturation, relaxation, and dissociation of excited triplet excitons in conjugated polymers, *Adv. Mater.*, **21**, 916–919 (2009).
[68] E. Hendry, M. Koeberg, J.M. Schins, L.D.A. Siebbeles, and M. Bonn, Ultrafast charge generation in a semiconducting polymer studied with THz emission spectroscopy, *Phys. Rev. B (Conden. Matter Mater. Phys.)*, **70**, 033202 (2004).

[69] E. Hendry, J.M. Schins, L.P. Candeias, L.D.A. Siebbeles, and M. Bonn, Efficiency of Exciton and Charge Carrier Photogeneration in a Semiconducting Polymer, *Phys. Rev. Lett.*, **92**, 196601 (2004).
[70] T. Virgili, G. Cerullo, L. Luer, G. Lanzani, C. Gadermaier, and D.D.C. Bradley, Understanding fundamental processes in poly(9,9-dioctylfluorene) light-emitting diodes via ultrafast electric-field-assisted pump-probe spectroscopy, *Phys. Rev. Lett.*, **90**, 247402 (2003).
[71] V. Gulbinas, Y. Zaushitsyn, V. Sundström, D. Hertel, H. Bässler, and A. Yartsev, Dynamics of the electric field-assisted charge carrier photogeneration in ladder-type poly(para-phenylene) at a low excitation intensity, *Phys. Rev. Lett.*, **89**, 1074011 (2002).
[72] C.J. Brabec, G. Zerza, G. Cerullo, S. De Silvestri, S. Luzzati, J.C. Hummelen, and S. Sariciftci, Tracing photoinduced electron transfer process in conjugated polymer/fullerene bulk heterojunctions in real time, *Chem. Phys. Lett.*, **340**, 232–236 (2001).
[73] K.G. Jespersen, F.L. Zhang, A. Gadisa, V. Sundstrom, A. Yartsev, and O. Inganas, Charge formation and transport in bulk-heterojunction solar cells based on alternating polyfluorene copolymers blended with fullerenes, *Org. Electr.*, **7**, 235–242 (2006).
[74] I.W. Hwang, D. Moses, and A.J. Heeger, Photoinduced carrier generation in P3HT/PCBM bulk heterojunction materials, *J. Phys. Chem. C*, **112**, 4350–4354 (2008).
[75] H. Tamura, J.G.S. Ramon, E.R. Bittner, and I. Burghardt, Phonon-driven ultrafast exciton dissociation at donor-acceptor polymer heterojunctions, *Phys. Rev. Lett.*, **100**, 107402 (2008).
[76] Y. Kanai and J.C. Grossman, Insights on interfacial charge transfer across P3HT/fullerene photovoltaic heterojunction from *ab initio* calculations, *Nano Lett.*, **7**, 1967–1972 (2007).
[77] R. Österbacka, C.P. An, X.M. Jiang, and Z.V. Vardeny, Two-dimensional electronic excitations in self-assembled conjugated polymer nanocrystals, *Science*, **287**, 839–842 (2000).
[78] T. Offermans, S.C.J. Meskers, and R.A.J. Janssen, Charge recombination in a poly(para-phenylene vinylene)-fullerene derivative composite film studied by transient, nonresonant, hole-burning spectroscopy, *J. Chem. Phys.*, **119**, 10924–10929 (2003).
[79] T. Offermans, P.A. van Hal, S.C.J. Meskers, M.M. Koetse, and R.A.J. Janssen, Exciplex dynamics in a blend of pi-conjugated polymers with electron donating and accepting properties: (MDMO-PPV) and (PCNEPV), *Phys. Rev. B*, **72**, 045213 (2005).
[80] S. De, T. Pascher, M. Maiti, K.G. Jespersen, T. Kesti, F.L. Zhang, O. Inganas, A. Yartsev, and V. Sundstrom, Geminate charge recombination in alternating polyfluorene Copolymer/Fullerene blends, *J. Am. Chem. Soc.*, **129**, 8466–8472 (2007).
[81] R.A. Marsh, C. Groves, and N.C. Greenham, A microscopic model for the behavior of nanostructured organic photovoltaic devices, *J. Appl. Phys.*, **101**, 083509 (2007).
[82] T.M. Clarke, A.M. Ballantyne, J. Nelson, D.D.C. Bradley, and J.R. Durrant, Free energy control of charge photogeneration in polythiophene/fullerene solar cells: The influence of thermal annealing on P3HT/PCBM blends, *Adv. Funct. Mater.*, **18**, 4029–4035 (2008).
[83] T. Kawatsu, V. Coropceanu, A.J. Ye, and J.L. Bredas, Quantum-chemical approach to electronic coupling: Application to charge separation and charge recombination pathways in a model molecular donor-acceptor system for organic solar cells, *J. Phys. Chem. C*, **112**, 3429–3433 (2008).
[84] C.R. McNeill, S. Westenhoff, C. Groves, R.H. Friend and N.C. Greenham, Influence of nanoscale phase separation on the charge generation dynamics and photovoltaic performance of conjugated polymer blends: Balancing charge generation and separation, *J. Phys. Chem. C*, **111**, 19153–19160 (2007).
[85] F.S. Bates, Polymer–Polymer phase behavior, *Science*, **251**, 898–905 (1991).
[86] N. Takeda, S. Asaoka, and J.R. Miller, Nature and energies of electrons and holes in a conjugated polymer, polyfluorene, *J. Am. Chem. Soc.*, **128**, 16073–16082 (2006).
[87] S. Westenhoff, I.A. Howard, and R.H. Friend, Probing the morphology and energy landscape of blends of conjugated polymers with sub-10 nm resolution, *Phys. Rev. Lett.*, **101**, 016102 (2008).
[88] P. Sreearunothai, A.C. Morteani, I. Avilov, J. Cornil, D. Beljonne, R.H. Friend, R.T. Phillips, C. Silva, and L.M. Herz, Influence of copolymer interface orientation on the optical emission of polymeric semiconductor heterojunctions, *Phys. Rev. Lett.*, **96**, 117403 (2006).
[89] A.C. Morteani, P. Sreearunothai, L.M. Herz, R.H. Friend, and C. Silva, Exciton regeneration at polymeric semiconductor heterojunctions, *Phys. Rev. Lett.*, **92**, 247402 (2004).

[90] A.C. Morteani, Ph.D. Thesis, The Electronics and Photophysics of Polymer Heterojunctions, University of Cambridge, 2005.
[91] A. Weller, Singlet- and triplet-state exiplexes. In *The Exciplex*, ed. M. Gordon and W.R. Ware, Academic Press Inc., New York, 1975, 23–38.
[92] H.J. Snaith, A.C. Arias, A.C. Morteani, C. Silva, and R.H. Friend, Charge generation kinetics and transport mechanisms in blended polyfluorene photovoltaic devices, *Nano Lett.*, **2**, 1353–1357 (2002).
[93] J.G.S. Ramon and E.R. Bittner, Exciton regeneration dynamics in model donor-acceptor polymer heterojunctions, *J. Phys. Chem. B*, **110**, 21001–21009 (2006).
[94] J.P. Schmidtke, R.H. Friend, and C. Silva, Tuning interfacial charge-transfer excitons at polymer-polymer heterojunctions under hydrostatic pressure, *Phys. Rev. Lett.*, **100**, 157401 (2008).
[95] M.M. Mandoc, W. Veurman, L.J.A. Koster, M.M. Koetse, J. Sweelssen, B. de Boer, and P.W.M. Blom, Charge transport in MDMO-PPV : PCNEPV all-polymer solar cells, *J. Appl. Phys.*, **101**, 104512 (2007).
[96] J. Nelson, Diffusion-limited recombination in polymer-fullerene blends and its influence on photocurrent collection, *Phys. Rev. B*, **67**, 155209 (2003).
[97] I. Montanari, A.F. Nogueira, J. Nelson, J.R. Durrant, C. Winder, M.A. Loi, N.S. Sariciftci and C. Brabec, Transient optical studies of charge recombination dynamics in a polymer/fullerene composite at room temperature, *Appl. Phys. Lett.*, **81**, 3001–3003 (2002).
[98] V.D. Mihailetchi, L.J.A. Koster, J.C. Hummelen, and P.W.M. Blom, Photocurrent generation in polymer-fullerene bulk heterojunctions, *Phys. Rev. Lett.*, **93**, 216601 (2004).
[99] S. Westenhoff, C. Daniel, R.H. Friend, C. Silva, V. Sundström, and A. Yartsev, Exciton migration in a polythiophene: Probing the spatial and energy domain by line-dipole Forster-type energy transfer, *J. Chem. Phys.*, **122**, 094903 (2005).
[100] S. Westenhoff, W.J.D. Beenken, R.H. Friend, N.C. Greenham, A. Yartsev, and V. Sundström, Anomalous energy transfer dynamics due to torsional relaxation in a conjugated polymer, *Phys. Rev. Lett.*, **97**, 166804 (2006).
[101] M.M.L. Grage, T. Pullerits, A. Ruseckas, M. Theander, O. Inganäs, and V. Sundström, Conformational disorder of a substituted polythiophene in solution revealed by excitation transfer, *Chem. Phys. Lett.*, **339**, 96–102 (2001).
[102] E. Collini and G.D. Scholes, Coherent intrachain energy migration in a conjugated polymer at room temperature, *Science*, **323**, 369–373 (2009).
[103] T.A. Ford, I. Avilov, D. Beljonne, and N.C. Greenham, Enhanced triplet exciton generation in polyfluorene blends, *Phys. Rev. B*, **71**, 125212 (2005).
[104] C.X. Sheng, M. Tong, S. Singh, and Z.V. Vardeny, Experimental determination of the charge/neutral branching ratio eta in the photoexcitation of pi-conjugated polymers by broadband ultrafast spectroscopy, *Phys. Rev. B*, **75**, 085206 (2007).
[105] J.S. Wilson, A.S. Dhoot, A. Seeley, M.S. Khan, A. Kohler, and R.H. Friend, Spin-dependent exciton formation in pi-conjugated compounds, *Nature*, **413**, 828–831 (2001).
[106] J. Peet, J.Y. Kim, N.E. Coates, W.L. Ma, D. Moses, A.J. Heeger, and G.C. Bazan, Efficiency enhancement in low-bandgap polymer solar cells by processing with alkane dithiols, *Nature Mater.*, **6**, 497–500 (2007).
[107] L.W. Barbour, M. Hegadorn, and J.B. Asbury, Microscopic inhomogeneity and ultrafast orientational motion in an organic photovoltaic bulk heterojunction thin film studied with 2D IR vibrational spectroscopy, *J. Phys. Chem. B*, **110**, 24281–24286 (2006).
[108] C.G. Yang, E. Ehrenfreund, and Z.V. Vardeny, Polaron spin-lattice relaxation time in pi-conjugated polymers from optically detected magnetic resonance, *Phys. Rev. Lett.*, **99**, 157401 (2007).
[109] M. Segal, M. Singh, K. Rivoire, S. Difley, T. Van Voorhis, and M.A. Baldo, Extrafluorescent electroluminescence in organic light-emitting devices, *Nature Mater.*, **6**, 374–378 (2007).
[110] A. Kadashchuk, A. Vakhnin, I. Blonski, D. Beljonne, Z. Shuai, J.L. Bredas, V.I. Arkhipov, P. Heremans, E.V. Emelianova, and H. Bassler, Singlet-triplet splitting of geminate electron-hole pairs in conjugated polymers, *Phys. Rev. Lett.*, **93**, 066803 (2004).
[111] S. Difley, D. Beljonne, and T. Van Voorhis, On the singlet-triplet splitting of geminate electron-hole pairs in organic semiconductors, *J. Am. Chem. Soc.*, **130**, 3420–3427 (2008).

[112] F.J.M. Hoeben, P. Jonkheijm, E.W. Meijer, and A. Schenning, About supramolecular assemblies of pi-conjugated systems, *Chem. Rev.*, **105**, 1491–1546 (2005).
[113] S. Edmondson, V.L. Osborne, and W.T.S. Huck, Polymer brushes via surface-initiated polymerizations, *Chem. Soc. Rev.*, **33**, 14–22 (2004).
[114] D. Veldman, J. Bastiaansen, B.M.W. Langeveld-Voss, J. Sweelssen, M.M. Koetse, S.C.J. Meskers, and R.A.J. Janssen, Photoinduced charge and energy transfer in dye-doped conjugated polymers, *Thin Solid Films*, **511**, 581–586 (2006).
[115] D. Beljonne, A.J. Ye, Z. Shuai, and J.L. Bredas, Chain-length dependence of singlet and triplet exciton formation rates in organic light-emitting diodes, *Adv. Funct. Mater.*, **14**, 684–692 (2004).

Part Three

14

Nanostructured Conducting Polymers for (Electro)chemical Sensors

Anthony J. Killard

Biomedical Diagnostics Institute, National Centre for Sensor Research, Dublin City University, Ireland

14.1 Introduction

Conducting polymers have been investigated for many years now for their electrical and electrochemical properties. The moderate range of conducting polymers now available, their many derivatives, broad range of counter-ion doping options, level of proton doping, and the many synthetic routes result in a large range of material properties in terms of conductivity, chemical sensitivity, selectivity, and redox characteristics. This allows them to participate in many chemical interactions which are suitable for chemosensing applications.

Nanotechnology allows conducting-polymer materials to be studied and applied to chemical sensing in a new way. Controlling the structure and morphology of conducting polymer materials at nanoscales brings the prospect of a range of enhancements not possible with traditional bulk materials. Traditional routes to polymer formation, such as chemical and electrochemical synthesis, lack any fine control on the tertiary structure of the growing polymer, and this lack of structural reproducibility has negative consequences for the performance of the material as a sensor interface. In addition, such polymerizations,

Nanostructured Conductive Polymers Edited by Ali Eftekhari

particularly electrochemical polymerization, cannot be easily scaled up and automated for large-scale production of sensors.

Nanostructured conducting polymers have several potential advantages over their bulk counterparts. Firstly, as synthesis is controlled at the nanoscale, the level of order and structural reproducibility should be much improved, thereby imparting more predictable and reproducible material behavior. Secondly, nanostructured materials provide enhanced surface-area-to-volume characteristics which vastly increase the interfacial area for chemical interactions and electron-transport processes to take place, overcoming other limitations of sensor performance such as diffusion. Thirdly, nanostructuring opens up an even wider array of composited materials which have new physical, electrical, and electrochemical properties resulting from these novel combinations. Fourthly, nanostructured materials may exhibit enhanced catalytic and electrocatalytic properties not possessed by their bulk counterparts due to surface structural features and quantum mechanical properties imparted by the nanostructuring process. Lastly, many nanofabrication techniques allow more and separate control of both the nanomaterial synthesis and the nanomaterial deposition processes, resulting in combined improvements in the fabrication of the sensors. The application of conducting-polymer nanostructured materials to chemical-sensing applications is a relatively new area of exploration and much current investigation is focused on the general behavior of various nanomaterials for sensing, rather than detailed and rigorous analytical evaluation, which must follow if we are to understand the real value of these materials.

If nanostructured conducting-polymeric materials are to be of value in chemical-sensing applications, they should achieve one or both of the following. They should undoubtedly lead to an improvement in the analytical performance of the sensor itself, in terms of sensitivity, limit of detection, reproducibility, stability, and interference rejection. They should also lead ultimately to improvements in the processability of the materials and their amenability to production as a real-world, working sensor device. This chapter will explore the range of polymers and nanostructured materials which have been used to produce chemical sensors and discuss their performance and ease of fabrication. It will examine the interaction between the polymer nanostructuring methodology and the application of the materials as sensors and how this combination of factors affects sensor performance. Definition of these materials in the literature is imprecise at present and some materials can be defined under more than one category. Some simplification of definition and categorization has been used, as appropriate.

14.2 Nanowires and Nanotubes

Template-assisted polymerization of conducting polymers has been an effective way to reproducibly fabricate conducting-polymer nanowires. Fundamentally, the technique employs a hard membrane template with pores of uniform length and diameter, typically composed of alumina. Polymerization can be performed chemically using a mixture of

monomer and oxidant, or the membrane can be attached to an electrode surface and the polymerization can proceed electrochemically. The nanowires are removed by sonication and dissolution of the template, yielding highly uniform nanowires. Nanowires composed of poly(pyrrole) (PPy) and poly(3,4-ethylenedioxythiphene/poly(styrene-sulfonate) (PEDOT/PSS) have been deposited at electrodes either through drop-coating or electrochemically. Others have enhanced the conducting-polymer nanowires with additional materials through the electrodeposition of nickel and gold (Figure 14.1). This has been used to evaluate responses to ammonia vapor [1] and was shown to be sensitive to 100 ppm using a conductimetric transduction methodology. These nanowires were used as the basis

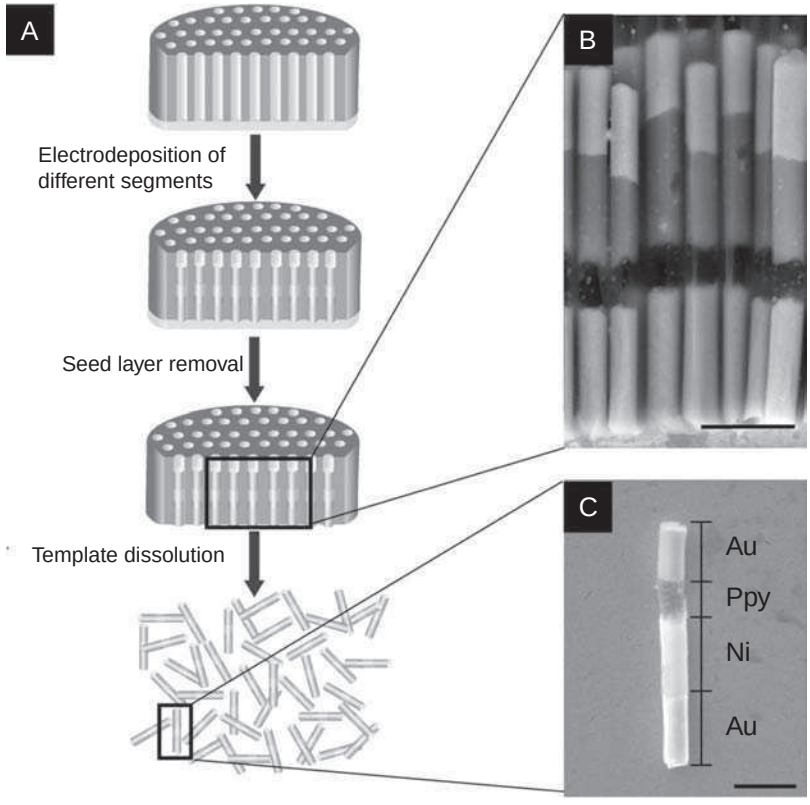

Figure 14.1 *Template-directed synthesis of conducting-polymer nanowires. Nanowires of PPy were synthesised by electropolymerization within an alumina template structure with a gold electrode base (A,B). Nanowires could be further functionalized by the growth of additional species such as nickel and gold (C). (Reprinted with permission from Electroanalysis, Magnetically Assembled Multisegmented Nanowires and Their Applications by M. A. Bangar, C. M. Hangarter, B. Yoo et al., 21, 1, 61–67. Copyright (2009) Wiley-VCH)*

of a sensitive chemical field-effect transistor (chemFET) device, described in the next section. A PEDOT/PSS-modified electrode was shown to be responsive to vapors of methanol, ethanol, and acetone in a conductimetric sensor [2]. However, there was little analytical characterization of the performance of the sensor to these gases, or comparison with other techniques, with resistance changes being ascribed to swelling of the polymer or changes in charge-carrier concentration of the PEDOT.

Others have fabricated PPy nanowires by template-free potentiostatic polymerization in $LiClO_4$ and Na_2CO_3 [3,4], which leads to the formation of disordered polymer mats at the electrode surface. These electrodes were used for the electrocatalytic reduction of nitrite and the oxidation of ascorbic acid. However, no comparisons were made between the nanostructured surfaces and bulk electropolymerized films.

Nanotubes are a distinct structure from nanowires in that they are fabricated with an empty core. Imaginative routes to nanotube fabrication have been developed by Gao *et al.* [5,6] for monitoring trimethylamine.

14.3 Nanogaps and Nanojunctions

The concept of the ChemFET has been in existence for some time. In such devices, a chemically selective component forms the gate of a conductor. In the case of conducting-polymer-based devices, the gate can be composed of a polymer nanowire. The chemical interaction of the polymer wire with analytes in its vicinity can lead to changes in the conductivity of the wire. It's small size and high aspect ratio means that it should be particularly sensitive to low concentrations of analyte, which should bring about relatively large and rapid changes in conductivity.

To fabricate the device, a nanojunction must first be formed. These tend to be created using gold electrodes through standard photolithographic techniques [7–9] or milling [10,11] to form gap junctions from 500 to 60 nm. The gap is then bridged either by the deposition of preformed nanotubes by drop-coating a dilute solution so a single nanotube lies fortuitously across the two gold electrodes [12–14], or they are grown electrochemically between the adjacent electrode faces [7–11]. Poly(aniline) (PANI), PPy and poly(thiophene) (PTh)-based sensors have been fabricated in this way. Several have been used for the detection of ammonia, one being capable of detection of 16 ppb, low enough to be used in the detection of ammonia in human breath samples [9]. Further functionalization of the conducting polymer nanostructures with chemoselective reagents such as metal chelators, e.g. nitrilo-triacetic acid (NTA), modification of PPy [12] or $(His)_6$ functionalization of PANI [8] has led to the enhanced sensitivity of the sensors to heavy-metal ions in drinking water with limits of detection for Cu^{2+} and Ni^{2+} as low as 0.6 ppt (10^{-14} M) and 23 ppt (0.4 nM), respectively. The PANI nanojunction device has also been used to measure the oxidation of dopamine, where as little as 100 nM could be detected in the presence of 1 mM ascorbic acid interferent [7]. Wang *et al.* used a four-electrode geometry and a PTh-modified gap junction to reduce interferences from parallel conduction pathways at such short length scales in the sensing of vanillin and 1-pentanol (Figure 14.2) [15].

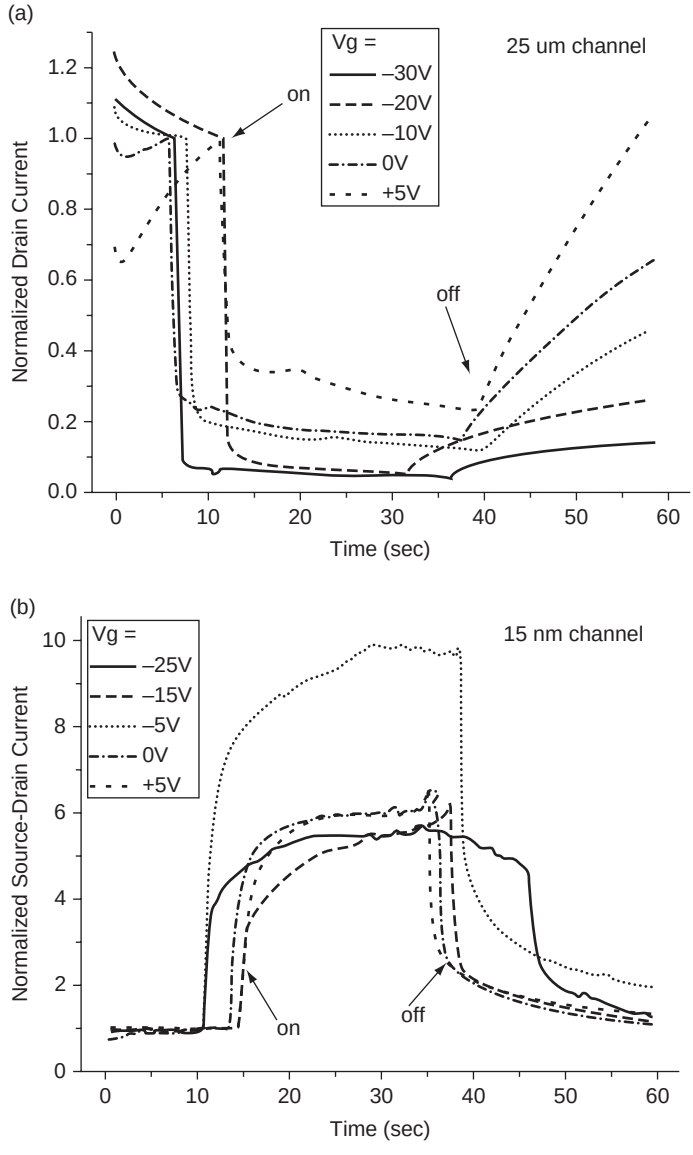

Figure 14.2 *Detection of 1-pentanol using a 4-electrode poly(3-hexylthiophene)-modified field effect transistor configuration: (a) shows the normalized source-drain current in response to exposure to 1-pentanol using the 15 nm cap junction over a range of gate voltages (Vg); (b) shows the 4-electrode nanogap junction configuration prior to modification with poly(3-hexylthiophene). Scale bar 100 nm. (Reprinted with permission from Sensors and Actuators B., L. Wang, D. Fine, S.I. Khondaker, T. Jung and A. Dodabalapur, Sub 10 nm conjugated polymer transistors for chemical sensing, 113, 539–544. Copyright (2006) Elsevier Ltd)*

14.4 Nanofibers and Nanocables

As with nanowires and nanotubes, nanofibers also benefit from the extremely high aspect ratio of this type of 1-D nanostructure, which again has benefits in chemical sensing, particularly with regard to sensitivity to doping and its impact on conductivity. Nanofibers are continuous polymer filaments and have been produced by electrospinning which can produce reasonable quantities of uniform, isolated fiber, but suffers from inherent scale-up issues, by wet-spinning [16], or chemical polymerization techniques popularized by the work of Huang and Kaner [17,18]. The spun fibers are typically deposited by their direct collection onto the sensor surface as a mat, or can be collected, dispersed, and drop-cast separately. It must be stressed that, as a result, there is little inherent control over the deposition localization, which is essentially random. Conductimetric chemical sensors based on conducting-polymer fibers of poly(*o*-toluidine) [19] and PANI [20], both of which were doped with camphorsulfonic acid (CSA) have been fabricated for the detection of alcohol vapors. Both groups showed similar resistance response ratios for exposure to ethanol vapor of 0.36 and 0.38, respectively, with the poly(*o*-toluidine) sensor showing better response to water (0.53). Pinto *et al.* made a further comparison between the nanofiber mat and the sensitivity of isolated nanofibers which showed response ratios for methanol, ethanol, and 2-propanol of 0.94, 0.94, and 0.97, respectively, compared to the mats which were 0.93, 0.38, and 0.18, respectively. Little difference in sensitivity thus resulted for methanol, but this improved for ethanol and propanol. Response times for the single nanofiber sensor were not necessarily better than the nanofiber mat. However, the recovery times were much improved, which may relate to improvements in the ratio of fiber mass and immobilized analyte mass in the isolated fiber system. No data were given as to the limits of detection of the films to these volatile vapors. Electrospun poly(diphenylamine), a derivative of PANI, has also been used as an ammonia sensor with 1 ppm detection and 1.5 minute response time [21].

The work of Kaner and coworkers has focused on the sensing of hydrogen gas on either PANI fabricated by the rapid mixing method [22–24] or PPy using the 'quick shake' reaction [25,26]. Concentrations of 0.06% were readily detectable. The CSA-doped nanofiber PANI was found to have 10-fold greater sensitivity over bulk polymer and had a response ratio of 0.03 [22]. However, HCl doped and undoped fibers had responses of 1.11 and 1.07, respectively [23]. The dedoped PANI films were also superior to PPy which had a response ratio of 0.12 and a response time of 43 s compared to the dedoped PANI with 28 s [25]. The dedoped PANI also showed the best stability and repeatability. This may relate to the sensing mechanism which appears to involve hydrogen bonding with the PANI nitrogens and which may be affected by protonation levels as well as competitive binding by interferences such as water vapor. Sensor response and response time were also affected by dopant and nanofiber size [24]. However, more studies need to be performed to determine which of these factors are responsible.

Nanocable chemosensors have been formed in which an inner core fiber filament is further modified by polymerization of the conducting polymer on its surface. This was first described for sensing by Zhang *et al.* in which a carbon fiber was used as the template for the electrochemical polymerization of a thin film of PANI [27]. The resulting nanoelectrode sensor was used to detect changes in pH resulting from the level of protonation in the polymer backbone. PPy nanofibers have been formed by the electrospinning of nylon fibers,

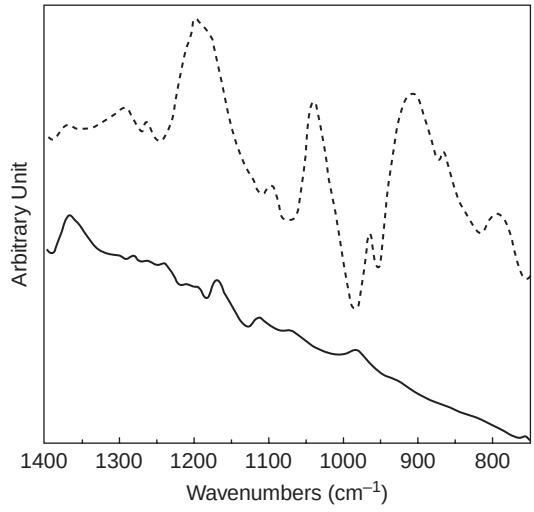

Figure 14.3 *(a) The fabrication of PPy coaxial nanofibers. Fibers of nylon/ferric chloride were first created through electrospinning at a field strength of 750 V cm^{-1} and deposited onto the metallic collector plate. Vapor deposition of PPy took place in a saturated pyrrole vapour at 15 mmHg for 22 hours [28]. (b) Nanofiber mats of nylon/ferric chloride/PPy on a metallic collector. Scale bar 2 μm. (Reprinted with permission from Electroanalysis, Disposable electrospun electrodes based on conducting nanofibers by F. Granato, M. Scampicchio, A. Bianco et al., 20, 1374–1377. Copyright (2008) Wiley-VCH)*

followed by the vapor deposition of pyrrole to form PPy [28] (Figure 14.3). Mats of the coaxial fibers were used for the amperometric detection of phosphate anions with applications in water-quality monitoring, where the limit of detection was found to be 1.2 μM with the suggestion of good long-term storage stability. A coaxial nanofiber based on electrospun poly(methyl methacrylate) and *in situ* solution polymerization has also been tested as a sensor for triethylamine (TEA) [29]. TEA is of significant interest in the food-processing and quality-monitoring fields as it is a volatile organic amine which results from the degradation of proteins and can be used to monitor food spoilage. The sensitivity to TEA vapor was shown to be dependent on the type of dopant used and the fiber diameter produced. Toluene sulfonic acid with 250-nm diameter fibers allowed the detection of 20 ppm TEA with a response ratio of 0.77 at 500 ppm.

As with nanowires and nanotubes, the advantage of nanofibers for chemical sensing lies in the high aspect ratio of the fibers, which leads to benefits in surface-area-to-volume ratio and improved sensitivity to doping and dedoping. However, little high-quality analytical data has yet been published to show the benefits of these materials over others. Nanofibers are mostly produced via electrospinning, which has issues of scale-up. However, continuous wet-spinning techniques can be adapted for continuous production and the physical properties of the fibers can be improved by their compositing as coaxial composites. Problems which remain are the lack of control of the fiber-deposition process, which remains essentially random and which may affect device performance and reproducibility.

14.5 Nanofilms

Sensor nanostructures have also been fabricated by controlling the layer thickness of conducting-polymer films. Bulk and electrochemical deposition of polymer films has been performed extensively in the past. Certainly, exerting greater control over the thickness of the deposited film may again improve surface-area-to-volume ratio effects and allow application in the traditional 2-D planar electrode configuration. This can be achieved either through bulk processing methodologies, in which the layer thickness is maintained at the nanometre scale, or by using already nanostructured materials from which a continuous 2-D film results. However, such an approach has not been extensively adopted for chemical-sensing applications.

The Langmuir–Blodgett (LB) technique is a well-established method of producing monolayers of highly ordered and orientated molecules at air–solution or solution–solution interfaces, which can then be transferred to solid surfaces via a dipping technique. This technique has been adapted using conducting-polymer nanowires and nanorods and applied to chemical sensing of ammonia. PEDOT nanowires doped with toluene sulfonic acid were fabricated using the template-directed oxidative polymerization method and then applied to the surface of an interdigitated electrode via the LB technique [30]. This resulted in the deposition of a highly ordered nanowire film. Unfortunately, no data is provided on the length of the nanowires, or the thickness of the LB film formed. In addition, the LB nanofilm did not show any improved performance over the unordered nanowire film in the detection of ammonia, with 20 ppm giving a response ratio on both surfaces of approx. 0.09. Detection of ammonia was observed at approx. 8 ppm. In contrast, Manigandan *et al.*, claim the formation of PANI 'rod-like' nanostructures of less than 100 nm in diameter formed by the lateral compression of cation-doped PANI in an LB trough [31]. However, these structures lacked uniformity, order and structural homogeneity. The authors quote a response ratio of 0.98 for an unknown quantity of ammonia vapor, with a response time of 52 s.

>Layer-by-layer (LbL) assembly is widely used to produce molecular monolayers and multilayers on sensor surfaces and has also been used to fabricate nanometric films of conducting polymers. The technique may involve repeated alternating deposition of the substrate into polycationic and polyanionic solutions. In one example, the polycation was the conductive polymer, PANI, and the polyanion, the counter-ion dopant, was poly(vinyl sulfonate) (PVS) or a metal-containing phthalocyanine complex [32]. Cyclic voltammetry revealed that greater discrimination of the oxidation peaks of ascorbic acid and dopamine could be achieved when iron was the metal selected as the metal guest. In other work, alternating layers of self-doped, anionic polymers such as poly(anilinesulfonic acid) (SPANI) with cationic poly(allyl amine) (PAH) have been assembled onto seed layers of PAH/poly(styrene sulfonate) (PSS) and evaluated as a humidity sensor [33]. Conversion of the polymer film from the leucoemeraldine to the emeraldine form due to proton transfer to water is suggested as the basis for the reduction in resistance of the film on exposure to water vapor [34]. A capacitance-based sensor for monitoring electrolyte concentration (NaCl) was also established using poly(*o*-ethoxyaniline)/PSS multilayered films [35].

Itoh *et al.* and Wang *et al.* have created an organic/inorganic hybrid nanofilm from the chemical vapor deposition of MoO_3, followed by the ion-exchange-induced intercalation

of PANI [36], poly(*o*-anisidine) [37], or poly(*N*-methylaniline) [38] between the molybdenum trioxide sheets, bringing about highly sensitive changes in conductivity, particularly to volatile organic carbons. These hybrid nanofilms had layer thicknesses of the order of 1.3 nm and were able to detect 25 ppb formaldehyde and acetaldehyde, which is suitable for applications such as sick building syndrome, in which the required sensitivity is 80 ppb. The PANI/MoO_3 hybrid showed the greatest sensitivity to formaldehyde at 50 ppm (0.08), and the poly(*o*-anisidine)/MoO_3 to acetaldehyde with a response ratio of 0.044 at 10 ppm (Figure 14.4).

The use of self-assembled monolayer formation has been adapted to the deposition of conducting-polymer nanofilms by the chemical polymerization of aniline at an amino-silane surface that acts as the seed layer for polymerization, which led to a more ordered nanofibrous growth than would be seen using bulk chemical polymerization [39]. This was shown to be capable of detection of 0.5 ppm ammonia vapor, with a

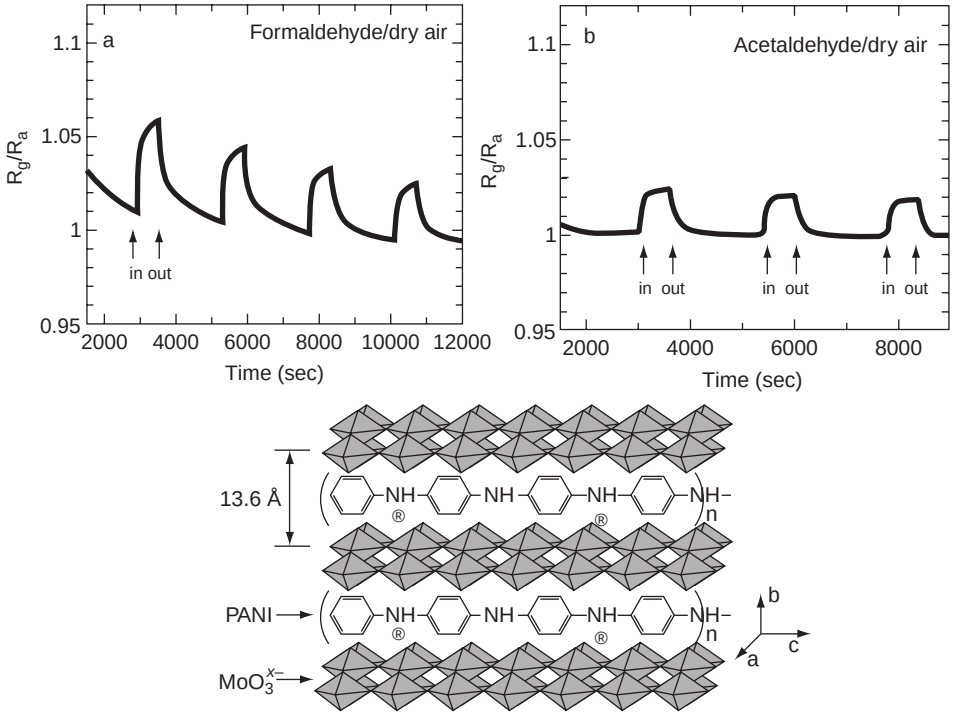

Figure 14.4 *Nanofilms for sensing of volatile organic compounds formed from PANI films intercalated with MoO_3. (a) Aniline monomer was intercalated within the MoO_3 film through a cation-exchange process with sodium ions and polymerized with ammonium persulfate. Conductimetric responses to 50 ppm of formaldehyde (b) and acetaldehyde (c) in dry air. (Reprinted with permission from Thin Solid Films, The preparation of polyaniline intercalated MoO3 thin film and its sensitivity to volatile organic compounds by J. Wang, I. Matsubara, N. Murayama et al., Thin Solid Films, 514, 329–333. Copyright (2006) Elsevier Ltd)*

response ratio of 2 at 20 ppm. Response time was from 60 to 100 s and recovery from 1 to 5 min.

14.6 Metallic Nanoparticle/Conducting-Polymer Nanocomposites

Probably the most exploited area of nanostructuring relating to conducting polymers and sensors lies in composites of nanostructured or unstructured conducting-polymer films and conductive materials with nanostructured morphologies. This is particularly so of metallic nanoparticles embedded within conducting-polymer films and materials. Metals, including noble metals and transition metals, have been extensively studied for their associated catalytic and redox behaviors and a wide variety of these phenomena have been applied to electrochemical sensors. Metallic nanoparticles have also been extensively investigated for their enhanced catalytic and electrocatalytic behaviors due to size, step-defect, and quantum-mechanical properties, which are extremely useful properties in electrochemical sensing [40]. Films of conducting polymers have long been seen as extremely useful substrates and carriers for such nanoparticles due to their excellent film-formation properties, and good levels of conductivity, as well as their open 3-D structures, which allow good diffusion of solution species to the surfaces of the embedded nanoparticles. Composites of these two species thus possess advantageous properties imparted by both materials and have the potential to improve sensor capability. Most attention for chemical-sensing applications has focused on the use of noble-metal catalysts such as Au, Pt, and Ag utilizing principally voltammetric techniques.

Sensors for the neurotransmitters dopamine and epinephrine have been constructed by the incorporation of Au nanoclusters through the reduction of $HAuCl_4$ onto the surface of an electropolymerized overoxidised PPy film [41]. The electrocatalytic oxidation of both dopamine and epinephrine was found to be enhanced significantly in the composite films, as compared with either polymer, nanoparticles, or gold alone, and the enhancements have been ascribed to a combination of the ability of the overoxidised film to accumulate dopamine and epinephrine due to the presence of greater numbers of carboxyl and carbonyl groups, as well as the increased gold electrode surface area imparted by the embedded nanoparticles. The two species could be measured simultaneously using differential pulse voltammetry with a limit of detection of 1 nM for epinephrine and 15 nM for dopamine. Similar techniques using PPy and PEDOT have also been illustrated for the detection of uric acid at nanomolar concentrations [42,43]. In a further modification, an electropolymerized overoxidised PPy film with nanowire morphology was shown to have improved sensitivity to the oxidation of hydrazine and hydroxylamine, which shows moderate enhancement over the electrodes modified with gold nanoclusters alone [44].

Nitrite is a common environmental pollutant. Electrochemically, it is a difficult species to reduce without the application of high overpotentials, and many have explored catalytic mechanisms to make it more amenable to reduction. Li and Lin [45] modified PPy nanowires with Pt nanoclusters and showed enhanced performance of the composite over an electrode modified by Pt nanoparticles alone, with increased reduction current

seen at –120 mV vs. Ag/AgCl, compared to –144 mV for the Pt film alone. The system was capable of detection of nitrite in water at 0.15 μM and a linear range from 0.5 to 1000 μM, and was illustrated for the determination of nitrite in rainwater, river water, and lake water, where the concentration varied between 2.4 and 4.8 μM, well within the range of the sensor device, with RSDs below 4%.

In two recent studies, conductimetric sensors for alcohol vapors were fabricated using metallic nanoparticles of Pd and Ag embedded in chemically synthesized bulk PANI films [46,47]. Both studies showed the enhanced detection of alcohol vapors, including methanol, ethanol, and propanol. However, the chemical interaction was explained in terms of the interaction of the alcohol groups with the imine nitrogen and the enhancement in the presence of the metal nanoparticles was only in terms of an increase in surface area brought about by the embedding of the nanoparticles in the film. However, PANI has an open, porous structure, which allows good diffusion and interaction with the polymer throughout its bulk. Greater consideration should be given to alternative polymer structures that result at the interface between the polymer and the nanoparticle which brings about such enhancements. In another alcohol-related application, an array of seven composites composed of PEDOT and Au or Pt nanoparticles modified with various surface coatings, was used to measure the differential pulse voltammetric responses to a number of Italian wines and was analyzed by principal-component analysis; according to the authors this was found to be a reliable way of distinguishing both style and vintage [48].

14.7 Metal-Oxide Nanoparticles/Conducting-Polymer Nanocomposites

Metal oxides are widely used as sensing materials in the semiconductor industry, particularly for gas sensing. Although their rigid inorganic crystalline structure is well-suited to fabrication using traditional electronics processing on rigid substrates, they are not suitable for alternative fabrication methodologies or deposition on flexible substrates. Sensors based on these metal oxides tend to require operation at high temperatures. Once again, combining these materials with conducting organic polymers has been seen as a way of obtaining synergistic properties in which the metal oxides impart their sensing functionality, while the conducting polymer provides a flexible conductive medium. This compositing is again achieved by fabrication of metal-oxide nanoparticles and their incorporation in or on polymer films.

Among the metal oxides, titanium dioxide (TiO_2) has attracted much interest as a composite material with conducting polymers. It is a relatively environmentally benign and stable n-type semiconductor, and has been applied to the sensing of several gases. However, it typically requires operation at elevated temperatures. Many have investigated the possibility of forming composites with nanoparticles of TiO_2 embedded in conducting-polymer films. The composite films are most easily and typically formed via the *in situ* polymerization of the monomer in the presence of the nanoparticles, which become embedded in the growing film. PANI is well known for its interaction with nitrogenous species such as ammonia and higher amines. PANI-TiO_2 nanoparticle

composites have been shown to have enhanced sensitivity to triethyl- and trimethylamine over PANI or TiO_2 alone [49,50]. However, the majority of this effect appears to be due to the conducting polymer, and its enhancement in the presence of TiO_2 nanoparticles may be merely due to the effect of polymer nanostructuring. PANI-TiO_2 nanoparticle composites were also shown to have better responses to ammonia than their unstructured counterparts [51], being 1.67 and 0.49, respectively, at the lowest measured value of 23 ppm. The sensor was also demonstrated to have decreased responses at elevated temperatures [52]. However, this phenomenon is typical of ammonia interaction with PANI and is probably independent of the effect of TiO_2 nanoparticles. The behavior of a PPy-TiO_2 nanoparticle composite was quite different, however, with the composite showing greater responses with increasing temperature, while the unstructured polymer showed a nonlinear response which was lower than the composite at elevated temperature [53]. This nanocomposite showed a response of 2.73 at 23 ppm with response and recovery quoted as 17 s and 60 s, respectively. It is far from conclusive at this time what benefit, if any, the TiO_2 may be bringing to the material beyond the nanostructured morphology that is achieved, although some temperature-dependent enhancements may be present.

Composites of PANI-TiO_2 and PANI-SnO_2 have also been investigated for their change in conductivity/impedance in response to CO vapors [54]. An LbL assembly approach was used to create a nanocomposite film. PANI was chemically polymerized around the deposited nanoparticles on a PSS monolayer. Both types of film showed good sensitivity to CO, with the PANI-TiO_2 film being particularly sensitive in the 0 to 100 ppm range. The PANI-SnO_2 film also demonstrated response and recovery times in 1 ppm CO of approx. 50 s and 60 s, respectively (Figure 14.5).

PPy-based TiO_2 nanoparticle composites have been investigated for humidity sensing. PPy was formed by *in situ* UV polymerization in the presence of TiO_2 nanoparticles and Ag NO_3 as oxidant [55,56]. Films have also been endowed with greater flexibility through the addition of the ionic polymer poly-[3-(methacrylamino)propyl] trimethyl ammonium chloride (PMAPTAC) [57]. Responses to humidity were either investigated impedimetrically or using a QCM mass balance. PPy-TiO_2 composites with and without the ionic copolymer both exhibited excellent responses to humidity. However, the PMAPTAC-modified film showed impedance changes over four logs, whereas the films without ionic copolymer showed impedance changes over two logs for humidities between 20 and 90% RH. Responses were also very frequency dependent, with good linearity at lower humidities at 1 kHz, becoming poorer at higher frequencies due to the rate of polarization of the adsorbed water. Response to 60% RH was 126 with CO (200 ppm) and CO_2 (500 ppm) being 1.83 and 4.18, respectively. The sensors exhibited rapid responses, switching to and from approx. 10% to 90% RH within 60 s. The QCM-based measurements were shown to detect water vapor at concentrations of 174 to 9700 ppm.

Several other examples of conducting-polymer/metal oxide nanocomposite materials also exist for chemical sensing of a range of analytes, including humidity [58,59], NO_2, [60,61], CO and H_2 [60], and H_2O_2 [62]. This latter example employed the use of Prussian blue, which is an iron complex with excellent catalytic properties, particularly towards O_2 and H_2O_2. Miao *et al.* [62] stabilized nanoparticles of Prussian blue with polymerization of a PANI shell to form a Prussian blue/PANI core–shell composite.

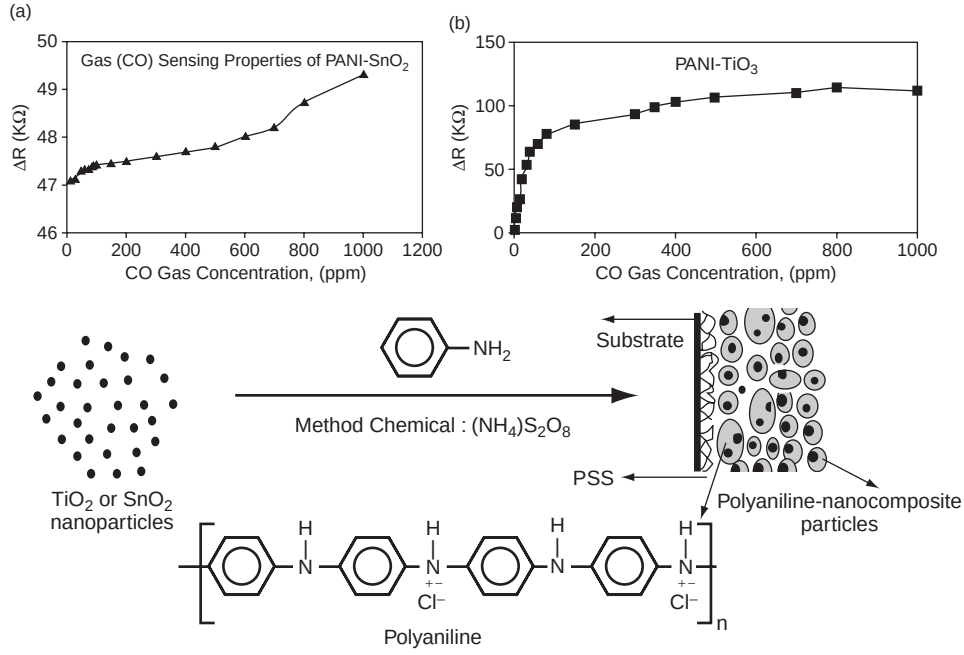

Figure 14.5 *Fabrication of PANI/polystyrene sulfonate-TiO_2 and -SnO_2 nanoparticle composites and sensitivity to CO gas. (a) Nanoparticles of either TiO_2 or SnO_2 were formed by mixing the nanoparticles with aniline monomer and chemically polymerizing onto a polystyrene sulfonate-modified substrate. Exposure of both SnO_2 (b) and TiO_2 (b) composites to CO from 0 to 1000 ppm showed increases in film resistance due to the oxidative nature of the gas. (Reprinted with permission from Thin Solid Films, The preparation of polyaniline intercalated MoO3 thin film and its sensitivity to volatile organic compounds by J. Wang, I. Matsubara, N. Murayama et al., Thin Solid Films, 514, 329–333. Copyright (2006) Elsevier Ltd)*

14.8 Carbon Nanotube Nanocomposites

Another area of intense interest in conducting-polymer nanomaterials for chemical sensing is their combination with carbon nanostructures, most particularly carbon nanotubes, either single-walled (SWNT) or multiwalled (MWNT). This again reflects the desire to combine the beneficial properties of both types of material to create new combinations with novel properties. CNTs empart high conductivity and high aspect ratios, which yield low percolation thresholds with nanodimensional structural order. This has led to their application as chemical sensors. However, CNT-based devices are difficult to fabricate, an issue which may be overcome by their dispersion in a conductive polymeric matrix.

In terms of fabrication, the focus is on the embedding or incorporation of the CNTs into the bulk polymer, with polymerization of the bulk polymer by conventional means, including chemical [63–68], electrochemical [69–71], photopolymerisation [72,73]and vapor deposition [74]. So, clearly, the main focus of the evaluation of the

nanocompsites is the enhancement brought by the incorporation of CNTs into traditional bulk materials. As well as more obvious enhancements in the conductivity of the composite films over conducting polymer alone, it has also been suggested that polymerization in the presence of the CNTs alters the polymerization process, leading to templating and growth orientation [75,63]. A PPy-SWNT conductimetric sensor for NO_2 detection was shown to be of comparative sensitivity to SWNTs alone when the composite was spin-cast and chemically polymerized [66] with a sensitivity of 0.9 at 3000 ppm. However, response and recovery times were slow, being approx. 30 min and 90 min, respectively. A PPy-MWNT electrode was investigated for its response to ethanol vapors [72]. Increases in film resistance were observed upon exposure to ethanol due to the highly electron-withdrawing oxygen in the ethanol molecule, whereas the MWNTs donate electrons and reduce absorption energy. Although the sensor response to the composite was not as good as PPy alone, being 1.19 and 1.24, respectively, the response times improved from a T_{90} of 40 s to 20 s at 30 000 ppm. A PPy-MWNT sensor has also been integrated with an active radio-frequency device for remote wireless monitoring of the anesthetic sevoflurane. This conductimetric sensor had a response of 1.1 at 150 ppm with a response/recovery time of approx. 75 s [73].

As detailed earlier, the conductivity of conducting polymers is very sensitive to the degree of proton doping. Not surprisingly, composites of conducting polymer and CNTs have been investigated for their response to acid environments, both liquid and vapor. PPy [74], PANI, [71] poly(2,5-dimethylaniline) [67], and poly(*o*-anisidine) [65] have all been investigated in this regard. However, the added value of the incorporation of CNTs into these films is far from clear. In most instances, CNTs, as well as conducting polymer/CNT composites, showed similar responses to changes in pH or HCl vapor concentration. It was also noted that CNTs alone had lower resistances than the semiconducting polymer/CNT composite [65], but that the response sensitivity to the composite was 10-fold greater than CNTs alone. Unfortunately, polymer films alone were not presented for comparison and it might be suggested that the addition of the CNTs, while marginally increasing film conductivity, is contributing little to the overall chemical sensitivity of the sensor to proton concentration. In the case of the PPy-carbon nanofiber 'nanocable' composite [74], the sensor did show increased sensitivity to low concentrations of HCl vapor over PPy alone. The response was also very rapid. However, the recovery times were in excess of 300 s at 20 ppm (Figure 14.6).

PANI and PPy-carbon nanotube composites have also been investigated for nitrogenous compounds such as ammonia, trimethylamine, and triethylamine [63,68,69,74] where, in general, significant improvements over polymer alone have been observed. In the case of a PANI/MWNT composite, the response to triethylamine vapor was also very dependent on the type of dopant used. The change from sulfosalicylic acid to *p*-toluene sulfonic acid changed the response sensitivity by more than twofold, reaching approx. 0.8 at 8 ppm [68]. The composite also showed much reduced response times over bulk polymer from 300 to 198 s. Recovery times were comparable. However, the exact mechanisms for these performance improvements remain unclear. Nonetheless, high sensitivity for detection of ammonia has been achieved with these composites, with 50 ppb being detectable using a PANI/SWNT composite [69] with response and recovery times of the order of 80 and 250 s, respectively, at 10 ppm ammonia.

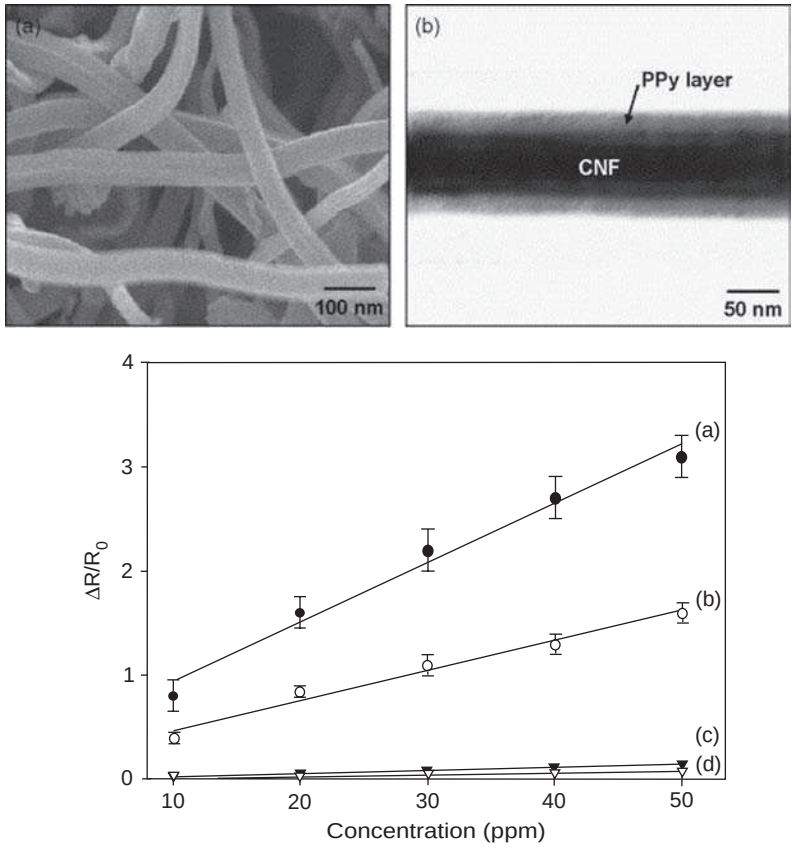

Figure 14.6 *Sensing of HCl and NH_3 using PPy/carbon nanofiber composites: (a) SEM image of the nanofiber mat and (b) TEM of a single composite nanofibers; (c) responses of the composite nanocables (a and b) and bulk PPy (c and d) to NH_3 (a and c) and HCl (b and d) (Reprinted with permission from Sensors and Actuators B: Chemical, CO gas sensing from ultrathin nano-composite conducting polymer film by M. K. Ram, O. Yavuz, V. Lahsangah and M. Aldissi, 106, 2, 750–757. Copyright (2005) Elsevier Ltd)*

14.9 Nanoparticles

Conducting-polymer nanoparticles are a distinct structural morphology with aspect ratios of roughly 1:1:1. As is the case with other forms of nanoparticle, such as metallic and metal oxides, these materials have several potential physical and chemical benefits. They have high surface-area-to-volume ratios and high radii of curvature which drastically alter the surface morphology in comparison to bulk polymer structures. This effect, in common with other nanostructures, may lead to enhancements of alterations in electrocatalytic processes. Nanoparticles can also be formulated to be stable suspensions, which can be processed as if they were a true solution. This has significant benefits for production and

fabrication processability, where solution processing can be employed with preformed polymer materials. The discrete particulate nature of the material is advantageous in certain types of deposition processes, such as inkjet printing, where ejection nozzles can be prone to clogging.

Several distinct nanoparticle structures can be synthesized via different synthetic routes. Micellar templates have been extensively employed in which amphiphilic micelles are formed which act as a site for polymerization of the monomer, such as in the fabrication of PANI nanoparticles on a dodecyl benzenesulfonic acid (DBSA) template [76]. However, there are only a limited number of examples of their application to chemical sensing. These PANI/DBSA nanoparticles have been optimized for deposition via inkjet printing [77] and used to fabricate printed sensor films [78]. These films were evaluated for their ability to detect ammonia in both aqueous and gaseous environments. For aqueous detection, an amperometric flow injection technique has been employed [79]. The sensor was shown to operate optimally at near neutral pH. Exposure to aqueous ammonia resulted in a transient current response at –0.3 V vs. Ag/AgCl ,where it becomes temporarily fully oxidized and recovers to the reduced form when the flow of buffer is restored. The nanoparticle sensor was shown to be capable of detection of ammonia across the industrially relevant range of 1 to 100 ppm, with a detection limit of 0.54 ppm (3.2 μM) with RSD below 5%. A range of common buffer interferences such as primary alcohols and salts were also investigated. For gaseous detection of ammonia, PANI/DBSA nanoparticles have been used in a conductimetric mode on screen-printed interdigitated electrodes [80]. The effect of the number of printed layers and operating temperature were also investigated in the industrially relevant range of 1–100 ppm. A T_{50} response time of 15 s was found for single layer films, irrespective of operating temperature. However, increasing the temperature to 80°C reduced recovery time to 210 s for 50 ppm ammonia. The sensitivity of the response was also shown to decrease with increased temperature and the sensor had a response of 0.24 for 100 ppm when operated at 80 °C. The background sensor response showed little dependence on the change in humidity from 35 to 98% at room temperature. These materials have been used in a noncontact, passive RF mode to detect ammonia inside a sealed container, which has applications for remote monitoring of food quality in so-called ‘smart packaging’ applications [81].

PANI/DBSA nanoparticles have also been studied for their oxidation of ascorbic acid [82]. The nanoparticles were drop-coated onto screen-printed carbon paste electrodes. The peak current response was achieved at approx. 250 mV vs. Ag/AgCl. However, the device also showed sufficient catalysis at 0.0 V vs. Ag/AgCl to allow measurements to be made at this potential where it was capable of detection of 8.3 μM ascorbic acid and was linear in the range of 0.5 to 8 mM.

The other type of nanoparticulate structure and fabrication morphology is the core–shell and associated hollow spheres. In this instance, a spherical nanostructure is established by polymerization onto a preformed nanoparticle. Different template materials have been used for fabrication. For chemical-sensing applications, the two most widely used have been silica and polystyrene, as highly monodisperse nanoparticles of these materials can be reliably synthesized. In addition, their surface chemistry can be modified to achieve different monomer interactions. Core–shell structures could be formed from the

electrochemical polymerization of aniline/PSS on sulfate-modified polystyrene nanoparticles [83]. The positively charged monomer adheres to the negatively charged particle surface and polymerization occurs on the particle surface. The polystyrene nanoparticle can be simply removed by solvent treatment to create associated hollow-sphere structures. Both the core–shell and hollow-sphere structures have been shown to have enhanced catalysis over bulk polymer in the oxidation of NADH, with hollow spheres showing the best performance. This may be due to enhancements in analyte diffusion throughout the film and available surface area for electrocatalysis.

Others have formed PANI-polystyrene core–shells and hollow spheres using chemical polymerization and decorated them with Au nanoparticles [84] (Figure 14.7). These composites were found to have improved conductivity over undecorated polymer nanoparticles. These were used to investigate dopamine oxidation using cyclic voltammetry. The peak oxidation potential was reduced due to the presence of the Au and the amperometric responses were increased significantly over Au nanoparticle or PANI-modified films alone, most likely due to the distribution of the Au nanoparticles and associated improvements in dopamine diffusion and access to the Au nanoparticle surfaces (Figure 14.8).

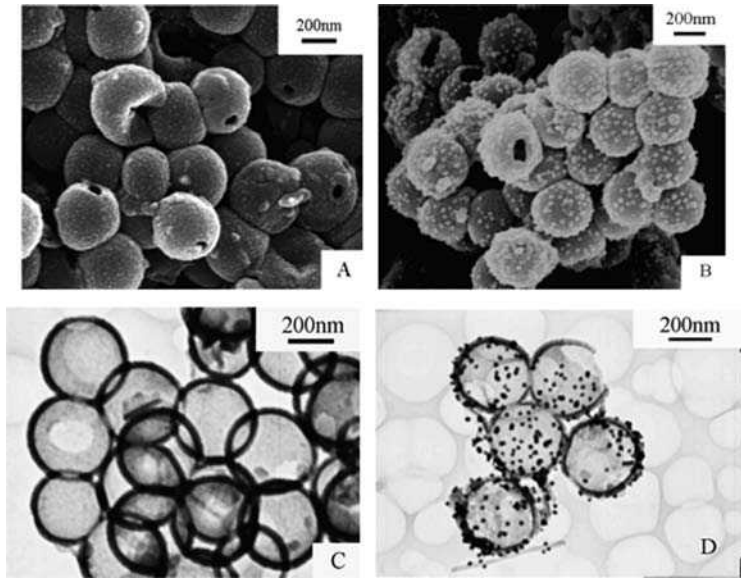

Figure 14.7 *TEM of PANI hollow spheres produced by chemical polymerization of aniline on polystyrene particles and removal with tetrahydrofuran, and decorated with gold nanoparticles. (Reprinted with permission from Langmuir, Polyaniline / Au composite hollow spheres: Synthesis, characterisation, and application to the detection of dopamine by X. M. Feng, C.J. Mao, G. Yang et al., 22, 9, 4384–4389. Copyright (2006) American Chemical Society)*

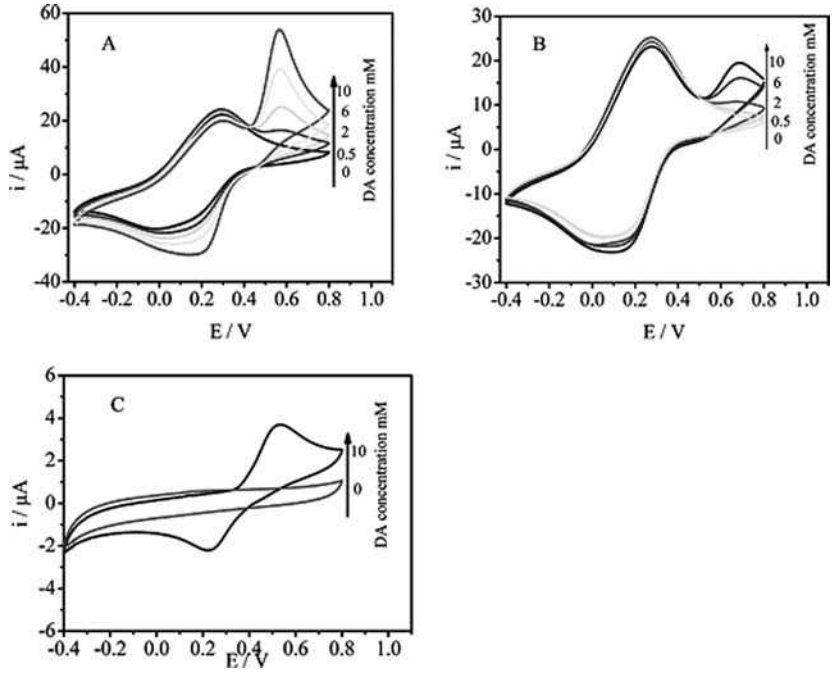

Figure 14.8 *Cyclic voltammograms of glassy carbon electrodes modified with PANI hollow spheres and gold nanoparticles (A), PANI alone (B) and gold nanoparticles alone (C) in a range of concentrations of dopamine (DA) at a scan rate of 100 mV* s^{-1} *vs. SCE. (Reprinted with permission from Langmuir, Polyaniline / Au composite hollow spheres: Synthesis, characterisation, and application to the detection of dopamine by X. M. Feng, C.J. Mao, G. Yang et al., 22, 9, 4384–4389. Copyright (2006) American Chemical Society)*

14.10 Nanoporous Templates

Solid templating methods have also been applied to the fabrication of nanoporous films and associated composites prior to the removal of the template. In this case, ordered, close packing of the template material must typically be achieved to create the porous networks (Figure 14.9(A)). Such films have been shown to have enhanced electrocatalysis to the reduction of nitrite over bulk polymer [85]. The amperometric responses to nitrite were nearly threefold higher in the nanocomposite material over bulk polymer at 50 mV vs. Ag/AgCl (Figure 14.9(B)). The amperometric response from the nanostructured composite was very dependent on the thickness of the deposited template layer, showing once again that the surface area enhancement due to nanotemplating enhances the catalytic efficiency of the film. Typically, inefficient diffusion of the species within the film may limit the catalysis achievable with bulk polymers, and this limitation appears to be overcome by nanostructuring. The optimized nanocomposite had a linear range for $NaNO_2$ of 5×10^{-7} to 1.4×10^{-3} M ($r = 0.999$, $n = 12$), a response time of 5 s, and a detection limit of 2.7×10^{-7} M (S/N = 3). The nanocomposites and nanoporous structures did exhibit comparable levels of catalysis which

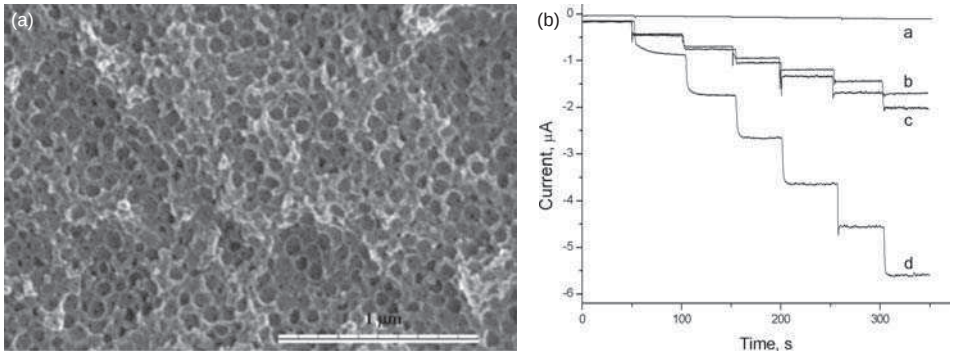

Figure 14.9 *The application of porous PANI films and composites to the sensing of nitrite. Scale 1 μm (A) Porous film of poly(aniline) formed from the in situ electrochemical synthesis in the presence of 100 nm polystyrene nanoparticle templates. (B) Enhanced electrocatalysis of concentrations of 50 μM nitrite in 0.1 M HCl at + 50 mV vs. Ag/AgCl of the nanocomposite film (d) compared to classy carbon (a), pre-treated glassy carbon (b) and bulk PANI [85]. (Reprinted with permission from Chemistry: A European journal, Nanocomposite and nanoporous polyaniline conducting polymers exhibit enhanced catalysis of nitrite reduction by X. Luo, A.J. Killard and M.R. Smyth, 13, 2138–2143. Copyright (2007) Wiley-VCH)*

suggests that in this instance the presence of the template was not a barrier to diffusion through the film. However, removal of the template did lead to decreases in electrochemical reproducibility, which may be due to collapsing or shrinkage of the film.

Greater enhancements in nitrite catalysis have been achieved by decorating the surface of bulk electropolymerized PANI films with polystyrene nanoparticles and repeating the polymerization process, forming either core–shell/hollow spheres or nanocomposite/nanopores, before and following template removal. In this way, multiordered structures have been formed with the bulk polymer exhibiting structure at the micrometer scale and the nanotemplating achieving order at the nanometer scale [86]. All types of multiordered film showed that catalysis was superior when the template was present. In the case of the core–shells, catalysis was greatest when the shell was thickest. However, for nanocomposites, the opposite was the case, with a single round of polymerization being optimal. In any case, a response of 16 μA at 500 μM was achieved (7.07 mm^2) which is double that achieved elsewhere [85].

14.11 Application Summaries

Table 14.1 gives an alphabetical listing of electrochemical sensors based on nanostructured conducting-polymer materials and composites. The main sensor characteristics have been extracted from the literature. The data given in the table are based on values extracted from the associated publications, either directly, or approximated from graphical data. The comments principally refer to abbreviations of the synthetic and deposition methods used, as well as other pertinent characteristics of the sensor. Responses or sensitivity values are based on either single data or slopes determined from calibrations. Detection limits are either formal limits of detection, or the lowest concentrations determined in the work, and

Table 14.1 *Alphabetical listing of analytes detected via electrochemical sensing employing nanostructured conducting polymer*

Analyte	Polymer material and morphology [a]	Method [b]	Response/ Sensitivity [c]	Analytical range	Detection limit	Response time[d]	Recovery time[d]	Comments[e]	Ref.
Acetaldehyde	PNMA-MoO_3 nanofilms	Cond.	$S_2 \sim 0.028$ @ 9.1 ppm	1–9 ppm	0.91 ppm	–	–	Chemical vapor deposition, chemical polymerization, ion exchange intercalation	[38]
	PANI-MoO_3 nanofilms	Cond.	$S_2 \sim 0.06$ @ 7 ppm	25–7000 ppb	25 ppb	–	–	Chemical vapor deposition, chemical polymerization, ion exchange intercalation	[87]
	PANI-MoO_3 nanofilms	Cond.	$S_4 = 1.04$ @ 50 ppm	50 ppm	50 ppm	~600 s	~1000 s	Chemical vapor deposition, chemical polymerization, ion exchange intercalation	[36]
Acetone	PEDOT/PSS nanowires	Cond.	–	20–80% saturation in N_2	<100 ppm	$T_{90} \sim 30$ s	~ 20 s	Template-directed electrochemical polymerization, dielectrophoretic deposition	[2]
Ammonia	PPy nanowire	Cond.	$S_3 = 6 \times 10^{-4}$/ ppm	40–300 ppm	40 ppm	–	–	Template-directed chemical polymerization, drop-coating	[13]
	PANI/SiW_{12} nanotubes	Cond.	$S_4 \sim 3$ @ 100 ppm	2–100 ppm	5 ppm	~1500 s	–	Template-directed chemical polymerization	[6]
	PANI/PEO nanowire/ nanojunction	Amp.	130 nA @ 50 ppm	0.5–50 ppm	0.5 ppm	~300 s	–	Electrospinning	[14]
	PANI nanowires/ nanojunctions	Cond.	$S_3 \sim 1.4$	0.1–100 $\times$ 10^{-6} bar	0.1 $\times$ 10^{-6} bar	≤60 s	–	Galvanostatic, template-free	[10,11]
	Nanojunctions	Cond.	0.42 μA/Log ppb	16–575 ppb	16 ppb	–	–	Electropolymerization, human breath	[9]
	Poly(diphenylamine)-PMMA nanofibers	Cond.	–	10–300 ppm	1 ppm	~ 1.5 min	–	Electrospinning	[21]
	PANI-DBSA nanoparticles	Cond.	$S_5 = 0.24$@ 100 ppm	1–100 ppm	1 ppm	$T_{50} = 15$ s	–	Micellar-templated chemical polymerization, inkjet printing, industrial detection	[80]
	PANI-DBSA nanoparticles	Amp.	6.8×10^{-4} A/ M	20 μM–10 mM	57 ppb	–	–	Micellar-templated chemical polymerization, inkjet printing, industrial detection	[79]

	PANI-DBSA nanoparticles	Imped.	RF signal ~250	–	–	–	–	Micellar-templated chemical polymerization, inkjet printing, RF, noncontact detection of ammonia	[81]
	PANI/CSA, PTSA, PFOA nanorods, nanoparticles	Cond.	$S_3 = 0.91-0.97$	–	–	52–120 s	–	Langmuir-Blodgett films	[31]
	PANI nanofibers	Cond.	$S_5 = 2$ @ 20 ppm	0.5–20 ppm	0.5 ppm	60–100 s	> 15 min	SAM-assembled nanofibers	[39]
	PEDOT/TSA nanowires	Cond.	$S_3 = 0.09$ @ 20 ppm	8–70 ppm	20 ppm	~7 s	~10 s	Langmuir-Blodgett films	[30]
	PANI/HCl/TiO_2 NP nanocomposite	Cond.	$S_5 = 9$ @ 141 ppm	23–141 ppm	23 ppm	2–8 s	19–70 s	*In situ* chemical polymerization, influence of synthesis temperature on response	[52]
	PANI-TiO_2 colloids nNanocomposite	Cond.	$S_5 = 6.6$ @ 141 ppm	23–141 ppm	23 ppm	5–18 s	16–69 s	*In situ* chemical polymerization	[51]
	PPy-TiO_2 nanocomposite/ nanofilm	Cond.	$S_5 = 0.08$ @ 141 ppm	23–141 ppm	23 ppm	12–19 s	60–85 s	Layer-by-layer assembly, chemical polymerization, impact of air and N_2 carrier on response	[53]
	PPy/CNF Nanocable (coaxial)	Cond.	$S_5 = 3$ @ 50 ppm	10–50 ppm	10 ppm	–	~500 s	Vapor deposition polymerization	[74]
	PANI-SWCNT Nanocomposite	Cond.	$S_3 = 0.02$/ppm	0–400 ppm	50 ppb	Minutes	Hours	Electrochemical polymerization	[69]
Ascorbic acid	PPy nanowires	Pot.	44.11 mA/M cm^2	5.0×10^{-4}–2.0×10^{-2} M	4.65×10^{-5} M	–	–	Template-free potentiostatic polymerization	[4]
	PANI-DBSA Nanoparticle	Amp.	10.75 μA/mM cm^2	0.5–8 mM	8.3 μM	–	–	Templated chemical polymerization, drop-casting, @ 0.0 V vs. Ag/AgCl	[82]
	PANI-phthalocyanine nanofilms	CV	–	–	–	–	–	Layer-by-layer, chemical polymerization, interferent in dopamine detection	[32]

(*continued overleaf*)

Table 14.1 (*continued*)

Analyte	Polymer material and morphology [a]	Method [b]	Response/ Sensitivity [c]	Analytical range	Detection limit	Response time[d]	Recovery time[d]	Comments[e]	Ref.
	PEDOT/Au NP Nanocomposite	DPV	–	0.5–3.5 mM	0.5 mM	–	–	Electrochemical polymerization, interferent in dopamine detection	[43]
Carbon monoxide	PANI-TiO_2 colloids Nanocomposite	Cond.	$S_5 \sim 1.8$ @141 ppm	23–141 ppm	23 ppm	–	–	*In situ* chemical polymerization, effect of humidity on background response shown	[51]
	PANI-TSA/PSS TiO_2/SnO_2 NPs Nanocomposite/ nanofilm	Imped./ Cond.	$\Delta R = 49–100$ kΩ @ 1000 ppm	1–1000 ppm	1 ppm	~80 s	~80 s	Chemical polymerization, LbL assembly	[54]
	PANI-CSA/In_2O_3 NP Nanofiber/ nanocomposite	SAW	2.0 kHz @ 500 ppm	60–1000 ppm	60 ppm	$T_{90} = 24$ s	$T_{90} = 36$ s	Chemical polymerization, drop casting	[60]
Chloroform	PANI-nitric acid/ benzoyl peroxide nanofiber	Amp.	$I/I_0 = 0.86$ in 2.2 % chloroform	–	–	$T_{90} = 50.2$ s	–	*In situ* UV polymerization	[88]
	PANI-Cu nanocomposite	Cond.	$S_3 = 1.5–3.5$	10–100 ppm	10 ppm	~ 5 min	–	Chemical polymerization, pelleting, chloroform vapor	[89]
Chloro-methanes	Poly(3-methylthiophene)-MWCNTs nanocomposite	Cond.	$S_3 = 3.6–11.9 \times 10^{-3}$/ppm	4–20 ppm		60–120 s		*In situ* chemical polymerization, drop-casting	[64]
Copper	PPy/NTA nanotubes/ nanojunctions	Cond.	$S_3 = 0.6$ @10^{-11} M	1×10^{-14}– 1×10^{-10} M	0.6 ppt	~ 50 s	–	Template-directed electrochemical polymerization and drop-casting	[12]
	PANI/PSS-peptide chelator nanojunctions	Cond.	–	0.06–1000 nM	62 pM	–	–	Drinking water analysis	[8]
Dimethyl methyl phosphonate (DMMA)	PTh-CNT nanocomposite/ nanofilm	Cond.	$S_3 = 0.08$ @ 0.6 ppm	0.05–25 ppm	0.6 ppm	–	–	Spin-coating	[90]

Dopamine	PANI nanojunctions	Cond./ Amp	–	–	100 nM	~ 40 s		ChemFET in the presence of 1 mM ascorbic acid	[7]
	PANI/Au hollow nanospheres	CV	54.1 μA @ 10 mM	0.5–10 mM	0.5 mM	–	–	Chemical polymerization, drop-coating	[84]
	PANI-phthalocyanines nanofilms	CV	–	0.25–8 mM	10^{-4} M	–	–	Layer-by-layer, chemical polymerization, ascorbic acid interference	[32]
	PPy-Au nanocluster nanocomposite	DPV	–	7.5×10^{-8}-2.0×10^{-5} M	1.5×10^{-8} M	–	–	Electrochemical polymerization and deposition	[41]
	PEDOT/Au NP Nanocomposite	DPV	0.2 μA/nM	20–80 μM	2 nM	–	–	Electrochemical polymerization, ascorbic acid interference	[43]
	Poly(anilineboronic acid)/CNT nanocomposite	CV	$S_1 = 0.45$ @ >30 nM	1–10 nM	0.6 nM	–	–	*In situ* electrochemical polymerization	[70]
Epinephrine	PPy-Au nanoclusters nanocomposite	DPV	3.58 μA/μM	0.3—21 μM	30 nM	–	–	Electrochemical polymerization and deposition	[42]
Ethanol	PEDOT/PSS Nanowires	Cond.	–	Nonlinear 10–100% saturation in N_2	<100 ppm	–	–	Template-directed electrochemical polymerization, dielectrophoretic deposition	[2]
	Poly(*o*-toluidine) camphorsulfonic acid fibers	Cond.	$S_3 = 0.360 \pm 0.063$	–	–	–	–	Electrospinning, surface collection	[19]
	PANI-CSA nanofibers	Cond.	$S_3 = 0.94$	–	–	20 s	20 s	Electrospinning	[20]
	PANI/Ag NP nanocomposite	Cond.	S_4= 0.002/ppm	0–500 ppm	100 ppm	102–52 s	~ 40 min	*In situ* chemical polymerization, pelleting, ethanol vapor	[47]
	PPy/MWCNT/ $NaClO_4$ nanocomposite	Cond.	S_4= 1.19@ 30 000 ppm	30 000–40 000 ppm	30 000 ppm	$T_{90} = 20$ s	$T_{90} = 20$ s	Spin-coating, UV polymerization, ethanol vapour in air. Acetone interference assessed	[72]
	PEDOT/PSS nanowires	Cond.	$S_3 = .55$@ 25 Torr	0–25 Torr	0.25 Torr	–	–	Ethanol vapour in N_2, block copolymer nanolithography	[91]

(*continued overleaf*)

Table 14.1 (*continued*)

Analyte	Polymer material and morphology [a]	Method [b]	Response/ Sensitivity [c]	Analytical range	Detection limit	Response time[d]	Recovery time[d]	Comments[e]	Ref.
Formaldehyde	PNMA-MoO_3 Nanofilms	Cond.	$S_2 \sim 0.026$ @ 9.1 ppm	1−9 ppm	0.91 ppm			Chemical vapor deposition, chemical polymerization, ion-exchange intercalation	[38]
	PANI-MoO_3 Nanofilms	Cond.	$S_2 \sim 0.06$ @ 5 ppm	25−5000 ppb	25 ppb	–	–	Chemical vapor deposition, chemical polymerization, ion-exchange intercalation	[87]
	PANI-MoO_3 Nanofilms	Cond.	$S_4 = 1.09$ @ 50 ppm	50 ppm	50 ppm	∼1000 s	∼3000 s	Chemical vapor deposition, chemical polymerization, ion-exchange intercalation	[36]
HCl	Poly(2,5-dimethylaniline)/ CNT nanocomposite	Cond.	–	–	–	–	–	Langmuir-Shaefer films and spin coating	[67]
	PAO-CNT nanocomposite	Cond.	$S_3 = 0.28$ @ 100 ppm	100−400 ppm	–	5 s @ 100 ppm	–	Pulsed plasma CNT alignment, chemical polymerization, Langmuir-Shaefer films	[65]
	PPy/CNF Nanocable (coaxial)	Cond.	$S_5 \sim 1.3$@ 50 ppm	10−50 ppm	10 ppm	–	∼150 s	Vapor deposition polymerization	[74]
Hexane	Poly(*o*-toluidine) camphorsulfonic acid fibers	Cond.	$S_3 = 0.015 \pm 0.014$ ($n = 4$)	–	–	–	–	Electrospinning, surface collection	[19]
Humidity	SPANI nanofilm	Cond.	–	50−90%RH	–	15 s @ Δ5%RH	–	Layer-by-layer technique	[33]
	PPy/Ag/TiO_2 NP nanocomposite	SAW	0.0069 Hz/ ppm @ 171.1 ppm	173.9−9711 ppm	173.9	12 s @ 55 ppm	20 s @ 55 ppm	Spin-coating, UV polymerization, low humidity detection	[55]
	PPy/TiO_2 NP/ PMAPTAC nanocomposite	Imped.	−0.05 Log Z/ %RH	30−90 %RH	–	11-90%RH in 40 s		Spin-coating, UV polymerization, effect of frequency and temperature studied	[57]
	PPy-TiO_2 NP, $AgNO_3$ nanocomposite	Imped.	−0.03 Log Z/ %RH	30−90% RH	–	30−80%RH in 40 s	–	UV photopolymerization	[56]
	PPy-Fe_3O_4 NPs nanocomposite	Cond.	$S_4 = 1000$ @ 75%RH	20−80%RH	–	10−15 s	20 s	Emulsion polymerization and pelleting	[58]

	POA/WO_3 Composite	Cond.	–	25−95%RH	–	50 s	49 s	Chemical polymerization, pelleting	[59]
Hydrazine	PANI/SiW_{12} nanotubes	Cond.	S_4∼ 0.1 @ 100 ppm	100 ppm	100 ppm	–	–	Template-directed chemical polymerization	[6]
	PPy-Au nanowire/ nanoparticle/ nanocomposite	DPV	63.0 μA/mM	1−500 μM	0.21 μM			Electrochemical polymerization and deposition	[44]
Hydrogen	PANI nanowires/ nanofibrils	CV, SAW		0.065−1% in air				Templated and template-free electropolymerization	[92]
	PPy nanofibers	Cond.	S_3= 0.12 @ 1%	0.06−1%	0.06%	43 s	–	Chemical polymerization, drop casting	[25]
	PPy nanofibers	SAW	Δf =20 kHz @ 1%	0.06−1%	0.06%	T_{90} = 39 s @ 1%	T_{90} = 219 s @ 1%	Chemical polymerization, drop casting	[26]
	PANI, PANI-HCl nanofiber	Cond.	S_1=1.11/1.07 @ 1%	0.06-1%	0.06%	28−32 s	–	Chemical polymerization, drop-casting	[23]
	PANI-CSA nanofibers	SAW	Δf = 14 kHz @ 1%	0.06−1%	0.06%	<250 s	<400 s	Template-free rapid mixing method, chemical polymerization	[24]
	PANI/CSA Nanofiber	Cond.	S_3 = -0.03	0−1%	0.1%	–	–	Chemical polymerization, airbrush deposition	[22]
	PANI-CSA/In_2O_3 NP nanofiber/ nanocomposite	SAW	11 kHz @ 1%	0.06−1%	0.06%	T_{90} = 30 s	T_{90} = 40 s	Chemical polymerization, drop casting	[60]
	PANI/WO_3 nanofiber	SAW	7 kHz @ 1%	0.06−1%	0.06%	T_{90} = 40 s	T_{90} = 100 s	Template-free chemical polymerization, 'quick-shake'	[93]
	PANI nanofiber	SAW	Δf = 9.2 kHz @ 1%	0.06−1%	0.06%	12 s	44 s	Electropolymerization	[94]
Hydrogen peroxide	PANI/PB NPs nanocomposite	CV		1−10 mM	1 mM			Chemical and electrochemical polymerization	[62]
	PPy-Au/PB nanoporous template	Amp.	–	10^{-4}−10^{-9} M	10^{-9} M	–	–	Nanotemplate lithography, galvanostatic polymerization	[95]
Hydroxy-lamine	PPy-Au nanowire/ nanoparticle/ nanocomposite	DPV	126 μA/mM	1−500 μM	0.20 μM	–	–	Electrochemical polymerization and deposition	[44]

(*continued overleaf*)

Table 14.1 (*continued*)

Analyte	Polymer material and morphology [a]	Method [b]	Response/ Sensitivity [c]	Analytical range	Detection limit	Response time[d]	Recovery time[d]	Comments[e]	Ref.
Methanol	PEDOT/PSS nanowires	Cond.	$S_4 = 1.01$	10−50% saturation in N_2	<100 ppm	T_{90} ~30 s	~ 20 s	Template-directed electrochemical polymerization, dielectrophoretic deposition	[2]
	PANI-CSA nanofibers	Cond.	$S_3 = 0.94$	–	–	32 s	20 s	Electrospinning	[20]
	PANI/Pd NP nanocomposite	Cond.	–	0−10 ppm	–	2−8 s	–	Chemical polymerization and pelleting, vapor in air	[46]
Nickel	PANI/PSS-peptide chelator nanojunctions	Cond.	–	0.1−1000 nM	0.4 nM	–	–	Electropolymerization, drinking water	[8]
Nitrate	PPy nanowires	Amp	1.17−1.65 nA/ μM	10 μM−1 mM	4.5±1 μM	–	–	Membrane template polymerization, dielectrophoresis, microfluidic device	[96]
Nitrite	PPy nanowires	Amp	55.84 mA/M cm^2	0−20 mM	–	–	–	Template-free electrochemical polymerization	[3]
	PPy-Pt nanowire/ nanocluster/ nanocomposite	CV	0.566 μA/μM	5×10^{-7}-1 $\times 10^{-3}$ M	1.5×10^{-7} M	–	–	Electrochemical polymerization and deposition	[45]
	PPy, Poly(*o*-anisidine), poly(1.3-DAB) and poly(1,2-DAB) nanotubes	Amp		10−1000 μM	2 μM	–	–	Template-directed electropolymerization, drinking water analysis	[97]
Nitrogen dioxide	PPy nanofibers	SAW	$\Delta f = 4.5$ kHz @ 2.1 ppm	–	2.1 ppm	$T_{90} = 133$ s	$T_{90} = 298$ s	Chemical polymerization, drop-casting	[26]
	PANI Nanofiber	Cond.	–	10−200 ppm	–	–	–	Interfacial polymerization, drop-casting	[98]
	PEDOT/SnO_2 and PTh-SnO_2 nanocomposites	Cond.	$\Delta R_t = 16$-120 kΩ @800−1000 ppb	0−1000 ppb	<100 ppb	–	–	Range of polymers studied, *in situ* surface polymerization	[99]

	PANI-CSA/In_2O_3 NP nanofiber/ nanocomposite	SAW	2.5 kHz @2.12 ppm	0.5−2.1 ppm	510 ppb	$T_{90} = 30$ s	$T_{90} = 65$ s	Chemical polymerization, drop-casting	[60]
	PANI/chitosan/WO_3 nanofiber/ nanocomposite	Amp.	–	100−500 ppb	–	8 s	–	Electrochemical polymerization	[61]
	Polypyrrole/CNT nanocomposite	Cond.	$S_5 \sim 0.9$	3000 ppm	3000 ppm	50 s	90 s	Chemical polymerization, drop-casting	[66]
1-Pentanol	PTh nanogaps/ nanojunctions	Amp	–	–	–	~ 2 s	>20 s	ChemFET, chemical polymerization and inkjet printing	[15]
pH	PANI-carbon nanofiber nanofiber/ nanocable	Pot.	-60.0 ±0.5 mV/ pH	pH 2.0−12.5	–	6−120 s	–	Electrochemical polymerization	[27]
	PPy/CNT, PANI/CNT nanocomposite	Pot.	$\sim$ -66.6 mV/pH	pH 1−13	–	–	–	Elecrochemical polymerization	[71]
Phosphate	PPy/nylon/$FeCl_3$ nanofibers	Amp.	1.35 μA/mM	0.1−1.2 mM	1.2 μM	–	–	Electrospinning	[28]
Propan-2-ol	PANI-CSA nanofibers	Cond.	$S_3 = 0.97$	–	–	>110	>50	Electrospinning, concentration not specified	[20]
Serotonin	PPy-Au nanocluster Nanocomposite	DPV		7.0×10^{-9}−2.2×10^{-6} M	1.0×10^{-9} M	–	–	Electrochemical polymerization and deposition	[41]
Sevoflurane	PPy/CNT nanocomposite	Cond.	30 MΩ	8%	8%	75 s	–	*In situ* UV polymerization, wireless RF monitoring of anaesthetic	[73]
Sodium chloride	POEA/PSS nanofilm	Imped.	7.6×10^{-8} F @ 10 mM	0.1−10 mM	10 μM	–	–	Layer-by-layer self-assembly	[35]
Toluene	PANI-nitric acid/ benzoyl peroxide nanofiber	Amp.	$I/I_0 = 0.413$	–	–	$T_{90} = 44.2$ s	–	*In situ* UV polymerization	[88]
Triethylamine	PANI/SiW_{12} nanotubes	Cond.	$S_3 \sim 10$ @ 100 ppm	100 ppm	100 ppm	~ 2000 s	–	Template-directed chemical polymerization	[6]
	PANI/egg shell membrane or PVA Nanotubes	Cond.	$S_3 = 9$	100 ppm	100 ppm	~200 s	–	Electrospun fiber template, eggshell membrane template, chemical polymerization	[5]

(*continued overleaf*)

Table 14.1 (*continued*)

Analyte	Polymer material and morphology [a]	Method [b]	Response/ Sensitivity [c]	Analytical range	Detection limit	Response time[d]	Recovery time[d]	Comments[e]	Ref.
	PANI/PMMA nanocable (coaxial)	Cond.	$S_3 = 0.77$ @ 500 ppm	20 − 500 ppm	20 ppm	–	–	Electrospinning, *in situ* solution polymerization	[29]
	PANI-nitric acid/ benzoyl peroxide nanofiber	Amp.	$I/I_0 = 0.074$	–	–	$T_{90} = 13.7$ s	–	*In situ* UV polymerization	[88]
	PANI-HCl, TiO_2 composite	Amp	–	–	5.14×10^{-7} mM	–	–	Spin coating, in-situ polymerization	[49]
	PANI/PSS-CNT nanocomposite	Cond.	$S_5 = 0.8$	0.5−8 ppm	ppb	$T_{90} \sim 200$ s	$T_{90} \sim 10$ min	*In situ* chemical polymerization	[68]
Trimethy-lamine	PANI/PSS/TiO_2 Nanocomposite	QCM	$R = 2.1 \times C$	10−200 ppm	10 ppm	–	–	Chemical polymerization	[50]
	PANI/CNT nanocomposite	Amp	0.5 μA @ 5.14×10^{-7} mM	–	–	–	–	Spin coating, *in situ* chemical polymerization	[63]
Uric acid	PPy-Au nanoclusters nanocomposite	DPV	1.81 μA/μM	0.05−28 μM	12 nM	–	–	Electrochemical polymerization and deposition	[42]
	PEDOT/Au NP nanocomposite	DPV	0.12 μA/nM	20−130 μM	2 nM	–	–	Electrochemical polymerization, ascorbic acid interference	[43]
Vanillin	PTh nanogaps/ nanojunctions	Amp	–	–	–	4 s	–	ChemFET, chemical polymerization and inkjet printing	[15]
White wines	PEDOT/Au and Pt nanocomposites	DPV	–	–	–	–	–	Principal component analysis	[48]

[a] PNMA, poly(*N*-methylaniline); PANI, poly(aniline); PEDOT, poly(3,4-ethylenedioxythiphene; PSS, poly(styrene-sulfonate), PPy, poly(pyrrole); PEO, poly(ethylene oxide); DBSA, dodecylbenzene sulfonic acid; CSA, camphor sulfonic acid; PTSA, poly(*o*-toluene sulfonic acid); PFOA, perfluoro-octanoic acid; TSA, toluene sulfonic acid; CNF, carbon nanofiber; SWCNT, single-walled carbon nanotube; NP, nanoparticle; MWCNT, multiwalled carbon nanotube; PTh, poly(thiphene); CNT, carbon nanotube; POA, poly(*o*-anisidine); SPANI, poly(anilinesulfonic acid); PB, Prussian Blue; DAB, 1,2-diamino benzene; POEA, poly(*o*-ethoxyaniline); PMMA, poly(methyl methacrylate).
[b] Cond, conductimetric; Amp., amperometric; Imped, impedimetric; Pot., potentiometric; CV, cyclic voltammetric; DPV, differential pulse voltammetric; SAW, surface acoustic wave; QCM, quartz crystal microbalance.
[c] See text for definitions of S.
[d] T_x, time taken to reach x% of final value.
[e] Fabrication and polymerization processes and points of note.

the analytical range is again that which was studied, either linear or nonlinear. Response and recovery times are also as stated. T_x values, where given, refer to the time to reach x% of the final signal.

Several methods are used to determine sensor response (S) in the literature, particularly in regard to conductimetric gas sensing, where the ratio of the test response to a control response is determined. The method used typically depends on whether the test response results in a signal that is either greater or lesser than some control value. To avoid confusion and allow standardization, five measures of S are used in this table, denoted S_1–S_5. In some publications, these values are further multiplied by 100 to yield a percentage response. However, in this work, all percentage values have been divided by 100 to yield the response quotient.

The five sensor response values are as follows:

$$\begin{aligned} S_1&=(R_c - R_t)/R_t \\ S_2&=(R_t - R_c) - 1 \\ S_3&=\Delta R/R_c \\ S_4&=R_t/R_c \\ S_5&=(R_t - R_c)/R_c \end{aligned} \tag{14.1}$$

Where R_c is the control response value, R_t is the test response value and ΔR is the difference between the control and test response values, either absolute or otherwise, as specified in the publication.

As can be seen from the table, several sensing applications tend to dominate, such as ammonia, dopamine, aldehydes, humidity, alkylamines, and other nitrogenous gases. This is no surprise as the chemistry of these polymers is dominated by conjugated ring structures possessing nitrogen atoms with associated electronic and doping characteristics. Thus, sensitivity to nitrogenous compounds, as well as to acids and water vapor is a common feature. However, chemical sensing using these polymers is thus dependent on their inherent chemical sensitivity, and the sensing aspect of the polymer is not separate from its selectivity characteristics. This severely limits the range of analytes that are amenable to detection with conducting polymers and also creates problems associated with sensor specificity. Nanostructuring, particularly nanocompositing is increasing the range of materials characteristics, bringing with it modifications in terms of the range of analytes these materials are sensitive to, as well as their selectivity/specificity characteristics. In addition, novel polymer derivatives are being synthesized with modified functionality and associated sensitivity/selectivity characteristics. Nonetheless, many improvements are still necessary in both the polymer chemistry and its nanomaterials control to bring about further improvements in these aspects of the sensing material. Significant improvements can be made to sensor selectivity by the addition of selective layers using the nanomaterials paradigm in much the same way as it has been used for bulk sensor development in the past.

14.12 Conclusions

The utility of conducting polymers as an electrochemical sensor interfacial material is being enhanced by nanotechnology through the fabrication of nanodimensional polymeric

materials and their compositing with a wide variety of conductive and inert nanomaterials. These are beginning to yield improvements in sensor analytical performance, as well as sensor design and fabrication. Continuing work in this field will see further refinements and improvements in the fabrication methodologies, expansion of the range of polymers and their nanostructural morphologies, and further compositing to improve sensitivity and selectivity.

References

[1] M.A. Bangar, C.M. Hangarter, B. Yoo, Y. Rheem, W. Chen, A. Mulchandani, and N.V. Myung, Magnetically assembled multisegmented nanowires and their applications, *Electroanal.*, **21**, 61–67 (2009).
[2] Y. Dan, Y. Cao, T.E. Mallouk, A.T. Johnson, and S. Evoy, Dielectrophoretically assembled polymer nanowires for gas sensing, *Sens. Actuat. B*, **125**, 55–59 (2007).
[3] Y. Tian, J.X. Wang, Z. Wang, and S.C. Wang, Solid-phase extraction and amperometric determination of nitrite with polypyrrole nanowire modified electrodes, *Sens. Actuat. B*, **104**, 23–28 (2005).
[4] J. S. Wang, J.X. Wang, Z. Wang, and S.C. Wang, Electrocatalytic oxidation of ascorbic acid at polypyrrole nanowire modified electrode, *Synth. Met.*, **156**, 610–613 (2006).
[5] Y. Gao, X. Li, J. Gong, B. Fan, Z. Su, and L. Qu, Polyaniline nanotubes prepared using fiber mats membrane as the template and their gas-response behavior, *J. Phys. Chem. C*, **112**, 8215–8222 (2008).
[6] Y. Gao, S. Yao, J. Gong, and L. Qu, Preparation of polyaniline nanotubes via 'thin glass tubes template' approach and its gas response, *Macromol. Rapid Commun.*, **28**, 286–291 (2007).
[7] E.S. Forzani, X. Li, and N. Tao, Hybrid amperometric and conductometric chemical sensor based on conducting polymer nanojunctions, *Anal. Chem.*, **79**, 5217–5224 (2007).
[8] A.D. Aguilar, E.S. Forzani, X.L. Li, N.J. Tao, L.A. Nagahara, I. Amlani, and R. Tsui, Chemical sensors using peptide–functionalized conducting polymer nanojunction arrays, *Appl. Phys. Lett.*, **87**, 193108 (2005).
[9] A.D. Aguilar, E.S. Forzani, L.A. Nagahara, I. Amlani, R. Tsui, and N.J. Tao, Breath ammonia sensor based on conducting polymer nanojunctions, *IEEE Sens. J.*, **8**, 269–273 (2008).
[10] N.T. Kemp, J. Cochrane, and R. Newbury, Patterning of conducting polymer nanowires on gold/platinum electrodes, *Nanotechnol.*, **18**, 145610 (2007).
[11] N.T. Kemp, D. McGrouther, J.W. Cochrane, and R. Newbury, Bridging the gap: Polymer nanowire devices, *Adv. Mater.*, **19**, 2634–2638 (2007).
[12] C.L. Aravinda, S. Cosnier, W. Chen, N.V. Myung, and A. Mulchandani, Label-free detection of cupric ions and histidine-tagged proteins using single poly(pyrrole)-NTA chelator conducting polymer nanotube chemiresistive sensor, *Biosens. Bioelectron.*, **24**, 1451–1455 (2009).
[13] S.C. Hernandez, D. Chaudhuri, W. Chen, N.V. Myung, and A. Mulchandani, Single polypyrrole nanowire ammonia gas sensor, *Electroanal.*, **19**, 2125–2130 (2007).
[14] H.Q. Liu, J. Kameoka, D.A. Czaplewski, and H.G. Craighead, Polymeric nanowire chemical sensor, *Nano Lett.*, **4**, 671–675 (2004).
[15] L. Wang, D. Fine, S.I. Khondaker, T. Jung, and A. Dodabalapur, Sub 10 nm conjugated polymer transistors for chemical sensing, *Sens. Actuat. B*, **113**, 539–544 (2006).
[16] J. Foroughi, G.M. Spinks, G.G. Wallace, and P.G. Whitten, Production of polypyrrole fibres by wet spinning, *Synth. Met.*, **158**, 104–107 (2008).
[17] J.X. Huang and R.B. Kaner, Nanofiber formation in the chemical polymerization of aniline: A mechanistic study, *Angew. Chem. Int. Ed.*, **43**, 5817–5821 (2004).
[18] J.X. Huang and R.B. Kaner, The intrinsic nanofibrillar morphology of polyaniline, *Chem. Commun.*, 367–376 (2006).

[19] D. Aussawasathien, S. Sahasithiwat, and L. Menbangpung, Electrospun camphorsulfonic acid doped poly(*o*-toluidine)-polystyrene composite fibers: Chemical vapor sensing, *Synth. Met.*, **158**, 259–263 (2008).
[20] N.J. Pinto, I. Ramos, R. Rojas, P. Wang, and A.T. Johnson Jr., Electric response of isolated electrospun polyaniline nanofibers to vapors of aliphatic alcohols, *Sens. Actuat. B*, **129**, 621–627 (2008).
[21] K.M. Manesh, A.I. Gopalan, K. Lee, P. Santhosh, K. Song, and D. Lee, Fabrication of functional nanofibrous ammonia sensor, *IEEE Trans. Nanotechnol.*, **6**, 513–518 (2007).
[22] S. Virji, R.B. Kaner, and B.H. Weiller, Hydrogen sensors based on conductivity changes in polyaniline nanofibers, *J. Phys. Chem. B*, **110**, 22266–22270 (2006).
[23] A.Z. Sadek, W. Wlodarski, K. Kalantar-Zadeh, C. Baker, and R.B. Kaner, Doped and dedoped polyaniline nanofiber based conductometric hydrogen gas sensors, *Sens. Actuat. A*, **139**, 53–57 (2007).
[24] A.Z. Sadek, C.O. Baker, D.A. Powell, W. Wlodarski, R.B. Kaner, and K. Kalantar-Zadeh, Polyaniline nanofiber based surface acoustic wave gas sensors – effect of nanofiber diameter on H_2 response, *IEEE Sens. J.*, **7**, 213–218 (2007).
[25] L. Al-Mashat, H.D. Tran, W. Wlodarski, R.B. Kaner, and K. Katantar-Zadeh, Conductometric hydrogen gas sensor based on polypyrrole nanofibers, *IEEE Sens. J.*, **8**, 365–370 (2008).
[26] L. Al-Mashat, H.D. Tran, W. Wlodarski, R.B. Kaner, and K. Kalantar-Zadeh, Polypyrrole nanofiber surface acoustic wave gas sensors, *Sens. Actuat. B*, **134**, 826–831 (2008).
[27] X.J. Zhang, B. Ogorevc, and J. Wang, Solid-state pH nanoelectrode based on polyaniline thin film electrodeposited onto ion-beam etched carbon fiber, *Anal. Chim. Acta*, **452**, 1–10 (2002).
[28] F. Granato, M. Scampicchio, A. Bianco, S. Mannino, C. Bertarelli, and G. Zerbi, Disposable electrospun electrodes based on conducting nanofibers, *Electroanal.*, **20**, 1374–1377 (2008).
[29] S. Ji, Y. Li, and M. Yang, Gas sensing properties of a composite composed of electrospun poly(methyl methacrylate) nanofibers and *in situ* polymerized polyaniline, *Sens. Actuat. B*, **133**, 644–649 (2008).
[30] J. Xu, Y. Jiang, Y. Yang, and J. Yu, Self-assembly of conducting polymer nanowires at air–water interface and its application for gas sensors, *Mater. Sci. Eng. B*, **157**, 87–92 (2009).
[31] S. Manigandan, A. Jain, S. Majumder, S. Ganguly, and K. Kargupta, Formation of nanorods and nanoparticles of polyaniline using Langmuir Blodgett technique: Performance study for ammonia sensor, *Sens. Actuat. B*, **133**, 187–194 (2008).
[32] V. Zucolotto, M. Ferreira, M.R. Cordeiro, C.J.L. Constantino, W.C. Moreira, and O.N. Oliveira, Nanoscale processing of polyaniline and phthalocyanines for sensing applications, *Sens. Actuat. B*, **113**, 809–815 (2006).
[33] R. Nohria, R.K. Khillan, Y. Su, R. Dikshit, Y. Lvov, and K. Varahramyan, Humidity sensor based on ultrathin polyaniline film deposited using layer-by-layer nano-assembly, *Sens. Actuat. B*, **114**, 218–222 (2006).
[34] S. Jain, S. Chakane, A.B. Samui, V.N. Krishnamurthy, and S.V. Bhoraskar, Humidity sensing with weak acid-doped polyaniline and its composites, *Sens. Actuat. B*, **96**, 124–129 (2003).
[35] N.K. Leonel Wiziack, L.G. Paterno, F.J. Fonseca, and L.H. Capparelli Mattoso, Effect of film thickness and different electrode geometries on the performance of chemical sensors made of nanostructured conducting polymer films, *Sens. Actuat. B*, **122**, 484–492 (2007).
[36] J. Wang, I. Matsubara, N. Murayama, S. Woosuck, and N. Izu, The preparation of polyaniline intercalated MoO_3 thin film and its sensitivity to volatile organic compounds, *Thin Solid Films*, **514**, 329–333 (2006).
[37] T. Itoh, I. Matsubara, W. Shin, N. Izu, and M. Nishibori, Analytical study of resistance drift phenomena on $(PANI)_{(x)}MoO_3$ hybrid thin films as gas sensors, *Bull. Chem. Soc. Jpn.*, **81**, 1331–1335 (2008).
[38] T. Itoh, I. Matsubara, W. Shin, and N. Izu, Synthesis and characterization of layered organic hybrid thin films based on molybdenum trioxide with poly(*N*-methylaniline) for VOC sensor, *Mater. Lett.*, **61**, 4031–4034 (2007).

[39] D. S. Sutar, N. Padma, D.K. Aswal, S.K. Deshpande, S.K. Gupta, and J.V. Yakhmi, Preparation of nanofibrous polyaniline films and their application as ammonia gas sensor, *Sens. Actuat. B*, **128**, 286–292 (2007).
[40] A. Wieckowski, E.R. Savinova, and C.G. Vayenas, *Catalysis and Electrocatalysis at Nanoparticle Surfaces*, CRC Press, Boca Raton, 2003.
[41] J. Li and X. Lin, Simultaneous determination of dopamine and serotonin on gold nanocluster, *Sens. Actuat. B*, **124**, 486–493 (2007).
[42] J. Li and X. Lin, Electrodeposition of gold nanoclusters on overoxidized polypyrrole film modified glassy carbon electrode and its application for the simultaneous determination of epinephrine and uric acid under coexistence of ascorbic acid, *Anal. Chim. Acta*, **596**, 222–230 (2007).
[43] J. Mathiyarasu, S. Senthilkumar, K.L.N. Phani, and V. Yegnaraman, PEDOT-Au nanocomposite film for electrochemical sensing, *Mater. Lett.*, **62**, 571–573 (2008).
[44] J. Li and X. Lin, Electrocatalytic oxidation of hydrazine and hydroxylamine at gold nanoparticle-polypyrrole nanowire modified glassy carbon electrode, *Sens. Actuat. B*, **126**, 527–535 (2007).
[45] J. Li and X. Lin, Electrocatalytic reduction of nitrite at polypyrrole nanowire-platinum nanocluster modified glassy carbon electrode, *Microchem. J.*, **87**, 41–46 (2007).
[46] A.A. Athawale, S.V. Bhagwat, and P.P. Katre, Nanocomposite of Pd-polyaniline as a selective methanol sensor, *Sens. Actuat. B*, **114**, 263–267 (2006).
[47] A. Choudhury, Polyaniline/silver nanocomposites: Dielectric properties and ethanol vapour sensitivity, *Sens. Actuat. B*, **138**, 318–325 (2009).
[48] L. Pigani, G. Foca, K. Ionescu, V. Martina, A. Ulrici, F. Terzi, M. Vignali, C. Zanardi, and R. Seeber, Amperometric sensors based on poly(3,4-ethylenedioxythiophene)-modified electrodes: Discrimination of white wines, *Anal. Chim. Acta*, **614**, 213–222 (2008).
[49] X.F. Ma, M. Wang, G. Li, H.Z. Chen, and R. Bai, Preparation of polyaniline-TiO_2 composite film with in situ polymerization approach and its gas-sensitivity at room temperature, *Mater. Chem. Phys.*, **98**, 241–247 (2006).
[50] J. Zheng, G. Li, X. Ma, Y. Wang, G. Wu, and Y. Cheng, Polyaniline–TiO_2 nano-composite-based trimethylamine QCM sensor and its thermal behavior studies, *Sens. Actuat. B*, **133**, 374–380 (2008).
[51] H. Tai, Y. Jiang, G. Xie, J. Yu, and X. Chen, Fabrication and gas sensitivity of polyaniline-titanium dioxide nanocomposite thin film, *Sens. Actuat. B*, **125**, 644–650 (2007).
[52] H. Tai, Y. Jiang, G. Xie, J. Yu, X. Chen, and Z. Ying, Influence of polymerization temperature on NH_3 response of PANI/TiO_2 thin film gas sensor, *Sens. Actuat. B*, **129**, 319–326 (2008).
[53] H. Tai, Y. Jiang, G. Xie, J. Yu, and M. Zhao, Self-assembly of TiO_2/polypyrrole nanocompsoite ultrathin films and application for an NH_3 gas sensor, *Int. J. Environ. Anal. Chem.*, **87**, 539–551 (2007).
[54] M.K. Ram, O. Yavuz, V. Lahsangah, and M. Aldissi, CO gas sensing from ultrathin nanocomposite conducting polymer film, *Sens. Actuat. B*, **106**, 750–757 (2005).
[55] P. Su and Y. Chang, Low-humidity sensor based on a quartz-crystal microbalance coated with polypyrrole/Ag/TiO_2 nanoparticles composite thin films, *Sens. Actuat. B*, **129**, 915–920 (2008).
[56] P. Su and L. Huang, Humidity sensors based on TiO_2 nanoparticles/polypyrrole composite thin films, *Sens. Actuat. B*, **123**, 501–507 (2007).
[57] P. Su and C. Wang, Flexible humidity sensor based on TiO_2 nanoparticles-polypyrrole-poly-[3-(methacrylamino)propyl] trimethyl ammonium chloride composite materials, *Sens. Actuat. B*, **129**, 538–543 (2008).
[58] R.P. Tandon, M.R. Tripathy, A.K. Arora, and S. Hotchandani, Gas and humidity response of iron oxide-polypyrrole nanocomposites, *Sens. Actuat. B*, **114**, 768–773 (2006).
[59] D. Patil, Y. Seo, Y.K. Hwang, J. Chang, and P. Patil, Humidity sensing properties of poly(*o*-anisidine), *Sens. Actuat. B*, **128**, 374–382 (2008).
[60] A.Z. Sadek, W. Wlodarski, K. Shin, R.B. Kaner, and K. Kalantar-Zadeh, A layered surface acoustic wave gas sensor based on a polyaniline, *Nanotechnol.*, **17**, 4488–4492 (2006).
[61] A. Tiwari and S. Gong, Electrochemical synthesis of chitosan-co-polyaniline/$WO_3.nH_2O$ composite electrode for amperometric detection of NO_2 gas, *Electroanal.*, **20**, 1775–1781 (2008).

[62] Y. Miao, J. Chen, and X. Wu, Electrochemical characterization of Prussian Blue nanoparticles, *Colloid J.*, **69**, 334–337 (2007).
[63] X.F. Ma, X.B. Zhang, Y. Li, G.A. Li, M. Wang, H.Z. Chen, and Y. Mi, Preparation of nanostructured polyaniline composite film via 'carbon nanotubes seeding' approach and its gas-response studies, *Macromol. Mater. Eng.*, **291**, 75–82 (2006).
[64] K.S.V. Santhanam, R. Sangoi, and L. Fuller, A chemical sensor for chloromethanes using a nanocomposite of multiwalled carbon nanotubes with poly(3-methylthiophene), *Sens. Actuat. B*, **106**, 766–771 (2005).
[65] L. Valentini, V. Bavastrello, E. Stura, I. Armentano, C. Nicolini, and J.M. Kenny, Sensors for inorganic vapor detection based on carbon nanotubes and poly(*o*-anisidine) nanocomposite material, *Chem. Phys. Lett.*, **383**, 617–622 (2004).
[66] K.H. An, S.Y. Jeong, H.R. Hwang, and Y.H. Lee, Enhanced sensitivity of a gas sensor incorporating single-walled carbon nanotube-polypyrrole nanocomposites, *Adv. Mater.*, **16**, 1005–1009 (2004).
[67] V. Bavastrello, E. Stura, S. Carrara, V. Erokhin, and C. Nicolini, Poly(2,5-dimethylaniline)-MWNTs nanocomposite: A new material for conductometric acid vapours sensor, *Sens. Actuat. B*, **98**, 247–253 (2004).
[68] Y. Li, H. Wang, X. Cao, M. Yuan, and M. Yang, A composite of polyelectrolyte-grafted multi-walled carbon nanotubes and in situ polymerized polyaniline for the detection of low concentration triethylamine vapor, *Nanotechnol.*, **19**, 015503 (2008).
[69] T. Zhang, M.B. Nix, B.Y. Yoo, M.A. Deshusses, and N.V. Myung, Electrochemically functionalized single-walled carbon nanotube gas sensor, *Electroanal.*, **18**, 1153–1158 (2006).
[70] S. R. Ali, Y. Ma, R.R. Parajuli, Y. Balogun, W.Y.-. Lai, and H. He, A nonoxidative sensor based on a self-doped polyaniline, *Anal. Chem.*, **79**, 2583–2587 (2007).
[71] N. Ferrer-Anglada, M. Kaempgen, and S. Roth, Transparent and flexible carbon nanotube/polypyrrole and carbon nanotube, *Phys. status solidi. B*, **243**, 3519–3523 (2006).
[72] R. Wu, Y. Huang, M. Yu, T.H. Lin, and S. Hung, Application of m-CNTs/$NaClO_4$/PPy to a fast response, room working temperature ethanol sensor, *Sens. Actuat. B*, **134**, 213–218 (2008).
[73] M. Chavali, T. Lin, R. Wu, H. Luk, and S. Hung, Active 433 MHz-W UHF RF-powered chip integrated with a nanocomposite *m*-MWCNT, *Sens. Actuat. B*, **141**, 109–119 (2008).
[74] J. Jang and J. Bae, Carbon nanofiber, *Sens. Actuat. B*, **122**, 7–13 (2007).
[75] T.M. Wu, Y.W. Lin, and C.S. Liao, Preparation and characterization of polyaniline/multi-walled carbon nanotube composites, *Carbon*, **43**, 734–740 (2005).
[76] S.E. Moulton, P.C. Innis, L.A.P. Kane-Maguire, O. Ngamna, and G.G. Wallace, Polymerisation and characterisation of conducting polyaniline nanoparticle dispersions, *Curr. Appl. Phys.*, **4**, 402–406 (2004).
[77] O. Ngamna, A. Morrin, A.J. Killard, S.E. Moulton, M.R. Smyth, and G.G. Wallace, Inkjet printable polyaniline nanoformulations, *Langmuir*, **23**, 8569–8574 (2007).
[78] A. Morrin, O. Ngamna, E. O'Malley, N. Kent, S.E. Moulton, G.G. Wallace, M.R. Smyth, and A.J. Killard, The fabrication and characterization of inkjet-printed polyaniline nanoparticle films, *Electrochim. Acta*, **53**, 5092–5099 (2008).
[79] K. Crowley, E. O'Malley, A. Morrin, M.R. Smyth, and A.J. Killard, An aqueous ammonia sensor based on an inkjet-printed polyaniline nanoparticle-modified electrode, *Analyst*, **133**, 391–399 (2008).
[80] K. Crowley, A. Morrin, A. Hernandez, E. O'Malley, P.G. Whitten, G.G. Wallace, M.R. Smyth, and A.J. Killard, Fabrication of an ammonia gas sensor using inkjet-printed polyaniline nanoparticles, *Talanta*, **77**, 710–717 (2008).
[81] N.B. Clark and L.J. Maher, Non-contact, radio frequency detection of ammonia with a printed polyaniline sensor, *React. Funct. Polym.*, **69**, 594–600 (2009).
[82] A. Ambrosi, A. Morrin, M.R. Smyth, and A.J. Killard, The application of conducting polymer nanoparticle electrodes to the sensing of ascorbic acid, *Anal. Chim. Acta*, **609**, 37–43 (2008).
[83] X. Luo, A.J. Killard, A. Morrin, and M.R. Smyth, Electrochemical preparation of distinct polyaniline nanostructures by surface charge control of polystyrene nanoparticle templates, *Chem. Commun.*, 3207–3209 (2007).

[84] X.M. Feng, C.J. Mao, G. Yang, W.H. Hou, and J.J. Zhu, Polyaniline/Au composite hollow spheres: Synthesis, characterisation, and application to the detection of dopamine, *Langmuir*, **22**, 4384–4389 (2006).
[85] X. Luo, A.J. Killard, and M.R. Smyth, Nanocomposite and nanoporous polyaniline conducting polymers exhibit enhanced catalysis of nitrite reduction, *Chem. Eur. J.*, **13**, 2138–2143 (2007).
[86] E. Kazimierska, M. Muchindu, A. Morrin, E. Iwuoha, M.R. Smyth, and A.J. Killard, The fabrication of structurally multiordered polyaniline films and their application in electrochemical sensing and biosensing, *Electroanal.*, **21**, 595–603 (2009).
[87] T. Itoh, I. Matsubara, W. Shin, N. Izu, and M. Nishibori, Preparation of layered organic-inorganic nanohybrid thin films of molybdenum trioxide with polyaniline derivatives for aldehyde gases sensors of several tens ppb level, *Sens. Actuat. B*, **128**, 512–520 (2008).
[88] Z. Li, F.D. Blum, M.F. Bertino, C. Kim, and S.K. Pillalamarri, One-step fabrication of a polyaniline nanofiber vapor sensor, *Sens. Actuat. B*, **134**, 31–35 (2008).
[89] S. Sharma, C. Nirkhe, S. Pethkar, and A.A. Athawale, Chloroform vapour sensor based on copper/polyaniline nanocomposite, *Sens. Actuat. B*, **85**, 131–136 (2002).
[90] F. Wang, H. Gu, and T.M. Swager, Carbon nanotube/Polythiophene chemiresistive sensors for chemical warfare agents, *J. Am. Chem. Soc.*, **130**, 5392–+ (2008).
[91] Y.S. Jung, W. Jung, H.L. Tuller, and C.A. Ross, Nanowire conductive polymer gas sensor patterned using self-assembled block copolymer lithography, *Nano Lett.*, **8**, 3776–3780 (2008).
[92] X. Yu, Y. Li, and K. Kalantar-zadeh, Synthesis and electrochemical properties of template-based polyaniline nanowires and template-free nanofibril arrays: Two potential nanostructures for gas sensors, *Sens. Actuat. B*, **136**, 1–7 (2009).
[93] A.Z. Sadek, W. Wlodarski, K. Shin, R.B. Kaner, and K. Kalantar-Zadeh, A polyaniline/WO_3 nanofiber composite-based ZnO/64° YX $LiNbO_3$ SAW hydrogen gas sensor, *Synth. Met.*, **158**, 29–32 (2008).
[94] R. Arsat, X.F. Yu, Y.X. Li, W. Wlodarski, and K. Kalantar-zadeh, Hydrogen gas sensor based on highly ordered polyaniline nanofibers, *Sens. Actuat. B*, **137**, 529–532 (2009).
[95] A. Lupu, P. Lisboa, A. Valsesia, P. Colpo, and F. Rossi, Hydrogen peroxide detection nanosensor array for biosensor development, *Sens. Actuat. B*, **137**, 56 (2009).
[96] S. Aravamudhan and S. Bhansali, Development of micro-fluidic nitrate-selective sensor based on doped-polypyrrole nanowires, *Sens. Actuat. B*, **132**, 623–630 (2008).
[97] V. Biagiotti, F. Valentini, E. Tamburri, M.L. Terranova, D. Moscone and G. Palleschi, Synthesis and characterization of polymeric films and nanotubule nets used to assemble selective sensors for nitrite detection in drinking water, *Sens. Actuat. B*, **122**, 236–242 (2007).
[98] X.B. Yan, Z.J. Han, Y. Yang, and B.K. Tay, NO_2 gas sensing with polyaniline nanofibers synthesized by a facile aqueous, *Sens. Actuat. B*, **123**, 107–113 (2007).
[99] M.K. Ram, O. Yavuz and M. Aldissi, NO_2 gas sensing based on ordered ultrathin films of conducting polymer and its nanocomposite, *Synth. Met.*, **151**, 77–84 (2005).

15

Nanostructural Aspects of Conducting-Polymer Actuators

Paul A. Kilmartin and Jadranka Travas-Sejdic

Polymer Electronics Research Centre, The University of Auckland, New Zealand

15.1 Introduction

Dimensional changes in conducting polymers such as polypyrrole (PPy), polyaniline (PANI), and poly(3,4-ethylenedioxythiophene) (PEDOT) during oxidation and reduction have been used for over 15 years to create movement, an actuating effect. This has opened up the possibility of the development of a new class of polymer-based, large strain, artificial muscles, to stand alongside other prospective materials, such as dielectric elastomers, shape-memory alloys, and carbon nanotube fibers [1]. Advantages of conducting polymers over more established actuator technologies, such as piezoelectric polymers, are seen in their low operation voltages, high work densities per cycle, and force generation capabilities, but with limitations seen in cycle life and energy conversion efficiencies [2].

However, a complete picture of the volume changes at work in conducting polymers has yet to be determined [3], and it is widely recognized that an understanding and better exploitation of nanostructural aspects of conducting-polymer actuators will be necessary to improve their performance as required for practical applications [4–7]. In this chapter we will outline the main mechanisms of actuation which have been investigated for conducting-polymer actuators, along with recent research to model actuator performance and develop applications. The effect of morphology and nanostructure, such as chain

Nanostructured Conductive Polymers Edited by Ali Eftekhari

alignment and conformational changes at the molecular level, will then be examined, before considering the role of the solvent, ion size, and conductivity on actuator performance and the use of composite materials with the likes of carbon nanotubes and hydrogels. Prospects for future research with a nanostructural focus will then be raised.

15.2 Mechanisms and Modes of Actuation

15.2.1 Ion Movement and Conducting-Polymer Electrochemistry

The mechanism behind the actuation of intrinsically conducting polymers has been recognized as being due, to a large extent, to the movement of ions and solvent in and out of the polymer during oxidation and reduction processes, as described in recent reviews [3,8–10]. Conducting-polymer actuators are generally formed by electrochemical polymerization on an inert electrode, and can be actuated either in contact with that electrode, or removed and operated as a free-standing film. When relatively small anions are present in the solution, expansion upon oxidation and contraction upon reduction is typically seen, often referred to as anion-driven actuation. The situation is reversed when larger anions become immobilized within the conducting polymer structure, in which case smaller cations instead move to maintain the charge balance, with expansion upon polymer reduction. This type of actuation is referred as cation-driven actuation. In many cases both anion and cation movement can be detected, which can cancel out the actuation of each of the ions – which ion will predominate can be difficult to predict.

Quartz crystal microbalance studies have shown that the movement of the solvent molecules associated with ions can be considerable. Using PPy prepared in sodium dodecyl sulfate, a mix of both cation- and anion-driven processes was seen when cycled in NaCl, and the mass changes involved indicated that four water molecules moved per Cl^- and 15 water molecules per Na^+ [11]. The role of solvent water molecules has also been examined for PPy in dodecyl benzene sulfonate (DBS), a very widely studied system, where the insertion of cations accounted for only 20% of the mass change upon polymer reduction, indicating that four water molecules were brought into the film with each Na^+ [12]. As the electrolyte concentration was changed from 0.1 M to 6 M, the total inserted mass became smaller and the mechanism moved from pure cation transport to an equal amount of anion transport [13]. These results were said to support an osmotic expansion model, whereby the difference in osmotic pressure between the electrolyte and polymer bulk (greater with more dilute electrolyte solutions) drives solvent movement.

Alongside swelling and deswelling effects, the role of conformational changes in the polymer backbone have been recognized as being equally important for certain systems (see below).

15.2.2 Bilayer and Trilayer Actuators

The first actuators described for conducting polymers in the early 1990s were ‘bilayer’ or ‘bending-beam’ structures in which a polymer film on a thin conductor would bend to well

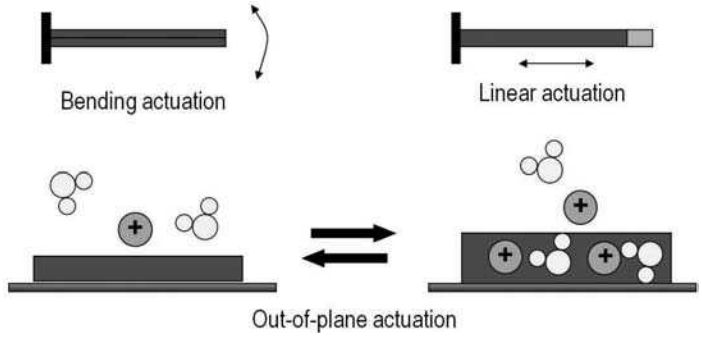

Figure 15.1 *Conducting-polymer actuation based upon bending of a bilayer or trilayer actuator in which 5–50-μm-thick polymer layers are typically grown on a metal-coated inert support; the linear stretching of a free-standing film, of several mm to cm in length; and the out-of-plane actuation of conducting-polymer films*

over 90° owing to the reversible expansion and shrinking of the film (Figure 15.1). These included a bilayer structure based upon PPy shown to act as an actuator by Otero [14], and a bending beam consisting of a 10 μm PANI layer used by the group at Linköping, Sweden, as a sensitive way to monitor volume changes in conducting polymers [4]. Various uses for conducting polymers as biopolymer muscles were envisaged owing to their high conductivity and electroactivity, although it was recognized even then that strain rates can be small owing to the redox processes being under the control of ionic diffusion, with the prospect that microporous materials with a more limited diffusion length could be used to increase strain rates [4]. Recently bilayer gold-polypyrrole 'nanofingers' 12–15 μm long and 250 nm in diameter have been prepared via a template synthesis and have been used to demonstrate electrochemically induced nanowire bending [15].

Soon after it was shown that PANI could be used as both anode and cathode in an all-plastic actuator in which the two conducting polymer films were assembled on either side of a solid polymer electrolyte (SPE) or similar material and operated in air [16]. An analogous 'trilayer' was demonstrated for PPy with two films working with respect to each other to achieve the bending motion [17]. Trilayer actuators have been shown to be able to move objects along a surface [18], and to allow very precise control of the position and movement of the actuator [19]. A range of solid polymer electrolytes have been used in further trilayer designs, with recent examples including PPy deposited on a polyurethane/$Mg(ClO_4)_2$ SPE [20], PPy layers on gold-coated 20-μm-thick cellophane papers [21], PANI in conjunction with poly(ethylene oxide) [22], PPy or PANI deposited onto cellulose paper, which showed enhanced displacement at the resonance frequency of the system around 3 Hz [23], and the use of nitrile rubber as the base elastomeric material with either PPy [24] or PEDOT [25].

Trilayer PPy actuators have also been constructed in which PPy is electrodeposited on either side of a gold electrode using the large DBS ion on one side (cation-driven PPy) and a smaller benzenesulfonate on the other (anion-driven PPy), which bent quickly in a co-operative manner as the trilayer was oxidized or reduced in 1 M $LiClO_4$ [26]. A problem with any design in which the conducting-polymer remains attached to an inert metal

electrode during actuation is eventual delamination from the surface as stresses are generated. The ease of delamination of a conducting-polymer actuator from a smooth thermally evaporated gold surface was lessened by additional gold electrodeposition to produce a much rougher surface. Along with better adhesion, the strain also increased by up to threefold and gave a more stable response [27]. A further design method which has been suggested to deal with the interfacial stresses which develop at the gold (Young's modulus of 83 GPa) and conducting-polymer interface (typically 0.2 GPa) is to include a 'buffer' layer of conducting polymer with a larger modulus value (~5 GPa) [28]. This layer remains conducting, but does not itself develop actuation strain, and is predicted to form zero strain at the polymer/gold interface at a particular buffer layer thickness.

An approach which creates an all-polymer bending actuator, and removes the delamination problem, is one in which two differently structured PPy layers are assembled on top of each other. The growth of an initial PPy layer containing an anion such as DBS, to produce a cation-driven layer, followed by further PPy deposition in the presence of *p*-phenol sulfonic acid (PPS) to produce an anion-driven layer, led to a 'bi-ionic' actuator which bends in the one direction as the whole assembly is either oxidized or reduced [29]. A stripe shape pattern of PPy bi-ionic actuators was also formed using a patterning technique to produce an electrochemically active spring which folded with a strain of some 60%. Problems remained with creep and mismatches of the size of the stroke of the spring elements [30]. The bi-ionic approach has been extended to include a central polythiophene layer as a high-strength conductive-polymeric support to two PPy layers, one doped with ClO_4^- to give an anion-driven film and the second a cation-driven film doped with DBS. The movement rate and extent of actuation was larger than for the alternative bi-ionic version [31]. In a further example, PPy doped with *p*-toluene sulfonic acid (*p*-TS) with cation-driven actuation was formed on top of PPy(ClO_4) with anion-driven actuation, to create an actuator which bent in response to an applied current [32].

15.2.3 Linear Actuators and the Inclusion of Metal Contacts

Bilayers and trilayers have proved to be very impressive in showing a high degree of angular movement, while the conducting-polymer film itself only lengthened by 1–2%. The desorption and sorption of water on a free-standing polypyrrole strip was also demonstrated to lead to contraction of around 1% upon applying a DC voltage, as an alternative to electrochemical doping [33], and more recently used to construct an 'oragami' folding actuator capable of caterpillar-like motion [34]. However, most studies have focused upon the electrochemically driven movement, and studies of 'linear' actuation movement have since been made which have allowed a range of actuation metrics to be evaluated [35]. With many conducting-polymer actuators, the conductivity of the polymer itself is not high enough to permit effective actuators to be constructed of any significant length. A development introduced by Santa Fe Science and Technology has been the production of fibers of PANI doped with 2-acrylamido-2-methyl-1-propane sulfonic acid with conductivities up to 1000 $S\,cm^{-1}$ for use in linear actuators. Solid-in-hollow linear actuators were constructed using a gel electrolyte [36]. With the advent of polymer-electrode combinations which permit the linear actuation to exceed 10%, more consideration is being given to linear actuators (see below).

Considerable improvement in the performance of linear actuators has been obtained by including a wire along the length of the conducting polymer to counter the drop in potential which severely limits performance for distances greater than 10 mm from the electrode contact, even with highly conducting polymer forms [37]. A very clear indication of the importance of conductivity to the performance of linear actuators was presented by Kaneto [38]. In considering PPy/CF_3SO_3 (triflate) films, a similar absolute length change was seen with linear actuators in the 14.5 to 55 mm range, giving a progressively lower percentage contraction as the actuator length increased. Maximum actuation was achieved many times faster when a gold sputtered layer was included which did not interfere with the overall actuator movement, developing 7% strain within a few seconds.

In further designs involving the addition of metal contacts, helical Pt wires included in hollow PPy tubes were found to be superior to hollow tubes on their own and to flat films [35]. The inclusion of the helical metal wire was found to improve the electrochemical efficiency of actuators several centimetres in length, with strain rates up to 13% s^{-1} [39]. Approaches to bundled 20 μm and hollow 350 μm PPy fibers, alongside the use of a Pt metal coating, have also been considered to optimize the strain and force generated [40,41]. A further approach to include a conductive metal wire within a PPy(BF_4) actuator, designed to push as well as to pull, has been to deposit the polymer electrochemically on a 0.25 mm tungsten microcoil. The larger contact area between metal electrode and conducting polymer lowered the voltage drop along the PPy actuator, and allowed strains of up to 11.6% to be achieved [42,43] A Pt zig-zag wire or Pt/Ir coil was used in certain high-strain PPy actuators to maintain strains of over 20%, although the Pt/Ir coil somewhat disturbed the actuation response [44,45] Through the use of a corrugated metal coating (4 μm deep with a corrugation period of 10 μm), the speed and extent of actuation (∼0.3% s^{-1} and 12%, respectively for PPy(DBS)) has been significantly improved [46].

15.2.4 Out-of-Plane Actuators

Another type of actuation which has been demonstrated is the 'out-of-plane' actuation of conducting-polymer films attached to an electrode substrate. PPy(DBS) out-of-plane actuation has been studied by Smela using atomic force microscopy, where a volume change of up to 35% was observed for films 1–15 μm thick, which is considerably larger than the linear actuation (∼2%) given for comparable PPy(DBS) films [47]. Films 1.5 μm thick were found to produce the greatest strain, as confirmed using a profilimeter. Reasons suggested for the anisotropy of the PPy(DBS) films included the effect of the DBS surfactant producing micelles during PPy deposition, through to a rearrangement of chains segments when the PPy(DBS) is first subject to a cathodic current and cation insertion [48]. The DBS surfactant is also believed to form a lamellar structure, leading to bilayers of PPy chains oriented parallel to the electrode surface, with very fast in-plane ion transport [49]. The out-of-plane actuator of PPy doped with polystyrene sulfonate (cation-driven) was also studied in a systematic manner using AFM [50]. Larger strains of up to 12.3% were obtained for thinner films (97 nm), which decreased as the PPy thickness was increased (to 5.5% strain for a 3.17 μm thick film). The strain with thicker films was also more dependent upon voltammetric scan rate, ascribed to a large increase in diffusion

time, raising the importance of polymer nanostructure in rate-limiting mechanisms involving ion diffusion.

15.2.5 Effect of Synthesis Conditions

It needs to be stressed that the performance of conducting-polymer actuators is heavily dependent upon their conditions of preparation, in that the quality of the films, including factors such as chain alignment and polymer density, can be readily altered as electropolymerization conditions are varied. Several synthetic conditions relevant to conducting-polymer nanostructure are included below.

Volume changes in PPy(DBS) bilayers grown from solutions across a range of pH values have been examined by Smela. The role of the large aromatic surfactant ion was outlined and the influence of the pH of the cycling solution [51]. A higher deposition current density in the electropolymerization of PPy(DBS) films led to small bilayer movement, ascribed to the formation of a denser PPy structure with more limited charge transfer [52]. In a further systematic evaluation of the performance of PPy(DBS) bilayer actuators, an increase in pyrrole or NaDBS concentration in the preparative solution lowered the potential of electropolymerization, and changed the resulting cyclic voltammograms of the materials, while a similar actuation performance was obtained with low, medium, and high concentrations. At the same time considerable variability was seen in both peak currents and bilayer tip displacements for actuators formed under the same conditions [53].

It has also been noted with PPy(ClO_4) that electropolymerization at a higher potential (0.9–1.0 V (Ag/AgCl)) produced an actuation 20% less than for films prepared at an optimum potential of 0.7 V. It was thought that the higher polymerization potential could lead to a higher degree of cross-linking and a lowering of the ability of the polymer to stretch [27]. PPy doped with *p*-toluene sulfonate also exhibited superior actuation performance when prepared at a lower current density [54]. A wide range of actuation measurements were made of stretched highly conducting PANI(AMPS) film and fiber actuators, in both HCl [37], and methanesulfonic acid [55], and related to formation conditions. With PPy(triflate) films formed in propylene carbonate electrolytes, we have found that an increased electrochemomechanical deformation was achieved when a higher concentration of pyrrole or $CF_3SO_3^-$ was used during electropolymerization, leading also to more highly conductive films [56], while the extent of linear strain decreased when a higher deposition current density was employed [57].

15.3 Modelling Mechanical Performance and Developing Device Applications

Relating chemical and material properties to actuation behavior has proven to be a major challenge, and remains an important area of investigation for several research groups, as efforts are made to systematically improve actuator performance in proposed devices. Properties at the nanoscale are being seen as increasingly important in this regard, as will be discussed in subsequent sections.

15.3.1 Modelling of Conducting-Polymer Actuation

The mechanical performance of PPy actuators has been characterized and modelled by Madden and Hunter. The relationships between load, displacement, voltage, and current have been considered, which confirmed that strain is directly proportional to the charge passed during actuation. On the other hand, electrochemical efficiencies were found to be low (~0.1%) for typical conducting-polymer actuators. The description predicts that high strain rates and power can be obtained through miniaturization of the actuators [58]. Limiting factors in the performance of conducting-polymer actuators include capacitance charging and diffusion rates, which can be represented in a transmission line model [59]. This model considers the polymer matrix as a double-layer capacitor, and was successfully applied to the electrochemistry of conducting polymers when variation of parameters such as polymer conductivity with polymer oxidation state were included [60]. In an attempt to better link material properties to performance, Madden has developed a diffusive elastic model to examine conducting-polymer charging and the associated diffusion of ions [61]. The model assumed that mass transport is limited by molecular diffusion within the polymer, which then expands in an elastic manner, while the polymer presents a negligible electronic resistance [59]. The model helps establish that actuation performance can be improved by: (a) increasing the charging rate, where smaller ions are expected to move more quickly into the films, and a larger concentration gradient can be built up using a higher electrode potential (so long as degradation processes are avoided), and where polymer morphology and thickness will be important; (b) increasing the strain-to-charge ratio, reliant on ion size and the involvement of the solvent; and (c) undertaking resistance compensation to control the voltage applied at the polymer–electrolyte interface. Some aspects of real conducting polymers which the model does not deal with include the voltage drop along the polymer due to its resistance, the creep which develops, polymer conformational changes and anisotropy, and what fraction of the actuation is due to ions of the one charge [61]. Substantial creep can develop especially for actuators subject to high loads [59], and the creep which cannot be subsequently recovered has been linked to irreversible degradation of polymer redox sites [62]. Further modelling using equivalent circuits has shown that better actuation speed will be obtained as smaller, more porous, and more highly conducting polymeric actuators are employed [63].

The oxidation and reduction of conducting polymers relies on both ion and electron movement. Smela has developed an experimental system designed to make ion transport the rate-limiting step and has studied the reduction reaction in PPy(DBS) (Figure 15.2).

It was shown that there are different rate-limiting processes at different electrode potentials for PPy reduction and the insertion of cations (e.g. diffusion in the electrolyte or electron transport), including a key role for migration in ion transport at more negative electrode potentials [64–66]. Modelling of the curvature of PPy(DBS) on gold bilayer actuators, including strain and modulus values, were also used to relate curvature to different gold and PPy thicknesses and lengths, and it was determined that the optimal PPy-to-gold thickness ratio was 5:1 [5].

Research groups at Wollongong, Australia, have examined a number of conducting-polymer performance criteria, such as the energy output (work) for different actuator geometries, and the way the strain typically decreases as the force under operation is increased. Part of the explanation for the behavior of conducting-polymer actuators can be

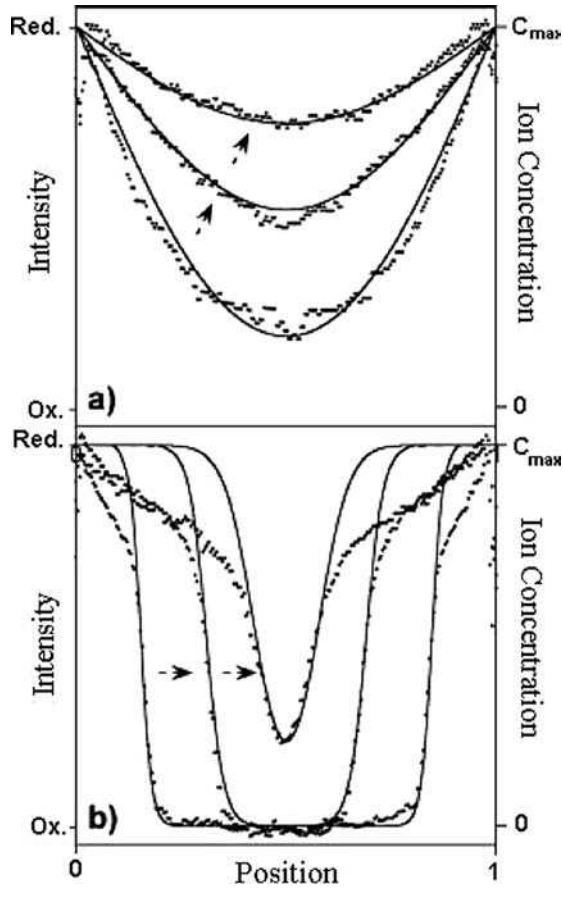

Figure 15.2 *Comparison of experimental (points) and modelling (lines) of ion concentrations for fronts moving inwards during PPy(DBS) reduction at: (A) –0.7 V (diffusion component greater than the drift component), and (B) –1.5 V (phase boundaries clearly visible, with migration playing the dominant role in ion transport). (Reprinted with permission from Advanced Materials, Visualizing ion currents in conjugated polymers by X. Wang, B. Shapiro and E. Smela, Adv. Mater., 16 18, 1605–1609. Copyright (2004) Wiley-VCH)*

related to a change in Young's modulus which occurs as PPy passes through different oxidation states – the elastic modulus tends to decrease as the polymer is reduced leading to a length increase under load, which can work against the contraction in length due to ion and solvent expulsion [35,67] The decrease in modulus for the reduced polymer has been explained as a lowering in interchain interactions, given that strong π–π stacking interactions within the oxidized polymer state lead to a stiffer structure [68]. Other groups have shown how the modulus varies with the applied potential [69], and that the modulus is dominated by the degree of counter-ion swelling for both anions and cations, with an emphasis on how critical the modulus changes will be to the mechanics of devices driven by polypyrrole actuators [70].

Conducting polymers are unusual as artificial muscles in that their work-per-cycle goes through a maximum as the applied stress is increased, again related to the change in modulus which occurs upon oxidation and reduction (by up to 500%) [71]. The application of mathematical models has allowed the geometry of trilayer bending actuators to be optimized for input parameters such as actuator thickness and input voltages. For certain PPy layers thicker than about 60 μm the extent of bending declined as the actuator could not overcome the increased rigidity of the system [72]. The force output at the tip of trilayer actuators has also been predicted using a mathematical model. Forces of the order of 1 mN were generated, and a general trend was obtained where a higher force is produced for a higher applied voltage [73]. At the same time it is recognized that the complex interplay of mechanical, chemical, and electrical parameters necessary to describe mass transfer in conducting-polymer actuators creates problems for the development of adequate models [74,75]. The creep observed in PPy(PF_6) trilayer bending actuators has also been modelled, and the mechanism of creep ascribed to the build up of osmotic pressure in the oxidized PPy layer leading to a spreading around of ions and solvent molecules and to further bending of the actuator [76]. Feedback control has enabled the effects of creep to be accounted for to establish better positioning ability of conducting-polymer actuators with continued operation [77].

15.3.2 Applications of Conducting-Polymer Actuators

A number of interesting device applications have been investigated based upon conducting-polymer actuation. An early approach was to use PPy actuators in conjunction with a solid ionic polyelectrolyte to create a steerable catheter which could be considered for use in minimally invasive surgery [78]. A more recent catheter design has been developed using laser-micromachining of polypyrrole actuators, including two-dimensional control made possible through the use of a four-electrode system [79]. A range of PPy/gold bilayer microactuators were developed by Smela and Inganas and used for applications such as closing a microvial, trapping living cells (Figure 15.3), to make self-assembling boxes [80], and these were strong enough to move silicon plates [81]. Through the microfabrication of conducting-polymer actuators, and the use of patterned electrodes and soft lithography, PPy(DBS) actuators as small as 10×40 μm were constructed on a silicon wafer and used to lift and move small loads [82]. 'Micromuscles' based upon the PPy(DBS)/Au bilayer have also been used to lift plates, to grab microscale objects, to construct a robotic arm, and to create various 3-D structures using hinge arrangements [83]. The application of conducting-polymer actuators in the biomedical context has also been reviewed by Smela [84]. This review provides a summary of actuator configurations, and particularly the use of microactuators. Current biomedical applications make use of the good biocompatibility of PPy to construct a blood-vessel connector, or a PPy valve for the control of urinary incontinence.

Conducting-polymer actuators have been developed for several applications by the Wollongong group [9]. These include the use of bilayer PPy actuators in a cochlear ear implant [85]. Hollow-tube actuators with helical wire interconnects have also been developed for use in an electronic Braille screen [39]. A trilayer actuator valve has been included in a combined sensor-actuator system to control a gas valve inlet for food

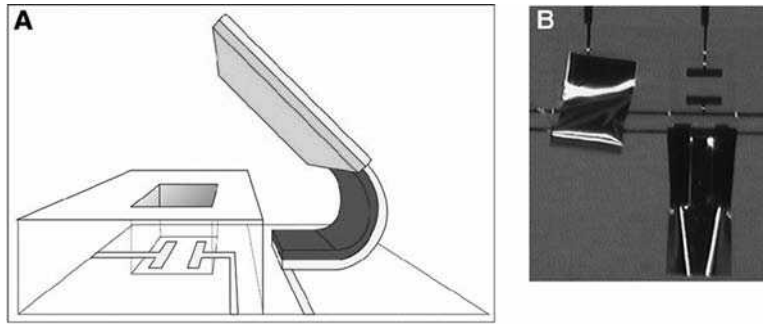

Figure 15.3 *Cell clinics constructed using PPy hinges to seal a 100 × 100 μm microcavity: (A) schematic with PPy hinge; and (B) picture of an open and closed cell clinic formed in a 20 μm thick SU-8 photoresist on a transparent class substrate. (Reprinted with permission from Science, Microfabricating conjugated polymer actuators by E. W. Jager, E. Smela and O. Inganas, 290 5496, 1540–1545. Copyright (2000) American Association for the Advancement of Science)*

packaging applications. While successful operation was demonstrated, difficulties remain with forming a tight closure of the gas opening and for achieving continued operation beyond about 50 hours [86]. A further area under consideration is in prosthetic applications, including a design where PPy fiber actuators are used to open and close a glove, while fabric strain gauges have been introduced to bring a sensing element into garments [87].

Further device applications have included the use of PPy actuators to vary the camber of propeller blades for underwater vehicles. While the extent of deflection obtained was appropriate, the forces generated were too small for the desired application [88]. Otero has joined four PPy bilayers and two plastic hinges to create a rhombic-shaped device. Contact failures and breakages around metal/polymer joints were found to be the most problematic [89]. Recently 3-D PPy(DBS) actuators have been produced using special fabrication procedures for use as micromanipulators, capable of gripping and lifting a cylindrical object [90]. Two PPy(PF_6) trilayer bending actuators with a carbon-fiber finger have also been combined to construct a microgripping system [76]. PPy(BF_4) actuators suitable to act as tremor suppressors have been considered, and by optimizing the synthesis conditions and the choice of electrolyte, a PPy actuator operating at up to 30 Hz with significant force has been constructed, relying on the stiffness change being much faster than the change in actuator length [91]. The inclusion of a bioadhesive polydopamine polymer layer on a gold-polypyrrole bilayer actuator has also led to a device capable of accumulating bacteria from aqueous solutions [92].

Conducting-polymer actuators have been employed in a number of designs for a micropump. Strong membrane-type PPy actuators have been employed in a diaphragm-based pump by the EAMEX group in Japan. A planate actuator has also been described in which anion- and cation-driven polypyrrole bimorph layers deform centrally within a test device, leading to fluid movement at the rate of 28 μl min^{-1} [93]. This group has also shown that PPy bilayer actuators can be combined to produce ring- and lip-type actuators [94]. A PPy tube configuration has been constructed at Wollongong in which pressure is

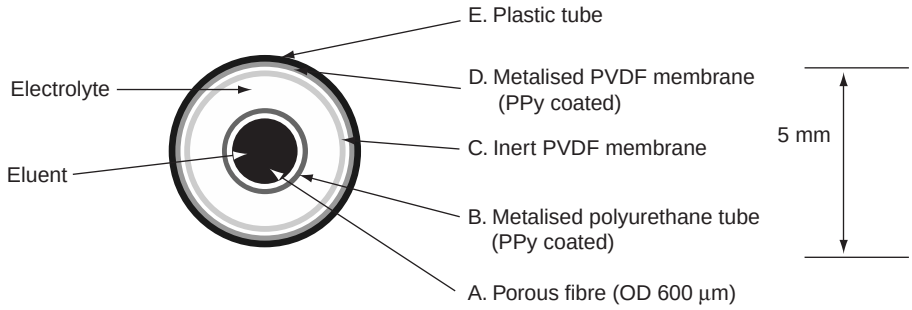

Figure 15.4 *Schematic of the TITAN microfluidic pump based upon a PPy-coated metallized polyurethane tube (1050 μm outer diameter). (Reprinted with permission from Smart Materials and Structures, TITAN: a conducting polymer based microfluidic pump by Y. Wu, D. Zhou, G. M. Spinks et al., 14, 6, 1511–1516. Copyright (2005) Institute of Physics)*

applied to a metallized polyurethane tube containing a PVDF porous support fiber, inducing a 12% volume change, and creating a tube in tube actuator node (TITAN) (Figure 15.4). Peristaltic fluid motion could be achieved using a series of the actuator tube units and flow rates of 2.5 μl min^{-1} [95].

The use of PPy-Nafion-PPy trilayers has enabled a low-power pump to be constructed at Dublin in which two trilayers act as tweezers in compressing the fluid inside a flexible polyurethane tube. Through the choice of conical inlets and outlets to create unidirectional fluid movement, flow rates of up to 1.6 μl s^{-1} were achieved [96]. A further pump design involving a polypyrrole-polydimethylsiloxane diaphragm with check valves has been developed, with a pumping rate of 52 μl min^{-1} [97].

A further microfluidics application for conducting-polymer actuators has been to consider the use of bilayers as valves. A number of valve designs were considered for a PANI-hydrogel composite, in which swelling of the blend was used to close a hole using a sphincter or plunger configuration [98]. A PPy bilayer has been used in the development of a miniaturized drug-delivery system, with an actuator valve just 200 μm in width [99]. The use of PPy(DBS) has been considered in this context, actuated by the movement of Na^+, because of the high concentration of Na^+ in extracellular fluid [100].

Controlled release of a drug from PEDOT nanotubes was demonstrated by electrical stimulation of PEDOT nanotubes at a potential of 1 V (vs. Ag/AgCl), which created a mechanical force within the nanotubes (Figure 15.5) [101]. PEDOT nanotubes were created by electropolymerizing PEDOT around a biodegradable polymer loaded with model drug molecules and electrospun on the electrode. The electrical stimulation caused expulsion of biodegradable polymer degradation products along with drug molecules from the nanotubes, although it was not clear whether this happened through the ends of the PEDOT nanotubes or through openings and cracks on the nanotube surface.

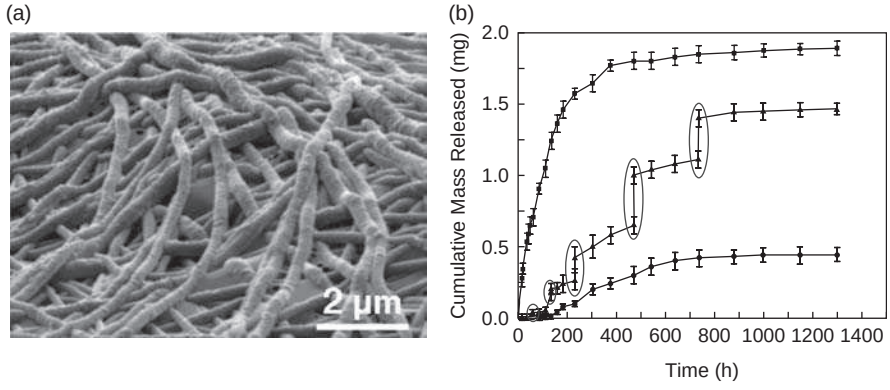

Figure 15.5 *Left: SEM image of PEDOT nanotubes on a neural probe tip; Right: mass release of dexamethasone from poly(lactide-co-glycolide) (PLGA) fibers (black), PEDOT-coated PLGA nanoscale fibers without electrical stimulation (red), and PEDOT-coated PLGA nanoscale fibers with electrical stimulation of 1 V at the times with the circled data. (Reprinted with permission from Advanced Materials, Conducting-polymer nanotubes for controlled drug release by M. R. Abidian, D.-H. Kim and D.C. Martin, 18, 4, 405–409. Copyright (2006) Wiley-VCH)*

15.4 Effect of Morphology and Nanostructure upon Actuation

The micro- and nanostructure of conducting polymers varies considerably based upon synthesis conditions with respect to properties important to actuation, such as conductivity, porosity, and alignment of polymer chains. It has been pointed out that electrochemical deposition itself tends to produce a nonuniform molecular structure and morphology in PPy films, since the material closer to the electrode is exposed to the polymerization voltage for a longer period of time, leading to more cross-linking and substitution reactions and more electronic defects (and ultimately a decrease in strain) [5]. The initial PPy deposition also proceeds via a nucleation and growth mechanism, while later polymerization on coalesced nuclei tends to produce columnar growth. Differences between various literature values for the same conducting polymer tested in the same electrolyte can be ascribed to preparation conditions and differences in the degree of polymer chain alignment [37]. Strategies to accentuate conducting-polymer alignment, anisotropy, porosity, and polymer conformation changes will be considered in this section.

15.4.1 Chain Alignment

The importance of the alignment of the polymer chains has been recently demonstrated in a study in which PPy(PF_6) films have been stretched to 96% [102]. The conductivity parallel to the stretch was increased, while the strain perpendicular to the stretch increased from 1.45 to 2.65% (but with more creep); at the same time very little strain could then be produced parallel to the stretch. The suggestion made was that counter-ions migrated to locations between the oriented polymer chains, producing strain perpendicular to this direction. The nanoscale chain configuration has also been altered by rolling as well as

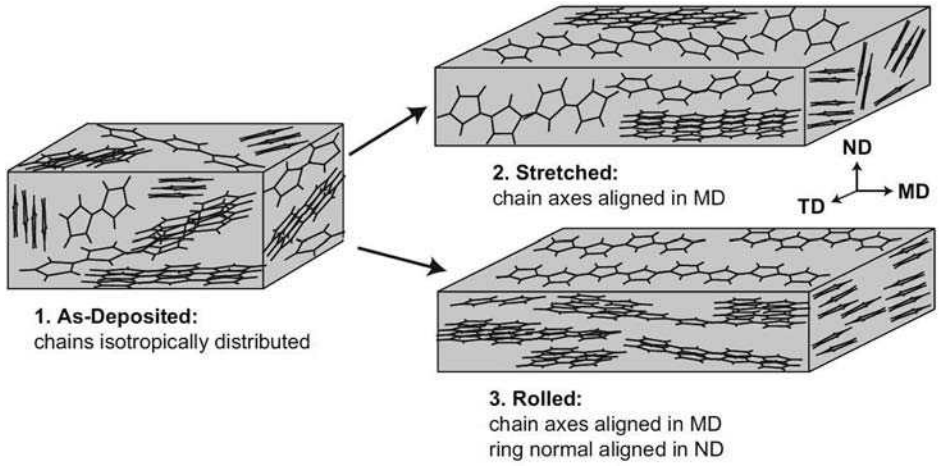

Figure 15.6 *Polypyrrole chain microstructure before and after processing using stretching or rolling leading to chain alignment in the machine direction (MD). (Reprinted with permission from Polymer, Anisotropic actuation of mechanically textured polypyrrole films by R. Z. Pytel, E. L. Thomas, Y. Chen, and I. W. Hunter, Polymer, 49, 5, 1338–1349. Copyright (2008) Elsevier Ltd)*

stretching PPy(PF_6) films [103]. Wide-angle X-ray diffraction showed how disordered PPy chains are held together by small crystalline bundles surrounded by solvent and counter-ions, with further texturing achieved through the rolling and stretching processing techniques where chains become orientated parallel to the machine direction (Figure 15.6). A 100% increase in active strain perpendicular to the machine direction was achieved through processing to strain values of up to 11.3%.

It has also been found that by using a tubular design (0.5 to 2 mm diameter) for a linear PPy(DBS) actuator, a strain of 7% was obtained (and larger for a thicker diameter tube), over twice that of a rectangular film. It was suggested that expansion in the cylindrical direction was effectively converted into the tube direction [104]. It has also been found that PANI actuators constructed in a tubular geometry produce a larger linear strain (2.0%) than comparable flat films (0.9%). The conductivity also increased fourfold by changing the geometric shape of the actuator. The amount of strain produced with the tubular PANI actuators increased further to 2.7% when a Pt wire helix was incorporated into the tube, likely through alignment of the polymer along the wire [105].

From an early stage in the development of conducting-polymer actuators, it was recognized that microstructures such as fibers (e.g. embedded in a solid electrolyte elastometric matrix) will offer a quicker electrochemical response compared to bulk films [106]. Recent research has examined the possibility of constructing actuators by assembling nanoscale fibers of conducting polymers. Bundles of parallel 43-μm-long PPy(DBS) nanowires, 200 nm in diameter, formed using an alumina template, were able to act as electrically controlled actuators. These nanowire actuators were able to lengthen by around 3%, with the prospect of nanoscale bilayers being constructed to produce a larger angular movement [6]. Bundles of PPy bilayer membranes have been formed using

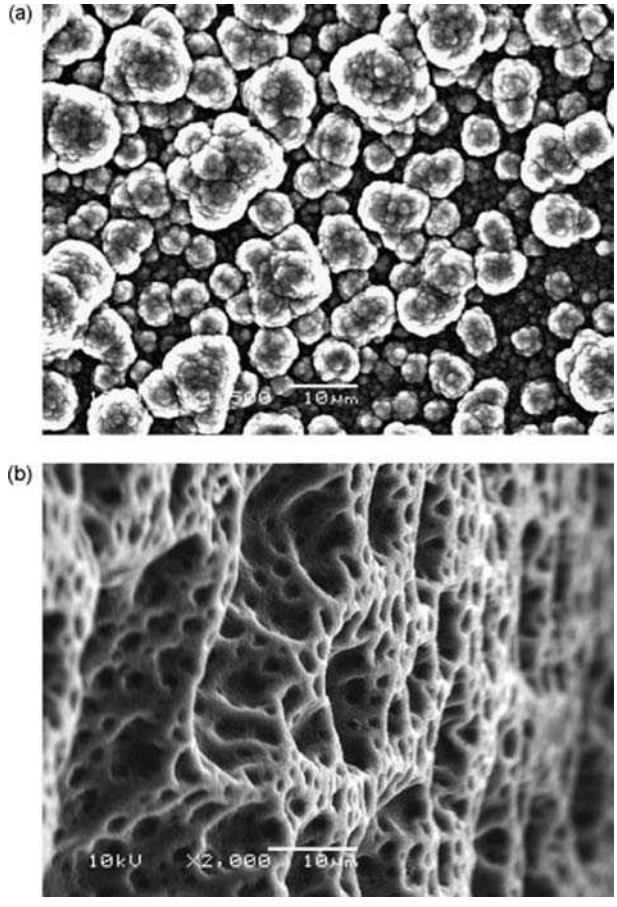

Figure 15.7 *SEM images: (A) regular PPy; and (B) templated PPy. (Reprinted with permission from Synthetic Metals, Templated polypyrrole electro-polymerization: Self-assembled bundles of bilayer membranes of amphiphiles and their actuation behavior by K. Kagawa, P. Qian, A. Tanaka and T. M. Swager, 157, 18–20, 733–738. Copyright (2007) Elsevier Ltd)*

an amphiphilic templating method [7]. The amphiphile chosen for this work formed supramolecular hydrogels with pyrrole in aqueous solutions, which acted as templates during PPy electropolymerization, leading to highly porous films (Figure 15.7). Fast diffusion of dopant ions was recorded through the porous films leading to a superior electrochemical response. The templated PPy also displayed a larger strain upon actuation in *p*-TSNa than typical PPy.

15.4.2 Anisotropy

A further nanostructured approach which has been undertaken is to establish a degree of anisotropy across a conducting-polymer film, often due to differences created at the inert

electrode compared to the solution side or some other interface during electropolymerization. The intrinsic anisotropy then leads to a bending actuation within the film during oxidation and reduction processes. When PPy films were prepared in a gap between PTFE films or within a PTFE pipe, considerable vertical anisotropy was introduced leading to a bending actuator. The surface in contact with the PFTE film was very smooth, while micrometer sized PPy particles were seen on the solution side, which was also five orders of magnitude less conductive than the smooth surface [107,108]. An asymmetry in PANI membrane actuators was also introduced when a thin dense skin layer was prepared next to a porous substructure, described as an integrally skinned asymmetric membrane [109]. An anisotropic PPy film has also been formed by successive electropolymerizations to form a pure PPy zone followed by one containing TiO_2 nanoparticles which produces a much looser structure. The resulting bilayer showed a fast response and large bending angle, again with a long lifetime due to elimination of the forces created in multilayer designs between stretching and supporting layers which otherwise lead to delamination and device failure [110].

Anisotropy has also been introduced into conducting polymers through the appearance of a very porous morophology on one side of the film. Preparation of PANI using a phase-inversion technique in hexane produced membranes with macrovoids distributed asymmetrically throughout the film (Figure 15.8) [111]. A larger Young's modulus (1.4 GPa) was obtained than for synthesis in water, owing to the denser structure formed, and the asymmetry meant that a single membrane was able to bend by up to 90°.

A single-layer PPy film, capable of bending actuation due to its intrinsic anisotropy, but without delamination problems, was constructed by electrochemical synthesis on a steel

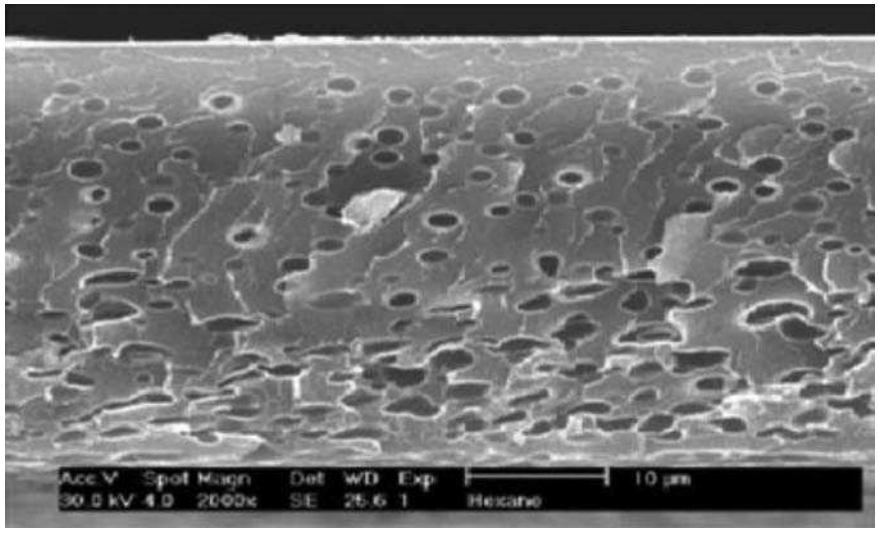

Figure 15.8 *SEM image of a PANI membrane prepared by the phase inversion technique with the appearance of macrovoids. (Reprinted with permission from Advanced Functional Materials, High-performance, monolithic polyaniline electrochemical actuators by J.-M. Sansinena, J. Gao and H.-L. Wang, H.-L., 13, 9, 703–709. Copyright (2003) Wiley-VCH)*

electrode in a mixed solvent containing an anionic surfactant [112]. The anisotropy was generated owing to the very porous morphology created on the PPy side in contact with the metal electrode, with pores up to 50 μm in size likely resulting from emulsion drops which initially form on the electrode surface. The electrolyte side was rough and compact and was able to be oxidized more efficiently.

15.4.3 Porosity

In other research, the creation of a highly porous structure has been used to improve the rate of exchange of ions in and out of the polymer film, thus leading to improvements in actuator performance. The linear actuation achieved with films of PPy(DBS) were found to increase from 2.5% to 5.6% when 1-pentanol was included as a cosurfactant during electropolymerization [113]. The morphology of the 1-pentanol films was quite different with large nodules on the solution side of the film and large voids on the side in contact with the stainless-steel electrode used for electropolymerization. Although the conductivity of the films was not greatly affected by the presence of 1-pentanol, it did lead to a higher doping level and a more isotropic film expansion. A change in PPy(β-naphthalene sulfonic acid)-film morphology was observed for electrochemical synthesis on different electrode substrates, with more compact films seen in one case on Pt than on ITO, while a highly porous structure was obtained on stainless steel, from which anions could be exchanged more easily [114]. The electrodeposition of PPy in the presence of an emulsion created by an anionic sulfosuccinate surfactant created a very porous structure and the presence of voids [115]. The subsequent cathodic expansion was sizeable owing to the ability of quite bulky cations to enter the films (Figure 15.9), including the tetrabutylammonium cation which had previously proven too large to enter PPy(DBS) films. The preparation of the PANI actuators using a phase-inversion technique also created a porous microstructure, with a change in pore size seen across a rather brittle film [105].

15.4.4 Conformational Changes

The role of conformational changes within the conducting polymer itself are continuing to be considered as an important aspect determining actuation behavior, with prospects for advances from improved nanostructuring. In an early study of PEDOT actuation, the volume changes observed were thought to be due to structural modifications within the polymer as much as to ion transport [116]. Upon oxidative doping the films were observed to first contract (but not due to cation ejection) and then expand. The fuller doping of PEDOT to a bipolaron state was suggested to generate a strong coulombic repulsion which would expand the polymer [116]. The actuation of integrally skinned asymmetric PANI membranes was ascribed mainly to changes in polymer conformation under electrochemical control, alongside ion movement into the membrane for chemical actuation [109]. *Ab initio* calculations have also recently been used to predict the shape change which can accompany the oxidation of PPy chains. These calculations show a helical shape for neutral PPy, whereas upon oxidation the chains become planar. This creates the possibility

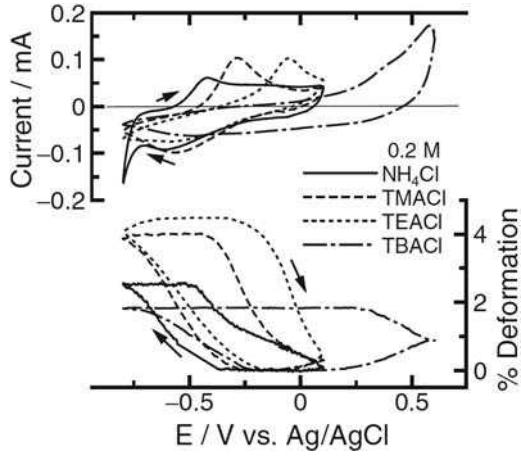

Figure 15.9 *Illustration of the high cathodic strains seen with larger cations in a PPy actuator formed in the presence of an emulsion: TMA = tetramethylammonium, TEA = tetraethylammonium, TBA = tetrabutylammonium. (Reprinted with permission from Chemistry Letters, Improved cathodic expansions of electrochemomechanical behavior in polypyrrole films electrodeposited from Aerosol OT emulsion by W. Takashima, S. S. Pandey and K. Kaneto, Chem. Lett., 33, 8, 996–997. Copyright (2004) Chemical Society of Japan)*

of a single-molecule actuation mechanism and may explain the conformational changes seen in related polythiophene-type conducting polymers [117].

The ability to create molecular level actuators has been taken even further in the example of thiophene-based molecular muscles by Madden and Hunter. Conformational rearrangement of the polymer backbone in molecules such as calix[4]arene-bithiophene was created at the molecular level [118]. This work has recently been reviewed and prospects for future research in this area considered [119].

15.5 Solvent and Ion Size Effects to Achieve Higher Actuation

15.5.1 Effect of Ion Size

In addition to nanostructural properties of the conducting polymer, considerable influence on actuation behavior has been demonstrated due to the choice of electrolyte. This has included properties of the solvent employed, and crucially the size of doping ions and their interaction with the conducting polymer. As mentioned above, PPy films doped with moderately small anions (e.g. Cl^-) lead to actuation driven by anion movement. By contrast, it is generally found that the inclusion of a large dopant anion (e.g. DBS) within PPy leads to cation-driven actuation, typically when a smaller cation is employed (e.g. Na^+). However, it is not always a simple matter of predicting which movement, anion or cation, will predominate for a particular electrolyte system, and for a particular type of

conducting polymer, related to its conditions of formation. Under some conditions dual ion movement has been observed. In the case of PEDOT in $TBAPF_6$, both anions and cations were found at times to play the dominant role in the actuation, meaning that the polymer films both contracted and expanded in response to single anodic and cathodic currents [120]. It is also possible to move from cation- to anion-driven actuation by first forming PPy in an electrolyte with a larger anion (e.g. β-naphthalene sulfonic acid or *p*-phenol sulfonate) and then cycling in an electrolyte containing a smaller anion (e.g. Cl^-), which eventually replaces the initial ionic dopant [121].

The size of the cations in PPy actuators was found to be a crucial factor, with a faster response given for smaller cations for cylindrical films formed in Na*p*-TS, showing that the bending mechanism was controlled by cation insertion and extraction [107]. For PPy films doped with $[Fe(CN)_6]^{3-}$, a larger deformation was established with increased solvation of the alkali-metal cation used, in the order $Li^+ > Na^+ > K^+$ [122]. This finding was confirmed in a further study using PPy(DBS) tubular films [104].

15.5.2 Ionic Liquids

The effect of anion size, independent of solvation effects, becomes most apparent when ionic liquids are used as the supporting electrolyte, as movement of solvent and osmotic processes are no longer involved. We can note here that a number of conducting-polymer actuation properties can be enhanced through the use of ionic liquids in place of aqueous or organic solvents. Low volatility, fast ion movement, and large electrochemical windows make ionic liquids attractive electrolytes for use with PANI and PPy actuators, where many thousands of cycles can be performed with little degradation [123]. In a case of a solid-state actuator consisting of PEDOT formed chemically on a nitrile rubber base containing different ionic liquids, an increased displacement was obtained when a larger anion was used, while it was recognized that conformational effects on the polymer chains will also influence the extent of actuation [25].

In further reports involving ionic liquids, an environmentally stable ethyl-methyl-imidazolium bis-(trifluoromethanesulfonyl) amide ionic liquid was employed with PPy trilayers on PVDF and in PPy polymer tube/Pt helix actuators. The ionic liquid served to overcome the PPy degradation observed at higher potentials in propylene carbonate, and also led to higher ionic conductivity and continued high strains with applied stress [124,125]. A higher degree of reproducibility and more stable strain response was obtained when ethyl-methyl-imidazolium tetrafluorosulfonic acid was employed as the ionic liquid electrolyte with a PPy actuator. The use of current pulse cycling instead of voltage cycling also improved actuator reproducibility and stability, in that it ensured that oxidation and reduction processes were equal in magnitude [126]. The Young's modulus for PPy actuators run in propylene carbonate can change by a factor of four as the polymer is oxidized and reduced (being larger in the oxidized, expanded state), while in an ionic liquid, a much smaller change ($\sim$8%) was seen [127]. On the other hand, for poly (3-methylthiophene), actuation in an ionic liquid led to the strain actually increasing a little (to 0.6% from 0.45%) as the applied stress was increased up to 4 MPa, in contrast to the large decline in strain seen in propylene carbonate. This resulted in much higher work per cycle at the higher operating stresses (3–4 MPa), even though the strain for zero applied

stress was greater in propylene carbonate (1.5%) [128]. Ionic liquids have also been used successfully with PEDOT to create a long-lasting actuator response without degradation [129].

15.5.3 Ions Producing Large Actuation Strains

In more recent times it has been found that certain moderately large anions, such as the triflate ion ($CF_3SO_3^-$), can produce large anion-driven actuation. Kaneto compared the performance of a number of tetrabutyl ammonium salts with various anions for inclusion in PPy films formed in methyl benzoate solutions and cycled in aqueous $NaPF_6$, all showing strains over 10% and stresses of over 20 MPa. Highly stretchable anion-driven films were obtained when BF_4^-, PF_6^-, or $CF_3SO_3^-$ were included in the polymerization solution [130]. Of these, PPy films formed with the triflate anion showed a longer mechanical elongation, ascribed to a lower degree of cross-reactions in the PPy formed [131]. It was suggested that a certain interaction between triflate or BF_4^- ions and pyrrole made them soluble in methyl benzoate and led to densely packed PPy chains upon electropolymerization to produce powerful actuators where conformational changes on the PPy chains could support the large stretching produced [132]. This type of PPy has subsequently been applied as powerful actuating elements in devices being developed by the EAMEX company in Japan [60]. Shu Yi Chu *et al*. also examined the influence of synthesis conditions (monomer and electrolyte concentration and deposition current density) on the formation of PPy(triflate) films from propylene carbonate solutions and tested in aqueous $NaPF_6$. The extent of actuation, of up to 10%, was found to be very sensitive to formation conditions [56,57].

Even larger actuation strains of 40% or more, approaching that of natural muscles, have been obtained in free-standing films involving insertion and expulsion of large bis(perfluoroalkylsulfonyl)imide anions [133]. In this case a very spongy and gel-like PPy morphology (less entangled PPy chains with weak interactions) was obtained (Figure 15.10) with stresses (2–10 MPa) intermediate between the stronger triflate ion films (50 MPa) and typical polymer gels (0.1–0.3 MPa). While the contraction of PPy films doped with the bis(trifluoroalkylsulfonyl)imide (TFSI) anion was relatively slow in aqueous solutions, the rate of contraction was faster in mixed water/propylene carbonate electrolytes (presumably giving a more swollen polymer), achieving values over 10% s^{-1} [134,135]. Exceptionally high actuation strains were also obtained using a trifluoromethylsulfonylmethide anion of over 30% (third cycle), with the best performing films being produced on a glassy carbon electrode (Figure 15.10A), but with a relatively low stress ($\sim$1 MPa) and slow response rate [136]. PPy actuators containing the TFSI ion have also been operated in ionic liquids, but with strain values for cation movement of less than 5%; some compromise between the higher stability afforded by ionic liquids and the greater degree of actuation achieved in organic solvents was seen with a 24% strain (due to anion movement) achieved in a mixed ionic liquid/propylene carbonate solvent [137].

PPy doped with TFSI has also been used to create a fast bending trilayer actuator, based upon a gold-coated PVDF membrane operated in air, relying on high diffusion rates through the gel-like polymer, more so than the size of the polymer conductivity. Tip displacements peaked for certain actuation frequencies (between 4 and 90 Hz, depending

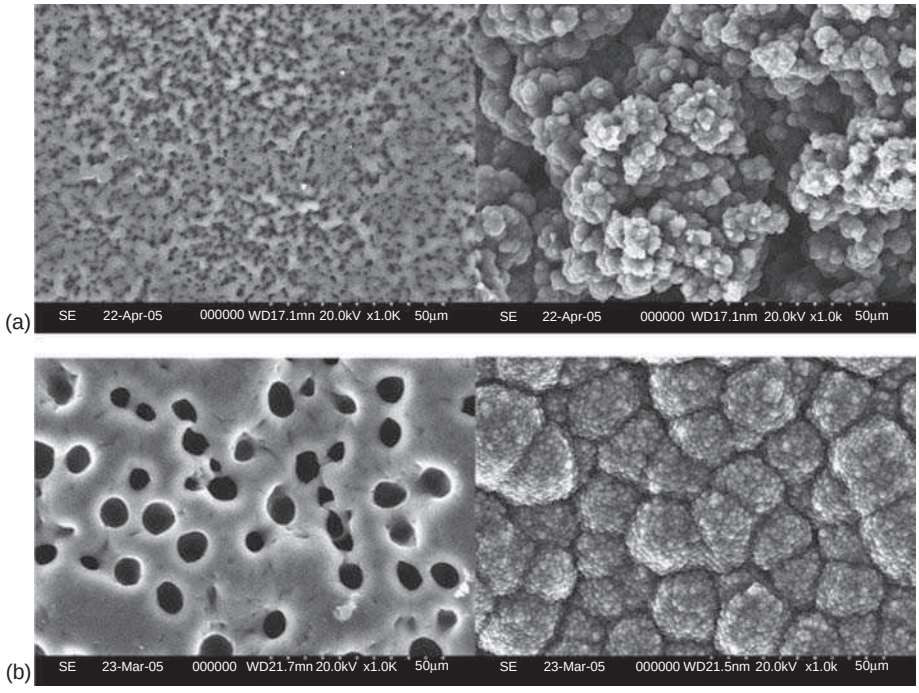

Figure 15.10 *SEM images PPy films doped with TFSI anions and prepared on: (A) a glassy carbon electrode; and (B) on a Pt electrode. The electrode side (with a macroporous morphology on Pt) is shown on the left in each case, and the solution side on the right. (Reprinted with permission from Synthetic Metals, Tris(trifluoromethylsulfonyl)methide-doped polypyrrole as a conducting polymer actuator with large electrochemical strain by S. Hara, T. Zama, W. Takashima and K. Kaneto 156, 2–4, 351–355. Copyright (2006) Elsevier Ltd)*

upon the length of the actuator), corresponding to the natural resonance frequency of the system [138]. The use of a laser ablation technique has allowed microsized actuators of this type to be produced (500 to 900 μm in length) that operate in air or in liquids [139].

Using the sequential deposition of selectively chosen sulfonic-acid-based dopants, giving firstly anion and secondly cation-driven PPy actuators, Kaneto was able to construct a linear artificial muscle which expanded by about 1% upon the application of both positive and negative electrode potentials [140]. In our own laboratory we were able to choose PPy preparative and test conditions which produced the same mixed-ion effect using a single PPy-triflate actuator system, and with a much larger actuation strain (up to 6% in both directions) (Figure 15.11A) [141]. This behavior is seen when employing nonaqueous solvents such as propylene carbonate (PC), to lessen the rate of polymer degradation, as an alternative to aqueous $NaBF_6$. An interesting feature of these systems is that potential steps in either direction (from –1 to +1 V (Ag/AgCl)) did not lead to an overall cancellation of actuation strain, but produced first film contraction followed by film expansion in both cases, showing that ion movement out of the polymer film (at a high concentration) occurs faster than ion movement into the polymer (which relies on diffusion

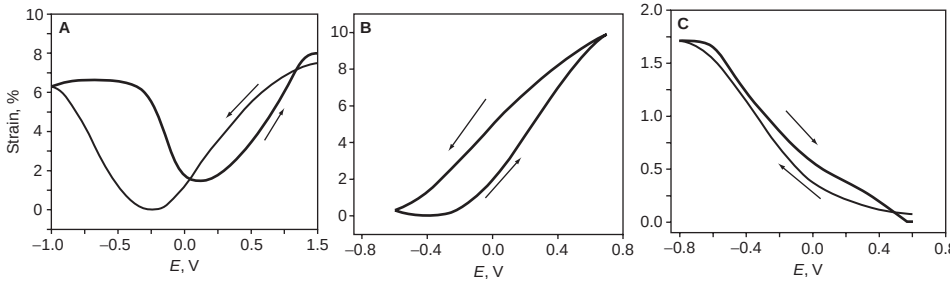

Figure 15.11 *Electrochemomechanical strain during cyclic voltammetry scans (2 mV s^{-1}, 2nd or 3rd cycle) for PPy films polymerized in PC/TBACF$_3$SO$_3$ and cycled in: (A) PC/TBACF$_3$SO$_3$; (B) NaPF$_6$ (aq.); and (C) a PEDOT film polymerized in PC/TBACF$_3$SO$_3$ and cycled in LiCF$_3$SO$_3$ (aq.)*

from a more dilute bulk solution). The cation-driven actuation can be largely suppressed by moving to an aqueous electrolyte (Figure 15.11B) [56], or while still employing propylene carbonate, through the use of a higher PPy formation potential [141], or by cycling in a PC/TBAPF$_6$ electrolyte [142]. By contrast we have found that PEDOT films doped with the triflate ion (TBACF$_3$SO$_3$) in either propylene carbonate or methyl benzoate showed exclusively cation-driven actuation of up to 3% in either PC [143], or aqueous electrolytes (Figure 15.11C).

15.6 Nanostructured Composite Actuators

In this section, consideration will be given to research in which conducting polymers have been combined with other materials to create a composite with improved actuation properties. This might involve the incorporation of a stiffer material (e.g. carbon nanotubes) to improve the stresses produced, or the inclusion of a gel to increase the amount of strain generated, albeit in a weaker actuator.

15.6.1 Blends of Two Conducting Polymers

A composite actuator was constructed using a copolymer of PPy and poly(methoxyaniline) formed in *p*-phenol sulfonic acid (PPS). Higher actuation deformations were seen at low pH. Pure PPy(PPS) initially showed mixed cation and anion actuation when tested in 1 M NaCl, but the cathodic expansion was removed by the inclusion of 30% poly(methoxyaniline) and the extent of electrochemical creep was also diminished [144]. The inclusion of poly(2-methoxyaniline-5-sulfonate) (PMAS) into PPy(DBS) films improved the cathodic expansion of the films. The presence of the PMAS also led to some anodic film expansion in some electrolytes (e.g. KCl), but exclusively enhanced cation expansion in other electrolytes (TBAPF$_4$) [145].

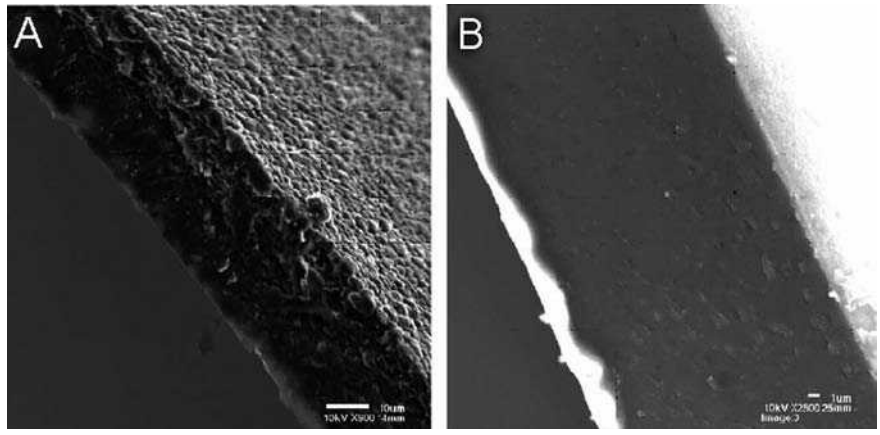

Figure 15.12 *SEM images of: (A) cross-section and bottom side of a PANI-graphite film; and (B) cross-section of a PANI film case without graphite. (Reprinted with permission from Polymer, Preparation and characterization of monolithic polyaniline-graphite composite actuators by W. Li, C. L. Johnson and H.-L. Wang, Polymer, 45, 14, 4769–4775. Copyright (2004) Elsevier Ltd)*

15.6.2 Graphite

The inclusion of conducting graphite powder in PANI(AMPS) actuators was found to improve conductivity for all PANI redox states, and allow larger bending angles to be achieved for longer (over 50 000 cycles) at a lower electrode potential [146]. The synthesis procedure resulted in a graphite-rich (stiffer) layer on one side of the 10-μm-thick PANI films (Figure 15.12). As the potential was evenly distributed along the actuator, the bending motion was achieved along the whole length of the film.

15.6.3 Carbon Nanotubes

Composites of PANI with carbon nanotubes (CNTs) in a mat form showed similar actuation patterns to the two constituents, behaving like PANI for low applied loads and like CNTs when a high load was applied to the sample (a reinforcing effect of the carbon nanotubes, which have a high Young's modulus). CNTs rely on non-Faradaic charging for their expansion, and continued high PANI actuation strains were obtained at higher stresses when CNTs were included in the composite [147]. Addition of CNTs lowered the creep of PANI actuators from 0.8% per cycle to 0.1% per cycle [148].

A PANI/CNT coating has also been applied to a PPy hollow fiber with a Pt helix. The inclusion of the Pt wire lowered the IR drop along the fiber, and thus increased actuation strain, while the addition of PANI and/or CNTs led to decreased strain [127]. CNTs have been added to PANI fibers to produce actuators with higher breaking strength and with larger modulus values (stiffness), even with an addition of only 0.76% of CNTs. Despite a lower free-stroke strain with zero applied stress, a higher charge-transfer efficiency was noted with the CNT-reinforced fibers leading to a higher

work-per-cycle output due to the higher strains achieved at much higher stresses [148]. The addition of 2% CNTs in wet-spun PANI fibers gave a maximum actuation of 2.2%, double that of PANI on its own, ascribed to a strong interaction between PANI and the CNTs [149].

15.6.4 Hydrogels

Blends of PANI, which provides the 'electronic backbone', and PHMEA hydrogels, which provide the 'ionic body' and high degree of swelling, were prepared by a combination of electropolymerization and UV hydrogel polymerization. A much larger swelling and shrinkage under electrochemical control was achieved than for the conducting polymer on its own. Of importance to valve applications, the blend was smooth in morphology and quite thick [98]. Conducting polymer/hydrogel composites were formed by the chemical oxidation of pyrrole in the presence of PEO as a stabilizer and added as a colloid to poly(acrylic acid). The gel composites were electroactive and could still be swollen with water [150].

PPy has been successfully grown within a thermosensitive microgel template using oxidative polymerization. While the PPy particles were found to interact strongly with the microgel network, similar reversible collapse-swelling properties were maintained [151]. Soft actuators have been formed using a polyacrylamide (PAMPS) gel composite with the inclusion of PPy. This procedure gave the gel a greater mechanical strength and conductivity, and allowed a gel rod to bend faster in an applied electric field [152].

An interpenetrating polymer network has been formed by preparing PANI within a chitosan hydrogel phase. Freeze-drying was employed to create a highly porous structure, after which a metal layer was added using electron-beam evaporation, to create an actuator which operated under an applied electric field [153,154]. This group has also incorporated conductive PANI/CNT fibers into a chitosan hydrogel composite. It was possible to use pH switching to achieve hydrogel swelling, and PANI redox reactions to produce a second (smaller) strain response under electrochemical stimulation [155].

Further approaches have recently been reported in which a conducting polymer/hydrogel composite is constructed and where a large swelling action is achieved. In one case, a hydrogel composed of acrylamide and maleic acid was doped with a PPy/carbon-black composite to create a fast acting and reversible electroactuator operating at neural pH [156]. PANI has been included within a polyacrylic acid-*co*-poly(vinyl sulfonic acid) hydrogel creating an interpenetrating network (IPN). The IPN was then able to undergo a reversible volume change upon application of an electrical stimulus of several volts. The PANI was included to help speed up the hydrogel response through expected changes in the local pH from redox switching reactions [157].

15.6.5 Other Interpenetrating Networks

An interpenetrating network of PEDOT and poly(ethylene oxide) formed a material capable of a reversible angular deflection owing to the built-in gradients of polymer and conductivities [158]. A further network of PEDOT and polybutadiene/poly(ethylene

oxide) was prepared and actuated in an ionic liquid [129,159]. A gradual dispersion of PEDOT through the IPN led to one-piece actuator devices designed to overcome delamination problems. In the presence of an ionic liquid, over a million bending deformations were achieved [160].

15.7 Prospects for Nanostructured Conducting-Polymer Actuators

Intrinsically conducting-polymer actuators have shown promising performance in a wide range of application designs, particularly on the microscale. However, due to the predominant actuation mechanism of (solvated) ion diffusion, larger-sized actuation elements with relatively fast actuation have been more difficult to construct. This limitation might be overcome by designing a controlled nanoporous conducting-polymer morphology which will allow the electrolyte solution to wet the whole bulk of the material, while at the same time not significantly diminishing the bulk polymer modulus. Some recent advances discussed in this chapter clearly support this idea [49,113,115]. Based on this past research, it has been shown that a more extensive nanoporous morphology can be achieved by adjusting synthesis conditions, such as the polymerization current density, polymerization potential, electrolyte salt, and solvent employed, through the use of nanostructured templates, or a post-polymerization processing to create ion channels.

Alongside mechanical testing of new conducting-polymer actuating elements, a fuller understanding of the underlying chemistry will be required to improve actuator performance. For example, the consistency and size of polymer chain lengths and the extent of cross-links or branched structures likely play a crucial role in defining actuator performance [131], and are very sensitive to polymerization conditions. The utilization of highly sensitive spectroscopic and surface analysis techniques (e.g. solid-state NMR, X-ray diffraction studies etc.) could well be applied more widely to link chemical structure with mechanical performance, both of newly formed actuators, and of actuators showing a loss of performance from prolonged use.

A further limiting factor at the present time is the relatively poor electrical conductivity of conducting polymers, which causes a significant IR drop in larger-sized actuators. New approaches are required to significantly increase polymer conductivity. Some developments lie in modifying the organic synthesis of the conducting polymers and their monomers to lower the band gap of the semiconducting polymer, along with enhancement of chain alignment (and lowering the extent of defects) during the synthesis, which will greatly affect polymer conductivity. The later can be achieved, for example, by using other well-aligned molecular templates, such as (polymer) liquid crystals [161], and by mechanical stretching [103].

In order to gain a better understanding of the structure–property relationships in conducting-polymer actuators, further advances in system modelling are also required. Although several significant models have been presented in the recent literature [58,59,63,64,66,71,72,74], a fuller description of the mechanical, chemical, and electrical phenomena in a conducting-polymer/electrolyte system is still sought. It will be particularly challenging to incorporate dynamic changes in material properties as the conducting polymer is cycled through a wide potential range (between oxidized and reduced states),

and to include the creep which develops (partly due to a viscoelastic property of the polymer material which differs with the redox state, and is affected by the kinetics of the osmotic pressures that develop). Advanced models would ideally take into the account changes in the polymer conformation with redox processes, and the effect of differences in the nanostructuring such as average pore size.

In the future there are many opportunities open to explore conducting-polymer nanostuctures (nanowires, nanorods, nanotubes, nanospheres) [162,163] that may ultimately posses higher conductivities then the bulk counterparts, due to more controlled synthesis conditions of the nanosized objects. Having such nanostructures available may also provide an easy means of preparing a wider range of composites of conducting polymers with carbon nanotubes, other conventional polymers etc., so long as the (solution-based) processing techniques (e.g. electrospinning of conducting-polymer fibers), provide a polymer structure with an equal or better mechanical performance, in terms of stress and strain output, as provided by the best of the electropolymerized films currently available.

References

[1] R.H. Baughman, Materials science: Playing nature's game with artificial muscles, *Science*, **308** (5718), 63–65 (2005).
[2] R.H. Baughman, Conducting polymer artificial muscles, *Synth. Met.*, **78** (3), 339–353(1996).
[3] M.T. Cortes and J.C. Moreno, Artificial muscles based on conducting polymers, *e-Polymers* (2003).
[4] Q. Pei, O. Inganaes, and I. Lundstroem, Bending bilayer strips built from polyaniline for artificial electrochemical muscles, *Smart Mater. Struct.*, **2** (1), 1–6 (1993).
[5] M. Christophersen, B. Shapiro, and E. Smela, Characterization and modeling of PPy bilayer microactuators. Part 1. Curvature, *Sens. Actuators, B*, **B115** (2), 596–609(2006).
[6] Y. Berdichevsky and Y.-H. Lo, Polypyrrole nanowire actuators. *Adv. Mater.*, **18** (1), 122–125 (2006).
[7] K. Kagawa, P. Qian, A. Tanaka, and T.M. Swager, Templated polypyrrole electro-polymerization: Self-assembled bundles of bilayer membranes of amphiphiles and their actuation behavior, *Synth. Met.*, **157** (18–20), 733–738 (2007).
[8] T.F. Otero, Artificial muscles. In *Handbook of Conducting Polymers*, 3rd Edn., **Vol. 2**, 2007, CRC Press, Boca Raton, FL,16/1–16/33.
[9] G.M. Spinks, P.G. Whitten, G.G. Wallace, and V.-T. Truong, An introduction to conducting polymer actuators, *Opt. Sci. Eng.*, **133**, 733–763 (2008).
[10] E. Smela, Conjugated polymer actuators, *MRS Bull.*, **33** (3), 197–204 (2008).
[11] D. Gimenez-Romero, P.R. Bueno, C. Gabrielli, C. Castano, H. Perrot, J.J. Garcia-Jareno, and F. Vicente, Mass/charge balance as a tool to estimate dimensional change in polypyrrole-based actuators, *Electrochem. Commun.*, **8** (1), 195–199 (2006).
[12] L. Bay, T. Jacobsen, S. Skaarup, and K. West, Mechanism of actuation in conducting polymers: osmotic expansion, *J. Phys. Chem. B*, **105**, 8492–8497 (2001).
[13] Y. Velmurugu and S. Skaarup, Ion and solvent transport in polypyrrole: Experimental test of osmotic model, *Ionics*, **11** (5 & 6), 370–374 (2005).
[14] T.F. Otero, J. Rodriguez, E. Angulo, and C. Santamaria, Artificial muscles from bilayer structures, *Synth. Met.*, **57** (1), 3713–3717 (1993).
[15] V.A. Pedrosa, X. Luo, J. Burdick, and J. Wang, 'Nanofingers' based on binary gold-polypyrrole nanowires, *Small*, **4** (6), 738–741 (2008).
[16] K. Kaneto, T. Kaneko, Y. Min, and A.G. MacDiarmid, *Synth. Met.*, **71**, 2211 (1995).

[17] J.M. Sansinena, V. Olazabal, T.F. Otero, C.N. Polo da Fonseca, and M.-A.D. Paoli, A solid state artificial muscle based on polypyrrole and a solid polymeric electrolyte working in air, *Chem. Comm.*, (22), 2217–2218 (1997).
[18] T.F. Otero and M.T. Cortes, Artificial muscles with tactile sensitivity, *Adv. Mater.*, **15** (4), 279–282 (2003).
[19] T.F. Otero and M.T. Cortes, Artificial muscle: movement and position control. *Chem. Comm.*, (3), 284–285 (2004).
[20] H.-R. Kang and N.-J. Jo, Solid-state conducting polymer actuator based on electrochemically-deposited polypyrrole and solid polymer electrolyte, *High Perform. Polym.*, **18** (5), 665–678 (2006).
[21] S.D. Deshpande, J. Kim, and S.-R. Yun, New electro-active paper actuator using conducting polypyrrole: actuation behaviour in $LiClO_4$ acetonitrile solution, *Synth. Met.*, **149** (1), 53–58 (2005).
[22] H. Yan, K. Tomizawa, H. Ohno, and N. Toshima, All-solid actuator consisting of polyaniline film and solid polymer electrolyte, *Macromol. Mater. Eng.*, **288** (7), 578–584 (2003).
[23] J. Kim, S.D. Deshpande, S. Yun, and Q. Li, A comparative study of conductive polypyrrole and polyaniline coatings on electro-active papers, *Polym. J.*, **38** (7), 659–668 (2006).
[24] M.S. Cho, J.D. Nam, Y. Lee, H.R. Choi, and J.C. Koo, Dry type conducting polymer actuator based on polypyrrole-NBR/ionic liquid system, *Mol. Cryst. Liq. Cryst.*, **444**, 241–246 (2006).
[25] M. Cho, H.J. Seo, J.D. Nam, H.R. Choi, J.C. Koo, K.G. Song, and Y. Lee, A solid state actuator based on the PEDOT/NBR system, *Sens. Actuat. B*, **B119** (2), 621–624 (2006).
[26] G. Han and G. Shi, High-response tri-layer electrochemical actuators based on conducting polymer films, *J. Electroanal. Chem.*, **569** (2), 169–174 (2004).
[27] M. Pyo, C.C. Bohn, E. Smela, J.R. Reynolds, and A.B. Brennan, Direct strain measurement of polypyrrole actuators controlled by the polymer/gold interface, *Chem. Mater.*, **15** (4), 916–922 (2003).
[28] B. Shapiro and E. Smela, Bending actuators with maximum curvature and force and zero interfacial stress, *J. Intell. Mater. Syst. Struct.*, **18** (2), 181–186 (2007).
[29] W. Takashima, S.S. Pandey, and K. Kaneto, Investigation of bi-ionic contribution for the enhancement of bending actuation in polypyrrole film, *Sens. Actuat. B*, **B89** (1–2), 48–52 (2003).
[30] W. Takashima, K. Kanamori, S.S. Pandey, and K. Kaneto, Patternable bi-ionic actuator: an example of new functionality of actuation, folding and unfolding of electrochemical spring, *Sens. Actuat. B*, **B110** (1), 120–124 (2005).
[31] G. Han and G. Shi, Conducting polymer electrochemical actuator made of high-strength three-layered composite films of polythiophene and polypyrrole, *Sens. Actuat. B*, **B99** (2–3), 525–531 (2004).
[32] E. Ochoteco, J.A. Pomposo, M. Bengoechea, H. Grande, and J. Rodriguez, Assembled cation-exchange/anion-exchange polypyrrole layers as new simplified artificial muscles, *Polym. Adv. Technol.*, **18** (1), 64–66 (2007).
[33] H. Okuzaki and T. Kunugi, Electrically induced contraction of polypyrrole film in ambient air, *J. Polym. Sci., Part B: Polym. Phys.*, **36** (9), 1591–1594 (1998).
[34] H. Okuzaki, T. Saido, H. Suzuki, Y. Hara, and H. Yan, A biomorphic origami actuator fabricated by folding a conducting paper, *J. Phys.: Conf. Ser.*, **127** 012001 (2008).
[35] G.M. Spinks, D. Zhou, L. Liu, and G.G. Wallace, The amounts per cycle of polypyrrole electromechanical actuators, *Smart Mater. Struct.*, **12** (3), 468–472 (2003).
[36] W. Lu, E. Smela, P. Adams, G. Zuccarello, and B.R. Mattes, Development of solid-in-hollow electrochemical linear actuators using highly conductive polyaniline, *Chem. Mater.*, **16** (9), 1615–1621 (2004).
[37] E. Smela, W. Lu, and B.R. Mattes, Polyaniline actuators, *Synth. Met.*, **151** (1), 25–42 (2005).
[38] T. Zama, S. Hara, W. Takashima, and K. Kaneto, Fast response polypyrrole actuators with auxiliary electrodes, *Jpn. J. Appl. Phys., Part 1*, **44** (11), 8153–8160 (2005).
[39] J. Ding, L. Liu, G.M. Spinks, D. Zhou, G.G. Wallace, J. Gillespie, High performance conducting polymer actuators utilising a tubular geometry and helical wire interconnects, *Synth. Met.*, **138** (3), 391–398 (2003).

[40] G.M. Spinks, T.E. Campbell, and G.G. Wallace, Force generation from polypyrrole actuators, *Smart Mater. Struct.*, **14** (2), 406–412 (2005).
[41] A.S. Hutchison, T.W. Lewis, S.E. Moulton, G.M. Spinks, and G.G. Wallace, Development of polypyrrole-based electromechanical actuators, *Synth. Met.*, **113** (1–2), 121–127 (2000).
[42] S. Hara, T. Zama, W. Takashima, and K. Kaneto, Polypyrrole-metal coil composite actuators as artificial muscle fibers, *Synth. Met.*, **146** (1), 47–55 (2004).
[43] S. Hara, T. Zama, S. Sewa, W. Takashima, and K. Kaneto, Polypyrrole-metal coil composites as fibrous artificial muscles, *Chem. Lett.*, **32** (9), 800–801 (2003).
[44] S. Hara, T. Zama, A. Ametani, W. Takashima, and K. Kaneto, Enhancement in electrochemical strain of a polypyrrole-metal composite film actuator, *J. Mater. Chem.*, **14** (18), 2724–2725 (2004).
[45] S. Hara, T. Zama, N. Tanaka, W. Takashima, and K. Kaneto, Artificial fibular muscles with 20% strain based on polypyrrole-metal coil composites, *Chem. Lett.*, **34** (6), 784–785 (2005).
[46] L. Bay, K. West, P. Sommer-Larsen, S. Skaarup, and M. Benslimane, A conducting polymer artificial muscle with 12% linear strain, *Adv. Mater.*, **15** (4), 310–313 (2003).
[47] E. Smela and N. Gadegaard, Surprising volume change in PPy(DBS): An atomic force microscopy study, *Adv. Mater.*, **11** (11), 953–957 (1999).
[48] E. Smela and N. Gadegaard, Volume change in polypyrrole studied by atomic force microscopy, *J. Phys. Chem. B*, **105** (39), 9395–9405 (2001).
[49] X. Wang and E. Smela, Fast switching of conjugated polymer films. In *Smart Structures and Materials 2006: Electroactive Polymer Actuators and Devices*, ed. Y. Bar-Cohen, SPIE, San Diego, 2006, p. 61680W.
[50] M.J. Higgins, S.T. McGovern, and G.G. Wallace, Visualizing dynamic actuation of ultrathin polypyrrole films, *Langmuir*, **25** (6), 3627–3633 (2009).
[51] S. Shimoda and E. Smela, The effect of pH on polymerization and volume change in PPy(DBS), *Electrochim. Acta*, **44** (2–3), 219–238 (1998).
[52] S. Maw, E. Smela, K. Yoshida, P. Sommer-Larsen, and R.B. Stein, The effects of varying deposition current density on bending behavior in PPy(DBS)-actuated bending beams, *Sens. Actuat. A*, **A89** (3), 175–184 (2001).
[53] S. Maw, E. Smela, K. Yoshida, and R.B. Stein, Effects of monomer and electrolyte concentrations on actuation of PPy(DBS) bilayers, *Synth. Met.*, **155** (1), 18–26 (2005).
[54] J. Sui, J. Travas-Sejdic, S.Y. Chu, K.C. Li, and P.A. Kilmartin, The actuation behavior and stability of p-toluene sulfonate doped polypyrrole films formed at different deposition current densities, *J. Appl. Polym. Sci.*, **111** (2), 876–882 (2009).
[55] E. Smela and B.R. Mattes, Polyaniline actuators - Part 2. PANI(AMPS) in methanesulfonic acid, *Synth. Met.*, **151** (1), 43–48 (2005).
[56] S.Y. Chu, P.A. Kilmartin, S. Jing, G.A. Bowmaker, R.P. Cooney, and J. Travas-Sejdic, The effect of monomer and electrolyte concentrations during synthesis on the actuation of PPy(CF3SO3) films in aqueous electrolytes, *Synth. Met.*, **158** (1–2), 38–44 (2008).
[57] S.Y. Chu, H. Peng, P.A. Kilmartin, G.A. Bowmaker, R.P. Cooney, and J. Travas-Sejdic, Effect of deposition current density on the linear actuation behaviour of PPy(CF_3SO_3) films, *Curr. Appl. Phys.*, **8** (3–4), 324–327 (2008).
[58] J.D. Madden, P.G. Madden, and I.W. Hunter, Polypyrrole actuators: modeling and performance, *Proc. SPIE-Int. Soc. Opt. Eng.*, **4329**, 72–83 (2001).
[59] J.D. Madden, P.G. Madden, and I.W. Hunter, Conducting polymer actuators as engineering materials, *Proc. SPIE-Int. Soc. Opt. Eng.*, **4695**, 176–190 (2002).
[60] M.R. Warren and J.D. Madden, Electrochemical switching of conducting polymers: A variable resistance transmission line model, *J. Electroanal. Chem.*, **590** (1), 76–81 (2006).
[61] P.G.A. Madden, J.D.W. Madden, P.A. Anquetil, N.A. Vandesteeg, and I.W. Hunter, The relation of conducting polymer actuator material properties to performance, *IEEE J. Oceanic Eng.*, **29** (3), 696–705 (2004).
[62] J.D. Madden, D. Rinderknecht, P.A. Anquetil, and I.W. Hunter, Creep and cycle life in polypyrrole actuators, *Sens. Actuat. A*, **A133** (1), 210–217 (2007).
[63] T. Shoa, J.D. Madden, C.-W.E. Fok, and T. Mirfakhrai, Rate limits in conducting polymers, *Adv. Sci. Technol.*, **61**, 26–33 (2008).

[64] X. Wang, B. Shapiro, and E. Smela, Visualizing ion currents in conjugated polymers, *Adv. Mater.*, **16** (18), 1605–1609 (2004).
[65] X. Wang and E. Smela, Color and volume change in PPy(DBS), *J. Phys. Chem. C*, **113** (1), 359–368 (2009).
[66] X. Wang, B. Shapiro, and E. Smela, Development of a model for charge transport in conjugated polymers, *J. Phys. Chem. C*, **113** (1), 382–401 (2009).
[67] G.M. Spinks, L. Liu, G.G. Wallace, D. Zhou, Strain response from polypyrrole actuators under load, *Adv. Funct. Mater.*, **12** (6–7), 437–440 (2002).
[68] M.R. Warren and J.D. Madden, A structural, electronic and electrochemical study of polypyrrole as a function of oxidation state, *Synth. Met.*, **156** (9–10), 724–730 (2006).
[69] G. Vazquez, T.F. Otero, and J.J. Lopez Cascales, Electro-chemo-mechanical response of a free-standing polypyrrole strip, *J. Phys.: Conf. Ser.*, **127**, 012005 (2008).
[70] R.Z. Pytel, E.L. Thomas, and I.W. Hunter, *In situ* observation of dynamic elastic modulus in polypyrrole actuators, *Polymer*, **49** (8), 2008–2013 (2008).
[71] G.M. Spinks and V.-T. Truong, Work-per-cycle analysis for electromechanical actuators, *Sens. Actuat. A*, **A119** (2), 455–461 (2005).
[72] P. Metz, G. Alici, and G.M. Spinks, A finite element model for bending behaviour of conducting polymer electromechanical actuators, *Sens. Actuat. A*, **A130–A131**, 1–11 (2006).
[73] G. Alici and N.N. Huynh, Predicting force output of trilayer polymer actuators. *Sens. Actuat. A*, **A132** (2), 616–625 (2006).
[74] G. Alici, P. Metz, and G.M. Spinks, A methodology towards geometry optimization of high performance polypyrrole (PPy) actuators, *Smart Mater. Struct.*, **15** (2), 243–252 (2006).
[75] G. Alici, B. Mui, and C. Cook, Bending modeling and its experimental verification for conducting polymer actuators dedicated to manipulation applications, *Sens. Actuat. A*, **A126** (2), 396–404 (2006).
[76] G. Alici and N.N Huynh, Performance quantification of conducting polymer actuators for real applications: A microgripping system, *IEEE/ASME Trans. Mechatron.*, **12** (1), 73–84 (2007).
[77] Q. Yao, G. Alici, and G.M. Spinks, Feedback control of tri-layer polymer actuators to improve their positioning ability and speed of response, *Sens. Actuat. A*, **A144** (1), 176–184 (2008).
[78] A.D. Santa, A. Mazzoldi, and D.D. Rossi, Steerable microcatheters actuated by embedded conducting polymer structures, *J. Intell. Mater. Syst. Struct.*, **7** (3), 292–300 (1996).
[79] K.K.C. Lee, N.R. Munce, T. Shoa, L.G. Charron, G.A. Wright, J.D. Madden, and V.X.D. Yang, Fabrication and characterization of laser-micromachined polypyrrole-based artificial muscle actuated catheters, *Sens. Actuat. A*, **153** (2), 230–236 (2009).
[80] E.W.H. Jager, E. Smela, O. Inganas, and I. Lundstrom, Polypyrrole microactuators, *Synth. Met.*, **102** (1–3), 1309–1310 (1999).
[81] E. Smela, M. Kallenbach, and J. Holdenried, Electrochemically driven polypyrrole bilayers for moving and positioning bulk micromachined silicon plates, *J. Microelectromech. Syst.*, **8** (4), 373–383 (1999).
[82] E.W. Jager, E. Smela, and O. Inganas, Microfabricating conjugated polymer actuators, *Science*, **290** (5496), 1540–1545 (2000).
[83] E.W.H. Jager, O. Inganas, and I. Lundstrom, Perpendicular actuation with individually controlled polymer microactuators, *Adv. Mater.*, **13** (1), 76–79 (2001).
[84] E. Smela, Conjugated polymer actuators for biomedical applications, *Adv. Mater.*, **15** (6), 481–494 (2003).
[85] D. Zhou, G.G. Wallace, G.M. Spinks, L. Liu, R. Cowan, E. Saunders, and C. Newbold, Actuators for the cochlear implant, *Synth. Met.*, **135–136**, 39–40 (2003).
[86] M.K. Andrews, M.L. Jansen, G.M. Spinks, D. Zhou, and G.G. Wallace, An integrated electrochemical sensor-actuator system, *Sens. Actuat. A*, **A114** (1), 65–72 (2004).
[87] G.M. Spinks, G.G. Wallace, L. Liu, and D. Zhou, Conducting polymers electromechanical actuators and strain sensors, *Macromol. Symp.*, **192** (7th Pacific Polymer Conference, 2001), 161–169, (2003).
[88] J.D.W. Madden, B. Schmid, M. Hechinger, S.R. Lafontaine, P.G.A. Madden, F.S. Hover, R. Kimball, and I.W. Hunter, Application of polypyrrole actuators: Feasibility of variable camber foils, *IEEE J. Oceanic Eng.*, **29** (3), 738–749 (2004).

[89] T.F. Otero and M. Broschart, Polypyrrole artificial muscles: a new rhombic element. Construction and electrochemomechanical characterization, *J. Appl. Electrochem.*, **36** (2), 205–214 (2006).
[90] T. Kikuchi, Y. Akiyama, M. Ueda, M. Sakairi, and H. Takahashi, Fabrication of a three-dimensional micro-manipulator by laser irradiation and electrochemical techniques and the effect of electrolytes on its performance, *Electrochim. Acta*, **52** (13), 4480–4486, (2007).
[91] S. Skaarup, L. Bay, and K. West, Polypyrrole actuators working at 2–30 Hz, *Synth. Met.*, **157** (6–7), 323–326 (2007).
[92] A. Liu, L. Zhao, H. Bai, H. Zhao, X. Xing, and G. Shi, Polypyrrole actuator with a bioadhesive surface for accumulating bacteria from physiological media, *ACS Appl. Mater. Interfaces*, **1** (4), 951–955 (2009).
[93] M. Fuchiwaki, K. Tanaka, and K. Kaneto, Planate conducting polymer actuator based on polypyrrole and its application, *Sens. Actuat. A*, **A150** (2), 272–276 (2009).
[94] M. Fuchiwaki, W. Takashima, S.S. Pandey, and K. Kaneto, Proposal of novel actuators using conducting polymer laminates, *Synth. Met.*, **135–136**, 135–136 (2003).
[95] Y. Wu, D. Zhou, G.M. Spinks, P.C. Innis, W.M. Megill, and G.G. Wallace, TITAN: a conducting polymer based microfluidic pump, *Smart Mater. Struct.*, **14** (6), 1511–1516 (2005).
[96] S. Ramirez-Garcia and D. Diamond, Biomimetic, low power pumps based on soft actuators, *Sens. Actuat. A*, **A135** (1), 229–235 (2007).
[97] J.H. Kim, K.T. Lau, R. Shepherd, Y. Wu, G. Wallace, and D. Diamond, Performance characteristics of a polypyrrole modified polydimethylsiloxane (PDMS) membrane based microfluidic pump, *Sens. Actuat. A*, **A148** (1), 239–244 (2008).
[98] L.M. Low, S. Seetharaman, K.Q. He, and M.J. Madou, Microactuators toward microvalves for responsive controlled drug delivery, *Sens. Actuat. B*, **B67** (1–2), 149–160 (2000).
[99] H.-K.A. Tsai, K.-S. Ma, C. Wang, H. Xu, C. Wang, J. Zoval, L. Kulinsky, and M. Madou, Development of integrated protection for a miniaturized drug delivery system, *Smart Mater. Struct.*, **16** (2), S295–S299 (2007).
[100] H. Xu, C. Wang, C. Wang, J. Zoval, and M. Madou, Polymer actuator valves toward controlled drug delivery application, *Biosens. Bioelectron.*, **21** (11), 2094–2099 (2006).
[101] M.R. Abidian, D.-H. Kim, and D.C. Martin, Conducting-polymer nanotubes for controlled drug release, *Adv. Mater.*, **18** (4), 405–409 (2006).
[102] R. Pytel, E. Thomas, and I. Hunter, Anisotropy of electroactive strain in highly stretched polypyrrole actuators, *Chem. Mater.*, **18** (4), 861–863 (2006).
[103] R.Z. Pytel, E.L. Thomas, Y. Chen, and I.W. Hunter, Anisotropic actuation of mechanically textured polypyrrole films., *Polymer*, **49** (5), 1338–1349 (2008).
[104] K. Yamato and K. Kaneto, Tubular linear actuators using conducting polymer, polypyrrole, *Anal. Chim. Acta*, **568** (1–2), 133–137 (2006).
[105] B. Xi, V.-T. Truong, V. Mottaghitalab, P.G. Whitten, G.M. Spinks, and G.G. Wallace, Actuation behaviour of polyaniline films and tubes prepared by the phase inversion technique, *Smart Mater. Struct.*, **16** (5), 1549–1554 (2007).
[106] A. Della Santa, D. De Rossi, and A. Mazzoldi, Characterization and modeling of a conducting polymer muscle-like linear actuator, *Smart Mater. Struct.*, **6** (1), 23–34 (1997).
[107] T. Okamoto, Y. Kato, K. Tada, and M. Onoda, Actuator based on doping/undoping-induced volume change in anisotropic polypyrrole film, *Thin Solid Films*, **393** (1,2), 383–387 (2001).
[108] M. Onoda, H. Shonaka, and K. Tada, Bending behaviour of polypyrrole films with anisotropy for artificial muscles, *J. Phys. D: Appl. Phys.*, **39** (12), 2596–2599 (2006).
[109] H.-L. Wang, J. Gao, J.-M. Sansinena, and P. McCarthy, Fabrication and characterization of polyaniline monolithic actuators based on a novel configuration: integrally skinned asymmetric membrane, *Chem. Mater.*, **14** (6), 2546–2552, (2002).
[110] X. He and G. Shi, Electrochemical actuator based on monolithic polypyrrole-TiO2 nanoparticle composite film, *Sens. Actuat. B*, **B115** (1), 488–493 (2006).
[111] J.-M. Sansinena, J. Gao, and H.-L. Wang, High-performance, monolithic polyaniline electrochemical actuators. *Adv. Funct. Mater.*, **13** (9), 703–709 (2003).

[112] G. Han and G. Shi, Electrochemical actuator based on single-layer polypyrrole film, *Sen. Actuat. B*, **B113** (1), 259–264 (2006).
[113] L. Bay, K. West, and S. Skaarup, Pentanol as co-surfactant in polypyrrole actuators, *Polymer*, **43** (12), 3527–3532 (2002).
[114] S.S. Pandey, W. Takashima, M. Fuchiwaki, and K. Kaneto, Effect of film morphology on the actuation behaviour in polypyrrole films, *Synth. Met.*, **135–136**, 59–60 (2003).
[115] W. Takashima, S.S. Pandey, and K. Kaneto, Improved cathodic expansions of electrochemomechanical behavior in polypyrrole films electrodeposited from Aerosol OT emulsion, *Chem. Lett.*, **33** (8), 996–997 (2004).
[116] X. Chen, K.-Z. Xing, and O. Inganäs, Electrochemically Induced Volume Changes in Poly(3,4-ethylenedioxythiophene), *Chem. Mater.*, **8** (10), 2439–2443 (1996).
[117] X. Lin, J. Li, E. Smela, and S. Yip, Polaron-induced conformation change in single polypyrrole chain: An intrinsic actuation mechanism, *Int. J. Quantum Chem.*, **102** (5), 980–985 (2005).
[118] P.A. Anquetil, H.-H. Yu, J.D. Madden, P.G. Madden, T.M. Swager, and I.W. Hunter, Thiophene-based conducting polymer molecular actuators, *Proc. SPIE-Int. Soc. Opt. Eng.*, **4695**, 424–434 (2002).
[119] P.A. Anquetil, J.D. Madden, H.-H. Yu, T.M. Swager, and I.W. Hunter, Biologically inspired large contraction actuators. In *Handbook of Organic Electronics and Photonics*, ed. H.S. Nalwa, American Scientific, Los Angeles, 2007.
[120] N. Vandesteeg, P.G.A. Madden, J.D. Madden, P.A. Anquetil, and I.W. Hunter, Synthesis and characterization of EDOT-based conducting polymer actuators, *Proc. SPIE-Int. Soc. Opt. Eng.*, **5051**, 349–356 (2003).
[121] S.S. Pandey, W. Takashima, and K. Kaneto, Conserved electrochemomechanical activities of polypyrrole film in complex buffer media, *Sens. Actuators, B*, **B102** (1), 142–147 (2004).
[122] Rajesh, S. S. Pandey, D. Kumar, W. Takashima, and K. Kaneto, Electrochemomechanical deformation studies of [Fe(CN)6]3- ion doped conducting polypyrrole film, *Thin Solid Films*, **467** (1–2), 227–230 (2004).
[123] W. Lu, A.G. Fadeev, B. Qi, E. Smela, B.R. Mattes, J. Ding, G.M. Spinks, J. Mazurkiewicz, D. Zhou, G.G. Wallace, D.R. MacFarlane, S.A. Forsyth, and M. Forsyth, Use of ionic liquids for p-conjugated polymer electrochemical devices, *Science*, **297** (5583), 983–987 (2002).
[124] D. Zhou, G.M. Spinks, G.G. Wallace, C. Tiyapiboonchaiya, D.R. MacFarlane, M. Forsyth, and J. Sun, Solid state actuators based on polypyrrole and polymer-in-ionic liquid electrolytes, *Electrochim. Acta*, **48** (14–16), 2355–2359 (2003).
[125] J. Ding, D. Zhou, G. Spinks, G. Wallace, D. Forsyth, M. Forsyth, and D. MacFarlane, Use of ionic liquids as electrolytes in electromechanical actuator systems based on inherently conducting polymers, *Chem. Mater.*, **15** (12), 2392–2398 (2003).
[126] G.M. Spinks, B. Xi, D. Zhou, V.-T. Truong, and G.G. Wallace, Enhanced control and stability of polypyrrole electromechanical actuators, *Synth. Met.*, **140** (2–3), 273–280 (2004).
[127] G.M. Spinks, B. Xi, V.-T. Truong, and G.G. Wallace, Actuation behavior of layered composites of polyaniline, carbon nanotubes and polypyrrole, *Synth. Met.*, **151** (1), 85–91 (2005).
[128] B. Xi, V.-T. Truong, P. Whitten, J. Ding, G.M. Spinks, G.G. Wallace, Poly(3-methylthiophene) electrochemical actuators showing increased strain and work per cycle at higher operating stresses, *Polymer*, **47** (22), 7720–7725 (2006).
[129] F. Vidal, C. Plesse, D. Teyssie, and C. Chevrot, Long-life air working conducting semi-IPN/ionic liquid based actuator, *Synth. Met.*, **142** (1–3), 287–291 (2004).
[130] S. Hara, T. Zama, W. Takashima, and K. Kaneto, Artificial muscles based on polypyrrole actuators with large strain and stress induced electrically, *Polym. J. (Tokyo, Japan)*, **36** (2), 151–161 (2004).
[131] T. Zama, S. Hara, W. Takashima, and K. Kaneto, Comparison of conducting polymer actuators based on polypyrrole doped with BF_4–, PF_6^-, $CF_3SO_3^-$, and ClO_4, *Bull. Chem. Soc. Jpn.*, **78** (3), 506–511 (2005).
[132] S. Hara, T. Zama, S. Sewa, W. Takashima, and K. Kaneto, Highly stretchable and powerful polypyrrole linear actuators, *Chem. Lett.*, **32** (7), 576–577 (2003).

[133] S. Hara, T. Zama, W. Takashima, and K. Kaneto, TFSI-doped polypyrrole actuator with 26% strain, *J. Mater. Chem.*, **14** (10), 1516–1517 (2004).
[134] S. Hara, T. Zama, W. Takashima, and K. Kaneto, Free-standing gel-like polypyrrole actuators doped with bis(perfluoroalkylsulfonyl)imide exhibiting extremely large strain, *Smart Mater. Struct.*, **14** (6), 1501–1510 (2005).
[135] S. Hara, T. Zama, W. Takashima, and K. Kaneto, Free-standing polypyrrole actuators with response rate of 10.8%s^{-1}, *Synth. Met.*, **149** (2–3), 199–201 (2005).
[136] S. Hara, T. Zama, W. Takashima, and K. Kaneto, Tris(trifluoromethylsulfonyl)methide-doped polypyrrole as a conducting polymer actuator with large electrochemical strain, *Synth. Met.*, **156** (2–4), 351–355 (2006).
[137] K. Yamato, K. Tominaga, W. Takashima, and K. Kaneto, Stability of electrochemomechanical strains in polypyrrole films using ionic liquids, *Synth. Met.*, **159** (9–10), 839–842 (2009).
[138] Y. Wu, G. Alici, G.M. Spinks, and G.G. Wallace, Fast trilayer polypyrrole bending actuators for high speed applications, *Synth. Met.*, **156** (16–17), 1017–1022 (2006).
[139] G. Alici, V. Devaud, P. Renaud, and G. Spinks, Conducting polymer microactuators operating in air, *J. Micromech. Microeng.*, **19** (2), 025017/1–025017/9 (2009).
[140] D.M/G. Preethichandra, A.K. Thakur, W. Takashima, and K. Kaneto, A combined bi-ionic polymer actuator with unidirectional extension against bipolar excitations, *Sens. Actuat. B*, **B122** (2), 587–590 (2007).
[141] R. Kiefer, S.Y. Chu, P.A. Kilmartin, G.A. Bowmaker, R.P. Cooney, J. Travas-Sejdic, Mixed-ion linear actuation behaviour of polypyrrole, *Electrochim. Acta*, **52** (7), 2386–2391 (2007).
[142] R. Kiefer, P.A. Kilmartin, G.A. Bowmaker, R.P. Cooney, and J. Travas-Sejdic, Actuation of polypyrrole films in propylene carbonate electrolytes, *Sens. Actuat. B*, **B125** (2), 628–634 (2007).
[143] R. Kiefer, G.A. Bowmaker, R.P. Cooney, P.A. Kilmartin, and J. Travas-Sejdic, Cation driven actuation for free standing PEDOT films prepared from propylene carbonate electrolytes containing $TBACF_3SO_3$, *Electrochim. Acta*, **53** (5), 2593–2599 (2008).
[144] S.S. Pandey, W. Takashima, and K. Kaneto, Electrochemomechanical deformation in conducting copolymers containing pyrrole and anisidine moieties, *React. Funct. Polym.*, **58** (2), 103–110 (2004).
[145] A. Tanaka, W. Takashima, and K. Kaneto, Improved cathodic expansions of polypyrrole films by poly(2-methoxyaniline-5-sulfonate) incorporation, *Thin Solid Films*, **499** (1–2), 179–184 (2006).
[146] W. Li, C.L. Johnson, and H.-L. Wang, Preparation and characterization of monolithic polyaniline-graphite composite actuators, *Polymer*, **45** (14), 4769–4775 (2004).
[147] M. Tahhan, V.-T. Truong, G.M. Spinks, and G.G. Wallace, Carbon nanotube and polyaniline composite actuators, *Smart Mater. Struct.*, **12** (4), 626–632 (2003).
[148] G.M. Spinks, V. Mottaghitalab, M. Bahrami-Samani, P.G. Whitten, G.G. Wallace, Carbon-nanotube-reinforced polyaniline fibers for high-strength artificial muscles, *Adv. Mater.*, **18** (5), 637–640 (2006).
[149] V. Mottaghitalab, B. Xi, G.M. Spinks, and G.G. Wallace, Polyaniline fibers containing single walled carbon nanotubes: Enhanced performance artificial muscles, *Synth. Met.*, **156** (11–13), 796–803 (2006).
[150] B.C. Kim, G. Spinks, C.O. Too, G.G. Wallace, and Y.H. Bae, Preparation and characterisation of processable conducting polymer-hydrogel composites, *React. Funct. Polym.*, **44** (1), 31–40 (2000).
[151] A. Pich, Y. Lu, V. Boyko, K.-F. Arndt, and H.-J.P. Adler, Thermo-sensitive poly (N-vinylcaprolactam-co-acetoacetoxyethyl methacrylate) microgels: 2. Incorporation of polypyrrole, *Polymer*, **44** (25), 7651–7659 (2003).
[152] T. Yamauchi, S. Tansuriyavong, K. Doi, K. Oshima, M. Shimomura, N. Tsubokawa, S. Miyauchi, and J.F.V. Vincent, Preparation of composite materials of polypyrrole and electroactive polymer gel using for actuating system, *Synth. Met.*, **152** (1–3), 45–48 (2005).
[153] M.-S. Kim, C.K. Lee, S.-R. Shin, S.-M. Lee, S.I. Kim, G.M. Spinks, and S.J. Kim, Enhancement of the electromechanical behavior of IPMCs based on chitosan/polyaniline

ion exchange membranes fabricated by freeze-drying, *Proc. SPIE-Int. Soc. Opt. Eng.*, **5759**, 454–463 (2005).
[154] S.J. Kim, M.S. Kim, S.I. Kim, G.M. Spinks, B.C. Kim, and G.G. Wallace, Self-oscillatory actuation at constant DC voltage with pH-sensitive chitosan/polyaniline hydrogel blend, *Chem. Mater.*, **18** (24), 5805–5809 (2006).
[155] G.M. Spinks, S.R. Shin, G.G. Wallace, P.G. Whitten, I.Y. Kim, S.I. Kim, and S.J. Kim, A novel 'dual mode' actuation in chitosan/polyaniline/carbon nanotube fibers. *Sens. Actuat. B*, **B121** (2), 616–621 (2007).
[156] E.A. Moschou, M.J. Madou, L.G. Bachas, and S. Daunert, Voltage-switchable artificial muscles actuating at near neutral pH, *Sens. Actuat. B,*, **B115** (1), 379–383 (2006).
[157] H.I. Kim, S.J. Park, and S.J. Kim, Volume behavior of interpenetrating polymer network hydrogels composed of polyacrylic acid-co-poly(vinyl sulfonic acid)/polyaniline as an actuator, *Smart Mater. Struct.*, **15** (6), 1882–1886 (2006).
[158] F. Vidal, J.F. Popp, C. Plesse, C. Chevrot, and D. Teyssie, Feasibility of conducting semi-interpenetrating networks based on a poly(ethylene oxide) network and poly(3,4-ethylenedioxythiophene) in actuator design, *J. Appl. Polym. Sci.*, **90** (13), 3569–3577 (2003).
[159] C. Plesse, F. Vidal, H. Randriamahazaka, D. Teyssie, and C. Chevrot, Synthesis and characterization of conducting interpenetrating polymer networks for new actuators, *Polymer*, **46** (18), 7771–7778 (2005).
[160] F. Vidal, C. Plesse, G. Palaprat, A. Kheddar, J. Citerin, D. Teyssie, and C. Chevrot, Conducting IPN actuators: From polymer chemistry to actuator with linear actuation, *Synth. Met.*, **156** (21–24), 1299–1304 (2006).
[161] J.F. Hulvat and S.I. Stupp, Liquid-crystal templating of conducting polymers, *Angew. Chem., Int. Ed.*, **42** (7), 778–781 (2003).
[162] L. Zhang, H. Peng, Z.D. Zujovic, P.A. Kilmartin, and J. Travas-Sejdic, Characterization of polyaniline nanotubes formed in the presence of amino acids, *Macromol. Chem. Phys.*, **208** (11), 1210–1217 (2007).
[163] L. Zhang, H. Peng, C.F. Hsu, P.A. Kilmartin, and J. Travas-Sejdic, Self-assembled polyaniline nanotubes grown from a polymeric acid solution, *Nanotechnology*, **18** (11), 115607/1–115607/6 (2007).

16

Electroactive Conducting Polymers for the Protection of Metals against Corrosion: from Micro- to Nanostructured Films

Pierre Camille Lacaze, Jalal Ghilane,
Hyacinthe Randriamahazaka and Jean-Christophe Lacroix

Laboratoire Interfaces Traitements et Dynamique des Systèmes (ITODYS),
CNRS – Université Denis Diderot Paris, France

16.1 Introduction

The first conducting polymers (named ICPs for intrinsically conducting polymers, or ECPs for electroactive conducting polymers) were discovered in the seventies by McDiarmid, Heeger, and Shirakawa [1] who showed that unsaturated conjugated polymers (polyacetylene, polyphenylene) became conductive when doped, corresponding to the chemical oxidation of the ethylene or polyphenyl carbon chain.

The electropolymerization technique, applied to oxidizable monomers (phenols and their derivatives) and developed in the seventies to obtain homogeneous thin dielectric films [2], was extended to heterocyclic conducting polymers as early as 1979 with polypyrrole (PPy) [3], and some time later to polyaniline (PANI, 1981) [4,5] and polythiophene (PT, 1982) [6]. It was shown that adherent homogeneous conductive solid

Nanostructured Conductive Polymers Edited by Ali Eftekhari

polymer films could be obtained through electro-oxidation of the corresponding monomers on a noble metal (platinum or gold). Their particularity of switching between conductive (1–100 S cm^{-1}) and insulating states (10^{-6}–10^{-9} S cm^{-1}) when they are successively oxidized (chemically or electrochemically) and reduced, is a unique polymer property which was found and continues to be extremely suitable for various analytical applications [7].

The use of conducting polymers for the protection of metals against corrosion was investigated a few years later, after DeBerry [8] (1985) found that a polyaniline film (PANI) obtained by electro-oxidation of aniline on stainless steel and mild steel in sulfuric acid solution could afford protection against corrosion. This was the beginning of a systematic research, which initially was based on the electropolymerization of pyrrole in neutral media and on commodity metals such as iron, mild steel, and stainless steel. The first attempts made in organic media [9,10] were somewhat disappointing, because the adherence of films to the metal was very poor and, moreover, considerable amounts of the metal were dissolved during the electrodeposition of the polymer. The reason was obvious, and intuitively this application would seem to be impossible, as the thermodynamic oxidation potential of the metal (corresponding to its dissolution) is much lower than that required for electropolymerization. Nevertheless, this difficulty was overcome by changing the relative rates of the two processes, i.e. slowing the dissolution reaction without preventing electropolymerization. In the case of pyrrole on iron, success was achieved by using solvents slightly more basic than water [11], or by chemically treating the electrode surface to make it less active [12,13]. However, the best way to inhibit metal dissolution is to select an electrolyte which, by reaction with the metal cation, leads to the formation of an insoluble metallic salt, providing a thin passivating layer. The formation of a passivating layer on the metal surface and its role in corrosion protection will be described in detail later. Various electrolyte salts were proposed by several groups for iron and steel [14,15] and also for extremely oxidizable nonferrous metals like zinc [16,17] and aluminium [18,19].

The most frequently used polymer in this field is certainly PPy, and the choice of pyrrole as monomer to achieve electropolymerization was not fortuitous. Indeed, the monomer is the only one which is soluble in neutral or weakly acidic aqueous media, its oxidation potential is relatively low and, besides, it is recognized as an environmentally friendly compound. These properties, favorable for electropolymerization on oxidizable metals, are not found with aniline and thiophene. The first monomer requires strongly acidic aqueous media, very aggressive towards oxidizable metals, and the second one, which has a very high oxidation potential, does not polymerize in aqueous media (except in the presence of surfactants [20,21] or complexants like cyclodextrin [22]. This is the main reason why PANI [23], and much later PPy and PT [24–25], were mostly used as suspensions of powders dispersed in organic solvents or blended with other polymers.

Several reviews have been written on this topic [26–27]. That by Tallman *et al.* in 2002 provides an excellent survey of all the reports up to 2001 concerning PPy, PANI, and PT, and their application to the protection of ferrous and nonferrous metals [27,28]. In addition, they show that many results appear contradictory, a fact they attribute to the variety of experimental conditions. In summarizing this work, they concluded that further investigations are needed for a better understanding of protection mechanisms. Besides, a distinction has to be made between PANI and other polymers (PPy and PT). Although PPy

and PANI can be oxidized by O_2 it is worth noting that this latter polymer exhibits some specific effects due to the protonic equilibrium between both oxidized forms, i.e. emeraldine salt (ES, green, conducting) and emeraldine base (EB, blue, nonconducting). The EB can be converted to ES by 'doping' with a 'strong' acid (with $pK_a < 5.5$) and vice versa for dedoping from ES to EB (using a base) [28–29]. This conversion does not exist with PPy, where a simple PPy(Ox)/PPy(Red) redox reaction is involved. We shall see along this chapter that PANI complex behavior has yielded to a proposed mechanism of protection specific to PANI, but also to some conflicting information.

After this brief historical summary illustrating the way conducting polymers have been progressively used to protect metals against corrosion, we shall examine the most significant recent results which provide new insights into the theories of protection by these materials. Finally, we shall move on to nanostructured conducting-polymer films and attempt to predict how they can be used for protection applications. However, this last topic is still in its infancy, and for the time being, the nanostructuration of the layer is used either to improve the adhesion of the conducting polymer to the surface or to increase its hydrophobicity, both factors being recognized as decisive for a good protection against corrosion. In the first case, the idea is to graft on the surface a bifunctional compound, where one end-group (phosphonic, sulphide, siloxane, or diazonium) will strongly interact with the metallic surface and the other one, similar to the monomer, will participate to the polymerization reaction and on the whole, provide a strong improvement of the adhesion of the coating. The second effect (lotus effect) is related to an increase of the hydrophobicity of the coating and is obtained through a microroughening of the surface involving a superficial nanostructuration of the polymer.

16.2 Protection Mechanisms Induced by Conducting Polymers

The use of organic coatings and paints to protect metals against corrosion is the traditional way which has been and continues to be widely applied. Several recommendations have been formulated for obtaining efficient coatings of ferrous and nonferrous metals. In general, an effective coating consists of several successive layers of different thicknesses: a primer which ensures adhesion to the metal (about 1 micron thick) and has inhibitor properties, followed by a thick polymer layer (about 20–30 μm) containing pigments and anticorrosion agents. Generally these layers are cured in order to achieve good cross-linking between the polymer chains and, finally, a thin top-coat with cosmetic ingredients is applied. A survey of this topic may be found in [30,31] and references therein. One of the key factors determining the performance of a paint coating is the barrier effect and the presence of inhibitors. Indeed, corrosion occurs through an electrochemical process consisting of two coupled anodic and cathodic half-cell electrode reactions taking place on different surface sites [32]. The metal M is oxidized, according to $M \rightarrow M^{n+} + ne^-$, while O_2 is reduced, according to either $O_2 + 2\,H_2O + 4\,e^- \rightarrow 4\,OH^-$ (in neutral or basic environment, pH > 7) or $O_2 + 4\,H^+ + 4e^- \rightarrow 2\,H_2O$ in acidic medium (pH < 7). Obviously, any means of decreasing the rate of either one or both reactions will contribute to increasing the performance of the coating. The first reaction, corresponding to the dissolution of M, can be considerably reduced if either the potential of the metal is shifted into the passivation domain, corresponding to the formation of a thin

metal-oxide film, or if a sacrificial coating (zinc deposited on steel, for example) or zinc powder mixed with the polymer is added in order to provide cathodic protection of the underlying metal. Any other insoluble and insulating compound firmly attached to the metal surface, resulting from a chemical or electrochemical treatment of the metal, will also contribute to its passivation.

A second means of slowing the rate of corrosion is to hinder the diffusion of O_2 and H_2O towards the metal surface and, therefore, good protection will be achieved through an efficient barrier effect of the coating, i.e. slow permeation of O_2 and H_2O. This effect increases with the thickness of the coating.

In general, both effects are combined to achieve good protection. However, good it may be a paint coating will never constitute an impermeable barrier to water and dioxygen, and it is imperative to slow the faradaic process of both electrochemical reactions. Up to now, the best way to achieve very good protection remains the use of various inhibitors in the coating (mainly chromate salts) associated with chemical conversion of the surface by chromic acid. A good survey of this topic can be found in [33,34] and the related references.

Unfortunately, chromate-based techniques, which provide outstanding passivation of metals like iron, zinc, and aluminium, are now prohibited by new environmental regulations. The need to find an alternative to chromates has given rise to much research, mainly centered on the replacement of Cr(VI) compounds by less toxic ones such as molybdates, cerium, and zirconium derivatives. Silica-based hybrid coatings obtained by the sol-gel process [35] constitute a promising alternative which has led to several good anticorrosive properties, as reported in recent reviews [36,37]. The use of electroactive conducting polymers (ECP) affords a new and original concept for the protection of metals. Although the topic is still debated, the way ECPs work to protect a metal against corrosion is very different from that usually accepted for insulating organic and hybrid coatings. Indeed, four mechanisms may be invoked to explain the protection properties of conducting polymers: (i) the displacement of the electrochemical interface from metal–solution to the ECP-surface–solution; (ii) the ennobling of the metal by the polymer in its oxidized state; (iii) the self-healing properties provided by counter-ions with inhibitor properties; (iv) a barrier effect (nonspecific), which will depend on an additional cross-linking of the polymer. All these points will be addressed in detail in the following.

16.2.1 Displacement of the Electrochemical Interface

The displacement of the electrochemical interface can be likened to the situation where an oxidizable metal is coated with a noble one (nickel or chromium) in order to prevent corrosion by completely isolating the underlying metal, which thus escapes from the aggressive environment. This amounts to saying that the electrochemical interface is no longer the oxidizable metal-solution, but the noble-metal–solution interface. However, the coating will only be efficient if the noble-metal layer is free from any defect, such as pinholes or scratches, whose presence would be disastrous, because of strong localized corrosion resulting from galvanic coupling between noble and oxidizable metals.

When an oxidizable metal is coated by a conducting-polymer film in its oxidized state the situation might seem to be similar to that described above. Indeed, the initial electrochemical interface moves from metal–solution to polymer–solution and, as long as the

polymer remains in its oxidized conductive state, we can infer that the electrical potential drop at the metal–polymer interface is small and thus the driving force for metal oxidation disappears. The underlying metal is no longer in contact with the aggressive environment.

Illustration of this effect in the case of a two-step process for aniline electropolymerization on mild steel and zinc from an aqueous electrolyte was reported by Lacroix *et al.*[38] In acidic medium (the usual conditions for the electrodeposition of PANI) the direct electropolymerization of aniline on zinc or steel fails, because large amounts of metal dissolve before the aniline polymerizes. This can be avoided if the surface is first treated by depositing a thin polypyrrole film in neutral salicylate medium. This PPy layer behaves as a thin noble-metal layer and can be used for the electrodeposition of a PANI film of controllable thickness in an acidic medium. Using this pretreatment, no or very little metal dissolution occurs in this second step. The films exhibit very stable electroactivity in acidic electrolytes, similar to that of PANI deposited on platinum, which indicates that the underlying oxidizable metal is fully protected (Figure 16.1).

The overall system has a bilayer structure, indicating that the electrochemical interface during aniline electrodeposition is the polypyrrole–solution interface. This confirms the concept of the displacement of the electroactive interface from its usual location (metal–solution) to the polymer–solution interface. The protection properties of such metal/PPy/PANI bilayers, as well as composites made of PANI and PPy, were confirmed by Iroh *et al.* on both aluminium alloys (AA 2024-T3 substrates) and low-carbon steel in sodium chloride solutions [39–40]. They concluded that these bilayer coatings lowered the porosity, improved the processibility and provided better protection than single coatings. More recently, Hasanov and Bilgic [41] also showed that steel substrates coated by PPy-PANI bilayers and immersed in aqueous sulfuric acid were better protected against corrosion than with single coatings, and that the steel/PPy/PANI bilayer coating was more

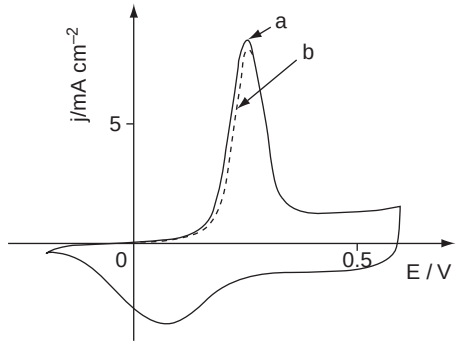

Figure 16.1 *Electrochemical cycling in 2 M* p*-toluene sulfonic solution of a mild-steel electrode coated by a PPy/PANI bilayer: (a) first cycle; (b) after cycling for 2 h. The bilayer system exhibits the same stability under potentiodynamic cycling as a platinum electrode coated by a PANI film in acidic medium. (Reprinted with permission from Journal of Electroanalytical Chemistry, Aniline electropolymerization on mild steel and zinc in a two-step process by J.-C. Lacroix, J.L. Camalet, P.C. Lacaze et al., 481, 1, 76–81. Copyright (2000) Elsevier Ltd)*

efficient than steel/PANI/PPy. It appears then that the first layer, which ensures the adherence of the second polymer, is a key to obtaining high protection.

Another illustration of the displacement of the electrochemical interface can be found in a recent study reported by Michalik and Rohwerder [42]. They were able to locate the oxygen reduction process on a metal–polymer system using an isotopic marker ($^{18}O_2$). The reduction of heavy oxygen will create $^{18}OH^-$ anions which can be recognized by mass spectroscopy. Sputter profiles performed by ToF-SIMS (time of flight-secondary ion mass spectroscopy) clearly demonstrated the presence of a significant number of heavy oxygen molecules only at the polymer surface. This indicates that the oxygen reduction process has been shifted from the metal–polymer interface to the top of the conductive coating. However, in these experiments, the conductive polymer is quickly reduced by corrosion in defects (introduced on purpose) and, when the coating is fully reduced, oxygen reduction takes place at the metal–polymer interface.

It can thus be stated that if such electrochemical interface displacement were permanent in a defect-free coating, and if no scratches were made during the lifetime of the coating, a steady state would be obtained in which the conductive polymer protects the underlying metal permanently, since no or minimal electrical potential drop arises at the metal–polymer interface.

However, the situation is not so simple as we might think. First, the polymer matrix is porous and, therefore, O_2 and H_2O can reach the metal surface through the pores, allowing corrosion reactions to take place in confined areas (through the pores the substrate would corrode even faster than on a bare electrode, because a local element would be formed, with metal exposed by the pores acting as an anode unless local passivation occurs). Second, the redox potential of the polymer is generally above that of the metal and thus P^{n+} is also capable of oxidizing M to M^{n+}, with a concomitant reduction of the polymer to a P state, in which the coating is not conducting any more, a situation where the electrochemical interface cannot be displaced, but where there is still a barrier effect (nonspecific). We will see in the next part that fast reduction of the polymer is needed to reach a high level of protection when small scratches are made in the coatings.

Furthermore, the kinetics of the reduction of $O_2 + H_2O$ largely depends on the potential of the metal, which is fixed by the redox potential of the polymer P^{n+}/P and thus by its time-dependent doping level. Indeed, as long as the polymer remains conductive, the potential of the metal–polymer electrode is above that of the redox couple of a bare metal electrode, whereas, when the polymer is reduced, the potential of the metal–polymer electrode drops to a lower value. This explains why open-circuit potential (OCP) vs. time curves have been considered as good criteria for testing protection efficiencies qualitatively. The longer the potential remains at a high value, the longer the protection. This simple test has nevertheless to be taken with caution. Indeed, it only reveals the time needed for P^{n+} reduction in a particular situation (pH, environment, electrolyte, film thickness) and for a particular coating, but does not give any clues about the corrosion current, which arises when the polymer is still in an oxidized/conductive state, nor its value when the polymer has reached a reduced/nonconductive state. Such tests should be compared only for films of similar thicknesses and with equivalent doping levels at the beginning of the test.

Finally, O_2 reduction on the polymer is crucial since it can help to maintain the polymer in an oxidized state as long as the O_2/H_2O oxidation potential is above that of the polymer

(note that poly-3,4-dioxyethylenethiophene, PPy and PANI are known to be stable in air in their oxidized state, whereas polythiophenes are stable in air in their neutral state).

For instance, with a PPy film deposited on a zinc electrode in aqueous salicylate solution, the reduction potential of the doped polymer is around −0.9 V/SCE [43], whereas the thermodynamic reduction potential of O_2 varies considerably with the pH, and can shift from 1.2 V/NHE (at pH 0, when the reduction involves four electrons) to 0.4 V in basic medium at pH 12 [44].

Clearly, O_2 can be reduced according to two reactions:

$$(n/4)O_2 + nH^+ + PPy \rightarrow n/2H_2O + PPy^{n+} \tag{16.1}$$

$$O_2 + 4H^+ + 4e^- \rightarrow 2H_2O \tag{16.2}$$

or

$$(n/4)O_2 + n/2H_2O + PPy \rightarrow nOH^- + PPy^{n+} \tag{16.1'}$$

$$O_2 + 2H_2O + 4e^- \rightarrow 4OH^- \tag{16.2'}$$

Reactions (16.1) and (16.1′) correspond to the chemical oxidation of the neutral PPy form by O_2 (in acidic and neutral media, respectively) and will occur if the redox potential of O_2/H_2O is more positive than that of the polymer, which is always the case for PPy. Reactions (16.2) and (16.2′) correspond to the electrochemical reduction of O_2 on the metal-like surface of the polymer (when it is in its conducting state) or at the metal–polymer interface (when the polymer is reduced). In a neutral medium, reaction (16.2′) will occur and, therefore, OH^- ions will be released.

The fact that the reduction of O_2 can take place at the polymer surface is also of great importance because this implies that the OH^- species, responsible for disbondment and delamination [38,39,41,42], has no effect on the adherence of the polymer. Unfortunately, as said previously, a conducting-polymer film is not fully impermeable, and some O_2 and H_2O will pass through the pores and be reduced at the metal–polymer interface with a release of OH^- ions and local delamination at the detriment of protection against corrosion. Delamination and disbondment of the coating upon reduction will be discussed later in this chapter, but it is useful to state that this is an important factor in the failure of the coating.

In conclusion, the displacement of the electrochemical interface can slow down corrosion for a time, but not indefinitely, and the ideal and permanent steady-state picture described above is rarely achieved.

16.2.2 Ennobling the Metal Surface

The ennobling of the metal surface is based on the assumption that the conducting polymer, in its oxidized state, will set the metal at a potential within its passive range where the dissolution rate is slow. This generally involves the formation of a thin insulating metallic oxide layer, more or less porous, the effect of which is to protect the metal from a rapid dissolution, and make it behave like a noble metal. To understand this effect it must be recalled that three distinct areas related to active, passive, and transpassive

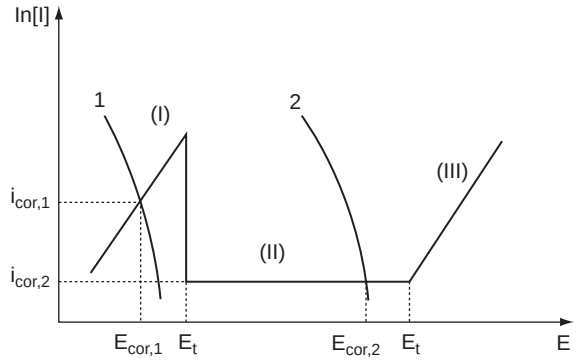

Figure 16.2 *Evans diagram of an oxidizable metal with a passivation range. In the active region (I) the metal dissolves rapidly up to E_f called the Flade potential or potential of passivation. This E_f potential corresponds to the formation of a thin, insoluble, and insulating metallic oxide film which leads to a resistive barrier involving a low corrosion current ($i_{cor,2}$, passive area, II). When the potential is higher than E_t, the oxide layer breaks down or dissolves, and metal oxidation is reactivated (transpassive area, III). When the medium in contact with the metal is a weak oxidant (i.e. H^+), the associated reduction process is represented by curve 1, and the corrosion current ($i_{cor,1}$) is high. Conversely, with a stronger oxidant (O_2, curve 2) the corrosion current ($i_{cor,2}$) falls in the passive range and is low. (Adapted from Manuel de peintures et vernis, edited by P. C. Lacaze and A. Revillon, Corrosion des métaux peints. Analyse des phénomènes et moyens de protection by M. Keddam and P. C. Lacaze, Chpt 13, Paris. Copyright (2007) Editions Hermann)*

potential domains are observed on the typical anodic polarization curve of an oxidizable metal. Therefore, as depicted in an Evans diagram and depending on the oxidant in contact with the metal (H^+, O_2, or oxidized conducting polymer), the corrosion potential may be set at more or less anodic potentials, corresponding to active or passive dissolution (Figure 16.2) [45].

Note that the width of the passivation area ($E_t - E_f$) and the current densities needed to reach this area depend on several parameters (metal, pH of the solution, nature of the anions in the vicinity of the metal). This last point is crucial since it is probably in the origin of some of the contradictory results reported in the literature. As an extreme case, let us just state that some anions, such as thiosalicylate, have tremendous passivation properties on zinc [46]. Thus, if a zinc-coated system is scratched in the presence of such an anion, passivation and ennobling of the scratch will occur easily and a very low current density will be needed to reach the passivation area. Unfortunately, a scratch on a zinc-coated system is rarely in contact with such anions and corrosion is possible. On the contrary, some environments give a very narrow passivation range and are associated with very high current densities in the active areas. Therefore, if there is a defect in a zinc-coated system, a very high current density will be needed to reach passivation. In this latter case, probably the coating could not provide the required electrical charge and self-healing passivation will not happen.

Nevertheless, when a conducting polymer in its oxidized state is coated on the metal, there is galvanic coupling between the metal and the polymer. The corrosion current has a kinetic origin and corresponds to a mixed potential resulting from the reduction of the

polymer and the oxidation of the metal. Of course, the most favorable situation for a low corrosion current is when the reduction of the polymer 'falls' in the passive area of the metal. As depicted in Figure 16.2, the magnitude of the corrosion current is then fixed by that of the passivation current.

This effect, which has been much debated since the pioneering work of DeBerry [8], is now widely accepted in the case of ferrous substrates coated by PANI in acidic media. Evidence for the protection of exposed bare steel areas was shown for the first time by Elsenbaumer *et al.* [47], who proved through XPS and Auger analysis that this effect was due to the formation of passivating iron oxides (γ-Fe_2O_3 and Fe_3O_4) induced by the galvanically coupled polyaniline in its oxidized state. These observations were confirmed by other groups [48–49,] and a general scheme to explain the formation of iron oxides in the case of PANI coatings (Figure 16.3) was proposed by Wessling [50]. According to this scheme, a redox reaction occurs between Fe and $(PANI)_{ox}$ (PANI oxidized state or PANI emeraldine salt) leading to $(PANI)_{red}$ (PANI neutral state or PANI leuco base) and to Fe^{2+}. In the presence of O_2 and H_2O it is assumed that the neutral form of PANI is reoxidized to $(PANI)_{ox}$, or PANI emeraldine salt (ES), while Fe^{2+} is oxidized to Fe^{3+} and transformed into Fe_2O_3 in the presence of OH^- resulting from the reduction of $O_2 + H_2O$. A more detailed interpretation of this ennobling effect was recently reported by Williams and McMurray [34] in the case of several metals (Fe, Al, Zn, and Mg) covered by coatings containing PANI/ES (ES of *p*-toluenesulfonic acid) dispersed in a polyvinylbutyral (PVB) binder and exposed to humid air. From potentiometric measurements performed with the scanning Kelvin probe (SKP) [51,52], they concluded that the efficiency of the ennobling effect was determined by the acid–base stability of the interface between PANI/ES and oxide covered metal. Indeed, they found that the open-circuit potential vs. time (E_{oc}) of the substrate considerably varied with the relative acidity of the corresponding oxides with regard to ES, the pK_a of which is around 5.5 [31]. Thus, with metal oxides (Fe and Al) more acidic than ES, PANI/ES remains in its doped state and, therefore, the E_{oc} (corresponding to the corrosion potential) is held in the passive region for a long time, providing a good ennobling effect. On the other hand, with less acidic oxides (Zn and Mg), ES is deprotonated and transformed into the nonconductive and electroinactive EB, shifting the E_{oc} to

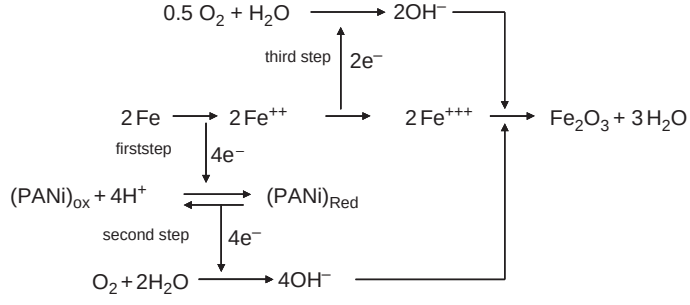

Figure 16.3 *Mechanism of iron protection against corrosion through a PANI coating. (Reprinted with permission from Synthetic Metals, Scientific and Commercial Breakthrough for Organic Metals by B. Wessing, 85, 1–3, 1313–1318. Copyright (1997) Elsevier Ltd)*

negative values, characteristic of the corrosion of the bare metal. In addition, they showed that the oxide layer thickness could be increased when the amount of PANI-pTS dispersed in the coating was increased, confirming the fact that the formation of the metal oxide resulted for a great part from the reduction of the PANI/ES, and also that the protection was improved as the thickness of the oxide increased. Very recently, the same group clearly showed that PANI/EB coatings did not induce oxide growth on Al, confirming in that case the absence of an ennobling effect [37].

These results provide new enlightenment on PANI ennobling, and could explain that some conflicting information reported in the literature on PANI ennobling, temporary or sustained, are probably linked to the conditions under which experiments are performed and in particular, how the reoxidation to PANI ES by oxygen is achieved. As noted by Williams and McMurray [34], the low concentration of dissolved oxygen in aerated water ($2.7\ 10^{-4}$ mol dm^{-3} at 20°C) may be insufficient to maintain cyclic reoxidation of the PANI ES indefinitely under immersion conditions. However, under dry atmospheric conditions, with much higher availability of oxygen, many authors have observed a long-term ennobling, especially with iron and zinc surfaces [53].

However, as previously described, this ennobling mechanism is only based upon steady-state considerations, and it does not adequately take into account electrochemical kinetics, which, depending on the experimental conditions (polymer, substrate, aeration of the environment . . . [41]), makes the protection efficiency vary considerably.

Rammelt *et al.* [54], in the case of polymethylthiophene (PMT) deposited on iron or steel surfaces, proposed a kinetic interpretation of the process through new experiments and, consequently, defined the conditions under which the ennobling mechanism works and provides protection against corrosion. They used an electrochemical corrosion cell similar to that of Elsenbaumer *et al.* except that the PMT was deposited on a noble metal (platinum) and not directly on the oxidizable metal (steel) (see Figure 16.4). The steel electrode was coated by an insulating epoxy polymer layer in contact with the electrolytic solution through a small pin hole. This arrangement avoids the presence of a possible additional passivating layer on the metal, which might mask the true ennobling effect, and which could be due to the deposition of an insulating layer resulting from the formation of an insoluble salt between iron ions and doping anions. Moreover, this configuration allows separation of the two processes occurring on the iron surface and in the polymer film.

In this experiment the PMT/Pt electrode is prepared by electrochemical oxidation of methyl-thiophene on platinum in organic medium. Then, the modified electrode is immersed in a $LiClO_4$ solution saturated with O_2. The potential of the PMT/Pt electrode is 0.5V/SCE and is found to correspond to the oxidized state of the polymer. When the steel/epoxy-hole electrode is galvanically coupled to the PMT/Pt electrode, its potential remains steady at 0.5 V, but it instantaneously decreases from 0.5 V to −0.5 V when disconnected from the PMT/Pt electrode, as depicted in Figure 16.5, and this can be repeated indefinitely. The fact that the potential drop is quasi-instantaneous means that the steel electrode has not been shifted to within the passive range, but is still in the active region and, therefore, under these conditions, the steel is not protected. It is important here to note that when the PMT/Pt electrode and the steel/epoxy-hole are connected the potential is positioned at +0.5 V/SCE, well above that of the metal oxidation potential. Surprisingly, oxidation of metal occurs vigorously despite this high potential, for which passivation is expected. In fact, the anodic potentiodynamic curve of steel carried out in $LiClO_4$ shows that no tendency to

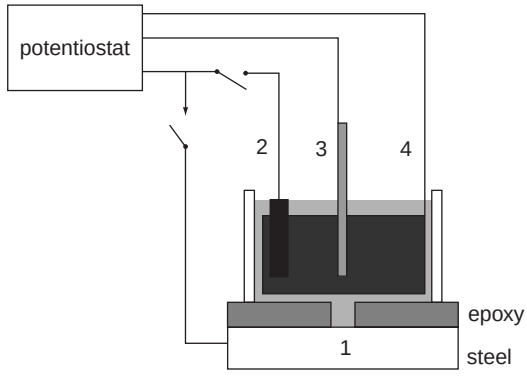

Figure 16.4 *Electrochemical corrosion cell used for testing the ennobling effect of a conducting polymer. The mild steel sample (1) is coated by a thin epoxy layer and is in contact with a 0.1 M $LiClO_4$ solution (aerated or deaerated) through a small hole. Polymethylthiophene (PMT) is deposited on a Pt electrode (2); a saturated calomel electrode (3) and a Pt counter-electrode (4) are used with either (1) or (2) as the working electrode. Electrodes (1) and (2) are galvanically connected and can be disconnected from the electrical circuit for specific measurements. (Reprinted with permission from Electrochimica Acta, Corrosion protection by ultrathin films of conducting polymers by U. Rammelt, P.T. Nguyen and W. Plieth, 48, 9, 1257–1262. Copyright (2003) Elsevier Ltd)*

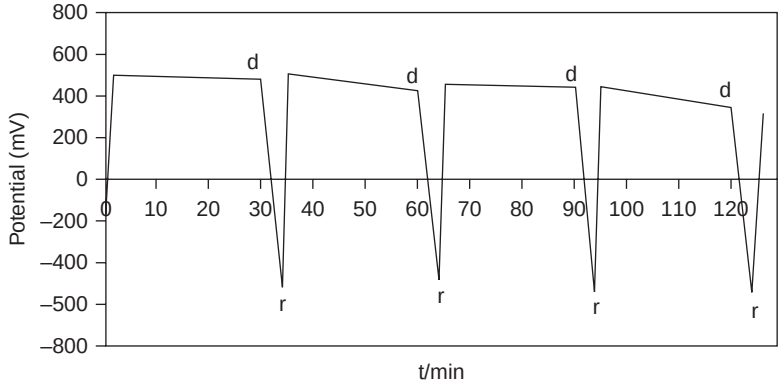

Figure 16.5 *Open-circuit potential (OCP) of the steel/epoxy-hole electrode vs. time in aerated 0.1 M $LiClO_4$ solution. r and d indicate the times at which the steel electrode is connected and disconnected, respectively, from the PMT/Pt electrode. (Reprinted with permission from Electrochimica Acta, Corrosion protection by ultrathin films of conducting polymers by U. Rammelt, P.T. Nguyen and W. Plieth, 48, 9, 1257–1262. Copyright (2003) Elsevier Ltd)*

passivation is found, i.e. no passivation areas are observed in the electrolytic medium used to perform this experiment, a result which also confirms that the conditions are inadequate for an efficient protection of steel with PMT. Nevertheless, from Tafel plots, the corrosion current was found to decrease by about two orders of magnitude (4.10^{-4} A cm^{-2} for bare steel and approximately 7.10^{-6} A cm^{-2} for the PMT-coated steel).

The situation is quite different in the case of PANI-coated steel (or stainless steel) in acidic medium (H_2SO_4). Experiments carried out by McDiarmid and Ahmad with steel and stainless steel (SS) samples coated with emeraldine base (EB) and immersed in H_2SO_4 are very significant [55]. Indeed, the open-circuit potential (OCP) vs. time curves differ drastically from those obtained with PMT: the potential of steel is set at very positive values corresponding to its passive state, and its decrease under OCP conditions is slow. Thus, with protonated EB-coated SS-410 the authors observed that in aerated 2 M H_2SO_4 solution the V_{oc} potential remained well above that of bare SS for about 50 days without potential breakdown. Similarly, a PANI SS-430 sample coated under the same conditions and immersed in a solution containing aggressive chloride ions (0.1 M H_2SO_4 + 0.1 M NaCl + 0.15 M Na_2SO_4) did not exhibit pitting corrosion for periods of more than 30 days. Furthermore, when a scratch was made through the coating, the V_{oc} fell for a short while but rose again, a fact which confirms that the PANI in its oxidized state (PANI/ES) had repassivated the exposed steel area, producing self-healing of the defect. At first sight, such different behaviors observed with PMT and PANI coatings are surprising. However, it must be recalled that PANI in its reduced form (PANI/leuco base) can be reoxidized by O_2 [35,65,66], but not PMT [64]. Very likely, PANI/ES, which is more conductive than PMT, can provide a higher current density capable of passivating the defect and passing over the Flade potential. This result could not be obtained with PMT prepared according to reference [64]. PMT was prepared by electrolysis in CH_2Cl_2 and then immersed in an aqueous chloride solution, whereas PANI was chemically coated on steel and then protonated in aqueous solution. In the first case, 480 mC were used to synthesize the PMT film in its oxidized state with an approximate thickness of 1 μm. Therefore, if a doping yield of around 0.2 is assumed, the available charge for oxidation of iron was about 100 mC. Moreover, as indicated in their paper, the resistance of the oxidized PMT film was only 50 Ω, while that of the hole was about 400 kΩ in an N_2-saturated solution and about 20 kΩ in an aerated solution. If a difference of potential of 0.5 V between PMT and iron is assumed, it may be deduced that the mean current for 1 s should be less than 25 μA. Consequently, the density on the iron pin-hole was less than 8 mA cm^{-2}, which is probably not enough to pass over the Flade potential (a value of 90 mA cm^{-2} was reported for steel-1018 in 2 M H_2SO_4 by Ahmad and McDiarmid [65]). It is worth noting that when the PANI is directly electrodeposited on the steel sample the interfacial resistance between the polymer and the metal is negligible and therefore the current density provided by the dedoping of the polymer is great enough to overcome the Flade potential and to passivate the metal. This could explain the good protection observed by several groups [56,57,58,59].

Polypyrrole (PPy) has also been widely investigated for the protection of metals. In contrast to PANI, the deposition of PPy on metals is generally carried out through electropolymerization of pyrrole in aqueous media. PPy is also easily oxidized by O_2 [56] and this property makes it behave like PANI and, therefore, the ennobling mechanism is expected to occur with iron and steel. Recently, Michalik and Rohwerder [51] clearly showed that, by using an electrochemical set-up similar to that of Rammelt *et al.* [64], PPy could protect small pin-holes from corrosion and was able to maintain the metal in the passive state for a few hours, but rapidly failed in a chloride-containing solution. The other parameter that should be considered is the size of the defect, which was also found to be critical for protection of the metal. In the presence of a large defect, the current density provided by the dedoping of PPy was assumed not to be high enough to passivate iron and,

therefore, the ennobling effect vanished. Furthermore, the O_2 reduction initially located at the PPy–solution interface, when PPy is in its oxidized state, shifts to the polymer–substrate interface after dedoping. Consequently, OH^- ions are produced at the polymer–metal interface and delamination occurs. They also note that in this latter case delamination is more rapid than with conventional coatings, a result which could be explained by the greater porosity of the PPy film in its reduced state.

Similar experiments using various electrolytes and, in particular, known passivating anions have also been reported. Such experiments are useful for rationalizing the so-called ennobling effects.

The ennobling effect of iron by ECPs was also studied by Nguyen *et al.* [57–58], in the case of single and composite conducting-polymer films electrodeposited from pyrrole or mixed pyrrole/1,5-diaminonaphthalene (Py-DAN) solutions in the presence of 2 M KNO_3. Film deposition (thickness fixed at around 2 μm) was obtained by cycling the potential between 0.24 V/SCE and various upper potentials 0.84, 0.94, and 1.14 V/SCE). It is worth noting that, in this procedure, the start potential (0.24 V/SCE) corresponds to the Flade potential, i.e. the beginning of the passivation range and, therefore, electropolymerization of Py occurs on the passivated iron. Thus, when the sample is immersed in a corroding solution, the oxidized polymer does not need a high current density to maintain the metal in its passivity range, since it is already passivated.

Interestingly, the OCP vs. time curves obtained when the samples were immersed in a sulfate solution (0.1 M K_2SO_4 at pH 4, less aggressive than the usual chloride solution) exhibited relaxation times of 1, 60, and about 3 hours with PPy films scanned up to 0.84, 0.94, and 1.14 V/SCE, respectively. Although no interpretation was given, it is probable that the time during which protection occurs is related to the stored charge in the polymer (greater at 0.94 V than at 0.84 V), and the fact that protection failed rapidly when the PPy was oxidized up to 1.14 V/SCE might be due to an overoxidation of the polymer. Its lower conductivity could mean that it can no longer provide the current density required to maintain the metal in the passivation range.

In the case of a composite film consisting of a poly-1,5-diaminonaphthalene (PDAN)/PPy bilayer they found that: (i) adhesion was dramatically improved (due to the fact that PDAN is deposited first) and (ii) the protection properties were considerably increased. The OCP vs. time curves exhibited a breakdown after around 50 days instead of hours as in the previous case. *In situ* Raman analysis of the outer PPy layer in the composite film showed an intensity enhancement of the band at 1610 cm^{-1} (characteristic of PPy in the doped state) with respect to the single PPy coating. This implies a larger amount of doped PPy than in the single PPy coating and, in our opinion, this could partly explain the protection improvement for a longer time. Moreover, since in each case the potential reached after breakdown was that corresponding to the iron depassivation state; this confirms that protection was due to an anodic ennobling mechanism.

In another paper [68], more details concerning the kinetics of the ennobling mechanism were given by the same group, through the use of an iron ring-disc electrode set-up. Doped PPy was electrodeposited on the ring (under the same conditions as previously) and the disc was bare iron. Immediately after immersion in a K_2SO_4 solution the disc potential was set to 0.15 V/NHE and, just after connection to the PPy-coated ring, it abruptly dropped to −0.3 V, as expected for bare iron in contact with a K_2SO_4 solution. A current peak was observed and, after that, for less than 2 min, the disc potential increased rapidly to 0.35 V and at the same

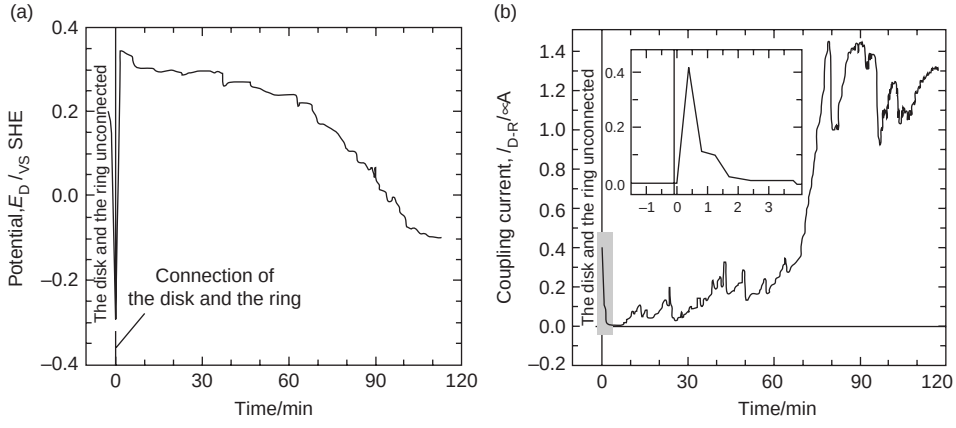

Figure 16.6 *Galvanic coupling between iron disc (0.25 mm diameter) and PPy-coated iron ring (5 mm outer diameter) immersed in 0.1 M K_2SO_4 solution (pH 4). The gap between the disc and the ring is 75 μm. (Reprinted with permission from Journal of Electroanalytical Chemistry, Mechanism for protection of iron corrosion by an intrinsically electronic conducting polymer by T.D. Nguyen, T.A. Nguyen, M.C. Pham et al., 572, 2, 225–234. Copyright (2004) Elsevier Ltd)*

time the current dropped from 0.4 μA (0.8 mA cm^{-2}) to 20 nA (40 μA cm^{-2}) (inset in Figure 16.6b). The initial polarization at 0.15 V was attributed to a partial passivation of iron during PPy deposition on the ring, and the coulombic charge passed during this transient current was about 32 mC cm^{-2}, in good agreement with the charge needed to passivate iron in a K_2SO_4 solution. Then, the current between the disc and the ring (i_{D-R}) increased slowly for about 1 hour to 0.3 μA and was marked by small fluctuations, associated with local pitting and self-healing, while the disc potential (E_D) slowly decreased. After that, the i_{D-R} increased more rapidly and the fluctuations were more pronounced, while E_D continued to decrease to negative potentials characteristic of the active range of iron. They also showed that, once the iron was in its active state, its passivation could not be achieved again, a fact they attributed to the presence of a resistive layer between the metal and the polymer, which impeded the delivery of a current density high enough for passivation.

A significant improvement of the ennobling effect was also observed when the PPy film on the ring was replaced by a composite film (PDAN/PANI) [59]. However, as previously, the ohmic drop between the bare metal and the coated area resulting from the slow corrosion impeded the repassivation of the exposed metal, and resulted in the disappearance of the ennobling effect.

With other metals, in particular with aluminium and its alloys, the ennobling mechanism is not clear-cut. Recent work by Yan *et al.* [60] carried out with PPy doped with electroinactive 1,3-benzene-disulfonic acid and electroactive sodium 4,5-dihydroxy-1,3-benzene-disulfonate and using a two-compartment cell similar to that of Rammelt *et al.* [64] seems to prove that the anodic protection model cannot be applied to the aluminum surface. Although the recharging of PPy by O_2 was demonstrated, they found that a small area of exposed aluminium (AA 2024-T3) simulating a defect in a coating and immersed in dilute Harrison's solution (0.35 wt% $(NH_4)_2SO_4$ + 0.05 wt% NaCl in water) did not

exhibit any passivity when galvanically coupled to oxidized PPy (electrodeposited on ITO). From the galvanodynamic polarization curves of aluminium obtained in the previous solution under air, O_2 or argon, and from the current density (1 mA cm^{-2}) observed when aluminium is coupled to the PPy-coated electrode, it was deduced that aluminium was set by the PPy in the active potential region and, therefore, could not be passivated under these conditions. Although no explanation was given, a possible cause of failing could be similar to the one previously given in the case of the PMT-coated iron electrode experiment, i.e. a too high internal resistance of the circuit.

However, other experiments performed by Seegmiller *et al.* [61] tend to prove that AA2024-T3 could be protected by coating with PANI. Indeed, with a polymethylmethacrylate/PANI blend (PMMA/PANI) doped with camphorsulfonic acid (CSA) and applied to this alloy, they showed through various techniques and, in particular, with scanning electrochemical microscopy (SECM) [62,63] that passivation in an artificial scratch was achieved, but not with PMMA alone.

In conclusion, the ennobling effect would be expected to occur with metals characterized by large passive potential ranges (iron, steel, and particularly stainless steel), and coated with conducting polymers which can be easily reoxidized by air (PANI, PPy). Although protection has been shown with polythiophene compounds [25,26] PMT does not fulfil the requirements for metal ennobling because it cannot be oxidized by air. Poly-3,4-dioxyethylenethiophene (PEDOT), which is more easily oxidizable and whose doped state is stable in air has recently been cited as a good iron corrosion inhibitor [64], could work in part according to the ennobling concept. It also appears that, to maintain the ennobling effect, the current delivered by the polymer must be high enough to pass over the Flade potential and, therefore, any chemical reaction leading to a resistive layer between the metal and the coating will be detrimental [69]. Moreover, it is worth noting that the anions in contact with the scratch will partially determine the Flade potential of the metal, the passivation area potential width and the current density needed to reach this area. It is thus obvious that a coating will not be able to protect the underlying metal in any conceivable electrolytic environment except if new strategies for controlling the electrochemical environment around the metal in the scratch are developed, as will be seen with self-healing.

Finally, much alike the displacement of the electrochemical interface, it can be stated that if small enough scratches occur during the lifetime of the coating in a favorable electrochemical environment, a steady state could be obtained in which the conductive polymer will permanently protect the underlying metal against corrosion. Small scratches will be repaired when the electrolytic medium around the defect provides a wide passivation range and if a small current density is required to reach it. A steady-state situation can be reached if the conducting polymer can be reoxidized by O_2. Unfortunately, this ideal and permanent steady-state picture described above is not easy to obtain and can be disrupted by several phenomena, such as delamination starting from the scratch (increase of the scratch surface) upon conductive-polymer reduction or slow reoxidation of the ECP.

16.2.3 Self-healing Effect with Doping Anions as Corrosion Inhibitors

It was shown previously that, when there is a small scratch on a metal coated by a conducting polymer, there is galvanic coupling between the metal and the polymer. This

galvanic coupling involves, on the one hand, the reduction of the polymer associated with release of the doping anions and, on the other hand, the oxidation of the metal. Furthermore, the reduction of O_2 either at the surface of the polymer, with concomitant reoxidation of the polymer, or at the surface of the scratch, also involves the formation of OH^- ions. Two effects can be predicted depending on the metal: either the potential of the metal will initiate the formation of metal oxides in the scratch (metal ennobling in the case of iron, aluminium, and copper), or the doping anions can act as anodic or cathodic inhibitors [65]. The idea that an inhibitor can be released when a small defect arises in the coating and that it can locally react with the bare metal and self-heal the defect is particularly attractive. This goal is easily achieved with a conducting polymer doped by anionic inhibitors. Indeed, the doping anions are not leached and are only released when corrosion starts, a fact which explains why conducting polymers were considered to be 'smart coatings' by Kending *et al.* [66] (Figure 16.7) after several groups proved that such coatings provided improved protection against corrosion [67–68].

Phosphonic acid derivatives (in particular, amino-tris-methylenephosphonic acid), well known for their anticorrosion properties, were used as doping anions in PANI formulations and were shown to out-perform other PANI formulations with conventional doping anions (i.e. *p*-toluene sulfonic acids and derivatives) [69].

Obviously, the efficiency of self-healing will depend on the mobility of the anion and on its aptitude to be released by the polymer. This latter property, related to the general process of doping-dedoping of the conducting polymers, was described by Chang and Miller [70] for application to biological drug release and more recently by Weidlich *et al.* [71], who studied the influence of size, mobility, and valence of ions on their release from or incorporation into conducting polymers.

Recently, with a view to a better understanding of the protection of iron by conducting polymers, the kinetics of the cathodic delamination of PPy doped with molybdate (MoO_4^{2-}) and phosphopolymolybdates ($PMo_{12}O_{40}^{3-}$) were considered by Paliwoda-Porebska *et al.* [72,73]. From a suspension of doped PPy nanoparticles (diameters ranging between 80 and

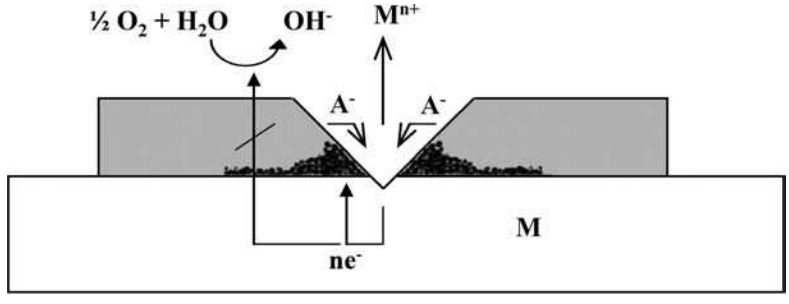

Figure 16.7 *Self-healing mechanism for a metal (M) coated by a conducting polymer (P^{n+}) doped with a corrosion inhibitor (A^-). Galvanic coupling between the polymer (P^{n+}) and the metal (scratch on the coating) releases A^-, which either interacts with M^{n+} and leads to an insoluble salt with inhibiting properties or is adsorbed onto M and provides anodic inhibition. (Reprinted with permission from Progress in Organic Coatings, 'Smart' corrosion inhibiting coatings by M. Kendig, M. Hon and L. Warren, 47, 3–4, 183–189. Copyright (2003) Elsevier Ltd)*

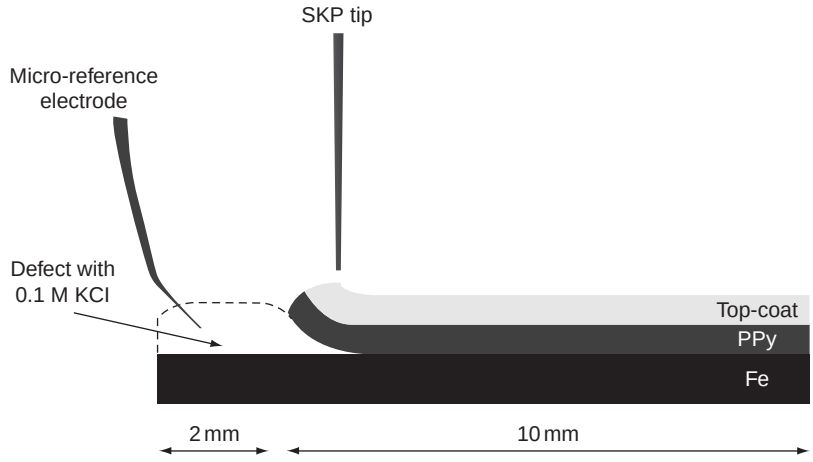

Figure 16.8 *Representation of the coated iron sample (PPy + top-coat) and its defect in contact with KCl solution. Delamination is followed by SKP measurements. (Reprinted with permission from Corrosion Science, On the development of polypyrrole coatings with self-healing properties for iron corrosion protection by G. Paliwoda-Porebska, M. Stratmann, M. Rohwerder et al., 47, 12, 3216–3233. Copyright (2005) Elsevier Ltd)*

130 nm) mixed in a nonconducting polymer matrix, a composite PPy film, whose thickness was close to that of the particles, was deposited on iron. The films were cured at 100 °C for 5 min., then top-coated by a polyacrylic resin, in order to mimic a situation close to that of an organic coating submitted to an aggressive environment. A defect was made and placed in contact with a drop of 0.1 M KCl solution; the delamination experiments were performed with the scanning Kelvin probe technique (SKP) (Figure 16.8).

Surprisingly, in contrast to PPy doped with $PMo_{12}O_{40}^{3-}$ (PPy-PMo), for which significant self-healing occurred, there was no passivation of steel in the defect (potential remained at -0.5V) and no decrease in the delamination rate in the case of the PPy film doped with MoO_4^{2-} (PPy-Mo). In the first case the potential in the defect increased from -0.5 V to -0.2 V (latter value characteristic of iron in the presence of molybdate) while in the second case it remained at -0.5 V (potential in the presence of chloride). Compared to a PPy film doped with a noninhibitor doping anion ($S_2O_8^{2-}$), for which the potential in the defect remained at about -0.5 V, the authors found that the delamination rate with PPy-Mo was the same as with PPy-$S_2O_8^{2-}$, while it was significantly lower with PPy-PMo.

These results are unexpected, since it was previously found that molybdate salts were released when submitted to a usual electrochemical reduction and, moreover, their inhibitor properties towards iron were confirmed. XPS analysis of the defect after delamination showed that, in contrast to PPy-PMo, no molybdate could be detected with the PPy-Mo film, confirming that under these conditions no molybdate is released with this doping salt and thus self-healing was absent.

The fact that $PMo_{12}O_{40}^{3-}$ was released and not MoO_4^{2-} is rather strange, and the interpretation given by the authors is not fully convincing. Indeed, they assumed that under aerated conditions a large amount of OH^- was released and would produce a marked

increase in the pH in the vicinity of the defect. Overoxidation of the PPy would result and cause a structural change responsible for the trapping of MoO_4^{2-} in the PPy-Mo film. On the other hand, in the case of PPy-PMo, the $PMo_{12}O_{40}^{3-}$ salt is decomposed by OH^- into MoO_4^{2-} and PO_4^{3-}, and a kind of buffering effect occurs which prevents the overoxidation of PPy and, therefore, does not impede the release of the two anions (PO_4^{3-} and MoO_4^{2-}) towards the defect.

Interestingly, at the same time and independently of the previous work, corrosion protection of PPy films (1–1.2 μm thick) electrodeposited on iron and doped with MoO_4^{2-} was also studied by Rammelt *et al.* [74]. They demonstrated the release of MoO_4^{2-} during the reduction of PPy and also the passivating effect of this anion in aerated aqueous 0.1 M NaCl solution.

The OCP vs. time curve of a coated PPy-Mo steel electrode clearly shows the passivation of iron, whose potential remains at about 0.35 V/SCE (potential corresponding to the redox process in the PPy film) for about eight hours. Then, the OCP curve reaches a second plateau at −0.2 V/SCE for 7–8 hours, which corresponds to the potential of mild steel immersed in sodium molybdate solution. When a small defect is made, the self-healing properties of this anion are also established, in contrast to a doping anion without inhibitor properties, such as PF_6^-. Indeed, the OCP remains at about −0.1 V (potential corresponding to the previous second plateau) for several hours. However, when the PPy is doped with PF_6^-, after only a few minutes the OCP falls to −0.5 V (potential corresponding to the active range of iron dissolution) demonstrating in this case the lack of protection by this anion, for probably the same reasons as those which we have indicated in the case of a PMT-coated mild-steel electrode [64].

These latter experiments illustrate all the complexity of the process and justify a thorough examination of the electrochemical conditions before any final decision is reached. In particular, it is worth noting that in this latter case the whole polymer film is immersed in the KCl solution, while in the previous work the liquid drop was in lateral contact with the metal and the polymer. Indeed, this arrangement could be the cause of this discrepancy between the two studies. In the previous experiment the MoO_4^- doped film is in contact with the electrolyte only through its section and not through all its volume, and this could explain that the anion release remains very small and insufficient to produce self-healing. The question remains open, and the very recent work of Rohwerder and Michalik [75] casts a new interesting light on the self-healing effect. Their work, based on delamination and SKP experiments, used a set-up similar to that described in [64], but PPy (also covered by a top-coat) was deposited on gold instead of iron.

The PPy was doped with *p*-toluene sulfonate (tosylate) or chloride and its delamination was tested with two chloride salt solutions injected in the defect (potassium chloride or tetrabutylammonium chloride). The aim of this work was to correlate the delamination rate with reduction of the polymer, corresponding either to the release of the doping anions or to the incorporation of cations. The measurements were carried out in air or in an oxygen-free atmosphere with the gold electrode polarized at a potential which simulates iron corrosion (−0.66 V vs. Ag/AgCl) (Figure 16.9).

The delamination curves differ markedly depending on the nature of the cation present in the electrolyte. Thus, under nitrogen atmosphere, where only the reduction of the polymer can occur, the delamination rate is very low with tetrabutylammonium in the defect, but it increases markedly when tetrabutylammonium is replaced by a smaller cation like

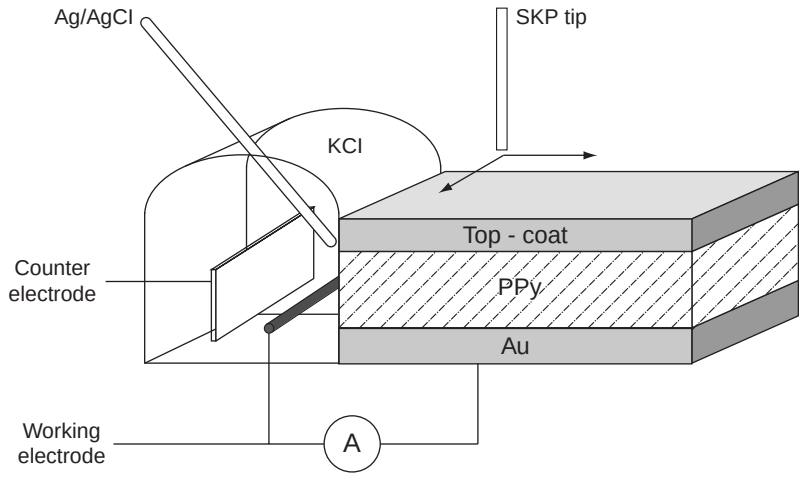

Figure 16.9 *Electrochemical set-up used to follow the delamination of electrochemically deposited PPy on a thin gold layer evaporated on glass. The gold edge is about 200 nm thick and constitutes the working electrode in contact with the electrolyte drop. The SKP chamber is in a humid atmosphere (air or N_2). (Reprinted with permission from Electrochimica Acta, Conducting polymers for corrosion protection: What makes the difference between failure and success? By M. Rohwerder and A. Michalik, 53, 3, 1300–1313. Copyright (2007) Elsevier Ltd)*

potassium. From these results they deduced that tosylate is slowly released and therefore involves a slow reduction of the polymer which cannot be accelerated when the chloride solution contains a bulky cation like tetrabutylammonium. Conversely, when tetrabutylammonium is replaced by potassium, whose mobility in the polymer is greater, reduction of the polymer increases rapidly, leading again to delamination. This seems also to prove that the de-adhesion of PPy occurs when its reduction is in progress, independently of any corrosion process. The reduction currents are roughly proportional to the film thickness, i.e. to the whole available amount of anion around the scratch, in the case of atmospheric corrosion, or in all the film when it is totally immersed. In presence of oxygen, the delamination moving front is very different from the previous one. Surprisingly, the delamination rate remains approximately the same for thick films (1.1 μm thickness) as under nitrogen, but it strongly decreases with thinner films (0.4 to 0.1 μm). Simultaneously, the potential in the delaminated area moves to more positive values (between −0.3 and −0.2 V instead of −0.45 V), and the galvanic current jumps significantly. The shift of the potential was attributed to a higher ohmic drop, and the galvanic current increase to simultaneous oxygen reduction at the gold electrode. They suggested that the slow delamination in the presence of oxygen for thinner films was due to ion transport along the delaminated interface, in contrast to thick films where it occurs within the polymer.

From their findings they concluded that for tosylate-doped thick PPy films, transport of small cations is very fast and is responsible for PPy reduction and delamination. This cationic transport in the film follows a percolation mechanism and, according to their view, good protection requires optimization of the percolation length, i.e. not too high a polymer conductivity, which implies an extended percolation system, but a percolation

network which only maintains a satisfactory electrochemical activity. However, the system used by the authors is far from a real one. The delamination observed on gold happens when the PPy is reduced, but this is not necessarily the case with other metals. Indeed, as will be described below, various solutions have been proposed to modify the metal surface in order to improve the adhesion of conducting polymers and to make delamination negligible, even when the polymer is in its reduced state.

Nevertheless, their conclusions about percolation mechanisms deserve to be considered, since this could be one of the factors which contribute to improving the protection properties of composite coatings incorporating conducting polymers, and for which extremely good results have been recently reported. It has to be noted that such a conclusion is in contradiction with those of Sections 16.2.2 and 16.2.3, in which a high conductivity of the polymer was required to provide the high discharge current density needed for the protection mechanism.

The self-healing effect, described in this section, is in our opinion an extension of the ennobling mechanism in which the release of anions, concomitant to polymer reduction, is used in order to control to some extent the electrolytic medium around the scratch and thus facilitate its passivation. Studies in this direction are still scarce and further work is needed to explore this concept. Some of the work described in Section 16.2.2 probably concerns self-healing properties, but this concept was not highlighted by the authors. It should be reanalysed in the light of recent work more focused on self-healing effects.

16.2.4 Barrier Effect of the Polymer

For a paint coating, the barrier effect constitutes one of the main features needed for good protection against corrosion. A strong barrier effect will indeed slow down O_2 and water diffusion through the coating and, consequently, considerably reduce corrosion at the interface [41,54]. However, diffusion through the coating of aggressive anions such as chloride is also a cause of corrosion, which also must be accounted for in the barrier effect. Independently of whether the polymer is or is not conducting, the diffusion rates of O_2 and H_2O depend mainly on the porosity of the polymer. Conversely, Cl^- diffusion occurs through ion exchange in the polymer and could be critical in the case of doped conducting polymers. Therefore, depending on the nature of the doping ion, this could be an important cause of corrosion [76]. In the following, we show how diffusion effects may be reduced for improving the protection.

16.2.4.1 Barrier Effect Related To Porosity

It is well known that the less porous the polymer, the better is the barrier effect, and the better the metal is protected against corrosion [41,42]. Unfortunately, native conducting polymers prepared by electropolymerization of a monomer in aqueous media and deposited directly onto the metal are very porous [77]. Moreover, polymer synthesis in aqueous media leads to native films containing large amounts of water, which are detrimental [41,42]. In general, the films are dried in air, but, even after that, the water content remains high. Clearly, submitting the material to thermal treatment, in order to remove all the water inside the polymer and make it more compact, should improve the barrier effect.

Another effect, which has often been disregarded, concerns the way the electropolymerization of the monomer is carried out, a point which could also explain the differing results reported for the same material, and which is also related to the porosity. In the following, these two points will be illustrated through two electropolymerization examples: pyrrole on zinc in the presence of salicylate salts, and pyrrole on iron in the presence of oxalic acid.

Decrease in Film Porosity Through Heat Treatment

This was observed with PPy films electrodeposited on zinc from an aqueous pyrrole solution in the presence of a mixture of sodium diisopropylsalicylate (DISac) and salicylate (Sac) [78]. Indeed, we found that the OCP vs. time curve of a native PPy film broke down immediately (shift of the potential after 10 min. from about 0 to −1 V) when the electrode was immersed in 3.5% chloride solution. A small improvement was observed when the same film was treated at 180 °C under N_2 for one hour before being immersed in the same chloride solution (breakdown in the OCP curve after half an hour). In fact, the barrier effect remained poor. Surprisingly, we found that it was dramatically improved when the thermal treatment was carried out in air. The initial OCP was at 0.2 V and remained around 0 V before dropping to −1 V (potential of zinc in salicylate medium) after more than 40 hours. Interestingly, the same treatment of a PPy film, obtained in the presence of Sac alone, gave the same effect, but to a lesser extent, with an initial OCP at −0.4 V and a breakdown of the OCP after only about 12 hours (Figure 16.10).

In both cases, this improvement of the barrier effect was attributed to high cross-linking of the PPy chains by O_2, similar to the cross-linking reactions occurring in air in the case of paints with a high oil content [38,39]. Self-healing was also observed, revealed by the small breakdowns in the OCP curve followed by a slow rise of the potential to its initial value. Besides, it is worth noting that the difference observed between the PPy films synthesized from salicylate mixture and those from the salicylate alone are correlated with an increase in the hydrophobicity of the film (PPy film synthesized in the presence of NaSac alone has a contact angle of 100° which shifts to 125° with DISacH). The hydrophobic character of a coating is in general a favorable property for protection [41,42], and thus could explain the improved protection observed with DiSacH.

In conclusion, native films electrosynthesized in aqueous media are strongly hydrated, and are highly porous. Dehydration is essential to improve the barrier effect.

Decrease in Film Porosity Through Different Modes of Electrodeposition

In recent work related to the electrodeposition of PPy from an aqueous pyrrole-oxalic acid solution, the influence of the iron surface pretreatment on the corrosion properties was reported by Van Shaftinghen, Deslouis *et al.* [79]. The performances of PPy-coated iron samples, obtained through three different electropolymerization techniques were tested: (i) electropolymerization at constant current (1 mA cm^{-2}) (denoted galstat), (ii) potentiostatic electropolymerization at 1V vs. Ag/AgCl in oxalic acid for 600 s followed by addition of pyrrole into the solution (denoted one-step), (iii) potentiostatic polarization in a two-step process identical to the previous one, except that a preliminary polarization at 0 V vs. Ag/AgCl for 600 s was carried out in the electrolyte alone (denoted two-step) (Figure 16.11). From the anodic curves of iron in oxalic acid alone, a first zone of potential ranging

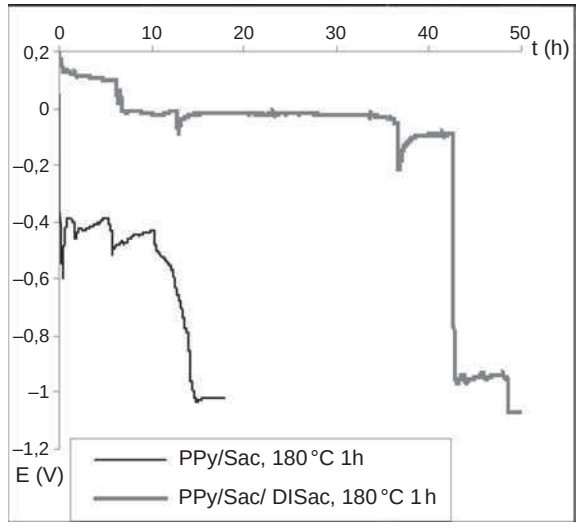

Figure 16.10 *OCP curves of coated PPy zinc electrodes cured in air for 1 h at 180 °C and immersed in 3.5% NaCl solution. PPy films (≈2 μm thick) were synthesized in 2 M NaSac + 0.5 M Py at pH 5 and 1.9 M NaSac + 0.1 M DISacH + 0.5 M Py at pH 5.4. (Reprinted with permission from Chemistry of Materials, Ultrafast electrosynthesis of high hydrophobic polypyrrole coatings on a Zinc electrode: Applications to the protection against Corrosion by E. Hermelin, J. Petitjean, P.C. Lacaze et al., 20, 13, 4447–4456. Copyright (2008) Elsevier Ltd)*

between –0.25 and +0.25 V with a negligible current density was identified as corresponding to the iron oxalate formation, while a second zone, also of low current density, between 0.75 and 1.25 V, was attributed to the formation of an oxide. After addition of pyrrole, and without any apparent modification of the first part of the polarization curve, it appears that pyrrole electropolymerizes in the second zone of potential, confirming that PPy deposits on an iron oxide layer (Figure 16.12). Interestingly, very different protection effects were reported for the three procedures. From OCP curves obtained in 3.5% NaCl solution, the best results were obtained in the case of the 'one-step' procedure, with a protection time of about 11 hours, whereas with the 'two-step' and the 'galstat' procedures the protection times dropped to about four hours and 20 min, respectively.

These differences are very significant and for the most part seem to be related to the structure of the interlayer formed between the metal and the PPy during the electrochemical process. From SEM (scanning electron microscopy) pictures obtained during the pretreatment of iron, it appears that in the case of the 'galstat' process (observation at a time corresponding to the passivation of iron, Figure 16.11a) the surface consists of small oxalate crystals, whereas, in the case of the 'one-step' process the surface was amorphous, more compact and characteristic of iron oxides [80]. In the case of the 'two-step' process the passivating layer exhibited an intermediate structure corresponding to a mixture of amorphous oxides and crystalline oxalate. Qualitatively, and although this was not claimed by the authors, it can be assumed that the porosity of these interlayers increases in the order: 'one-step', 'two-step' and 'galstat' procedures, and that barrier effects and,

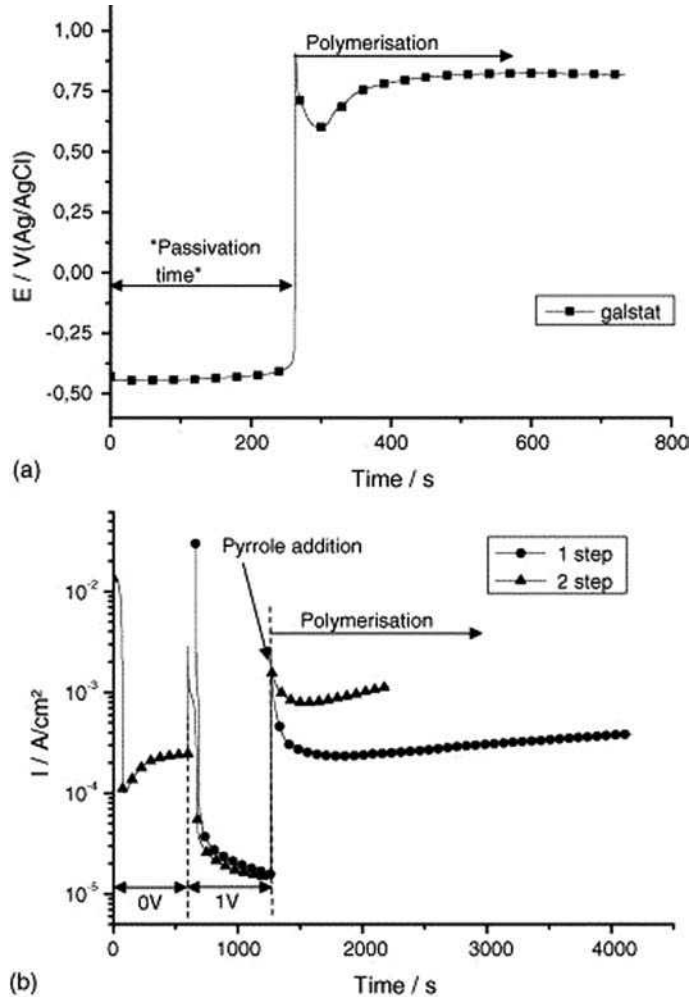

Figure 16.11 *Three electropolymerization procedures used for the deposition of PPy films on iron (0.9 C cm^{-2} corresponding to about 1.5–2 μm thickness): (a) electropolymerization at constant current (1mA cm^{-2}) of a 0.05 M oxalic acid + 0.05 M pyrrole solution (galstat); (b) one-step and two-step procedures (see text for explanation). (Reprinted with permission from Electrochimica Acta, Influence of the surface pre-treatment prior to the film synthesis on the corrosion protection of iron with polypyrrole films by T. Van Schaftinghen, C. Deslouis, A. Hubin and H. Terryn, 51, 8–9, 1695–1703. Copyright (2006) Elsevier Ltd)*

therefore, protection performance decrease in the same order. Electrochemical impedance spectroscopy (EIS) experiments seem to confirm this point of view; indeed, the 'one-step' procedure led to the highest impedance of the passive layer, and this could be related to a better barrier effect. The poorest protection, provided by the 'galstat' procedure, is probably due to a poor compactness of the interlayer, but also to a greater porosity of the PPy layer. These structural changes in the porosity of the material constitute an

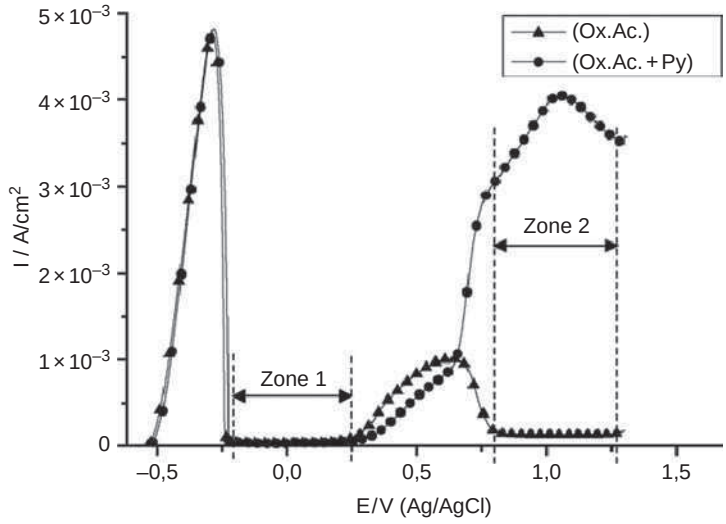

Figure 16.12 *Anodic polarization curves of iron in 0.05 M oxalic acid (Ox.Ac) and in 0.05 M oxalic acid + 0.05 M pyrrole (Ox.Ac.+Py). Polarization rate 5 mV sec^{-1}. (Reprinted with permission from Electrochimica Acta, Influence of the surface pre-treatment prior to the film synthesis on the corrosion protection of iron with polypyrrole films by T. Van Schaftinghen, C. Deslouis, A. Hubin and H. Terryn, 51, 8–9, 1695–1703. Copyright (2006) Elsevier Ltd)*

additional proof that a strong barrier effect is needed for protection, independently of all other effects, in particular assuming that the adhesion of PPy remains about the same when the morphology of the passive interlayer is changing.

16.2.4.2 Ionic Cross-Exchange

The ion-exchange properties of doped conducting polymers have been widely investigated in the case of PANI. These properties are highly dependent on pH, and involve a protonic equilibrium between EB and ES forms. The ion-exchange mechanism is different with EB and ES. EB can sequester both proton and anionic species, forming the protonated PANI-emeraldine salt, while ES undergoes simple anion exchange like a polyelectrolyte. These ion-exchange properties have been used for practical applications such as the recovery of Cr(VI) in aqueous solutions [81] or for ion exchange of various anions [82]. In the case of PPy and polythiophene derivatives, protonation is not as efficient as in the case of PANI and, therefore, the ion-exchange mechanisms are only related to doping and dedoping processes.

Hien *et al.* [88] showed that PPy electrodeposited on iron in the presence of tetraoxalate provided anodic protection of the metal (ennobling effect) which was effective as long as the aggressive anions (Cl^-) did not reach the oxidized metal. This effect remained poor when the polymer was doped only with tetraoxalate, but could be considerably improved when large anions such as polystyrene sodium sulfonate (PSS) or sodium dodecylsulfonate (SDS) were included in the polymer as dopants, and were trapped in the polymer matrix. However, since direct electropolymerization in the presence of these anions led to PPy

films with poor adherence, a two-step process was used. A first electropolymerization of pyrrole was carried out in the presence of sodium tetraoxalate in order to get a good adherence of PPy to iron, and also to provide iron passivity and the self-healing effect. Then, on this modified electrode, a second PPy layer was electrodeposited from a pyrrole solution containing either PSS or SDS. The whole bilayer was found to be extremely adherent to iron, a property which constitutes the first requirement for good protection against corrosion. Comparison of OCP curves obtained with such coated iron electrodes immersed in 3.5% NaCl clearly showed a marked improvement of the protection when PPy was doped with SDS. Indeed, the time at which the potential shifted from the passive to active iron state was about 500 hours with films doped by SDS, whereas with PSS and tetraoxalate, the same event occurred at times of about 50 and 40 hours, respectively (Figure 16.13).

The time of 500 hours was obtained for an optimized concentration of 0.025 M SDS corresponding to the formation of spherical micelles in the solution. A higher concentration (0.04 M) was detrimental because of a change in the organization of pyrrole in the solution. However, the surface energy of the coating, which was not taken in consideration in this paper, might also be significant for the barrier effect [41,42], and it is probable that the replacement of PSS by DS would lower the surface energy of the coating. Such an effect was observed in the case of PPy electrodeposition on zinc when salicylate was replaced by diisopropylsalicylate, for which a more hydrophobic surface was obtained and also an improved barrier effect [90].

In conclusion, independently of the usual effects encountered with organic coatings (hydration, cross-linking and compactness, hydrophobicity), specific effects due to the presence of doping anions must be taken in consideration. This mainly concerns ion

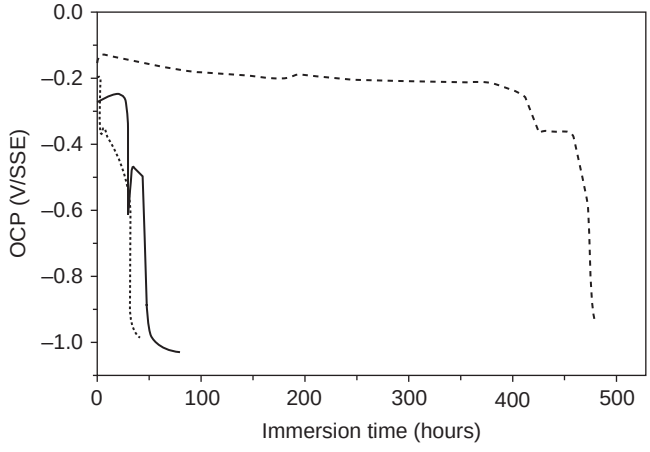

Figure 16.13 *OPC vs. time curves for oxalate-doped (. . .), PSS–Na-doped (—) and SDS–Na-doped (. . .) PPy films immersed in 3.5% NaCl solution. The same amount of charge was used for the synthesis of films (2 C cm^{-2}, i.e. 3 μm thick); the potential is referred to a saturated sulfate reference electrode (SSE). (Reprinted with permission from Electrochimica Acta, Role of doping ions in the corrosion protection of iron by polypyrrole films by N.T.L. Hien, B. Garcia, A. Pailleret and C. Deslouis, 50, 7–8, 1747–1755. Copyright (2005) Elsevier Ltd)*

exchange between the doping anion and the ions present in the environment, in particular the very aggressive chloride anions, whose diffusion into the coating can be slowed down if bulky doping anions are inserted in the conducting polymer. A thin passivating layer, generally produced by the electrodeposition process, will also contribute to increasing the barrier effect, and therefore improve the protection properties.

16.3 Conducting-Polymer Coating Techniques for Usual Oxidizable Metals: Performances of Conducting-Polymer-Based Micron-Thick Films for Protection against Corrosion

Recently, many new investigations have been developed for the replacement of inorganic inhibitors currently used for the protection of active metals [83–84]. Efficient systems including conducting polymers have been proposed and the improvements observed compared to experiments of the eighties are extremely promising; the protection properties can already be considered as competitive with the best usual systems, in particular with prohibited, but highly performing pigmented Cr^{VI}-based coatings [39]. Many means of exploiting the specific properties of conducting polymers to achieve an organic coating have been described. They have been included as primers directly deposited onto the metal as a film (by an electrochemical or chemical process) followed by application of a top coat. They were also used in blends with other nonconducting polymers or as an additive to modify the protection properties of conventional coatings. Moreover, in contrast to the first studies, which were principally devoted to PANI, recently a new trend has arisen with many studies devoted to PPy and PT derivatives, for which very promising results have been obtained. In the following we shall describe the most relevant results obtained by means of the two techniques.

16.3.1 Coatings Consisting of a Conducting Primer Deposited by Electropolymerization

The technique offers many advantages compared to the chemical-based formulation process. Undoubtedly, the possibility of obtaining a polymer film of controlled thickness in an aqueous medium by the simple electrochemical oxidation of a monomer is of great practical interest. Indeed, the process may be easily automated and thus its transfer to various industrial coating applications can be envisaged. Another advantage of the technique is that it provides an excellent electrical contact between the metal and the polymer, the first requirement for good redox behavior of the conducting polymer and ennobling and self-healing. However, as has been previously indicated, the electrodeposition of a conducting-polymer film on an active metal is not straightforward and requires that the metal be prepassivated in order to allow oxidation of the monomer without the metal being dissolved. This point is indeed crucial, which explains why so much effort has been expended in finding in each case the best metal-monomer system capable of overcoming this difficulty, which, in fact, could be considered as an advantage over casting from ECP

formulations (in contrast to the latter technique, if partial delamination occurs, the metal surface is already passivated when it comes in contact with air or with an electrolytic medium and, therefore, self-healing is facilitated).

Finally, electrodeposition can be achieved either through a two-step process (pre-treatment of the electrode, then electropolymerization) or through a single electropolymerization step of the monomer in presence of a suitable electrolyte. The first way, particularly used in the past, has now been replaced by the direct one-step electropolymerization technique, which is preferred for practical and cost considerations.

The adherence of the ECP to the metal, in particular when dedoping has occurred, is also extremely important, and critical for good protection, but, unfortunately, is not always specified. A thin passive interlayer firmly anchored to the metal and to the polymer, generally resulting from a precipitation reaction between the metal ion and the doping anion, may improve the adhesion of the material. Of course, this implies a suitable choice of the electrolyte, which will depend both on the monomer and on the metal. Thus, in the following, a distinction will be made between ferrous and nonferrous metals, but also between the most usual conducting polymers (PPy, PANI, PT, and derivatives).

16.3.1.1 Ferrous Metals

PPy Coatings

Undoubtedly, electrodeposition of conducting polymers on iron is the process most studied. The first PPy coating of iron in aqueous media was carried out by Schirmeisen and Beck [85] in the presence of nitrate salts, then, by Lacaze *et al.* [12,13] who improved the process and achieved good protection after the iron surface had been pretreated by dilute nitric acid in order to improve the adhesion [86,87]. Just as in the nitrate process, this procedure provided a passivation of iron, but also involved an increase of the roughness of the surface resulting from a slight attack on the surface by the acid, the effect of which was to improve the mechanical adherence [88].

After that, the use of oxalate salts was adopted, and in spite of a slight dissolution of the metal during the electropolymerization, very adherent (11.5 MPa adherence) and homogeneous films were obtained by Beck and Michaelis [14,15]. Some time later, the study was taken up again by Su and Iroh who studied the effects of various electrochemical process parameters on the synthesis and the properties of PPy electrodeposited on iron [89–90]. They confirmed that in acidic medium the pyrrole electrochemical polymerization takes place on the passivated electrode coated with crystalline iron(II) oxalate, and that PPy is deposited after the desorption of oxalate. As mentioned previously, the work of Shaftinghen, Deslouis *et al.* [91] showed that the protection properties of the material were dependent on the pyrrole electropolymerization conditions.

Other electrolytes have been tested. Saccharin sodium hydrate was recently proposed by Bazzaoui *et al.* [91], as well as saccharin added to oxalic acid as supporting electrolyte [92]. In this latter case an improvement with respect to the oxalic acid electrolyte was attributed to a reinforcement of the barrier effect of the passive layer. Less usual ways have been explored with ionic liquids as media for electropolymerization. Formation of highly conducting PPy on iron in 1-butyl-3-methylimidazolium hexafluorophosphate was reported [93]; however, it does not seem promising because such solvents are expensive and also because adhesion to the metal is poor.

PANI Coatings

Since the pioneering work of Wessling, who was the first to propose a commercial product based on PANI formulations for the protection of iron (Ormecon International, Zipperling Kessler) [94], the electrochemical technique has also been used for the deposition of PANI films on iron. After the work of DeBerry, several electrolytes were systematically tested. Sazou and Georgolios [95] found oxalic acid to be the most suitable, but the performance was poor and, without special pretreatment of the surface, the films were very porous and did not resist for long an aggressive chloride solution. An alternative was found with the prior deposition of a thin acid-resistant conducting-polymer film such as PPy [46,96], or by electropolymerizing mixtures of monomers such as 1,5-diaminonaphthalene (DAN) and aniline [70], and pyrrole and aniline [47–50], for which it appeared that bilayer films were formed with, in general, PANI being the outer layer of the film. However, in spite of these promising results, it is worth noting that PANI coating from formulations remains more popular than the electrochemical technique.

Polythiophene and Derivatives

In contrast to other polymers (PPy and PANI), thiophene cannot be electropolymerized in pure aqueous media, on account of its insolubility and also because the cation-radical is extremely reactive towards nucleophilic species (i.e. water). Moreover, its oxidation potential is the highest of the common heterocycles (≈1.8 V/SCE in $LiClO_4$–acetonitrile) which means that electropolymerization on active metals has been carried out with bis-thiophene, whose oxidation potential is much lower (≈0.7 V), rather than with thiophene. This explains why polythiophene (PT) was first electrodeposited on iron using bis-thiophene in mixed aqueous–organic media [97], and with thiophene in organic media [98,99]. Later, in order to get rid of organic solvents, Bazzaoui, Aeiyach, and Lacaze [100] developed a new method for the electrosynthesis of PT on platinum and iron, which was based on the use of a neutral micellar solution in water. By using SDS as the surfactant mixed with a small amount of butanol in aqueous $LiClO_4$ solution, bis-thiophene was oxidized on iron at low potential (0.7 V) and PT could be easily electrodeposited at constant current. Protection properties were later reported by Kousik *et al.* [118] for thick (≈20 μm) PT films electrodeposited on iron from a solution of thiophene in acetonitrile. They concluded from EIS experiments and after extended immersion in chloride solutions that significant protection was provided by these coatings. The principle of iron pretreatment with the prior adsorption of a bifunctional compound (2-(3-thienyl) ethylphosphonic acid) followed by electropolymerization of 3-methylthiophene (MT) was successfully applied by Rammelt *et al.* [101]. They showed that a PMT film could be synthesized galvanostatically in CH_2Cl_2 on the pretreated steel surface and was covalently bonded by the thienyl end of the adsorbed layer (Figure 16.14).

When the steel/adhesive/PMT samples were top-coated by an alkyd layer (40 μm thick) very good protection was observed in delamination tests in chloride solution and under cathodic polarization. The delamination tests failed when the alkyd layer was deposited directly either on bare steel or on steel coated only with PMT.

A similar procedure, already used with PANI on iron and zinc [46], was also followed by Tüken *et al.* [102]. However, in this case, the thin adhesive layer consisted of PPy, previously electrodeposited from a pyrrole–oxalic acid solution. Then, thiophene was electropolymerized from a thiophene–$LiClO_4$ solution in acetonitrile. It was found that

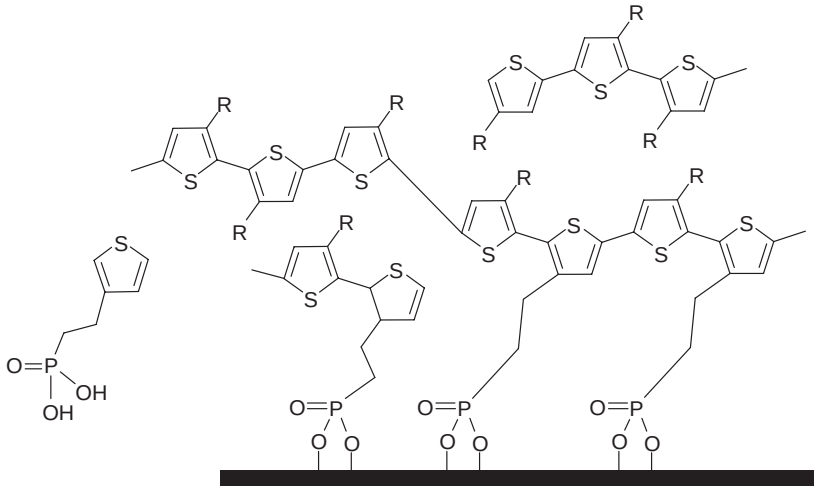

Figure 16.14 *Schematic representation of the PMT film bonded to a first adhesive monolayer of a bifunctional compound. According to this process, the bifunctional compound is first attached to iron through the $PO(OH)_2$ group, then, electropolymerization of MT is performed on this modified surface and leads to PMT chains covalently bonded to the thienyl end of the bifunctional compound. (Reprinted with permission from Electrochimica Acta, Protection of mild steel by modification with thin films of polymethylthiophene by U. Rammelt, P.T. Nguyen and W. Plieth, 46, 26–27, 4251–4257. Copyright (2001) Elsevier Ltd)*

these PPy/PT bilayer coatings had very low porosity and exhibited an excellent barrier effect. Once again, this seems to prove that strong adhesion of the coating is needed for a good protection.

16.3.1.2 Nonferrous Metals

For practical and economic grounds, three main metals, aluminium, zinc, and copper have been the most studied. Aluminium and its alloys (AA-2024 T3, AA 7075) are widely used in the aircraft industry and, in contrast to iron, they are naturally protected by a thin insulating oxide layer. However, it is worth noting that aluminium alloys contain other metals, such as copper and zinc, and this might explain the electrochemical discrepancies sometimes observed between pure aluminium and alloys. Zinc is principally used in the automobile and building industries, sometimes alloyed with other metals (Ni, Cu). It is deposited as a thin layer about 10 μm thick on large steel sheets in order to provide cathodic protection of iron (more than 10 years guarantee against corrosion claimed by the manufacturers is partly due to the presence of zinc on steel). Copper is also a critical component of modern industry and is used not only for wiring, but also in plumbing and heating work. Although relatively stable in the natural atmosphere, nevertheless the three metals are subject to corrosion and have to be protected by suitable paints, as with ferrous metals. The replacement of chromating procedures by more eco-friendly treatments is also required and, for this reason, the use of conducting polymers was also suggested.

Aluminium and Alloys

Most direct electropolymerization reactions of heterocyclic monomers were performed with pyrrole, while PANI and PT coatings were generally applied from pigmented solutions. Electropolymerization on aluminum differs considerably from that on iron or steel. The alumina film acts as an insulating barrier, inhibits electron transfer, and makes electropolymerization difficult. First significant results with PPy electrodeposition were obtained by Beck *et al.* [18,19] by using oxalic acid, which is well known to produce a porous aluminium oxide [103], essential for successful deposition through the pores. Naoi *et al.* [104] showed that various sodium sulfonate surfactants, such as *n*-dodecylbenzenesulfonate (SDBS), butylnaphthalenesulfonate (BNS), and *n*-dodecylsulfate (SDS), allowed to deposit simultaneously porous Al_2O_3 and PPy with a high current efficiency. They assumed that PPy growth was due to the presence of electronically conducting paths in the Al_2O_3 layer. A great improvement for direct PPy electrodeposition on aluminium alloys was reported by Tallman *et al.* [105,106] who used Tiron as an electron-transfer mediator. In this latter case the deposition potential was shifted by 0.5 V to lower potentials, the current efficiency was nearly 100%, the films were very homogeneous, and the adherence was considerably improved compared to solvent-cast films (adherence of ≈6 MPa with Tiron, ≈2 MPa with usual formulations). The use of catechol as a mediator mixed with tosylate was also found to be suitable for PPy electrodeposition on aluminium. The protection properties of polyurethane (PU) top-coated PPy-Al samples, submitted to long-term immersion and Prohesion^{TM} exposure, were tested by EIS. A good barrier effect was reported after several months exposure [125]. More recently, Bazzaoui *et al.* [107] described the successful use of saccharin sodium hydrate to deposit adherent PPy films on aluminium. They showed a significant barrier effect with thick PPy films (11 μm) immersed in 0.1 M HCl. However, in contrast to the previous procedure, a high overvoltage was needed and, therefore, the PPy was probably overoxidized.

Electrodeposition of PANI derivatives was achieved by Shah and Iroh [108] in the case of Al alloy (2024) and *N*-ethylaniline in aqueous oxalic acid solution. The coating was electrodeposited by cyclic voltammetry by application of an unusually large potential range (–1V to +3V/SCE). Corrosion current was measured in chloride solutions from Tafel plots and was found to be significantly lower (about one order of magnitude) than that of bare Al-2024. Multifunctional coatings (PPy/PANI) were also achieved on aluminium by coelectropolymerization of aniline and pyrrole (in a feed ratio of 3:7) in oxalic acid solution, but protection performances were not given [109,110].

Zinc and Other Nonferrous Metals

Plated zinc steel sheets are currently used in the automobile industry, and, as for other metals, chromating processes have been excluded in painting procedures, justifying the search for other solutions, in particular the electrodeposition of conducting polymers. As a large amount of zinc-plated steel sheet is already produced by an electroplating process, it is obvious that the electrodeposition of a conducting polymer on zinc constitutes a simple procedure particularly well adapted to an industrial process. However, it must be noted that several properties of zinc render its use in electrochemistry difficult: (i) its electronegativity is higher than that of iron and, therefore, it oxidizes at very low potentials (–0.98 V/SCE), (ii) it is not protected by a thin insulating layer like aluminium, and (iii) its passivity

range is restricted, is not as broad as for iron and occurs at a high pH, unfavorable for the application of conducting polymers. These preliminary considerations mean that the ennobling effect is not expected with conducting polymers and, therefore, protection against corrosion can be achieved only through self-healing and barrier effects. Of all the available conducting polymers, and for the same reasons as previously indicated, PPy was found to be the best adapted. However, with zinc as a substrate, the main difficulty was to find a suitable doping salt which would allow rapid deposition of the polymer and impede dissolution of the metal. Sodium salicylate fulfils these requirements perfectly [111,112], and ultrafast deposition rates compatible with industrial coating procedures were achieved. Very high current densities could be used with 100% current efficiency, and adherent PPy films (1 μm in 3 s) were obtained. Salicylate is essential; electropolymerization took place on a thin zinc salicylate layer (15 nm thick) and the pyrrole electrolysis process was quite similar to that performed on a platinum electrode. However, no significant reduction in the deposition potential was noted compared to other salts, like sodium nitrate, and, thus, a possible catalytic effect, as in the case of Tiron [124], was not proved. In addition, it is worth noting that this supporting electrolyte could work with most metals (iron, copper, aluminium...). As indicated previously, protection properties were dramatically improved by using mixtures of sodium salicylate and sodium diisopropylsalicylate and also after heat treatment in air [90]. Cross-linking between PPy chains and an increase in the hydrophobicity improved the barrier effect, and a self-healing effect was provided by salicylate anions, which are known also for their corrosion inhibition properties [113]. From a practical point of view it was found that a 1 μm thick PPy film was equivalent to a 1 μm zinc layer deposited on iron. Recently, Martins *et al.* [114] used sodium tartrate as a doping salt to deposit PPy on zinc at constant current. Several zinc-plated steel samples coated with thick PPy films (15–20 μm) were tested with salt spray. Very good protection was obtained for times as long as 600 hours in the case of PPy coatings deposited at 15 or 20 mA cm^{-2} with ultrasonic stirring. This latter is particularly effective in improving both the protection and the mechanical properties of the film. However, the faradaic yield was relatively poor (50% of the faradaic charge is lost in secondary processes related probably to partial dissolution of the metal), and this might constitute a serious drawback for an industrial process. The OCP curves revealed no self-healing and, therefore, the protection properties may be attributed to a strong barrier effect, resulting also from the use of rather thick PPy films.

Copper

Electrodeposition of conducting polymers on copper has been investigated by several groups, and various salts have been tested to achieve the electrochemical polymerization of pyrrole from aqueous solutions in a one-step process. No serious difficulty was found, and electrolytes used previously on iron, such as oxalic acid [115,116], salicylates [117,118], and tartrate [119] were found suitable for PPy electrodeposition on copper and its alloys; aqueous phosphate solutions were also found to provide highly adherent and homogenous films [120]. In all cases, PPy electrodeposition occurred after the preliminary passivation of copper through a mixed copper salt, copper oxide, or copper hydroxide layer. A two-step process, where an oxalate-doped PPy underlayer (PPy-Oxalate) is first deposited, followed by a dodecylbenzenesulfonate-doped PPy layer

(PPy-DBS), was reported by Wang *et al.* [121] and protected copper very effectively in chloride solutions.

Other Nonferrous Metals

Corrosion is of less concern than with aluminium, zinc, or copper, and work devoted to titanium [122], nickel [123], and lead [124] is related to other applications and will not be treated in this chapter.

16.3.2 Coatings Made from Conducting-Polymer Formulations

The main difficulties related to electropolymerization processes have been ruled out, and theoretically, no metal specificity is involved in the procedure which could restrict the application, except the case of PANI whose acidity properties can conflict with different metal oxides, as previously stated in Section 16.2. The main problem lies in the fact that all the conducting polymers are generally insoluble and, therefore, mixing them with paint will involve either the fabrication of particle dispersions or functionalization of the polymer in order to make it soluble in an organic solvent. Initially centred on PANI formulations, the process has been progressively extended to other conducting polymers like PPy, PT, and their derivatives.

16.3.2.1 PANI Formulations

Much work has been devoted to the use of PANI formulations for the protection of metals against corrosion. Two main methods of application have been described. In one case, the PANI formulation is applied to the metal as a primer, and then top-coated by a conventional polymer layer. In the second case, the PANI is diluted in a polymer matrix; it may be a blend of PANI and another polymer, or it may be included in the coating.

PANI as a Primer

According to this technique, a commercial product made of PANI dispersions (Versicon^{TM}, Allied, and then Corrpassiv^{TM}, Ormecon Chemie, Ammersbek, Germany) was proposed by Wessling, at the beginning of the nineties [23,125]. Mild-steel samples coated with these PANI solutions and overcoated with an epoxy paint exhibited corrosion rates in aqueous 3.5% NaCl solutions or in 0.1 M HCl 100 times lower than samples coated with epoxy paint alone [56]. It was claimed that these PANI dispersions outperformed all other similar products, such as PANDA, developed in the same time by Monsanto [126]. The Corrpassiv^{TM} product (about 2% PANI in the liquid coating) could be applied on iron, steel, zinc, and aluminium. The ennobling mechanism was clearly established in the case of iron and steel, and it was claimed that these formulations performed better than zinc-rich epoxy paints, even at significantly lower coating thickness (20 μm instead of 60–80 μm). Success of these 'organic-metallic' paints was assumed to be due to the nanosize of the PANI particles, and to their specific formulation, different from true solutions. Other approaches, consisting in applying a neutral *N*-methyl pyrrolidone-PANI 'solution' to steel, subsequently doped by immersion in a solvent containing the dopant, have been proposed by several groups[127,128,129]. Cecchetto *et al.* described a silane pretreatment of aluminium samples (AA5182) in neutral environment for improving corrosion-resistance performances of

emeraldine-base coatings [130]. Both laboratory and beach site testing indicated an effective protection significantly better than epoxy or polyurethane top-coat alone. In contrast to these latter results, it must be mentioned that Araujo *et al.* [131] obtained opposite results. Testing mild-steel and galvanized-steel samples coated by a pure undoped PANI layer (about 15 μm thick) and top-coated by a thick epoxy layer (70–80 μm), they found that performances, in terms of underfilm corrosion and adhesion loss, were indeed markedly lower than those of other reference coating systems. These apparent contradictions, which have been often cited in the literature, are not surprising, because the adhesion of undoped polymers to metals is known to be generally poor, and good adhesion to the substrate is the first condition for good protection against corrosion.

In parallel with the previous technique based on PANI formulations containing doping salts without inhibiting properties, which only allow the ennobling of the metal by the oxidized PANI, it has been shown previously (Section 16.2.4) that efficient protection can be obtained also when the PANI is doped by inhibiting anions. In that case, as previously indicated, the PANI is considered as a source of inhibiting species which are released when it is reduced, and which could be used for the self-healing of a small scratch in the coating [75–81,84,85]. Phosphonates and, in particular, amino trimethylene phosphonic acid (ATMP), camphorsulfonic acid, and also Prussian blue and hexacyanoferrate anions (used for the protection of stainless steel against pitting corrosion) [132] were the main doping anions which were tested to provide passivation through a self-healing effect.

PANI Pigmented Paints

More recently, a new tendency consisting of the application of conventional paint coatings containing PANI additives has been developed. Thus, the protection properties of iron with a coating (100–200 μm thick) of polymethylmethacrylate (PMMA), epoxy, or water-soluble epoxy (WSE), each blended with PANI or poly-*o*-ethoxyaniline (PEtOANi), have been reported by Huh *et al.* [133]. Various acids (camphorsulfonic acid, dodecylbenzene sulfonic acid, HNO_3, HBF_4 . . .) were used as the dopants of PANI and PEtOANi. It was found that the blended coatings performed better than the unblended coatings when submitted to long-term immersion in 3% chloride solution. Corrosion protection of mild-steel samples coated with a styrene–butyl acrylate copolymer (≈80 μm thick) containing various amounts (from 0.1 to 20 wt%) of HCl-doped PANI were tested by Samui *et al.* [134]. Interestingly, paints containing less HCl/PANI performed better than those containing more. This was shown to be due to more noble characteristics and to a very low water-vapor permeability of the more lightly loaded paints. In constrast, adhesion strength of the HCl/PANI paint was found to increase from 4 to 6 MPa with the amount of HCl/PANI, but on the whole it remained fairly good during the corrosion tests. Similar studies were reported by Seegmiller *et al.* [72] for AA 2024-T3 coated with a blend of camphorsulfonate-doped PANI and PMMA, and also by Sathiyanarayanan *et al.* [135] in the case of carbon steel coated by a PANI pigmented vinyl resin paint. Very recently, emeraldine base (0.3 wt%) mixed with $Zn_3(PO_4)_2$ (10%) and with an epoxy resin was reported by Armelin *et al.* [136] to perform better than the same resin containing PANI salt, a result in apparent contradiction of those of Araujo *et al.* and Williams and McMurray previously cited. In fact, the coatings were prepared according to two distinct procedures and, besides, the presence of $Zn_3(PO_4)_2$ in the coating, which is well known for its inhibiting properties, will obviously contribute to improve the protection properties of

this complex coating and could act as a Lewis acid for transforming EB into ES. Very recently, soya oil alkyd coatings pigmented by composite nanostructured PANI and polynaphthylamine (PNA) were reported by Riaz *et al.* [137]. From corrosion rates, open-circuit potential measurements and SEM studies, far superior corrosion resistance was found compared to the PANI/alkyd system.

The same blending technique was applied to PANI doped with anions involving inhibiting properties. Thus, the corrosion performance of a PANI-pigmented epoxy resin coated on steel (40 μm thick) was reported by Azim *et al.* [138]. PANI was chemically synthesized and doped with amino trimethylene phosphonic acid (ATMP-PANI); ATMP-PANI pigment particles were obtained (mean size 4 μm) and were dispersed in an epoxy resin (30 wt%). Interestingly, when such a coated steel sample is immersed in 3% chloride solution, the OCP initially shifts to negative potentials; afterwards, it slowly shifts towards less negative potentials (−0.22 V) and remains stable after about 40 days immersion. This potential variation was attributed to the formation of a passive layer on iron due to the release of the phosphonic acid.

Paints with PANI and Inorganic Pigments

Recently, new research has been developed with paints blended with inorganic pigments coated or mixed with PANI. Kalendova *et al.* [139] synthesized mixed metal oxides (spinel and perovskite structures), silicate and graphite, subsequently coated with PANI phosphate and included as additives in epoxy-resin-based paints. The concentration of pigment in paints was 15 vol% and about 20 wt% of PANI was present in the surface-modified pigments. Tests in the presence of corroding substances (SO_2 and NaCl) did not exhibit an improvement in the case of mixed metal oxides coated with PANI, but very efficient protection was found for PANI-coated graphite. A similar strategy was applied to carbon steel by Meroufel *et al.* [140]. HCl-doped polyaniline (HCl/PANI) powder (2.1 wt%) was incorporated into a powdered zinc-rich epoxy primer (ZRP). ZRP pigments are known to provide cathodic protection, and the coating of ZRP pigments with PANI-Cl was assumed to enhance electronic conduction inside the coating through a percolation mechanism. It was found that the OCP remained cathodic and constant for up to 100 days immersion in 3% chloride solution. From EIS and Raman spectroscopy results it was concluded that only a fraction of zinc particles in contact with PANI-Cl were passivated, whereas the rest remained active. In contrast to ZRP coatings, zinc corrosion products (white corrosion) were not observed at the surface of the PANI-ZRP coating, confirming the good performance of these coatings. This improved protection was assumed to be due to an enhancement of the barrier properties.

16.3.2.2 PPy and PT Formulations

Many publications have appeared during recent years and some results seem very promising.

PPy Formulations

Very interesting results were obtained by Gelling *et al.* [141] with poly-3-octyl pyrrole (POPy) and poly-3-octadecyl pyrrole (PODPy) solubilized in an organic solvent and cast on Al 2024 T3 (2–3 μm thick), then top-coated by a ∼20 μm-thick polyurethane (PU)

layer. The protection properties of the various PPy-PU bilayers were compared to usual coatings where the PPy layer was replaced by a 20-μm-thick chromated epoxy primer. In long-term immersion tests with dilute Harrison's solution they found that after about 600 days of immersion, four of six controls (chromated-epoxy primer/polyurethane top coat) were damaged (blistering), while for the six POPy/polyurethane top-coat samples there was no damage; this result is probably related to the ennobling mechanism.

Very recently, another strategy was developed by Tallman *et al.* [142]. They synthesized PPy-modified alumina nanoparticles and used them as coating filler for the protection of AA 2024-T3. Aluminium hydroxide monohydrate nanoparticles (AMN) dispersed in water (average size 15 nm) were chemically coated by the simultaneous polymerization of pyrrole and 1,2-dihydroxybenzene (DHB), providing modified alumina nanoparticles (PDMAN). The PDMAN were dispersed in a branched polyester–urethane (BPEU) yielding a gel which was coated on aluminium as a film about 10–15 μm thick, then top-coated by BPEU. The protective behavior found was assumed to be due to an increase in the barrier effect; very good adhesion also provided by the presence of DHB contributed to improving the protection.

PT Formulations

The use of polythiophene derivatives as paint additives is new and until now few results have been reported. Very recently, application of a polythiophene derivative as an anticorrosion additive for paints was reported by Ocampo *et al.* [143]. The protection properties of selected primers specially recommended for marine steel (F111) were compared to the same primers modified by addition of 0.2 wt% of regio-regular poly(3-decylthiophene). From long-term immersion in 3.5% NaCl solutions, it was found that a two-component epoxy–amine resin-coated steel (films about 100–200 μm thick) exhibited degradation after three days immersion, whereas the same coatings with polythiophene as additive were not damaged until 30 days immersion. Interestingly, with PEDOT mixed with epoxy paints the best protection was obtained with the paint formulation containing PEDOT in the highest doping state [144]. This result is particularly significant, since PEDOT is well known to be stable in its oxidized state, and, therefore, it might mean that the protection not only works through a barrier effect, but also through an ennobling mechanism corresponding to the passivation of steel[1].

16.4 Nanostructured Conducting-Polymer Coatings and Anticorrosion Protection

New research trends have emerged in the last few years in which nano- or microstructuring of coatings (or some parts of coatings) is used to overcome some of the problems described above and to improve their anticorrosion properties.

---

[1] PEDOT was obtained by electrochemical polymerization of EDOT in $LiClO_4$–CH_3CN on a stainless steel electrode. It was collected and ground, then added to the paint formulation. Steel samples were coated with the paint formulation (film about 100 μm thick) and submitted to accelerated corrosion test cycles (up to 700) of about one hour each and consisting in successive immersion in NaCl solution, wringing, heat drying, and cooling at room temperature.

As shown previously, anticorrosion properties are the result of a complex steady-state situation in which several phenomena are in action: (i) displacement of the electrochemical interface, (ii) ennobling and self-healing effects, (iii) barrier effect offering nonspecific protection.

Protection mechanisms (i) and (iii) are ineffective when a defect appears in a coating, and mechanism (ii) will fail for large defects, even though it may induce excellent protection for small ones. Furthermore, delamination of the coating upon reduction of the conductive polymer as well as the progressive incorporation of water and electrolyte within the coating can be responsible for failure.

In any cases, it is clear that adhesion of the ECP on the metal is an essential requirement for anticorrosion properties. It is also clear that O_2 and electrolyte diffusion inside a coating has to be avoided. It is against these two main causes of failure that micro- and nanostructuring of coatings can bring new improvements.

16.4.1 Improving ECP Adhesion to Oxidizable Metals

One of the major problems is the usually weak and short-term adhesion between the ECP layers and substrates of a completely different nature. The most desirable situation by far is the covalent bonding of the ECP chains. Such control of the substrate/ECP interface is not reached when ECPs are chemically or electrochemically deposited on surfaces through oxidation of a monomer. While ECPs such as PPy and PANI are usually strongly adherent on oxidizable metals when in their oxidized state, they are generally poorly adherent in their reduced state. Indeed, the interface between the two materials is ill defined and not controlled. More importantly, no covalent bonds between the two materials are generated, and adhesion is mainly due to electrostatic interactions and weak chemical interactions. When a small scratch in the coating occurs, reduction of the polymer, which is supposed to induce self-healing, also causes delamination around the scratch. As a consequence, the scratch size increases and the ideal steady state described above is disrupted; further reduction of the polymer is needed to repair this new area in which there is direct contact between the bare metal and the environment. Ultimately this will lead to a complete failure of the coating and to corrosion extending from the initial scratch to large areas of the metal.

An advantage of incorporating ECPs into a binder such as epoxy or polyurethane is the good adhesion that such binders provide, and the actual performance of coatings based on formulation may be due to the fact that the adhesion is better than that obtained by electropolymerization. However, this strategy leads to less contact between metal and ECP and, in view of the protection mechanisms described in Section 16.2, this may be to the detriment of the anticorrosion properties.

Several strategies have been used to improve adhesion of ECP upon oxidizable metal. Bilayer coatings, composed of two types of ECP deposited electrochemically, are among these strategies and several groups have reported that they provide better protection by enhancing the adherence of the first layer to the metal. Many examples have already been described in Section 16.2 of this chapter. However, the interface between the metal and the first layer remains ill defined with no covalent bonds between the metal and the polymer.

An ultrathin layer (few nanometers) of material covalently bonded both to the metal surface and to the ECP should constitute an outstanding adhesion primer. This could be

achieved by using bifunctional coupling agents capable of chemically reacting with the metal and with the polymer. Such coupling reagents comprise two functional groups, one like siloxane, thiol, or phosphonate, which will strongly react with metal hydroxides or oxides and the other, an unsaturated group or a monomer moiety, which will react with the polymer.

Several attempts have been made using organosiloxanes as adhesion primer layers on top of which the ECP could be deposited. In this case, the silanol functions covalently bind to pendant OH groups on still ill-defined surfaces of the metal and various oxidation products [145–146]. An excellent survey devoted to the use of silane coupling agents for anticorrosion was provided by Van Ooij *et al.* [147–148]. However, it has to be noted that organic silanes are not easy to handle on an industrial scale; such surface treatments take time and this might constitute a severe drawback for anticorrosion coatings. This may be the reason why the combined use of silane and conductive polymers has been studied more for applications such as solid electrolyte capacitors, nano- or micropatterning and electroluminescent devices.

The same applies to thiol-based pretreatments, which show some potential for specific applications, but also require quite a long time to reach complete coverage of the metal surface through the formation of a well-defined monolayer [149,150].

Another interesting and promising research direction is based on the electroreduction of diazonium salts on oxidizable metals. This reaction first developed on carbon substrate [151–152] was extended to several metals (iron, mild steel, Ni, Co, Al . . .) [153–154] and makes it possible to graft thin layers of organic compounds on solid surfaces. The layers generated are usually just a few nanometers thick and are assumed to be covalently attached to the metal. They consist of small oligoaromatic chains (generally based on oligophenylene moieties). Such layers have been studied for anticorrosion properties. Of course, without a top-coat, their effects remain modest, but, nevertheless, the barrier effect is important. These layers have been used as primary layers for the surface polymerization of various monomers leading to nonconducting polymers [155–156]. However, this method has, to the best of our knowledge, rarely been used for the electrochemical deposition of a second material. The main reason is that the grafted layers resulting from the reduction of diazonium salts are poorly conducting and, once deposited, any electrochemical processes is difficult to trigger on these modified surfaces.

Recently, this difficulty was overcome when the starting diazonium was the aniline dimer (4-aminodiphenylamine or ADPA) [157]. In that case the grafted layer is electroactive and aniline oxidation remains possible in aqueous sulfuric acid and leads to a strongly adherent PANI film on the modified surface. The first experiments were performed on carbon and extension to an oxidizable metal has not yet been reported. However, as it has been proven that the covalent grafting of diazonium salts was also successful with iron and other oxidizable metals [178–182], we think that the same procedure might be applied in the case of iron. A strong increase of the adhesion should be expected, and therefore an improvement of the protection properties.

16.4.2 Nanostructured Surfaces Displaying Superhydrophobic Properties

We have seen that failure of the coating can also be the result of water or electrolyte incorporation in the coatings. This can be considerably reduced when the surface repels water. Hydrophobic anions have therefore been incorporated into ECP coatings and have

proven to increase corrosion protection. For instance, polypyrrole film containing a perfluorinated dopant exhibited hydrophobicity, while ClO_4^--doped polypyrrole was hydrophilic [158]. Similar effects were obtained when diisopropylsalicylate was used instead of salicylate in PPy coatings deposited on zinc [90].

Water and electrolyte incorporation within the coating is due to the surface wettability. This is an important property for most solid materials and is defined by both the surface energy and surface morphology. Superhydrophobicity is a fairly recent term used to describe the extreme water repellency of a rough hydrophobic surface. A surface with a large water contact angle ($\geq$150°) is described as superhydrophobic [159]. The large contact angle is the result of the combination of a rough microstructure and a rough nanostructure [160,161]. The biological surfaces to which this term was originally applied were often found to have roughness on several scales, typically with features of several micrometers with nanometer-scale roughness as well (Figure 16.15).

The ability to control the morphology of the surface on the micron and nanometer scales is the key to achieving nonwetting surfaces [162]. This decoupling of wetting from simple surface energy opens up many possibilities for engineering surfaces and suggests very important opportunities in the area of corrosion inhibition.

Direct fabrication of superhydrophobic coatings on metal surfaces has indeed brought new research trends to the corrosion problem. Two main approaches have been developed

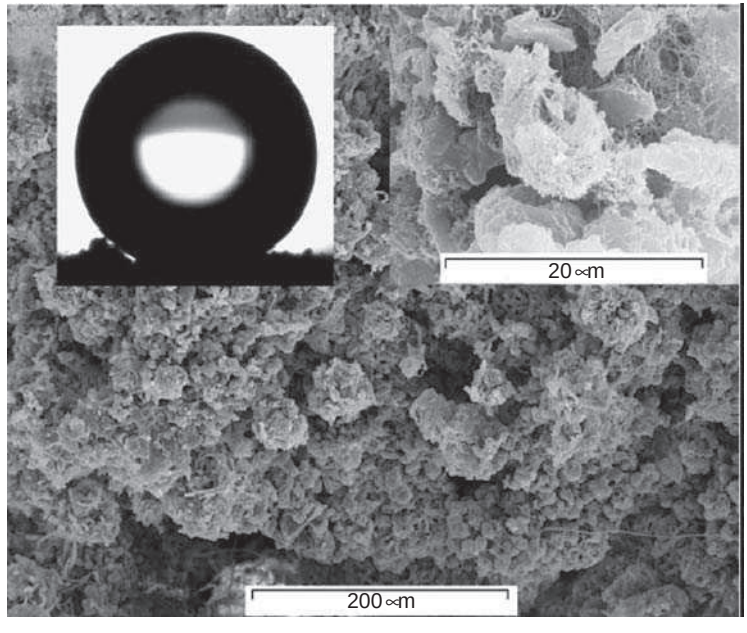

Figure 16.15 *Superhydrophobic surfaces in biology: the lichen* Lecanora conizaeoides *showing high roughness with inset showing water drop 155 ± 4°. (Reprinted with permission from Journal of Plant Physiology, A lichen protected by a super-hydrophobic and breathable structure by N.J. Shirtcliffe, F. B. Pyatt, M.I. Newton and G. McHale, 163, 1193–1197. Copyright (2006) Elsevier Ltd)*

to generate superhydrophobic surfaces [190,163]. One is to increase directly the surface roughness of low-surface-energy materials; the other is to fabricate a suitable surface roughness with certain materials and then to modify the as-prepared surface by grafting hydrophobic molecules onto it.

In order to realize practical applications, methods for the elaboration of superhydrophobic coatings should be as cheap and easy as possible. Electrochemical methods are thus widely used to form rough structures [164]. The concept of templateless growth of conducting polymer nanowires is of interest for anticorrosion, however, to our knowledge, no example has been reported for oxidizable surfaces. Liu *et al.* reported that polyaniline nanowires were grown from the surface of a platinum electrode by redox polymerization, using a programmed constant-current method designed to control the nucleation and growth rates [194] (Figure 16.16). On the one hand, they showed that uniform and oriented nanowires were formed only when the current density was progressively reduced and, on the other, that the separation of nucleation and growth events was required for obtaining oriented polymer nanowires.

Another strategy for synthesizing conducting-polymer nanofiber arrays based on a two-phase system has also been reported by Li *et al.* [165]. This system ensures a very low concentration of monomer, for instance pyrrole, in the polymerization process (Figure 16.17).

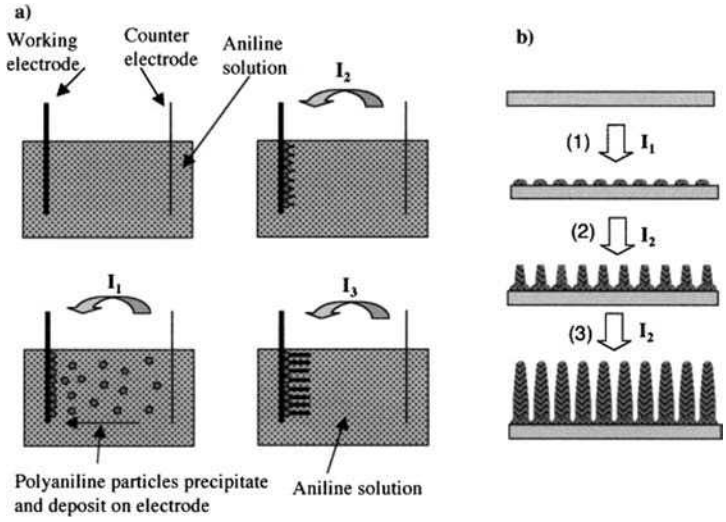

Figure 16.16 *Schematic drawing of the steps for growing oriented polymer nanowires: (a) reactions in the electrochemical cell, (b) growth after nucleation. (Reprinted with permission from Chemistry: A European Journal, Templateless assembly of molecularly aligned conductive polymer nanowires: a new approach for oriented nanostructures by J. Liu, Y. Lin, L. Liang et al., 9, 604–611. Copyright (2003) Wiley-VCH)*

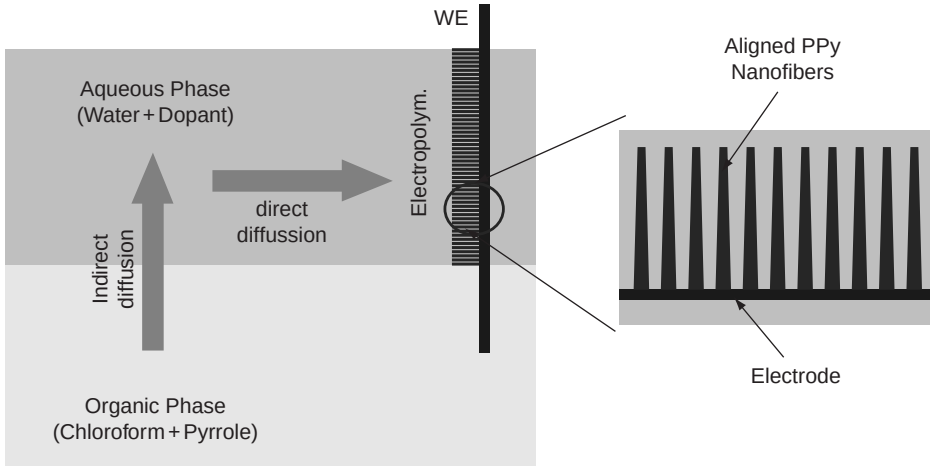

Figure 16.17 *Schematic illustration of two-phase electropolymerization: (a) Pyrrole diffuses from the organic phase into the aqueous phase slowly (indirect diffusion). Then polypyrrole is deposited by the diffusion of pyrrole to the electrode (direct diffusion). (b) Aligned polypyrrole nanofibers are produced by successive CV electropolymerizations. (Reprinted with permission from Journal of Materials Chemistry, Polypyrrole nanofiber arrays synthetized by a biphasic electrochemical strategy by M. Li, Z. Wei and L. Jiang, 18, 2276–2280. Copyright (2008) Royal Society of Chemistry)*

With successive cyclic voltammetric (CV) electropolymerizations, the length of the polypyrrole nanofibers could be controlled from several hundred nanometers to several micrometers (Figure 16.18).

Xu *et al.* reported a simple electrochemical process to fabricate superhydrophobic conducting polypyrrole films [188]. Interestingly, they demonstrated that reversible switchable

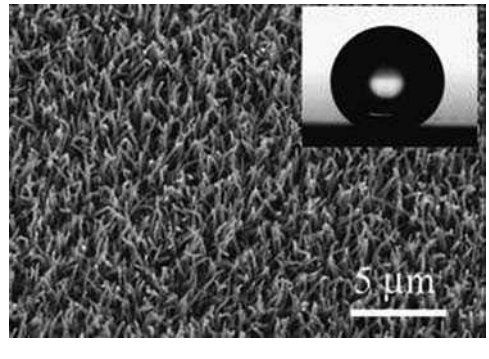

Figure 16.18 *SEM image of the superhydrophobic aligned polypyrrole nanofiber film after 30 CV scanning cycles using L-camphorsulfonic acid as dopant. Right inset: digital camera image of a water drop on the nanofiber film; the contact angle is about 165°. (Reprinted with permission from Journal of Materials Chemistry, Polypyrrole nanofiber arrays synthetized by a biphasic electrochemical strategy by M. Li, Z. Wei and L. Jiang, 18, 2276–2280. Copyright (2008) Royal Society of Chemistry)*

surface wettability between superhydrophobic (doped or oxidized state) and superhydrophilicity (dedoped or neutral state) was obtained upon changing the applied potential.

Superhydrophobicity of a surface is also a means to struggle against biofouling corresponding to the undesirable adherence of micro-organisms, plants, algae, and animals on submerged surfaces. The antibiofouling properties of superhydrophobic coatings have been investigated [166]. Bioadhesion is a complicated phenomenon that involves different types of interactions between organisms and the surface. Protein adhesion to a superhydrophobic surface can be inhibited to a great extent due to the water repellency of this surface, which prevents protein solution penetration [167]. It is well known that biofouling will induce biocorrosion [168]. Thus, superhydrophobic surfaces which are able to withstand salt and protein solutions in a wide range of concentrations may open up a new avenue for applications, especially to marine engineering materials.

In summary, one-step or other simple techniques are greatly needed for the fabrication of superhydrophobic surfaces on a large scale and with good homogeneity, and may prove very useful for improving ECP anticorrosion properties. Furthermore, stimuli-responsive superhydrophobic surfaces will provide interesting functional materials beyond those found in nature. This field is in its infancy and new research efforts are required to evaluate the full potential of these approaches to the design of chromium-free organic coatings for protecting metals against corrosion.

16.5 Conclusions

The use of electronic conducting polymers for protection against corrosion is a topic which has considerably progressed in the last years. From the analysis of the published work it is obvious that much effort has been made to understand the protection mechanisms but, also, many new metal systems have been tested and, at this time, we consider that some results are very promising and already compare well with the prohibited chromating processes.

A simple conducting-polymer film cannot alone provide full protection to a metal, and this means that to be efficient it must be top-coated by another polymer film. Under these conditions, and when a small defect occurs in the coating (small scratch which puts the metal in direct contact with the environment) two specific ways of protection may be expected, each corresponding to a kind of self-healing: the ‘ennobling’ and ‘self-passivation’ effects. The first is obtained by metals characterized by a wide passivation potential range, corresponding to the formation of an oxide (aluminium, iron, or steel), which inhibits metal dissolution. Self-healing will occur through the reduction of the ECP resulting from galvanic coupling with the metal, which moves the potential of the metal into the passivation range, where the corrosion current is very low. Two conditions are, however, required for this effect to be observed. Firstly, the polymer must be oxidizable in air (PPy, PANI, PEDOT), in order to maintain a steady state. Secondly, the galvanic current density provided by reduction of the oxidized polymer must be higher than that corresponding to the Flade potential (transition between the active and the passive zones of the metal). This latter point is extremely important and has been rarely taken in consideration. We think, as was outlined in our discussion, that this might be at the origin of many discrepancies reported in the literature.

The second self-healing effect, related to ECP doped with anions with inhibiting properties, is more general. It depends only on the formation of a thin adsorbed insoluble salt layer in the defect, and results from the precipitation of metal ions with the doping anion. In our opinion, this effect is similar to the ennobling effect, the difference being in the nature of the passivation of the metal, and in the fact that the kinetics of the reduction of the polymer is not as important as in the ennobling case.

The adherence is probably one of the most crucial properties for long-term protection. Disbonding of the coating generally occurs through the simultaneous reduction of the ECP and the production of OH^- species at the metal–polymer interface (resulting from the displacement of the electrochemical interface which moves from the polymer–environment to the metal–polymer). The adherence may be dramatically improved by an appropriate pretreatment of the metal to provide tight bonding with the polymer

Other nonspecific effects, such as the compactness of the polymer and probably the more or less hydrophobic character of the polymer, may also play an important role for good protection to be achieved. The compactness of the polymer, which will determine its porosity and its barrier effect, may be improved by thermal treatments, a general procedure used in the paint industry to improve the cross-linking between unsaturated polymer chains. The affinity of the polymer for water (detrimental towards protection), depending on the porosity, may be also modulated by incorporating more (or less) hydrophobic doping anions into the polymer. This should slow the diffusion of water through the coating and, therefore, improve the protection. Elaboration of superhydrophobic surfaces on a large scale is a new challenge which could also provide the solution to some specific cases of corrosion.

Finally, the choice between the electropolymerization technique and that of ECP formulations is not straightforward and will depend on the difficulties and the relative advantages encountered with a specific metal–polymer association. The electrochemical technique seems better adapted than the cast formulation technique when very thin polymer layers are required and if the system will not be exposed to a very aggressive environment.

Acknowledgement

We are indebted to Dr J. S. Lomas for critical discussion and for correcting the manuscript.

References

[1] C.K. Chiang, M.A. Druy, S.C. Gau, A.J. Heeger, E.J. Louis, A.G. MacDiarmid, Y.W. Park, and H. Shirakawa, Synthesis of highly conducting films of derivatives of polyacetylene, (CH)x, *J. Am. Chem. Soc.*, **100**, 1013–1015 (1978).

[2] M.C. Pham, J.E. Dubois, and P.C. Lacaze Obtaining thin films of 'reactive polymers' on metal surfaces by electrochemical polymerization. Reactivity of functional groups in a carbonyl substituted polyphenylene oxide film, *J. Electroanal. Chem.*, **86**, 147–157 (1978).

[3] A.F. Diaz, K.K. Kanazawa, and G.P. Gardini, Electrochemical polymerization of pyrrole *J.C.S. Chem. Comm.*, 635–636 (1979).

[4] G. Mengoli, M. Munari, P. Bianco, and M. Musiani, Anodic synthesis of polyaniline coatings onto Fe sheets, *J. Appl. Polym. Sci.*, **26**, 4247–4257 (1981).

[5] E.M. Genies, A.A. Syed, and C. Tsintavis, Electrochemical study of polyaniline in aqueous and organic medium, Redox and kinetic properties, *Mol. Cryst. Liq. Cryst.*, **121–124**, 181–186 (1985).
[6] G. Tourillon and F. Garnier, New electrochemically generated organic conducting polymers, *J. Electroanal. Chem.*, **135**, 173–178 (1982).
[7] J. Jang, Conducting polymer nanomaterials and their applications, *Adv Polym Sci.*, **199**, 189–259 (2006).
[8] D.W. DeBerry, Modification of the electrochemical and corrosion behavior of stainless steels with an electroactive coating, *J. Electrochem. Soc.*, **132**, 1022–1026 (1985).
[9] K.M. Cheung, D. Bloor, and G.C. Stevens, Characterization of polypyrrole electropolymerized on different electrodes, *Polymer*, **29**, 1709–1717 (1988).
[10] G. Troch-Nagels, R. Winand, A. Weymeersch, and L. Renard, Electron conducting organic coating of mild steel by electropolymerization, *J. Appl. Electrochem.*, **22**, 756–764 (1992).
[11] C.A. Ferreira, S. Aeiyach, M. Delamar, and P.C. Lacaze, Electropolymerization of pyrrole on iron electrodes. Influence of solvent and electrolyte on the nature of the deposits, *J. Electroanal. Chem.*, **284**, 351–369 (1990).
[12] P.C. Lacaze, C.A. Ferreira, S. Aeiyach, and J.J. Aaron, French Patent, (PSA-Citroën), 9214091 (1992).
[13] C.A. Ferreira, S. Aeiyach, J.J. Aaron, and P.C. Lacaze, Electrosynthesis of strongly adherent Ppy coatings on iron and mild steel in aqueous media, *Electrochim. Acta*, **41**, 1801–1809 (1996).
[14] F. Beck and R. Michaelis, Strongly adherent, smooth coatings of polypyrrole oxalate on iron, *J. Coatings Technol.*, **64**, 59–67 (1992).
[15] F. Beck, R. Michaelis, F. Schloten, and B. Zinger, Film forming electropolymerization of pyrrole on iron in aqueous oxalic acid, *Electrochim. Acta*, **39**, 229–234 (1994).
[16] P.C. Lacaze, J. Petitjean, S. Aeiyach, and M. Hedayatullah, Process and bath for the electrolytic deposition of polypyrrole on an oxidizable metal surface by electro-polymerization, French Patent SOLLAC-USINOR 93 15385, (1993), US Patent 5522981.
[17] J. Petitjean, S. Aeiyach, J.-C. Lacroix, and P.C. Lacaze, Ultra-fast electropolymerization of pyrrole in aqueous media on oxidable metals in a one-step process, *J. Electroanal. Chem.*, **478**, 92–100 (1999).
[18] P. Hülser and F. Beck, Electrodeposition of polypyrrole layers on aluminium from aqueous electrolytes, *J. Appl. Electrochem.* **20**, 596–605 (1990).
[19] F. Beck and P. Hülser, Electrodeposition of polypyrrole on aluminium from non-aqueous solutions *J. Electroanal. Chem.*, **280**, 159–166 (1990).
[20] E.A. Bazzaoui, S. Aeiyach, and P.C. Lacaze, Electropolymerization of bithiophene on Pt and Fe electrodes in an aqueous SDS micellar medium, *Synth. Met.*, **83**, 159–165 (1996).
[21] N. Sakmeche, E.A. Bazzaoui, M. Fall, S. Aeiyach, M. Jouini, J.C. Lacroix, J.J. Aaron, and P.C. Lacaze, Application of sodium dodecylsulfate (SDS) micellar solution as an organized medium for electropolymerization of thiophene derivatives in water, *Synth. Met.*, **84**, 191–192 (1997).
[22] C. Lagrost, J. C. Lacroix, S. Aeiyach, M. Jouini, K. Chane Ching, and P. C. Lacaze, Host guest complexation : a new strategy for electrodeposition of processable polythiophene composites from aqueous Medium, *Chem. Comm.*, 489–490 (1998).
[23] B. Wessling, Passivation of metals by coating with polyaniline: corrosion potential shift and morphological changes, *Adv. Mat.*, **6**, 226–228 (1994).
[24] V.J. Gelling, M.M. Wiest, D.E. Tallman, G.P. Bierwagen, and G.G. Wallace, Electroactive-conducting polymers for corrosion control 4. Studies of poly(3-octyl pyrrole) and poly(3-octadecyl pyrrole) on aluminum 2024-T3 alloy, *Prog. Org. Coat.*, **43**, 149–157 (2001).
[25] J. I. Iribarren, E. Armelin, F. Liesa, J. Casanovas, and C. Aleman, On the use of conducting polymers to improve the resistance against corrosion of paints based on polyurethane resins, *Mat. Corr.*, **57**, 683–688 (2006).
[26] D.E. Tallmann, G. Spinks, A. Dominis, and G.G. Wallace, Electroactive conducting polymers for corrosion control. Part 1. General introduction and a review of non-ferrous metals, *J. Solid State Electrochem.*, **6**, 73–84 (2002).

[27] P. Zarras, N. Anderson, C. Webber, D.J. Irvin, J.A. Irvin, A. Guenthner, and J.D. Stenger-Smith, Progress in using conductive polymers as corrosion-inhibiting coatings, *Radiation Phys. Chem.*, **68**, 387–394 (2003).
[28] C. Menardo, M. Nechtschein, A. Rousseau, J.P. Travers, and P. Hany, Investigation on the structure of polyaniline: carbon-13 NMR and titration studies, *Synth. Met.*, **25**, 311–322 (1988).
[29] G. Williams and H.N. McMurray, Polyaniline inhibition of filiform corrosion on organic coated AA2024-T3, *Electrochim. Acta*, **54**, 4245–4252 (2009).
[30] D. Stoye and W. Freitag (Eds.), *Paints, Coatings and Solvents*, Wiley-VCH, Weinheim, 1998.
[31] A. Revillon and P.C. Lacaze (Eds.), *Manuel de Peintures et Pernis* (T I, T II), Hermann, Paris, 2007.
[32] D. Landolt, In *Corrosion et Chimie de Surface des Métaux*, Presses Polytechniques et Universitaires Romandes, Lausanne, Switzerland, 1993.
[33] N.L. Thomas, The barrier properties of paint coatings, *Prog. Org. Coatings*, **19**, 101–121 (1991).
[34] Nivedita S. Sangaj, and V.C. Malshe, Permeability of polymers in protective organic coatings. Review, *Prog. Org. Coatings* **50**, 28–39 (2004).
[35] C. Sanchez, B. Julian, P. Belleville, and M. Popall, Applications of hybrid organic-inorganic nanocomposites, *J. Mater. Chem.*, **15**, 3559–3592 (2005).
[36] M. Pagliaro, R. Ciriminna, and G. Palmisano, Silica-based hybrid coatings, *J. Mater. Chem.*, **19**, 3116–3126 (2009).
[37] D. Wang and G.P. Bierwagen, Sol-gel coatings on metals for corrosion protection, *Prog. Org. Coatings*, **64**, 327–338 (2009).
[38] J.-C. Lacroix, J.L. Camalet, S. Aeiyach, K.I. Chane-Ching, J. Petitjean, E. Chauveau, and P.C. Lacaze, Aniline electropolymerization on mild steel and zinc in a two-step process, *J. Electroanal. Chem.*, **481**, 76–81 (2000).
[39] R. Rajagopalan and J.O. Iroh, Development of polyaniline-polypyrrole composite coatings on steel by aqueous electrochemical process, *Electrochim. Acta*, **46**, 2443–2455 (2001).
[40] J.O. Iroh, Y. Zhua, K. Shah, K. Levine, R. Rajagopalan, T. Uyar, M. Donley, R. Mantz, J. Johnson, N.N. Voevodin, V.N. Balbyshev, and A.N. Khramov, Electrochemical synthesis: a novel technique for processing multi-functional coatings, *Prog. Org. Coatings* **47**, 365–375 (2003).
[41] R. Hasanov and S. Bilgic, Monolayer and bilayer conducting polymer coatings for corrosion protection of steel in 1M H2SO4 solution, *Prog. Org. Coatings*, **64**, 435–445 (2009).
[42] A. Michalik and M. Rohwerder, Conducting polymers for corrosion protection: a critical view. *Z. Phys. Chemie*, **219**, 1547–1560 (2005).
[43] J. Petitjean, J. Tanguy, J.C. Lacroix, K.I. Chane-Ching, S. Aeiyach, M. Delamar, and P.C. Lacaze, Interpretation of the ultra-fast electropolymerization of pyrrole in aqueous media on zinc in a one-step process: The specific role of the salicylate salt investigated by X-ray photoelectron spectroscopy (XPS) and by electrochemical quartz crystal microbalance (EQCM), *J. Electroanal. Chem.*, **581**, 111–121 (2005).
[44] M. Pourbaix, Atlas of Electrochemical Equilibria, 2nd Edn., NACE, Houston, TX, 1974.
[45] M. Keddam and P.C. Lacaze, Corrosion des métaux peints. Analyse des phénomènes et moyens de protection. In *Manuel de Peintures et Vernis*, ed. A. Revillon and P.C. Lacaze, Hermann, Paris, 2007, Ch. 13.
[46] J. Petitjean, Ph. D. Thesis, University of Paris, France, 1994.
[47] W.-K. Lu, R.L. Elsenbaumer, and B. Wessling, Corrosion Protection Of Mild Steel By Coatings Containing Polyaniline, *Synth. Met.*, **71**, 2163–2166 (1995).
[48] M.C. Bernard, A. Hugot-Le Goff, S. Joiret, N.N. Dinh, and N.N. Toan, Polyaniline layer for iron protection in sulfate medium, *J. Electrochem. Soc.* **146**, 995–998 (1999).
[49] A. Cook, A. Gabriel, and N. Laycock On the Mechanism of Corrosion Protection of Mild Steel with Polyaniline, *J. Electrochem. Soc.*, **151**, B529–B535 (2004).
[50] B. Wessling, Scientific and commercial breakthrough for organic metals, *Synth, Met.*, **85**, 1313–1318 (1997).
[51] M. Stratmann and H. Streckel, On the atmospheric corrosion of metals, which are covered with thin electrolyte layers, Part 1: Verification of the experimental technique, *Corros. Sci.*, **30**, 681–696 (1990).

[52] A. Leng, H. Streckel, and M. Stratmann, The delamination of polymeric coatings from steel. Part 1. Calibration of the Kelvin probe and basic delamination mechanisms, *Corros. Sci.*, **41**, 547–578 (1999).
[53] A.P. Nazarov and D. Thierry, Scanning Kelvin probe study of metal/polymer interfaces, *Electrochim. Acta*, **49**, 2955–2964 (2004).
[54] U. Rammelt, P.T. Nguyen, and W. Plieth, Corrosion protection by ultrathin films of conducting polymers, *Electrochim. Acta*, **48**, 1257–1262 (2003).
[55] N. Ahmad and A.G. McDiarmid, Inhibition of corrosion of steels with the exploitation of conducting polymers, *Synthetic Metals*, **78**, 103–110 (1996).
[56] A. Wu, C. Everaldo, E.C. Venancio, and A.G. McDiarmid, Polyaniline and polypyrrole oxygen reversible electrodes, *Synth. Met.*, **157**, 303–310 (2007).
[57] T. D. Nguyen, M.C. Pham, B. Piro, J. Aubard, H. Takenouti, and M. Keddam, Conducting polymers and corrosion PPY-PPy-PDAN composite films. Electrosynthesis and characterization, *J. Electrochem. Soc.*, **151**, B325–B330 (2004).
[58] H. Nguyen Thi Le, B. Garcia, C. Deslouis, and Q. Le Xuan, Corrosion protection and conducting polymers: polypyrrole films on iron, *Electrochim. Acta*, **46**, 4259–4272 (2001).
[59] A. Meneguzi, M.C. Pham, J.-C. Lacroix, B. Piro, A. Adenier, C.A. Ferreira, and P.C. Lacaze, Electroactive poly(aromatic amine) films for iron protection in sulfate medium, *J. Electrochem. Soc.* **148**, B121–B126 (2001).
[60] M. Yan, D.E. Tallman, and G.P. Bierwagen, Role of oxygen in the galvanic interaction between polypyrrole and aluminum alloy, *Electrochim. Acta*, **54**, 220–227 (2008)
[61] J.C. Seegmiller, J.E. Pereira da Silva, D.A. Buttry, S.I. Cordoba de Torresi, and R.M. Torresi, Mechanism of action of corrosion protection coating for AA2024-T3 based on poly(aniline)-poly(methylmethacrylate) blend, *J. Electrochem. Soc.*, **152**, B45–B53 (2005).
[62] A.J. Bard and M.V. Mirkin (Eds.), *Scanning Electrochemical Microscopy*, CRC Press, Boca Raton, 2001.
[63] P. Sun, F.O. Laforge, and M.V. Mirkin, Scanning electrochemical microscopy in the 21st century, *Phys. Chem. Chem. Phys.*, **9**, 802–823 (2007).
[64] E. Armelin, R. Oliver, F. Liesa, J.I. Iribarren, F. Estrany, and C. Aleman, Marine paint formulations: conducting polymers as anticorrosive additives, *Prog. Org. Coatings*, **59**, 46–52 (2007).
[65] A. Cook, A. Gabriel, D. Siew, and N. Laycock, Corrosion protection of low carbon steel with polyaniline: passivation or inhibition? *Curr. Appl. Phys.*, **4**, 133–136 (2004).
[66] M. Kendig, M. Hon, and L. Warren; 'Smart' corrosion inhibiting coatings, *Prog. Org. Coatings*, **47**, 183–189 (2003).
[67] J.N. Barisci, T.W. Lewis, G.M. Spinks, C.O. Too, and G.G. Wallace, Conducting Polymers as a Basis for Responsive Materials Systems, *J. Intel. Mat. Syst. Str.*, **9**, 723–731 (1998).
[68] S. de Souza, J. E. Pereira da Silva, S. I. Cordoba de Torresi, M.L.A. Temperini, and M.R. Torresi, Polyaniline based acrylic blends for iron corrosion protection, *Electrochem. Solid-State Lett.*, **4**, B27–B30 (2001).
[69] P. J. Kinlen, Y. Ding, and D. C. Silverman, Corrosion protection of mild steel using sulfonic and phosphonic acid-doped polyanilines, *Corrosion*, **58**, 490–497 (2002).
[70] A.C. Chang and L.L. Miller, Electrochemically controlled binding and release of salicylate, TCNQ and ferrocyanide from films of oligomeric 3-methoxythiophene, *J. Electroanal. Chem.*, **247**, 173–184 (1988).
[71] C. Weidlich, K.-M. Mangold, and K. Jüttner, EQCM study of the ion exchange behavior of polypyrrole with different counterions in different electrolytes, *Electrochim. Acta*, **50**, 1547–1552 (2005).
[72] G. Paliwoda-Porebska, M. Stratmann, M. Rohwerder, K. Potje-Kamloth, Y. Lub, A.Z. Pich, and H.-J. Adler, On the development of polypyrrole coatings with self-healing properties for iron corrosion protection, *Corros. Sci.*, **47**, 3216–3233 (2005).
[73] G. Paliwoda-Porebska, M. Rohwerder, M. Stratmann, U. Rammelt, L.M. Duc, and W. Plieth, Release mechanism of electrodeposited polypyrrole doped with corrosion inhibitor anions, *J. Solid State Electrochem.*, **10**, 730–736 (2006).
[74] U. Rammelt, L. M. Duc, and W. Plieth, Improvement of protection performance of polypyrrole by dopant anions, *J. Appl. Electrochem.*, **35**, 1225–1230 (2005).

[75] M. Rohwerder and A. Michalik, Conducting polymers for corrosion protection: What makes the difference between failure and success? *Electrochim. Acta*, **53**, 1300–1313 (2007).
[76] N.T.L. Hien, B. Garcia, A. Pailleret, and C. Deslouis, Role of doping ions in the corrosion protection of iron by polypyrrole films, *Electrochim. Acta*, **50**, 1747–1755 (2005).
[77] A. Hallik, A. Alumaa, H. Kurig, A. Jänes, E. Lust, and J. Tamm, On the porosity of polypyrrole films, *Synth. Met.*, **157**, 1085–1090 (2007).
[78] E. Hermelin, J. Petitjean, J.-C. Lacroix, K.I. Chane-Ching, J. Tanguy, and P.C. Lacaze, Ultrafast electrosynthesis of high hydrophobic polypyrrole coatings on a Zinc electrode: Applications to the protection against Corrosion, *Chem. Mater.*, **20**, 4447–4456 (2008).
[79] T. Van Schaftinghen, C. Deslouis, A. Hubin, and H. Terryn, Influence of the surface pretreatment prior to the film synthesis on the corrosion protection of iron with polypyrrole films, *Electrochim. Acta*, **51**, 1695–1703 (2006).
[80] H. Nguyen Thi Le, M.C. Bernard, B. Garcia-Renaud, and C. Deslouis, Raman spectroscopy analysis of polypyrrole films as protective coatings on iron, *Synth. Metals*, **140**, 287–293 (2004).
[81] R. Ansari, Application of polyaniline and its composites for adsorption/recovery of Cr(VI) from aqueous solutions. *Acta Chim. Slov.*, **53**, 88–94 (2006).
[82] N. Endo, Y. Takeda, M. Higa, and K. Matsusaki, Ion-exchange properties of colloidal particle consisting of polyaniline and poly(vinyl alcohol) fixed on silica-gel powder, *Analyt. Sci.*, **19**, 721–725 (2003).
[83] G.B. Deacon, M. Forsyth, P.C. Junk, and W.W. Leeb, From chromates to rare earth carboxylates: a greener take on corrosion inhibition *Chem. Austral.* **75**, 18–21 (2008).
[84] S. R. Taylor, G.J. Shiflet, J.R. Scully, R.G. Buchheit, W.J. Van Ooij, K. Sieradzki, RE. Diaz, C. J. Brinker, and A. L. Moran, Increasing the functionality of military coatings using nanodimensioned materials. *Corr. Rev.*, **25**, 491–522 (2007).
[85] M. Schirmeisen and F. Beck, Electrocoating of iron and other metals with polypyrrole, *J. Appl. Electrochem.* **19**, 401–409 (1989).
[86] C.A. Ferreira, S. Aeiyach, J.J. Aaron, and P.C. Lacaze; Electrosynthesis of strongly adherent Ppy coatings on iron and mild steel in aqueous media, *Electrochim. Acta* **41**, 1081 (1996).
[87] K. Fraoua, S. Aeiyach, J. Aubard, M. Delamar, P.C. Lacaze, and C.A. Ferreira; XPS and SERS evidence for iron nitrates species responsable of the strong adherence of polypyrrole on iron or steel treated with nitric acid, *J. Adhesion Sci. Technol.* **13**, 517 (1999).
[88] P.C Lacaze, C.A. Ferreira and S. Aeiyach, unpublished results.
[89] W. Su and J.O. Iroh, Formation of polypyrrole coatings onto low-carbon steel by electrochemical process, *J. Appl. Polym. Sci.*, **65**, 417–424 (1997).
[90] J.O. Iroh and W. Su, Characterization of the passive inorganic interphase and polypyrrole coatings formed on steel by the aqueous electrochemical process, *J. Appl. Polym. Sci.*, **71**, 2075–2086 (1999).
[91] M. Bazzaoui, J.I. Martins, S.C. Costa, E.A. Bazzaoui, T.C. Reis, and L. Martins, Sweet aqueous solution for electrochemical synthesis of polypyrrole Part 2. On ferrous metals, *Electrochim. Acta*, **51**, 4516–4527 (2006).
[92] N. Attarzadeh, K. Raessi, and M.A. Golozar, Effect of saccharin addition on the corrosion resistance of polypyrrole coatings, *Prog. Org. Coatings*, **63**, 167–174 (2008)
[93] A.M. Fenelon and C.B. Breslin, The formation of polypyrrole at iron from 1-Butyl-3-methylimidazolium hexafluorophosphate, *J. Electrochem. Soc.*, **152**, D6–D11 (2005)
[94] B. Wessling and J. Posdorfer, Corrosion prevention with an organic metal (polyaniline):corrosion test results, *J. Electrochim. Acta*, **44**, 2139–2147 (1999)
[95] D. Sazou and C. Georgolios, Formation of conducting polyaniline coatings on iron surfaces by electropolymerization of aniline in aqueous solutions, *J. Electroanal. Chem.*, **429**, 81–93 (1997)
[96] C.K. Tan and D.J. Blackwood, Corrosion protection by multilayered conducting polymer coatings, *Corros Sci.*, **45**, 545–557 (2003)
[97] U. Barsch and F. Beck, Electrodeposition of polythiophene from bisthiophene onto iron, *Synth. Met.*, **55**, 1638–1643 (1993).
[98] S. Aeiyach, E.A. Bazzaoui, and P.C. Lacaze, Electropolymerization of thiophene on oxidizable metals in organic media, *J. Electroanal. Chem.*, **434**, 153–162 (1997)

[99] G. Kousik, S. Pitchumani, and N.G. Renganathan, Electrochemical characterization of polythiophene-coated steel, *Prog. Org. Coatings*, **43**, 286–291 (2001)
[100] E.A. Bazzaoui, S. Aeiyach, and P.C. Lacaze, Electropolymerization of bithiophene on Pt and Fe electrodes in an aqueous SDS micellar medium, *Synth. Met.*, **83**, 159–165 (1996).
[101] U. Rammelt, P.T. Nguyen, and W. Plieth, Protection of mild steel by modification with thin films of polymethylthiophene, *Electrochim. Acta*, **46**, 4251–4257 (2001).
[102] T. Tuken, B. Yazici, and M. Erbil, A new multilayer coating for mild steel protection, *Prog. Org. Coatings*, **51**, 205–212 (2004).
[103] C.A. Foss, Jr., G.L. Hornyak, J.A. Stockert, and C.R. Martin, Template-Synthesized Nanoscopic Gold Particles: Optical Spectra and the Effects of Particle Size and Shape, *J. Phys. Chem.*, **98**, 2963–2971 (1994).
[104] K. Naoi, M. Takeda, H. Kanno, M. Sakakura, and A. Shimada, Simultaneous electrochemical formation of Al2O3:polypyrrole layers (I): effect of electrolyte anion in formation process, *Electrochim. Acta*, **45**, 3413–3421 (2000).
[105] D. E. Tallman, C. Vang, G.G. Wallace, and G.P. Bierwagen, Direct Electrodeposition of polypyrrole on aluminum and aluminum alloy by electron transfer mediation, *J. Electrochem. Soc.*, **149**, C173–C179 (2002).
[106] D.E. Tallman, M.P. Dewald, C.K. Vang, G.G. Wallace, and G.P. Bierwagen, Electrodeposition of conducting polymers on active metals by electron transfer mediation, *Current Applied Physics*, **4**, 137–140 (2004).
[107] M. Bazzaoui, J.I. Martins, S.C. Costa, E.A. Bazzaoui, T.C. Reis, and L. Martins, Sweet aqueous solution for electrochemical synthesis of polypyrrole. Part 1-A. On non-ferrous metals. *Electrochim. Acta*, **51**, 2417–2426 (2006).
[108] K. Shah and J. Iroh, Electrochemical synthesis and corrosion behavior of poly(N-ethyl aniline) coatings on Al-2024 alloy, *Synth. Met.*, **132**, 35–41 (2002)
[109] G.S. Akundy, R. Rajagopalan, and J.O. Iroh, Electrochemical deposition of polyaniline-polypyrrole composite coatings on aluminum, *J. Appl. Polymer Sci.*, **83**, 1970–1977 (2002).
[110] J.O. Iroh, Y. Zhu, K. Shah, K. Levine, R. Rajagopalan, T. Uyar, M. Donley, R. Mantz, J. Johnson, N. N. Voevodin, V.N. Balbyshev, and A.N. Khramov, Electrochemical synthesis: a novel technique for processing multi-functional coatings, *Prog. Org. Coatings*, **47**, 365–375 (2003)
[111] J. Petitjean, S. Aeiyach, J.-C. Lacroix, and P.C. Lacaze, Ultra-fast electropolymerization of pyrrole in aqueous media on oxidable metals in a one-step process, *J. Electroanal. Chem.*, **478**, 92–100 (1999).
[112] J. Petitjean, J. Tanguy, J.C. Lacroix, K. I. Chane-Ching, S. Aeiyach, M. Delamar, and P.C. Lacaze, Interpretation of the ultra-fast electropolymerization of pyrrole in aqueous media on zinc in a one-step process: the specific role of the salicylate salt investigated by x-ray photoelectron spectroscopy (XPS) and by electrochemical quartz crystal microbalance (EQCM), *J. Electroanal. Chem.*, **581**, 111–121 (2005).
[113] M. Forsyth, C.M. Forsyth, K. Wilson, T. Behrsing, and G.B. Deacon, ATR characterisation of synergistic corrosion inhibition of mild steel surfaces by cerium salicylate, *Corros. Sci.*, **44**, 2651–2656 (2002).
[114] J.I. Martins, T.C. Reis, M. Bazzaoui, E.A. Bazzaoui, and L. Martins, Polypyrrole coatings as a treatment for zinc-coated steel surfaces against corrosion, *Corros. Sci.*, **46**, 2361–2381 (2004).
[115] T. Tüken, B. Yazıcı, and M. Erbil, The electrochemical synthesis and corrosion performance of polypyrrole on brass and copper, *Prog. Org. Coatings*, **51**, 152–160 (2004).
[116] P. Herrasti, A.I. del Rio, and J. Recio, Electrodeposition of homogeneous and adherent polypyrrole on copper for corrosion protection, *Electrochim. Acta*, **52**, 6496–6501 (2007).
[117] A.C. Cascalheira, S. Aeiyach, J. Aubard, P.C. Lacaze, and L.M. Abrantes, Electropolymerization of Pyrrole on oxidizable metals: role of salicylate ions in the anodic behaviour of copper, *Russ. J. of Electrochemistry*, **40**, 294–298 (2004).
[118] L.M. Martins Dos Santos, J.-C. Lacroix, K.I. Chane-Ching, A. Adenier, L.M. Abrantes, and P.C. Lacaze, Electrochemical synthesis of polypyrrole films on copper electrodes in acidic and neutral aqueous media, *J. Electroanal. Chem.*, **587**, 67–78 (2006).

[119] M. Bazzaoui, J.I. Martins, E.A. Bazzaoui, T.C. Reis, and L. Martins, Pyrrole Electropolymerization on Copper and Brass in a Single-Step Process from Aqueous Solution, *J. of Appl. Electrochem.*, **34**, 815–822 (2004).
[120] M.I. Redondo and C.B. Breslin, Polypyrrole electrodeposited on copper from an aqueous phosphate solution: Corrosion protection properties, *Corros. Sci.*, **49**, 1765–1776 (2007).
[121] J. Wang, Y. Xu, X. Sun, S. Mao, and F. Xiao, Polypyrrole films electrochemically doped with dodecylbenzenesulfonate for copper protection, *J. Electrochem. Soc.*, **154**, C445–C450 (2007).
[122] S.T. Earley; D.P. Dowling, J.P. Lowry, and C.B. Breslin, Formation of adherent polypyrrole coatings on Ti and Ti-6Al-4V alloy, *Synth. Met.*, **148**, 111–118 (2005).
[123] P. Xu, X. Han, C. Wang, D. Zhou, Z. Lv, A. Wen, X. Wang, and B. Zhang, Synthesis of Electromagnetic Functionalized Nickel/Polypyrrole Core/Shell Composites, *J. Phys. Chem. B*, **112**, 10443–10448 (2008).
[124] A. Eftekhari, I. Ahmadi, Electrodeposition of smooth and adherent film of polypyrrole on lead electrode, *Prog. Org. Coatings*, **57**, 371–375 (2006).
[125] B. Wessling, scientific engineering of anti-corrosion coating systems based on organic metals (polyaniline), http://www2.zipperling.de/Research/Documents/PIOC/PIOC-KRZ.en.html.
[126] P.J. Kinlen, D.C. Silverman, and C.R. Jeffreys, Corrosion protection using polyaniline coating formulations, *Synth. Met.*, **85**, 1327–1332 (1997).
[127] D.A. Wroblewski, B.C. Bencewicz, K.G. Thompson, and C.J. Bryan, Corrosion Resistant Coatings from Conducting Polymers. *Polym. Prepr.*. **35**, 265–266 (1994).
[128] R. Racicot, T. Brown, and S.C. Yang, Corrosion protection of aluminum alloys by double-strand polyaniline, *Synth. Met.*, **85**, 1263–1264 (1997).
[129] M. Fahlmann, S. Jasty, and A. Epstein, Corrosion protection of iron/steel by emeraldine base polyaniline: an X-ray photoelectron spectroscopy study, *Synth. Met.*, **85**, 1323–1326 (1997).
[130] L. Cecchetto, A. Denoyelle, D. Delabouglise, and J.-P. Petit, A silane pre-treatment for improving corrosion resistance performances of emeraldine bse-coated aluminium samples in neutral environment; *Appl. Surf. Sci.*, **254**, 1736–1743 (2008).
[131] W.S. Araujo, I.C.P. Margarit, M. Ferreira, O.R. Mattos, and P.L. Neto, Undoped polyaniline anticorrosive properties, *Electrochim. Acta*, **46**, 1307–1312 (2001).
[132] M. Galkowski, M.A. Malik, P.J. Kulesza, H. Bala, K. Miecznikowski, R. Wlodarczyk, L. Adamczyk, and M. Chojak, Protection of steel against corrosion in aggressive medium by surface modification with multilayer polyaniline-based composite film, *J. Electrochem. Soc.*, **150**, B249–B253 (2003).
[133] J.H. Huh, E.J. Oh, and J.H. Cho, Investigation of corrosion protection of iron by Pani blend coatings, *Synth. Met.*, **137**, 965–966 (2003).
[134] A.B. Samui, A.S. Patankar, J. Rangarajan, and P.C. Deb, Study of polyaniline containing paint for corrosion prevention, *Prog. Org. Coatings*, **47**, 1–7 (2003).
[135] S. Sathiyanarayanan, S. Muthukrishnan, G. Venkatachari, and D.C. Trivedi, Corrosion protection of steel by polyaniline (PANI) pigmented paint coating, *Prog. Org. Coatings*, **53**, 297–301 (2005).
[136] E. Armelin, C. Aleman, and J.I. Iribarren, Anticorrosion performances of epoxy coatings modified with polyaniline:A comparison between the emeraldine base and salt forms, *Prog. Org. Coatings*, **65**, 88–93 (2008).
[137] U. Riaz, S. Ahmad, and S. M. Ashraf, Comparison of corrosion protective performance of nanostructured polyaniline and poly(1-naphthylamine)-based alkyd coatings on mild steel, *Mat. Corr.*, **59**, 1–7 (2008).
[138] S. Syed Azim, S. Sathiyanarayanan, and G. Venkatachari, Anticorrosive properties of PANI–ATMP polymer containing organic coating, *Prog. Org. Coatings*, **56**, 154–158 (2006).
[139] A. Kalendova, D. Vesely, J. Stejskal, and M. Trchova, Anticorrosion properties of inorganic pigments surface-modified with a polyaniline phosphate layer, *Prog. Org. Coatings*, **63**, 209–221 (2008).
[140] A. Meroufel, C. Deslouis, and S. Touzain, Electrochemical and anticorrosion performances of zinc-rich and polyaniline powder coatings, *Electrochim. Acta*, **53**, 2331–2338 (2008).

[141] V.J. Gelling, M.M. Wiest, D.E. Tallman, G.P. Bierwagen, and G.G. Wallace, Electroactive-conducting polymers for corrosion control. 4. Studies of poly(3-octyl pyrrole) and poly (3-octadecyl pyrrole) on aluminum 2024-T3 alloy, *Prog. Org. Coatings*, **43**, 149–157 (2001).
[142] D.E. Tallman, K.L. Levine, C. Siripirom, V.G. Gelling, G.P. Bierwagen, and S.G. Croll, Nanocomposite of polypyrrole and alumina nanoparticles as a coating filler for the corrosion protection of aluminium alloy 2024-T3 *Appl. Surf. Sci.*, **254**, 5452–5459 (2008).
[143] C. Ocampo, E. Armelin, F. Liesa, C. Aleman, X. Ramis, and J.I. Iribarren, Application of a polythiophene derivative as anticorrosive additive for paints, *Prog. Org. Coatings*, **53**, 217–224 (2005).
[144] F. Liesa, C. Ocampo, C. Aleman, E. Armelin, R. Oliver, and F. Estrany, Application of electrochemically produced and oxidized Poly(3,4ethylenedioxythiophene) as anticorrosive additive for paints: influence of the doping Level, *J. Appl. Polym. Sci.*, **102**, 1592–1599 (2006).
[145] W. Shengxian, W.D. Wayne, X. Jun, W. Chang, Z. Zhixin, and Z. Yanrong, Coating compositions and methods of making and using them, US Patent Application, 2006134339 (2006).
[146] A. Najari, P. Lang, P.C. Lacaze, and D. Mauer, A new organofunctional methoxysilane bilayer system for promoting adhesion of epoxidized rubber to zinc, *Prog. Org. Coatings*, **64**, 392–404 (2009).
[147] W.J. van Ooij, Improved service life of coated metals by engineering the polymer–metal interface. In *Service Life Prediction of Organic Coatings - A Systems Approach*, ed. D.R. Bauer and J.W. Martin, ACS Symposium Series No. 722, American Chemical Society, Oxford University Press, 1999, 354–377.
[148] A. Seth, W.J. Van Ooij, P. Puomi, Z. Yin, A. Ashirgade, S. Bafna, and C. Shivane, Novel, one-step, chromate-free coatings containing anticorrosion pigments for metals – An overview and mechanistic study *Prog. Org. Coatings*, **58**, 136–145 (2007)
[149] S. Hayes, P. J. Kinlen, J. Rawlins, M. D. Blanton, and Y. Ulyanova, Multi-layer and composite corrosion resistant coatings and applying corrosion resistant coatings to metal substrates, USPTO Application 2008 0317962 PCT International Application , WO 2008143735 A2 20081127, (2008).
[150] E. Jaehne, S. Oberoi, and H-J. P. Adler, Ultra thin layers as new concepts for corrosion inhibition and adhesion promotion, *Prog. Org. Coatings* **61**, 211–223 (2008).
[151] P. Allongue, M. Delamar, B. Desbat, O. Fagebaume, R. Hitmi, J. Pinson, and J.M. Savéant, Covalent Modification of Carbon Surfaces by Aryl Radicals Generated from the Electrochemical Reduction of Diazonium Salts, *J. Am. Chem. Soc.*, **119**, 201–207 (1997).
[152] A O. Solak, L. R. Eichorst, W. J. Clark, and R. L McCreery, Modified carbon surfaces as ''organic electrodes'' that exhibit conductance switching, *Anal. Chem.*, **75**, 296–305 (2003).
[153] A. Adenier, E. Cabet-Deliry, T. Lalot, J. Pinson, and F. Podvorica, Attachment of polymers to organic moieties covalently bonded to Iron surfaces. *Chem. Mater.*, **14**, 4576–4585 (2002).
[154] T. Shimura and K. Aramaki, Preparation of a self assembled monolayer on iron by the formation of covalent bond between carbon and iron atoms, *Corros. Sci.* **48**, 3784–3801 (2006).
[155] A. Adenier, E. Cabet-Deliry, T. Lalot, J. Pinson, and F. Podvorica, Attachment of polymers to organic moieties covalently bonded to Iron surfaces. *Chem. Mater.*, **14**, 4576–4585 (2002).
[156] V. Mevellec, S. Roussel, L. Tessier, J. Chancolon, M. Mayne-L'Hermite, G. Deniau, P. Viel, and S. Palacin, Grafting polymers on surfaces: a new powerful and versatile diazonium salt-based one-step process in aqueous media. *Chem. Mat.*, **19**, 6323–6330 (2007).
[157] L. M. Santos, J. Ghilane, C. Fave, P.-C. Lacaze, H. Randriamahazaka, L. M. Abrantes, and J.-C. Lacroix, Electrografting polyaniline on carbon through the electroreduction of diazonium salts and the electrochemical polymerization of aniline, *J. Phys. Chem. C*, **112**, 16103–16109 (2008).
[158] L. Xu, W. Chen, A. Mulchandani, and Y. Yan, Reversible conversion of conducting polymer fims from superhydrophobic to superhydrophilic, *Angew. Chem. Int. Ed.*, **44**, 6009–6012 (2005).
[159] T. L. Sun, L. Feng, X. F. Gao, and L. Jiang, Bioinspired surfaces with special wettability, *Acc. Chem. Res.*, **38**, 644–652 (2005).

[160] X. Zhang, F. Shi, J. Niu, Y. Jiang, and Z. Wang, Superhydrophobic surfaces: from structural control to functional application, *J. Mater. Chem.*, **18**, 621–633 (2008).
[161] N.J. Shirtcliffe, F.B. Pyatt, M.I. Newton, and G. McHale, A lichen protected by a superhydrophobic and breathable structure, *J. Plant Physiol.*, **163**, 1193–1197 (2006).
[162] N. J. Shirtcliffe, G. McHale, M. I. Newton, G. Chabrol, and C. C. Perry, Dual-scale roughness produces unusually water-repellent surfaces, *Adv Mater.*, **16**, 1929–1932 (2004).
[163] M. Ma and R. M. Hill, Superhydrophobic surfaces, *Curr. Opin. Colloid Interface Sci.*, **11**, 193–202 (2006).
[164] J. Liu, Y. Lin, L. Liang, J.A. Voigt, D.L. Huber, Z.R. Tian, E. Coker, B. Mckenzie, and M. Mcdermott, Templateless assembly of molecularly aligned conductive polymer nanowires: a new approach for oriented nanostructures, *Chem. Eur. J.*, **9**, 604–611 (2003).
[165] M. Li, Z. Wei and L. Jiang, Polypyrrole nanofiber arrays synthetized by a biphasic electrochemical strategy, *J. Mater. Chem.*, **18**, 2276–2280 (2008).
[166] Y. Zhang, R. Lamba, and J. Lewis, Engineering nanoscale roughness on hydrophobic surface—preliminary assessment of fouling behaviour, *Sci. Technol. Adv. Mater.*, **6**, 236–239, (2005).
[167] Y. Wang, C. E. Sims, P. Marc, M. Bachman, G. P. Li, and N. L. Allbritton, Micropatterning of living cells on a heterogeneously wetted surface, *Langmuir*, **22**, 8257–8262, (2006).
[168] W.G. Characklis, Biofouling: effects and control. In *Biofouling and Biocorrosion in Industrial Water Systems* ed. H. C. Flemming and G.G. Geesey, Springer, Berlin, 1991, 7–27.

17

Electrocatalysis by Nanostructured Conducting Polymers

Shaolin Mu[a] *and Ya Zhang*[b]

[a]*Department of Chemistry, Yangzhou University, China*
[b]*School of the Environment, Nanjing University, China*

17.1 Introduction

Many conducting polymers, such as polyaniline [1–3], polypyrrole [4–6], polythiophene [7,8], poly(p-phenylene) [9] and so on, have been synthesized, since the exciting discovery of the dramatic increase in conductivity of polyacetylene after doping was achieved 30 years ago [10]. Clearly, the appearance of conducting polymers opened a significant way to prepare a new type of material. The conducting polymers have received a great deal of interest and are particularly appealing because they exhibit electrical, electronic, magnetic, and optical properties similar to metals or semiconductors while retaining their flexibility, and ease of processing, and moreover, have good redox reversibility and the electrochromic properties. These properties are favorable to their applications in the electronic, physical, chemical, biochemical, and environmental protection fields. Research on conducting polymers is also closely related to the rapid development in nanofibers, nanowires, nanotubes [11–20] and molecular electronics [21]. The nanostructured conducting polymers have aroused considerable attention in their unique properties [22–25] and potential applications [26–32].

Nanostructured Conductive Polymers Edited by Ali Eftekhari

The specific surface area of a nanostructured conducting polymer is much larger than that of the bulk. Martin's research group [13] has shown that the conductivity of the nanostructured conducting polymer, such as polypyrrole, is higher than that of the bulk sample of the same polymer because the former polymer is aligned and ordered. These properties are very advantageous to electrocatalysis. Therefore, the electrocatalytic properties should be observed in nanostructured redox polymers. The reversible redox of a conducting polymer is a basic condition for the electrocatalytic reaction of species, in which the conducting polymer acts as a redox mediator to play an important role in charge transfer. The catalytic activity of a conducting polymer is dependent on its redox activity, which is related to the pH values, applied potentials, and its surface area. Beyond the usable ranges of pH and potential, the conducting polymer loses its electrochemical activity and suffers from an irreversible degradation. Therefore, enhancing the usable ranges of pH, potential, and surface area are very important for conducting polymers used as electrocatalytic materials and are also a challenge to scientists.

In this chapter, we discuss electrocatalysis caused by nanostructured conducting polymers prepared using only electrochemical methods. The electrochemical synthetic techniques of a large variety of conducting-polymer nanocomposites incorporated with nanoparticles of metals [33–38] or metal oxides [39–43] have been previously reviewed [44–46]. Their catalytic activity was mainly caused by nanoparticles of metals or metal oxides themselves, while conducting polymers played an important role in improving dispersion and enhancing stability of nanoparticles of metals and metal oxides. Therefore, the synthetic techniques of these conducting-polymer nanocomposites are kept outside the scope of this chapter, but their electrocatalytic properties are discussed here.

17.2 Electrochemical Synthetic Techniques of Nanostructured Conducting Polymers

The electrochemical synthetic techniques of nanostructured conducting polymers are mainly carried out using galvanostat, potentiostat, and cyclic voltammetry (CV). The advantages of electrochemical over chemical preparation are that the sizes of the nanoparticles are easily controlled by the applied potential, current density, scan rate, and the number of cycles, and especially that the nanostructured conducting polymer deposited on the electrode material can be directly used to investigate its electrochemical properties and *in situ* spectroelectrochemical characteristics.

17.2.1 Synthesis by Cyclic Voltammetry

In order to immobilize enzymes in conducting polymers to fabricate biosensors, the electrochemical synthesis of polypyrrole films was studied under different conditions. It was found that the size and morphology of polypyrrole films synthesized using cyclic voltammetry were affected by the concentration of the supporting electrolyte at a scan potential range between 0.0 and 1.0 V (vs. SCE), and at a scan rate of 48 mV s^{-1} [47]. The diameters of particles prepared in a solution containing 0.10 M pyrrole and 0.10 M NaCl

with pH 2.0 are in the range 20–50 nm, which are tightly arranged on the platinum foil. However, the diameters of polypyrrole particles, obtained in the same solution, but containing 1.0 M NaCl, are in the range 70–400 nm, which is much larger than those prepared in a solution containing 0.10 M NaCl. This difference is attributed to the concentration of the supporting electrolyte. It is known that the oxidation of the conducting polymer is accompanied by the transfer of anions from the solution to the polymer matrix, and vice versa for reduction. The rate of anion exchange between the conducting polymer and the solution increases with increasing electrolyte concentration during repeated potential cycling, because of an increase in the reaction rate. The increase in the rate of anion exchange is disadvantageous for the formation of the polypyrrole nuclei. Therefore, as electrolysis continues, the polymerization of pyrrole takes place preferably on the polypyrrole nuclei due to autocatalytic polymerization [48,49], which results in the formation of polypyrrole particles with larger diameters due to the rapid growth of the polypyrrole nuclei in the concentrated electrolyte.

Gao *et al.* reported the synthesis of aligned coaxial nanowire of carbon nanotubes with polypyrrole or polyaniline using a cyclic voltammetric technique [50]. DC conductivity of the polyaniline-coated nanotube film was measured to be 10 S cm^{-1}, which is higher than that of polyaniline film electrochemically deposited on a gold plate under the same conditions. This is possibly due to the 'doping' effect associated with carbon nanotubes.

Choi and Park synthesized nanosized polyaniline wires and nanorings on a gold electrode using molecular templates [51]. The polymerization was carried out using cyclic voltammetry between –0.10 and 0.90 V (vs. Ag/AgCl in saturated KCl), in a solution containing 20 mM aniline and 1.0 M sulfuric acid. The nanoring shown in Figure 17.1 is about 85 nm in diameter with a ring radius of about 535 nm, leading to about 3.4 μm in total length. The electrolytic time was controlled by scans. The strategy for this technique is that the gold electrode is modified with a self-assembled monolayer of well-separated thiolated cyclodextrins prior to placing in the above electrolyte. Thiolated aniline monomer is

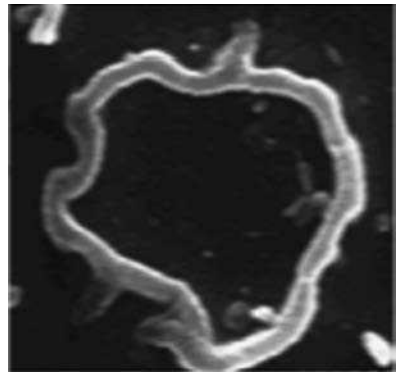

Figure 17.1 *SEM picture of polyaniline nanoring grown potentiodynamically. (Reprinted with permission from Advanced Materials, Electrochemical growth of nanosized conducting polymer wires on gold using molecular templates by S.J. Choi and S.M. Park, 12, 20, 1547–1549. Copyright (2000) Wiley-VCH)*

anchored to the surface within the cyclodextrin cavity and forms an initiation point for polyaniline wire growth.

Vasilieva *et al.* synthesized redox polymers poly[M(Schiff)] (M = Ni, Pd; Schiff = tetradentate Schiff bases) with nanowire diameters in the range 20–200 nm using cyclic voltammetry [52]. They demonstrated that nanostructures based on redox polymers have conductivities that are more than an order of magnitude greater than bulk samples of the same polymers.

The fabrication of polypyrrole wires via electropolymerization within poly(methyl methacrylate) nanochannels on an indium tin oxide (ITO) substrate was reported by Chen *et al.* [53]. The electrochemical synthesis of polypyrrole was performed by a cyclic voltammetry method in aqueous 0.1 M $NaClO_4$ containing 0.1 M pyrrole monomer. The potential was scanned 10 times between –0.7 and +0.6 V vs. Pt at a scan rate of 100 mV s^{-1}. The nanochannels act as templates for electropolymerization of polypyrrole nanowires.

Liu's research group reported a simple method to synthesize polypyrrole or poly (*N*-methylpyrrole)/carbon-nanotube composite films using an ionic surfactant as the electrolyte [54]. The single- or multi-walled CNTs were first dispersed in an aqueous solution containing SDS (sodium dodecyl sulfate), then pyrrole or *N*-methylpyrrole was added to the above mixture; finally the electrochemical polymerization of pyrrole or *N*-methylpyrrole was carried out using repeated potential cycling between –0.2 and +0.8 V (vs. SCE). The typical electrolyte was an aqueous solution of 0.1 M SDS, 25 mM monomer, and 0.17 g l^{-1} CNTs. The SEM image of polypyrrole showed that a uniform film was deposited at the surface of the Au electrode. There were many one-dimensional nanostructures that stood almost vertically on the deposited film. These nanostructures were of roughly uniform size with diameters in the range of several hundreds of nanometers and heights of up to several micrometers. Surfactant SDS not only served as electrolyte and dopant, but dispersed and stabilized the CNTs in the aqueous solution.

In general, the synthesis of nanostructured conducting polymers using the cyclic voltammetry technique was carried out in a single potential window. However, Si *et al.* used cyclic voltammetry in different potential windows to synthesize functional polythiophene nanoparticles on an Au (111) surface [55]. The electrolyte solution consisted of 2 mM (4-benzeno-15-crown-5 ether)-thiophene-3-methylene-amine (BTA), 30 mM $HClO_4$, and 0.1 M $NaClO_4$. Self-assembly of BTA monomers on Au(111) surfaces promoted ordered polymerization to form polymer nanoparticles or clusters by which the size of the polymer nanoparticles could be controlled electrochemically. In the first potential range, the potential window was set a range of –0.1 to +0.9 V (vs. SCE). The purpose of this was probably to produce radical cations. The potential scan was then extended anodically to 1.45 V to form the polymer. The BTA-based polymer films displayed selective sensitivity to potassium ions with a linear dependence on ion concentration over four orders of magnitude.

Polyaniline nanowires with different sizes were synthesized by cyclic voltammetry at different scan rates, in the presence of ferrocenesulfonic acid [24]. The scan potential was controlled at a range between –0.10 and +0.92 V (vs. SCE). Figure 17.2 shows SEM images of polyaniline films obtained by four cycles at scan rates of: (a) 6, (b) 12, and (c) 30 mV s^{-1}, and by six cycles at (d) 60 mVs^{-1}. The SEM images in Figure 17.2 reveal the fact that all films are constructed of interwoven nanofibers with different diameters and

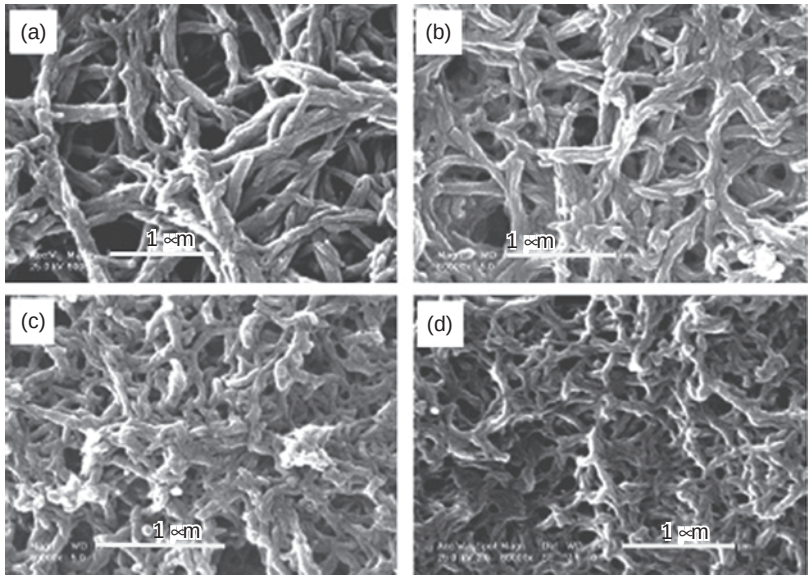

Figure 17.2 *SEM images of polyaniline films obtained at different scan rates: (a) 6; (b) 12; (c) 30; (d) 60 mV* s^{-1}*, scale bar is 1 μm. (Reprinted with permission from Journal of Physical Chemistry B, Spectral Characteristics of Polyaniline Nanostructures Synthesized by Using Cyclic Voltammetry at Different Scan Rates by Shaolin Mu et al., 112, 37, 11558–11563. Copyright (2008) American Chemical Society)*

lengths. The nanofibers in Figure 17.2a have an average diameter of about 130 nm, with lengths varying from 300 nm to 2.6 μm, and the structure is the loosest among the plots in Figure 17.2. As the scan rate increases, the diameter and the length of the nanofibers become smaller and smaller, and the nanostructures become more and more compact. At a scan rate of 60 mV s^{-1}, the nanofibers in Figure 17.2d have an average diameter of about 80 nm with lengths varying from 270 nm to 1.1 μm. It is obvious that the size of polyaniline nanofibers can be controlled by the potential scan rate. There are two steps involved in the electrochemical polymerization of aniline. They are, first, the formation of the polyaniline nuclei and, second, their growth. In general, aniline in an acidic solution can be oxidized, beginning at 0.70 V (vs. SCE), to form polyaniline. For the synthesis of polyaniline using cyclic voltammetry, a slower scan rate is favorable to slow the formation of polyaniline nuclei. This is because, at the slower scan rate, the retention time becomes longer in the aniline oxidation region of 0.70 to 0.92 V under the experimental conditions, which leads to rapid growth of polyaniline nuclei. As a result, the rate of film growth increases due to the longer time allowing more film growth. Therefore, only a few polyaniline nanofibers with large diameters are found in Figure 17.2a. As the electrolysis proceeds slowly at a scan rate of 6 mVs^{-1}, polyaniline continuously forms on the polyaniline nuclei since polyaniline can catalyze the oxidation of aniline [48,49]. In this case, the polymerization of aniline still takes place preferably on the polyaniline nuclei rather than at the naked platinum surface. This is why polyaniline nanofibers in Figure 17.2a are the largest in diameter and the longest in length. Increasing the scan rate from 6 to 12, 30, and 60 mV s^{-1}

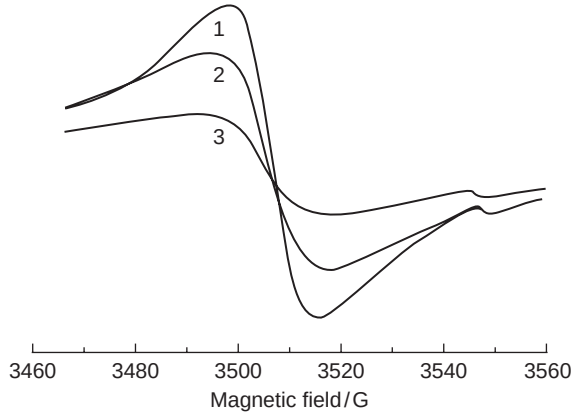

Figure 17.3 *ESR spectra of nanostructured polyaniline samples (each of 10 mg) prepared at different potential scan rates: (1) 6, (2) 12, and (3) 60 mV s^{-1}. (Reprinted with permission from Journal of Physical Chemistry B, Spectral Characteristics of Polyaniline Nanostructures Synthesized by Using Cyclic Voltammetry at Different Scan Rates by Shaolin Mu et al., 112, 37, 11558–11563. Copyright (2008) American Chemical Society)*

is favorable for quicker formation of the polyaniline nuclei, but slower growth. As a result, the amount of polyaniline nuclei deposited on the platinum surface increases with increasing scan rate. Therefore, the images in Figures 17.2a–d show that the surface structure of polyaniline becomes more and more compact and that the nanofiber sizes get smaller and smaller in diameter and shorter and shorter in length as the scan rate increases. Ferrocenesulfonic acid has a large size with positive charge. On the forward scan, the oxidation of aniline results in the formation of polyaniline; meanwhile, ferrocenesulfonic acid with positive charge in the polyaniline film is repelled into the solution due to electrostatic interaction. Regular doping and dedoping processes are favorable for the formation of smaller nanofibers. Therefore, ferrocenesulfonic acid acts as a molecular template for the synthesis of polyaniline nanofibers. Ordered changes in the spectra of X-ray diffraction and ESR with the nanofiber sizes of polyaniline are observed. The crystallinity of polyaniline increases with decreasing diameter of polyaniline nanofibers; the ESR spectra reveals the fact that the decrease in the intensity of the ESR signal is accompanied by increases in the value of the peak-to-peak line width ΔH_{pp} as the diameter of polyaniline nanofiber decreases, which is shown in Figure 17.3.

17.2.2 Synthesis by Potentiostat

As discussed previously, the size of polypyrrole particles synthesized using cyclic voltammetry is affected by the concentration of the supporting electrolyte [47], and also by the electrochemical technique used. Images of polypyrrole film, synthesized at a constant potential of 0.70 V (vs. SCE) and in a solution containing 0.10 M pyrrole and 1.0 M NaCl, show a compact structure composed of nanotubes with diameters of 50–90 nm and lengths varying from 70–160 nm, which are regularly arrayed at the electrode surface. The sizes of these tubes are much smaller than those synthesized using cyclic voltammetry in the same

solution [47]. This is because the periodic doping and dedoping processes of the conducting polymer occur during repeated potential cycling, whereas the doping process only occurs during constant potential electrolysis. Therefore, it is expected that the concentration and size of anion dopants will have larger effect on the morphology of the conducting polymer and the size of polymer particles synthesized using cyclic voltammetry, compared to the constant potential technique.

Kan's research group reported the synthesis of polyaniline spherical nanoparticles in the presence of a magnetic field [56–58]. The electrolytic solution consisted of 0.2 M aniline and 1.2 M HCl. The electrochemical polymerization of aniline was carried out at a constant potential of 0.7 V (vs. SCE) and an applied magnetic field of 780 mT. Images of the polyaniline films indicated that polyaniline nanoparticles synthesized in the presence of the magnetic field were uniformly dispersed on the electrode surface and had an average diameter of about 95 nm (Figure 17.4a); however, polyaniline film synthesized in the absence of magnetic field showed an irregular flake structure with large sizes (Figure 17.4b). It is clear that the applied magnetic field strongly affected the morphology of the polyaniline film and the size of the particles. This is attributable to the orientation effect of a magnetic field on aniline polymerization, since aniline in strongly acidic solution exists in the protonated form with a positive charge. However, the spherical nanoparticles were also produced in a solution containing 0.2 M aniline, 1.0 M HCl, and 0.2 M $CeCl_2$ or other chlorides, such as $NiCl_2$, $CuCl_2$, and $ZnCl_2$ [59]. The electrochemical polymerization of aniline in this solution was carried out at a constant potential of 0.8 V (vs. SCE) in the absence of a magnetic field. The average diameter of most of polyaniline particles obtained in this manner was in the range 50–200 nm. The formation mechanism of polyaniline nanoparticles in this system was suggested by the authors to be as follows [59]: the polyaniline chains are first formed on the ITO electrode surface in the early stages of electropolymerization, then Co^{2+}, Ni^{2+}, Cu^{2+}, or Zn^{2+} in the solution are coordinated with the lone-pair electrons of N atoms in the polyaniline chains. The coordination effect makes polyaniline chains transform into a complex molecule with a polar group, which is similar to a surfactant. According to shaping theory, when the size of a molecule with polar

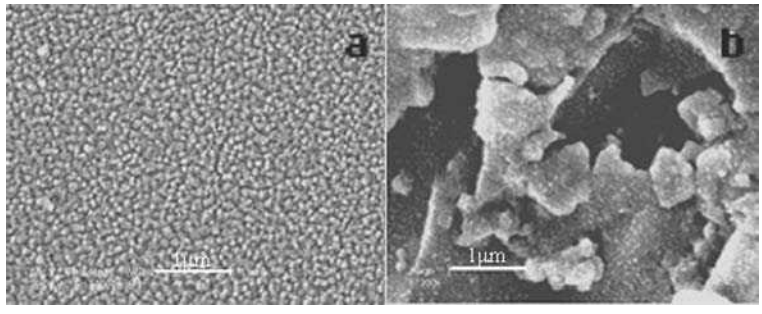

Figure 17.4 *Effect of magnetic field on the morphology of polyaniline films, in the presence (a) and in the absence (b) of a magnetic field at 780 mT, respectively. (Reprinted with permission from Materials Chemistry and Physics, Studies on synthesis and properties of uniform and ordered polyaniline nanoparticles in the magnetic field by J. Kan, Y. Jiang and Y. Zhang, 102, 2-3, 260–265. Copyright (2007) Elsevier Ltd)*

group approaches the proportions of spherical particle morphology, it tends to aggregate spherical particles [60].

Kan's research group also investigated the effect of alcohols on the electrochemical polymerization of aniline at a constant potential of 0.8 V (vs. SCE) [61]. They found that the presence of alcohols favors formation of nanofibers. This is attributed to hydrogen bonding between alcohols and polyaniline chains, which results in the polymer chains being pushed apart [62].

Polypyrrole nanotubes synthesized at a constant potential using the pores of nanoporous polycarbonate (PC) particle track-etched membranes as a template [63,64] and polypyrrole nanowires synthesized at a constant potential of 0.9 V (vs. SCE) using nanochannels of proton-modified natural zeolite clinoptilolite [65] have been reported. Their electrochemical properties were improved compared to the conventional polypyrrole.

Polyaniline nanotubes were synthesized using nanoporous polycarbonate particle track-etched membranes as templates at a constant potential of 0.8 V (vs. Ag/AgCl) [66]. The electrolytic solution consisted of 0.3 M aniline and 1 M HCl and the polymerization time was defined. It was found that the nanostructured polyaniline showed an enhancement of the electronic conductivity compared to analogous polymer bulk conductivity. Tagowska *et al.* investigated the effect of anions on conformation and oxidation states of polyaniline nanotubes by Raman spectroscopy, in which polyaniline nanotubes were synthesized at a constant potential of 0.8 V (vs. Ag/AgCl) using polycarbonate filtration membranes with pore diameters of 100 nm as a template [67]. Figure 17.5 shows the typical SEM picture of polyaniline nanotubules synthesized in 1 M HCl solution. Raman spectra demonstrated a significant result that the kind of anions influenced not only the morphology of the polyaniline nanotubules, but also their oxidation and conformation states. In the presence of ClO_4^- anions, they obtained polyaniline nanotubules in a semioxidized polaronic state and a planar conformation, while in the presence of Cl^- anions polyaniline nanotubules were formed in a fully oxidized state (bipolaronic form) and the chains were twisted. This indicates that polyaniline nanotubules synthesized in the presence of ClO_4^- were not

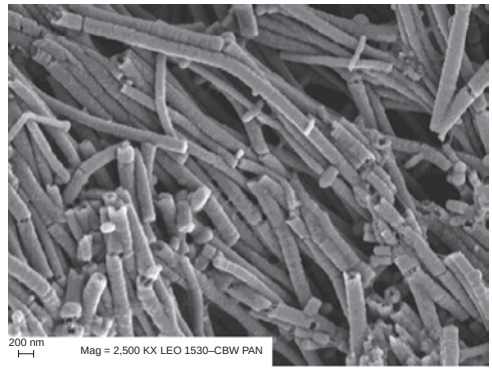

Figure 17.5 *SEM of typical polyaniline nanotubules. (Reprinted with permission from Synthetic Metals, Polyaniline nanotubules—anion effect on conformation and oxidation state of polyaniline studied by Raman spectroscopy by Magdalena Tagowska, Barbara Palys and Krystyna Jackowska, 142, 1-3, 223–229. Copyright (2004) Elsevier Ltd)*

easily overoxidized compared to those formed in the presence of Cl^-, even though the polymerization of aniline in the two different solutions was carried out at the same potential. This indicates that the electrochemical properties of polyaniline synthesized in the presence of ClO_4^- anions are better than those of polyaniline synthesized in the presence of Cl^- ions because there was less tendency for overoxidation.

Shi's research group reported the electrochemical synthesis of polypyrrole nanowires with diameters of 120–500 nm and lengths of several micrometers [68]. The polymerization of pyrrole was performed in a solution containing pyrrole and 1-pyrenesulfonic acid (PSA), in which PSA acts as both surfactant and dopant. The potential was fixed at 1.1 V (vs. SCE). Electrochemical investigation demonstrated that polypyrrole wires have much stronger electrochemical activity than the conventional flat polypyrrole film because of their higher specific surface area. They suggested that the polypyrrole wires were possibly formed through a micelle-guided growth process. The structures of the micelles might change from spherical to rod- and lamellar-shaped as the concentration of the surfactant was increased, which would influence on the morphology of the polypyrrole wires. Therefore, the micelles adsorbed on the electrode surface would act as the templates.

Zhang *et al.* reported the template-free electrochemical synthesis of a superhydrophilic polypyrrole nanofiber network at a constant potential of 0.85 V (vs. Ag/AgCl) [69]. The electrolyte solution consisted of pyrrole, $LiClO_4$, and phosphate. A 300-nm thick gold film deposited on silicon wafer with an intermediate layer of Ti was used as the working electrode. As shown in Figure 17.6, a homogeneous polypyrrole nanofiber network was synthesized at a large scale without the assistance of any 'hard' or 'soft' template. The diameters of the nanofibers were in a range 50–220 nm, and could be simply controlled by the reaction time, from 2 min (Figure 17.6c) to 1 h (Figure 17.6d). The authors proposed the mechanism of nanofiber formation to be as follows [69]. It is known that pyrrole can form various oligomers and further randomly aggregate or self-assemble, strongly dependent on the nature of its interaction with the anion present and/or the surface of the electrode. Therefore, the presence of hydrogen bonding between phosphate and pyrrole oligomers is essential to producing the 1-D nanofiber structure, and the electrostatic interactions between dopant ions and pyrrole oligomers leads to an irregular nanostructure [69]. This is a simple, environmentally friendly and one-step approach to fabricate a polypyrrole film with a unique nanostructure.

Xiao *et al.* investigated the electrochemical synthetic mechanism of conducting-polymer nanotubes in a porous alumina template using poly(3,4-ethylenedioxythiophene) (PEDOT) as a model compound [70]. The electrochemical polymerization of EDOT was performed potentiostatically at various potentials from 1.0 to 1.8 V (vs. Ag/AgCl) in a solution containing EDOT, $LiClO_4$, and acetonitrile. They found that the tubular portion of the nanotube structure increased as the applied potential increased from 1.4 to 1.8 V at a fixed concentration of EDOT, while the tubular portion decreased with increasing monomer concentration from 10 to 100 mM at a fixed potential of 1.6 V.

The synthesis of polypyrrole–heparin nanotubes was performed at a constant potential of 0.8 V (vs. SCE), using a nanoporous membrane as a template [71]. Heparin, which is a bioactive polyelectrolyte, was used as the doping anion. The use of a bioactive doping compound, which provides interesting biological properties in the composite sample, allows the fabrication of functionalized surfaces able to promote direct electronic communication between biological species and substrates. This result also confirmed that the

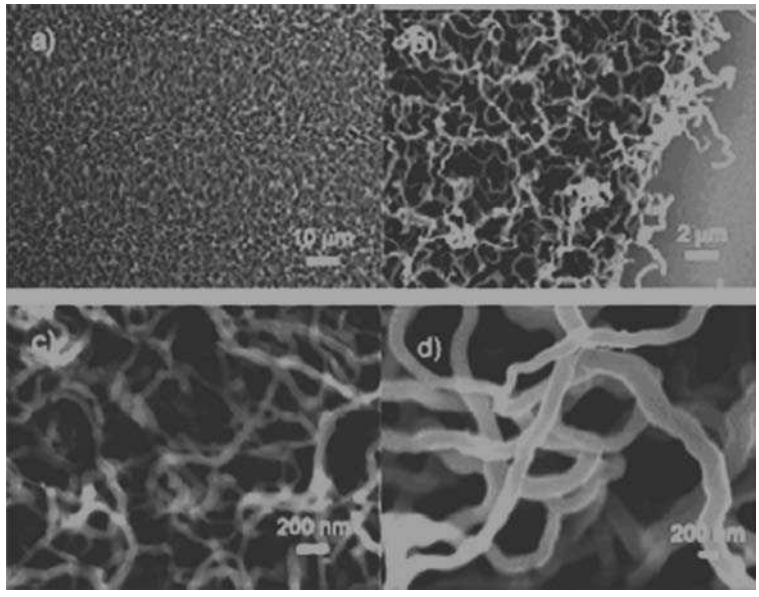

Figure 17.6 *FESEM images of polypyrrole nanofiber network: (a) Low magnification image and (b) edge view of the polypyrrole nanofiber network. High magnification images of polypyrrole nanofiber network formed at (c) 120 s and (d) 1 h. (Reprinted with permission from Macromolecules, Template-Free Electrochemical Synthesis of Superhydrophilic Polypyrrole Nanofiber Network by J.F. Zhang, C. M. Li, S. J. Bao et al., 41, 19, 7053–7057. Copyright (2008) American Chemical Society)*

morphology of conducting polymers is strongly affected by the nature of the anions used as dopants during the electrosynthesis.

17.2.3 Synthesis by Galvanostat

Liang *et al.* reported the direct electrochemical synthesis of large arrays of uniform and oriented nanowires of polyaniline with diameters much smaller than 100 nm, on a variety of substrates, without using a supporting template [72]. They designed a three-step electrochemical deposition procedure with different current densities. In the first step, a large current density was used to create the nucleation sites on the substrate. The initial stage was followed by continued polymerization at reduced current density in a two-step procedure. A typical procedure involved electrochemical deposition in an aniline-containing electrolyte solution, by using the substrate as the working electrode. This process involved 0.08 mA cm^{-2} for 0.5 h, followed by 0.04 mA cm^{-2} for 3 h, which was then followed by another 3 h at 0.02 mA cm^{-2}. Reducing the current density produced uniform and oriented nanowires. They suggest that the nanowires are formed by the following mechanism: (i) nucleation on the substrate at a high current, and (ii) continued nucleation and growth at the low current density.

Tseng's research group reported a template-free, site-specific, and scalable electrochemical method for the fabrication of individually addressable polyaniline nanoframework electrode junctions (PNEJs) in a parallel-oriented array [73]. These polyaniline nanoframeworks, which are composed of numerous intercrossing polyaniline nanowires that have uniform diameters ranging from 40 to 80 nm, can be used for the chemical sensing of HCl and NH_3 gases, and ethanol vapour, and for sensing the pH of aqueous NaCl solutions. They chose to prepare 10 PNEJs simultaneously by growing 10 polyaniline nanoframeworks site-specifically from one set of electrodes to other set of electrodes across 2-μm gaps. The electrochemical process could be divided into three continuous steps. In the first step, a constant current (50 nA) was applied to introduce the polyaniline nuclei onto the Pt working junction electrodes. This relatively high current enables a large quantity of the initial polyaniline nuclei to form on the electrode surface. They serve as seeds for the growth of the nanoframeworks during the following two steps. After this first step, the current was reduced to 25 nA. During the second step, the polyaniline nanoframeworks began to propagate from the working junction electrodes to the other set of junction electrodes. Finally, the current was further decreased to 12 nA. After 180 min, the 10 PNEJs were obtained simultaneously in a parallel array with each polyaniline nanoframework positioned precisely within the 2-μm gap between its electrodes. It is clear that this method is very similar to the report by Liang *et al.* [72].

Ramanathan *et al.* reported a facile technique for fabrication of individually addressable polyaniline and polypyrrole nanowire arrays of controlled dimension and high aspect ratio (100 nm wide by up to 13 μm long), and site-specific positioning, using a single-step electrodeposition between electrodes in channels [74]. The electropolymerization was performed in the galvanostatic mode by applying a desired current, while the potential of the working electrode was monitored continuously with respect to a pseudo reference electrode. This technique is capable of producing arrays of individually addressable nanowire sensors, with site-specific positioning, alignment, and chemical compositions. Based on this technique, they fabricated field-effect transistors based on single nanowires of conducting polymers (i.e., polyaniline and polypyrrole) [75].

The nanostructured polyaniline was synthesized at a constant current in the presence of an ionic liquid (1-ethyl,3-methylimidazolium bromide) [76]. The electrolytic solution consisted of 1 M aniline, 1 M HCl, and 2 M ionic liquid. The ionic liquid acts as a supporting electrolyte as well as a dopant. Also, polyaniline nanofibers were synthesized at a constant current using a stainless-steel plate as a working electrode in a solution containing 0.5 M aniline and 2.0 M H_3PO_4 [77]. The authors assumed that the nanofibers may be derived from the gels formed during the electrochemical deposition [77]. They also found that the dendritic degree of polyaniline nanofibers is related to dopants, and the order is as follows: PANI-H_3PO_4 > PANI-H_2SO_4 > PANI-HNO_3. No nanofibers were obtained using CH_3COOH as dopant due to the high solubility of PANI-CH_3COOH [77].

Lu's research group electrochemically synthesized polypyrrole nanotubes using stainless steel as a working electrode [78]. The electrochemical polymerization was performed under a constant current density of 1 mA cm^{-2} in a solution containing pyrrole, KNO_3, and methyl orange. It is worthy of note that methyl orange is not a surfactant molecule since it lacks surfactant properties such as effective lowering of the surface tension and a well-defined critical micelle concentration, while it can form a fibrillar precipitate on the electrode via electric flocculation in a neutral aqueous solution prior to the polymerization

of pyrrole. Thus, the fibrillar precipitate of methyl orange acts as a template for the subsequent growth of polypyrrole nanotubes. It is interesting that polypyrrole nanotubes synthesized in this manner showed a high conductivity and an ability to alter photochemically the electrical behavior.

For all the above electrochemical synthetic techniques, the electrolysis time for the synthesis of nanostructured conducting polymers must be controlled, depending on the experimental methods and conditions, as the sizes of the conducting polymers, such as nanoparticles, nanorods, nanofibers, and nanotubes, will continuously grow with time.

17.3 Electrocatalysis at Nanostructured Conducting-Polymer Electrodes

An electrocatalytic reaction almost always involves a nonelectroactive species (Z) in the following chemical reaction, which regenerates starting material [79]:

$$O + ne \rightleftharpoons R \tag{17.1}$$

$$R + Z \rightleftharpoons O + Y \tag{17.2}$$

If species Z is present in large excess compared to O, then (17.2) is a pseudo-first-order reaction. To compare conveniently catalytic activity between the nanostructured conducting polymer and the bulk polymer, the key thing is that the amounts of the conducting polymer deposited on the electrode should be equal. The characteristics of the electrocatalytic reaction are related to the electrochemical techniques used. These characteristics are an increase in current density for potentiostat; a shift in peak potentials for oxidation and reduction toward less positive potentials and more positive potentials, respectively, for galvanostat; and an increase in the oxidation or reduction peak current, or a shift of the peak potentials of oxidation and reduction toward less positive potentials and more positive potentials, respectively, or both for cyclic voltammetry.

17.3.1 Electrocatalysis by Pure Nanostructured Conducting Polymers

Some conducting polymers themselves have catalytic ability [80–84] because they can be oxidized and reduced reversibly, which provides an advantageous condition for enhancing the charge-transfer rate. However, a necessary condition for electrocatalysis is that the redox potential of the species to be oxidized or reduced by the conducting polymer is within the potential range in which the conducting polymer itself is electroactive. In general, the electric activity of the conducting polymer is dependent on pH. In fact, each conducting polymer has own useable potential and pH range, which should be considered before choosing the conducting polymer as a catalyst in the electrocatalytic field. For an electrocatalytic reaction caused by a conducting polymer, the catalytic activity of the nanostructured conducting polymer must be greater than that of the corresponding bulk polymer because of the smaller specific surface area in the latter case. For convenience, synthesis methods, electrocatalytic methods, and electrocatalytic characteristics of pure nanostructured conducting polymers are listed in Table 17.1.

Table 17.1 *Synthesis methods and electrocatalytic characteristics of nanostructured conducting polymers*

Polymer	Synthesis method and electrode material	Catalyzed species	Electrolysis method	*Characteristics*	*Ref.*
PAN	Galvanostat, PAN/MWNTs/Au, PAN/PS/GC	Nitrite reduction	Potentiostat	Increase in the reduction current	[85,86]
3-D POA	Galvanostat with a three-step procedure, 3-D POA/Pt	Cytochrome c redox	CV	Negative shift of the formal potential	[90]
PAN/polycatechol	CV with two steps, polycatechol/ PAN/Pt	Oxidation of ascorbic acid	CV	Negative shift of the oxidation peak potential	[91]
PANOA	CV with different scan cycles, PANOA/Pt	Catechol oxidation	CV	Negative shift of the oxidation peak potential and an increase in the peak current	[92]

Nitrite is more difficult to reduce. However, it was found that nitrite could be reduced at the polyaniline (PAN) carbon nanotube composite-modified electrode, which was fabricated by galvanostatic electropolymerization of aniline on a multiwalled carbon nanotube (MWNTs)-modified gold electrode. This electrode exhibited enhanced electrocatalytic behavior for the reduction of nitrite and facilitated the detection of nitrite at an applied potential 0.0 V (vs. SCE) [85]. Evidence for the catalytic behavior was that no obvious response was observed at a bare gold electrode, indicating that nitrite is difficult to reduce at a bare gold electrode at 0.0 V. The carbon nanotubes used here did not take part in the electrochemical reaction, but played an important role in enhancing the surface area of the electrode. The above experimental result was confirmed by Luo *et al.* [86]. They used the polyaniline/polystyrene (PS) nanocomposite electrode to study the reduction of nitrite. The electrode was prepared on an electrochemically pretreated glassy carbon (GC) electrode, which had been previously modified with multilayer of PS nanoparticles with a diameter of 100 nm. Polyaniline was electropolymerized and grown through the interstitial spaces between the PS nanoparticles, which formed a nanocomposite film of polyaniline and PS nanoparticles on the electrode surface. The experimental result demonstrated that the catalytic response of the polyaniline/PS nanocoposite film to nitrite was more than 10-fold greater than that of an equivalent bulk-polyaniline film. On the basis of the electrocatalytic reduction of nitrite on the nanostructured polyaniline, both were used to detect the concentration of nitrite.

It is known that cytochrome c often exhibits direct quasi-reversible voltammetric responses at metal oxide [87] and nonmetal electrodes [88], but shows almost no voltammetric redox peaks at bare metal electrodes [89] because of its very slow electron-transfer rate. However, Dong's research group observed the direct electrochemistry of cytochrome

c at the 3-D poly(orthanilic acid) (POA) nanonetwork-coated platinum electrode [90]. The significant evidence for this is that a pair of well-defined redox waves with formal potential ($E^{0'}$) of –0.032 V (vs. Ag/AgCl) was achieved at a scan rate of 20 mVs^{-1}. The interaction between cytochrome c and poly(orthanilic acid) makes the formal potential shift negatively compared to that of cytochrome c in solution ($E^{0'} = 0.017$ V, $\upsilon = 20\,mV\,s^{-1}$). This is caused by electrocatalytic redox due to the nanonetwork conducting polymer.

It was found that polyaniline nanofibers coated with polycatechol (60–90 nm) have good electrochemical activity over a wide pH range and can catalyze the oxidation of ascorbic acid in a 0.1 M citrate buffer solution of pH 5.6 [91]. An oxidation peak of ascorbic acid appears at 0.05 V (vs. SCE). The catalytic characteristics are that its oxidation peak potential is lower than that at the bare platinum electrode and that polymer nanofibers with the diameters of 60–90 nm have a higher catalytic activity (current density) than those with diameters of 140–210 nm.

Copolymer poly(aniline-co-*o*-aminophenol) (PANOA) nanostructured fibers with average diameters in the range 70–107 nm exhibited electrocatalytic oxidation to catechol in a Na_2SO_4 solution with pH 5.0 [92]. Figure 17.7A shows a cyclic voltammogram for the electrochemical oxidation of catechol on the bare platinum electrode. An anodic peak appears at 0.55 V (vs. SCE) that is attributed to the oxidation of catechol. This platinum electrode was used to synthesize the copolymer films for experiments on the oxidation of ascorbic acid. Curves 1–4 in Figure 17.7B are the cyclic voltammograms of the electrochemical oxidation of catechol on copolymer films with different sizes of fibers that were synthesized by using repeated potential cycling for 8, 10, 14, and 18 cycles at a scan rate of 60 $mV\,s^{-1}$, respectively, in a solution containing aniline, *o*-aminophenol, ferrocenesulfonic acid, and sulfuric acid. Their corresponding average diameters were

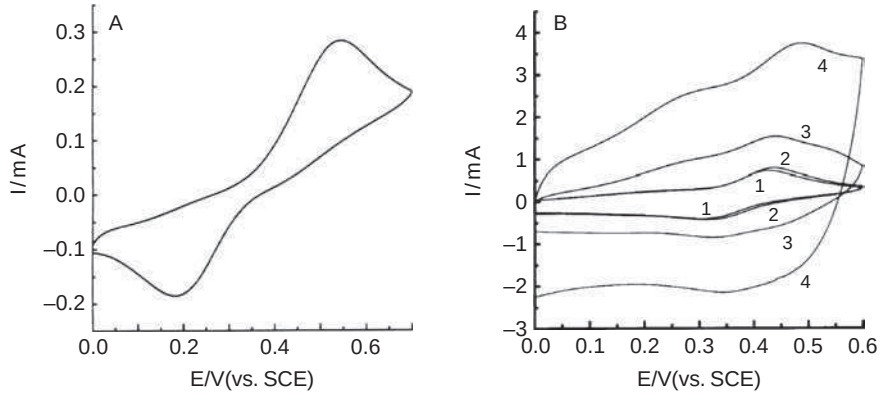

Figure 17.7 *(A) Cyclic voltammogram of catechol on a platinum electrode. (B) Effect of poly(aniline-co-o-aminophenol) fiber diameter on the electrochemical oxidation of catechol, at a scan rate of 60 mV s^{-1}. Average fiber diameter: (1) 70 nm, (2) 90 nm, (3) 100 nm, (4) 107 nm, in a solution consisting of 5 mM catechol and 0.3 M Na_2SO_4 with pH 5.0. (Reprinted with permission from Electrochimica Acta, Poly(aniline-co-o-aminophenol) nanostructured network: Electrochemical controllable synthesis and electrocatalysis by Shaolin Mu, 51, 17, 3434–3440. Copyright (2006) Elsevier Ltd)*

70, 90, 100, and 107 nm, respectively. The potentials of anodic peaks on curves 1–4 are 0.423, 0.434, 0.442, and 0.485 V, respectively, which are attributed to the oxidation of catechol on the copolymer electrodes. All these peak potentials are less positive than that of the catechol oxidation on the bare platinum electrode (Figure 17.7A). This is strong evidence for electrocatalytic oxidation. Additional evidence is that the oxidation current of catechol on the copolymer electrode is higher than that on the bare platinum electrode under exactly the same conditions, for example the anodic peak current of catechol on the bare platinum electrode is 0.28 mA in Figure 17.7A, and that of catechol on the copolymer electrode is 0.75 mA on curve 1 and 1.5 mA on curve 3 in Figure 17.7B. The currents of the anodic peaks on curves 1 and 3 in Figure 17.7B are caused by both the oxidation of the copolymer itself and the oxidation of catechol. However, the anodic peak currents of the two copolymers are 0.22 and 0.80 mA (CVs omitted here) in the same solution, but without catechol. Therefore, the net oxidation currents of catechol in curves 1 and 3 in Figure 17.7B are 0.53 and 0.70 mA, respectively. It is obvious that the net oxidation current of catechol on the copolymer electrode is much higher than that on the bare platinum electrode, even if their anodic peak potentials in Figure 17.7B are lower than that on the bare platinum electrode in Figure 17.7A. Figure 17.7B also shows that the oxidation potential of catechol increases with increasing diameter of the copolymer fibers, for example the anodic peak potential on curve 1 is lower than that on curve 2. This result is expected because of the smaller average diameters of the fibers in the former case.

17.3.2 Electrocatalysis at the Electrodes of Conducting-Polymer Nanocomposites

Inorganic nanoparticles of different natures and sizes can be combined with conducting polymers to form conducting-polymer nanocomposites using both chemical and electrochemical routes. A large variety of metal nanoparticles have been chosen for the preparation of conducting-polymer nanocomposites [44]. However, only metals having catalytic activity, such as Pt, Au, etc. are focused on in this section. The applications of conducting-polymer nanocomposites in the electrocatalytic field and their catalytic characteristics are listed in Table 17.2.

17.3.2.1 Electrocatalysis of Oxygen Reduction

The electrocatalysis of oxygen reduction is a very interesting research area due to its great importance in fuel cells and sensors. Among all the electrodes reported [93,94], the noble metals, in particular platinum and its alloys, are considered to be the best electrocatalysts for oxygen reduction. However, the disadvantages of high cost, the very sluggish kinetics of oxygen reduction, poisoning by impurities, and biofoiling in biological systems limit their practical applications in energy conversion and biosensors. Nanoparticles of Pt or other noble metals with high surface-area-to-volume ratios exhibit promising reactivity toward the reduction of oxygen and the oxidation of hydrogen or methanol. In this case, the dispersion of nanoparticles during preparation and the stability of nanoparticles in high ionic strength environments become very important. The conducting polymer/metal or

Table 17.2 *Electrocatalytic characteristics of conducting polymer nanocomposites*

Polymer nanocomposites	Catalyzed species	Catalysis method	Characteristics	Ref.
PAN/PMo_{12}/Pt	Oxygen reduction	CV	High reactivity toward oxygen reduction	[95,96]
PPy/Au/ITO	Oxygen reduction	CV	Increase in reduction current density	[33]
TPPS/Co/PPy TPPS/Co/PAN	Oxygen reduction	CV	Positive shift of the reduction peak potential and an increase in peak current	[98,35]
POA/Pt/GC	Oxidation of hydrogen and methanol	CV	Increase in the anodic peak current density and negative shift of the onset potential	[100,101]
PAN/Au with NSA	Oxidation of ascorbic acid	CV	Negative shift of the anodic peak potential and increase in the oxidation current	[102]

Metal particles used here are nanometer sized.

metal oxide nanocomposites play an important role in improving the dispersion and stability of the nanoparticles.

An electrode constructed of phosphomolybdate ($PMo_{12}O_{40}^{3-}$) or ($PW_{12}O_{40}$)-decorated Pt nanoparticles (immobilized within ultrathin polyaniline film) was used to investigate oxygen reduction [34,95]. The electrolyte was 0.5 M H_2SO_4 saturated with oxygen. The cyclic voltammogram shows that the reduction of oxygen at a PMo_{12}-protected Pt (with polyaniline film) electrode appeared at 0.51 V (vs. Ag/AgCl). This peak potential value is comparable to those reported previously for oxygen reduction at polycrystalline Pt or platinized tungsten oxide electrodes [96]. Therefore, the phosphomolybdate-decorated Pt nanoparticles showed promising reactivity toward the electroreduction of oxygen.

Li and Shi reported the preparation of two-dimensional gold nanostructures via electrochemical deposition of gold nanoparticles onto an indium tin oxide (ITO) glass substrate modified with thin polypyrrole (PPy) film [33]. By controlling the electrodeposition conditions, gold nanoparticles with dendritic rod-, sheet-, flower- (consisting of staggered nanosheets), and pinecone-like structures were generated. Among them, the flower-like gold nanoparticles showed high catalytic activity for the electrochemical reduction of oxygen, and its activity (reduction current density) was measured to be approximately 25 times that of gold pinecones and 10^4 times that of gold nanosheets in terms of gold weight, and 20.3 times that of gold wire in terms of film area. The electrolyte was an aqueous solution of 0.01 M $LiClO_4$ and 0.1 M $HClO_4$ with saturated oxygen. The pinecone-like naonoparticles can form a compact film with nano-/microscale structures like a lotus-leaf.

Zhou *et al.* reported template-synthesized cobalt porphyrin/polypyrrole (TPPS-Co/PPy) nanocomposite and its electrocatalysis of oxygen reduction in a phosphate buffer solution (PBS) [97]. With the assistance of ultrasonication and different preparation procedures, the nanocomposite can be electrochemically synthesized with uniform 2-D and 3-D nanostructures. Lines (a) and (b) of Figure 17.8 show the cyclic voltammograms of a cobalt

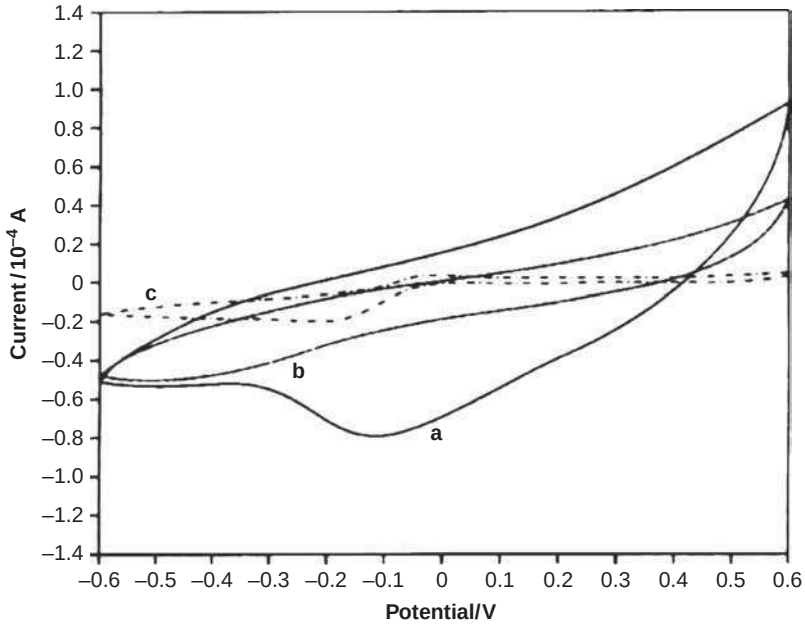

Figure 17.8 *Cyclic voltammograms of: (a) the TPPS-Co/PPy nanocomposite-coated electrode in the O_2-saturated PBS (solid line); (b) the TPPS-Co/PPy nanocomposite-coated electrode in the N_2-saturated PBS, and (c) the bare Au electrode in the O_2-saturated PBS; scan rate is 50 mV s^{-1}. (Reprinted with permission from Journal of Physical Chemistry C., Template-Synthesized Cobalt Porphyrin/Polypyrrole Nanocomposite and Its Electrocatalysis for Oxygen Reduction in Neutral Medium by Qin Zhou, Chang Ming Li, Jun Li et al., 111, 30, 11216–11222. Copyright (2007) American Chemical Society)*

porphyrin/polypyrrole nanocomposite-modified gold electrode in O_2- and N_2-saturated PBS (0.01 M, pH = 7.4), respectively. It can be observed that there is a new and pronounced cathodic process over a wide range of potentials in the O_2-saturated PBS. In addition, compared with the bare Au electrode in the O_2-saturated PBS (Figure 17.8C), the peak potential (or the onset potential) of the oxygen reduction shifts positively and the peak current increases greatly. These results are clear indications of the occurrence of considerable electrolysis at the nanocomposite-modified electrode for the oxygen reduction. In order to exclude the effect of polypyrrole itself, the electrocatalytic activity of pure polypyrrole was checked by cyclic voltammograms in the O_2- and N_2-saturated PBS, respectively. The results showed that there was no obvious electrocatalysis caused by pure polypyrrole in the neutral medium (not shown here). On the basis of all these experimental results, it can be concluded that the TPPS-Co/PPy nanocomposite is a good electrocatalyst for oxygen reduction in a neutral medium. The authors presented a catalytic mechanism of this nanocomposite [97]: TPPS-Co in the nanocomposite acts as the electroactive center for the oxygen reduction, and the high density of three-dimensional nanorods provides a high concentration of the electroactive centers for the oxygen reduction. Additionally, the interaction between the π-electron conjugated system of TPPS-Co and that of polypyrrole

enhances electron-transfer through the nanocomposite, which can allow rapid electron transfer from the electrode to the active metal centers.

A TPPS-Co/polyaniline nanocomposite-modified glassy carbon electrode also showed significant electrocatalytic activity for the oxygen reduction in acidic solution with the number of electrons close to four [35]. In 1 M HCl, the activity of the nanocomposite-modified GC electrode is comparable to that of a Pt disk electrode in terms of both the number of electrons involved and the electrode potential. These features make the nanocomposite attractive for some applications, especially as an oxygen reduction electrode in HCl solutions.

17.3.2.2 Electrocatalysis of the Oxidation of Hydrogen and Methanol

Electrochemical oxidation of methanol is important for application in direct methanol fuel cells. Among metal catalysts, platinum is generally used as an electrocatalyst for such an oxidation. However, it suffers from poisoning by CO, formed as a by-product, and other adsorbed species. A promising way to enhance electrocatalytic activity of Pt and reduce its poisoning effect is to fabricate conducting polymer/Pt composite electrodes.

Dispersing metallic particles inside conducting polymers gives the possibility of electrocatalytic electrodes. Indeed, the polymer provides the possibility of higher surface areas and is conducting in the potential range where the organic molecule is oxidized. A platinum-modified polyaniline electrode was fabricated via the electrochemical deposition of platinum particles in the polyaniline film, which was achieved by electrolysis at a constant potential using an acidic hexachloroplatinate solution [98]. This electrode was used to investigate the oxidation of hydrogen and methanol, and was found to have a higher electrocatalytic activity than the bulk platinum electrode. Moreover, the poisoning effect was drastically decreased, as proved by *in situ* EMIRS spectrum studies, which showed no significant CO_{ads} signal. The kinetic results showed that the methanol electro-oxidation was first order with respect to methanol and that the main oxidation product was formaldehyde.

Based on the stepwise oxidation (three-step method with constant potential) of *o*-anisidine, nanofibrillar porous poly(*o*-anisidine) (POA) film was formed on a glassy carbon electrode [99]. Then loading of Pt nanoparticles into a nanofibrillar POA matrix was performed by a two-step process: first, doping or sorption of $[PtCl_6]^{2-}$ ions by simply dipping into a Pt complex solution for 1 to 2 min and allowing the polymer film to dry for 15–20 min; next, reduction of Pt(IV) metal ions to Pt(0) metallic nanoparticles was carried out under a constant potential, which resulted in Pt particles (10–20 nm) distributed throughout in the polymer matrix. A POA/Pt composite formed in this way was used to investigate the electrocatalysis of methanol oxidation [99]. The results indicated that this electrode had higher electrocatalytic activity because of its very high surface area (17 times higher than bulk Pt) and less poisoning effects than bulk Pt. The peak current density of electrochemical oxidation of methanol was found to be approximately 8.6 times higher than that of bulk Pt. In addition, the chronoamperometry result revealed that POA/Pt composite catalyst prepared by this stepwise procedure showed 1.5 times higher catalytic activity than POA/Pt composite catalyst prepared by the potential cycling method. The enhanced rate of electrocatalytic activity may be due to finely dispersed Pt nanoparticles in a POA nanofibrillar matrix and attributed to POA encapsulation of Pt nanoparticles.

Zhao *et al.* reported the preparation of a nanostructured polypyrrole/carbon composite electrode via Pt particles with 3–4 nm diameter deposited on a polypyrrole/carbon composite with naphthalene sulfonic acid (NSA) as dopant, which was used as the anode of fuel cells for hydrogen or methanol oxidation [100]. Cyclic voltammograms of hydrogen and methanol oxidation showed that this electrode exhibited better catalytic activity than those on plain carbon. This result might be due to higher electrochemically available surface area, electronic conductivity, and easier charge transfer at polymer/carbon particle interfaces allowing high dispersion and utilization of deposited Pt nanoparticles [100].

17.3.2.3 Electrocatalysis of the Oxidation of Ascorbic Acid

Granot *et al.* found that composite materials consisting of polyaniline/poly(4-styrenesulfonate) (PAN/PSS) or polyaniline/Au nanoparticles capped with 2-mercaptoethane sulfonic acid (PAN/Au-NPs) are able to catalyze the oxidation of ascorbic acid [101]. Figure 17.9 shows the electrochemical oxidation of ascorbic acid by PAN/Au-NPs, PAN/PSS, and bare Au electrodes. The electrocatalyzed oxidation of ascorbic acid by PAN/Au-NPs is about twice as efficient as with the PAN/PSS system (the two electrodes include the same content of PAN, $\sim 1.9 \times 10^{-8}$ mol cm^{-2}). For comparison, they studied also the oxidation of ascorbic acid by a bare Au electrode. The anodic peak current was observed at more positive potentials than with the PAN-modified electrodes, implying that the polymer matrixes act as catalysts for the oxidation of ascorbic acid. Figure 17.10 shows the anodic current at 0.1 V (vs. SCE) developed by the two PAN-modified electrodes and the bare Au electrode. The overpontential required for the oxidation of ascorbic acid was controlled by the modifier associated with the electrode, and the lowest overpotential was observed with the PAN/Au-NP-modified film. This is due to enhanced charge transport through the PAN/Au-NP system.

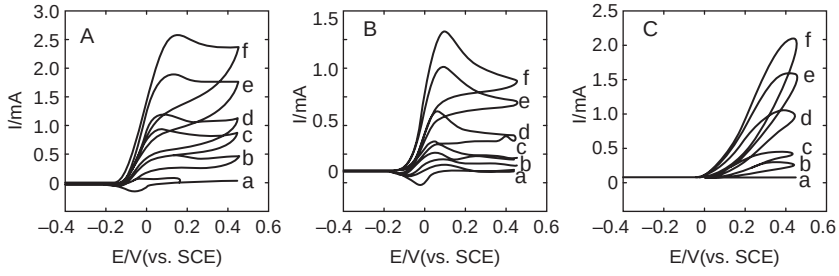

Figure 17.9 *Cyclic voltammograms of electrochemical oxidation of ascorbic acid: (A) a planar film composed of PAN/Au-NPs; (B) a planar film composed of PAN/PSS; (C) a bare Au electrode, in different concentrations of ascorbic acid: (a) 0 mM, (b) 5 mM, (c) 10 mM, (d) 20 mM, (e) 30 mM, and (f) 40 mM. The data were recorded in 0.1 M phosphate buffer, pH 7.5. Oxygen was removed from the background solution by bubbling Ar. Potential scan rate, 5 mV s^{-1}. (Reprinted with permission from Chemistry of Materials, Enhanced Bioelectrocatalysis Using Au-Nanoparticle/Polyaniline Hybrid Systems in Thin Films and Microstructured Rods Assembled on Electrodes by E. Granot, E. Katz, B. Basnar and I. Willner, 17, 18, 4600–4609. Copyright (2005) American Chemical Society)*

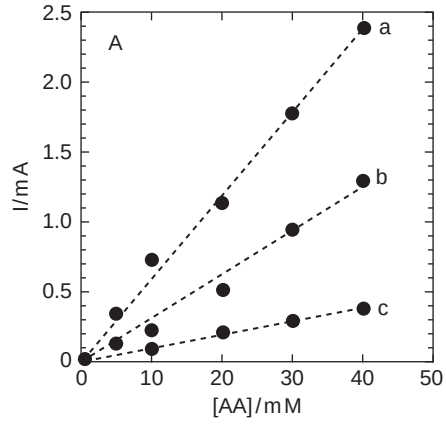

Figure 17.10 *Calibration plots corresponding to the electrochemical oxidation of ascorbic acid derived from the cyclic voltammograms at 0.1 V (vs. SCE): (a) the PAN/Au-NP system; (b) the PAN/PSS system; (c) the bare Au electrode. (Reprinted with permission from Chemistry of Materials, Enhanced Bioelectrocatalysis Using Au-Nanoparticle/Polyaniline Hybrid Systems in Thin Films and Microstructured Rods Assembled on Electrodes by E. Granot, E. Katz, B. Basnar and I. Willner, 17, 18, 4600–4609. Copyright (2005) American Chemical Society)*

17.4 Conclusion

Nanostructured conducting polymers have attracted a great deal of interest in their synthesis and applications during the past few years. Many techniques have been used to prepare variant nanostructures of the conducting polymer and synthesize nanostructured conducting polymers. The successful synthesis of nanostructures in this field provides a convenient way to study the properties, applications, and formation mechanisms of nanostructured conducting polymers. On the basis of the present reports, it seems that the synthetic techniques show great potential and the formation mechanism of conducting-polymer nanostructures is getting clearer and clearer. Although, there are several different techniques, the feature that all the synthetic techniques have in common is that a fast polymerization rate is needed at the beginning of the reaction in both chemical and electrochemical methods. The purpose of this is to produce a large quantity of polymer nuclei, which enable nanostructures to form; the nuclei growth is then controlled by polymerization time or by reducing the polymerization rate. The latter is especially suitable for electrochemical synthesis because of the continuous growth of polymer nuclei with electrolysis time. However, the electrolysis time is also controlled even if the polymerization rate is reduced. The sizes of nanostructures synthesized using the electrochemical method are more readily controlled than when using the chemical method because the electrochemical parameters are easily changed and controlled. Although the synthesis of conducting-polymer nanostructures has been achieved successfully, several challenges still remain in the field of molecular electronics, including the synthesis of ordered and oriented arrangements of nanowires and the enhanced conductivity of nanowires. This is because the random structures and misalignment of the conducting polymers

are not ideal for high efficiency and faster kinetics of the electrode reaction; the ordered and oriented arrangement of nanowires is a basic condition for molecular devices; and the low conductivity will produce an appreciable iR_s drop when current passes through the nanowire circuit. In comparison with reports on the synthesis of conducting-polymer nanostructures, electrocatalysis by pure nanostructured conducting polymers is scarce. It is expected that electrocatalysis by pure nanostructured conducting polymers will develop rapidly in the foreseeable future.

References

[1] J. Bacon and R.N. Adams, Anodic oxidations of aromatic amines, III. Substituted anilines in aqueous media, *J. Am. Chem. Soc*., **90**, 6596–6599 (1968).

[2] A.F. Diaz and J.A. Logan, Electroactive polyaniline films, *J. Electroanal. Chem*., **111**, 111–114 (1980).

[3] A.G. MacDiarmid, J.C. Chiang, M. Halpern, W.S. Huang, S.L. Mu, N.L.D. Somasiri, W.Q. Wu, and S.I. Yaniger, 'Polyaniline': Interconversion of metallic and insulating forms, *Mol. Cryst. Liq. Cryst*., **121**, 173–180 (1985).

[4] A.F. Diaz and K.K. Kanazawa, Electrochemical polymerization of pyrrole, *J. Chem. Soc. Chem. Commun*., 635–636 (1979).

[5] E.M. Genies, G. Bidan, and A.F. Diaz, Spectroelectrochemical study of polypyrrole films, *J. Electroanal. Chem*., **149**, 101–113 (1983).

[6] Y.F. Li, Effect of anion concentration on the kinetics of electrochemical polymerization of pyrrole, *J. Electroanal. Chem*., **433**, 181–186 (1997).

[7] G. Tourillon and F. Garnier, New electrochemically generated organic conducting polymers, *J. Electroanal. Chem*., **135**, 173–178 (1982).

[8] G.Q. Shi, S. Jin, G. Xue, and C. Li, A conducting polymer film stronger than aluminum, *Science*, **267**, 994–996 (1995).

[9] J.G. Speight, P. Kovacic, and F.W. Koch, Synthesis and properties of polyphenyls and polyphenylenes, *J. Macromol. Sci. Rev. Macromol. Chem*., **5**, 295–386 (1971).

[10] H. Shirakawa, E.J. Louis, A.G. MacDiarmid, C.K. Chiang, and A.J. Heeger, Synthesis of electrically conducting organic polymers: Halogen derivatives of polyacetylene, $(CH)_x$, *Chem. Commun*., 578–580 (1977).

[11] W.S. Huang, B.D. Humphrey, and A.G. MacDiarmid, Polyaniline, a novel conducting polymer, morphology and chemistry of its oxidation and reduction in aqueous electrolytes, *J. Chem. Soc., Faraday Trans. 1*., **82**, 2385–2400 (1986).

[12] C.R. Martin, Template synthesis of electronically conductive polymer nanostructures, *Acc. Chem. Res*., **28**, 61–68 (1995).

[13] Z.H. Cai, J.T. Lei, W. B. Liang, V. Menon, and C.R. Martin, Molecular and supermolecular origins of enhanced electric conductivity in template-synthesized polyheterocyclic fibrils. 1. Supermolecular effects, *Chem. Mater*., **3**, 960–967 (1991).

[14] X.Y. Zhang, W.J. Goux, and S.K. Manohar, Synthesis of polyaniline nanofibers by 'nanofiber seeding', *J. Am. Chem. Soc*., **126**, 4502–4503 (2004).

[15] J.X. Huang and R.B. Kaner, A general chemical route to polyaniline nanofibers, *J. Am. Chem. Soc*., **126**, 851–855 (2004).

[16] J.X. Huang and R.B. Kaner, Nanofiber formation in the chemical polymerization of aniline: A mechanistic study, *Angew. Chem. Int. Ed*., **43**, 5817–5821 (2004).

[17] D.M. Sarno, S.K. Manohar, and A.G. MacDiarmid, Controlled interconversion of semiconducting and metallic forms of polyaniline nanofibers, *Synth. Met*., **148**, 237–243 (2005).

[18] H.J. Ding, M.X. Wan, and Y. Wei, Controlling the diameter of polyaniline nanofibers by adjusting the oxidant redox potential, *Adv. Mater*., **19**, 465–469 (2007).

[19] M. X. Wan, *Conducting Polymers with Micro or Nanometer Structure*, Tsinghua University Press, Beijing and Springer-Verlag GmbH, Berlin, 2008.
[20] G. G. Wallace and P.C. Innis, Inherently conducting polymer nanostructures, *J. Nanosci. Nanotech*., **2**, 441–451 (2002).
[21] A.G. MacDiarmid, 'Synthetic metals': A novel role for organic polymers (Nobel leture). *Angew. Chem. Int. Ed*., **40**, 2581–2590 (2001).
[22] C.C Wang, J.F. Song, H.M. Bao, Q.D. Shen, and C.Z. Yang, Enhancement of electrical properties of ferroelectric polymers by polyaniline nanofibers with controllable conductivities, *Adv. Function Mater*., **18**, 1299–1306 (2008).
[23] H.J. Wang, L.W. Ji, D.F. Li, and J.Y. Wang, Characterization of nanostructure and cell compatibility of polyaniline films with different dopant acids, *J. Phys. Chem. B*, **112**, 2671–2677 (2008).
[24] S.L. Mu and Y.F. Yang, Spectral characteristics of polyaniline nanostructures synthesized by using cyclic voltammetry at different scan rates, *Phys. Chem. B*, **112**, 11558–11563 (2008).
[25] Y. Yan, Z. Yu, Y. W. Huang, W.X. Yuan, and Z.X. Wei, Helical polyaniline nanofibers induced by chiral dopants by a polymerization process, *Adv. Mater*, **19**, 3353–3357 (2007).
[26] S. Virji, R.B. Kaner, and B.H. Weiller, Hydrogen sensors based on conductivity changes in polyaniline nanofibers, *J. Phys. Chem. B*, **110**, 22266–22270 (2006).
[27] J. Jang, J. Ha, and J. Cho, Fabrication of water-dispersible polyaniline-poly(4-styrenesulfonate) nanoparticles for inkjet-printed chemical-sensor applications, *Adv. Mater*, **19**, 1772–1775 (2007).
[28] H.B. Zhao, L. Li, J. Yang, and Y.M. Zhang, Nanostructured polypyrrole/carbon composite as Pt catalyst support for fuel cell applications, *J. Power Sources*, **184**, 375–380 (2008).
[29] D. Li, J.X. Huang, and R.B. Kaner, Polyaniline nanofibers: A unique polymer nanostructure for versatile applications, *Acc. Chem. Res*., **42**, 135–145 (2009).
[30] A. Malinauskas, Electrocatalysis at conducting polymers, *Synth. Met*., **107**, 75–83 (1999).
[31] A.J Heeger, Semiconducting and metallic polymers: The fourth generation of polymeric materials (Nobel lecture), *Angew. Chem. Int. Ed*., **40**, 2591–2611 (2001).
[32] K. Doblhofer and K. Rajeswar, *Handbook of Conducting Polymers*, Marcel Dekker, New York, 1988, Chapter 20.
[33] Y. Li and G.Q. Shi, Electrochemical growth of two-dimensional gold nanostructures on a thin polypyrrole film modified ITO electrode, *J. Phys. Chem. B*, **109**, 23787–23793 (2005).
[34] P.J. Kulesza, K. Karnicka, K. Miecznikowski, M. Chojak, A. Kolary, P.J. Barczuk, G. Tsirlina, and W. Czerwinski, Network electrocatalytic films of conducting polymer-linked polyoxometallate-stabilized platinum nanoparticles, *Elctrochim. Acta*, **50**, 5155–5162 (2005).
[35] Q. Zhou, C.M Li, J. Li, and J.T. Lu, Electrocatalysis of template-electrosynthesized cobalt-porphyrin/polyaniline nanocomposite for oxygen reduction, *J. Phys. Chem. C*, **112**, 18578–18583 (2008).
[36] E. Pintér, R. Patakfalvi, T. Fülei, Z. Gingl, I. DéKány, and C. Visy, Characterization of polypyrrole-silver nanocomposites prepared in the presence of different dopants, *J. Phys. Chem. B*, **109**, 17474–17478 (2005).
[37] V. Ruiz, P.G. Nicholson, S. Jollands, P.A. Thomas, J.V. Macpherson, and P.R. Unwin, Molecular ordering and 2D conductivity in ultrathin poly(3-hexylthiophene)/gold nanoparticles composite films, *J. Phys. Chem. B*, **109**, 19335–19344 (2005).
[38] A.Z. Ernst, S. Zoladek, K. Wiaderek, J.A. Cox, A. Kolaryzurowska, K. Miecznikowski, and P.T. Kulesza, Network films of conducting polymer-linked polyoxometalate-modified gold nanoparticles: preparation and electrochemical characterization, *Elctrochim. Acta*, **53**, 3924–3931 (2008).
[39] H. Yoneyama, A. Kishimoto, and S. Kuwabata, Charge-discharge properties of polypyrrole films containing manganese dioxide particles, *J. Chem. Soc. Chem. Commun*., 986–987 (1991).
[40] M. Li, J.Y. Yuan, and G.Q. Shi, Electrochemical fabrication of nanoporous polypyrrole thin films, *Thin solid Films*, **516**, 3836–3840 (2008).
[41] L.J. Sun, X.X. Liu, K.K. Lau, L. Chen, and W.M. Gu, Electrodeposited hybrid films of polyaniline manganese oxide in nanofibrous structures for electrochemical supercapacitor, *Elctrochim. Acta*, **53**, 3036–3042 (2008).

[42] M. H. Huang, L.H. Bi, Y. Shen, B.F. Liu, and S.J. Dong, Nanocomposite multiplayer film of preyssler-type polyoxomatalates with fine tunable electrocatalytic activities, *J. Phys. Chem. B*, **108**, 7980–7986 (2004).
[43] J. Dexmer, C.M. Leroy, L. Binet, V. Heresanu, P. Launois, N. Steunou, C. Coulon, J. Maquet, N. Brun, J. Livage, and R. Backov, Vanadium oxide-PANI nanocomposite-based macroscopic fibers:1D alcohol sensors bearing enhanced toughness, *Chem. Mater.*, **20**, 5541–5549 (2008).
[44] R. Gangopadhyay and A. De, Conducting polymer nanocomposites: A brief overview, *Chem. Mater.*, **12**, 608–622 (2000).
[45] S.V.N.T. Kuchibhatla, A.S. Karakoti, D. Bera, and S. Seal, One dimensional nanostructured materials, *Prog. Mater. Sci.*, **52**, 699–913 (2007).
[46] D. Chen, G. Wang, and J.H. Li, Interfacial bioelectrochemistry: fabrication, properties and applications of functional nanostructured biointerfaces, *J. Phys. Chem. C*, **111**, 2351–2367 (2007).
[47] Y.F. Yang, S.L. Mu, and H. Chen, Electrochemical synthesis of polypyrrole for the immobilization of galactose oxidase, *Synth. Met.*, **92**, 173–178 (1998).
[48] D.E. Stilwell and S.M. Park, Electrochemistry of conductive polymers, II. Electrochemical studies on growth properties of polyaniline, *J. Electrochem. Soc.*, **135**, 2254–2262 (1988).
[49] S.L. Mu and J.Q. Kan, Evidence for the autocatalytic polymerization of aniline, *Electrochim. Acta*, **41**, 1593–1599 (1996).
[50] M. Gao, S.M. Huang, L.M. Dai, G. Wallace, R.P. Gao, and Z.L. Wang, Aligned coaxial nanowires of carbon nanotubes sheathed with conducting polymers, *Angew. Chem.*, **112**, 3810–3813 (2000).
[51] S.J. Choi and S.M. Park, Electrochemical growth of nanosized conducting polymer wires on gold using molecular templates, *Adv. Mater.*, **12**, 1547–1549 (2000).
[52] T.S. Vasilieva, S. Logvinov, A. Timonov, R. Amadelli, and D. Bartak, Electrochemical synthesis and characterization of redox polymer nanostructures, *Langmuir*, **19**, 9005–9012 (2003).
[53] J.M. Chen, S.W. Liao, and Y.C. Tsai, Electrochemical synthesis of polypyrrole within PMMA nanochannels produced by AFM mechanical lithography, *Synth. Met.*, **155**, 11–17 (2005).
[54] X.T. Zhang, J. Zhang, and Z.F. Liu, Conducting polymer/carbon nanotube composite films made by in situ electropolymerization using an ionic surfactant as the supporting electrolyte, *Carbon*, **43**, 2186–2191 (2005).
[55] P.C. Si, Q.J. Chi, Z.S. Li, J. Ulstrup, P.J. Møller, and J. Mortensen, Functional polythiophene nanoparticles: size-controlled electropolymerization and ion selective response, *J. Am. Chem. Soc.*, **129**, 3888–3896 (2007).
[56] R.G. Lv, S.L. Zhang, Q.F. Shi, and J.Q. Kan, Electrochemical synthesis of polyaniline nanoparticles in the presence of magnetic field and erbium chloride, *Synth. Met.*, **150**, 115–122 (2005).
[57] J.Q. Kan, Y. Jiang, and Y. Zhang, Studies on synthesis and properties of uniform and ordered polyaniline nanoparticles in the magnetic field, *Mater. Chem. Phys.*, **102**, 260–265 (2007).
[58] S.L. Zhang, R. Tang, and J.Q. Kan, Effect of magnetic field and rare-earth ions on properties of polyaniline nanoparticles, *J. Appl. Poly. Sci.*, **103**, 2286–2294 (2007).
[59] S. Zhou, T. Wu, and J.Q. Kan, Effect of Co^{2+}, Ni^{2+}, Cu^{2+} or Zn^{2+} on properties of polyaniline nanoparticles, *J. Appl. Poly. Sci.*, **106**, 652–658 (2007).
[60] S. Härtel, M.L. Fanani, and B. Maggio, Shape transitions and lattice structuring of ceramide-enriched domains generated by sphingomyelinase in lipid monolayers, *Biophys. J.*, **88**, 287–304 (2005).
[61] S. Zhou, T. Wu, and J.Q. Kan, Effect of methanol on morphology of polyaniline, *European Poly. J.*, **43**, 395–402 (2007).
[62] C.K. Tan and D.J. Blackwood, Interactions between polyaniline and methanol vapor. *Sensors and Actuators B*, **71**, 184–191 (2000).
[63] S.D. Champagne, E. Ferain, C. Jérôme, R. Jérôme, and R. Legras, Electrochemically synthesized polypyrrole nanotubules: Effects of different experimental conditions, *Eur. Poly. J.*, **34**, 1767–1774 (1998).
[64] D.D. Pra and S.D. Champagne, A comparative study of the electronic structure and spectroelectrochemical properties of electrosynthesized polyaniline films and nanotubes, *Thin Solid Films*, **479**, 321–328 (2005).

[65] M. Trueba, A.L. Montero, and J. Rieumont, Pyrrole nanoscaled electropolymerization: Effect of the proton, *Electrochim. Acta*, **49**, 4341–4349 (2004).
[66] M. Delvaux, J. Duchet, P.Y. Stavaux, R. Legras, and S.D. Champagne, Chemical and electrochemical synthesis of polyaniline micro-and nano-tubules, *Synth. Met*., **113**, 275–280 (2000).
[67] M. Tagowska, B. Palys, and K. Jackowska, Polyaniline nanotubules-anion effect on conformation and oxidation state of polyaniline studied by Raman spectroscopy, *Synth. Met*., **142**, 223–229 (2004).
[68] G.W. Lu, C. Li, and G.Q. Shi, Polypyrrole micro- and nanowires synthesized by electrochemical polymerization of pyrrole in the aqueous solutions of pyrenesulfonic acid, *Polymer*, **47**, 1778–1784 (2006).
[69] J.F. Zhang, C.M. Li, S.J. Bao, X.Q. Cui, Q. L. Bao, and C.Q. Sun, Template-free electrochemical synthesis of superhydrophilic polypyrrole nanofiber network, *Macromolecules*, **41**, 7053–7057 (2008).
[70] R. Xiao, S. Cho, R. Liu, and S.B. Lee, Controlled electrochemical synthesis of conductive polymer nanotube structures, *J. Am. Chem. Soc*., **129**, 4483–4489 (2007).
[71] J.S. Moreno, S. Panero, and B. Scrosati, Electrochemical polymerization of polypyrrole-heparin nanotubes: Kinetics and morphological properties, *Electrochim. Acta*, **53**, 2154–2160 (2008).
[72] L. Liang, J. Liu, C.F. Windisch, Jr., G.J. Exarhos, and Y.H. Lin, Direct assembly of large arrays of oriented conducting polymer nanowires, *Angew. Chem. Int. Ed*., **41**, 3665–3668 (2002).
[73] J. Wang, S. Chan, R.R. Carlson, Y. Luo, G.L. Ge, R.S. Ries, J. R. Heath, and H.R. Tseng, Electrochemically fabricated polyaniline nanoframework electrode junctions that function as resistive sensors, *Nano Lett*., **4**, 1693–1697 (2004).
[74] K. Ramanathan, M.A. Bangar, M.H. Yun, W. Chen, A. Mulchandani, and N.V. Myung, Individually addressable conducting polymer nanowires array, *Nano Lett*., **4**, 1237–1239 (2004).
[75] A.K. Wanekaya, M.A. Bangar, M.H. Yun, W. Chen, N.V. Myung, and A. Mulchandani, Field-effect transistors based on single nanowires of conducting polymers, *J. Phys. Chem. C*, **111**, 5218–5221 (2007).
[76] M. Deepa, S. Ahmad, K.N. Sood, J. Alam, S. Ahmad, and A.K. Srivastava, Electrochromic properties of polyaniline thin film nanostructures derived from solutions of ionic liquid/polyethylene glycol, *Electrochim. Acta*, **52**, 7453–7463 (2007).
[77] Y.P. Guo and Y. Zhou, Polyaniline nanofibers fabricated by electrochemical polymerization: A mechanistic study, *Eur. Poly. J*., **43**, 2292–2297 (2007).
[78] X.M. Yang, T. Y. Dai, Z.X. Zhu, and Y. Lu, Electrochemical synthesis of functional polypyrrole nanotubes via a self-assembly process, *Polymer*, **48**, 4021–4027 (2007).
[79] A. J. Bard and L.R. Faulkner, *Electrochemical Methods, Fundamentals and Applications*, 2nd Edn., John Wiley & Sons, Inc., New York, 2001, p. 473.
[80] Z. Mandić and L. Duić, Polyaniline as an electrocatalytic material, *J. Electroanal. Chem*., **403**, 133–141 (1996).
[81] A. Malinauskas, Electrocatalysis at conducting polymers, *Synth. Met*., **107**, 75–83 (1999).
[82] S.L. Mu, The electrocatalytic oxidation of gallic acid on polyaniline film synthesized in the presence of ferrocene phosphonic acid, *Synth. Met*., **139**, 287–294 (2003).
[83] Y.F. Yang and S.L. Mu, Determination of hydrogen peroxide using amperometric sensor of polyaniline doped with ferrocenesulfonic acid, *Biosens. Bioelectron*., **21**, 74–78 (2005).
[84] S.L. Mu, Direct determination of arsenate based on its electrocatalytic reduction at the poly(aniline-*co*-*o*-aminophenol) electrode, *Electrochem. Commun*., **11**, 1519–1522 (2009).
[85] M.L. Guo, J.H. Chen, J. Li, B. Tao, and S.Z. Yao, Fabrication of polyaniline/carbon nanotube composite modified electrode and its electrocatalytic property to the reduction of nitrite, *Anal. Chim. Acta*, **532**, 71–77 (2005).
[86] X.L. Luo, A.J. Killard, and M.R. Smyth, Nanocomposite and nanoporous polyaniline conducting polymers exhibit enhanced catalysis of nitrite reduction, *Chem. Eur. J*., **13**, 2138–2143 (2007).

[87] M.A. Harmer and H.A.O. Hill, The direct electrochemistry of redox proteins at metal oxide electrodes, *J. Electroanal. Chem*., **189**, 229–246 (1985).
[88] J. Wang, M. Li, Z. Shi, N. Li, and Z. Gu, Direct electrochemistry of cytochrome c at a glassy carbon electrode modified with single-wall carbon nanotubes, *Anal. Chem*., **74**, 1993–1997 (2002).
[89] N.S. Lewis and M.S. Wrighton, Electrochemical reduction of horse heart ferricytochrome c at chemically derivatized electrodes, *Science*, **211**, 944–947 (1981).
[90] L. Zhang, X. Jiang, L. Niu, and S.J. Dong, Syntheses of fully sulfonated polyaniline nanonetworks and its application to the direct electrochemistry of cytochrome c, *Biosens. Bioelectron*., **21**, 1107–1115 (2006).
[91] S.L. Mu, Novel properties of polyaniline nanofibers coated with polycatechol, *Synth. Met*., **156**, 202–208 (2006).
[92] S.L. Mu, Poly(aniline-*co*-*o*-aminophenol) nanostructured network: Electrochemical controllable synthesis and electrocatalysis, *Electrochim. Acta*, **51**, 3434–3440 (2006).
[93] T.J. Schmidt, V. Stamenkovic, M. Arenz, N.M. Markovic, and P.N. Ross Jr., Oxygen electrocatalysis in alkaline electrolyte: Pt(hkl), Au (hkl) and the effect of Pd-modification, *Electrochim. Acta*, **47**, 3765–3776 (2002).
[94] J. S. Yang and J.J. Xu, Nanoporous amorphous manganese oxide as electrocatalyst for oxygen reduction in alkaline solutions, *Electrochem. Commun*., **5**, 306–311 (2003).
[95] P.J. Kulesza, M. Chojak, K. Karnika, K. Miecznikowski, B. Palys, and A.L. Wieckowski, Network films composed of conducting polymer-linked and polyoxometalate-stabilized platinum nanoparticles, *Chem. Mater*., **16**, 4128–4134 (2004).
[96] P.J. Kulesza, B. Grzybowska, M. A. Malik, and M.T. Galkowski, Tungsten oxides as active supports for highly dispersed platinum microcenters: Electrocatalytic reactivity toward reduction of hydrogen peroxide and oxygen, *J. Electrochem. Soc*., **144**, 1911–1917 (1997).
[97] Q. Zhou, C. M. Li, J. Li, X.Q. Cui, and D. Gervasio, Template-synthesized cobalt porphrin/polypyrrole nanocomposite and its electrocatalysis for oxygen reduction in neutral medium, *J. Phys. Chem. C*, **111**, 11216–11222 (2007).
[98] H. Laborde, J.M. Léger and C. Lamy, Electrocatalytic oxidation of methanol and C1 molecules on highly dispersed electrodes Part: 1: platinum in polyaniline, *J. Appl. Electrochem*., **24**, 219–226 (1994).
[99] C. Sivakumar, Finely dispersed Pt nanoparticles in conducting poly(*o*-anisidine) nanofibrillar matrix as electrocatalytic material, *Electrochim. Acta*, **52**, 4182–4190 (2007).
[100] H.B. Zhao, L. Li, J. Yang, and Y.M. Zhang, Nanostructured polypyrrole/carbon composite as Pt catalyst support for fuel cell applications, *J. Power Sources*, **184**, 375–380 (2008).
[101] E. Granot, E. Katz, B. Basnar, and I. Willner, Enhanced bioelectrocatalysis using Au-nanoparticle/polyaniline hybrid systems in thin films and microstructured rods assembled electrodes, *Chem. Mater*., **17**, 4600–4609 (2005).

18

Nanostructured Conductive Polymers as Biomaterials

Rylie A. Green, Sungchul Baek, Nigel H. Lovell, and Laura A. Poole-Warren

Graduate School of Biomedical Engineering, University of New South Wales, Sydney, Australia

18.1 Introduction

Conductive polymers (CPs) are an emerging technology in the field of biomaterials. While CPs retain a predominantly investigative role in the field of medical implants, they have shown potential across a wide range of applications, including neural interfaces, biosensors, nerve grafts, and drug-delivery devices.

CPs have been extensively explored for addressing the limitations of conventional neuroprosthetic implant devices which employ metallic electrodes to interface with neural tissue. In this application CPs have the potential to provide a conductive interface with properties more suited to soft-tissue integration. Unlike conventional conductive materials CPs are relatively soft, with a textured surface conducive to cell attachment. The high surface area relative to the geometric base area means these materials also have good charge-transfer properties, with low impedance and negligible bilayer capacitance, a substantial limitation of existing neural-stimulation electrode technologies. These types of properties have resulted in much investigation of conductive polymers for a range of other medical applications, including biosensors, nerve regeneration templates, and for drug-delivery applications.

Nanostructured Conductive Polymers Edited by Ali Eftekhari

18.2 Biomedical Applications for Conductive Polymers

18.2.1 Electrode Coatings

The most common biomedical applications for which CPs have been explored are implantable bioelectrodes for stimulating or recording from tissues. Typical neuroprosthetic implant electrodes are fabricated from platinum, gold, or alloys of these metals and iridium oxide. Despite recent advances in surface modification to increase the available surface area of conventional electrodes, their minimal interaction with neural tissue limits their ability to provide optimal stimulation of and recording from neural cells [1]. The provision of a conductive-polymer coating has the potential to surmount these limitations by providing a softer interface with a high surface area for delivering higher charge densities with lower thresholds.

Bioelectrodes are used extensively in the area of biological-machine systems integration (BMSI), particularly in relation to neural interfacing. The primary purpose of the BMSI is to provide neural interfaces for both sensory (recording) and actuation (neurostimulation) purposes. The majority of recent advances in BMSI for manipulation and locomotion are in the domain of neural and rehabilitation engineering, the motivation being to improve the quality of life of the severely paralyzed or those suffering from profound losses to various sense organs.

The cochlear implant, bionic eye, and deep brain stimulators are examples of stimulating devices. In the case of the latter device, direct electrical stimulation of cortical and deep brain structures has been carried out for many years to control epileptic seizures and symptoms associated with degenerative neurological disorders such as Parkinson's disease. Replacing a loss of motor control through functional electrical stimulation (FES) of nerve fibers and muscle is another example. While these prostheses are used to electrically evoke responses in specific neural tissue through controlled stimulation paradigms, in many cases they are also required to perform recording functions that output information relating to characteristics of the neural-tissue interface – typically the interfacial impedance. Existing neural recording devices are typically more research-based, with intensive investigation underway in the areas of brain–computer interfacing and nerve interfacing for prosthetic control purposes.

The cochlear implant is a commercially available device that has for several decades restored hearing percepts to patients suffering from sensorineural deafness. This device communicates with neural tissue via a flexible electrode array inserted in the cochlea. While the electrodes are fabricated from platinum and provide an effective long-term stimulation platform, it is hypothesized that CP electrodes could reduce implant power consumption and improve signal fidelity by increasing the electroactive surface area. This would benefit patients by allowing more complex signal modulation resulting in an improved dynamic range. The psychophysical outcome of such technology would be clearer hearing percepts of sounds, which are currently poor due to high background noise, such as music and speech in crowded environments [2]. Additionally, the modification of CPs to incorporate biofunctional molecules might be used to both reduce tissue damage resulting from implantation and rescue or aid in the survival of diseased neural cells [1,3].

The vision prosthesis, also known as the bionic eye, is a stimulating device which is currently under development. Several groups around the world [4–6] are designing implants to restore perception of sight to blind patients by bypassing the degenerative photoreceptor tissue and electrically stimulating the remaining functional cells. Such devices are designed to aid patients blinded by degenerative diseases of the retina such as age-related macular degeneration (AMD) and retinitis pigmentosa (RP) [4,6,7]. In both these diseases the photoreceptor layer regresses, but a number of cell types within the retina, such as the retinal ganglion cells (RGCs) remain functional and can be electrically stimulated by electrodes placed in close apposition to the target cells [8,9]. One of the major technological barriers in developing such a device is the construction of the high-density electrode array [1]. CPs can potentially offer one alternative to allow small electrodes to be constructed with appropriate characteristics for long-term charge delivery [1].

In stimulating electrode applications the current density supplied by the electrode and the current threshold required for cell activation are integral in determining the quality of the delivered signal. As the size of the electrodes is reduced to increase the number of discrete stimulation points (or resolution), the current density inversely increases. For conventional platinum electrodes this is a major limitation, as the typical charge-carrying capacity of this metal is 6 mC cm^{-2} [10] and the safe charge injection limit is 250 μC cm^{-2}, above which hydrolysis of the platinum can result in the evolution of toxic chemical species that can cause adverse tissue reactions [11]. Conventional CPs have been reported as carrying charge densities of up to approx. 200 mC cm^{-2} [12,13]. It has been proposed that CP coatings can provide significantly higher charge-carrying surface areas available per geometric electrode area.

CPs have also found application in neural recording and sensing of many organ systems in the body, with particular emphasis in brain (cortical) interfacing to provide so-called brain–computer interfaces (BCIs). Other applications include improving biosignal detection in diagnostics and mapping approaches for corrective surgery. Studies have shown that the distance between the recording electrodes and neural tissue has a significant influence on the signal-to-noise ratio (SNR) [14,15]. The application of a CP coating provides closer apposition between the recording electrode and neural tissue, resulting in improved signal detection with less noise. An improved SNR can potentially be used to distinguish previously unattainable signals, leading to better diagnostics and improved surgical outcomes through more accurate localization and mapping [16].

18.2.2 Alternate Applications

18.2.2.1 Biosensors

A biosensor is a device having a biological sensing element either intimately connected to or integrated within a transducer. The aim is to produce a digital electronic signal, which is proportional to the concentration of a specific biochemical or enzyme. CP conductivity is sensitive to chemical agents, and this allows them to be structured for use as biosensors, with the conductivity being proportional to the detected biochemical. The ability to alter the CP molecular structure and morphology makes them a superior choice for biosensors

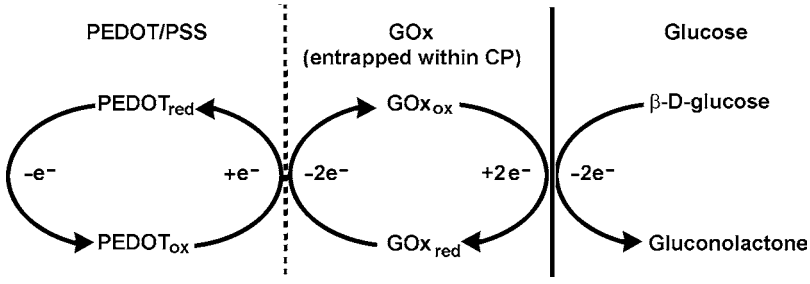

Figure 18.1 *Schematic of conducting polymer PEDOT functionalized with GOx, operating as a biosensor for detecting glucose levels*

which are easily tailored to enhance the sensitivity and selectivity of a device to specific biochemicals [17].

Amperometric biosensors based on CPs with incorporated enzymes such as glucose oxidase (GOx), alcohol dehydrogenase, glutamate oxidase, and peroxidase [18–21] have found application in both the biomedical and food industries. The most common CP-based biosensor is used in the detection of glucose for diabetic patients. In this CP-based biosensor, GOx is immobilized on the surface of either polypyrrole (PPy) or poly(3,4-ethylene dioxythiophene) (PEDOT). As shown in Figure 18.1, the GOx enzyme catalyses the conversion of glucose to D-gluconolactone and the electron release from the oxidation reaction alters the current passing through the CP in proportion to the concentration of converted glucose in solution [17].

18.2.2.2 Nerve Grafts

Nerve grafts or conduits guide the repair of injured neural tissue. Neural repair in the central nervous system, as in the case of spinal injury, as well as peripheral nerve damage associated with trauma, often result in uncontrolled growth of neural tissue. The result is that no effective conduction path is obtained and both movement and sensory response can be lost in the body portion distal to the injury.

CPs have potential application in nerve-graft technology, where an electroactive path is desirable for guiding tissue growth to bridge the gap in a damaged neural conduction path. CPs can be patterned to form channels along which neural cells extend and the preferential adherence of cells to CPs may limit uncontrolled growth which could lead to cross-talk and poor reconstruction of the damaged nerve. Currently CPs are not frequently used because most are nonbiodegradable, but recent developments of novel composite CPs consisting of degradable block copolymers indicate these materials will potentially provide superior scaffolds for nerve repair [22,23].

18.2.2.3 Drug Delivery

The ability to nanostructure CPs allows biological signaling factors to be incorporated into these materials, through a variety of routes [3,13,24]. Electrochemical reduction of oxidatively doped CPs can conceivably allow the release of microscopic doses of

biological inclusions to controllably supply tissues with appropriate biological cues [19,25]. Biological release profiles can also be controlled through either polymer composition and structure or through the application of electrical potentials, which releases charged biomolecules via ionic flux [26].

Such bioactive CPs can be designed for targeted cell responses. This functionality has been predominantly exploited in the field of neuroprostheses to promote neural cell growth towards microelectrodes and is hypothesized to aid in the survival and rescue of degenerative cells [3,27,28]. The provision of cell adherence proteins and growth factors within CPs have significantly improved *in vivo* cell interactions with electrodes [3,14], but wider applications of bioactive CPs have not been thoroughly investigated. It is hypothesized that bioactive CPs could find application in the prevention of infection and reduction of inflammation through the provision of antibiotics, anti-inflammatories, and other appropriate drug formulations.

18.3 Polymer Design Considerations

18.3.1 Conduction Mechanism

Conductivity in electroactive polymers arises from the presence of conjugated double bonds along the backbone of an otherwise insulative structure. In conjugation, the bonds between the carbon atoms are alternatively single and double. Every bond in the backbone contains a localized 'sigma' (s) bond which forms a strong chemical bond and every double bond also contains a less strongly localized 'pi' (p) bond [29]. This alternate bond arrangement produces a low energy state and introduces a conduction band [30].

The polymer is transformed into a conductor by doping it with either an electron donator or an electron acceptor. The main criteria for a conducting-polymer dopant is that it must oxidize or reduce the polymer without lowering its stability [30,31]. In oxidative doping an electron is removed from the p-system of the backbone producing a free radical and a spinless positive charge. The radical and cation are coupled to each other via local resonance and the combination is called a polaron. Upon further oxidation the free radical of the polaron is removed, creating a new spinless defect called a bipolaron [32]. Eventually, with continued doping, continuous bipolaron bands can be formed along the conducting polymer backbone, as shown on the left side of Figure 18.2.

On application of a potential across a conducting-polymer film, the main mechanism of conduction is the movement of charge carriers between localized sites or between bipolaron states. Ion movements in or out of the film are dependent on dopant charge and

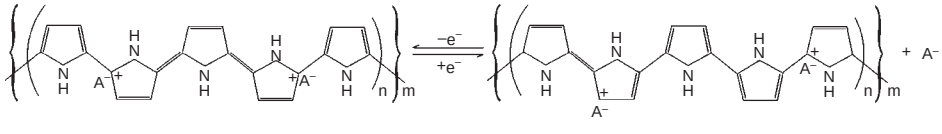

Figure 18.2 *Bipolaron conduction of charge across polypyrrole chains*

motility, but can be ideally represented by the reaction in Figure 18.2 [27]. Although bipolarons are known to be the main source of charge carriers, the precise mechanism of charge transport through conducting polymers is not fully understood [30]. It is important to consider that most conducting polymers are highly disordered, consisting of both amorphous and crystalline regions. Charge transport is known to occur not only along the polymer chains, but also between chains and the complex boundaries established by the multiple phases.

18.3.2 Conventional Components

The performance of a CP in any given application is highly dependent on the monomer, the dopant and the solvent from which the CP is evolved or cast, all of which may have significant impact on the properties of the resulting polymer. The first widely recognized CP was polyacetylene (PA), which when doped with iodine was found to have a 10-million-fold increase in its conductivity [33]. This polymer has not been extensively studied for biomedical applications due its low thermal and chemical stability in air [34]. Today, one of the most commonly used CPs in the biomedical literature is polypyrrole (PPy) which was first described as early as 1968 [35]. The monomer units from which these polymers are derived are integral in determining their physicochemical properties and the cyclic polyenes depicted in Figure 18.3 are the most prevalent CPs reported for biomedical use. PPy, polythiophene (PTh), and polyaniline (PANI) have emerged as the predominant class of CPs that exhibit thermal stability, high conductivity, and ease of synthesis.

Neural electrodes are often used for chronic implant applications that demand chemical and electrical stability of materials. Yamato *et al.* found that PPy has limited electrical response under cyclic voltammetry because of structural defects along the CP backbone

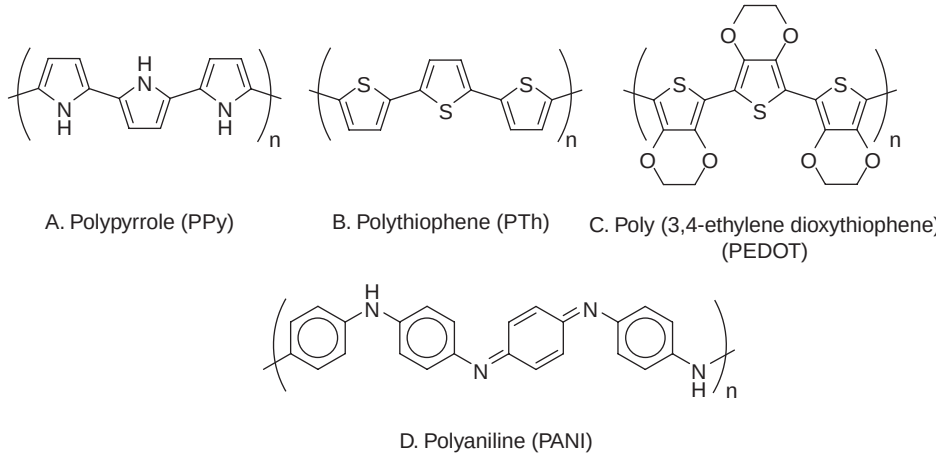

Figure 18.3 *Chemical structures of common conductive polymers for biomedical applications*

[36]. Derivatives of PTh such as poly(ethylene dioxythiophene) (PEDOT) (Figure 18.3C), have been increasingly investigated for their superior electrochemical stability and ability to be tailored for altered functionality [36–39].

Xiao *et al.* investigated PEDOT derivatives poly(hydroxymethylated-3,4-ethylenedioxylthiophene) (PEDOT-MeOH) and PEDOT doped with sulfonatoalkoxy ethylene dioxythiophene (SEDOT) to improve water solubility of EDOT and consequently increase incorporation of biologic agents into the CP [37,38]. Films of polythiophene with different alkyl side chains were successfully synthesized by Li *et al.*, who found that hydrophobicity of the films could be adjusted by introducing alkyl side chains with different lengths [39]. Hydrophobic polythiophene films with long alkyl side chains experienced higher protein adsorption and neural cell proliferation.

While investigation of PANI has been limited, Bidez *et al.* [40] and Kamalesh *et al.* [41] have demonstrated that films evolved from anilines do have potential application as biomaterials. The emeraldine salt of PANI, EPANI was found to be both conductive and support cardiac myoblast growth and proliferation [40]. Li *et al.* produced electrospun nanofibres incorporating PANI and gelatin [42] which were conductive and supported attachment and proliferation of cardiac myoblasts equivalent to that observed on tissue culture plastic.

The dopant ion required for polymer conductivity is one of the most important components of a CP. Its structure, number of available balancing charges and interaction with the polymer backbone are key to the overall performance of the material. In biomedical applications the dopant also needs to be nontoxic or restrained by the polymer matrix. A number of dopant types have been investigated for use in biomedical applications, including small anions, polymeric anions, buffer salts, and biologically active anions. Table 18.1 summarizes various dopant types and solvents that have been reported in the

Table 18.1 *Sample of the variety of polymer, dopant and solvent combinations investigated for conducting polymers in biomedical applications*

Polymer	Dopant (MW)	Solvent	Ref.
PPy	Polystyrene sulfonate (PSS, ~100 kDa)	H_2O	[12,15,43]
PPy	*p-T*oluene sulfonate (pTS, 194 Da)	H_2O	[44–46]
PPy	Benzene sulfonate (BS, 180 Da)	H_2O	[45]
PPy	Silk-like protein fragments (SLPF, ~110 kDa)	H_2O	[47]
PPy	Hyularonic acid (HA, 2100 kDa)	H_2O	[48]
PEDOT	PSS	H_2O/acetonitrile (AN)	[12,49]
PEDOT	pTS	H_2O/AN	[12]
PEDOT	Lithium perchlorate ($LiClO_4$, 106 Da)	H_2O	[50,51]
PEDOT	Sulfonatoalkoxy-EDOT (S-EDOT, 315 Da)	H_2O	[37]
PEDOT	DCDPGYIGSR (1 kDa)	H_2O/AN	[13,14,52]
PEDOT	DEDEYFQRYLI (1.6 kDa)	H_2O /AN	[13,24]
MeOH-PEDOT	PSS	H_2O	[38]
PANI	Undoped	*n*-Methyl-pyrrolidone	[40]
Emeraldine PANI	Hydrochloric acid (HCl, 36 Da)	*n*-Methyl-pyrrolidone	[40]

literature. Generally, these dopants have relatively low toxicity [1] and other criteria, such as their impact on physical and electrical properties, drive their selection as dopants.

The most common solvent used in electropolymerization of CPs is water. This is mainly due to the desire for more biocompatible materials without residual chemical solvents that might have toxic effects on the biological environment. In some cases the monomer is not sufficiently soluble in water, as in the case of PEDOT, and here acetonitrile (AN) is employed to provide increased solubility. Harsh solvents are avoided when biofunctional additives are used in the electrolyte solution, as discussed in Section 18.3.3. Strong solvents are likely to degrade biomolecules, reducing their functionality *in vivo*, and requiring higher concentrations to be used during polymerization to account for this loss.

18.3.3 Biofunctional Additives

The next generation of implantable devices are likely to require biomaterials that are more interactive with tissues, being designed to interact with specific target biomolecules of relevance to the specific application. Although conventional PPy and PTh films have shown adequate biocompatibility for many biomedical applications, their lack of biofunctional activity results in poor cell interactions and limits their potential as an implantable material.

Specific biological tissue interactions can only be driven by appropriate functional biomolecules, which can be incorporated into CPs through a variety of routes. Biological functionality has been imparted to CPs through doping, entrapment, physical adsorption and covalent bonding, as shown in the schematic in Figure 18.4. Some biological signaling factors which have been used in CP applications have included silk-like protein fragments (SLPF), hyaluronic acid (HA), various laminin peptides, enzymes, polymeric amino acids, growth factors, and whole cells [12,13,47,48,53,54]. The main challenges in creating a bioactive CP are first in maintaining the concentration and

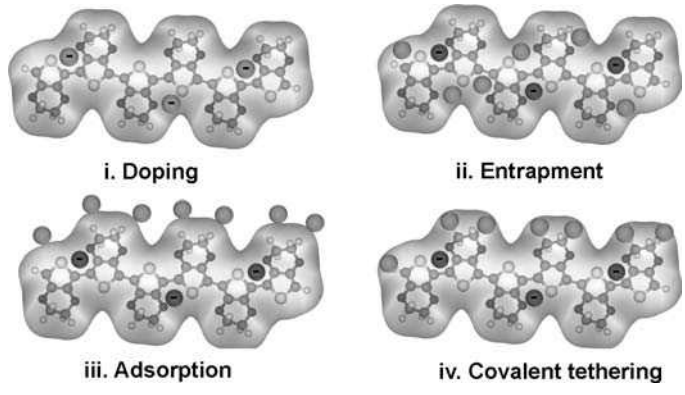

Figure 18.4 *Schematic of conventional biological modification routes of CPs, shown for poly(3,4-ethylene dioxythiophene). The green molecule represents the biofunctional additive and the negatively charged purple molecule is the dopant anion (See colour Plate 10)*

function of the biological components throughout fabrication, and second in retaining biofunctionality for the required duration.

There are advantages and disadvantages to all methods of incorporating biologicals into CPs. The concentration of biological entity required to functionalize a CP is usually much higher than that required if the entity is supplied directly to the biological environment. The method of polymer modification influences the amount of biomolecule required during fabrication to ensure biofunctionality. Strong solvents used during electrochemical polymerization or post-process chemical modification may degrade biologicals, and higher concentrations need to be supplied to account for degradation. When biofunctional molecules are used to dope a CP, high concentrations need to be supplied in the electrolyte solution to ensure enough anions are available for polymerization to proceed. It has also been shown that biomolecules in the electrolyte solution limit the efficiency of electrodeposition and may degrade the mechanical and electrical performance of the polymer [13,24,48].

Both biomolecule doping and entrapment are likely to maintain CP biofunctionality for a longer period than if the biological molecules are adsorbed to the polymer surface post-processing. Adsorption relies on ionic interactions at a material surface which dynamically alters when placed in a biological environment. The presence of molecules with stronger affinities for either the target molecule or the CP will result in displacement of the biomolecule from the CP surface.

While covalent bonding of biomolecules to the CP surface presents the opportunity to provide signalling factors at optimal concentration and orientation, current processing methods are time-consuming with low efficiency of bonding [55]. There is also evidence that significant surface morphology changes can result from chemical processing that might affect CP electrical and mechanical performance [53,55]. Ideally, biosynthetic CPs need to be based on a flexible design that permits interaction with varied cell types by a simple exchange of the incorporated biomolecules. Novel techniques for the incorporation of biofunctional additives are required to optimize their performance in CPs.

18.4 Fabrication of Nanostructured Conductive Polymers

CPs can be fabricated through a variety of routes which are classified as either predominantly electrochemical or chemical. While electrochemical synthesis has been more widely used for preparing nanoscale CP thin films for biomedical applications, chemical polymerization can produce large quantities of CP thick films or colloidal dispersions at low cost. Despite these advantages, chemical techniques have found relatively little application in biomedical applications. The advantages and disadvantages of electrodeposition and chemical synthesis are summarized in Table 18.2.

The main advantage of electrodeposition is its simplicity and reproducibility. CP thin films of controlled thickness and morphology can be electropolymerized on conductive surfaces, conventionally platinum, gold, or indium tin oxide (ITO), by varying the applied number of charges passed through the electrolyte solution. However, not all CPs can be formed electrochemically. For efficient electropolymerization, the chosen monomer must be able to readily oxidize into its radical cation at the potential applied to the electrolyte.

Table 18.2 *Comparison of Conventional Polymerization Techniques*

Polymerization Technique	Advantages	Disadvantages
Electrodeposition	Short polymerization time (~15 min) Ease of set up Uniform thin film (20 nm–100 μm) on conducting surface (control of film thickness) Ability to entrap/dope biological entities into polymer matrix	Limited number of processible monomers Inability to coat nonconducting surface Minimal control over the molecular weight (MW) and the structural features
Chemical Synthesis	Flexibility of polymerization scheme Coatings of nonconducting surfaces Control over the MW and the structural features Post-processibility Mass-producibility	Complexity of fabrication process Powdery end product (requires post-processing) Intricacy of incorporating complex bulky dopant Use of oxidants

Furthermore, electrodeposition provides limited control over the resulting polymer molecular weight (MW) and backbone features such as conformation (the regular 180° rotation of adjacent monomers), regio-regularity, and cross-linking [56]. Chemical defects such as hydroxyl and carbonyl groups or hydrogenation may also occur if the CP is over-oxidized [57].

For CPs with asymmetrical monomers, several backbone coupling variants, depicted in Figure 18.5, can occur. The term region-regularity refers to the amount of defect-free 2–5′coupling within the backbone. This α–α coupling (alternately referred to as 2–5′ coupling) provides the ideal torsional angle between monomers (and thereby low energy

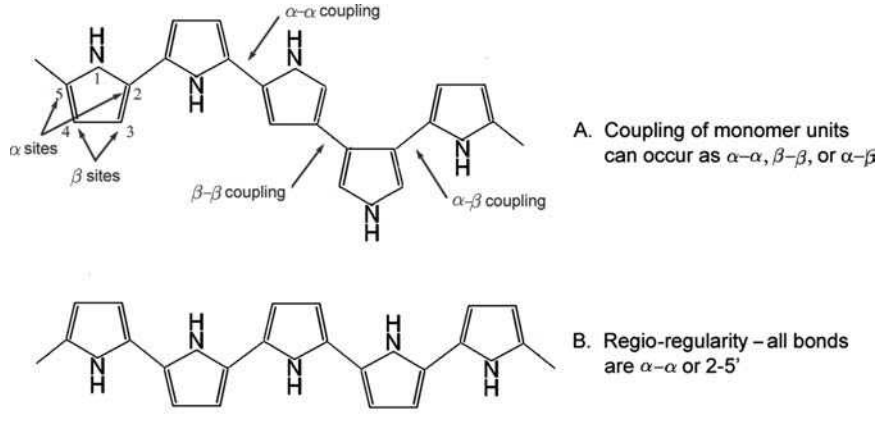

Figure 18.5 *Structural assembly of CP backbone using the asymmetrical monomer PPy: A. Coupling variants include α–α, β–β and α–β; and B. When all bonds are α–α regio-regularity is achieved*

planar conformation and low steric hindrance). This produces a polymer backbone with an increased degree of p-conjugation and delocalisation. Accordingly, when defective α–β and β–β couplings occur during polymerization, properties of CP are degraded [36]. Since electrodeposition provides minimal control over the structural features of the resulting CPs, controlling the properties of electrodeposited films through variation of the fabrication conditions is difficult. This inability to regulate properties and the difficulties associated with upscaling this type of reaction system, limits the ability to commercialize electrodeposited CPs. Further details of electrodeposition are discussed in Section 18.4.1.

Chemical synthesis is a an alternative fabrication technique that may prove to be more versatile by providing several polymerization routes for CPs. Chemical synthesis has the benefit of permitting CP fabrication on any deposition surface while providing greater control over the backbone structure, and is likely to be more economical when producing large quantities of polymers compared to electrodeposition. While these advantages make chemical synthesis promising for fabricating CPs for commercial purposes, its intricate fabrication process make it unattractive for biomedical applications, as explained in Section 18.4.2. Recently, a number of CPs with modified backbone structures have been investigated. These and other modification techniques of CPs are described in Section 18.4.3.

18.4.1 Electrodeposition

Electrochemical deposition of a CP is generally carried out in a single compartment, three-electrode (working, counter, and reference electrodes) cell with a solution of a monomer and an electrolyte (dopant) dissolved in an appropriate solvent. A schematic of a typical electrochemical deposition rig is shown in Figure 18.6. Upon galvanostatic (constant current), potentiostatic (constant potential), or potentiodynamic (pulsed current or pulsed

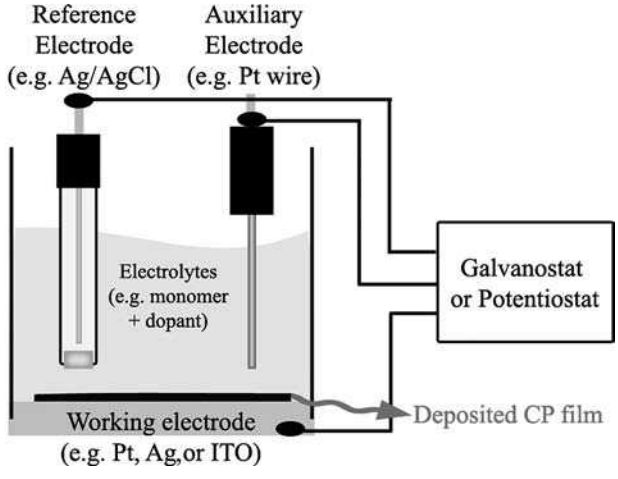

Figure 18.6 *Schematic of three-electrode cell used for electrodeposition*

potential) oxidation of the monomer, free-standing, homogeneous polymer thin film is formed on the working electrode (anode) surface.

In typical electrochemical oxidation, the monomer is oxidized to its radical cation and the coupling of two radicals form a dimer. The oxidation potential of the dimer is lower than that of the monomer and, therefore, consequent reoxidation of the dimer induces a further coupling with a monomeric radical until an insoluble oligomer is formed and precipitates onto the anode [58]. Several studies have suggested that subsequent polymer growth involves nucleation and three-dimensional growth processes and the electrode material has a direct effect on this nucleation-initiated growth [59]. Platinum electrodes are particularly beneficial as they can provide a high density of initial nucleation sites which help produce compact CPs with high conductivities [59,60].

Previous studies have shown that experimental conditions during electrodeposition, including solvent/electrolyte system, deposition charge, and time, pH level, and temperature will influence the morphology, conductivity, and mechanical properties of the final polymer film [61]. Conducting polymers can be synthesized in both aqueous and organic solvents. The most commonly used solvent in biomedical applications, water, is an oxygen nucleophile. While beneficial in a biological system, it is not an ideal solvent for polymer formation. When water is reduced, the oxygen forms hydroxide which reacts with radical intermediates and disrupts chain growth. A aprotic, non-nucleophilic solvent is likely to be more advantageous to forming polymers with good conductivity.

However, dopant solubility and pH level must be considered, as these are also dependant on the choice of solvent. As mentioned previously, conventional sodium sulfonate dopants and anionic biomolecules are easily dissolved in water. Aqueous sodium sulfonate electrolytes have a pH range (pH 7–9) close to the body pH level and this would help to minimize pH-induced cytotoxicity when implanted in the body. Temperature can affect the solubility of dopant and even the viscosity of electrolyte. Generally, low temperature helps to produce smoother, more conductive films, but the reduced dopant solubility and the increased viscosity can be problematic [62].

18.4.2 Chemical Synthesis

The mechanism of the chemical oxidation process has not yet been explained and most researchers assume that it is analogous to that of electrochemical oxidation. Two major techniques of chemical synthesis are oxidative coupling and metal-catalyzed cross-coupling. In oxidative coupling, the monomer solution of a CP is dissolved in an organic solution, such as chloroform, and added drop-wise to a flask filled with an organic solution of mild Lewis-acid catalysts under inert gas. Typical catalysts used are $FeCl_3$, $Fe_2(SO_4)_3$, or $CuCl_2$. The monomer solution mixture is then stirred for several hours to polymerize. The schematic in Figure 18.7A and associated chemical equation in Figure 18.7B, depicts the oxidative coupling of PPy dissolved in chloroform and catalyzed in the presence of $FeCl_3$.

Properties of CPs synthesized via oxidative coupling strongly depend on the reaction conditions, including the type and amount of constituents, polymerization time and temperature. To obtain films with high conductivity, an excessive amount of the oxidant species is added to the mixture in order to compensate for the oxidant molecules that are

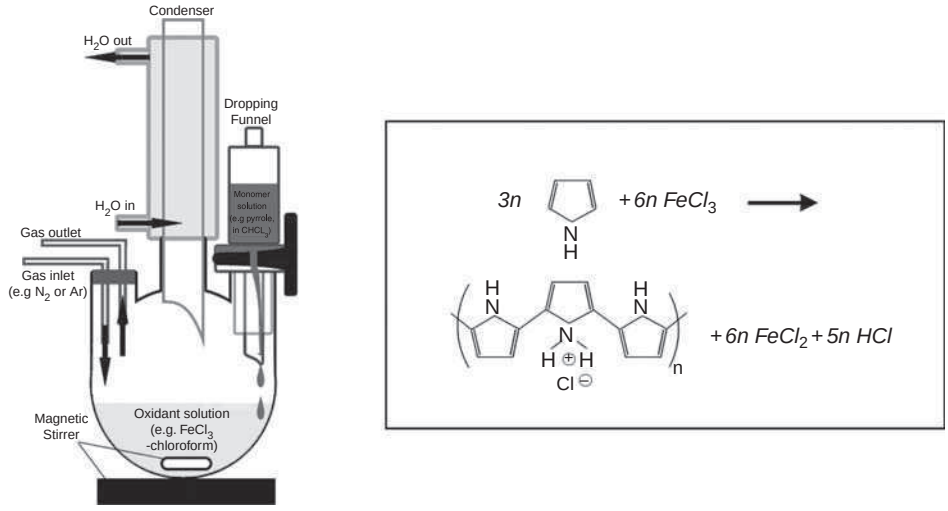

Figure 18.7 *Chemical synthesis of CP by oxidative coupling: (A) apparatus and (B) example of conventional reaction for fabrication of polypyrrole (PPy)*

consumed by acid by-products. In Figure 18.7B, HCl is the byproduct of the polymerization which causes the complexation of $FeCl_3$ to $FeCl_4$. A low polymerization temperature is desirable as this slows the oxidation rate of monomer and helps to fabricate region-regular chains by providing a small amount of cations to react with the growing chain at any given time [63].

While oxidative coupling has produced CPs with moderate regio-regularity of up to 90% for poly(3-alkylthiophene) (P3AT) [63], metal-catalyzed cross-coupling is superior with regio-regularity of greater than 95% reported for the same CP [64]. As a result of improved regio-regularity, metal-catalyzed CPs are more conductive. Metal-catalyzed cross-coupling has been widely studied for CPs in electronic applications and coupling variations employed thus far are summarized in Table 18.3. While the high conductivity of cross-coupled CPs may be attractive for some bioapplications, the use of toxic catalysts in

Table 18.3 *Metal-catalyzed cross-coupling reactions for CPs*

R-A	+	R-B	→	CPs	
A		B	Catalysts	CPs	Ref
MgBr		Br, I	Pd or Ni	*PT, PPP, PF	[65] [66]
Alkyne		Br, I	Pd and Cu	PPE	[67,68]
ZnX		Br, I	Pd or Ni	PT	[69]
SnR3		OTf	Pd	PT, PPP, PF	[70]
B(OH)2		Br, I	Pd	PT, PPP, PF	[71]

*R = conducting polymer monomer unit; PT = poly(thiophene)s; PPP = poly(p-phenylene)s; PF = Poly(fluorine)s; PPE = poly(phenylene ethynylene)s.

the process would increase the cytotoxicity of the resulting CP and therefore the cross-coupling technique has rarely been implemented for biomedical applications.

18.4.3 Alternate Processing Techniques

Most studies in last two decades focused on improving the electrical properties of CPs by optimizing reaction conditions. While a rigid conjugated backbone provides good CP conductivity, its strong interchain electron transfer results in intractable, insoluble polymers which are not thermally processible. The lack of processibility, along with the lack of bioactive functional groups on the chain, has limited the commercial exploitation of conventional CPs for biomedical applications. In an effort to overcome these difficulties, both covalent and noncovalent modification techniques have been studied. The fabrication of composite materials intended to take advantage of the properties of both constituent materials is another common route of exploration. Additionally, the processing of CPs by novel methods such as supercritical fluids or the manufacture of novel CP structures, such as nanotubes, have gained interest in recent years.

18.4.3.1 Copolymer Composites

Properties of copolymers and composites are derived from the combination of the characteristics of parent constituents. Accordingly, copolymerization and fabrication of composites of CPs with biofunctional nonconducting polymers have been studied to combine the electrical properties of the former with the processibility, bioactivity, and biostability of the latter.

Several conducting copolymers have been synthesized by copolymerizing a CP with either a conventional organic (nonconducting) polymer or another CP. Copolymerizations of two different heterocyclics, for example pyrrole and analine [72], or two variants of the same heterocyclic such as thiophene and 3-alkylthiophene [73], have been investigated. This type of copolymerization is used to stabilize the polymer backbone by providing variations in the torsion angle between adjacent aromatic rings and has been studied as a method to increase processibility. To improve solubility CPs, water-soluble conducting PPy graft copolymers have been prepared by using a poly-(sodium styrenesulfonate) (PSS)-linked-pyrrole monomer as a polymerization precursor. The resulting polymer was soluble in both water and the polar solvent DMSO [74].

Biodegradable polymer components have been employed to impart degradation characteristics to CPs produced as block copolymers [23,75]. Rivers *et al.* produced copolymers of conductive pyrrole-thiophene oligomers and biodegradable ester-aliphatic chain [75]. Initial biocompatibility tests showed that the copolymer was degradable by enzymes in the body and had toxicity similar to poly (lactic-co-glycolic) acid (PLGA), supporting cell attachment and proliferation. However, the conductivity of iodine-doped polymer was only around 10^{-4} S cm^{-1} [76]. Huang *et al.* fabricated a block copolymer of polylactide (PLA) with an aniline pentameter, producing a potential nerve repair scaffold with conductivity around 5×10^{-6} S cm^{-1} [23]. The use of longer conjugated segments and different doping techniques have been suggested to improve copolymer conductivities [76].

Conjugation of CP oligomers with protein sequences have been theorized to provide an optimal bioactive CP, providing the advantages of both components. Klok *et al.* have studied the combination of thiophene variants, tetra(3-hexylthiophene), with silk inspired peptide sequences to produce block copolymers with a self-assembled nanostructure [77,78]. These studies anticipated that the peptide or protein sequence would improve solubility, biocompatibility, and provide control over the structure formation of CP through protein folding. The use of the thiophene oligomers were propounded to prevent enzymatic degradation of the polymer while retaining an electrically conductive material. However, the specific properties of these novel polymers are unknown as studies thus far have been concentrated on the structural modeling of the copolymer. Despite minimal results, these biosynthetic CPs have the potential to provide new avenues of investigation for producing the desired combination of electrical and biological properties.

18.4.3.2 Hydrogel Composites

The role of hydrogels in CP composites can be divided into two categories: (i) a matrix for CP particle deposition and (ii) a template for confining the structure of CPs. The properties of these CP composites strongly depend on the concentration and structure of the CP within the hydrogel. A number of CP-filled hydrogel matrices have been used to obtain an electrically conducting composite with high mechanical and biological stability. A PPy/PSS–alginate composite was fabricated by electrodepositing PPy/PSS on alginate-coated Au electrodes [79]. The lowest impedance (7 kΩ) of the resulting composite at 1 kHz was two orders lower than that of the pure PPy film (∼100 kΩ). While no mechanical properties or the PPy content of the composite were reported, the alginate hydrogel increased the surface area of the PPy and produced a composite with low impedance.

Similarly, PPy was electrodeposited on an UV-polymerized poly(2-hydroxyethyl methacrylate) (pHEMA) matrix [80–82]. The addition of PPy in the pHEMA hydrogel reduced the electrical resistivity of pHEMA from 350 Ω to 52 Ω. The overall impedance of the composite was constantly low at less than 100 Ω across the frequency range of 1 mHz–60 kHz. Again, no mechanical properties or the CP content of the composite were reported.

CP composites of both poly(vinyl alcohol) (PVA) [83–88] and poly(ethylene glycol) (PEG) [87,89,90] have been fabricated by both chemical and electrochemical polymerization of either monomer solution loaded or dispersed into hydrogel networks. Li *et al.* reported that tetraethylammonium perchlorate (TEAP) doped PPy-PVA composite was more hydrophilic than PPy/TEAP film and showed less fibrinogen adsorption on the surface than the CP control film. The PPY-PVA composite maintained intrinsic conductivity of PPy/TEAP film (7 S cm^{-1}) and the porous structure of the composite promoted neural cell attachment and spreading in the model clonal line, PC12 [86].

PPY-PVA and PPY-PEG composites were fabricated by vapor polymerization of pyrrole onto $FeCl_3$-loaded hydrogel matrices [87]. $FeCl_3$-loaded PVA and PEG matrices were freeze-dried to form microstructures. The resulting composites have fine foam-like lattice structure with low weight density. The tensile strength and conductivity of 20 wt% PPy-PVA were 2.0 ± 0.2 MPa and ∼0.1 S cm^{-1}, respectively.

18.4.3.3 Carbon Nanotube Composites

The unique combination of high mechanical stability, electrical conductivity, and surface area make carbon nanotubes (CNTs) a popular material for a wide range of biomedical applications, from microbial fuel cells to biochemical sensors [91–94]. Accordingly, CP composites have been investigated to synergize both mechanical and electrical properties of CNTs.

PPy or PEDOT/CNT composites are conventionally synthesized by electrodeposition from a monomer/CNT electrolyte solution [93–100]. In general, the presence of CNTs has increased the conductivity of CPs and improved their sensitivity when applied to biosensors. Wu *et al.* [101] reported that the electrical conductivity of 3 wt% multiwalled carbon nanotube (MWNT)/PPy composites was 150% higher than that of bulk PPy film. While Long *et al.* [98] reported two orders of magnitude increase in conductivity for MWNT-PPy composites. However, CNTs, especially single-walled nanotubes (SWNTs), have been reported as potentially cytotoxic [102,103]. Sayes *et al.* reported that addition of carboxyl or sulfonyl phenyl chains to the sidewall of SWNTs reduced their cytotoxic effect [104].

Further studies to evaluate the intrinsic cellular toxicity of CNTs and the mechanical stability of the resulting composites are required for practical bioapplications.

18.4.3.4 Supercritical Fluid Modifications

Supercritical fluids (SCFs), in particular supercritical carbon dioxide (Sc-CO_2), have been attracting great interest as processing solvents for use in biomaterial fabrication. SCFs are considered advantageous, due to their high diffusion coefficient and solubility, low surface tension and viscosity, and negligible toxicity. The supercritical status of CO_2 is achieved when both temperature ($T_{C,\,CO2} = 31.1\ °C$) and pressure ($P_{C,\,CO2} = 72.9$ bar) are above the critical values [105]. At this critical point, shown in Figure 18.8, the liquid- and gas-phase boundary disappears and becomes a single supercritical phase. Hence, supercritical fluids exploit the advantageous properties of both liquid (high solubility) and gas (high diffusivity and low viscosity).

Sc-CO_2 can either be used as a 'green' solvent [106] for chemical polymerization of CP or as a penetrant for impregnating chemical entities into the CP matrix. Armes *et al.*

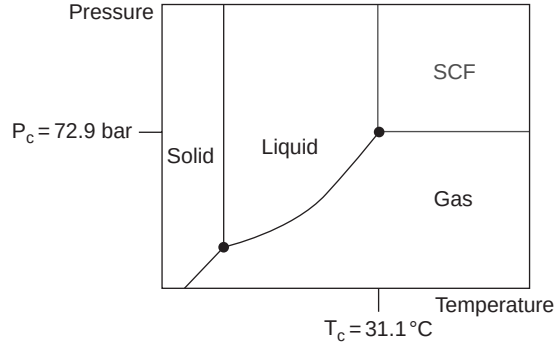

Figure 18.8 *Schematic pressure vs. temperature phase diagram for supercritical CO_2*

reported that both the pyrrole monomer and $Fe(CF_3SO_3)_3$ oxidant are soluble in Sc-CO_2, allowing the chemical fabrication of PPy films without harsh solvents [107]. Similarly, several CP composites have been fabricated by simple two-step processing using Sc-CO_2 as a solvent [108–111]. In the first step, porous matrices of polyethylene (PE) [108], polystyrene (PS) [109], or polyurethane (PU) [110,111] were loaded with Sc-CO_2-solubilized oxidant ($FeCl_3$, $Fe(CF_3SO_3)_3$, $Fe(CF_3CO_2)_3$, or I_2). Then the pyrrole vapor was applied to the oxidant-loaded matrix to form PPy within the matrix by chemical polymerization. Kurosawa *et al.* [109] and Shenoy *et al.* [110] have reported that the amount of PPy formed was directly related to the amount of oxidant impregnated in the substrate. Shenoy *et al.* further demonstrated that the use of ethanol helped to solubilize oxidant in $Fe(CF_3SO_3)_3$ in Sc-CO_2 [110].

Generally, CO_2 is used only as a solvent for nonpolar molecules with low molecular weights [112]. Thus, most polar molecules and many polymers cannot be dissolved in pure CO_2 under standard conditions ($<100\,°C$, <350 bar), which limits the applicability of Sc-CO_2 to CPs. The development of alternate SCFs and CP structures will be required to produce optimal biomaterials with this technology.

18.4.3.5 Novel CP Structures

A number of novel methods for nanostructuring CPs have been investigated to produce materials with specific properties and functionalities for biomedical systems. The synthesis methods for nanostructured CPs can be generally divided into two main categories, template and nontemplate approaches.

In a template synthesis, CP is polymerized within the pores or channels of a nanoporous template to obtain the controlled structure and morphology upon removal of the template. Templates can be either a masking of a confined area that CP can grow in or a structured surface that CP is deposited upon. Masking type templates, namely nanoporous anodic aluminium oxide (AAO also commonly known as Al_2O_3, alumina, or anodisc^{TM}) [113–118], hydrogels [119,120] and latex particles [121–130], have been used to prepare nanoscale fibrils, particles, and tubules of CPs.

Kim *et al.* [118] electrodeposited 40-μm long, 100- or 200-nm thick PPy, PANI, and PEDOT nanowires on an Au surface using AAO templates with cylindrical nanopores. The diameters of the resulting nanowires were dictated by the pore sizes of the template used, with 100 nm pores resulting in 100 nm CP wires. The polymerization was initiated along the wall of the AAO template as the anionic template attracted cationic CP [131]. Consequently, instead of nanowires, nanotubes with wall thicknesses of 10–30 nm were formed initially. Then, as polymerization time increased, the nanotubes were filled to yield nanowires.

A major challenge in developing templated CPs is in the removal of templates to obtain free-standing CP films. Kim *et al.* [132] removed the alumina template used to produce CP nanowires by application of hydrofluoric acid or alternatively sodium hydroxide, following polymerization. The use of strong acidic or basic solutions were shown to decrease the CP conductivity from 30 S cm^{-1} prior to alumina dissolution, to 7 S cm^{-1} for the HF treatment and 1×10^{-2} S cm^{-1} for the NaOH treatment. The dedoping effect of NaOH solution, through the ion exchange between the intercalated anion and OH^-, accounts for the sharp loss of conductivity [132].

As an alternate approach, Abidian *et al.* [119] electrodeposited 50–100-nm thick, 100–600 nm diameter PEDOT nanotubes by using electrospun poly(L-lactic acid) (PLLA) nanofibers as a template. The PLLA nanofibers were spun onto the microfabricated neural electrode and either PEDOT or PPy was electrodeposited on the Au conducting sites around the electrospun PLLA. After the polymerization, the PLLA template was removed by soaking the probe tip in dichloromethane, forming nanotubes on the neural probe. The resulting PEDOT and PPy nanotubes showed very low impedances at 1 kHz, of 4 kΩ and 80 kΩ, respectively, when compared to uncoated Au sites (800 kΩ). Additionally, the charge-transfer capacity of electrode sites modified with PEDOT nanotubes increased by approx. three orders of magnitude due to the increased surface area. In their more recent work, poly(lactic-co-glycolic acid) (PLGA) nanofibers were used as a template instead of PLLA nanofibers. Biodegradable PLGA offered an additional controlled drug-release function while maintaining the function as a template.

Colloidal composite microparticles have been prepared by polymerizing *N*-methyl pyrrole on structured poly(*N*-isopropylacrylamide) (PNIPAAm) microgel particles . The maximum amount of CP that can maintain colloidal status of the formed composite was 4.5 vol% relative to the microgel volume, and the conductivity of the composite was on the order of 10^{-5}–10^{-6} S cm^{-1} [133]. Similar colloidal dispersions of CP composites have been fabricated by coating sterically stabilized polystyrene (PS) [121–127] or silica [128,129] latex nanoparticles with a thin layer of CP. PS and silica latex cores were then dissolved respectively in tetrahydrofuran (THF) and HF to form hollow CP nanoparticles resembling the shapes of ''broken egg-shell'' [122].

Tran *et al.* [134,135] reported a template-free fabrication method of CP nanofibers using CP oligomers. Addition of small amounts (1–20 wt% of the monomer) of oligomers (e.g. bipyrrole) into the conventional chemical oxidation reagents (e.g. monomer (pyrrole) and oxidant ($FeCl_3$)) yielded the formation of 20 nm PPy nanofibers instead of conventional granular agglomerates after the conventional chemical oxidation procedure (Figure 18.7). The resulting PPy nanofibers were water dispersible and readily cast into films for biosensing applications. Additionally, no special purification/removal steps were required to obtain CP nanofibers.

18.5 Polymer Characterization

CPs designed for biomedical applications generally require good electrical conductivity, physicochemical and mechanical stability, and biocompatibility to effectively interact with biological system. A wide range of analytical techniques to characterize the feasibility of conducting polymers as biomaterials are summarized here.

18.5.1 Surface Properties

It is well known that the surface properties, such as roughness, porosity, wettability, chemical composition, and morphology, are critical to the *in vivo* performance of a biomaterial. Thus, surface characteristics of CPs have been studied using various methods.

Surface chemistry and morphology of CPs have been investigated using high-vacuum methods such as scanning electron microscopy (SEM) with energy-dispersive X-ray analysis (EDX), X-ray photoelectron spectroscopy (XPS), auger electron spectroscopy (AES), and matrix-assisted laser desorption/ionization time-of-flight mass spectroscopy (MALDI-TOF-MS).

SEM provides nanoscale details, including shape, structure, roughness, and porosity of CP surfaces and can also be used to measure the thickness of CP films. Additionally, with EDX functionality SEM can be used to identify the elemental composition of a CP surface. Similarly, XPS (x,y spatial resolution $\sim$1 μm) and AES (resolution $\sim$5 nm) can provide quantitative data on the chemical composition of a material surface. Accordingly, XPS and AES have been widely used to identify the doping level/species of CP films, while MALDI-TOF-MS have been used for qualitative identification of biomolecules incorporated in CP matrices.

Other techniques, such as atomic force microscopy (AFM), and dynamic contact angle measurement (DCA) have been performed to measure the surface roughness and hydrophilicity of the sample, respectively.

18.5.2 Mechanical Properties

Since cell interaction is affected by the mechanical properties of the surrounding entity, mechanical properties, including stiffness and elastic modulus of biomedical CPs must be considered. Due to insolubility of most CPs, it is very hard to prepare a free-standing CP sample for conventional tensile testing, thus reports on microtensile test data are scarce. Lang and Dual showed films formed from commercially available PEDOT/PSS dispersion (also known as Baytron) had an ultimate tensile strength of 1–2.7 GPa and yield strength of 25–55 MPa [136]. Nanoindentation is, and may be, the only mechanical testing method available for quantitatively testing the stiffness of electrodeposited nonsoluble CPs, which must be fabricated on a substrate. However, there have been a few reports on measuring the mechanical properties of CP by indention. Yang and Martin used nanoindentation to show a correlation between softer films and low impedances [51]. However, various systematic errors associated with imperfect tip geometry and adhesion of the film to the tip makes this technique problematic.

Secure adhesion of the CP film on a substrate is another important mechanical property for long-term function of a bioimplant device. Pull-off tests (ASTM standard procedure D-4541-95) and other ASTM adhesion and hardness assays may provide valuable information on the adherence of CP films to metal substrates [1,137].

18.5.3 Electrical Properties

Electrochemical stability is an essential requirement for CPs designed for any long-term bioelectric applications. Cyclic voltammetry (CV) is used to measure the electrochemical characteristics of a CP sample, including the reduction/oxidation potentials and reversibility. By performing CV over multiple cycles the long-term electrochemical stability of a sample can be assessed. This technique has been shown to be particularly important in the

design of CPs. Variation of the monomer and dopant type of a CP can significantly affect the long-term electrochemical performance of the material. CPs based on PPy are, in general, less stable than those based on PEDOT, with Yamato observing a loss in electrochemical stability of 95% for PPy doped with PSS, compared to 11% for identically doped PEDOT [36]. CV has also shown that variation of dopant type or size can impact on the CP stability. PPy doped with the small pTS anion results in an electrochemically instable film when compared to PPy doped with the larger anionic polymeric PSS chain [12].

Quantitative conductivity of a CP sample is typically measured by a four-point probe technique. CPs for biomedical applications have typically yielded conductivities of between 1 and 200 S cm^{-1} [44–46,49,50,138]. However, four-point probe measurements can be problematic, as the CP film must be removed from the substrate prior to testing. There have been a number of different methods used for film removal, including double-sided tape, razor blades, and backing the film with polydimethylsiloxane (PDMS) [61]. Fonner *et al.* found the double-sided tape technique to be most effective, as the CP film was removed from the substrate undamaged and the presence of the tape did not affect the conductivity measurement [61].

Finally, electrochemical impedance spectroscopy (EIS) can be used to quantify the impedance characteristics of a CP. The vast majority of literature has shown that CP coating of conventional electrode materials can reduce the interface impedance by several orders of magnitude [12,52,79,139]. This has widely been attributed to the increase in surface area available for charge transfer when CPs are employed. Importantly, EIS is also used to model the electrode interface. CPs reportedly alter the capacitive behavior of conventional electrode materials to produce a predominantly resistive interface with significantly smaller phase angles at low frequencies [12,51,139,140].

The assessment of a variety of electrical properties can provide important information regarding the potential performance of CPs for biomaterial applications. The properties of electrochemistry, conductivity, and impedance are not mutually exclusive and all must be quantified to design an optimal CP.

18.5.4 Biological Performance

The *in vitro* biocompatibility of CPs has been generally investigated by cell viability, proliferation and cytotoxicity assays of various cell types, including rat pheochromocytoma cells (PC12), rat Schwann cells, cardiac myoblasts, astrocytes, and various neural tissue explants [13,27,43,47]. Studies on a wide variety of CPs have indicated good *in vitro* cell responses, with minimal cytotoxicity and, in several cases, preferential adherence of cells to the CP surface, compared to conventional implant materials. However, the majority *in vitro* studies examine the passive or nonelectrochemically activated state of CPs. Due to the application-specific nature of biocompatibility, passive CP assessment, although a useful preliminary study, is an imperfect characterization of CP biological performance for most implant applications.

Electrical stimulation has been shown to increase the growth of neurites from neural tissue both on conventional culture substrates and in the presence of CPs [141]. Electrically stimulated CPs have been assessed *in vitro*, with both clonal cell lines and explant tissue demonstrating increased survival and growth on activated CPs when

compared to passive CP controls [27,141,142]. Kotwal and Schmidt have hypothesized that increased neurite outgrowth is due to electrically mediated protein absorption onto the CP surface [142]. Optimizing this mechanism may provide insight into the design of CPs for ideal cell adherence and growth.

In vivo characterization is more suited to the assessment of CP biological performance, with studies tailored for the intended implant application. *In vivo* CP studies have been largely limited to electrode recording applications, where CPs have been shown to temporarily improve signal quality [52]. This is due primarily to neural interactions, discussed further in Section 18.6. Future biological characterization of CPs must focus on *in vivo*, long-term studies in anatomically appropriate sites with on-going assessment of electrical performance.

18.6 Interfacing with Neural Tissue

The main focus of CP technology in the biomedical field is the alteration of bioelectrodes for neuroprosthetic applications. CPs have been found to significantly improve the interactions of neural tissue with conventional electrodes through the creation of a more conducive environment for cell adherence and growth [3,12,14,40,48,143]. When placed in a biological environment the smooth metallic or glassy surface of conventional electrode constructs does not interact significantly with the surrounding tissue. The result is that the neural interface contains a small fluid gap through which the electrical stimulation or recording must be transduced [1], depicted in Figure 18.9A. High impedance with large bilayer capacitance is evident at this interface and as a consequence the electrical stimulation parameters must be sufficiently large such that the stimulation reaches the target neural cells with a high enough current to cause depolarization of the cell's transmembrane potential to a threshold value. The introduction of a CP coating, depicted in Figure 18.9B, aims to remove the fluid gap and create an intimate connection between the electrode and target neural tissue, effectively reducing the current required to reach the desired cell depolarisation threshold.

Maintenance of contact with neural cells is integral to the performance of the implant device and the use of biosynthetic CP coatings will potentially improve the long-term efficacy of such devices. Limited research is available on the long-term interactions of CPs with neural tissue. Two studies by the Martin research group at Michigan University have examined the chronic performance of nanostructured PEDOT on neural recording electrodes [52,144]. The microelectrode arrays coated with surfactant-templated PEDOT and

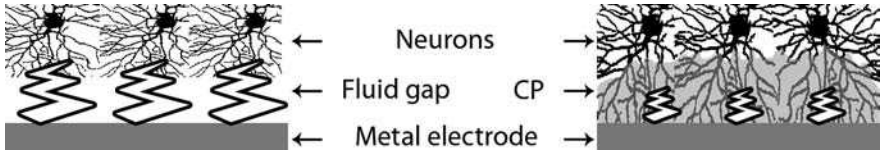

Figure 18.9 *Schematic of neural interaction and passage of electrical stimulation for: (left) conventional metal electrodes and (right) CP-coated electrodes with neural ingrowth*

PEDOT nanotubes were implanted in rat cortex for periods of six and seven weeks, respectively. In both studies the SNR of the PEDOT-coated electrodes was significantly improved compared to the bare electrode control in the initial period following implantation. However, the benefit provided by the nanostructured PEDOT substantially decreased over the subsequent weeks such that no significant difference was observed between the PEDOT coated and control electrodes by day 15. This decline in CP performance was attributed to the wound-healing response which caused separation between the microelectrode and neural tissue in both studies [52,144]. It is hypothesized that a combination of neurotrophins and anti-inflammatories will be required to control the wound-healing response and promote neural in-growth to the electrode sites before fibrous encapsulation and scar tissue displace the electrodes [52]. While Abidian *et al.* [145] have incorporated the anti-inflammatory drug dexamethasone into copolymer nanotubes of PLGA/PEDOT and demonstrated release profiles *in vitro*, their chronic *in vivo* performance has not been reported. Despite the need for more research in this area, novel nanostructures of drug-loaded CPs show promise for revolutionizing the functionality of electrode interfaces and implant devices.

In neuroprosthetic applications it is important to note that the interfacial neural tissue is not likely to be healthy. Electrical current is applied to cells where the native input has been compromised through injury or disease, with the artificial stimulation bypassing the damaged tissue. Both injury and disease cause cascade degeneration along the neural path, and, as such, the remaining functional tissue being stimulated is typically in a state of regressing functionality. It has been shown that the application of external electric charge can aid in the rescue and delay the onset of transneuronal degeneration in the remaining functional cells [3,142,146]. However, a desirable neural interface would promote cell regeneration and maintain the interface for the implant and conceivably patient lifetimes.

Nanostructured bioactive CPs aim to improve cell rescue and limit continued degeneration through the creation of an interface with optimal mechanical and morphological properties, improved electrical transduction, allowing the use of smaller, safer charge injections, combined with a controlled supply of appropriate biological signaling factors. Numerous studies have outlined the efficacy of supplying damaged neural tissue with a combination of both electrical stimulus and neurotrophins [27,142,146,147], but very limited *in vivo* data is available on the supply of neurotrophins via CPs. A pioneering study by Richardson *et al.* on guinea-pig cochleae indicated that electrical stimulation in combination with controlled release of neurotrophin, NT-3, from PPy can rescue damaged neural cells if they are in the direct path of current passage, but the surrounding cells continue to degenerate [3]. Additionally, it was found that rescued cells continued to degenerate once the supply of neurotrophin was exhausted, a period of two weeks. A major challenge in the future development of CPs will be the on-going provision of neurotrophins through controlled release.

18.7 Conclusions

Conducting polymers are an exciting alternative to conventional metal biomaterials for use in a range of implant applications with a requirement for electroactivity. The development

of commercially applicable CPs for the biomedical field will rely on novel methods of CP fabrication and the careful choice of components to minimize impact on the resulting polymer properties. Both the method of fabrication and components of a CP contribute to material physicochemical and biological properties, and ultimately determine CP safety and performance in a biological environment.

A major challenge in the development of bioactive CPs is in creating a material that can provide biological cues for both the regeneration and long-term maintenance of tissue, as well as being physically robust and electrically stable. Nanostructuring conducting polymers via incorporation of biological signals or via fabrication of CNT and hydrogel composites offer novel solutions to some of the issues that arise through use of conducting polymers alone. These approaches for developing polymers with optimal electrical, mechanical, and biological performance will potentially lead to the development of advanced materials with application across numerous fields in the biomedical industry.

References

[1] R.A. Green, N.H. Lovell, G.G. Wallace, and L.A. Poole-Warren, Conducting polymers for neural interfaces: Challenges in developing an effective long-term implant, *Biomaterials*, **29**, 3393–3399 (2008).

[2] C.Q. Huang and R.K. Shepherd, Reduction in excitability of the auditory nerve following electrical stimulation at high stimulus rates. IV. Effects of stimulus intensity, *Hearing Res.*, **132**(1–2), 60–68 (1999).

[3] R.T. Richardson, A.K. Wise, B.C. Thompson, B.O. Flynn, P.J. Atkinson, N.J. Fretwell, J.B. Fallon, G.G. Wallace, R.K. Shepherd, G.M. Clark, and S.J. O'leary, Polypyrrole-coated electrodes for the delivery of charge and neurotrophins to cochlear neurons, *Biomaterials*, **30**, 2614–2624 (2009).

[4] J. Weiland and M. Humayan, Past, present and future of artificial vision, *Art. Organs*, **27**, 961–962 (2003).

[5] E. Zrenner, Will retinal implants restore vision?, *Science*, **295**, 1022–1025 (2002).

[6] N.H. Lovell, L.E. Hallum, S. Chen, S. Dokos, P. Byrnes-Preston, R.A. Green, L.A. Poole-Warren, T. Lehmann, and G.J. Suaning, Advances in retinal neuroprosthetics. In *Handbook of Neural Engineering*, ed. M. Akay, WileyBlackwell, London, 2007.

[7] M.S. Humayun, Pattern electrical stimulation of the human retina, *Vision Res.*, **39**(15), 2569–2576 (1999).

[8] M.S. Humayun, M. Prince, E. De Juan, Jr., Y. Barron, M. Moskowitz, I.B. Klock, and A.H. Milam, Morphometric analysis of the extramacular retina from postmortem eyes with retinitis pigmentosa, *Invest. Ophthalmol. Vis. Sci.*, **40**(1), 143–148 (1999).

[9] M.S. Humayun, E. De Juan, Jr., G. Dagnelie, R.J. Greenberg, R.H. Propst, and D.H. Phillips, Visual perception elicited by electrical stimulation of retina in blind humans, *Arch. Ophthalmol.*, **114**(1), 40–46 (1996).

[10] D.R. Kim, M. Abidian, and D.C. Martin, Synthesis and characterization of conducting polymers grown in hydrogels for neural applications, *Mat. Res. Soc. Symp. Proc.*, **1**, 1–6 (2004).

[11] T.L. Rose and L.S. Robblee, Electrical stimulation with Pt electrodes. VIII. Electrochemically safe charge injection limits with 0.2 ms pulses, *IEEE Trans. Biomed. Eng.*, **37**(11), 1118–1120 (1990).

[12] R.A. Green, Ph.D. Thesis, Conducting polymers for neural interfaces: Impact of physicochemical properties on biological performance, Graduate School of Biomedical Engineering, University of New South Wales (2009).

[13] R.A. Green, N.H. Lovell, and L.A. Poole-Warren, Cell attachment functionality of bioactive conducting polymers for neural interfaces, *Biomaterials*, **30**(22), 3637–3644 (2009).

[14] X. Cui, J. Wiler, M. Dzaman, R.A. Altschuler, and D.C. Martin, In vivo studies of polypyrrole/peptide coated neural probes, *Biomaterials*, **24**(5), 777–787 (2003).
[15] D.H. Kim, S.M. Richardson-Burns, J.L. Hendricks, C. Sequera, and D.C. Martin, Effect of immobilized nerve growth factor on conductive polymers: Electrical properties and cellular response, *Adv. Funct. Mater.*, **17**(1), 1–8 (2006).
[16] A. Snellings, D.J. Anderson, and J.W. Aldridge, Use of multichannel recording electrodes and independent component analysis for target localization in deep brain structures, *Proceedings of the 1st International IEEE EMBS Conference on Neural Engineering*, Capri Island, Italy, 305–308 (2003).
[17] J. Liu, M. Agarwal, and K. Varahramyan, Glucose sensor based on organic thin film transistor using glucose oxidase and conducting polymer, *Sens. Actuat. B Chem.*, **135**(1), 195–199 (2008).
[18] M. Gao, L. Dai, and G.G. Wallace, Glucose sensor based on glucose-oxidase-containing polypyrrole/aligned carbon nanotube coaxial nanowire electrodes, *Synth. Met.*, **137**, 1393–1394 (2003).
[19] T.V. Vernitskaya and O.N. Efimov, Polypyrrole: A conducting polymer; its synthesis, properties and applications, *Russ, Chem. Rev.*, **66**(5), 443–457 (1997).
[20] J. Wang and M. Musameh, Carbon-nanotubes doped polypyrrole glucose biosensor, *Anal. Chim. Acta*, **539**, 209–213 (2005).
[21] J. Huang, S. Virji, B.H. Weiller, and R.B. Kaner, Nanostructured polyaniline sensors, *Chemistry*, **10**(6), 1314–1319 (2004).
[22] G.C.W. De Ruiter, M.J.A. Malessy, M.J. Yaszemski, A.J. Windebank, and R.J. Spinner, Designing ideal conduits for peripheral nerve repair, *J. Neurosurg.*, **26**(2) (2009).
[23] L. Huang, J. Hu, L. Lang, X. Wang, P. Zhang, X. Jing, X. Wang, X. Chen, P.I. Lelkes, A.G. Macdiarmid, and Y. Wei, Synthesis and characterization of electroactive and biodegradable ABA block copolymer of polylactide and aniline pentamer, *Biomaterials*, **28**, 1741–1751 (2007).
[24] R.A. Green, N.H. Lovell, and L.A. Poole-Warren, Impact of co-incorporating laminin-peptide dopants and neurotrophic growth factors on conducting polymer properties, *Acta Biomater.*, **6**, 63–71 (2010).
[25] Y. Li, K.G. Neoh, L. Cen, and E.T. Kang, Controlled release of heparin from polypyrrole-poly(vinyl alcohol) assembly by electrical stimulation, *J. Biomed. Mater. Res. A*, **73A**(2), 171–181 (2005).
[26] J. Isaksson, P. Kjall, D. Nilsson, N. Robinson, M. Berggren, and A. Richter-Dahlfors, Electronic control of Ca^{2+} signalling in neuronal cells using an organic electronic ion pump, *Nat. Mater.*, **6**(9), 673–679 (2007).
[27] R.T. Richardson, B. Thompson, S. Moulton, C. Newbold, M.G. Lum, A. Cameron, G. Wallace, R. Kapsa, G. Clark, and S. O'Leary, The effect of polypyrrole with incorporated neurotrophin-3 on the promotion of neurite outgrowth from auditory neurons, *Biomaterials*, **28**(3), 513–523 (2007).
[28] B.C. Thompson, S.E. Moulton, J. Ding, R. Richardson, A. Cameron, S. O'leary, G.G. Wallace, and G.M. Clark, Optimising the incorporation and release of a neurotrophic factor using conducting polypyrrole, *J. Contr. Rel.*, **116**(3), 285–294 (2006).
[29] A.J. Heeger, A.G. Macdiarmid, and H. Shirakawa, The nobel prize in chemistry, 2000: Conductive polymers, *The Royal Swedish Academy of Sciences* (2000).
[30] C. Pratt, *Conducting Polymers*, Kingston University, London, 1996.
[31] A.J. Heeger. *Handbook of Conducting Polymers II*, ed. T.A. Skotheim, Marcel Dekker, New York, 1986.
[32] N.K. Guimard, N. Gomez, and C.E. Schmidt, Conducting polymers in biomedical engineering, *Prog. Polym. Sci.*, **32**, 876–921 (2007).
[33] H. Shirakawa, E.J. Louis, A.G. MacDiarmid, C.K. Chiang, and A.J. Heeger, Synthesis of electrically conducting organic polymer: Halogen derivatives of polyacetylene (CH)x, *J. Chem. Soc. Chem. Comm.*, 578–580 (1977).
[34] A. Guiseppi-Elie and G.E. Wnek, Stability of iodine-doped polyacetylene in aqueous environments, *J. Physique*, **3**(6), 193–197 (1983).

[35] A. Dall'Olio, G. Dascola, V. Varacca, and V. Bocchi, Electron paramagnetic resonance and conductivity of an electrolytic oxypyrrole black, *CR Acad. Sci. Ser. C*, **267**, 433–435 (1968).
[36] H. Yamato, M. Ohwa, and W. Wernet, Stability of polypyrrole and poly(3,4-ethylenedioxythiophene) for biosensor application, *J. Electroanal. Chem.*, **397**(1–2), 163–170 (1995).
[37] Y. Xiao, X. Cui, and D.C. Martin, Electrochemical polymerization and properties of pedot/s-edot on neural microelectrode arrays, *J. Electroanal. Chem.*, **573**, 43–48 (2004).
[38] Y. Xiao, X. Cui, J.M. Hancock, M. Bouguettaya, J.R. Reynolds, and D.C. Martin, Electrochemical polymerization of poly(hydroxymethylated-3,4-ethylenedioxythiophene) (pedot-meoh) on multichannel neural probes, *Sens. Actuat. B Chem.*, **99**, 437–443 (2004).
[39] D.-F. Li, H.-J. Wang, J.-X. Fu, W. Wang, X.-S. Jia, and J.-Y. Wang, Preparation of a hydrophobic polythiophene film to improve protein adsorption and proliferation of pc 12 cells, *J. Phys. Chem. B*, **112**(51), 16290–16299 (2008).
[40] P.R. Bidez, S. Li, A.G. Macdiarmid, E.C. Venancio, Y. Wei, and P.I. Lelkes, Polyaniline, an electroactive polymer, supports adhesion and proliferation of cardiac myoblasts, *J. Biomater. Sci., Polym. Ed.*, **17**, 199–212 (2006).
[41] S. Kamalesh, P. Tan, J. Wang, T. Lee, E.T. Kang, and C.H. Wang, Biocompatibility of electroactive polymers in tissues, *J. Biomed. Mater. Res.*, **52**, 467–478 (2000).
[42] M. Li, Y. Guo, Y. Wei, A.G. Macdiarmid, and P.I. Lelkes, Electrospinning polyaniline-contained gelatin nanofibers for tissue engineering applications, *Biomaterials*, **27**(13), 2705–2715 (2006).
[43] X. Cui, J.F. Hetke, J.A. Wiler, D.J. Anderson, and D.C. Martin, Electrochemical deposition and characterization of conducting polymer polypyrrole/pss on multichannel neural probes, *Sens. Actuat. A Phys.*, **93**(1), 8–18 (2001).
[44] L.F. Warren, J.A. Walker, D.P. Anderson, and C.G. Rhodes, A study of conducting polymer morphology: The effect of dopant anions upon order, *J. Electrochem. Soc.*, **136**(8), 2286–2295 (1989).
[45] H. Masada and D.K. Asano, Preparation and properties of polypyrrole, *Synth. Met.*, **135–136**, 43–44 (2003).
[46] R.A. Khalkhali, Electrochemical synthesis and characterization of electroactive conducting polypyrrole polymers, *Russ. J. Electrochem.*, **41**(9), 1023–1935 (2005).
[47] X. Cui, V.A. Lee, Y. Raphael, J.A. Wiler, J.F. Hetke, D.J. Anderson, and D.C. Martin, Surface modification of neural recording electrodes with conducting polymer/biomolecule blends, *J. Biomed. Mater. Res.*, **56**(2), 261–272 (2001).
[48] J.H. Collier, J.P. Camp, T.W. Hudson, and C.E. Schmidt, Synthesis and characterization of polypyrrole-hyaluronic acid composite biomaterials for tissue engineering applications, *J. Biomed. Mater. Res.*, **50**, 574–584 (2000).
[49] T.A. Skotheim and J.R. Reynolds, *Conjugated Polymers: Theory, Synthesis, Properties, and Characterization*, CRC Press, Boca Raton, FL, 2007.
[50] F. Estrany, R. Oliver, E. Armelín, H.I. Iribaren, F. Liesa, and C. Alemán, Electroactive properties and electrochemical stability of poly(3,4-ethylenedioxythiophene) and poly(n-methylpyrrole) multi-layered films generated by anodic oxidation, *Port. Electrochim. Acta*, **25**, 55–65 (2007).
[51] J. Yang and D.C. Martin, Impedance spectroscopy and nanoindentation of conducting poly(3,4-ethylenedioxythiophene) coatings on microfabricated neural prosthetic devices, *J. Mater. Res.*, **21**(5), 1124–1132 (2006).
[52] K.A. Ludwig, J.D. Uram, J. Yang, and D.C. Martin, Chronic neural recordings using silicon microelectrode arrays electrochemically deposited with poly(3,4-ehtylenedioxythiophene) (pedot) film, *J. Neural Eng.*, **3**, 59–70 (2006).
[53] H.K. Song, B. Toste, K. Ahmann, D. Hoffman-Kim, and G.T.R. Palmore, Micropatterns of positive guidance cues anchored to polypyrrole doped with polyglutamic acid: A new platform for characterizing neurite extension in complex environments, *Biomaterials*, **27**, 473–484 (2006).
[54] A.J. Hodgson, M.J. John, T. Campbell, A. Georgevich, S. Woodhouse, T. Aoki, N. Ogata, and G.G. Wallace, Integration of biocomponents with synthetic structures – use of conducting polymer polyelectrolyte composites, *SPIE*, **2716**, 164–176 (1996).

[55] N. Gomez and C.E. Schmidt, Nerve growth factor-immobilized polypyrrole: Bioactive electrically conducting polymer for enhanced neurite extension, *J. Biom. Mater. Res. Part A*, **81A**(1), 135–149 (2007).
[56] S.H. Cho, K.T. Song, and J.Y. Lee, Recent advances in polypyrrole. In *Handbook of Conducting Polymers*, ed. T.A. Skotheim and J.R. Reynolds, CRC Press, Boca Raton FL, (2007).
[57] K.M. Cheung, D. Bloor, and G.C. Stevens, Characterization of polypyrrole electropolymerized on different electrodes, *Polymer*, **29**(9), 1709–1717 (1988).
[58] A.Z. Diaz, J.I. Castillo, J.A. Logan, and W.Y. Lee, Electrochemistry of conducting polypyrrole films, *J. Electroanal. Chem.*, **129**, 115–132 (1981).
[59] J. Roncali, Conjugated poly(thiophenes): Synthesis, functionalization, and applications, *Chem. Rev.*, **92**(4), 711–738 (1992).
[60] A. Yassar, J. Roncali, and F. Garnier, Conductivity and conjugation length in poly(3-thiophene) thin-films, *Macromolecules*, **22**(2), 804–809 (1989).
[61] J.M. Fonner, L. Forciniti, H. Nguyen, J.D. Byrne, Y.-F. Kou, J. Syeda-Nawaz, and C.E. Schmidt, Biocompatibility implications of polypyrrole synthesis techniques, *Biomed Mater.*, **3**(3) 034124 (2008).
[62] K. West, L. Bay, M.M. Nielsen, Y. Velmurugu, and S. Skaarup, Electronic conductivity of polypyrrole-dodecyl benzene sulfonate complexes, *J. Phys. Chem. B*, **108**(39), 15001–15008 (2004).
[63] S. Amou, O. Haba, K. Shirato, T. Hayakawa, M. Ueda, K. Takeuchi, and M. Asai, Head-to-tail regioregularity of poly(3-hexylthiophene) in oxidative coupling polymerization with fecl3, *J. Polym. Sci. A, Polym. Chem.*, **37**(13), 1943–1948 (1999).
[64] R.C. Hiorns, A. Khoukh, B. Gourdet, and C. Dagron-Lartigau, Extremely regio-regular poly (3-alkylthiophene)s from simplified chain-growth grignard metathesis polymerisations and the modification of their chain-ends, *Polym. Int.*, **55**(6), 608–620 (2006).
[65] M. Kumada, Nickel and palladium complex catalyzed cross-coupling reactions of organometallic reagents with organic halides, *Pure Appl. Chem.*, **52**(3), 669–679 (1980).
[66] R.D. Mccullough and R.D. Lowe, Enhanced electrical conductivity in regioselectively synthesized poly(3-alkylthiophenes), *J. Chem. Soc. Chem. Commun.*, 70–72 (1992).
[67] K. Sonogashira, Y. Tohda, and N. Hagihara, A convenient synthesis of acetylenes: Catalytic substitutions of acetylenic hydrogen with bromoalkenes, iodoarenes and bromopyridines, *Tet. Lett.*, 4467–4470 (1975).
[68] K. Sonogashira, Development of Pd-Cu catalyzed cross-coupling of terminal acetylenes with sp(2)-carbon halides, *J. Organomet. Chem.*, **653**(1–2), PII S0022-328X(02)01158-0 (2002).
[69] E. Negishi, A.O. King, and N. Okukado, Selective carbon-carbon bond formation via transition metal catalysis, *J. Org. Chem.*, **42**(10), 1821–1823 (1977).
[70] J.K. Stille, The palladium-catalyzed cross-coupling reactions of organotin reagents with organic electrophiles, *Angew. Chem. Int. Ed. Eng.*, **25**(6), 508–523 (1986).
[71] N. Miyaura, T. Ishiyama, H. Sasaki, M. Ishikawa, M. Satoh, and A. Suzuki, Syntheses of functionalized alkenes, arenes, and cycloalkenes via a hydroboration coupling sequence, *J. Am. Chem. Soc.*, **111**(1), 314–321 (1989).
[72] P.R. Solanki, S. Singh, N. Prabhakar, M.K. Pandey, and B.D. Malhotra, Application of conducting poly(aniline-co-pyrrole) film to cholesterol biosensor, *J. Appl. Polym. Sci.*, **105**(6), 3211–3219 (2007).
[73] A. Buzarovska, L. Arsov, N. Hebestreit, and W. Plieth, Synthesis and characterization of thiophene/3-alkylthiophene random cooligomers, *J. Solid State Electrochem.*, **7**(1), 49–54 (2002).
[74] W.J. Bae, K.H. Kim, W.H. Jo, and Y.H. Park, A water-soluble and self-doped conducting polypyrrole graft copolymer, *Macromolecules*, **38**(4), 1044–1047 (2005).
[75] T.J. Rivers, T.W. Hudson, and C.E. Schmidt, Synthesis of a novel, biodegradable electrically conducting polymer for biomedical applications, *Adv. Funct. Mater.*, **12**(1), 33–37 (2002).
[76] N.K.E. Guimard, J.L. Sessler, and C.E. Schmidt, Toward a biocompatible and biodegradable copolymer incorporating electroactive oligothiophene units, *Macromolecules*, **42**(2), 502–511 (2009).

[77] H.-A. Klok, A. Rösler, G. Götz, E. Mena-Osteritz, and P. Bäuerle, Synthesis of a silk-inspired peptide-oligothiophene conjugate, *Org. Biomol. Chem.*, **2**(24), 3541–3544 (2004).
[78] G.W.M. Vandermeulen and H.-A. Klok, Peptide/protein hybrid materials: Enhanced control of structure and improved performance through conjugation of biological and synthetic polymers, *Macromol. Biosci.*, **4**(4), 383–398 (2004).
[79] D.H. Kim, M. Abidian, and D.C. Martin, Synthesis and characterization of conducting polymers grown in hydrogels for neural applications, *Mat. Res. Soc. Symp. Proc.*, **1**, F5.5.1–5.5.6 (2004).
[80] S. Brahim, D. Narinesingh, and A. Guiseppi-Elie, Polypyrrole-hydrogel composites for the construction of clinically important biosensors, *Biosens. Amp. Bioelectr.*, **17**(1–2), 53–59 (2002).
[81] S. Brahim and A. Guiseppi-Elie, Electroconductive hydrogels: Electrical properties of polypyrrole-poly(HEMA) and electrochemical composites, *Electroanalysis*, **17**(7), 556–570 (2005).
[82] S. Brahim, G. Slaughter, and A. Guiseppi-Elie. Electrical and electrochemical characterization of electroconductive ppy-p(HEMA) composite hydrogels. In *Smart Structures and Materials 2003: Active Materials: Behavior and Mechanics*, ed. D.C. Lagoudas, Proceedings of the SPIE, **5053**, 1–12 (2003).
[83] A. Pron and K. Wojnar, *Characterization of Polypyrrole-Polyvinyl Alcohol Composite Prepared by Chemical Oxidation Of Pyrrole*, Springer-Verlag, Berlin, 1987.
[84] H.N.M. Ekramul Mahmud, A. Kassim, Z. Zainal, and Y. Wan Mahmood Mat, Fourier transform infrared study of polypyrrole-poly(vinyl alcohol) conducting polymer composite films: Evidence of film formation and characterization, *J. Appl. Polym. Sci.*, **100**(5), 4107–4113 (2006).
[85] M. Makhlouki, J.C. Bernede, M. Morsli, A. Bonnet, A. Conan, and S. Lefrant, Xps study of conducting polypyrrole-poly(vinyl alcohol) composites, *Synth. Met.*, **62**(2), 101–106 (1994).
[86] Y. Li, K.G. Neoh, L. Cen, and E.T. Kang, Porous and electrically conductive polypyrrole- poly (vinyl alcohol) composite and its applications as a biomaterial, *Langmuir*, **21**(23), 10702–10709 (2005).
[87] H. Bai, C. Li, F.E. Chen, and G. Shi, Aligned three-dimensional microstructures of conducting polymer composites, *Polymer*, **48**(18), 5259–5267 (2007).
[88] Y. Li, K.G. Neoh, L. Cen, and E.T. Kang, Porous and electrically conductive polypyrrole-poly(vinyl alcohol) composite and its applications as a biomaterial, *Langmuir*, **21**(23), 10702–10709 (2005).
[89] L.M. Yee, H.N.M.E. Mahmud, A. Kassim, and W.M.M. Yunus, Polypyrrole-polyethylene glycol conducting polymer composite films: Preparation and characterization, *Synth. Met.*, **157**(8–9), 386–389 (2007).
[90] T.J. Wang, Y.Q. Qi, J.K. Xu, X.J. Hu, and P. Chen, Effects of poly(ethylene glycol) on electrical conductivity of poly (3,4-ethylenedioxythiophene)-poly(styrenesulfonic acid) film, *Appl. Surf. Sci.*, **250**(1–4), 188–194 (2005).
[91] A. Callegari, S. Cosnier, M. Marcaccio, D. Paolucci, F. Paolucci, V. Georgakilas, N. Tagmatarchis, E. Vazquez, and M. Prato, Functionalised single wall carbon nanotubes/polypyrrole composites for the preparation of amperometric glucose biosensors, *J. Mater. Chem.*, **14**(5), 807–810 (2004).
[92] S.S. Wong, E. Joselevich, A.T. Woolley, C.L. Cheung, and C.M. Lieber, Covalently functionalized nanotubes as nanometre-sized probes in chemistry and biology, *Nature*, **394**(6688), 52–55 (1998).
[93] Y.J. Zou, C.L. Xiang, L.N. Yang, L.X. Sun, F. Xu, and Z. Cao, A mediatorless microbial fuel cell using polypyrrole coated carbon nanotubes composite as anode material, *Int. J. Hydr. En.*, **33**(18), 4856–4862 (2008).
[94] X.Q. Cui, C.M. Li, J.F. Zang, Q. Zhou, Y. Gan, H.F. Bao, J. Guo, V.S. Lee, and S.M. Moochhala, Biocatalytic generation of PPy-enzyme-CNT nanocomposite: From network assembly to film growth, *J. Phys. Chem. C*, **111**(5), 2025–2031 (2007).
[95] J.H. Fan, M.X. Wan, D.B. Zhu, B.H. Chang, Z.W. Pan, and S.S. Xe, Synthesis, characterizations, and physical properties of carbon nanotubes coated by conducting polypyrrole, *J. Appl. Polym. Sci.*, **74**(11), 2605–2610 (1999).

[96] S. Bhandari, M. Deepa, A.K. Srivastava, C. Lal, and R. Kant, Poly(3,4-ethylenedioxythiophene) (pedot)-coated MWCNTs tethered to conducting substrates: Facile electrochemistry and enhanced coloring efficiency, *Macromol. Rapid Commun.*, **29**(24), 1959–1964 (2008).
[97] J.Y. Kim, K.H. Kim, and K.B. Kim, Fabrication and electrochemical properties of carbon nanotube/polypyrrole composite film electrodes with controlled pore size, *J. Power Sources*, **176**(1), 396–402 (2008).
[98] Y.Z. Long, Z.J. Chen, X.T. Zhang, J. Zhang, and Z.F. Liu, Electrical properties of multi-walled carbon nanotube/polypyrrole nanocables: Percolation-dominated conductivity, *J. Phys. D Appl. Phys.*, **37**(14), 80510–80512 (2004).
[99] C. Peng, J. Jin, and G.Z. Chen, A comparative study on electrochemical co-deposition and capacitance of composite films of conducting polymers and carbon nanotubes, *Electrochim. Acta*, **53**(2), 525–537 (2007).
[100] G.Z. Chen, M.S.P. Shaffer, D. Coleby, G. Dixon, W.Z. Zhou, D.J. Fray, and A.H. Windle, Carbon nanotube and polypyrrole composites: Coating and doping, *Adv. Mater.*, **12**(7), 522 (2000).
[101] S.-H.L. Tzong-Ming Wu, Characterization and electrical properties of polypyrrole/multi-walled carbon nanotube composites synthesized by in situ chemical oxidative polymerization, *J. Polym. Sci. B Polym. Phys.*, **44**(10), 1413–1418 (2006).
[102] A. Magrez, S. Kasas, V. Salicio, N. Pasquier, J.W. Seo, M. Celio, S. Catsicas, B. Schwaller, and L. Forro, Cellular toxicity of carbon-based nanomaterials, *Nano Lett.*, **6**(6), 1121–1125 (2006).
[103] N. Lewinski, V. Colvin, and R. Drezek, Cytotoxicity of nanoparticles, *Small*, **4**(1), 26–49 (2008).
[104] C.M. Sayes, F. Liang, J.L. Hudson, J. Mendez, W.H. Guo, J.M. Beach, V.C. Moore, C.D. Doyle, J.L. West, W.E. Billups, K.D. Ausman, and V.L. Colvin, Functionalization density dependence of single-walled carbon nanotubes cytotoxicity in vitro, *Toxicol. Lett.*, **161**(2), 135–142 (2006).
[105] J.A. Darr and M. Poliakoff, New directions in inorganic and metal-organic coordination chemistry in supercritical fluids, *Chem. Rev.*, **99**(2), 495–541 (1999).
[106] E.J. Beckman, Supercritical and near-critical co2 in green chemical synthesis and processing, *J. Supercrit. Fluids*, **28**(2–3), 121–191 (2004).
[107] F.M. Kerton, G.A. Lawless, and S.P. Armes, First example of a conducting polymer synthesised in supercritical fluids, *J. Mater. Chem.*, **7**(10), 1965–1966 (1997).
[108] L.N. Nikitin, M.O. Gallyamov, A.Y. Nikolaev, E.E. Said-Galiyev, A.R. Khokhlov, S.S. Bukalov, G.I. Magdanurov, V.V. Volkov, E.V. Shtykova, K.A. Dembo, and G.K. Elyashevich, Structure of composites prepared via polypyrrole synthesis in supercritical CO_2 on microporous polyethylene, *Polym. Sci. Ser. A*, **48**(8), 827–840 (2006).
[109] S. Kurosawa, A.S. Teja, J. Kowalik, and L. Tolbert, Supercritical carbon dioxide processing of conducting composites of polypyrrole and porous crosslinked polystyrene, *Polymer*, **47**(9), 2997–3004 (2006).
[110] S.L. Shenoy, P. Kaya, C. Erkey, and R.A. Weiss, Synthesis of conductive elastomeric foams by an in situ polymerization of pyrrole using supercritical carbon dioxide and ethanol cosolvents, *Synth. Met.*, **123**(3), 509–514 (2001).
[111] Y. Fu, D.R. Palo, C. Erkey, and R.A. Weiss, Synthesis of conductive polypyrrole/polyurethane foams via a supercritical fluid process, *Macromolecules*, **30**(24), 7611–7613 (1997).
[112] A.I. Cooper, Polymer synthesis and processing using supercritical carbon dioxide, *J. Mater. Chem.*, **10**(2), 207–234 (2000).
[113] E. Ekanayake, D.M.G. Preethichandra, and K. Kaneto, An amperometric glucose biosensor with enhanced measurement stability and sensitivity using an artificially porous conducting polymer, *IEEE Tran. Instrument. Meas.*, **57**(8), 1621–1626 (2008).
[114] E. Ekanayake, D.M.G. Preethichandra, and K. Kaneto, Polypyrrole nanotube array sensor for enhanced adsorption of glucose oxidase in glucose biosensors, *Biosen. Bioelectr.*, **23**(1), 107–113 (2007).
[115] M. Lu, X.H. Li, and H.L. Li, Synthesis and characterization of conducting copolymer nanofibrils of pyrrole and 3-methylthiophene using the template-synthesis method, *Mater. Sci. Eng. A Struct. Mater. Prop. Microstruct. Proc.*, **334**(1–2), 291–297 (2002).

[116] X.H. Li, X.G. Zhang, and H.L. Li, Preparation and characterization of pyrrole/aniline copolymer nanofibrils using the template-synthesis method, *J. Appl. Polym. Sci.*, **81**(12), 3002–3007 (2001).
[117] R.M. Hernandez, L. Richter, S. Semancik, S. Stranick, and T.E. Mallouk, Template fabrication of protein-functionalized gold-polypyrrole-gold segmented nanowires, *Chem. Mater.*, **16**(18), 3431–3438 (2004).
[118] B.H. Kim, D.H. Park, J. Joo, S.G. Yu, and S.H. Lee, Synthesis, characteristics, and field emission of doped and de-doped polypyrrole, polyaniline, poly(3,4-ethylenedioxythiophene) nanotubes and nanowires, *Synth. Met.*, **150**(3), 279–284 (2005).
[119] M.R. Abidian and D.C. Martin, Experimental and theoretical characterization of implantable neural microelectrodes modified with conducting polymer nanotubes, *Biomaterials*, **29**(9), 1273–1283 (2008).
[120] M.R. Abidian and D.C. Martin, Multifunctional nanobiomaterials for neural interfaces, *Adv. Funct. Mater.*, **19**(4), 573–585 (2009).
[121] Y. Yang, Y. Chu, F.Y. Yang, and Y.P. Zhang, Uniform hollow conductive polymer microspheres synthesized with the sulfonated polystyrene template, *Mater. Chem. Phys.*, **92**(1), 164–171 (2005).
[122] C. Barthet, S.P. Armes, S.F. Lascelles, S.Y. Luk, and H.M.E. Stanley, Synthesis and characterization of micrometer-sized, polyaniline-coated polystyrene latexes, *Langmuir*, **14**(8), 2032–2041 (1998).
[123] D.B. Cairns, S.P. Armes, and L.G.B. Bremer, Synthesis and characterization of submicrometer-sized polypyrrole-polystyrene composite particles, *Langmuir*, **15**(23), 8052–8058 (1999).
[124] M.A. Khan and S.P. Armes, Synthesis and characterization of micrometer-sized poly(3,4 ethylenedioxythiophene)-coated polystyrene latexes, *Langmuir*, **15**(10), 3469–3475 (1999).
[125] M.A. Khan and S.P. Armes, Conducting polymer-coated latex particles, *Adv. Mater.*, **12**(9), 671 (2000).
[126] M.A. Khan, S.P. Armes, C. Perruchot, H. Ouamara, M.M. Chehimi, S.J. Greaves, and J.F. Watts, Surface characterization of poly(3,4-ethylenedioxythiophene)-coated latexes by x-ray photoelectron spectroscopy, *Langmuir*, **16**(9), 4171–4179 (2000).
[127] M.K. Park, K. Onishi, J. Locklin, F. Caruso, and R.C. Advincula, Self-assembly and characterization of polyaniline and sulfonated polystyrene multilayer-coated colloidal particles and hollow shells, *Langmuir*, **19**(20), 8550–8554 (2003).
[128] L.Y. Hao, C.L. Zhu, C.N. Chen, P. Kang, Y. Hu, W.C. Fan, and Z.Y. Chen, Fabrication of silica core-conductive polymer polypyrrole shell composite particles and polypyrrole capsule on monodispersed silica templates, *Synth. Met.*, **139**(2), 391–396 (2003).
[129] F.Y. Yang, Y. Chu, S.Y. Ma, Y.P. Zhang, and J.L. Liu, Preparation of uniform silica/polypyrrole core/shell microspheres and polypyrrole hollow microspheres by the template of modified silica particles using different modified agents, *J. Colloid Interface Sci.*, **301**(2), 470–478 (2006).
[130] D.B. Cairns, M.A. Khan, C. Perruchot, A. Riede, and S.P. Armes, Synthesis and characterization of polypyrrole-coated poly(alkyl methacrylate) latex particles, *Chem. Mater.*, **15**(1), 233–239 (2003).
[131] C.A. Foss, G.L. Hornyak, J.A. Stockert, and C.R. Martin, Template-synthesized nanoscopic gold particles – optical-spectra and the effects of particle-size and shape, *J. Phys. Chem.*, **98**(11), 2963–2971 (1994).
[132] Y.F. Li and R.Y. Qian, Studies on the chemical compensation of conducting polypyrrole by naoh solution, *Synth. Met.*, **26**(2), 139–151 (1988).
[133] J. Mrkic and B.R. Saunders, Microgel particles as a matrix for polymerization: A study of poly(n-isopropylacrylamide)-poly(*n*-methylpyrrole) dispersions, *J. Colloid Interface Sci.*, **222**(1), 75–82 (2000).
[134] H.D. Tran, K. Shin, W.G. Hong, J.M. D'arcy, R.W. Kojima, B.H. Weiller, and R.B. Kaner, A template-free route to polypyrrole nanofibers, *Macromol. Rapid Commun.*, **28**(24), 2289–2293 (2007).
[135] H.D. Tran, Y. Wang, J.M. D'arcy, and R.B. Kaner, Toward an understanding of the formation of conducting polymer nanofibers, *ACS Nano*, **2**(9), 1841–1848 (2008).

[136] U. Lang and J. Dual, Mechanical properties of the intrinsically conductive polymer poly(3,4-ethylenedioxythiophene) poly(styrenesulfonate) (PEDOT/PSS), *Key Eng. Mater.*, **345–346**, 1189–1192 (2007).

[137] D.E. Tallman, C. Vang, G.G. Wallace, and G.P. Bierwagen, Direct electrodeposition of polypyrrole on aluminum and aluminum alloy by electron transfer mediation, *J. Electrochem. Soc.*, **149**(3), C173–C179 (2002).

[138] R.A. Green, L.A. Poole-Warren, and N.H. Lovell. Novel neural interface for vision prosthesis electrodes: Improving electrical and mechanical properties through layering. In *Proceedings of the 3rd International IEEE EMBS Conference on Neural Engineering*, Kohala Coast, Hawaii, USA (2007).

[139] X. Cui and D.C. Martin, Electrochemical deposition and characterization of poly(3,4-ethylenedioxythiophene) on neural microelectrode arrays, *Sens. Actuat. B Chem.*, **89**(1–2), 92–102 (2003).

[140] X. Cui and D.C. Martin, Fuzzy gold electrodes for lowering impedance and improving adhesion with electrodeposited conducting polymer films, *Sens. Actuat. A Phys.*, **103**(3), 384–394 (2003).

[141] C.E. Schmidt, V.R. Shastri, J.P. Vacanti, and R. Langer, Stimulation of neurite outgrowth using an electrically conducting polymer, *Proc. Natl. Acad. Sci. USA*, **94**(17), 8948–8953 (1997).

[142] A. Kotwal and C.E. Schmidt, Electrical stimulation alters protein adsorption and nerve cell interactions with electrically conducting biomaterials, *Biomaterials*, **22**(10), 1055–1064 (2001).

[143] D.D. Ateh, H.A. Navsaria, and P. Vadgama, Polypyrrole-based conducting polymers and interactions with biological tissues, *J. R. Soc. Interface*, **3**, 741–752 (2006).

[144] M.R. Abidian, L.G. Salas, A. Yazdan-Shahmorad, T.C. Marzullo, D.C. Martin, and D.R. Kipke. In-vivo evaluation of chronically implanted neural microelectrode arrays modified with poly (3,4-ethylenedioxythiophene) nanotubes. In *Proceedings of the 3rd International IEEE EMBS Conference on Neural Engineering* Kohala Coast, Hawaii, USA, 2007.

[145] M.R. Abidian, D.H. Kim, and D.C. Martin, Conducting-polymer nanotubes for controlled drug release, *Adv. Mater.*, **18**(4), 405–409 (2006).

[146] R.B. Borgens, Electrically mediated regeneration and guidance of adult mammalian spinal axons into polymeric channels, *Neuroscience*, **91**(1), 251–264 (1999).

[147] P.C. Roehm and M.R. Hansen, Strategies to preserve or regenerate spiral ganglion neurons, *Curr. Opin. Otolaryngol. Head Neck Surg.*, **13**(5), 294–300 (2005).

19

Nanocomposites of Polymers Made Conductive by Nanofillers

Haiping Hong[a], Dustin Thomas[a], Mark Horton[a], Yijiang Lu[b], Jing Li[b], Pauline Smith[c], and Walter Roy[c]

[a]Department of Material and Metallurgical Engineering, South Dakota School of Mines and Technology, Rapid City, SD, USA
[b]Nanotechnology Branch, NASA Ames Research Center, Moffett Field, CA, USA
[c]Army Research Lab, Aberdeen Proving Ground, MD, USA

19.1 Introduction

Nanofillers, carbon nanotubes (CNTs), especially single-walled carbon nanotubes (SWNTs), have attracted a great deal of interest due to their low density, large aspect ratio, superior mechanical properties, and unique electrical and thermal conductivities [1–4]. They can find potential applications in many fields, such as chemical sensing, gas storage, field emission, scanning microscopy, catalysis, and composite materials.

Nanofillers were first discovered by Japanese Scientist S. Iijima in 1991 as helical microtubules of graphitic carbon [1]. Dr Richard E. Smalley of Rice University, USA was awarded the 1996 Nobel Prize in Chemistry for his codiscovery of buckyballs (C_{60}) and has made significant contributions in carbon nanotube synthesis and potential applications [2,3].

Carbon nanotube fillers include three main categories: single-wall, multiwall, and double-wall. Figure 19.1 shows transmission electron microscope (TEM) images of each category.

Nanostructured Conductive Polymers Edited by Ali Eftekhari

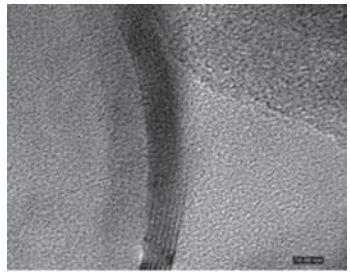

A: Single Wall Carbon Nanotube

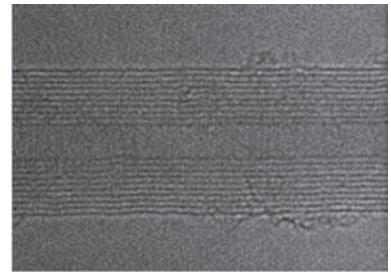

B: Multi Wall Carbon Nanotube

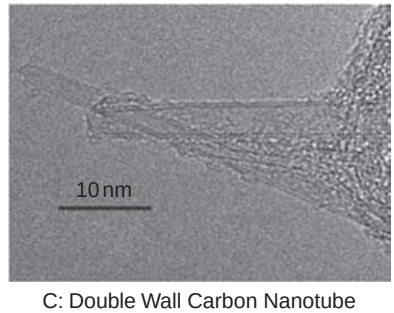

C: Double Wall Carbon Nanotube

Figure 19.1 *TEM images of different nanotube categories*

Nanofillers have superb thermal and electrical properties. All nanotubes are expected to be very good thermal conductors along the tube axis, exhibiting a property known as 'ballistic conduction,' but good insulators laterally to the tube axis. It has been reported that single-wall carbon nanotubes exhibit thermal conductivity (TC) values as high as 2000–6000 W mK^{-1} [4] under ideal circumstances. The temperature stability of carbon nanotubes is estimated to be up to 2800 °C in a vacuum, and about 750 °C in air. By comparison, metals have TC values of several hundred W mK^{-1}, and water and oil have TC values of only 0.6 W mK^{-1} and 0.2 W mK^{-1}, respectively. Table 19.1 lists the thermal conductivities of various materials, including nanofillers (nanotubes), metals, and oils.

Because of the symmetry and unique electronic structure of graphene, the structure of a nanotube strongly affects its electrical properties. For a given (n,m) nanotube, if $n - m = 3q$ (where q is an integer), then the nanotube is metallic, otherwise the nanotube is a semiconductor. Thus, all armchair ($n = m$) nanotubes are metallic, and nanotubes (5,0), (6,4), (9,1), etc. are semiconducting. In theory, metallic nanotubes can have an electrical current density more than 1000 times greater than metals such as silver and copper [5].

Scientists have reported four-probe measurements on single nanotubes made by lithographic deposition of tungsten leads across the tubes and found that each multishell nanotube has unique conductivity properties [6]. Both metallic and nonmetallic behaviors are observed, as well as abrupt jumps in conductivity as the temperature is varied. The differences between the electrical properties of different nanotubes are far greater than expected. The results suggest that differences in geometry play a profound part in determining the electronic behavior.

Table 19.1 *Thermal conductivity of various materials*

Material	TC value (W/mK)
Single-wall carbon nanotube (SWNT)	2000–6000 (ideal)
Multiwall carbon nanotube (MWNT)	Around 2000 (ideal)
Copper	394
Silver	418
Aluminum	238
Stainless steel	13
Water	0.60
*BP166 oil (polyalphaolefin)	0.18
*Royco 500 oil (polyol ester)	0.17
*Royco 808 oil (polyol ester)	0.18

*BP is a registered trademark of British Petroleum Inc.; Royco is a registered trademark of Anderol Inc.; Royco 500 and 808 are formulated lubricants containing polymer (polyol) esters as the base stock. They are fortified with performance additives.

Since carbon nanotube fillers have extremely superior thermal and electrical properties, many efforts have been made to produce large quantities of carbon nanotubes and investigate their potential commercial application opportunities. There are many US-based high-tech corporations that are capable of producing large quantities of good-quality carbon nanotubes, including Hyperion Catalysis, Carbolex, CNI (now Unidym), Helix Material Solutions, MER, Nanolab, South West Nanotechnology etc. Table 19.2 shows a detailed description of some nanotubes suppliers, production rate, cost, and type.

Recently, Professor Xie Youchang of Peking University, China discovered a method to synthesize single-wall carbon nanotubes through CH_4 [7]. High-purity single-wall carbon nanotubes were synthesized by catalytic decomposition of carbon-containing gases with Fe, Co, Ni, Mo, and W catalysts in the presence of a small amount of water vapor, which can prohibit the generation of amorphous carbon and multiwall carbon nanotubes on the surface of the catalysts and promote the generation of single-wall carbon nanotubes. Since CH_4 is the main component of natural gas and the cost is moderately priced, it is quite certain that the price of SWNTs should decrease significantly in the near future.

Figure 19.2 shows a typical TEM image of SWNTs made by Professor Xie. The purity of SWNTs is more than 80% with some thin-wall (double-wall) CNTs. The concentration of amorphous carbon is $<5\%$ and ash is $<2\%$. The price for these CNTs is around \$20 per gram. In the future, the price may be even lower if the process and facility can be further improved. A more reasonable price for carbon nanotubes will make it possible to pursue projects in which large quantities of nanotubes are needed.

Very recently, a US-based high-tech corporation, SouthWest NanoTechnologies (SWeNT®), announced that in the near future, they could produce new SWNTs at less than \$1 per gram in ton quantities that will be the most conductive material they've ever made [8].

Typical commercial greases consist of a polyalphaolefin base oil and a metal-soap thickener, such as lithium, calcium, or aluminium. The thickener is needed to ensure the grease has stable pseudo-plasticity. Literature reports indicate that polyalphaolefin oils

Table 19.2 *The price of various nanofiller (carbon nanotube) (2008 data)*

Company	Production	Cost (per gram)	Type
Beijing Boda		$20	SWNT
Carbolex	~35 g/day [up to 250g/week]	$60–100	SWNT
Catalytic Materials	1.2 kg/day	$40–60	MWNT
Cheap Tubes		$10–300	MWNT, SWNT, functional tube
Helix Material Inc		$28–210	MWNT, SWNT, DWNT
Hyperion Catalysis		$100–200	High-quality MWNT
MER	—	$8–400	MWNT, SWNT, DWNT
Nanocyl	10 kg/day (end 2004)	$6–485	MWNT, SWNT, DWNT
NanoLab	20–100 g/day 120 g/day	$200–2000 $64–85 (c)	High-purity SWNT, DWNT SWNT
Nanoamor	30–50 kg/day	$3–500	MWNT, SWNT, DWNT
Rosseter Holding	100–200 g/day	$20–25	MWNT
SWeNT™	competitive amount (tons) in next couple of months	< $1 as-produced	Various types of SWNT High conductivity
Unidym		$50-900	SWNT, high-purity SWNT, DWNT, high-purify DWNT, F-SWNT

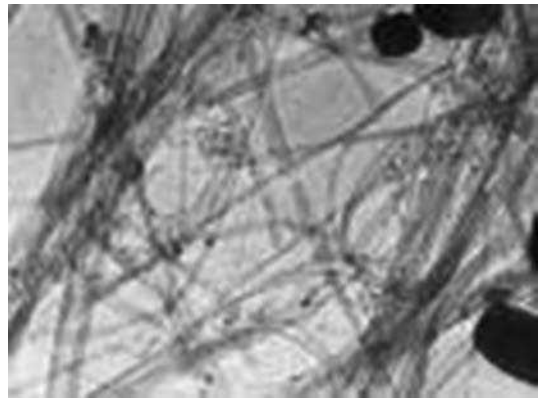

Figure 19.2 *Typical TEM images of SWNTs made by Professor Xie of Peking University. (Reproduced with kind permission from Youchang Xie, University of Peking)*

containing various concentrations of CNT show a dramatic increase in viscosity with increasing concentration of CNT [9–11]. The results suggest that, given appreciable concentrations, CNT could be used exclusively as a thickening agent to create carbon nanotube grease, or CNT grease.

It has been reported that incorporating magnetically sensitive metal oxide nanoparticles or magnetically sensitive metal-coated carbon nanotubes into heat-transfer nanofluids results in an enhancement of the thermal conductivities of the nanofluids [12–15]. This enhancement is due to the magnetic particles forming connected networks, which tend to get partially oriented in the direction of the magnetic field, resulting in more physical contacts. It will be interesting to investigate the effects of these magnetically sensitive metal oxide nanoparticles or metal-coated carbon nanotubes in the grease structure.

The rheology of particle suspensions has been studied to great extents, and many theoretical and empirical models exist, describing the viscous response of the suspension. Groundbreaking work conducted by Einstein in 1906 and 1911 describing the interaction of dilute suspensions of rigid spherical particles initiated interest in studying the viscous response of particle suspensions of nearly all concentrations and morphologies. In all cases, it is seen that the presence of particles in a medium increases the viscosity of the medium due to the dissipation of extra energy, caused by the modification of the velocity distribution of the medium as it moves around the particle [16]. Obviously, it makes sense to compare the CNT suspensions to suspensions containing axisymmetrical particles of large aspect ratios. Brenner *et al.* and Rahnama *et al.* have conducted significant research, studying the effect of particle aspect ratio on the viscosity of suspensions [17–19]. In each case, it was noted that the orientation of these axisymmetrical particles had a dramatic effect on the velocity field of the medium around the particle. Dramatic shear thinning was seen, due to particle alignment in the direction of shear flow. This work also explained the dramatic increase in viscosity with increasing particle concentration. In dilute suspensions, the particle is free to rotate in three dimensions. As the particle is crowded by an increasing number of neighboring particles, its motion is limited to two or even one dimension which increases the stress required to initiate particle flow and alignment.

The study of the rheological behavior of CNT suspensions is a relatively emergent field. Work has been done describing the relationship between the intrinsic shear viscosity and the mean CNT length in water and super-acid-based SWNT suspensions [20,21]. Other research on the rheological behavior of moderate concentrations, up to 10 wt%, of MWNTs in polyalphaolefin oils has been conducted [22]. Yang and Grulke have determined the effects of particle concentration, dispersant concentration, and dispersion energy on the viscosity of the nanofluid, while Hobbie and Fry determined the rheological properties of nanofluids with concentrations ranging from semidilute to concentrated. Recent work has compared the viscoelastic characteristics of the MWNT suspensions to that of axisymmetrical long fibers [23]. This work explains that particle orientation and distribution of the CNT is controlled by hydrodynamic forces and also explains the shear thinning behavior of the CNT suspension.

In this chapter, we will report efforts to successfully make homogeneous and stable nanogreases based on carbon nanotubes and polyalphaolefin oils (DURASYN® 166). Some physical properties of these greases (electrical conductivity, thermal conductivity, dropping point, oil leakage percentage, viscosity, copper corrosion, penetration length, etc.) will be characterized. Also, the rheological impact of polyalphaolefin (PAO) oil-based carbon nanotube (CNT) grease will be investigated. In addition, time-dependent magnetic experiments conducted through greases containing magnetically sensitive metal oxide nanoparticles or metal-coated carbon nanotubes are detailed. Finally, the electrical conductivities of various fillers (nanotubes) in solid phase are measured and discussed.

19.2 Experimental

19.2.1 Materials and Equipment

Carbon nanotubes (single-wall and multiwall) were purchased from Helix Material (Richardson, Texas), Carbolex (Broomall, PA), and Carbon Nanotechnologies Incorporation (CNI, Houston, Texas, now Unidym Inc). The carbon nanotubes were used as received without any further purification or functionalization. Therefore, there are some impurities such as carbon black and metal in the samples.

DURASYN® 166 is a commercial polyalphaolefin oil product purchased from Chemcentral (Chicago, IL). Magnetically sensitive Fe_2O_3 nanoparticles with an average diameter of 5–25 nm was purchased from Sigma Aldrich. A three-roll mill (Ross Engineering Inc, New York) was used to make the stable and homogeneous greases. Grease containing Fe_2O_3 nanoparticles was made by mixing the Fe_2O_3 particles and carbon nanotubes together in the polyalphaolefin oils under continuous stirring and heating, then the slurry samples were poured into three-roll mill. The milling process was repeated 5–8 times until the slurry samples became homogeneous greases. It is expected that Fe_2O_3 was scattered well within the grease structure. Due to limited sample size of nickel-coated single-wall carbon nanotubes, these greases had to be hand mixed. The magnetic field was provided by a pair of spaced Ba-ferrite magnet plates ($4 \times 6 \times 1$ inch dimensions), placing the sample in the middle of the gap between the magnets.

The acid number (AN) per ASTM D664 was determined for the oil-based fluids (polyalphaolefin and polyol ester). The relative amounts of acidic constituents present in products can be determined by titrating with bases. The acid number is a measure of the amount of acidic substance. (The acid number, n, is the quantity of base expressed in milligrams of potassium hydroxide per gram of sample required to titrate a sample to a specified end point). This test is considered to be a comparison test for the purpose of identifying chemical activity that may have occurred due to the addition of nanomaterials.

Viscosity of the oil-based fluids was determined at different temperatures per ASTM D445 by a Brookfield LV viscometer. Usually temperatures of 40 °C and 100 °C are chosen as the range to indicate the change of viscosity.

Detection of copper corrosion from lubricating grease was measured by ASTM D4048-02 Standard Test Method. This test method measures the tendency of lubricating grease to corrode copper under specific static conditions. It may be of some value in predicting possible chemical attack on lubricated parts, such as bearings that contain copper or copper alloys. Such corrosion, for example, can cause premature bearing failures.

Pour point, the lowest temperature at which movement of the test specimen is observed under prescribed conditions of test, was determined per ASTM D97 for the polyalphaolephin-based nanogreases. Pour point as used here is an indicator of potential physical change.

Lubricating greases [24] consist of lubricating oil in which a thickener is dispersed as a microscopic second phase. One of the more important physical aspects of the greases is the stability of the grease structure as provided by the oil thickener interaction. Two tests that

measure this aspect of grease rheology were chosen for the grease samples in this program: dropping point and oil separation. Dropping point was determined using ASTM D2265, and oil separation was measured using Federal Test Method (FTM) 321.3. These tests were performed at two conditions: 24 hours at 100°C, and 24 hours at 177 °C. The dropping point is defined as the temperature at which a drop of oil or grease falls out of the bottom of the sample test cup. This test is useful in helping to characterize the grease's top temperature of sustained operation, and the various categories of commercial greases (as identified by their thickener type) will have well-known typical dropping points. The relationship between the grease's oil and its thickener is also characterized by oil separation.

Grease consistency [25] was measured by the ASTM D217 unworked and worked (60 strokes) penetration method. For a limited amount of samples, the corresponding ASTM D1403 half-scale penetration method was used. Shear stability was determined using ASTM D217 worked 100 000 stroke penetration. In this method, the grease was worked for 60 strokes and the penetration was measured. Then the grease was worked for 99 880 strokes. Once the grease had cooled to ambient temperature, it was worked another 60 stokes, then measured for its final penetration. The difference between the worked 100 000 strokes (w/100 000) value and the worked 60 strokes (w/60) value is considered a measure of the shear stability of the greases.

Thermal conductivity data [26] was obtained using the Hot Disk^{TM} thermal constants analyzer, using the following parameters: measurement depth 6 mm, room temperature 25 °C, power 0.025 W, measurement time 16 s, sensor radius 2.001 mm, TCR 0.0471 K^{-1}, disk type kapton, temperature drift rec yes. The diagram is shown in Figure 19.3.

The electrical conductivity data of grease was obtained by volume resistivity test cells made by Electro-Tech Systems, Inc. (ETS) [27]. The cell dimensions automatically calculate the volume resistivity of the material being tested by multiplying the measured resistance by either 10 (large cell) or 100 (small cell). The stainless-steel container acts as both an electrostatic shield and provides containment of material overflow. The test cell is made from PVC and uses stainless-steel electrodes. Figure 19.4 shows a diagram of the test cell.

The electrical conductivities of various fillers (nanotubes) in the solid phase were measured by a Keithley 2002 digital multimeter and an Agilent 34401 DMM.

Figure 19.3 *Hot Disk^{TM} thermal constants analyzer: (a) sensor; (b) equipment diagram. (Reproduced with kind permission from NLGI. Copyright (2010) NLGI)*

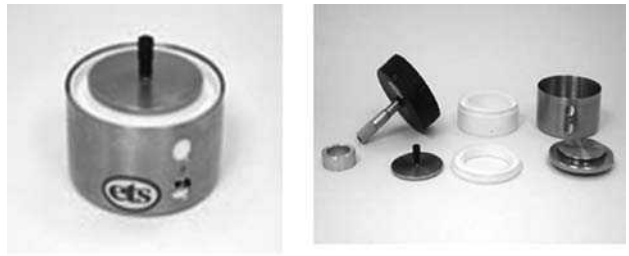

Figure 19.4 *Volume resistivity test cells: (a) assembled; (b) in parts. (Reproduced with kind permission from NLGI. Copyright (2010) NLGI)*

The SWCNT samples were deposited on the interdigitated electrodes (IDE) to form a thin coating. The IDE is made by a P-type boron-doped silicon (100) wafer with a resistivity of 0.006–0.01 Ω cm and thickness of 500±25 μm. A layer of 0.5 μm silicon dioxide was thermally grown on top of the Si substrates. A layer of 200 nm platinum on top of 20 nm titanium was deposited on the SiO_2 layer onto the designed finger patterns. These patterns consisted of 4, 8, 12, and 50 μm finger gaps with 10 μm finger width [28]. The IDE used for the conductivity measurement is listed in Figure 19.5 with finger width: 10 μm, and gap width: 12 μm.

A Bohlin CVO controlled stress rheometer was used to study the rheological behavior of each sample. A parallel plate system was used to conduct the measurements. The system allowed for a relatively large gap, which easily allows the measurement of carbon nanotube grease with aggregated particulate. A gap of 250 μm was experimentally determined and allowed for a large range of applied shear stress, ease of sample loading, and a lack of jamming caused by the aggregates. Figure 19.6 shows a Bohlin CVO rheometer, as used in the experiments.

During the ramped shear stress tests, the range of applied shear stress was not held constant. In order to see the characteristic response of each grease sample, altering the stress range was required due to the differing viscosities of the samples. The criteria to select the stress range for each sample was that it allowed pure viscous flow and showed the sample's response to a relatively large range of shear stress.

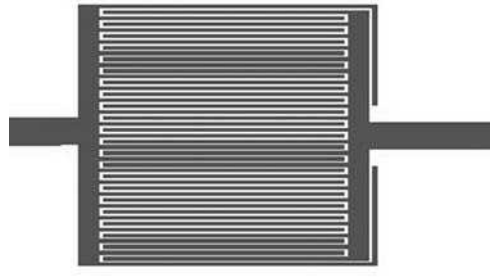

Figure 19.5 *Interdigitated electrode (IDE) chip for measuring samples. (Reproduced with kind permission from NLGI. Copyright (2010) NLGI)*

Figure 19.6 *Bohlin CVO-controlled stress rheometer. (Reproduced with kind permission from NLGI. Copyright (2010) NLGI)*

A creep test was performed to examine the viscoelastic properties of the CNT-grease. A shear stress of 5 Pa was used for 5.0 and 7.0 wt% nanotube loading, while 40 and 100 Pa was used for 10.0 wt% and 12.0 wt% nanotube loading. These stresses were considered to be below that of instantaneous pure viscous flow for each sample. Each creep test was sequenced for 1000 s, followed by a 100 s creep-recovery analysis.

The yield stress of each CNT grease was determined via an increasing shear stress ramp. The yield stress in these experiments shall be defined as the stress at which the sample's instantaneous viscosity rapidly decreases from an increasing or constant value. This will determine the shear stress required for the onset of pure viscous flow. Again, the range of shear stress was chosen to compliment each individual sample.

19.2.2 Preparation of Nanocomposite (Nanotube Grease)

Table 19.3 lists the polymeric material (oils) that were used to make the nanocomposite (greases). Polyalphaolefin oils with different viscosities were mainly used. Selected polymeric oils, such as polyol ester and naphthalene, were used when necessary.

Figure 19.7 shows a carbon nanotube composite (grease) made from the polymer DURASYN® 166 oil [29,30]. The nanocomposite (grease) is black, opaque, and homogeneous. The compositions of the four nanotube greases that are used in this chapter are listed in Table 19.4. Two of the samples were made by dispersing approximately 10–12 wt% SWNTs in the oil, and the other two samples are made by dispersing approximately

Table 19.3 *Base polymer (oils) used to make nanocomposite (greases)*

Product Name	Supplier	Product Description	Density, g/ml	Typical Vis, 40 °C, cSt
Durasyn 166	BP	6 cSt PAO	0.837 @ 15.6 °C	31
SHF403	ExxonMobil	40 cSt PAO	0.849 @ 15.6 °C	391
Esterex NP4101	ExxonMobil	Neopolyol ester	0.928 @ 15.6 °C	58.3
KR-015	King Industries	Alkylated naphthalene	0.884 @ 25 °C	114

19–20 wt% MWNTs in the oil. The volume concentration of each sample is calculated using Equation 19.1 below.

$$C_{volume} = \frac{C_{weight}}{{}^{\rho_{particle}}/_{\rho_{basefluid}} + \left(1 - {}^{\rho_{particle}}/_{\rho_{basefluid}}\right) C_{weight}} \tag{19.1}$$

where: $\rho_{\text{Particle}} = 1.40\text{g cm}^{-3}$ and $\rho_{\text{basefluid}} = 0.86\text{g cm}^{-3}$.

At this level of volume concentration, it is very likely that nanofillers (nanotubes) form some sort of network (at least locally) because of their large aspect ratio and nanosize. The

Figure 19.7 *Picture of the nanocomposite (grease) made from the nanofiller (carbon nanotubes) and polymer (DURASYN® 166 oil). (Reproduced with kind permission from NLGI. Copyright (2010) NLGI)*

Table 19.4 *Composition of selected four types of carbon nanotube composites (greases)*

Sample Number	9-1	9-2	9-3	9-4
PAO, 6 cSt (wt%)	35.36		32.00	
PAO, 40 cSt (wt%)	53.04	44.75	48.00	40.50
Esterex NP4104 (wt%)		44.75		40.50
SWNT (wt%)	11.60	10.50		
MWNT (wt%)			20.00	19.00
Carbon nanotube thickener (wt%)	11.60	10.50	20.00	19.00
Carbon nanotube thickener (vol%)	7.05	6.98	13.30	12.58

networks add to the increased thermal and electrical conductivities that are observed from experimental data. The network explanation also agrees with results such as high dropping points and good temperature resistance.

Lubricating greases consist of lubricating oil in which a thickener (for example, nanotubes) is dispersed as a microscopic second phase. One of the very important physical aspects of greases is the stability of the grease structure provided by the oil–thickener interactions. Two types of tests were chosen for the grease samples in this study: the dropping point and oil separation. Various categories of greases (as identified by their thickener types) have well-known typical dropping points. This test is useful for characterizing the upper temperature limit for a grease to sustain operation. The relationship between grease oil and its thickener is also characterized by the oil separation. The dropping points of the four greases were shown to be above 271 °C, and the oil separation held relatively constant over the three test temperatures spanning 100 to 177 °C. The results indicate that the nanotube greases are high-temperature resistant. Also, the four greases were passive to copper at both 100 °C and 177 °C. This is significant since it has been previously determined that some graphites in greases typically become aggressive towards copper at high temperatures, such as 177 °C.

The grease consistency and stiffness were determined by the penetration length measurements. The thickening power of the SWNTs and MWNTs in polyalphaolefin oils is shown in Figure 19.8a. It clearly shows that the SWNTs provide about twice as much thickening power as the MWNTs. Also, the worked penetration length decreases with increasing carbon nanotube concentration for both SWNTs and MWNTs. The lower penetration length at high carbon nanotube concentrations means that the grease becomes stiffer with higher carbon-nanotube loading. Figure 19.8b shows the worked penetration as a function of the carbon nanotube concentration using different base-oil systems. It is obvious that, within experimental error, there is no synergism between the different oil systems (polyalphaolefin and polyol ester).

It is interesting to point out that stable CNT greases can still be made without an appropriate chemical surfactant. The dropping point still remains high (>271 °C).

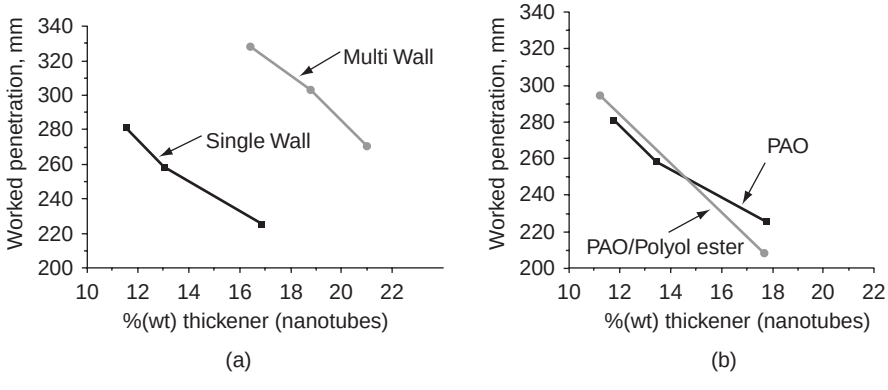

Figure 19.8 *(a) Thickening power of carbon nanotubes in PAO oils. (b) Effect of base oil on thickening power of carbon nanotubes. (Reproduced with kind permission from NLGI. Copyright (2010) NLGI)*

Different types of surfactants (containing various types and concentrations of alcohols and water) don't change the dropping point of the grease. This phenomenon may be associated with the high-temperature reflux (>120 °C) of the nanotubes and oils in the grease-making process. Eventually, alcohols and water will evaporate and leave the grease. However, it remains unknown why homogeneous grease can be made without a chemical surfactant. In the lubricant fluids, nanotubes would immediately precipitate in the oil if there were no chemical surfactants. The relatively high concentration of nanotubes (>10 wt%) probably produces Van der Waals forces between the nanotubes and the oils and forms some kind of three-dimensional network, which makes them attach well.

19.3 Results and Discussion

19.3.1 Thermal and Electrical Properties of Nanocomposites (Nanotube Greases)

Table 19.5 shows the characterization of the four nanocomposites (greases). The thermal conductivity seems saturated and stays around 0.25–0.27 W mK^{-1}. Compared to the values of 0.17–0.18 W mK^{-1} for the base polymeric oils (polyalphaolefin and/or polyol ester), the effective thermal conductivities of the nanocomposites (nanogreases) have increased by about 60–70%. Also, it is possible to theoretically predict the effective thermal conductivity k_e of greases using the Fricke equation (Equation 19.2) or the

Table 19.5 *Characterization of selected four types of nanocomposites (carbon nanotube greases)*

Sample Number	9-1	9-2	9-3	9-4
Experimental Thermal Conductivity (TC, W mK^{-1})	0.26	0.27	0.25	0.27
Theoretical TC (by Fricke equation)	0.98	0.97	0.41	0.40
Theoretical TC (by Hamilton-Crosser equation)	0.33	0.33	0.52	0.50
Electrical Resistivity (Ωcm)	3000	3500	2000	4000
Viscosity @ 40 °C (cSt)	142.00	142.00	151.00	151.00
Penetration, 1/4 scale, ASTM D1403:				
Unworked (mm)	286	270	278	292
Worked/60 (mm)	285	269	279	292
Worked/100 000 (mm)	290	297	308	ND
Dropping Point (°C, ASTM D2265)	>271	>271	>271	>271
Oil Separation (wt%, FTM 321.3):				
24 hr, 100 °C	3.56	0.79	4.22	ND
24 hr, 150 °C	5.06	2.81	4.37	ND
24 hr, 177 °C	5.93	4.42	5.23	ND
Copper Corrosion, ASTM D4048:				
24 hr, 100 °C	1B	1B	1B	1B
24 hr, 177 °C	1B	1B	1B	1B

Note: ND: not determined.

Hamilton–Crosser equation (Equation 19.3), knowing the base fluid thermal conductivity k_m and the carbon nanotube thermal conductivity k_p :Fricke equation [31,32]

$$k_e = k_m + \frac{1}{3} v_p \sum_{i=a,b,c} \frac{k_p - k_m}{k_m + d_{pi}(k_p - k_m)} k_m \tag{19.2}$$

where the depolarization factor $d_{pi}((i = a, b, c)$ is defined by

$$d_{pi} = \frac{abc}{2} \int_0^\infty \frac{1}{(i^2 + w)\sqrt{(a^2 + w)(b^2 + w)(c^2 + w)}} \mathrm{d}w$$

which satisfies

$$d_{pa} + d_{pb} + d_{pc} = 1$$

Hamilton–Crosser equation [33]

$$k_e = k_m + 3\Psi^{-1} v_p \frac{k_p - k_m}{(3\Psi^{-1} - 1)k_m + k_p - v_p(k_p - k_m)} k_m \tag{19.3}$$

where the sphericity Ψ is the ratio of the surface area of a sphere to that of a particle having the same volume. Parameters used in the calculations are $k_m = 0.17$ W mK^{-1}, $k_p = 2000$ W mK^{-1}, $a = 1750$ nm, $b = 0.7$ nm and $c = 0.7$ nm.

The calculated TC is also listed in Table 19.5. The less than calculated thermal conductivity value demonstrates the existence of thermal contact resistance and lack of efficient nanotube–nanotube physical contacts in the greases [34,35].

There are several factors that are very crucial to the thermal performance of the nanocomposites (nanogreases), including the stability of the suspension, the size distribution of the nanotubes/particles, the agglomerations of the nanotubes/particles, and the interface between the nanotubes/particles and oil in the suspension [36].

Figure 19.9 shows the thermal conductivity vs. nanofiller (nanotube) weight concentration in the polymeric oil (polyalphaolefin oil). It is clearly seen that thermal conductivity increases with increasing nanotube concentration. The curve tends to saturate at high concentrations (>10 wt%).

Electrical conductivities of the four nanocomposites (greases) were measured by volume resistivity test cells. All the samples showed volume resistance of around 2000–4000 Ω cm. Usually, any materials with less than 10 000 Ω cm are considered to be electrical conductors. The results indicate that these nanocomposites (nanogreases) are electrically conductive, compared to the insulating polymeric base oils (polyalphaolefin and/or polyol ester) and commercial greases (lithium, calcium, aluminum, and polyurea). However, the conductivity values of the nanocomposites (nanogreases) are not very high. With the development of new nanofiller (carbon nanotube) manufacture techniques, the electrical conductivities of pristine carbon nanotubes are expected to enhance dramatically [8], which could have a significant impact on the electrical conductivity of the nanocomposite (grease). Also, aligning nanofillers (nanotubes) or adding additives such as Ag could significantly increase the electrical conductivity of the grease [37].

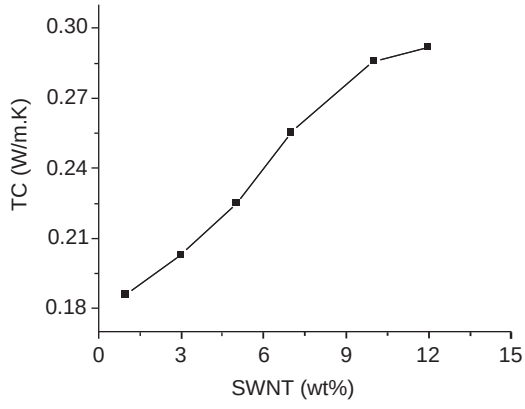

Figure 19.9 *Thermal conductivity vs. nanofiller (nanotube) weight concentration in the polymeric oil (polyalphaolefin oil). (Reproduced with kind permission from NLGI. Copyright (2010) NLGI)*

Table 19.6 *Thermal conductivities of grease, water, and water/grease mixtures*

Sample Number	Measured TC (W/mK)	Calculated TC by ideal mixture (W/mK)
Sample 9-2 grease	0.27	
Water	0.60	
20 wt% water/80 wt% grease	0.30	0.33
33 wt% water/67 wt% grease	0.33	0.37

Another interesting phenomenon is that the homogeneous nanocomposites (greases) can be made when water is added. Actually, adding water to grease is a physical mixing process during which water is packed into the grease. Table 19.6 lists the thermal conductivities of the grease, water, and water/grease mixtures. It is clearly seen that the effective thermal conductivities have been significantly increased when water is added, due to the higher thermal conductivity of water (0.60 W mK^{-1}). The measured thermal conductivity data are very close to the calculated values for an ideal mixture, indicating that water is packed very well within the grease structures.

It seems that no currently established theory or model can well explain the above interesting results as presented for the carbon nanotube greases. Additional efforts are needed to better understand the fundamental science in this new emerging and promising field of nanotechnology.

19.3.2 Rheological Investigation of Nanocomposite (Nanotube Grease)

19.3.2.1 Stress Ramp Test

Figure 19.10 illustrates the viscosity as a function of shear stress of the 5, 7, and 10 wt% CNT greases, and the data for the 12 wt% CNT grease is shown in Figure 19.11. As can be

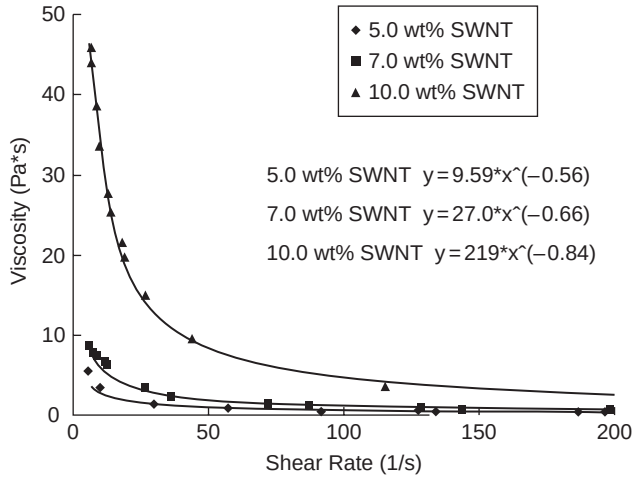

Figure 19.10 *Stress ramp test for three CNT greases. The 5.0 wt% SWNT CNT grease was subjected to a stress range of 80–300 Pa, while the 7.0 wt% SWNT CNT grease was subjected to a stress range of 50–500 Pa, and the 10 wt% SWNT CNT grease was subjected to a stress range of 300–800 Pa. (Reproduced with kind permission from NLGI. Copyright (2010) NLGI)*

seen in Figures 19.10 and 19.11, each CNT grease sample exhibits shear thinning behavior over the entire shear stress range. It also shows that the response of each CNT grease closely follows the power law (or Ostwald) rheological model, as expressed in Equation 19.4 [16].

$$\eta = k\gamma^{n-1} \tag{19.4}$$

where: η = viscosity; k = consistency coefficient; γ = shear rate; n = power law index.

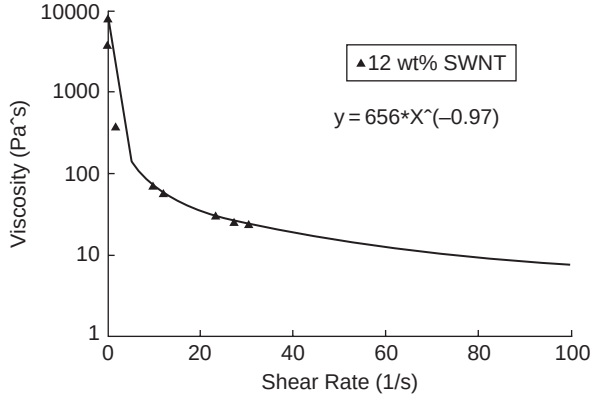

Figure 19.11 *Stress ramp test for CNT-grease containing 12.0 wt% SWNT. The grease was subjected to a stress range of 700–850 Pa. (Reproduced with kind permission from NLGI. Copyright (2010) NLGI)*

Table 19.7 *Consistency coefficient and power law index for each CNT-grease sample*

Sample	Consistency (k)	Index (n)
5.0 wt% SWNT	9.59	0.44
7.0 wt% SWNT	27.0	0.34
10.0 wt% SWNT	219	0.16
12.0 wt% SWNT	656	0.03

Table 19.7 shows the consistency coefficient and power law index for each CNT grease. The power law index allows one to obtain the degree of shear thinning that the sample exhibits. The closer n is to zero, the higher the severity of shear thinning. As seen in Table 19.7, the consistency and shear thinning behavior increases with increasing concentration.

The interactions between the nanoparticles have a profound effect on the viscosity of the system. At low concentrations, each individual nanoparticle is free to rotate in three different planes, which allows the surrounding medium to easily move around the nanoparticles under a shear stress. In more concentrated systems, like the CNT greases, the nanoparticles aggregate, due to intermolecular attractive forces (Van der Waal forces). This aggregation limits the suspended nanoparticle's motion to a single plane, about its axis of symmetry, and forms a mechanical lock. Similar interactions have been seen in fiber suspensions [38]. Therefore, increasing particle concentration leads to increasing aggregate size and increases the energy required for the medium to move around the aggregate, which increases the resulting viscosity of the system [39]. This particle interaction explains the significant (exponential) viscosity increase with increasing nanotube loading.

Figure 19.12 shows the dramatic increase in viscosity for increasing concentrations of SWNT. The results also indicate that CNT dispersion in oil is similar to polymer dispersion

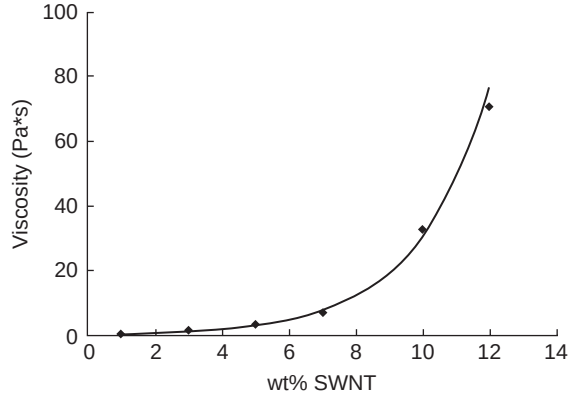

Figure 19.12 *Viscosity vs. SWNT concentration at a fixed shear rate of 10 1 s^{-1}. (Reproduced with kind permission from NLGI. Copyright (2010) NLGI)*

in oils, which suggests the presence of polymer-like entanglements within the suspension. The large aspect ratio of the CNT causes dynamic motion, coils, and entanglements [40–42].

As can be seen in Figure 19.9, small increases in shear stress resulted in dramatic decreases in viscosity. The dramatic shear thinning behavior of the CNT grease suggests the formation of a structural network consisting of entangled nanotubes. This shear thinning phenomenon also suggests the disassembly of the aggregated nanotubes. With increasing shear stress, the energy introduced into the system is significant enough to overcome the intermolecular and mechanical forces holding the aggregates together. This increasing energy breaks the aggregated particles into smaller aggregates and causes the orientations of the nanotubes to be directed in the direction of shear flow. Due to the large aspect ratio of the CNTs, their orientation in the direction of shear drastically reduces the viscosity of the suspension. Work conducted by Yang, *et al.* showed the same shear thinning response in relatively low concentrations of MWNT in polyalphaolefin oil [10,11].

19.3.2.2 Yield Stress Test

Figure 19.13 shows the yield stress of the CNT grease: (A) 5.0 wt% SWNT, (B) 7.0 wt% SWNT, (C) 10.0 wt% SWNT, and (D) 12 wt% SWNT, while Table 19.8 lists the peak yield stress for each sample. The peak yield stress in these experiments is defined as the stress at which the sample's instantaneous viscosity rapidly decreases from an increasing or constant value.

The results from the yield stress tests further support the assumption of a network structure in the grease. As can be seen in Figure 19.13, a sharp increase in viscosity is seen with low stresses. This likely corresponds to nanotube aggregation in the grease structure upon the onset of motion. The aggregation continues to lead the increase of viscosity, until enough shear stress is present to break up these aggregates and the viscosity

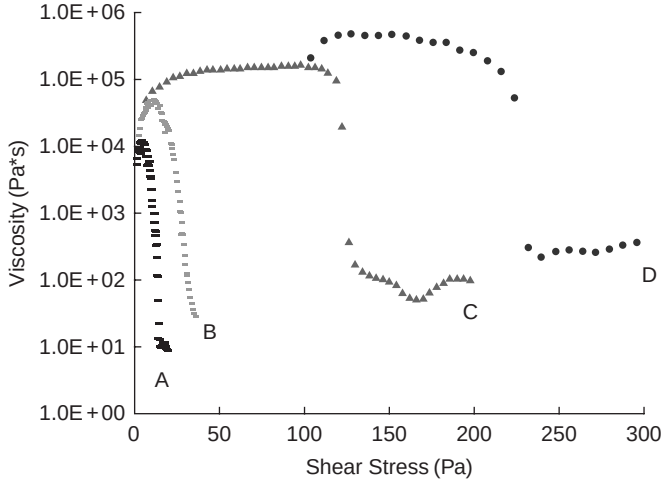

Figure 19.13 *Yield test for CNT-grease: (A) 5.0 wt% SWNT, (B) 7.0 wt% SWNT, (C) 10.0 wt% SWNT, and (D) 12 wt% SWNT. (Reproduced with kind permission from NLGI. Copyright (2010) NLGI)*

Table 19.8 *Experimental yield stress*

Sample	Yield Stress (Pa)
5.0 wt% SWNT	4.6
7.0 wt% SWNT	10.2
10.0 wt% SWNT	98.5
12.0 wt% SWNT	152.0

starts to decrease. This shear stress value is defined as the peak yield stress. The fact that the viscosity gradually decreases suggests that the large aggregates are not totally dismembered immediately, but rather the numbers of particle entanglements are continually reduced as shear stress increases [43].

Similarly to the shear stress ramp tests, the yield stress tests produced results which suggest particle–particle interactions in the grease structure. The yield results are also similar to that of polymer suspensions [38].

19.3.3 Nanocomposites (Nanotube Greases) with Magnetically Sensitive Nanoparticles

Figure 19.14 shows several materials: (A) Fe_2O_3 nanoparticles, (B) nanocomposite (grease) made from 10 wt% SWNT and 10 wt% Fe_2O_3, and (C) nanocomposite (grease) made from 10 wt% SWNT. Although the color of Fe_2O_3 nanoparticles is brown, the color of nanocomposite (grease) made from 10 wt% SWNT and 10 wt% Fe_2O_3 remains black. It indicates that Fe_2O_3 particles disperse well in the grease structure; otherwise, the brownish color would appear.

Figure 19.14 *Picture of several materials: (A) Fe_2O_3 nanoparticles; (B) grease made from 10 wt% SWNTs and 10 wt% Fe_2O_3; and (C) grease made from 10 wt% SWNTs. (Reproduced with kind permission from NLGI. Copyright (2010) NLGI)*

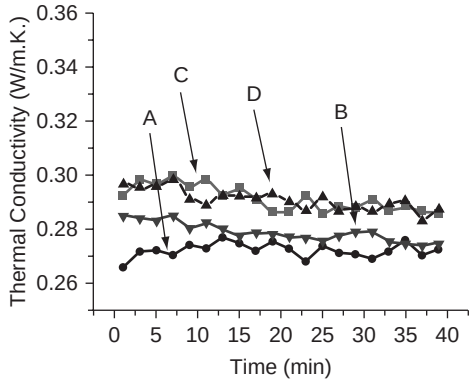

Figure 19.15 *Thermal conductivity vs. time for nanocomposite (grease) with 10 wt% SWNT and different Fe_2O_3 loading concentrations under a magnetic field (0.62 kG): (A) 0 wt%; (B) 5 wt%; (C) 10 wt%; and (D) 20 wt%. (Reproduced with kind permission from NLGI. Copyright (2010) NLGI)*

Figure 19.15 shows the thermal conductivity vs. time for nanocomposite (grease) with 10 wt% SWNT and different Fe_2O_3 loading concentrations under magnetic field (0.62 kG). Unlike the heattransfer nanofluids containing SWNT and Fe_2O_3 particles, which show significant enhancement of TC initially [12–15], it is clearly seen that the four curves are all straight within the experimental error, indicating that TC values are independent of time.

A possible explanation for the above results is the existence of three-dimensional networks formed by Van der Waals forces in the nanocomposite (carbon nanotube grease) structure. The network structures increase the thermal and electrical conductivities; consistent with high dropping points and good temperature resistance. Since the CNTs are already tangled and have reasonably good contacts with each other, they are not going to move much in the presence of an applied magnetic field. Therefore, even under a strong external magnetic field, there is no obvious TC enhancement observed within 40 minutes, or even longer [34].

Since the viscosity of the nanocomposite (grease) is high, the magnetic force may not be enough to move the CNTs right away, which is another possibility for not observing TC enhancement. In order to exclude this possibility, we have measured grease samples with 10 wt% SWNT and 20wt% Fe_2O_3 for 24 hours. The TC data did not change.

Figure 19.15 also shows that with increasing Fe_2O_3 loading concentration from 0 to 10 wt%, the TC value increases from 0.26 W mK^{-1} to 0.30 W mK^{-1} (an increase of around 15%). This may be due to the accumulation of Fe_2O_3 particles themselves. It is well known that Fe_2O_3 also has a high TC value (hundreds of W mK^{-1}). Higher concentrations of Fe_2O_3 increases the chance of particles contacting each other, hence the enhanced TC is observed. It is still unknown why the TC value is saturated at high Fe_2O_3 particle concentrations. In Figure 19.15, the difference in TC value for 10 wt% and 20 wt% Fe_2O_3 concentrations is negligible.

Figure 19.16 shows the results of thermal conductivity measurements taken in various magnetic fields for nanocomposite (grease) with 10 wt% SWNT and different Fe_2O_3

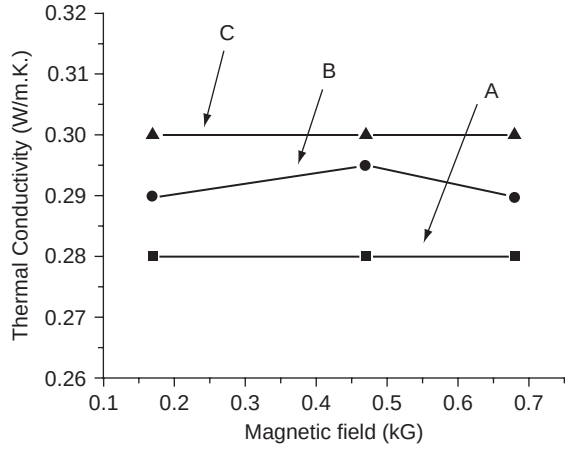

Figure 19.16 *Thermal conductivity vs. different magnetic field strengths for grease with 10 wt% SWNTs and different Fe_2O_3 loading concentrations: (A) 5 wt%; (B) 10 wt%; and (C) 20 wt%. (Reproduced with kind permission from NLGI. Copyright (2010) NLGI)*

loading concentrations. For all three samples, the TC values remain identical under the different magnetic fields (0.68 kG, 0.47 kG, and 0.17 kG). Of course, the TC increases with increasing Fe_2O_3 concentration in every specified magnetic field.

The quantitative data correlating the distance between the two magnets, the magnetic field, the TC average value with 10 wt% SWNT, and the different Fe_2O_3 loading concentrations (1 wt%, 5 wt%, 10 wt%, and 20 wt%) are listed in Table 19.9.

Also, the quantitative data correlating the distance between the two magnets, the magnetic field, the TC average value with 20 wt% MWNT and different the Fe_2O_3 loading concentrations (1 wt%, 5 wt%, and 10 wt%) are listed in Table 19.10. The two tables show the same trend.

After completely evaluating and testing greases containing carbon nanotubes and magnetically sensitive Fe_2O_3, it will be very interesting to study nanocomposites (greases) containing just singlewall nanotubes with a magnetically sensitive nickel layer coating. However, several initial attempts failed and it seems very difficult for Ni-coated nanotubes

Table 19.9 *TC values in different magnetic fields with 10 wt% single wall nanotube and different weight percentage Fe_2O_3*

Distance between two magnets (mm)	Magnetic Field (kG)	TC average value with different Fe_2O_3 concentrations (W mK^{-1})			
		1 wt%	5 wt%	10 wt%	20 wt%
46	0.68	0.26	0.28	0.29	0.30
85	0.47	N/A	0.28	0.30	0.30
182	0.17	N/A	0.28	0.29	0.30

Table 19.10 *TC values in different magnetic fields with 20 wt% multiwall nanotube and different weight percentage Fe_2O_3*

Distance between two magnets (mm)	Magnetic field (kG)	TC average value with different Fe_2O_3 concentrations (W/m.K.)			
		1 wt%	5 wt%	10 wt%	20 wt%
46	0.68	N/A	N/A	0.28	N/A
85	0.47	0.26	0.27	0.28	N/A
182	0.17	N/A	N/A	0.27	N/A

to form a grease in Durasyn 166 oil, even with the total Ni-coated SWNT concentration taken up to roughly 16.5 wt%. The results show that the Ni-coated SWNTs did not have the same thickening effect as previously seen with as pristine SWNTs. In the latter case, the grease could be formed at 7–8 wt% nanotubes. A possible explanation is that Ni coating changes the nanotube surface energy and configuration. Therefore, pristine nanotubes were mixed with Ni coated nanotubes in order to make suitable quality grease.

Previously grease containing only pristine nanotubes could be mixed using a hotplate with a magnetic stir bar. The nanocomposite (nanogrease) containing Ni-coated SWNTs and pristine nanotubes had to be manually stirred and mixed, due to the Ni-coated nanotubes attraction to the magnetic stir bar. The average thermal conductivity (TC) for this grease was found to be 0.27 W mK^{-1}, which is close to the TC value for grease containing only 10 wt% pristine SWNTs. The similarity in TC between the sample containing only 10 wt% pristine SWNT and this new sample containing a combined total weight percent of Ni-coated SWNTs and pristine SWNTs of roughly 21 wt% can be explained by the following. Firstly, the volume-to-weight ratios of Ni-coated SWNTs and pristine SWNTs vary greatly. The Ni-coated nanotubes have a much lower volume-to-weight ratio, and therefore, there is a very large drop in the total number of individual nanotubes in the Ni-Coated SWNTs in comparison to as-produced SWNTs at the same total weight. Secondly, Ni has a much lower TC than CNTs, and therefore, the transfer of heat from one nanotube to the next could be severely hindered by this coating. Lastly, in order to produce the Ni coating on the CNTs, the surface must first be modified, which could lead to partially damaged or broken CNTs, which, again, would lower the heat transfer rate.

Various magnetic fields were also used with the Ni-coated SWNT grease to see if the magnetic field had any effect on the thermal conductivity. This time, the sample was placed into magnetic field strengths of 0.64 kG, 0.90 kG, and 1.12 kG, for nearly 11 hours, while conducting scheduled TC measurements, which showed no noticeable change in the TC, as shown in Figure 19.17 below.

The sample was then placed in a magnetic field with a strength of 1.76 kG for 24 hours, with the same results, as shown in Figure 19.18.

Even after being exposed to a magnetic field (1.46 kG) for more than 72 hours, there was no apparent TC change in the sample. The combined results for all of the thermal conductivity measurements of the grease containing the Ni-coated carbon nanotubes can be found in Table 19.11.

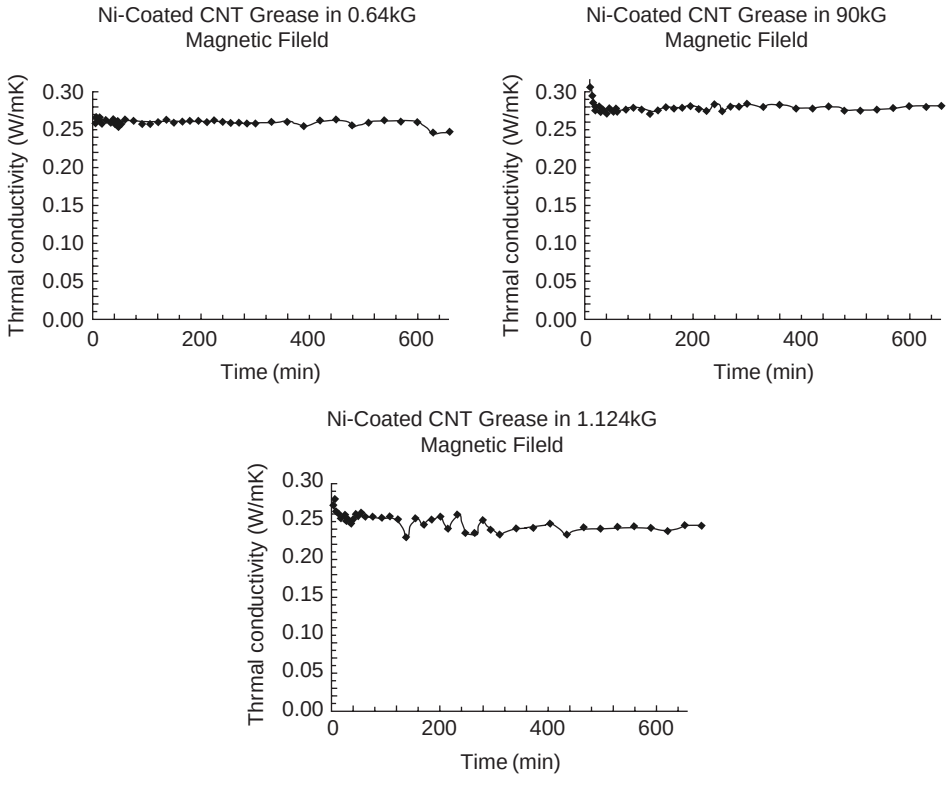

Figure 19.17 *The thermal conductivity results for Ni-coated SWNT nanogrease in multiple magnetic fields for 11 hours: (a) 0.64 kG; (b) 0.90 kG; and (c) 1.12 kG. (Reproduced with kind permission from NLGI. Copyright (2010) NLGI)*

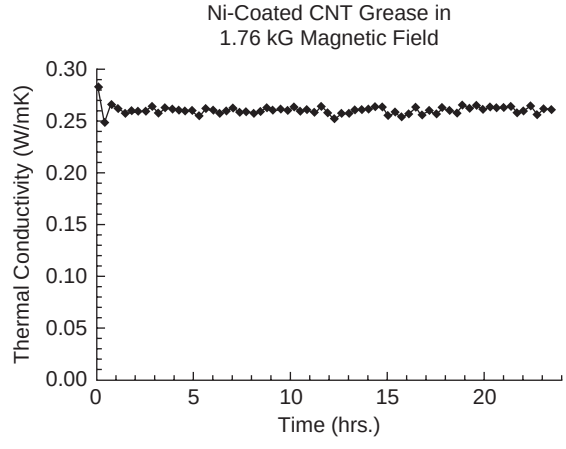

Figure 19.18 *Thermal conductivity results for Ni-coated SWNT nanogrease in a 1.76 kG magnetic field for 24 hours. (Reproduced with kind permission from NLGI. Copyright (2010) NLGI)*

Table 19.11 *Average thermal conductivity of the Ni-coated SWNT nanogrease in multiple magnetic fields*

Magnetic Field Strength(kG)	Time(hrs)	Average Thermal Conductivity(W/mK)
—	—	0.27
0.64	11	0.26
0.90	11	0.27
1.12	11	0.26
1.76	24	0.26
1.46	72	0.27

As shown in Table 19.11, there were insignificant changes in the TC due to the magnetic field.

19.3.4 Electrical Conductivities of Various Nanofillers (Nanotubes)

In order to better understand and improve the conductivities of nanocomposites (nanotube greases), the electrical conductivities of various fillers (nanotubes) in the solid phase were measured.

Table 19.12 lists five nanofillers (nanotubes) with different functional groups and chemical structures. In order to get uniform sample coating on each sensor, appropriate solvent and concentrations were chosen as follows. Considering the solvent polarities, in which water is 9 and DMF is 6.4, nanofillers (nanotubes) are easy to aggregate in water and DMF, having the highest polarity among the organic solvents. Therefore, we used DMF for all samples. Pristine SWCNTs are not distributed as well as others, even when ultrasonicated for 15 min. Pristine nanotubes are hydrophobic and not functionalized. The functional groups on the SWCNTs help their dispersion the DMF solvent.

Table 19.13 lists the conductivity (resistivity) data of the above five samples with and without voltage applied. We could draw the following conclusions based on the conductivity (resistivity) results. The conductivities of functionalized nanotubes (fluorinated SWNTs and sulfonated SWNTs) are decreased significantly. The alignment effect was observed in sulfonated SWNTs because the material contains the charge inside the

Table 19.12 *Types of nanofillers, concentrations and solvents*

	Type of Nanofiller	Concentration	Solvent Type
1.	*Pristine SWNT*	0.0324%	DMF
2.	*Fluorinated SWNT*	0.0364%	DMF
3.	*COOH SWNT (school of mines)*	0.0363%	DMF
4.	*COOH SWNT (outside campus)*	0.0365%	DMF
5.	*Sulfonated SWNT*	0.0366%	DMF

Figure 19.19 *Pictures of five nanofiller (nanotube) solutions with different functional groups and chemical structures. (Reproduced with kind permission from NLGI. Copyright (2010) NLGI)*

molecule. It seems that COOH SWNTs show good conductivity, probably due to partial oxidization by acid [44].

It seems that the pristine nanotube results are somewhat controversial. The alignment effect is observed with the pristine nanotubes, however, it shouldn't be observed. We are collecting more samples, such as purified nanotubes, Ni-coated nanotubes, strong-acid-treated nanotubes, which will be tested at NASA Ames Research Center. It is expected that with more samples, we will better understand the relationship between conductivity and structure.

Table 19.13 *Conductivity (resistivity) data of the above five samples with and without voltage applied*

Sensor chip	Coating sample	Agilent 34401 DMM	Keithley 2002 DMM
GSFP-05_S2	Pristine SWNT	256 kΩ	270 kΩ
GSFP-05_S4	Pristine SWNT*	29.9 Ω	29.9 Ω
GSFP-08_S2	Fluorinated SWNT	41.2 kΩ	40.5 kΩ
GSFP-08_S4	Fluorinated SWNT*	39.1 kΩ	39.2 kΩ
GSFP-09_S2	COOH SWNT(S3)	12.0 Ω	12.0 Ω
GSFP-09_S4	COOH SWNT(S3)*	16.1 Ω	16.2 Ω
GSFP-15_S2	COOH SWNT(S4)	18.5 Ω	18.2 Ω
GSFP-15_S4	COOH SWNT(S4)*	17.8 Ω	17.8 Ω
GSFP-14_S2	Sulfonated SWNT	5.34 kΩ	5.29 kΩ
GSFP-14_S4	Sulfonated SWNT*	25.6 Ω	25.7 Ω

An electric field of 3V across the fingers with a gap size of 12mm was applied while the SWCNT samples were being coated on the IDE. Instrument used for the resistance measurement: Keithley2002 digital multimeter and Agilent 34401 DMM.

19.4 Conclusion

In summary, homogeneous and stable nanocomposites (nanogreases) based on nanofillers (carbon nanotubes) and polymers (polyalphaolefin oils, DURASYN® 166) have been produced. Characterization results indicate that these types of nanocomposites (greases) have high dropping temperatures (>271 °C) and very low oil-leaking percentages, even at high temperatures. Also these nanocomposites are not aggressive to copper at temperatures up to 177 °C. In this way, nanotube fillers distinguish themselves from more common graphitic materials that for many years have been commonly used as solid grease additives.

Rheological research has shown that the nanocomposites (nanogreases) exhibit pseudoplastic behavior, which has a typical power law response and a definable yield stress. It provides convincing evidence that a metastable network structure is formed inside the nanocomposite with high nanofiller (nanotube) concentrations.

The use of nanofillers (carbon nanotubes) as a thickening agent in polyalphaolefin oils to create nanocomposites (nanogreases) has significant merit. Given the abnormally high thermal and electrical conductivities of carbon nanotubes, it is conceivable that nanocomposites could exhibit excellent thermal and electrical conductivities. The rheological response of these nanocomposites is important for two reasons: to determine if the composite will have sufficient lubricating properties; and to provide critical information on the structure and particle–particle interactions of nanotube suspensions. The knowledge gained concerning the structure of nanotube suspensions will allow their manipulation to achieve better physical properties.

Time-dependent magnetic experiments were performed using nanocomposites (greases) with different concentrations of Fe_2O_3 nanoparticles or Ni-coated carbon nanotubes. The results demonstrated that, even under the influence of a strong applied magnetic field and the addition of magnetically sensitive materials, the TC value remains constant. A possible explanation for these results is that the nanofillers (carbon nanotubes) become associated with each other through Van der Waals forces in the composite structure to form three-dimensional networks, which make magnetic alignment of the nanotubes extremely difficult or impossible.

The results of electrical conductivities indicate that the conductivities of functionalized fillers (fluorinated SWNTs and sulfonated SWNT)s decrease significantly. The alignment effect has been observed in sulfonated SWNT filler because the material contains the charge inside the molecule.

Although there are many unknown or uncertain factors related to the fundamental nature of nanocomposites (nanotube greases), the increased electrical and thermal conductivities by addition of nanofillers strongly indicate that these nanotube greases could replace the current commercial greases (lithium, calcium, aluminum, and polyurea) and have a promising future in commercial applications.

Acknowledgments

H. Hong would like to thank the US Army Research Lab (Cooperative agreement DAAD19-02-2-0011) for financial support, Professor Sungho Jin of University of

California, San Diego for comments regarding the magnetic results, Dr. Wenhua Yu of Argonne National Lab for his simulation and modeling, Andy Waynick of NCH for the initial grease samples, and Jesse Wensel and Brian Wright for the thermal conductivity measurements of some grease samples.

References

[1] S. Iijima, Helical microtubules of graphitic carbon, *Nature*, **354**, 56–58 (1991).
[2] J. Liu, A.G. Rinzler, H.J. Dai, J.H. Hafner, R.K. Bradley, P.J. Boul, A. Lu, T. Iverson, K. Shelimov, C.B. Huffman, F. Rodriguez-Macias, Y.S. Shon, T.R. Lee, D.T. Colbert, and R.E. Smalley, Fullerene pipes, *Science*, **280**, 1253–1256 (1998).
[3] C.B. Huffman, V.C. Moore, M.S. Strano, E.H. Haroz, K.L. Rialon, P.J. Boul, W.H. Noon, C. Kittrell, J.P. Ma, R.H. Hauge, R.B. Weisman, and R.E. Smalley, Band gap fluorescence from individual single-walled carbon nanotubes, *Science*, **297**, 593–596 (2002).
[4] S. Berber, Y.K. Kwon, and D. Tománek, Unusually high thermal conductivity of carbon nanotubes, *Phys. Rev. Lett.* **84**, 4613–4616 (2000).
[5] P.G. Collins and P. Avouris, Nanotubes for electronics, *Sci. Amer.*, **283**, 62 (2000).
[6] T.W. Ebbesen, H.J. Lezec, H. Hiura, J.W. Bennett, H.F. Ghaemi, and T. Thio, Electrical conductivity of individual carbon nanotubes, *Nature*, **382**, 54–56 (1996).
[7] Y. Xie, J. Liu, and Y. Zhu, US Patent application pending US 2006/0245996 A1
[8] South West Nano Technologies (SWeNT®), Nano News Letter, April 1, 2009.
[9] Y. Yang, E. Grulke, Z. George Zhang, and G. Wu., Thermal and rheological properties of carbon nanotube-in-oil dispersions, *J. Appl. Phys.*, **99**, 114307 (2006).
[10] Y. Yang, E. A. Grulke, Z. G. Zhang, and G. Wu, Rheological behavior of carbon nanotube and graphite nanoparticle dispersions, *J. Nanosci. Nanotech.*, **5**, 571–579 (2005).
[11] Y. Yang, E. A. Grulke, Z. G. Zhang, and G. Wu, Temperature effects on the rheological properties of carbon nanotube-in-oil dispersions, *Colloids Surf. A*, **298**, 216–224 (2007).
[12] J. Philip, P.D. Shima, and B. Raj, Nanofluid with tunable thermal properties, *Appl. Phys. Lett.*, **92**, 043108 (2008).
[13] J. Philip, J.M Laskar, and B. Raj, Magnetic field induced extinction of light in a suspension of Fe_3O_4 nanoparticles, *Appl. Phy.s Lett.*, **92**, 221911 (2008).
[14] B. Wright, D. Thomas, H. Hong, L. Groven, J. Puszynski, E. Duke, X. Ye, and S. Jin, Magnetic field enhanced thermal conductivity in heat transfer nanofluids containing Ni coated single wall carbon nanotubes, *Appl. Phy.s Lett.*, **91**, 173116 (2007).
[15] H. Hong, B. Wright, J. Wensel, S. Jin, X. Ye, and W. Roy, Enhanced thermal conductivity by the magnetic field in heat transfer nanofluids containing carbon nanotube, *Synth. Met.*, **157**, 437 (2007).
[16] C.W. Macosko, *Rheology: Principles, Measurements and Applications*, John Wiley & Sons. Inc. New York, 1994, 425–514.
[17] H. Brenner, Rheology of a dilute suspension of axisymmetric Brownian particles, *Int. J. Multiphase Flow*, **1**, 195 (1974).
[18] H.L. Goldsmith and S.G. Mason, *Rheology*, **Vol. 4**, ed. F.R. Eirich, Pergamon, New York, 1967.
[19] M. Rahnama, D. L. Koch, and E. S. G. Shaqfeh, The effect of hydrodynamic interactions on the orientation distribution in a fiber suspension subject to simple shear flow, *Phys. Fluids*, **7**, 487 (1995).
[20] M.S. P. Shaffer and A.H. Windle, Analogies between polymer solutions and carbon nanotube dispersions, *Macromolecules*, **32**, 6864 (1999).
[21] V.A. Davis, L.M. Ericson, A.N.G. Parra-Vasquez, H. Fan, Y. Wang, V. Prieto, J.A. Longoria, S. Ramesh, R.K. Saini, C. Kittrell, W.E. Billups, W.W. Adams, R.H. Hauge, R.E. Smalley, and M. Pasquali, Viscoelasticity of single wall carbon nanotube suspensions, *Macromolecules*, **37**, 154 (2004).

[22] E.K. Hobbie and D.J. Fry, Rheology of concentrated carbon nanotube suspensions, *J. Chem. Phys.*, **126**, 124907 (2007).
[23] S. Lin-Gibson, J.A. Pathak, E.A. Grulke, H. Wang, and E.K. Hobbie, Elastic flow instability in nanotube suspensions, *Phys. Rev. Lett.*, **92**, 4 (2004).
[24] A. Waynick, South West Research Institute Report, No. 08-10813 (2006).
[25] A. Waynick, South West Research Institute Report, No. 08-12518 (2007).
[26] See www.hotdisk.se for detailed information.
[27] See www.electrotechsystems.com for detailed information.
[28] J. Li, Y. Lu, Q. Ye, L. Delzeit, and M. Meyyappan, A Gas sensor array using carbon nanotubes and microfabrication technology, *Electrochem. Solid State Lett.*, **8**(11), 100–102 (2005).
[29] H. Hong, A. Waynick, and W. Roy, Heat transfer nanolubricant and nanogrease based on carbon nanotube, *NLGI Spokesman*, **71**(6), 23 (2007).
[30] H. Hong, A. Waynick, W. Yu, P. Smith, and W. Roy, manuscript to be submitted.
[31] H. Fricke, A mathematical treatment of the electric conductivity and capacity of disperse systems, *Phys. Rev.*, **24**, 575–587 (1924).
[32] H. Fricke, The Maxwell–Wagner dispersion in a suspension of ellipsoids, *J. Phys. Chem.* **57**, 934–937 (1953).
[33] R.L. Hamilton and O.K. Crosser, Thermal conductivity of heterogeneous two-component systems, *Indust. Eng. Chem. Fund.*, **1**, 187 (1962).
[34] H. Hong, D. Thomas, M. Horton, Y. Xiangrong, J. Sungho, P. Smith, and W. Roy, Constant magnetic field thermal conductivity in carbon nanotube grease containing magnetic sensitive Fe_2O_3 nano particles, in preparation.
[35] H. Hong, D. Thomas, A. Waynick, Y. Wenhua, P. Smith, W. Roy, Carbon nanotube grease with enhanced thermal and electrical conductivities, *J. Nanopart. Res.*, **12**, 529–535 (2010).
[36] P. Keblinski, J.A. Eastman, and D.G. Cahill, Nanofluids for thermal transport, *Mater. Today*, **8**(6), 36–44 (2005).
[37] F. Du, J. E. Fischer, and K. I. Winey, Effect of nanotube alignment on percolation conductivity in carbon nanotube/polymer composites, *Phys. Rev. B*, **72**, 121404, (2005).
[38] W.W. Graessley, The entanglement concept in polymer rheology, *Adv. Polym. Sci.*, **16**, 1 (1974).
[39] P. Hiemenz and R. Rajagopalan. *Principles of Colloid and Surface Chemistry*, Marcel Dekker, Inc., New York, 1997, 145–187.
[40] M.C. Williams, Stresses in concentrated polymer solutions: Part I. Shear dependence of viscosity, *A.I. Ch. E. J.*, **12**, 1064–1070 (1966).
[41] W.W. Graessley, Viscosity of entangling polydisperse polymers, *J. Chem. Phys.*, **47**, 1942–1953 (1967).
[42] W.W. Graessley, Molecular entanglement theory of flow behavior in amorphous polymers, *J. Chem. Phys.*, **43**, 2696–2703 (1965).
[43] M. Horton, H. Hong, and P. Smith, A rheological investigation of carbon nanotube grease, in preparation.
[44] B.S. Shim, J. Zhu, E. Jan, K. Critchley, S.S. Ho, P. Podsiadlo, K. Sun, and N.A. Kotov, Multiparameter structural optimization of single-walled carbon nanotube composites: toward record strength, stiffness, and toughness, *ACS Nano*, **3**(7), 1711–1722 (2009).

Index

References to figures are given in italic type: reference to tables are given in bold type.

Nanostructured Conductive Polymers Edited by Ali Eftekhari

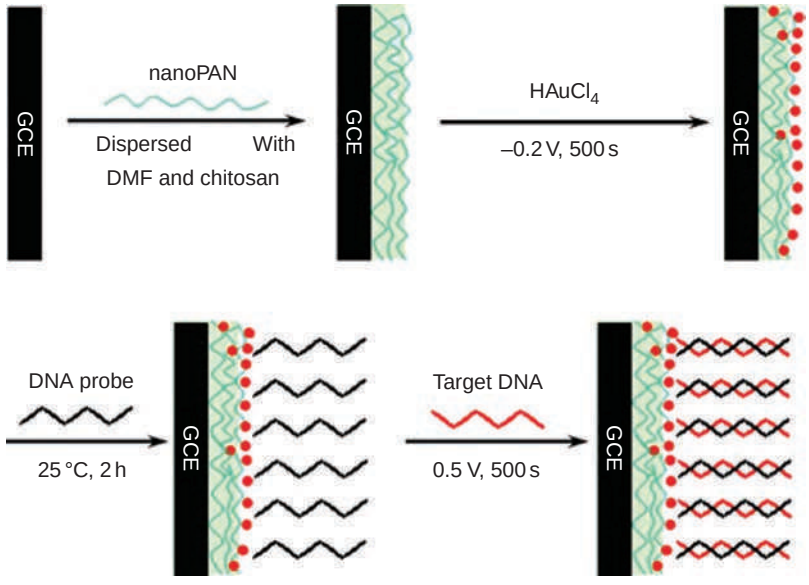

Plate 1 *Schematic diagram of the immobilization and hybridization of DNA on Au/nanoPAN/GCE. (Reprinted with permission from Analytica Chimica Acta, Enhanced Sensitivity for deoxyribonucleic acid electrochemical impedance sensor: Gold nanoparticle/polyaniline nanotube membranes by Y. Feng, T. Yang, W. Zhang, C. Jiang and K. Jiao, 616, 2, 144–151. Copyright (2008) Elsevier Ltd) (See Figure 2.31)*

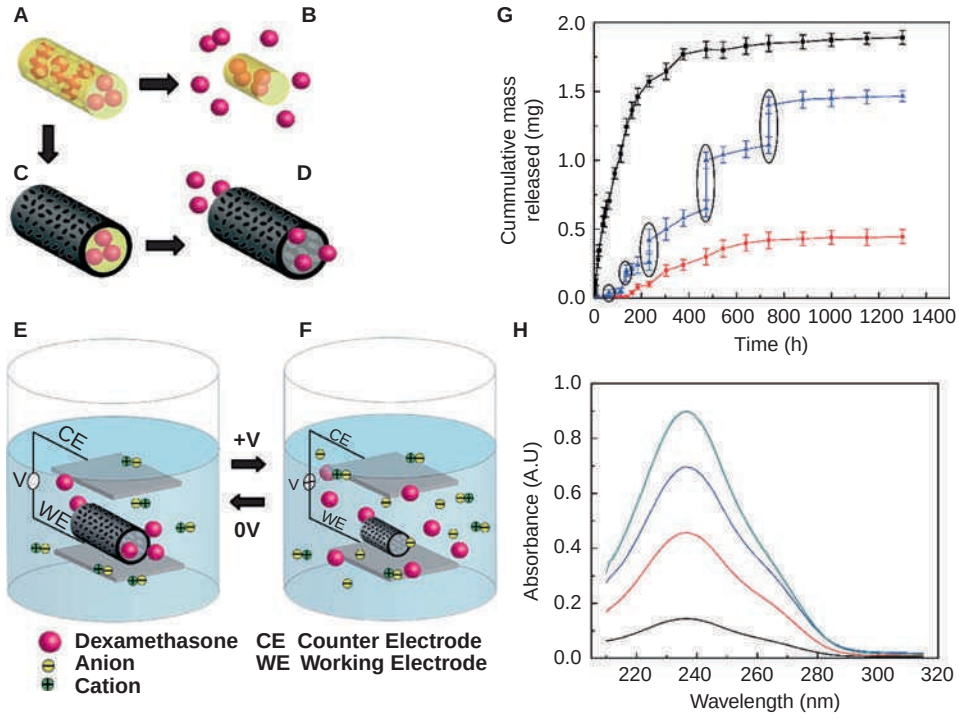

Plate 2 *Schematic illustration of the controlled release of dexamethasone: (A) dexamethasone-loaded electrospun PLGA, (B) hydrolytic degradation of PLGA fibers leading to release of the drug, and (C) electrochemical deposition of PEDOT around the dexamethasone-loaded electrospun PLGA fiber slows down the release of dexamethasone (D). (E) PEDOT nanotubes in a neutral electrical condition. (F) External electrical stimulation controls the release of dexamethasone from the PEDOT nanotubes due to contraction or expansion of the PEDOT. By applying a positive voltage, electrons are injected into the chains and positive charges in the polymer chains are compensated. To maintain overall charge neutrality, counter-ions are expelled towards the solution and the nanotubes contract. This shrinkage causes the drugs to come out of the ends of tubes. (G) Cumulative mass release of dexamethasone from: PLGA nanoscale fibers (black squares), PEDOT-coated PLGA nanoscale fibers (red circles) without electrical stimulation, and PEDOT-coated PLGA nanoscale fibers with electrical stimulation of 1 V applied at the five specific times indicated by the circled data points (blue triangles). (H) UV absorption of dexamethasone-loaded PEDOT nanotubes after 16 h (black), 87 h (red), 160 h (blue), and 730 h (green). The UV spectra of dexamethasone have peaks at a wavelength of 237 nm. Data are shown with a ±standard deviation (*n* = 15 for each case). (Reprinted with permission from Advanced Materials, Conducting-Polymer Nanotubes for Controlled Drug Release by M. R. Abidian, D.-H. Kim and D. C. Martin, 18, 4, 405–409. Copyright (2006) Wiley-VCH) (See Figure 4.19)*

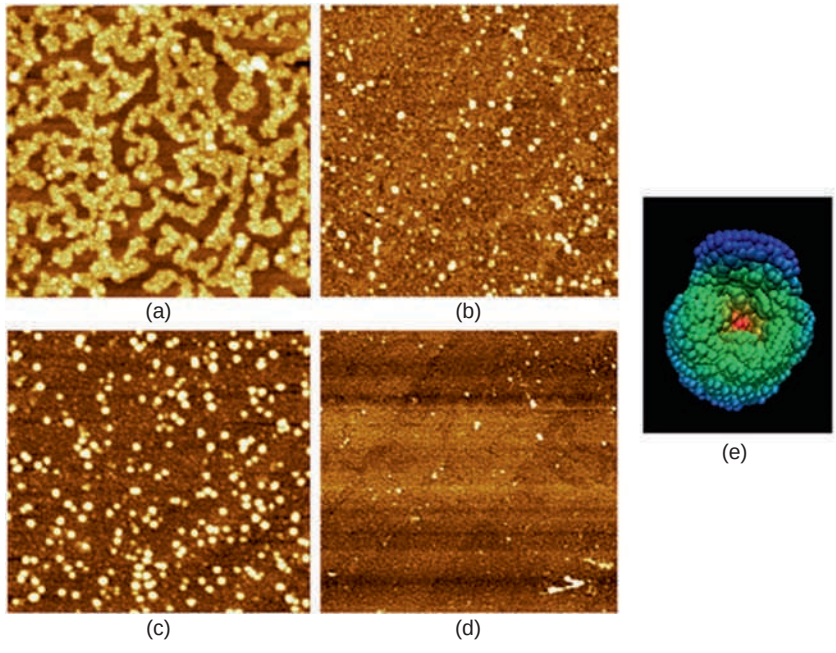

Plate 3 *AFM images (10 × 10 μm) of POEA-EB (pH 10.0) for immersion times of (a) 1s, (b) 3s, (c) 5s, (d) 180s, and (e) average DAM for POEA-EB. (Reprinted with permission from Journal of Colloid and Interface Science, Nanoscale conformational ordering in polyanilines inestigated by SAXS and AFM by F. L. Leite, M. de Oliveira Neto, L. G. Paterno et al., 316, 2. Copyright (2007) Elsevier Ltd) (See Figure 9.5)*

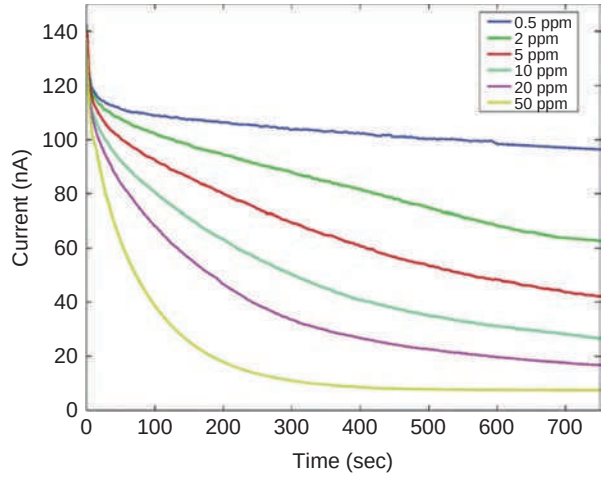

Plate 4 *Measured time-dependent current through an individual CPNW sensor upon exposure to NH_3 gas. The nanowire device being tested was about 335 nm in diameter. (Reprinted with permission from Nano Letters, Polymeric Nanowire Chemical Sensor by H. Liu et al., 4, 4, 671–675. Copyright (2004) American Chemical Society) (See Figure 10.44)*

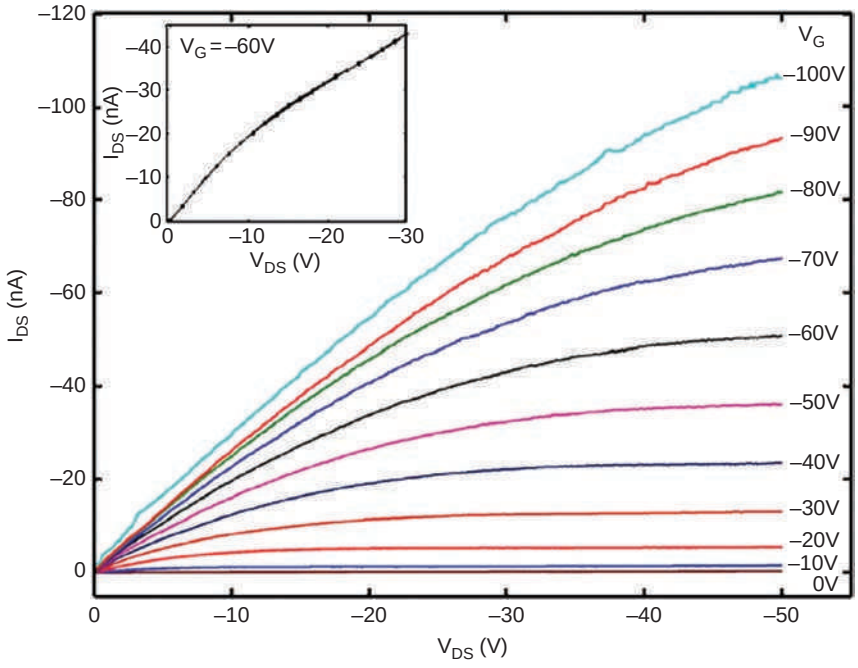

Plate 5 *I_{DS} vs. V_{DS} characteristics of a regio-regular P3HT nanofiber FET, with an effective channel length of 10 μm and diameter of 180 nm, showing accumulation mode operation when a different negative gate bias is applied. Inset: The forward and reverse sweeps exhibit negligible hysteresis of the device. (Reprinted with permission from Applied Physics Letters, Single electrospun regioregular poly(3-hexylthiophene) nanofiber field-effect transistor by H. Liu, C. H. Reccius and H. G. Craighead, 87, 25. Copyright (2005) American Institute of Physics) (See Figure 10.51)*

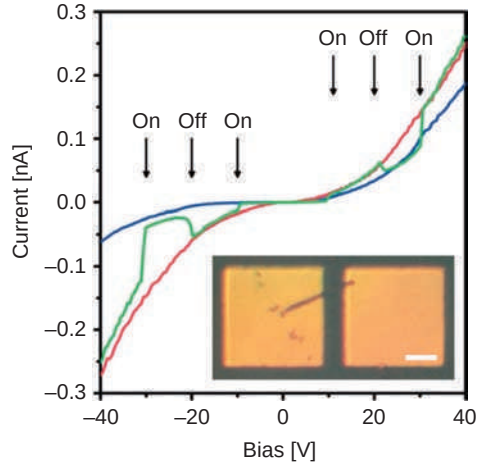

Plate 6 *I–V characteristics of a top-contacted F8T2 nanowire acquired in the dark (blue line) and under 405 nm illumination (red line). Reversible switching in I–V data measured under manually chopped 405 nm illumination is also shown (green line). Inset: optical microscopy image of a typical top-contacted F8T2 nanowire device. Scale bar: 10 μm. (Reprinted with permission from Advanced Materials, A Single Polymer Nanowire Photodetector by G. A. O'Brien, A. J. Quinn, D. A. Tanner and G. Redmond, 18, 18, 2379–2383. Copyright (2006) Wiley-VCH) (See Figure 10.56)*

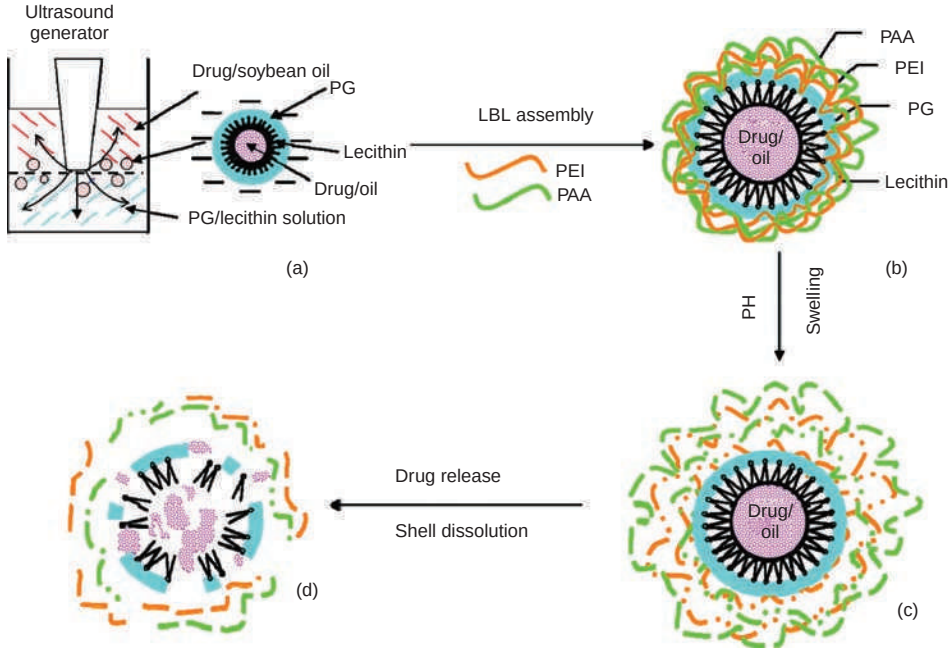

Plate 7 *Schematic illustration of the formation of LBL-synthesized containers and drug release after pH changes (PG, polyglutamate; PEI, polyethyleneimine; PAA, poly(acrylic acid); LBL, layer-by-layer): (a) Formation of oil-loaded polyglutamate containers in an ultrasonic field; (b) LBL assembly of a PEI/PAA shell; (c), (d) swelling and dissolution of the container shell by changing the pH value of the surrounding circumstance. (Reprinted with permission from Langmuir, A Novel Drug Carrier: Lipophilic Drug-Loaded Polyglutamate/Polyelectrolyte Nanocontainers by X. Rong Teng, D.G. Shchukin, and H. Mohwald, 24, 2, 383–389. Copyright (2008) American Chemical Society) (See Figure 11.1)*

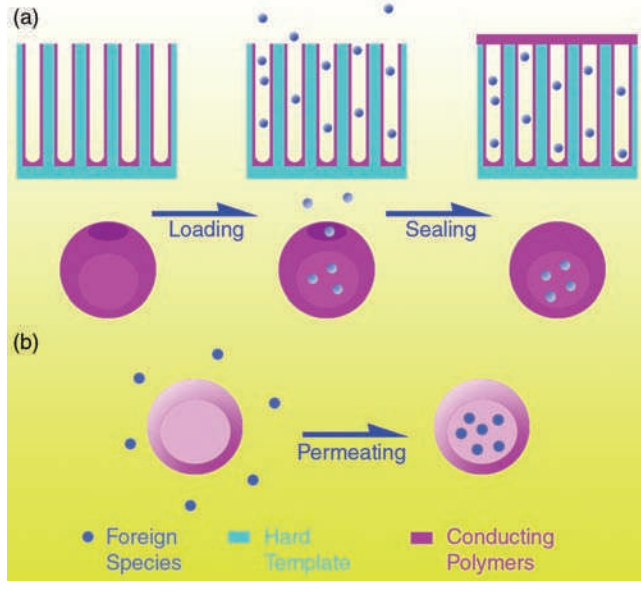

Plate 8 *A schematic illustration of the encapsulation approaches: (a) loading the content after the synthesis process and then sealing the open ends of the CPCs by a further polymerization; (b) entrapping the chemical species by their permeation phenomenon (See Figure 11.12)*

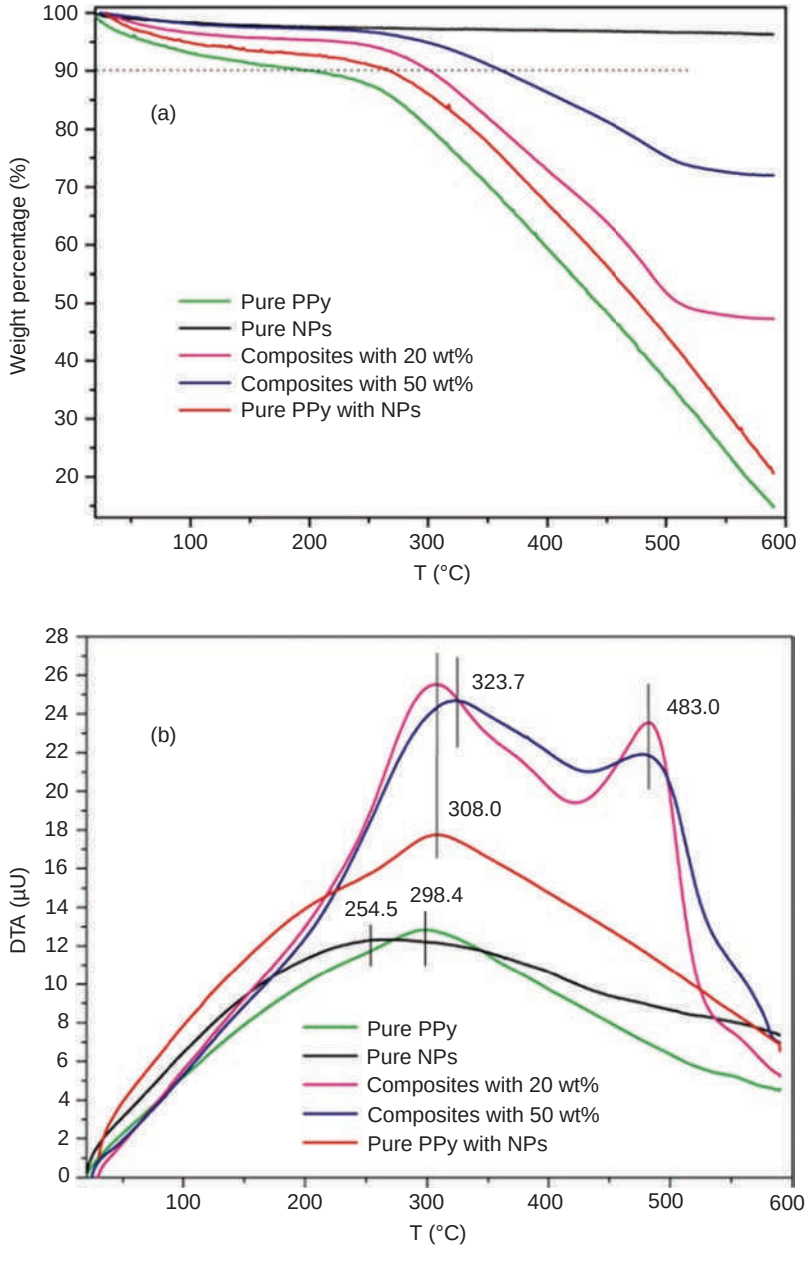

Plate 9 *(Reprinted with permission from Journal of Nanoparticle Research, Fabrication and Characterization of Iron Oxide Nanoparticles Reinforced Polypyrrole Nanocomposites, by Z. Guo, K. Shin, A. B. Karki et al., 11 (6) 1441–1452. Copyright (2009) Springer Science + Business Media (See Figure 12.5)*

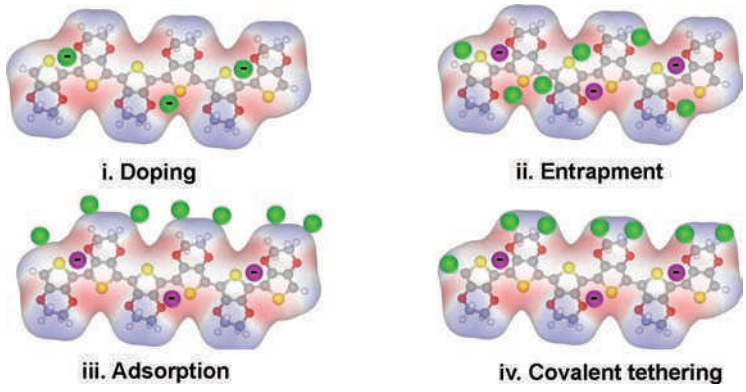

Plate 10 *Schematic of conventional biological modification routes of CPs, shown for poly(3,4-ethylene dioxythiophene). The green molecule represents the biofunctional additive and the negatively charged purple molecule is the dopant anion (See Figure 18.4)*